PROCEEDINGS OF THE

36th POWER SOURCES CONFERENCE

6-9 JUNE 1994

36th Power Sources Conference

Hyatt Cherry Hill
Cherry Hill, New Jersey
June 6-9, 1994

Sponsored by the
Power Sources Division
Electronics & Power Sources Directorate
U.S. Army Research Laboratory

36th Power Sources Conference Organizing Committee

General Conference Chair:
Robert P. Hamlen
U.S. Army Research Laboratory, EPSD
Ft. Monmouth, NJ

Technical Program Chair:
Sol Gilman
U.S Army Research Laboratory, EPSD
Ft. Monmouth. NJ

Information Chair:
Sue McArthur
U.S. Army Research Laboratory, EPSD
Ft. Monmouth, NJ

Conference Coordinator:
Ralph Nadell
Palisades Institute for Research Services, Inc.
New York, NY

Exhibition Manager:
Erika Suresky
Palisades Institute for Research Services, Inc.
New York, NY

Technical Program Committee Members:

James Barnes
Naval Surface Warfare Center
Silver Spring, MD

Wishvender Behl
U.S. Army Research Laboratory, EPSD
Ft. Monmouth, NJ

Harold Christopher
U.S. Army Research Laboratory, EPSD
Ft. Monmouth, NJ

Patrick Davis
Naval Surface Warfare Center
Silver Spring, MD

A. Goldberg
U.S. Army Research Laboratory
Adelphi, MD

Guido Guazzoni
U.S. Army Research Laboratory, EPSD
Ft. Monmouth, NJ

T. Richard Jow
U.S. Army Research Laboratory, EPSD
Ft. Monmouth, NJ

Richard Marsh
Wright Laboratory
Wright-Patterson AFB, OH

Timothy C. Murphy
Naval Surface Warfare Center
Silver Spring, MD

Edward Reiss
U.S. Army Research Laboratory, EPSD
Ft. Monmouth, NJ

Mark Salomon
U.S. Army Research Laboratory, EPSD
Ft. Monmouth, NJ

Patricia H. Smith
Naval Surface Warfare Center
Silver Spring, MD

Martin Sulkes
U.S. Army Research Laboratory, EPSD
Ft. Monmouth, NJ

Ray Sutula
U.S. Department of Energy
Washington, DC

Steve Vukson
Wright Laboratory
Wright-Patterson AFB, OH

Clinton Winchester
Naval Surface Warfare Center
Silver Spring, MD

Table of Contents

Session 1: CAPACITORS

Session 2: PRIMARY AQUEOUS BATTERIES

Table of Contents (Continued)

Table of Contents (Continued)

Table of Contents (Continued)

Table of Contents (Continued)

Session 9: RECHARGEABLE AQUEOUS BATTERIES I

Table of Contents (Continued)

Session 10: LITHIUM / POLYMER BATTERIES

Table of Contents (Continued)

Session 11: RECHARGEABLE AQUEOUS BATTERIES II

Session 12: HIGH-TEMPERATURE / THERMAL BATTERIES

Table of Contents (Continued)

Session 13: PRIMARY LITHIUM BATTERIES I

Table of Contents (Continued)

Session 14: THERMAL BATTERIES

Session 15: PRIMARY LITHIUM BATTERIES II

NOTES

Author Index

PROGRESS WITH ADVANCED MATERIALS FOR HIGH-ENERGY-DENSITY CAPACITORS

Clive W. Reed, Michael W. DeVre, Steven M. Gasworth, and Stefan J. Rzad
GE Corporate Research and Development
Schenectady, New York 12301

Abstract

A program funded by the US Army Electronics and Power Sources Directorate/ Army Research Laboratory, Fort Monmouth, NJ, has been completed in which the objectives were to demonstrate and develop new dielectric materials which will enable the future development of pulse power storage capacitors with energy densities in excess of 10 J/g. Four candidate materials were investigated: diamond-like carbon (DLC) films, chemical vapor-deposited (CVD) diamond films, Ultem® polyetherimide films, and computer-designed modified polyetherimides. Each of these approaches presented unique challenges, but there was a unified technical approach in addressing them: that of synthesis, surface modification, metallization, and clearing to improve their breakdown performance. The status of the work is reported for each approach; with electrical measurements, enhancement of breakdown via surface modification and clearing, and the fabrication and testing of test capacitors. It is concluded that DLC and Ultem® films offer the most immediate promise for meeting the target energy densities.

Introduction

High energy delivery systems, such as high power lasers, high power microwave, directed energy weapons, and power electronics, require large amounts of energy to drive them. In stationary systems, this can be achieved using power supplies of large physical size. But, for mobile devices, the energy sources must be compact. One of the essential parts of the supply is the energy storage device, typically a capacitor or battery. When capacitors are used, a high energy density is a pre-requisite in order to minimize the overall size of the power supply. Capacitors of tens of J/g are highly desirable; however, such energy densities are an order of magnitude higher than present state-of-the-art technology. State-of-the art reviews of high-energy-density capacitors are given in references 1-3.

The program reported here is focused on materials for high-energy density capacitors with 10 kV rating, 1 Hz repetition rate, and energy densities of tens of J/g. Preliminary results on this program were reported at this meeting in 1992[4]. Results at the completion of this two-year program are reported here.

State-of-the-Art

Materials for capacitors typically fall into three general categories: 1) ceramic, such as Ta_2O_5 and $BaTiO_3$; 2) electrolytic, such as alumalytic and tantalytic, and 3) polymeric, such as polypropylene and polyvinylidene fluoride, each with or without an impregnating liquid. Electrolytic capacitors are characterized by large capacitance densities, and high energy densities have been achieved[5]. However, such capacitors do not have good bipolar capability, and their voltage capability and resistivity are too low for high voltage applications such as those of present interest[1]. Ceramics, on the other hand, have high dielectric constants and relatively high breakdown strengths. For example, Ta_2O_5, with a dielectric constant of 27 and a thin film breakdown strength of 4-8 $x10^6$ V/cm^2, has an energy density of 19 J/cm^3. However, the best quality Ta_2O_5 films are those formed electrolytically and they are *not* fully bipolar. Ferromagnetics, such as $BaTiO_3$, have the problem that the dielectric constant changes with the applied electric field and with temperature, with a sharp drop at the Curie temperature[6]. Ceramics have two other severe problems: their inherent brittleness and the great difficulty in making defect-free large areas. The latter problem is compounded by the fact that, unlike polymer materials, ceramics are not "clearable" so that defects cannot be eliminated; this severely limits the electric stresses at which ceramics can be operated, with a consequent limitation in energy density.

There are several, complementary reasons why polymers look to be the most attractive approach for achieving very high energy density. First, they can be made into films in very large areas and with very high quality. (Fortunately, many polymer films have applications outside of capacitors, so considerable development in film making methods are at our disposal). Second, although the polymers themselves typically have low dielectric constants, inherently they have very high resistivities (> 10^{13} Ω.cm) and very high breakdown strengths (> 10^6 V/cm). And, third, very effective methods have been developed for enhancing breakdown performance in metallized polymer films designs: these involve the use of self healing and the use of liquid impregnants. The former is very effective in eliminating defects from the films, while the latter prevents discharges external to the film that might otherwise trigger breakdown at lower levels. These discharges might occur between the layers, at the metallization edges, or at the electrode contact. This combination of qualities, coupled with low dielectric losses and relatively stable dielectric constant over a wide temperature range, make polymer films the preferred choice for many applications.

Technical Approach

The volumetric energy density (D) in a capacitor is given by:

$$D = \varepsilon\varepsilon_0 E^2/2 \quad J/cm^3 \qquad (1)$$

where ε = relative dielectric constant of the material
ε_0 = permittivity of free space = 8.85×10^{-14} F/cm
and E = applied electric field in V/cm (this is the operating field).

To obtain the energy density per unit weight, W (J/g), D must be divided by the mass density, ρ (g/cm^3):

$$W = \varepsilon\varepsilon_0 E^2/2\,\rho \quad J/g \qquad (2)$$

Equation (1) shows that increased energy density requires either increased dielectric constant or operating electric stress or both. To increase the energy density per unit weight, low density materials are preferred. Unfortunately, as noted above, materials with high dielectric constants often have low dielectric strengths, low resistivities, and large dielectric losses. The latter leads to undesirable, even unacceptable, dielectric heating, which could require thermal management that could reduce the overall energy density. As a consequence, since energy density increases as the square of the electric field but only linearly with dielectric constant, the primary objective of the present work has been to increase the electric stress. Secondarily, we have tried to maximize dielectric constant within the material systems which have been studied.

It is of interest at this point to compare the voltage rating and breakdown strengths of the candidate materials investigated in this work against other candidates. This is done in Figure 1.

High Operating Stresses: Clearing, Pulse Conditioning, and Surface Modification

A primary objective throughout this program, with each of the material technologies, has been to push the dielectric materials to as high a stress as possible and to develop new methods for doing so. Basically, three methods were used: 1) clearing, 2) pulse conditioning, and 3) surface modification. As indicated above, clearing ("self-healing") represents an avenue to remove defect sites within the respective material films by deliberately forcing the material to breakdown, but in doing so strictly limiting the energy involved so that minimal damage is done to the surrounding material. The method is used extensively to improve the performance of low voltage metallized film capacitors; but, until the present work, has been surprisingly little used for high voltage capacitor development. The method is of course not applicable to foil electrodes; rather, it is restricted to capacitors with metallized electrodes, applied by vapor deposition using metals such as aluminum. When a voltage is applied, a defect in the dielectric such as that shown schematically in Figure 2, undergoes highly localized breakdown. The resulting arc vaporizes the thin metal electrodes, interrupts the current flow, and quenches the breakdown. Defects are therefore removed both physically and electrically, with minimal loss of capacitance, and the remaining dielectric can be operated at a higher stress. By continuing to raise the voltage, and repeating the process, increasingly higher stresses can be sustained. The method has been successfully applied to each of the polymer film materials used in this program.

The second method, pulse conditioning, is a novel adjunct to the method of clearing. It uses short, high-voltage pulses to promote clearings prior to the application of a ramp voltage.

Once the film has been cleared, then the electric strength is that of the "defect free" material. In the third method to improve breakdown strength, surface modification, we begin to prevent the injection of electrons at the electrode surface, which are the initiators of the "intrinsic" electronic processes of breakdown. Preliminary results of such an effect were presented at this meeting in 1992[4]. The effect is further investigated in this work; included is a surface fluorination treatment using CF_4 gas. Other researchers have also been investigating surface modification methods for improving capacitor performance[7]. It should be noted, that as the electric stress is increased, into the upper MV/cm range, (as desired to meet the target energy densities) extrinsic qualities such as impurities and inherent dielectric losses can limit breakdown performance, leading to thermally driven breakdown. The present materials were selected to avoid such limitations. They are the reasons why, for example, the polymer polyvinylidene fluoride, an otherwise excellent material, cannot be operated at high stress other than for very short duty cycles.

Experimental

Diamond Like Carbon Films

DLC is an amorphous mixture of carbon and hydrogen which exhibits polymer-like properties (low dielectric constant and high breakdown strength) and is typically produced by low pressure plasma-enhanced chemical vapor deposition techniques. More commonly investigated for its tribological qualities, DLC films of good electrical quality can be obtained under a specific range of deposition conditions. We previously reported small area DLC capacitors exhibiting improved electrical properties, relative to our initial electrical-grade films, including high resistivity (~10^{16} Ω.cm) and breakdown strength (~5 MV/cm). These improvements were achieved by modifying the plasma power level, the substrate electrode temperature and the carrier gas composition[4]. Polarization is essentially electronic, and frequency independent dielectric constant and low loss characteristics were demonstrated between 100 Hz and 1 MHz. We have since pursued further improvement of electrical properties, especially breakdown strength, by process modification. Additionally, methods for fabricating thick film multilayer capacitors were developed to meet the high voltage rating requirements.

With a view toward productivity improvement we have demonstrated the capability of depositing good quality DLC films using a variety of hydrocarbon feedstock sources. Table I lists some electrical properties for three hydrocarbon sources. Electrical measurements were generally made on 1 μm thick MIM structures. Electrodes were typically 1000 Å sputtered aluminum, to facilitate clearing. Breakdown measurements were done using a manually controlled ramp voltage at a rate of approximately 5 V/sec on an electrode area of 0.317 cm^2. The use of C_2H_2 resulted in a seven-fold improvement in the deposition rate over the CH_4, while the C_4H_6 showed a three-fold improvement with no sacrifice in electrical performance.

On the other hand, substrate surface smoothness plays a critical role in determining the ultimate breakdown strength of the deposited films. For example, the range of breakdown strengths (3 - 4 MV/cm) observed for "baseline" films, those which have not been process optimized or surface modified, is due to variations in the surface quality of the silicon substrate material. On the best silicon substrate surfaces, films from a process optimized for breakdown strength exhibit values of about 6 MV/cm. To be able to accommodate more practical substrates, including those with rough surfaces, we applied field-grading layers (a form of surface modification) consisting of low resistivity DLC or hydrogenated amorphous silicon, resulting in breakdown strengths three times greater than for non-graded structures on the same substrate.

With respect to energy density, Figure 3 shows that a tradeoff must be made between dielectric constant and breakdown strength. In this figure, process conditions are the independent parameter. As noted under Technical Approach, energy density increases more rapidly with breakdown strength than with dielectric constant, so we generally prefer conditions favoring the former. Fortunately, these same conditions also tend to give the highest resistivities and lowest dissipation factors[4].

In order to meet the high voltage rating requirements for high energy density capacitor applications, DLC films in the range of 7 - 10 μm are necessary. DLC films were deposited from 5 to 11 μm in thickness without loss of adhesion, a major concern considering the mechanical stresses associated with plasma deposited films. In addition, multilayer capacitors were fabricated consisting of two layers of 7.5 μm DLC and three 1000Å aluminum electrode layers with a combined electrode area of approximately 70 cm^2.

We have demonstrated the capability of increasing the small area breakdown strength of DLC films into the 6 MV/cm range by incorporating charge trapping species into the bulk film. The ability to fabricate thick film multilayer capacitors, while maintaining good electrical and mechanical integrity, demonstrates the prospects for this new technology.

CVD Diamond Films

Diamond is attractive for high energy density storage based on the intrinsic properties of single crystals[8]. These include high resistivity and high breakdown strength (10 MV/cm), absence of dielectric losses due to atomic or orientation polarization, radiation hardness, high service temperature, high thermal conductivity and chemical inertness. In the form of thick polycrystalline films grown by CVD, diamond should lend itself to high voltage operation. The challenges are to (i) approach in CVD diamond the high resistivity and breakdown strength observed in single crystal diamond and (ii) overcome the some of the extrinsic features of

CVD diamond: roughness, limited deposition area of free-standing crack-free films, and relatively high cost. Since the extrinsic issues are widely addressed outside the present work we focused on the intrinsic electrical properties.

High resistivities were obtained with low to moderate nominal electric fields. However, the resistivity invariably decreased with increasing field at a rate that would preclude high energy density storage because conduction through the film would compete with the intended load for the stored charge, and because of the possibility of thermal breakdown.

Time and frequency domain measurements on the single layer structures (Figures 4 and 5) reveal a space charge polarization which we attribute to a separation of the centers of native positive and negative charge carriers under the influence of applied voltage. This process could account for the field-dependent resistivity and low breakdown strengths typical of CVD diamond. Efforts to improve electrical properties included post-deposition heat, chemical and plasma treatments as well as nitrogen doping for electrical compensation of the extrinsic p-type conduction, and thinning to eliminate surface roughness of the as-grown film. Comparison of the dielectric constants and loss tangents (as functions of frequency) for the best undoped and the best nitrogen-doped CVD diamond films showed that space charge polarization was reduced by the doping.

The encouraging result of the nitrogen doping effort suggests that electrical compensation, either by nitrogen doping or by electron irradiation, is a promising approach. At present, however, CVD diamond's breakdown strength and volumetric energy density are roughly factors of 10 and 100, respectively, below those of DLC and Ultem®. Optimization of CVD diamond for application as a high energy density dielectric will require further fundamental effort, most likely aimed at a combination of electrical compensation, thinning, and tailored electrical contacts.

Beyond the intrinsic issue of dielectric performance, however, is the issue of CVD diamond availability in the form of the large-area free-standing layers needed to construct high energy density capacitors of practical scale and quantity. Present CVD diamond growth technology produces small-area free-standing films. Moreover, without dramatic improvements in rates and yields, the cost will remain much greater than for the other candidate dielectric materials. Thus, for CVD diamond to emerge as a viable candidate for high energy density storage at high voltage significant progress is required both in the dielectric performance and in film growth technology.

Ultem® Polyetherimide Films

Ultem® polyetherimide has a very attractive combination of properties for a high-energy density capacitor film[9]: a dielectric constant of 2.94, low dielectric losses and stable dielectric constant over a wide temperature/frequency range, and high breakdown strength. Breakdown strengths of up to 7 MV/cm have been achieved with several films, implying an energy density of around 6 J/g. Also, its excellent thermal stability, typically up to 200C in air, allows a high use temperature, well above that of polypropylene or polyvinylidene fluoride, without loss of its excellent physical and mechanical properties. Finally, its solubility in various solvents and non-crystalline nature make it amenable to solvent casting as required to achieve the highest breakdown strength.

In the prior report at this meeting[4], data was given for various commercial extruded Ultem® films with thicknesses of around 1 mil. In this paper data is given for both extruded and solvent cast films. Whereas the extruded film was 1 mil thick, the solvent cast films were considerably thinner: 3.5 and 8 μm thick.

A comparison of the quality of extruded and solvent cast Ultem® films comes from the dc breakdown data (25 V/s) as function of temperature over the range -20C to 100C (Figure 6). These measurements were done with evaporated aluminum electrodes (thickness = 1000Å; area = 0.4 cm^2), and were essentially free of clearing events, thus affording an assessment of the inherent quality of the two films. Clearly, the breakdown data for the solvent cast film is better than that of the extruded film over a wide range of temperature and it is tempting to conclude that the difference is due to a superior quality of the solvent cast film. However, it is possible that the difference is related to the different thicknesses of the two films, since electronic breakdown of amorphous polymers exhibits increasing breakdown with decreasing thickness. Unfortunately, commercial films were not available at different thicknesses in order to be able to resolve the correct explanation.

As found with extruded films of Ultem®, the solvent cast films were similarly (20-30%) improved in their breakdown behavior as a consequence of surface treatment with oxygen-containing coatings and by a fluorine treatment of the polymer surface using CF_4 gas. In each case we speculate that the effect derives from a trapping of electrons; but fluorine also enhances adhesion of the aluminum electrodes and therefore it may prevent discharge initiated breakdown. Measurements of the current at breakdown do not readily permit one to distinguish between the two possibilities.

A major theme in the present work is "clearing" of the capacitor structure by controlled voltage application to electrically isolate defects. This is illustrated by Figures 7a and 7b, which show the voltage pulse supported by a single layer structure of 8.67μm thick Ultem® before and after clearing. Figure 7a represents the first application of the pulse, which initiated some clearings. Figure 7b shows the second application of the same waveform, which is now fully supported by the structure. In Figure 7b the first (negative) peak of the waveform at 6.4 kV corresponds to an electric stress of 7.4 MV/cm and a raw energy density of ~7 J/cm^3. This stress and energy density are, respectively, factors of ~1.5 and ~2 greater than observed with a ramp voltage. This strong dependence of breakdown results on voltage waveform reinforces the importance of reflecting conditions of the intended application in the test waveform.

Figure 7b also shows that following the 1 millisecond (negative) pulse, the structure tolerates significant voltage reversal. The importance of tolerance for voltage reversal in pulse applications is the elimination of circuit components otherwise needed to protect the capacitor from reversal. The case shown, with reversal of about 70%, occurring in about 10 μs or 1% of the pulse width, does not represent a limiting tolerance for this structure.

Clearing also occurs during excitation by a voltage ramp, promoting a higher final (shorting) breakdown voltage than would otherwise occur. We discovered that ramp breakdown voltages for the Ultem® single layer structures are further enhanced if the structures are first subjected to sequences of short (10 - 100 μs) high voltage (1 - 6kV) pulses. The pulse-conditioned structures exhibited breakdown strengths as much as 10% higher (i.e. 20% higher energy density) under the subsequent ramp test (25 V/s) than without pulse conditioning. This effect depends upon several parameters (metallization thickness and conductivity, pulse duration, circuit parameters of the test apparatus, experimental technique, pulse conditioning protocol), and further work is needed to optimize it.

With Ultem® film, the developments were extended to the fabrication of trial 10 kV, 0.5 kJ capacitors; potentially, a step toward the application of interest. Based on the 10 kV requirement, the 1 mil extruded film was selected over the thinner

solvent-cast films. One mil thick, single-side aluminum metallized Ultem® film was wound into a cylindrical configuration; edge electrodes were applied by the standard "schooping" technique[10] and the clearing and breakdown performance of a number of the rolls were measured to establish the voltage capability per roll. Breakdowns of the individual rolls occurred in the range 2-3 MV/cm; hence it was decided to use an applied stress of 1 MV/cm for the final capacitor. Each individual roll in the final capacitor was dc cleared up to a level of 1.6 MV/cm before final assembly.

This trial capacitor was made with very little attempt to optimize the fabrication steps such as the winding conditions, metallization thickness, or clearing procedure. The Ultem® film itself may not have been optimal for this size of capacitor; a solvent cast film of suitable thickness was not available at the time. With so many features that could be improved upon, the final result (energy density ~ 1 J/g) is considered as very encouraging.

Modified Polyetherimide

Work was also continued during Year 2 on the use of computer modeling to predict modified polyetherimide structures with increased dielectric constant over Ultem®[11]. The approach continues to show promise and would be expected to further enhance the performance potential shown by Ultem® polymer.

Summary

Each of the four material technologies investigated in this program, plasma-polymerized diamond-like carbon films, chemical vapor deposited carbon, Ultem® polyetherimide films, and computer-modelled modified polyetherimides, has shown some degree of promise for meeting the objective of a capacitor energy density of greater than 10 J/g, based on the dielectric only. DLC and Ultem® films are the most attractive approaches, because they offer promise for application in the relatively near term, subject to further development. Several avenues for improving breakdown strength have been developed during the program: this suggests that the strategy of using polymer films and progressively increasing their breakdown performance has validity as a long term approach for high-energy-density capacitors. Molecular modelling of modified polyetherimides to increase dielectric constant, remains promising, especially since it would naturally build upon any developments realized with Ultem® films; but improvements in methodology are still needed and large-scale polymer synthesis and film making would need to be implemented. CVD diamond is fundamentally an attractive dielectric material, but additional work is needed on many technical aspects.

Acknowledgments

This work was supported by the United States Army under contract No. DAAAL01-91-C-0149. The authors are greatly indebted to Drs. T. R. Jow and S. Gilman, of the US Army Electronics and Power Sources Directorate, and Professor W. J. Sarjeant, of the Department of Electronics and Electrical Engineering, SUNY Buffalo, New York, for technical guidance and helpful discussions, and to Dr. K.W. Browall for project management.

References

1. Sarjeant, W.J. Capacitors, Trans IEEE, EI 25, 861-922 (1990).
2. Gerstenberg, D., Handbook of Thin Film Technology, Maissel, L.I. and Glang, R., Eds., McGraw Hill , 1970.Ch. 19. pp 1-36.
3. Rose, M.F., High Energy Density Capacitors for Source Power Conditioning, IEEE AES Magazine, pp 17-22 (1989).
4. Rzad, S.J., Gasworth, S.M., Reed, C.W., and DeVre, M.W., Advanced Materials for High Energy Density Capacitors, paper at 35th Power Sources Conference, 1992.
5. Lee, H., Bullard, G.L., Mason, G.E., and Kern, K., Improved Pulse Power Sources with High Energy Density Capacitor, IEEE Trans Mag. 25, 324-330 (1989).
6. Shirn, G.A., and Burn, I., Proc. Symp. High Energy Density Capacitors and Dielectric Materials, Reed, C.W., Ed. NRC, 49-66 (1981).
7. Yializis, A., Binder, M., and Mammone, R.J., "Plasma Treatment of Polymer Dielectric Films to Improve Capacitive Energy Storage", NASA 2000 paper.
8. Properties of Diamond, Field, J.E., Ed., Academic Press, London, 1979.
9. Theoleyre, S. and Reed, C.W., Dielectric Properties of Polyetherimide Films, NAS-NRC Conference on Electrical Insulation and Dielectric Phenomena, 1984.
10. Shaw, D.G., Cichanowski, S.W., and Yializis, A., A Changing Technology: Failure Analysis and Design Innovation, Proc. Symposium High Energy Density Capacitors and Dielectric Materials, Reed, C.W. Ed. NRC 13-48 (1981).
11. Bendler, J. and Takekoshi, T., Molecular Modelling of Polymers for High Energy Storage Capacitors, paper at 35th Power Sources Conference, 1992.

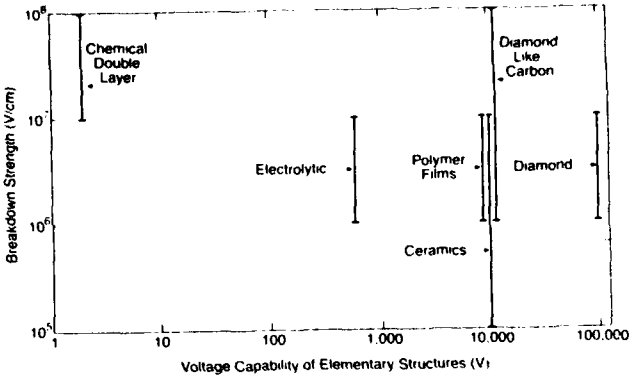

Figure 1 Electrical breakdown strength and voltage capability of elementary structures for different capacitor technologies

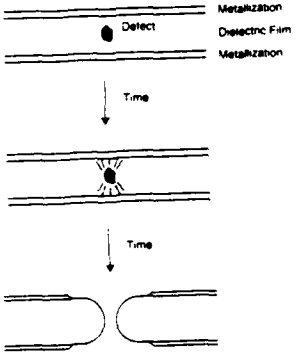

Figure 2 Schematic Picture of Clearing

Table I

Comparison of 1KHz Dielectric Properties for DLC Films Processed Using Different Hydrocarbon Precursors

Precursor	ε	Tanδ	ρ(ac)
CH_4	3.5	0.0068	$7.5X10^{10}$
C_2H_2	3.1	0.0039	$1.5X10^{11}$
C_4H_6	2.8	0.0019	$3.9X10^{11}$

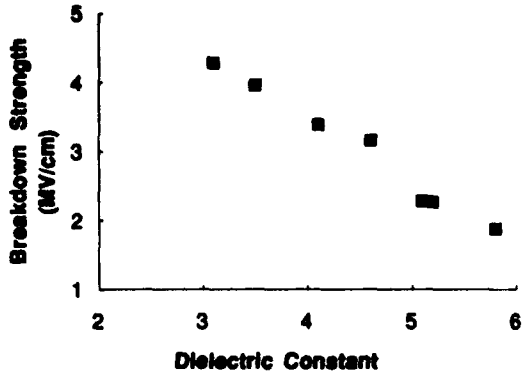

Figure 3 Relation between DLC dielectric constant and breakdown strength as deposition process conditions are varied.

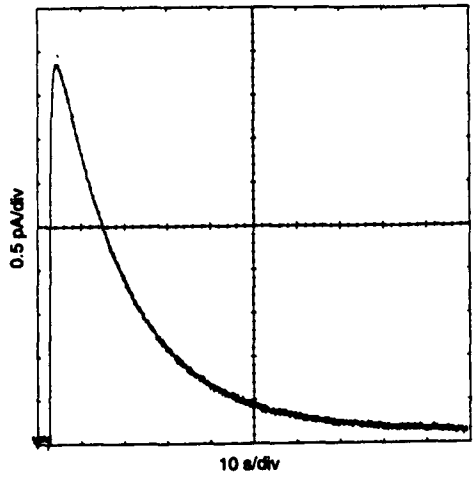

Figure 4 Time domain current response of single layer capacitor structure incorporating a 250μm thick diamond film to a 1 V step. Only the charging transient is shown, with the current zero near the bottom of the plot. The steady state current indicates a resistivity of about 10^{14} Ω.cm

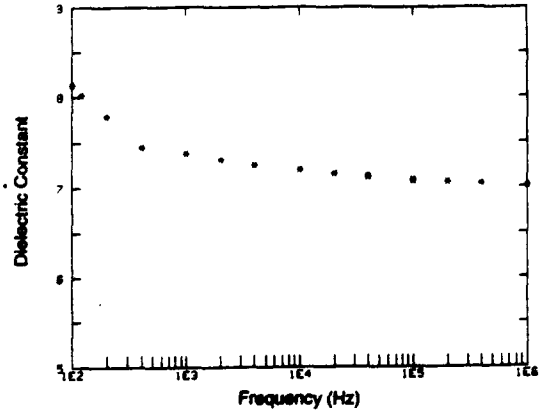

Figure 5 Dielectric constant as a function of frequency for the same structure as in Figure 4. An error in the assumed vacuum capacitance accounts for the high frequency limit greater than diamond's nominal value of 5.7

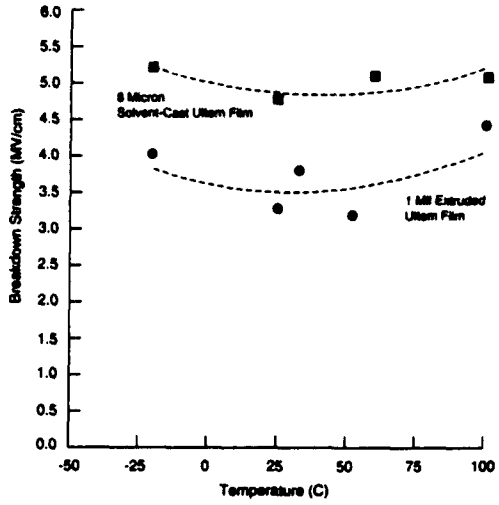

Figure 6 Effect of temperature on the dc breakdown strength of 8 μm thick solvent-cast and 1 mil thick extruded Ultem® films

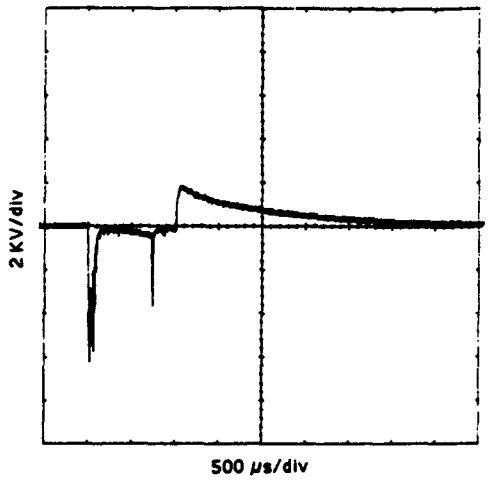

Figure 7a Oscilloscope trace of voltage applied to a single layer capacitor structure incorporating 8.67μm thick Ultem®. Several clearing events are evident.

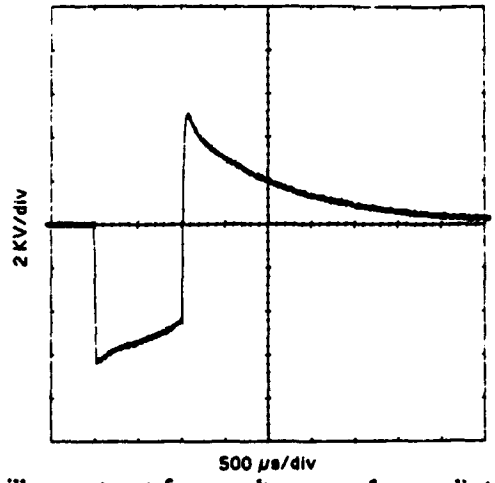

Figure 7b Oscilloscope trace of same voltage wave-form applied to the same single layer structure as in Figure 7a. Droop in (negative) pulse amplitude after the initial peak is an artifact of the test apparatus. This trace, showing the structure holding off 6.4 kV, was made after that shown in Figure 7a.

ELECTROCHEMICAL CAPACITORS FOR ELECTRIC VEHICLES - A TECHNOLOGY UPDATE AND RECENT TEST RESULTS FROM THE IDAHO NATIONAL ENGINEERING LABORATORY

A.F.Burke
Idaho National Energy Laboratory
EG&G Idaho, Inc.
Idaho Falls, ID 83415-3830

Abstract

The DOE Electrochemical Capacitor (ultracapacitor) Development Program is reviewed and the technologies being pursued to meet the near-term and advanced energy density goals of 5 Wh/kg and 15 Wh/kg, respectively, are identified and their status assessed. Capacitor testing at the Idaho National Engineering Laboratory (INEL) is summarized with special attention being given to tests of the Panasonic 3 V, 1500 F device at temperatures between -25°C and +65°C and tests of a 168 V pack of Panasonic 3 V, 500 F devices at powers up to 25 kW.

Introduction

The first paper on the use of electrochemical (double-layer) capacitors for electric vehicle applications was given at the 34th Power Sources Symposium in June 1990 (Reference 1). Specifications for devices to be used in vehicles were presented at that time and the United States Department of Energy (DOE) initiated a program to develop devices that would meet those specifications in 1992. At the present time (1994), it is now widely recognized that high energy density capacitors (often referred as ultracapacitors) can be used to load level the batteries in electric vehicles thereby reducing the peak power requirement for the battery. This permits the battery to be designed for maximum energy density and cycle life and minimum cost with much less attention being given to peak power. There are now programs underway in the United States, Europe, and Japan to develop capacitors for electric and hybrid vehicle applications. The goals of the DOE Ultracapacitor Program are given in Table 1, but the goals of the programs outside the United States are thought to be essentially the same.

The conclusion reached in 1990 that capacitors could be developed with an energy density of at least 5 Wh/kg and suitably low resistance (about 0.1 ohm-cm^2) was based in large part on the work on mixed metal oxide capacitors that was underway at Pinnacle Research Institute (References 2 and 3). Since 1990, work on a number of other material technologies for ultracapacitors has been started and there appear to be several technologies that show good promising of meeting the DOE advanced ultracapacitor goal of 15 Wh/kg. A summary of the current DOE Ultracapacitor Program is given in Reference 4 and that paper also contains a bibliography of recent publications pertinent to the DOE Program. In this paper, an update of ultracapacitor technology, as of 1993, is given along with recent test data taken at the Idaho National Engineering Laboratory (INEL) as part of the ongoing DOE Ultracapacitor Program.

Work supported by the U.S. Department of Energy Assistant Secretary for Energy Efficiency and Renewable Energy (EE), under DOE Idaho Operations Office, Contract DE-AC07-76ID01570

The Status of Ultracapacitor Technology (1993)

There are a number of ultracapacitor development projects in progress in the United States and abroad. The distinguishing characteristic of each of these programs is the material being used in the electrodes, which include the following:

- Carbon/metal fiber composites
- Foamed (aerogel) carbon
- Activated, synthetic, monolithic carbon
- Doped conducting polymer films on carbon cloth
- Mixed metal oxides

A summary of the status of each of these technologies as of the end of 1993 is given in Table 2. When available data permitted, the performance values given in Table 2 for the various technologies are based on testing done at the INEL. The status of several of the technologies is discussed briefly in the following paragraphs.

The only high energy density power capacitors commercially available are those from Panasonic, which utilize particulate carbon with a binder on an aluminum foil and an organic electrolyte in a spiral wound, 3 V single cell configuration. Panasonic now markets 70 F, 500 F, and 1500 F devices. All these devices, which have been extensively tested at the INEL, have energy densities of 2.3 Wh/kg and 2.9 Wh/L for charging to 3 V. The resistance of the 500 F device is 3 to 4 milli-ohms permitting discharge at a power density of 500 W/kg with a relatively small IR voltage drop. The Panasonic capacitors are suitable for performing laboratory testing of battery and capacitor systems, but their energy densities are not high enough for packaging in electric vehicles.

Laboratory tests of single cells and bipolar stacks of devices fabricated as part of the DOE Ultracapacitor Development Program have shown energy densities of 1 to 2 Wh/kg for devices using aqueous electrolytes (sulfuric acid and KOH) and 6 to 8 Wh/kg using organic electrolytes. The resistances of the 1 V cells using aqueous electrolytes are in the range of 0.2 to 0.5 ohm-cm^2 and for the 3 V cells using organic electrolytes, the range is 1 to 2 ohm-cm^2. PSFUDS testing of cells using aqueous electrolytes has shown round-trip efficiencies of 90 to 92% and those using organic electrolytes efficiencies of 85 to 88%. Tests of bipolar stacks have indicated that stacking capacitors should not prove difficult as only minimum difficulty with cell imbalance has been encountered with both the carbon-based and mixed metal oxide technologies. The test results obtained in 1993 indicate that it will be difficult to reach the DOE near-term goal of 5 Wh/kg in carbon-based devices using an aqueous electrolyte unless the carbon loading can be increased to at least 1 gm C/cm^3. However, test results indicate that the near-term goal can be reached or exceeded in carbon-based devices using an organic electrolyte, but with a significant increase in cell resistance. Work on packaging cells and bipolar stacks in a completely sealed manner is progressing well with indications that within a year packaged bipolar devices will be available with energy densities of 2 to 3 Wh/kg using aqueous electrolytes and 6 to 10 Wh/kg using organic electrolytes.

Future Projections of Ultracapacitor Performance and Cost

The major questions regarding ultracapacitor technology are concerned with energy density and cost. As indicated in Table 1, the DOE energy density goal is 5 Wh/kg for the near-term and 15 Wh/kg for the long-term. The cost goal is to achieve $ 0.5 to 1.0/Wh. There appear to be at least three technical approaches that have a reasonable chance of meeting the long-term energy density goal. They are:

1. Highly loaded (>1 gmC/cm^3), carbon-based substrates using an organic electrolyte
2. Mixed metal oxides with 10 to 20 micron thick substrates with an aqueous or organic electrolyte
3. Doped polymer substrates with an organic electrolyte

For the electric and hybrid vehicle applications, it is necessary to meet the energy density goal and at the same time have a low enough resistance that the capacitor can be discharged at a power density of at least 1.5 kW/kg. In addition, cycle life and cost goals must also be met. Results of a simple analysis of the carbon-based technologies are shown in Tables 3 and 4 for the case of a carbon loading of 1 gm/cm^3 in the substrates of the cell. The results indicate that meeting the long-term goal of 15 Wh/kg requires a cell voltage of at least 2 to 3 V (in other words, the use of non-aqueous electrolytes) and that meeting the cost goal of $0.5 to 1/Wh requires a carbon cost of $2 to 5/lb even for devices having energy densities of 10 Wh/kg or greater.

Recent Capacitor Testing at the INEL

Testing of high energy density capacitors for electric vehicle applications has been underway at the INEL since 1991. Summaries of the test procedures used and results obtained are given in References 5 through 8. The test equipment now available at the INEL for capacitor testing is listed in Table 5. This equipment, which was designed to be used for testing batteries, has been adapted for testing capacitors with little difficulty. The standard types of tests performed on capacitors are listed in Table 6.

In addition to testing capacitors delivered to the INEL from industrial contractors and the National Laboratories as part of the DOE Ultracapacitor Development Program (Reference 4), testing has been performed in recent months to determine the characteristics of the Panasonic 3 V, 1500 F devices and modules and packs consisting of up to one-hundred sixty eight (168) of the Panasonic 3 V, 500 F devices, which will used at INEL to test capacitor/battery systems with and without interface electronics between the capacitor and battery packs. Photographs of the Panasonic devices, modules, and packs are shown in Figures 1 through 3. Test data for the Panasonic 1500 F device are given in Table 7 for constant current and constant power discharges. The constant power discharge data are compared in Figure 4 with similar data for the 500 F devices. The characteristics of the larger 1500 F device scale as expected from those of the smaller 500 F device in that the energy density of the two devices are essentially the same and the resistance of the larger device is approximately one-third that of the smaller device.

A four-cell string of the Panasonic 1500 F devices was tested at temperatures between -20°C and +65°C in an environmental chamber. The data for 100 A and 300 A discharges of the cells are shown in Figure 5 and Table 8. The test results indicate that the capacitance is essentially independent of temperature, but the resistance increases monotonically with decreasing temperature due primarily to the decreasing conductivity of the electrolyte. The resistance of the capacitor at -20°C is about 20% higher and at +65°C, it is about 20% lower than at a standard ambient temperature of 25°C.

Prior to assembling the one-hundred sixty eight (168) 3 V, 500 F devices into fourteen (14) 12 V modules, each of the devices was characterized using a standard test in which they were successively charged and discharged at 25, 50, and 100 A. The average capacitance of each device was calculated based on the measured charge/discharge times for each current. The average capacitance and standard deviation for the 170 devices are given in Table 9. Fifty-six sets of three devices for the fourteen 12 V modules were formed by taking successively one device from each end (low and high) and one from the middle of the distribution. The capacitance of the three device sets was 1470 F with a very small standard deviation of 0.93 F indicating the distribution of the capacitances of the devices themselves was very symmetric about the mean of 489 F. The capacitor pack of the fourteen (14) 12 V modules was then discharged at constant powers up to 25.5 kW (500 W/kg) and on the PSFUDS cycle for several hours. The capacitor pack functioned satisfactorily in all the tests and is ready for further testing with a battery pack and interface electronics.

References

(1) Burke, A.F., Hardin, J.E., and Dowgiallo, E.J., "*Applications of Ultracapacitors in Electric Vehicle Propulsion Systems*," Proceedings of the 34th Power Sources Symposium, Cherry Hill, NJ, June 25-28, 1990.

(2) Tong, R.R., Mason, G.E., Lee, H.L., and Bullard, G.L., "*Power Characteristics of the Ultracapacitor*," Proceedings of the 33rd International Power Sources Symposium, Cherry Hill, NJ, June 13-16, 1988.

(3) Bullard, G.L., Alcazar, H.B.S., Lee, H.L., and Morris, J.L., "*Operating Principles of the Ultracapacitor*," IEEE, 4th Symposium on Electromagnetic Launch Technology, Austin, TX, April 1988.

(4) Burke, A.F., Electrochemical Capacitors for Electric and Hybrid Vehicles - The DOE Program and the Status of the Technology-1993, The Annual Automotive Technology Development Contractor's Coordination Meeting - 1993, October 1993.

(5) Burke, A.F., "*Laboratory Testing of High Energy Density Capacitors for Electric Vehicles*," EG&G Idaho, Inc. Report No. EGG-EP-9885, October 1991.

(6) Burke, A.F., "*The Development of Ultracapacitors for Electric and Hybrid Vehicles - The DOE Program and the Status of the Technology*," The Annual Automotive Technology Development Contractors' Coordination Meeting, 1992, SAE P-265, pp 377-389, October 1992.

(7) Burke, A.F., and Dowgiallo, E.J., "*Ultracapacitors for Electric and Hybrid Vehicles - A Technology Update*," Proceedings for the 11th International Electric Vehicle Symposium, Florence, Italy, September 1992.

(8) Burke, A.F., "*Testing of Ultracapacitors and Batteries for Electric Vehicle Applications*," Proceedings of the Third International Seminar on Double Layer Capacitors and Similar Energy Storage Devices, Deerfield Beach, FL December 1993.

Table 1. Near-term and advanced goals for the DOE Ultracapacitor Development Programs.

Battery w/o Capacitor	Near-Term	Advanced
Weight (kg)	500 to 600	200 to 300
Power Density (W/kg) Average Gradeability Peak (accel)	 10 30 to 50 80	 20 110 to 160 375 to 550
Ultracapacitor Unit		
Energy stored (Wh)	500	750
Maximum Power (kW)	50	80
Weight (kg)	<100	<50
Volume (L)	<40	<20
Energy density (Wh/kg)	>5	>15
Maximum useable power density (W/kg)	>500	>1600
Round trip efficiency (%)	>90	>90
Vehicle Acceleration		
0 to 88 km/h (sec)	<20	<8

Table 3. Simple calculations of energy density (carbon-based ultracapacitors).

V_{cell}	(F/gmC)(1)	Wh/kg(2)
1	250	5.75
2	175	16.1
3	125	25.9
4	90	33.1

(1) Capacitance for a single electrode

(2) Cell is 66% carbon by weight

$$\frac{Wh}{kg} = \frac{1}{8}\,\frac{(F/gmC)}{1.5}\,\frac{V^2}{3.6}$$

Table 2. Summary of ultracapacitor technology (Status 1993, Future Projections).

	Construction			Performance						Status			
Name	Config.	Electrode Mat'l	Electrolyte	Wh/kg	Wh/L	Resistance ohm-cm²	(W/kg)pk(1)	Effic(2) (%)	Cost	Size (cm²)	Voltage	Cap. (F)	Basis for Projection
NEC Supercap													
FY	prismatic	carbon	sulfuric acid	0.33	0.55	45	"	"	low	4	5	2.2	Mfg Spec Sheet
FE	prismatic	carbon	sulfuric acid	0.01	0.18	1.9	"	"	low	4	5	1.5	Mfg Spec Sheet
Panasonic	spiral wound, single cell	carbon	organic	2.2	2.9	7	400	80-90	low	single cell	3 V	500-1500	Lab Tests
Evans	prismatic	carbon	sulfuric acid	0.2	0.5	1	"	"	low	6	11	0.5	Mfg Spec Sheet
Seiko Instruments	button cell	polyacene polymer	organic	1.9	4.9	12	"	"	"	3	5	2.5	Mfg Spec Sheet
Pinnacle Research Institute	bipolar	mixed oxides (Ru, Ta) Adv. Design	sulfuric acid	5	14	$<10^{-2}$	>10,000	>95	high	2	100 V	0.01	Mfg Testing
				13	40	$<10^{-2}$	"	>95	med	200	"	"	Projections
Maxwell/ Auburn	bipolar	carbon/metal composite	KOH	1.2	2	0.2	800	90	med	20	1 V	55	Lab Tests
			organic	7	9	1.5	2000	"	med	20	3 V	13	Lab Tests
Livermore Nat'l Lab	bipolar	aerogel carbon particulate	KOH	1	1.5	"	"	90	med	58	1 V	35	Lab Tests
Sandia Nat'l Lab	bipolar	synthetic, activated carbon	aqueous	1.4	1.7	0.35	1000	"	med	2	1 V	3.5	Lab Tests
Los Alamos Nat'l Lab	bipolar	conducting polymer on carbon	organic	10-20	"	"	"	"	low	"	"	"	Projections

(1) Maximum power at which the energy recoverable from capacitor is at least 80% of that recoverable at 100 W/kg.

(2) Efficiency on the PSFUDS cycle for the peak power step at (W/kg)pk = 300.

Table 4. Simple calculations of cost (carbon-based ultracapacitors).

	$/Wh			
$/lbC	5 Wh/kg	10 Wh/kg	20 Wh/kg	30 Wh/kg
2	0.59	0.30	0.15	0.10
5	1.47	0.74	0.37	0.25
10	2.9	1.45	0.73	0.49

$$\$/Wh = \frac{(\$/kgC)}{1.5\,(Wh/kg)_{dev}}$$

Table 5. Test equipment at the INEL for capacitor testing.

Bitrode Tester (2)

- Up to 20 V
- 500 A discharge, 150 A charge
- Sequential charge/discharge cycles with programmable current or power and voltage limits for both charge and discharge

Maccor Tester

- 5 channels 20 V, 12.5 A
- 2 channels 100 V, 12.5 A
- 1 channel 100 V, 50 A
- All channels program for power and current and voltage limits
- Can do sequential charge/discharge cycles
- Used to test 1 V cells

Energy Systems Tester (1)

- 500 V, 500 A limits
- Can do sequential charge/discharge cycles with programmable voltage limits
- Used to test a capacitor unit. It tracked power in discharge of less than one second

Table 6. Standard ultracapacitor tests.

1. Constant current charge/discharge
2. Constant current charge/constant power discharge
3. PSFUDS cycle (200 sec) $(W/kg)_{max}$ = 300 or 500
4. Self-discharge test from rated voltage (48 hours)
5. Leak current test at rated voltage (3 hours)
6. Repeat test 1 through 5 at temperatures above and below ambient (-20° to 55°C)

Table 8. Calculation of the effect of temperature on cell resistance and capacitance.

Temp °C	V_1[1]	V_2[2]	R/cell mohm	V_3	V_4	C/cell farads
100 A DISCHARGE						
65	10.25	9.62	1.58	9.0	6.85	1860
40	10.3	9.7	1.50	9.1	7.03	1932
25	10.2	9.45	1.88	8.84	6.65	1826
5	10.2	9.45	1.88	8.84	6.6	1786
-10	10.1	9.28	2.05	8.63	6.26	1688
-20	9.98	9.08	2.25	8.35	6.03	1724
300 A DISCHARGE						
65	10.25	8.2	1.7	7.58[5]	5.55[6]	1773
40	10.3	8.45	1.54	7.86	5.8	1747
25	10.2	8.2	1.67	7.58	5.55	1773
5	10.2	8.2	1.67	7.58	5.45	1690
-10	10.1	7.65	2.04	7.05	5.03	1782
-20	10.0	7.23	2.31	6.6	4.74	1777

(1) Voltage at t = 0 before discharge

(2) Voltage at t = 0 after discharge is initiated

(3) Voltage at t = 3 sec

(4) Voltage at t = 13 sec

(5) Voltage at t = 1 sec

(6) Voltage at t = 4 sec

$$R = (V_1 - V_2)/I$$

$$C = \frac{(\Delta t)(I)}{V_3 - V_4}$$

Table 7. Summary of test data for a Panasonic 3 V, 1500 F capacitor.

Test Condition	Test No.	Charge Time (sec)[1]	Dischg Time (sec)[2]	Amp-Sec[4]	Watt-Sec	Resist. mOhms[3]
CONSTANT CURRENT						
100 A	1	53.5	42.4	-4238.5	-7074.7	1.247
100 A	2	53.5	42.6	-4259.8	-7139.6	1.232
100 A	3	52.5	42.2	-4219.4	-7047.0	1.301
50 A	4	52.5	70.5	-3525.1	-6702.8	1.467
50 A	5	52.5	70.5	-3525.1	-6747.9	1.400
50 A	6	52.5	71.0	-3550.1	-6786.0	1.467
150 A	7	53.5	22.5	-3359.6	-6251.2	1.299
150 A	8	52.5	22.0	-3314.6	-6153.6	1.299
150 A	9	52.5	22.2	-3314.5	-6160.5	1.199
300 A	10	53.0	9.7	-2856.1	-4973.8	1.399
300 A	11	53.0	9.9	-2916.4	-5101.9	1.299
300 A	12	53.0	10.0	-2946.1	-5151.4	1.299
CONSTANT POWER						
90 W	13	50.5	71.0	-3302.2	-6431.9	1.365
90 W	14	50.5	71.5	-3314.6	-6476.0	1.365
90 W	15	50.5	71.5	-3307.7	-6476.1	1.290
180 W	16	50.5	33.8	-3131.6	-6105.6	1.245
180 W	17	50.5	33.6	-3122.2	-6069.1	1.241
180 W	18	50.5	33.6	-3126.2	-6070.7	1.241
360 W	19	50.5	14.6	-2713.3	-5227.9	1.199
360 W	20	50.5	14.8	-2736.3	-5302.1	1.299
360 W	21	50.5	14.6	-2704.7	-5229.7	1.199
450 W	22	50.5	10.7	-2481.4	-4759.7	1.299
450 W	23	50.5	10.9	-2537.9	-4851.0	1.299
450 W	24	50.5	10.9	-2537.9	-4851.0	1.299
720 W	25	50.5	6.1	-2336.6	-4098.5	1.299
720 W	26	51.5	6.1	-2336.9	-4098.1	1.199
720 W	27	50.5	6.0	-2324.6	-4007.4	1.299
900 W	28	51.5	5.1	-2316.5	-3836.7	1.299
900 W	29	51.5	5.3	-2405.3	-3975.6	1.299
900 W	30	51.5	5.2	-2353.8	-3930.0	1.299

Device Characteristics:
Weight: 887 gm — Diameter: 7.7 cm
Length 14.9 cm — Single Cell
Spiral wound — Carbon-based
Organic electrolyte

(1) All charge done at 100 A between 0 to 3 V

(2) Discharge to 0.5 V

(3) Resistance calculated from voltage change from end-of-charge to beginning of discharge

(4) Maximum test current is 500 A during constant power discharges

Table 9. Statistical characteristics of Panasonic 3 V, 500 F power capacitors.

Weight (grams)

Average	307.4
Standard deviation	3.47

Capacitance (Farads)

Average	489.4
Standard deviation	15.7
99% confidence	489 ±40

Statistics based on tests of 170 devices.

Figure 1. The Panasonic 3 V, 150 F power capacitor.

Figure 2. A 12 V module of 3 V, 500 F Panasonic power capacitors.

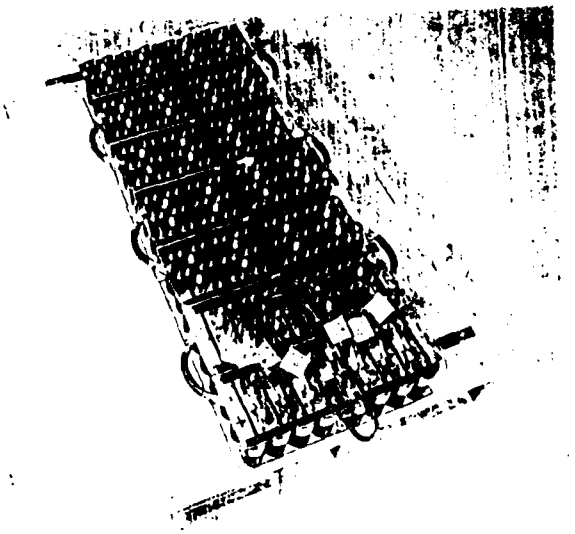

Figure 3. The 168 V pack of 3 V, 500 F Panasonic power capacitors.

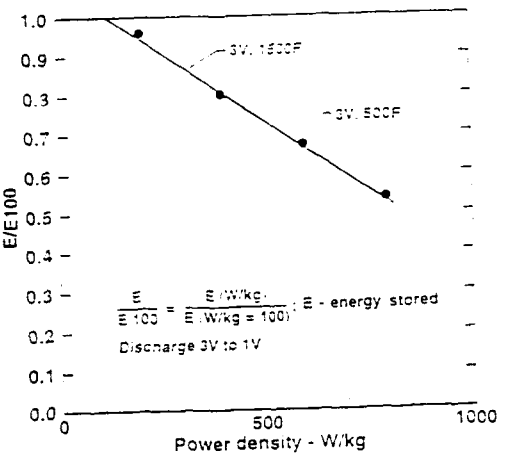

Figure 4. Comparison of discharge data for the Panasonic 3 V, 500 F and 1500 F capacitors.

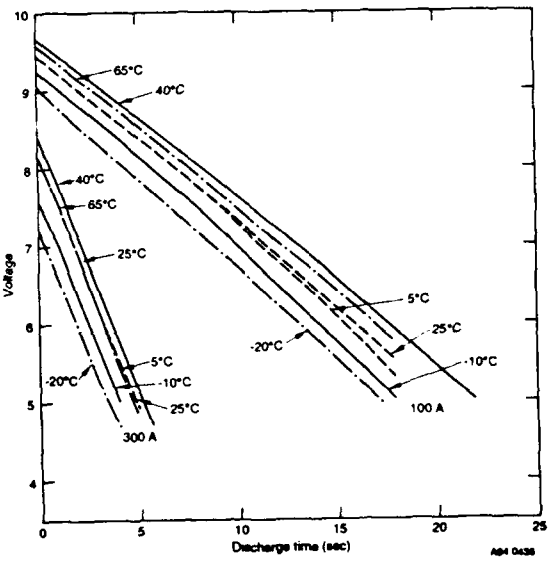

Figure 5. Discharge characteristics of the Panasonic 3 V, 1500 F capacitor at temperatures between -20° and 65°C.

A FORTY-KILOJOULE CARBON DOUBLE-LAYER CAPACITOR

David A. Evans
The Evans Company
33 Eastern Avenue
East Providence, RI 02914

Abstract

A high performance carbon double-layer capacitor (DLC) was constructed using a five element equivalent circuit model. It was designed for 15, 30, 60, or 120 V operation, depending on buss connections. Activated carbon with sulfuric acid was used to form its electrodes. The prototype had a mass of 27.5 kg and a volume of 17 liters. It stored more that 40 kJ of energy.

Power performance was measured using resistance, constant-current, and constant-power loads. Currents as high as 400 A and power levels up to 23 kW were used. The capacitor would reproducibly deliver 5 kW for 4 s, 10 kW for 1.1 s, 15 kW for 0.5 s, or 20 kW for 0.1 s. Voltage imbalance problems were not encountered. Capacitor self-discharge power was below 1 W. The feasibility of this approach was clearly demonstrated. Design and construction details are reported. Methods to further reduce the size and weight of large double layer capacitor power units are described.

Introduction

Evans was awarded a Small Business Innovation Research (SBIR) grant from the Department of the Navy to determine if carbon double layer capacitor (DLC) technology could be used as a bridge DC power source for submarine computer systems. The Navy is interested in the technology because DLCs have high power density, require no maintenance, and are free of the hazards commonly associated with batteries.

The proposed work had three main objectives. First, to design a DLC power source capable of a 15 kW average discharge rate for a minimum of 100 ms. The operating voltage was to be selected by external buss connections at 15 to 120 volts. And, the unit needed to be sealed to prevent contamination and electrolyte loss. Second, to fabricate the device according to this design. Third, to measure the electrical characteristics, evaluate power performance, and report the results to the Navy.

Discussion

Evans Capattery 1 F and 1.5 F type RE cell stacks were evaluated for use in the 15 kW capacitor. Both are eight-cell stacks providing reliable operation at 7.5 V (0.94 V/cell). These were evaluated for power performance using ac impedance methods.

An equivalent circuit model was developed for the cell stacks using complex impedance measurements. A five capacitor element RC network model was used to develop an equivalent circuit model for a 15 kW capacitor. Performance of this model was then simulated with Micro-Cap (Spectrum Software) circuit analysis software.

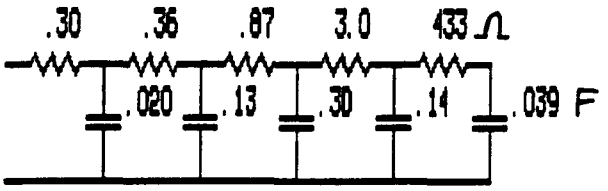

Figure 1. Equivalent circuit model for two series-connected 1.5 F RE cell stacks derived from impedance data.

Model calculations showed that approximately 10,000 F of capacity (at 0.94 V/cell) was needed to meet the power performance requirements. A minimum of 780 1.5 F cell stacks would be needed to supply the required capacity. For mechanical considerations, 816 cell stacks were specified for the design.

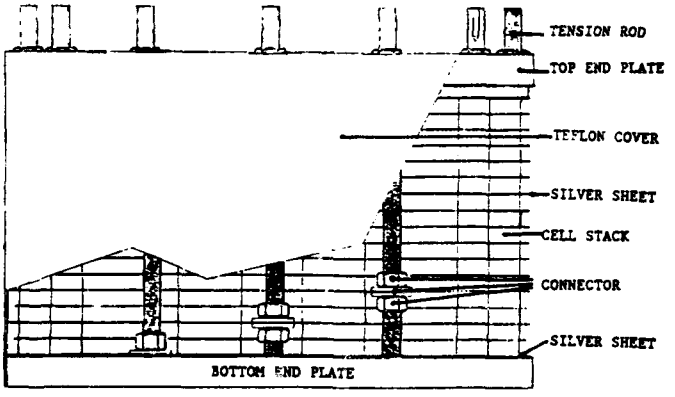

Figure 2. Assembly diagram of the 15 kW capacitor.

The capacitor was divided into 16 tiers, each containing 51 cell stacks. Provision for 15, 30, 60, and 120 V operation was made by connections to metal plates located between tiers. For 120 V operation, the 16 tiers were placed in series by connecting to the two end plates. Connecting the two end plates to one polarity and connecting the center plate to the opposite polarity gave 60 V operation. Configurations for 30 V and 15 V were similarly developed.

DLC cells using particulate carbon electrodes need compressive loading sufficient to establish low resistance contact among the carbon particles. In the case of Capattery cell stacks, this load is approximately equal to 100 pounds per square inch of cell geometric area. For the Navy device, this translated into a total axial load of roughly 9000 pounds. Because the load was distributed on a 13" circular area, and total deflection was to be held to 0.010", 0.75" thick 6061-T6 aluminum end plates were selected.

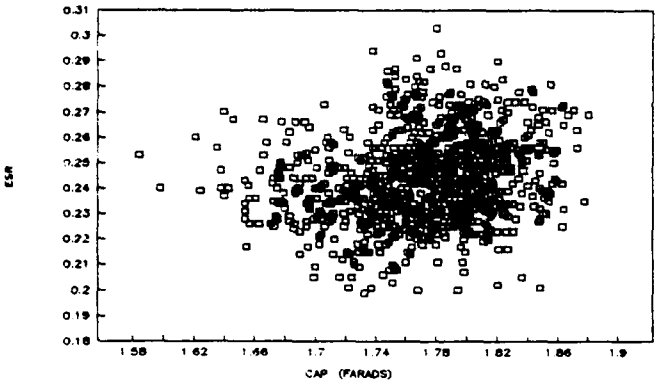

Figure 3. Scatter plot of ESR vs. capacitance shows the distribution of parts selected for the device.

To equalize voltage among the 16 tiers of cell stacks, a computer aided procedure was used to match cell stacks based on individual capacitance and ESR. Additionally, a precision 1 kohm resistor was connected in parallel with the capacitors on each tier. The current (7.5 mA) in the parallel circuit was on the order of 20 times the leakage current of the device. The combined strategies resulted in very well-balanced voltages during dynamic and static testing. Voltage distribution at charge and partial discharge conditions is given in Figure 11.

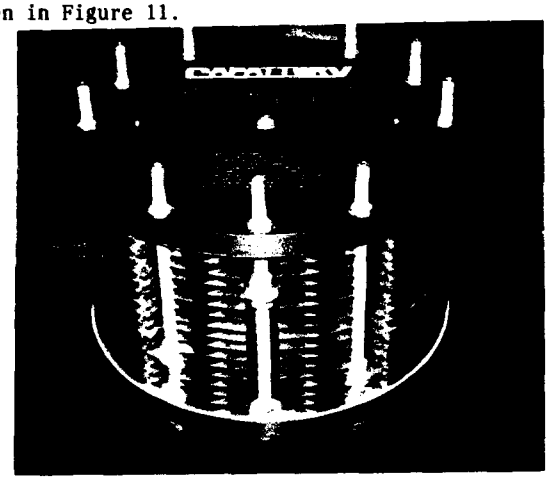

Figure 4. Photograph of the capacitor. The dimensions are 13 inches diameter by 8 inches high to the outside of the end plates.

Electrical Properties and Performance Measurements

The ESR was measured at 1 kHz according to the method in DOD-C-29501. Measurements were made at each of the four voltage setups. The results are shown in Table 1.

TABLE 1

Equivalent Series Resistance Values

Setup voltage (V)	ESR (ohms)
15	0.005
30	0.009
60	0.026
120	0.088

Capacitance was measured by constant-current charging and by ac impedance spectroscopy. Comparison of the results can reveal non-ideal behavior.

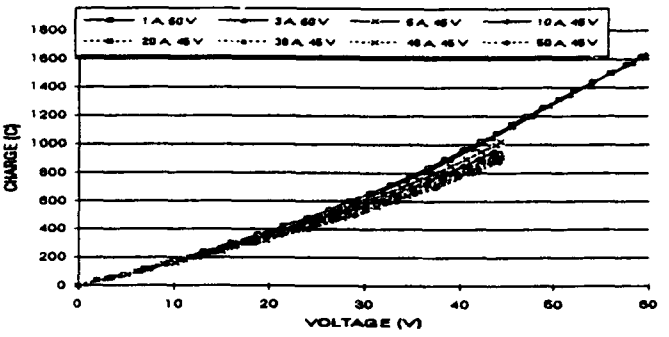

Figure 5. Stored charge vs. voltage for eight charging currents (60 V setup). C = Q/V is calculated at 26.7 F for the 1 A charging current. Stored energy is 48 kJ at 60 V.

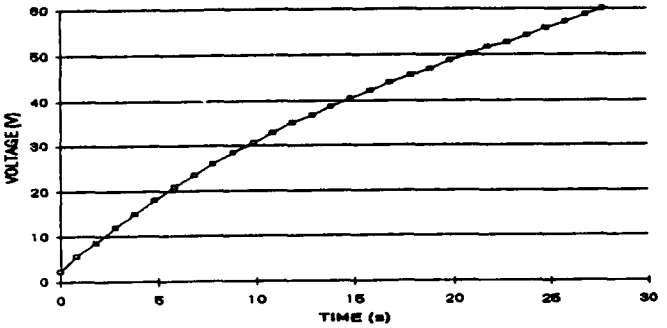

Figure 6. Capacitor voltage vs. time when charged at 50 A in the 60 V setup. The capacitance calculated from this data is 22.5 F.

Figure 7 is a plot of the small-signal impedance data taken at the 120 V setup with a Schlumberger 1260 frequency response analyzer. Measurements are shown over the frequency range 300 uHz to 10 kHz.

Ideal 4.8 F capacitor behavior is exhibited at frequencies below 0.4 Hz. At higher frequencies, the capacitance declines. The observed self-resonance at 1 kHz corresponds to a device inductance of about 5nH. The ESR (resistance at self-resonance) is 0.09 ohms.

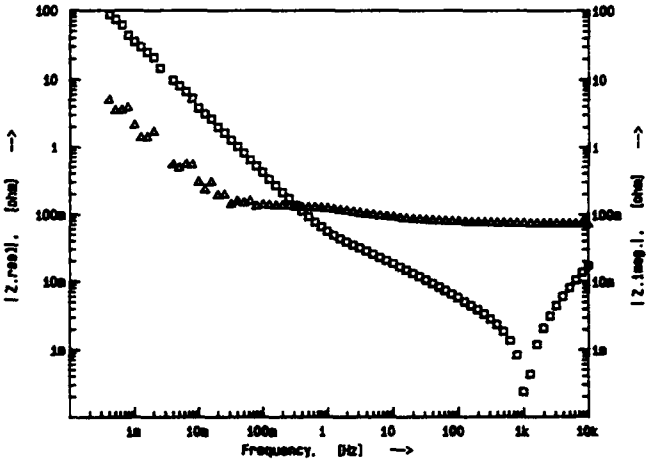

Figure 7. Reactance and resistance vs. frequency in the 120 V setup.

Capacitor power performance was measured using three types of loads--resistance, current sink, and power sink. Test procedures and results follow.

For resistance discharges, a low-inductance, water-cooled "dump" resistor was used. A precision, low-inductance 2000-A-capacity 50 uohm shunt resistor was in the circuit to measure current.

The capacitor was first charged to its setup voltage, usually with 3 A current. The charging supply was then disconnected. Capacitor and shunt voltage connections were made to a 50 MHz dual-channel digital storage oscilloscope, which triggered at switch closing. Delivered power was calculated as the product of the capacitor voltage and circuit current. This procedure eliminated the need to have numerous, high-precision, high-power dump resistors since voltage on the entire load (cables, dump resistor, and shunt resistor) was measured.

Figure 8 shows delivered power versus time for three capacitor discharges. Two were at the 120 V setup and one was at the 60 V setup. An average power of 15 kW was delivered for nearly 500 ms. Many additional discharge tests were conducted using resistance loads, all with comparable results.

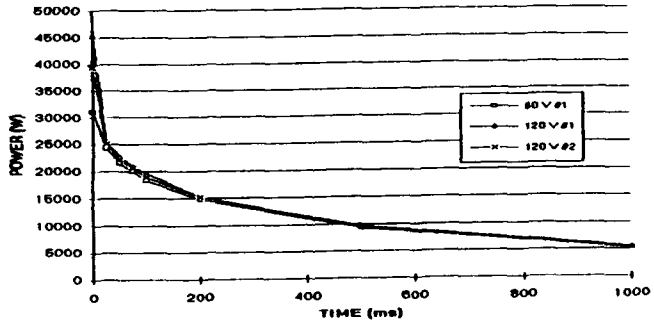

Figure 8. Power performance with resistive loads in the 60 and 120 V setups. More than 15 kW was delivered for the 100 ms time period. An average power of 15 kW was delivered for 500 ms.

The Energy Systems tester located at INEL was used for constant-power discharge testing. It was comprised of a programmable control module, a power absorbing module, and a data acquisition module. The rise-time of the power absorbing module was 10 us (10 to 90% at 500 A). Data was acquired and recorded at 100 ms time increments. Measurement and control resolution were both 0.025% (12 bit). The tester incorporated an on-line calibration system to maintain its accuracy. Two 4/0 cables from the tester were connected to the prototype capacitor for testing. Mr. Ed Martin, under the direction of Dr. Andrew Burke (both of INEL), conducted the capacitor tests. Dr. John R. Miller from JME, Inc. witnessed them.

These results shown in Figure 9 confirm the power potential of the prototype capacitor. Results also show the extraordinarily high power capability of double layer capacitor technology. Consistent results during consecutive discharge cycles were also demonstrated.

The INEL tester was also used to obtain constant-current discharge data. A similar 50 A, 100 s charge to 120 V was used. Power performance for the constant-current discharge tests is shown in Figure 10.

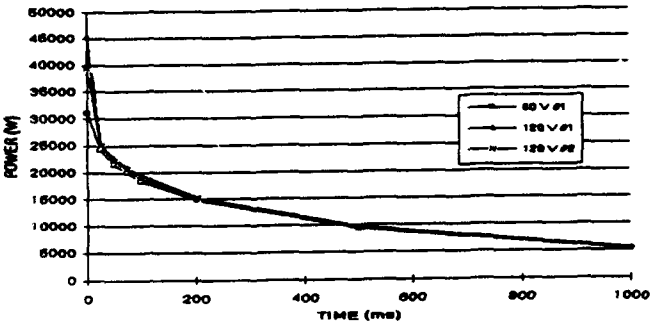

Figure 9. Three consecutive constant-power discharges at 15 kW (120 V setup).

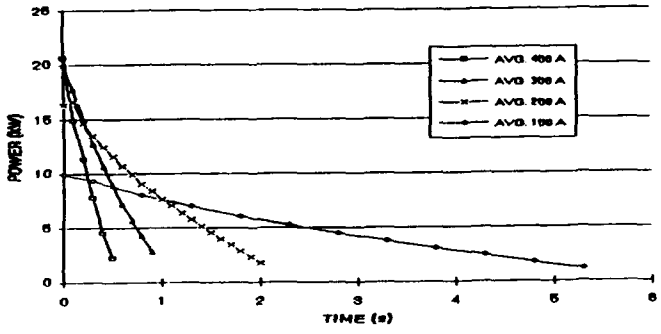

Figure 10. Delivered power during discharges at four current levels from 100 to 400 A (120 V setup).

The equivalent of 128 capacitor cells are series connected in the 120 V setup. Performance problems could occur if any were charged to a voltage higher than 1.22 V. As previously described, careful attention was given to cell stack matching in the prototype capacitor to avoid over-voltage. Balancing resistors were also used to help maintain a uniform voltage distribution along the cell stacks.

Measurements were made to determine the effectiveness of these approaches for establishing and then maintaining cell voltage balance. Figure 11 shows voltage measurements between pairs of terminals obtained after a 3 A charge to 120 V (120 V setup). Voltages appear well-balanced. Each was well below 19 V, the critical potential for electrolysis. The voltage distribution after discharge of the capacitor to 60 V through a 0.5 ohm resistor is also shown. A uniform voltage distribution is evident.

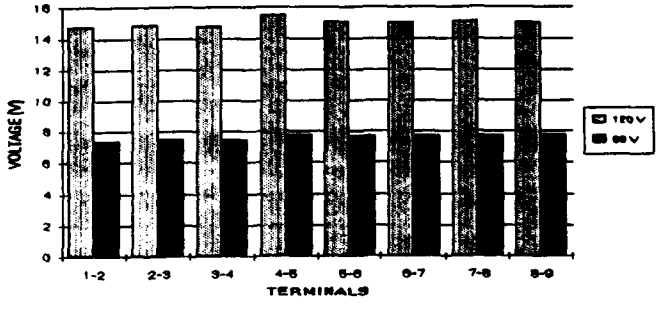

Figure 11. Voltage distribution in the capacitor after a 3 A charge to 120 V (120 V setup). Voltages are given between pairs of terminals. Also shown are voltage measurements after a subsequent 0.5 ohm discharge to 60 V.

The capacitor was made up of 816 1.5 F modules. Each module had eight cells and was individually sealed. Optimization of a large device does not allow the volume or weight required for sealing hundreds of small modules. Redundant packaging and seals could be eliminated by building larger cells. Work is ongoing to design devices with improved energy density. The main effort is to develop higher capacity, large geometric area particulate carbon electrodes. Large increases in energy density would be achievable by reducing the amount of inactive material used for seals and supporting packaging, and incorporating improved carbon electrodes. Designs with at least 60 % volumetric packaging efficiency should be readily attainable. Figures 12 and 13 show the volume and weight fraction of the various materials of construction for the capacitor.

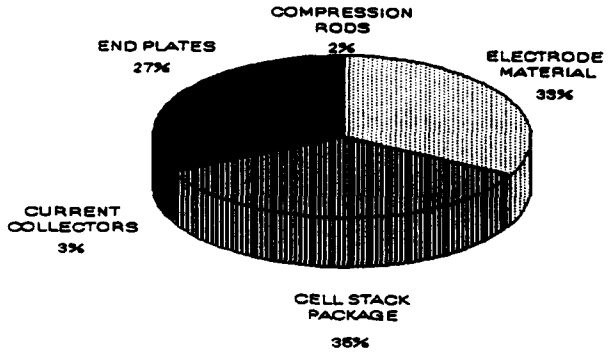

Figure 12. Volume percent of each material used in the prototype capacitor. The electrode material occupied just 33% of the total volume. Larger area capacitor cells would significantly reduce the volume fraction in the cell stack package.

These changes should also reduce the cost of building large devices. In addition to material savings, there should be substantial time and labor savings. These savings are critical to the marketability of these capacitors.

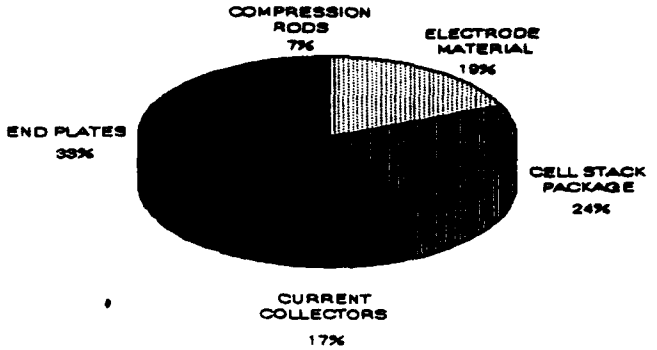

Figure 13. Weight percent of each material used in the prototype capacitor. The electrode material comprised 19% of the total.

Conclusion

It is possible to accurately predict the performance of large DLCs by the application of models based on smaller DLCs. Demonstrating this approach, a 120 V, 5 F capacitor was designed and constructed using models developed for 7.5 V, 1.5 F modules. DLCs with extremely high power performance can be built. The potential exists for significant improvement in energy density.

ELECTROCHEMICAL CAPACITOR VOLTAGE BALANCE:

CELL UNIFORMITY REQUIREMENTS FOR HIGH-VOLTAGE DEVICES

John R. Miller

JME, Inc.
17800 Parkland Drive
Shaker Heights, Ohio 44122

Abstract

This paper presents results from our investigation of cell uniformity requirements for high-voltage electrochemical capacitors (ECs). A lumped-element equivalent circuit model is first derived to simulate the electrical response of a single cell. Complex impedance data is used for this. Then a high voltage EC model is created by series connecting these single-cell circuits. Finally, model performance is statistically evaluated using a Monte Carlo analysis. Both static and dynamical performance is reported. Cell voltages are obtained as a function of the specified tolerances for each element in the single-cell equivalent circuit model.

The presented approach establishes the relationship between cell uniformity specifications and the maximum average cell voltage that a multicell EC can be operated at reliably. This approach can readily be extended to include thermal management specifications.

Introduction

Electrochemical capacitors (ECs) are attractive power sources for many reasons. One is energy density--ECs typically have 10- to 100-times higher values than conventional capacitors. Unfortunately, the operating voltage of an EC cell is low, typically in the 1- to 3-V range depending on electrolyte. Thus, many cells must be series-connected to form a practical device. For example, hundreds of series-connected cells are needed to satisfy the voltage requirements of the electric vehicle (EV) load-leveling application. Consequently, cell-to-cell property and performance uniformity is critically important in order to maintain acceptable voltage balance within the cell-stack.

For reliable EC operation, it is imperative that the voltage on every one of the series-connected cells never exceeds V_C, the breakdown potential of the electrolyte. This must be met under all operating conditions. That is during static situations, where the EC is held at its maximum voltage for extended times, to dynamic operation, where it is rapidly charged or discharged. Consequently, voltage balance must be maintained at all frequencies.

Significant advantages are offered by reducing cell variability and thereby being able to operate it at a higher voltage. For example, if cell variability were reduced so that the average cell voltage could be increased by just 10%, then the energy density of the device would increase by over 22%.

The above energy density calculation was made as follows. A cell-voltage increase of 10% reduces the required number of series-connected cells (each of the same size and rating) by 10%. In other words, 10% fewer cells are needed to obtain the same operating voltage. Thus, EC capacitance will increase by 10% along with the stored energy. But fewer cells are used--the mass of the EC will be 10% lower. Consequently, the resultant energy density increases by a factor of 1.1/0.9 = 1.22 or 22%.

Similar calculations show that a 20% increase in the average cell voltage of a multicell capacitor produces a 50% increase in its energy density!

There are advantages in addition to energy density for operating an EC at the maximum possible average cell voltage. One is reliability. An EC should be more reliable with fewer cells. A second is cost. It should be lower when fewer cells are used. And a third is power performance. EC equivalent series resistance (ESR) will be lower with fewer cells.

Circuit Models

A multicell EC is schematically shown in Fig. 1. It is comprised of N series-connected cells, each obtained from a specified population. The voltage on an individual cell in this string is equal to its impedance times the circuit current. Because the cells do not all have identical impedances, the voltage on each one is different and in fact characteristic of the impedance population.

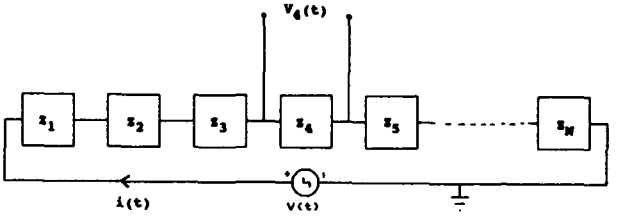

Figure 1: Schematic of a high-voltage electrochemical capacitor. The current i(t) is equal to the voltage V(t) divided by the sum of the cell impedances. The voltage on a cell is equal to i times its impedance.

Fig. 2 is an equivalent circuit model for one of the above cells. It is a five-time-constant ladder network that simulates the distributed resistance and capacitance present in an EC cell. Resistor R_L is established by the leakage current. Resistor R_s is determined by the high-frequency resistance of a cell, i.e. the impedance at self-resonance, or equivalently, by the IR drop during a step-change in current. Other circuit parameters are derived using cell impedance data with a complex-nonlinear-least-squares (CNLS) fitting routine. Collectively, the five-capacitor/six-resistor circuit model can accurately simulate the impedance of one EC cell at all frequencies [1].

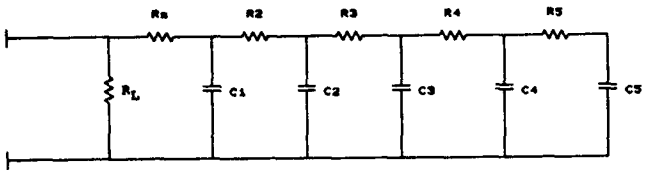

Figure 2: Equivalent circuit model for a single cell. This five-time-constant ladder network is derived using ac impedance measurements.

The above circuit model can be simplified in the limits of low and high frequencies. In the low-frequency or dc limit, all five capacitors in the Fig. 2 circuit model act as open circuits so that the model reduces to a single resistor R_L. In the high frequency limit, the five capacitor elements act as shorts. Then the model reduces to a single resistor R_s. Here, R_s is assumed to be much less that R_L, a condition always met in practical devices.

In summary, a circuit model that is accurate for a typical EC cell in the low- and the high-frequency limits is very simple. It is just one resistor.

Model Results

High- and Low-Frequency Limits

The equivalent circuit model for an EC cell in the low- and high-frequency limits is a single resistor. Consequently, the current flowing in a circuit comprised of N series-connected EC cells is $i(t) = V(t)/(\sum R_x)$. Here, V(t) is the time-dependent voltage applied to the N-cell capacitor and R_x is the resistance value of cell x.

For a large number of cells N, and where the width of the resistance distribution of the cells is small compared to its mean value R_o, the current can be well approximated as $i_o = V(t)/(NR_o)$ [2]. Thus in the low- and the high-frequency limits, the voltage on cell x is equal to $i_o R_x$, where R_x can be either the cell's R_L or R_s. Consequently, the distribution of cell voltage exactly mimics the distribution of cell resistance values in these limits.

Consider the distribution of cell voltages in the multicell EC shown in Fig. 3. Here, $V_a = i_o R_o$ is the average cell voltage and V_c is the critical electrolyte breakdown potential, a value that can cause irreversible performance change in a cell if exceeded.

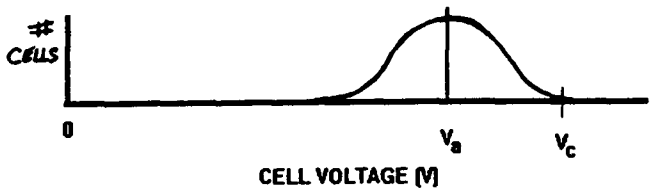

Figure 3: Cell voltage distribution in a multicell electrochemical capacitor. The average cell voltage is V_a and the cell operating voltage limit is V_c, the breakdown potential of the electrolyte.

If cell resistance values (R_s or R_L) are specified to have a tolerance of $\pm$ Y%, then it is imperative that $V_a + (V_a Y/100) \leq V_c$ for reliable operation. Rearranging, $V_a \leq V_c/(1 + Y/100)$ gives the maximum average cell voltage as a function of resistor tolerance. Table 1 lists the maximum allowable cell voltages calculated from this equation for an aqueous electrolyte (V_c = 1.2 V).

TABLE 1: MAXIMUM AVERAGE CELL VOLTAGE FOR AN AQUEOUS ELECTROLYTE

Cell Resistance Tolerance (%)	Maximum Average Cell voltage (V)
5	1.14
10	1.09
20	1.00
30	0.92
40	0.86
50	0.80

As listed in the table, the maximum average cell voltage is 1.00 V for a distribution of cells having a resistance tolerance of $\pm$ 20%. Average cell voltage decreases to 0.92 V for a tolerance of $\pm$ 30%. And with a tolerance of $\pm$ 50%, the maximum average cell voltage is 0.80 V.

EC operating reliability can be estimated at a given average cell voltage if resistance tolerances are further specified. For example, if 99.9% of the cell resistors meet a $\pm$10% tolerance, then 0.1% could be outside this range. Therefore in a 300-cell EC operating at the maximum average cell voltage listed in the Table, approximately 300 X 0.001/2 = 0.15 cells in the string will have voltages greater than V_c.

Consequently, every sixth 300-cell EC, on the average, potentially will have a serious flaw, i.e. a "bad cell." In other words, ~16% of the ECs assembled from such a population of cells may fail during either dc or high-frequency operation if operated at the calculated maximum average cell voltage of 1.09 V.

As a second example, successful operation of an aqueous EC at an average cell voltage of 1.0 V requires a cell resistance tolerance of 20%. Assuming that the cell resistance populations are normal (Gaussian) and that tolerances are set at the 99.9% level, then the required standard deviation for the resistance values is 20/3.29 = 6.1%. (3.29 standard deviations includes 99.9% of the area under a normal curve.)

Thus R_L and R_s in this example, if normally distributed, need to have a standard deviation of less than 6.1% in order to provide reliable operation of an aqueous EC at an average cell voltage of 1.00 V in the dc and the high-frequency limits. For operation at an average cell voltage of 1.10 V, the corresponding standard deviation in resistance values is 2.7%. These may need to be reduced further, as mentioned before, to permit acceptable manufacturing yields.

Intermediate-Frequency Region

Voltage-balance determination at intermediate frequencies is more complicated than at the limits. Here the complete circuit model (Fig. 2) is needed to accurately describe the dynamical response of an EC. Variability in each circuit element will affect the cell voltage in some very complicated manner. For example, one cell in a series string may experience above-average voltage when charged at one rate and below-average voltage when charged at a different rate, depending on the exact values of its circuit elements from the specified distributions.

The cell voltage distribution at intermediate frequencies was statistically determined using a Monte Carlo approach. This involved creating a multicell circuit using elements randomly selected from the specified populations. Then this circuit was analyzed

to obtain the voltage on a single cell. Next, another multicell circuit was randomly generated and analyzed to obtain a second voltage value for the cell. This sequence was repeated numerous times to establish the distribution of cell voltages for the EC.

The Monte Carlo approach is demonstrated using the single-cell circuit shown in Fig. 4 as the "building block." Cell circuit elements were derived using impedance data from a 53-F, 0.012-ohm-ESR, single-cell, aqueous electrolyte, double layer capacitor.

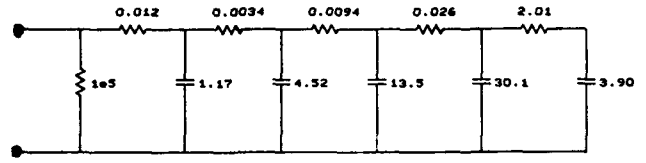

Figure 4: Single-cell circuit model used to perform the Monte Carlo voltage distribution analysis. This model was derived using impedance data from a 53 F prototype capacitor. The listed values are in Farads and Ohms.

Four separate situations are analyzed. The first examines influences on the cell voltage distribution due to variability in the ESR. Here all circuit elements except R_s are held fixed. The second examines influences due to variability in all of the resistor elements. The third examines influences due to variability in all of the capacitor elements. And the fourth examines influences due to variability in all of the circuit elements collectively.

In each situation, the distribution of values for the circuit elements was assumed to be normal. A 20% tolerance at the 99.9% confidence level was selected for this example. High confidence in the simulation data was developed by evaluating 500 individual randomly-generated circuits for each of the four situations.

Simulations were performed by applying sinusoidal voltage waveforms to the multicell EC. The corresponding average signal amplitude on each cell was 0.25 V.

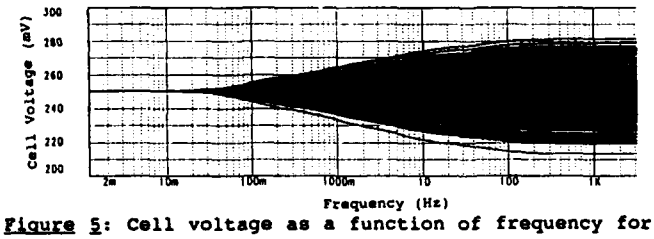

Figure 5: Cell voltage as a function of frequency for a multicell EC comprised of Fig. 4 cells. The average cell voltage is 0.25 V. Data from 500 simulations are shown. Only ESR has variability. It is characterized by a normal distribution with a ±20% tolerance at the 99.9% confidence level. For this EC, the high-frequency limit is reached at ~100 Hz.

Fig. 5 shows the cell voltage for the first situation where only ESR variability exists. If R_s had been fixed in these simulations, then the cell voltage would have been 0.25 V at all frequencies. As shown in the figure, ESR variability has a progressively greater effect as the frequency is raised above ~50 mHz (charge/discharge times of ~10 s or less). From the simulations, it is evident that the capacitor reaches its high-frequency limit at ~100 Hz. At frequencies above this value, the width of the cell voltage distribution is constant and at a value consistent with the analytical results obtained in the high-frequency limit.

Fig. 6 shows cell voltage versus frequency in the situation where all circuit resistor elements have variability. The width of the voltage distribution is greater than seen in Fig. 5. As previously shown, a distribution in the resistances primarily creates voltage variability in the high-frequency region.

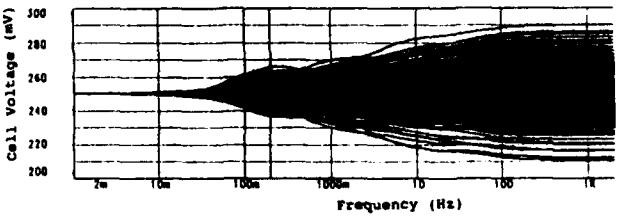

Figure 6: Cell voltage versus frequency for 500 simulations. Resistance values were randomly selected from normal distributions having 20% tolerance limits at the 99.9% confidence level. Capacitance values are fixed. The mean cell voltage was 0.25 V.

The influence of capacitance variability on the cell voltage distribution is shown in Fig. 7. The low-frequency region is affected predominantly here. The width of the cell voltage distribution increases progressively as the frequency is reduced, reaching a maximum value at ~20 mHz (~25 s charge or discharge times).

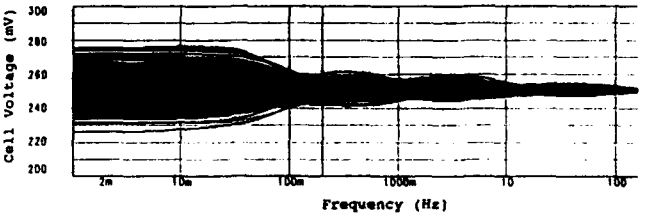

Figure 7: Cell voltage as a function of frequency in the multicell EC having an average voltage of 0.25 V. Each of the five capacitor elements has variability, characterized as normal distributions with 20% tolerances at the 99.9% confidence level.

Every circuit element has variability in the Fig. 8 simulations. The width of the cell voltage distribution is greatest at high frequencies. The minimum width of the voltage distribution is in the region ~90 mHz to ~500 mHz.

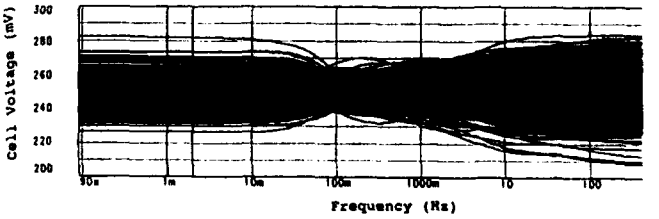

Figure 8: Cell voltage versus frequency for a multicell EC. The average cell voltage is 0.25 V. Voltages for the 500 trials show the collective influence of variability in all circuit elements. Element values have normal distributions with means given in Fig. 4 and tolerances of 20% at the 99.9% confidence level.

The simulation trials shown above can be further analyzed to quantify the cell voltage distribution. Histograms of cell voltages for the case where all circuit elements have variability are shown in Fig. 9. Results are given for three frequency bands, 0.01 to 0.02 Hz, 0.1 to 0.2 Hz, and 1 to 2 Hz. The mean of each distribution is very close to 0.25 V, the value expected. Standard deviations for each band are

respectively 0.0077 V, 0.0055 V, and 0.0077 V. The maximum observed voltages in each band are similar and equal to approximately 0.27 V.

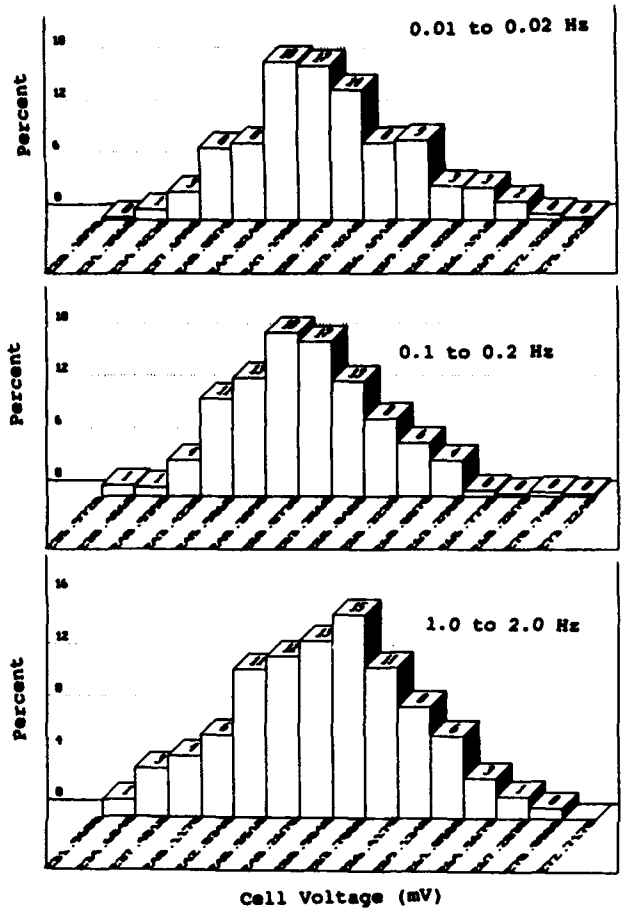

Figure 9: Cell voltage histograms in three frequency bands obtained via Monte Carlo simulations of a multicell EC (Fig. 8 data). The average cell voltage was 0.25 V. All circuit elements have variability characterized by normal distributions and 20% tolerance limits at the 99.9% confidence level.

A Monte Carlo transient analysis simulation was also performed on the same multicell EC for the situation where all circuit elements have variability. Here, the average cell voltage was ramped linearly from 0.5 V to 1.0 V in 30 s followed by a linear decrease to 0.5 V in 10 s. Fig. 10 shows the voltage-time results for the 500 trials.

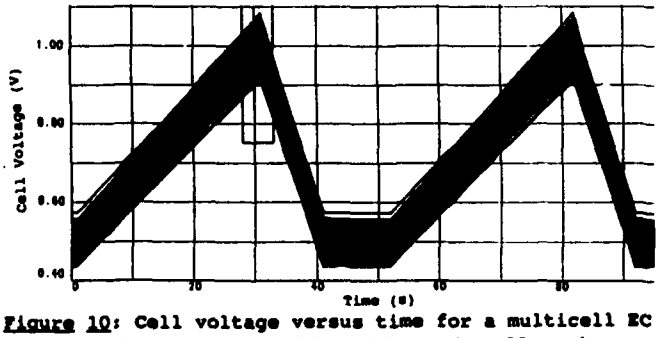

Figure 10: Cell voltage versus time for a multicell EC formed using Fig. 4 cell models and a 30-s charge, 10-s discharge waveform. Each circuit element had variability characterized by a normal distribution with 20% tolerance limits at the 99.9% confidence level. The average peak cell voltage was 1.0 V.

A histogram of peak cell voltages for the above simulation is shown in Fig. 11. The mean of the distribution was 1.004 V, the standard deviation was 0.029 V, and the maximum cell voltage was 1.084 V.

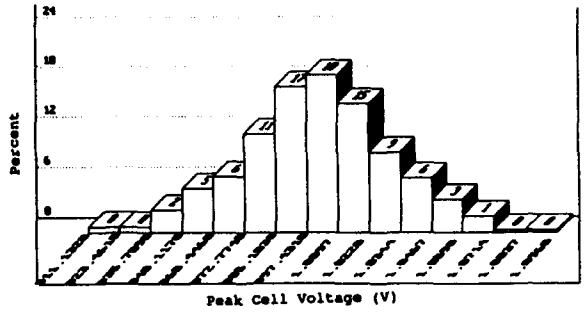

Figure 11: Histogram of peak cell voltages obtained for a 500-trial Monte Carlo transient analysis simulation of a multicell EC. The average peak cell voltage was 1.00 V. The maximum cell voltage observed in the simulations was 1.084 V.

Discussion

The distribution of cell voltages in a multicell EC depends on the distribution of cell impedances. Because the cell impedance is complex, the voltage distribution will be frequency dependent. Results from this study show that the width of the cell voltage distribution is greatest at the high- and low-frequency limits. Thus, voltage imbalance situations are most problematic during high-rate charging or discharging and during constant-voltage conditions.

The above conclusion is based on three assumptions. First, elements in the circuit model of a cell are independent random variables. Second, they all fit a normal distribution. And third, their tolerances are identical. For a specific multicell EC, the population of cells used to assemble it must be characterized and used to establish the actual distributions of circuit element values. Then in using the described approach, the maximum average cell voltage for reliable EC operation can be accurately determined.

This approach should also be useful for establishing thermal management specifications in large, multicell ECs. EC properties and performance are strongly dependent on temperature [1]. Thus, thermal gradients may create voltage uniformity problems even if every cell is identical. Temperature coefficients can be determined for each element in the equivalent circuit model of a cell and used in Monte Carlo simulations. Thus, temperature as well as cell property uniformity requirements can be established.

Acknowledgments

This work was supported in part by the DOE under EG&G Idaho, Inc. contract number C93-170332.

References

[1] J.R. Miller, "Performance of Mixed Metal Oxide Pseudocapacitors: Comparison with Carbon Double Layer Capacitors," Proc. 2nd Int. Seminar on Double Layer Capacitors and Similar Energy Storage Devices, Deerfield Beach, FL (Dec. 7-9, 1992).

[2] see for example, Chapter 6 "Functions of Random Variables" in Probability and Random Processes: An Introduction for Applied Scientists and Engineers, by W.B. Davenport, McGraw-Hill, (1970).

OPTIMIZATION OF FABRICATION PARAMETERS FOR CARBON-BASED CHEMICAL DOUBLE LAYER CAPACITORS

W. T. Owens, M. F. Rose, C. Johnson, and B. Stephens
Space Power Institute
231 Leach Center
Auburn University, AL
(205) 844-5894, FAX 844-5900

Abstract

Chemical double layer capacitors have high energy densities compared to electrolytic capacitors and high power densities compared to batteries. These properties make CDL capacitors applicable to various applications such as load leveling in electric vehicles. Some shortcomings of carbon-based CDL capacitors are relatively high equivalent series resistance, pressure requirements, and difficulty in maintaining uniformity. Auburn composite electrode technology, which is described within, addresses all of these problems. Some of the routes taken towards optimum processing conditions and composite electrode formulations will also be discussed.

Introduction

The history, fundamentals, and general uses of chemical double layer (CDL) capacitors have recently been reviewed[1,2,3]. CDL capacitors possess much higher energy densities than electrolytic capacitors and their power densities outstrip batteries by orders of magnitude. Furthermore since CDL energy is a physical phenomenon, the number of charge-discharge cycles is not limited by factors normally affecting rechargeable batteries. Carbon-based CDL capacitors do have some shortcomings. Namely the equivalent series resistance (ESR) is relatively high, pressure is required to maintain physical contact between high surface area carbon particles[1,2], and uniformity is difficult to obtain (as evidenced by in-house characterization of purchased CDL capacitors). Auburn composite electrode technology addresses all of these problems.

Specifically these composite electrodes consist of a dispersion of high surface area activated carbon fibers within a bonded conductive metal fiber network. The metal fiber network serves as an extension of the foil, to which it is bonded, into the charge storage medium. The result is low ESR and no pressure requirement for operational capacitors. Electrode preforms are made by combining metal and carbon fibers with a suitable binder using a conventional paper-making process which yields homogeneity and uniformity both within sheets and from one sheet to the next. Since paper production is a well established art, the transition from laboratory scale to plant scale production would be relatively smooth. Another advantage to this technology is the ability to tailor the electrodes to particular power or energy densities as demanded by an application. This is accomplished primarily through selection of electrode formulation (i.e. carbon:metal:binder ratio) but care must be taken not to adversely affect the carbon during the sintering process which is required to bond the metal fibers to one another and to foils. This paper describes methods used to determine electrode formulations for maximum energy densities while maintaining low ESR as well as the procedures used to produce finished electrodes without degradation of the active carbon.

Experimental

Materials

Chopped activated carbon fibers (2 mm length, 8 μm diameter) with surface area ca. 1500 m^2/g were obtained from Federal Fabrics. The cellulose binder was a cotton based ashless paper (Whatman). Chopped nickel fiber (2 mm length, 2 μm diameter) was purchased from Ribtec. Airco provided argon (99.997%) and hydrogen (99.95%), which were used without additional purification. Electrolyte, 6.1 M KOH, was prepared from a 45% solution (Fisher Scientific) using distilled water as a diluent. Nickel foil (13 μm thick) was acquired from Fine Metals.

Preform Fabrication

Particular carbon-metal-cellulose formulations were selected and appropriate amounts of each component were blended together until homogeneous. Sheets of approximately 20x20 cm were made using an Adirondack sheet mold. All of these operations were carried out using distilled water to limit ion contamination. Disks 0.57 cm in diameter were punched out of sheets, aligned on foils, sandwiched between fused silica plates and held in place with fused silica clips.

Sintering

Clipped assemblies were lowered into a 10 cm ID fused silica reactor tube which was heated with an ATS tube furnace. After purging, various steps were implemented as will be detailed below. The reactor was equipped with a K-type thermowell inserted axially to locate the tip at the center of the region where the samples were placed. This provided more reliable local temperatures than the furnace thermocouples which were external to the reactor tube and in fact closer to the heating elements than to the center of the flowing reactant stream. Gas flow rates were determined and controlled with calibrated rotameters. Total flow rates (except during purging periods) were set at about 500 ml/min (STP) which corresponds to a linear flow rate of about 6.2 cm/min. All reactions were carried out at atmospheric pressure.

Electrode Characterization

Finished electrodes were impregnated with electrolyte and assembled in pairs with ion-permeable polymer separators. This assembly was positioned between two nickel plates which served as the electrical connections. Sample capacitors of this type were then charged under a

potential of 0.98-1.02 V for two minutes followed by discharge into a known load. Charge-discharge cycles were monitored with a Lecroy 9450a oscilloscope. Waveforms were downloaded and analyzed to determine capacitance, ESR, energy, etc. After a series of tests, the samples were weighed to allow calculation of the gravimetric energy density and specific capacitance.

Results and Discussion

Sintering Procedures

Bonding of metal fibers to one another and to the foil is critical to formation of the conductive network which reduces ESR and also provides mechanical strength to the resultant electrodes. Sintering basically involves the use of thermal energy to accelerate diffusion processes which cause bonding at every metal-metal contact. Initial work involved the use of hydrogen to remove surface oxides which tend to impede sintering[4,5]. Hydrogen also promotes gasification rather than pyrolysis of cellulose and, of course, would tend to reverse the oxidation of metals which could occur by reaction with certain cellulose gasification products. Unfortunately many metals catalyze hydrogasification of carbon at metal sintering conditions. In fact hydrogasification of amorphous carbon can occur below typical sintering temperatures of nickel without the presence of a catalyst. In either case surface area and thus charge storage area would be lost. One approach for reduction of carbon losses from gasification was to adjust sintering temperatures to take advantage of the difference in activation energies of diffusion and catalyzed gasification, which has been illustrated with electrodes containing stainless steel[6,7]. This procedure involved a room temperature purge followed by immersion of the reactor into a hot furnace. The approach taken here, however, was to break the procedure into additional steps in order to completely prevent hydrogen induced carbon damage rather than reducing it.

Procedure 1 includes three steps, namely purging, drying, and sintering. The drying step was added based on evidence that, in the presence of nickel, hydrogen-water mixtures more readily gasify graphite than either component alone[8]. Addition of the drying step had little impact on the total time of the reaction sequence since it was actually incorporated by heating to 200°C during a portion of the purging step required to remove oxygen prior to addition of hydrogen to the reactor. Following the drying step hydrogen (1% H_2/Ar) was admitted and the reactor temperature was increased to a sintering temperature of 1050°C. Data from electrical characterization of samples made using procedure 1 and other procedures are listed in Table 1. Since complete gasification of cellulose would leave a void to be filled with electrolyte, the second procedural adaptation, labeled procedure 2 included a 500°C pyrolysis step carried out in the same argon flow used during drying. Pyrolysis was followed by a sintering step with 1% H_2/Ar. The rationale was that the potential void could be left filled with a carbonized cellulose fiber which would provide a modest addition to the charge storage surface area. Table 1 indicates that this pyrolysis step, while affecting the specific capacitance in only a limited fashion, resulted in significantly lower energy density as compared with the previous procedure.

Table 1. Evaluation of Sintering Procedures.

procedure number	Voltage V	Spec. Capac. F/g carbon	ESR Ω	Energy J/g	Density Wh/kg
1	1.01	139	0.06	4.22	1.17
2	1.01	143	0.05	3.89	1.08
3	1.01	116	0.09	5.02	1.39
4	1.01	175	0.05	6.01	1.67
5	1.02	190	0.04	6.36	1.77

There seemed to be little to gain from use of pyrolyzed cellulose and some question about the fate of the cellulose pyrolyzation products. Specifically if any of these products were relatively high molecular weight hydrocarbons then the potential existed that these molecules would adsorb and remain on the active carbon under these conditions. It was also possible that these species would pyrolyze rather than volatilize as the temperature was raised during the actual sintering step. This would result in loss of charge storage area especially if pore openings were blocked.

The next change in procedure was the addition of 5% hydrogen to prevent pyrolysis of cellulose and to promote formation of low molecular weight cellulose gasification products which would be less likely to adsorb on the activated carbon at these temperatures. This procedure, labeled 3, also eliminated hydrogen from the sintering step altogether. Inclusion of hydrogen at 500°C should be sufficient to remove surface oxides from nickel, and since cellulose was removed no hydrogen was necessary during the sintering step to reverse oxidation of metal by gasification products. Procedure 3, in summary, includes a purging/drying step, a cellulose elimination/metal reduction step, and an argon sintering step. As Table 1 shows, these changes further enhanced the energy density while the specific capacitance decreased. The capacitance decrease was probably caused by active carbon surface area reduction due to cellulose gasification products as explained above. The greater energy density suggests that elimination of cellulose, as opposed to pyrolysis, was favorable. This was understandable in light of the fact that the interstices between fibers were never completely filled with electrolyte so leaving them filled with relatively low surface area carbonized cellulose was paramount to adding dead weight.

Procedures 4 and 5 involved the use of successively larger concentrations of hydrogen during the cellulose elimination/metal reduction step for the purpose of further promoting the formation of low molecular weight cellulose gasification products. The data in table 1 show that this approach was successful. In fact the specific capacitance improvements support the idea that cellulose gasification products can lead to loss of surface area. Further work should be done to refine the temperatures and duration used for each step.

Generally comparisons of sintered and unsintered samples show that, while sintering improves ESR and energy density (due to better utilization of carbon and removal of cellulose), the specific capacitance always decreases due to some degradation of the carbon. The data in Table 2 seem to indicate that procedure 5 improves the carbon. It is possible the improved capacitance might be due to improved utilization of the carbon allowed by the conductive network. Nonetheless this illustrates that this reaction sequence is certainly not detrimental to the carbon. Also note the vast improvement in ESR and concomitant

increase in energy density afforded by the conductive network.

Table 2. Comparison Between Sintered and Unsintered Electrodes.

Sample number	Voltage V	Spec. Capac. F/g carbon	ESR Ω	Energy J/g	Density Wh/kg
48 sintered	1.01	187	0.10	6.27	1.74
unsintered	1.01	134	0.83	5.02	1.39
59 sintered	1.01	152	0.05	6.32	1.76
unsintered	1.01	103	0.80	4.92	1.37

Preform Formulation

Effect of Cellulose: A carbon:metal ratio of 6:1 was chosen to study the effect of cellulose content on the performance of finished electrodes. Sheets with cellulose contents of 1-30% by weight were made, and electrodes were fabricated using procedure 5 discussed above. As shown in Figure 1, cellulose content did not appear to dramatically effect energy density at levels from 5-20%. Above 20% two effects were probably detrimental. First, greater void volume was left when cellulose was gasified, and to the extent that the voids were filled with electrolyte greater device masses and lower energy densities resulted. The second effect was that with larger amounts of cellulose greater quantities of gasification products were formed and could have potentially resulted in reduction of activated carbon surface area by surface fouling as detailed above. Interestingly at the lowest cellulose content tested, namely 1%, the energy density was a bit low. The cellulose binder was necessary to ensure metal-metal contacts. With reduced contact there was reduced bonding which led to an inferior conductive network and inefficient utilization of active carbon area. The cellulose content should probably remain in the range of 2-10% for best carbon utilization and minimal degradation of carbon.

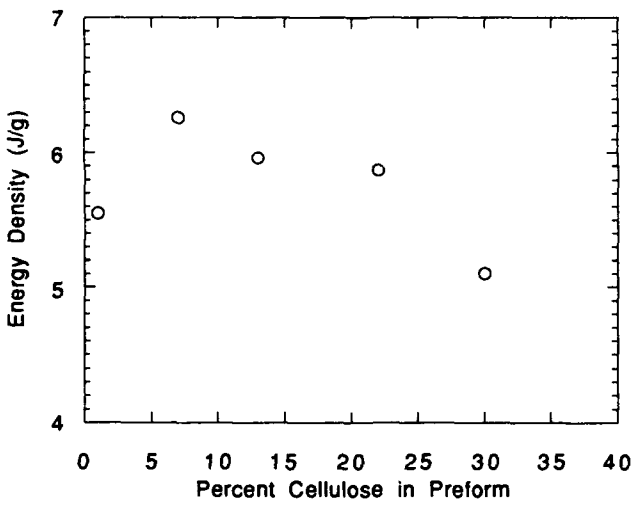

Figure 1. Effect of Cellulose Content of Electrode Preforms.

Carbon:Metal Ratio: With cellulose content in the range specified above, formulations were chosen to study the effect of the carbon:metal ratio. Sample electrodes were made according to procedure 5 detailed above. The results shown in Figure 2 indicate that lower percentages of carbon result in lower energy densities as expected. When the metal content was too low the energy storage capability of the carbon was not realized and again the energy density was low. It appeared that the optimal ratio of carbon to metal for maximum energy density was in the range 85-90%. It should be noted that higher metal content will generally result in lower ESR and higher power densities. The metal-carbon formulation can be manipulated to tailor capacitors to various power or energy density specifications as demanded by a given application.

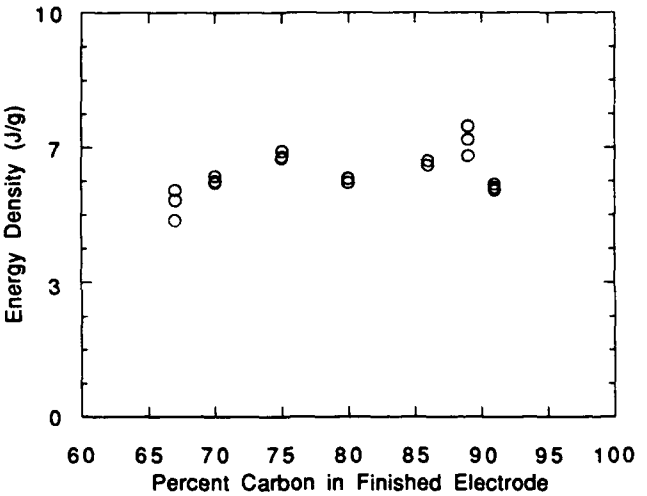

Figure 2. Effect of Carbon to Metal Ratio.

Conclusions

A reaction sequence can be used to prevent rather than simply reduce hydrogen-induced degradation of the active carbon charge carrying substrate.

Cellulose content should remain in the range of 2-10% for maximum energy densities.

The carbon content relative to metal should lie in the range 85-90% to maximize energy densities.

Acknowledgements

This research was funded by the U.S. Department of Energy through Maxwell Laboratories, Inc. under subcontract number MLS-CR92-1098.

References

(1) M.F. Rose, *Proc 33rd Int. Power Sources Symp.*, Cherry Hill, NJ, USA, 1988, The Electrochemical Society, Pennington, NJ, USA, pp. 572-592.

(2) M.F. Rose, C. Johnson, W.T. Owens and B. Stephens, J. Power Sources, **47**, 303, (1994).

(3) A. Yoshida, K. Imoto, H. Yoneda and A. Nishino, IEEE Trans. Comp. Hybr. Man. Tech, **15**, 133.

(4) D. Kohler, J. Zabasajja, A. Krishnagopalan and B. Tatarchuk, J. Electrochem. Soc., **137**, 136 (1990).

(5) B.J. Tatarchuk, M.F. Rose, A. Krishnagopalan, U.S. Patent 5,102,745.

(6) B.J. Tatarchuk, U.S. Patent 5,096,663.

(7) D. Kohler, J. Zabasajja, M.F. Rose and B. Tatarchuk, J. Electrochem. Soc., 137, 1750 (1990).

(8) R.T.K. Baker and R.D. Sherwood, J. Catal., 20, 198, (1990).

Optimization of Carbon Fibers Used in Electrochemical Capacitors for Electric Vehicle Applications

C. J. Farahmandi, Ed Blank, Deborah Hileman, John Dispennette, Karl Lambert
Maxwell Laboratories, Inc.
1500 Pumphrey Avenue
Auburn, AL
(205) 821-4366

Introduction

Double layer capacitors (DLCs) are energy storage devices that have gained acceptance in recent years. Their energy and power density make them attractive for applications whose performance requirements fall between traditional electrostatic capacitors and rechargeable batteries. They store more energy per weight than traditional capacitors, and they discharge the energy at a higher power density than rechargeable batteries. The cycle life of these devices exceeds that of any rechargeable battery system because of the highly reversible nature of charge adsorbed in the double layer. Charge/Discharge cycles of 300,000 times have been reported.[1]

An application for DLCs that has recently drawn attention is the use of these devices to level the load of batteries in electric vehicles.[2] This would reduce the peak power requirements of the batteries and allow them to be designed for higher energy density and longer cycle life. In the spring of 1992, Maxwell Laboratories was awarded a multi-year development contract by the Department of Energy (DOE) and EG&G Idaho to develop high-energy-density, high-power-density electrochemical capacitors. The goal of this contract is to manufacture devices that meet the DOE design specifications for a load leveling device in an electric vehicle. The performance criteria for this device are the delivery 5 Wh/kg with a power rating of 600 W/kg. The capacitor must also have an overall charge/discharge efficiency of 90% and a useful life of over 100,000 discharge cycles. Maxwell's technical approach is to develop bipolar double layer capacitors using high-surface-area carbon fiber electrodes. This bipolar capacitor stack will operate at 350 V and stores 1.8 MJ of energy.

Early in this contract two design approaches were adopted. The first uses an aqueous solution as the solvent for the electrolyte. Because of the high ionic conductivity of aqueous based solutions, capacitors employing these solutions tend to have low equivalent series resistances. However, the operating voltage of these solutions is typically below 1.0 volts, which limits the amount of energy that can be stored in these devices. The second design uses an organic solvent to dissolve the electrolytic salt. Capacitors made from these solutions can operate at a higher cell voltage, and thus they can store more energy. A lower ionic conductivity, however, increases the equivalent series resistance.

Both the aqueous and organic designs use high-surface-area carbon fiber in the electrodes. This material was chosen because of its high performance, availability, and relative low cost. Porous carbon has been recognized as a high performance material for DLCs since the first units were developed.[3] Early designs used activated carbon paste electrodes.[4] These electrodes were made from a slurry of activated carbon powder and the electrolytic solution. These electrodes had to be held under high pressures to overcome contact resistance between carbon particles. The high pressure is acceptable for small electrodes, but, as the electrodes are scaled to larger sizes, the packaging pressure increases dramatically. Because of the size of the capacitor being developed for the electric vehicle application, this approach is unacceptable. Maxwell has been developing metal/carbon composite electrodes that reduce the packaging pressure and internal resistance. These improvements are accomplished by reducing the number of carbon-carbon contacts that current must flow through to reach highly conductive metal directly connected to the current collector. Maxwell's main approach utilizes a sintered carbon/metal electrode.

In addition to reducing the internal resistance in the capacitor, the electrode must posses a high capacitance. The capacitance is determined by the characteristics of the carbon fiber. The surface area, density, pore volume, and pore diameter of the fiber may all change the performance of the capacitor. Results may also vary widely depending on which electrolytic solution is used. Cost is also an important factor when selecting a fiber for a DLC. The fiber price increases dramatically as the surface area per mass increases. It is important to determine which fiber provides the optimum performance from a cost perspective. This paper summarizes a study that was undertaken at Maxwell Laboratories to find an optimum carbon fiber for both the aqueous and organic electrolyte designs. Four carbon fibers of varying physical characteristics were examined for performance when employed in a sinter-fused composite electrode. The optimum fiber for both electrolytic solutions is identified. A comparison between capacitors made with the organic and aqueous electrolytes is also made in relation to the program goals.

Work supported by the U.S. Department of Energy, under INEL EG&G Idaho , Subcontract #C91-103647.

Experimental Methods

Capacitor Fabrication

The carbon fibers examined in this study were tested in sinter-fused carbon/nickel composite electrodes. This fabrication process has been described in detail elsewhere.[5,6] Briefly, electrodes were fabricated by first creating paper-like electrode precursors consisting of a mixture of carbon, nickel, and cellulose fibers. Presintered electrodes were cut from these paper sheets, pressed against nickel foil, and run through a two stage heating process that sinter-fuses the nickel fibers to themselves and to the nickel foil. This process greatly reduces the number of carbon-carbon contacts current must flow through to reach a metal fiber that is connected directly to the current collector. Thus, the resistance of the device is reduced. The carbon fibers used for this study were approximately 9 μm in diameter and 3 mm in length. The nickel fibers were 2 μm in diameter and 3 mm in length, and the cellulose fibers were 8 μm in diameter and 5 mm in length.

Capacitors made for this study consisted of two sinter-fused composite electrodes of approximately 20 cm^2 surface area and 0.028 cm thickness. An ionic separator was placed between the two electrodes. The composite electrodes and cell separator were vacuum impregnated with the electrolytic solution. The assembled capacitor was then placed into a cell holder which sealed the device. Figure 1 shows a diagram of the capacitor and cell holder.

Testing Methods

Once the capacitors were fabricated and assembled in the cell holders, the equivalent series resistance and capacitance were measured. The series resistance was determined from the initial voltage drop during constant current discharge. Determination of capacitance was not as straightforward as that of the resistance, because the charge delivered by a DLC can vary, depending on the rate of discharge. Often the voltage dropped more quickly than expected during a rapid discharge; if the capacitor was allowed to stand after discharge the voltage recovered to the expected level. To help quantify this effect two different techniques were used to measure the capacitance.

The first technique was designed to measured the total charge stored in the capacitor. This measurement was accomplished with a potential step test. In this test, the capacitor was charged to full voltage. Then it was subsequently discharged through a 1.0 ohm resistor, with a potential step from the initial voltage down to zero volts. As the capacitor discharged into the resistor, the current was measured and integrated to obtain the charge. The discharge was allowed to continue for ten minutes, and the capacitor was then left at open circuit so the voltage could stabilize. After several hours, the final voltage was recorded. The voltage recovered was subtracted from the initial voltage; then the capacitance was calculated.

The second method of measuring capacitance was designed to more closely represent the electric vehicle application. In this test, a constant current charge/discharge cycle at 50 mA/cm^2 was used to measure the capacitance. This method counts only the charge that is available for rapid utilization. The test consisted of a constant current charge followed by a rest period, then a constant current discharge. Both the charge and discharge were conducted at 50 mA/cm^2. The rest period was one third of the charge time. The capacitance was calculated from the slope of the voltage response. This test method is the more important of the two for determining performance in the electric vehicle application. For this application, only the charge that is available for rapid, continuous cycling is important. The potential step test does, however, provide important information about the total charge stored in the capacitor.

Results

Carbon Fiber Density

Four types of activated carbon fiber with varying physical characteristics were used in this study. The characteristics of the fibers are shown in Table 1. It can be seen that as the surface area increases, the pore radius and pore volume dramatically increase. This relationship suggests that the fiber density is dropping and that some of the increase in surface area is due solely to changes in fiber density arising from an increasing fiber porosity. From the pore volume data, the fiber density and porosity can be calculated.[7] The fiber porosity (ε_f) is defined as:

$$\varepsilon_f = \frac{\text{pore volume}}{\text{total fiber volume}} = \frac{mV_f}{mV_f + m\left(\frac{1}{\rho_s}\right)} = \frac{V_f \rho_s}{V_f \rho_s + 1}$$

where:
m = mass of the fiber
V_f = pore volume of the fiber
ρ_s = density of solid carbon --assume to be 1.8g/cm^3

The fiber density (ρ_f) is calculated from:

$$\rho_f = \frac{\varepsilon_f}{V_f}$$

Figure 2 shows how the fiber density decreases with increasing surface area. Also shown is the surface area on a volume basis. This surface area remains relatively constant as the surface area increases on a mass basis.

Table 1

Physical Characteristics of Carbon Fibers

Fiber	Surface Area (m^2/g)	Pore Radius (Å)	Pore Volume (ml/g)
GF10	1,000	9	0.22
GF15	1,500	12	0.5
GF20	2,000	16	0.75
GF25	2,500	22	1.2

Aqueous Electrolyte Results

The results of the aqueous electrolyte tests are shown in Figure 3. The potential step test measured consistently higher capacitance than the constant current test. This result is obtained because a fraction of the total capacitance is not available for rapid discharge. The higher surface area carbons had a higher capacitance. However, these performance gains are negated by the fact that the high surface area fibers have a lower fiber density. This relationship leads to thicker electrodes that require more electrolytic solution. Given that the high surface area carbon fibers cost many times more than the low surface area fibers, it will be more cost effective to use the low surface area carbon with this design.

Organic Electrolyte Results

The organic electrolyte test results are shown in Figure 4. These results differ dramatically from the aqueous electrolyte tests. First, there is not a large difference in capacitance between the voltage step test and the constant current tests. This shows that a larger fraction of the charge is available for rapid discharge with this electrolyte. Figure 4 further shows that there is a dramatic increase in performance with increasing surface area. The aqueous electrolyte capacitors did not show this dependence. The reason for the large increase may be due to a dependence on pore radius. The organic electrolyte may not be able to enter a small pore. A stronger dependence on pore radius would be expected, because larger molecular weight salts are used to compensate for the poorer solvation power of the organic solvents. Large electrolytic salts cannot enter small pores. It can be concluded from these tests that the highest surface area carbons should be used with the organic electrolyte design.

Conclusions

The ultimate goal of this research project is to meet the design requirements of the DOE's electric vehicle program. From the data gathered for this paper, a comparison between the two studied electrolytic solutions can be made. Figure 5 is a Rygone plot of the two candidate designs for electric vehicle applications. It should be noted that, while the aqueous electrolyte data for this plot were taken from capacitors using the nickel composite electrodes, the organic electrolyte capacitors were not. The optimal high surface area carbon fibers were still used; however, instead of a nickel sinter-fused electrode structure, these capacitors employed an aluminum/carbon composite structure. For the organic electrolyte design, this approach has proven to be superior. The aluminum structure is used because it can be charged to a higher voltage than nickel electrodes. In the figure it is shown that the organic electrolyte design is superior to the aqueous both in terms of energy and power density. The higher energy density is expected for the organic devices because of the high operating voltage (one volt for the aqueous versus three volts for the organic). The higher power density for the organic is more surprising because the organic electrolytic solution has a low ionic conductivity. However, three aqueous cells need to be stacked in series to match the voltage of one organic cell. Therefore, the equivalent series resistance should be multiplied by three when comparing it to the organic devices. The results of these tests show that the organic electrolyte design is able to meet the DOE electric vehicle goals; whereas, it does not appear likely that the aqueous electrolyte will be able to meet these goals. The results of the investigation show clearly that the organic electrolyte design provides superior performance over the aqueous electrolyte design.

References

1. Burke, A. F. , "Laboratory Testing of High Energy Density Capacitors for Electric Vehicles," Proceedings of The International Seminar on Double Layer Capacitors and Similar Energy Storage Devices, Florida Educational Seminars, December, 1991.
2. Burke, A. F., Hardin, J. E., and Dowgiallo, E. J., "Application of Ultracapacitors in Electric Vehicle Propulsion Systems," Proceedings of the 34th Power Sources Symposium, Cherry Hill, N. J., June 25-28, 1990.
3. Becker, H. I., U. S. Patent Number 2,800,616, "Low Voltage Electrolytic Capacitor," July 1957.
4. Boos, D. L. and J. E. Metcalfe, U. S. Patent Number 3,634,736, "Electrolytic Capacitors Employing Paste Electrodes," 1972.
5. Kohler D. , et. al., J. Electrochemical Society. , vol. 137, p. 136, 1990.
6. Kohler D. , et. al., J. Electrochemical Society. , vol. 137, p. 1750, 1990.
7. Smith, J. M., Chemical Engineering Kinetics, third edition, McGraw-Hill, p.334, 1981.

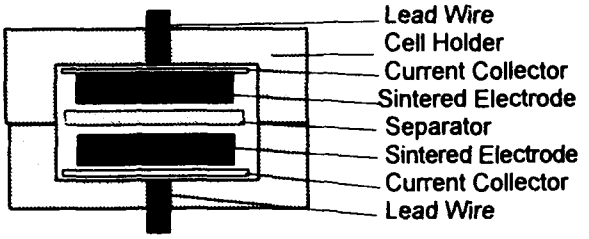

Figure 1. Basic design of capacitors used to test carbon fibers.

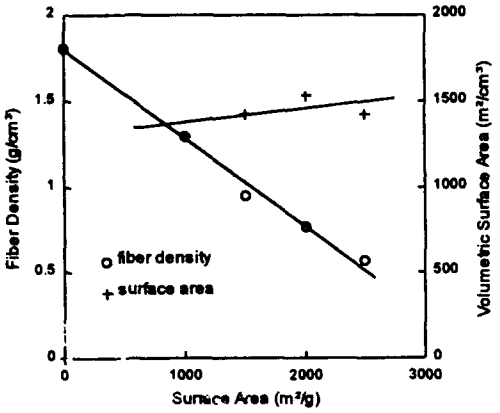

Figure 2. Fiber density decreases with increasing gravimetric surface area. This makes volumetric surface area remain constant.

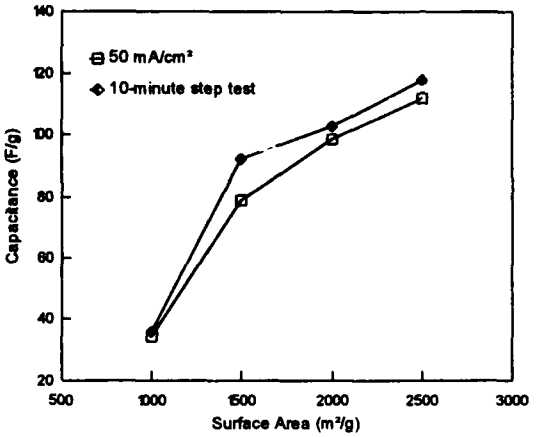

Figure 4. Organic Electrolyte Test Results --The step tests show total fiber capacitance per dry mass of carbon on an electrode basis. The tests at 50 mA/cm² show the fraction of capacitance available for rapid discharge.

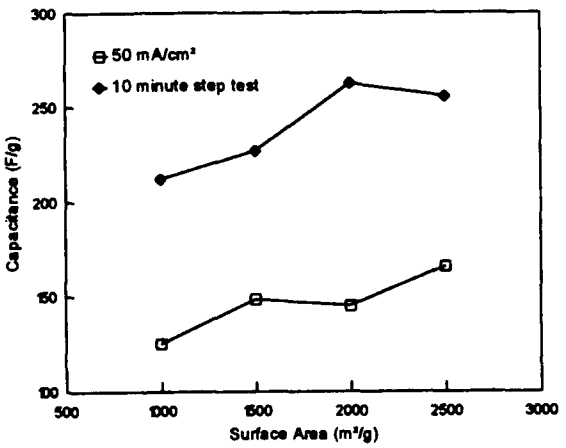

Figure 3. Aqueous Electrolyte Test Results -- The step tests show total fiber capacitance per dry mass of carbon on an electrode basis. The tests at 50 mA/cm² show the fraction of capacitance available for rapid discharge.

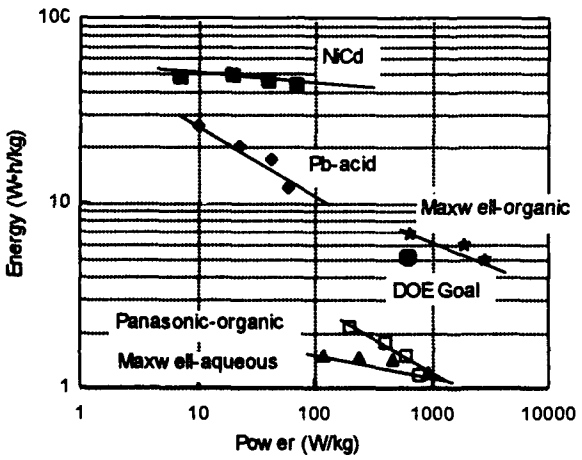

Figure 5. Rygone plot showing performance of Maxwell's double layer capacitors in comparison to competing technologies. Maxwell's energy densities are based on unpackaged device weight (includes two composite electrodes, one current collector, separator, and electrolyte). Packaged devices are expected to weigh 15-25% more than unpackaged devices.

An Overview of Electrochemical Capacitor Technology and Application

Dr. Sumner P. Wolsky
Ansum Enterprises, Inc., Boca Raton, FL
Richard S. Wissoker, P.E.
Wissoker Associates, Lexington MA

Introduction

This paper provides a brief overview of the status of electrochemical capacitors with an emphasis on applications and market potential. A major purpose of this presentation is to encourage further work in the field by demonstrating the sizable opportunity available. The information presented here is based primarily on the recently published International Technology and Market Study.[1]

The Electrochemical Capacitor

The term **Electrochemical Capacitor** in this discussion encompasses all devices usually referred to as a *double layer capacitor, supercapacitor, ultracapacitor,* or *pseudocapacitor*. An electrochemical capacitor stores energy through charging at a solid electrode liquid interface [double layer capacitance (DL)] and Faradaic reactions occurring at or near a solid surface [pseudocapacitance (PSC)]. Both types of behavior can occur in a device and the capacitive effects are additive. The DL occurs most prominently in carbon electrode based systems, while PSC dominates in redox, intercalation, and similar reactions.

The electrochemical capacitor is a relatively new device. Based on electrochemical principles discovered by Helmholtz[2] in 1879, it was first patented by Becker of the General Electric Company[3] in 1957 and offered for sale commercially by SOHIO in the late 1960's. The SOHIO patents were ultimately licensed to NEC in Japan. Electrochemical capacitors have been marketed since the late 1970's by Japanese companies: NEC, Matsushita (Panasonic), ELNA/Asahi, and Murata. There has been comparatively little effort in the United States, and that mostly R&D directed at special military and electric vehicle (EV) applications.

It has been only in the last five years that exciting new research directions and market opportunities have led to rediscovery of the electrochemical capacitor internationally as a potentially valuable energy source for a variety of important, high discharge rate uses.

The electrochemical capacitor is attractive because it can store several hundred times as much energy on a weight and volume basis as a conventional electrolytic capacitor, while retaining its ability to deliver that energy at high discharge rates. The performance of the device can exceed that of a battery in those applications requiring high power density and discharge rates in the minutes to less than seconds range. The electrochemical capacitor can also be used in combination with a battery to reduce peak power demands and thereby extend battery life. It is the latter use that has attracted much recent attention.

Advantages and Limitations

Some of the most important advantages of the device are:

- Cycle life in excess of 100,000 cycles
- High power density
- Discharge rates in the range of minutes to milliseconds
- Safety - tolerates high rate charge/discharge and overcharge
- Wide operating temperature range

Important limitations are:

- Low energy density relative to a battery
- Maximum cell voltages of 5 V with non-aqueous electrolytes
- Reliability of series stacked high voltage capacitors
- High cost of some potentially useful materials

Key Issues

There are several key issues which will determine the future of the electrochemical capacitor as a significant energy storage device.

Technology

The goal of present electrochemical capacitor research is to obtain cost effective devices with useful high energy and power densities. The original technology, which employed carbon electrodes in aqueous solutions, has been broadened to encompass other interesting materials such as higher surface area carbons, mixed metal oxides and doped conducting polymer electrodes. These materials in combination with non aqueous electrolytes provide the possibility of higher energy storage devices.

Energy and power densities of 5 wh/kg and 500 w/kg respectively are said to have been achieved in the laboratory and even greater values are projected for the future.

Markets

The present electrochemical capacitor products are made almost exclusively in Japan on high volume production equipment. They are used primarily for memory backup power in consumer electronic equipment. The United States electrochemical capacitor market represents a small fraction of the total world use, but it is growing at a substantial rate.

A serious impediment to US market development is the general unfamiliarity of design engineers and component manufacturers with the nature and performance of the device. Successful use of the electrochemical capacitor in commercial, military, or other applications requires an intimate knowledge of both the properties and performance capability. Further rapid market growth is anticipated as the engineers become more familiar with the device.

The development of higher power, greater energy density, more rapid discharge rate electrochemical capacitors has opened a wide range of possible markets. The following are among the new and expanded potential applications for the electrochemical capacitor:

- Hybrid and electric vehicles
- Auto subsystems
- Medical
- Actuators
- Power backup
- Military

The hybrid and electric vehicle application, in which the electrochemical capacitor is used to load level the battery, will be substantial if present plans to institute reduced vehicle emission requirements are enforced in California and elsewhere. It is this application which has principally

spurred the recent interest in the electrochemical capacitor.

The EV and hybrid EV applications have tended to mask the possibilities of the other market areas shown above. These additional markets can conceivably match or even exceed the demand for EV use. It has been estimated that an addressable market volume of approximately $1.35 billion is possible by the year 2000.

Satisfying the performance demands of these markets will not be easy. The requirements are difficult. There are competitive devices. The cost will have to be economically feasible.

The outlook is optimistic, but it will take the combination of improved technology, reasonable cost and intensive marketing to fullfill these expectations.

Competitive Environment

It is too early to tell which companies will dominate the future electrochemical capacitor markets. The competitors will require the technical, marketing and financial resources to pursue these important, new applications. European and US efforts are focused on the EV application. The US programs are being supported primarily by the Department of Energy as part of their EV development program. There are other confidential activities in progress at several important companies which could significantly impact the competitive picture.

The Japanese have a broader view, recognizing the potential for small reliable high power sources in a growing world of portable products, as well as the EV market. The Japanese also have the advantage of a long-standing history in the field and the commitment of major industrial groups.

More than 1150 relevant patents have been issued in the electrochemical capacitor field since 1942. Of all issued patents, 78.8% are from Japan, compared to a much smaller fraction from the United States. Recent novel technical approaches by US and European groups provide indications of a strong competitive market environment in the future.

Conclusion

The technology and market outlooks for the electrochemical capacitor are optimistic. Electrochemical capacitor research is still in its infancy. Broader US industry and government support is necessary to accelerate research and development of these devices. The competition will likely increase as the reality of the opportunity is more widely recognized. The device stands an excellent chance of becoming a key energy storage device of the future.

References

[1] Wolsky, S.P. and Wissoker, R.S. The International Technology and Market Study of Electrochemical Capacitors. Florida Educational Seminars, Inc., Boca Raton, FL. (1994)

[2] Helmholtz, H. von, Ann. Physik Vol. 3; pp. 337 (1879)

[3] General Electric Company (Becker), US Patent 2,800,616 "Low voltage electrolytic capacitor." Issued 7/23/57

PERFORMANCE OF LOW MERCURY ZINC/MANGANESE DIOXIDE ALKALINE CELLS

R.W. Nolan and G.J. Donaldson
Directorate of Research & Development Air
Research & Development Branch
National Defence Headquarters
Ottawa, Canada
K1A 0K2

Abstract

The Canadian armed forces use large quantities of alkaline cells, often in cold field conditions. In recent years the manufacturers of alkaline cells have been gradually lowering the mercury content of these cells, primarily because of the environmental hazards of mercury. The present study was undertaken because of the concern that the removal of mercury might adversely affect performance, especially in the cold, and also diminish the resistance to mechanical shock and vibration, and shelf life. This investigation of some of the performance characteristics of alkaline cells was conducted in comparison with older cells which contained higher levels of mercury. It was found that the room temperature performance of alkaline cells was excellent. However, between 5°C and -20°C, low-mercury cells manufactured since 1992 had performance that was inferior to the older cells.

Introduction

The zinc/potassium hydroxide/manganese dioxide cell, commonly referred to as the alkaline cell, became a widely available consumer product during the 1970's. It is estimated that worldwide annual use is more than five billion cells.[1] Historically, mercury has been an important additive in the manufacture of these cells, being amalgamated at up to 8% by weight with the zinc anode. The use of mercury resulted in less zinc corrosion and extended shelf life compared to the zinc/carbon Leclanche cell.[2,3] There was also enhanced interparticulate contact in the zinc powder, producing better electrode conductivity[4,5] and improved resistance to mechanical shock and vibration.

In recent years, primarily in response to environmental pressure, manufacturers have been reducing the amount of mercury contained in alkaline cells,[6,7] some of which are now advertised as being "environmentally-friendly" and containing less than 0.001% Hg. Consumers have been assured that the mercury removal program has not caused any loss in cell performance. Notwithstanding these claims, it was decided to conduct an objective assessment of the effects of moving to low-mercury alkaline cells.

Experimental Program

In February 1993 it was learned that a large military stock of AA-size and C-size cells had been declared "time-expired" and was slated for disposal. The military supply system considers alkaline cells to be "time-expired" when they have been stored for 30 months from their date of manufacture (DOM). The only D-size cells in stock were manufactured in 1992. For comparative purposes, a quantity of commercially available, "mercury-free" D cells was purchased locally: DOM - June 1992.

In all, six groups of cells were available for the study:

1. AA size - DOM 01/92 - military stock
2. AA " - DOM 03/89 - military stock
3. C size - DOM 01/92 - military stock
4. C " - DOM 05/89 - military stock
5. D size - DOM 02/92 - military stock
6. D " - DOM 06/92 - commercial

It was verified that all cells in the test program were produced by the same manufacturer. The following measurements were made on the cells in each group: open circuit voltage, resistance (ac value at 1 kHz) and mass.

Undischarged cells from each group were dissected and samples of the zinc anode were removed, weighed and dissolved in concentrated HCl/HNO_3. The concentration of mercury in each of these solutions was then determined using inductively-coupled argon plasma atomic absorption spectrophotometry. The dry mass of the anode sample was used to calculate the mercury content as a percent by weight.

In a typical alkaline cell application, such as operating a flashlight, the rate of discharge is approximately 250 milliamperes, corresponding to a load of about 5 ohms. Thus the majority of cells from each group was resistively discharged at this load. Some additional experiments were conducted using 1Ω and 10Ω loads. Cell capacity was determined to the industry standard end of test voltage: 0.8 volts, although in many cases discharging was continued to below 0.1 volts.

For each experiment, cells were equilibrated prior to discharging for a minimum of four hours in an environmental test chamber at the desired temperature, between -40°C and 60°C. A 12 W resistor was then connected across each cell. The voltage drop across the load was measured every two minutes throughout the discharge period using a PC-controlled data acquisition unit. The capacity was determined by integrating the computed current over the elapsed time using Simpson's rule.

Results and Discussion

There were only minor differences between the open circuit voltages of cells of each size group and no significant differences in

weights. The two groups of D-size cells had very similar impedance values. However, the impedance of the AA- and C-sized cells that were manufactured in 1989 was significantly lower than those manufactured in 1992. The mercury content of the anode in the 1989 cells was found to be about 0.8% and that of the 1992 cells was approximately an order of magnitude lower. During a subsequent conversation with the manufacturer, it was learned that all alkaline cells made by this company since 1990 were "ultra-low mercury", (i.e. less than 0.025% mercury).[8] Our analyses indicated that the mercury content stated by manufacturers must be relative to the total cell mass rather than the mass of the zinc anode. These results are summarized in Table I.

TABLE I

MERCURY CONTENT OF ANODES AND MEAN IMPEDANCE MEASUREMENTS

Group	Cell Size	DOM	Mercury Content (%w/w anode)	Mean Impedance (mohms)
1	AA	01/92	0.10	165 ± 7.4*
2	AA	03/89	0.74	89 ± 5.1
3	C	01/92	0.07	131 ± 11.9
4	C	05/89	0.82	79 ± 6.5
5	D	02/92	0.08	96 ± 15.1
6	D	06/92	0.07	98 ± 19.0

* standard deviation

Since one of the effects of amalgamating mercury with the zinc anode is to increase the conductivity of the electrode, the impedance data confirmed that 1992 cells contained less mercury than the 1989 cells. The impedance data also suggested that the mercury content of the military D cells was similar to that of commercial "low-mercury" cells.

Typical results for the discharge of alkaline C cells at 25°C are given in Figure 1. In this experiment, two 1989 cells and three 1992 cells were discharged simultaneously. During the first several minutes after the load was applied, voltages dropped quickly from about 1.5 volts to 1.3 volts. After this initial period, the voltage curve sloped gradually, taking between 25 and 30 hours to fall to 0.8 volts. It then quickly decreased to a minimum value of about 0.1 volts. At temperatures above 10°C, the newer cells outperformed the older cells by about two to fours hours. This was expected on the basis of the reported 3% to 4% annual loss of capacity for storage of alkaline cells at 20°C.[5,9] It was also noted that the voltage of the 1989 cells was marginally higher than the 1992 cells during the first 15 hours of the experiment. Similar comments pertain to the groups of AA-size cells.

The typical discharge curves obtained for a similar experiment which was conducted at 0°C are shown in Figure 2. In this experiment the output of the 1989 cells remained above 0.8 volts for about twice as long as for the 1992 cells (19.5 h vs 9.2 h) and on average their capacity was twice as great (3.8 Ah vs 1.9 Ah). These results were unexpected, thus prompting a more detailed evaluation of low temperature performance.

Numerous discharge experiments at 1Ω, 5Ω and 10Ω were conducted to compare the performance of the two groups of C cells over a range of temperatures between -40°C and 60°C. The capacity results for these experiments are given in Table II (5Ω only) and in Figure 3 in slightly different representations. The data were averaged over at least five replicate cell discharge experiments at each temperature. Above 5°C, the capacity, as represented by the time to reach 0.8 volts, of the 1992 cells was about 10% more than that of the 1989 cells, but between 5°C and -20°C the capacity of the 1989 cells was significantly greater (in some cases more than 100%) than that of the 1992 cells (e.g. see Table II). Table II also indicates that there was a substantial increase in standard deviations for the data between 5°C and -5°C and at 45°C, most notably for the 1992 cells.

TABLE II

MEAN CAPACITY OF C CELLS DISCHARGED THROUGH 5 OHM LOAD

Temperature (°C)	Time to 0.8 v (hours)	
	1989	1992
60	32.0 ± 0.5*	35.1 ± 0.3*
45	28.7 ± 1.1	32.6 ± 1.1
30	28.5 ± 0.3	30.5 ± 0.2
20	25.6 ± 0.3	28.5 ± 0.1
10	23.6 ± 0.3	25.9 ± 0.5
5	22.2 ± 0.2	23.9 ± 0.8
0	19.7 ± 0.4	12.6 ± 4.4
- 5	16.0 ± 0.9	7.1 ± 1.6
-10	11.2 ± 0.1	5.5 ± 0.1
-15	7.8 ± 0.1	4.5 ± 0.1
-20	5.2 ± 0.1	4.2 ± 0.1
-30	2.3 ± 0.0	2.4 ± 0.1
-40	1.0 ± 0.0	0.4 ± 0.0

* standard deviation

The difference in the capacity for higher versus lower mercury-content cells was plotted in Figure 3 against the test temperature for C-size cells that were discharged at 1Ω, 5Ω and 10Ω. It shows that the cells with higher mercury content performed better overall, but there was a rate dependence for the magnitude of the difference which varied with the temperature. At the 1Ω rate the older, higher mercury-content cells were better at all temperatures, but excelled in the 10°C-30°C range.

A comparison of the performance of AA cells manufactured in 1989 and in 1992 indicated a similar, but less pronounced discrepancy at temperatures between 0°C and -30°C.

For the D-size cells discharged on a 5 ohm load, the only significant difference between the capacity of the two groups of cells occurred at -5°C. This anomaly is

illustrated in Figure 4 which shows the very dissimilar discharge curves for commercial and military cells. At this temperature, the difference in time to reach 0.8 volts was almost 60% while at all other temperatures this difference was always less than 7%. The discrepancy at -5°C was verified as significant by repeating the experiment on 10 additional cells from each group. There was only a small difference in the mercury content of the anodes for these two groups of cells (see Table I) and the impedance values were also indistinguishable. This suggests that only a small change in the mercury content of the zinc electrode can have a profound effect on performance at certain temperatures. Why this should occur at temperatures near to or just below 0°C is unknown and may warrant further study. Except for -5°C, there would appear to be no significance performance differences between cells produced for the military and those for the consumer market.

At temperatures below approximately 0°C there were notable irregularities in the discharge curves for all of the low-mercury alkaline cells. Figure 4 shows this behaviour for D cells from both groups as indicated, and Figure 5 for C-size cells discharged in this case at 0°C. What was typical of the low mercury cells of all sizes, as shown by the examples in Figures 4 and 5, was the instability of the voltage below approximately 0.8 volts and the tendency for the cell voltage to increase after several hours of discharging below 0.4 volts. The voltage fluctuations may be caused by a loss of electrical continuity in the anode. None of the 1989-dated cells exhibited these features.

The effects of low-mercury on the shelf life and resistance to mechanical shock and vibration are currently being studied and will be the subject of a future publication.

Conclusions

At temperatures above 5°C the performance of each of the three sizes of alkaline cells used by the Canadian military was found to be excellent, often exceeding the manufacturer's performance claims. However, between 5°C and -20°C, AA-size and C-size cells that were procured since 1992 had performance characteristics which were inferior to those of older cells. The older cells contained more mercury in the zinc anode and despite the marginal loss of capacity over three years of storage, still produced more energy at lower temperatures than the newer, low mercury cells. The lower mercury content of 1992 cells compared to 1989 cells was confirmed by chemical analysis of the anode. Lower mercury cells also had higher impedance values.

The performance of the military stock of D cells and commercial D cells with comparable DOM was only different at -5°C. The slight differences in composition of the zinc/mercury anode may have been responsible.

Acknowledgements

The authors would like to acknowledge the continued support of the Directorate of Research and Development Air, Canadian Armed Forces and the Electrochemical Science and Technology Centre, University of Ottawa.

References

1. K. Kordesch, Ch. Faistauer and J. Daniel Ivad, 8th International Battery Symposium, Brussels, May 9-13, 1993.

2. C. Huang, et al, "A new type of nonpoisonous addition agent for substituting mercury in zinc/manganese dry cells", J. Power Sources, 45 (1993) 169-175.

3. K.V. Kordesch, "Alkaline manganese dioxide cells", in "Handbook of Batteries & Fuel Cells", (D. Linden, ed.), McGraw-Hill, 1984.

4. J.Y. Huot, "Resistivity and anodic discharge of mercury-free gelled zinc anodes", Power Sources 14 (1993) (A. Attewell and T. Keily, eds.).

5. K.V. Kordesch, "Alkaline manganese dioxide zinc batteries", in "Batteries, Vol 1", K.V. Kordesch (ed.), Marcel Dekker, Inc., New York, 1974.

6. D. Spahrbier, "Mercury reduction programme for primary batteries", Chemistry & Industry, July 1990.

7. M. Meeus, et al, "New Developments in Reduction of Mercury Content in Zinc Powder for Alkaline Dry Batteries", Power Sources 11 (1986), (L. J. Pearce, ed.).

8. Private communication; manufacturer's representative and author (RWN), 30 Sept 1993.

9. Manufacturer's Battery Engineering Data, published 1992.

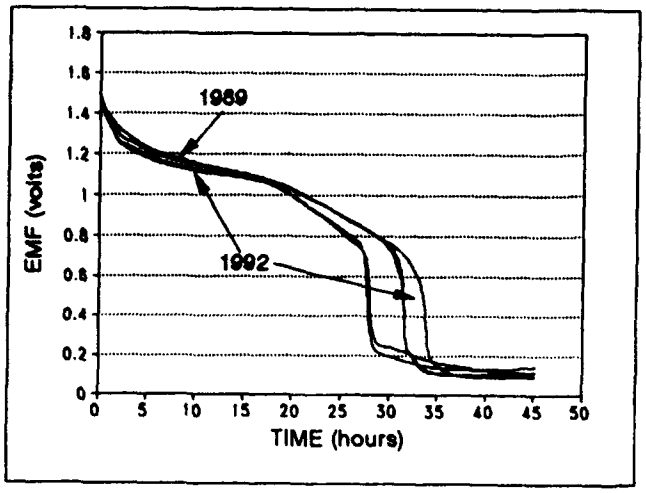

Figure 1. C Cells: Discharge Curves @ 20°C, 5 ohm Load.

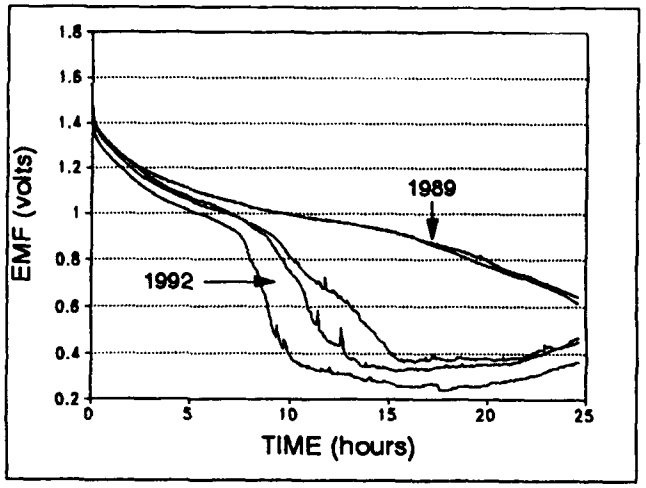

Figure 2. C Cells: Discharge Curves @ 0°C, 5 ohm Load.

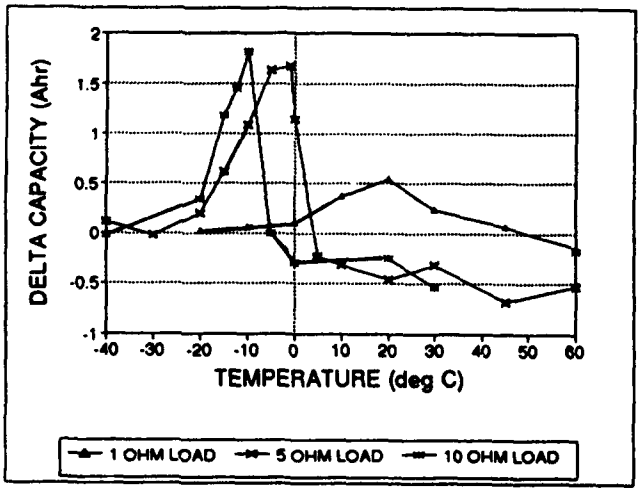

Figure 3. Mean Difference in Capacity: High Mercury - Low Mercury C Cells versus Load and Temperature.

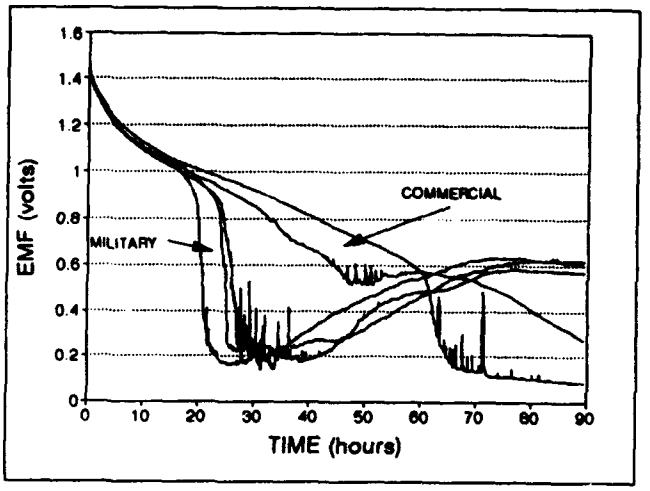

Figure 4. D Cells: Discharge Curves @ -5°C, 5 ohm Load (Discharging continued beyond 0.8 volts).

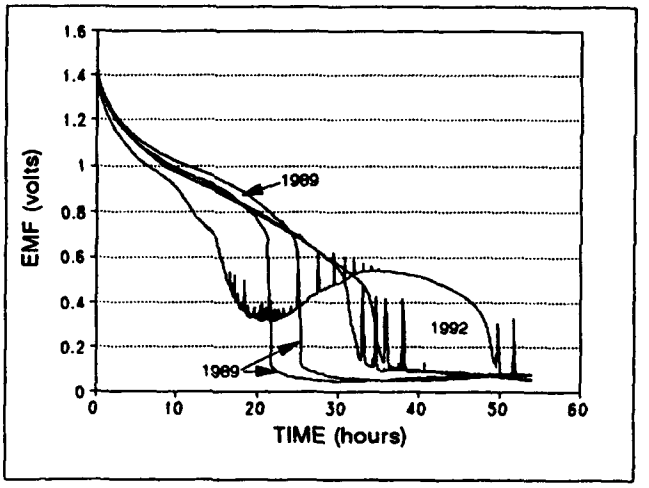

Figure 5. C Cells: Discharge Curves @ 0°C, 5 ohm Load (Discharging continued beyond 0.8 volts).

THE COPPER / MAGNESIUM SEAWATER CELL FOR NEAR SURFACE OPERATION.

Øistein Hasvold[*] and Reidar Kjennbakken[**]

[*]Norwegian Defence Research Establishment, Division for Weapons and Materiel, PO. Box 25 N-2007 Kjeller, Norway
[**]Norwegian Coast Directorate, PO. Box 8158, Dep, 0033 Oslo, Norway

Abstract

The paper describes a power source recently adapted by the Norwegian lighthouse authorities for application in light buoys. The power source is based on an electrochemical cell which uses magnesium as fuel, seawater as electrolyte and oxygen dissolved in the seawater as oxidant. Under load, the magnesium anode dissolves, but as sea water contains typically 1.2 kg of magnesium per ton, the cell reaction does not affect the environment. The cathode is a copper structure with a high surface area. The cathode surface is protected against biofouling by cuprous ions, generated from copper corrosion.

The complete power supply consists of a single seawater cell, a DC/DC converter and an accumulator. The cell power is limited by the rate of water exchange in the cathode. Typical performance is 2 W average from a cell 1 m high with a diameter of 50 cm. Cell deterioration is caused by biofouling and deposition of calcareous layers on the copper cathode, copper corrosion and by anode depletion. After cleaning, the cathode surface is as new. Anode capacity is sufficient for 5 years, thus the required maintenance on the cell can be done in conjunction with the periodic maintenance of the light buoy. After 5 years, the cell is exchanged or recharged with a new magnesium anode depending on the condition of the cell.

Off shore navigational light buoys with different sea water cell design have been used by the Norwegian Coast Directorate since 1989. The results show that the system is safe, reliable, easy to maintain and with a potential for very low cost.

Introduction

Primary cells based on metal anodes (e.g. alloys of magnesium or aluminium) which use seawater as the electrolyte and oxygen dissolved in the seawater as the oxidant with inert cathodes have been known for some time [1,2,3,4]. Such cells need a continuous renewal of the seawater to supply the cathode with fresh seawater and to remove the products of the cell reaction(s). Because of this they must have an open structure, causing leakage currents between serially connected cells to be high. This is why power sources for low rate discharge are based on a single cell or cells connected in parallel. A DC/DC-converter converts the low cell voltage (0.4 to 2 V depending on the particular cell system) into a regulated voltage (e.g. 14 V). A secondary battery may be charged from the DC/DC-converter. Compared to conventional power sources, such seawater cells gives a very high theoretical energy density, as only the anode material is consumable. They have a potential for moderate cost, excellent safety and infinite storage ability when dry. Until recently however, low power density and cathode deterioration caused by fouling by marine organisms and formation of calcareous layers on the cathode surface have precluded the realisation of a commercially viable power source based on this concept. The cathode reaction

$$O_2 + 2\,H_2O + 4\,e^- = 4\,OH^-$$

leads to an alkalisation of the cathode surface. This pH increase may lead to precipitation of calcium carbonate on the cathode surface[7]:

$$Ca^{++} + HCO_3^- + OH^- = CaCO_3 + H_2O$$

The development of methods to reduce this problem were necessary steps toward the development of a commercial seawater battery.

In 1989 the Norwegian Coast Directorate established a Project group to adapt the seawater battery technology to light buoys and at the XIIth International Association of Lighthouse Authorities Conference, we described a prototype installation of a light buoy powered by a seawater cell [5]. These cells are based on a centrally mounted anode with a concentric cathode made from copper. Later, improved cells developed at NDRE have been used as power sources for underwater surveillance systems, surface buoys and for the propulsion of a small unmanned underwater vehicle (UUV), [6]. The power source for the UUV is dependent on a forced flow of seawater for the transport processes in the cell whereas the low rate cells depend on natural convection (sea current, waves)[7].

Anodes

Magnesium anodes have lower cost and give higher cell voltage than aluminium anodes. Corrosion reduces the specific capacity from the theoretical value of 2000 Ah/kg to roughly 1200 Ah/kg depending of alloy and anodic current density. Typical potential under load for the magnesium aluminium zinc alloy AZ63 is -1.49 V_{SCE}. The anode shows very little polarisation over the current density range of interest, but voltage delay is observed.

In light buoys, cylindrical AZ63 anodes with a diameter of 190 mm and a length of 1000 mm have been used. Initial anode weight is 50 kg. Assuming discharge to 50% reduction in anode diameter, the corresponding capacity is 50000 Ah.

The DC/DC-converter

Most converters use MOS-FET transistors. Their exceptionally low on-resistance makes it possible to achieve a high efficiency, typically above 75%, but they need a gate voltage higher

than the cell voltage to be turned on. Thus they need an auxiliary power source for start-up. This may be a secondary battery or another converter. Systems with auxiliary converters have excellent storage ability in contrast to systems based on auxiliary power from accumulators.

Galvanic separation between input and output is preferred as a short between the steel structure of the light buoy and the cell connections will lead to a malfunction of the power source and in the case of a short to the positive terminal, to corrosion of the light buoy. The 300 W converter for the UUV has galvanic separation between input and output and a 2 W converter for light buoys with galvanic separation is under development. All experiments with light buoys have been undertaken with converters without galvanic separation.

The safe load on a seawater cell with respect to calcareous film formations depend on the temperature and the rate of exchange of the water at the cathode surface. This rate of exchange varies with the design of the cell, the sea current and the wave action on the buoy. Generally speaking: the worse the weather, the better the cell. At the same time, the converter must sense the status of the accumulator to avoid overcharging and waste of energy. In converters for light buoys, these functions are built in. The size of the secondary battery should at least be sufficient to take care of the longest possible continuous calm period and the converter should have sufficient excess power for the recharge of the accumulator under normal conditions. This is similar to the considerations that must be taken with solar power sources.

Because of this dependence on the hydrodynamic conditions, this power source is unsuitable for use in areas with exceptionally calm conditions.

Cell development

Seawater cells with inert cathodes are intended for deep sea use where light induced growth of algae is absent or for short time discharge. They can give a cell voltage of 1.6 V under load, but close to the surface, as in light buoys, biofouling may reduce the life of such cells to a few weeks in the growth season. This made it necessary to develop cathodes which releases a substance into the seawater that is toxic to marine life. The cell used in light buoys is based on cathodes of copper or copper alloys which corrode at a controlled rate, thereby releasing copper ions into the seawater. Copper is toxic to marine life and copper compounds are used in the bottom paints for boats ("Anti fouling") for the same reason.

The first cell with copper cathodes operated at a depth of 60 m from November 19, 1987 until March 13, 1990 at which time 80% of available anode capacity (60000 Ah) was used. Except for a decrease in cell voltage from 1.1 to 0.9 V caused by the reduction in anode diameter with time (increased IR loss) and some areas with a calcareous deposit, the reduction in performance with time was small. Biofouling was not observed at the cathode, but strength members and moorings were covered with nematodes, tube worms and sea anemones. After retrieval, the cell was cleaned with a high pressure power cleaner, but this was unable to remove calcareous deposits. Copper corrosion was less than 0.05 mm over 2.5 years. Copper corrosion under open circuit is estimated to roughly 0.08 mm per year [8]. Under load, the copper structure has some degree of cathodic protection, making the rate of corrosion less. The cell was equipped with a new anode and a new cable and re-deployed on March 22, 1990. At the time of redeployment, the cathode surface was green from exposure to air and felt very "coarse". This had obviously decreased the cell performance as the load had to be reduced from 3 W to 2 W. Gradually then, the performance decreased further.

From the spring of 1989, seawater batteries with plate cathodes have powered two light buoys, one at Rakke and one at Ytre Hausene at the southern coast of Norway [5]. Inspections in the autumn 1990 have shown that biofouling of the cathode had not occurred after two growth seasons whereas the buoy itself was covered by biofouling. Biofouling (mainly mussels) on the supporting cell structure and on the buoy was removed with a high pressure power cleaner and the buoy redeployed. The experiment at Rakke was terminated because the converter was flooded by seawater.

Table 1 summarises the experience with seawater cells with copper cathodes. The oldest seawater cells used on Flakk (in the Trondheims fjord), Rakke and Ytre Hausene had cathodes made from copper plates arranged radially around the central anode[5]. The newer cells have cathodes made from a sheet of expanded copper coiled in a spiral and subsequently locked in shape with glass reinforced polyurethane resin in the top and bottom[9] as shown schematically in figure 1.

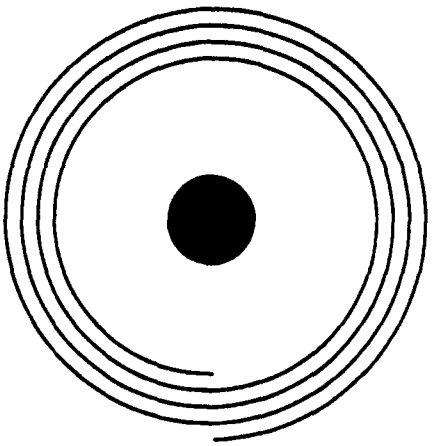

Figure 1 *Schematic of a seawater cell with the anode in centre and a spirally wound expanded metal cathode.*

The cells Horten 1 and 2 (on the south east coast) and Runde (on the west coast) were experimental buoys which were not used for navigation. Their main purpose was to establish the maximum safe load for seawater cells. In light buoys, the cell is open in the bottom and closed at the top. In this way, wave action leads to an active pumping of the seawater through the expanded metal cathode [10]. Figure 2 shows a tail tube buoy with a seawater cell. The buoy has a diameter of 2.0 m and is 9.5 m high. The tail tube is 0.5 m in diameter, and the seawater cell is located in a steel cage in the lower part of the tube. The cell voltage under load was between 0.9 and 1.1 V for all cells. Typical load for a navigational light was 1.5 W in the dark. In addition to this load, between 0.1 to 1.5 W must be added, depending on the no load current drain of the converter and the state of charge and self-discharge rate of the accumulator. In the navigational lights, and in some test buoys, sealed lead acid batteries (Sonnenschein A200/12V/9.5 Ah) were used together with a LBEA-85 lantern.

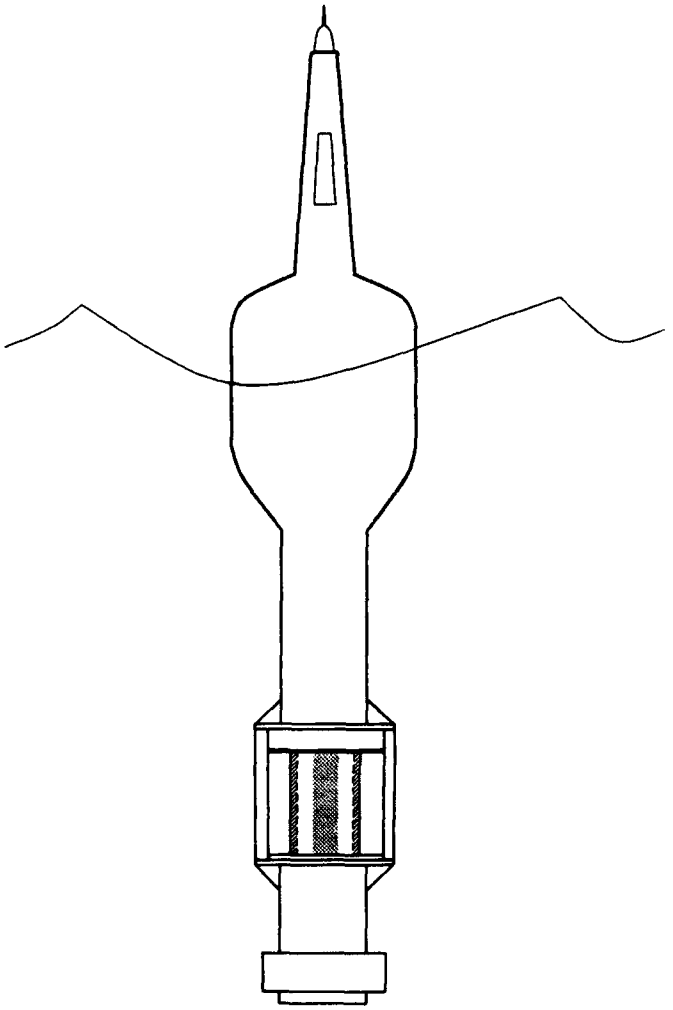

Figure 2 *Schematic of a tail tube navigational light buoy with the seawater cell located above the balance weight.*

Table 1. Summary of the experiments with seawater cells:

Seawater cell:	Start of discharge	Duration/ days	Load:	Terminated because of
Flakk	19.Nov.87	847	2.5 - 3 W	Anode depletion
Flakk, continued	22.Mar.90	420	2 W	Calcareous film
Rakke L B	20.Jun.89	960	Nav Light	Seawater leak
Ytre H L B	05.Sep.89	449	Nav Light	Cleaned at Sea
Ytre H L B	28.Nov.90	666	Nav Light	OK, taken to Base
Horten1	27.Sep.89	342	Nav Light	Anode depletion*
Horten2	03.Nov.89	503	2.5 W	Calcareous film
Runde	06.Dec.90	634	Nav Light	Failure of lead acid
Runde, cleaned	15.Dec.92	212	Nav Light	Seawater leak
Kroppen L B	9.Oct.93	in service	Nav Light	
Fauskane L B	11.Oct.93	in service	Nav Light	

*Hollow anode

Figure 3 shows the cell voltage and the accumulator voltage after the buoy was deployed at Runde on April 22, 1991 after an adjustment of the converter. The accumulator was discharged at the start, thus the converter was continuously running at full power over the first five days until the accumulator was recharged. The lantern load was Fl 2, 10s, 10 W bulb, 14% on. The light extinguished on Nov 12, 1992. This was caused by one shorted cell in the accumulator. Because of the cell short, the converter ran continuously and biofouling started. The biofouling and the build-up of a calcareous layer subsequently lead to cell failure. No cleaning of the cell was done between its fabrication in the autumn of 1990 and its retrieval in November 1992. Then, the defective buoy was cleaned and the calcareous layer on the cathode removed by wet sand blasting from the outside, leaving the calcareous deposit on the inside intact. Equipped with a new accumulator and a 5 W bulb, the buoy was functional until a seawater leak destroyed the electronics. At this time, no sign of new calcareous deposit was observed.

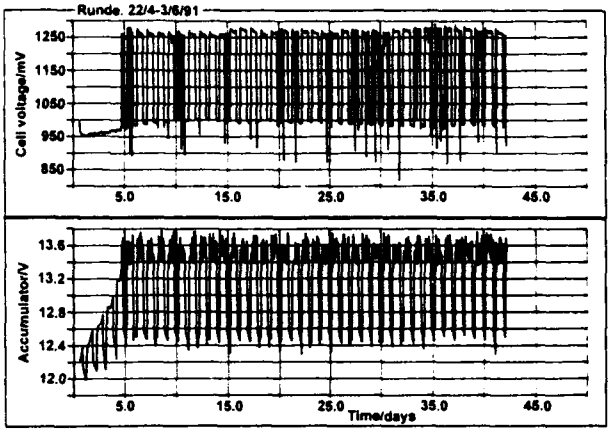

Figure 3 *Power source at Runde from April 22, 1991. Upper curve: seawater cell voltage, lower curve: lead acid battery.*

Discussion

The use of oxygen dissolved in the seawater makes it possible to make batteries with very high energy density. Compared to air, the rate of diffusion and the concentration of oxygen in seawater is low and makes the power density of such batteries low compared to conventional and metal/air batteries. Whereas the energy content of the cell is determined by the cell voltage and amount of magnesium, the rate by which this energy can be extracted from the cell is mainly determined by the rate of seawater exchange in the cathode, the cathode materials and structure.

For cells with copper cathodes, cell life is restricted by the corrosion of copper or by the consumption of magnesium if the cathode current density is kept sufficiently low. For cells with a medium current density, a gradual deterioration takes place as parts of the copper surface become insulated by calcium carbonate. As the free surface area decreases, the local current density increases further, thereby increasing the rate of calcium carbonate deposition and decreasing the rate of copper corrosion to a value insufficient to avoid biofouling. If this happens, the buoy must be taken up for cleaning. Conservative data for safe load in open sea for a cell with an optimal structure have been established. These data predict a cell life in excess of 4 years in a light buoy.

The last two cells, Kroppen and Fauskane, power navigational lights in a very exposed area on the west coast of Norway. Compared to the experimental cells at Runde and Horten, the cathode current density has been decreased by a factor of 2, ensuring a safe margin with respect to calcareous film formation and biofouling.

The cell can be restored to the "as new" condition if the scale on the cathode is removed. This may be done mechanically (wet sand blasting) or chemically with an acid etch. Calcium carbonate is easily dissolved, thus weak acids such as 1% hydrochloric acid is suitable. Both processes are routine and blasting may be done at sea. The life of the anode is between 3 and 5 years after which the cell may be refitted with a new anode, making this power source well suited for low cost, low power applications of long duration.

Future production of cells and converters will be made by Simrad Subsea A/S, Norway.

Acknowledgements

We would like to thank the Norwegian Coast Directorate, Simrad Subsea A/S and the Norwegian Defence Research Establishment for the permission to present this work.

References

[1] Lidorjenko N S, V A Naumjenko, A T Kopjov, L P Esajan and D V Kurygitsa (1976): Russian Patent SU-5509307

[2] Walsh M (1990): "Single cell seawater batteries". Proceedings of the 34th International Power Sources Symposium, Cherry Hill, New Jersey. pp 110-111

[3] Lauer J S, Jackovitz J F and Buzzelli E S (1990): "Seawater Activated Power Source for long Term Missions". Ibid pp 115-117

[4] Hasvold Ø (1990): "Seawater batteries for low power, long term applications". Ibid pp 50-52

[5] Kjennbakken R and N Størkersen (1990): "Sea Water Primary Battery". XIIth Conference of the International Association of Lighthouse Authorities (IALA). Holland,

[6] Hasvold Ø (1993): "A Magnesium - Seawater Power Source for autonomous underwater vehicles". Power Sources 14 (Ed. A Attewell and T Keily), pp 244 - 255

[7] Hasvold Ø (1991): "Seawater batteries for long Term Application". Power Sources 13 (Ed. T Keily and B W Baxter), pp 307 - 318

[8] Wood R J K, Hutton S P, and Sciffrin D J (1990): "Mass transfer effects of non-cavitating seawater on the corrosion of Cu and 70Cu-30Ni". Corr. Sci.., Vol 30, pp 1177-1201

[9] Hasvold Ø, Garshol T and Østvold T (1989): "Seawater cell". Norwegian Patent 168145. US Pat No 5.256.501

[10] Hasvold Ø (1990): "Seawater cell" Norwegian patent 171087.

INVESTIGATIONS ON COPPER OXIDE AS DEPOLARIZER IN ALUMINIUM PRIMARY BATTERY

GOPU KUMAR, A.SIVASHANMUGAM, N.MUNIYANDI and S.BASKARAN*
Central Electrochemical Research Institute (CSIR),
Karaikudi - 623 006, TamilNadu, India

Introduction

Aluminium (Al), a battery negative, with its acclaimed merits like low equivalent weight, easy availability, low cost, easy machining, environmentally stable[1] etc.,has undergone very few attempts[2-4] for developing aqueous primary reserve batteries in conjunction with different inorganic positives.

Aluminium sea-water reserve batteries were reported by several authors[5] utilizing either oxygen reducing or hydrogen evolving cathodes and are found to be well suited for a variety of oceanographic applications[5,6] ofcourse, at very low current densities (0.100 to 10 mA cm^{-2}) and voltages (1.4 to 0.5V). Al/MnO_2 reserve batteries[2] are used for low power, long duration undersea trasponders. Very recently, Licht et.al.,[4] have demonstrated a novel aqueous Al/Sulphur activated battery ,for possible use in electric vehicles[7] wherein they have realised an energy density of 110 Wh/kg and compared favourably with conventional batteries like lead-acid (35 Wh/kg), Zn/MnO_2 (95 Wh/kg) etc.

Hence, it is evident from the above studies that aluminium based reserve batteries are useful in civilian as well as military applications. However, only a few inorganic depolarizers (MnO_2,S and AgO) have been investigated inspite of the fact that they are associated with limited capacity output (0.17 to 0.43 Ah/g). We were, therefore, interested to conduct a comprehensive examination on the higher capacity cupric oxide (CuO) [ie., 0.67 Ah/g] as a possible depolarizer for aluminium reserve battery, which is hitherto not reported. The basic reaction involved is :

$$2Al + 3CuO + 3H_2O \longrightarrow 2Al(OH)_3 + 3Cu$$

In the present paper, we report the performance of CuO in aluminium reserve batteries at different current drains and with sodium hydroxide (NaOH) and potassium hydroxide (KOH) electrolytes.

Experimental

Chemicals : CuO (Loba Chemie,AR), KOH and NaOH (Fischer, AR) and acetylene black (AB) were used as such without further purification.

Cell Fabrication and Optimization of Electrolyte Composition

Cathodes of 3 cm X 2 cm area were prepared by spreading the cathode mix containing depolarizer (1g CuO),conducting material (0.4g AB) and aqueous binder (2 to 3% carboxymethyl cellulose) uniformly over a metallic current collector (copper mesh) and pressed at an optimised load of 6 tonnes. The anodes of 3 cm X 2 cm size were the cut pieces from 2S grade aluminium sheets(0.4% Fe, 0.3% Si, 0.1% Mg and 0.1% Mn) of 1.5 mm thickness. Al/CuO cells were assembled in a plastic container by placing a cathode between two anodes and were seperated by multilayers of cellophane.

The cells were activated using 20 ml of the test electrolyte like KOH or NaOH at varying concentrations (0.5, 1, 2 and 3 M) and discharged at 25 mA current drain at room temperature (30 $\pm 1^{\circ}C$). All experiments were repeated for concordancy and were reproducible within $\pm 2\%$.

Optimization of AB

Conducting materials like acetylene black, graphite etc are blended with inorganic depolarizers[8] in order to enhance their conductivity and for achieving large surface area electrodes.

In the present study, AB was added in various proportions (up to 70%) with 1g of CuO and 1 cc of binder. Cathodes were prepared using the above mix and pressed at an optimum load of 6 tonnes. The cells were assembled as described earlier and were discharged at constant current drains of 25 mA corresponding to a current density of 2.1 mA cm^{-2} in 0.5 M KOH electrolyte.

Discharge Study

A number of Al/CuO cells were assembled and discharged at various current drains (25, 50 and 100 mA) corresponding to current densities of 2.1, 4.3 and 8.6 mA cm^{-2} respectively after initial optimization of AB content and electrolyte concentration.

Linear Sweep Voltammetry (LSV) Studies

0.17 g of CuO was mixed with 40% AB and very small amounts of binder. The mix was spread on both sides of a copper mesh current collector of 1 cm X 1 cm size and pressed at an optimized pressure. LSV experiments were performed using a three electrode system consisting of CuO cathodes as working, platinum as counter and Ag/AgCl as reference electrodes in 1 M NaOH solution using a Wenking potentiostat (LB 75, Germany) attached to a scan generator (VSG 72, Germany) and a X -Y recorder (Rekidemi, Japan).

Results and Discussion

Fig 1 presents the discharge curves obtained from Al/CuO cells using cathodes containing AB from 20 to 60% by weight of CuO in 0.5 M KOH at a constant current drain of 25 mA. It is evident from the

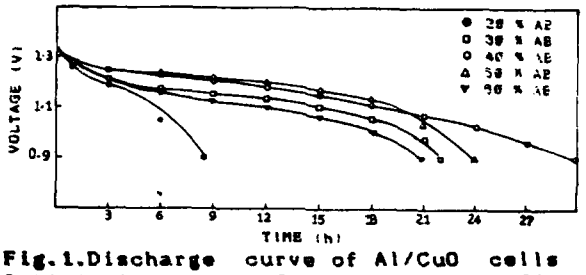

Fig.1.Discharge curve of Al/CuO cells : Optimization of AB (0.5 M KOH, 25 mA current drain)

curves that the capacity of the cells were enhanced upto 40% AB content and thereafter not much significant improvement is observed. Moreover, the open circuit voltage (OCV) of the cells remains constant (1.51 to 1.55 V) with varying AB composition. Interestingly, the constant OCV of the Al/CuO cells at varying AB content is in agreement with our earlier observations on Mg/PNP cells[9] and is true as suggested by Tye et. al.[10] Further, a marginal decrease in capacity of Al/CuO cells at higher AB contents (above 40%) could be associated to the decrease in the reaction sites by masking of the electroactive species ie, CuO. Therefore, 40% AB content was taken as the optimized composition for further investigations on Al/CuO cells.

Figs 2 and 3 depict the performance of Al/CuO cells using different concentrations of aqueous electrolyte solutions of NaOH and KOH (0.5,1,2 and 3 M) at the optimized AB content and at 25mA current drain at room temperature. It is clear from the discharge profile that the capacity of the cells employing either 0.5M KOH or 1M NaOH show higher reduction effficiency and thereby higher capacity

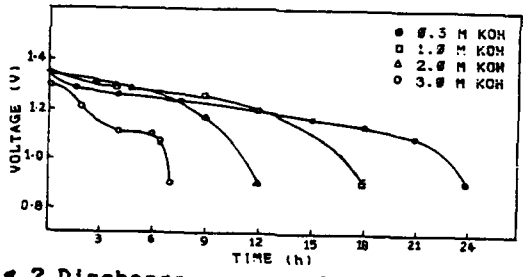

Fig.2.Discharge curve of Al/CuO cells in various concentration of KOH (40% AB, 25 mA current drain)

output. This could probably be due to the aggressive corrosive nature of these electrolytes forming insoluble/soluble Na or K aluminates. Hence, 1M NaOH and 0.5M KOH were taken as the optimised electrolyte composition.

Discharge behaviour of Al/CuO cells in the above optimised AB and electrolyte concentration at different current drains (25,50 and 100 mA) are presented in figs 4 and 5. As can been seen from these figures, the cell voltage initially falls at lower current drain (<50 mA) thereafter it follows a flat profile and the average operating voltage is seen to be 1.15 to

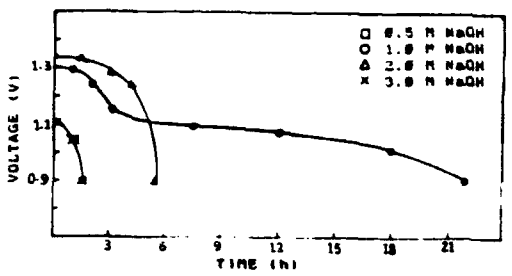

Fig.3.Discharge curve of Al/CuO cells in various concentration of NaOH (40% AB, 25 mA current drain)

1.2 V. However, at higher current drains (>50 mA) a sloping discharge curve is obtained with a steep fall in the capacity of the cells. Moreover, the internal resistance of the cells employing a NaOH electrolyte was found to be lesser (≃ 2.3 ohms)than KOH electrolyte. These large internal resistance could probably be due to the non-conducting nature of cupric oxide[11] and may also be ascribed to the formation of insoluble aluminates.

It is observed that Al/NaOH/CuO cells show better current capability (Fig.5) ie., 100 mA in comparison to Al/KOH/CuO cells. This behaviour is rather surprising considering the higher conductivity of KOH over NaOH electrolyte.[12] However, since we were concerned in the present studies only to evaluate the performance of CuO in alkaline medium, no special attention was given for improving the electrolytes.[13] Furthermore, Tseung et al.,have reported recently that a mixed electrolyte containing 30% NaOH + 50% KOH and viceversa would be an ideal electrolyte solution for aluminium reserve batteries. In view, of these studies, we could safely attribute our observations to the formation of insoluble potassium aluminate salts during discharge of the cells in KOH solution.

The average operating voltage at higher current drains (>50 mA) is ≃1.2V for cells employing NaOH as electrolyte and therefore capable of operating at higher current densities.

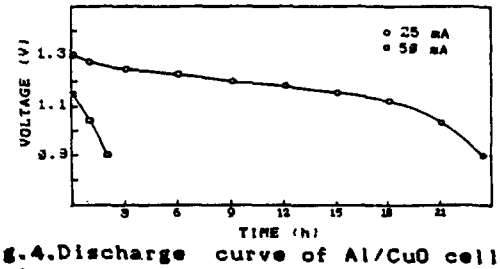

Fig.4.Discharge curve of Al/CuO cells at various current drain (40% AB, 0.5 M KOH)

Table I presents the capacity, reduction efficiency and number of electrons transferred for CuO in Al/CuO cells at different current drains and electrolytes. It can be seen that at lower current drains almost similar capacities are obtained suggesting maximum efficiency

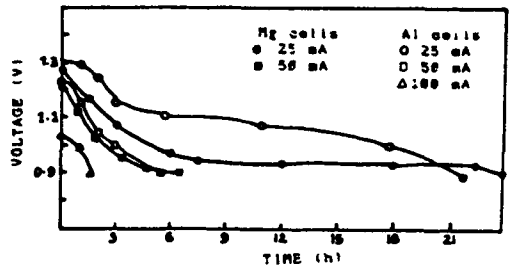

Fig.5.Discharge curve of Al/1M NaOH/CuO and Mg/CuO cells at various current drain

and electron transfer for both the electrolytes. However, at higher current drains (>50 mA) Al/NaOH/CuO cells show better performance. Cells employing NaOH solutions show higher efficiency and electron transfer. These results are interesting considering the higher mobilities and conductivities of K^+ over Na^+ ions. The above results could be assigned to the smaller size of the cations ie., Na^+ thereby indicating higher hydration number[12] and thus enhancing the solubility of Na aluminates as compared to their potassium counterparts.

A comparison of our results on Al/CuO cells with Zn/CuO cells[14] indicate higher operating voltages. We have also compared our investigations with Mg/CuO reserve cells as shown in Fig.5. It can be seen from the discharge curves that higher operating voltages are obtained in the case of Al/CuO cells at both the investigated current drains (25 and 50 mA) for Mg/CuO cells. However, at 100 mA current drains Mg/CuO cells showed operating voltages below the cut off voltage in the present study. Further, a marginal increase in capacity is noticed for cells employing magnesium anodes. Moreover, the energy densities (based on dry weight) of Al/CuO cells are found to be 140 Wh/Kg and is higher than Mg/CuO cells (100 Wh/kg).

In order to arrive at the practical condition of CuO cathode during discharge of an Al/CuO cell, pressed powder electrodes[15] as in the case of the discharge studies were subjected to LSV studies at significantly reduced sweep rates (V) ie., 2.5,10 and 25 mV/s in the potential range of 000 tp -500 mV in 1M NaOH medium. It can be seen from Fig.6 that only cathodic peak (-300 to - 350 mV) are observed and they shift further cathodic with increasing sweep rates (upto 25mV/s). However, no peak is obtained at higher

Table I

Capacity (Ah), Cathodic Efficiency (%) and Number of electrons transferred (n) in Al/CuO cells at various current drains (C.D) and electrolytes.

C.D	NaOH			KOH		
(mA)	Ah	%	n	Ah	%	n
25	0.55	82	1.6	0.60	89	1.8
50	0.28	43	0.8	0.10	15	0.3
100	0.20	30	0.6	--	--	--

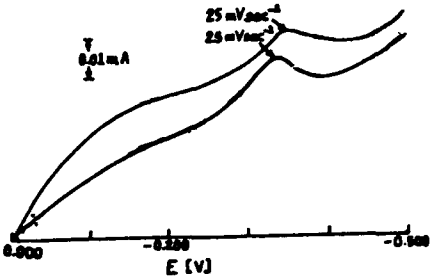

Fig.6.Typical linear sweep voltammogram of CuO cathode.

sweep rates. These facts suggest that the reduction of CuO via Cu_2O is a slow process. Further, a sudden fall in current after the peak potential may be ascribed to the stability of the reduction product. A linear relationship of i_p with square root of scan rate confirms that the process of CuO reduction is diffusion controlled.

Conclusion

1. Aluminium / Cupric Oxide reserve batteries are capable of operating at higher current densities (up to 6.6 mA cm^{-2}) in a NaOH medium.

2. Cathodic efficiency of CuO is 80% at low current drains and 30% at higher current densities.

3. Higher operating voltage (1.20 V) are obtained for Al/CuO cells in comparision to conventionally used reserve Mg/CuO (1 V) or Zn/CuO (0.6 V) cells.

4. Energy density of Al/CuO cells is 140 Wh/kg and is higher as compared to Mg/CuO cells ie., 100 Wh/kg.

Finally, in addition to the above advantages, aluminium is a cheaper anode material.

Acknowledgement

One of the authors (GK) thanks Prof.G.V.Subba Rao, Director, CECRI, Karaikudi and the organizers for their generous financial support for presenting this paper.

* ME project student.

References

(1) D.Linden, Handbook of Batteries and Fuel Cells, McGraw Hill, Inc.,(USA), 1984, Chap.6.

(2) E.R.Dublious, T.C.Murphy, B.M.L. Rao, Extended Abstracts., The Electrochem. Soc. Inc., USA, 92-2, 1992, 675.

(3) K.V.Rao., Trans SAEST., 27, 1992, 119.

(4) S.Licht and D.Peramunage., J. Electrochem., 140, 1993, L4.

(5) P.K.Shen, A.C.C. Tseung and C.Kuo., J.Power Sources., 47, 1994, 119.

(6) B.M.L.Rao, J.Zakrzewshi and R.P.Hamlen.,Extended Abstracts, The Electrochem. Soc. Inc.,USA, 89-1, 1989,15.

(7) S.Licht and D.Peramunage., Science., 261, 1993, 1029.

(8) R.Jasinski, High Energy Batteries, Plenum, New York, 1967.

(9) Gopu Kumar, A.Sivashanmugam and R.Sridharan, J.Electrochem. Soc., 140, 1993, 3087.

(10) F.G.Fischer and Wissler, in Battery Material Symposium, Vol.1, A.Kozawa and M.Nayayama,Editors., p 120, IBA publication, Brusski (1994); Dr Tye, ibid, Discussion.

(11) G.W.Vinal, Primary Batteries, John Willey and Sons, Inc., USA, 1950, chap.8.

(12) I.N.Levine, Physical Chemistry,McGraw - Hill, Inc., USA, 1978, chap.16.

(13) A.C.C.Tseung, R.L.Quarshie, Z..Lin, Extended Abstract, The Electrochem. Soc. Inc.,USA, 89-1, 1989,16.

(14) C.D.S.Tuck., Modern Battery Tech - nology., Ellis Horwood., England, 1991.

(15) J.McBreen, Power Sources 5., D.H.Collins (Eds), Academic Press, London, 1975.

IMPROVED MAGNESIUM BATTERY

Louis P. Jarvis
US Army Research Laboratory
Electronics and Power Sources Directorate
Fort Monmouth, NJ 07703-5000

Abstract

Following a twenty month developmental contract with Rayovac Corporation, One-hundred prototype BA-4590 magnesium/ manganese dioxide (magnesium) batteries were fabricated. Half the batteries (lot A) were fabricated with no chromates in the cathode. The corrosion inhibition system was sodium metavanadate in the cathode and electrolyte, and a cottonseed oil anode treatment. The remaining fifty batteries (lot B) were fabricated with a 50% reduction of barium chromate in the cathode mix .

Throughout continuous discharge testing lot B batteries outperformed lot A. The magnesium batteries of both lots also "ran" hot. The external temperature of six batteries exceeded 45 °C. During intermittent usage, lot A magnesium batteries lost 15% more capacity to anodic corrosion than lot B batteries. During SINCGARS simulation, lot A batteries delivered no service hours; whereas, lot B delivered 0.5, 7.1, and 9.2 hours at 4.4, 21.1, and 43.3 °C respectively.

Overall, the magnesium BA-4590 incorporating barium chromate has the potential for battery cost savings only under low power, tepid operating temperature conditions.

Introduction

Faced with budget cuts, the US. Army is interested in reducing battery training costs. The projected low unit cost of the magnesium chemistry makes the prototype BA-4590 an attractive candidate as a cost effective training battery replacement for the BA-5590/U lithium battery. Shortcomings inherent with the standard magnesium electrochemical systems, however, have made this replacement unrealistic.

Precious efforts [1,2] have dealt with the development of the magnesium BA-4590 battery. The most recent work entails the investigation of anode corrosion inhibitor systems alternate to the standard inhibitor system of barium chromate.

Following a twenty month developmental contractual effort with Rayovac corporation, one-hundred prototype BA-4590 magnesium batteries were fabricated. This paper focuses on the testing and evaluation of the magnesium batteries under various discharge conditions (rate, temperature and duty cycle). Additionally, effect of intermittent usage, SINCGARS radio simulated drain, and accelerated storage was investigated.

Approach

Tests were performed to characterize the following parameters of the two lots (A and B) of the prototype magnesium BA-4590/U batteries: (1) weight and dimensions, (2) continuous discharge, (3) intermittent discharge, (4) SINCGARS simulation and (5) accelerated storage.

The 16-cell Prototype magnesium battery consists of two 15.0-volt electrical sections. Each portion consists of a 2.25 ampere slow-blow electrical fuse and 8 cells connected in series. The battery is utilized in either series or parallel arrangement. Nominal voltage is 30.0 volts (series) or 15.0 volts (parallel).

The cells are designated 1602-M. The cell, cylindrical in shape, is 52.88 mm in height and 25.81 mm in outside diameter. The cells are bobbin construction. The anode, the can itself is magnesium alloy (AZ21). This is the same anode material utilized in the Rayovac production magnesium battery, the BA-4386/U. The alloy consists of magnesium (95.65%), aluminum (2.0%), zinc (1.0%), and minute quantities of magnesium (0.2%) and calcium (0.15%). The anode corrosion inhibition utilized in lot A battery consists of sodium matavanadate (cathode and electrolyte) and cottonseed oil treatment of the magnesium alloy cans. For lot B batteries, the corrosion inhibitor system consists of barium chromate (cathode) and lithium chromate (electrolyte).

The cathodes mix of the two battery lots are as follows:

Lot A	Component	Lot B
52.00%	Magnesium dioxide	52.00
6.95	Acetylene carbon black	6.95
0.82	Magnesium hydroxide	0.82
-----	Barium Chromate	0.82
0.16	Sodium metavanadate	-----
40.07	Electrolyte	39.41

For lot A the electrolyte consists of 3.5N magnesium perchlorate and sodium metavanadate (.2g/l). Lot B electrolyte consists of 3.5 magnesium perchlorate with lithium chromate (.2g/l).

Experimental Procedure

Before testing, dimensions and weight of all batteries were measured. Following discharge, battery dimensions were recorded and compared to initial values. Dimensions prior to and following testing were compared to BA-5590/U

dimensions as specified in MIL-B-49430(ER).

Electrical testing consisted of continuous constant current discharge, intermittent discharge, SINCGARS radio simulation and accelerated storage. A 16 channel Techware Automated Battery Cycler performed all discharge and data acquisition. Five and one-quarter inch disks stored all discharge data. A Tenny Jr temperature chamber was employed to maintain the battery environment at the appropriate temperature.

Continuous Discharge

Continuous constant current discharge was performed at 4.4, 21.1, and 43.3°C. Batteries were soaked for 8 hours at the appropriate temperature prior to discharge. The discharge rate varied from 500 to 1250 mA. Throughout testing internal and battery skin temperatures were recorded. The discharge time to 20.0 volts was used to calculate capacity.

Intermittent Discharge

Testing was performed at 500 mA and 21.1°C. The batteries were partially discharged for three hours. The batteries were then stored at 21.1°C for one or four weeks. Discharge at 500 mA and 21.1°C was then continued to an endpoint of 5.0 volts. The time to 20.0 volts was used for calculation of capacity. Battery performance was compared to that obtained for continuous discharge at 500 mA and 21.1°C.

SINCGARS Simulation

Testing simulated typical usage of the SINCGARS radio. One BA-5590/U battery in the parallel mode powers the radio, which operates at constant power. The discharge scenario consists of 1 minute at 26.4 watts (transmit) followed by 9 minutes at 3.6 watts (receive). This cyclic regime was continued to a battery potential of 5 volts under the transmit mode. Testing was performed at 4.4, 21.1 and 43.3°C. Prior to discharge, all batteries were soaked at the appropriate temperature for 8 hours. The calculation of useful capacity used the time to 10.0 volts..

Accelerated Storage

Batteries were stored for four weeks at 71.1°C prior to discharge. The batteries were then discharged at 500 mA at 21.1°C to 0.0 volts. The time to 20.0 volts was used for calculation of capacity. Battery performance was compared to that obtained for continuous discharge at 500 mA and 21.1°C.

Results

Weight and Dimensions

The lithium BA-5590/U requirements for weight and dimensions are as follows:

maximum weight: 1058 grams
height: 125.40 to 127.00 mm
length: 110.16 to 111.76 mm
width: 60.63 to 62.23 mm

All the magnesium BA-4590/U batteries were within the weight specification. The mean battery weight is 974 grams.

Following discharge, the dimensions of all magnesium batteries exceeded the specifications. The length of all the batteries surpassed the maximum limit of 111.76 mm. The smallest dimensional increase was the height. Fourteen batteries exceeded the height limit of 127.00mm. Battery expansion was a direct result of the individual cells swelling. The formation of magnesium hydroxide $Mg(OH)_2$ between the anode and cathode exerted internal pressure on the anode (can). This caused the individual cells to swell and crack open.

Continuous Discharge

Table 1 shows the dependence of magnesium BA-4590 performance on discharge conditions (temperature and rate).

Table 1.

Constant Current Discharge

Discharge Conditions		Average Capacity to 20.0 Volts (Ah)		
Temperature (°C)	Rate (Amps)	Lot A	Lot B	Lithium
4.4	0.50	1.80	2.74	6.70
21.1	0.50	6.56	6.88	7.10
21.1	1.00	1.30	2.64	7.00
21.1	1.25	0.00	1.21	7.00
43.3	1.00	2.33	2.5	6.90

Lot B (reduced chromate) outperformed Lot A (sodium metavanadate and cottonseed oil) batteries throughout the continuous discharge regime. The magnesium BA-4590 also ran hot. At elevated test conditions (discharge rate and ambient temperature), the internal battery operating temperature increased. This inherent characteristic of the magnesium system is beneficial at cold temperatures. The generated heat warms the battery and improves performance. At elevated discharge rates and operating temperature the additional heat could pose a handling problem. The maximum recorded skin temperature of six batteries exceeded 45°C. This is the pain threshold for skin [3]. Unlike the magnesium, the lithium battery performance is highly stable throughout the various discharge conditions and it does not "run" hot.

Intermittent Discharge

Partially used magnesium batteries do not store well as a result of anodic corrosion. The initial discharge of 3 hours of 500 mA removed the magnesium hydroxide film that protects the anode from corrosion. Once removed the film does not reform to its original degree of protection.

Lot A batteries lost an average of 0.13 hr per day due to the anodic corrosion; whereas, Lot B batteries lost 0.11 hr per day. This represents a 15% greater anodic corrosion capacity loss for Lot A. Lot A contained no chromates, only sodium metavanadate and cotton seed oil as corrosion inhibition. Lot B corrosion inhibition system was a 50% reduction in barium chromate from 0.12 to 0.06 g per cell.

SINCGARS Simulation

Table 2 below shows the SINCGARS simulation test results. Performance of the magnesium batteries is highly dependent upon temperature; whereas, lithium BA-5590/U operation is considerably stable. Compared to Lot B magnesium batteries, the lithium battery provided 390% greater service. Regardless of the discharge temperature, lot A magnesium batteries provided no service time.

Table 2

SINCGARS Simulation

Discharge Temp. (°C)	Time to 10.0 Volts (hr)		
	Lot A	Lot B	Lithium
4.4	0.0	0.5	33.3
21.1	0.0	7.1	34.5
43.3	0.0	9.2	36.0

Accelerated Storage

The effect of 4 weeks at 71.1°C is shown below in Table 3.

Table 3

Accelerated Storage

Battery Number	Lot	Service Time (hr)	Weight Loss (g)
13	A	0.00	41
14	A	0.00	46
15	A	0.00	40
16	A	0.00	44
17	B	6.35	10
18	B	6.04	10
19	B	5.84	10
20	B	6.30	9

Lot A magnesium batteries delivered no service following accelerated storage; an average of 6.56 hours was lost. Lot B batteries delivered an average of 6.13 hours of operation. The corresponding reduction in battery weights is evidence of the anodic corrosion that rendered the poor performance of Lot A batteries. Post mortem analysis of the failed cells revealed much of the anode can had corroded and the cathode mix was very dry. The Lot A corrosion inhibition system did not perform well - anodic corrosion via $Mg+2H_2O \rightarrow Mg(OH_2) + H_2$ was uncontrollable. Eventually the cathode mix "dried out" and battery performance was drastically reduced.

Cost Analysis

A comparison of battery operating cost between the prototype magnesium BA-4590 and the lithium BA-5590/U was performed. Continuous discharge and SINCGARS simulation was investigated. The analysis is based on the following:

1. One day (24 hr) of radio operation
2. Battery unit costs:
   Lithium BA-5590/U: $51.50
   Magnesium BA-4590/U: $18.40

The above unit prices are estimates of the actual cost incurred by the soldier.

Table 4 compares the magnesium and lithium battery operating costs for continuous usage. At 4.4°C, the magnesium BA-4590/U is cost effective at approximately 500 mA and below. At 21.1°C, savings are realized at 1.0 amperes and below. At 43.3°C, the magnesium battery is cost effective below 1.0 amperes.

Table 4

Continuous Discharge Battery Operating Costs

Temp. (°C)	Rate (A)	Battery Operating Cost ($/day)		
		Lot A	Lot B	Lithium
4.4	0.50	122.7	80.6	92.2
21.1	0.50	33.7	32.1	87.0
21.1	1.00	339.7	167.3	176.6
21.1	1.25	no service	456.2	220.7
43.3	1.00	189.5	176.1	179.1

Table 5 displays the SINCGARS simulation battery operation costs. Only at elevated temperatures (>43°C) is the magnesium BA-4590/U cost effective.

Table 5

SINCGARS Simulation Battery Operating Costs

Temp. (°C)	Battery Operating Costs ($/day)		
	Lot A	Lot B	Lithium
4.4	no service	883.2	37.1
21.1	no service	62.2	35.8
43.3	no service	48.0	34.3

The cost analysis assumes continuous battery usage. Intermittent operation of the magnesium system would reduce any potential cost savings.

Conclusions

The corrosion inhibition system of sodium metavanadate and cottonseed oil (lot A) performed

extremely poor. Throughout the entire test regime, lot A magnesium system showed no performance advantage over lot B (50% $BaCrO_4$ reduction) magnesium batteries. Following four weeks of 71.1°C storage, lot A magnesium batteries delivered zero service hours; whereas, lot B delivered an average of 6.1 hours. Similar results were observed for SINCGARS simulation testing. Regardless of temperature, lot A delivered no operational hours; whereas, lot B BA-4590 batteries delivered 0.5, 7.1 and 9.2 hours at 4.4, 21.1. and 43.3°C respectively

Overall, the prototype magnesium battery did not perform well at extreme conditions. At 4.4°C and below and at rates greater than 1.0 amperes, BA-4590 performance was significantly reduced. Additionally, the battery dimensions were not stable and the external temperatures exceed 45°C at certain conditions. The lithium BA-5590/U performance was far superior. SINCGARS simulation tests showed that only at elevated temperatures (>43°C) is magnesium BA-4590 usage cost effective versus lithium BA-5590/U. Regarding continuous usage, the cost effective break even point is 1.0 amperes at 21.1 and 43.3°, and 0.5 amperes at 4.4°C.

References

1. Spellman, P. J., Dittberner,K.L., Ekern,D.M., Larsen,D.M., and Oxley,J.E., "Low-Cost High-Rate Magnesium Battery", Research and Development Technical Report, SLCET-TR-89-0921-F (1992).

2. Jarvis, Louis, "Low Cost Improved Magnesium Battery", Proceedings of the 35th International Power Sources Symposium, p.26 (1992).

3. Parker, F. James and West, Vita R., "Bioastronautics Data Book", Second Edition, NASA (1973), p. 68

ANODIC BEHAVIOUR OF MAGNESIUM-LITHIUM ALLOY IN AQUEOUS MAGNESIUM PRIMARY BATTERY

GOPU KUMAR, A.SIVASHANMUGAM, N.MUNIYANDI and A.K.VADIVEL*
Central Electrochemical Research Institute (CSIR),
Karaikudi - 623 006, TamilNadu, India

Introduction

Magnesium batteries, both reserve and dry types are, nevertheless, very attractive than zinc/lithium batteries.[1,2] Investigations on magnesium anode either individually or in conjunction with different depolarizers have attained remarkable dimensions, which is evident from recent literature scan.[3-5] The reason acclaimed to the potentialities of magnesium anode like high energy, environmentally friendly and, ofcourse, technologically comfortable.[6]

Studies on the improvement of shelf-life and potential realization of magnesium have been attempted through various means either by introducing inhibitors, eliminating certain degrading elements, surface coating or alloying with metals like Al, Zn, Pb, Sn etc. Some magnesium alloys (AZ 31, AZ 21, AP 65, AT 61) have been extensively investigated and few are well established in certain practical applications.[1,7]

However, the idea of alloying lithium with magnesium is quiet interesting so as to enjoy the higher potential/energy characteristics of lithium and till date very few reports[8,9] are available to elucidate the possibility of exploiting magnesium - lithium (Mg-Li) alloy as a battery anode. The addition of lithium to magnesium has been reported to have a corrosion resistance[10] similar to other magnesium alloys and give higher voltage and better discharge characteristics.

Hence, in the present paper, we have carried out a comprehensive investigation on the performance characteristics of Mg-Li alloy as a half cell(single electrode) as well as Mg-Li/CuO cell in selected electrolytes.

Experimental

Chemicals : Mg-Li alloy (13% Li), $MgCl_2$, $MgBr_2$, $Mg(ClO_4)_2$, $Mg(COOCH_3)_2$ and CuO (Loba Chemie, AR) were used.

Determination of Self Corrosion

Weight loss method was used for comparing the self corrosion of Mg-Li alloy in various electrolytes. 1 cm × 1.5 cm specimen were intially cleaned and then weighed. These sheets were completely immersed in 100 ml of the investigating electrolyte for 15 hours at 30±1°C. During the course of this experiment the solutions were not stirred, since in an actual battery the electrolyte is under stagnent condition, when the current is not drained.

Galvanostatic Polarization Measurements

Anodic and cathodic polarization of Mg-Li alloy anode in various electrolytes mentioned earlier were carried out by impressing direct current from a constant current generator. The experimental cell was a typical three electrode assembly using platinum foil as counter, Ag/AgCl as reference and Mg-Li (3 cm × 2 cm) as working electrodes. The Mg-Li pieces were cloth buffed in the presence of pumice and then degreased with trichloroethylene before use. Polarization measurment was started after an immersion time of 5 min, when a steady state potential (open circuit) was obtained. Current densities in the range of 10 - 250 mA cm^{-2} were impressed on the working electrode and the steady potential was measured at each current density. Current and potential measurments were made using high impedance multimeter.

Preparation of Electrodes and Cell Assembly

Mg-Li alloy sheets of 3 cm × 2 cm size and 0.15 cm thickness were used as anode. Cathodes were prepared by pressing a loose powder mix containing 1g CuO, 0.4g acetylene black and 2 to 3 ml of aqueous binder on both sides of a 3 cm × 2 cm copper current collector at an optimized pressure. Thus, a cell assembly consists of two anodes and one cathode seperated by cellophane arranged alternatively and loosely wound by nylon thread for keeping the electrodes intact to minimize the ohmic resistance. Electrodes were assembled in a PVC container and activated with the required volume of the investigated electrolytes and discharged at constant current drains of 25, 50, 75 and 100 mA at room temperature up to a cut off voltage of 0.8 V. Voltage vs time were recorded at time intervals. The weight of anode consumed was also determined from the initial and final weight of the anodes taken before and after discharge respectively. The anodes were cleaned by a standard procedure[11] before weighing.

Results and Discussion

The work described here relates to the studies on the anodic behaviour of Mg-Li alloy metal undertaken either individually or in combination with cathode in the presence of various electrolytes such as $MgCl_2$, $MgBr_2$, $MgSO_4$, $Mg(ClO_4)_2$ and $Mg(COOCH_3)_2$ solutions.

Corrosion Rate Measurement

It is well known that the corrosion rate depends on electrolyte concentration,

alloy composition and pH of the solution. The corrosion rate of Mg-Al alloy is highest in chloride medium and lowest in perchlorate medium. This was ascribed to the parasitic corrosion occuring in Mg-Al alloys.[11]

However, in Mg-Li alloy the rate of corrosion is maximum and minimum in $Mg(ClO_4)_2$ and $MgCl_2$ electrolyte solutions respectively (Table I). Further, the corrosion rate increased at higher electrolyte concentration due to the increase in the anion content[12] and the corrosion rate of Mg-Li alloy in 2 M solution of various electrolytes are in the order of $MgCl_2$ < $Mg(COOCH_3)_2$ < $MgSO_4$ < $MgBr_2$ < $Mg(ClO_4)_2$.

Table I

Corrosion rate measurement of Mg-Li alloy in different electrolytes

Corrosion rate (mg cm^{-2} min^{-1})	Concentration (Molar)		
	1.0	1.5	2.0
$MgCl_2$	0.0031	0.0042	0.0059
$MgBr_2$	0.0046	0.0057	0.0168
$Mg(ClO_4)_2$	0.0054	0.0074	0.0422
$MgSO_4$	0.0038	0.0052	0.0072
$Mg(COOCH_3)_2$	0.0053	0.0060	0.0067

Table II presents a comparison of the corrosion rate of Mg-Li alloy with the widely used Mg AZ 31 alloy.

Table II

Corrosion rate measurment of Mg-Li alloy and Mg AZ 31 alloy in 2.0 molar concentration

Electro-lyte	Corrosion rate (mg cm^{-2} min^{-1})	
	Mg-Li	Mg AZ 31
$MgCl_2$	0.0059	0.1032
$MgBr_2$	0.0168	0.0810
$Mg(ClO_4)_2$	0.0422	0.0029
$MgSO_4$	0.0072	0.0033
$Mg(COOCH_3)_2$	0.0067	0.0034

The maximum and minimum rate of corrosion is observed for Mg-Li alloy in $Mg(ClO_4)_2$ and $MgCl_2$ electrolyte solution respectively.

The above observations are interesting considering the difference in the corrosion behaviour of Mg-Al and Mg-Li alloys. In the case of Mg-Al alloys, the onset of parasitic reaction and subsequent formation of highly acidic $AlCl_3$ salt, enhances the rate of corrosion in $MgCl_2$ medium. However, in Mg-Li alloy, the anodically generated electrolyte salt, LiCl accumulates untill it precipitates[13] out as an impervious layer in the pores of the superficial hydroxide layer and thereby increasing the corrosion resistance of this alloy. Further, these facts may also be supplemented by the newer mechanical properties associated with this alloy.[8]

Open Circuit Potential Measurements

Open circuit potential (OCP) measurments have been carried out for Mg-Li alloy (vs Ag/AgCl) in 1.0, 1.5 and 2.0 molar concentrations of $MgCl_2$, $MgBr_2$, $Mg(ClO_4)_2$, $MgSO_4$ and $Mg(COOCH_3)_2$ electrolytes.

It is evident from table III that the OCP of Mg-Li alloy is found to increase slightly with increasing electrolyte concentration. The OCP is marginally higher in the case of $MgCl_2$ or $MgBr_2$ electrolyte and this could be ascribed to the slightly acidic nature[4] of these electrolytes. It is interesting to compare our observations with the OCP of Mg-Al alloys,[11] wherein higher potential differences are realized in $MgCl_2$ medium than $Mg(ClO_4)_2$ ie., 0.15 V. However, in the present study the difference is only by 0.08 V. This fact could be ascribed to the adherent passive film formed by LiCl. The formation of corrosion product, high reactivity of alloy, internal resistance caused by the magnesium hydroxide film formation and the entry of hydrogen gas into the electrode surface resulting in the reduction of the effective surface area are the likely reasons for the sharp drop in the OCP of these electrolytes.

Table III

Open circuit potential of magnesium-lithium alloy in various electrolytes with respect to Ag/AgCl reference electrode

Electrolyte	Open Circuit Potential (V)		
(Molar)	1.0	1.5	2.0
$MgCl_2$	-1.46	-1.48	-1.50
$MgBr_2$	-1.47	-1.48	-1.52
$Mg(ClO_4)_2$	-1.42	-1.42	-1.44
$MgSO_4$	-1.36	-1.38	-1.42
$Mg(COOCH_3)_2$	-1.38	-1.40	-1.46

Galvanostatic Polarization Measurements

Figs.1(a-c) show plots of potential against log current density for Mg-Li alloy in various electrolytes when subjected to galvanostatic polarization. It is observed that the cathodic polarization was more pronounced than the anodic polarization. This reveals that the corrosion of this alloy in these electrolytes is controlled cathodically. Similar behaviour is observed in the case of Mg AZ31 alloy [Figs.2(a-c)]. It can be seen from these figures that electrolytes like $MgSO_4$ and $Mg(COOCH_3)_2$ show more positive value and hence these electrolytes are not suitable.

Discharge Behaviour

Magnesium reserve cells were fabricated using Mg-Li alloy, CuO as anode and cathode material respectively. The discharge characteristics of Mg-Li / $MgCl_2$ / CuO cells have been carried out galvanostatically under continuous discharge at various current densities. Table IV summerizes the performance of the above cell at various current drains (25, 50, 75 and 100 mA) corresponding to

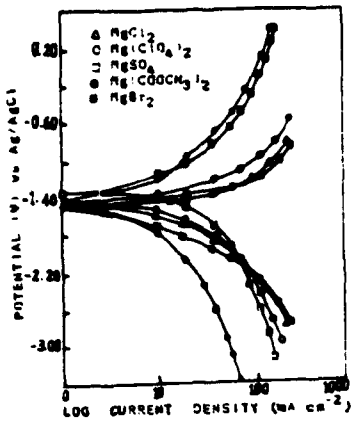

(a)

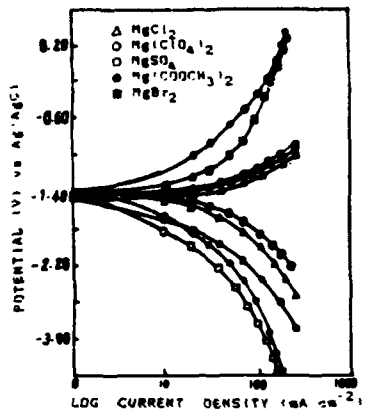

(b)

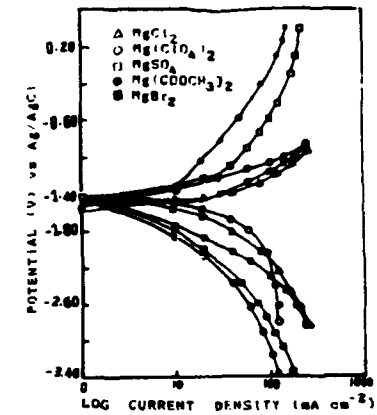

(C)

Fig.1 Galvanostatic Polarization of Mg-Li Alloy in Various Electrolytes
a) 1 M b) 1.5 M c) 2 M

current densities of 2.1, 4.2, 6.3, 8.3 mA cm^{-2} respectively. It is noted that increase in current densities results in loss of cell capacity which could be attributed to the increased cathodic polarisation during the discharge of the respective cells.

Table IV
Various energy parameters of Mg-Li / $MgCl_2$ / CuO cell

Cell parameters	C.D. (mA cm^{-2})			
	2.1	4.2	6.3	8.6
Cell Voltage (V)	1.24	1.06	0.92	0.67
Capacity (Ah)	0.64	0.63	0.48	0.35
No. of elect -rons transf -erred	1.91	1.66	1.19	1.04
Cathod'c efficiency(%)	95	93	69	53
Anodic efficiency(%)	65	68	73	81

Fig.3 shows the discharge behaviour of Mg-Li / $MgCl_2$ / CuO cells. The open circuit voltage of 1.62 V decreased on applying load to a constant working voltage of 1.24 V. This is due to the internal resistance of the cell. The capacity output or the cathode efficiencies were found to be 95% and 53% at lower and higher current drains respectively indicating higher electron transfer at lower drains. A comparison of these results with Mg AZ 31 / CuO cell at 25 and 50 mA current drains (Fig.3) suggests that the incorporation of lithium in the present investigation not only

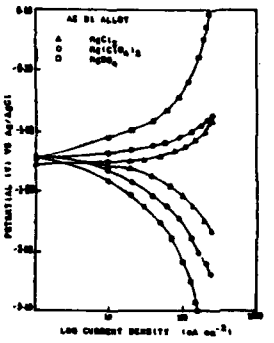

(a)

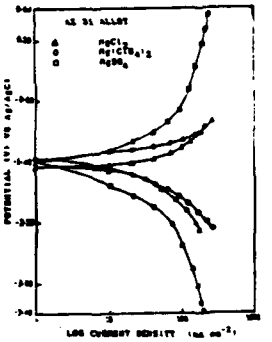

(b)

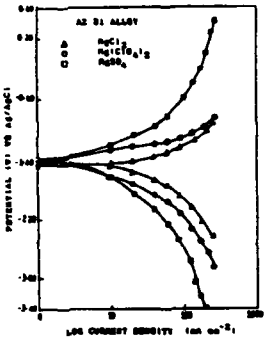

(C)

Fig.2 Galvanostatic Polarization of Mg A231 Alloy in Various Electrolytes
a) 1 M b) 1.5 M c) 2 M

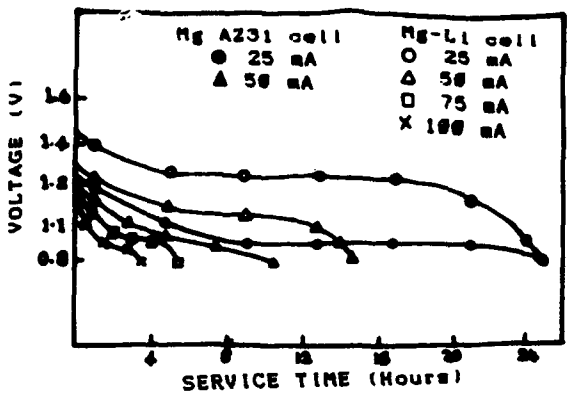

Fig.3. Discharge Behaviour of Mg-Li/CuO and Mg AZ31/CuO Cells at Various Current Drains

shows increase in operating voltage of 0.3 to 0.4 V but also enhances the cell capacity. This may be explained due to the cubic crystal structure[10] of this alloy. These results are in agreement with the earlier assumptions.[14]

The anodic efficiences of Mg-Li/$MgCl_2$/CuO cells at various current densities are presented in table IV. It is seen that the efficiences increase with increasing current densities ie., at 8.6 mA cm^{-2} it is 81%. This may be due to the higher concentration of hydroxyl ions as well as the passivation of lithium caused by the electrolyte salt ($MgCl_2$) in superficial anolytes. The above facts are in agreement with the observations of Wiesener et.al.[15]

Conclusion

1. Higher OCP for Mg-Li alloy are observed in 2 M $MgCl_2$ and $MgBr_2$ electrolyte medium.

2. The corrosion rate of Mg - Li alloy is found to be in the order of $MgCl_2$ < $Mg(COOCH_3)_2$ < $MgSO_4$ < $MgBr_2$ < $Mg(ClO_4)_2$.

3. Mg-Li alloys exhibit higher (81%) anodic efficiencies even when the current density is increased to 8.6 mA cm^{-2}.

4. Mg-Li/$MgCl_2$/CuO cells give higher operating voltage and capacity than Mg Al counterpart.

5. Galvanostatic polarisation studies have demonstrated that the corrosion of Mg-Li in $MgCl_2$, $MgBr_2$, $Mg(ClO_4)_2$, $MgSO_4$ and $Mg(COOCH_3)_2$ electrolytes is cathodically controlled.

Finally, in view of the above advantages, Mg-Li alloy is a potential anode material for magnesium batteries.

Acknowledgement

One of the authors (GK) thanks Prof. G.V.Subba Rao, Director, CECRI, Karaikudi and the organizers for their generous financial support.

References

1) G.W.Heise and C.N.Cahoon., "The Primary Batteries" Vol. 1, John Wiley & Sons, Inc., N.Y.(USA) (1960).

2) L.Jarvis., J.Power Sources., 32 (1990) 271.

3) Gopu Kumar, A.Sivashanmugam and N.Muniyandi., J. Power Sources., 30 (1992) 121.

4) Gopu Kumar, A.Sivashanmugam and N.Muniyandi., J. Appl. Elect. Chem., 23, (1993) 265.

5) Gopu Kumar, A.Sivashanmugam and R.Sridharan., J. Electchem. Soc., 140 (1993) 3087.

6) T.D.Gregory, R.J.Hoffman and R.C.Winterton., J. Electrochem. Soc., 137 (1990) 775.

7) N.C.Cahoon and G.W.Heise.,The Primary Batteries, Vol. 2, John Wiley & Sons, Inc., N.Y. (USA), (1976).

8) Y.Iwadate, M.Lassouani, F.Lautelme and M.Chemla., J. Appl.Electrochem., 17 (1987) 385.

9) M.L.Saboungi and M.Blander., J. Electrochem. Soc., 17 (1975) 1631.

10) M.Sahoo and J.T.N.Atkinson., J.Mater. Sci., 17 (1982) 3564.

11) R.Udhayan, N.Muniyandi and P.B.Mathur British corrosion journal., 27 (1992) 68.

12) R.Udhayan and D.P.Bhatt., J. Power Sources, 39 (1992) 107.

13) S.D.James., Proc. Sym. Lithium Batteries., 84(1) (1984) 18.

14) R.Jasinski., High Energy Batteries., Plenum Press, N.Y. (USA), (1967).

15) L.Wiesener, W.Glaeser and R.Pelz., Power Sources 5., Academic Press, London, (1975).

ELECTROLYTE LEAKAGE PHENOMENON IN RESERVE ORDNANCE BATTERY FOR U.S. ARMY M732 ELECTRONIC PROXIMITY FUZE

Mel Morganstein
Reserve Battery Technology Branch
Electronics and Power Sources Directorate
Army Research Laboratory
2800 Powder Mill Road
Adelphi, MD 20783-1145

The PS115 Reserve Power Supply

The M732 electronic fuze is the principle proximity fuze system used in the U.S. Army and Marine Corp's 105 , 155 , 175 , and 8-inch artillery and 4.2-inch mortars. Millions of these fuzes are in the field stockpiles worldwide. Energy for the fuze is provided by a liquid electrolyte reserve battery designated the PS115. To meet storage requirements over the required 20 year plus shelf life and under a wide range of conditions (–40° to about 65°C), the battery is a reserve system that is inert prior to use. As such, the fluoboric acid electrolyte is stored apart from the cells in a copper can or ampule.

An ordnance battery must also withstand very high mechanical stresses during operation, viz. linear accelerations of over 25,000 g's (over 35,000 g's in rocket-assisted projectiles) and spin rates over 300 rps.

The rugged 19-cell assembly (Figure 1) is fabricated into an integral unit by the thermal lamination of a series of steel-based, electroplated, bipolar, circular plates, alternately stacked with separators made of polyethylene-coated, highly impervious paper. A grooved brass plate bonded between the ampule and cell stack assembly works in conjunction with a series of holes in each of the electrode plates and acts as a manifolding system to route the fluoboric acid electrolyte into the cells when the battery is activated. The electrodes utilize lead and lead dioxide as the active cell materials. To minimize thickness and withstand the extreme mechanical forces, these materials are electroplated in layers about 0.025 mm thick onto a nickel-flashed, 0.065-mm-thick steel base stock to create a bipolar material.

Since the batteries are built into the fuzes and must activate automatically at gun launch, liquid electrolyte reserve ordnance batteries incorporate a unique mechanism within the ampule that automatically pierces the container and releases the liquid at projectile launch. This mechanism takes advantage of the extreme mechanical forces available only at that time, a combination of linear setback and angular acceleration forces. Centrifugal force generated by projectile spin then moves the electrolyte into the cells and activates the battery in a few milliseconds.

To eliminate the intercell electrolyte short-circuit that persists after the electrolyte is distributed throughout the series-connected assembly, the PS115 makes use of an immiscible, non-conducting organic liquid in an extraordinary fashion. This solvent, methylene bromide ($MeBr_2$, specific gravity = 2.497, twice that of the electrolyte) is held in a special inner can and is metered out through small holes after the aqueous electrolyte, quickly displacing the conductive electrolyte from the common distribution channel and eliminating the intercell short. To retain the $MeBr_2$, the unsealed inner cartridge contains a polypropylene fiber pad, a material that is wetted by oleagenous substances such as $MeBr_2$, but not by aqueous solutions such as the fluoboric acid electrolyte. Thus, the pad absorbs the $MeBr_2$ like a sponge, retaining *virtually* all of the liquid, even after decades of storage.

Since initial compatibility studies of the materials comprising the ampule system indicated chemical compatibility, no extraordinary effort had been made to isolate the fluoboric acid electrolyte from the $MeBr_2$. Thus, the cartridge holding the $MeBr_2$ was not sealed in the initial production design, but included small holes to meter out the $MeBr_2$ after the acid electrolyte. As will be shown, this proved to be a critical design flaw.

The Leakage Mechanism of Early Design PS115 Power Supplies

The degradation problem was first discovered in PS115 battery engineering samples in 1983. It was seen in advanced cases as external destruction of the molded glass-filled polycarbonate battery case (Figure 2). When samples were removed from M732 fuzes and returned from the field during a followup study, researchers quickly learned that internal electrolyte leakage could be severe enough to destroy the paper separators without being evident externally (Figures 3 and 4). The separator degradation permitted electrolyte short circuits to develop down the outside of the stack of cells, drastically reducing output voltage, and thus affecting the electronic operation. Although the fuze would revert to the backup ground impact mode function, there would be a loss in combat effectiveness. Only in the most advanced cases did it appear that the fuze mechanism itself would be attacked to the degree that it would fail to function at all. A high-level study was sponsored by the Army to determine the extent that this was also occurring within fielded M732 fuzes, what was causing it, and what could be done to mitigate or eliminate the problem both in the current stockpile and future production.

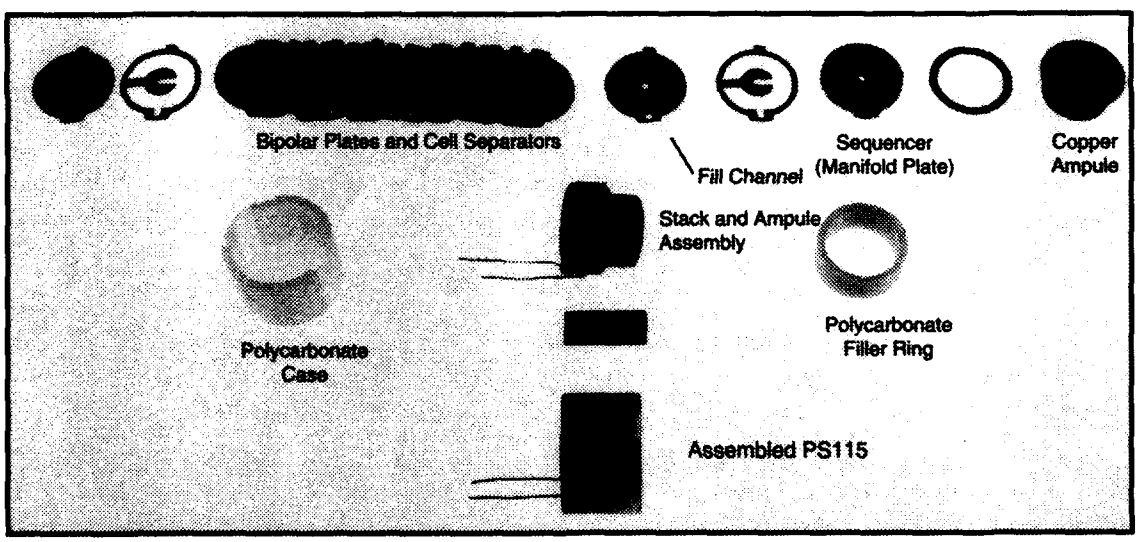

Figure 1. PS115 Reserve Battery, exploded view at top; assembled at bottom.

Because the initial studies had not shown any material incompatibility, this problem came somewhat as a surprise to the battery's developers at the Harry Diamond Laboratories (HDL).* The pure ETP (Electrolytic Tough Pitch) copper from which the ampule is made had been proven to be extremely resistant to attack from the fluoboric acid electrolyte. Common chemistry texts indicated no direct reaction, and this conclusion had seemingly been demonstrated after long-term, high-temperature storage tests. Consistently, ampules were intact even after accelerated-aging tests at 71°C (160°F) that *ostensibly* simulated storage well beyond the 20-year requirement.

*Now part of the U.S. Army Research Laboratory.

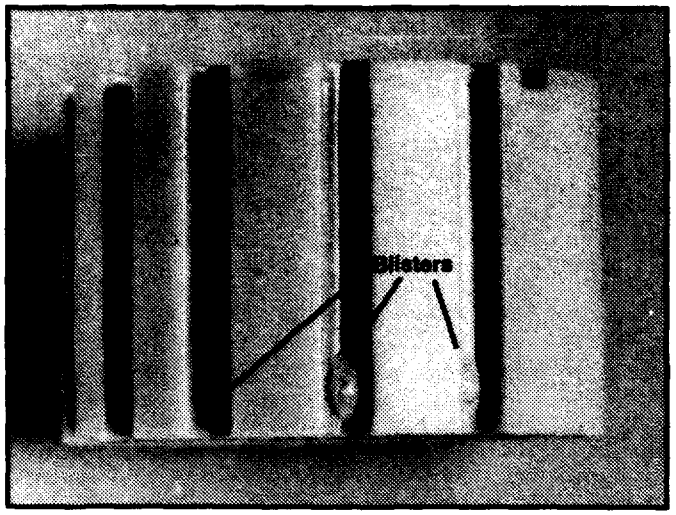

Figure 2. Degradation of polycarbonate case by leaking methylene bromide.

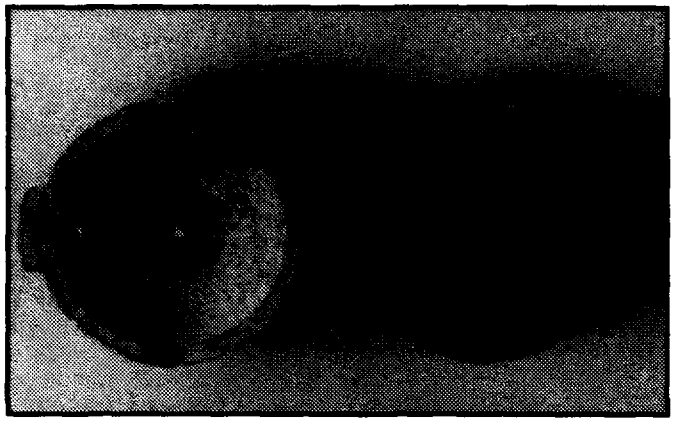

Figure 3. View of good battery split between cell stack and sequencer.

Figure 4. View of leaking battery split between cell stack and sequencer. Note corrosion on electrode plate and destruction of separator.

Investigators found that leakage took place through pinholes eaten through the 0.076-mm-thick frangible copper diaphragm. In fact, extensive pitting was discovered in the interior surface of the copper ampule where it was wetted by the acid (Figure 5). While this microscopic pitting was not deep enough to perforate the thicker 0.25-mm-thick walls of the cylindrical ampule cup itself, it often penetrated the much thinner diaphragm. (This can be seen in Figures 6 and 7.) Also noted was a white precipitate of an insoluble copper salt coating much of the interior of the ampule.

In the post-leakage study, it was ultimately established that complex chemical interaction *was* taking place between the acid electrolyte, the supposedly inert $MeBr_2$ insulating fluid, and the copper of the ampule. Where the liquid reactants are in contact with the copper, pitting will occur. Depending on storage conditions, perforation—and thus leakage—will often occur if the liquids are in contact with the thin diaphragm. This chemical process proceeds until the partial pressure of one of the reaction products, methane gas, reaches about 6 atm. If this is prior to a perforation, the process effectively stops and the ampule remains intact. This is borne out by plots of cumulative leakage v. time, wherein the leakage incidence approaches a limiting level (see Figure 9). The corrosion mechanism is documented[1] in detail and is discussed in the next section.

Chemistry of Corrosion Process

Exposure of the copper comprising the ampule and diaphragm to atmospheric oxygen inevitably produces some oxidation on the surface. It was well known that this thin oxide coating reacts readily with the acid electrolyte.

$$Cu_2O+2H^+ \rightarrow 2Cu^+ + H_2O \quad (1)$$

$$CuO+2H^+ \rightarrow Cu^{+2} + H_2O \quad (2)$$

Despite the fact that copper is found above hydrogen in the regular electromotive series, it has been demonstrated that copper will nontheless react with a non-oxidizing acid[2] such as HBF_4. This will liberate hydrogen until the concentration of the gas is such that the potential established for equilibrium (3) is equal to that established for (4).

$$H_2 \leftrightarrow 2H^+ + 2e^- \quad (3)$$

$$2Cu^+ + 2e^- \leftrightarrow 2Cu \quad (4)$$

When this occurs, the EMF disappears, terminating the corrosion. That is, the following reaction,

$$2Cu+2H^+ \rightarrow 2Cu^+ + H_2\,, \quad (5)$$

proceeds until a sufficient hydrogen partial pressure is reached. This supports the observation that copper is not seemingly attacked by the fluoboric acid electrolyte within the sealed ampule, unless some mechanism occurs to remove the hydrogen and/or copper ions.

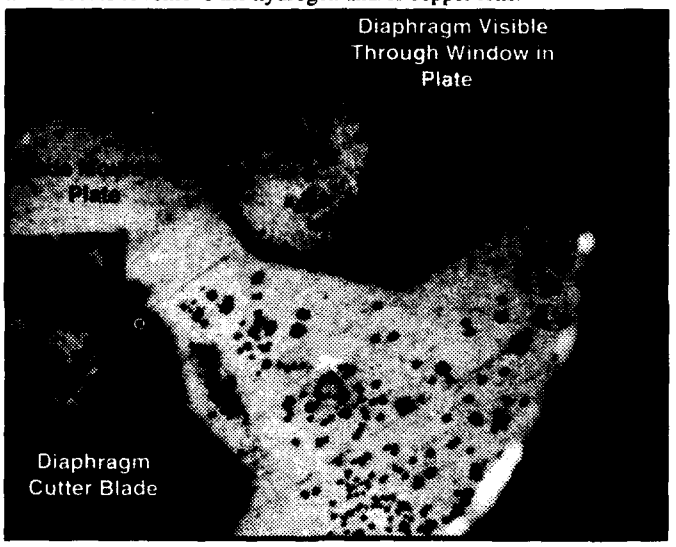

Figure 5. Interior view of ampule showing extensive pitting on cutter blade mounting plate and diaphragm.

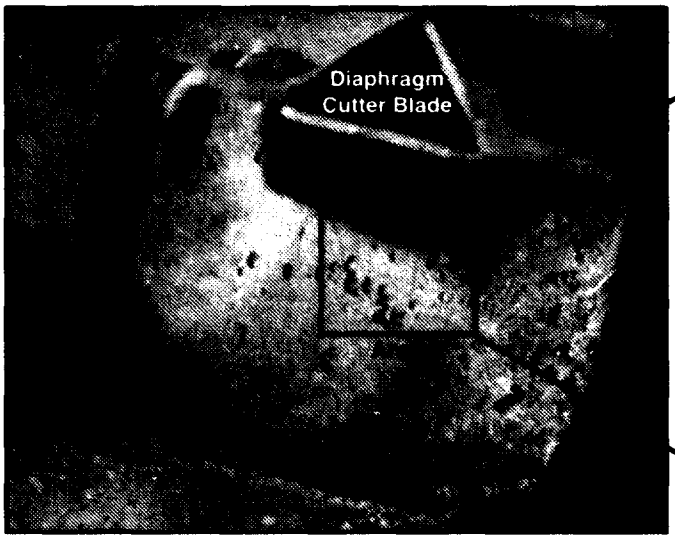

Figure 6. View of diaphragm showing perforation.

Figure 7. Magnification of Area A showing pits and perforation.

Equations (1) through (5), in addition to the known equilibria between metallic copper and copper ions,

$$Cu+Cu^{+2}\leftrightarrow 2Cu^{+} \quad (6)$$

determine the initial concentrations of cuprous (Cu^{+}) and cupric (Cu^{+2}) ions and hydrogen in the acidic phase.

The availability of $MeBr_2$ (either in vapor or liquid phase contact) provides a means to *remove* hydrogen from the system, i.e., the catalyzed reduction (hydrogenation) of methylene bromide in an acid medium at a metallic surface.

$$CH_2Br_2+H_2 \xrightarrow[\Delta]{Me} CH_3Br+HBr \quad (7)$$

This critical reaction is considered the rate-controlling step in the corrosion process. In addition to constantly removing hydrogen formed in equation (5), it produces HBr, a product which will react with and precipitate out the copper ions formed in that reaction.

$$Cu^{+}+HBr\rightarrow H^{+}+CuBr\downarrow \quad (8)$$

$$Cu^{+2}+2HBr\rightarrow H^{+}+CuBr_2\downarrow \quad (9)$$

Thus, the $MeBr_2$ hydrogenation reaction (7) removes both the reaction products produced in (5), causing the acid to attack the metallic copper ampule parts as long as the former reaction continues to consume hydrogen. The established presence of both methyl bromide (CH_3Br) and bromide ions (from the HBr) in corroded ampules is strong evidence that the reaction shown in (7) occurs.

The presence of methane (CH_4) in ampules in battery samples returned for study is explained by a second hydrogen ion-copper catalyzed reaction that succeeds the process in (7)

$$CH_3Br+H_2 \xrightarrow[\Delta]{Me} CH_4\uparrow+HBr\,. \quad (10)$$

which produces methane and additional bromide ions. It is the latter product that not only precipitates out copper ions, but further depletes hydrogen and thus drives reaction (5) toward the right, consuming metallic copper in the process.

Precipitates of both chlorides and fluorides of copper are also formed, and are explained by the co-presence of both cuprous and cupric ions, present in minute amounts in the acid electrolyte.

What is of critical importance in the understanding of the processes involved in ampule perforation is the role played by the gaseous product created in reaction (10), methane. It is the increasing partial pressure of this gas that can eventually drive the reaction in the reverse direction and effectively bring the degradation to a halt. Thus, if this occurs before the ampule is perforated, its integrity will, most likely, never be compromised, and the battery will remain fully intact and operational.

The Pitting Mechanism

One thrust of the study was to determine the cause for pitting, i.e., *localized* reaction sites, rather than a phenomenon in which the attack was evenly distributed across the entire wetted interior surface. It was eventually established that this pitting was a result of the deposition of an insoluble white copper salt precipitate on the wetted surface. Since the precipitate tended to create a protective coating on the wetted copper as the reaction proceeded, it progressively restricted the metal surface available for reaction. This continued until the active area was reduced to a number of extremely small sites that had to bear the brunt of the attack. If equilibrium was reached before the copper was perforated, the ampule would remain intact; if not, we had a "leaker."

Why this Phenomenon was Missed During Battery Development

Clearly, M732 fuzes stored for years at ambient conditions were developing leaks in the batteries. Yet, no such leakage was observed in samples of ampules stored in 71 C (160 F) compatibility studies during the battery development program. An important part of this investigation was to determine the cause of this significant disparity.

Reaction rate theory dictates that a chemical process proceeds more quickly and equilibrium is reached sooner with increasing temperature. By assuming that reaction rates double with every 10 C rise in temperature, one can simulate 16 years (192 months) of storage at 20 C ambient temperature in only about three months by raising the storage environment to 80 C, i.e. an increase of 60 C above ambient. Since the temperature-reaction rate factor here is normally somewhat higher than 2.0 (established in extensive storage tests of newly manufactured ampules), one year of storage at 60 C is normally considered equivalent to 20 years in the stockpile at ambient temperature (slightly less than 20 C). An Arrhenius plot of the storage data (extrapolated to ambient temperature) is shown in Figure 8. This *normally* allows product researchers to predict extended storage capabilities in reasonable development time-frames.

In fact, the normal temperature-reaction rate relationship is borne out by plots of cumulative ampule leakage v. time data at various fixed temperatures, where the onset of leakage occurs earlier (and the maximum leakage incidence is greater) as the temperature is increased. In the special study, large groups of samples were stored in environmental conditioning ovens at various temperatures. As expected, ampule diaphragm corrosion pitting, with the accompanying leakage, was observed in a portion of the samples. As fully predicted, for temperatures up to about 60 C (140 F), the onset of this leakage occurred sooner as the storage temperature increased (see Figure 9, a simplified representation of the phenomenon). More details of this conditioning study were published in another HDL report.[4]

Most extraordinary, however, was that the percentage of ampules that leaked began to decrease sharply with increasing temperature above about 60 C (140 F). In fact, the rate dropped to zero at at about 71 C (160 F). When ampules were stored above this threshold temperature, the leakage phenomenon disappeared altogether. None of the leakage that occurred at

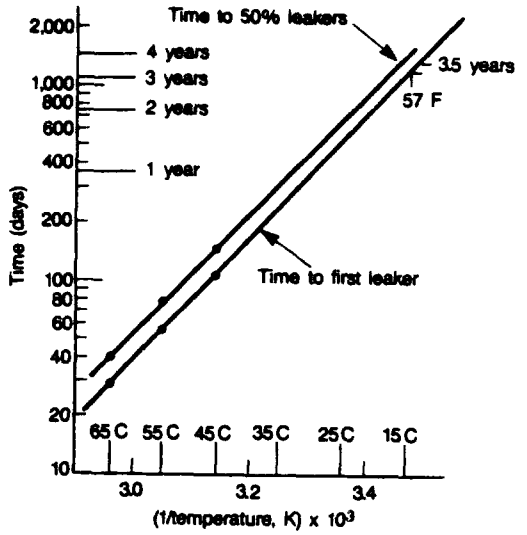

Figure 8. Arrhenius plot of storage data.

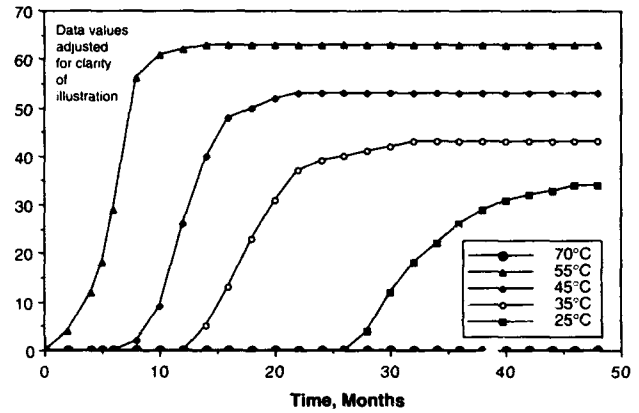

Figure 9. Ampule leakage rate v. time at fixed storage temperature.

lower temperatures was evident. Chemical tests indicated that the same reactions had taken place, but the physical results were significantly different.

Examination of the inside surfaces of the ampule can and diaphragm of samples stored above the threshold temperature showed that the surface of the copper was subtly changed to a matte-like appearance with no pitting. This clearly indicated that a chemical reaction involving the copper had still occurred, but the reaction was now evenly distributed across the entire wetted surface, and not confined to very localized areas so as to cause pitting. It was evident that the process that caused pitting and perforation no longer acted at 71°C. It was eventually established that above about 60°C (140°F), increased solubility of the copper precipitates prevented the formation of the masking protective coating and eliminated the unique mechanism that caused the pitting. Although unknown during the development period, it was now evident that the original storage compatibility tests of the ampules at 71°C were invalid since the higher temperature did not merely accelerate the effect of storage, it altered the internal processes and eliminated the very cause of the leakage.

Solutions to the Ampule Leakage Problem

The investigation produced several ways of dealing with the problem, depending on whether we were dealing with batteries yet to be produced, batteries that had yet to be built into fuzes, or the existing M732 fuze stockpile.

Batteries Yet to be Produced

For batteries produced after the cause of the problem had been identified, the ampule was redesigned to eliminate all contact between the fluoboric acid electrolyte and the methylene bromide insulating liquid. The "bromide" capsule was modified so as to be a completely sealed container within the larger acid ampule. Thin copper diaphragm panels that would be torn open during gun launch by a second set of internal cutter blades were added to the capsule.

Saving the Existing Battery Inventory, the "Bakeout" Program

During the research program, it quickly became evident that the reaction products did not affect battery performance, and that ampules could be "heat treated" to reduce the potential for leakage. By merely raising the temperature of the ampules to the critical threshold level, 74°C±3°, and storing them at this level for three days, the reaction could be driven to equilibrium, i.e., to stability, without the formation of pits. While this new insight could not salvage any PS115 batteries already built into fuzes, it could be used to preserve battery inventory that was in the "pipeline" after the fuze production lines were shut down following discovery of the problem. Consequently, the Army funded a program to save this quantity of approximately 500,000 batteries by "baking" them in a controlled process.

Preserving the Existing Fuze Stockpile

Further, a partial solution was developed to halt the continuing degradation of the existing stockpile. The ampule study included tests which demonstrated that the incidence of battery leakage was a maximum when the diaphragm was down and fully wetted, less when the ampule was on its side and the wetted area reduced, and virtually non-existent when the diaphragm was at the top and thus untouched by the liquid. Since the fuze inventory was largely stored pointing nose upward, with the battery ampule diaphragms wetted, it was clear that the degradation could be arrested by inverting the fuzes. Acting on recommendations of the technical staff at HDL, the U.S. Army directed that the entire inventory of M732 fuzes throughout the entire world be positioned nose downward.

M732 Fuze Stockpile Surveillance Program

Unfortunately, the inversion operation only served to help prevent further degradation: batteries which had already leaked could not be saved. Under the direction of the Army, a surveillance of the fuze stockpile was begun to statistically assess the real condition of the fuze batteries at various locations on a lot-by-lot basis. It was planned that through this program, the Army would be able to determine which assets should be disposed, which could be accepted as is, and which should be completely screened by some non-destructive test method, e.g., X-rays, to screen out fuzes with leaking power supplies.

The study to date has demonstrated that storage environments in the many locations, including depots and ammunition supply points in the continental United States, the Middle East, Europe, and the Republic of Korea, have differed significantly from nominal parameters that had been used for the original estimates of nominal stockpile condition. It is clear that these variations have significantly affected the condition of the stockpile at different locations and with different histories. It has been learned, for example, that fuzes stored in desert environments with minimal insulative storage were in significantly worse condition than those retained in magazines with adequate earth cover, where the temperature was consistent and fairly cool. In the latter case, older fuzes are in significantly better condition, and most newer fuze lots are in perfect condition. Samples are currently being taken from sites around the world.

References

1. Jeffrey T. Nelson, HDL report, HDL-TR-84-6, "Corrosion Mechanism in the M732 Fuze Power Supply" (April 1984).
2. U.R. Evans, "The Corrosion and Oxidation of Metals," pages 312-313 (1960).
3. Hartman & Schrobilgen, "Inorganic Chemistry," Vol. 11, No. 5, pages 940-951 (1971).
4. Jeffrey T. Nelson, HDL Report, HDL-TR-2110, "M732 Fuze Stockpile Evaluation" (April 1987).

Bi-POLAR Ag-Zn BATTERY

John Giltner
Eagle-Picher Industries, Inc.
Joplin, Mo.

Introduction

The silver-zinc (Ag-Zn) battery system has been uniquely efficient to safely satisfy high power demand applications with low mass and volume. However, a new generation of defense, aerospace and commercial applications will impose even higher power demands. These new power demands can be potentially satisfied by the development of a bi-polar battery design.

Applications

Electromechanical Actuators

Electromechanical actuators (EMA's) for space launch boosters for use by DOD, NASA, and commercial space programs are potential application for this high power battery system.

EMA's could replace hydraulic actuators which are often costly for procurement, maintenance and operability. They have often caused launch delays. Recent advances in electrical components, motors and power processing make high power EMA's a practical alternative which could reduce cost for hardware and launch operations.

Silver-zinc is considered most practical for high power capability with good voltage response control and excellent energy density. Bi-polar design could extend the silver-zinc advantage for this application where load varies from 40 to 400 amperes and voltage control of ± 15% is desired.

For example, standard secondary (rechargeable) silver-zinc design for high power, 270 volt EMA's has been estimated at over 620 lbs. EP's previous research on bi-polar design projects a weight estimate of 196 lbs.

Medical Devices

Another potential application is in the emerging technologies of the medical community. Battery operated hand tools and portable instruments provide advantage of no power cord and use on remote sites. This application is the result of recent advances in miniature brushless dc motor technology. This motor type has several advantages over AC induction motors, including high efficiency and linear speed control.

This application is at opposite end of energy spectrum from EMA's requiring very small batteries. However, it is similar to EMA's with relatively high power output for size and weight and also requiring high energy density and close voltage control. This field is wide open to advantages of bi-polar design.

Advantages

Ag-Zn batteries have been unique for many years in their ability to safely satisfy high power demands with low mass and volume and with good voltage control.

Typical applications include:

1. Remote-activated for missile systems and military applications.
2. Rechargeable for space missions and high energy efficiency requirements.

Bi-polar design can improve on standard system by reducing the weight and volume of the individual cell. This design concept also increases the voltage output thereby reducing the number of cells required. Some of the factors involved are:

1. Reduced Weight and Volume:
   A. Elimination of the plastic cell container
   B. Elimination of plate leads and intercell connector
   C. Elimination of internal plate current collector.

2. Increased Voltage
   A. Eliminate resistance of current collector
   B. Eliminate resistance of plate lead
   C. Eliminate resistance of intercell connector

Additionally, the components of a bi-polar design lend themselves to a "stacking" assembly operation. This provides potential for an automated, high volume production line which would lower manufacturing labor cost.

Problem Areas

EPI worked previously (1974-75) on development of a secondary bi-polar silver-zinc battery. This development demonstrated the electrical capability of the system and manufacturing techniques.

One difficulty with this development was mechanical problems with the seals. However, recent improvements in plastics and adhesives should eliminate the major problem of maintaining a seal around the periphery of the bi-polar module. The seal problem is not as significant for a primary battery application or for a requirement for only a few discharge cycles.

A second difficulty encountered was with activation (introducing electrolyte into the cell) and with venting gas from the cell without loss of electrolyte.

The bi-polar design presents some unique problem areas due to its unusually thin cell thickness and construction requirements. These concerns are detailed as follows:

Activation: Entrapped gas bubbles are difficult to remove. Thorough wetting requires pulling vacuum several times.

Initial Charging and Conditioning: Evolution of gas from charge becomes entrapped causing high charge voltage by increase in internal resistance. A few charge/discharge cycles are required to realize optimum efficiency.

Loss of Seal: Construction defects are difficult to test for. Seal breakdown may occur due to substrate corrosion from charge/discharge conditioning or cycling. Electrolyte leakage from more than one cell in stack can cause high resistance external discharge which reduces stand capability.

Vent System: Improved vent system is recommended to provide removal of entrapped gas.

Design Concept

In this design concept the power consuming, inter-electrode, current conductors are eliminated while the current is then conducted via the large cross section, electrode substrate. Negative and positive active materials are applied to opposite sides of a solid silver foil substrate.

The relationship of components for the silver-zinc bi-polar is shown in Figure 1 below. The design shown represents materials utilized in the previously mentioned development effort. Our current program is evaluating additional new materials.

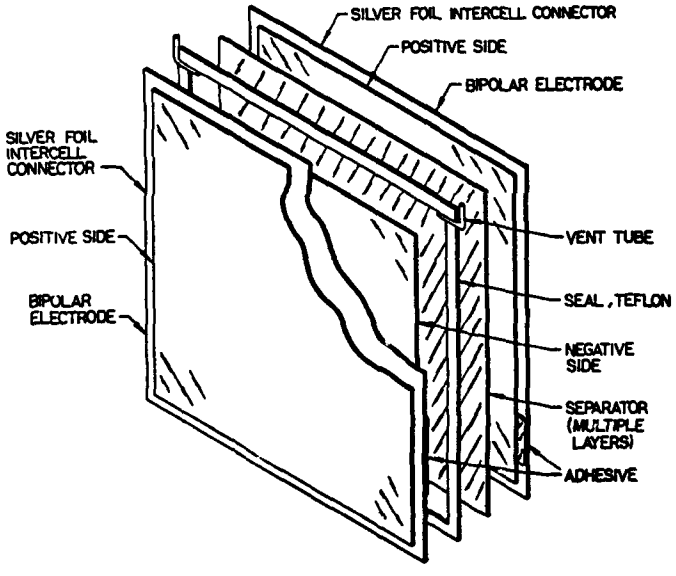

Figure 1. Relationship of components

The bi-polar electrode is further detailed in Figure 2. The positive side consists of sintered porous silver. The negative side consists of a vacuum deposited zinc bottom layer and a sprayed zinc oxide top layer. The substrate (or intercell connector) is silver foil with an electrochemical etch.

The seal (or cell frame) consists of porous Teflon with assembly accomplished using a two-part epoxy adhesive. The separator system utilizes two absorbent types, Webril and Viskon, and a barrier type of cellophane.

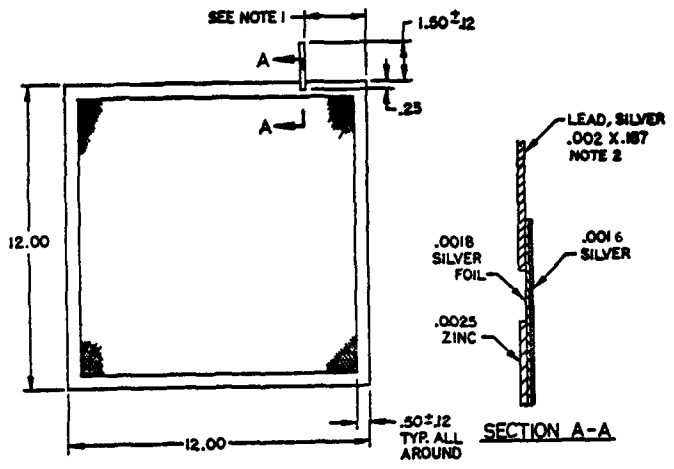

Figure 2. Bi-polar electrode

The bi-polar cells are assembled into a ten cell stack or module which is shown in Figure 3. The reservoirs on each side of the module are initially filled with electrolyte for activation. Activation is accomplished by pulling an external vacuum which evacuates air from each cell through the fill / vent tubes. After release of vacuum and cell filling, then these tubes also provide for venting of gas or excess electrolyte into the reservoirs.

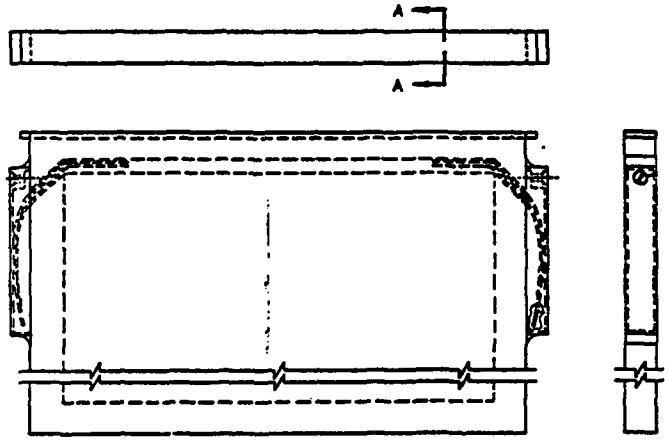

Figure 3. Ten-cell bi-polar module

TEST DATA

A portion of the test data generated during the previous development effort is provided herein in Figures 6, 7 and 8. Figure 6 shows cell voltage versus time at four different current densities. Figure 7 shows cycle life as a function of depth of discharge. Figure 8 shows cell voltage at 5, 15 and 30 seconds during the cycle life of the cell. Note that voltage continues to improve throughout the cycle life until capacity degradation becomes a factor after about 40 cycles.

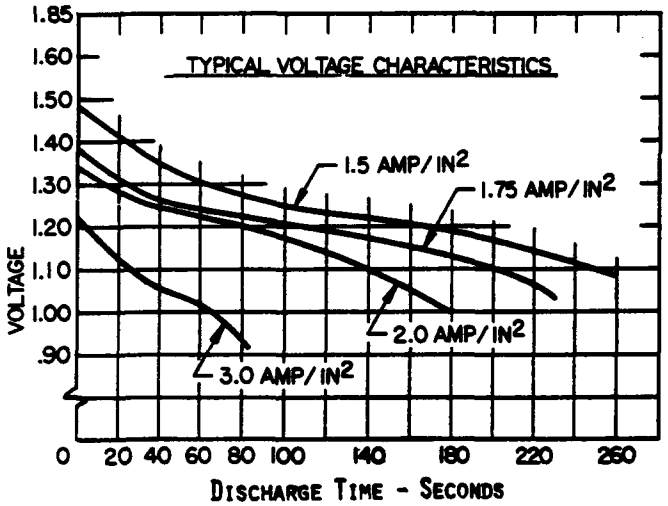

Figure 4. Cell voltage versus discharge time

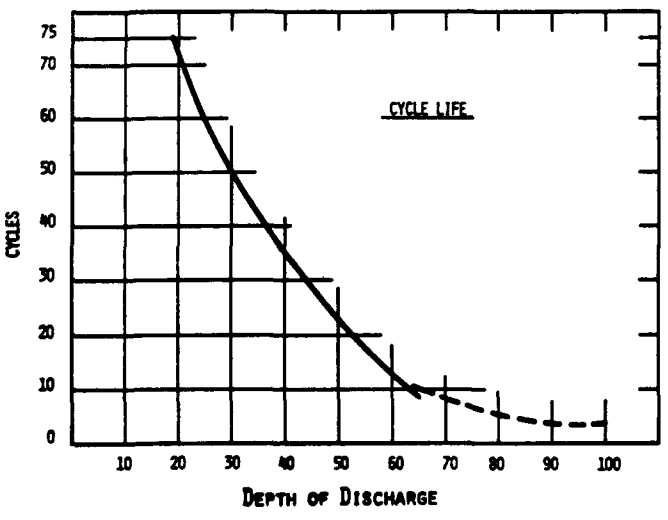

Figure 5. Cycle life versus depth of discharge

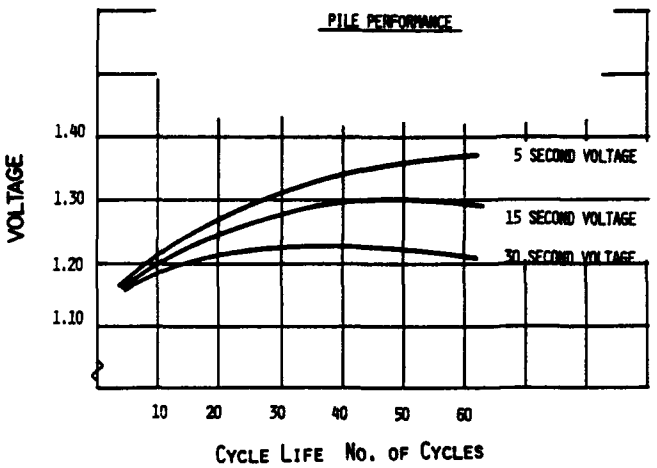

Figure 6. Cell voltage versus cycle life
1.5 amps/in^2, 25% depth of discharge

SYSTEM WEIGHT AND VOLUME PROJECTIONS

During previous work, the following projections for energy density were made from test data for a high power system which demonstrated in excess of 50 discharge/charge cycles.

Projected system power = 100 kilowatts
Discharge time = 30 seconds
Discharge current density = 1.75 amps/in^2
System Weight = 86 lbs (9.7 WH/lb)
System Volume = 1071 in^3 (.78 WH/in^3)

CURRENT PROGRAM GOALS

EPI is currently working on a development program to produce a bi-polar silver-zinc battery design for NASA. The potential application would be to power electromechanical actuators for space launch vehicles.

Base Load	=	40 amps
Steady High Load	=	200 amps
Peak High Load	=	400 amps
System Voltage	=	270 volts
Peak High Watts	=	108 kilowatts
Avg. Load	=	53.3 amps
Discharge Time	=	10 minutes
Capacity	=	8.89 amp-hours

The Lithium Polymer Battery: A Competitive System or a Promising Technology?

Fausto Croce, Bruno Scrosati and Mark Salomon *
Dipartimento di Chimica, Università 'La Sapienza'
00185 Roma, Italy

*On leave from the U.S. Army Research Laboratory, Fort Monmouth, N.J.,U.S.A.

The lithium polymer battery is presently under development in various academic, governement and industrial laboratories throughout the world. The question, however, which still remains to be solved is whether this battery has effectively reached the state of passing from a promising electrochemical technology to a competitive commercial reality. An analysis of the electrolde and electrolyte materials most commonly used for the production of lithium polymer batteries would suggest that key aspects which still require particular attention are the phenomena at the electrode interfaces. In this review these aspects are discussed and the lines of research which are currently in progress in our laboratory to contribute to their understanding and, hopefully, to their solution, are illustrated.

Introduction

In the late seventies Michel Armand[1] proposed the use of polymer or polymer-like materials for the fabrication of thin-film, rechargeable lithium batteries, and this idea has gained increasing popularity and attention. Over the last decade several academic, governement and industrial laboratories have been engaged in the development of this fascinating battery concept. Many important results have been obtained and the lithium polymer battery (LPB) has progressed from laboratory scale to the fabrication of prototype systems with a rate which is without precedent in the history of the development of advanced batteries.

Today, the United States, Japan and the European Community are investing heavily for developing technology for the large scale production of LPBs with the final aim of winning the race for the production of an advanced electrochemical source suitable for powering electric vehicles and consumer electronic devices. The important question, however, which still remains to be answered is whether the progress in the field of LPBs has reached a level such that all the related challenging technological goals have been met and, therefore whether these batteries have indeed passed from being a promising electrochemical technology to a competitive commercial reality. Reliability, durability, safety and cost are the main requirements which have to be realized. An analysis of the electrode and the electrolyte materials most commonly used for the production of LPBs would suggest that the key aspects to which detailed attention should be addressed are the phenomena at the interfaces. Data reported by various laboratories clearly demonstrate that the lithium electrode interface is inevitably affected by passivation phenomena which may influence the cyclability and the reliability of the battery. Chemical and electrochemical reactions may also occur at the other, postive (intercalation electrode) interface which will also affect the capacity and the discharge efficiency of the battery. In this work we will attempt to illustrate and discuss these problems, and review the lines of research which are currently in progress in our laboratory to contribute to their understanding and, hopefully, to their solution.

LPB concept and features

The basic structure of LPBs is well known: in its most common form it combines a lithium ion conducting polymer membrane with two lithium reversible electrodes, namely, a lithium metal foil anode and a cathode based on a reversible intercalation compound (e.g. V_6O_{13} , TiS_2 or $LiMO_2$,M= Co, Ni). The latter is blended with the polymer elecrolyte and carbon to form a plastic composite which is backed by a metal foil current collector. LPB prototypes are formed by a simple lamination of the three components to obtain thin-layer, flexible structures which in principle may be fabricated in any desired shape and form. Such a straighforward and versatile fabrication procedure, combined with the high energy content of the electrodic system, are the major key features of LPBs. In fact, the scaling-up of the LPB production can be conveniently achieved by adapting existing winding machines routinely used in the capacitor industry for the lamination of the components in various battery designs. Thus one can envision the appealing possibility of obtaining solid-state batteries which are produced in any form to be placed in any available empty space of a specific portable electronic device or automobile body. Indeed, LPBs can presently be readily prepared in flat, thin design for powering 'smart' credit cards, in prismatic packaging for powering portable computers, in 'C'-cell configurations for powering consumer electronic devices and in high-capacity cyindrical, spiral assembly or prismatic stack modules for electric vehicle applications[2]. Such unique configurations promises highly efficient packing, and thus quite high energy densities may be anticipated for LPBs. Indeed, direct tests on practical prototypes confirm that LPBs may offer energy densities consistently higher than lead-acid and nickel-cadmium batteries[3].

The key LPB component: the electrolyte

The success of LPBs is directly linked to the availability of a satisfactory electrolyte, namely of a membrane which combines high ionic conductivity with flexibility, extended temperature range of operation, wide electrochemical stability, lithium transport number approaching unity and compatibility with the electrode materials. In the inital stage of development, membranes formed by complexing lithium salts with poly(ethylene oxide) PEO, have been widely used[4]. However, these first generation polymer elecrolytes, although of great importance and continuing interest, suffer by a temperature-dependent conductivity which assumes

practically acceptable values (i.e. of the order of 10^{-3} S cm^{-1}) only around 100°C[5]. An electrolyte requiring high temperatures to achieve suitable ionic conductivities clearly limits the application range of the battery, and many alternative routes are presently being pursued with the goal of obtaining mechanically stable polymer membranes having high ionic conductivity at and below room temperature. The basic structure of the first generation, PEO-based electrolytes and the type of their transport mechanism (which requires high polymer chain flexibility to allow fast lithium ion transport[4,5]) exclude the possibility of combining the two desired properties whatever changes are made in the nature of the components and in their reciprocal compositions. Therefore, this class of electrolyte cannot provide high ionic transport at temperatures much below 100 °C. Consequently, alternative structures and configurations have been considered for the development of 'new generation' ionically conducting membranes. Generally, the most successful concept has been that of trapping liquid solutions into polymer cages with an immobilization procedure which varies from case to case and whch includes UV crosslinking, and gelification and casting. The transport characteristics of these "wet" polymer electrolytes which have been termed as "gel electrolytes"[6], "hybrid electrolytes"[7] or, more recently "gelionics"[8], are reported in detail in another paper of this Conference[9]. Here it will be only remarked that these new membranes have conductivities of the order of 10^{-3}S cm^{-1} at room temperature, an electrochemical stability window exceeding 4.5V, and a lithium ion transference number averaging around 0.6. Therefore, one may conclude that in terms of transport characteristics, progress has been outstanding and that today a large variety of ionically conducting membranes are available for use as separators in low-resistance, thin-layer lithium batteries. As an example, Figure 1 illustrates the room temperature discharge curves of a LPB using a new generation electrolyte obtained by immobilizing a propylene carbonate-ethylene carbonate, PC-EC, solution of $LiAsF_6$ in a poly(acrylonitrile) PAN matrix.

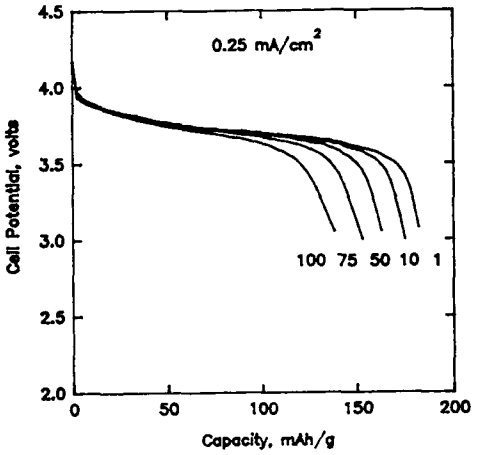

FIGURE 1 -Discharge performance of a Li / $LiAsF_6$-EC-PC-PAN/ $LiCoO_2$ battery cycled at room temperature and at 0.25 $mAcm^{-2}$. The number of cycles is indicated in the figure. The molar composition of the electrolyte is: 4.7-44.3-39-12.

The problem of the interfaces

Figure 1 shows that the performance of the LPB tends to decay upon cycling since a high fraction of the theoretical capacity is delivered only at the initial cycles after which a consistent decline in capacity occurs. The phenomenum, although at different extents, is quite common to all LPBs and it is still one of the major problems which affect their development. Kinetic limitations, quite likely related to degradation at the electrode interfaces resulting from the repeated plating-stripping cycles at the lithium metal anode and the repeated insertion-deinsertion cycles at the composite cathode, may be responsible for the effect. This conclusion, which is supported by impedance analysis[10], suggests that the cycling performance of LPBs may be improved by following two main strategies: (i) by the optimization of the electrolyte configuration and nature, with the aim of reducing the lithium passivation phenomena and (ii) by optimization of the cathode morphology and compositon, with the aim of improving homogeneity among the components. While the latter condition may be successfully accomplished by reducing the particle size of the intercalation compound, by determining its most suitable concentration and by the realization of optimized mixing techniques, considerable difficulties are still encountered in controlling the response of the lithium electrode: presently the anode-electrolyte interface problem constitutes the major drawback of LPBs.

The lithium metal electrode

Low internal resistance and high energy density, although important properties, are not sufficient to make a battery successful in practical terms. Also reliability and safety are crucial requirements. The latter are directly related to the stability of the lithium interface, which in turn is a direct consequence of the interactions of metal with the electrolyte. Results obtained in our[11,12] and in other[13] laboratories have clearly demonstrated that the lithium electrode undergoes serious passivation when in contact with the new generation, "wet" polymer electrolytes. This is not surprising since these gels contain materials (such as PC) which are very aggressive towards lithium. As well known, uncontrolled passivation phenomena affect the cyclability of the lithium electrode - and thus, of the entire LPB- and may eventually lead to a serious safety hazard.

Therefore, it appears of paramount importance to fully control chemical and electrochemical reactions at the interface, and this requires a clear understanding of the nature and the morphology of the passivation film growing on the lithium electrode when in contact with a given electrolyte. With the aim of achieving this important goal, we have investigated the impedance response of the lithium electrode in contact with a typical example of the new generation electrolytes, namely a $LiClO_4$-EC-PC-PAN membrane, and used the results to develop a model of the interface. According to this model which is illustrated in Figure 2, upon initial contact with the electrolyte lithium experiences an initial passivation reaction with the formation of a compact layer which grows directly on the metal surface (or on a native film). On prolonged contact time, the passivation phenomena give rise to an additional, porous layer, whose nature and morphology probably depend upon the type of solvent, the type and amount of impurities and upon other unpredictable causes (e.g. direct reaction with the host polymer and physical separation of the anode from the gel electrolyte). As long as this additional layer remains porous, the rise in the interfacial

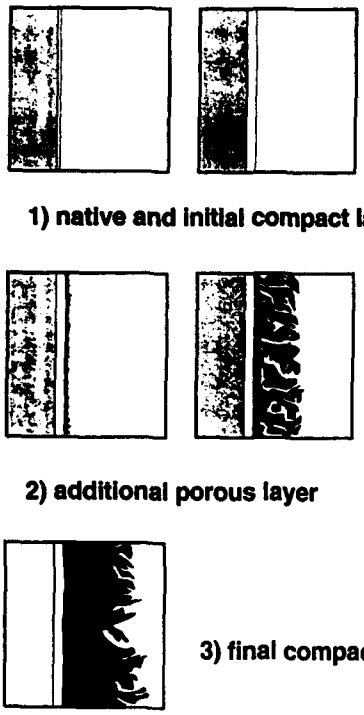

FIGURE 2- Model of the passivation occuring at the lithium electrode-PAN-based electrolyte interface.

resistance is not greatly reduced; however, with extended contact time, the layer becomes progressively denser to finally collapse on the electrode interface, with a consequent sharp rise in the interfacial resistance. Therefore, the model of Figure 2 suggests that is the second thick layer the one which mostly affects the lithium electrode performance and hence, that studies should be directed to inhibit its formation and growth. One approach in this direction is the selection of electrolytes based on components which are expected to be the less aggressive towards the lithium metal. A second approach is the addition to the electrolyte of materials which may act as impurity-getters, namely of substances capable of trapping the impurities so preventing their flow to the interface. Ceramic fillers, like γ-lithium alluminate or zeolites, are expected[14-16] to satisfactorily fulfill this action. These expectations are confirmed by practical results, and in fact addition of zeolites to the PAN EC/PC $LiClO_4$ electrolyte considerably alleviates the passivation of the lithium electrode as shown in Figure 3 which compares the trend of the interfacial resistance of a Li electrode in contact with the base electrolyte and with the electrolyte with added zeolite.

The beneficial effect of the ceramic fillers on the response of the interface is further confirmed by the induced improvements in the lithium cycling efficiency which increases from 72 % in plain PAN, EC/PC $LiClO_4$ electrolyte to a value of 85% for a cell using a composite (PAN EC/PC $LiClO_4$+10 weight percent zeolites) electrolyte. Further improvements can also be obtained when substituting poly(acrylonitrile) with poly (methyl methacrylate) as the polymer component[9]. However, although encouraging, these improvements are still not sufficient for practical purposes. In fact, for assuring acceptable applicability, the efficiency should fall between 97 and 99% and, at the present stage of knowledge, it is difficult to foresee that such efficiency values can be achieved in the case of PAN-based lithium cells.

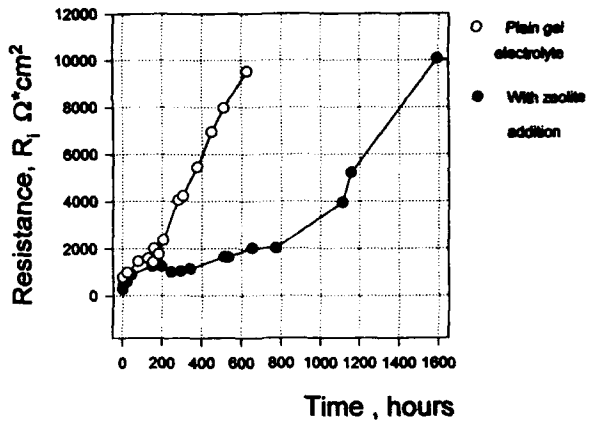

FIGURE 3 -Time evolution of the interfacial resistance, Ri, of the lithium electrode in base electrolyte (--o--) and in zeolite-added (--●--)$LiClO_4$-EC-PC-PAN electrolyte (Room temperature).

In conclusion, concern should be taken when proposing new electrolytes for applications in electrochemical devices. If the envised application is in lithium batteries, beside transport properties, electrode compatibility should additionally be chosen among the most crucial requisites. From the results discussed here, there are indications that the PAN-based electrolytes, and quite likely the majority of the wet polymer electrolytes which generally contain aggressive liquid components, do not fulfill the requirements for applications such as long-life, rechargeable lithium metal batteries. If one wants to successfully exploit the outstanding transport properties of these electrolytes, some interfacial-stabilizing additives should be added or new configurations be developed where any contact with the lithium metal is avoided. The latter solution can be achieved in 'rocking-chair' cells where the lithium metal electrode is replaced by a lithium ion source electrode. The validity of this concept is confirmed by the present trend in reserearch and developments of LPBs.

Rocking chair LPBs

As well known, the most common configuration of rocking chair batteries uses lithiated carbon Li_xC_6 as the negative electrode, a lithium metal oxide $LiMO_2$ (M=Co, Ni) or $LiMn_2O_4$ as the positive electrode and liquid organic solutions as the electrolyte[17-19]. Due to the high oxidizing character of the selected $LiMO_2$ cathode, these batteries may suffer from solvent decomposition upon cycling. Therefore, the replacement of the liquid electrolyte with a solid, thin-layer, Li-ion conducting membrane would be highly beneficial in terms of performance, especially if this membrane has a high ionic conductivity and a wide electrochemical stability window. The gel-type polymer electrolyte seem to fulfill these conditions and thus, they appear to be quite compatible with the use of Li_xC_6/$LiMO_2$ couples, as indeed, practically demonstrated in our and in other laboratories[13].

However, one should be aware that Li_xC_6 lithiated carbon coke, although being the most popular rocking chair anode, suffers from some drawbacks, the most serious being the voltage excursion upon charge (Li^+ uptake)- and discharge (Li^+ release) which may extend up to 1.5V upon the exchange of the total removable lithium ($0<x<0.5$)[19]. This can be an undesired performance especially if the cells are directed to the electronic market where voltage stability is often a priority requirement. Consequently, other intercalation compounds, having better voltage regulation than carbon coke, should be considered.

Large variation in potential with concentration are generally related to large changes in the electrochemical potential of the electroactive species[20]. In the case of Li_xC_6 one may assume that changes in the chemical and the electrochemical potential of the Li^+ ions are associated with interactions between these ions and the host structure which may be basically described in terms of disorded, randomly packed graphite units[21].

As alternatives to Li_xC_6 based on carbon-coke one may then consider such materials as pure graphite and/or open-structured compounds offering expectations of weak interactions with the intercalated lithium ions. One example of the latter is the layer-structured titanium disulphide, TiS_2, where the intercalation of the lithium ions within the Ti-S-Ti layers is accompanied by a modest free energy change and, thus, by a limited voltage variation[22], i.e. 0.7V passing from x=0 to x=1.

To evaluate the effectiveness of this choice, we have assembled a rocking chair cell where titanium disulphide, TiS_2, serves as the negative, 'lithium-sink' electrode and lithium cobalt oxide, $LiCoO_2$ as the positive, 'lithium-source' electrode, while the electrolyte was the PAN-EC/PC,$LiClO_4$ polymer membrane. This cell is represented by:

$$TiS_2 \,/\, \text{PAN-EC/PC,}LiClO_4 \,/\, LiCoO_2 \qquad [1]$$

It should be noted that TiS_2, which is one of the commonest cathodes in conventional lithium battery configurations, is used here as the anode to accept Li^+ ions from $LiCoO_2$ during charge and release them during discharge, according to the process

$$TiS_2 + LiCoO_2 \underset{\text{discharge}}{\overset{\text{charge}}{<=======>}} Li_xTiS_2 + Li_{(1-x)}CoO_2 \qquad [2]$$

The cell, assembled in the discharged state exhibits an open circuit voltage (OCV) of 0.3V at room temperature. After charging at a current density of 0.02 $mAcm^{-2}$ the cell assumed a charged state voltage of 2.1V. The cell was then discharged at the same current density to a voltage cutoff level of 0.5V, and the cycling regime was repeated several times obtaining the typical trend illustrated in Figure 4.

In conclusion, the results reported here, although in a preliminary stage, confirm that the rocking chair concept is quite applicable for the development of reliable and versatile LPBs. The performance of the example discussed in this work and those of other types currently under test in other laboratories[13,19], concur that this concept may ultimately be the winning one in assuring widespread commercialization of LPBs.

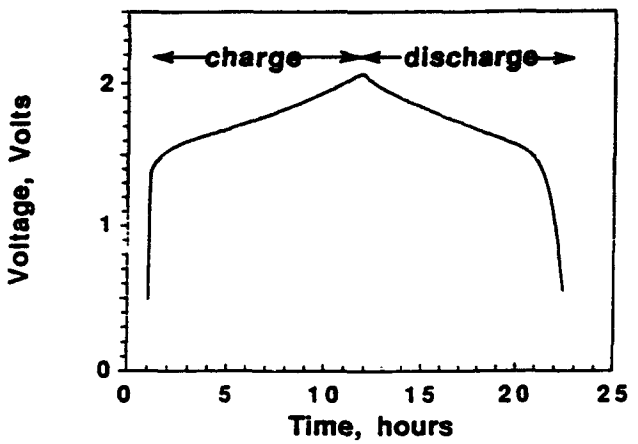

FIGURE 4-Typical charge-discharge cycle at 25 °C of the Li_xTiS_2 / $LiClO_4$/-EC-PC-PAN / $Li_{(1-x)}CoO_2$ thin-layer, rocking-chair LPB. Cycling current density: 0.02 $mAcm^{-2}$.

Acknowledgements

One of us (M.S.) is grateful to the University of Rome for a Visiting Scientist Fellowship.

References

1) M.B. Armand,J.M.Chabagno, and M.J. Duclot (1978) Second Internat. Symp. Solid Electrolytes, St.Andrews,Scotland, paper 6.5.
2) B.Scrosati and R.J.Neat (1993), Applications of Electroactive Polymers, B.Scrosati Ed., Chapman & Hall, London, p. 183.
3) B.B. Owens (1992) Proceedings 35th Internat. Power Sources Symp., IEEE, Cherry Hill, N.J.,p.271.
4) F.M.Gray (1991) Solid Polymer Electrolytes, VCH, New York.
5) J.MacCallum and C.A.Vincent Eds. (1987) Polymer Electrolyte Reviews-1, Elsevier Applied Science, London .
6) K.M.Abraham (1993), Applications of Elecroactive Polymers, B.Scrosati Ed., Chapman & Hall, London, p. 75.
7) K.Arbizzani, M.Mastragostino, L.Meneghello, X.Andrieu and T.Vicedo (1993) Mat.Res.Soc. Symp. Proceedings, vol. 293, p. 169.
8) G.B.Appetecchi, F.Croce and B.Scrosati (1994), J.Electroanal.Chem., submitted
9) G.B.Appetecchi, F.Croce and B.Scrosati (1994), This Proceedings, paper 10.2
10) F.Capuano, F.Croce and B.Scrosati (1992), J.Power Sources, 37 p.369.
11) F.Croce and B.Scrosati(1993), J.Power Sources, 44 p. 9.
12) F.Croce, F.Gerace, G.Dautzenberg, S.Passerini, G.B.Appetecchi and B.Scrosati (1994), Electrochim.Acta, in press.
13) K.M.Abraham and M.Alamgir(1993), J.Power Sources, 44 p. 195.
14) F.Croce and B.Scrosati (993), Polym. Adv. Techn., 4, p.198.
15) M.Borghini, M.Mastragostino, S.Passerini and B.Scrosati (1994), J.Electrochem. Soc., submitted.
16) S.Slane and M.Salomon (1994), in course of publication.
17) T.Nagura and K.Tazawa (1990), Prog.Batteries Solar Cells ,9 (1990) p. 203.
18) B.Scrosati (1992), J. Electrochem.Soc., 139 p.2776.
19) J.M.Tarascon and D.Guyomard (1992), J.Electrochem. Soc.,139 p. 937.
20) H.Gerischer, F.Decker and B.Scrosati (1994), J.Electrochem.Soc., in press
21) R.W.Ruland (1965), Acta Cryst., 18 p. 992.
22) S.M. Whittingham, Progress in Solid State Chem.(1978), 41.

DEVELOPMENT OF CARBON ANODE FOR RECHARGEABLE LITHIUM CELLS

C.-K. Huang, S. Surampudi, G. Halpert

Jet Propulsion Laboratory
California Institute of Technology
4800 Oak Grove Drive
Pasadena, California 91109

INTRODUCTION

Conventionally, rechargeable lithium cells employ a pure lithium anode. To overcome problems associated with the pure lithium electrode, it has been proposed to replace the conventional electrode with an alternate material having a greater stability with respect to the cell electrolytes. For this reason, several graphitic and coke based carbonaceous materials were evaluated as candidate anode materials[1]. Graphitic carbons were found to exhibit higher reversible lithium capacity compared to the coke based materials. At JPL, Ethylene Propylene Diene Monomer (EPDM) was selected as a suitable binder material for the fabrication of carbon electrodes[2]. The results of the electrode fabrication studies indicated that the amount of binder required for a carbon material is dependent on its surface area. Excessive amounts of binder were found to reduce the reversible lithium capacity and also the rate capability of the electrode. JPL has developed a two step procedure for the formation of Li_xC electrode[3]. This process involves the intercalation of lithium into carbon in two different steps. Electrodes prepared by this method exhibited higher reversible Li capacity compared to those prepared by the single step process. Lithium capacity and reversibility of the carbon electrodes were also found to be significantly dependent on the nature of the electrolyte and its composition[4]. In this paper, we summarized the results of the studies on Li-ion cell development.

EXPERIMENTAL

The electrochemical performance of the graphite material was investigated using half cells employing Li as the negative electrode and carbon as the positive electrode. Both nickel and copper grid can be used as current collector and substrate for the carbon electrode. Carbon electrodes were made by pressing and then formed by electrochemical intercalation with Li. The pressing technique was found suitable for the electrode fabrication. Ethylene propylene diene monomer (EPDM) was used as a binder. All electrodes were prepared by mixing the carbon powder with a solution of EPDM binder in cyclohexane until a uniform slurry was obtained. The slurry was spread on both sides of the grid to form the electrodes. Then, the carbon/EPDM coating is dried by allowing the cyclohexane to evaporate. As a final step , both sides of the grid were pressed between a pair of stainless steel plates, to a pressure of about 450 lbs/in2. Typically, electrodes were coated with 10 - 15 mg of carbon per cm2, and were 10-15 mil thick. Electrochemical cells were constructed using these electrodes, lithium foil (Foote Mineral Corp.), porous polypropylene separators (Celgard no. 2400), and selected electrolytes.

Mixed (by volume ratio) solvent electrolytes containing ethers and carbonates were chosen for this study. Lithium hexafluoroarsenate (LiAsF6) and Lithium hexafluorophosphate (LiPF6) were used as electrolyte salts. Specifically, six different groups of electrolytes were studied: (1) 1.5M LiAsF6 in {x% Ethylene carbonate [EC] + (100-x)% 2-Methyl tetrahydrofuran [2-MeTHF]}, where x = 10, 50 and 70 (These electrolytes will be abbreviated as SE2MeTHF(x%).), (2) 1.0M LiAsF6 in {(70% EC + 30% Dimethoxy ethane (DME)}, this electrolyte will be abbreviated as SEDME(70%) & 1.0M LiPF6 in (70% EC + 30% DME), and this electrolyte will be abbreviated as PEDME(70%). (3) 1.0M LiAsF6 in {70% EC + 30% Dimethyl carbonate (DMC)}, this electrolyte will be abbreviated as SEDMC(70%) and 1.0M LiPF6 in (70% EC + 30% DMC), this electrolyte will be abbreviated as PEDMC(70%). (4) 1.0M LiAsF6 in {x% EC + (100-x)% Diethyl carbonate [DEC]}, where x = 10, 30, 50 and 70 (These electrolytes will be abbreviated as SEDEC(x%).), (5) 1.0M LiPF6 in {x% EC + (100-x)% DEC}, where x = 10, 30, 50 and 70 (These electrolytes will be abbreviated as PEDEC(x%).), and (6) 1.0M LiAsF6 in (33.3% EC + 33.3% 2-MeTHF + 33.4% DEC) with or without the addition of 2.5% 2-Methyl furan [2-MeF] (These electrolytes will be abbreviated as S(1/3) and S(1/3+2MeF).). The experimental cells were evaluated for charge/discharge characteristics, faradaic utilization of the carbon active material, rate capability and cycle life. Constant current was used for charging and discharging the cells. Experiments were conducted in an oxygen and moisture free dry box.

RESULTS & DISCUSSIONS

(A) Electrochemical Intercalation Techniques: Once a suitable carbon electrode is formed, difficulties arise in incorporating lithium ions into the carbon anode. To incorporate lithium ion, a carbon electrode is typically immersed within an electrolyte bath with a lithium ion source which may be a lithium-containing electrode such as a piece of lithium metal, lithiated titanium disulfide TiS_2, or lithiated cobalt oxide, etc.. A current is then applied between the lithium source and carbon electrodes. Two electrochemical intercalation methods have been developed. The first of these is an intermittent discharge method. The initial application of current causes a portion of the lithium ions to react with carbon atoms on the surface of the carbon electrode, without any intercalation. Because the voltage (v.s. Li) of the carbon electrode drops to near 0 volts, it may appear that the electrode is no longer useful. The current is then deactivated and reapplied several times. Each subsequent re-application of current causes a greater reaction with lithium ions and ultimately results in reversible intercalation (Figure 1). The second method involves application of current in two stages wherein the second current level is substantially lower than the first current level. However, the second current is applied only once and results in substantial intercalation of lithium ions. In the first method, four or more steps are required to achieve substantially full intercalation. In the two stage method, substantially full intercalation is achieved in two stages. Figs. 2 illustrate a second method in which one current is used for an initial discharge stage and then a lower current is used for subsequent discharge stages. The processes for the step one discharge were studied by complex impedance measurements using three electrodes at different stages during the step one discharge. The results are given in Figure 3. At stage one, we found one semi-circle & a straight (capacitor) line that reflects the initial film from the binder or other impurities. Ultimately, we found two semi-circles which reflects the formation of a new film (Figure 3). These results indicated that all the Li transferred during the step one discharge results in a stable film with no intercalation. Therefore the step one discharge is irreversible. The chemistry of the film was examined by EDX at four conditions including (1) Fresh carbon electrode, (2) Fresh carbon electrode dipped in the electrolytes (1.5 M LiAsF6 in 10% EC + 90% 2-MeTHF) and then washed by using pure solvent (2-MeTHF) to clean up the residual salts, (3) Cycled carbon electrodes, and (4) Cycled carbon electrode then washed by pure solvent. The most important finding is that the film contains oxygen (Figure 4).

(B) Binder Effect: For ambient temperature fabrication of carbon electrode, a binder material must be provided to hold the carbon particles together. However, if too much binder is provided with the graphitic carbon, low specific energy, poor rate capability and inadequate lithium reaction occurs. Conversely, if an insufficient amount of binder is provided, the graphitic carbon particles tend to disperse or dissolve within the electrolyte bath. In Fig. 5, voltage is

charted as a function of the value of x in LiXC for 0.5%, 1% and 3% EPDM compositions to illustrates the effect of the amount of EPDM binder on the reaction of lithium-ions with graphitic carbon. The discharge curves were obtained using the first stage of a two stage technique. A relatively low current level of 0.188 mA/cm2 was used for the discharge of the 3% EPDM carbon electrode. These results illustrate that even at the relatively low current, very little lithium ion reaction was achieved for a 3% EPDM composition. Nevertheless, even with 2% EPDM, very little intercalation was found to occur. Fig. 6 illustrates electrochemical intercalation and deintercalation curves for lithium into and out of a graphitic carbon having a 0.5% EPDM composition.

Although 1% EPDM can be used to achieve a reversible cell, 1% is not an optimal EPDM binder percentage. The use of a 0.5%, by weight, EPDM binder allows for adequate cohesion of the graphitic carbon particles while also allowing for an effective subsequent intercalation of lithium ions into the carbon. Although a composition of 0.5% EPDM is optimal, a composition of up to 1% EPDM may also be effective for binding the carbon. In general, the most effective percentage of EPDM depends on the total surface area of the graphitic carbon. Table I provides rate capability information for a lithium cell incorporating a 0.5% EPDM/carbon-based electrode. In a 1 ampere-hour cell, a C/20 discharge rate and a C/3 charge rate is achieved while maintaining a capacity greater than 200mAh/gm. These results verify that a graphitic carbon electrode having a 99.5% carbon and 0.5% EPDM binder composition is an effective composition for use as a carbon/lithium-ion electrode in a lithium cell. The EPDM percentage of 0.5% is effective for use with most commercial grades of graphitic carbon. Other percentages within the rage of 0.5% - 1.0% may also be effective. However, as noted above, the optimal EPDM percentage depends upon the surface area of the graphitic carbon.

(C) Evaluation of carbon materials: The carbon materials that had been evaluated include: pitch coke material, the same type of petroleum coke materials with different particle size, PAN carbon fiber, and graphite materials. The coke materials that we have evaluated showed a typical powder x-ray diffraction pattern of broad peaks compared to the sharp and narrow peaks for graphite materials. Two step Li reaction of pitch coke material with initially high current, followed by a low current Li intercalation, showed about 50 % of Li capacity to be reversible. For petroleum coke materials, we examined the Li reversible capacity (by 1V cut off) of the same petroleum coke materials but with different particle size. Experimental results showed that the reversible Li capacity is about the same (0.06 Li per carbon) for both petroleum coke materials having different particle size. The major difference is that the irreversible Li capacity is much larger for the small particle size coke materials. These indicated that the surface of carbon material plays an important role in the electrochemical intercalation process. Also, the reversible Li capacity in the PAN-based carbon fiber material was evaluated. The results indicated that about 0.1 Li per carbon can be reversibly cycled at a slow charge and discharge rate. For the case of graphite material, 0.124 Li per carbon can be reversibly cycled after a two step Li reaction. To make a comparison, reversible Li capacity of different types of carbon materials is summarized in Table II.

(D) Type of electrolyte and its composition: Seventeen different mixed solvent electrolytes containing ethers and carbonates were evaluated as candidate electrolytes for Li-ion cells. The results obtained to date indicate that the electrochemical performance of the carbon material identified is dependent significantly on the nature of the electrolyte employed. The experimental results of Li/C cells containing various electrolytes are summarized below:

(1) The reversible Li capacity for the cells containing SE2MeTHF electrolyte having various amount of EC was approximately 0.12 Li/C. However, the irreversible Li capacity increases sharply with increase in the amount of EC. These results indicate increased electrolyte decomposition in electrolytes containing higher levels EC.

(2) The interfacial resistivity was very high for cells containing PEDME, SEDME, PEDMC and SEDMC electrolytes. Due to the high resistivity, these cells were not able to be cycled. Detailed analysis of these cells revealed that the separator used (Celgard 2400) was not wet. The dry condition may have been caused by the high percentage (70%) of EC used, which, in turn, increased the electrolyte viscosity.

(3) The discharge curves (Figure 7) of Li/LixC cells containing SEDEC electrolytes reveal a high peak voltage (1.2 V vs. Li) which may be an effect of the LiAsF6 salt. This peak voltage decreases slightly with increase in the EC content in the electrolyte. The cells activated with electrolytes containing more EC exhibited higher voltage discharge profiles under the same discharge current density. The higher voltages may be explained by increase in the practical surface area of the carbon electrodes which, in turn, is probably due to the EC solvent co-intercalation into the carbon particles. The increased Li capacity of the first step discharge is mostly used for the formation of a protective film on the carbon to cover the increased surface area. The Li capacity used for film formation is actually a waste of Li and electrolyte. For all the four combination of EC in the SEDEC group, the reversible Li capacity is in the range of 0.12 Li/C. However, the irreversible Li consumption increases sharply as the EC amount in the electrolyte increases to above 30% (Figure 9).

(4) Figure 8 exhibits the first step discharge of half cells containing PEDEC with various amount of EC. The discharge Li capacity in the Li/C Cells containing PEDEC electrolytes had a similar trend as cells containing SEDEC electrolytes. However, the peak voltage of these cells was lower (0.6 - 0.7 Volts vs. Li). For cells containing PEDEC electrolytes, the reversible Li capacity was in the range of 0.13 Li/C. Figure 9 shows that the irreversible Li consumption increases sharply as the EC amount increases, and eventually reaches a state of having more irreversible capacity than reversible capacity for PEDEC(70%). Therefore, the optimum EC amount in PEDEC electrolyte used in rechargeable Li cells with a LixC anode is between 30 and 50%.

(5) Li/C cells containing S(1/3) and S(1/3+2-MeF) electrolytes delivered about the same amount of total discharge capacity (0.19 Li/C). However, the cells having 2-MeF in the electrolyte showed slightly less charge capacity (0.075 Li/C) than those not containing 2-MeF (0.08 Li/C).

Experimental results obtained so far indicate that increase of ethylene carbonate (EC) was found to improve the rate capability of the cells. However, the increase in EC content was also found to increase the amount of electrolyte decomposition. The electrolytes containing EC and diethyl carbonate (DEC) with lithium hexafluorophosphate ($LiPF_6$) salt were found to be promising for Li ion cells.

(E) Lithium-ion Cell Development:

(a)$Li_xC/LiCoO_2$ system: Experimental $Li_xC/LiCoO_2$ cells were fabricated and the cycle testing of these cells is in progress (Figure 10). PEDEC electrolyte was selected as the candidate electrolyte for these in-house Li-ion cells. Aluminum and nickel grids were used as the current collectors for the $LiCoO_2$ cathode and graphitic carbon anode respectively. The cells so far have completed 19 cycles and have no noticeable loss in discharge capacity.

(b) Li_xC/Li_xTiS_2 system: Although the Li_xC/Li_xTiS_2 cell has lower voltage than the $Li_xC/LiCoO_2$ cell . it may have comparable specific energy because Li_xTiS_2 has higher specific lithium capacity than $LiCoO_2$. Earlier work at JPL showed that the Li metal-TiS_2 cell was attractive in terms of specific energy and reversibility. However, some difficulties were encountered during the fabrication of LixC/LixTiS2 cells. This comes from the intrinsic problems in the areas of: (a) instability of lithiated TiS2 and lithiated carbon materials in the dry room environment, (b) salt precipitation on the electrode surface during the drying process after the preparation of lithiated carbon and lithiated TiS2 electrode, and (c) difficulty in cell fabrication. The difficulty of Li_xC/Li_xTiS_2 cell fabrication is due to the complicated handling procedures involving initial preparation of active materials (lithiated TiS2 or lithiated carbon) in one cell and then transfer of one of these to the final cell. For these reasons, the work on Li_xC/Li_xTiS_2 cell fabrication was temporarily postponed.

SUMMARY

This study includes fabrication steps for forming a carbon electrode composed of graphitic carbon particles adhered by an ethylene propylene diene monomer binder. An effective binder composition is determined for achieving a carbon electrode capable of subsequent intercalation by lithium ions. Two differing multi-stage intercalation processes are proposed. In the first, a fixed current is repetitively applied. In the second, a high current is initially applied, followed by a single subsequent lower current stage. Resulting carbon/lithium-ion electrodes are well suited for use as an anode in a reversible, ambient temperature, lithium cell. In addition, the electrochemical intercalation of lithium into carbon was also investigated in several mixed solvent electrolytes containing ethers and carbonate. The results obtained to date indicate that electrolyte decomposition occurs at the carbon electrode surface during the initial stages of the discharge process. The extent of decomposition was found to be significantly dependent on the electrolyte composition. Electrolytes containing higher percentages of EC showed improved rate capability, but also, more electrolyte decomposition. Electrochemical performance of the carbon electrodes is closely related with the type of electrolytes used. Some carbon and electrolyte combinations may yield reversible Li capacity of more than 300 mAh/gm. However, these electrodes can not be practically used as anode material for rechargeable Li cells if the irreversible Li capacity is too large.

ACKNOWLEDGEMENTS

The work described here was carried out at Jet Propulsion Laboratory, California Institute of Technology, under contract with the National Aeronautics and Space Administration.

REFERENCES

(1) R. Yazami, PH. Touzain, J. of Power Sources, p. 368 (1983) 9.

(2) "Alternate Anode Materials for Ambient Temperature Secondary Lithium Cells", C.-K. Huang, S. Surampudi, A. Attia and G. Halpert, Presented at the 180th Meeting of Electrochem. Soc., Phoenix, Arizona, Oct. (1991).

(3) "Evaluation of Carbon Anodes for Rechargeable Lithium Cells", C.-K. Huang, S. Surampudi, A. Attia and G. Halpert, Proceedings of the 182nd Meeting of Electrochem. Soc., Toronto, Canada, Oct. (1992).

(4) "Effect of Electrolyte Composition on Carbon Electrode Performance", C.-K. Huang, S. Surampudi, D. H. Shen and G. Halpert, Proceedings of the 184th Meeting of Electrochem. Soc., New Orleans, Louisiana, Oct. (1993).

TABLE I. Rate Capability of Li out (C) and Li in (D) in LixC Anode

CURRENT (mA)	CAPACITY (mAh)
D 26	783
C 50	789
D 26	791
C 100	763
D 50	728
C 50	741
D 50	734
C 100	716
D 50	714
C 200	697
D 50	710
C 300	670

* CAPACITY: > 200 mAh/gm at 1 mA/cm2.

TABLE II. The Comparison of Reversible Li Capacity of Carbon Materials Evaluated

(1) PITCH COKE:	0.070 Li PER CARBON
(2) PETROLEUM COKE:	0.057-0.077 Li PER CARBON
(3) PAN FIBER:	0.097 Li PER CARBON
(4) GRAPHITE:	0.124 Li PER CARBON

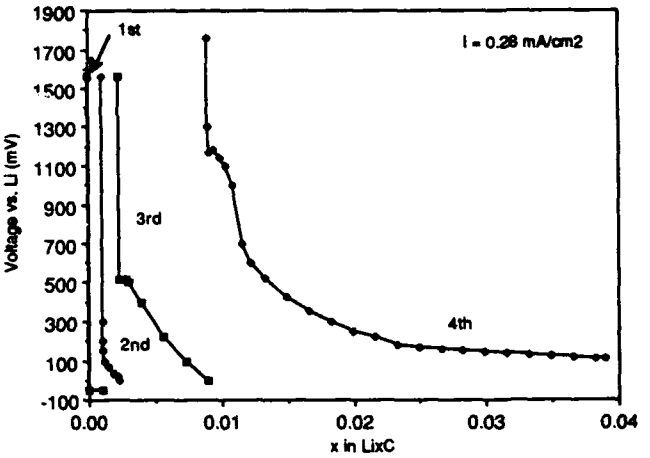

Figure 1. The improved discharge performance of Li intercalating into carbon using intermittent discharge technique.

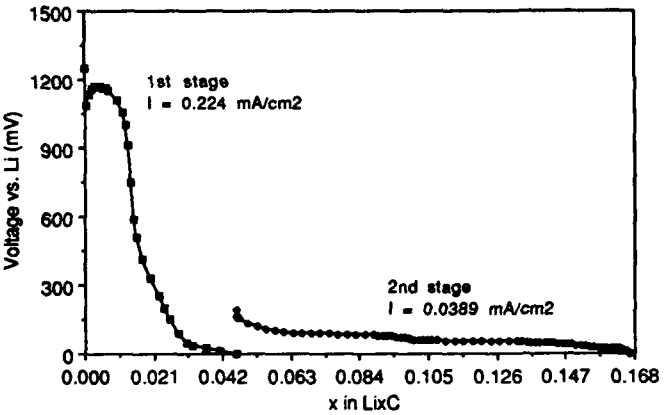

Figure 2. Electrochemical intercalation of Li into graphite by two-stage method.

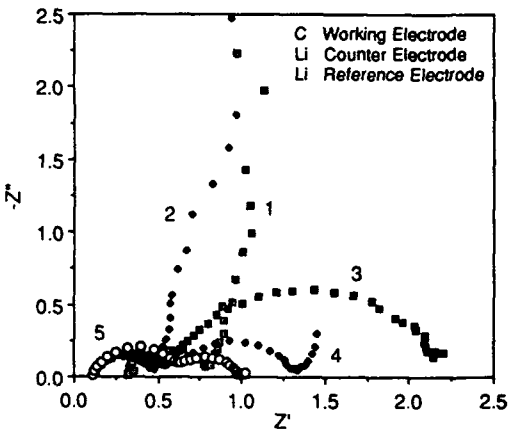

Figure 3. AC measurement of Li/C cell at different stages during first discharge of the two-step intercalation technique.

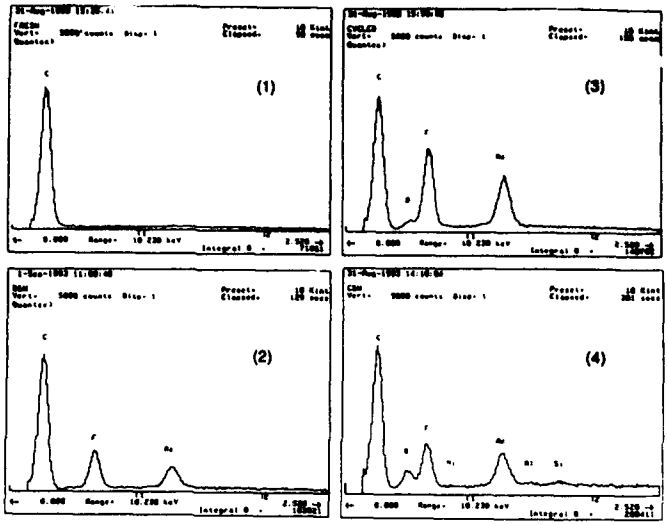

Figure 4. The chemistry of carbon surface film was examined by EDX at four condition: (1) Fresh carbon electrode (2) Fresh carbon electrode dipped in the electrolytes and then washed by using pure solvent to clean up the residual salts (3) Cycled carbon electrodes (4) Cycled carbon electrode then washed by pure solvent.

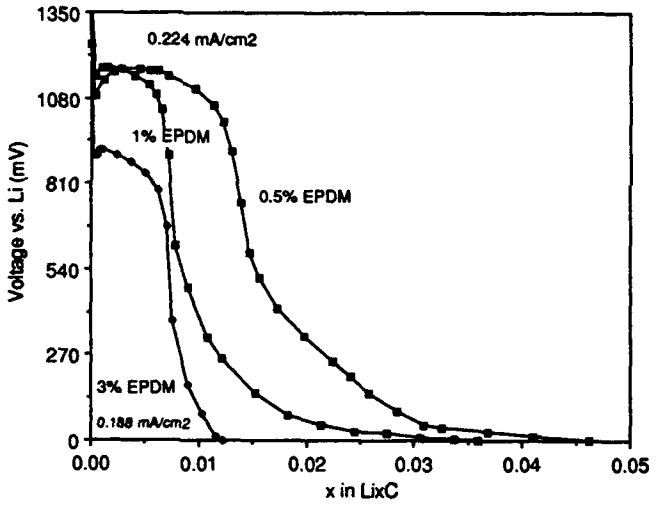

Figure 5. The effect of the percent amount of EPDM binder on the reaction of lithium with graphitic carbon.

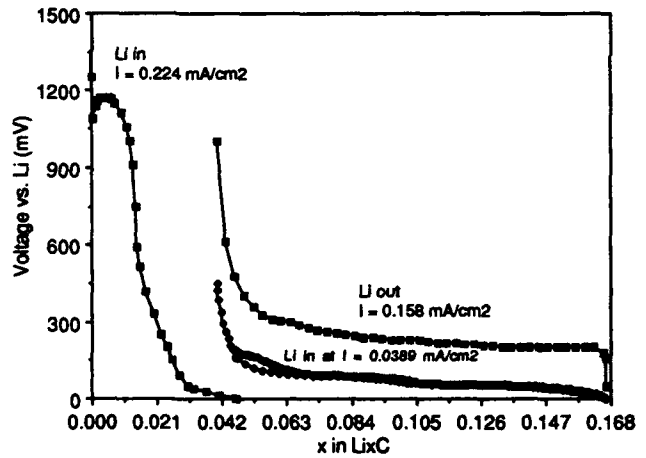

Figure 6. Electrochemical Li intercalation and de-intercalation in graphite.

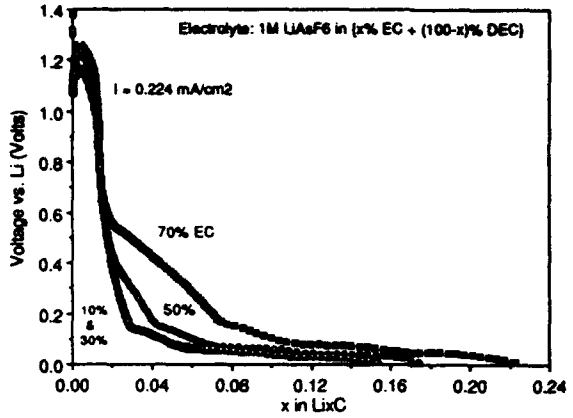

Figure 7. Comparison of the first step discharge of Li/LixC cells containing electrolyte having different amount of EC.

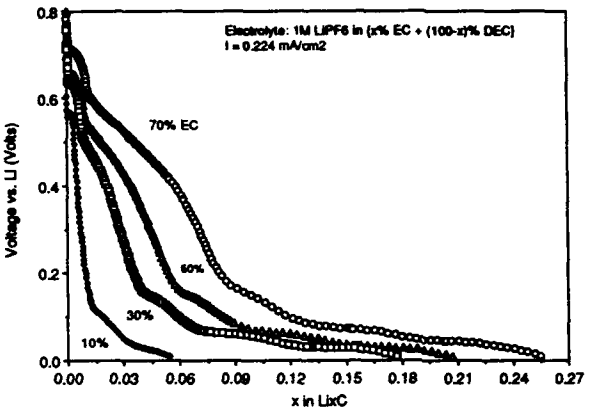

Figure 8. Comparison of the first step discharge of Li/LixC cells containing electrolyte having different amount of EC.

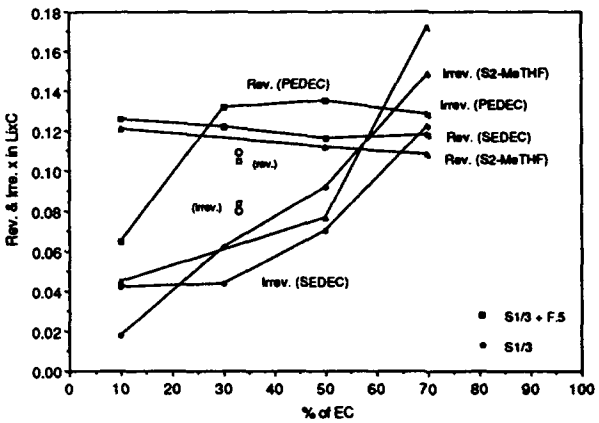

Figure 9. Comparison of the reversible and irreversible Li capacity of Li/LixC cells containing various electrolytes.

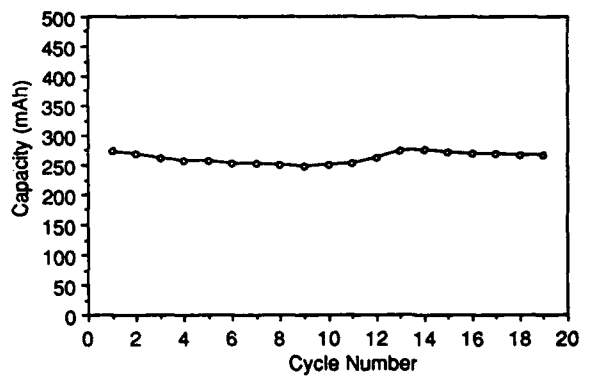

Figure 10. Cycling performance of a C/LiCoO2 250 mAh cell.

DEVELOPMENT OF A HIGH ENERGY DENSITY RECHARGEABLE LITHIUM-ION CELL TECHNOLOGY

Walter Ebner, David Fouchard, Like Xie and Sid Megahed
Rayovac Corporation, Madison, WI

Abstract

Lithium-ion cells are attractive for many consumer and military applications. However, to achieve the performance goals for Naval applications, high capacity anode materials are needed that can boost specific energy beyond present levels. Graphitic carbons offer twice the theoretical capacity of petroleum coke and, thus, represent attractive second generation anode materials. The feasibility of using graphitic carbon anode materials has been demonstrated in AA-cells where a 48 percent increase in capacity was achieved at low discharge rates. However, the rate capabilities of these cells were poor compared to cells with petroleum coke anodes. This paper discusses work in progress to improve the rate capabilities of graphitic carbon anode materials considering both the type of graphitic carbon and the effects of the electrolyte solution.

Introduction

Lithium-ion batteries represent an exciting new technology that offers much promise for a wide range of applications and markets. These batteries offer a high level of safety combined with long cycle life, good rate capabilities and low temperature performance, and energy densities that surpass all traditional rechargeable battery technologies. Sony and Toshiba have already introduced lithium-ion batteries into the U.S. consumer market for camcorders and portable computers, respectively, and more batteries by these and other manufacturers are expected to follow later this year.

Lithium-ion batteries also offer much promise for military applications and at Rayovac we are pioneering their development under contracts to both ARL and NSWC. This paper describes work being done under our NSWC contract directed at developing a prismatic lithium-ion cell technology to power auxiliary equipment on underwater vehicles. In the present program, we are developing an 8 Ah cell to demonstrate the feasibility of the lithium-ion technology. Subsequent phases of the program will incrementally scale-up the technology to a 200 Ah cell which will be the building block for battery development. The final battery would incorporate 24 cells configured in a series-parallel arrangement yielding a 24V, 14KWh battery.

Our present development efforts are directed at the $LiNiO_2$/carbon system. $LiNiO_2$ was selected over $LiCoO_2$ because its lower operating voltage offers many advantages which more than offset the reduction in energy density and specific energy. These advantages include better high temperature stability, lower self-discharge rates, better safety characteristics during overcharge, and the use of a wider range of electrolyte solutions. The latter consideration is especially important to achieve the rate capabilities and low temperature performance needed for military applications. For example, DME-based solutions, which offer good rate capabilities and low temperature performance, can be used with $LiNiO_2$ but not with $LiCoO_2$.

Our baseline technology employs a petroleum coke anode combined with either a 1.0M $LiN(CF_3SO_2)_2$/PC-DME (50:50) (coin cells only) or 1.0M $LiPF_6$/PC-DME (50:50) electrolyte solution. This technology has been found to offer excellent performance characteristics(1).

The main deficiencies of the $LiNiO_2$/petroleum coke system are capacity and specific energy. A key performance goal for the prismatic cell technology is to achieve a specific energy of ≥115 Wh/kg in the 200 Ah cell and projections made using a computer model indicated that it would be very difficult to realize that goal using the baseline technology (Figure 1). To boost specific energy, we are pursuing the development of alternate, high capacity carbon anode materials. The projections shown in Figure 1 indicate that a specific capacity of 320 mAh/g will be sufficient to meet the specific energy goal.

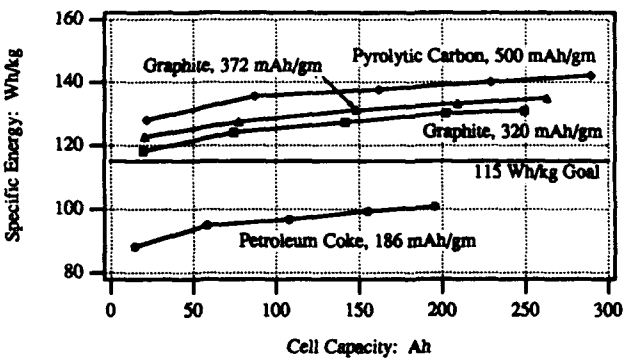

Figure 1. Specific Energy Projections for Prismatic $LiNiO_2$/Carbon Lithium-Ion Cells as a Function of Carbon Type and Cell Size.

Based on these projections, we are pursuing the development of graphitic carbon anode materials for the prismatic cell technology which offer a theoretical capacity of 372 mAh/g. This paper discusses the progress to date in implementing a graphitic carbon. Although our investigations are not complete, we have substantially increased our understanding of the behavior and characteristics of graphitic carbons for use as anode materials in lithium-ion cells.

Results and Discussion

Our initial evaluations of graphitic carbons employed Lonza KS synthetic graphites. These materials are readily available commercially at low cost and have been shown to give reasonably good performance as a lithium intercalation electrode(2). Electrolyte solutions were EC-based since they have been reported to give good reversibility with graphitic carbons(3).

Figure 2 compares AA-cell capacity as a function of rate capabilities for a Lonza KS-15 graphite anode versus a petroleum coke anode. At low current densities, the cell with the graphite anode performed quite well, delivering a capacity of 620 mAh versus 420 mAh for the petroleum

coke cell. This represents a 48 percent capacity improvement. Under these conditions, the graphite anode delivered a specific capacity of 356 mAh/g, very close to the theoretical 372 mAh/g for graphite. At higher current densities, however, the capacity of the graphite cell dropped off much more rapidly than the petroleum coke cell. At 5 mA/cm^2 and beyond, the petroleum coke cell actually yielded higher capacities.

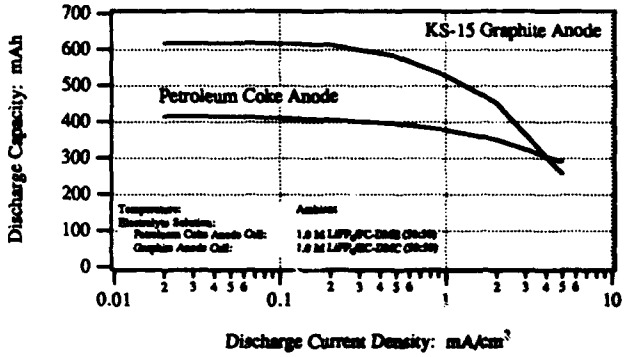

Figure 2. Discharge Rate Capability Comparison of AA-Cells Incorporating a Lonza KS-15 Graphite Anode Versus a Petroleum Coke Anode.

These initial investigations showed that graphitic carbons were indeed viable anode materials for lithium-ion cells and could realize the significant gains in capacity projected for them. However, the results also showed that significant improvements in rate capabilities were needed before these gains could be achieved at practical current densities. Therefore, increasing the rate capabilities of cells employing graphitic carbon anode materials has become a major focus of our work, To accomplish this, we investigated two approaches: the use alternate graphitic carbons and the use alternate electrolyte solutions.

Alternate Graphitic Carbons

There are a wide range of graphitic carbons commercially available and it was of interest to determine how they compared as intercalation anode materials. Investigations were therefore undertaken to determine the specific capacities, irreversible capacities, and rate capabilities for a variety of graphitic carbons. We also wanted to try to correlate performance with physical properties of the graphite in an effort to determine the most important properties. These could then be used to select other candidate materials and, ultimately, to engineer new high capacity carbons.

Table 1 summarizes the graphitic carbons evaluated along with their known physical properties. Figure 3 compares the reversible and irreversible capacities measured for each carbon in lithium coin half-cell tests at 0.1 mA/cm^2. The highest reversible capacity was achieved with the IBA natural graphite followed by SFG-75. These results indicate that large Lc values may be beneficial to performance. Comparing the results for SFG-6 with those for SFG-75, it appears that increased surface area decreases reversible capacity and increases irreversible capacity.

Based on these results, graphitic carbons having high Lc values (e.g. >2,000 A) and low surface areas (e.g. < 5 m2/g) are indicated to give the best overall performance, considering reversible and irreversible capacities.

Table 1. Summary of Graphitic Carbons Evaluated for Use as Lithium-Ion Anode Materials

Graphitic Carbon	d(002) (Å)	Lc (Å)	True Density (g/cc)	Surface Area (m^2/g)
KS-44 Synthetic Graphite	3.34	>1,000	2.26	10.0
SFG-6 Synthetic Graphite	3.34	>1,000	2.26	15.2
SFG-44 Synthetic Graphite	3.34	<2,000	2.26	4.2
SFG-75 Synthetic Graphite	3.34	>2,000	2.26	3.5
IBA Natural Graphite	3.34	>2,000	–	–
Sumitomo FPA-405 Natural Graphite	3.35	>2,000	2.26	5.7
EC-110 Isotropic Graphite	–	–	–	9.5

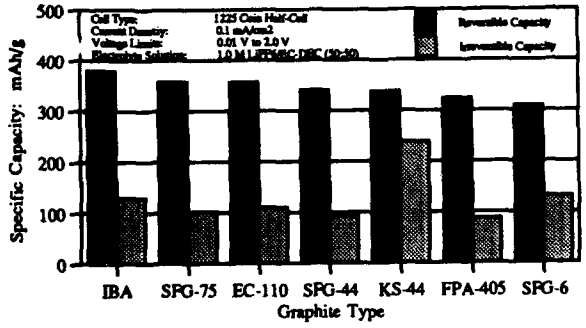

Figure 3. Specific Reversible and Irreversible Capacities for Various Graphitic Carbons

Rate capabilities for some of the graphites were determined using stepwise intercalation/deintercalation tests and then fitting the capacity versus current density results to an empirical equation, derived by Selim and Bro(4), using a nonlinear curve fitting technique. We have found this to be an excellent method for evaluating rate capabilities in both half-cells and full lithium-ion cells(1). The curve fitting process gives best fit values for three empirical parameters, Qo, R, and A which provide a quantitative measure of rate capability. R is of particular interest because it provides an estimate of the maximum practical current density for a given cell design or electrode configuration. Thus, cells should be designed to operate at current densities ≤R to ensure efficient operation.

Table 2 compares fitted parameters from the Selim-Bro Equation for petroleum coke versus two graphitic carbons. For all three carbons tested, the intercalation R-values were much smaller than the deintercalation R-values. We attribute this to the effects of ion desolvation during the intercalation process. Significantly, the intercalation rates in graphite are indicated to be much lower than in petroleum coke. The deintercalation rate capabilities, as given by the R-values, are all indicted to be of similar magnitude. These results, therefore, indicate that graphitic carbons offer discharge rate capabilities similar to those of petroleum coke.

Table 2. Fitted Parameters from the Selim-Bro Equation Defining the Rate Capabilities of Petroleum Coke Versus Two Graphitic Carbons.

	Intercalation			Deintercalation		
Carbon	Qo (mAh/g)	R (mA/cm²)	A	Qo (mAh/g)	R (mA/cm²)	A
Petroleum Coke	241	1.24	1.46	234	9.54	0.53
Sumitomo FPA-405 Natural Graphite	365	0.43	0.86	336	11.26	0.58
EC-110 Isotropic Graphite	400	0.44	0.91	364	10.86	0.60
Electrolyte Solutions Used: Petroleum Coke: 1.0M $LiN(CF_3SO_2)_2$/PC-DME (50:50) Graphites: 1.0M $LiPF_6$/EC-DEC (50:50)						

The lower rate capabilities observed in the AA-cell tests with graphitic carbon anodes are, therefore, attributed to solution properties rather than to the graphite anodes. As shown in Table 3, the EC-based solutions required for use with graphitic carbons are considerably less conductive and more viscous than the PC-DME solution used with petroleum coke. Reduction in rate capabilities by the EC-based solutions was confirmed in AA-cell tests using petroleum coke anodes with a 1.0M $LiPF_6$/PC-DME versus a 1.0M $LiPF_6$/EC-DEC solution. The results, shown in Figure 4, clearly show lower rate capabilities for the EC-DEC solution. The fitted R-value from the Selim-Bro equation was reduced by 44 percent (e.g. 1.89 versus 3.39 mA/cm^2 for the PC-DME solution).

Table 3. Physical Properties of Key PC- and EC-Based Electrolyte Solutions at 25°C.

Electrolyte Solution	Conductivity (mS/cm)	Viscosity (cP)
1.0M $LiPF_6$/PC-DME (50:50)	14.3	2.62
1.0M $LiPF_6$/EC-DMC (50:50)	10.9	3.34
1.0M $LiPF_6$/EC-DEC (50:50)	7.8	4.71

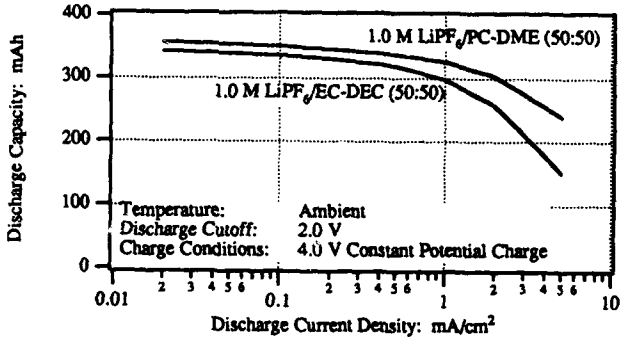

Figure 4. $LiNiO_2$/Petroleum Coke AA-Cell Discharge Rate Capability Comparison Showing Performance for a EC-DEC Electrolyte Solution Versus a PC-DME Solution.

Based on these results, it appears that the type of graphite has little impact on the discharge rate capabilities of lithium-ion cells. Instead, solution properties are indicated to be the dominating factor. Thus, to improve discharge rate capabilities, alternate high conductivity electrolyte solutions are needed that can work reversibly with graphitic carbon anodes and, at the same time, offer the oxidative stability needed for the high potential cathode materials used in lithium-ion cells

Alternate Electrolyte Solutions

To date, EC-based solutions are the only solutions known to work reversibly with graphitic carbons. The most widely used solutions employ mixtures of EC with DMC (5,6) or DEC (6), although EC can be used alone. However, to improve the rate capabilities of lithium-ion cells employing graphitic carbon anodes, other solutions must be identified. To accomplish this, we must first understand what solvent qualities are needed to achieve reversible performance with graphitic carbons and then use that information to engineer higher performance solutions.

As a first step in the learning process, we have conducted low rate intercalation/deintercalation cycle tests of KS-44 synthetic graphite in a variety of single and mixed solvents. These tests employed lithium coin half-cells.

Figure 5 shows the reversible and irreversible capacity observed with each solvent. Both EC and DMC yielded high reversible capacities but accompanied by high irreversible capacities as well. DEC, on the other hand, exhibited very poor performance, with virtually no reversible capacity. The ethers, DME and 1,3-dioxolane, gave poor performance. PC gave the worst performance, exhibiting a specific irreversible capacity of 1030 mAh/g and no reversible capacity.

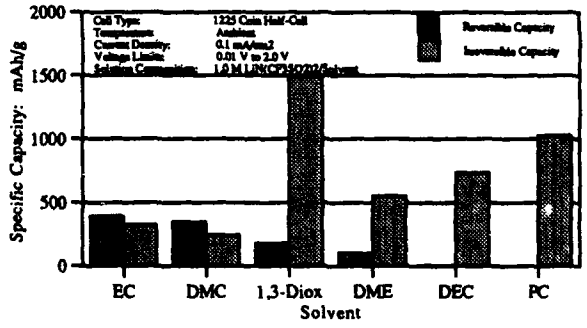

Figure 5. Specific Reversible and Irreversible Capacities for Lonza KS-44 Graphite with Various Single-Solvent Electrolyte Solutions.

Figure 6 shows results for mixed solvents. As expected, the best results were achieved with EC-DMC and EC-DEC. All other solvent mixtures gave poor performance.

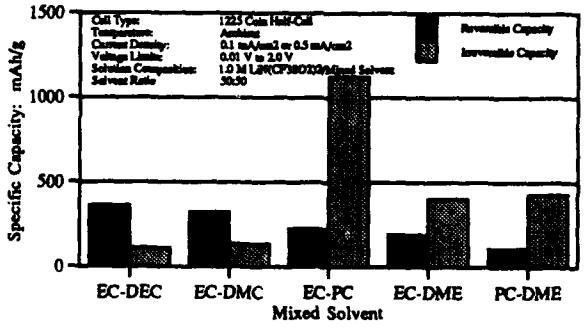

Figure 6. Specific Reversible and Irreversible Capacities for Lonza KS-44 Graphite with Various Mixed-Solvent Electrolyte Solutions.

It is believed that the reason that most solvents do not work with graphitic carbons is that they are cointercalated

along with the lithium ions. This solvent cointercalation results in extensive exfoliation of the graphite which continually exposes fresh surfaces that can react with the electrolyte solution. Furthermore, it is believed that the cointercalated solvent molecules undergo reductive decomposition producing gaseous byproducts that can further exfoliate the graphite.

To achieve reversible operation, it is essential that the protective film that forms on the surface of the carbon during the first charge (SEI layer) be completely formed prior to the onset of intercalation. We also believe it important that the SEI layer be highly inorganic in nature. Evidently, EC is able to form a compact film very rapidly at potentials of about 1.0V or more positive to lithium.

Although the results to date are limited, they do provide some insight into the types of solvents that are suitable for use with graphitic carbons. For example:

- DMC has been shown to yield high reversible capacities with graphitic carbons. To date, EC and DMC are the only solvents identified that can be used as primary solvents with graphitic carbons.
- Molecular weight seems to be important to the performance of carbonate solvents. Those having molecular weights above 100 perform poorly as primary solvents but can be used as cosolvents if they have a low dielectric constant.
- Aliphatic and cyclic ethers perform poorly as either primary solvents or cosolvents.
- A low dielectric constant appears to be important for cosolvents to be used with EC

These findings will now be used to select additional solvents and cosolvents for evaluation with graphitic carbons. We plan to pursue a wide range of solvents and solvent types in a systematic approach to develop high performance electrolyte solutions for use with the $LiNiO_2$/graphite lithium-ion technology. We also plan to explore the use of additives as a means to control and enhance SEI layer properties in a wide range of electrolyte solutions.

SUMMARY AND CONCLUSIONS

The $LiNiO_2$/graphite lithium-ion technology is an attractive system, capable of boosting cell capacity and specific energy well beyond present levels achieved using petroleum coke anodes. However, improvements in rate capabilities are needed before these enhancements can be realized at practical discharge rates.

Through half-cell investigations, we have found that the reduced rate capabilities are not due to slower kinetics at the graphite electrode but, rather, to effects of the EC-based electrolyte solutions used with the graphitic carbons. These results, therefore, substantiate the need for development of new, high performance electrolyte solutions suitable for use with graphitic carbon anodes.

Although the type of graphite does not appear to strongly affect rate capabilities, it does impact reversible and irreversible capacities. Our goal is to maximize reversible capacity and minimize irreversible capacity and the best overall performance has been achieved with graphites having large Lc values and low surface areas.

Initial half-cell investigations of KS-44 synthetic graphite with a variety of single and mixed solvent electrolyte solutions have been used to develop a better understanding of the types of solvents that are suitable for use with graphitic carbons. These results will now be used to select additional solvents and solvent types for evaluation and to guide future experimentation.

Through development of improved electrolyte solutions and selection of graphitic carbons with optimized physical properties, we are confident that a $LiNiO_2$/graphite prismatic cell technology can be achieved that will meet or exceed all performance requirements for Naval applications.

ACKNOWLEDGMENTS

The authors gratefully acknowledge the Office of Naval Technology under the High Energy Battery Project (Naval Surface Warfare Center, White Oak) for their support of this work under Contract N60921-93-C-0023. Also, the AA-cell tests were conducted under ARL Contract DAAL01-93-C-3363, and we gratefully acknowledge the U.S. Army Research Laboratory in Fort Monmouth, New Jersey for their support of that portion of the work.

REFERENCES

1. W. Ebner, D. Fouchard and L. Xie. Submitted to Solid State Ionics (1994).
2. J.R. Dahn, A.K. Sleigh, Hang Shi, J.N. Reimers, Q. Zhong, and B.M. Way, Electrochemica Acta, Vol 38, No. 9, p. 1179 (1993).
3. R. Fong, U. von Sacken, and J.R. Dahn, J. Electrochem Soc., 137, p. 2009 (1990).
4. R. Selim and P. Bro, J. Electrochem. Soc., 118, 829 (1971).
5. D. Guyomard and J.M. Tarascon, U.S. Patent No. 5,192,629 (1993).
6. J.R. Dahn, A.K. Sleigh, Hang Shi, B.M. Way, W.J. Weydanz, J.N. Reimers, Q. Zhong and U. von Sacken in "Lithium Batteries - New Materials, Developments and Perspectives", pg.1. Edited by G. Pistoia. Published by Elsevier, Amsterdam, 1994.

DEVELOPMENT OF A LITHIUM-ION BB-2847 BATTERY

David Fouchard, Walter Ebner and Sid Megahed
Rayovac Corporation, Madison, WI

Abstract

A program, sponsored by the Army Research Laboratories (ARL), was undertaken at the Rayovac Corporation, to develop lithium-ion technology suitable for military applications and to demonstrate the technology in a BB-2847 battery for the AN/PAS-13 application. Current options for the AN/PAS-13 are either a primary lithium battery or a rechargeable nickel cadmium battery. The former provides high capacity but at a high cost, particularly for training missions. The latter is relatively inexpensive over its lifetime, but provides only limited operating time. A higher energy density secondary battery is therefore needed that can extend performance beyond the levels presently achieved with nickel cadmium batteries, and that can offer a significant cost advantage over primary lithium batteries for training missions.

The system selected for initial development was the carbon/$LiNiO_2$ "rocking chair" or "lithium-ion" system. Development was undertaken stepwise through coin cells, AA-cells, D-cells and the BB-2847 battery with two D-cells and an integrated battery controller. The development resulted in a safe secondary battery with significant energy density advantages over the nickel cadmium battery.

Introduction

The Army needs superior, cost effective, rechargeable batteries to provide power to an increasingly wide range of man-portable electronics equipment(1). While traditional rechargeable batteries such as Ni/Cd and Pb-acid batteries have received limited use in these applications, they are heavy and often cannot provide sufficient energy in a man-portable package. What is needed is a new generation of safe, lightweight, high energy rechargeable batteries.

To fulfill this need, considerable effort has been made during the past decade to develop rechargeable lithium cells. These systems offered promise of high specific energies, excellent charge retention and good low temperature performance. However, no practical rechargeable lithium batteries have been achieved to date, primarily due to the failure to resolve serious safety issues(2).

More recently, the rocking chair (RCT) or lithium-ion technology has emerged as a viable alternative to rechargeable lithium cells(3). This is a lithium-like technology that replaces the problematic metallic lithium anode with a low molecular weight intercalation electrode, typically petroleum coke or a pyrolytic carbon. By doing this, the safety issues related to the presence of metallic lithium and the dendritic deposition of metallic lithium are eliminated. Thus, lithium-ion is intrinsically a much safer technology than a rechargeable lithium technology. It also offers long cycle life combined with moderate capacities, rate capabilities, and an energy density that exceeds all long lived aqueous rechargeable batteries. The lithium-ion technology also has a high commercial (dual use) potential. This paper describes the development of such a technology for military applications, and its demonstration in a BB-2847 battery for the AN/PAS-13 application.

Approach

The BB-2847 battery is a nominal 6 V system, rectangular in shape, measuring 3.75" by 2.55" by 1.50" . For the AN/PAS-13 application, continuous discharge rates of approximately 2 A are required, with a pulse capability to 5 A. Our approach was to use 2 series connected D-cells, using the carbon/$LiNiO_2$ lithium-ion system. The dimensions of the BB-2847 are such that 2 D-cells and a small control circuit can be accommodated. The use of a dedicated controller can greatly enhance the performance and safety of such a system, and as such, was an important component of the battery.

Cell Design

The materials chosen for this development effort were petroleum coke (Conoco) for the anode and $LiNiO_2$ for the cathode. The $LiNiO_2$ was prepared in-house by reacting LiOH and $Ni(OH)_2$ under O_2. Electrodes were prepared from the materials by slurry coating both sides of 25 μm metal foils, copper for the anode and aluminum for the cathode. After coating and drying, the electrodes were densified by repetitively passing through compression rollers with successively smaller gap settings. Typically, the cathodes were 225 μm thick with a density of 2.4 g/cm^3 and the anodes 275 μm thick with a density of 1.3 g/cm^3, producing a working surface area of 1,100 cm^2 in a D-cell. The electrodes were spirally wound with Celgard 2400 separator and inserted into standard D-size cans. After beading and attaching tabs, the cells were closed by crimping around a molded polypropylene header having an integral vent panel and a stainless steel feed-through. Cells were then vacuum filled through the feed-through and sealed by forcing a stainless steel ball into the opening.

D-Cell Performance

Discharge rate capability determination of cells was carried out by sequentially discharging to 2.0 V at progressively lower currents with a 30 minute rest between each discharge. The data from such a test are shown in Figure 1 which plots cumulative discharge capacity as a function of discharge current. It can be seen that the delivered capacity ranged from 3.25 Ah at 4.4 A (4 mA/cm^2) to 3.71 Ah at 0.018 A (0.02 mA/cm^2). The energy density values calculated from these data are 226 Wh/l and 104 Wh/kg at 2 A, and 252 Wh/l and 115 Wh/kg

at low rates. The material utilization values as a function of current density for the same cell are shown in Figure 2. Note that the anode utilization ranged from 166 to 190 mAh/g while the cathode ranged from 128 to 146 mAh/g. These values are all close to Δx of 0.5, a value typical for both petroleum coke (Li_xC_6) and Li_xNiO_2.

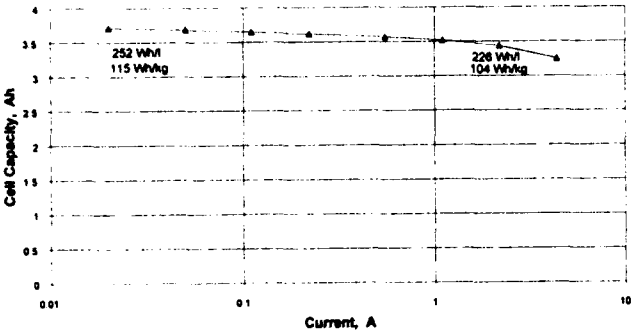

Figure 1. Discharge Rate Capability of the Lithium-Ion D-Cell at 25°C

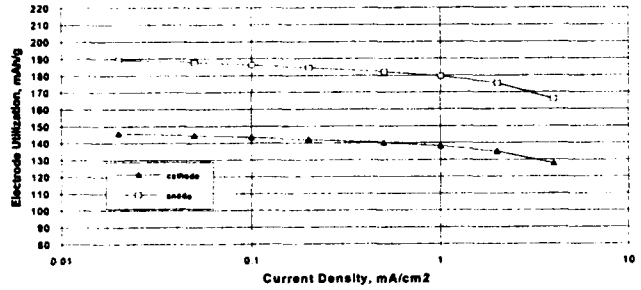

Figure 2. Electrode Utilization Values as a Function of Current Density for the Lithium-Ion D-Cell at 25°C

Battery Controller

A dedicated control circuit was developed for the BB-2847 in order to achieve maximum performance, reliability and safety from the battery. A block diagram of the circuit is shown in Figure 3. Note that the circuit is entirely analog. The two series-connected D-cells interface with separate charge and discharge connectors. A number of protective devices are common to both the charge and discharge ports, and are wired in series with the cells. They are:

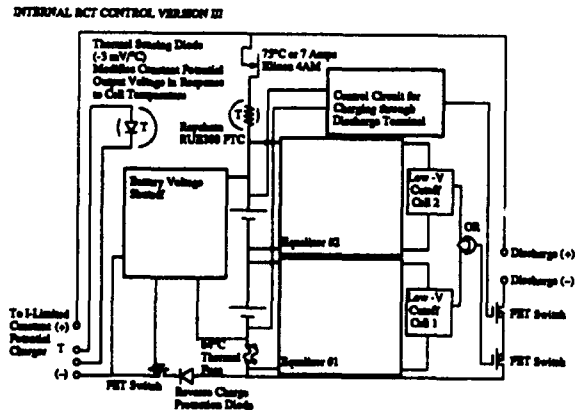

Figure 3. Block Diagram of the Control Circuit for the BB-2847

- PTC fuse (Raychem Polyswitch), the primary current limiting device
- Klixon device (Texas Instruments), the secondary current limiting device and the primary over-temperature control device (75°C),
- Thermal fuses (Elmwood), the secondary over-temperature control device (85°C).

All of the devices are auto-resetting except the thermal fuses.

The charge control section of the controller incorporates the following functions:

- Diode protection for polarity reversal
- Cell equalization
- High voltage cutoff
- Temperature compensation.

Cell equalization consists of parallel bypass resistors for each cell, controlled through an operational amplifier and a precision voltage reference. When a cell reaches 4.0 V during charge, the bypass resistor is connected across the cell, limiting its voltage while the cells continue to charge. Near the end of charge, both cells would normally be in the bypass mode. The system corrects for minor differences in cell capacity, enabling full battery capacity to be realized. The high voltage protection circuit monitors battery voltage and will turn off a FET switch if voltage levels exceed 8.35 V, stopping the charge. This protection would be required in the event of a charger malfunction, or the use of a high voltage, non-standard charger. The voltages of the high voltage protection and equalization circuits are temperature compensated at -6 mV/°C and -3 mV/°C respectively. This was done to match the -6mV/°C temperature compensation of the charger. The purpose of the temperature compensation was two-fold; to raise the charging voltage at low temperatures to ensure complete charging in a reasonable time, and to limit charge voltages at high temperatures to extend battery life.

The discharge control section of the controller contains a lower voltage cutoff function, and a protective circuit to limit charging through the discharge connector. Individual lower voltage cutoffs for each cell are used, set at 1.8 V. When either cell reaches this value, a FET switch is turned off, stopping the discharge. The voltage loss associated with using a diode to prevent charging through the discharge port was deemed too large in a 2-cell battery such as the BB-2847, therefore an alternate circuit was required. The circuit senses both voltage and charge current in the discharge port, and turns off a second FET switch if either is excessive. The voltage penalty for the second FET is only 25 mV, rather than several hundred mV for a diode, and therefore does not introduce significant energy losses.

The quiescent current of the control circuit is approximately 120 μA. This represents a storage period of 1.4 years for a 50% loss of battery capacity . The circuit was fabricated on a custom PC board measuring 2.4 x1.3",

equivalent to the cross-sectional area of the BB-2847 case. The complete layout of the battery is shown in Figure 4. A molded ABS case was used, with charge and discharge connectors on the front face. The complete package weighed approximately 295 g.

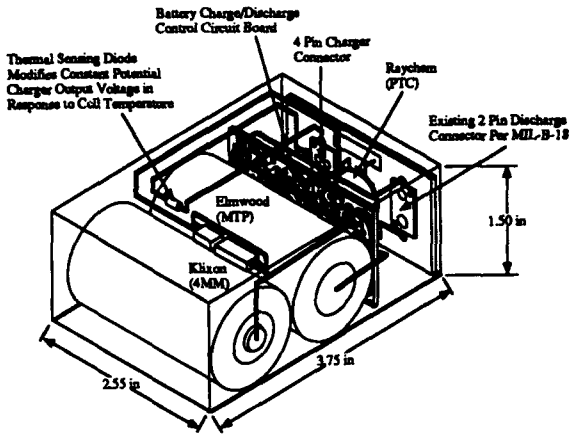

Figure 4. General Layout of the Lithium-Ion BB2847 Battery.

Battery Performance

A charging curve for a BB-2847 battery is shown in Figure 5. Battery voltage, cell voltages, capacity and the voltage across the equalization resistors are all plotted versus charging time. The charger voltage was set at 8.30 V in order to achieve a nominal 8.0 V across the 2 series cells and 0.3 V across the series diode. With the current limited to 1 A, the first cell reached 4.0 V in 2.8 h, whereupon the equalization circuit activated as evidenced by a voltage appearing across the bypass resistor. After 4.4 h, the second cell reached 4.0 V, and that equalization circuit activated, indicative of a complete charge. Shortly after this, an over-voltage condition was deliberately created by raising the charger voltage. The battery voltage and current increased over the next 1.2 h, until the over-voltage protection circuit activated, stopping the charge. Peak voltage values were 8.38 V for the battery, and 4.16 and 4.18 V for the cells.

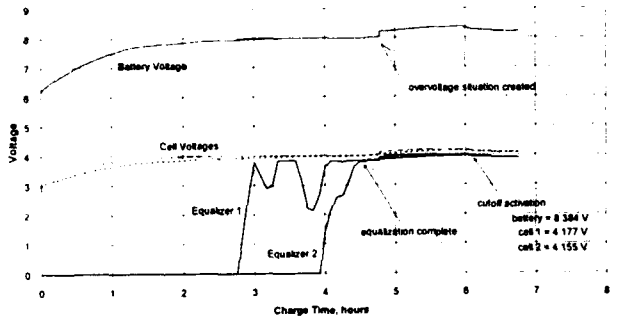

Figure 5. Illustration of the Equalization and High Voltage Protection Systems in the BB-2847 Controller

Typical discharge curves for the BB-2847 at 2 A, including 25°C and -20°C ambient, are shown in Figure 6. In this case the capacity at 25°C was 3,147 mAh, while the -20°C capacity was 2,389 mAh, 76% of the room temperature value. Average voltage values were 6.05 V and 5.86 V respectively. An illustration of the pulse discharge capability of the battery is shown in Figure 7. After charging to 8.0 V, the battery was discharged to 4 V in a pulse sequence of 5 A for 20 s followed by a 40 s rest. The battery was then rested for 30 minutes, and finally discharged at 1 A to 4.0 V to determine the residual capacity. The graph shows battery voltage and capacity versus time. It can be seen that 96 pulses were achieved within the specified voltage limits, equivalent to 2,666 mAh. The 1A residual capacity was 523 mAh, for a total of 3,189 mAh.

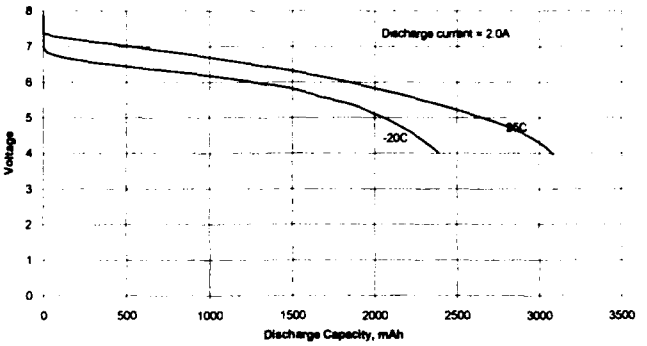

Figure 6. Comparison of Discharge Profiles at 25°C and -20°C for BB-2847 Battery 046. Discharge Rate 2A to 4.0V

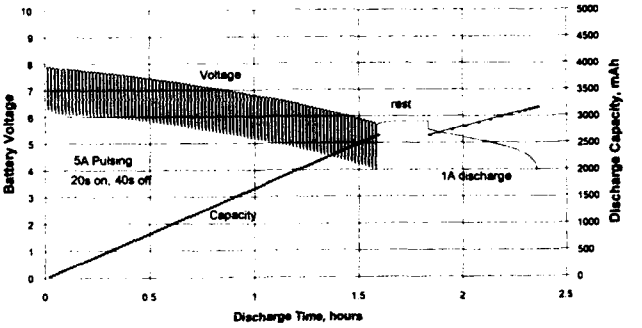

Figure 7. Discharge Profile for BB-2847 Battery 017 for the High Rate Pulse Discharge Test at 25°C

A cycle life test of a typical battery is shown in Figure 8. The voltage range was 8.0/4.0 V with a 2 A discharge rate. Every 20 cycles, the discharge was continued until the lower voltage cutoff of the battery activated (one cell reaching 1.8 V). The capacity for this battery was 3,316 mAh initially, 2,903 mAh after 50 cycles and 2,528 mAh after 80 cycles. This represents 88% retained capacity after 50 cycles and 76% after 80 cycles. It should be noted that these cells were optimized for capacity and rate, with a cycle life requirement of only 100 cycles.

There is considerable latitude to extend the cycle life with minor tradeoffs in capacity, and this is illustrated in figure 9. This figure compares cycling performance of AA-cells optimized in different ways. In one case the cell was optimized for maximum capacity and a cycle life requirement of 100 cycles, similar to the D-cells for the BB-2847 batteries. The other cell was optimized for

longer cycle life at a lower capacity. Cycling conditions were 4.0 to 2.0 V, with a discharge rate of 2 mA/cm^2. It can be seen that the high capacity cell delivered approximately 30% more capacity initially, but faded to 80% of its peak capacity in 140 cycles, versus 500 cycles for the other cell. This demonstrates the flexibility of the technology in fulfilling a wide variety of applications.

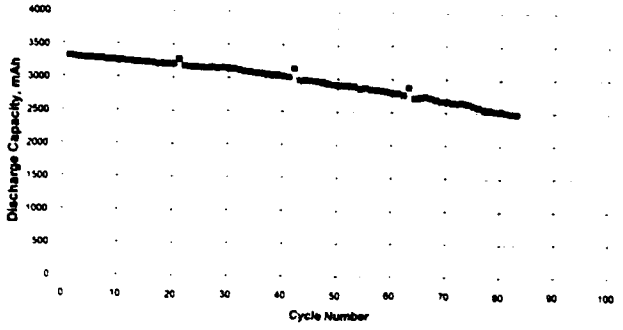

Figure 8. Cycle Life Test of BB-2847 Battery 012. Voltage Range 8/4V, Discharge at 2A, Room Temperature

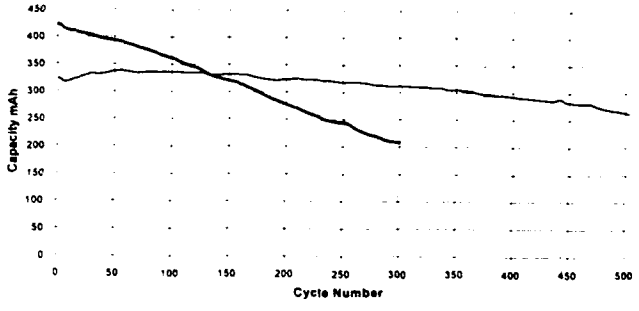

Figure 9. Comparison of Cycle Life of AA-Cells Optimized for a 100 Cycle Requirement With Those Optimized for Longer Cycle Life. Voltage Range 4/2V, Discharge 2 mA/cm^2.

Summary

A lithium-ion technology, suitable for military applications was developed and demonstrated in a BB-2847 battery. Using petroleum coke and $LiNiO_2$ active materials, D-cells having energy density values of 252 Wh/l, 115 Wh/kg at low rates and 226 Wh/l, 104 Wh/kg at a 2 A rate were demonstrated. Using 2 D-cells in conjunction with a dedicated battery controller and charger, a complete system offering high performance, reliability and abuse tolerance was achieved. The system offers an attractive alternative to the present options of an expensive, high performance lithium primary battery, and an inexpensive but limited performance Ni/Cd system.

Acknowledgments

The authors gratefully acknowledge the U.S. Army Research Laboratory in Fort Monmouth, New Jersey for their support of the work conducted at Rayovac.

References

(1) S. Gilman, Proceedings of the Tri-Service Lithium Battery R&D Workshop, Lake Placid, NY, June 23, 1993.

(2) D.P. Wilkinson, J.R. Dahn, U. von Sacken and D.T. Fouchard, Abstracts 53 and 54, p.85 and 87, The Electrochemical Society Extended Abstracts, Vol. 90-2, Seattle, WA, October 14-19 (1990).

(3) T. Nagaura and K. Tozawa, Progress in Batteries & Solar Cells, Vol. 9, p. 209 (1990).

LITHIUM LIKE RECHARGEABLE BATTERY

Robert J. Staniewicz, Angela S. Gambrell, and Gabriel Castro
Saft R&D Center
107 Beaver Court
Cockeysville, MD 21030

Introduction

A lithium like rechargeable battery replaces metallic lithium with a lithium ion intercalation carbon electrode which operates somewhat positive of the Li°/Li^{+} potential. Carbon intercalation negatives offer a cycle life of at least 1,000 cycles, promise of consumer type safety, and rapid charge between C/6 to C rates to 100% DOD, all superior characteristics compared metallic lithium rechargeable cells. Presently, energy density of a LiON® Li(C)/$LiNiO_2$ cell, referenced to a small Ni-Cd or Ni-metal hydride cell offers between 100 to 150% improvement at 113 Wh/kg and 250 Wh/L.

Our work has focused on designing and building proof-of-concept D cells and small prismatic cells with $LiNiO_2$ positives and graphite negative electrodes. Some studies have focused on electrode binder studies and evaluation of D cell power capabilities, and cycling life. The LiON® chemistry in the present configuration offers the promise of dual use technology - able to meet projected applications as the BB-2847 or BB-2590 for the military and consumer use.

General Experimental Methods

The positive material, $LiNiO_2$, was synthesized by the method in US Patent 4,980,080 while graphite carbon was used as the negative. Positive electrodes were prepared by two methods, a previously reported PTFE aqueous process[1] used expanded Al screen while the other method, a $LiNiO_2$ suspension [prepared with PVDF and N-methylpyrolidone (NMP)] which was coated onto an Al foil substrate and then dried at approximately 120 °C. The graphite electrode was PTFE bonded onto an expanded Cu substrate or coated onto Cu foil using an emulsion of graphite, PVDF and NMP. Binder content as a percentage of active material was generally between 4 to 12% depending on the process. Cylindrical D cells were constructed from the PTFE bonded electrodes while small prismatic cells used the PVDF bonded electrodes. The separator was Celgard 2400, electrolyte was 1M $LiPF_6$ EC/DMC prepared in house, and cell hardware was Ni plated steel. Cells were charged the first cycle at a C/10 to C/20 rate to 4.1 V while subsequent cycles used considerably faster charging rates at C/6 to C/2. Discharge was performed to a 2.5 V cutoff and MACCOR testing equipment was used for all charge/discharge characterizations.

Results and Discussion

A key point to designing lithium ion cells is to understand the electrochemical performance of the half cell materials, since there is no reference electrode when complete Li ion cells are built and tested. A convenient approach is to study the behavior of metallic Li/graphite and metallic Li/$LiNiO_2$ cells, the lithium negatives also served as quasi reference electrodes. These lithium half cells of $LiNiO_2$ and graphite exhibited the following intrinsic behavior under C/10 charging rate and C/3 discharge rates:

1. LiNiO2 showed a capacity of 180 mAh/g when charged to the 4.10 V limit, or 0.65 lithium de-intercalated from $LiNiO_2$.
2. Saft's graphite required 450 mAh/g when charged to 0 V.
3. The first charge of the graphite consumed approximately 30% of the charge (135 mAh/g) to form an SEI layer.
4. Maximum reversible graphite capacity at C/3 was 320 mAh/g, or $Li_{0.86}C_6$.
5. Reversible capacity for $LiNiO_2$ was 126 mAh/g based on the 70% reversible capacity of the graphite.

With these experimentally determined electrochemical constants, it was then possible to design complete cells using graphite negatives and $LiNiO_2$ positives.

The cycling performance of our first D cell, built in February, 1993, is shown in Figure 1. The electrodes used in this D cell were PTFE bonded on Al or Cu expanded grids. The discharge rate was 1 A to a 2.5 V cutoff while the charging method approximated a C/6 rate. The charging voltage limit was changed four times, giving rise to the stepped nature of the curve shown in Figure 1, the first limit was 3.9 V, then 4.0 V to 80 cycles, 4.05 V to 500 cycles, 4.1 V to 800 cycles and, finally, 4.2 V after 800 cycles. Since these first generation D cells had less than 10 Wh total energy, we knew that improvements in energy were possible. This led to the latest generation of D cells using PTFE bonded electrodes. These 13 Wh D cells have energy densities of 113 Wh/kg and 264 Wh/L at a C/3 discharge rate. The performance is tabulated in Table 1 for various constant current and constant power rates. This cell was also tested via a dynamic stress test (DST) which is used to evaluate potential rechargeable candidates for electric vehicle applications. The DST profile consists of pulse discharge at various power levels and regenerative charging pulses, all of which are indexed to a peak demand of 120 or 150 Wh/kg. The Saft graphite/$LiNiO_2$ electrochemistry, as tested in D cells (Figures 2 and 3), provides 108 Wh/kg when a 120 W/kg peak power is demanded and 102 Wh/kg at 150 W/kg peak power.

Evaluations of reverse roll coated electrodes of $LiNiO_2$ on 0.0178mm Al foil and graphite on 0.01mm Cu foil have been made using PVDF as a binder for both electrodes. We decided to evaluate these electrodes in small prismatic cells with an internal volume of 14 cm^3. Since the first charge for a lithium ion cell involves SEI formation on graphite, there is a solvent reduction on the graphite surface, giving rise to some gas evolution[2]. We reasoned that this gas could cause deformation of the case, therefore, the cells were not sealed and the gases were allowed to escape via tubing to an inverted buret filled with mineral oil (roughly 3 - 7 cm^3 of gas was measured for a 1 Ah charge). Following the first three cycles, the fill port was then welded shut. The discharge capacity as a function of cycle number is shown in Figure 4. This cell, having an active surface area of 325 cm^2, was

discharged at C/3, or 0.25 A, and charged in two hours to a voltage cutoff of 4.1 V and a taper charge of 50 mA.

An interesting experiment was conducted with another prismatic cell of nominal 0.45 Ah at 100% DOD to 2.5 V. This cell was initiated on a 60% DOD discharge profile to 0.27 Ah at 0.225 A and the charge was 90 mA to a 0.27 Ah cutoff. This means the charge was not terminated to a fixed voltage cutoff but was allowed to seek its own equilibrium to deliver 0.27 Ah. The charge voltage cutoff was initially 4.02 V and declined with cycling. We chose to cycle the "middle" 60% of capacity (0.27 Ah) of the 0.45 Ah cell, leaving 20% of the charged capacity (0.09 Ah) uncycled. The results are somewhat surprising in that the average discharge and charge voltage decreased with cycle number. This means that the cell reached a lower discharge cutoff voltage with successive cycles and a lower charge cutoff voltage with successive cycles. We speculate that this behavior occurred because of a constant but slow self-discharge of the uncycled 0.09 Ah capacity. Self-discharge could cause the discharge to reach lower voltages because the "state of change" of the cell is decreasing. This behavior, in turn, gives rise to the lower charge cutoff voltage. The overall behavior occurs because the charge in and out are perfectly matched and there is no excess charge to compensate for the self-discharge.

Conclusions

The LiON® electrochemistry shows good cycling and energy behavior for some early proof-of-concept cells. Both PTFE and PVDF bonded electrodes have been investigated, at this early point in our investigations we cannot conclude which electrode technology is electrochemically superior. Energy density in D cells was demonstrated at 113 Wh/kg (compared to 45 Wh/kg Ni-Cd®) and 250 Wh/L (compared to 90 Wh/L Ni-Cd®).

References

1. R. Staniewicz, A. Romero, M. Broussely, F. Berton, and J. Labat, Proc. 35th Int. Power Sources Symposium, 332(1992).

2. D. Aurbach, Y. Ein-Eli, O. Chusid, Y. Carmeli, M. Balai, and H. Yamin, J. Electrochem. Soc., 141, 603(1994).

Acknowledgement

Part of this work was funded by US Army Research Laboratory, contract number DAAL01-93-C-3379. We thank Mr. Martin Sulkes for his valuable advice.

Description	Results	Comments
C/3 Capacity Verification	3.76 Ah 113.4 Wh/kg 263.6 Wh/l	Taper Charge to 4.1 V 1.235 A CC Discharge to 2.5V
Constant Current @ C/3 Constant Current @ C/2 Constant Current @ C	3.76 Ah 3.76 Ah 3.43 Ah	1.235 A CC Discharge to 2.5V 1.853 A CC Discharge to 2.5V 3.705 A CC Discharge to 2.5V
Constant Power @ 85 W/kg Constant Power @ 57 W/kg Constant Power @ 28 W/kg	3.43 Ah 3.52 Ah 3.64 Ah	9.75 W Discharge to 2.5V 6.00 W Discharge to 2.5V 3.25 W Discharge to 2.5V
DST Cycle	108.0 Wh/kg 101.7 Wh/kg	120 W/kg Peak Power 150 W/kg Peak Power

Table 1. 13 Wh D cell characterization. This cell had 29.6 g of $LiNiO_2$ and 11.8 g of graphite. Interfacial area was 940 cm^2

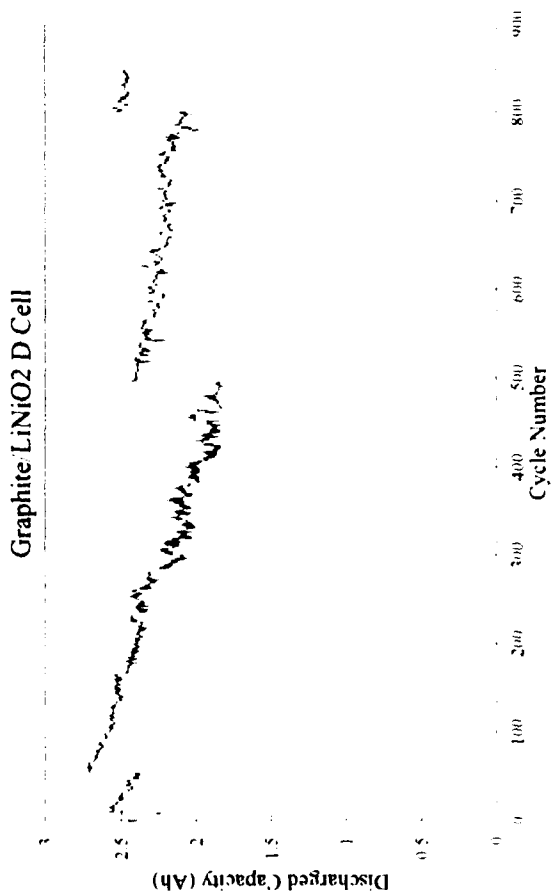

Figure 1. D Cell built in 2/93. Active LiNiO2 weight was 29.6g and graphite weight was 8.5g.

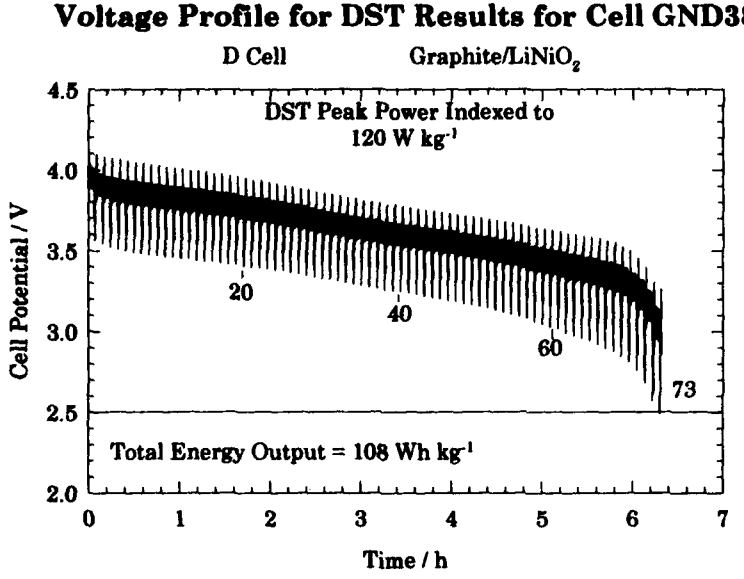

Figure 2. 13 Wh D cell discharged and charged indexed to 120 W/kg peak power. DST is a test of the USABC.

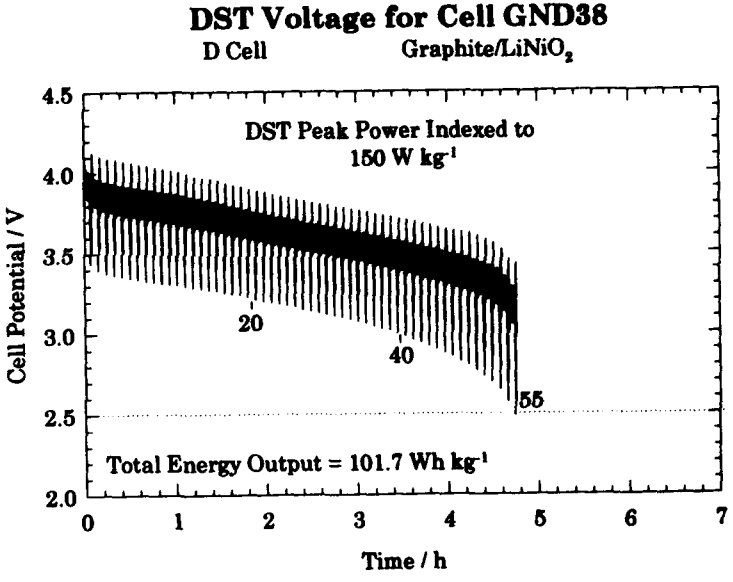

Figure 3. 13 Wh D cell discharged and charged indexed to 150 W/kg peak power. DST is a test of the USABC.

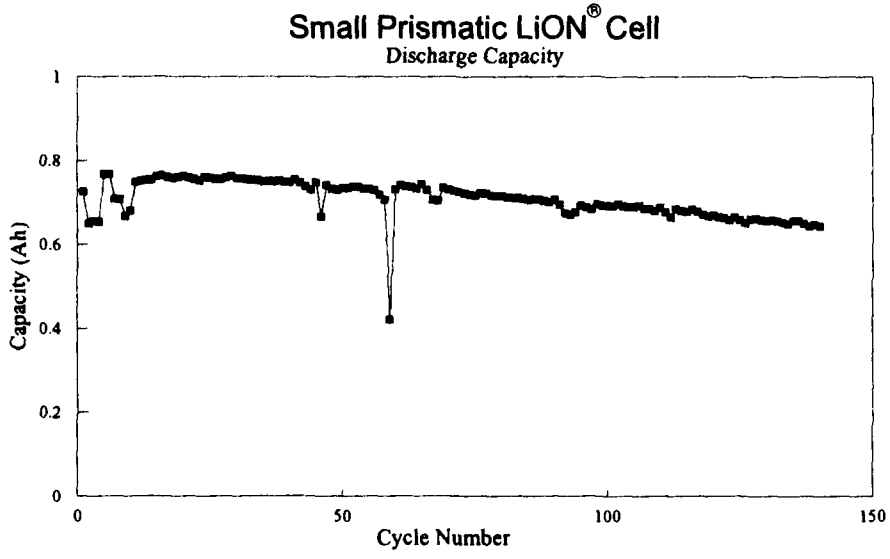

Figure 4. Nominal 0.75Ah prismatic cell; charge time is 2 hours with a taper charge; discharge is 0.25A (C/3).

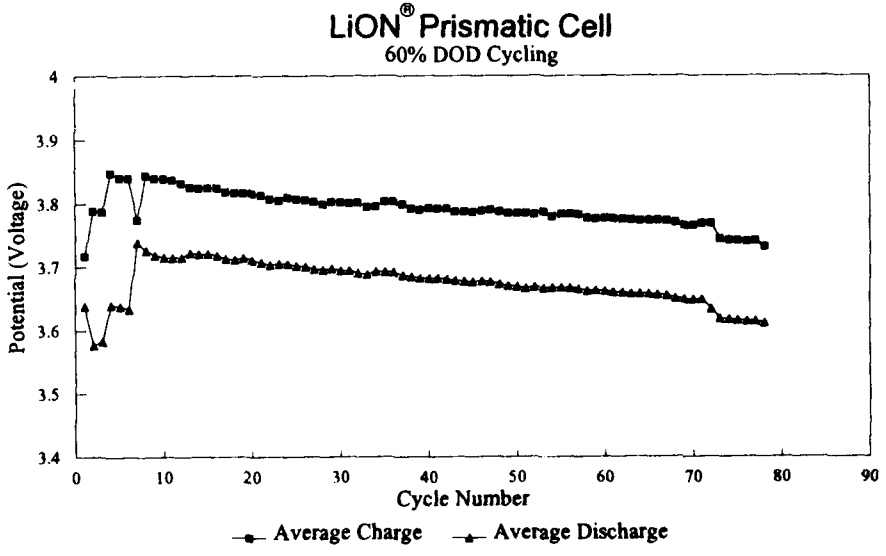

Figure 5. Prismatic cell discharged and charged to a fixed 0.27 Ah (60% DOD).

INVESTIGATIONS OF DOPING EFFECTS IN THE $LiMn_2O_4$ SPINEL SYSTEM

Jeffrey A. Read, Ralph Wise, C. C. Liang
Ultralife Batteries Inc., Newark, NY

Introduction

The $LiMn_2O_4$ spinel system has been investigated as a cathode material in the next generation of rechargeable lithium ion batteries[1]. The main advantages of the $LiMn_2O_4$ spinel system are cost, lack of toxic metals such as cobalt or nickel, and high cathode potential versus lithium[2]. The main disadvantages are low capacity and cyclability as compared to $LiCoO_2$ and $LiNiO_2$.

To investigate the possibility of improving both the capacity and cycle life of $LiMn_2O_4$ materials, the spinel system was doped with Ag and Cu in mole ratios of approximately 1% to 8% of the Mn content. The objective was to perturb the lattice structure in order to improve the electrochemical properties. Galvanostatic cycling studies were conducted to investigate the effects of doping on both capacity and cycling behavior.

Experimental

Ag and Cu doped $Li_{1.05}Mn_2O_4$ spinels were prepared from Li_2CO_3, MnO_2 , and either $AgNO_3$ or pure Cu metal. Ag was doped at a level appropriate to form $Li_{1.05}Ag_{.04}Mn_2O_4$. Cu was doped at appropriate levels to form spinels with the formulas $Li_{1.05}Cu_{2x}Mn_{2-x}O_4$ where x= .01, .02, and .08. Samples were prepared by reacting the starting materials at 800°C for 3 days, grinding the products, then annealing for 3 more days at 800°C.

Electrodes were prepared by mixing the spinel, carbon black and an Ethylene Propylene Diene Monomer (EPDM) rubber in a ratio of 92:4:4 in cyclohexane. The resulting slurries were then spin coated onto pretreated aluminium disks. Electrodes were dried at 200°C under vacuum for 12 hours, then compressed to a density of approximately 2.3 g/cc.

Electrodes with typical active weights of .01 g to .04 g were cycled at .5mA/cm^2 versus a lithium counter electrode. A lithium reference electrode was used. The electrolyte used for all cycling studies was $LiPF_6$ in EC:DMC (67:33 by weight). Cycling studies were carried out on a Schlumberger SI1280 Electrochemical Measurement Unit.

X-Ray powder patterns were recorded on a Scintag PAD-V diffractometer with CuK_α radiation. Atomic Emission spectra were recorded on a Perkin-Elmer ICP/6500.

Results

The powder x-ray diffraction patterns of the doped spinels are identical to the undoped material. The crystalinity remains high in the doped materials as indicated by the sharp powder lines. There are no extra phases observed.

Atomic emission spectra of the electrolyte solutions used for cycling studies reveal the presence of Ag^+, Cu^+, and Mn^{2+} ions. The weight of Ag^+ ion found in these electrolyte solutions is equivalent to the weight of Ag originally doped into the spinel electrodes. Typically 0.4 mg to 1.0 mg of Ag would be present in the doped electrode. After several cycles all of the silver would be found in the electrolyte. The weight of Cu^+ ion detected in the electrolyte solutions is equivelent to 1% of the weight of Cu doped into the electrodes. Typically 0.2 mg to 1.6 mg of Cu is present in the doped electrodes. The electrolyte solutions typically contain .0025 mg of Cu^+ ion after cycling. Cu^{2+} ions cannot be detected in the electrolytes at an instrument detection limit of .01 ppm. Mn^{2+} is detected in all of the electrolyte solutions but only in amounts that represent less than .1% of the Mn content in the electrodes.

The first charge / discharge cycle for $Li_{1.05}Ag_{.04}Mn_2O_4$ is shown in figure 1. The charge curve shows two distinct plateaus, one at 4.04 V and a second at 4.16 V. This behavior is similar to the undoped material shown in figure 2. The capacity on discharge is depressed in the doped material as compared to the undoped spinel. The capacity of the Ag doped spinel remains constant at 84 mAh/g upon cycling.

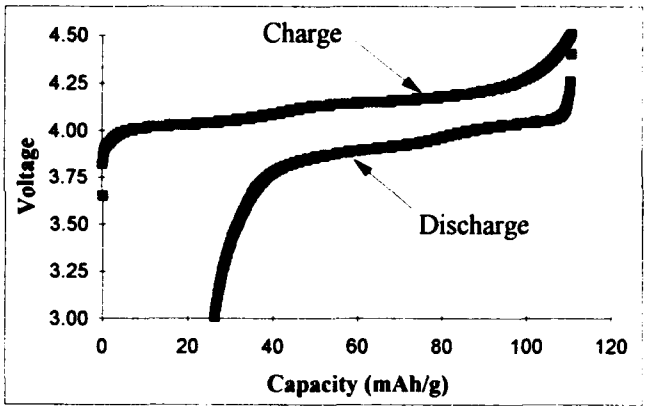

Figure 1. First charge / discharge cycle for $Li_{1.05}Ag_{.04}Mn_2O_4$.

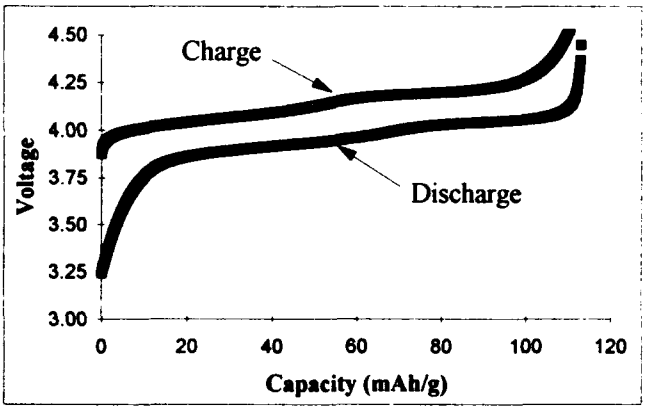

Figure 2. Charge / discharge cycle for $Li_{1.05}Mn_2O_4$.

$Li_{1.05}Ag_{.04}Mn_2O_4$ electrodes were also discharged below 3.0 V to observe the 2.7 V lithium intercalation plateau. The discharge curve is shown in figure 3. The electrode material accepts lithium ions at 2.7 V, but subsequent cycling behavior is severely damaged. The next discharge cycle shown in figure 4 gives a capacity above 3.0 V of only 32 mAh/g as compared to 84 mAh/g on the previous discharge. Figure 4 shows that the 4.0 V sites in the spinel are being lost or modified when lithium is allowed to enter the lower potential sites. The sloping of the discharge curve indicates that there is mixing of high and low potential sites in the material.

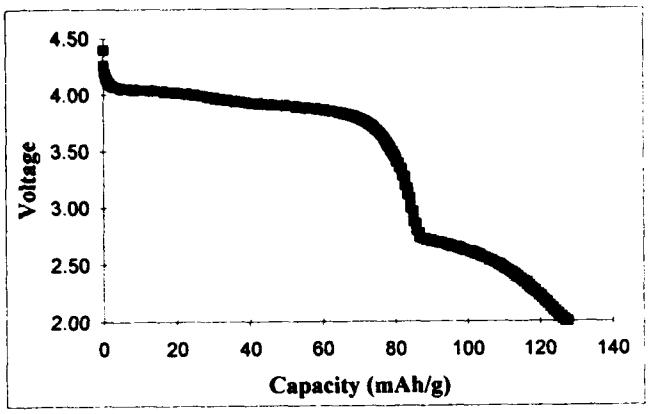

Figure 3. $Li_{1.05}Ag_{.04}Mn_2O_4$ discharge below 3.0 V.

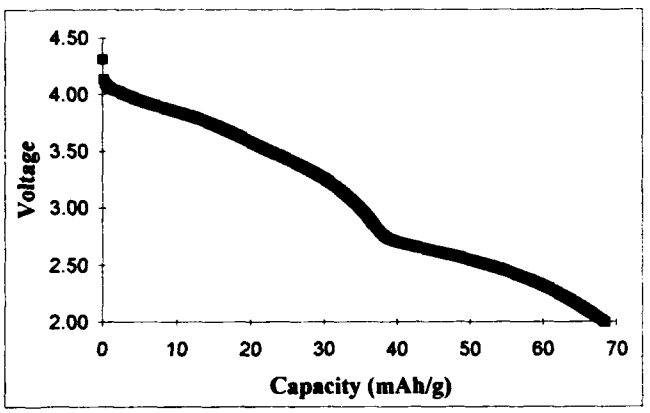

Figure 4. Discharge of $Li_{1.05}Ag_{.04}Mn_2O_4$ electrode after cycling below 3.0 V.

The first charge curves for the $Li_{1.05}Cu_{2x}Mn_{2-x}O_4$ materials with x= .01, and .08 are shown in figure 5. The x=.02 material shows the same charge and discharge curves as for the x=.08 material. The x=.01 material appears to be similar to the undoped spinel, shown in figure 2, with slightly decreased capacity. The charging curve for the x=.08 material in contrast shows a large decrease in capacity and a lack of flat plateau regions. The first discharge curves for these materials are shown in figure 6. Discharge capacity is severely depressed as the doping concentration increases. In addition, the x=.08 electrode does not show a level discharge. The Cu doped materials were discharged below 3.0 V and show capacity in the 2.7 V region.

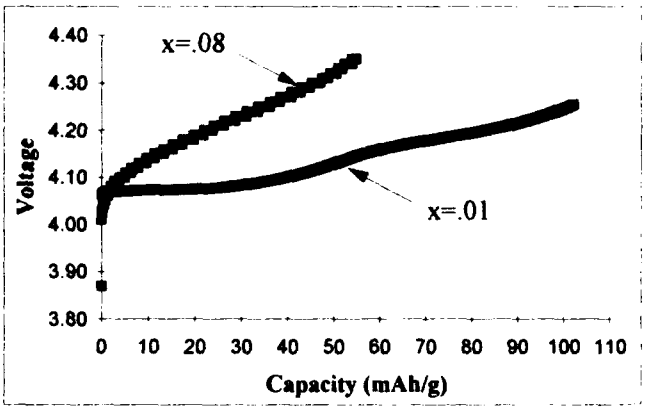

Figure 5. Charging curves for the $Li_{1.05}Cu_{2x}Mn_{2-x}O_4$ materials with x=.01 and x=.08.

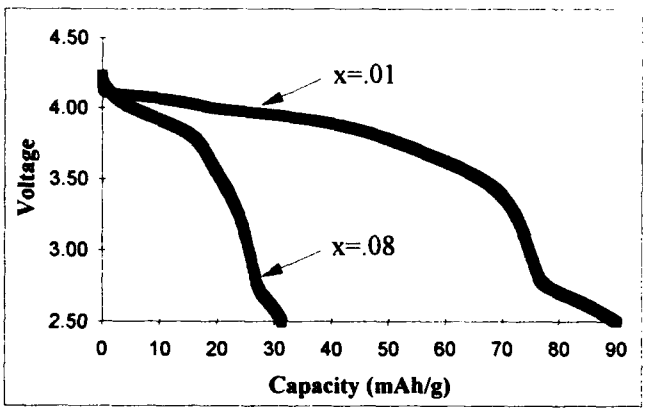

Figure 6. Discharge curves for the $Li_{1.05}Cu_{2x}Mn_{2-x}O_4$ materials with x=.01 and x=.08.

Discussion

$Li_{1.05}Ag_{.04}Mn_2O_4$ clearly looses all of its Ag in the form of Ag^+ ions upon cycling as shown by the analysis of the electrolyte. The charge and discharge curves of the Ag doped material show distinct voltage plateaus. The powder x-ray diffraction pattern is sharp, indicating a high degree of crystalinity. The cycling behavior also indicates a stable and ordered lattice structure. The doping of Ag into the lattice does not appear to disturb the normal spinel behavior. The Ag ions may simply act as a substitute for Li^+ ions in the lattice. The Ag^+ ions leave the lattice along with the Li^+ ions when the

spinel electrode is charged, and remain in solution as Li^+ ions cycle in and out of the spinel lattice.

Discharge of the $Li_{1.05}Ag_{.04}Mn_2O_4$ material below 3.0 V does result in the intercalation of Li^+ ions into 2.7 V sites. The discharge of lithium into the lattice at 2.7 V results in a decrease in capacity upon the next discharge cycle. The intercalation of lithium into these 2.7 V sites must therefore change the lattice structure, altering the structure around the 4.0 V sites and possibly creating defects in the lattice.

The Cu doped materials show a small loss of Cu^+ ions from the lattice. Approximately 1% of the Cu is lost into the electrolyte from the electrodes. No Cu^{2+} ions are observed in the electrolyte. The small loss of Cu from the doped spinel materials would indicate that most of the Cu atoms occupy sites in the spinel lattice normally occupied by Mn atoms. The small percentage of Cu^+ ions found in the electrolyte could arise either from breakdown of the lattice structure or from de-intercalation of Cu^+ ions doped into Li^+ lattice positions. These results would indicate that at least 99% of the Cu atoms doped into the spinel occupy positions normally occupied by Mn atoms. Therefore, the formula for the materials is correctly written as $Li_{1.05}Cu_{2x}Mn_{2-x}O_4$.

The charge and discharge curves for $Li_{1.05}Cu_{2x}Mn_{2-x}O_4$ with x=.01 show distinct voltage plateaus. The powder x-ray diffraction pattern is sharp, indicating a high degree of crystalinity. The cycling behavior also indicates a stable and ordered lattice structure. The doping of Cu into the lattice at this level does not appear to disturb the normal spinel behavior, and may simply act as a substitute for Mn^{+4} ions in the lattice.

The charge and discharge curves for $Li_{1.05}Cu_{2x}Mn_{2-x}O_4$ with x=.02 and x=.08 do not show flat voltage plateaus. The cycling behavior is poor. The sloping charge and discharge curves, particularly obvious in the x=.08 material, are proof the lattice is disordered. These curves also indicate, that a degree of mixing has occured between the 4.0 V and 2.7 V sites. The doping of Cu into the lattice at these levels has disturbed the normal cycling behavior. The substitution of Cu^{+2} ions into Mn^{+4} sites may have resulted in the presence of a large number of defects. A large number of defects would create an unstable lattice, resulting in poor cycling behavior.

Discharge of the $Li_{1.05}Cu_{2x}Mn_{2-x}O_4$ materials below 3.0 V does result in the intercalation of Li^+ ions into 2.7 V sites. The discharge of lithium into the lattice at 2.7 V results in a decrease in capacity upon the next discharge cycle. The intercalation of lithium into these low potential sites must change the lattice structure and alter the environment around the 4.0 V sites.

Conclusions

The doping of Ag and Cu into the $LiMn_2O_4$ materials decreased the capacity of the spinel system. The Ag atoms occupy positions in the spinel structure normally occupied by Li atoms. Ag is lost from the lattice upon charging and does not affect the cycling behavior. The Cu atoms occupy positions in the lattice normally occupied by Mn atoms. At low doping levels of Cu, the spinel cycling behavior is unaffected. At higher doping levels the capacity was greatly decreased and the cycling behavior was poor.

1. J.M. Tarascon and D. Guyomard, *Electrochemica Acta*, Vol 38, 9, 1221 (1993).

2. I. Faul and J. Knight, *Chem. and Ind.*, 24, 820 (1989).

PEM FUEL CELLS FOR PASSIVE OPERATION

Otto J. Adlhart and Peter Rohonyi
AF Sammer Corporation
Ringwood, New Jersey

Introduction

The PEM fuel cell first developed by the General Electric company for the Gemini program in the 1960's (1) has undergone substantial changes in recent years. With the availability of high performance ionexchange membranes the PEM fuel cell became suitable for a broad range of power requirements.

The new PEM cell relies on non-porous graphite structures and bipolar construction. (2) The non-porous bipolar plates have the disadvantage that product water removal has to rely on oxygen or air recirculation.

This problem was overcome by the patented PEM cell developed by the EPSI division of AF Sammer Corp. (3,4) The Sammer cell (Figure 1.) relies on an ABA construction with porous carbon collector A elements and gas-impervious sheet metal B elements for reactant separation. The porous collector facilitates mobility of product water in the cell and makes possible its eventual passive rejection from the cell stack by means of a gas/water separator.

This unique feature facilitates integration of the PEM fuel cell with a chemical hydrogen generator. The chemical hydrogen generator utilizes the fuel cell product water to react with a metal hydride forming hydrogen and hydroxides. Depending on the choice of the hydride the quantity of hydrogen formed can equal that consumed in the fuel cell, eliminating the need for disposal considerations. This is an important aspect in closed systems i.e. underwater vehicles.

Development Objectives

The key objective of the effort discussed below was the development of a rugged, reliable, cost effective and versatile hydrogen fueled PEM fuel cell suitable for operation with either oxygen or air. For the fabrication of this advanced fuel cell conventional manufacturing technology and non-exotic materials of construction were to be utilized.

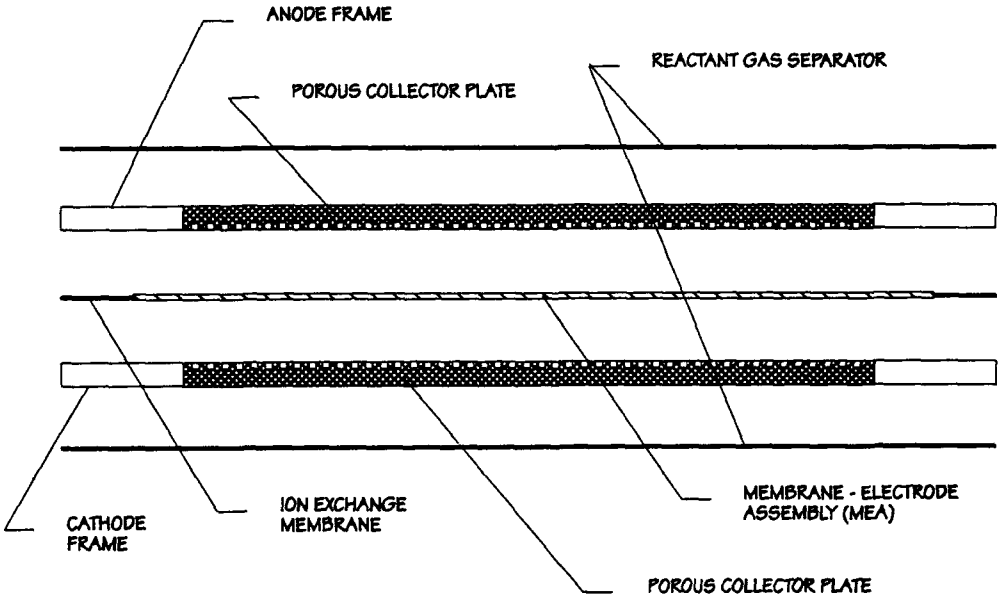

Figure 1.

AF Sammer PEM Cell Configuration

Development Results

The development effort resulted in a PEM fuel cell with salient features as detailed below:

- **Non-metallic "B" element**, consisting of impervious glassy carbon, which in addition to the cell separation function also acts as a frame, housing the "A" element.(Figure 2.)

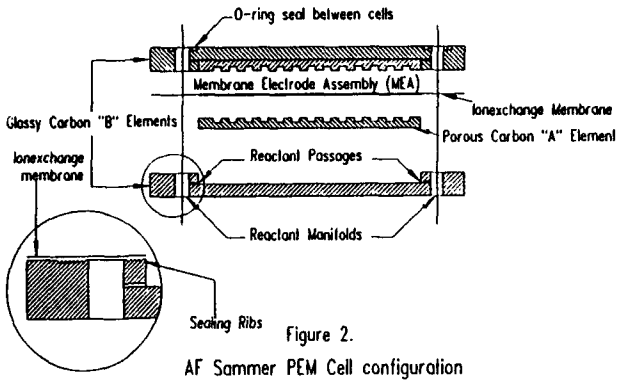

Figure 2.
AF Sammer PEM Cell configuration

- **Hydrophilic "A" element**, comprising of a porous carbon disc which permits prehumidification of the reactants by the product water. The prehumidified reactants enter the flow field at a predetermined location eliminating the risk of membrane dry out. (Figure 3.)

- **Product water** collects easily in the flow field and gravitates towards the wicking manifold port to be wicked to and rejected via a water/gas separation port from the cell stack.

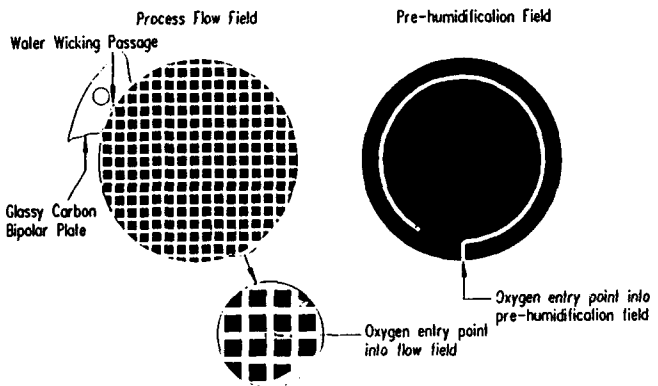

Figure 3.

Sammer Fuel Cell - Hydrophilic Carbon Collector with Reactant Prehumidification

- **The water/gas separation port,** (Figure 4.) relies on a hydrophilic microporous membrane to reject the product water to ambient or to be used in a chemical hydride hydrogen generator which is also being developed by Sammer.

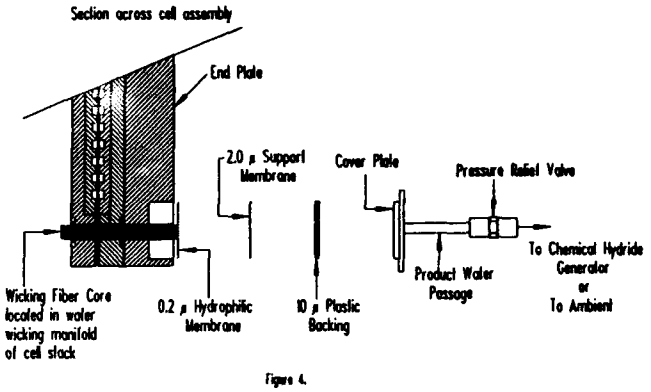

Figure 4.

Sammer Fuel Cell - Passive Water Removal Arrangements with Water/Gas Separation Port

- **Sealing** is done by commercial "Viton" O-rings of sufficient cross section to permit for manufacturing irregularities and still seal reliably.

- **Cooling** is facilitated either by designated cooling cells interspersed through the stack for internal water cooling or by an external water cooling jacket. Forced air cooling is also a viable option for lower power levels as the heat is conducted to the stack surface by the cell components.

- **Unitized individual cells** facilitate assembly and disassembly.

- **External tie and positioning rods** facilitating assembly and trouble shooting are being used.

Draper Laboratory PEM Cell

The combination of some of the above salient features have been utilized in the Sammer 20 Ampere stack under construction for Draper Laboratories. (Figure 5).

The PEM fuel cell for Draper Laboratories consists of four stacks of 36 cells each, designed to provide 115 Volts @ 20 Amps. It is to operate with an external water cooling jacket where contact between the stack and the jacket will be ensured by heat transfer grease.

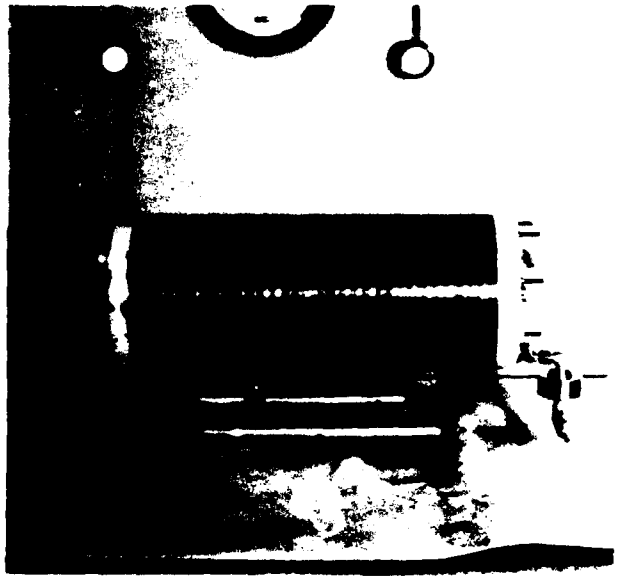

Figure 5.

The Draper Laboratories Fuel Cell

The Sammer 150 Ampere Stack

The 150 Ampere PEM fuel cell is the building element for the development of 2 and 5 kw water cooled stack modules (Figure 6.). These modules will be integrated into fully automated hydrogen/oxygen power plants. As the Draper cell it relies on a circular cell configuration. The active area of this cell is 300 cm^2.

External tie and positioning rods are utilized. This feature together with the unitized cell construction facilitates the removal or exchange of individual cells.

References

1. NASA JSC Report Number TTA E063-67-1, 1967

2. U.S. 4,175,165 Fuel cell system utilizing ion exchange membrane with bipolar plates. Assigned to Engelhard Corp. July 1977

3. U.S. 4,826,741 "Proton Exchange Membrane Fuel Cell With Improved Water and Thermal Management", Assigned to EPSI May 2, 1989

4. "An Assessment of the Air-Breathing Hydrogen-fueled SPE Fuel Cell". Proceedings of the 28th Power Sources Symposium, pp. 29-32, June 1978.

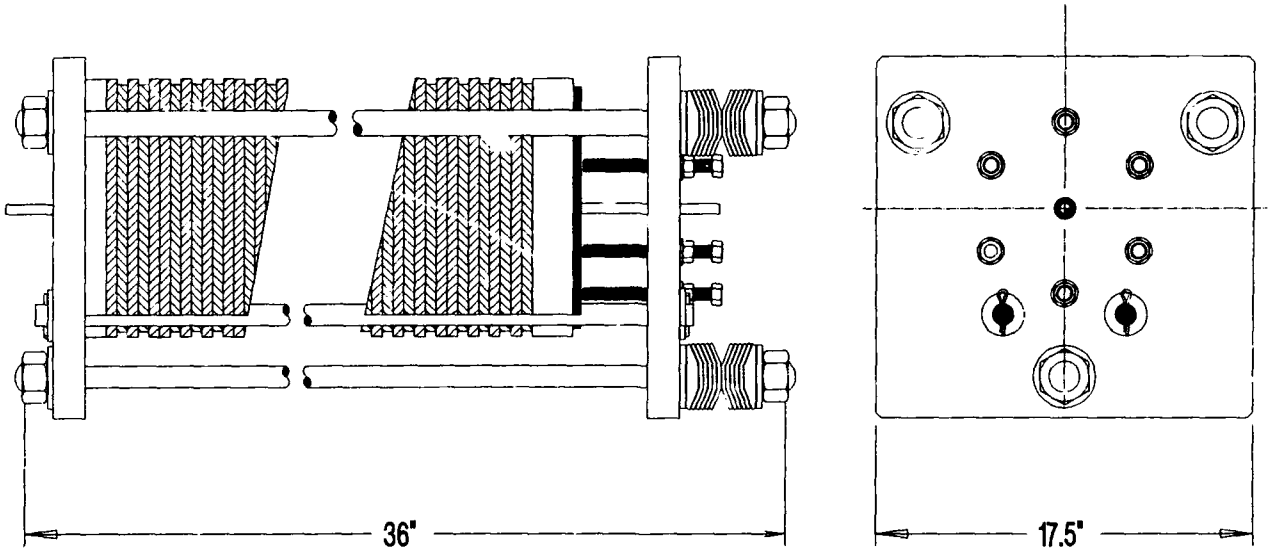

Figure 6.

Sammer 2 kw PEM fuel cell

NOTES

Heat Removal in Ambient Pressure PEM Cell Stacks

V. Marshall, J. Kelland, P. Grosjean, D. Bloomfield
Analytic Power Corp., Boston, MA

Introduction

In recent years PEM fuel cell technology has evolved to the point where compact, lightweight stacks are practical in the range of 25 to 500 watts. Extended operation however requires proper heat and water management in the fuel cell. The vapor pressure characteristics of water and the hydrophilic nature of the ion exchange membranes intimately link the heat and water balance of these cells. Coupling also occurs between the cell performance and the heat and water management. This paper concentrates on the heat removal requirements of these cells and the consequences of inadequate thermal management. We also identify the limitations of free convection and detail the benefits of forced convection cooling for PEM cells. While testing was conducted on stacks in the range of 25 to 250 watts, the concepts discussed are applicable to higher power levels and power densities.

Thermal & Water Management Model

A model of the stack cathode with an integral cooler is shown in Figure 1. The stacks run dead-ended on pure H_2, so, to simplify the model we chose to neglect any mass transfer to or from the anode.

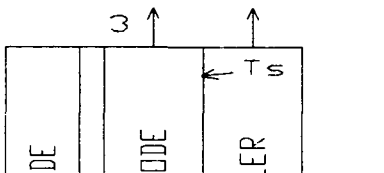

Figure 1 - Ambient Cell Model

Flow in the cathode and coolant cavities is co-current and air is assumed to be at 70°F, 40% r.h. and 1 atm. Our model balances the water exiting the cathode at (3) with that entering with the reactant air at (1) plus the amount produced in the cell at (2). We assume that all of the water leaves the cathode as vapor and that the relative humidity there is 100%. The temperature at the cathode exit is then calculated using steam tables and the mole fraction of water at the exit. This exit temperature represents steady state equilibrium of water into and out of the cathode of the cell. We refer to this as the cell equilibrium temperature.

If there is good thermal conductivity between the cathode and cooler cavities then the cathode exit temperature will tend to follow the cooler exit temperature (T_s). The equilibrium temperature at the cathode therefore determines the maximum temperature differential available for convective heat transfer. The heat flux from the cell reaction depends on the cell performance and is calculated by:

$$Q_c = 3.413 * J * (E_o / V_c - 1) \quad (Btu/hr\text{-}ft^2)$$

Where J is the current density (A/ft^2), E_o is the open circuit cell potential, and V_c is the cell operating voltage at J. External heat loss from the outside of the stack is neglected and heat transfer is assumed to occur only as convection to the coolant air. The required convective heat transfer coefficient is calculated by:

$$h_c = Q_c / (T_s - T_{amb}) \quad (Btu/hr\text{-}ft^2\text{-}°F)$$

For modeling purposes we used the performance curve shown in Figure 2 and assumed that it remained constant. This performance is an average of several 122 cm^2 cells in a stack cooled by forced convection. The cell performance will of course change during operation but, our approach is conservative in that the performance used for the model corresponds to a maximum performance level and therefore a lower heat flux. The heat transfer coefficients calculated in this manner are therefore minimum allowable values given the assumptions made.

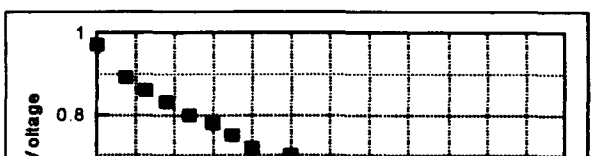

Figure 2 - Cell Performance

The cathode stoichiometric oxygen flow at (1) is:

$$M_{O2} = 2.056E\text{-}5 * V_c * J \quad (lb\text{-}mol/hr\text{-}ft^2)$$

with an oxygen utilization UO, the cathode dry inlet air flow is:

$$M_{cath} = (M_{O2} * 4.76) / UO * 28.97 \quad (lb/hr\text{-}ft^2)$$

The cooling flow of air to remove the heat of the cell per unit of cell area is given by:

$$M_{cool} = Q_c / (C_p * (T_{exit} - T_{amb})) \quad (lb/hr\text{-}ft^2)$$

Effects of Reactant Flow on Cooling Requirements

Using the model outlined above, heat transfer coefficients were calculated as a function of cell operating voltage for constant oxygen utilizations of 20,40, and 60%. At this point the mode of cooling is completely arbitrary, we are simply identifying minimum heat transfer requirements for the assumed performance level. The results are shown in Figure 3 along with the corresponding cathode exit equilibrium temperatures for each case.

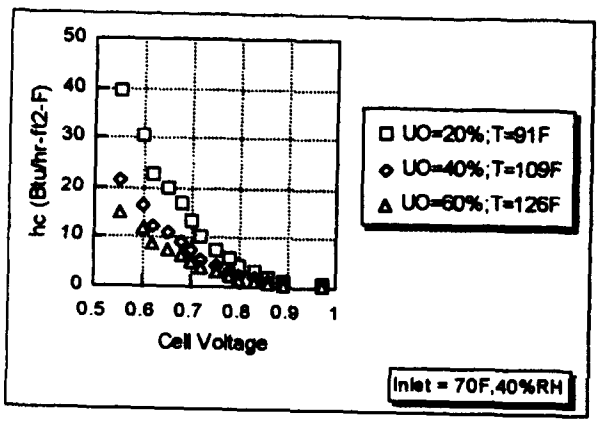

Figure 3 - Minimum Heat Transfer Coefficients

The effect of cathode reactant flow is twofold. Since the cathode reactant comes in at less than 100% r.h., higher flows (lower utilizations) carry more water out of the cell. In order for the system to balance the water and keep the cell from drying out at higher flow rates, the cathode exit temperature must be kept lower than if the flow rate was small. This lower temperature differential requires a much higher heat transfer coefficient to remove waste heat than the same cell operating at the same level but at a higher utilization. In other words, two identical cells operating at the same level and generating the same quantity of heat, can have significantly different heat transfer requirements simply because of differences in their cathode flow rates. The graph shows that, from a heat transfer point of view, it is advantageous to be able to operate the cathode at high utilizations.

In designing air-cooled stacks it is important to know the ratio of air used for cooling and that used for cell reaction. We define a flow ratio R_f which is simply the amount of cooling air divided by the amount of reactant air required at equilibrium conditions. An interesting result of our model is shown in Figure 4. This is a plot of the flow ratios as a function of cell voltage for three constant reactant flows (as opposed to constant utilizations). Note that the ratio is independent of the cathode flow and is a direct function of the cell voltage. It is also significant that the smallest ratio is about 10 at .9 volts/cell. This means that even at low heat fluxes you still need about 10 times the reactant flow just to cool the cell.

Since volumetric flows are generally determined by pressure drop and geometry, it is theoretically possible to design the geometry of the cooling and reactant channels around a specific cell voltage. The problem here is that this curve represents *equilibrium* conditions - operating the cell below the curve would result in too little cooling flow (overheat) while operation above the curve would result in flooding. To complicate things even further, the curve is continually shifting up and down itself as the cell performance changes.

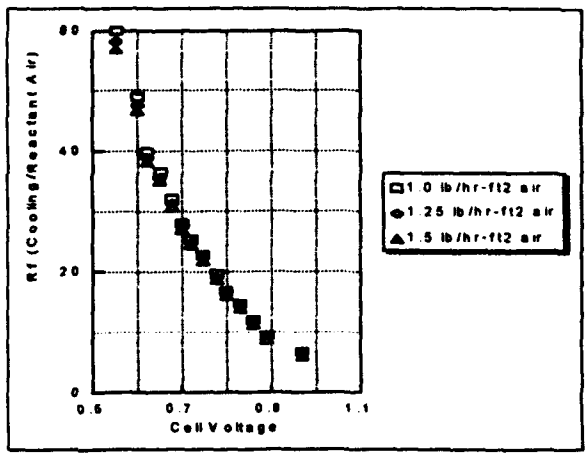

Figure 4 - Cooling/Reactant Ratios

Limitations of free convection

Table 1 shows typical accepted heat transfer coefficients for various conditions. The model we have presented suggests that the minimum operating voltage a cell cooled by free convection should be about .8 volts since this is where the minimum heat transfer coefficients exceed 5 Btu/hr-ft^2-°F. A more detailed analysis of the heat transfer coefficient in terms of the geometry of the stack and the available temperature differentials however, results in even lower values.

Table 1[1]
Convective Heat Transfer Coefficients

Condition	h (Btu/hr-ft^2-°F)
Air, free convection	1-5
Air, forced convection	5-50
Oil, forced convection	10-300
Water, forced convection	50-2,000

For simple vertical plates in air at standard conditions, the following approximation for the heat transfer coefficient can be used[1]:

$$h_c = 0.28 * [(\Delta T)/L]^{1/4} \qquad (\text{Btu/hr-ft}^2\text{-°F})$$

For a 4" high plate at 160°F, h_c is about 1.1 Btu/hr-ft^2-°F. Since the cooler cavities are integral with the cell stack, we can consider them instead as two parallel vertical plates with a height L and spaced some distance b (ft) apart. To dissipate the maximum amount of heat with a diatomic gas, Kreith[2] gives the following approximation for the optimum spacing:

$$b_{opt} = 2.9 * (L^{1/4} * u_s^{1/2} * T^{1/4}) / (g^{1/4} * d_s^{1/2} * (T_s - T)^{1/4})$$

Where L is the plate height (ft), T is the mean gas temperature (°R), T_s is the surface temperature of the plate (°R), u_s is the gas viscosity (lb_m/ft-sec) at T_s, d_s is the gas density (lb_m/ft^3) at T_s, and g is 32.2 ft/sec^2. The maximum heat transfer coefficient can then be calculated by:

$$h_c = k_s / b_{opt} * Nu_b \qquad (\text{Btu/hr-ft}^2\text{-°F})$$

Where k_s is the thermal conductivity of the gas at T_s

and Nu_b is the average Nusselt number calculated for *b*. Both equations give similar numbers for h_c.

Nusselt numbers which represent maximum heat transfer rates per unit area are given in Figure 5.

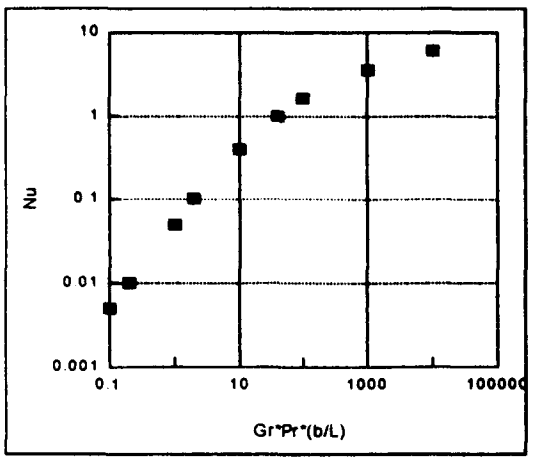

Figure 5 - Nusselt Numbers for Free Convection

Based on this data, a series of curves were generated (Figure 6) which show the maximum heat transfer coefficient as a function of the flow length (plate height L) for plate surface temperatures of 100, 130, and 160°F. Again we assumed an ambient air temperature of 70°F. Note that heat transfer coefficients greater than 2 only appear for extremely short flow lengths. For flow lengths of 1-10 in, which would correspond to the cathode path length for stacks in the 25 - 500 watt power range, the coefficient is limited to between 1 and 2. It is also significant that there is little gain in heat transfer between plates at 100°F and those at 160°F. This is important since it precludes the use of high ΔT's to significantly enhance heat transfer.

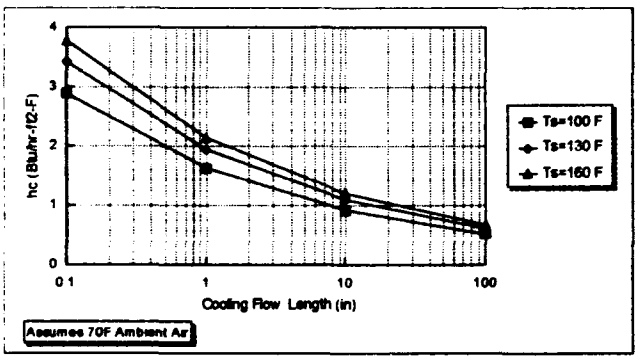

Figure 6 - Maximum Theoretical Heat Transfer Coefficients

By matching the theoretical coefficients in Figure 6 with the required coefficients of Figure 3 we see that the lowest design cell voltage for free convection would be limited to values above .90 volts/cell. While operation at this point may be very efficient, at best the power density is only about 16 W/ft^2, making it impractical for most applications.

Single Cell 1 Atm Testing

While it is obvious that excessive overheating of an ambient pressure PEM cell will eventually result in dry out of the membrane, we were interested in the rate at which this might occur and whether the effect could be reversed if the cell were operating on dry H_2 and air. To examine these effects we ran a single 40 cm^2 cell in test hardware which consisted of carbon fiber flowfields sandwiched between 1/2" water cooled plates. The results of the tests are shown in Figures 7 & 8.

The cell's performance was surprisingly high for 1 atm operation on dry gases -- it operated steadily at about .5 volts and 430 A/ft^2 and showed a limiting current density of about 900 A/ft^2. The cell maintained this level until about 160 minutes into testing when the cell temperature was deliberately increased to 155 °F over the next 40 minutes. The effect on performance was significant. The cell resistance climbed from 4.5 milliohms to 687 milliohms and the limiting current density fell to just 23 A/ft^2. After operating the cell at this condition for several minutes it was then cooled down to 110°F in 25 minutes while being operated at limiting current density. In this time the cell resistance fell and the limiting current rose steadily. When the temperature fell back to 110°F the load on the cell was adjusted so that the cell voltage was again at .5 volts. The current density here was now about 370 A/ft^2. This is about 86% of its initial performance level.

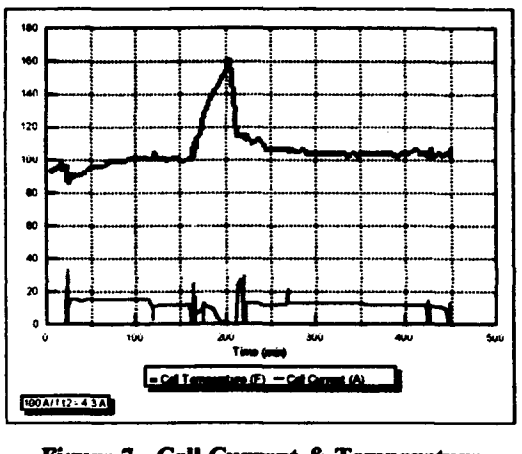

Figure 7 - Cell Current & Temperature

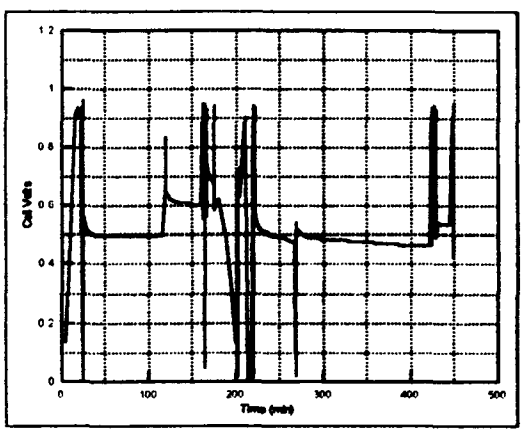

Figure 8 - Cell Voltage

The difference in the performance levels might be explained by the hysterisis which Nafion exhibits when dried at high temperatures and subsequently re-hydrated. This test not only shows the importance of heat removal in regards to cell performance, but it also implies that cells which have been dried out may regain much,

if not all, of their initial performance level once proper heat transfer is re-instituted.

Results of stack testing

Figures 9 and 10 show the relative performance of a 25 cell free convection stack and an 18 cell forced convection stack. Both stacks are comprised of identical cells with active areas of about 18.9 in^2. The free convection stack has no separate coolers so all of the cooling air must flow past the cathode of the cell. The forced convection stack on the other hand has separate cooler elements which effectively split the cooling and reactant air. It is clear that the forced convection stack achieves higher performance – especially around .7 volts/cell.

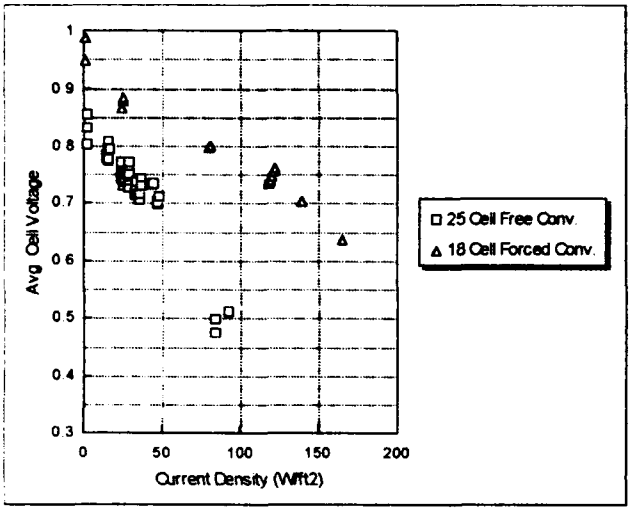

Figure 9 - Cell Voltage vs. Current Density

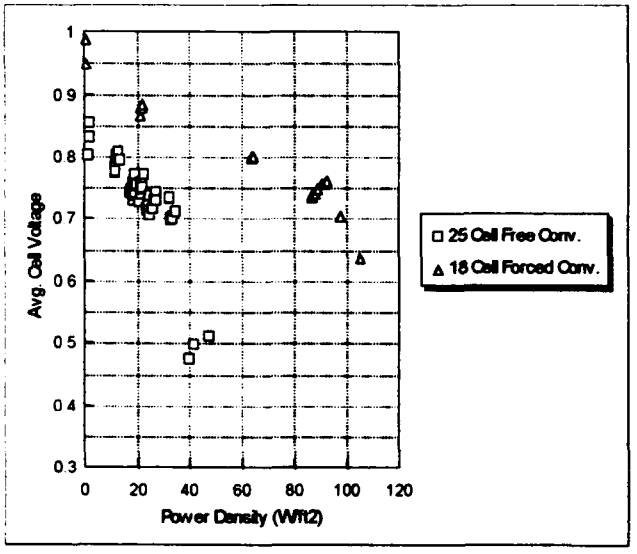

Figure 10 - Cell Voltage vs. Power Density

As Figure 10 shows, forced convection effectively triples the power density of ambient PEM cells. The data of the free convection stack show higher power densities than predicted by our model but, these operating conditions are not steady state. The forced convection data are, on the other hand, very nearly steady state as these stacks have demonstrated continuous operation for several hours.

Conclusions

To date most research and modeling of PEM cells has concentrated on pressurized operation. The problems of thermal and water management in these cells is well documented. The ambient pressure stack appears, on the outside, to be a lower power density, simplified version of these pressurized units. The reality is that ambient pressure stacks represent the extreme of the thermal and water management problem. The low operating pressure makes these cells sensitive to utilization and allows significantly higher mole fractions of water than are possible in pressurized stacks. The low power density compounds the problem by limiting the amount of water being added to the gas stream. The result is a unit which is super-sensitive to reactant and coolant flows, yet as our tests have shown can operate steady state at moderate power densities if properly controlled.

The results of testing of both free and forced convection cooled, ambient pressure stacks have shown that free convection is impractical for design cell voltages below .8 volt/cell. Operation of stacks at lower cell voltages (higher power densities) results in overheating and dry-out of the membrane with a corresponding loss of performance. Forced convection stacks with identical anode and cathode structures but with separate integral coolers have shown continuous operation at power densities of 90 W/ft^2 and voltages of .7 volts/cell. Although these stacks have an additional structural element which increases their size and weight, the higher power density results in an overall reduction in the specific weight, volume, and cost. The penalty in parasite power is about 1% of the gross power.

Modeling of the heat and mass transfer, as well as the geometry of the cathode of ambient pressure stacks has shown that the limiting factor in the power density of stacks cooled by free convection is the low overall heat transfer coefficients. For continuous operation of free convection stacks cell voltages should be kept around .9 volts/cell. Heat transfer coefficients for forced convection in the temperature range of interest will probably not exceed 10 $Btu/hr\text{-}ft^2\text{-}^oF$. This will allow forced convection to handle the heat transfer requirements of cells down to operating voltages of .6 volts/cell based on present performance. However, power densities in excess of about 110 W/ft^2 will have to be achieved through increases in cell performance for forced convection air to remain effective.

References

(1) Marks' Standard Handbook for Mechanical Engineers; 8th ed.

(2) Kreith, F. (1966); Principles of Heat Transfer

COST REDUCTION AND PERFORMANCE IMPROVEMENTS IN PEM FUEL CELLS

J. P. Maceda
H. Power Co.
Belleville, NJ

Paper not received in time for publication

Paper not received in time for publication

Paper not received in time for publication

Paper not received in time for publication

Paper not received in time for publication

Paper not received in time for publication

TREATMENT OF PERFLUORINATED ION-EXCHANGE MEMBRANES (NAFION®) TO INCREASE WATER ABSORPTION AND IONIC CONDUCTIVITY.

Shoibal Banerjee
DuPont Company, Wilmington, DE

Introduction

The need for development of higher performance membranes becomes clear from the following considerations. The polarization curve of a fuel cell plots voltage vs. current density and defines power output. A typical polarization curve has three distinct regions. At low current density, ohmic losses are small, and polarization at the cathode controls the cell potential. As the current density increases, ohmic loses grow and the curve becomes roughly linear, in this region the slope is inversly proportional to the electrical conductivity. The proton conductivity of the polymer electrolyte membrane contributes significantly to the overall electrical conductivity of the PEM fuel cell assembly. Further increase of current density causes an even sharper drop in the polarization curve caused by reactant mass transfer limitations.

The intermediate region of the polarization curve is where the power output of the cell is normally useful for practical applications. The conductivity of the membrane controls the slope in this region, and it depends mainly on two interrelated factors. In the low current density region, conductivity depends upon inherent membrane properties such as total water content or degree of hydration for a given thickness. As the current density is increased, more water is dragged from the anode (electro-osmotic drag) and a concentration gradient builds up to counteract the electro-osmotic drag, thus increasing the resistance of the membrane to proton conduction. One key to developing higher performance fuel cells is to develop PEMs that have inherently higher degree of hydration provide (improved conductivity) and for improved water management.

In our laboratory we have discovered that irradiating Nafion® polymers with electron beam causes significant change in the structure of the polymer which results in increased water absorption and conductivity without sacrificing mechanical strength. The results of this work are presented in this paper.

Experiments & Results

Infrared Studies

Two forms of the Nafion® polymer , the sulfonyl fluoride form and the sulfonate salt (potassium) form were irradiated under vacuum at four different dosage levels (1,3,5 and 9 mega rad). FTIR spectra of the sulfonyl fluoride form of Nafion® as a function of irradiation dosage were obtained. The spectrum of the un-irradiated sample (control) was subtracted from the spectrum of the irradiated samples. The resulting spectra shows that two carbonyl bands at 1778 cm^{-1} and 1811 cm^{-1} grows with increasing radiation dosage. These bands are assigned as dimeric acid type C=O at 1778cm^{-1} and monomeric acid type C=O at 1811cm^{-1}.

In order to determine whether the electron beam is affecting the sulfonyl fluoride group on the side chain or the perfluorinated back bone we carried out a semi-quantitative analysis of the infrared bands. We determined the integrated area of the 1778 cm^{-1} band normalized it to the area of the 2359 cm^{-1} band which is an over tone of the C-F bending mode and has been used as the internal standard. Similarly the area of the sulfonyl fluoride side group band at 2703 cm^{-1} was also normalized. Figure 1 shows the plot of

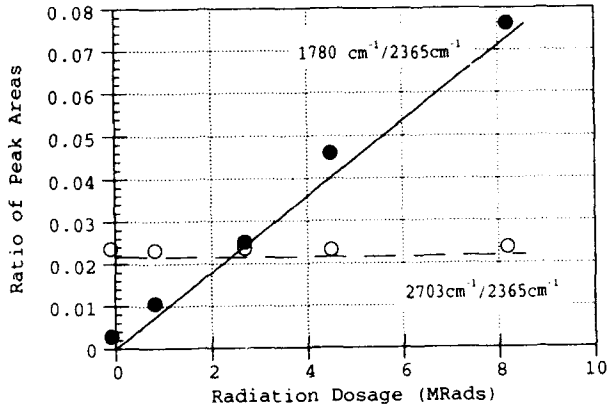

Figure 1

these normalized areas as function of radiation dosage, here we see that the 1778 cm^{-1} band is growing almost linearly with the dosage whereas the sulfonyl fluoride band does not change with radiation dosage. This indicates that the sulfonyl fluoride group remains relatively unaffected by the radiation where as the C=O functional groups are probably forming on the fluorocarbon backbone.

The irradiated samples were hydrolyzed and the FTIR spectra of the irradiated and hydrolyzed membranes were obtained In Figure 4 we see that the 1811 cm^{-1} band has disappeared and in addition to the 1778 cm^{-1} band two other bands have appeared at 1692 cm^{-1} and 1628 cm^{-1}. The new bands are assigned as carboxylic salt C=O at 1692 cm^{-1} and water at 1628 cm^{-1} A semi-quantitative analysis similar to Figure 1 was done on these spectra and the results are displayed in Figure 2, here we see that both the amount of the carboxylate C=O formed as evidenced by the growth of the 1692 cm^{-1} band

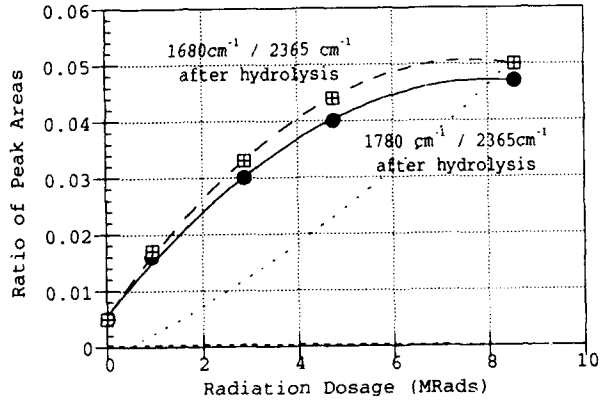

Figure 2

and the carboxylic acid type C=O at 1778 cm^{-1} increase with the radiation dosage. The carboxylate C=O is primarily formed by conversion of the monomeric acid type C=O at 1811cm^{-1} , and may be a reactive species is formed which gets converted to the carboxylate salt when the samples are hydrolyzed.

Irradiation of the sulfonate form of Nafion®

FTIR spectra of the sulfonate (K^+) form of the polymer irradiated at different dosage levels were also obtained. The results show the growth of the 1778 cm^{-1} band (the dimeric acid type C=O), but unlike the sulfonyl fluoride form there is no appearance of the monomeric acid type C=O band at 1811 cm^{-1} . Figure 3 shows a plot of the normalized band (1778 cm^{-1}) area versus irradiation dosage, the data shows that although the

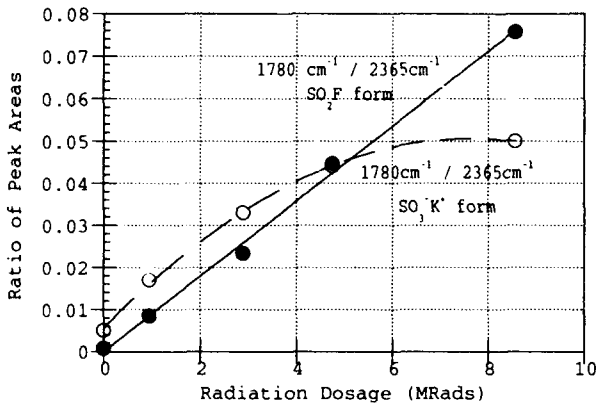

Figure 3

area grows with irradiation, it levels out beyond 4.5 Mrads, unlike the sulfonyl fluoride form.

To determine if the acid type C=O species in the irradiated polymer is reactive, we re-hydrolyzed the irradiated films. FTIR spectra of the irradiated, re-hydrolyzed membranes were obtained, and the spectra shows that unlike the sulfonyl fluoride form the 1778 cm^{-1} band has completely disappeared and two new bands at 1692 cm^{-1} and 1628 cm^{-1} have appeared, as before these bands are assigned to carboxylate type C=O and water respectively.

To determine whether nonvolatile low molecular products were formed in the polymer films due to irradiation, Soxhelt extraction of the irradiated membranes were carried out. FTIR analysis of both the extracted films and the extract did not show any significant formation of non-volatile low molecular products.

Water Absorption

Figures 4 and 5 show the water absorption of the irradiated films as a function of the radiation dosage.

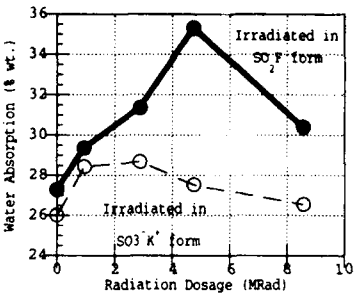

Figure 4

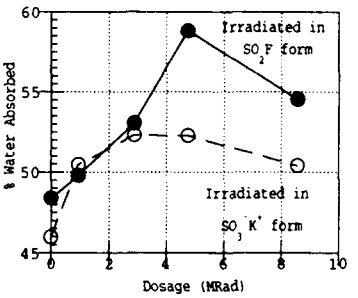

Figure 5

In Figure 4 both sets of films are in the potassium salt form and in Figure 5 they are in the acid form. These data show that firstly, the water absorption increases on irradiating the Nafion® membranes, secondly the increase in water absorption for the membranes that were irradiated in the sulfonyl form is significantly higher than the films that were irradiated in the potassium salt form at all levels of radiation dosage, and finally there is a maximum in water absorption around 4 mega rads dosage for both forms of the membranes.

A possible explanation for the higher water absorption of the XR films that were irradiated in the sulfonyl fluoride form may be the presence of the carboxylate C=O species at 1692 cm^{-1} which is ionic and would absorb more water. We tested this speculation by measuring the water absorption of the XR films that were irradiated in the

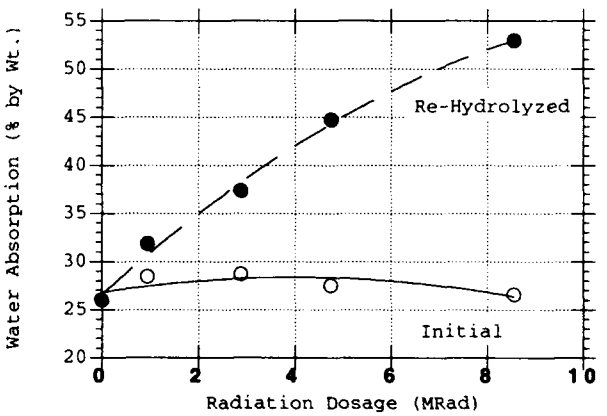

Figure 6

potassium salt form and then re-hydrolyzed because these films have the similar carboxylate C=O (1692 cm^{-1}) species. The water absorption data is shown Figure 6. Here it can be seen that the water absorption of the re-hydrolyzed film is significantly higher than the original films at all levels of radiation dosage.

Tensile Properties

The tensile properties were measured in the sulfonic acid form of both the films. The films were dried overnight at 100 degC.

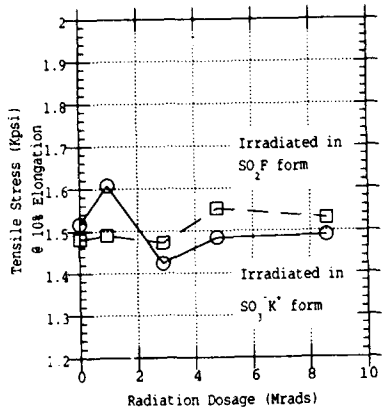

Figure 7

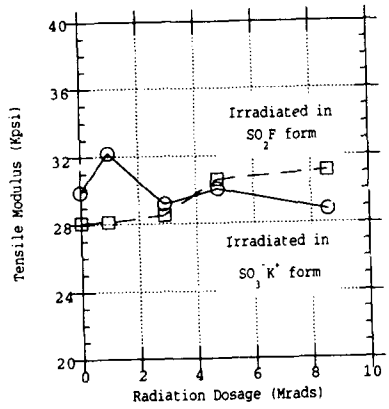

Figure 8

The tensile modulus and the tensile stress at 10% elongation as a function of radiation dosage are displayed in Figures 7 and 8 respectively. From the plots it is seen that at these levels of irradiation none of these properties are significantly altered.

Ionic Conductivity

Ionic conductivity of electron beam irradiated membranes were determined by dielectric analysis. The polymers used in this case was our standard commercial N115 membranes. The membranes were conditioned at 50% relative humidity (RH) for one week and the measurements were done in controled environment to maintain the RH conditions.

Figure 9 shows the variation of conductivity with temperature for membranes irradiated 0, 1, 5, 10 and 20 Mrads we see that the conductivity increases significantly as the radition dosage is increased. The increase in conductivity is maximum at 10Mrad dose where it about two orders of magnitude higher than the (unirradiated) control sample.

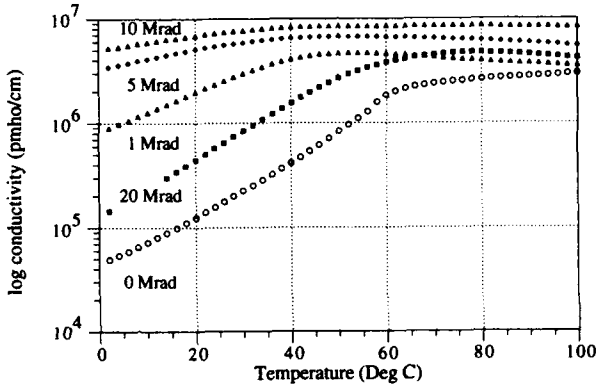

Figure 9

Conclusion

Electron beam irradiation treatment of perfluorosulfonic acid membranes generates ionic groups in the polymer structure. These ionic groups are responsible for increased water absorption and conductivity of the membranes.

NOTES

Recent Advances in Direct Oxidation Fuel-Cell Technology

S. Surampudi, H. Frank, S. Narayanan, and G. Halpert
Jet Propulsion Laboratory
and
C. Cropley, J. Kosek, and A. Laconti
Giner, Inc.

ABSTRACT

Development of fuel cells that can operate directly on fuel such as methanol and hydrocarbons has been pursued since the 1950s. Several synthetic fuels such as hydrocarbons, alcohols, aldehydes, glycols, and hydrazine have been considered for direct-fuel cell applications. Among these fuels, methanol has received most attention in view of its widespread availability. Prior to 1990, the existing DMFCs exhibited limited performance, i.e., low operating voltages (less than 0.3 V) at low rates (less than 30 mA/cm^2). This performance level is far short of the power density required to compete with batteries. Recently, there has been a breakthrough in the development of DMFC technology at JPL in collaboration with Giner, Inc. and USC. This breakthrough involved demonstration of an output of 300 mA/cm^2 at 0.5 V at 90°C which is 20× higher than that reported to date.

DIRECT METHANOL FUEL CELL STACK DEVELOPMENT

Donald L. Maricle, Brian L. Murach, Leslie L. Van Dine
International Fuel Cells, South Windsor, Ct

Introduction

The ARPA Low Temperature Direct Oxidation Fuel Cell Program has the objective of advancing direct oxidation fuel cells to the stack demonstration level. IFC as a commercial fuel cell manufacturer performs two major functions in the ARPA program: 1) Identify potential DOD applications for direct oxidation fuel cells, and set cell performance goals that would meet the application's power requirements in a fully learned-out power module. 2) Demonstrate direct oxidation advances accomplished on this program, in a low temperature, full area, fuel cell stack.

Applications were identified through site visits, literature searches and calls to appropriate DOD agencies. This paper focuses on the person-portable micro climate cooling application. Methanol fuel was assumed, since logistic fuels are presently beyond the capability of low temperature fuel cells. A polymer electrolyte membrane (PEM) fuel cell was selected for both the application studies and a stack demonstration. PEM is the only developed near room temperature fuel cell compatible with carbon containing fuels.

The major technical problems limiting the application of direct methanol fuel cells are well recognized: Slow oxidation kinetics resulting from the accumulation of by-product anode poisons on the catalyst is the most severe limitation. Cross diffusion of the water miscible methanol from the anode to the cathode is the second. The latter causes mixed potential reduction in the cathode performance, loss of fuel (low Faradaic efficiency), and excess thermal load in the stack.

Conceptual systems have been identified for both MeOH/O_2 and MeOH/air power modules. A 2 cell full-area stack has been run to assess the present status of direct methanol technology against the goals established by the system study.

System Analysis and Performance Goals

A simple, light weight MeOH/air system is illustrated in Figure 1. It assumes: the fuel is fed as a liquid to anode flow field of the stack (liquid feed); water is recovered to supply the required water to the anode; ambient pressure operation; no air saturation is required due to the flow of liquid water/methanol by the anode; the stack voltage is 12V DC; the methanol crossover was allocated to be equivalent to 50 ASF of electrochemical consumption.

This system offers several advantages. The use of a single condenser to recover water *and* methanol from both the anode and cathode exhaust divorces the system methanol loss rate (due to saturation of spent air and product CO_2 exhaust streams with water/methanol), from the stack operating temperature. The use of dry air provides evaporative cooling, and eliminates the need for cooling capability in the anode recycle loop, but limits the stack operating temperature to 170°F.

A thermodynamic analysis of this system was used to determine the fuel cell performance needed to meet the application requirements of: 250 watts, 1000 watt hours, 11 pounds total system weight including stack, accessories, and fuel. Figure 2 shows the stack, accessories, fuel, and total weight based on 0.6 V/cell (and the above assumptions) as a function of current density at which the 0.6 V/cell is achieved. This analysis indicates that the 11 pound weight goal can be met for a 250 watt 1000 watt hour direct methanol power module if an electrochemical performance of 0.6V at 220 ASF can be achieved by an ambient pressure MeOH/air cell with no more than 50 ASF equivalent methanol crossover.

The voltage sensitivity of the total system weight is displayed in Figure 3. For example the goal can also be met by 0.7V at 170 ASF, or 0.57V at 250 ASF. Similarly a performance of 0.5V at 250 ASF misses the weight goal by 1.4 pounds.

Results of cell and stack testing conducted on the ARPA program has indicated that meeting the 50 ASF equivalent methanol crossover allocation is challenging. Figure 4 illustrates the weight penalty that would be accrued by increasing the crossover up to 200 ASF, assuming all the crossover methanol is lost by oxidation to CO_2 on the Pt black cathode catalyst. This increase in total system weight is a consequence of the extra methanol fuel that must be carried to compensate for the low Faradaic efficiency. A significant advantage of the system analyzed here is that most of the methanol not oxidized to CO_2 as it passes through the cathode is recovered and recycled to the anode. Development of an O_2 reduction catalyst not capable of oxidizing methanol would completely solve the crossover problem when used in the system described here.

The methanol air system has a potential liability for battlefield applications. Chemical warfare agents may poison the air cathode, requiring an air clean up system not considered in the above analysis. One solution to this is a MeOH/O_2 power module. This trades the weight of the oxygen and extra tankage against the weight of an air clean up system.

Figure 5 Illustrates the simple MeOH/O_2 system analyzed to establish performance goals. The assumptions are similar to the air system except that 45 psia operating pressure is assumed, and without N_2 associated water loss on the cathode side, a 220°F stack operating temperature can be achieved to promote the slow methanol oxidation kinetics.

Figure 5 shows two condensers and cooling fans. In reality one fan and a condenser with two parallel sections would be used. A cathode vent is required to eliminate the CO_2 produced by the crossover methanol. A cathode recycle is required to allow a high CO_2 level on the cathode to minimize the O_2 lost from the cathode vent. Both liquid and vapor water rejection is required since the gases venting at the condenser exit temperature do not eliminate all the product water.

Figure 6 illustrates the weight breakdown as a function of current density with the same 250 watt, 0.6V/cell, 1000 watt hour assumptions used in the air case. In this case, the extra weight of the O_2 precludes meeting the weight goal at any reasonable current density with these assumptions. The voltage sensitivity displayed in Figure 7 demonstrates that 330 ASF at 0.7V/cell is required to meet the weight goal with this O_2 system. Figure 8 shows the extra

weight penalty for excess crossover. This now includes the weight of both extra methanol fuel and O_2.

Direct Methanol Stack Testing

A Pt/Ru black catalyst developed by PSIT was chosen as the catalyst development most ready for a stack demonstration. Initial application of this catalyst to direct methanol oxidation in a PEM cell was accomplished at the 2.25x2.25 inch sub scale level using Nafion® 117 as the electrolyte. Performance of 0.52V at 100 ASF against 50 psia O_2, 180°F, was obtained using vapor fed 1.5/1 molar ratio water/methanol.

Full scale (5x8 inch active area) single cell and stack hardware capable of either vapor or liquid feed was developed. Vapor feed performance equivalent to the sub scale result was achieved in a full size single cell with the PSIT Pt/Ru catalyst. Use of the liquid feed hardware option required increasing the temperature to 220°F in order to produce an anode limiting current over 100 ASF. A performance point of 0.6V at 100 ASF, against 50psia O_2, was recorded with 1.5/1 water to methanol molar ratio liquid, fed directly to the cell at this temperature.

On the basis of these results a 2 cell stack was built using the same type anode and cell hardware. It was run in the liquid feed mode at 220°F. Initial performance at the same conditions, shown in Figure 9, matched the single cell result. Good uniformity between cells was achieved. The 100 ASF point was held for 5 hours. Figure 10 displays the relatively stable 0.6V performance obtained for both cells. This is among the best reported performance results for direct methanol fuel cell stacks.

Conclusion

IFC has demonstrated that direct methanol oxidation can be accomplished in a low temperature PEM stack. Improvement in electrode performance and methanol crossover is required to meet the performance goals established for the person-portable micro climate cooling application.

Acknowledgment

This work was supported by ARPA under a contract managed by ONR.

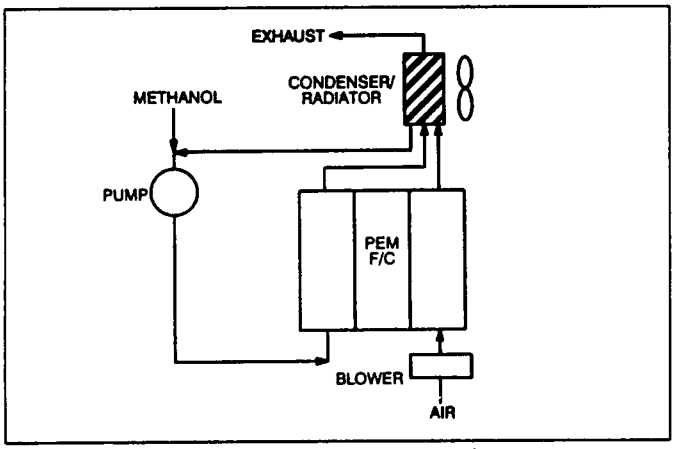

Figure 1 Direct Oxidation Methanol/air Power System

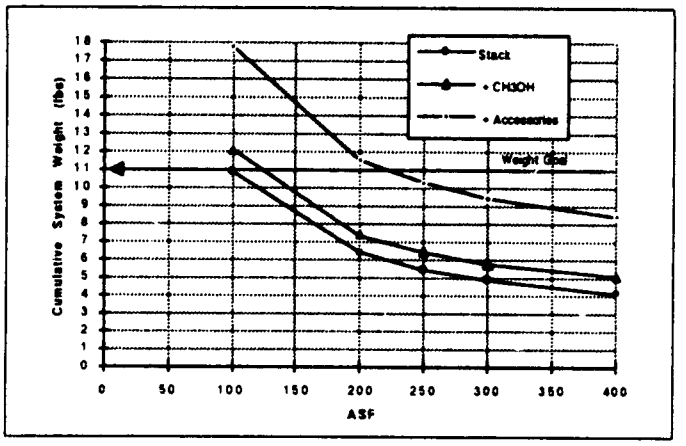

Figure 2 MeOH/air System Weights vs. Current Density @ 0.6V/cell, 250 watts, 1000 Whr, 50 ASF MeOH X-over, 170°F, 14.7 psia

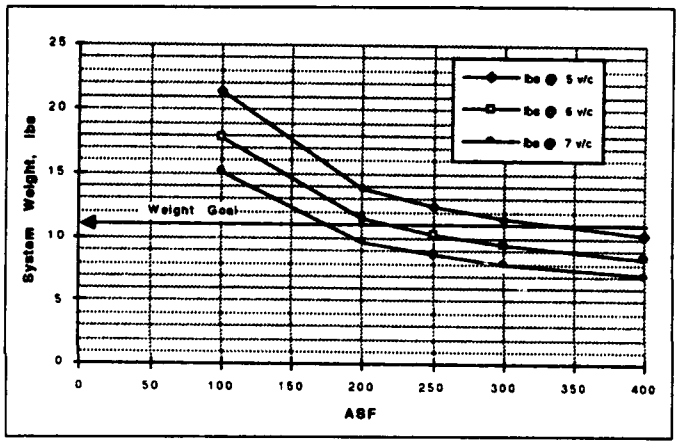

Figure 3 Total System Weights of MeOH/air vs. Current Density, as a Function of Cell Voltage. Same Conditions as Above

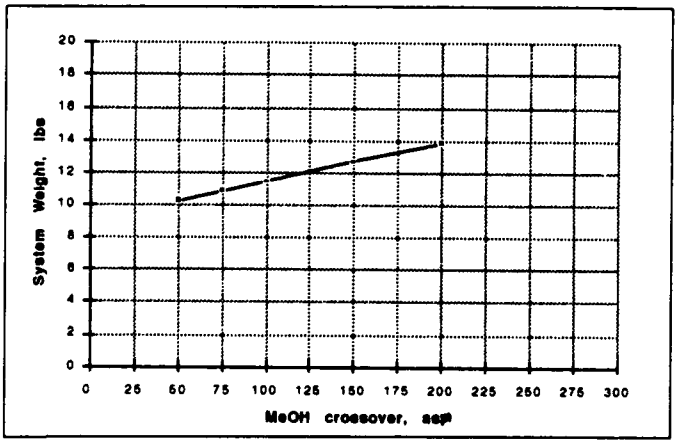

Figure 4 Impact of MeOH Crossover on MeOH/air System Weight. Same Conditions as Above

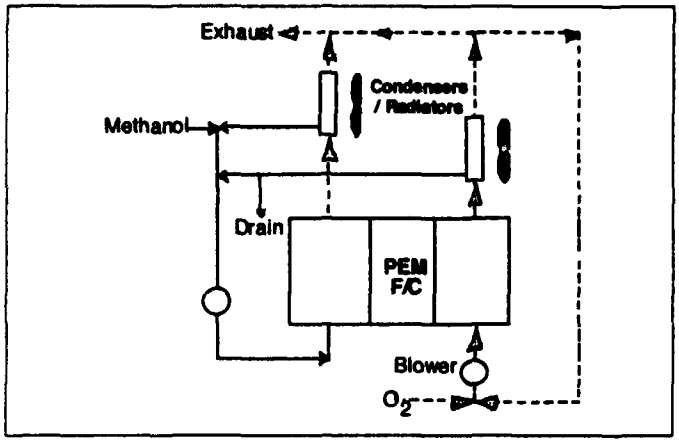

Figure 5 Direct Oxidation MeOH/O_2 PEM Power System

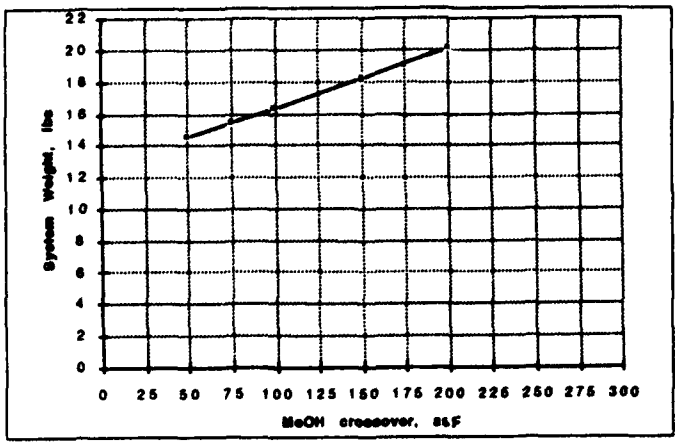

Figure 8 Impact of MeOH Crossover on MeOH/O_2 System Weight. Same Conditions as Above

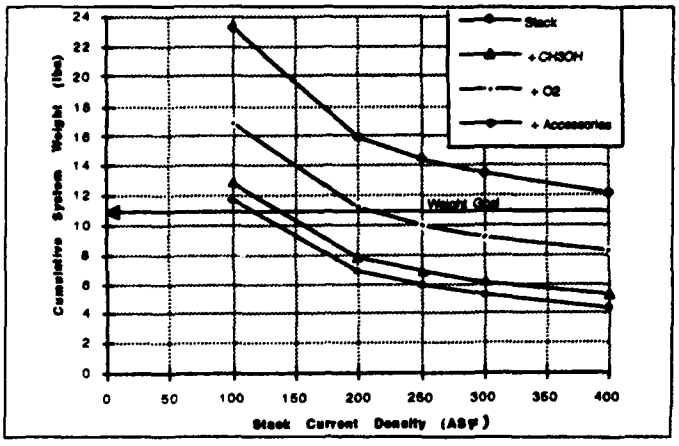

Figure 6 MeOH/O_2 System Weight vs. Current Density @ 0.6V/Cell, 45psia, 250 watts, 1000 Whr, 50 ASF MeOH X-Over.

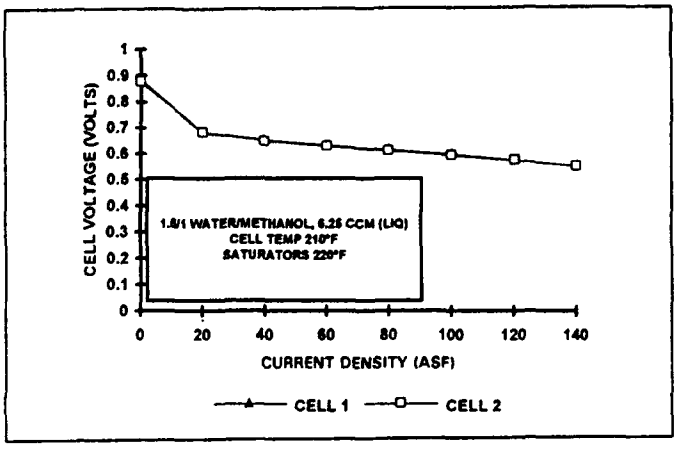

Figure 9 Two Cell Stack MeOH/O_2 50 psia Performance

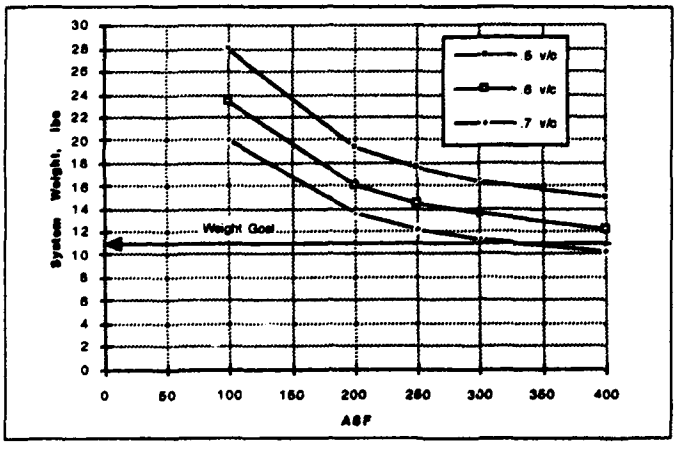

Figure 7 Total System Weights of MeOH/O_2 vs. Current Density, as a Function of Cell Voltage. Same Conditions as Above

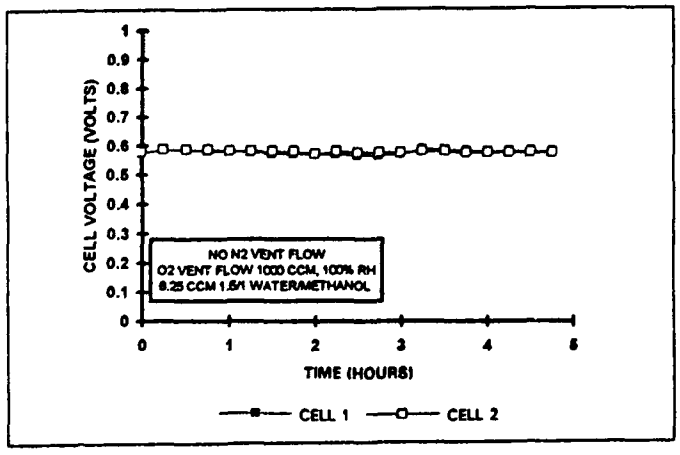

Figure 10 Short term MeOH/O_2 Stack Stability Test

FUEL CELL POWER PLANTS FOR BARE-BASE AND FIXED-BASE APPLICATIONS

Sandors Abens and George Steinfeld
Energy Research Corporation, Danbury, CT

Introduction

Energy Research Corporation is initiating the development of fuel cell power plants for fixed and bare-base DoD applications under the ARPA "Fuel Cell Power Plant Initiative." ERC will adapt its direct carbonate fuel cell power plant technology in combination with a logistic fuel processing system for dual use application.

Features of the fuel cell power plant design include:

- Multifuel operation on logistic fuels DF-2 and JP-8, as well as natural gas,
- Logistic fuel preprocessor design compatible with direct internal reforming fuel cell operation,
- High efficiency - leading to 40% lower fuel consumption as compared with diesel engine gensets,
- Use of non-noble catalyst materials - eliminating any undue dependency on foreign sources,
- Rugged fuel cell construction employing metallic cell hardware - for ease of transportation under military conditions,
- Water recovery system for water self-sufficiency, and
- Low thermal and acoustic signature, as well as negligible emissions.

After initial analysis and bench-scale verification of the fuel preprocessing system, which started in early 1994, a brassboard system will be constructed. In parallel, an approach for fuel cell stack weight and volume reduction will be developed and verified at subscale and incorporated in a 32kW stack with full area cells. The brassboard fuel feed system and the 32kW stack will be tested with both diesel (DF-2) and JP-8 fuels. The results will be utilized to derive preliminary power plant designs for fixed and bare-base applications. Maximum power rating for a single fuel cell generator set, as well as a transportable multiple-skid power plant will be defined, and the corresponding design will be provided considering the bare-base requirements specified by DoD. This development is expected to improve the efficiency, fuel flexibility, emissions, and thermal and acoustic signatures of future fixed- base and mobile power plants.

Team members for the proposed project include ERC and its wholly-owned subsidiary, Fuel Cell Manufacturing Corporation; Haldor Topsoe, Inc. and its parent company, Haldor Topsoe A/S; Fluor Daniel Corporation; and Illinois Institute of Technology.

Logistic Fuel Processing:

Logistic fuels such as DF-2 and JP-8 provide a high energy density fuel offering transportability advantages for mobile applications and a source of back-up fuel for fixed base applications when natural gas is available. Table 1 summarizes some of the characteristics of interest for processing these fuels into a fuel useable by fuel cells. The higher sulfur content and lower H/C ratio makes DF-2 somewhat more challenging from a fuel processing point of view compared to JP-8.

Table 1
Properties of Logistic Fuels JP-8 and DF-2
Both Fuels Have Similar Characteristics, But DF-2 Poses a Greater Processing Challenge

PROPERTY	JP-8	DF-2
Molecular Formula (avg)	$C_{12.4}H_{21.2}$	$C_{14.6}H_{24.8}$
Molecular Weight	170	200
H/C Ratio (Molar)	1.80	1.70
Sulfur Mass %	0.3 (max.)	0.5 (max)
Specific Gravity	.805	.850
Gross Heating Value Btu/lb	19,780	19,570
Gross Heating Value Btu/gal	132,600	138,600

Source: U.S. Army, Fort Belvoir Research Development and Engineering Center

Desulfurization:

The key step in processing logistic fuels for fuel cell application is the desulfurization step. Sulfur compounds in these fuels, which can be present up to 0.5 wt% according to Federal Specification VV-F-800D for Diesel Fuel, must be reduced below 1 ppm to maintain the catalytic activity of downstream catalysts. While commercial suppliers are already preparing to reduce sulfur levels to 0.05 wt% (500 ppm) in diesel fuel to meet clean air regulations, this level is still high for fuel cell applications, and must be reduced further.

The approach planned is based on utilizing available hydrodesulfurization catalysts at pressures sufficiently high to lower the sulfur level to below 1 ppm. This hydrotreating step also lowers the aromatics content of the fuel, making it easier to reform without carbon formation.

Preconversion:

Following the desulfurization step, an adiabatic preconversion step will be used to convert the higher hydrocarbons in DF-2 and JP-8 to methane as follows:

$C_nH_m + nH_2O \rightarrow nCO + (n + m/2)H_2$ endothermic
$CO + 3H2 \rightarrow CH_4 + H_2O$ exothermic
$CO + H_2O \rightarrow CO_2 + H_2$ exothermic

This approach has been shown in a previous DoD-funded project to be feasible for operating carbonate fuel cells with diesel-like fuels[1].

The endothermic steam reforming of hydrocarbons can be considered irreversible for all higher hydrocarbons (n>1) which are converted directly to carbon oxides and hydrogen with no intermediate products. The reaction is then followed by the exothermic methanation and water-gas shift reactions which adjust the chemical equilibrium between the carbon oxides, methane, hydrogen and water. Typical conditions and exit compositions for a diesel preconverter based on equilibrium calculations and earlier subscale testing indicate that a high methane content can be achieved. This makes operation on diesel fuel or jet fuel appear to the fuel cell as operation on natural gas, with a small variation in the gas composition. This facilitates the use of the same fuel cell design for logistic fuels as for natural gas, maximizing dual use which builds on technology already developed for the commercial sector.

Fuel Cell Power Plant:

The fuel cell power plant is based on internal reforming carbonate fuel cell technology, the Direct Fuel Cell, developed at Energy Research Corporation. The Direct Fuel Cell concept, is depicted in Figure 1. Methane fuel is first reformed in the anode compartment of the carbonate fuel cell to produce CO and H_2. Both H_2 and CO are oxidized by the carbonate ion ($CO_3^{=}$) to H_2O and CO_2, discharging two electrons. The carbonate ions are formed on the cathode side of the fuel cell by reaction of O_2 and CO_2 plus two electrons from the external circuit. Since methane reforming is endothermic, it serves to remove heat produced in the fuel cell, minimizing fuel cell cooling requirements. Because methane conversion in the fuel cell is achieved by using waste heat, the direct fuel cell is inherently more efficient than conventional fuel cells operating on externally reformed fuel.

Individual fuel cell stacks are grouped in modules which will be identical to commercial natural gas power plant designs, with the exception of the stack design changes developed under the stack militarization task. This allows a dual use application for both commercial and military systems. Figure 2 depicts a 1MW fuel cell module which incorporates four carbonate fuel cell stacks. Two of these modules are required for a 2MW power plant.

Preliminary Power Plant Development for Fixed- Base Applications:

The fixed-base power plant, rated at 2 MW, will be capable of operating on logistic fuels, DF-2 and JP-8, as well as on natural gas. Such a multifuel capability provides independence and versatility for military installations in the event of commercial power

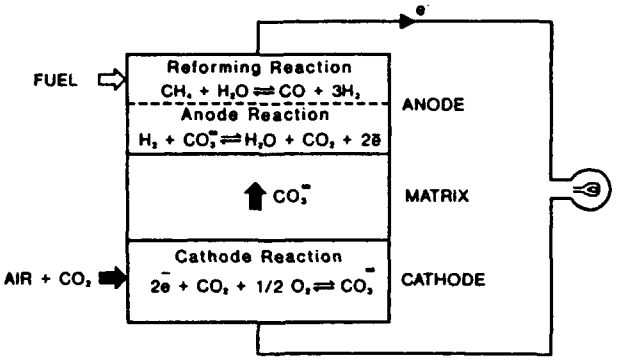

Figure 1
Direct Fuel Cell Concept

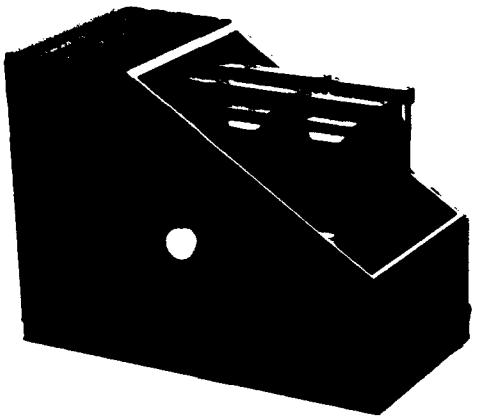

Figure 2
Engineering Model of a 1MW
Carbonate Fuel Cell Module
Two modules containing four stacks each are required in a 2MW Plant

interruption or outage caused by natural disaster, accident, sabotage, vandalism and/or attack.

The logistic fuel processing front-end will be added to an existing natural gas plant design with minor changes in the remainder of the plant. However, a water recovery system will be added to make the power plant water self- sufficient.

The Direct Fuel Cell power system concept is shown in Figure 3. Oxygen and carbon dioxide are supplied to the cathode by a burner which combusts the residual fuel in the anode tailgas with excess air. Stack exhaust is used to raise the steam needed for reforming the fuel to hydrogen.

Overall power plant specifications are estimated on DF-2 and JP-8 at a thermal-to- electric efficiency of 57.8% and 57.2%, respectively, and at 61.2% on natural gas, all on a lower heating value basis. Heat recovery to produce 66-80 gallons of hot water per minute at 150°F can be provided, increasing the overall plant electric and thermal efficiency to 80-85%.

All three design fuels can produce the rated power of 2MW using eight stacks, with natural gas

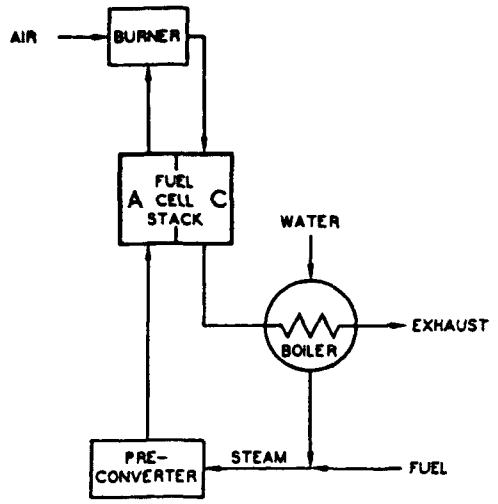

Figure 3
Direct Fuel Cell System Concept

performance slightly above performance on logistic fuels.

Preliminary Power Plant Development for Bare- Base Applications:

Bare-base power systems are required to rapidly establish a sustainable operation at a bare-base location vital to various military missions. These power systems may be used globally, in all seasonal environments, and in any of the climatic extremes listed in MIL-STD-210B. The power systems must be rugged, portable, reliable, affordable, and simple to maintain.

The detailed design requirements of bare-base deployment will be defined in a pre-design mission analysis to evaluate design options that are consistent with bare-base deployment needs.

Transportation requirements for C-130 transport will define the maximum size of the bare base power plant which is currently anticipated to be in the size range of 300 kW.

A skid mounted unit containing fuel processing, fuel cell stacks and power conditioning sections of the plant will be packaged in a ruggedized unit for transportability and field operation. Trade-offs will be considered between a single maximum rating unit transportable in one shipment by C-130 versus a larger modular power plant transportable on multiple skids which can be readily assembled in the field.

Performance will be similar to the 2 MW power plant for fixed-base application, with some possible trade-offs to meet transportability requirements.

References:

1. Abens, S.G., and Kumm, W.H., (1992). Evaluation of Reformation of Diesel Type Fuel in an MCFC Stack. Proceedings of the 35th International Power Sources Symposium, pp. 46-48.

Acknowledgement:

This work is performed by Energy Research Corporation and its subcontractors as part of the ARPA Fuel Cell Power Plant Initiative with technical and management direction provided by the NASA Lewis Research Center under Contract NAS3-27021.

Evaluation of Stack Design and Electrode Performance for Alkaline Fuel Cells

HONG-KI LEE*, JOONG-PYO SHIM, HYUNG-JIN KIM**, YEONG-KYUNG KONG***, and JU-SEONG LEE

Dept. of Industrial Chemistry, **Dept. of Chemical Engneering, Hanyang Univ., *Dept. of Chemistry, Woosuk Univ., ***Agency for Defense Developement, Korea.

Astract

The characteristic of electrode and matrix according to the manufacturing process was studied and also the design of 100W stack was performed for the basic research of the developement of 3KW AFC system. The performances of electrodes were investigated with mass activity, Tafel slope, impedance analysis, chemisorption and particle size analysis. Raney nickel containing 2.0% of Ti with particle size of 5.7 μm was shown the highest mass activity of 2.4 A/g. New technology to load silver particles on carbon black with colloidal method was carried out for oxygen electrode catalyst and 200Å of silver particle size was shown the 38.5 m^2/g of the highest surface area and 84 A/g of mass activity. Potassium titanate was used as new material for matrix and 2:1 of whisker and powder mixture was shown 160% of wettability, 62% of porosity and 230 mmHg of bubble pressure. The stack was assembled with epoxy resin reinforced with glass fiber for preventing thermal shock and the cell performances were evaluated at various operating condition.

INTRODUCTION

The serious environmental pollution resulted from combustion of fossil fuels have demanded the developement of fuel cell as new clean energy system. Fuel cell which can convert the chemical energy of fuel into the electrical energy has several advantages ; favorable higher conversion efficiency of fuel, recovery of exhaust heat, noiseless conversion, lower production of pollutants and minimal siting restriction. The first successful H_2-O_2 alkaline fuel cell(AFC) was started in 1932 by Bacon and culminated in 5KW system in 1955 which was used 30% KOH as an electrolyte and was operated at 200℃.[1] Technical developement of AFC was accomplished by NASA in the early 1960's and many scientists proved that it is suitable in application where only small uints are required such as space shuttle, military purpose and electrical vehicles. AFC has several advantages over Phosphoric Acid Fuel Cell(PAFC)[2-3]; (A) potentially higher energy efficiency caused from the higher rates of oxygen reduction, (B) low operating temperature and better material torelance and (C) better performances. To maintain the competition for the commercial application, non-noble metal is recommended as catalyst and its amount should be diminished without decrease of electrode performance.

In this study, optimum condition of preparing Raney nickel catalyst for hydrogen electrode and the effects of the electrochemical characteristics at porous electrode according to the promotor were investigated. For oxygen electrode, the colloidal method for impregnation of silver on carbon black was carried out and the dispersity of carbon black was studied. The stack was assembled with potassium hexatitanate matrix and the influence of design and operating condition were confirmed.

EXPERIMENTAL

Preparation of Materials.

The various mass fraction of nickel and aluminum powder was mixed in mortar thoroughly, then pelleted by pressing at 200kg/cm^2, sintered at 700℃. Aluminum was leached in 6N NaOH solution at 80℃ for 24 hours and obtained Raney nickel was partially oxydized and stored in vacuum prior to use. Silver particles were impregnated on carbon black with colloidal method and used as catalyst for oxygen electrode. 1:4 of K_2CO_3 and TiO_2 mixture was sintered at 850℃, was prepared potassium hexatitanate powder. It was detailed in previous work[4-6]

Manufacturing Process of Electrode

The manufacturing process of porous catalytic layer of hydrogen electrode was followed. Raney nickel was mixed with polytetrafluoroethylene (PTFE; Teflon 30J, Du Pont) and homogenizing with Ultrasonic Generator (US-300T, Japan) and dried until it bacame paste. The obtained paste was pelleted by pressing or rolling method with isopropyl alcohol on 60 mesh stainless steel net for the mechanical support and was treated at 340℃ in N_2 atmosphere for 1 hr. The gas diffusion layers were prepared with the Toray carbon paper(TGP-H-60, porosity 73%, thickness 0.17mm) containing 40 w/o of PTFE. They were attached to the catalytic layer by hot press and soxhlet in acetone to remove residual surfactant which was originally mixed in PTFE dispersion.

Methods of Measurement

Potentiostat/Galvanostat(EG&G PARC Model 273A) connected with IBM computer system and Solatron 1255(Schlumbeger) were used for measuring the electrochemical characteristics[7-10]. The counter electrode was Pt gauze and the reference electrode was NHE. The IR drop was reduced by closing the reference electrode through the luggin capillary to the working electrode. The whole cell assembly was sealed to prevent the precipitation of potassium bicarbonate and/or carbonate. CO-chemisorption was carried out with Cahn 2000 Microbalance and the gasflow were controlled with Multiple-Dyne-Blender. Investigation of morphology was carried out with SEM(JSM 350. JEOL).

RESULT and DISCUSSION

Improvement of Hydrogen Electrode Performance

The electrochemical characteristics of the electrode were considerably influenced by the portion of nickel and aluminum content for Ni-Al alloy. When the catalysts were obtained from 60w/o of nickel and 40w/o of aluminum, the

electrode shown the highest current density of 450 mA/cm^2 and these tendencies could be explained with following two reason. First, residual Al were exist as contaminant and finally the catalytic activity was worse and the amount of unleached Al was increased with the increase of $NiAl_3$ Second, the diffusion of hydroxyl ion could interrupt at fine pore and resulted the increase of resistance. From pore size distribution data, the ratios below 0.1um pore size was decreased with increase of Ni content during Ni-Al alloy formation as shown in Fig. 1. From the binary phase diagram[11], 40w/o of nickel content indicated the region of $NiAl_3$ and 60w/o indicated of the Ni_2Al_3. With our XRD data, the intensity of characteristic XRD peak of $NiAl_3$ was diminished as the increase of nickel content.

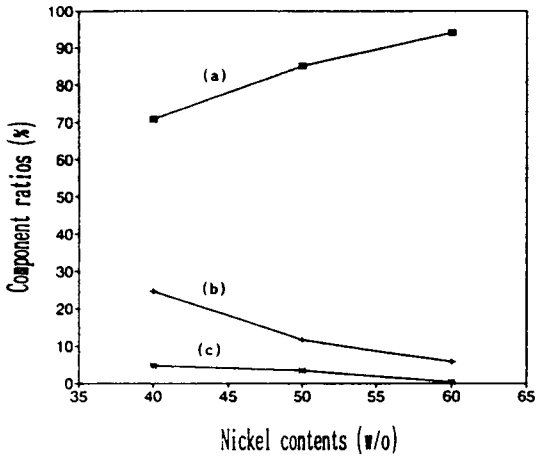

Fig. 1. Component ratios of pore size at the Raney nickel obtained from various Ni portion for Ni-Al alloy.
(a) 10μm ~ 1μm of pore size
(b) 1μm ~ 0.1μm of pore size
(c) below 0.1μm of pore size

The mass activity were increased when the electrode manufactured with the Raney nickel catalyst containing Ti. And the particle size of Raney nickel was decreased with the increase Ti content during Ni-Al alloy formation. Similar size distribution was found from the linear slope when 1.5-2.0 w/o of Ti was contained. It could be concluded that titanium was textual promotor and there was no evidence from polarization curve that the activity of catalyst was increased. Without Ti, the surface area and mean particle size of Raney nickel had the value of 0.6436 m^2/cc, 12.36μm, but 1.3129 m^2/cc and 5.7μm was evaluated when 2.0 of Ti was added respectively. Fig.2 was shown impedance spectra in the form of a Cronigs-Kramer plot. Distinguished two semicircle was obtained and high frequencies circle attributed to the

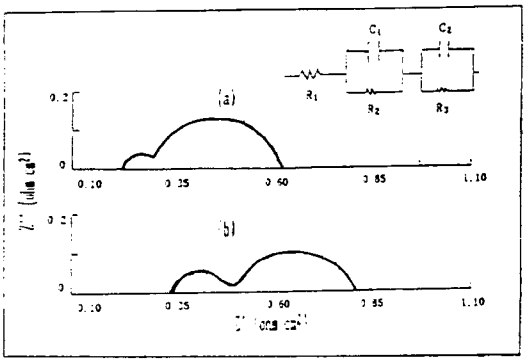

Fig. 2. Impedance spectra of Raney nickel electrode.
(a) Raney nickel
(b) Raney nickel containing 2w/o of Ti

electrolyte resistance and the effective capacitance of the electrode. Low frequencies circle may correspond to hydrogen transport impedance in the pore and transport of hydroxide ions from electrode. With the addition of Ti, the resistance and capacity were changed from 0.35 cm^2 to 0.30 cm^2, from 0.307 F/cm^2 to 0.42 F/cm^2, respectively.

Improvement of Oxygen Electrode Performance

Silver particle impregnated on carbon black by colloidal method was used as catalyst for oxygen electrode. The increase of catalytic surface area and its activity could accomplished by minimizing of silver particle size, but small particles could aggromerate each other and the active surface area was decreased. As shown in Fig.3, when the silver particle shown 200Å of particle size, the maximum surface area of 40 m^2/g was calculated with the result of O_2

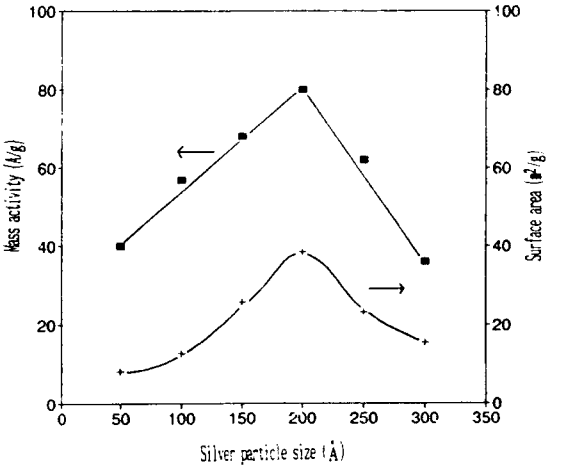

Fig. 3. Mass activity and surface area vs. various silver particle size.

chemisorption and almost 80 A/g of mass activity at the electrode was obtained. According to our calculation, real distance of each particle was 250Å. After 5mg/cm^2 of loading amount, almost it had the saturation value of specific activity. The particle size of silver catalyst with non-homogenizing carbon black used as supportor was shown almost 250Å, but with homogenized carbon black, it had 130Å of silver particle size. From this result, silver particle size would influenced according to dispersity of carbon black. The pore size distribution of non-homogenized carbon black had only macropore and transitional pore by interparticle pore with 17m^2/g of pore surface area. But as soon as homogenizing was began, sharp micropore peak was appeared with increase of pore surface area and it had maximum value of 88m^2/g when homogenizing 30sec. More than 30sec of homogenizing time, the micropore was disappeared, since active small particle was reagglomerated. The pore area was increased as to homogenizing and could be expected the increase of corrosion rate. But, as shown in Fig.4, there is no evidence that the increase of corrosion compare to the pore area of carbon black.

Matrix and Stack Assembly

The matrix has the functions of electrode seperation and electrolyte containment. The matrix may be a limiting factor with the respect of compatibility with the electrolyte, good ionic conductivity, effectiveness as a barrier, proper strength and flexibility. Potassium hexatitanate powder matrix was shown only 50% of wettability but strong mechanical properties and whisker matrix was shown 170% of

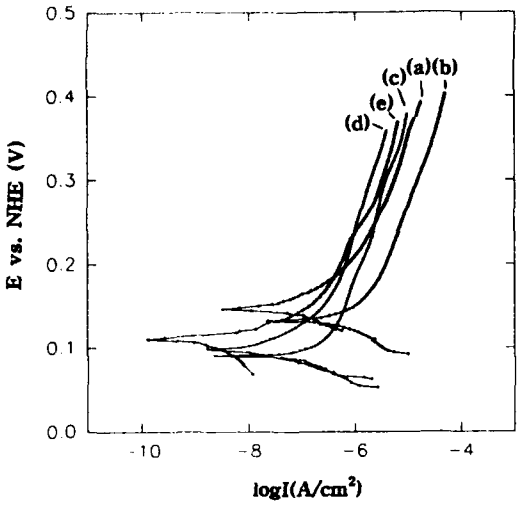

Fig. 4. The potentiodynamic anodic polarization curve of carbon according to dispersion time.
(a) 20sec (b) 30sec (c) 40sec (d) 50sec (e) 60sec

wettability with weak mechanical properties. The matrix made by mixture with 1:2 of powder and whisker had appropriate wettability and ionic conductivity. It was represented in Fig.5.

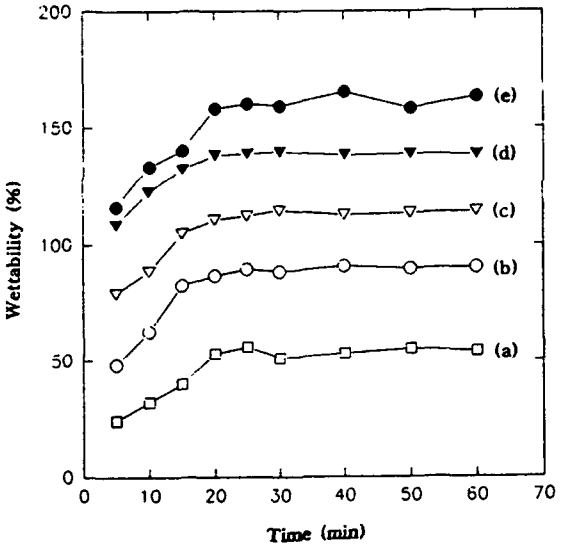

Fig. 5. Time dependance fo wettability with various $K_2O \cdot 6TiO_2$ matrix.
(a) powder : wisker = 1 : 0
(b) powder : wisker = 2 : 1
(c) powder : wisker = 1 : 1
(d) powder : wisker = 1 : 2
(e) powder : wisker = 0 : 1

The arrangement of stack and final product was shown in Fig.6 and Fig.7. To prevent the leak of gas, epoxy casting mold was used and also the epoxy resin was reinforced with glass fiber. The dimension of electrode was 12×16 cm^2 and active area was 100 cm^2. In Fig.8, the stack which was constructed with nickel foam as gas channel was illustrated, each component was sealed with PTFE followed molding with epoxy resin.

CONCLUSION

From these results, the following conclusions can be drawn;

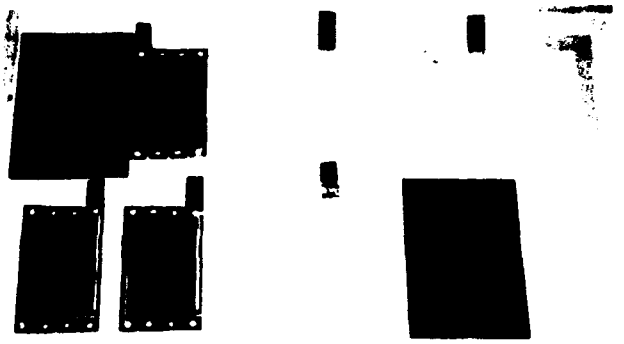

Fig. 6. Electrodes and matrix.

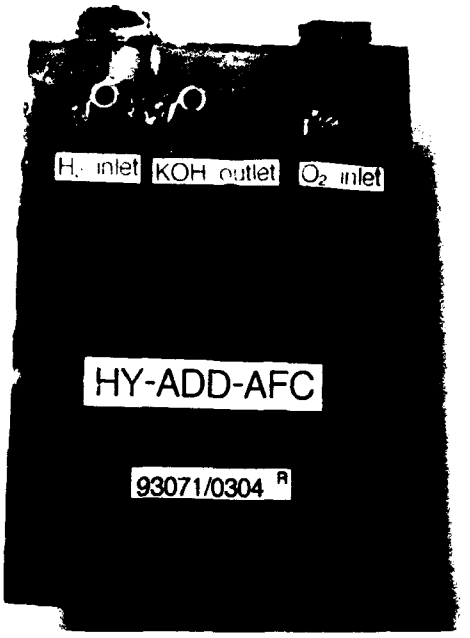

Fig. 7. Arrangement of 30W alkaline fuel cell stack.

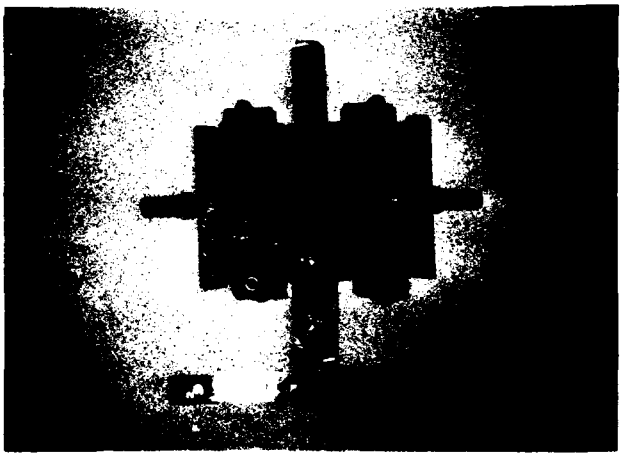

Fig. 8. Arrangement of 10W alkaline fuel cell stack.

1. Raney nickel catalyst obtained from the 60% of nickel and 40% of aluminum mixture showed the optimum electrochemical characteristics.

2. The increase of electrode performance could accomplished with the addition of titanium.

3. With the colloidal method, silver catalyst could impregnated on carbon black and reduced the amount of silver was accomplished.

4. Particle size of silver catalyst for the oxygen electrodee should maintain 200Å.

5. The matrix which had good wettability mechanical properties could made by the mixture of potassium hexatitanate powder and whisker.

ACKNOWLEDGEMENT

This work has been supported by the basic reseach program of Agency for Defense Developement in KOREA. The authors express the appreciation to the ADD.

References

1. A.A.Adams, F.T.Bacon, and R.G.H.Watson, "Fuel Cell", W.Mitchell, Jr., Academic Press, NY.(1963)
2. A.J.Appleby, and F.R.Foulkes, "Fuel Cell handbook" Von Nostrand Reinhold, NY. (1990)
3. H.Ewe, E.W.Justi, and H.J.Selbach, Energy Convers Manage, 24, 97(1984)
4. H.K.Lee, and J.S.Lee, J. of Kor. Ind. & Eng. Chem., 3(2), 189(1992)
5 H.K.Lee, and J.S.Lee, J. of Kor. Ind. & Eng. Chem., 3(4), 701(1992)
6. J.P.Shim, H.K.Lee, and J,S,Lee, J. of Kor. Ins. Sur. Eng., 26, 6, 299(1993)
7. T.Kenjo, Bull. Chem. Soc. Jpn., 54, 2563(1981)
8. T.Tomida, and I.Nakabayashi, J. Electrochem. Soc., 136, 3296(1989)
9. U.A.Tracey, Powder Metallurgy, 2, 45(1979)
10. T.Tomida, and I.Nakabayashi, J. Electrochem. Soc., 136, (1989)
11. J.L.Murray, L.H.Bennett, and H.Baker, "Binary Alloy Phase Diagram", American Society for Metals, vol 1, 142(1986)

$Fe_2(SO_4)_3$ as a Cathode Material for Rechargeable Lithium Batteries

S. OKADA, K.S. Nanjundaswamy, A. Manthiram and J.B. Goodenough
Center for Materials Science & Engineering, ETC 9.102
The University of Texas at Austin
Austin, TX

H. Ohtsuka, H. Arai and J. Yamaki
NTT Interdisciplinary Research Laboratories
Tokai, Ibaraki, Japan.

INTRODUCTION

Among the known Li-insertion compounds, layered rocksalt-type $LiCoO_2$[1] and $LiNiO_2$[2] and spinel-type $LiMn_2O_4$[3] are pursued intensively at present as cathode materials for rechargeable lithium batteries. They are phases in which Li can be inserted reversibly at voltages higher than 3.5 V with respect to Li. However, the higher voltage (> 4 V) associated with $LiCoO_2$ and $LiNiO_2$ may lead to an instability of the electrolyte, while the low lithium mobility associated with $LiMn_2O_4$ limits the power capability. In addition, these high-voltage cathodes are problematic in terms of cost and the availability of the transition metals. It should be emphasized that the Wh/$ is a more important factor than Wh/g in the case of the larger size batteries as for an electric vehicle or a load-leveling system.

These considerations prompt an identification of alternate cathodes, and iron compounds are especially attractive. Because Fe is abundant, inexpensive and less toxic than Co, Ni or Mn. To date, several iron-compound cathodes such as $FePS_3$[4], FeOCl[5], FeS_2[6] and FeOOH[7] have been proposed, but most of them have relatively poor rechargeability and a low discharge voltage. To develop an inexpensive high-voltage cathode, we have focused our attention on $Fe_2(SO_4)_3$ and its isostructural relatives; it has the highest open-circuit voltage (OCV) of the iron-compound cathodes.

$Fe_2(SO_4)_3$ has a NASICON-related framework in which the SO_4 tetrahedra share corners with FeO_6 octahedra and *vice versa* to form a three-dimensional network. The interstitial space can accommodate four guest cations per formula unit, but only two Li atoms are needed to reduce the Fe^{3+} ions to Fe^{2+}. Initial studies[8] found that the framework of monoclinic $Fe_2(SO_4)_3$ transforms to a new, apparently orthorhombic symmetry in $Li_2Fe_2(SO_4)_3$ with a constant OCV of 3.6 V *versus* a Li anode, but hexagonal $Fe_2(SO_4)_3$ remained hexagonal and the OCV decreased monotonically with increasing Li concentration. The high OCV was attributed to the strong polarization of the oxygen toward the sulfur, which lowers the covalent component of the Fe-O bonding. A subsequent study[9] found that hexagonal $Fe_2(SO_4)_3$ may also give a nearly flat OCV curve of 3.6 V *versus* Li and an initial capacity of two Li atoms per formula unit.

In this paper, the synthesis, characterization and electrochemical characteristics of the two $Fe_2(SO_4)_3$ modifications are presented. In an attempt to improve the rechargeability of an $Fe_2(SO_4)_3$ cathode, a small quantity of $LiTi_2(PO_4)_3$ was added to provide a buffer at 2.5 V against the extrusion of metallic iron. In addition, the OCV of $Li_{3+x}Fe_2(PO_4)_3$ was obtained to see the effect of the polyanion PO_4 *versus* SO_4 on the energy of the Fe^{3+}/Fe^{2+} couple.

EXPERIMENTAL

Preparation of monoclinic $Fe_2(SO_4)_3$

Monoclinic $Fe_2(SO_4)_3$ was prepared according to Long[10] by refluxing ferrous sulfate heptahydrate $FeSO_4 \cdot 7H_2O$ (Fisher Scientific) in conc. H_2SO_4 for about 2 hours. To remove absorbed moisture and sulfuric acid, heat treatment was done in an alumina crucible at 350 °C for 12 hours as described elsewhere[9]. In this work, we tried an oxidation reaction with hydrogen-peroxide solution (30 w/o) as follows;

$$2FeSO_4 \cdot 7H_2O + H_2SO_4 + H_2O_2 \rightarrow Fe_2(SO_4)_3 \cdot 9H_2O$$

After the rapid exothermic neutralization reaction, fine pale-pink crystals were deposited in the bottom of the flask. The fine-particle diameter was less than 20 μm and approximately one 50th of the crystal diameter obtained by the above reflux method. The weight loss on TGA profile in Fig. 1 means that the product fine particles are ferric sulfate nonahydrate $Fe_2(SO_4)_3 \cdot 9H_2O$. The precipitate was filtered *via* reduced pressure and washed with alcohol. After dehydration at 300 °C for 10 hours in air, it was identified as anhydrous monoclinic (space group $P2_1/n$) $Fe_2(SO_4)_3$ (JCPDS No.42-229) by X-ray diffraction. This synthesis method has some advantages; rapid, cheap, no residual product except water and fine particles.

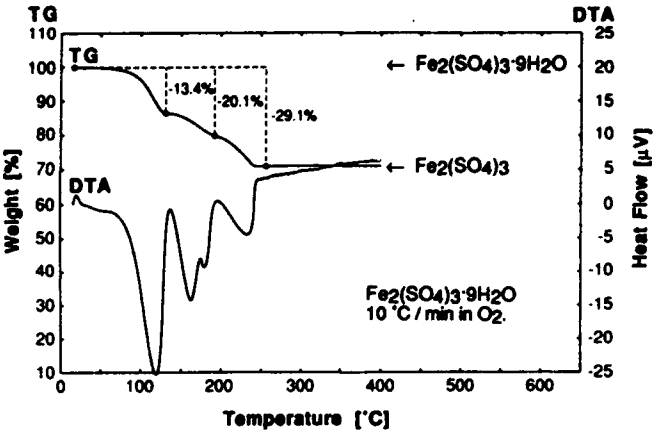

Fig. 1. TGA and DTA curves of $Fe_2(SO_4)_3 \cdot 9H_2O$ made by oxidation reaction with H_2O_2.

Preparation of hexagonal $Fe_2(SO_4)_3$

Hexagonal (space group $R\bar{3}$) $Fe_2(SO_4)_3$ can be prepared by three methods. The first is dehydration of as-received ferric sulfate hydrate, $Fe_2(SO_4)_3 \cdot nH_2O$ (Kanto Chemical). The TGA result of $Fe_2(SO_4)_3 \cdot nH_2O$ showed more than 250 °C is necessary to remove the crystal water from the $Fe_2(SO_4)_3$ host matrix[9]. Anhydrous hexagonal $Fe_2(SO_4)_3$ was obtained by heating as-received $Fe_2(SO_4)_3 \cdot nH_2O$ samples at 250 °C for several hours in air, followed by heating in a sealed quartz tube at 600 °C for 20 hours. A simple one-step heating of the hydrated ferric sulfate in flowing Ar or vacuum was tried at several temperatures T < 600 °C, but all attempts failed to yield a single hexagonal phase.

The second method involves a thermal decomposition of ammonium ferric sulfate, $NH_4Fe(SO_4)_2 \cdot 12H_2O$:

$$2NH_4Fe(SO_4)_2 \cdot 12H_2O \rightarrow Fe_2(SO_4)_3 + 25H_2O\uparrow + 2NH_3\uparrow + SO_3\uparrow$$
$$(41.5w/o) \quad (46.7w/o) \quad (3.5w/o) \quad (8.3w/o)$$

Hexagonal $Fe_2(SO_4)_3$ was obtained by heating $NH_4Fe(SO_4)_2 \cdot 12H_2O$ (Kanto Chemical) in an alumina crucible for 15 hr at 500 °C in Ar. In this reaction, Ar atmosphere is required to prevent the formation of Fe_2O_3. The synthesis temperature was determined from the TGA curve of $NH_4Fe(SO_4)_2 \cdot 12H_2O$ shown in Fig. 2. The 57.2 % weight loss of $NH_4Fe(SO_4)_2 \cdot 12H_2O$ at 500 °C agrees with the theoretical value (58.5 %) within experimental error. The further weight loss at temperatures over 600 °C, Fig. 2, corresponds to the thermal decomposition from $Fe_2(SO_4)_3$ to Fe_2O_3.

The third method consists of a thermal decomposition of ammonium ferrous sulfate, $(NH_4)_2Fe(SO_4)_2 \cdot 6H_2O$, as follows;

$$2(NH_4)_2Fe(SO_4)_2 \cdot 6H_2O \rightarrow Fe_2(SO_4)_3 + 14H_2O\uparrow + 4NH_3\uparrow + SO_2\uparrow$$
$$(51.0w/o) \quad (32.1w/o) \quad (8.7w/o) \quad (8.2w/o)$$

The heat treatment of $(NH_4)_2Fe(SO_4)_2 \cdot 6H_2O$ (Kanto Chemical) was done in an alumina crucible for 15 hours at 500 °C in air. In this reaction ferrous ion is oxidized to ferric ion. The synthesis temperature was determined from the TGA curve of $(NH_4)_2Fe(SO_4)_2 \cdot 6H_2O$ shown in Fig. 3. The 49.03 % weight loss of $(NH_4)_2Fe(SO_4)_2 \cdot 6H_2O$ at 500 °C agrees with the theoretical value (49.01 %).

All of these products were identified as the anhydrous hexagonal $Fe_2(SO_4)_3$ (JCPDS No.42-229) by X-ray diffraction. Of the above three methods, the last one in air is the most convenient for large-scale production. In addition, the synthesis temperature is not high and the operating temperature range from 450 to 550 °C is conveniently broad. We used here the hexagonal sample made by the third method.

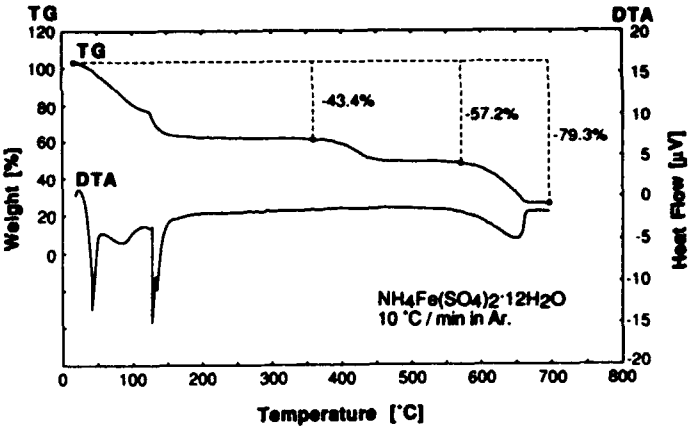

Fig. 2. TGA and DTA curves of $NH_4Fe(SO_4)_2 \cdot 12H_2O$ in Ar.

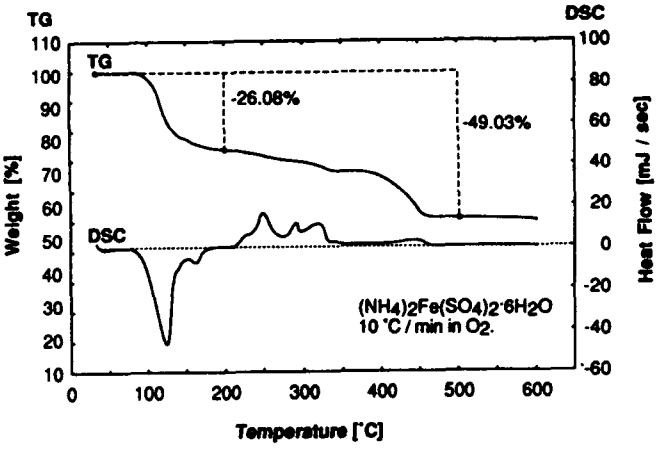

Fig. 3. TGA and DSC curves of $(NH_4)_2Fe(SO_4)_2 \cdot 6H_2O$ in O_2.

Preparation of $LiTi_2(PO_4)_3$ and $Li_3Fe_2(PO_4)_3$

Two other NASICON-related cathode materials, $LiTi_2(PO_4)_3$ and $Li_3Fe_2(PO_4)_3$, were prepared by high-temperature solid-state synthesis:

$$2TiO_2 + 3NH_4H_2PO_4 + 0.5Li_2CO_3 \rightarrow LiTi_2(PO_4)_3 + 4.5H_2O\uparrow + 3NH_3\uparrow + 0.5CO_2\uparrow$$

$$Fe_2O_3 + 3NH_4H_2PO_4 + 1.5Li_2CO_3 \rightarrow Li_3Fe_2(PO_4)_3 + 4.5H_2O\uparrow + 3NH_3\uparrow + 1.5CO_2\uparrow$$

Stoichiometric amounts of the reactants were mixed and ground finely in an agate mortar. The starting mixtures were calcined first at 200 - 400 °C for several hours to remove NH_3 and H_2O and to prevent the loss of Li_2O; the temperature was then gradually raised to 850 °C. After firing at 850 °C for 2 days with intermittent grinding, the mixtures were pelletized and further sintered at 1000 °C for 12 hours in air. The products were identified as $LiTi_2(PO_4)_3$ (JCPDS No.35-754, space group $R\bar{3}c$) and $Li_3Fe_2(PO_4)_3$ (space group $P2_1/n$)[11] by X-ray diffraction.

Cell preparations

The discharge and cycling properties of these cathodes were examined in coin-type cells. The cathode materials were ground to fine particles with a milling machine (Spex #8000 mixer/mill). The cathode mixture was obtained by blending $Fe_2(SO_4)_3$ with acetylene black and polytetrafluoroethylene in a weight ratio 70 : 25 : 5 and was pelletized with a hand press having properly spaced rollers. The electrolyte used was 1 M $LiClO_4$ in a 1:1 (by volume) mixture of propylene carbonate (PC) and dimethoxyethane (DME).

Measurements

Cell performance was evaluated at various constant currents at room temperature. X-ray diffraction experiments with Cu-Kα radiation at 40 kV and 40 mA were carried out during the first cycle at the four points shown in Fig. 5; (a) the initial $Fe_2(SO_4)_3$, (b) the intermediate discharged state $Li_{0.5}Fe_2(SO_4)_3$, (c) the full discharged state $Li_{1.5}Fe_2(SO_4)_3$ and (d) the full recharged state $Fe_2(SO_4)_3$ after the full discharge. The cathode pellets were electrochemically charged and discharged to these states at a rate of 0.05 mA/cm^2 in the coin cell, and enough resting time was allowed for the cells to achieve equilibrium before X-ray analyses were initiated. Discharged and charged cathode pellets were washed with anhydrous PC in a dry box and dried under vacuum for at least 1 hour. Owing to the sensitivity to moisture, the X-ray patterns were recorded from samples sealed in an evacuated holder. The background noise in the pattern was improved by a special configuration of the holder.

RESULTS and DISCUSSION

Fig. 5 shows the crystal structures of the two $Fe_2(SO_4)_3$ modifications[12-14]. The open framework of FeO_6 octahedra sharing corners with SO_4 tetrahedra gives a three-dimensionally

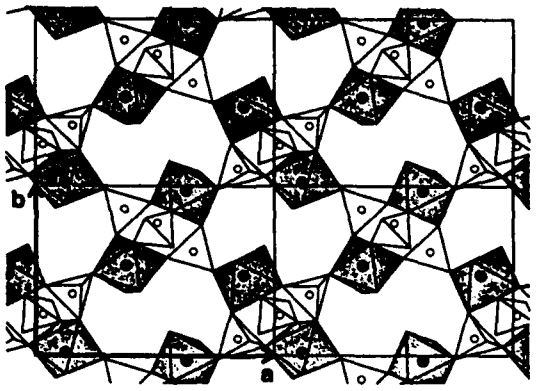

Monoclinic $Fe_2(SO_4)_3$ (after Sudreau)

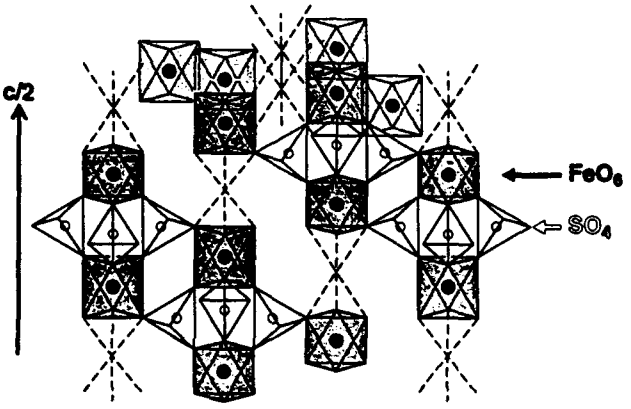

Hexagonal $Fe_2(SO_4)_3$

Fig. 4. Crystal structure of the two $Fe_2(SO_4)_3$ modifications.

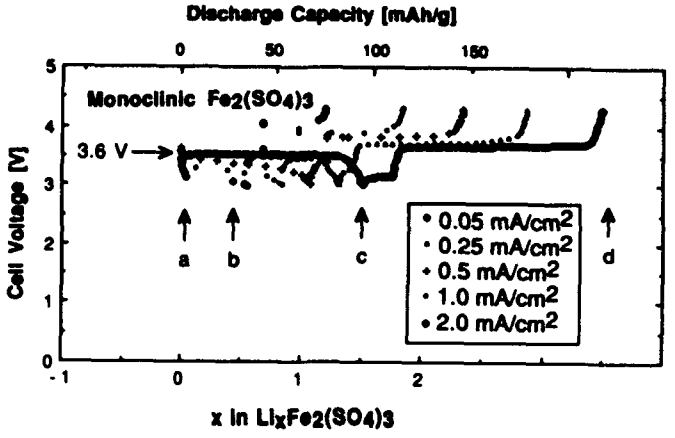

Fig. 5. Charge-discharge profile of monoclinic $Fe_2(SO_4)_3$.

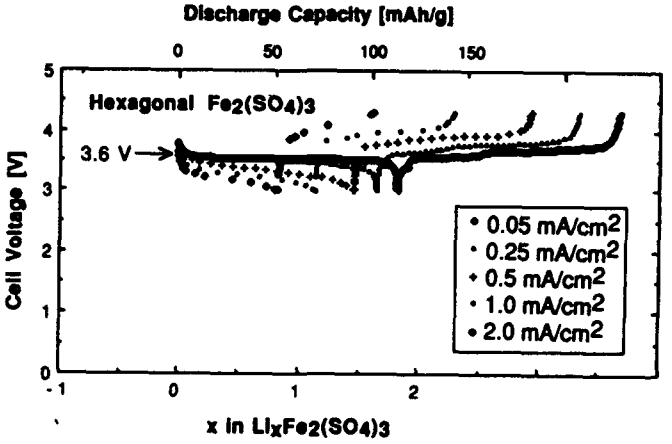

Fig. 6. Charge-discharge profile of hexagonal $Fe_2(SO_4)_3$.

connected interstitial space in which the Li^+ ions are highly mobile. However, the FeO_6 octahedra are isolated from one another, which hinders electron transport *via* the Fe^{3+}/Fe^{2+} redox couple of the Fe-atom array. This situation may reduce the power capability of the cathode. To improve the cathode properties, the particle size of hexagonal and monoclinic $Fe_2(SO_4)_3$ was reduced by mechanical milling or by adopting the H_2O_2 oxidation method of synthesis. Figs. 5 and 6 show, respectively, the OCV curves for the monoclinic and the hexagonal starting materials; in both cases, a flat curve at 3.6 V relative to a Li anode was obtained.

The X-ray diffraction patterns of Fig. 7 show the structural evolution of the monoclinic $Fe_2(SO_4)_3$ cathode, Fig. 7(a), on lithium insertion. The final discharge product $Li_2Fe_2(SO_4)_3$ is orthorhombic (space group Pcan) and isostructural with $Li_3Fe_2(PO_4)_3$, Fig. 7(c). In the intermediate range $0 < x < 2$, $Li_xFe_2(SO_4)_3$ contains both the monoclinic and the orthorhombic phases, as can be seen in Fig. 7(b) as well as inferred from the flat OCV curve. On recharge, the monoclinic phase is almost fully restored, Fig. 7(d). These results demonstrate that monoclinic $Fe_2(SO_4)_3$ is converted reversibly to orthorhombic $Li_2Fe_2(SO_4)_3$ *via* a displacement transition of the NASICON framework. The flat OCV at 3.6 V *versus* Li is a consequence of the coexistence of the parent $Fe_2(SO_4)_3$ and discharged $Li_2Fe_2(SO_4)_3$ phases.

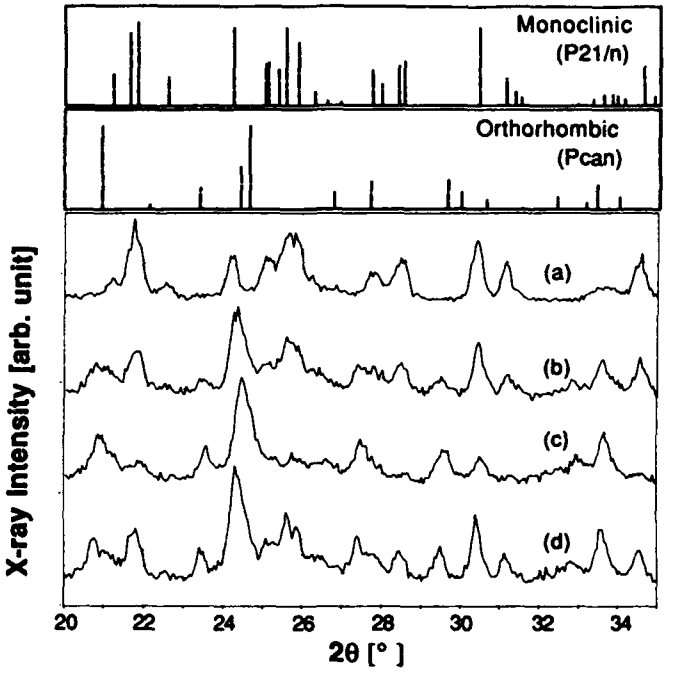

Fig. 7. X-ray diffraction patterns of monoclinic $Fe_2(SO_4)_3$ during the first cycle.

Although good reversibility at 3.6 V *versus* Li is proved for $0 < x < 2$ in $Li_xFe_2(SO_4)_3$, an abrupt voltage drop occurring for $x > 2$ is irreversible. Suspecting the reduction of iron to the elemental state, we sought to protect the cathode from this reaction by introducing hexagonal $LiTi_2(PO_4)_3$ as a buffer. As shown in Fig. 8, $LiTi_2(PO_4)_3$ exhibits an OCV with a plateau at 2.5 V

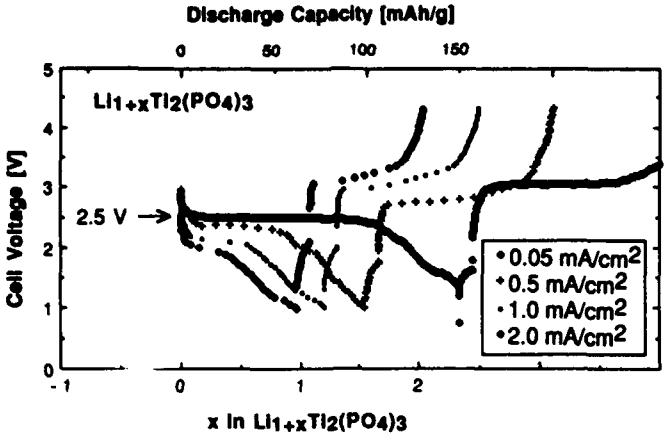

Fig. 8. Charge-discharge profile of $LiTi_2(PO_4)_3$.

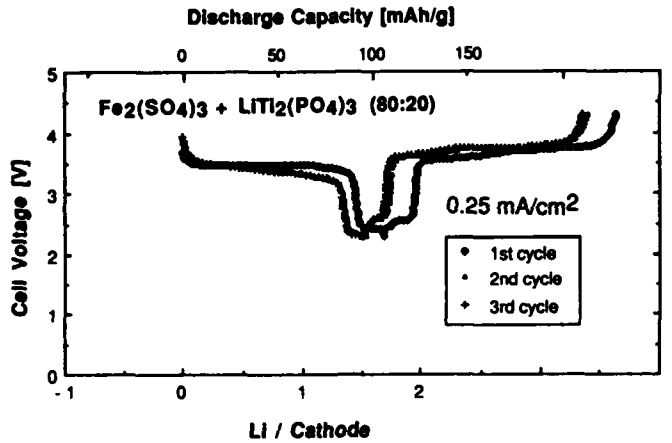

Fig. 9. Rechargeability of mixed cathode with 20 w/o $LiTi_2(PO_4)_3$ and 80 w/o $Fe_2(SO_4)_3$.

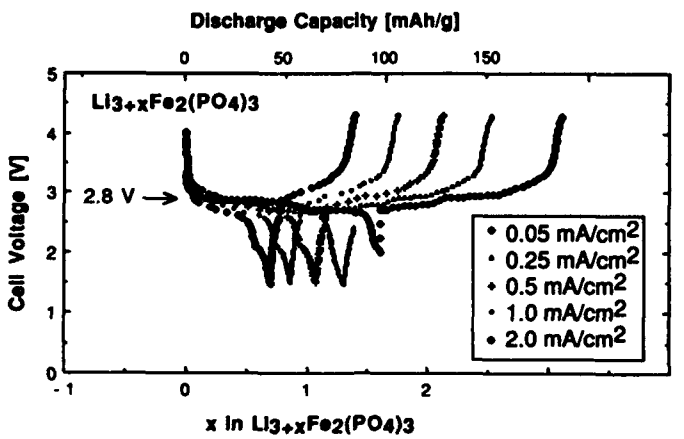

Fig. 10. Charge-discharge profile of $Li_{3+x}Fe_2(PO_4)_3$.

versus Li where hexagonal $LiTi_2(PO_4)_3$, $R\bar{3}c$ space group, coexists with orthorhombic $Li_{1.5}Ti_2(PO_4)_3$, Pbca space group[15]. Fig. 9 shows the OCV curve for a 20 - 80 w/o mixture of $LiTi_2(PO_4)_3$ and $Fe_2(SO_4)_3$ in the initial cathode; the 3.6 V plateau is followed by a 2.5 V plateau *versus* Li as anticipated. Although a loss of capacity was still observed in the second cycle, there was no further loss in capacity in the third cycle. This preliminary result is encouraging and suggests that a more intimate mixing of the $LiTi_2(PO_4)_3$ and $LiTi_2(PO_4)_3$ starting phases may improve the reversibility of the electrode.

Finally, the behavior of $Li_3Fe_2(PO_4)_3$ as a cathode was investigated, Fig. 10, to determined the influence of a charge of polyanion from $(SO_4)^{2-}$ to $(PO_4)^{3-}$ on the Fe^{3+}/Fe^{2+} redox potential. The $Fe_2(PO_4)_3$ framework was expected to accept four Li atoms, but $Li_{4+x}Fe_2(PO_4)_3$ apparently transforms to a structure that accepts 4.5 Li atoms, Fig. 10. A plateau at 2.8 V *versus* Li shows a shift in the redox potential of 0.8 V. This result is compatible with a smaller polarization of the O^{2-} ions towards P (V) than S (VI); the OCV of 3.0 V *versus* Li for $Li_xFe_2(MO_4)_3$, M = Mo or W, indicates an intermediate polarization.

CONCLUSIONS

Both monoclinic and hexagonal forms of $Fe_2(SO_4)_3$ have been shown to give a flat OCV of 3.6 V *versus* Li on insertion of Li to $Li_2Fe_2(SO_4)_3$. The flat OCV reflects the coexistence of two phases, and the phase transition is reversible. To prevent decomposition with the extrusion of elemental iron on rapid discharge, $Fe_2(SO_4)_3$ was mixed with $LiTi_2(PO_4)_3$, which provides a Ti^{4+}/Ti^{3+} redox potential at 2.5 V *versus* Li to act as a buffer. Preliminary results are encouraging. Finally, $Li_3Fe_2(PO_4)_3$ was shown to have an Fe^{3+}/Fe^{2+} redox energy 0.8 V higher than that of $Fe_2(SO_4)_3$.

REFERENCES

(1) K.Mizushima, P.C.Jones, P.J.Wiseman and J.B.Goodenough, Mat. Res. Bull., 15, 783 (1980).
(2) M.G.S.R.Thomas, W.I.F.David and J.B.Goodenough, Mat. Res. Bull., 20, 1137 (1985).
(3) T.Ohzuku, M.Kitagawa and T.Hirai, J. Electrochem. Soc., 137, 769 (1990).
(4) A.Le Mehaute, G.Ouvrard, R.Brec and J.Rouxel, Mat. Res. Bull., 12, 1191 (1977).
(5) M.S.Whittingham, Prog. Solid State Chem., 12, 41 (1978).
(6) R.Brec and A.Dugast, Mater. Res. Bull., 15, 619 (1980).
(7) K.Kanamura, C.Zhen, H.Sakaebe and Z.Takehara, J. Electrochem. Soc., 138, 331 (1991).
(8) A.Manthiram and J.B.Goodenough, J. Power Sources, 26, 403 (1989).
(9) S.Okada, H.Ohtsuka, H.Arai and M.Ichimura, Proceedings of the Symposium on New Sealed Rechargeable Batteries and Super Capacitors, 93-23, 431 (1993).
(10) G.J.Long, G.Longworth, P.Battle, A.K.Cheetham, R.V. Thundathil and D. Beveridge, Inorg. Chem., 18, 624 (1979).
(11) A.B.Bykov, A.P.Chirkin, L.N.Demyanets, S.N.Doronin, E.A. Genkina, A.K.Ivanov-Shits, I.P.Kondratyuk, B.A.Maksimov, O.K.Mel'nikov, L.N.Muradyan, V.I.Simonov and V.A.Timofeeva, Solid State Ionics, 38, 31 (1990).
(12) P.B.Moore and T.Araki, Neues Jahrb. Mineral. Abh., 121, 208 (1974).
(13) F.Sudreau, D.Petit and J.P.Boilot, J. Solid State Chem., 83, 78 (1989).
(14) J.B.Goodenough, H.Y-P.Hong and J.A.Kafalas, Mat. Res. Bull., 11, 203 (1976).
(15) S.Wang and S-J.Hwu, Chem. Mater., 4, 589 (1992).

Bulk Syntheses and Electrochemical Properties of Submicron Powders of $Li_xMn_2O_4$

E.M.Kelder, L.Chen, X.Huang, and J.Schoonman,*

Laboratory for Inorganic Chemistry,
Delft University of Technology,
2628 BL Delft, The Netherlands,
Tel.:+31.15.782667 Fax:+31.15.782655

* **Institute of Physics**
Academia Sinica, P.O.Box 603,
Beijing 100080, China

Abstract

Submicron powders of $Li_xMn_2O_4$ with spinel structure were synthesized by a wet chemical method, the index x being the lithium content in the starting precursor materials. The kind of powders formed depends on the value of x, and can be divided into three compositional regimes as determined by XRD. These are: α-Mn_2O_3 + $LiMn_2O_4$, $Li_yMn_2O_4$ ($1 \le x \le 1.5$), and $Li_{1.5}Mn_2O_4$ + Li_2MnO_3, for $x \le 1$, $1 \le x \le 1.5$, and $x \ge 1.5$, respectively. The electrochemical properties of the powders were studied in a galvanic cell Li/1M $LiAsF_6$ in PC+DME/$Li_xMn_2O_4$. The lithium chemical diffusion coefficient $\tilde{D}$, the Warburg impedance W_c, the relative capacity of the cell, and the internal resistance of the cell R_i were obtained. Two maxima versus composition are observed in all measurements, and are explained by interfacial defects formed in the two-phase systems $LiMn_2O_4$ + α-Mn_2O_3 and $Li_{1.5}Mn_2O_4$ + Li_2MnO_3.

1. Introduction

Several cathode materials for thin film rechargeable lithium batteries are known. Among these, the transition metal oxides show very promising results [1-7]. The lithium ions are assumed to intercalate easily into the host lattice of the oxide. Due to environmental demands manganese dioxides appear to be the most promising of these transition metal cathodes. Manganese dioxide appears in several different lattice structures such as β-MnO_2, γ-MnO_2, and λ-MnO_2, all of which are able to intercalate lithium ions. The λ-MnO_2 is of the spinel structure and does have much interstitial space for lithium ions to be intercalated [8]. This λ-MnO_2 has shown intercalation concentrations of lithium ions up to a mole ratio of unity, i.e. $Li_2Mn_2O_4$, where Mn_2O_4 refers to the spinel structure [9].
It is well known that the size of the primary particles affects strongly the diffusion behavior of the lithium ions [8]. In fact, the smaller the primary particles are the higher the diffusion coefficient becomes. Rapid diffusion of lithium ions in the cathode material is highly desirable for good battery operation.
Here we report on the results of a wet-chemical synthesis of submicron powders of lithium manganese oxide with the stoichiometry $Li_yMn_2O_4$, and with y ranging from 1 to almost 1.5. The powders are characterized by X-Ray Diffraction (XRD) and Scanning Electron Microscopy (SEM). The lithium diffusion coefficient is measured using Galvanostatic Intermittant Titration Technique (GITT).

2. Experimental Aspects

The submicron powders were synthesized by a novel wet chemical route using manganese acetate and lithium hydroxide with various ratios of Li/Mn ($1/2x$) [10]. A calcining step of 600 °C is used to oxidize the precursors. For the chemical composition of the powders the nominal input concentration ratio Li/Mn of the starting materials, i.e. $Li_xMn_2O_4$, is used for simplicity. Hereafter, the material $Li_yMn_2O_4$ refers to the single phase lithium manganese oxide having the spinel structure with various y values. The details of this synthesis will be reported separately.
The powders were characterized by SEM (JEOL 35) and XRD (Philips, PW 1840, CuKα).
Prior to being used as an electrode, all the $Li_xMn_2O_4$ powders were dried at 150 °C for 24 hours to remove any water contamination.
The electrochemical properties of the powders were studied in a galvanic cell which comprises

$$Li/1M\ LiAsF_6\ in\ PC+DME/Li_xMn_2O_4$$

In particular, the following parameters were determined:
(1) the lithium chemical diffusion coefficient $\tilde{D}$ in the cathode material using the Galvanostatic Intermittent Titration Technique (GITT) [11] (Galvanostatic/Potentiostatic System Modes 273 Princeton Applied Research). It was assumed that at a voltage variation of less than 5 mV per day the system was at equilibrium;
(2) the diffusional behavior (W_c) in the AC response using Impedance Spectroscopy (Solartron 1255 Frequency Response Analyzer and a Solartron 1286 Electrochemical Interface). The impedance data were measured at the equilibrium potential, i.e. under conditions of the absence of a DC current. In order to achieve this, the open circuit voltage was measured and subsequently a negative voltage was applied to the system by the Electrochemical Interface. In the instance of a very small current, the system was assumed to be at equilibrium. The impedance data were analyzed using a non-linear least-squares (NLLS) computer fit program developed by B.A.Boukamp [12];
(3) the relative capacity using the same Galvanostatic/Potentiostatic system combined with an X-Y recorder. The scan rate was 1 mV/s.
(4) the internal resistance of the battery R_i by measuring the current and voltage drop during discharging the cell.

3. Results and Discussion

3.1. Structural characterization of the powders

3.1.1 X-ray diffraction (XRD)

The kind of powder formed depends on the nominal value x in $Li_xMn_2O_4$, and can be divided into three regimes as determined by XRD (Fig.1). These compositional regimes are: α-Mn_2O_3+$LiMn_2O_4$, $Li_yMn_2O_4$ ($1 \le y \le 1.5$), and $Li_{1.5}Mn_2O_4$+Li_2MnO_3, for $x \le 1$, $1 \le x \le 1.5$, and $x \ge 1.5$, respectively. As a result, the color of the products changes from black to orange on going to higher nominal x values. Note that α-Mn_2O_3 as well as the spinel $Li_yMn_2O_4$ is black. Thus, it becomes possible to synthesize powders of $Li_yMn_2O_4$ with the spinel structure with y ranging from 1 to almost 1.5. Higher values of x consequently result in the formation of co-deposits of Li_2MnO_3. Lower values of x result in the formation of α-Mn_2O_3 in addition to $LiMn_2O_4$.

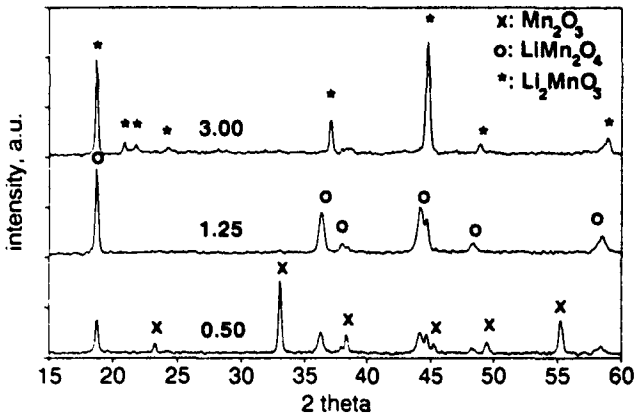

Fig.1. XRD-spectra of the synthesized powder with nominal values of x in $Li_xMn_2O_4$ as indicated.

3.1.2 Scanning electron microscopy

The primary particle size of the powders is in the order of 0.6 μm as can be seen in the SEM micrograph shown in Figure 2. The particle size did not depend strongly on the nominal value of x.

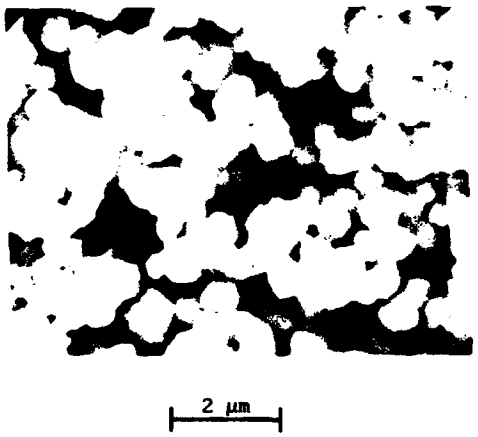

Fig.2. A SEM micrograph of a typical $Li_xMn_2O_4$ powder.

3.2. The electrochemical properties

3.2.1 The lithium chemical diffusion coefficient $\tilde{D}$

The lithium chemical diffusion coefficients are gathered as a function of the nominal value x in Figure 5. The lithium chemical diffusion coefficients are greater by at least one order of magnitude with respect to the lithium chemical diffusion coefficients obtained by solid state reaction reported in [8,13,14], i.e. about $5\times10^{-9}cm^2/s$. The values obtained here range from $3.3\times10^{-8}cm^2/s$ to $7.7\times10^{-7}cm^2/s$. In addition, the powder made by solid state reaction reveals lithium chemical diffusion coefficients which are almost independent of the primary particle size [13-15]. The variation in primary particle size was reported to be determined by the calcining temperature [15]. The primary particle size here was observed to be about 0.6 μm as already mentioned above. Therefore, the enhancement in the lithium chemical diffusion coefficient cannot be related to the primary particle size but is probably due to defects on the particle surface, like composition inhomogeneities, nonstoichiometry, and poor crystallization.

Another striking phenomenon is the appearance of two maxima in the lithium chemical diffusion coefficient as a function of the nominal value x. These maxima appear near x=0.75 and near x=1.75. From XRD data it was shown that at these nominal concentrations a two-phase system occurs of either α-Mn_2O_3 in addition to $LiMn_2O_4$, or $Li_yMn_2O_4$ ($1\le y\le1.5$) in addition to Li_2MnO_3. Since these co-deposits were a result of a proper choice of the amounts of the starting materials, they were highly dispersed into the matrix of the spinel. In the instance of composite ionic conductors, which are composed of a two-phase system having an inert oxide with a high surface area in addition to an ionic conductor, enhanced ionic conductivity has been observed [16-18]. Even two orders of magnitude in the enhancement of the ionic conductivity in LiX(Al_2O_3) (X is an halide) has been reported. The mechanism of the ionic conductivity enhancement is suggested to be the formation of highly conductive interfacial regions between particles of the two phases. The maximum conductivity appears at about 25 m/o of the second phase in the composite conductors. The maximum diffusion enhancement in the present case agrees quite well with the 25 m/o of the second phase of either α-Mn_2O_3 or Li_2MnO_3 relative to either $LiMn_2O_4$ and $Li_yMn_2O_4$ ($1<y<1.5$), respectively. While at x=0.75 and x=1.75, the lithium chemical diffusion coefficient reaches maximal values, the further addition of the second phase component, relative to the amount of $Li_yMn_2O_4$ spinel, consequently results in a predominant presence of this component, and, hence, a decrease of the lithium chemical diffusion coefficient due to the lower bulk diffusion of this inert second phase component.

3.2.2 The relative capacitance

A typical cyclic voltammogram is plotted in Figure 3. The voltage separation between the peaks in the oxidation and in the reduction scan is a measure of the polarization. The higher the separation the higher the polarization, and, hence, the chemical diffusion coefficient. For the nominal value x=0.75 this separation is the smallest. In addition, the area covered by the cyclic voltammogram represents the capacity of the cell during oxidation and reduction because the Y-axis represents the current and the X-axis measures the time interval of the cycle. The relative capacities of the cell as a function of the nominal value x are gathered in Figure 5. Two maxima appear near the same x-values as observed for the lithium chemical diffusion coefficient. Some other factors such as the electrolyte resistance, the interface between the electrolyte and the cathode as well as the anode will also influence the cell capacity. However, impedance analysis do not support this as will be reported in a separate paper [19].

3.2.3. The diffusional behavior

Figure 4 shows an example (x=1.25) of the recordedimpedance spectra. The impedance of the cell is composed of a double layer capacitance, a charge transfer resistance, and a Warburg impedance of both electrodes. However, the Warburg impedance of the lithium metal electrode is neglected. In addition to these electrode impedances, the electrolyte contributes a resistance to the system. Therefore, a simplified equivalent circuit as shown in the insert of Figure 4 has been taken to fit the impedance data using NLLS fitting. Figure 4 shows the experimental data as well as the fit results. The values of the reciprocal Warburg impedance as a function of the nominal value x are gathered in Figure 5. Qualitatively the reciprocal Warburg prefactor is proportional to the chemical diffusion coefficient. Figure 5 clearly shows this

proportionality. In fact, the results of the Warburg impedances support the observations of the chemical diffusion coefficient by GITT.

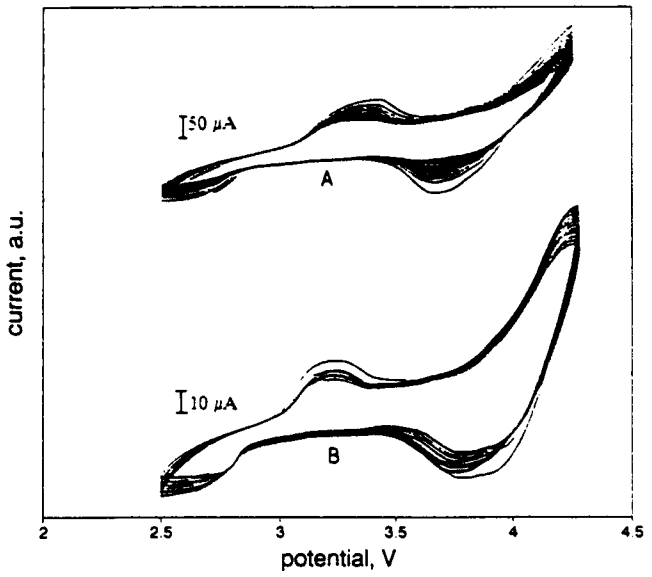

Fig. 3. Cyclic voltammograms of the cell as given in the text, with A x=0.75 and B x=1.5 in $Li_xMn_2O_4$.

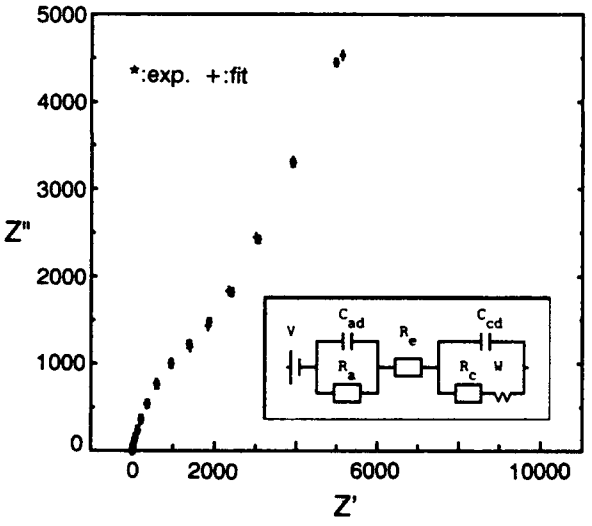

Fig. 4. A typical impedance spectrum and NLLS fit result of the cell as given in the text, with x=1.25. The insert shows a simplified equivalent circuit of the galvanic cell with V the externally applied voltage, R_e the resistance of the electrolyte, R_a and R_c the charge transfer resistances of the anode and cathode, respectively, C_{ad} and C_{cd} the double layer capacitances between anode or cathode and the electrolyte, respectively, and W_c the Warburg impedance of the cathode.

3.2.4. The internal resistance

The internal resistance R_i was calculated using Equation (1),

$$\frac{LCV}{OCV} = -1\left(\frac{R_i}{OCV}\right) + 1 \qquad (1)$$

with LCV, OCV, i and R_i the load circuit voltage, the open circuit voltage, the current, and the internal dc resistance, respectively. The inverse internal resistance represents the battery conductivity and is, therefore, a measure of the diffusion of the conductive species. The calculated values are gathered in Figure 5. Again, two maxima are observed near the same x-values as mentioned above. Hence, the R_i measurements, too, support the concept of enhanced chemical diffusion coefficients.

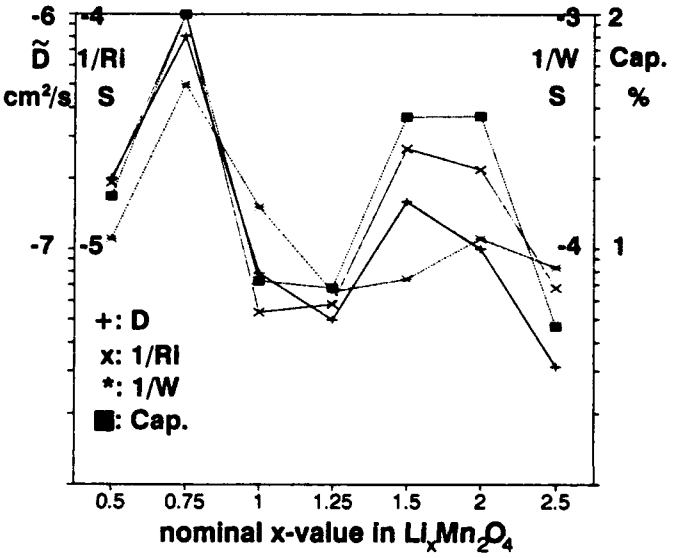

Fig. 5. The lithium chemical diffusion coefficient $\tilde{D}$, the cell capacity Cap., the reciprocal Warburg impedance W^{-1}, and the reciprocal internal resistance R^{-1} as a function of the nominal value of x in $Li_xMn_2O_4$.

4. Conclusions

Submicron powders of $Li_xMn_2O_4$ with nominal values of $0<x<3$ are synthesized by a wet-chemical technique. Three regimes can be distinguished: α-Mn_2O_3 + $LiMn_2O_4$, $Li_yMn_2O_4$ ($1 \le y \le 1.5$), and $Li_yMn_2O_4$+Li_2MnO_3, for $x \le 1$, $1 \le x \le 1.5$, and $x \ge 1.5$, respectively. The chemical diffusion coefficients are at least 10 times higher compared to $\tilde{D}$ values of powders made by solid state synthesis techniques. In addition, an interfacial diffusion enhancement has been observed in two two-phase regions near x=0.75 and x=1.75. The cathodes with these nominal compositions showed an improved reversibility, a higher capacity, and a lower Warburg impedance.

References

[1] J.R.Dahn, U.Von Stacken, and R.Fong, Abstract 42, p.66, The Electrochem.Soc., Extended Abstracts, Vol.90-2, Seattle, WA, October 14-19 (1990).

[2] T.Nagaura, 4th Int.Rechargeable Battery Seminar, Deerfield Beach, Florida (1990).

[3] Y.Nishi, H.Azuma, and A.Omaru, U.S.Pat.4,959,281 (1990).

[4] J.C.Hunter, J.Solid State Chem. 39 (1981) 142.

[5] M.M.Tackeray, W.I.F.David, P.G.Bruce, and J.B.Goodenough, Mat.Res.Bull. 18 (1983) 461.

[6] M.M.Tackeray, P.J.Johnson, L.A.de Piciotto, P.G.Bruce, and J.B.Goodenough, Mat.Res.Bull. 19 (1984) 179.

[7] T.Ohzuku, M.Kitagawa, and T.Hirai, J.Electrochem. Soc. 137 (1990) 769.

[8] J.M.Tarascon, E.Wang, F.K.Shokoohi, W.R.McKinnon, and S.Colson, J.Electrochem.Soc. 138 (1991) 2859.

[9] J.M.Tarascon and D.Guyomard, J.Electrochem.Soc. 138 (1991) 2864.

[10] E.M.Kelder and J.Schoonman, submitted for publication.

[11] W.Weppner and R.A.Huggings, J.Electrochem. 124 (1977) 1569.

[12] B.A.Boukamp, Internal Report, CT 89/214/128.

[13] Chen Liquan and J.Schoonman, Solid State Ionics 67 (1994) 17.

[14] D.Guyomard and J.M.Tarascon, J.Electrochem.Soc. 139 (1992) 937.

[15] P.Barboux, J.M.Tarascon, and F.K.Shokoohi, J.Solid State Chem. 94 (1990) 185.

[16] C.C.Liang and L.H.Barnette, J.Electrochem.Soc. 123 (1976) 453.

[17] G.Wang, Z.R.Li, L.Q.Chen, and Z.Y.Zhao, Acta Phys. Sinica 30 (1981) 1569.

[18] Chen Liquan, WangLianZhong, Che Guancan, Wang Gang and Li Zirong, Solid State Ionics 14 (1984) 149.

[19] L.Chen, X.Huang, E.M.Kelder, and J.Schoonman, to be published.

Effect of Cell Design on Cycling Life and Safety Behavior of Rechargeable Li/Li_xMnO_2 cells

Y.Geronov, E.Mengeritski, I.Yakupov and P.Dan
Tadiran Battery Division
P.O.Box 75, Rehovot 76100, Israel

Abstract

The effect of cell design on cycling life of Li_xMnO_2 AA cells is studied. It is found that an increase in depth of discharge of Li anode from 22% to 38% reduces the figure of merit from 80 to 60. At lower d.o.d the cells can be cycled about 300 times with 60/250 mA. A substantial improvement of the cycling life at low discharge rates is obtained by using charge current densities of about 0.1 mA/cm^2. The safety tests at abuse conditions show that the cells are safe independently on the accumulated capacity during cycling.

Introduction

In a previous communication [1] we showed that Li_xMnO_2 cathode can be cycled more than 500 times until the cathode capacity decreases from 170 to 120 mAh/g. In a practical cell e.g. in AA size this number of cycles drops substantially due to a limited efficiency of the Li (metal) anode.

A tremendous number of publications [2,3] was devoted to this problem. However the key to reach the maximum Li efficiency in practice is still not found. On the other hand safety of lithium(metal) rechargeable cells is still the subject of many concerns [4,5]. It is quite probable that the safety behavior of the Li secondary cells is closely connected to the Li cycleability and it is ruled out by the similar mechanisms. A recent study of Pasquariello et al [6] have shown that lithium does not contribute essentially in the heat evolution and that safety problems are mainly provoked by the electrolyte decomposition. These findings change a common understanding about the role of Li in the safety events of Li rechargeable cells.

This study is aiming to study: i) how the design of Li_xMnO_2 rechargeable AA size cell affects the Li cycling efficiency and ii) in what extent the accumulated capacity, respectively the Li surface influences the safety behavior.

Experimental

"Jelly roll" AA cells with various anode to cathode capacity ratio and a layer of "Celgard" separator were built in dry room. The different depth of discharge (d.o.d.) of the cells were obtained (for the same cathode mixture) by changing the cathode thickness respectively. the length of the rollon. The thickness of the Li foil was the same for all versions. The charge/discharge current density was the same for all cells and equal to 0.3 mA/cm^2 during charge and 1.0 mA/cm^2 during discharge. Cycling was performed galvanostatically in a voltage limit of 2 to 3.4 V.

A nondestructive method was employed to investigate the state-of-health during cycling of cells with different d.o.d. The method consists in measuring the cell impedance at 1000 Hz with a home made instrument.

A standard version of 0.75 Ah AA size cell specified as TLR-7301 was used for all safety tests. The safety behavior of the charged cells was studied at different amount of accumulated cycling capacity. The short circuit test was performed by cell shorting through 0.01 ohm. Cell current and temperature were recorded simultaneously. Overcharge and overdischarge were made at a constant current of 1000 mA by using a ten volt power supplier.

Results and discussion

Effect of lithium depth of discharge on its cycling efficiency

According to the well known equation, the relationship between the accumulated capacity during cycling and cycling efficiency of the Li anode, E, res. the figure of merit, FOM , is given by :

$Q_a = Q_{ex}/(1 - E)$ (1) respectively,

$Q_a = Q_{ex} * FOM$ (2)

In these equations the accumulated capacity, Qa is expressed as a sum of discharge capacities, q during cycling until the cell capacity drops to 65 % of its capacity at the second discharge; $Q_{ex} = Q_0 - Q_1$,where Q_0 is the capacity equivalent to the weight of the Li anode in the AA cell and Q_1 - the capacity used for lithiation of Li_xMnO_2 cathode during the first discharge. A typical value of Q_1 for our cathodes is 0.17 Ah/g

The expression (1-2) implies that for a certain electrolyte and at a constant cycling conditions the value of Qa should be independent of q if the Li cycling efficiency does not change during cycling.

It was of our special interest to understand how the depth of discharge of Li in AA size Li_xMnO_2 cells affects the Li cycling efficiency. Fig. 1 presents this dependence for the cells with different variation of d.o.d. The depth of discharge is calculated from the expression $q_a/(Q_0 - Q_1)$, where q_a is the average discharge capacity determined by dividing the accumulating cycling capacity by n.

It is obvious from Fig. 1 that the cycling efficiency, respectively. FOM strongly depends on d.o.d. The relationship between d.o.d. and FOM is linear in all range of studied d.o.d. A slight deviation from linearity was observed at higher d.o.d. An increase of d.o.d. from about 22% to about 38% gives rise to a decrease in FOM from 80 to 60 resp. the cycling efficiency, E from 0.987 to 0.983. According to eqs 1 and 2 the cycling number also decreases with d.o.d which is presented in the same figure.

A similar relationship was reported by Makrides et al [7] and Post and Takeuchi [8] for the AA size Li/TiS_2 accumulators.

For elucidation of the reasons for the discrepancy between the requirements of eq.1 and the experimental results obtained (Fig.1), the cell impedance at 1000 Hz was followed simultaneously during cycling. In order to consider a contribution of each electrode impedance to the overall cell impedance , preliminary impedance measurements at OCV of the charged cells in the range of 100 kHz to 0.1 Hz were

performed by using a Li/Li^+ reference electrode. It was observed that at 1000 Hz the impedance includes the electrolyte resistance and part of the anode impedance. The cathode impedance was negligibly small.

Fig.2 presents the cell impedance Z_{1000} as a function of the accumulated capacity during cycling at three different d.o.d. of 30, 38 and 47 %. As one could see from the figure the rate of impedance change with cycles is comparatively small in most part of the cycling life until a critical value of accumulated capacity is reached. Then at a certain amount of Qa a steeper increase of Z was observed. The increase of cell impedance coincides well with a higher rate of capacity dropping in the end of the cycling life (Fig 3). This led us to a suggestion that the anode is responsible for the observed increasing of cell impedance . Post mortem analysis of the cells confirmed our prediction. It was found that independent on the d.o.d. applied during cell cycling, the bulk Li was nearly completely exhausted and the anode lost its integrity even in the cell containing enough electrolyte after long cycling.Therefore the reduced amount of Qa found at higher d.o.d. is because of lower Li cycling efficiency as was shown in Fig. 1. The mechanism of this process is under investigation.

Cycling life at some special conditions

It is well known [9,10] that lithium rechargeable cells substantially reduced their cycling life at low discharge rates e.g. 15-20 hrs. Fig. 4 presents the results of cycling test of TLR -7301 cells at 40 mA discharge and 60 mA charge. All cells completed their life after 50-60 cycles because of much higher than permitted 10% difference between the charge and discharge capacity. This is considered [9] as an indication of a soft short circuit because of dendrite formation.. An improvement in the cycling life was obtained by using of a special separator (curve 2). Following findings of Juzkow [10], we cycled the cells with a charge current of 20 mA instead of 60 mA keeping the same discharge current of 40 mA. The results are summarized in curve 3 at the same figure. After 6 months the cells are still cycling collecting 170 cycles with an accumulated capacity of 120 Ah without appreciable disbalance between charge and discharge capacity. Considering a very low rate of impedance change in the last 100 cycles (see the same figure) it would be predicted that the cells could reach a cycling life close to that at the standard regimes(see also Fig. 2 and 3). This drastical improvement in the cycling life supports an idea that the formation of a thick passive layer on the Li surface during a long discharge is responsible for the dendrite formation and it could be overcome by reducing the charge current density to a value of about 0.1 mA/cm^2.

One of drawbacks of the Li rechargeable cells is their shorter cycling life at temperatures about 0 and 50 °C. Fig. 5 presents the results of cycling tests of TLR-7301 at 0°C and 45°C. The cycling was performed at the same conditions as at room temperature (60/250 mA). Because of higher electrolyte resistivity at 0°C the cell capacity was reduced by about 30%

Nevertheless more than 120 cycles were obtained at this temperature. After end of life the cells kept their reliability for cycling at RT delivering the remaining accumulated capacity.

Probably because of some acceleration of the passivation processes on Li and the electrolyte decomposition at higher temperature the cycling life at 45°C is reduced to about 150 cycles .

Safety behavior at short circuit at different Qa

In a series of papers [11,12] it was demonstrated that the probability of safety hazards for Li/Li_xMnO_2 and Li/MoS_2 accumulators increases with cycle number. Recently Laman et al [13] presented data showing that the termal stability of the cells decreases with accumulated capacity and only by using a safety low melting separator the peak temperature at short circuit experiment could be kept below a critical temperature at which explosion can occur.

Fig.6 presents a dependence of the peak temperature on accumulated capacity, Qa of our TLR-7301 Li/Li_xMnO_2 cells at short circuit through 0.01 ohm.The cells were prepared only with one layer of standard "Celgard" separator and were cycled as was described in the experimental. A very small increase in the peak temperature with accumulating capacity was found. An appreciable dropping of the peak temperature at short circuit was observed approximately after a half of the accumulated capacity probably because of cell impedance increasing (see also Fig.3). However even at the highest peak temperatures neither explosion or opening vent with fire were observed demonstrating very high safety reliability of our cells and its independence on the accumulated capacity during cycling. Similar to the finding in [6] this results suggest that the contribution of Li in the heat evolution is negligible if other factors as e.g. electrolyte decomposition could be limited during abuse conditions.

The preliminary short circuit test (Fig. 7) of a 2,5 Ah C size cell showed similar to that of AA size cell behavior. The cell was tested after 10 cycles. The temperature was less than 110°C when a smooth opening of the vent occurred. Compared to published results for C size $Li/LiMoS_2$ rechargeable cells[14] no external cooling or fuses were used in this experiment.

It is expected that the relationship between the peak temperature and accumulated capacity for our C size rechargeable cells is similar to that presented in Fig. 6. The experiments to clarified this dependence are well under way.

Safe test at overcharge and overdischarge

Fig. 8 shows the behavior of the cell at overcharge under a constant current of 1000 mA. The maximum temperature measured at the can was 120°C. At this moment of the peak temperature cell voltage raised to the cut off voltage of the charger of 10V. The cell was kept at this voltage about 30 min. more and no events were observed. By that time the temperature dropped and the charger was disconnected.

No events were observed also at 300-500% overdischarge with a current of 1000 mA. The cells exposed to these tests were not protected by electronic devices and reached in some cases -10 V without hazards.

Crush tests to 30% of the o.d. and nail penetration were performed and no fire, explosion or cell decomposition were observed.

Conclusions

AA size Li/Li_xMnO_2 (TLR-7301) rechargeable cells with maximum specific energies of 290 wh/l and 125 wh/kg were developed. The cells can be cycled at room temperature between 2 and 3.4 V more than 300 times at 3 hours discharge rate and about 150 times at 0 and 45°C. An average rate of capacity decline of 0.12 % per cycle was measured for

the most part of the cycling life.

AA size Li/Li_xMnO_2 (TLR-7301) rechargeable cells demonstrated safe behavior at abuse conditions as short circuit, overcharge and overdischarge as well as at crush and nail penetration. The preliminary tests with 2.5Ah C size cells showed also very safe behavior.

References

1. Y. Geronov, P. Dan, E. Mengeritski, Ext. Abstract 6th IMLB, Munster, Germany (1992)
2. M. Abraham and S. B. Brummer, in Lithium Batteries (Ed. J. Gabano), Chap. 13 (1983)
3. M. Abraham, Electrochimica Acta, 38, 1233 (1993)
4. K. Brandt, 5-th International Seminar on Li Battery Technology and Applications, Deerfield Beach, Florida, March (1991)
5. D. Fouchard, K. Brandt, L. Lechner, Ext. Abst. 180th Meeting AES, Phoenix Ar (1991)
6. P. M. Pasquariello, K.M. Abraham, E.B.Willstaed, D. Chen and S. Surampudi, Proc. Symposium on Li Batteries, ed. V. Koch, p.v. 93-24, p.106 (1993)
7. A. C. Makrides, K. M. Abraham, G. L. Hollek, T.H. Nguyen, R.J. Hurd, 34th Power Sources Symp. p. 167. Pennigton, New Jersey (1990)
8. J. Post and E. S. Takeuchi , 35th Power Sources Symp., Cherry Hill, N. J. (1992)
9. K. Brandt, M. Juzkow, Ext. Abstr. 5th IMLB, Beijing, China p. 180 (1990)
10. M. W. Juzkow, Ext. Abstr. 178th Meeting AES, Seattle, WA(1990)
11. D. Wilkinson, J. Dahn, U. v. Sacken, D. Fouchard, Ext. Abstract 178th Meeting AES, Seattle, WA (1990)
12. L. Lehner and H. Woo, Ext. Abstract 180th Meeting AES, Phoenix Ar (1991)
13. F. C. Laman, Y. Sakurai, T. Hirai, J. Yamaki and S. Tobishima, Ext. Abstract 6th IMLB, Munster, Germany (1992).
14. K. Brandt, D. Fouchard, J. A.R. Stiles, Proc. 31th Power Sources Symp., Atlantic City, New Jersey(1984).

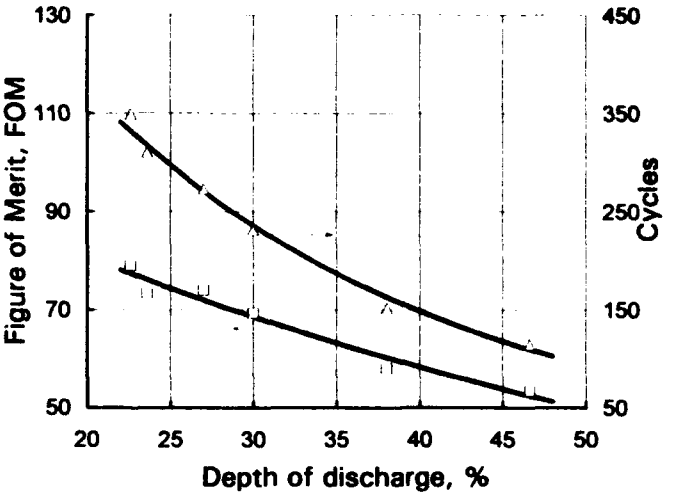

Fig. 1. Effect of depth of discharge, d.o.d., on Figure of Merit, FOM, and cycle number

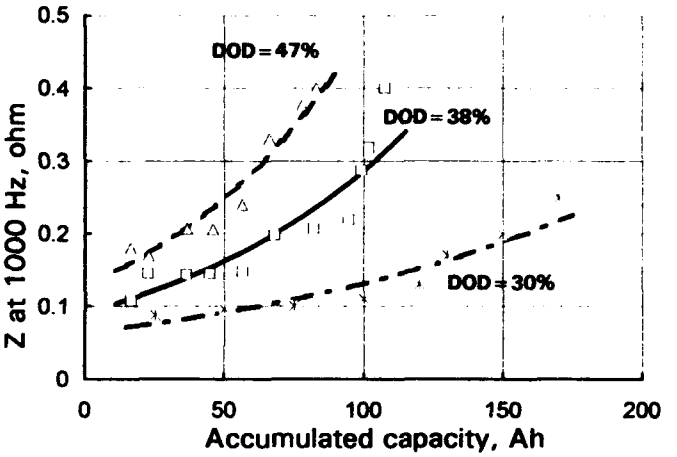

Fig. 2. Change of impedance at 1000 Hz with accumulated capacity at different d.o.d.

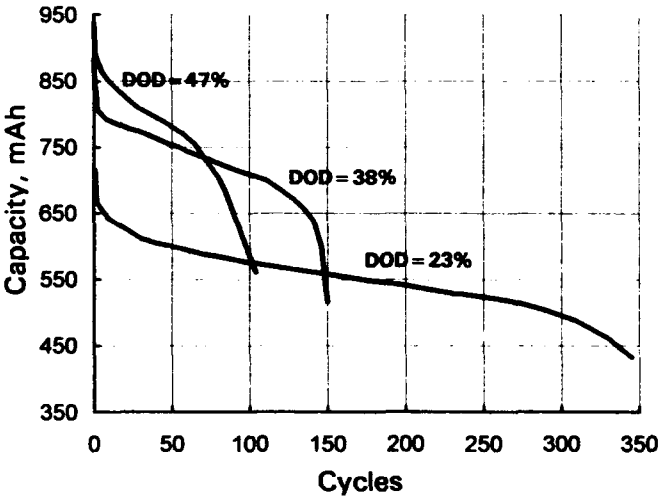

Fig. 3. Capacity - cycles dependence for AA size Li/LixMnO2 cells at different d.o.d.

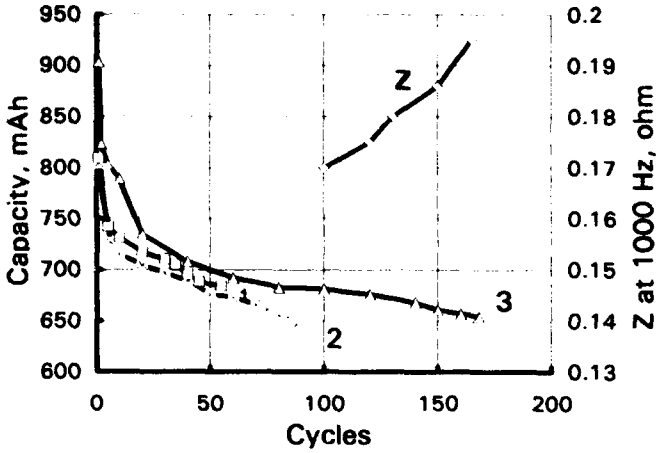

Fig. 4. Effect of low discharge rate (40 mA) on cycling life. Charge currents: 1 - 60 mA; 2 - 60 mA (special separator); 3 - 20 mA.

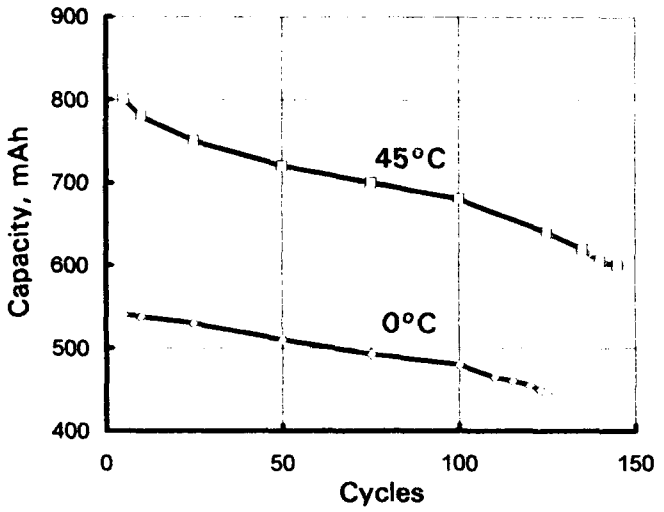

Fig. 5. Cycling of TLR-7301 at 0°C and 45°C.

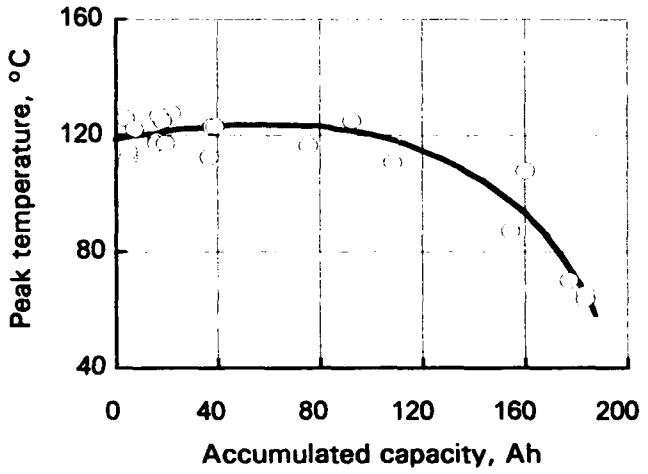

Fig. 6. Effect of accumulated capacity on peak temperature at short circuit test of AA size Li/LixMnO2 cells.

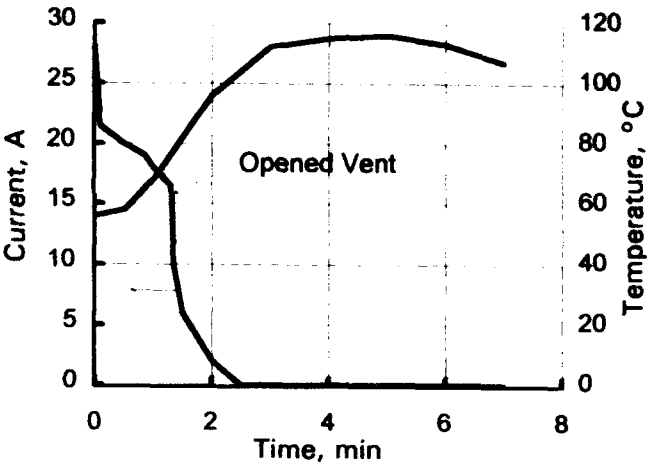

Fig. 7. Short circuit of a 2.5 Ah C-size Li/LixMnO2 cell.

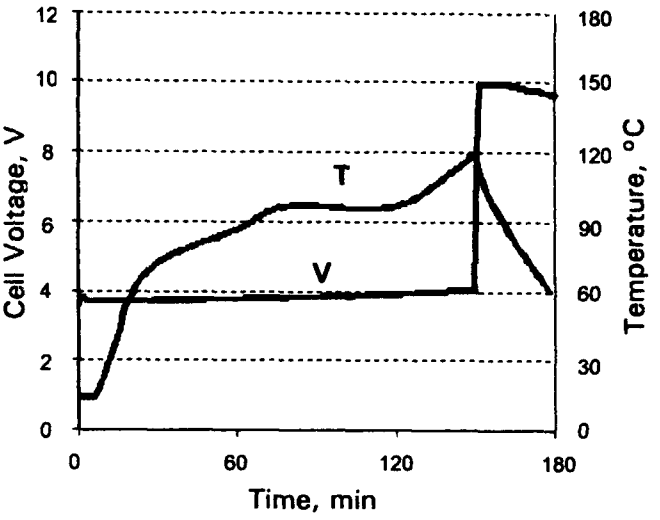

Fig. 8. Overcharge at 1000 mA after 60-th cycle. Power supply - 10V.

HIGH RATE BIPOLAR LITHIUM-ION BATTERIES

Sohrab Hossain
Yardney Technical Products, Inc.
82 Mechanic Street
Pawcatuck, CT 06379
and

Richard Marsh
Wright Laboratory
Wright Paterson Air Force Base
Dayton, OH 45433

Abstract

Lithium-ion rechargeable battery system has been examined in a bipolar configuration using petroleum coke and graphite anode and $LiCoO_2$ cathode materials in 1M $LiClO_4$ (PC/DME or EC/DMC) electrolytes. The continuous and pulse cycling behavior was evaluated. The effects of overcharge and overdischarge on performance was also examined.

Introduction

Since the first announcement of its commercialization, lithium-ion rechargeable battery system has received considerable interest. The use of carbon materials as anodes instead of metallic lithium provides excellent cycling efficiency and safety characteristics of the system. Li-ion moves back and forth between the lithiated transition metal oxide cathode and carbon anode in the presence of aprotic electrolyte during the charge/discharge process and no metallic lithium is plated.

Cathode reaction:

$$LiMO_2 \underset{\text{discharge}}{\overset{\text{charge}}{\rightleftharpoons}} Li_{1-x}MO_2 + xLi^+ + xe^-$$

Anode reaction:

$$C + xLi^+ + xe^- \underset{\text{discharge}}{\overset{\text{charge}}{\rightleftharpoons}} Li_xC$$

The Li-intercalation process involves three principal steps:

- diffusion or migration of solvated Li^+ ions to the Helmholtz plane of the double layer at the host lattice
- desolvation and injection of Li^+ ions into the vacancy structure at the near surface of the host, and
- diffusion of Li^+ into the bulk of the host lattice.

The inherent characteristics, e. g., slow intercalation process, organic electrolytes of relatively low ionic conductivity and non-metallic electrodes make the Li-ion system a relatively low rate system.

The rate of any battery system can be improved through the improvement of mass transport behavior (ionic path) and/or design parameters (electronic path). In an attempt to improve the rate capability, Li-ion battery system has been examined in a bipolar configuration. In bipolar design, there is

- no bus bars or intercell connectors
- insignificant resistance losses along or across electrodes
- minimal resistance losses in between cells, and
- uniform current and potential distribution.

The unique combination of the above characteristics minimizes uneven utilization of materials and prevents polarization losses that could lead to direct plating of metallic lithium on the carbon rather than intercalating into the electrode structure particularly at relatively high rate. Li-ion system in bipolar design is suitable for continuous high rate and high pulse power applications.

Experimental

The carbon materials used as anodes in this study were either petroleum coke (Conoco) or graphite (Lonza). The active carbon material was mixed with 5% polyvinyledene fluoride (PVDF) in cyclopentanone and spray-coated on copper substrate. The positive electrode was made from a mixture of $LiCoO_2$ (Johnson Matthey), carbon black and either PVDF or TFE binder. Microporous polypropylene (Celgard 2400) was used as separator.

The electrolyte was 1M $LiClO_4$ either in a mixture of propylene carbonate and dimethoxyethane (1:1 v/v) or ethylene carbonate and dimethyl carbonate (1:2 v/v). The electrolyte was stored under lithium chips at least 48 hours prior to activation of the cell. The water content of the electrolyte was less than 20 ppm (by Carl Fisher Coulometer).

Figure 1 shows the arrangement of a single cell Li-ion system in bipolar configuration. The negative and positive electrode plates (end plates of a true bipolar battery) were placed over each other with the separator in between them and compressed with the screws around the edges. A Teflon O-ring was used to seal the cell. The cell was vacuum-filled with the electrolyte through an opening at the top of the negative electrode plate. The opening was kept closed with a two-way valve. The geometrical electrode area is 70 cm^2.

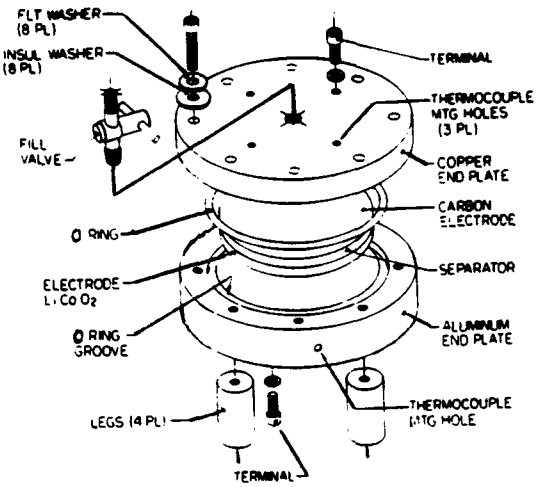

Fig. 1: Single Cell Arrangement

For multicell stack assembly, thin bimetallic substrate was used. The copper side of the bimetallic substrate was bonded with the lithiated cobalt dioxide cathode materials and the aluminum side with the carbon anode materials. High density polyethylene polymer ring was molded around the edges of the substrate, which was used for insulation and seal of each cell. After activation with proper amount of the electrolyte in argon-purge dry room area, the multicell bipolar stack was compressed using a flange around the edges. The compression provides good sealing. Additional sealing was assured by melting and bonding the outside polypropylene ring. Figure 2 shows the multicell assembly of the Li-ion bipolar battery.

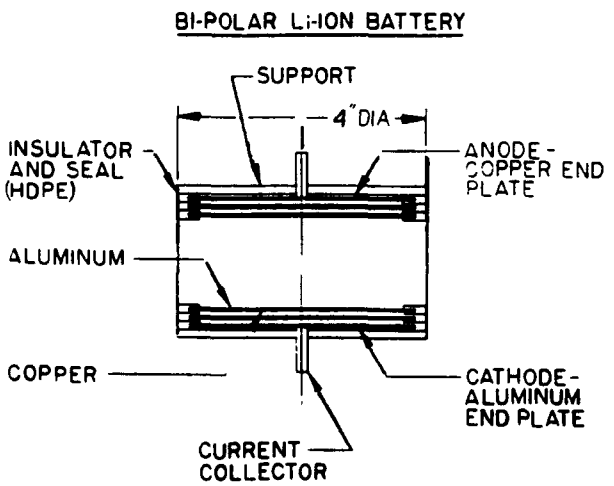

Fig. 2: Multicell Assembly

The electrochemical measurements for single cells were carried out using a Maccor 32-station cycler programmed with a computer to control duty cycle and to monitor and store data. A home-made cycler was used for multicell bipolar battery. The single cells and multicell batteries were galvanostatically charged and discharged between a specified voltage limits.

Results and Discussion

Single Cell Tests

Continuous Discharge Characteristics

Figures 3 and 4 show the second discharge profiles of two single cells made from petroleum coke and graphite anode materials, respectively. Both the cells were charged to 4.0 V vs. Li at 1.5 mA/cm^2 and then, after 5 minutes of rest period (at OCV), the cells were discharged to 2.75 at 1.5 mA/cm^2. The cell with petroleum coke anode had delivered a capacity of 255 mAh/g of carbon with a slopping discharge profile. Much higher capacity (336 mAh/g of carbon) was obtained from the cell with graphite anode and the discharge profile was almost flat.

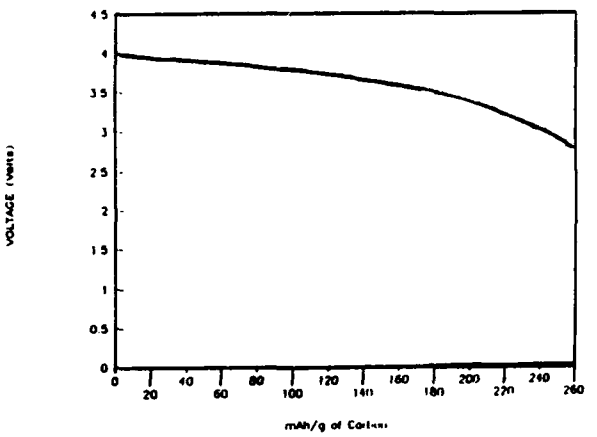

Fig. 3: Discharge behavior of a Li-ion single cell (end plates of a bipolar battery) at 1.5 mA/cm^2. Cathode: $LiCoO_2$; Anode: Petroleum Coke; Electrode Area: 70cm^2

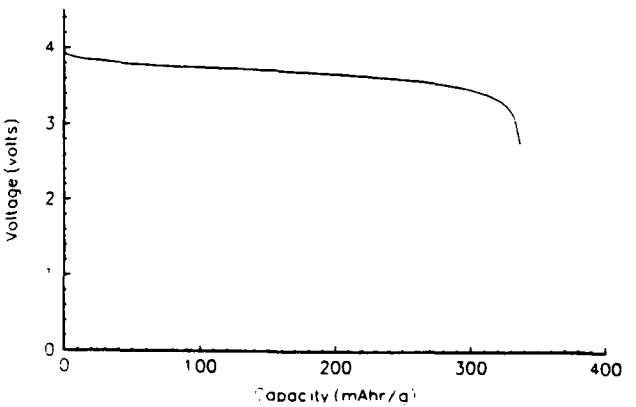

Fig. 4: Discharge behavior of a Li-ion single cell at 1.5 mA/cm^2. Cathode : LiCoO2; Anode: Graphite; Electrode Area: 70 cm^2.

Pulse Discharge/Charge Characteristics

The cell made with graphite anode was charged at 2 mA/cm² to 4.0 V and then continuously discharged and charged between the voltage limits 2.75 and 4.1 V for 3000 times. The cell was discharged at 45 mA/cm² for 5 seconds and charged at 5 mA/cm² for 45 seconds. The charge/discharge characteristics are shown in Fig.5. Figure 6 shows the end of discharge voltage vs. cycle number.

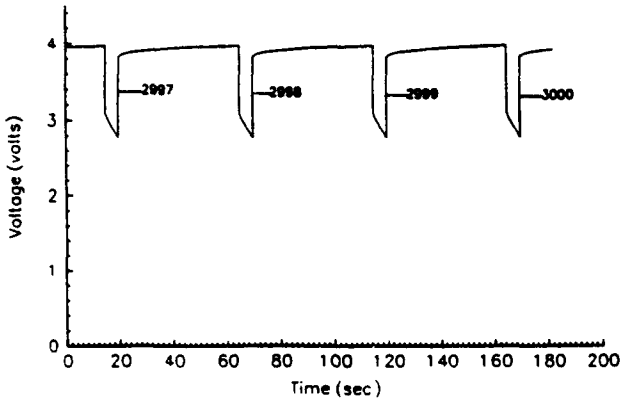

Fig. 5: Charge/Discharge behavior of a Li-ion single cell at 45 mA/cm² discharge for 5 seconds and 5mA/cm² charge for 45 seconds. Cathode: $LiCoO_2$; Anode: Graphite; Electrode Area: 70 cm²

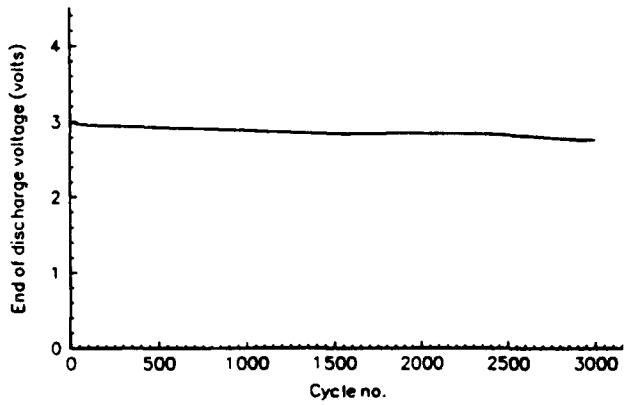

Fig. 6: End of Discharge Voltage vs. cycle number of a Li-ion single cell. Cycling conditions are as in Fig. 5.

Continuous Discharge Characteristics after Pulse Cycles

After 3000 pulse cycles, the cycling was intentionally terminated in order to examine again the continuous discharge behavior of the cell. The cell was charged to 4.1 V and then discharged to 2.75 V at 2 mA/cm². Figure 7 represents the discharge profile. The cell delivered a capacity of 334 mAh/g of carbon.

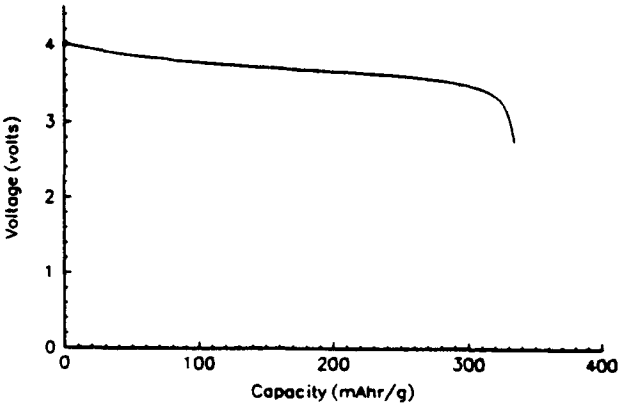

Fig. 7: Discharge behavior of a Li-ion single cell at 2 mA/cm² (after delivering 3000 pulse cycles).

Effect of Overdischarge/Overcharge

Figure 8 shows the effect of overdischarge of the Li-ion single cell made with graphite anode and $LiCoO_2$ cathode. The cell, after charging to 4.1 V at 2 mA/cm² (total charge capacity = 325 mAh/g of carbon), was allowed to discharge at 2 mA/cm² for 30 minutes and then a load of 50 mA/cm² was applied until the cell went to reversal. The cell was then again discharged at 2 mA/cm² for another 30 minutes (total capacity delivered in this discharge process = 153 mAh/g of carbon).

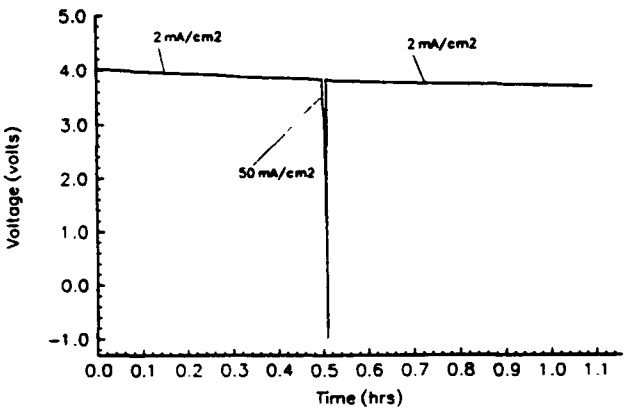

Fig. 8: Discharge/over discharge behavior of a Li-ion single cell.

The same cell was then charged at constant voltage of 4.1 V (current load went up to 0.85 Ampere, 12 mA/cm²) for 30 minutes and then at 4.9 V (current load went upto 2.4 Ampere, 35 mA/cm²) for 30 seconds and finally again at 4.1 V for another 30 minutes (total capacity in this charge process = 142 mAh/g of carbon). After overcharging, the cell was then discharged to 2.75 V at 2 mA/cm². The capacity delivered in this discharge process is 307 mAh/g of carbon. The variation of voltage and current with time for the whole operation is shown in Fig.9.

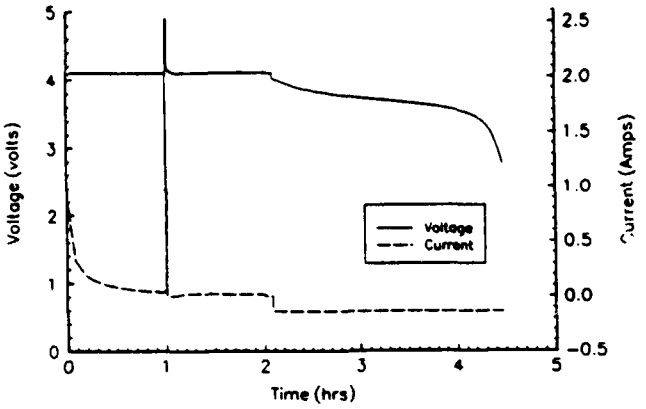

Fig. 9: Variation of voltage, current and time during charge/overcharge and discharge of a Li-ion single cell.

Multicell Stack Test

A four-cell stack bipolar battery was made with petroleum coke anode and $LiCoO_2$ cathode materials. The battery was cycled at 1.5 mA/cm^2 between the voltage limits 16.4 V and 11.0 V. The charge/discharge behavior of the battery is shown in Fig.10. The battery failed to cycle due to electrolyte leakage around the seal after delivering 72 cycles.

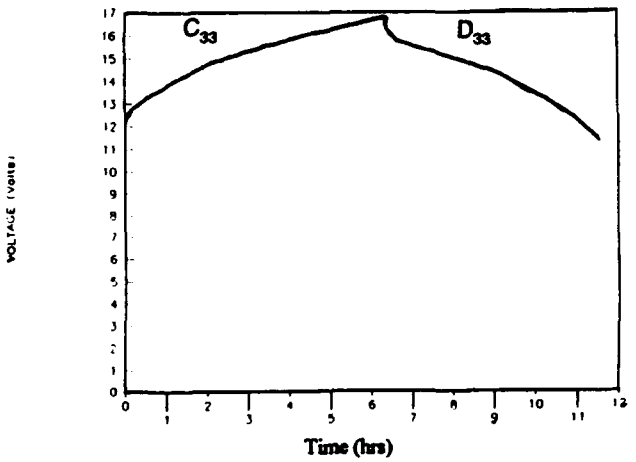

Fig. 10: Discharge behavior of a 4-cell stack bipolar Li-ion battery at 1.5 mA/cm^2. Cathode: $LiCoO_2$; Anode: Petroleum Coke

Summary

The test results indicate that Li-ion system in bipolar configuration

- can deliver excellent capacity even at relatively high rate of charge/discharge
- can deliver more than 3000 high rate pulse cycles
- can provide continuous charge/discharge cycles even after delivering several thousands of high rate pulse cycles
- can accept limited overdischarge/overcharge

Acknowledgement

The authors would like to thank Greg Kozlowski, Paul Paterno, Sheila Danahey and Hasmukh Patel for help in preparing cells and materials. This work was partly supported by the U.S. Air Force (WPAFB) under Contract No. F33515-91-C-2107.

Development of an Aluminum-air Portable Power Fuel Cell System for Field Charging of Military NiCd and Lead-acid Power Packs.

Stanley T. Winarski, STW Contract Services, 200 Antietam Court, Hampton, VA 23669
Dr. Bhaskara Rao, Explorex, 6 Finchley Court, Southampton, NJ 08088
Rene DuBois, Robert Martin, Chris Cestone, Pete Guggenheim; Alupower ,150 Mt. Bethel Rd. Warren, NJ 07059
Dr. Robert P. Hamlen, Director, Power Sources Division, USArmy Research Laboratory, Ft. Monmouth, NJ 07703

Abstract

This paper reviews the development of an aluminum-air field charger for military NiCd power packs. The electrolyte for this six cell device is prepared in the field using water from virtually any source to dissolve a packet of salt. The device, filled with the electrolyte, charges a military BB 590/U (2 Ah 24 V NiCd) Power Pack in 4 hours using pulse charging and a sophisticated charge termination routine. It contains no hazardous materials and it is reusable.

Introduction

Concept

The Special Technology Office of the Secretary of Defense for Command, Control and Communications (OSD-C3I, ST) directed the examination of aluminum-air technology to determine if it could be adapted for use as a field charger for Special Operations Forces. SOF require a charger that is highly reliable but one that places little demand on the operator so that he may attend to other business. The two charging technologies presently used by SOF, solar panels and hand cranked generators, have serious drawbacks which limit their operational usefulness. Both require direct operator involvement throughout the charging cycle. The use of solar panels is weather dependent. They require regular repositioning, and they risk exposing the operator's position to a searching enemy. Hand cranked generators, while more covert and weather and time of day independent, require rigorous operator effort to use.

The concept was to design a collapsible aluminum-air device that could have very long shelf life, occupy a minimum of space when not in use, and be stored and transported safely even when carried by troops being air dropped into operational areas. The concept called for the device to be able to be filled with electrolyte and emptied in the field. It was required to be capable of reliably charging a single BB590/U Power Pack (2 Ah, 24V NiCd battery) with each fill of electrolyte and have the capability of being used 7 times.

Background

Because of its high practical energy density (between 200 and 400 Wh/kg), aluminum-air technology has been under study and development for military applications for several years[1]. An earlier development effort resulted in the design of an alkaline based aluminum-air system capable of powering an EHF satellite communications radio.[2] That research demonstrated that man portable applications of aluminum-air technology were very feasible.

The key elements in all aluminum-air systems are the aluminum alloy anode which must operate at high columbic efficiency over a wide range of current density and an economical high performance air electrode. Figure 1 is a schematic diagram of an aluminum-air cell, with the chemical reaction at each electrode.

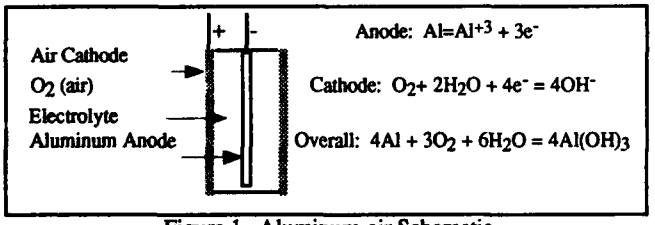

Figure 1 Aluminum-air Schematic

Development Program

Cell Development

Aluminum-air cells were developed through modeling and experimentations to define optimum performance characteristics for this application. Bearing on this analysis were issues of current density, electrolyte volume, surface area and volume of anode, anode-cathode gap spacing, heat management, considerations regarding filling and emptying, and weight and volume constraints.

Electrodes: Alcan AB alloy was selected for the anode for this application. This alloy has low polarization loss, low self-discharge and high (70-75%) utilization efficiency in this application. The cathode used was Alupower's AC65 gas diffusion electrode (Figure 2). This electrode consists of two layers of impregnated carbon fibers covering both faces of a nickel grid current collector. The air side is a hydrophobic Teflon® coating to prevent electrolyte leakage.

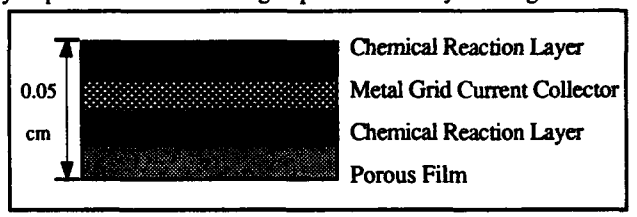

Figure 2 Cathode Composition

Heat Management: The chemical reactions that occur in aluminum-air cells are exothermic, with heat and power released in generally equal quantities. Heat management was achieved by natural convection of the electrolyte within the cell. The results are that the cells reach a steady state of 42°C, well below the targeted maximum operating temperature of 65°C.

Cell Construction: Analysis of cell construction methods proved a more complicated task than the cell chemistry. To obtain the surface area and the capacity needed, cells approximately 8" x 5" by 0.5" thick capable of containing 300 ml of electrolyte were needed. Because of the large surface areas required for the cathode and anode and the restrictions on the overall size of the device, it was essential to minimize the amount of inactive surface area, volume, and material weight.

Three solutions were devised. Two versions feature a composition skeleton frame assembly, one of extruded and the other of machined plastics, which serve as a housing for the anode and as a two sided "picture" fame to which the cathode is attached to both faces by adhesives. The third version is a single face unit of molded epoxy with the edges of the cathode molded in. Two frames are fused together around a centrally positioned anode to form a single cell.

High initial set up costs precluded furthering this line of research beyond identifying acceptable candidate manufacturing solutions. For the proof-of-concept prototypes delivered under the contract, an unframed cell was devised. This cell consists almost totally of cathode material, folded at right angles at the bottom and sides and glued to form an open, box-like envelope (Figure 3). It works so well that it may be the configuration of choice when this device enters manufacturing.

Collapsibility: The initial concept was to design a collapsible unit in which at least the air space between cells could be eliminated

when the unit was prepared for transport. Ideally, even the anode-cathode gap (which is empty when the device is not in operation), would be closed. This seemed necessary based on early analysis which suggested the cells would need to be larger than proved necessary.

This became less important as much thinner cells were required for this application (0.5") than had been anticipated and the required air space between them was also substantially reduced (0.25"). Attempts to incorporate collapsibility within these already compact cells caused severe problems with regard to manufacturability and cost, as well as in the design of a filling and draining solution. No economical solution was found at the time and that aspect was abandoned.

A fixed cell configuration was therefore adopted consisting of cells 0.5" thick with a 0.25" space between them capable of supplying the approximately 12.5 Ah discharge at 1.0V per cell required. A header top plate was fabricated onto which the cells are mounted and fastened in place with adhesives. The plate has an opening at one end to facilitate rapid filling and draining of the cells.

Electrolyte Development: Preliminary investigations led to the formulation of a trisodium citrate-based saline electrolyte. Although this met the operating requirements of the charger, testing revealed that if the cells were not drained soon after being used to full capacity (worse case performance - charging a NiCd that had been drained further than normal), the electrolyte gelled in the cell precluding their reuse. Because of the requirement to reduce the overall size of the cells, the cells were configured to contain only the minimum volume of electrolyte. When stressed to full potential, the electrolyte performed its mission but the accumulated volume of aluminum hydroxide in solution saturated it and precipitated as a gel. This was unacceptable. The soldier in the field needed a wider margin for error. In addition, the total weight of trisodium salt needed to enable the chemical process in each of the seven cycles of use exceeded the weight limits established for the program. It was necessary to devise an improved electrolyte.

New Formula: Experiments were conducted varying the cation in the electrolyte, varying the complexing agents, mixing of complexing agents, and employment of partially neutralized citrate or citric acid. This work resulted in creation of a new electrolyte using 3 wt% sodium chloride with 12 wt% disodium monohydrogen sesquihydrate, a commercially available salt. This new patented electrolyte not only eliminated the gelling problem during rated use of the charger, it also reduced the weight of required salt for the 7 cycles by almost 38%. Further weight reduction of 10 % could be possible should a commercial source for anhydrous citrate could be found.

Cold Weather Electrolyte: Cold condition experiments corroborated that the electrolyte conductivity decreases during extremely cold conditions. Voltage delivered by the charger was reduced to 2.5 V. However, as the electrolyte warms up due to the heat released during the cell discharge, the voltage improves. A special Cold Weather electrolyte was devised adding a portion of Sodium Hydroxide. The heat generated by neutralization of the acid and the base during the dissolution of the salts warmed the solution so that the cold start problem is eliminated.

Fill and Drain Mechanism Development

To ensure satisfactory field performance, the charger must be capable of being filled and drained easily and rapidly. The narrow cell gap, the need for six cells, and the requirement that there be air space between the cells during operation of the charger compounded the issue of how to fill and drain the unit. This issue was already complicated by the need for the electrolyte level in each cell to be relatively equal. An electrical shunt path between the cells was not acceptable. The electrolyte in the cells had to be isolated one from another.

A simple solution was devised which accommodates a very wide margin for error when operated in the field. A low box frame has been formed in the cell top plate. The box is covered with a hinged lid. (See Figure 3) To fill the charger, the soldier opens the lid exposing the openings into each of the cells, pours the electrolyte into the box only needing to be careful to ensure that none of it is spilled outside the box. The liquid will find its own way into the cells, overfilling some and under filling others. After pouring all the electrolyte into the box, the soldier snaps the cover down and tips the entire charger to the side permitting the electrolyte to flow back into the box finding its own level. When the unit is righted, the liquid will fill each cell with equal amounts of electrolyte.

The closed box serves as a catchment manifold and condenser for water vapor generated during operation of the device enabling it to return to the cells as a liquid.

Power Conditioning and Management

Options Developed: Several methods were devised to convert the output of various aluminum-air cell configurations to the level of power and energy required.

One method involved using 14 smaller cells. This result unit produced 15V capable of charging the NiCd at the 3 hour rate. This used a constant current charge routine to feed power to the NiCd until it reached "saturation" at its rated capacity. This procedure works well with saline based aluminum-air technology since the aluminum-air cells can be designed to specific performance parameters.

One excursion with this configuration explored using the Power Supply Adapter (PSA) to furnish more positive cutoff control and to positively reduce the charging current to 200 mA when the BB 590/U voltage reaches a preset temperature compensated limit. The PSA is from the government's OP-177/U Power Supply Assembly, the kit containing the solar panel arrays and hand crank generator currently issued to SOF units. This approach was abandoned after repeated failures of the two PSA furnished by the government. These were both early production items loaned to the program from a static display. Follow up research in this area may be appropriate in view of the fact that the OP-177/U remains in the SOF inventory.

Selected Design: The configuration selected for incorporation into the demonstration models employs 6 aluminum-air cells in series to generate 6 V at 6 Amp.

DC/DC Conversion: A DC/DC converter, designed by Wall Industries, Inc., Exeter, NH, converts the output of the cell stack to 28 Volts. The output of the DC/DC converter in series with the 6 Volts directly from the cell stack results in 34 Volts, 0.75A. This supplies the power and energy needed to charge a fully exhausted BB 590/U in about 4 hours.

Charge Protocol: The heart of the control electronics is Integrated Circuit System's ICS 1700 Charge Controller, a 16 pin DIP large scale integrated circuit which uses Christie Electric Corporation's patented Reflex® principle of charging and time derivative charge termination. This control module simplifies the charging task for the soldier. It determines autonomously when full charge has been attained and automatically switches to a maintenance mode. LED displays indicate the charging activity, alerts the soldier to faults in the NiCd or in the connections.

Packaging

Cell Housing: A molded housing to protect the cell stack was designed to be light and rugged and ensure that the cells would be able to "breathe". This cell housing fastens to the cell top plate, a molded unit configured so that 6 cathode cell shells could be attached to it to align them with the fill and drain openings. This top plate contains the fill trough and space for the power management and charge control electronics. It contains a protected area in which the connections between the anode of one cell is connected to the cathode of the adjacent cell. It also provides a dock into which the power conditioning and charge management power module can be inserted.

Power Management Component: The concept for the charger specified that it would be discarded after its last use. However, the

electronics are not depleted during use and are reusable almost indefinitely. Rather than waste these components, the design was modified to consolidate the electronics into a self contained module. The cell top plate was modified to permit easy "slip in and slip out" of the module. (See Figure 3) Once a charger has been exhausted in the field, the power module can be removed and retained for reuse with other cell stacks.

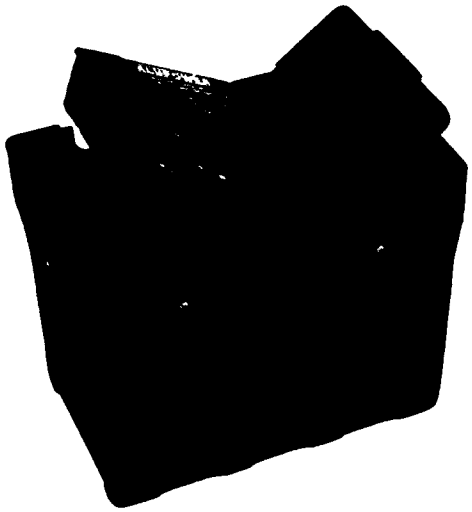

Figure 3 Final Package Design

Salt Packets: The development of the new electrolyte permitted reduction in the volume of salt needed to support the discharge process that occurs in the aluminum-air cells. It was determined that 2 grams of complexing agent is needed in the electrolyte for each ampere-hour discharge of the aluminum-air cell. Sodium chloride is needed at about 3-5 % by weight to provide the required conductivity in the cells. Measured quantities of these salts were prepared and placed in moisture-proof polymer film bags and heat sealed. The heat seal is torn off in the field when the electrolyte is to be mixed with water. To prevent any of the salt from being lost during the tearing process, the bag contains a second pressure sensitive seal just below the heat seal. That is spread open after the heat seal is torn off, and the salt can then be poured into the electrolyte mixing container.

Mixing Container: A collapsible opaque vinyl wide mouth bottle is supplied. It serves as a water collection vessel, is marked for measurement of the correct amount of water for each cycle, and provides a container for mixing the salt and water prior to pouring the solution into the cells.

NiCd Connector: A cable with color coded plugs is supplied to connect the NiCd to the aluminum-air charger.

Testing and Evaluation

Developmental Testing: The charger supplied 2.30 Ah into the NiCd power packs, which produced 2.05 Ah on discharge. This equated to about 85% efficiency. Operating the device presented no difficulty. It filled and drained successfully and showed tolerance for abuse. A wide range of water quality was used for electrolyte, to include muddy ground water taken from vehicle tracks at a construction site. The device worked well during hot and cold testing. The salt packages, mixing container, and cable each work well.

Government Testing: Government testing was conducted at the Electrochemical Power Systems Department, Naval Surface Warfare Center, Crane, Indiana. Partially depleted and full exhausted NiCds were charged with excellent results. One test was conducted charging a prototype super NiCd (3.0Ah) with total success. Because of a special interest in lead-acid batteries at Crane, one test was conducted charging a 1.8Ah BB 490/U lead-acid power pack. The Power Module was modified in the field to bypass the ICS 1700 chip and successfully directly charged the battery. Hot and cold testing substantiated earlier testing results.

User Evaluation: Demonstration models of the chargers were field tested by soldiers of the USA Special Operations Command. Every soldier who tested the device praised its performance and reported that it would fill a very real need on the battlefield and that they would like to have this capability for charging batteries in the field. The demonstration models, however, were deemed to be too bulky in their present prototype configuration. They recommended that the device be repackaged as separable smaller modules for ease of packing.

The Evaluation Report stated that the aluminum-air technology would be a "substantial improvement" to the Special Operations Power Sources (OP-177/U) currently fielded to Special Operations Detachments and that it has "extremely promising potential".

Future Plans: Teaming partners with experience in packaging are being sought to complete commercialization of this device. Phase II designs now incorporate an elongated cell stack which, when not in use, will fold flat like a book eliminating the air space between each cell. During operation, it will fan open allowing air to circulate between the cells. The Power Module will be a totally separate component, capable of charging either a NiCd, lead-acid, or metal hydride battery. It will connect to the cell stack and to the battery by a wire harness. Alternative charging protocols have been examined and there are many that can be employed. Efforts to marry aluminum-air technology with Electronic Power Technology's (EPTI) impressive new charging process are underway.

Conclusions

This development program shows that aluminum-air technology employing saline electrolyte can be configured successfully in man portable applications to meet real needs of customers.

Acknowledgements

The success of this development program was made possible by contributions from a host of people who became enthused with the concept and devoted their efforts and talents to ensure success. The management, scientists and engineers of Alupower. Tom Gossie & Bob Rex, Integrated Circuit Systems, Valley Forge, PA. Scott Marvel and Bill Monagle, Christie Electric, Gardena, CA. Susan Melvin, Wall Industries, Exeter, NH.

References

1. J. Stannard and G. Deuchars, "Low Power Fuel Cell Study", Dept. of Def., EHF Satcom R&D Project, Ottawa, Canada, August 17,1990.

2. B.M.L. Rao, et al., "Aluminum-air Batteries For Military Applications", Proceedings, Power Sources Symposium, Cherry Hill, NJ, June 22-25, 1992.

High Energy Density Primary Zinc–Air Battery Characterization

Terrill B. Atwater
US Army Research Laboratory
Electronics and Power Sources Directorate
ATTN: AMSEL-EP-PA
Fort Monmouth, NJ 07703

Ronald A. Putt
MATSI, Inc.
430 Tenth Street NW
Suite S-007
Atlanta, GA 30318

Deborah Bourland and Bob Bragg
National Aeronautics & Space Administration
Lyndon B. Johnson Space Center
Houston, TX 77058

ABSTRACT

The ever increasing use of portable communications equipment and portable computing devices as well as remote monitoring and sensing equipment has increased the need for a high energy density power source. The development of advanced capability zinc–air batteries helps fill the need for high energy sources that also supply sufficient power to operate the new generation of portable equipment. Current state-of-the-art zinc–air batteries designed by MATSI, Inc. for NASA–JSC have been characterized for their energy and power density. These batteries have achieved an specific energy of greater than 500 W·hr/kg (520 W·hr/l) and can deliver 24 W/kg (25 W/l) of power at a specific energy of 200 W·hr/kg. This power and energy density capability makes state-of-the-art zinc–air batteries suitable for the portable communications and electronics market.

INTRODUCTION

Due to its inherent safety and high specific energy density, the zinc–air (oxygen) electrochemical system is a very attractive energy source. However, for most portable power applications both energy and power are required. This requirement has excluded zinc–air electrochemical systems available to date. NASA–JSC has contracted with MATSI, Inc. to develop a commercially viable zinc–air cell which will meet present demands of power and energy required by portable electronic equipment.

Historically zinc–air cells have been produced in two configurations; very low rate cells, used for industrial batteries, and button cells, used primarily in hearing aids. Both of these cells are designed for their specific applications and do not supply the power needed for portable electronics. Next generation primary zinc–air batteries, developed by MATSI, Inc., overcome the rate limitation of industrial cells and capacity limitation of button cells.

Initial efforts resulted in the development of two cell sizes, Large Capacity (LC) cells with greater than 200 A·hr at 6 milliamperes/cm^2 and High Rate (HR) cells with a capacity of 30 A·hr at 14 milliamperes/cm^2. Table 1 lists the dimensional aspects of each cell type along with performance characteristics. These cells are prismatic, with the electrodes fitted into machined plastic cell cases. They can then be stacked to achieve the application-specific requirements for the final battery. This flexible design allows for tailoring battery designs and configurations.

Design Specifications for
LC and HR Zinc–Air Cells

	LC Cell	HR Cell
Battery Surface	13 cm. × 25 cm.	6 cm × 12 cm.
Active Surface	290 cm^2	55 cm^2
Thickness	0.8 cm.	0.7 cm.
Weight	540 g.	93 g.
Spacer Thickness	0.8 cm	0.6 cm.
Capacity	200 A·hr @ 2 A.	30 A·hr @ 1 A.
Specific Energy	440 W·hr/kg	375 W·hr/kg

Table 1. Design and performance specifications for LC and HR zinc–air cells.

The design flexibility of this system has led to the development of a third cell size which will supersede the previous designs. The specifications of this new cell, designated MAC, are shown in Table 2.

Design Specifications for
MAC Zinc–Air Cells

	MAC Cell
Battery Surface	9.25 cm. × 8.5 cm.
Active Surface	55 cm^2
Thickness	1 cm.
Weight	125 g.
Spacer Thickness	.5 cm.
Capacity	37 A·hr @ 1 Amps. 32 A·hr @ 2 Amps.
Specific Energy	340 W·hr/kg @ 1 A. 270 W·hr/kg @ 2 A.
Energy Density	540 W·hr/l @ 1 A. With out spacer
Maximum Output Power	3 W @ 3 Amps.
Power Density	24 W/kg @ 3 Amps. 38 W/l @ 3 Amps.

Table 2. Design and performance specifications for MAC zinc–air cells.

This paper will present performance characterization data of the enhanced capability zinc–air cell.

BACKGROUND

As described in earlier work[1-3], the advanced capability zinc–air cell design consists of: 1) an anode and electrolyte mixture consisting of a paste of amalgamated zinc powder in a gelled potassium hydroxide electrolyte, 2) a microporous polymeric separator and 3) a PTFE-bonded carbon cathode. These components are configured as a prismatic cell in a molded plastic case.

Experiments described in earlier work were used to determine the optimum electrode and electrolyte formulations. Test cells, with different zinc content, were fabricated and discharged. The resultant plot of capacity versus weight percent zinc showed that a energy density maxima occurs at a zinc concentration of 70 weight percent[1-3].

Additional experiments were designed to optimize the potassium hydroxide concentration. These experiments were designed to examine the electrolyte's sensitivity to the ambient humidity. The data showed that a potassium hydroxide concentration of 35 weight percent achieved higher anode utilization and was less sensitive to the ambient humidity[1-3].

The oxygen electrode consists of two layers producing a high performance oxygen electrode. The electrolyte side of the cathode includes a high surface area carbon for oxygen reduction and a metal oxide catalyst for peroxide decomposition. The air side of the cathode has a higher PTFE content to prevent electrolyte weepage[1]. The oxygen electrode was also studied by examining cell performance with and without a peroxide decomposition catalyst. This study showed the cells with the catalyst out performed the cells without; the cells with the catalyst had improved voltage and better anode utilization[1-3].

The resultant cell has the capability of high rate discharge wile maintaining the high energy density of the zinc–air electrochemical system.

EXPERIMENTAL

Two zinc–air cell types, LC and MAC, were tested to determine the discharge characteristics of the advanced capability zinc–air cell. Tests were designed and conducted to determine the cells' capability to operate portable electronic equipment. Initial tests performed on LC cells were conducted at various discharge rates and temperature to determine the viability of the system for portable power. Additional testes on MAC cells were conducted to characterize the system.

Initial characterization tests were performed to determine the power verses energy curve for the LC cell. The cells delivered 480 W·hr/kg at a discharge rate of 0.8 W/kg (1.7 mA/cm^2) and 300 W·hr/kg at 18 W/kg (21 mA/cm^2). The power density for these batteries is low, however the high energy density achieved warranted further investigation of the system. Subsequent testing of the MAC cells showed that the system could produce 24 W/kg (55 mA/cm^2) power while maintaining 200 W·hr/kg of energy. Figure 1 shows the Watt/kg versus Watt·hr/kg curve for both the LC and MAC cells.

Specific Power Vs. Specific Energy Curves
For LC and MAC Zinc–Air Cells.

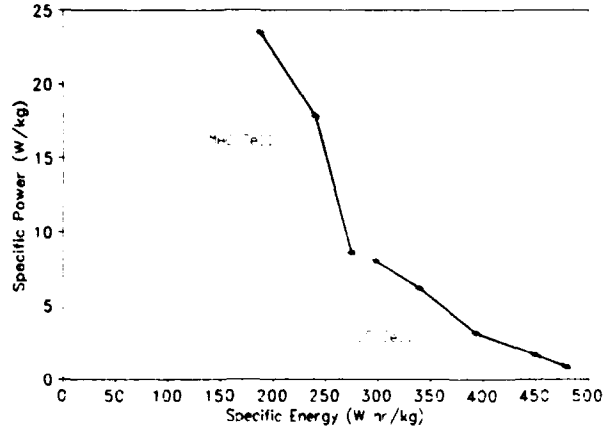

Figure 1. Specific power versus specific energy for LC and MAC zinc–air cells.

Prior to the power-versus-energy data collection MAC cells were used to determine the polarization and power curve for the zinc–air system. Figure 2 shows the polarization curve and power profile of the MAC cell. Peak power is achieved at 3.2 amperes at 3.0 watts, corresponding to 24 W/kg at 58 milliamperes/cm^2. This promising energy density led to continued testing of the system.

Polarization and Power Curve for
MAC Zinc–Air Cell.

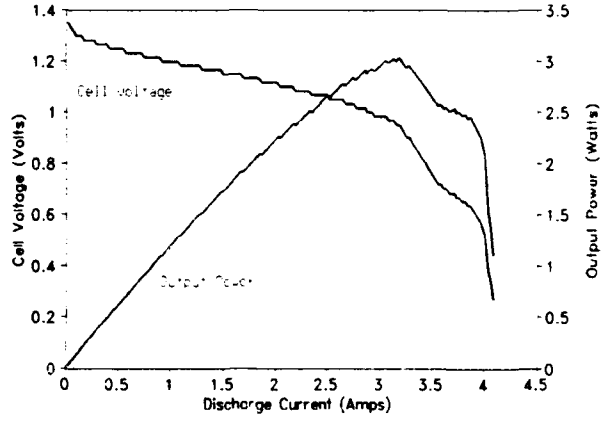

Figure 2. Polarization and power curve for MAC zinc–air cells.

MAC cells were discharged at 1.0, 2.0 and 3.0 Amperes at 25°C and 1.0 Ampere at 0°C. Figure 3 shows typical discharge curves for the MAC cell. This graph shows little loss of capacity from 1.0 ampere discharge to 3.0 ampere discharge, i.e. 30 Amp·hrs and 24 Amp·hrs respectively. Cells discharged at 1.0 ampere at 0°C achieved capacities in the order of 16 Amp·hrs.

Typical Discharge Curve for
MAC Zinc–Air cell at 25°C

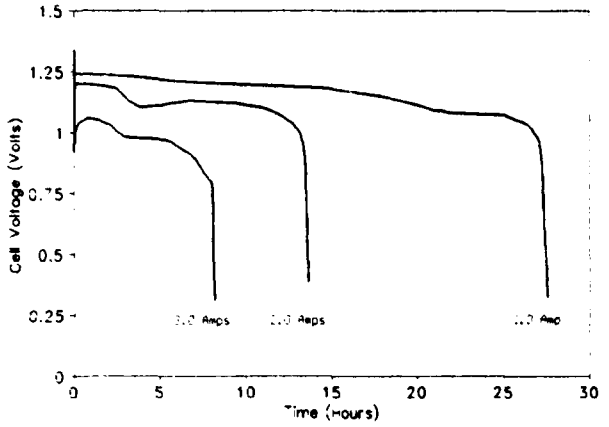

Figure 4. 1.0, 2.0 and 3.0 Ampere Discharge curves for MAC zinc–air cells.

DISCUSSION

Both energy and power are required for most electronic equipment. In addition portable electronic equipment puts weight and volume constraints on the power source. The zinc–air cells tested showed that they can deliver both the energy and power required for electronic equipment and this energy and power are available in a small, light-weight packages.

The MAC cells tested had a specific power of 24 W/kg (25 W/l). These cells also have an energy density of 500 W·hr/kg (520 W·hr/l). Additionally the cells suffered minimal capacity loss from a discharge rate of 1.0 ampere to 3.0 amperes. The cells also maintained a respectable capacity when discharged at 0°C, i.e. 50% of the 25°C capacity.

These encouraging characteristics led to the fabrication of a six cell battery that would operate a laptop computer. The battery pack was designed to replace a rechargeable external battery pack. The zinc–air battery, comprising six MAC cells, has approximately the same weight and volume as the battery it replaces (862 g. and 18.3 cm. × 26.0 cm. × 1.3 cm.). However the rechargeable battery has an operating time of 5 hours of less while the zinc–air battery has an operating time of 30 hours.

Prototype laptop computer batteries were fabricated and tested. The batteries were tested under simulated load conditions, some simulating a black and white (B&W) computer load and some were tested simulating a color computer load. The average load for the B&W computer is 1.2 amperes and 2.0 amperes for the color computer. The zinc–air battery realized its potential and delivered 26 hours of service and 14.5 hours of service for the B&W and color computers respectively.

CONCLUSION

The advanced capability zinc–air cell developed by MATSI, Inc. has shown that zinc–air technology is capable of powering portable electronic equipment. Batteries comprising of six MAC zinc–air cells have been demonstrated in laptop computer applications. The power density and energy density of this zinc–air design enables its use not only in portable electronics equipment but also in high pulse power/high energy hybrid battery systems. These hybrid systems would use the energy density and power capability of the zinc–air system coupled with a very high power rechargeable battery. The zinc–air battery would supply the base energy as well as energy to recharge the pulse battery while the high power pulse battery would supply the high power pulses whenever required by the system.

REFERENCES

1. Bob Bragg, Debbie Bourland, Glenn Merry and Ron Putt, "Primary Zinc–Air Batteries For Space Power", The 1991 NASA Aerospace Battery Workshop, NASA Conference Publication 3140.

2. Ronald Putt and Glenn W. Merry, "Zinc–Air Primary Batteries", Proceedings of the 35th International Power Sources Symposium, IEEE, Piscataway NJ, 1992.

3. Ron Putt and Glenn Woodruff, "Zinc–Oxygen Battery Technology", Proceedings of the 28th IECEC, Atlanta GA, ACS, Washington DC., p 1.1085, 1993.

A HIGH ENERGY DENSITY ALUMINUM/OXYGEN CELL

Daniel W. Gibbons and Eric J. Rudd, ELTECH Research Corp., 625 East St., Fairport Harbor, OH 44077
Dane Gregg, Loral Defense Systems - Akron, 1210 Massillon Road, Akron, OH 44315

Abstract

Aluminum is an attractive anode material for metal/air batteries, particularly for propulsion applications where weight and volume are crucial. With a higher specific energy than nearly all other metals, it is also environmentally acceptable, non-reactive, and presently available in large production quantities. A closed cycle aluminum/oxygen system is currently under development for an unmanned, underwater vehicle (UUV) with more than three times the energy density of existing silver/zinc batteries. Recent work has focussed on low corrosion aluminum alloys and an Electrolyte Management System (EMS) for processing the byproducts of the energy producing reactions. Single cells have produced nearly 6000 Amp-hrs from a single aluminum plate at 97% current efficiency.

Introduction

Aluminum, zinc, lithium, and iron systems have all been demonstrated, but only aluminum provides a high energy and power density in an environmentally acceptable package that is easy to handle, safe to operate, and readily available. The chemistry of the Al/O_2 integrated fuel cell system is shown below. The net result of this reaction sequence is the consumption of aluminum, oxygen, and water to produce aluminum trihydroxide and energy.

Anode	$Al + KOH + 3OH^- \rightarrow KAl(OH)_4 + 3e^-$	(1)
Cathode	$3/4\ O_2 + 3/2\ H_2O + 3e^- \rightarrow 3OH^-$	(2)
Overall	$Al + KOH + 3/4\ O_2 + 3/2\ H_2O \rightarrow KAl(OH)_4$	(3)
Corrosion	$Al + KOH + 3H_2O \rightarrow KAl(OH)_4 + 3/2H_2$	(4)
Crystallization	$KAl(OH)_4 \rightarrow KOH + Al(OH)_3\downarrow$	(5)
Recombination	$H_2 + 1/2O_2 \rightarrow H_2O$	(6)

During cell discharge, aluminum is dissolved (Equation 1) to form an aluminate species while the alkali metal hydroxide is consumed. A corrosion reaction also occurs, again forming the soluble aluminate together with hydrogen gas (Equation 4). This corrosion reaction is a coulombic inefficiency and, therefore, must be minimized. Since KOH is consumed as the battery operates, the conductivity of the electrolyte decreases until precipitation or crystallization of aluminum trihydroxide occurs (Equation 5) , replenishing "free" hydroxide. Thus a "steady state" condition may be achieved with respect to electrolyte composition and conductivity, at which time the electrolyte will contain crystals of aluminum trihydroxide (hydrargillite). As will be discussed later, controlling the electrolyte composition is very important to maximize performance. In addition, hydrogen destruction by recombination is necessary for closed cycle applications where simple venting is not practical.

A complete Al/Air power source is a multi-component system that includes several unit operations such as thermal management, solids removal, and gas-liquid separation as indicated in Figure 1. Aluminum cannot be electrodeposited from aqueous solutions, so that the Al/Air battery is not a true secondary battery. The anode must be replaced mechanically, requiring novel features in the cell design, but offering relatively rapid refuelability. Oxygen or air may be used as the oxidant, but air fueled systems require a scrubber to reduce CO_2 content from ambient levels of 350 ppm to less than 50 ppm.

Recent progress in electrode and EMS development at the single cell and sub-module level will be summarized in this manuscript.

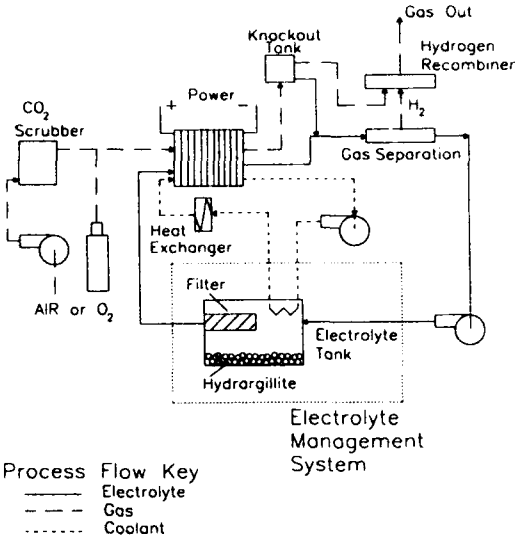

Fig. 1. Schematic of an Al/Air or Al/O_2 battery system.

Electrode Development

Anode Alloys

Aluminum reacts rapidly and irreversibly with oxygen to form a strongly-adhering oxide film, which largely determines the electrochemical behavior in aqueous electrolytes. This oxide layer produces a material that does not corrode in neutral solutions despite being thermodynamically unstable. To achieve stability in alkali solutions, modification of the behavior of the oxide layer through the formation of aluminum alloys has been extensively explored [1-5]. The incorporation of small concentrations of metals such as magnesium, calcium, zinc, gallium, indium, thallium, lead, mercury, and zinc, usually in combinations as ternary or quaternary alloys, has been effective in achieving activation (high current capability) and inhibition of corrosion. The use of solution inhibitors such as sodium stannate has not been nearly as successful in reducing corrosion in our laboratories.

The presence of certain impurities in the aluminum can markedly affect the electrochemical behavior. For example, the corrosion rate is particularly sensitive to the concentration of iron in the metal. Using manganese as an alloying element has been shown to reduce the rate of corrosion of primary aluminum (99.9% purity), which contains high levels of iron [6]. Today's state of the art low corrosion alloys rely on high purity starting material, e.g., 99.995% and 99.999% Al. Once a suitable alloy has been identified, the transition from fabrication at the laboratory-scale (bookmold ingots of weight approximately 3-5 lbs.) to the pilot-scale (150-250 lb. ingots) is not always readily achieved. The electrochemical performance of the large ingot material can be variable and often is inferior to that of the bookmold material. Fabrication practice and the resultant alloy microstructure can have a dramatic effect on both the corrosion and polarization behavior [7].

In the recent program to develop a power source for a UUV, emphasis has been upon mission life and vehicle range. Identification of an alloy with a low rate of corrosion that maximizes the utilization of the metal fuel then became essential. An added advantage was that the hydrogen gas handling requirements within the system are minimized, very beneficial for this closed cycle application where no gases or liquids can be vented.

The percent utilization for several candidate alloys is presented as Figure 2, together with data for pure 99.995% aluminum. As the applied load is increased, the percent utilization improves dramatically. The electrochemical characteristics of the three low corrosion alloys are shown in Figure 3, showing the dependence of the anode potential upon the external load. As shown, a judicious selection of alloying elements and fabrication practice produces anode materials with properties far superior to pure aluminum.

These alloy materials were fabricated as large ingots by conventional industry practice, although the data shown in Figures 2 and 3 were obtained in laboratory-scale cells. Alloy ERC-4 is clearly superior, achieving high utilization while maintaining acceptable polarization behavior. Alloys ERC-2 and ERC-3 closely approached the utilization targets, but ERC-3 tended to passivate at high current densities with aluminate present in the electrolyte. Full-scale (700 cm^2) experiments conducted with ERC-4 showed excellent agreement with lab-scale data and was therefore chosen as the alloy for this demonstration.

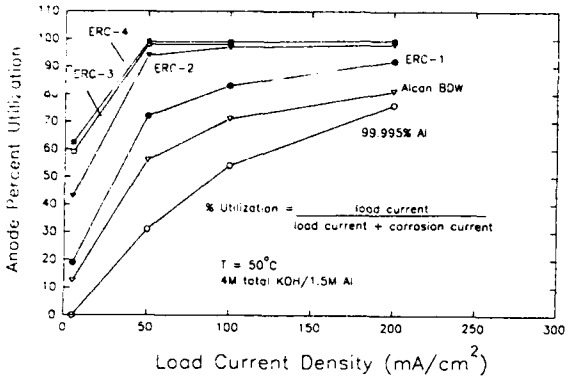

Fig. 2. Corrosion of selected aluminum alloys at 50°C.

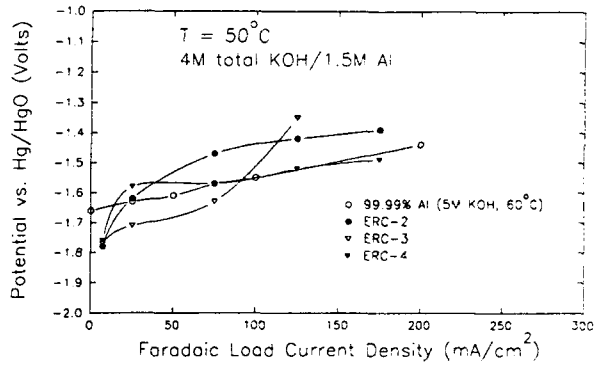

Fig. 3. Polarization behavior of aluminum and selected alloys at 50°C.

The Air Cathode

The reaction at the cathode is the reduction of oxygen, which can only be sustained at practical rates by using a gas diffusion electrode. A three-phase boundary between the catalyst, electrolyte, and reactant oxygen must be established and this demands a unique electrode structure. The air cathode used in the recent programs to develop the Al/Air battery as the power source in (a) an electric vehicle [8], and (b) an unmanned, underwater vehicle is a high performance, two layer structure composed primarily of carbon and teflon. The development of air cathode technology has been described elsewhere [7,8].

This type of electrode has shown excellent extended performance under both constant current operation and cyclic operation. In addition, for the UUV application, it is necessary that the transport of oxygen gas through the electrode into the electrolyte(which contains hydrogen gas) be prevented, or at least minimized. A porous barrier layer was added, bonded to the nickel mesh and surface of the active layer. During operation the pores of this layer readily fill with electrolyte, providing an effective barrier to the transport of oxygen gas into the electrolyte. The performance of the modified electrode, over the range of current densities of interest, is shown as Table 1.

Because the UUV cell stack features a moving anode, cathode uniformity is critical to prevent uneven dissolution of the anode which hampers the ability to maintain a small, constant electrode gap. A novel quality control procedure, dubbed the "voltage mapping technique," was developed to ensure uniformity. The voltage map cell, see Figure 4, features a 0.552 cm^2 cylindrical, aluminum anode operated at 100 mA/cm^2 and encapsulated in a Tygon tube to maintain a 0.050" electrode gap. One can then mount a cathode face-up, cover with electrolyte, and thus create a small Al/O_2 battery at specific areas on the cathode where the measured cell voltage is proportional to cathode activity. Probe position can easily be controlled by the use of a simple acrylic template. In this manner, changes to the microporous barrier layer could be made and quickly tested to optimize the cathode's reactivity and permeability resistance.

Table 1. Performance of the modified cathode at 60°C in 4M KOH with dry O_2.

	IR corrected Cathode Potential (volts) vs. Hg/HgO at				
Time on Line @ 50 mA/cm^2	OCV	25 mA/cm^2	50 mA/cm^2	100 mA/cm^2	200 mA/cm^2
27 hours	0.06	-0.07	-0.10	-0.13	-0.19
313 hours	0.06	-0.06	-0.09	-0.12	-0.18
1000 hours	0.07	-0.07	-0.09	-0.13	-0.21

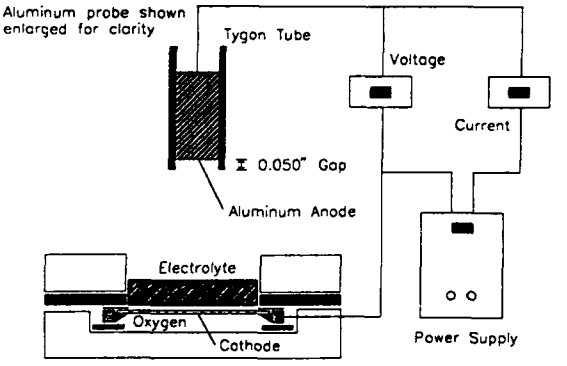

Fig. 4. Voltage map test apparatus.

The Electrolyte Management System

Development of the Filter/Crystallizer

The Al/Air battery may operate in two basic modes, Batch or Steady State, depending on the treatment of the aluminate species generated by reactions (1) and (4). In the Batch mode, fresh electrolyte is charged into the system and operation continues until the level of aluminate reaches saturation. This situation corresponds to an end of charge condition; no solids are formed during Batch operation. Conversely, a near constant electrolyte composition can be maintained in the Steady State mode by promoting the crystallization of the aluminate species into an insoluble hydroxide called hydrargillite, $Al(OH)_3$ (equation 5). During the cell refueling operation, the electrolyte tank is emptied and the $Al(OH)_3$ crystals may be sent to a Hall-Heroult cell for processing back into aluminum.

The performance of a Batch operation battery is electrolyte volume limited and off-board facilities to process the supersaturated solutions of potassium aluminate are required. Steady state operation produces a battery with greater capacity and a more constant voltage profile versus time for a given load. By promoting the crystallization of $Al(OH)_3$ and regenerating KOH, the energy capacity of the battery is significantly enhanced for a given electrolyte tank volume.[9]

The limitations of Batch operation, low capacity and a sloping voltage profile, are shown in Figure 5. Cell voltage at 100 mA/cm^2 drops by 0.25 volt as the conductivity decreases by a factor of 3 over the length of the test. The high aluminate concentration combined with the lack of "free" hydroxide leads to potential oscillations and eventual cell failure. This type of behavior has been observed with pure aluminum and several of the alloys that have been tested in our laboratory in Batch mode.

Previous studies have shown that optimization of Al/O_2 energy and power density requires an Electrolyte Management System [10,11]. ELTECH's patented filter/crystallizer unit [12] maintains system simplicity, since only a filter and two additional valves are required. Mission duration is increased by continuously regenerating potassium hydroxide for subsequent reaction at the anode and storing cell discharge products compactly as a crystalline hydroxide species, $Al(OH)_3$. Continuous crystallization maintains a high and nearly constant electrolyte conductivity; therefore, stack voltage remains steady throughout the discharge cycle. As the stack is discharged, a crystal cake forms and gradually increases in thickness with a subsequent increase in pressure drop across the filter. When the pressure drop reaches a predetermined level, the cake is pulsed off the filter by backflushing (flow reversal achieved simply by valve actuation) to settle in the bottom of the tank.

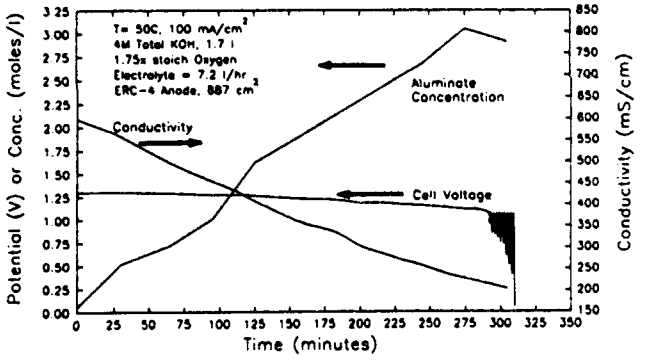

Fig. 5. Conductivity, aluminate, and cell voltage as a function of time for an Al/O_2 without the filter/crystallizer.

Filter/Crystallizer Operation

Figure 6 displays the results of a filter test for a power load of 40.3 Amps. This experiment was run in conjunction with an aluminum half-cell driven by a power supply in which H_2 was evolved at the nickel counter-electrode. Total hydroxide concentration was kept constant by water addition since the cathode reaction and anode corrosion consume water. Electrolyte conductivity was continuously monitored by a Foxboro model 872 conductivity meter with an electrodeless sensor, 871EC.

Backflushes occurred at 5 psi or 202 Ah, whichever came first and, in the figure, a hollow circle indicates a backflush. A software bug prevented the system from backflushing properly for the first 20 hours. Operation began again at 40 hours after the necessary software modifications were made. Despite the system upsets the filter performed well for more than 250 hours, maintaining the conductivity between 300 and 400 mS/cm. Further improvements in filter lifetime are expected by an optimized selection of: (1) the anode alloy, (2) the filter material, and (3) the backflush algorithm.

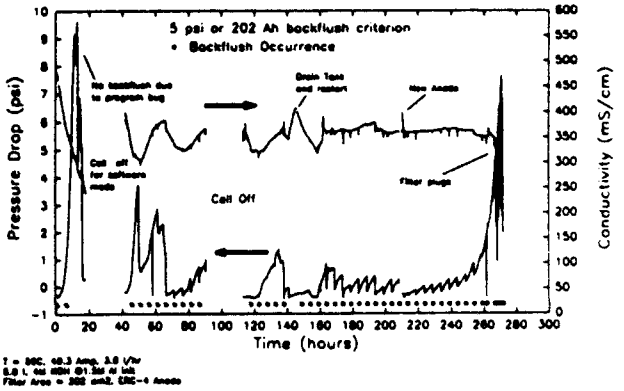

Fig. 6. Filter/crystallizer test at constant current discharge of 40.3 Amps.

Integrated Battery System Performance

Aluminum/Oxygen Single Cell Performance

Full-scale Al/O_2 cells (active electrode area of 690 cm^2) have been integrated with the filter/crystallizer unit for a series of studies. The cell featured a fixed anode with backside temperature control and a modified AE-100 Eltech cathode to minimize electrolyte leakage and oxygen gas blowthrough. The anode alloy, ERC-4, was manufactured from high purity aluminum as a 150 lb. ingot using conventional practice and thermo-mechanical processing. The process streams were all maintained at 50°C with an oxygen gas flowrate of 1.75x stoichiometry. The unreacted oxygen was recycled to the cell using a peristaltic pump.

A single cell was operated at a constant current density of 50 mA/cm^2, drawing nearly 5,700 amp-hours, during which time the cell voltage declined from 1.45 volts to 1.39 volts (see Figure 7). This decline in the cell voltage may be entirely attributed to the increasing inter-electrode gap in this particular (fixed electrode of 0.5" thickness) cell design. Therefore the UUV cell stack features a movable anode to prevent this ohmic voltage loss and is essential to achieve the required high energy density. The data shown represent an energy yield of 3.9 kilowatt-hours/kilogram aluminum, which is significantly better than that obtained with earlier aluminum alloys. The value of the EMS is particularly evident when the performance shown in Figure 7 is compared to the data in Figure 5.

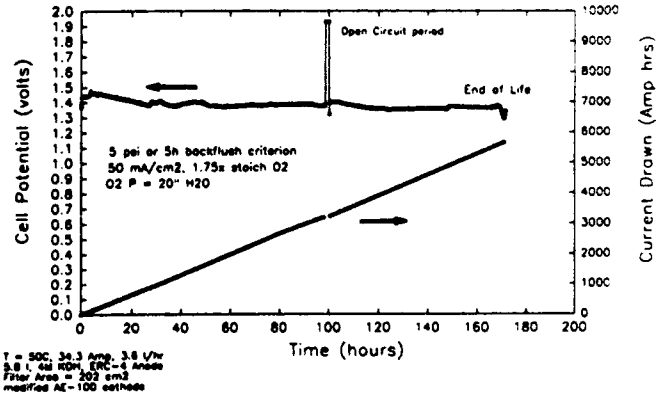

Fig. 7. Full-scale cell performance during constant current discharge.

Sub-Module Testing

The component development described here enabled the construction of a 1.5 kW 9-cell "short stack" test bed where *9 full-scale cells* are integrated with scaled versions of the electrolyte management system, hydrogen recombiner, etc. The hydrogen recombiner consists of Ag/Pd tubes surrounded by Pd catalyzed alumina pellets. The entire

system is computer controlled via Keithley's Viewdac software. Oxygen is supplied on demand by mass flow controllers utilizing the cell stack oxygen pressure as the control variable. The system also included liquid accumulators to account for movement of the anode which increases the cooling volume on the anode backside as the stack is discharged.

Polarization data was recorded periodically and is presented as Figure 8; cell to cell agreement is excellent. The large decrease in cell voltage observed from open circuit to 25 mA/cm^2 is a consequence of the irreversibility of both the aluminum anode and the oxygen cathode reactions. At higher current densities the slope of the polarization curve decreases markedly, the voltage presumably being dominated by the concentration and ohmic overpotentials in the cell.

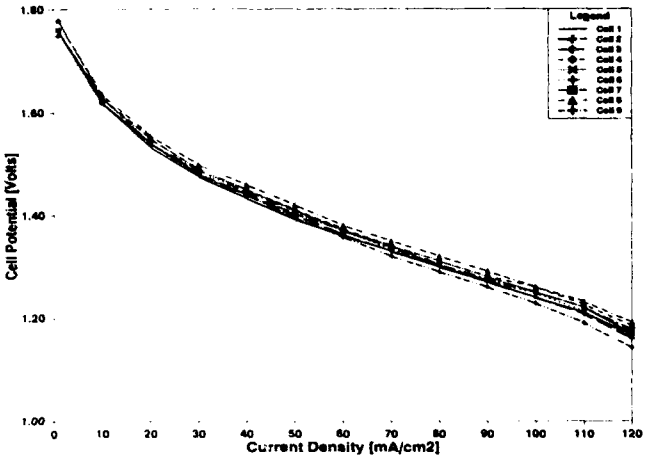

Fig. 8. Individual cell voltages for 9-cell short stack test.

Of particular concern for flow batteries and fuel cells, the system's transient response must not limit vehicle performance. The 9-cell stack's response to a sudden load increase is shown in Figure 9. The battery's response is essentially instantaneous; less than 0.5 milliseconds are required to reach the steady state voltage value.

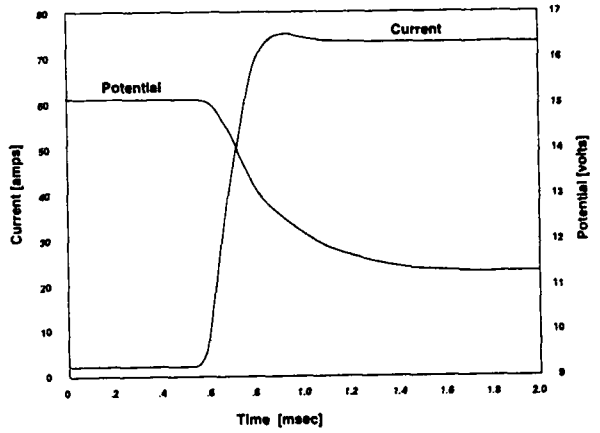

Fig. 9. Transient response of 9-cell short stack.

Conclusions

The advances described here for the electrodes and Electrolyte Management System have resulted in the design of a 15 kW Al/O_2 power source with an energy yield in excess of one Megawatt-hr. Construction will begin soon of this propulsion system for an unmanned, underwater vehicle. The specific energy density based on anode weight is nearly 4 kWh/kg aluminum.

Acknowledgements

A substantial part of this work was performed under the auspices of the Advanced Research Projects Agency, Contract Number MDA-972-91-C-0040.

References

1. Reding, J. T.; Newport, J. J., *Materials Protection*, 5, 15 (1966).
2. Sakano, T., et al., *Materials Protection*, 5, 45 (1966).
3. *The Metallurgy and Electrochemistry of the Aluminum Anode*, a report from the Fontana Corrosion Center for ELTECH Research Corporation, May 1984.
4. Valand, T., *The Behavior of Aluminum in Aqueous Solutions*, a report to the Norwegian Defense Research Establishment, NRDE-PUBL-81/1003, 1981.
5. *Aluminum-Air Battery Development*, Final Report to Lawrence Livermore National Laboratory from ELTECH Research Corporation, Contract Number 1806205, Sections VIIIC, VIIID, and X, November 1987.
6. Scott, D. H., *Effect of Manganese Additions on the Performance of Aluminum Anode Alloys*, a progress report to Lawrence Livermore National Laboratory, UCRL-15473, May 1982.
7. *Development of Aluminum-Air Batteries for Application in Electric Vehicles*, Final Report to Sandia National Laboratories from ELTECH Research Corporation, Contract Number SAND 91-7066, December 1990.
8. Rudd, E. J. "Status of the Aluminum-Air Battery Technology," Proceedings of the Workshop on Structure Effects in Electrocatalysis and Oxygen Electrochemistry, Volume 92-11, The Electrochemical Society, Inc., NJ (1992).
9. Gibbons, D. W., and Rudd, E. J., "The Development of Aluminum/Air Batteries for Propulsion Applications," *Proceedings of the 28th IECEC*, The American Chemical Society, vol 1, p. 1091, (1993).
10. Gibbons, D. W., et al., "Aluminum/Oxygen Fuel Cell with Continuous Electrolyte Management," *Unmanned Systems*, 9, 38, (1991).
11. Maimoni, A.; Cooper, J. F., "Development of the Aluminum-Air Battery for an Electric Vehicle," *Energy Technology Review*, Lawrence Livermore National Laboratory, p. 9, April 1988.
12. Coin, R. J., et al., "Metal-Hydroxide Crystallizer and Filter," *U.S. Patent 4,994,332*, (1991).

THE ALUMINUM FUEL CELL IN TRANSPORTATION APPLICATIONS

Geoffrey M. Scamans, Alupower Inc., Warren, NJ
David K. Creber and John H. Stannard, Alupower Canada Limited, Kingston, Ontario

Introduction

In a conventional fuel, cell hydrogen and oxygen from the air are combined to produce electricity, heat and water. In an aluminum fuel cell, aluminum is used instead of hydrogen and the reaction products are electricity, heat and aluminum hydroxide. Unlike a battery, a fuel cell is not electrically recharged and will provide power for as long as fuel, in this case aluminum, is supplied. Aluminum as a fuel in an aluminum fuel cell provides the same energy, weight for weight, as gasoline used in an internal combustion engine and is volumetrically more energy dense than hydrogen stored as a high pressure gas, as liquid hydrogen or as a metallic hydride.

This means that the aluminum fuel cell power source (FCPS) competes favorably with hydrogen fuel cells in transportation applications where the requirement is for a compact power source. Particular examples where the aluminum FCPS has been demonstrated are as a range extender in a Chrysler minivan and as a long endurance energy source in a 21-inch diameter unmanned underwater vehicle (UUV).

The key to this development has been the provision of aluminum alloy anodes that are stable in strongly alkaline electrolytes and can release their stored energy efficiently over a wide range of power densities. This has reduced the engineering complexity of the aluminum FCPS and has significantly accelerated prototype power source production and in-vehicle testing. The cost of aluminum as a fuel depends on the tolerance to iron impurities present in lower cost grades of aluminum and to date, aluminum fuel has had to be made from more expensive superpure aluminum as the anode alloy base. However, recent developments have shown that it may now be possible to make efficient anodes directly from pot-line aluminum.

The paper summarizes the present state of development of the aluminum FCPS by Alupower and its partners for both land and sub-sea applications and describes aluminum anode development and the tolerance to iron impurities and its consequent effect on the aluminum fuel economy.

In-Vehicle Demonstration Programs

An electric vehicle aluminum FCPS demonstration program was completed by Alupower at the end of 1991 with the road test of a 7.5 kW range extender module fitted to a Chrysler minivan[1]. A total of 24.4 hours of operation at various power levels was achieved over a fourteen day period and the system provided 74.4 kWh of electrical energy. A range of 211 km of city driving was demonstrated compared to the range of 300 km predicted from earlier dynamometer testing. The lead-acid batteries provided an additional 17 kWh which would have limited the range of the vehicle to only 50 km if used alone.

The range extender module in the minivan contains a 56-cell stack with cells connected in series. Electrolyte is pumped from a reservoir through the cell stack and through a heat exchanger to control a maximum electrolyte temperature of 60°C. Each cell contains an aluminum anode which is 6 mm thick and has a surface area of 1000 cm^2. There is a sufficient volume of the 8M KOH electrolyte (180 l) such that the system runs without the precipitation of aluminum hydroxide and at the end of discharge all the aluminum fuel consumed remains as a soluble aluminate ion in the electrolyte. This simplifies the refuelling operation.

Sea trials of an aluminum FCPS fitted to the Applied Remote Technology XP-21 unmanned underwater vehicle were completed at the end of 1993[2,3]. The power source was configured as two 76-cell modules which could provide 1.25 kW and 50 kWh as single units or 2.5 kW and 100 kWh when connected in series. The complete power source occupied an 88-inch (2235 mm) long section of the 21-inch (533 mm) diameter vehicle. Oxygen was supplied to the FCPS from high pressure gas spheres at 4000 psig (27.7 MPa).

The trials provided a wealth of operational experience of the aluminum FCPS operating in a closed hull environment including stop-start operation and discharge at a wide range of power levels. A total of four 76-cell modules were discharged. The energy density of the system, at a power density of 4.4 W/l was 260 Wh/l which is almost twice the energy density of silver-zinc batteries. The energy density of the aluminum FCPS could be improved by cell design optimization and the use of liquid oxygen to nearly 500 Wh/l.

Each cell of the 76-cell power source module has an individual electrolyte reservoir and the cell contains a 4 mm thick 360 cm^2 anode. The 4.5M KOH electrolyte is circulated by the natural convection set up by heat generated in the cell gap and this type of cell is known as the self-managing cell. As the aluminum hydroxide precipitates from the electrolyte it settles and accumulates at the bottom of the cell and at the end of discharge the aluminum anode is consumed and the cell is filled with reaction product. The power source is refuelled by replacement of the complete 76-cell module.

Aluminum Anode Development

The anode in a power source is the reservoir of electricity and candidate anode materials can be rated by their charge density, which is the number of electrons available, either per unit weight or per unit volume. The most energy dense anode materials are liquid hydrogen (26.59 Ah/g, 2.04 Ah/cm^3) beryllium (5.95 Ah/g, 11.0 Ah/cm^3), lithium (3.86 Ah/g, 2.06 Ah/cm^3) and aluminum (2.98 Ah/g, 8.05 Ah/cm^3). Aluminum is therefore a good candidate power source fuel from both a gravimetric and volumetric perspective and is also non-toxic compared to beryllium, safe compared to lithium and a solid at ambient temperature compared to hydrogen. Aluminum is also the third most abundant element in the earth's crust after oxygen and silicon. Also, the aluminum hydroxide reaction product generated in a power source may be recycled back to aluminum metal through the same pot-lines used for aluminum production.

Although the earliest reference to the use of aluminum in batteries is in 1855[4], it was only in 1989 that an anode composition was patented that is stable in a highly alkaline battery electrolyte and is efficient over a wide range of current densities. This anode is an alloy with tin (0.07 wt%) and magnesium (0.5 wt%) which is used with a low level addition of tin, as stannate, to the electrolyte [5,6].

The present era of development of the aluminum-air fuel cell began with the work of Zaromb[7], who published work on the combination of an aluminum anode with a semi-permeable carbon

based catalytic membrane for the reduction of oxygen from the air. However, the aluminum anodes used suffered from high polarization (low cell voltage), passivity under load and high levels of corrosion both at open circuit and under load. This high rate of corrosion produced copious quantities of hydrogen. This situation was significantly improved by Pryor[8] who developed a family of aluminum-tin alloys based on some earlier observations that tin could promote the dissolution of aluminum utensils. Pryor also added gallium and magnesium to his favoured anode composition which became known as A6.

Tin could also be introduced to the power source by using sodium stannate dissolved in the electrolyte and the use of this addition at the 0.06M level became a ubiquitous addition as a, so called, corrosion inhibitor[9]. The consequence of this was that using this addition to the electrolyte masked almost all effects brought about by changes in anode alloy chemistry through the phenomenon of electrochemical dominance which will be explained later. However, Moden[10] was able to patent a variant of A6 where all the tin was added to the electrolyte rather than the anode and his aluminum-gallium-magnesium alloy became known as RX808 and was the benchmark composition for subsequent anode development programs. The big advantage over A6 was in castability.

In 1982, Alcan began its aluminum anode development program, following the promotion by Cooper[11] of the aluminum-air FCPS for a fully traffic compatible electric vehicle. The Alcan program used 99.999% super purity aluminum to which trace single additions were made of gallium, indium and tin. This work showed that for an alloying addition to be effective, it had to be held in solid solution in the aluminum crystal structure. When mixed compositions containing more than one of the three elements were tested, in every case when tin was present in the anode system, the anode behaved as if it was an aluminum-tin alloy. Tin dominated electrochemically over indium and gallium and in the total absence of tin, indium dominated over gallium[12]. This could all be explained in simple terms by referring to the relevant Pourbaix diagrams. For an element to modify the electrochemical behaviour of an aluminum anode, it had to be dissolved either in the anode or the electrolyte, to not dissolve as aluminum dissolved from the anode surface and to have a lower melting point than aluminum. Only ten elements satisfy these simple criteria: antimony, zinc, lead, cadmium, thallium, bismuth, tin, indium, gallium and mercury - listed in decreasing melting point order and in order of decreasing electrochemical dominance. To see the electrochemical characteristic of any element in the list, then all those elements higher in the list have to be absent from the anode and the electrolyte. Cell voltage increases as dominance and melting point reduces so the optimum additions are at the end of the list provided corrosion rates are acceptable. Unfortunately, mercury and gallium which provide the highest cell voltages can't be used as anode corrosion rates are extremely high and such anodes are better suited for hydrogen generators rather than use in a power source. The operational problem of aluminum-indium anodes is that the corrosion rate increases progressively with discharge time, particularly at low current density, leading again to excessive heat and hydrogen production and unacceptable anode performance. This can be improved by addition of manganese and magnesium to the basic binary alloy, resulting in an alloy known as BDW[13]. However, BDW is not suitable for use in aluminum power sources with high energy density.

By far, the best anodes are based on the aluminum-tin anode system with as much tin as possible in solid solution in the aluminum. This is limited to 0.07 wt% as although the maximum solubility is 0.12 wt%, anodes with higher levels of tin are difficult to cast as sound ingots, particularly as the ingot size is increased. The addition of stannate to the electrolyte compensates for the lower than ideal level of tin in the alloy and the anode corrosion rate is further improved by the addition of magnesium at the 0.5 wt% level. Magnesium controls a high hydrogen production state of the aluminum anode surface that is prevalent at the start of discharge and can be maintained at low operating current densities[5]. The high efficiency aluminum-tin-magnesium alloy is known as EB. Although gallium can improve anode potential by up to 50 mV, it is specifically excluded from the anode composition as the anode corrosion rate is increased both on and off load and the tolerance to iron bearing impurities in the aluminum is significantly reduced[14].

Aluminum Anode Efficiency

The rate of corrosion of anode alloy EB depends on the anode potential as determined by the operating current density, the temperature and molarity of the electrolyte, the stannate concentration and the iron level in the anode. Corrosion rate decreases with increasing current density as the anode potential is reduced but increases with temperature, electrolyte molarity and iron level. An addition of stannate in the range 0.004 to 0.02M is a compromise between increasing the level of tin available to the anode whilst avoiding the risk of the development of tin dendrites on the anode surface that can bridge between the anode and the air cathode. Figure 1 shows

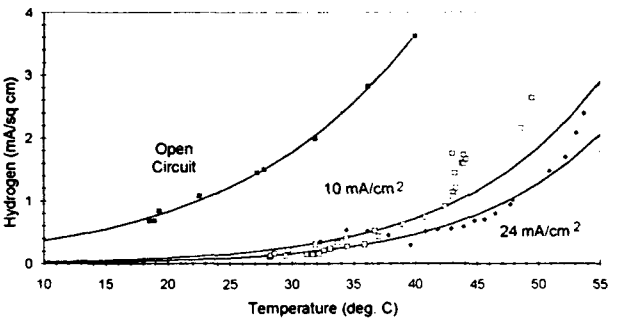

Figure 1. Hydrogen Evolution Current

the rate of hydrogen production using anode alloy EB with an iron level of less than 10 ppm in a cell of the type used in the XP-21 aluminum FCPS as a function of operating current density and electrolyte temperature in the range of 18 to 54°C. The cell was filled with 660 cm^3 of 4.5M KOH + 0.01M sodium stannate and the kinetics of the hydrogen evolution reaction were monitored continuously by pumping air across the top of the electrolyte which was then passed into a calibrated Analygas Systems Model 62 hydrogen monitor. Currents were set at 0 A, 3.75 A (10 mA/cm^2) and 8.5 A (24 mA/cm^2) to examine anode efficiency at low current density and under open circuit conditions.

From the data shown in Figure 1 it can be seen that the hydrogen evolution rate increases as expected with both increasing temperature and decreasing current density and the empirical data can be fitted to an Arrhenius rate equation. The anodic coulombic efficiencies calculated from the data in Figure 1 are listed in Table 1.

If cells are run at temperatures between 55 and 65°C, then the current density needs to be 20 mA/cm^2 or higher to ensure that the anode efficiency remains above 90%. The rate of hydrogen production at 10 mA/cm^2 is 10 cm^3/min for an anode area of 350 cm^2. This means that the 50 kWh XP-21 power source will produce about 0.8 l/min of hydrogen when operating at a low power of 150 W.

Table 1
Anode Efficiency in 4.5M KOH + 0.01M Stannate

	Electrolyte Temperature		
Current Density	20°C	40°C	50°C
10 mA/cm²	99.5%	94%	85%
24 mA/cm²	99.8%	98%	95%

A similar set of results is shown in Figure 2 for alloy EB using a flowing electrolyte cell and assessing coulombic efficiency using weight loss techniques after extensive anode discharge. Hydrogen measurements were also carried out to estimate the hydrogen evolution rate from the range extender power source using 8M KOH electrolyte in the temperature range 60 to 80°C at current densities of 0, 40, 80 and 160 mA/cm². The results of these test are summarized in Table 2.

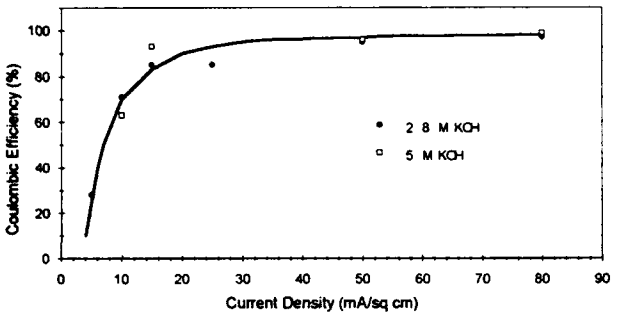

Figure 2. Anode Coulombic Efficiency (Flowing Electrolyte Cell)

If the electrolyte temperature increases above 60°C then efficiency will drop below 90% at current densities below 40 mA/cm². From the above data, the 56-cell stack of the range extender will generate approximately 1.9 l/min of hydrogen at 130 mA/cm² and 80°C which drops to 0.25 l/min at the normal operating temperaure of 60°C.

Table 2
Anode Efficiency in 8M KOH + 0.01M Stannate

	Electrolyte Temperature	
Current Density	60°C	80°C
40 mA/cm²	95.4%	75.0%
80 mA/cm²	98.2%	93.6%
160 mA/cm²	99.6%	97.0%

Open Circuit Corrosion Rate

The target open circuit corrosion rate for an aluminum anode was set at 1 mA/cm² by the DOE aluminum-air traction program led by LLNL. As a comparison, the corrosion rate of zinc in 4M KOH at 50°C has been measured as 0.25 mA/cm² and amalgamated zinc powder has a corrosion rate as low as 0.01 mA/cm² in 9M KOH at 50°C[15,16]. The open circuit corrosion rate of alloy EB in 5M KOH + 0.01M stannate was measured by weight loss after 45 days at 25°C in a self-managing cell and was 0.011 mg/cm²/min which corresponds to 2.0 mA/cm². A similar measurement after 10 days in a flowing cell at 25°C using 2.8M KOH + 0.01M stannate electrolyte gave a corrosion rate of 0.0052 mg/cm²/min which corresponds to 1.0 mA/cm².

The open circuit corrosion rate of alloy EB has also been measured at higher electrolyte temperatures using the hydrogen measurement method. In a flowing cell using 8M KOH + 0.01M stannate, corrosion rates of 0.6 mA/cm² at 40°C, 4.6 mA/cm² at 60°C and 20 mA/cm² at 80°C were measured. This can be compared to the open circuit corrosion rate as a function of temperature in a self-managing cell as shown in Figure 1 where the rate varies from less than 1 mA/cm² at 20°C to nearly 4 mA/cm² at 40°C.

These measurements show that although there is variation, the open circuit corrosion rate of anode alloy EB is of the order of 1 mA/cm² at 25°C which satisfies the LLNL target. However, this rate doubles with every 10°C rise in electrolyte temperature. This is shown in Table 3 as a loss of cell capacity as a function of time for the XP-21 power source cell assuming an original capacity of 567 Ah from the weight of anode in the cell. A complete self-discharge takes approximately 80 days at 20°C.

Table 3
Anode Self Discharge Rate at Open Circuit

	1 min	1 hour	1 day	10 days
20°C	0.005 Ah (0.001%)	0.28 Ah (0.05%)	6.8 Ah (1.2%)	68 Ah (12%)
40°C	0.02 Ah (0.003%)	1.3 Ah (0.23%)	32 Ah (5.6%)	316 Ah (55.7%)

Impurity Tolerance

Extensive studies of the effect of impurities in aluminum on anode efficiency have concluded that iron is the most significant impurity which controls the corrosion rate of aluminum in power source electrolytes[14]. This is shown in Figure 3 which shows how the efficiency of alloy EB drops as the iron level increases. This figure has been compiled from anode release test data. There is no similar correlation with any other contaminant. The anode efficiency is acceptable (>90%) if the iron level is less than 10 ppm.

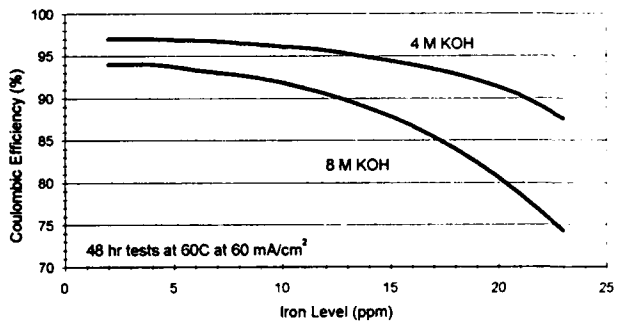

Figure 3. Effect of Iron Level on Anode Efficiency

Higher levels of iron may be tolerated by heat treatment to take the iron into solid solution in the aluminum. Iron impurities form second phase particles which act as local cathodes to stimulate corrosion as iron is relatively insoluble in aluminum[17]. Heat treatment at high temperature can dissolve these particles and can

restore anode efficiency. For example, an EB alloy with an iron level of 20 ppm and a coulombic efficiency of 77% at 60 mA/cm^2, provided an efficiency of over 93% when given a heat treatment to solutionize iron particles. Since the maximum solubility of iron in aluminum at 640°C is 340 ppm (0.034 wt%) this represents the maximum level of iron impurity that may eventually be tolerated in aluminum anodes. It is also possible to moderate the effect of second phase iron particles by using manganese additions which reduce their effect as cathodic sites[18]. This method is much less effective than heat treatment to remove the particles completely.

These results show that efficient anode alloys can be made from 99.99% super purity aluminum rather than 99.999% superpurity aluminum which reduces the cost of the base metal by a factor of two. The best pot-line aluminum available is 99.9% which typically contains a minimum of 350 ppm (0.035 wt%) iron. In order to make anode alloys from pot-line aluminum then better control of iron impurity levels is required to produce low iron metal (ideally less than 200 ppm) in a single reduction step from a pot-line cell.

The Aluminum Fuel Economy

The market price of super purity aluminum made by the Hoopes electrolytic refining process ranges from $6.80/kg for 99.999% down to $3.50/kg for 99.99% which is the lowest purity grade available. Selected 99.9% pot-line metal with iron at <350 ppm can be obtained at a $0.11/kg premium compared to 99.85% pot-line aluminum which is presently trading at $1.25/kg.

Production capacity of super purity metal is of the order of 15,000 tonnes/year in the western world with a capacity of up to 80,000 tonnes/year in CRS, Poland and Romania. Energy consumption to refine aluminum by the Hoopes process is between 12.5 kWh/kg up to 16 kWh/kg which has to be added to the minimum of 13 kWh/kg used to produce pot-line aluminum. The cost to produce super-purity aluminum is of the order of $2.15/kg when power costs, metal loss, labor and depreciation are considered[19].

In addition to the metal cost, there is an anode production cost that involves the alloying, casting, analysis, extrusion, machining and testing of anodes which varies with production volume. Present costs for 99.99% super pure aluminum using a 12 tonne production furnace are $11/kg. Using this price, the cost of aluminum as a fuel is $3.3/kWh assuming an anode efficiency of 94% and an average cell voltage of 1.2V which translates to 3.36 kWh/kg. This could be reduced to $3.66/kg and $1.08/kWh by using selected pot-line metal and alloying and making anodes directly on a continuous caster.

If, eventually, the demand for aluminum as a fuel is high enough to require one million tonnes of aluminum per year and the aluminum hydroxide is recovered from the used power source electrolyte, then aluminum fuel costs could be reduced further to $1.54/kg or $0.46/kWh. For this to happen, the aluminum hydroxide reaction product has to be calcined directly to alumina which is then fed into the pot-line cells. This will also reduce iron contamination as the original bauxite ore is a major source of iron contamination in the final pot-line aluminum. Iron is also introduced from the carbon anodes of the pot-line reduction cell, from steel studs in the pots and from steel tools used for melting and casting. Using best practices and recycled reaction product alumina it should be possible to make 99.95% purity metal this way with iron at less than 100-200 ppm. This approach ofers the potential to reduce the cost of aluminum as a fuel to 7¢/km which compares to the cost of driving on gasoline at 3.5¢/km or electricity from the utilities at 0.5¢/km, assuming an energy requirement of 150 Wh/km. These figures are consistent with those reported by LLNL[20] but are very different from the present best production price estimate of $11/kg which is 50¢/km.

Presently, while the cost of aluminum as a fuel is high and the cost of gasoline is low, aluminum as a fuel in transportation applications is only suitable for electric vehicle range extension where the aluminum FCPS is only activated occasionally or for use in electric propulsion applications where high energy density and covertness of operation are essential as in the air independent propulsion of underwater vehicles.

Summary

The high energy density aluminum FCPS has been successfully demonstrated in both land based and sub-sea vehicle applications. These systems utilize the development of a highly efficient aluminum anode composition, EB, which achieves a coulombic efficiency of more than 90% over a wide range of operating power levels and has a low open circuit corrosion rate at ambient temperature. The EB anode alloy can be made tolerant of iron impurities by heat treatment. Presently the cost of aluminum as a fuel is very high compared to the cost of gasoline but this could be reduced significantly by the direct use of low iron pot-line metal and by the recycling of the aluminum hydroxide reaction product.

References

(1) Lapp S P, Dawson, J., Testing Results and Running Cost Projections for an Aluminum-Air Lead Acid Battery Hybrid Electric Van". 11th International Electric Vehicle Symposium, 1991.

(2) Collins, K, Stannard J H, Dubois R and Scamans G M, "An aluminum-oxygen fuel cell power system for underwater vehicles," Underwater Intervention, New Orleans, January 1993.

(3) Scamans G M, Stannard J H, Tregenza J E, Creber D K and Dubois R, "High energy aluminum oxygen power source fro a 21" diameter unmanned underwater vehicle," Oceanology International, Brighton, UK, March 1994.

(4) Hulot M, *Compte Rend*, 40, 1148, 1855.

(5) Hunter J A, Scamans G M and Sykes J M, "Anode development for high energy density aluminum batteries," *Power Sources 13*, pp 193-212, 1991.

(6) Hunter J A, Scamans G M, O'Callaghan W B and Wycliffe P A, US Patent 5004654, 1991.

(7) Zaromb S, *J Electrochem Soc*, 109, 1125, 1962.

(8) Pryor M J, US Patents 3186836, 3189486, 3240629, 3240688, 3250649, 3282688, 3368953 and 3368958, 1965-1968.

(9) Katoh M, US Patent 3563803, 1967.

(10) Moden J R and Perkons G, US Patents 4107406 and 4150204, 1978-1979.

(11) Cooper J F and Behrin E, " The aluminum-air battery for electric vehicles: an update," Energy and Technology Review, LLNL, November 1980.

(12) Scamans G M, Hunter J A and Holroyd N J H, "A surface engineering approach to the corrosion of aluminum." Aluminum Alloys Contemporary research and Applications, Academic Press pp 486-500, 1989.

(13) Scamans G M, O'Callaghan W B, Fitzpatrick N P and Hamlen R P, "The present status of aluminum-air battery development," Proceedings of the 21st Interscience Energy Conversion Conference, San Diego, August 1986.

(14) Wycliffe P A, unpublished work, Alcan International, Kingston, 1990.

(15) Macdonald D D, Lee K H, Moccari A and Harrington D, "Evaluation of alloy anodes for Al-air battery studies." *Corrosion Science*, 44, 652, 1988.

(16) Meeus M, Strauven Y and Groothart L, "New developments in reduction of mercury content in zinc powder for alkaline dry batteries," *Power Sources 11*, pp 281-300, 1986.

(17) Tuck C D S and Gilmour A, "The chemistry and electrochemistry of battery systems," Modern Battery Technology, Ellis Horwood, pp 31-80, 1991.

(18) Scott D H, "The effect of manganese additions on the performance of aluminum-air battery anode alloys," Progress report to LLNL, UCRL 15473, May 1982.

(19) Creber D K, unpublished work, Alcan International, Kingston, 1991.

(20) Cooper J F, "Aluminum-air power cell research and development progress report," Electric and Hybrid Vehicles Systems Assessment Seminar, Gainsville, December 1983, UCRL 90465, February 1984.

REGENERATIVE ZINC/AIR AND ZINC/FERRICYANIDE BATTERIES FOR STATIONARY POWER APPLICATIONS

by
John F. Cooper, Larry E. Keene, Jon Noring, Arturo Maimoni and Keith Peterman
Lawrence Livermore National Laboratory • Livermore CA 94550

Abstract

We report a novel configuration for a zinc-particle, packed-bed anode in which an open structure of high hydraulic permeability is maintained indefinitely in a cell with closely spaced walls by the formation of particle bridges and associated gaps. The configuration minimizes electrolyte pumping costs, allows rapid refueling and partial recharge, and provides for 100% zinc consumption. This approach benefits zinc/air fuel batteries by allowing nearly continuous operation and fuel recycle without commercial infrastructure; it benefits $Zn/[Fe(CN)_6]^{-3}$ batteries by eliminating shape-change and polarization problems found with planar anodes.

Introduction

Zinc/air batteries have long attracted interest in mobile and stationary power applications because of low cost and high energy density (150-350 Wh/kg). Zinc batteries might be classified into four broad types: (1) primary, (2) secondary, i.e., electrically recharged; (3) reconstructable cell; and (4) refuelable cell. Primary batteries have found widespread application in disposable batteries for hearing aids, and have been developed for military field electronics as well as recyclable lap top computers. Primaries have high life cycle costs and contain RCRA land-banned materials limiting disposal: zinc and often corrosion inhibitors (such as mercury or cadmium). Secondary batteries using bifunctional air electrodes can be cycled at most a few hundred times, and compete poorly with secondary batteries (lithium polymer, Ni/H_2, etc.) of comparable energy density but greater durability and power. Electric storage batteries using the $Zn/[Fe(CN)_6]^{-3}$ couple are limited by shape change and show low power densities (W/m^2) characteristic of planar zinc electrodes.[1]

Electric Fuel, Ltd. (Israel) recently tested reconstructable-cell zinc/air batteries in postal vans in Germany, demonstrating anode replacement using robotics and energy densities up to 200 Wh/kg. Zinc consumption is incomplete, and the undischarged zinc is recovered along with discharge products in a complex anode fabrication process requiring industrial infrastructure.[2]

Laboratory zinc/air cells using stationary bed anodes have been developed at University of California (Berkeley). Discharge results in precipitation of solid ZnO without passivation and out of contact with the zinc/electrolyte interface, giving cells in this configuration a loading capacity of ~400 Ah/liter-electrolyte. Ducts allow electrolyte circulation by density-driven ("solutal") convection, which obviates the use of electrolyte pumps. The cell is refurbished using a jet of electrolyte to dislodge and fluidize a product cake consisting of zinc oxides and zinc, after which fresh electrolyte and zinc particles may be added.[3]

A zinc/air battery refueled with a particle/alkaline slurry was pursued by CGE (France)[4] and by Pinnacle Research Institute (California).[5] CGE developed tubular zinc cells through which the reactive slurry is circulated during discharge. To avoid abrasion, the battery tubes were of heavy construction using thick, resistive asbestos separators. The weight and cell resistance reduced energy and power densities below 100 Wh/kg and 50 W/kg.

Technical Approach

Renewed commercial interest in zinc/air applications have encouraged efforts at this laboratory to develop refuelable zinc/air batteries for stationary and mobile (electric vehicle) applications that avoid major limitations of the existing technologies cited above.[6] Specifically, we have developed and demonstrated a novel self-feeding cell which uniquely provides the following: (1) the cell is rapidly refueled by hydraulic transfer of a slurry of 0.5-1 mm zinc particles after pumping out the exhausted electrolyte (an alkaline liquid containing zincates and colloidal zinc oxides); (2) 100% of the zinc introduced into the battery is consumed to produce electric power; (3) the design provides for partial recharge, recharge under load, and equalization of individual cell capacities; (4) the cell is robust because nearly all of the reactant mass is stored outside of cell, protecting the fragile air electrode and separator membranes from abrasion during refueling or damage during handling or road shocks; and (5) electrolyte pumping power is negligible, consuming less than 0.1% of the gross power output.[7]

The cell design (Figure 1) is based on a phenomenon of two-phase flow. When particles of nearly uniform size are introduced into a channel having a width only a few times larger, the particles do not close pack. Rather, a stationary bed is formed which has network of arches and bridges spanning the gap. As zinc anode particles discharge and decrease in dimensions, the open network persists if the bed tapers in the direction of flow such that the gap is always less than about 5 times the average particle dimension. This open structure persists even under conditions of agitation. Particles enter the cell under gravity flow and move both downwards and normal to the cathode surface (where particle discharge is favored). The solid fraction of the bed has been estimated from macrophotographs to be between 40- and 50% by volume, and no doubt is a function of surface friction coefficients of zinc and current collectors, polarization, agitation, and electrolyte composition.

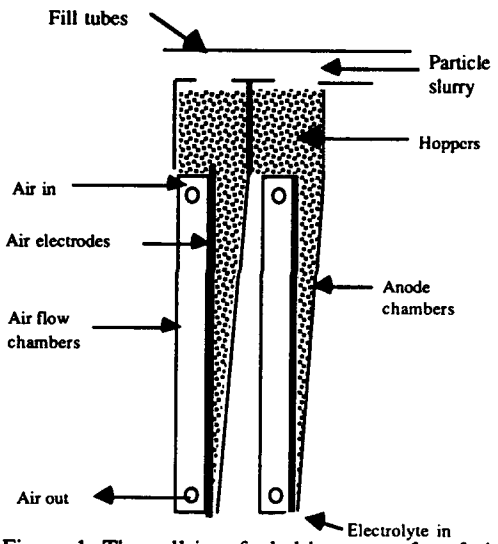

Figure 1. The cell is refueled by a transfer of zinc particles into hoppers, which gravity feed to the cells. A particle bridging phenomenon prevents close packing and maintains a low hydraulic resistance regardless time of discharge.

Cells are refueled from a particle slurry flowing through an adjacent duct. As the slurry is passed over an orifice atop each cell, a fraction of the particles fall into the hopper. Since the interiors of the cells are not disturbed, the slurry velocity in the fill tubes can be quite large. We have filled cells in less than 2 minutes by this technique. The time to fill multicells in parallel is limited by the capacity of the slurry pump. Before discharge, the fill tubes are drained and the orifices are closed.

The recycling of zinc products is done by a user-owned and operated unit. For example, an electrodeposited zinc plate may be shredded into fuel particles.[6] We have developed a technique which combines proprietary electrochemical and mechanical processes to generate particles of zinc from battery reaction products. The equipment can be housed at the home base of the user, and in some applications should be miniaturized and placed within the battery. In either case, no commercial infrastructure whatsoever is required to collect, transport or recycle products into fuel.

Technical Status and Experimental Results

The self-feeding cell has been tested on 80-, 600-, and 1000-cm^2 scales, and a stand-alone battery with a bipolar stack of twelve

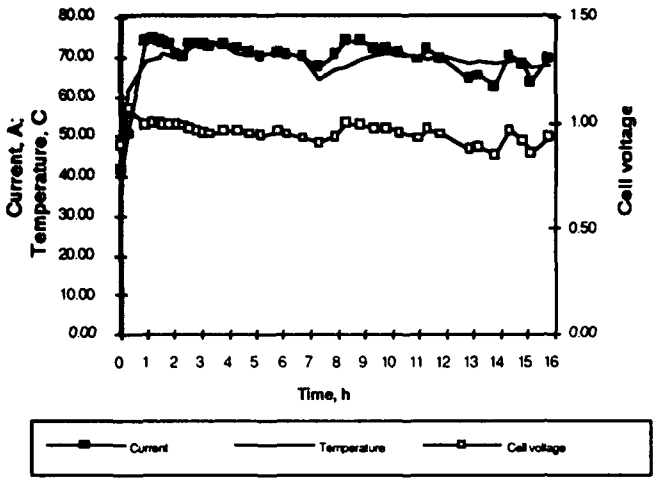

Figure 2. Current, temperature and voltage were stable in a 600-cm^2 Zn/air cell using a Ag-catalyzed cathode (Alupower, Inc.). The cell was discharged at 70 °C in flowing 12 N KOH solution, with intermittent refueling with zinc.

250 cm^2 cells is under construction for mobile testing.

Long duration tests were conducted using a silver-catalyzed air electrode (Alupower, Inc., Warren NJ). Figure 2 shows stable operation at 1.15 kA/m^2 and 70 C for fixed load discharges without active heat rejection. This monopolar cell was fed from a hopper (top 2 cm in the photograph of Figure 3) which was periodically replenished with weighted quantities of zinc. Particle bridges formed even when the cell was discharged on a shaker table under conditions normally leading to powder compacting (20-50 mG horizontal and vertical accelerations at 60 and 120 Hz). Anode current collection was from a nickel expanded metal screen separated from the cathode by a porous polymer membrane. Coulomb efficiencies approached 99% after 2 h of operation, and determined by comparing the time-integrated load current with the amount of zinc added to maintain a constant level in the hopper.[6]

The scaleup of self-feeding configurations was tested in 1000 cm^2 cells with tapered (1-6 mm) anode chambers and having a modular design for either monopolar or bipolar stacking. The air electrode was housed in a replaceable internal cassette, which mated with a permanent frame containing internal air and electrolyte flow channels. Cell voltage suffered because of high resistance in central feed-throughs (1.05 V at 60 A, 35 °C). The particle bridge and gap formation was found for 1 mm particles (Figure 4), and hydraulic power dissipation for electrolyte flow was negligible despite the 30 cm height of the cell. (Table 1).

Improved peripheral current collection and positive rib support within air and zinc chambers was tested in 80 cm^2 cells designed for bipolar assembly. These laminated cells have internal electrolyte and air distribution channels. The improved polarization in Figure 6 results from (1) an improved air electrode catalyst and (2) an air-electrode support structure which compresses the cathode, separator and anode current collector between opposing rib-like structures. The air electrode (model AE 100, catalyzed with of Co tetramethyl-phenyl-porphyrin, CoTMPP) was supplied by Eltech, Inc. Similar polarization with an Alupower, Inc. electrode using CoTMPP have been reported. This proprietary configuration has been replicated into fully engineered 250-cm^2 bipolar cell stacks with internal circulation of air and electrolyte. The stack will be tested (1994) as a refuelable, stand-alone replacement for commercial lead/acid electric-bus batteries, delivering twice the energy in a unit having the same dimensions and half the weight.

Existing laboratory cells allowed time-lapse video and still macrophotography of the evolution of the bed during extended discharge periods. Except for the 1000 cm^2 scale, the bed is sufficiently narrow to allow observations of the anode current collector and separator. The following summarizes our observations: (1) A steady-state population of gaps and bridges develops in about 1 hour at 1 kA/m^2, starting at the base of the cell and proceeding upwards. (2) the open structure is maintained in a dynamic balance between gap formation and collapse, with a time constant on the order of 100 s. (3) Approximately 40-50 vol.-% of the bed consists of solid particles. (4) Small particles (< 0.1 mm) are entrained in the ~ 1 cm/s phase flow, and collect and discharge at the top of the cell. (5) Agitation appears to increase the number and to decrease the size of the gaps. (6) The particle flow is normal to cathode at the separator surface, but downwards at the opposing wall (transfer plate). The particle flow pattern results in a layer of particles of nearly uniform size adjacent to the bipolar transfer plate, maintaining an open structure of nearly constant hydraulic resistance.

Table 1 collects the data relevant to forced convection of air and electrolyte. Hydraulic power dissipation for electrolyte flow is negligible. We favor forced convection for high power applications because it provides a means for decoupling the control of heat and mass transport from the internal state of the battery.

Table 1. Measured power dissipation for flow circuits in Zn/air cells

Cell size, cm^2	Total electro-lyte head, cm	Electro-lyte. flow, ml/s	Electro-lyte flow power, mW	Air flow, l/min	Air flow power, mW	Total parasitic power, %*
80	22	1.5	3.4	1.5	80	0.50
600	50	5.0	18.4	6.0	760	0.65
1000	60	13	69	13.8	2100	1.1

*Total passive power dissipation for air and electrolyte flow circuits, for rated cell power of 2 kW/m^2.

Applications and analyses

Experimental zinc/ferricyanide load leveling batteries were limited to a few hundred cycles by anode shape change, and exhibited the relatively high polarization characteristic of planar zinc electrodes. Capacity was limited by the amount of zinc supported on the anode.[1] The development of a self-feeding cell obviates problems of shape change and cycle life, while the high surface area of particles lowers the cell resistance and increases power. Since both reactants may now be stored outside of the cell and injected on demand, the capacity is arbitrarily large and fully independent of power rating.

Stationary zinc/air power sources for emergency or silent power benefit from indefinite dry shelf life, low standby losses once activated, and the ability to be refueled indefinitely by exchange of reactants. Hydraulic refueling allows partial recharge, cell equalization, and refueling under load. The use of hoppers as buffers between individual cells and a rapidly flowing slurry protects the fragile interior components of the cells and minimizes the impulse imparted to the electrodes by handling or road shocks.

Mobile applications of this technology (reported in open[6,7] and in detailed proprietary documents) exploit both the high energy density and rapid refuelability to increase range and to allow nearly continuous operation by means of periodic refueling.

The weight (W) and volume (V) of the battery of current design can be represented by a linear combination of peak rated power (P) and nameplate energy (E):

$$W = K_1 P + K_2 E, \text{ and } V = K_3 P + K_4 E. \quad (1)$$

For the bipolar stack and support auxiliaries under construction, K_1 = 5 kg/kW, K_2 = 1.1 kg/kWh, K_3 = 5.6 liters/kW, and K_4 = 0.74 liters/kWh. The specific energies and powers implied by (1) are not as high as found with paste-type zinc anodes. We have gained the benefits of rapid and simple refueling without infrastructure by imposing the constraint of maintaining reaction products as pumpable fluids. This constraint determines the size of K_2 and K_4.

The manufacturing cost of the battery depends strongly on the cost of the air electrode and its plastic holder (~ \$120/m^2 for lots of 500,000 m^2) and the rated power of the cell (5 kW/m^2). An assembled system will cost wholesale about \$50/kW-rated power + \$2/kWh nameplate capacity, when the costs of auxiliaries, assembly labor, materials and markups are counted.

Problems and Discussion

The limiting aspects of this technology are (1) air electrode life, a function of duty cycle; (2) limiting electrolyte capacity (Ah/liter) for maintaining fluidity of discharge products; (3) tolerance of air/electrolyte seals and junctions to mechanical fatigue and chemical attack; and (4) polarization of the air-electrode (which limits surface power density).

Air electrode life is greatest under conditions of fixed-rate discharge at 2-3 kA/m^2 and moderate temperatures (55-65 °C); under these conditions, operation without failure for 12,000 hours have been achieved in similar alkaline electrolytes.[8] Cycling to high power levels and long periods on standby reduce life. Electrolyte loading capacities of 250 Ah/liter limit energy densities to about 200 Wh/kg; this is sufficient for many applications. The use of hoppers minimizes stress on the air electrode and air/liquid barriers compared with other designs. The rate of fatigue failure of the seals resulting from pressure fluctuations and vibrations has not been determined, but it is likely to be controlling. Because of the moderate surface power density of Zn/air (5 kW/m^2), the desire to minimize air electrode area to minimize cost, and the favorable operating lifetimes achieved with low fixed discharge rates, some applications will benefit from hybridization with a high power device (supercapacitor or high-rate battery) to provide for peak power excursions and electrical regeneration.

Conclusions

When both anode and cathode reactants are fluids which are readily transferred on demand into the cell, electrode morphology and shape change no longer determine life-cycle cost and the high surface/volume ratio of the anode particles decreases polarization losses. We believe we have solved a fundamental problem of stationary particle bed anodes by providing a configuration of low hydraulic resistance in the steady-state, through the formation of particle bridges and gaps between closely-spaced and tapered walls. Electrolyte forced convection, necessary for mass transport and for effective thermal control, may be achieved with only a trivial parasitic power loss.

The use of hoppers to receive and store zinc particles isolates the fragile interior of the cell from feed stream, allowing high transfer rates without fear of damaging the cell. The hoppers also allow partial recharge, cell equalization, and can be modified for refueling under load without danger of shorting.

The value of this technology derives from two unique attributes. (1) The cost of the battery (per rated power and especially per nameplate capacity) is very low compared with existing or projected secondary or reconstructable batteries. (2) The ability to be rapidly refueled by zinc recovered by the owner in a simple process obviates the need for commercial recycling infrastructure.

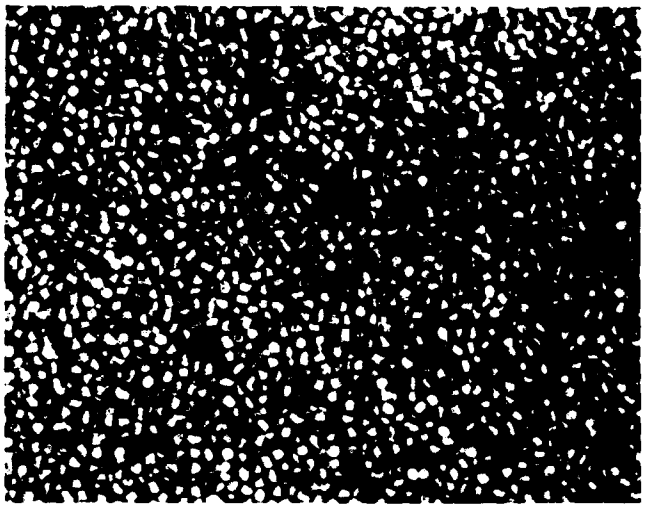

Figure 4. Particles (1-mm x 1 mm) form bridges in stationary beds up to 5 mm thick. Shown here is a mature bed segment in a 1000 cm^2 cell (horizontal field of view, 45 mm).

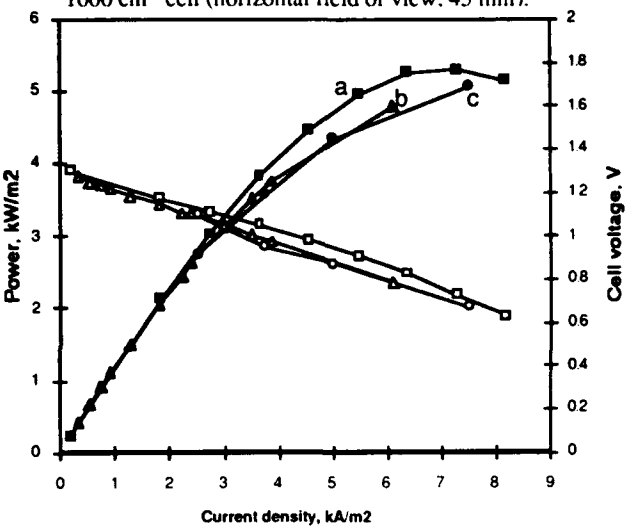

Figure 5. Polarization curves from the discharge of 80-cm^2 cells were recorded at successive stages of electrolyte exhaustion: (a) 36-, (b) 54- and (c) 126 Ah/liter at 65 °C.

Figure 3. A steady-state network of bridges and gaps allow flow with negligible hydraulic resistance. Shown here is a 30 cm x 20 cm cell after 15 hours of operation (left); 0.1 mm fines are entrained by the electrolyte and collect and discharge at the top of the bed (right).

Acknowledgments Work performed under the auspices of the U.S. Department of Energy by the Lawrence Livermore National Laboratory under contract number W-7405-ENG-48.

References

1. Hollandsworth, R.P., Zegarski, J. and Selman, J.R., Zinc/Ferricyanide Battery Development Phase IV, *Final Report: 9 May 1983-15 February 1985*, SAND85-7195, May 1985.
2. Jonathan R. Goldstein and Binyamin Koretz, Tests of a full-sized mechanically rechargeable zinc-air battery in an electric vehicle, *Proc. Intersociety Energy Conversion Engineering Conference*, Paper no. 93410, Atlanta Georgia, August 1993.
3. Evans, J. W. and Savaskan, A zinc-air cell employing a packed bed anode *J. Appl. Electrochem.*, **21**, 105-110 (1991)
4. Appleby, J. and M. Jacquier The C. G. E. Circulating Zinc/Air Battery, *J. Power Sources* vol. 1, pp. 17-34 (1976/77)
5. Sierra Alcazar H. B., Nguyen P. D. and Pinoli, A. A., *Technology Base Research on Zinc/Air Battery Systems*, LBL-Report No. 23960, September 1987.
6. J. Noring, S. Gordon, A. Maimoni, M. Spragge, and J. F. Cooper, Mechanically Refuelable Zinc/Air Electric Vehicle Cells, *Proc. 183rd Meeting of the Electrochemical Society*, Honolulu HI, May 1993; LLNL Report UCRL-JC-112422.
7. John F. Cooper, Larry Keene, Arturo Maimoni, Jon Noring, and Keith Peterman, A continuous feed zinc/air fuel battery for fleet electric vehicle applications, *Proc. 185th Meeting of the Electrochemical Society*, San Francisco, CA May 22-27, 1994.
8. Private communication: Eric Rudd (Eltech, Inc.) to J. F. Cooper, July 1993.

USER EXPERIENCE OF THE ALUMINUM-AIR RESERVE POWER SYSTEM

S P Lapp, Alupower Canada Limited, Kingston, Ontario
S M Warner, Alupower/Chloride Limited, Swinton, England
G M Scamans and R DuBois, Alupower Inc., Warren, NJ

Introduction

The first aluminum-air reserve power unit (RPU) was developed at the request of British Telecom (BT) who required a compact standby power unit that would fit in their System X equipment rack and provide an output of 500 W for 48 hours. This unit was developed in Alcan's Kingston research center and was tested at BT's test facility in the UK within six months[1]. The prototype unit satisfied the BT requirement and had an energy density of over 300 Wh/kg and a three year development program was then started with BT. During this development period the BT requirement changed progressively to 1200 W for 48 hours and eventually to 6000 W for 5 days. Although a 1200 W system, which was essentially the smaller unit with a double stack of cells and a larger electrolyte reservoir, was developed and tested, the final requirement was beyond the economic feasibility of an aluminum-air RPU compared to a diesel generator.

The development of the RPU in Europe has then focused on an application for France Telecom (FT) whose requirement was 500 W for 100 hours for reserve power for a new rural exchange network. The FT test program which began in 1989 should be completed later this year and field deployment should begin this year. A similar program is underway with the Italian telecom company SIP who are presently field testing two 1200 W units.

More recently the cellular network and cable network companies in the UK represented by Mercury One-2-One and NYNEX have been evaluating the aluminum-air RPU as a compact source of quiet reserve power to provide extended protection against power outages. A unit deployed by Mercury in a live site at an important network node supported a loss of power for over 35 hours which was the first operating site discharge of a RPU.

In North America and Japan the reserve power requirement tends to be higher than in Europe which has led to the development of a 6 kW, 12 hour unit based on the use of a larger electrode area cell design. This unit is at the final prototype test stage and is undergoing customer evaluation for a range of telecom standby power applications from central offices to controlled environment vaults (CEVs). NYNEX, however, have strong interest in the 1200 W unit modified to fit a standard Lineage 2000 equipment rack in the same space that could be occupied by a 330 Ah lead-acid battery. They are at the stage of starting field trials.

The paper will present the basic technology of the aluminum-air RPU and will then detail the user experience that has been made available for publication and demonstrates particular features of RPU operation.

The development of the aluminum-air RPU has been described in publications presented at specialized Telecom power conferences and have also developed the economic argument for the use of this system compared to lead-acid batteries or diesel generators[2-8]. The purpose of the present paper is to bring the aluminum-air RPU to a wider power source audience.

Core Technology

The aluminum-air RPU depends on the use of aluminum as a compact energy storage medium. For the power source to be successful aluminum anodes must be supplied at low cost whilst providing the highest possible coulombic efficiency and the minimum open circuit corrosion rate[9]. This is essential to minimize heat and hydrogen production during discharge and to ensure re-start of a partially discharged cell stack. All RPU power sources use an aluminum alloy anode, known as EB, which contains low level additions of tin and magnesium and is used with a low level of tin dissolved in the power source electrolyte to maximize anode efficiency. The aluminum anode and the electrolyte are replaced after each complete system discharge or when the capacity of the system after partial use is less than the minimum specified reserve time.

The cathodic reactant is oxygen which is supplied from the ambient air through a carbon based catalytic membrane. Such electrodes are widely available but are not made by a continuous production technique as employed by Alupower to minimize production costs[10]. The critical cathode issue for use in a RPU system concerns re-use as at least three complete cell discharges are required, using new anodes each time, to minimize the cost of system re-fuelling. The RPU cell uses a laminated cathode of active carbon catalyzed with silver which shows a low level of polarization at current densities up to 160 mA/cm^2.

Initially, the electrolyte used was 4.5M KOH which allowed precipitation of the aluminum hydroxide reaction product to occur which maximized energy density as electrolyte capacity was of the order of 1000 Ah/l. However precipitation of the reaction product was difficult to control with the required reliability so the electrolyte strength was increased to 8M KOH to maximize dissolved aluminum solubility to prevent any solid product forming even when the aluminum anode was fully discharged. This electrolyte has a capacity of 500 Ah/liter so twice the volume of electrolyte is required for the same power source capacity as before. Solids-free operation provides the essential system reliability and simplifies the re-fuelling and refurbishment operation.

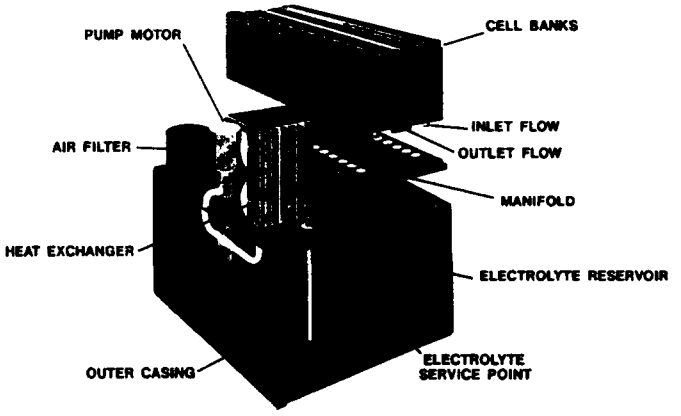

Figure 1. Schematic drawing of the AL-600 reserve power unit

The main components of an aluminum-air RPU are shown in Figure 1 which is a schematic of the AL-600 unit. The cell stack is a bank of twelve twin cells connected to a manifold with connections for electrolyte flow. The electrolyte reservoir holds the 8M KOH electrolyte which is pumped into the cell stack to activate discharge and is returned to the reservoir when the system is deactivated. The system is also provided with an air blower to supply air to the cathodes, a heat exchanger and fans to control electrolyte temperature to a maximum of 67°C, an electrolyte pump and a controller which can be either mounted on the front panel of the unit or positioned as a separate rack-mounted unit. The control unit monitors and controls all RPU operations and has an RS232 data port for external communications. The AL-1200 unit uses the same twin cells but has a second bank of cells positioned over a larger electrolyte reservoir. the 48 cells of this unit can be connected either in series to provide a nominal 48 V or as banks of 24 cells in series connected in two parallel stacks to provide a nominal 24 V. The AL-6000 unit has a larger cell with an electrode area of 1000 cm^2 compared to 340 cm^2 for each cell of the twin cell. This unit can also be configured as a AL-3000 unit using a smaller heat exchanger. The discharge performance of the four units as a function of output power is shown in Figure 2.

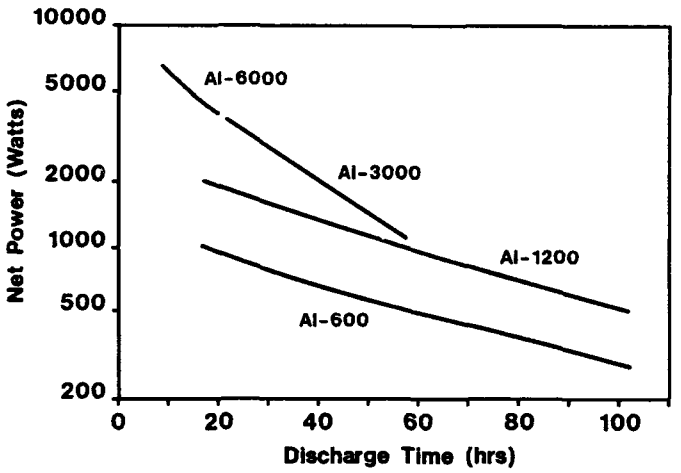

Figure 2. Discharge duration as a function of power level

The RPU is deployed as part of a reserve power system with lead-acid batteries to respond to the initial loss of external power. The lead-acid battery is sized to cover the majority of power breaks and usually has capacity for 1-5 hours of discharge. The RPU is only activated during extended power outages on a low voltage signal from the lead-acid battery which also provides the initial power to activate the RPU. The RPU may be connected directly in parallel with the lead-acid battery or can be interfaced through a DC/DC converter to the load equipment.

System Evaluation

Discharge Duration

A deliberately instigated discharge of a modified AL-1200 RPU by NYNEX in New York is shown in Figure 3(a)-(c). The RPU was connected in parallel with an AT&T,24X,VR300E lead-acid battery which was discharged from a fully charged 54.5 down to 44 V which activated the RPU. As can be seen from the current/time curves in Figure 3(a) the RPU, which had 44 rather than 48 cells to provide a better voltage match with the lead-acid batteries,

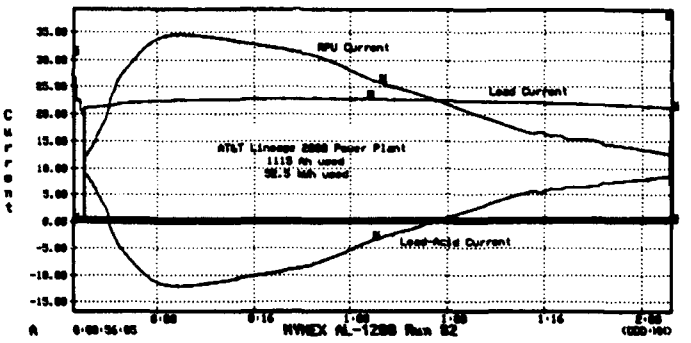

Figure 3(a). Current/time discharge of the 44-cell AL-1200 RPU showing both RPU and lead-acid currents.

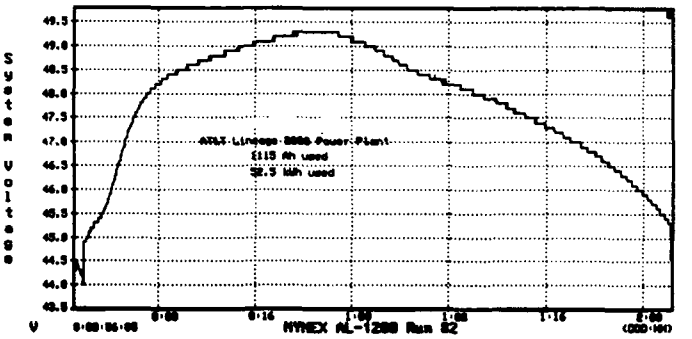

Figure 3(b). System voltage during the discharge of the AL-1200 RPU.

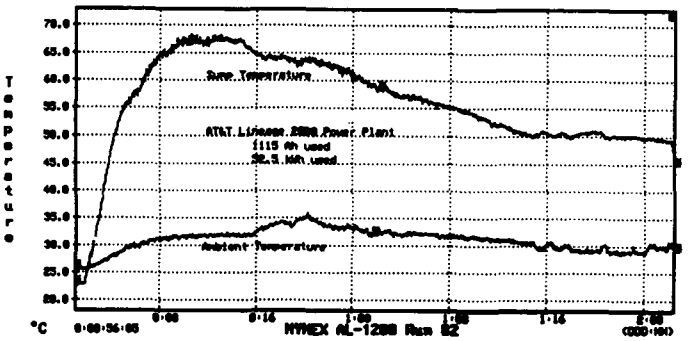

Figure 3(c). Electrolyte reservoir (sump) and ambient temperature during the AL-1200 RPU discharge.

supported both the load current and recharged the lead-acid batteries for thirty hours after which time the load was supported by both the RPU and the recharged lead-acid batteries until the RPU had provided a total of 52.5 kWh. This is equivalent to 57.3 kWh from a 48 cell AL-1200 unit which is very close to the nominal rating at 1200W of 48 hours discharge which is 57.6 kWh as shown in Figure 2. System voltage was at all times between 44 and 49.5V which was within the required voltage window set by NYNEX as shown in Figure 3(b). The maximum electrolyte temperature when the RPU was at maximum power was 67°C. The ambient temperature varied from 30 to 35°C during the 52 hour discharge as shown in Figure 3(c).

An AL-1200 unit was supplied to Mercury One-2-One on a three month trial basis as part of a reserve power system for an important transmission high site of their cellular network. Within one week of installation the unit operated for 7 hours after the lead acid batteries were discharged. On its second operation, two weeks later, the unit ran for a further 35 hours and in total provided 59.7 kWh which is 1136 Ah/cell. The unit was regenerated with new anodes and by electrolyte replacement and was again called into operation one week later for 2 hours. The unit has now been stored for a further 7 months on active standby since this activation and shut down.

Cell Re-use

In-house testing has shown that under release test conditions of a 48 hour discharge at 80 mA/cm^2 of a cell from either the AL-600 or AL-1200 RPU that the cell voltage decays from an average initial value of 1.35V down to 1.16V at the end of discharge. Most of this decay in cell voltage is due to increased cell gap as the anode is consumed and a loss of electrolyte conductivity as it becomes more and more saturated with dissolved aluminate. Washing of the cathode and re-use restores performance to 1.34V which decays down to 1.15V after a second 48 hour cell discharge. Similarly runs three and four decay from 1.33V down to 1.14V and 1.30V down to 1.10V respectively. On the fifth run the performance of the cathode is marginal as the cell voltage decays from 1.23V down to 1.00V which is the minimum acceptable voltage. This data shows that at least three cell re-uses are possible using the same cathode.

Similar testing of repeated discharge of the larger cell for the AL-6000 unit has shown that after three twelve hour discharge cycles at a constant current of 125 A using new anodes and electrolyte each time then the loss of cathode potential is less than 50 mV/discharge. On the fourth cycle the cell reached 1.00 V after nine hours of discharge.

Re-start Capability

Time to full power depends on the temperature of the electrolyte, the characteristics of the DC/DC converter (if fitted), the capacity and state of discharge of the lead-acid batteries and the discharge and storage history of the RPU cells. At temperatures of 15°C and above full power is achieved in 10-30 minutes for a unit with new cells and electrolyte. The spread is due to the variation in lead-acid battery requirements which changes the maximum load needed from the RPU. Below 15°C the time to full power increases progressively as the electrolyte temperature falls and it is advisable to fit a low power electrolyte heater pad which maintains the electrolyte temperature above 15°C.

In addition to our own studies of re-start capability both Ontario Hydro and France Telecom have subjected RPUs to repeated re-start tests. FT started and ran an AL-600 unit for three hours, then left the unit in standby mode for three weeks and achieved a total of 14 re-starts using this operational cycle. Loss of re-start capability was due to the high level of dissolved aluminate which reduces electrolyte conductivity and limits re-start capability to the point where the unit has been 50-60 % discharged. This can be improved by increasing the volume of electrolyte available to reduce the aluminate concentration. Re-start becomes difficult once an electrolyte capacity of 240 Ah/l has been reached which is nearly half the maximum solids free capacity of 500 Ah/l.

Ontario Hydro ran a series of repeated discharges of an AL-600 unit over a test period of seven months in 1992. The unit was started with electrolyte temperatures in the range 20-50°C depending on both the ambient temperature and the time between discharges as the electrolyte remains warm for several hours after discharge and the time to achieve 600 W output power was noted. The unit was then discharged at 600 W for times up to three hours. Satisfactory re-start was achieved twelve times up to 40 % discharge when the unit took more than 2.5 hours to reach 600 W. Further restarts were then achieved with new anodes and new electrolyte.

Figures 4(a) and 4(b) show the consecutive discharge of an AL-600 unit with six days of standby between each discharge. The first five discharges are shown in Figure 4(a) which show that the time to reach an output level of 500 W increases progressively as the total time of discharge accumulates. On the fifth run the unit was unable to provide a re-charge of the lead-acid battery before its voltage had declined to a minimum pre-set level. Renewal of the electrolyte as shown in Figure 4(b) restored start-up performance for the sixth discharge.

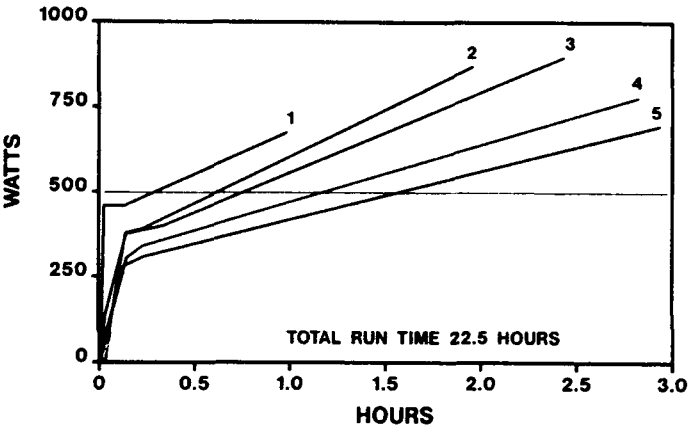

Figure 4(a). Consecutive discharges of an AL-600 RPU with 6 days storage between discharges.

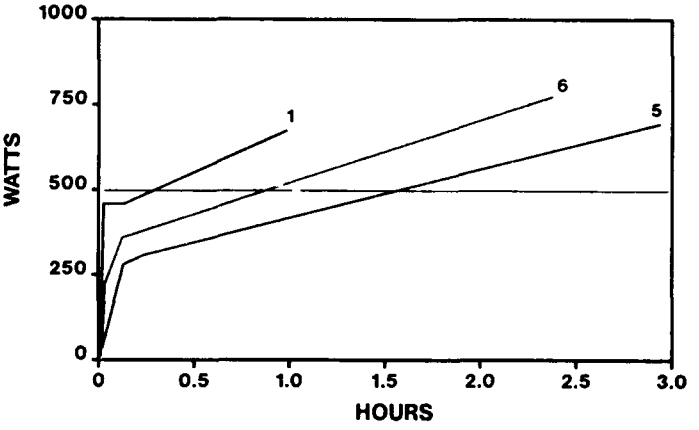

Figure 4(b). Discharge of the AL-600 RPU after electrolyte renewal

Extended Standby

Although a newly installed RPU in the un-activated condition has a virtually unlimited shelf life as neither the anode nor the cathode degrade and carbonation of the electrolyte is insignificant the issue is how long a unit can remain on standby after activation and still be capable of effective re-start and further discharge.

To examine this, at the cell level, cells were put through a simulated start up and lead-acid battery re-charge and then stored them over baths of electrolyte for 10 days at 60°C after which time they were discharged again and then stored for a further 23 days. After this discharge the cells were stored for a further 63 days at 60°C and re-tested. The time to reach a power level of 45 W/cell which is equivalent to a high power level of 2160 W for a AL-1200 unit extended progressively from 1.5 hours, to 2 hours, to 2.5 hours and finally to 3 hours. Even after repeated discharge and a total storage time of 96 days at 60°C these results show that the RPU in tandem with a lead-acid battery can still activate and support an external load and provide extended duration support for telecoms.

RPU Performance

The volumetric and gravimetric energy and power densities of the AL-600, which has a volume of 209 l and weighs 160 kg, are shown in Table 1(a) as a function of output power level. At low powers of operation the hotel loads are a significant proportion of the net power and hence energy density is reduced. Reduced energy density at the higher power levels is due to electrode polarization as the current density increases. The AL-1200 has slightly higher energy and power densities as the AL-600 at twice the output power level in each case. This is because the AL-600 has a 60 l electrolyte reservoir whereas the present AL-1200 has a 100 l electrolyte reservoir. The energy and power density figures for the AL-6000 RPU, which has a volume of 626 l and a weight of 440 kg when filled with electrolyte, are shown in Table 1(b).

Net Power (W)	Power Density (W/l)	Energy Density (Wh/l)	Specific Power (W/kg)	Specific Energy (Wh/kg)
200	1.0	126	1.3	165
400	1.9	153	2.5	200
600	2.9	144	3.8	188
800	3.8	115	5.0	150
1000	4.8	86	6.3	112

Table 1(a). Energy and power density as a function of output power for the AL-600 RPU

Net Power (W)	Power Density (W/l)	Energy Density (Wh/l)	Specific Power (W/kg)	Specific Energy (Wh/kg)
2000	3.2	141	4.6	201
3000	4.8	144	6.8	205
6000	9.5	115	13.6	164

Table 1(b). Energy and power density as a function of output power for the AL-6000 RPU

Summary

The aluminum-air RPU has been in development since 1986 as an extended duration standby power source for applications in telecom networks. The power range of units developed to date has been from 200W to 6000W and discharge times are from 12 to over 100 hours depending on the particular unit and the power level.

Extensive user evaluation has been completed both by established major telecom companies and by emerging cellular network companies. These evaluations have substantiated discharge duration times and have confirmed that multiple restart is possible up to electrolyte capacities of 240 Ah/l. Extended standby life after activation looks promising from accelerated testing of single cells.

The present solids free RPU design has an energy density of the order of 160-200 Wh/kg over most of its operational range.

The first unit activated on a live site as part of a cellular network provided the expected level of standby power integrated over two separate discharge events. Field demonstrations are in progress with several major telecom companies in North America, Europe and Japan.

Acknowledgements

Development of the aluminum-air RPU has been a team effort and the extensive efforts of all those involved is gratefully acknowledged particularly Bob Moore, Tony Warburton and Allan Williams at Alupower/Chloride, John Dawson, Graham McGregor and Mike Schoeneweiss at Alupower Canada and Chris Cestone, Bill Hoge, Bhaskara Rao and John SanGiacomo at Alupower Inc.

References

(1) O'Callaghan W B, Fitzpatrick N P and Peters K, "The aluminum-air reserve battery - a power supply for prolonged emergencies," Intelec 89, Eleventh International Telecommunications Energy Conference, Firenze, Italy.

(2) O'Connor J A, "A new dual reserve power system for small telephone exchanges," Intelec 89, Firenze, Italy.

(3) Hodgson P and Heath M, "Interfacing the aluminum-air battery with telecommunications equipment," Intelec 90, Orlando, 1990.

(4) Warner S M, "The operation of aluminum-air reserve power systems," Intelec 91,

(5) Scamans G M and Warner S M, "Operation of aluminum-air reserve power systems," ERA Battery Conference, London, 1991.

(6) Warner S M, "Standby power - a practical range extender," ERA Battery Conference, London, 1992.

(7) Scamans G M, Lapp S P, Warner S M and Holmes D, "Further development of the aluminum-air telecommunications reserve power source," Intelec 92, Washington, 1992.

(8) Warner S M, "Extending the reliability of DC power in a telecommunications network," Intelec 93, Paris 1993.

(9) Scamans G M, Creber D K and Stannard J H, "The aluminum fuel cell in transportation applications," Power Sources 36, Cherry Hill, 1994.

(10) Hoge W, " An approach to the mass production of gas diffusion electrodes," Power Sources 35, Cherry Hill, 1992.

HIGH PERFORMANCE THERMOPHOTOVOLTAIC EMITTERS*

Robert E. Nelson
Tecogen Division
Thermo Power Corporation
45 First Avenue
Waltham, MA 02254-8995

Introduction

Thermophotovoltaics (TPV) is the direct energy conversion process where a primary energy source (chemical flame, nuclear reactor, concentrated solar energy, etc.) is used to elevate a radiating structure to incandescent temperatures. The radiant energy is collected on an array of semiconductor photoconverters which transforms the incident radiation directly into electrical power. When this process was invented[1] about thirty years ago, most of the early developers[2] of this technology utilized black- (or gray) bodies as the radiant source. Since conventional photovoltaic converters are responsive efficiently only over a narrow bandwidth interval, these early investigators attempted to reflect nonphotoconvertible (mostly long wavelength) radiation back to the source with interference filters or other means in an attempt to enhance the conversion efficiency of the TPV process. Various losses including filter absorption, view factor considerations, and reabsorption problems at the emitter combined to cause a search for selective emitters which did not require these kinds of filtering mechanisms.

Selective Emitters

In the 1970's, investigators at the U.S. Army Fort Monmouth Laboratory determined that the rare earth oxides provided a potential source of selective emitters for TPV applications. The rare earth elements are unique among the stable elements insofar as they appear to be chemically similar. That is, they have the same number of valence electrons (3), but all, of course, have different atomic numbers. This set of conditions can be satisfied only if electronic vacancies exist in the inner electron shells. These vacancies permit electronic transitions that energetically fall into the visible and near IR portions of the electromagnetic spectrum. In addition, all the rare earth elements form stable oxides that are refractory with about the same melting point (about 2600°C). Guazzoni[3] was the first investigator to report the high temperature emittance of selected rare earth oxides, and he identified ytterbia and erbia as important TPV candidate emitters to illuminate elemental silicon and germanium photoconverters, respectively.

Guazzoni and coworkers attempted to fabricate practical monolithic emitters out of erbia by employing conventional ceramic fabrication processes such as slip casting as well as pressing and sintering. Because of thermal stress fracturing, these emitters were incapable of surviving thermal cycles in excess of 1000°C.[4] Guazzoni and coworkers developed a composite emitter structure comprised of a core material, silicon carbide, which was capable of surviving thermal cycling to higher temperatures, and a thin coating of erbia deposited over the silicon carbide. Since a thin coating of erbia is transparent (diathermous) in the infrared except for narrow band opaqueness arising from the electronic transition mechanism, Guazzoni's composite emitter resembled a gray body emitter arising from the properties of the silicon carbide core with superimposed emissions arising from the rare earth electronic transitions peculiar to erbia (a dominant emission at 1.55 μm in the IR and a smaller monochromatic green emission at 530 nm in the visible). These composite emitters were capable of reaching the temperatures necessary for TPV service, but the substantial amount of broadband emission was not a significant improvement over the earlier gray body emitters.

*This work has been supported by the Basic Research Group of the Gas Research Institute, Chicago, Illinois.

Fibrous Emitters

During the 1980's, high performance emitter development was carried out at The Gillette Company. Gillette was interested in fossil fuel powered emitters that generated radiant output in the visible and near IR. This work, in addition, was devoted exclusively to fibrous refractory oxide ceramic emitters. Small diameter (10 μm diameter) fibers were chosen as the emissive medium because fibrous structures have several advantages over monolithic ceramic emitters. First, a small diameter fiber survives thermal stress because no appreciable thermal stresses are built up in the small diametral dimension. Thermal stress built up along the axis of the fiber is relieved by a flexing of the fiber. Furthermore, the fibrous network couples well to the flame's combustion products. In fact, the 10 μm fibers are in approximate thermal equilibrium with the combustion gases, where fiber temperatures ranging from 1500 to 1700°C are possible with conventional fossil fuel (gasoline, diesel fuel, propane, natural gas, etc.) flames. In addition, a small diameter fiber allows some control of unwanted (or broad band) emission. Most oxide ceramics have a high temperature gray body emittance from 0.2 to 0.4 over the spectral region of interest to us, 0.5 to 5 μm. This leads to substantial broadband emission in conventional monolithic emitters. When the ceramic emitter is composed of small diameter fibers, this optically thin structure does not generate appreciable gray body emission. Fiber dimensions, however, cannot be reduced to arbitrarily small sizes because the desirable emission from the selective electronic transitions in certain rare earths will be affected. Finally, the small diameter fibers exhibit a rapid thermal response time. With the high thermal transfer coefficient and low heat capacity of the small volume fibers, a thermal response time of 20 milliseconds has been experimentally determined[5] for fibrous emitter structures similar to ours. This rapid thermal response time has desirable implications. Emitters can be brought up to operating temperatures quickly, and load following or power regulation is practical in TPV energy conversion systems.

A filamentary network of small diameter fibers is, in fact, a common emitter structure inasmuch as the Welsbach gas lighting mantle[6] is well known and the most efficient converter of the heat of gas combustion into luminous output. The unique material composition (99.3% by weight of thoria and 0.7% by weight of ceria) of the Welsbach mantle exhibits in fibrous form an unusual spectral emittance[7] that is very high in the visible and very low in the near IR. The Welsbach mantle exhibits also a significant detriment, and for those who use camping lanterns with mantles, the fragility of these delicate light emitters is an obvious problem. Generally speaking, ceramic fibers fracture because they contain flaws which originate during the fabrication process and which act as stress raisers that cause flaws or cracks to propagate and result in fiber failure far below the ceramic's intrinsic tensile limit.

We have developed a fiber fabrication process[8] that greatly reduces the density and severity of these flaws to increase substantially the mechanical impact resistance of these devices. We employ a specialized cellulosic support process to fabricate the mantle. We begin with a textile precursor in the form of a closed end cylinder that is knitted, woven, or braided out of rayon yarn. The textile precursor is impregnated with aqueous salt solutions of the metals of interest. The treated rayon is subsequently thermally processed to (1) convert the metal salt to the desired refractory oxide and to (2) pyrolyze away the rayon precursor to yield the final product composed of refractory ceramic. The final product has the morphology of the precursor but with greatly reduced final dimensions. Uncontrolled pyrolysis such as the simple burning of the impregnated rayon precursor generates large volumes of decomposition gas in the interior of the rayon filament. Large rifts occur in the rayon as the gases escape. These rifts may be so large that they do not heal or sinter during final processing. Our process begins with a thermal treatment to facilitate the escape of these gases, and our process carefully controls the pyrolysis step to permit the orderly decomposition of the precursor. With our procedure, an improvement in impact resistance that is about two orders of magnitude improvement over conventionally processed devices is possible.

Mechanical Impact Strength

Even though mantle emitters of enhanced mechanical strength are possible with the aforementioned specialized processing, the mantle geometry still has shortcomings. We have performed a simplified mechanical analysis of the mantle geometry by evaluating the maximum stresses developed in the mantle fibers at the attachment point when the mantle is subject to inertial forces. A cantilevered hollow beam analogue has been chosen to represent the mantle. The maximum bending stress S_b turns out to be

$$S_b/\rho a = L^2/D$$

where L is the mantle's length (from the attachment plane to the free end) and D is the mantle's diameter at the attachment plane. ρ is the density of the mantle material, and "a" is the acceleration (or deceleration) in, say, g's. In the analysis the thickness of the mantle fabric drops out of the formulation when it is assumed, realistically, that the thickness is much less than either mantle dimension L or D. We have little control of ρ since the optical characteristics govern the ceramic choice. Since the stress per unit g is proportional to L^2/D in this bending analysis, some comments on overall mantle strength can be made. Long slender mantles are more vulnerable to damage than short, squat structures. Typically, commercial mantles exhibit a mantle diameter which is approximately equal to the mantle's unsupported length. Thus, a second conclusion may be made which is intuitively acceptable. As the mantle size increases (L or D increases), the bending stress increases proportionally with either dimension. Therefore, large mantles are more vulnerable to damage than small mantles. Caution must be used here to avoid extending the aforementioned stress relationship to small L's in order to reduce bending stress. This is an improper use of the cantilevered hollow beam model and a drumhead model would be more appropriate for L's substantially smaller than D's.

Supported Continuous Fiber Emitter

For applications requiring large emitters, we have pointed out the vulnerability of large mantles to mechanical damage. An array of small conventional mantles may be considered but this approach generally involves complexity, and view factors are adversely affected. A new construction[9] has been developed that preserves the desirable properties of fibrous emitters in robust structures of arbitrary size. One embodiment of this novel construction is shown in Figure 1. Here the optically active fibers are anchored to a porous substrate called Celcor which is an extruded cordierite product manufactured by Corning as a catalytic support. An air/fuel premix, in the simplest embodiment, is delivered to the structure from the plenum side. The flame front is located in a plane above the substrate but within the fiber network where a high rate of thermal transfer from the combustion products to the optically active fibers takes place. The substrate, to first order, does not participate in the radiation process because its temperature is far lower than that of the radiating fibers. The substrate, therefore, may be chosen for practical considerations such as cost, mechanical strength, etc. and other substrate characteristics such as thermal stability, thermal coefficient of expansion, and optical properties are unimportant. The substrate, furthermore, acts as a fuel/air delivery system, and substrate porosity is adjusted to provide flame stability (prevention of flashback) and to maximize the turn down ratio.

The structure of Figure 1 is fabricated by impregnating rayon yarn with the appropriate molarity of an aqueous metal salt solution. The metal salt, of course, is chosen to yield the ceramic with the desired optical characteristics. The treated yarn bundles are subsequently inserted into the Celcor substrate as an uncut looped pile. Controlled thermal processing of the imbibed rayon yarn completes the conversion of the treated rayon precursor into the desired durable fibrous ceramic.

Selective Rare Earth Candidates

Ytterbia and erbia have already been identified as emitter candidates for TPV applications. In fibrous form, these rare earths can be very selective.[10] Normalized exitances of fibrous (10 μm diameter filaments) ytterbia and erbia are shown in Figures 2 and 3, respectively. These emitters are powered by isobutane/air flames. Ytterbia has a single emission at 0.98 μm with a full width at half maximum (FWHM) of about 150 nm. Erbia's dominant emission is at 1.55 μm with a FWHM that can be as low as 65 nm. There may be TPV applications that are powered by sources with temperatures far lower than those of chemical flames. We include a fibrous holmia example in Figure 4 with a selective emission at about 2 μm which is best powered by a 1500 K thermal source. A number of other rare earths exhibit selective emission with substantial radiant output in the interval from 1 to 2.5 μm.

Conclusion

Rare earth oxides in fibrous form provide many candidate emitter options that are compatible with available photoconverters. The fibers, which can be fabricated in durable form and incorporated into support structures, are refractory and stable in flame environments. Very selective emission with low off-band emission is available for TPV applications. Small diameter fiber emitters exhibit rapid thermal response times along with high radiation efficiencies and thermal stress resistance.

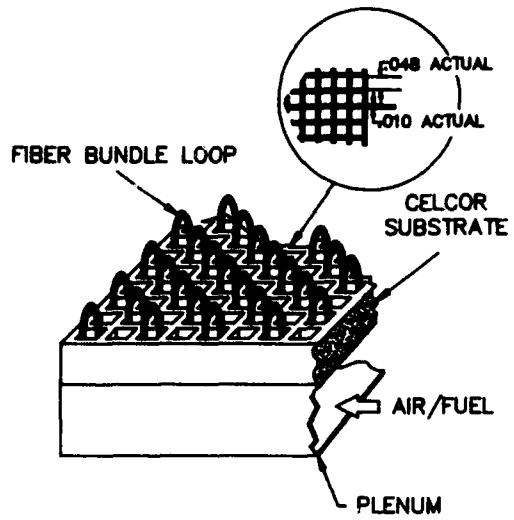

Figure 1. Supported Continuous Fiber Emitter. Pore spacing in substrate has been exaggerated for clarity. Inset demonstrates actual pore/web relationship.

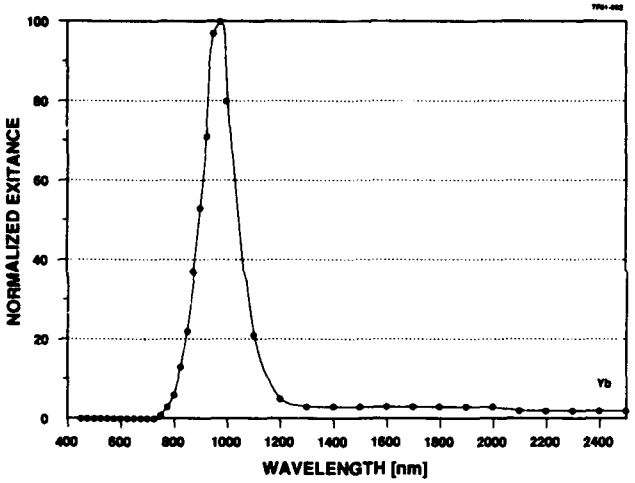

Figure 2. Normalized Spectral Exitance of Fibrous Ytterbia

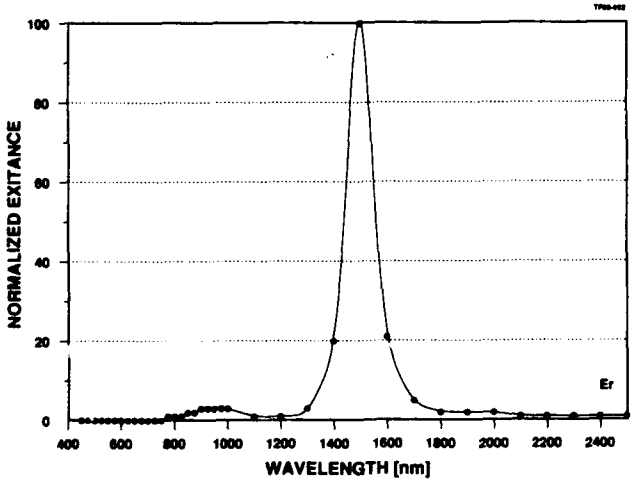

Figure 3. Normalized Spectral Exitance of Fibrous Erbia

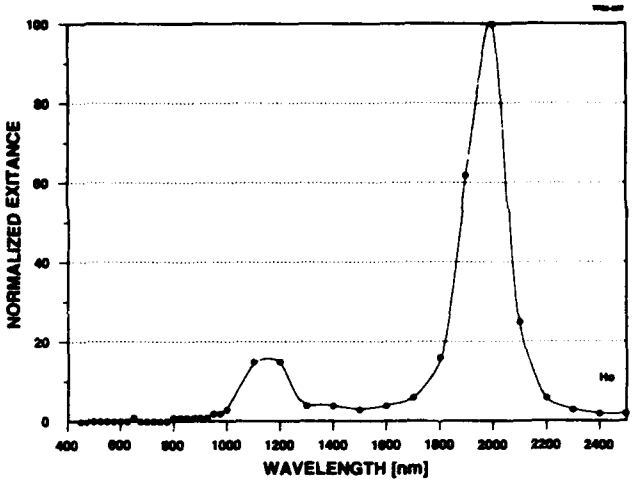

Figure 4. Normalized Spectral Exitance of Fibrous Holmia

References

(1) D.C. White and R.J. Schwartz, "P-I-N Structures for Controlled Spectrum Photovoltaic Converters," Proceedings of NATO AGARD Conference, Cannes, France. March 16-20, 1964. Published by Gordon & Breach Science Publishers, London, 1967. pp. 897-922.

(2) J.J. Werth, "Thermo-Photovoltaic Converter with Radiant Energy Reflective Means," U.S. Patent No. 3,331,707. Filed July 31, 1963. Issued July 18, 1967.

(3) G.E. Guazzoni, "High Temperature Spectral Emittance of Oxides of Erbium, Samarium, Neodymium and Ytterbium," Applied Spectroscopy, Vol. 26, No. 1, 1972. pp. 60-65.

(4) G. Guazzoni and E. Kittl, " Cylindrical Erbium Oxide Radiator Structures for Thermophotovoltaic Generators," Research and Development Technical Report ECOM-4249, U.S. Army Electronics Command, Fort Monmouth, New Jersey. August 1974.

(5) S.A. Pollack and D.B. Chang, "Selective Thermal Radiators," U.S. Patent No. 4,755,673. Filed October 24, 1984. Issued July 5, 1988.

(6) H.E. Ives, E.F. Kingsbury, and E. Karrer, "A Physical Study of the Welsbach Mantle," Journal of the Franklin Institute, Vol. 186, No. 4, October 1918. pp. 401-438. Concluded in November 1918. pp. 585-625.

(7) H. Rubens, "Über das Emissionsspektrum des Auerbrenners." Annalen der Physik, IV Folge 18, 1905. pp. 725-738.

(8) W.J. Diederich and R.E. Nelson, "Refractory Metal Oxide Processes," U.S. Patent No. 4,883,619. Filed August 16, 1982. Issued November 28, 1989.

(9) C.R. Parent, B.P. McFadden, and J.F.S. Olow, "Emission Technology," U.S. Patent No. 5,137,583. Filed April 17, 1991. Issued August 11, 1992.

(10) R.E. Nelson, "Thermophotovoltaic Technology," U.S. Patent No. 4,584,426. Filed September 2, 1983. Issued April 22, 1986.

HIGH TEMPERATURE EMITTERS FOR THERMOPHOTOVOLTAIC POWER SYSTEMS

P. Adair, M. F. Rose, T. Owens and K. Schroeder
Space Power Institute
231 Leach Science Center
Auburn University, AL 36849

Abstract

Thermophotovoltaics is the term applied to the technique for energy conversion whereby the energy emitted by an incandescent source is converted to electrical energy by a photovoltaic cell. The selective line emitters are made from oxides of the rare earths such as erbia. These emitters are made through a specialized series of processes which begin with nitrates of the rare earth and end with rare earth oxide filaments. A special requirement for these applications is the need for a robust large area emitter which could take the shock and vibration of Army applications. Conventional paper making techniques have been used to combine materials suitable as binders with the radiating material. As a result, this technique allows for fabrication of large area robust emitters which were heretofore unobtainable. These radiators will be described in some detail as representative of the process and will be used to illustrate the manufacturing technology developed at Auburn University. Another approach considered in our laboratory is to produce a "modified" blackbody emitter which can withstand sufficiently high temperature operation and produce a significant amount of radiant energy. With this approach, preliminary estimates indicate that efficiencies are comparable to those which can be obtained with selective line emitters.

Introduction

All matter is continually emitting radiant energy as a result of the thermal vibration of the particles of which it is composed. By definition, a blackbody radiator absorbs all radiant energy incident upon it and emits the maximum possible amount of flux per unit area at any given wavelength or wavelength interval for any body at its temperature. All real materials reflect part of the radiant energy incident upon them and emit less radiant energy than a black body radiator at the same temperature. The radiant power density from a blackbody is given by the Stefan-Boltzmann equation as:

$$P = \sigma T^4 \qquad (1)$$

where the power density, P, is in watts/meter^2, the constant σ is the Stefan-Boltzman constant and temperature, T, is in Kelvin. For a non-blackbody source, the above equation is modified by the emissivity, a factor between 0 and 1, which describes the deviation from a blackbody. The spectral or wavelength, λ, distribution of this flux is given by the Planck equation as:

$$P_\lambda = c_1\lambda^{-5}[e^{c2/\lambda T} - 1]^{-1} \qquad (2)$$

in which the parameter P_λ is the spectral emissive power per meter^2 per meter wavelength interval and c_1 and c_2 are the first and second radiation constants. It is this spectrum against which the performance of selective line emitters must be judged with respect to spectral content and efficiency.

Clearly the intensity at a given wavelength is a function of the temperature and it is this temperature which will also determine the efficiency of selective line emitters. If the short wavelength cutoff for the black body spectrum is at a wavelength longer than that required to excite a specific line radiator, there will be little or no emission from the sample. However, the intensity at a particular wavelength is exponential in temperature which should result in a strong temperature dependence for line emission. This is in fact what is observed. In the experiments described below, the experimental set up has a limited capability for exploring the temperature dependence of the emissions.

It has been shown theoretically[1] that certain rare earth oxides are capable of emitting as much as 70% of their total radiated energy when heated at high temperatures in a single line characterized by their electronic structure. The reason that this is possible is the unique electronic structure of the rare earths. At short wavelengths, in the ultraviolet region of the spectrum, the rare earth oxides tend to have a high emissivity. Fortunately, these modes are only excited efficiently at extremely high temperatures. On the other end of the spectrum, in the far infrared, similarly, there is little energy emitted even though there is a high emissivity for these materials. For the temperatures contemplated for thermophotovoltaics, the emissivity of these materials is effectively low except at the line frequency. As a result, in crystalline solids of these materials, the radiative characteristics of these elements are narrow band emissions, rather than a more broad band continuum superimposed upon a line spectrum. The rare earths, in oxide form, which have received significant interest are Nd_2O_3, Ho_2O_3, Er_2O_3, and Yb_2O_3. Table 1 is a listing of some of the electronic parameters for these selected rare earth elements[1].

The line emission from these elements should be at the following wavelengths respectively. Nd - 2.5 microns;

Table 1

Radiative Characteristics of Potential Rare Earth Emitters

Element	Electronic Transition	Photon Energy	Bandwidth	Maximum Efficiency	Approximate Temp. at Max. Eff.
		(eV)	($\Delta E_g/E_g$)	(%)	(K)
Yb	$^2F_{5/2} \rightarrow {}^2F_{7/2}$	1.29	0.18	70	3000
Er	$^4I_{13/2} \rightarrow {}^4I_{15/2}$	0.83	0.05	55	2000
Ho	$^5I_7 \rightarrow {}^5I_8$	0.62	0.10	72	1500
Nd	$^4I_{13/2} \rightarrow {}^4I_{9/2}$	0.50	0.15	55	1400

Ho - 2.0 microns; Er - 1.5 microns and Yb - 0.95 microns. Note that some of these materials (Table 1) approach maximum efficiency at temperatures well within the range of those already in use in the industry. Further, Chubb's[1] theoretical analysis indicates that the optimum geometry for a radiator is in the form of a fiber with a thickness on the order of, or less than, the optical depth at the line frequency. The advantage of the thin fibers is in the small optical thickness of the fibers. Small fibers effectively limit off-band absorption and emission, characteristic of free carrier absorption and lattice defects. Guazzoni[2] has measured emittances for some of the rare earth oxides at the characteristic wavelength to be in the 0.4-0.6 range. This is comparable to values listed in the materials handbook[3] and indicates that a substantial power density can be radiated from structures made from these oxide emitters. A typical blackbody like radiator has a hemispherical emissivity on the order of 0.75. Until robust large area samples of these materials can be fabricated, it is impossible to determine the efficiency of conversion from the heat of combustion or electrical input to line emission.

Experimental

Radiator Fabrication

The fundamental prerequisite for selected line emitters for our application is that they must be strong enough to survive in a battlefield scenario. Furthermore, they must be easy to fabricate, capable of fabrication in any geometry, and relatively inexpensive. The basic technology used in the fabrication of our emitters is covered by U. S. Patents 5,080,963 , 5,096,663 , and 5,102,745 , with significant additions applicable to the unique materials requirements placed on selected emitters. Standard paper making techniques are used. The preliminary form of the radiator consists of a suitable precursor for the rare earth oxide, cellulose, and quartz fibers which have been blended and made into a standard sheet of paper. By using this technique, highly uniform sheets can be made which can be molded into any form while still wet. When dry, the sample is oxidized to produce a composite structure. The "radiator" is then annealed at a high temperature in a reducing atmosphere to remove the cellulose and sinterbond the quartz fibers. The sinterbonding provides an excellent mesh which effectively holds the radiating material in place as well as providing structural strength. Quartz is ideal and can be purchased in a number of sizes. By varying the constituents, thick paper can be made to the point of being essentially optically opaque over a wide range of wavelengths. We have used this technique to produce robust radiators from erbium, holmium, and neodymium.

Experimental Set Up

Figure 1 is a block diagram of the experimental assembly used to measure the emission from the emitter surfaces. We have constructed the apparatus to allow both a combustion and electrical heat source. In order to make accurate efficiency measurements, it would be desirable to heat the samples electrically. In that manner, the input power to the heating element must be equal to the power radiated from the surface plus any losses due to convection and conduction. For accurate measurements, it may be necessary to conduct this experiment in a vacuum and with long cylindrical samples where end effects would be negligible.

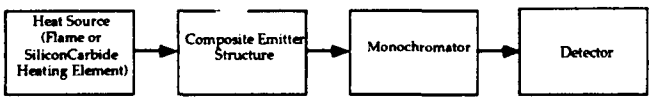

Figure 1: Block diagram of experimental test setup by flame or electrical heating.

For our test setup, we thermally heated the composite emitter structures via a combustion flame source or by flowing current through a silicon carbide heating element. The composite emitters were molded into a cylindrical tube shape in order to maximize the thermal coupling to the silicon carbide heating element. The composite emitters, in the form of a tube, could also then be placed in the flow of a combustion flame to be thermally excited. When heated, the spectral content of the composite emitter output was determined by using a Jarrell Ash Quarter Meter Ebert Monochromator which contained a diffraction grating with a 295 grooves per millimeter ruling and a 2.1 micron blaze. A thermopile detector was placed at the exit slit of the monochromator to determine the relative amount of radiation at each wavelength. A thermopile detector was used because of its uniform absorption over a wide range of wavelengths. The power impinging upon the detector head at each scanned wavelength was then logged using a data recorder.

Results and Discussion

The basic technique for fabricating unique composites allows the construction of a homogeneous, moldable structure from components which normally are incompatible. Using this technique, we have also fabricated essentially a blackbody mantle comprised of silicon carbide fibers with quartz as a binder. We were interested in this moldable radiator structure because one option for thermophotovoltaic applications is to fabricate a tandem photovoltaic cell which is sensitive to two regions of the spectrum. This of course places the burden for efficiency on the cell construction. Conversations with solid state physicists indicate that cells as high as 30% efficiency could be constructed. Conversion from heat of combustion to blackbody radiation using one of these radiators is highly efficient with the structure emissivity approaching 1. The small size of the fibers ensures high efficiency. Figure 2 illustrates the emission spectrum from this sample along with a blackbody spectrum at the same temperature calculated from Equation 2. The "dip" in the silicon carbide curve is due to absorption from water vapor in the air.

The technique above has also resulted in "mantle" structures containing rare earth oxides which are robust enough to make cylindrical structures 1" in diameter and 6" long. They are easily handled and have survived dropping to the floor in the process of changing mantles. This is of interest because rare earth oxides are very brittle and fragile in nature and cannot be used in large area emitters without the structural support of some type of reinforcing material such as quartz fibers. The strength is governed by the appropriate heat treatment of the mantle and the ratio of the constituents. For our application, we feel that this issue is solved and strong mantles can be made in most geometries

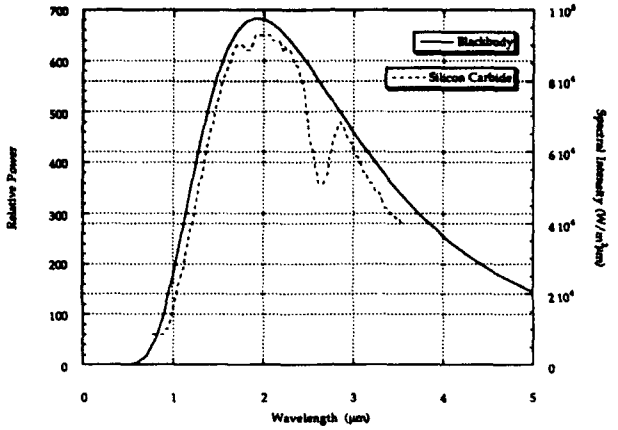

Figure 2: Silicon carbide composite emitter versus blackbody curve at same temperature.

and if necessary with surface areas of several square feet using our equipment. We have observed radiation from mantles excited both electrically and with combustion heat sources. Figures 3-5 are a compilation of the results of the rare earth oxide composite emitters when heated with a combustion flame. Note that for holmia, the peak to background ratio is 6:1 and the bandwidth at half maximum is 400 nanometers. Also noteworthy is the fact that all of the composite emitters have line emissions corresponding to the values listed in Table 1 with significant peak to background ratios. A wide bandwidth may be good for thermo-photovoltaic applications from the perspective of cell output power design. Under certain circumstances, it may be desirable to broaden the emission profile or to have radiation at two distinct wavelengths. The technique described above is readily adaptable to producing "two line" emitters. Figure 6 is the output spectrum of an erbia/holmia composite emitter.

In an attempt to construct an experimental arrangement which would allow accurate characterization of efficiency, an electrically heated unit was constructed. The silicon carbide heating element was powered by the laboratory main through a variac power controller. In this manner, the heating element should be capable of achieving temperatures of 1500 K. Our first experiments with this assembly have resulted in the expected line emission but superimposed upon the line emission is a blackbody like spectrum which manages to penetrate the mantle and is

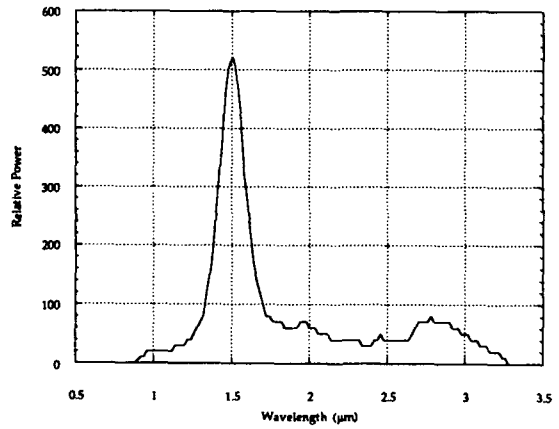

Figure 3: Erbia composite emitter heated with a combustion flame.

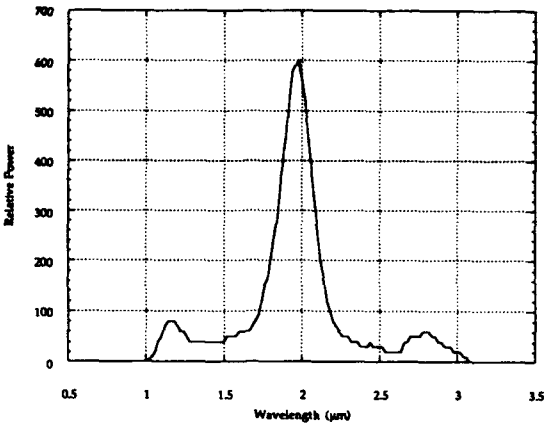

Figure 4: Holmia composite emitter heated with a combustion flame.

characteristic of the silicon carbide heating element. Thicker emitter structures should effectively eliminate that problem. Figures 7-9 illustrate the data from erbia, holmia, and neodymia. Note that a small peak occurs at the predicted wavlength of the rare earth oxide but blackbody radiation penetrates the fibrous mantle structure lowering the peak to background ratio.

One significant problem encountered during testing was determining the temperature accurately at the high temperatures required for line emission. Because the composite emitters are of a fibrous nature, good surface contact with the oxide fibers and a thermocouple junction is virtually impossible. Another possibility for temperature measurement is the use of an optical pyrometer. With this type of temperature measurement, the emittance of the observed sample must be known. Unfortunately, the very nature of the rare earth oxides yields a material with an emittance that varies with wavelength and more importantly temperature. Therefore, it is impossible to accurately determine the sample temperature by simply observing the composite emitter with an optical pyrometer. The sample temperature in general was greater than 1200 K for the data displayed in Figures 3-7. At present, other methods for accurately determining the surface temperature of the composite emitters are being explored such as using a high temperature paint, whose emissivity can be measured, to place a small dot on the emitter surface.

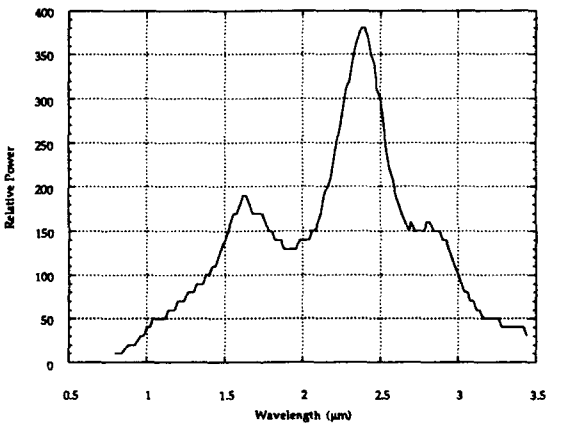

Figure 5: Neodymia composite emitter heated with a combustion flame.

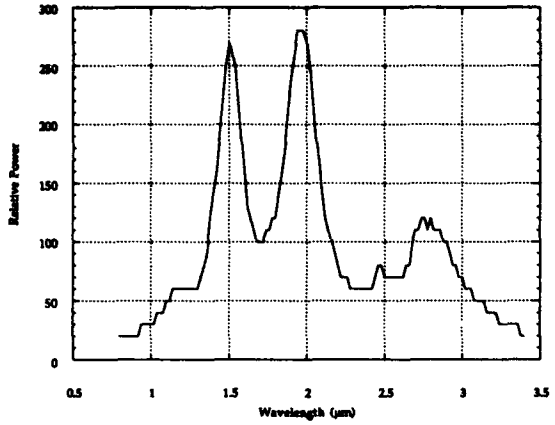

Figure 6: Erbia/Holmia composite emitter heated with a combustion flame.

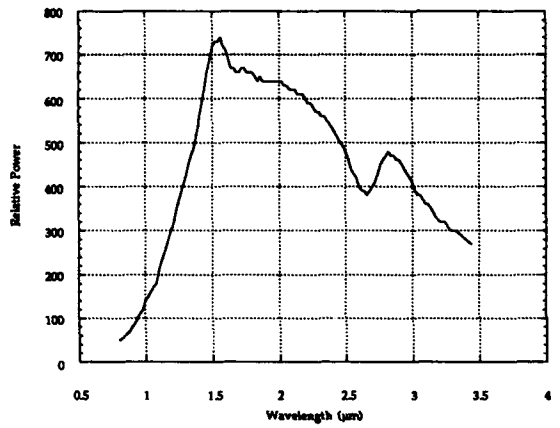

Figure 7: Erbia composite emitter heated by SiC heating element.

In closing, we have succeeded in the manufacture of robust samples using composite techniques which we feel can have significant applications to thermophotovoltaics.

Acknowledgments

The authors would like to take this opportunity to thank the Army Research Office for their funding and support under research grant DAALO39260205-1. We would also like to thank Dr. Randy Criss for his help and knowledge on infrared spectroscopy.

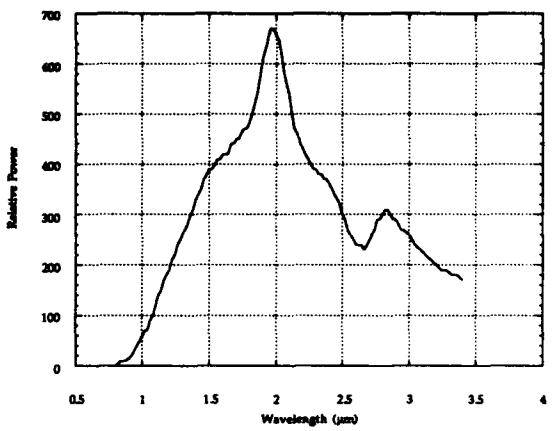

Figure 8: Holmia composite emitter heated by SiC heating element.

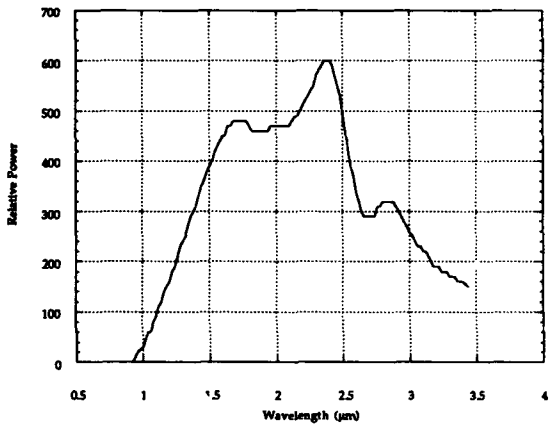

Figure 9: Neodymia composite emitter heated by SiC heating element.

References

(1) Chubb, D. L. (1990). Reappraisal of Solid Selective Emitters. NASA Tech. Memo 103290.

(2) Guazzoni, G. E. (1972). High-Temperature Spectral Emittance of Oxides of Erbium, Samarium, Neodymium, and Ytterbium. Applied Spectroscopy, Vol. 26, #1, pp. 60-65.

(3) Touloukian, Y. S., and DeWitt, (1972) D. P. Thermal Radiative Properties Nonmetallic Solids. Thermophysical Properties of Matter, Vol. 8.

HYBRID THERMOPHOTOVOLTAIC POWER SOURCES

G.Guazzoni and B.Pizzo
Electronics & Power Sources Directorate
Army Research Laboratory, Ft. Monmouth, N.J.

Abstract

The spectral matching of the radiation from an Ytterbium Oxide emitter with the absorption characteristics of the photovoltaic Si cell allows the design of high efficiency/high power density thermophotovoltaic generators. The use of the Si cell allows the development of hybrid thermophotovoltaic power sources operating with solar radiation and with thermal energy from a hydrocarbon fuel combustion. A hybrid thermophotovoltaic system can therefore provide output power in the presence of sunlight and at night or in adverse environmental conditions.

Introduction

The experimental results and design analysis reported in this paper represent an approach to provide military, tactical power sources that can be operated by either solar radiation and thermal energy emitted by a hydrocarbon fuel operated burner. Advances in the thermophotovoltaic (TPV) energy conversion technology, which have been realized through research and development work in the past few years, have been utilized in this study.

Hybrid TPV generators in the 10-30 watt output power range can support Special Operations Forces critical missions providing day and night source of power to recharge essential communication equipment's batteries. Larger power range (100-3000 watt output) hybrid TPV units can provide silent, reliable, efficient source of electric power for Army shelters and other applications.

Discussion

A TPV generator consists of a light source (burner or other heat source heating a mantle-emitter) and an array of photovoltaic (PV) cells that directly convert part of the radiation from the emitter into electric power. A hybrid TPV system also consists of a unit that controllably can burn hydrocarbon fuel heating a ceramic mantle with selective spectral emission chosen to optimize the match with the spectral response characteristic of a Si cell array. However, the Si cell array can be disassembled from the rest of the unit and used directly in conjunction with the sun. If high intensity Si cells are used, a foldable concentrator will be deployed to collect larger amounts of solar radiation. A hybrid TPV power source can therefore operate and provide electric power output both, in the presence of solar radiation and at night or in adverse environmental conditions.

Hybrid Thermophotovoltaic Unit for the Special Operations Forces

The Special Operations Power Sources (SOPS) are deployed by tactical elements of the Special Operations Forces (SOF) into denied or targeted areas to provide a long term means of recharging outstation C-E equipment batteries. The preferred source of power is a passive system, (two solar panel assemblies) which can recharge the batteries and produce power output without the presence of a full time operator. Each solar panel assembly consist of two rectangular (23 cm x 33 cm) cell panels containing 39 multicrystal Si cells for a total cell area of approximately 2400 cm^2. The Si Cell efficiency is approximately 13.5 % and under one full sunlight conditions at 1.5 air mass, the two solar panel assemblies produce approximately 30 watts at a nominal 16 volts. During periods when the solar panels are not effective (darkness, reduced visibility or adverse environmental conditions) an active system, consisting of a Man-Operated Generator (MOG) provides means to generate electric power. The SOPS kit also contains DC-DC adapters , universal power cables and connection plugs. All components of the kit are throw away items with the exception of the MOG which is the heaviest and most expensive component. It has to be carried back from the field and if damaged must be exchanged for a fully functional unit.

A possible hybrid use of the SOF solar panels is their operation in connection with an artificial source of light when sun radiation is not available. This source of light can be provided by a propane, butane or natural gas burner (tip of a gas lantern) equipped with an emitting mantle spectrally tuned to the Si cell characteristics, for example, a ruggedized Welsbach mantle doped with a selective emitting rare earth oxide with strong radiating bands in the Si cell spectral absorption region. The actual solar panel assemblies used by the SOF can be redesigned, still maintaining the same kind and number of cells, into a multi-panel configuration capable of completely encircle and cover the artificial source of light for maximum light collection and to avoid visible detection. A schematic representation of this concept is illustrated in Figures 1, 2 and 3. Figure 1 is the schematic of a six-panel array of state-of-the-art

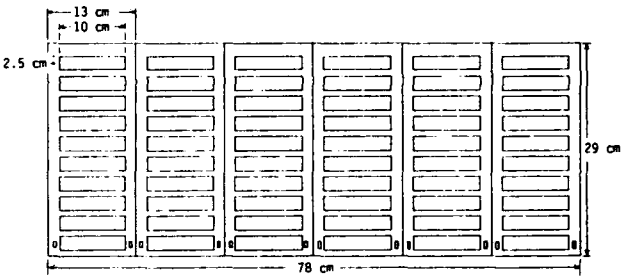

Figure 1. Six-panel array (60 series connected Silicon cells).

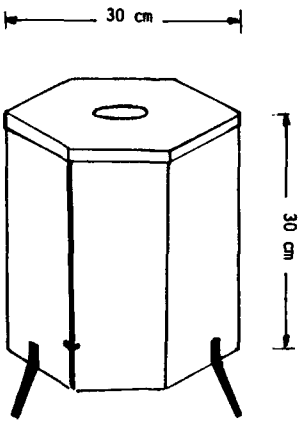

Figure 2. Hexagonal enclosure formed with the six-panel array.

multicrystal Si cells with a conversion efficiency of 13.5 % which was utilized in the experimental demonstration of the feasibility of this approach. The six-panel array is comprised of 60 series connected cells. Figure 2 is a representation of the six-panel hexagonal enclosure that can be formed by assembling the panels around the burner-mantle. The enclosure is closed on the top with an hexagonal cover provided with louvers to exhaust heat and combustion gases. The inside surface of the cover is aluminum coated to reflect light back to the cells. Figure 3 is a cross sectional view of the enclosure-burner assembly.

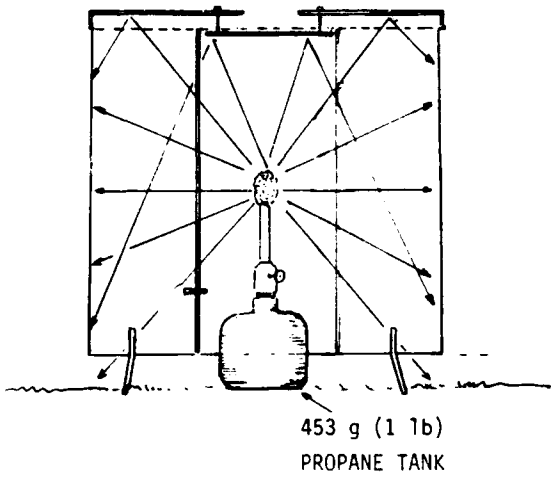

Figure 3. Cross sectional view of the panels-burner enclosure.

Preliminary tests to demonstrate the feasibility of this approach were conducted using commercially procured lantern burners and gas mantles. Operating the burner with propane fuel at a fuel rate of 50.5 grams per hour the combustion on the mantle generates approximately 645 thermal watts (2,200 BTU/hour). To express the effect of a light source over a surface enclosing it, a term is necessary which is constant when summed over a spherical shell enclosing the source but which can vary as individual zones of the shell are considered. Luminous flux measured in lumens performs this function. Basic literature data[1] on commercial gas light mantles perform indicate that a mantle combustion generating 2,200 BTU/hour produces between 138 and 271 lumens (depending on the mantle orientation and the ratio of fuel to air) over a complete spherical shell. Because two lumens correspond to one watt of radiating energy, the mantle utilized in these preliminary tests emitted, in the best operating conditions, no more than 135 watts of radiation. This translates in a mantle radiating efficiency of 21% (e.g. 21% of the energy generated by the fuel combustion is converted into light) which can be considered in accordance with literature data on commercial burner-mantle units that, without heat regeneration sections, are characterized by emission efficiencies between 10 and 20%.

Approximately ninety-seven (97) watts (72% of the energy radiated by the mantle) fall on the 6-panel hexagonal structure, with the remaining 28% equally distributed over the top and bottom openings of the enclosure. The radiation falling on the opening at the bottom of the unit (19 watts) is completely lost. The radiation hitting the top cover, is partially reflected and it is estimated that approximately 8 watts reach the cell panels. The sixty (60) series connected Si cells account for 1500 cm^2 of the panel surface (66% of the total panels area). Therefore the cells receive a maximum of 72 watts of radiation (64 watts directly from the mantle and 8 watts reflected back by the enclosure cover).

The average intensity of the cell illumination is approximately 48 mw/cm^2, less than half a full sunlight illumination. If all the radiation were impinging normally on the cell surface and were uniformly distributed over the entire active cell area, the cell array, with a conversion efficiency of 13.5% , could generate an electric output of up to 9.7 watts. The tests conducted on the demonstration unit, Figure 4, produced a total electric output of 1.7 watts, corresponding to a system overall efficiency (electric output divided by the heat of content of the fuel used) less than 1%.

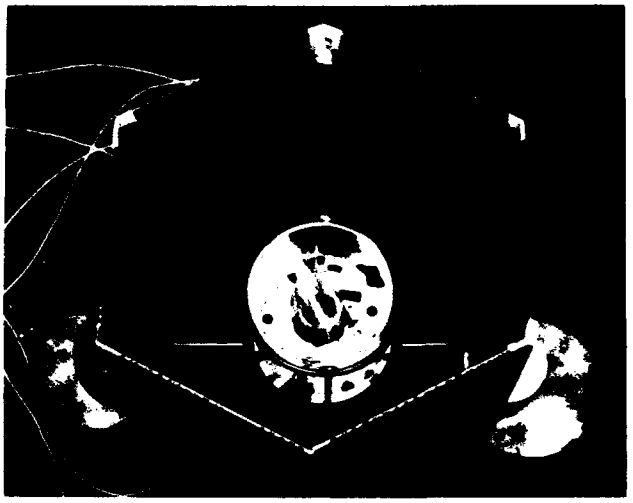

a) Demonstration unit with upright mantle suspended above the burner

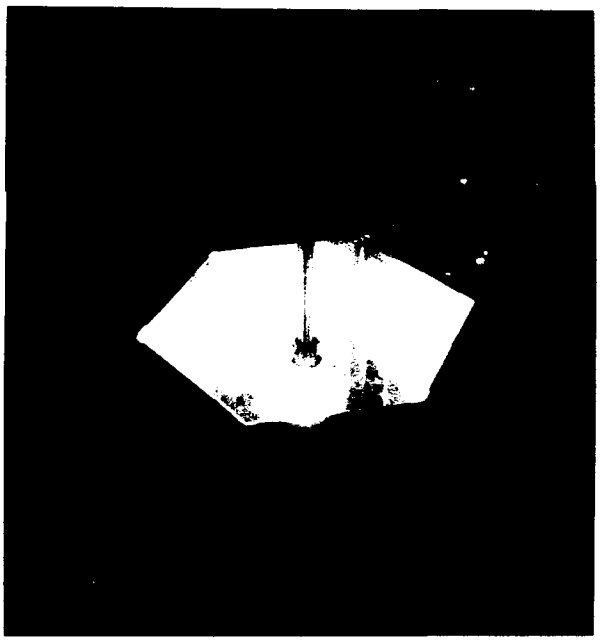

b) Demonstration unit with inverted mantle suspended below burner port

Figure 4. Six-panel demonstration unit.

Two major reasons for the poor performance of this first proof-of-principle demonstration were immediately identified; a) cells uneven illumination and, b) spectral mismatch between the emission characteristics of the mantle and the absorption characteristic of the Si cell. As shown in Figure 1, every panel contained 10 series connected cells. The mantles used, 2-3 cm long, were positioned at the middle point of the 29 cm long panels. Therefore, the illumination of the cells resulted quite disuniform. Measurements conducted with a calibrated solar flux meter indicated that the two cells at the middle of each panel, directly facing the mantle at a minimum distance of 12 cm, were illuminated with

light intensity of 80-90 mw/cm^2 while the cells located in the top and bottom rows of the panels were illuminated at intensities of only 20-25 mw/cm^2. These peripheral cells generate substantially fewer free carriers than the other cells and because they are all series connected, they limit the output of the entire panel to the level of current that they can sustain. If longer mantles can not be fabricated and utilized, the next demonstration prototype will be designed with shorter cell panels, 10 - 12 cm long, each consisting of two Si cells vertically oriented and bridging the entire panel length. In this way every cell will be equally illuminated. The mantles utilized in these tests were procured from 3 different manufacturers of gas lanterns. They were commercial gas mantles whose chemical composition is optimized to provide high intensity emission lines in the human-eye visible part of the spectrum (400-700 nm). These emission lines correspond to wavelengths shorter than the wavelength range where the Si cell has the pick of its absorption curve (900-1050 nm) resulting in reduced output from the cell.

Rare earth oxides have been proven to be chemically stable up to temperatures close to their melting point (above 2000° C) and to maintain their spectral emission characteristics for an indefinite time, even in highly oxidizing atmosphere.[2] A strong radiation band at relatively shorter wavelengths (850-1150 nm) from an Ytterbium Oxide mantle heated at temperatures in the 1300 - 1700°C range, was found to be an optimal match for the Si cell absorption characteristics providing a high efficiency conversion of the mantle radiation into electric power.[3,4] Even if a commercial, low cost mantle design must be utilized for this SOF application, the mantle composition must be reformulated to include Ytterbium Oxide. During the last few years emitters have been constructed of fine (5-10 μm) rare-earth oxide fibers similar in design to the Welsbach mantles used in gas lanterns.[5] Some of these mantles made of 100% ytterbia, have demonstrated substantial improvement in mechanical properties and spectral match with the Si cell characteristics (5 fold higher electric output from the cell as compared with commercial gas mantles operated at the same temperature and fuel consumption rate.)

Tactical, Portable Hybrid TPV Generators

New ceramic mantle processing techniques, applicable to several refractory oxides, have resulted in effective selective emitter mantle compositions with significant improved mechanical and thermal shock resistant characteristics. Several rare earth oxides (Erbium Oxide, Niodimium Oxide, Ytterbium Oxide, etc.) have been formed in innovative mantle designs with increased selective thermal emission capability characterized by strong energy bands in the wavelength range between 800 and 2500 nm.

Planar sources of selective emission, called supported continuous fiber emitters, were recently developed with over 10 watts/cm^2 surface radiating intensity. These flat mantle structures, alternative to the traditional close end cylinder configuration, provide an effective innovative design for the mantle of portable TPV Power Sources with

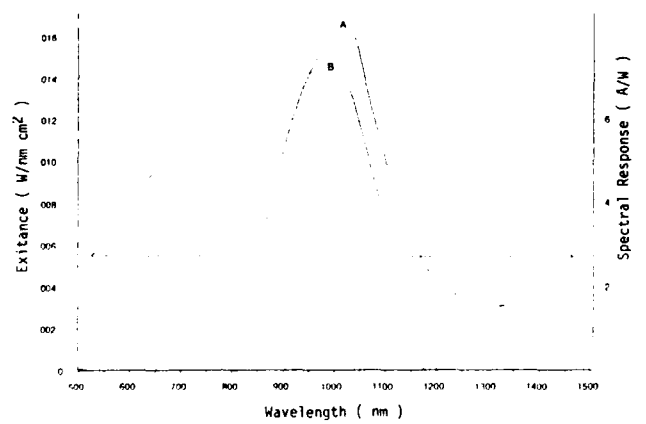

Figure 5. Spectral exitance of Ytterbium Oxide (A) and spectral response of high intensity advanced Si cell (B).

larger power output (from hundreds of watts to few kilowatts). In addition, recent advances have been made in the development of high intensity Si cells which have been fabricated with conversion efficiencies ranging between 20 and 33% at concentrations levels in the 20-200 suns. The overlapping of Si cell response and Ytterbium Oxide emitter output is shown in Figure 5.[6] The combined result of both, spectrally improved selective emitters with high emission flux density and high intensity Si cells provides the possibility for the development of high power density/high conversion efficiency TPV generators. The use of Si cells also allows the design of a hybrid TPV unit capable of working with both hydrocarbon combustion and sunlight. Figure 6 is a conceptual representation of a 90 watt electrical output portable TPV power source comprising a 100 cm^2 flat design, Ytterbium Oxide fiber mantle and a PV panel with 100 cm^2 of high intensity Si cell active area. When operated with combustion from hydrocarbon fuel and using realistic output and view factors, 3 watt/cm^2 of the radiating energy from the Ytterbium Oxide mantle are available in the spectral range usable by the Si cell. With a cell conversion efficiency around 33%, the cell array will provide 1 watt of electrical output for every square centimeter of active cell area. The only ancillary power requirement (~10 watts) is for the operation of a small fan to provide forced air cooling of the Si cells which work at approximately 30 times full sun radiating intensity. The fan is directly powered by the cell panel output with no need for a starting battery. Using state-of-the-art components the weight of the unit (without fuel) is less than 3 kg. with a power density of approximately 30 watt/kg.

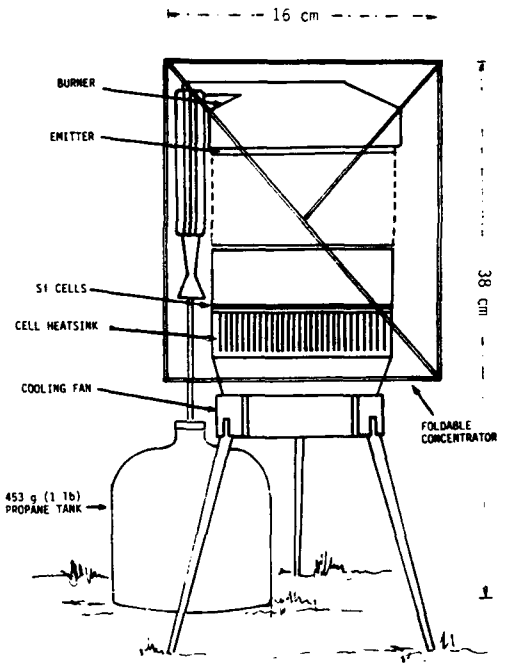

Figure 6. Conceptual representation of a 90-watt Hybrid Thermophotovoltaic Tactical Power Source

Recent developments in spectrally selective holographic concentrators indicate the possible use of holography as spectral splitting for PV and TPV energy conversion.[7] A single element hologram, between emitter and cell array, can defract away from the cells and out of the system the unwanted infrared radiation. This will reduce cell cooling requirement and provide an effective, simplified design approach for waste heat recovery. The overall efficiency of the 90 watt TPV unit (net electrical output divide by the heat of content of the fuel) is strongly dependent on the burner efficiency. Without any preheating of the air-fuel mixture, 453 grams (1 lb) of fuel operate the 90 watt power source for

approximately 1 1/2 hours with a unit efficiency of 2.2%. With an effective heat recuperation section, burner efficiencies in the 40-50% range are achievable resulting in a system efficiency in the 6-7% range. In Figure 7 the cells-cooling fan section of the unit is disassembled from the burner system and equipped with a simple design (truncated pyramid) concentrator for operation on sunlight. Concentration of solar radiation becomes necessary when higher intensities are desired than can be obtained with a flat collector alone or when the cost of the receiver per unit area (e.g. high intensity cells) is higher than the cost of a concentrator per unit aperture area. Closely related to sunlight concentration is the "acceptance angle", i.e. the angular range over which all rays are accepted without moving all or part of the collector. Thermodynamics defines the maximum possible concentration for a given collector acceptance angle. The simple concentrator design depicted in Figure 7 which can be made of foldable aluminum foil sections can be engineered to form integral part of the TPV unit shroud, however it is an inefficient concentrator structure and involves a compromise with its optical and thermal properties. In military applications the cell-concentrator assembly may be required to be fixed on the ground and a too narrow acceptance angle may call for continuous, periodic reorientation of the unit to collimate with the sun. Among concentrators which approach the thermodynamic limit of concentration are the "compound parabolic concentrators" (CPC).[8] They consist of parabolic reflectors which funnel the radiation from aperture to absorber (Figure 8). The right and left half of the CPC illustrated in Figure 8 or for a 3 dimensions CPC, the opposite sections (branches) of the concentrator belong to different parabolas as expressed by the name CPC. The axis of the right branch, for instance, makes an angle θ with the axis of the collector, and its focus is at A. At the end point C, the slope is parallel to the collector's axis. The CPC have a unique angular acceptance characteristic: all rays incident on the aperture within the acceptance angle will reach the absorber while the others will bounce back and forth between the reflector sides and eventually re-emerge through the aperture. Equipping the TPV power source with a CPC designed for a specific acceptance angle will provide longer (few hours) unattended, operation of the cell panel before need for unit reorientation.

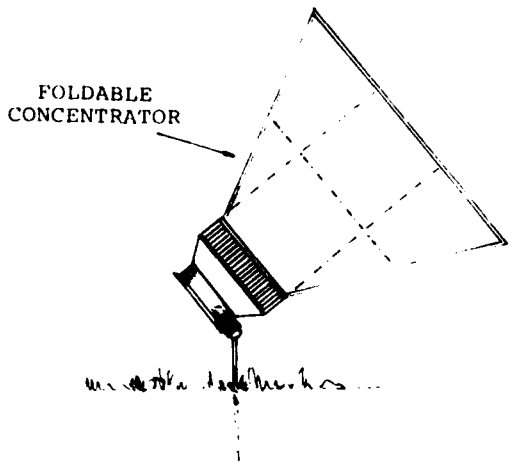

Figure 7. Si cells-concentrator assembly operating on sun radiation

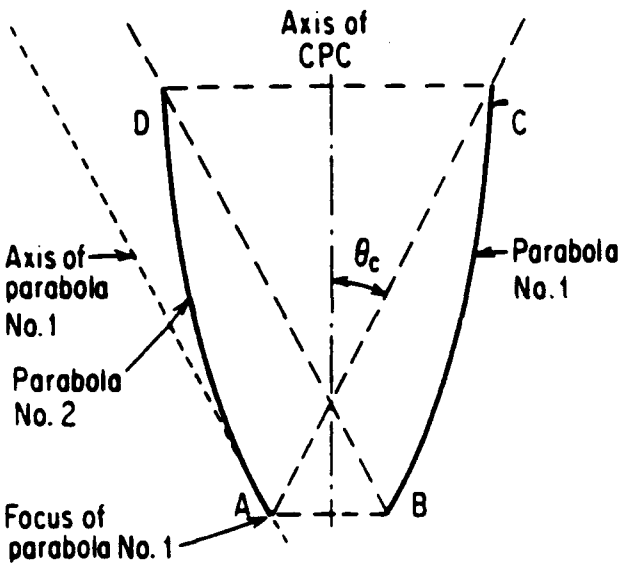

Figure 8. Compound Parabolic Concentrator showing foci, axes, and parabola branches

Conclusion

The utilization of the Si cell as PV converter in the design of a thermophotovoltaic generator allows the hybrid use of the unit with both, sunlight and radiation from a hydrocarbon fuel combustion. The use of high intensity radiators with strong emission bands in the Si cell spectral absorption region is a key factor for the development of lightweight, high power density, hybrid thermophotovoltaic power sources. Holography can provide an innovative approach for the removal (scattering) and the management (focusing on specific areas) of the unusable infrared radiation, resulting in a highly effective waste heat recovery (preheating of the air-fuel mixture) with substantial increase of the generator overall efficiency.

References

(1) R. J. Zielinski,(1962) "Gas Light Performance and Design", Research Bulletin 91, American Gas Association Laboratories

(2) G. E. Guazzoni, (1969)"Rare-Earth Oxide Radiators for Thermophotovoltaic Energy Conversion", R & D Tech Report ECOM-3116

(3) G. E. Guazzoni, (1972)"Applied Spectroscopy" , Vol. 26 , 1972 pp 60-65

(4) R. E. Nelson (1986) "Rare Earth Oxide TPV Emitters", proceedings of the 32nd International Power Sources Symposium. pp.95-110

(5) C. R. Parent and R.E. Nelson (1986)" Thermophotovoltaics Energy Conversion with a Novel Rare Earth Oxide Emitter", Proceedings of the 21 st IECEC, Vol II, 1986, pp.13141317.

(6) R. E. Nelson and P.A. Iles (1993) "Possible Applications of Selective Emitters for Space Power" proceedings of the Joint Solar Engineering conference ASME. pp 529-537

(7) J.E. Ludman, J.L. Sampson, R.A. Bradbury, J. G. Martin, J.R. Riccobono, G. Sliker, E. Rallis, (1992) "Photovoltaic Systems Based on Spectrally Selective Concentrators", Proceedings of the SPIE, Volume 1667,1992, pp 182-189.

(8) J. F. Kreider and F. Kreith (1979) "Solar Energy Handbook" McGraw-Hill

ALPHA IRRADIATIONS OF InP SOLAR CELLS: IMPLICATIONS FOR RADIONUCLIDE BATTERIES

Charles C. Blatchley, Edward A. Burke, Claudia W. Colerico, Pascale M. Gouker, Harvey B. Serreze
Spire Corporation, Bedford, MA

Introduction

In this study, the first reported alpha particle bombardments of InP were completed, and the Non-Ionizing Energy Loss (NIEL) formalism expressing radiation dose as an equivalent fluence of 1 MeV electrons was precisely verified for InP. With this approach any ionizing exposure, at any incident energy, can be converted to a common condition for comparisons. Consequently, simple alpha particle exposures can be generalized. Their high equivalent doses are ideal for testing solar cells or other semiconductor devices that must work reliably in a radiation environment. In addition, carrier removal was found to cause two previously undetected effects, a plateau above the simple diffusion-length predicted curve due to an expanded depletion region, followed by a sharp drop in performance as additional carrier loss chokes off power conversion altogether. Both effects have significant implications for radio-voltaic batteries.

Previous attempts to employ radioisotopes to power silicon voltaic cells were limited to beta emitters with relatively short half lives and low energies to avoid radiation damage. This limited both power and effective lifetime. Compared with more common semiconductors (silicon and gallium arsenide), InP exhibits a marked resistance to radiation damage, opening the possibility of an alpha-emitter battery. In addition, indium phosphide anneals at relatively low temperatures, in many instances at room temperature.

Initial tests of alpha irradiated InP photocells using visible light (AM0 solar spectrum) agreed well with NIEL predictions model. However, degradation in alpha excited cells was higher than calculated for AM0. Low temperature annealing is insufficient to overcome this discrepancy. We conclude that even with the best material characteristics reported in the literature, long-lived alpha particle powered cells could be made but not as compactly as historical beta cells using silicon.

Computational Modeling

Two computer models were essential to interpretation of these measurements. First, the TRIM Monte Carlo code[1] calculates charge carrier generation and displacement production along an ion track in solids. The second is the PC-1D device model,[2] a one dimensional, finite element approach to semiconductor transport equations, for predicting device performance as a function of material parameters, *e.g.*, minority carrier lifetime.

Radiation induced displacement damage has been studied in InP with electrons, protons, and cobalt-60 gamma radiation[3-8] but not previously with alpha particles. Fortunately, the NIEL method permits available displacement damage information to be generalized. Once the damage distribution is calculated, it can be correlated with previous data from other radiation types to determine changes in carrier diffusion length and dark current. These in turn permit the prediction of cell parameters, such as short circuit current, open circuit voltage, fill factor, and maximum power point.

Because the most relevant radiation damage studies have been for solar cells used in space, a convenient standard for comparing radiation doses is the damage produced by 1 MeV electrons. At other energies, electrons produce the non-ionizing energy loss shown in Figure 1. This permits an estimate of damage produced by beta rays from a particular nuclide relative to 1 MeV electrons.

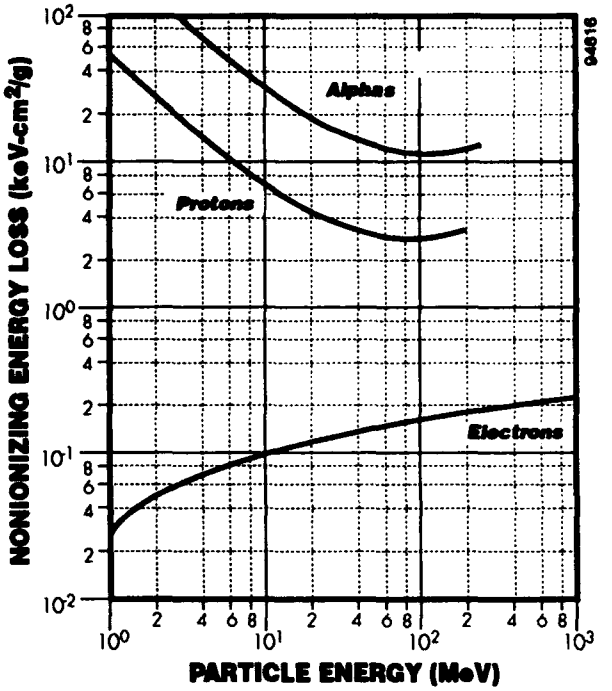

Figure 1 *NIEL in InP for electron and proton bombardment as a function of incident energy.*

The dominant adverse effect of radiation on semiconductor performance is a reduction in diffusion length L, given by

$$\frac{1}{L^2} - \frac{1}{L_o^2} = K_d \Phi \qquad (1)$$

where L_o is the diffusion length prior to irradiation, Φ is the radiation fluence and K_d is the damage coefficient. A series of diffusion lengths are calculated over the range of fluence values of interest and these are entered into the PC-1D device modeling code to determine their effect on key quantities such as voltage and current at maximum power. Other parameters are based on growth conditions or measurements made during fabrication.

Measurements under AM0 of open circuit voltage, short circuit current, and efficiency were first modeled with PC-1D by adjusting initial diffusion lengths and dopant concentrations until an optimal fit to BOL (beginning of life) performance was obtained. Keeping the doping constant, the diffusion length could then be changed as a function of dose to generate curves for all three outputs. If all

parameters were kept constant except the damage coefficient, this effectively allowed a best fit determination of the damage constant from AM0 readings as a function of dose.

In a planar battery design, the damage rate is proportional to the amount of alpha emitting radioisotope per cm^2 of voltaic cell. TRIM calculates displacement damage along an alpha particle track as shown in Figure 2. When corrected for source geometry, this determines the displacement-damage energy profile in the semiconductor.

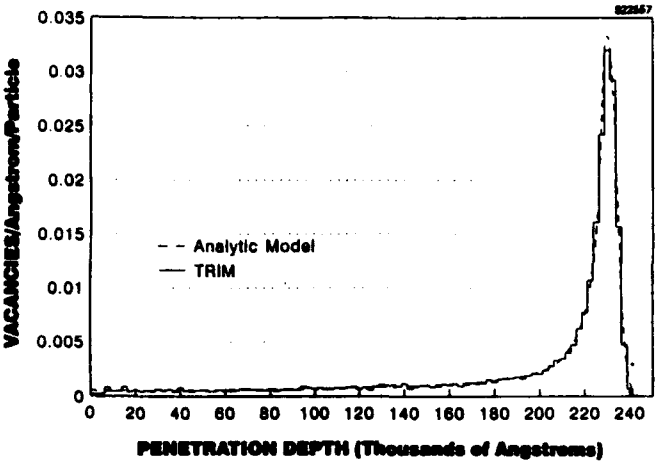

Figure 2 *Vacancies created along the track of a 5.5 MeV alpha particle in InP calculated by the TRIM code.*

Experiments

Samples studied were shallow homojunction n/p InP cells grown by metalorganic chemical vapor deposition. Cell design was identical to the high conversion efficiency solar cells developed at Spire and widely reported in the literature. It includes a highly doped back surface field p-InP buffer, a 3.5 μm low-doped p-InP base and a thin highly- doped n^+-InP emitter. The cell front contact grid and 25 mm^2 active area were defined using standard photolithography techniques. Cells were individually diced for evaluation and radiation testing.

Alpha bombardments were completed in air and vacuum, depending on the size of the cells and test requirements, using three 1 mCi Am-241 sources. Two of the sources had thin windows for in-air irradiation, and one had mesh reinforcing for vacuum. Evaluation of cell performance relied mostly on standard solar cell characterization techniques (AM0, dark/illuminated I-V curves, and quantum efficiency), but several were monitored during alpha illumination.

A dry nitrogen chamber at room temperature protected cells in storage, since some degradation was possible with exposure to humidity. Irradiations to 1 MeV equivalent electron fluences above 10^{17} agree strongly with the NIEL/PC-1D predictions based on previous (1989) electron irradiations of Spire MOCVD n/p cells made with silicon doping, although levels of damage observed were well beyond previous reports. This excellent agreement between alpha and electron irradiation data strongly vindicated the NIEL damage correlations.

Typical relative efficiency, J_{sc}, and V_{oc} under AM0 illumination for Am-241 irradiated cells are shown in Figures 3 through 5. Readings from n/p cells are shown as solid squares representing average measurements from five different cells at each fluence level. Data points at the highest fluence levels are single cell readings, because of the long irradiation times needed to achieve these levels.

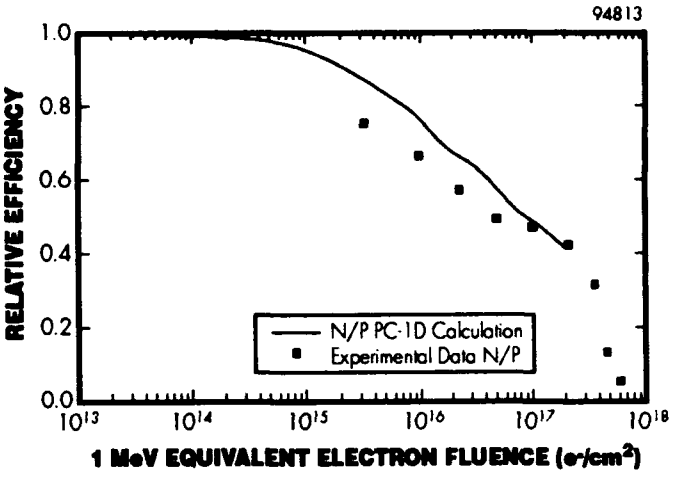

Figure 3 *AM0 efficiency for n/p type InP solar cells as a function of 1 MeV equivalent electron fluence compared to a PC-1D. Starting AM0 efficiency 16.7%*

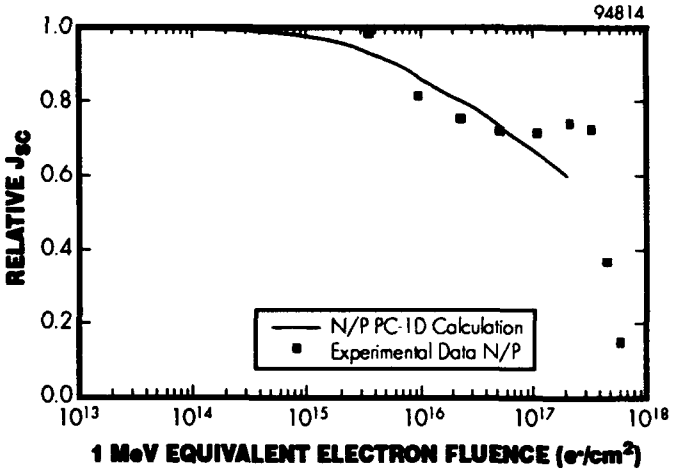

Figure 4 *Normalized AM0 J_{sc} for the same cells shown in Figure 3. Starting value = 32.5 mA/cm^2.*

The solid line is the PC-1D calculation for an n/p cell based on damage coefficients that were consistent for both previous Si-doped cells and these Se-doped n/p cells. Based on Yamaguchi's measured damage coefficients, p/n material should be more radiation resistant (lower damage coefficient) than the n/p material. However, these indicate the contrary.

At high particle fluences, short circuit current, for both AM0 and alpha illumination departed markedly from the monotonic decrease observed with less than 10^{16} cm^{-2}. This enhancement typically started at about 6 x 10^{16} cm^{-2} and persisted until about 4 x 10^{17} cm^{-2}. where the short circuit current began a precipitous

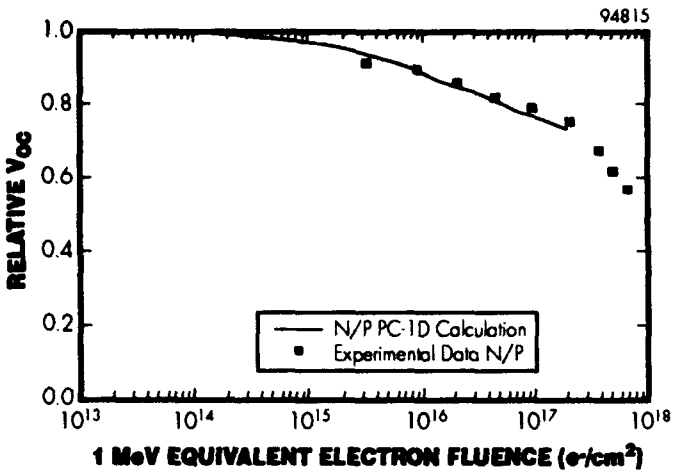

Figure 5 *V_{oc} under AM0 for the cells in Figure 3. Starting value: - 0.865V.*

drop just before 10^{16} cm^{-2}. Neither phenomena appear in the open-circuit voltage. This "plateau and plummet" in the short circuit current can be explained by including effects of carrier removal, which were reported and modelled by Yamaguchi.[9] At low exposures, carrier concentration can be described analogously to diffusion length:

$$N_o - N = K_c \cdot \Phi \qquad (2)$$

where N_o is the majority carrier concentration before irradiation and N the concentration after a particle fluence Φ. K_c is the carrier removal rate in units of cm^{-1}, analogous to the damage coefficient for diffusion length and a function of the particle, its energy, and the dopant concentration.

The plateau is due to the growth of the space charge region as carrier concentration drops, which collects carriers are more efficiently by drift in the space charge field than by diffusion from the field free region of the base. Enhanced collection compensates for the reduction in diffusion length. Ultimately carriers are so diminished that the cell ceases to function. Changes in voltage are not as apparent as in the current due to the logarithmic dependence of voltage on current.

Conclusions

To date, all of our data with MOCVD and diffused-junction InP cells indicate damage coefficient about 300 times larger than the original measurement from NTT. This may be due to differences in measurement techniques rather than material structure some of which were similar. PC-1D modelling generally agrees with all measurements, provided the appropriate damage coefficient was used.

The plateau in J_{sc} above the PC-1D curve most likely results from expansion of the depleted region as carriers are removed by trapping at defects. This effect, equivalent to a reduction in dopant concentration, was not at first modeled by PC-1D which only included the change in diffusion length. The effective reduction in dopant concentration eventually overwhelms the enhancement of the depletion region by creating a large series resistance, exactly the effect observed near end of cell life. Carrier removal thus explains both the plateau in efficiency near the 50% point and the final drop at end-of-life.

In spite of the tentative conclusion that InP alpha cells are not practical, alpha particle bombardments damaged cells well beyond levels previously tested, and verified the Non-Ionizing Energy Loss (NIEL) formalism. Behavior of n/p InP photocells at extremely low power levels was found to be substantially different from that under AM0 illumination, where p/n generally performs better. Under very low illumination, or alpha stimulation, n/p cells are better.

References

(1) J.F. Ziegler, J.P. Biersack and U. Littmark, *The Stopping and Range of Ions in Solids Vol-1*, Pergamon Press, New York (1985).

(2) P.A. Basore, D.T. Rover and A.W. Smith, "PC-1D Version 2: Enhanced Numerical Solar Cell Modeling," 20th IEEE Photovoltaic Specialist Conference, 389-396 (1988).

(3) M. Yamaguchi, C. Uemura, A. Yamamoto, "Radiation Damage in InP Single Crystals and Solar Cells," J. Appl. Phys. **55**, 1429-1436 (1984)

(4) M. Yamaguchi, K. Ando, "Mechanism for Radiation Resistance of InP Solar Cells," J. Appl. Phys. **63**, 5555-5562 (1988).

(5) C.J. Keavney, S.M. Vernon, V.E. Haven, M.J. Nowlan, R.J. Walters, R.L. Statler, G.P. Summers, "Radiation-Hard High Efficiency InP Solar Cell and Panel Development," 26th IECEC, 321-326 (1991).

(6) R.J. Walters, S.R. Messenger, G.P. Summers, E.A. Burke, C.J. Keavney, "Proton and Electron Irradiation of MOCVD InP Solar Cells: Experimental Results and Radiation Modelling," Proceedings of the 22nd IEEE Photovoltaic Specialists Conference, pp. 1560-1565 (1991).

(7) R.J. Walters, C.J. Keavney, S.R. Messenger, G.P. Summers, E.A. Burke, "The Effect of Dopant Density on the Radiation Resistance of MOCVD InP Solar Cells," Proceedings of the 22nd IEEE Photovoltaic Specialists Conference, pp. 1588-1592 (1991).

(8) R.J. Walters, S.R. Messenger, G.P. Summers, E.A. Burke, C.J. Keavney, "Space Radiation Effects in InP Solar Cells," IEEE Transactions on Nuclear Science, **38**, 1153-1158 (1991).

(9) M. Yamaguchi, C. Uemura, A. Yamamoto and A. Shibukawa, *Jpn. J. Appl. Phys.*, **23**, 302 (1984).

U.S. DEPARTMENT OF ENERGY ELECTROCHEMICAL BATTERY PRODUCTION DUAL USE CONCEPTS

Clifford G. Wagner, Principal Engineer
Martin Marietta Specialty Components, Inc.,
Largo, Florida

Introduction

The Department of Energy (DOE) has initiated a program designed to convert its defense production plants from nuclear weapons production to commercial/Department of Defense (DoD) utilization, wherever practical, in order to make the plant's high technology capabilities available to the American manufacturing community, and to minimize the economic impact of ending the plant's DOE-defense mission.

The Pinellas Plant, located near St. Petersburg, Florida, managed and operated by Martin Marietta Specialty Components, Inc., (Specialty Components) is planning to participate in a dual use program; to fulfill the DOE mission, while at the same time making its resources available to community partnerships for local business development.

This paper is limited to an introduction to the dual use concept and technical information relevant to three areas, thermal batteries, lithium ambient battery packs and double-layer capacitor packs.

Dual Use Concepts

Several programs have been initiated to assist American industry involvement in this process. The Pinellas Plant can be accessed through the following mechanisms:

1. Private Use
2. Cooperative Research and Development Agreements (CRADA), through a National Laboratory
3. Cooperative Agreements

The DOE has granted Specialty Components permission for private use of the Pinellas Plant, in addition to current DOE mission work. This private use involves leasing facility space and equipment by Martin Marietta or its subsequent contractor(s) for commercial endeavors at the plant. One may either seek services or products from Specialty Components, or seek alliances or partnerships with Specialty Components to achieve specific programmatic goals.

CRADAs can be structured to conjoin the efforts of a National Laboratory, the Pinellas Plant and the work initiator to accomplish the desired goal.

Cooperative Agreements can be established between the DOE and a participant, who will perform work at the Pinellas Plant.

One area in which Specialty Components is actively pursuing dual use is thermal battery production. This paper updates some of the technologies and processes in use at the Pinellas Plant. The Pinellas Plant has produced thermal batteries since 1974, when it was assigned thermal battery procurement responsibility for the weapons program under the design guidance of the Sandia National Laboratories (SNL) in Albuquerque. The plant has also served as a backup and limited production facility with 8000 square feet of dry room space.

Thermal Battery Leak Detection

It has been a nuclear weapons design requirement through the years to produce thermal batteries for applications specifying shelf lives of a minimum of 25 years [1]. Many aspects of battery design concerning individual component design must be controlled to ensure material compatibility and stability over the requisite time span. Igniters must also be specifically designed to stand up to the internal atmosphere of the stored battery. While this paper targets the leak aspect of battery life assurance, we do not mean to denigrate the component stability and compatibility aspects.

Given adequate long life component design in typical thermal batteries, performance deterioration from aging has been attributed mainly to water vapor; and, secondarily, to oxygen [1,2,3]. Both contaminants degrade the lithium by reacting with it, thereby removing it from its normal electrochemical accessibility.

Moisture exposure is minimized during battery construction by working in dry rooms, or otherwise controlling accessibility of water to the battery components. Lithium/lithium-alloy handling is also controlled to minimize oxygen exposure. The battery is sealed, usually by welding, to produce a hermetically sealed assembly, i.e., one that essentially is impervious to the exchange of water vapor or oxygen between the battery and the environment. Small leaks in finished batteries allow more oxygen than moisture to enter the battery. Batteries made this way have shown no practical deterioration in performance after storage times of up to 25 years, or after accelerated aging.

In leak detection work, absolute zero leak rates are not reasonably demonstratable. Testing, therefore, is designed to show that any leaks present are below a specified leak rate. A gas other than those which normally affect the product's life is used to seek out the leak. Assumptions and correlations must be made to use leak check data to predict the systems actual life expectancy.

The Pinellas Plant has used two techniques for leak detection: bubble checking and helium leak checking. The bubble test is performed by placing the battery in a container, pressurizing the container with the tracer gas, removing the battery and submerging it in a liquid, and watching for any bubble streams, indicating a leak. The helium leak check is a bomb type check which starts by placing the battery in a container, pressurizing the container with the tracer gas, removing the battery; but then the battery is place in a chamber attached to a mass spectrometer to measure the helium concentration (in the chamber) which is the result of helium leakage from a defective battery.

A leak is almost always a dynamic defect. Because the leak is allowing gas exchange all the time, it is necessary to calculate the actual leak rate from the leak test data. The concentration of tracer gas inside the battery varies with leak size, internal free volume, bombing pressure, bombing time and elapsed time between bombing and testing. The actual leak rate is defined as the reading that would be given by the leak detector if the battery contained 100% helium at normal atmospheric pressure in its free space [4].

Factors complicating interpretation of data include a lack of a precise physical descriptions of each battery, definition of all significant transport rates, definition of all significant degradation reaction rates, and a knowledge of the history of all variations in the temperature, gas pressure, and gas concentrations during all stages of the battery's pretest and testing activities [1]. An example of a particular thermal battery complication is tracer gas permeation and slow release inside the battery by materials such as a header encapsulant. Since this data has never (to the author's knowledge) been assembled leak rate interpretation has been approached through various simplifying assumptions by different investigators.

Calculations indicate that bubble leak testing cannot be relied upon to reveal all leaks which would deteriorate batteries held in storage for 25 years [1]. Helium bomb leak testing, however, can give this level of protection.

Leak test theory based on simple container and leak designs indicate that gross leaks can be missed by helium bomb leak testing. However, tests at the Pinellas Plant have shown that the release of the helium from inside the battery with a gross leak is sufficiently affected by the materials of construction of the battery so that the gross leaker shows up reliably during the testing.

Five-Cell And Single-Cell Testing

Five-cell testing is a method of discharge testing, initially performed by the SNL in Albuquerque, that employs a reusable test container sized to hold five cells of a given diameter. The reusable test container allows for simplified assembly of the igniter, header, leads and case without welding or soldering. A greater or lesser number of cells can be assembled simply by changing the length of the reusable container's case wall.

The assemblies are usually tested on a special time-temperature-voltage (TTV) tester which imposes a background load and a package of pulse loads. The loads may be fixed resistance or constant current. The pulse load's magnitude, duration and duty cycle is preset before testing. Temperatures in the cell stack are also measured. The tester collects voltage output information every millisecond during rise time and during pulses.

The testing is particularly useful in studying the effects of heat balance, insulation design or pellet modifications upon electrical performance, especially during pulsing. Figure 1 shows overall performance comparison of five cell tests with one test having steel, muffle collectors present and the other having no collectors present. Figure 2 shows comparative pulse performance polarization data. These batteries had the same heat balance factor of 82 calories per gram of unit cell. As can be seen the muffle collectors prolonged the active life and pulse carrying capability of the battery significantly. The muffle collectors also seemed to produce a more controlled and faster rise time (50 ohm load). The background load was ten ohms fixed resistance and the pulse load was one ohm fixed resistance. The ohmic resistance, as indicated by the instant drop voltage value, was similar early in the battery's life but appear to have been higher in the presence of the muffle collectors later in the active life. More testing is needed to confirm this observation. Internal temperatures were higher in the muffle collector battery in spite of the same heat balance factor. The muffle collector effectively controls the movement of heat and is useful for longer life designs using lower heat balance factor values.

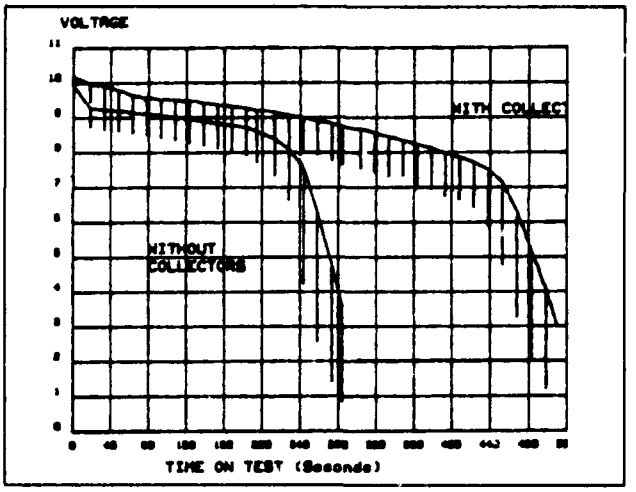

Figure 1. Muffle Collector Effects, batteries with and without collectors, TTV Testers - 82 Cal/Cell Heat

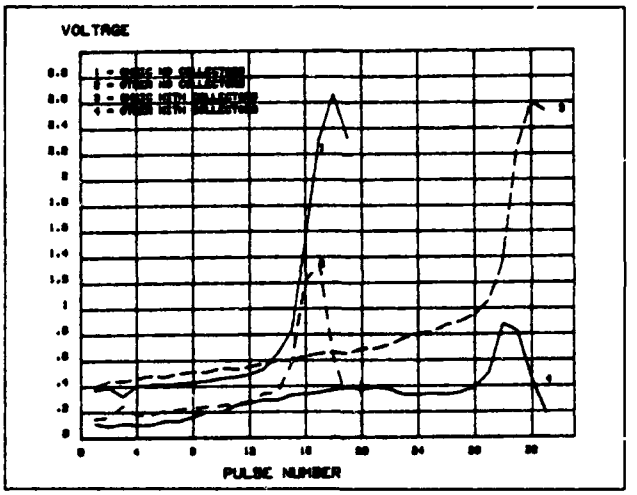

Figure 2. Muffle Collector Effects, Ohmic and Total Polarization, with and without collectors

Experience with this tester shows it to complement the single-cell and full-up battery tests. Because the test is sensitive to thermal management problems, temperatures are taken. This tester is useful in design work for pellet design changes including: chemistry differences, stack loading, end insulation and initial heat balance studies. It's chief use is to reduce the cost associated with pursuing these questions. It is also useful for routine material control work where electrical performance of different batches of materials is being compared.

Single-cell testing, using heated platens instead of heat pellets, is useful for more basic studies of cell performance, because of the ability to control temperatures over a predetermined range of values. The testing at the Pinellas Plant is being modified to use a controlled atmosphere fixture in place of a glove box.

Spin Battery Design

High spin rate (18,000 rpm) battery development utilizes minimal cell diameters to minimize the centrifugal forces on the molten electrolyte. This is counter balanced by current density

limitations. The power leads are isolated from the stack as much as possible to prevent cells from shorting to the leads, which might occur if electrolyte leaked through the insulation and touched the leads. Moderately insulating materials only seems usable at the higher spin rates because of the tendency of the highly insulating, high void volume materials to pulverize during spinning. Normal MgO binder levels in the LiCl/KCl separator (40%) yield adequate molten electrolyte immobilization. Lateral insulation needs to be tightly bound to the stack, if radially ignited, to insure adequate heat strip contact with the pellet stack.

Header/Case Welding

Microplasma and pulsed gas tungsten arc (GTA) welding have been helpful in minimizing thermal stressing of the headers during closure welding of the battery case. These thermal stresses can lead to glass cracking and failure at the terminals. Both welding processes have the capability of producing a "soft" start that reduces displacement of molten metal at arc initiation, which is important in the welding of thin metals. The processes allow for the addition of small amounts of hydrogen to the shielding gas flow to produce a localized reducing atmosphere that increases the arc energy, raises the fluidity of the molten metal and aids the shielding gas in preventing oxidation. The tungsten electrode is recessed in the microplasma welding head, which assures the electrode cannot contact the weld, thus eliminating a source of contamination. The smooth surface of the welds produced by these two processes aids in visual weld inspection.

Closed Mold Header Encapsulation

Headers, after attachment of igniter, monitor and internal leads, are usually encapsulated using alumina filled epoxy resins. This may be done in an open mold or a closed mold. The open mold is simpler to make and use, but requires an additional machining step for dimension control. Closing the mold and pouring through a sprue yields acceptable as-cast dimensions, and in addition allows for vacuum de-airing, thereby giving an improved encapsulant integrity.

Heat Powder Handling for Safety

The heat powder used in the Pinellas Plants thermal batteries is iron/potassium perchlorate blends varying from 88%Fe/12%$KClO_4$ to 84%Fe/16%$KClO_4$. These powders have been classified variously from flammable solids to explosives 1.3. The powders are received in small bags in approximately one gallon containers and are stored in minimum quantities to minimize dangers. Powder handling is limited to dry rooms. Screening of heat powder and transfer to jars for special handling is performed in an air curtain bench. Wrist grounding straps are worn when screening the powders. Latex gloves are required when handling the material in powdered form. Heat powder contaminated surfaces are cleaned with a canister type, high efficiency particulate air (HEPA)-filtered vacuum cleaner, except when large amounts of powder are to be cleaned such as from an accidental spill.

Battery stacking stations have been constructed using a remotely operated, quick release canister system containing Lith-X (Western Litho Plate and Supply Co.) extinguishing material which is dropped over and surrounds an ignited battery stack to control the burn. Premature ignition may result during the application of glass tape to battery stacks if static electrical potential is sufficient to precipitate an electrical arc. Personal grounding is required during pellet stacking. Pressure compensating stack presses are not utilized for wrapping of Li(Si)/FeS_2 batteries because if burning is accidentally started the press acts to squeeze separator out of the stack increasing anode to cathode contactability.

Iron Disulfide Purification

Results on the techniques of size reduction and purification of iron disulfide have been reported previously and only a summary and brief update on this process will be reported here [5]. The iron disulfide is ground and sized and then purified by acidic washings. The iron disulfide is leached with concentrated hydrogen fluoride (HF) acid to remove quartz (SiO_2) impurities and siliceous gangue that act to reduce the effective capacity of the FeS_2. These materials are generally held below 2% by weight [6]. Concentrated hydrochloric acid (HCl) is used to remove acid-soluble Fe impurities and any other electroactive impurities that affect the voltage output of the battery.

The use of concentrated HF requires elaborate precautions because of the health and safety hazards it presents to personnel handling it. Solutions of HF generate corrosive fumes and must be used in a strictly controlled environment with adequate ventilation. Concentrated HF can cause severe burns and ulcerations upon contact with the skin. In addition, there are substantial costs and problems associated with disposal of waste HF solutions.

A reaction kettle is used for the purification step. The acids are prediluted and handled with double wall piping. Personnel are not exposed to the acid at any time.

Dry Powder Blending Without Freon®

One step in the procedure for the preparation of small batches of the separator mix is mixing MgO into the LiCl/KCl powder using Freon and a Waring Products Blender. Freon served as a good mixing media because it did not contaminate the powders and was easy to evaporate away after mixing, but its use is being discontinued at the Pinellas Plant because of its chlorofluorocarbons committee (CFC) classification. The powders are now being dry-blended in a Turbula®® mixer for approximately 30 minutes. The sides of the jar must be scraped down by hand several times during mixing to assure a complete mixing. The completed mixture is then fused, crushed and ground, sized and stored.

Aqueous Degreasing of Metal Parts

Work was performed to evaluate the effectiveness of several CHC/CFC solvent replacements in removing contaminants from 304L stainless steel coupons. Contaminants evaluated were various mixtures of fatty acids, mineral oils, sodium and potassium hydroxides, pine oil, monohydric alcohols, petroleum hydrocarbons, ethers and silicone grease. Approximately ten cleaner materials were evaluated including aliphatic hydrocarbons, aliphatic esters, terpenes and mixtures. No "universal" cleaner among the selected cleaning agents was found. Oakite Products, Inc., Aluminum Cleaner NST, a mild alkaline, aqueous mixture with organic and inorganic, aliphatic and aromatic ingredients, was selected.

®Trademark, E. I. DuPont de Nemours
®®Trademark, Willy A Bachofen Maschinenfabrik Basel Switzerland

A water-drop contact angle technique was used as a rapid method for measuring surface cleanliness. The correlation of contact angle measurements to surface cleanliness was investigated using a limited XPS analysis of cleaned coupons. The XPS data showed that as the contact angle increased, the amount of surface carbon increased with a concomitant decrease in the oxygen level. This indicated that the coupons with high contact angles had more contamination than the coupons with low contact angles.

Toluene Diisocyanite (TDI) Reduction in Lithium Ambient Batteries and Double Layer Capacitor Packs

TDI is an ingredient in polyurethane elastomers and resins used in the Pinellas Plant in the manufacture of several Lithium Ambient Battery Packs and Double Layer Capacitor Packs. Goals were set to eliminate or reduce the amount of TDI, a suspected carcinogen, used.

We use an elastomeric system to glue parts together and changed from Adiprene® L-100 (10% free TDI) and Cyanacure (amine curing agent) to PET 90 with only 0.05 % free TDI, used with E 300 amine curing agent. In addition to a reduction in the TDI, the new system also gave higher butt tensile adhesion strengths (227 versus 882 psi) and higher lap shear adhesion strengths (989 versus 677 psi).

TDI was also reduced in the polyurethane potting resin by substituting the TDI with polymeric methylene diphenyl diisocyanate (MDI) and reformulating the resin. The two systems gave similar base line strengths, fill characteristics and adherence to metal and plastic parts when confined to rise to similar densities. The MDI system had a higher free rise volume and shorter pot life. The change-over was authorized for certain products.

Low Hazardous Solder Flux Removal Materials

Double Layer Capacitor (DLC) Packs are constructed and evaluated at the Pinellas Plant. Safety considerations necessitate minimization or elimination of certain chemicals commonly used in solder cleaning/flux removal processes; particularly Trichloroethane (TCE) at the Pinellas Plant. The soldering involves cable attachment to connectors and splice interconnection between DLCs. Attempts to solder the cables to the connectors using fluxless soldering failed because of poor wetting of the solder. Use of alcohol only for cleaning gave poor flux removal. Therefore, other candidate materials were evaluated as both a presolder cleaner and a solder defluxer.

D-Limonene and Citridet, terpene based products, were evaluated with fair results but did not yield the best cleaning based on visual and Epi-fluorescence microscopy. In addition it appears that the handling requirements for strong terpene cleaning solutions will not differ greatly from those needed for present materials.

Three additional non-aqueous, non-terpene based products (Armakleen 2000, Ionox HC and SAI 2000) were evaluated and gave good to very good results. SAI 2000 gave superior results. All flux was removed including that which wicked up between the wires and insulation. TCE and the other candidates, which left traces of flux behind, were inadequate to clean the wicked flux. No solvent residues were found by FTIR, Auger, or SEM examination. Accelerated corrosion testing (ASTM D2247: 100% Humidity at 100°F for 7 days) did not generate any corrosion.

Upon humid exposure a green exudate was observed which appears to be Copper Abietate Dehydrate. Upon tinning the wires, the tinning rosin creeps a slight distance up the wire/insulation interface. Upon subsequent cleaning the capillary motion can transport dilute rosin further up the wires. The abietic acid reacts with the copper through any cracks in the silver on the wires. The resulting product is non-corrosive and no harmful effects have been discovered; however it is an aesthetic issue [7].

The new cleaner was less harmful to the connector than the TCE had been. Gasket material in the connector experienced a 220% weight change when stored immersed in TCE but only a 100% change in the new cleaner. This appears to be leaching of the plasticizer out of the gasket material.

Tank Round and Bomb Retrofit Batteries

In support of the dual use program, studies are underway aimed at making the Pinellas Plant's equipment and technology available for other than DOE dedicated use; that is, in DoD or commercial applications. In particular the thrust is to transmute the very high reliability battery design and manufacturing methodologies into an optimized cost/reliability production capability. Higher production rate methods are being developed while designing appropriate reliability levels, specific to each application, into the batteries.

Initial optimization thrusts are towards typical system power and higher voltage control battery designs.

Acknowledgements

The author wishes to express his sincere appreciation to those individuals whose work has been discussed here; the Sandia National Laboratories Thermal Battery Group who, throughout the years, have initiated and supported most of the work reported in this paper, and the many individuals at the Pinellas Plant who have been responsible for various projects.

References

1. J. Q. Searcy and James R. Armijo "Additional Experiments Relative to the Shelf Life of Li(Si)/FeS_2 Thermal Batteries" SAND84-1510.
2. C. S. Winchester "Aging Studies of the LAN and Li(X)/FeS_2 Thermal Battery System".
3. J. Q. Searcy and P.G. Neiswander "Aging Study of Li(Si)/FeS_2 Thermally Activated Batteries" SAND80-0423.
4. S.G. Burnet "Leak Detection of Sealed Parts" and "Basic Technology and Terminology of Leak Detection" Presentations. Locations and Dates Unknown.
5. R. A. Guidotti, F.W.Reinhardt "Characterization of Electrolyte-Binder Mixes for use in Thermal Batteries" SAND90-2103, UC-213.
6. R. L. Poole "Characterization of Materials in Support of the Li(Si)/FeS_2 Electrochemical System" GEND - GEPP-TM-542
7. W. J. Ricket "Reliable and Visually Clean Hand Soldering of Cable Assemblies Using Low Solids Flux and No Cleaning.

DUAL USE TECHNOLOGY FOR ARMY APPLICATIONS

Edward H. Reiss, Jr., Fee Chan Leung
Army Research Laboratory, Fort Monmouth, NJ

Introduction

Unique electrochemistries and battery configurations powering portable electronic devices may no longer meet the changing military priorities for the twenty-first century. The first major priority change occurred several years ago when the Army assessed the cost of batteries directly to the military unit consuming the batteries rather than to a general support fund. Increased, negative feedback caused Program Managers, developers and logisticians to realize the balance between cost and readiness. Next, the soldier's complaints focused upon performance, availability and cost. The typical comment was "Why can't we purchase high-quality, cheap batteries from the local supermarket?" Recognize that the expected performance related to lightweight, high energy dense lithium non-rechargeable batteries. A further complication affecting the trade-off between performance and military objectives is the desire for small, light, more powerful, more energetic and safer batteries to give the soldiers a winning advantage on any battlefield whether in actual combat or training.

Manpower and monetary cutbacks affect us all. In the military this simply means do more with less. We have a multifaceted approach that addresses our needs; our procurement methods and strategies; and our research and development objectives. Performance attributes of future battlefield requirements necessitate careful scrutiny to establish operational readiness or military need documents reflecting decisive weapons and devices yet attainable within the manpower and fiscal constraints. This process coordinates the material and system developers with the combat doctrine developers. New players in this process are the Battlelabs. The procurement process has demonstrated "best value" type solicitations along with multiyear delivery schedules in order to obtain required batteries in sufficient quantities at acceptable prices from a stable industrial or commercial base.

The remainder of this paper will focus on blending our research and development objectives with industrial or commercial interests and to relate dual use technologies to specific non-rechargeable, rechargeable and alternative power sources as well as Army specific applications.

General Discussion

For this paper, dual use technologies are those electronic or electrochemical processes and products allowing both the military and commercial or industrial users to benefit. A prime example is the family of alkaline cells. Standardized in size and voltage, readily available throughout the world, and produced by the millions, these relatively inexpensive cells power hundreds of military electronic devices and thousands of commercial devices in all sectors of society. Competition in a growing marketplace keeps the price low and availability high. Stability exists. On the negative side, alkaline batteries are inadequate or inappropriate for all applications. Cameras, computers, telephones and tools generally require smaller, lighter, more energetic alternatives than alkaline.

Dozens of papers at this forum and numerous other meetings have defined exciting new breakthroughs in electrodes, electrolytes, systems, materials, processes and applications. Creating a win-win combination for these new, electrochemical advances is really our challenge for the near and far terms if we are truly to benefit. Table 1 is a partial listing of various electrochemical and related systems favorable as dual use technologies and the near-term likelihood of being fielded by the Army. Shown are conventional non-rechargeable and rechargeable battery technologies as well as alternative power source considerations.

Table 1

POTENTIAL DUAL USE TECHNOLOGIES

Lithium Manganese Dioxide	Non-rechargeable	High
Lithium Thionyl Chloride	Non-rechargeable	Medium
Metal Air	Non-rechargeable	Medium
Lithium Sulfuryl Chloride	Non-rechargeable	Low
Lead Acid, Sealed and Gelled	Rechargeable	High
Nickel Metal Hydride	Rechargeable	High
Lithium Ion	Rechargeable	High
Metallic Lithium	Rechargeable	Medium
Metal Air	Rechargeable	Medium
Lithium Polymer	Rechargeable	Low
State-Of-Charge	Alternative	High
Power and Energy Management	Alternative	High
Solar	Alternative	Medium
Thermal Photovoltaic	Alternative	Low

Non-rechargeable Technologies

Of the four non-rechargeable technologies listed, the first three systems currently power one or more military, portable devices. These systems are by no means fully developed, neither for performance nor configuration. The fourth is under development for possible use in the Land Warrior or Soldier System. Our reasons for considering these four are demonstrated in Figure 1 which shows the relative energy densities of the alternatives. Lithium Sulfur Dioxide is plotted as representative of the standard for combat operation of Command, Control, Communication, Computer and Intelligence (C4I) equipment. Clearly, performance is very desirable.

Lithium Manganese Dioxide (LMD) and Lithium Thionyl Chloride (LTC) batteries operate relatively low power commercial and military devices. The Mini Eyesafe Laser Infrared Observation Set (MELIOS), currently in development, requires relatively high power from a small, lightweight battery. Recent attempts to use commercially available LMD cells packaged into eight or nine cell battery configurations were unsuccessful due to performance limitations. The Army also developed a LTC battery, the BA-6516/U, to meet the MELIOS's performance objectives. For another device, the Thermal Weapon Sight (TWS), also needing high power, light weight, and sufficient energy to last over 12 hours, we identified a LTC battery, the BA-6847/U, to meet the performance requirements. However, the

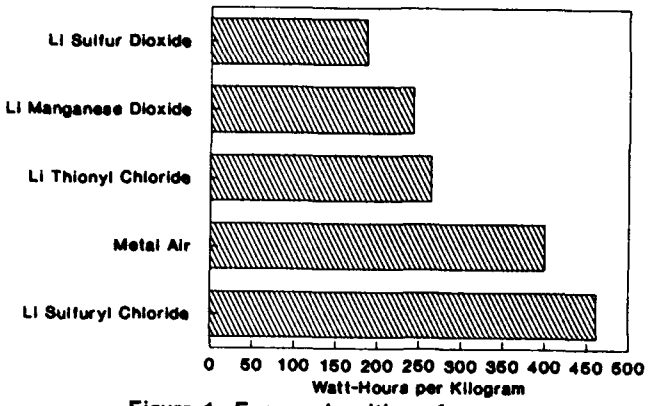

Figure 1. Energy densities of non-rechargeable dual use technologies

expected high costs of these unique LTC batteries dictate a reevaluation of the requirements of the MELIOS's and TWS's missions. Can we identify other battery types that are more justifiable in terms of dollars per mission or "best value"?

Let's view the above examples as positive endorsements of dual use technologies. All were attempts to adapt readily available products into new applications for mutual gain. Potential benefits to the Army were decreased developmental costs since the battery industry was already knowledgeable about each battery chemistry from its own research, development and production experience. Industry stood to gain by selling an existing cell size, without costly engineering or design costs, using existing production equipment and tooling. Maybe we were premature. The performance and cost trade-offs must still be resolved before we attain true dual use.

Investigations of potential solutions are underway. The LMD electrochemistry can be packaged in cylinders or in foil packets or pouches. With and without government sponsorship, industry is pursuing development aimed at increasing the power and energy available from a given battery size by incorporating flat plates of electrodes and electrolytes sandwiched together and sealed in foil pouches. This will allow greater volumetric efficiency and due to material handling simplifications will allow decreased production costs. With the introduction of commercial applications such as laptop computers, a slow but increasing demand is foreseen for power and energy from small, lightweight batteries. This may spur the advancement of cylindrical LMD cells with higher rate capabilities.

We are less enthusiastic about the LTC than the LMD. Over the next two to three years, design changes to achieve lower costs must also maintain performance features without compromising safety. Technical approaches in this direction are not promising. While an order for tens of thousands of batteries could reduce the cost, justification of large purchase orders from the Army for unique LTC batteries is questionable at this time.

Metal air batteries find use in the military primarily for special missions with highly trained operators. Commercially, metal air batteries are in low power hearing aids, emergency equipment and special purpose devices. With the exception of the hearing aid batteries, few batteries are purchased or used, availability is restricted and costs are high. Zinc and Aluminum air batteries have shown promising advances in power and energy densities. However, continued advances are needed. The ability to add water available at the site of use makes these systems attractive to a growing number of military users.

The potential for the highest energy density of sealed batteries makes the Lithium Sulfuryl Chloride (LSC) battery very attractive for the military. The 21st Century Land Warrior and Soldier System require power to operate an electronic package integrating: two radios, a global positioning system, day and night vision enhancement, target detection, aiming assist, a computer, displays and possibly a backpack cooler. Ideally a battery complement will operate the non-cooling systems at an average of 10 watts for up to 72 hours. Operating at 250 watts, the cooler demands very high power. Practical limitations on size, weight and energy will reduce the mission time for a battery operated cooler to four hours -- far less than the full mission. High energy is the key for the remainder of the system and energy translates into weight or energy density. Weight and volume are extremely critical since the soldier must carry all the electronics plus his normal combat gear. Early awareness of probable performance characteristics and costs will help direct our efforts toward a viable solution. As shown above for the TWS, meeting only one of the parameters is not acceptable. Performance, cost and availability must be improved for the LSC to enter the Army's inventory. Additional commercial interest is necessary for it to become an effective dual use technology. Our preliminary efforts are aimed at: improvements in power density without a compromise in energy density, and overcoming self discharge.

Rechargeable Technologies

Until recently, the Army utilized very few rechargeable batteries in C4I equipment. These applications usually required power levels beyond that attainable from primary batteries, i.e., the AN/GVS-5 laser rangefinder and the AN/TAS-4 TOW missile launcher. The predominate choice was Nickel Cadmium -- certainly a dual use technology. Sealed Lead-acid was occasionally used.

Today we are faced with new philosophies on cost, training and the environment. Cost has risen in importance, the phrase "train as you fight" no longer applies in all peacetime training exercises. Simply stated, rechargeable batteries can save significant money during peacetime training. The greatest gains exist when the rechargeable battery's characteristics match those of the replaced primary battery during training missions. The high potential for cost avoidance resulting from rechargeable batteries drives the Army to identify, develop and use improved rechargeable batteries. Adapting our needs to utilize dual use technology increases the benefit.

Figure 2 shows the potential, dual use, rechargeable electrochemistries and their relative energy densities. The sealed or gelled Lead-acid batteries offer few performance advantages over the Nickel Cadmium. They do offer low cost and are readily available in a variety of sizes. Their biggest drawback is weight per hour of use making them unsuitable for most conventional Army missions of moderate length. For use in the AN/PRC-119, SINCGARS radio, a Lead-acid battery weighing slightly less than two kilograms will operate for about 6 hours. The corresponding

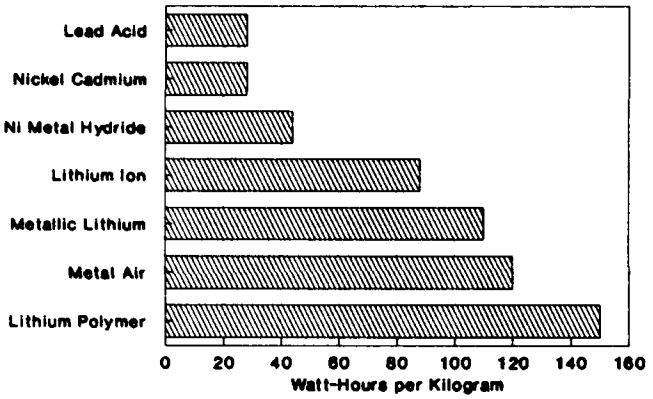

Figure 2. Energy densities of rechargeable dual use technologies

primary battery, BA-5590/U, weighing one kilogram operates for 24 hours.

Nickel metal hydride batteries offer a reasonable increase in energy density and are emerging as one of the preferences for commercial video cameras, cellular telephones and laptop computers. Detailed chemical, design and performance characteristics of these and other new rechargeable batteries are discussed elsewhere in the proceedings by George Au and Martin Sulkes. The first adaptation of this chemistry by the Army will be as a replacement for a 6 volt, 7 ampere-hour, primary battery, the BA-5847/U, to support the fielding of the Thermal Weapon Sight. This battery will contain commercial cells not optimized for the BA-5847/U's volume. Potential for success is high. Optimization requires a blend of performance traits and choice of the most cost effective cell size. The latter is driven by commercial applications.

Lithium ion batteries are beginning to appear in small quantities in relatively small cell sizes from a limited commercial base. Performance attributes favor continuation of this product for both military and commercial applications. Our development efforts address: increasing the cell size to a "D" cell; maintaining safety; and optimizing the charge process without degrading the cycle life, depth-of-discharge or energy characteristics. With over 40 Army portable C4I systems designed to operate from the BA-5590/U and an expected large usage in the TWS, our major thrust centers on the "D" cell. Our belief is that Lithium ion batteries require the additional development before they will replace the Nickel metal hydride system. Commercial advances will be watched.

Metallic Lithium has demonstrated superior performance for a rechargeable battery. However, limited supporting data coupled with earlier safety failures foster skepticism. Numerous breakthroughs in electrolytes and electrodes foretell great things are about to happen. Time will tell. Realistically the introduction of a cost effective, logistically available, metallic Lithium battery as both a commercial and a military battery within the next three years is doubtful.

Another battery system of medium risk is the rechargeable, metal air. While limited cycle life is possible, the ability to remove and replace the electrolyte and electrodes has benefits. Negligible Army funds are pursuing this technology. As with its non-rechargeable counterpart, applications tend to be special purpose both in the military and commercially.

The last rechargeable system of interest is the Lithium polymer. Prototypes exist but tend toward low rate designs. Conceptually a bi-polar arrangement of thin membranes, produced by inexpensive lamination techniques will benefit the Army and create many new commercial applications. With current research focusing on fundamental properties, i.e., conductivity of membranes and electrolytes, production quantities will not exist for many years.

Alternative Technologies

State-of-charge (SOC), power and energy management technologies offer an immediate benefit. Battery power is expensive by comparison to 110 volt AC power. Discarding a partially used battery and powering circuits when not needed wastes expensive energy.

SOC meters and circuits exist for Lithium Sulfur Dioxide batteries. The meter determines remaining capacity only when the battery is removed from its equipment. A good concept for depots but of limited use to soldiers in combat. Our experience with SOC circuits showed they were accurate. Costing $2 to $5, they are not yet cheap enough for installation in every battery. When such a circuit is developed, users of the SINCGARS radio, which was already modified to accept a SOC input, will benefit.

Power and energy management begin with the functional design of equipment and continue throughout the entire development process. Low voltage analog and digital microelectronics, reconfigurable architectures, auto-shutdown and adaptive sleep modes are emerging as potential approaches. Our guidance to industry is design not to use power, design the most efficient circuits and then conserve energy whenever possible.

Applications for solar and thermal photovoltaic technologies are increasing though still limited to special purposes, i.e., float charge and small, low power devices. Obviously the Army can not rely on the availability of abundant sunshine. We can not expect to create artificial sunlight while on the move in combat. Hopefully, peacetime training exercises will foster creative applications as the power per square meter increases. An immediate, large scale change is unlikely.

Fuel cells are of benefit when mission times are long, power is relatively high and low weight is critical. The Soldier System's backpack cooler is a good example. Industrial consortiums, private enterprise and government agencies promise prototypes within the next few years, however, production of fuel cells meeting the Army's missions is not likely until the end of the century.

Conclusions

Changes in economics, politics, threat and technology perturb our priorities. Elevation of cost increases the desirability of rechargeables. Who and where we fight alter how we fight and hence redefine equipment performance. Scientific breakthroughs occur but are unscheduled. Our plans for the future blend our priorities with industry concerns. Incorporation of dual use technology is seen as critical if the Army is to achieve its goals in a rapid, cost effective manner.

Update on the USN Program to Reduce Aircraft Battery Maintenance Costs

Baird C. Newman
Crane Division
Naval Surface Warfare Ctr.
Crane, IN 47522

Paul A. Scardaville
Saft America Inc.
711 Industrial Blvd.
Valdosta, GA 31601

Flight Test Program

In January 1993, three Saft batteries, Ultra Low Maintenance versions of MIL-B-81757/9 (or BB433), were entered into a 14-month flight test at Camp Pendleton, California.

One battery was assigned to each of three USMC Helicopter Squadrons flying AH-1 helicopters. The batteries are kept in constant use.

One battery was capacity checked at 2 months, the second at 4 months, and the third at 8 months. No water additions were made. All three batteries were clean when checked, with only microampere case leakage currents observed. Capacities measured have been above minimum specification requirements.

On 1 March 1994, all batteries will be checked again. Thus, the second round maintenance free intervals on the 14 month, 1 March 1994, checkpoint will be: 12 months since recharge at 2 months; 10 months since recharge at 4 months; and 6 months since recharge at 8 months.

20 Ah (MIL-B-81757/8 & /11) Prototype

A prototype for the 20 Ah batteries was supplied by Saft in November 1993. This battery has also demonstrated superior cycling capabilities, power, and capacity as compared to the standard QPL 20 Ah battery. At cycle 1200 of the MIL-81757 standard cycle test (except for shorter rests and recharge times 1/2 of the standard), the ULM battery performance is better than the cycle 46 performance of the standard MIL-B-81757 20 Ah batteries.

Schedule for Submission of Qual. Test ULM Batteries

(1) MIL-B-81757/8 and /11 formats, 20 Ah: December 1993

(2) MIL-B-81757/7 format, 10 Ah: December 1993

Schedule for Submission of Prototype Evaluation Batteries:

Size	Application	Date
15 Ah	F-18E/F	November 1993
17 Ah	AH-64	January 1994
7 Ah	UH/AH-60	February 1994
35 Ah	AH1W	April 1994

EVALUATION OF COMMERCIAL AA-SIZE LITHIUM CELLS FOR NAVY MINE APPLICATIONS

Julie A. Banner, Clinton S. Winchester and William P. Kilroy
Naval Surface Warfare Center, Silver Spring, MD

Introduction

The Navy is establishing a "Standard Family of Cells for Navy Mine Applications" in an effort to reduce the expense and increase the availability of batteries for Navy mine and mine countermeasure systems. The Standard Family currently includes #6-, C- and A-size cells. It is our goal to identify a commercially available, AA-size lithium cell to become the fourth member of this standardized group of cells.

A survey of commercially available lithium AA-size cells was completed.[1] Eight different lithium-based chemistries produced in the AA-size were considered as potential candidates for testing. After performing a critical evaluation of performance data, product availability, and level of technical maturity, five cell models were chosen for in-depth testing and evaluation. Cells were ordered from either the manufacturer or an authorized distribution house in February of 1992.

The test plan was based on requirements that are characteristic of mine and mine countermeasure power sources. Test parameters were taken from weapon specifications for six power supplies that would be targeted for replacement using the new AA-size cell. Variables in the test plan included four discharge rates, three pulse loads, three discharge temperatures, three storage temperatures, and two storage durations. This report summarizes the performance of the five cell models tested using this test plan. This evaluation effort will be continued as cells with other chemistries and designs are added to the commercial market.

Some mine applications require a low-magnetic signature power source. Preliminary studies indicated that commercially available cells do not meet this requirement. However, the magnetic signature is a secondary characteristic of a desirable cell technology. The primary emphasis of this program was to characterize the performances of cells under discharge conditions typical of mine warfare applications.

Experimental Methods

Four lithium/thionyl chloride ($Li/SOCl_2$) cell models and one lithium/manganese dioxide (Li/MnO_2) cell model were chosen for evaluation. The manufacturers of the $Li/SOCl_2$ cells were: Electrochem Industries (E•I), SAFT France, Power Conversion, Inc. (PCI), and Eagle-Picher (EP). The E•I cells were manufactured for E•I in Japan. The Li/MnO_2 cells were purchased from Varta. Table 1 lists the manufacturers of the test cells along with the cells' chemistries, model numbers, designs and rated capacities. The EP cell should not be considered a standard AA-size cell because it is a square prism instead of a cylinder. This volume difference accounts for the ~25% additional rated capacity as compared to the other four cell designs.

Table 1. Test Cell Characteristics

	Chemistry	Model	Design	Rated Capacity
EP	$Li/SOCl_2$	LTC-30P	Prismatic	2.6 Ah @ 7.4 mA
E•I	$Li/SOCl_2$	QTC85	Bobbin	1.9 Ah @ 0.1 mA
PCI	$Li/SOCl_2$	TCL T06/41	Bobbin	1.8 Ah @ 0.18 mA
SAFT	$Li/SOCl_2$	LS6	Bobbin	1.8 Ah @ 3 mA
Varta	Li/MnO_2	CR AA	Bobbin	2 Ah @ 2 mA

Abbreviations in Table 1: Ampere-hours (Ah), milliamperes (mA)

An initial inspection was performed on all cells upon receipt at the laboratory. The following data were taken: open circuit voltage, weight and AC resistance. Closed circuit voltage tests were performed with a 200Ω load on ten cells from each manufacturer, five at ambient temperature and five at -2°C.

All cells were discharged using resistive loads. The cells were fixed in a horizontal position during discharge. Unless otherwise indicated, five cells per manufacturer were used for each test. The cells to be discharged fresh were kept in a refrigerator at 10°C prior to testing. Cells to be discharged after high temperature storage were stored in calibrated environmental chambers (Tenney Jr. units). Cells were allowed to equilibrate at the discharge temperature for at least 4 hours prior to each test. Data were taken using Fluke data loggers.

Low Rate Tests and Results

3 mA Discharge at 23°C

The baseline performances of fresh cells were determined by discharging the cells at 3 mA at room temperature. At the 3 mA rate, all but the E•I cells met or exceeded the manufacturers' rated capacities (see Table 1) to a 2.0 volt (V) cutoff. The E•I cells were rated at 1.9 Ah at a 0.1 mA rate and provided an average of 1.76 Ah when tested at the 3 mA rate. While the capacity delivered by these cells was less than the rated capacity, the deviation is not significant considering the difference in rates. All cells showed good voltage regulation during this test. The $Li/SOCl_2$ and Li/MnO_2 cells had mid-discharge voltages of 3.5V and 2.8V respectively.

3 mA Discharge at 49°C

When fresh cells were discharged at 3 mA at 49°C, the average capacity of all of the $Li/SOCl_2$ cells decreased. The SAFT cells lost 8.4% capacity relative to room temperature discharge at the same rate. The cells from E•I, EP and PCI lost 13%, 16.3% and 17% respectively. The Li/MnO_2 cells from Varta delivered 1.8% more capacity when discharged at elevated temperature.

3 mA Discharge at -2°C

Low temperature operation (-2°C) is of particular interest for mine and mine countermeasure power source applications. Both SAFT and PCI cells delivered approximately the same capacity at -2°C as compared to room temperature at a 3 mA rate. The E•I cells, however, provided 4% more capacity at -2°C than at room temperature. The EP cells exhibited a depressed discharge voltage and lost 10% of capacity relative to room temperature when discharged at -2°C. The Varta cells lost 22% of capacity during this low temperature discharge and had a significantly lower mid-discharge voltage.

0.25 mA Discharge at -54°C

Mine batteries may be required to provide an extremely low current for memory retention once the system has been programmed. Extreme temperatures are reached during high-altitude transport on an airplane wing. To simulate this scenario, the test cells were discharged at 0.25 mA at -54°C for four days. The four Li/$SOCl_2$ cells met the minimum requirement of 4 hours and continued to discharge in the 3.3 to 3.5V range for >120 hours, when the test was terminated. The E•I cells had the highest mid-discharge voltage for this test: 3.5V. The Li/MnO_2 cells from Varta also met the minimum requirement, however the voltages dropped to 0 after 28 hours of discharge.

High Rate Tests and Results

Most mine and mine countermeasure power sources function for long times at low rates. However, one mine battery application that is a potential for retrofit using the AA-size cell would require 0.4 Ah to be delivered at a rate of 50 mA. Also, some applications require a high pulse (>100 mA) from the power source, possibly near the end of battery life. Therefore, tests were conducted on fresh cells to determine the high rate and pulse capabilities of the various test models.

50 mA Discharge at -2°C with Pulse

A 65Ω load was applied to the Li/$SOCl_2$ cells for four hours, followed by a 28Ω load for >0.5 hours. The corresponding loads for the Li/MnO_2 cells were 50Ω and 20Ω. This test was carried out at -2°C. The EP and the Varta cells performed poorly. During the first four hours, the EP cells delivered an average of 20 mA, with a voltage around 1.25V. The Varta cells provided a peak of 55 mA when the load was applied, with an initial voltage of 2.5V. By the end of the 4 hour portion of the discharge, the current had dropped to 20 mA, with a corresponding voltage of 1V. Neither the EP nor the Varta cells delivered any additional current when the pulse load was applied.

The E•I cells discharged below 2.0V during the 50 mA portion, and provided an average peak pulse current of only 45 mA. Four of the five PCI cells discharged for four hours at 50 mA with a flat voltage of about 3V and provided an average peak pulse current of 105 mA. The voltage of the fifth PCI cell fell to below 1.0 volt upon application of the load and never recovered. The SAFT cells provided the best performance in this high rate test, with all cells discharging at 50 mA with a voltage above 3.0V. These cells provided an average peak pulse current of 110 mA.

High Rate Discharge at -2°C

The second high rate test was performed to determine cell capacity to a cutoff of 2.0V. The Li/$SOCl_2$ cells that would not discharge with a 65Ω in the first high rate test were discharged with a 170Ω load. The Varta (Li/MnO_2) cells were discharged with a 125Ω load. A population of three cells per manufacturer was used in this test.

Table 2 summarizes the results. Only the SAFT and the PCI cells met the requirement of providing 0.4 Ah capacity at a 50 mA rate. The EP and E•I cells generated some useful capacity when discharged at 20 mA. It is clear that the Varta cells were not effective under these discharge conditions.

Table 2. High Rate Discharge Performance

Manufacturer	Rate of Test (mA)	Avg. Capacity to 2.0V (Ah)
EP	20	1.35
E•I	20	1.49
PCI	**50**	**0.89**
SAFT	**50**	**0.94**
Varta	20	0.09

Storage Tests and Results

Mine and mine countermeasure power sources are routinely required to have a shelf life of greater than five years. This long-life requirement, when coupled with the potential for high temperature storage and low temperature discharge, provides a challenging scenario for a battery. Storage tests were completed to characterize the response of these commercial cells to high temperature exposure followed by low temperature discharge. The following tests were designed to provide comparison data for the five cell types being evaluated and should not be interpreted as correlating to a longer duration at a lower storage temperature.

Storage at 66°C for 45 Days

Cells were stored for 45 days at 66°C, then discharged at 3 mA. The discharges were run at both ambient temperature and -2°C. Table 3 summarizes the data from these tests, and also includes the comparable data from tests performed on fresh cells.

Table 3. Capacity to 2.0V in Ah of Cells Discharged at 3 mA as a Function of Storage and Discharge Temperature

	23°C Discharge	23°C Discharge	-2°C Discharge	-2°C Discharge
	Fresh Cells	45 Days/66°C Storage	Fresh Cells	45 Days/66°C Storage
EP	2.96	2.91	2.67	2.65
E•I	1.76	1.76	1.84	1.82
PCI	1.85	1.63	1.83	1.62
SAFT	2.04	2.02	2.03	2.02
Varta	2.02	1.94	1.57	1.44

Several interesting observations were made based on the data in Table 3. The EP cells showed no appreciable change in capacity between fresh and stored cells, yet delivered approximately 10% more capacity at room temperature relative to -2°C. The E•I cells also exhibited no capacity loss due to 45 days storage at 66°C, but delivered almost 5% more capacity at -2°C than at room temperature. This is the only cell model tested that consistently yielded more capacity at -2°C than at room temperature.

The PCI cells were not affected by the variation in discharge temperature, but lost 11% of capacity after high temperature storage. The Varta cells were affected by both discharge temperature and storage conditions; these cells delivered less capacity as the conditions become more harsh. The SAFT cells consistently delivered ~2 Ah regardless of discharge temperature or storage for 45 days at 66°C.

Storage at 41°C for Six Months

High rate discharges were performed on cells that had been stored for six months at 41°C. These tests were performed on populations of three cells per manufacturer and involved both 20 mA and 50 mA discharge rates, depending on the capabilities of the cells. All discharges were performed at -2°C. Table 4 summarizes the data from these tests and compares the results with the previously given data from the fresh cells discharged at high rates.

Table 4. Stored and Fresh Cells Discharged at High Rates at -2°C

Manufacturer	Rate of Test (mA)	Capacity to 2.0V (Ah)	
		Fresh	6 Months @ 41°C
EP	20	1.35	1.24
E•I	20	1.49	0.66
PCI	**50**	**0.89**	**0.40**
SAFT	**50**	**0.93**	**0.85**
Varta	20	0.09	0.04

The SAFT cells displayed the least capacity degradation after six months storage at 41°C. These cells lost approximately 8.6% of baseline capacity. The EP cells also exhibited an 8% loss, but as was mentioned previously, could not be discharged at the 50 mA rate. PCI cells were able to meet the 50 mA rate requirement, but lost >50% of capacity as a result of 6 months storage at 41°C. The fresh E•I cells performed well at the more moderate, 20 mA rate, but lost 55.7% of capacity after storage. The Varta cells did not deliver any appreciable capacity at the 20 mA rate.

Summary and Continuing Work

Upon completion of the testing, the SAFT LS6 cells were identified as the best performers of the five cell models tested. The SAFT cells delivered the highest capacity of the four standard-size cells, performed the most consistently from cell to cell, provided the best high rate capabilities, and retained the most capacity after six-month storage. The EP LTC-30P cells provided the highest capacity at low rates due to the non-standard shape. However, the high rate tests demonstrated that the EP cells were unable to meet both the 50 mA discharge and the >100 mA pulse requirements. The E•I 3B940 cells were also limited by a failure to perform well at the highest rates. The PCI T06/41 cells showed good high rate and pulse capability, but exhibited significant capacity loss after high temperature storage. The Varta CR AA cells, the only Li/MnO_2 design tested, were limited both by capacity losses when discharged at low temperature, and an inability to discharge at moderate to high (20-50 mA) rates.

The commercial cell test program generated a comprehensive data base of the capabilities of the five test cells chosen for evaluation. We plan to purchase and evaluate new AA-size cells as they are added to the commercial market. These may include Li/MnO_2 spiral cells produced by PCI and Dowty, and Li/$SOCl_2$ spiral cells produced by EIC Laboratories, Inc. and Yardney Technical Products. We have also evaluated specially designed non-magnetic Li/$SOCl_2$ cells developed by ECO, Inc.[2]

References

(1) Kilroy, W. P., Freeman, W. A., Banner, J. A., and Hoff, G. F. (1993). Lithium AA-Size Cells for Navy Mine Applications: I. Selection and Test Plan. NSWCDD/TR-92/210

(2) Kilroy, W. P., Banner, J. A., and Walsh, F. (1994). Development of AA-size cells for mine batteries. Proceedings of the 36th Power Sources Conference.

RECHARGEABLE BATTERY DEVELOPMENT FOR THE AN/PAS-13 THERMAL WEAPONS SIGHT

Martin Sulkes and George Au, Army Research Lab,
Electronics and Power Sources Directorate, Fort Monmouth, NJ

Abstract

Rechargeable Lithium and Lithium-ion batteries in several electrochemical systems have been and are currently being investigated as potential candidates to provide power for training missions to the AN/PAS-13, "Thermal Weapons Sight (TWS)". Because of a unique combination of power, weight, voltage and operating cost requirements, this equipment was deemed the ideal candidate to first field a rechargeable lithium battery in significant quantities. The specific requirements of the TWS and the capabilities of the various battery types investigated will be discussed.

Introduction

The AN/PAS-13, "Thermal Weapons Sight (TWS)," (Shown in Figure 1), is a class of low cost, lightweight infrared imaging devices of medium to high resolution to be used for the fire control of individual and crew served weapons during both daylight and darkness. TWS is required to operate in adverse weather and battlefield conditions. It will be procured in large quantities for provision down to the infantry squad level.

When originally conceived, the key factors driving the choice of a battery power source were: lightweight(0.55 lbs) due to the mounting location and a 12 hour operating time to minimize battery changes. These goals were achievable only with the BA6847, a 2 "D" cell Lithium-Thionyl Chloride throwaway battery. Unfortunately these superior performance attributes come at a cost of approximately $1/wh. Even the Lithium Sulfur-dioxide, BA5847/U, throwaway battery which provided only 1/2 or less of the BA6847's service came at a cost of approximately $0.60/WH. Original cost projections, in 1990, when Lithium sulfer-dioxide demand was high, were about 2/3's of the costs given above.

Therefore, using throwaway batteries only, could result in a 20 year operating and support (O & S) cost of $80M per 1000 TWS units. Based on the projected deployment schedule of many thousands of TWS's and heavy training requirements, costs of this magnitude are unacceptable, except for the most critical military needs. The cost factor has become even more critical in 1994, when field units are required to budget and pay for the batteries they use.

As such, the Electronics and Power Sources Directorate of the Army Research Lab was tasked by the Project Manager for Night Vision in early 1991 to develop a high capacity, lightweight, rechargeable battery, that even with a cycle life as short as 50 cycles, could reduce the cost of portable battery power by 6-10 times compared to Lithium Throwaway types. An examination of the system requirements, shown in table 1, determined that the TWS was an almost ideal candidate for a 30 watt-hour rechargeable Lithium System. One particularly unique discharge load factor aiding the use of a rechargeable lithium battery was the fact that the average and peak loads decreased as temperatures dropped.

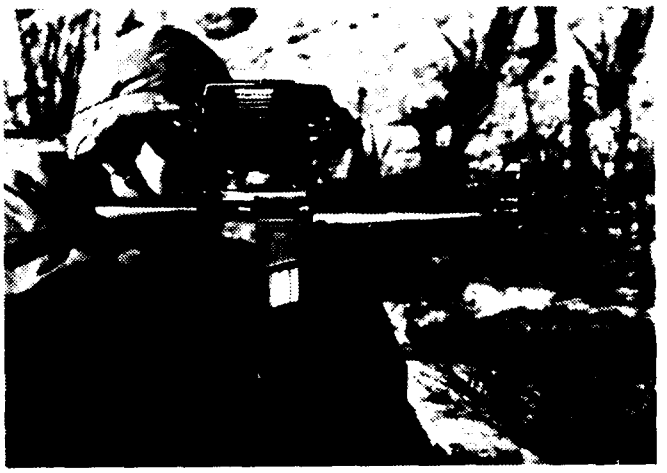

Fig. 1 AN/PAS-13, Thermal Weapons Sight

Table 1. TWS RECHARGEABLE BATTERY REQUIREMENTS

Voltage Range	4-8 volts	
Input Power		
@50°C	12.4/4W for 2.9/7.1 minutes	Typical
	13.0W Continuous	Maximum
@25°C	10/3W for 2.9 min/7.1 min	Typical
	10.5W Continuous	Maximum
@-20°C	9.2/2.2W for 2.9 min/7.1 min	Typical
	9.5W Continuous	Maximum

Desired operating time: 4-6 hours on typical load equals 20 to 30+ watt-hours

Weight - No more than 0.75 lbs (0.34kg)

Size - 2.55 X 3.75 X 1.5 inches = 14.3 in^3 (0.23L)

Approach

After considering the state-of-the-art of rechargeable Lithium batteries at the time and the tradeoffs shown in table 2, the choice was made to initially concentrate on the Li-V_2O_5 system. The reasons were it had a more mature technology, lower self discharge, simpler charge control and a high capacity based on the insertion of 1.8 Lithium per V_2O_5 (1). At the same period of time, development was continuing on Lithium Nickel Oxide and Lithium-Cobalt Dioxide as potentially higher energy systems. Also, investigation was started on Lithium-Ion or "rocking chair" technology in order to respond to requirements for increased safety. Another approach, pursued in cooperation with The Advanced Research Projects Agency (ARPA) was the demonstration of Lithium-Polymer technology in a BB2847 battery, where the Polymer system's high volume utilization could provide a higher capacity than traditional round cells. Table 3 lists the various related contractual efforts in chronological order. However, as time has passed, factors unrelated to battery performance, such as the industrial base for each technology, its dual use potential and total cost of ownership are being given greater weight in the choice of a rechargeable battery for the TWS.

Table 2. LITHIUM METAL OXIDE COMPARISON

	LiV205	LiNi02	LiCo02
END OF CHARGE	3.8V	4.1V	4.2V
SHARP END OF CHG	YES	NO	NO
END OF DISCHG	2.5/2.0V	2.8V	3.0V
AVG DISCHG VOLT	3.35/2.75	3.7	3.9
ASSEMBLY STATE	CHGED	DISCHG	DISCHG
SELF DISCHARGE			
1 MONTH @45C	5%	5% *	10% *
WH/KG PER CELL	110/50	168	175

* SOME PERMANENT LOSS

Results And Discussion

Li/V_2O_5: The specifics of the Li/V_2O_5 "D" cells developed for the BB2847 were given by Staniewicz and Broussely (2). When discharged at 2 amperes (2-3 ma/cm^2) these cells provided more than 50 cycles, starting at 16 wh, each and remaining above 10 wh. Based on these encouraging results, 2 cell prototype batteries were assembled using only the minimal controls and thermal protection devices thought necessary for this system. They were then operated at the TWS 10 watt load. Figure 2 compares the results from cell data with that actually obtained in a battery configuration. As can be seen, a third of the battery's capacity is lost, compared to what was expected. Circuit voltage losses increased the current so that the lower plateau was below the cutoff point of the equipment. In addition, cycle life was much less than expected because of cell imbalance, caused by

Table 3. BB-2847 Related Contractual Efforts

Contract (agency)	Contractor	Electrochemical Systems
DAAL01-90-C-0034 (ARL)	SAFT	Li-V_2O_5/Li-$LiNiO_2$
DAAL01-90-C-0036 (ARL)	SAFT	Li-$LiNiO_2$/Li-$LiCoO_2$
DAAL01-92-C-0221 (ARL)	Rayovac	Li-C/$LiNiO_2$
MDA972-93-C-0013 (ARPA)	Valence	Li/SPE/Vanadium Oxide
BAA 93-32 for flexible	Multiple	Li/SPE/$LiCoO_2$
manufacturing (ARPA)	Awards	Li-C/SPE/$LiMn_2O_4$,

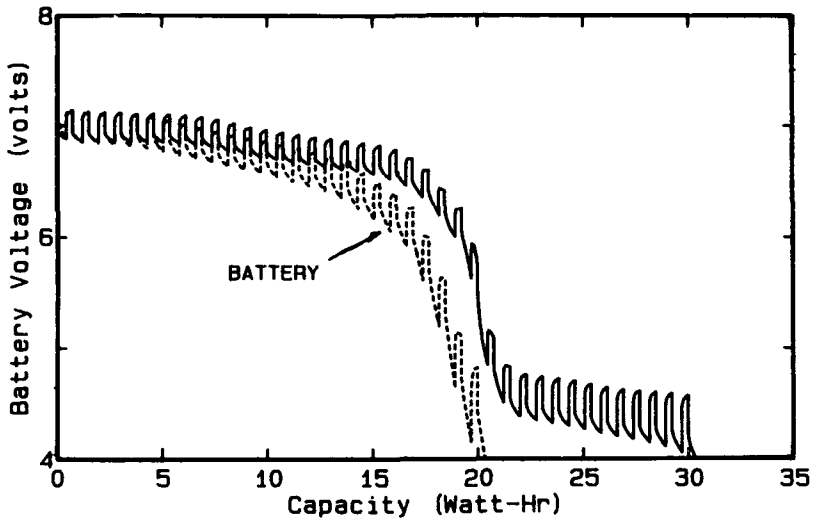

FIG 2. Lithium/V205 BB2847 Battery on TWS Load.
- Comparison With Cell Data Without Thermal Controls.

intermittent dendritic shorting. Because charge and discharge were controlled on overall battery voltage, individual cells were driven to extremes of voltage which accelerated the batteries deterioration. As a result of these problems and significant improvements in the capacity of $LiNiO_2$ "D" cells by the SAFT R&D Center the decision was made to drop the V_2O_5 chemistry for the BB2847.

$LiNiO_2$: The general design characteristics of the Li/$LiNiO_2$ "D" cells and the battery and charge controls are described by Staniewicz, Romero and Gambrell in reference 3. Figure 3 shows a Li/$LiNiO_2$ battery with charge controls. This rechargeable battery system had many advantages for the TWS while presenting some difficulties that required unique solutions. These advantages included a high cell voltage (3.7 volt average) which minimizes current demand, a cell energy density up to 170 wh/kg and ability to provide extra capacity at high temperatures as required by the equipment. Figure 4 shows TWS operating time as a function of temperature based on cell performance. Figure 5 shows battery discharge output at high and low temperature. Note that the battery internal cutoff is temperature compensated to prevent the excessive intercalation of lithium that can take place at high temperatures with deleterious effects because of the limited (2x) lithium capacity built into these cells. The actual battery capacities from figure 3, were 12% lower at high temperature than cell data would project because of the power loss across a diode and a high voltage end of discharge cutoff. At low temperature (-20°C), battery output is more than 2X higher due to battery self heating.

Disadvantages of the Li/$LiNiO_2$ battery are those common to most metallic Lithium batteries, and include short cycle life, low recharge rate, the need for individual cell controls and extensive safety protection. Again, because the BB2847 is only a 2 cell battery, this did not present an insurmountable obstacle. In order to meet safety needs, the Li/$LiNiO_2$ - BB2847 used a dedicated charger which individually charges each cell through a separate charging port by a current limited (0.4A), constant potential of 4.1 volts. Typical charge time is 12-15 hours. A microprocessor control in the battery provides resetable protection in the event of overcurrent, overtemperature, and cell imbalance. It also communicates with the charger microprocessor to limit change time and indicate any fault.

A total of 30 prototype batteries and 5 chargers were delivered for evaluation. These hand made units, when good, provided high capacity, (31 wh at 20°C/and 60 cycles to 20 whr). In all cases there were no safety problems. However, additional work would be required to improve and control all manufacturing processes and to reduce the sensitivity of the digital control circuits to spurious signals before this technology could be considered for limited fielding. Based on a 1993 market analysis, it was apparent that large metallic lithium cells and batteries using this technology would not be available with an acceptable reliability and cost within the foreseeable future. Nevertheless, much of the technology developed could be applicable to a lithium-ion version of the BB2847.

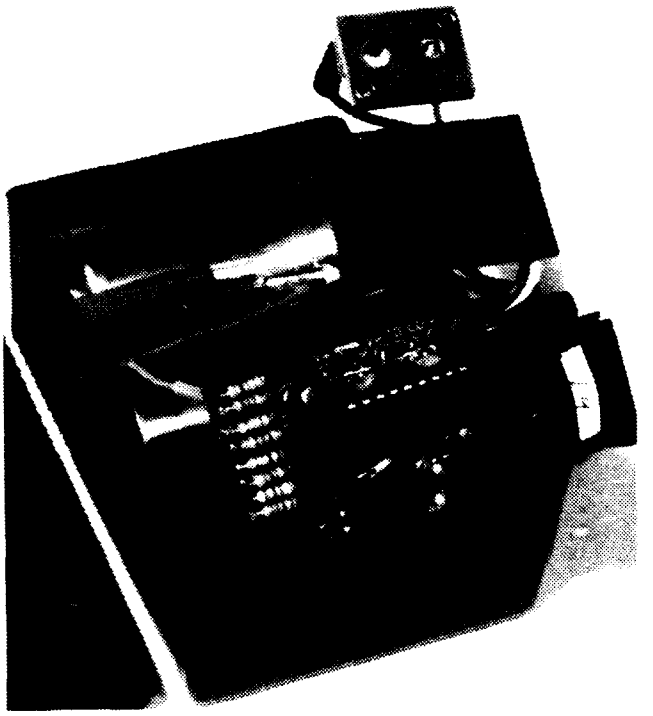

Fig. 3 Prototype Li/$LiNiO_2$ BB2847 Rechargeable Battery

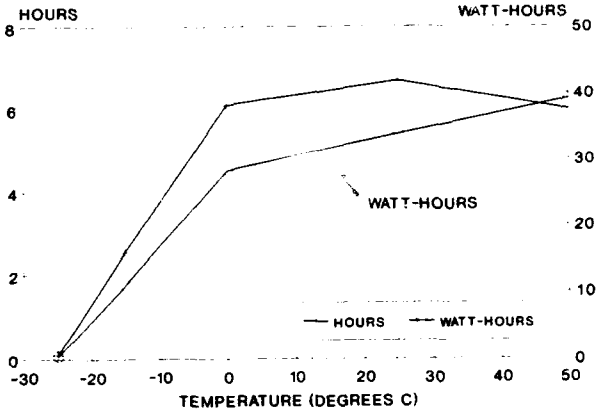

FIG 4. TWS SERVICE WITH LiNiO2 BATTERY

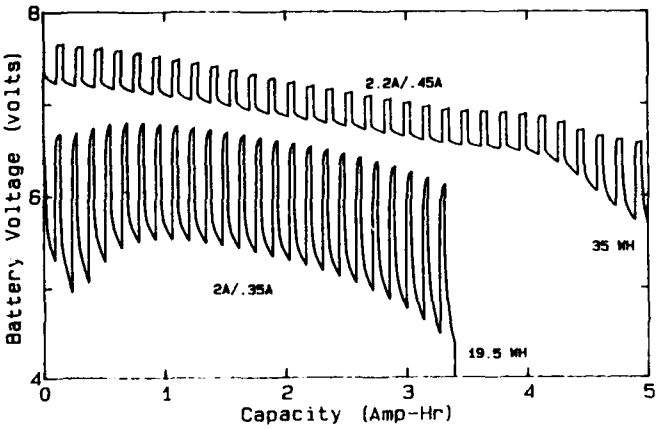

FIG 5. Discharge Profile of Li/LiNiO2 Batteries At -20 C And 50 C On Simulated Constant Current TWS Loads

Li-C/$LiNiO_2$: One version of the BB2847 using a petroleum coke anode is discussed in detail by Fouchard (4), including both cell and control information. A total of 30 of these batteries and 5 chargers have been delivered to ARL for evaluation. Initial evaluations of these prototypes have indicated that the Rayovac RCT battery can provide 20 wh at 67 wh/kg for 100 or more cycles. Low temperature performance is excellent with approximately 75% of ambient service time being attainable at -30°C. On the other hand, high temperature service at 50°C is reduced by about 25%. This occurs because of the desire to maximize battery life and safety at high temperature. Accordingly, a lowered voltage limit is placed on charge and cell voltage which results in about 3% less capacity. Additional evaluations are being carried out to determine life and storageability under a variety of conditions.

Another approach to the design of Li-ion "D" cells, that have been demonstrated in BB2847 batteries, is described by Staniewicz, Gambrell and Castro (5) and employs a graphite anode with an ethylene carbonate (EC) electrolyte. Evaluation of a limited number of battery samples has been initiated using a charge control based on individual cell charging at a 4.1 volt constant potential.

Li-C/$LiCoO_2$: Another approach to achieve a BB2847 battery in minimum time is also being explored. This would make use of commercially available lithium-ion cells such as the 18650 size. A total of 6 of these cells would fit the BB2847 box and could provide 20wh at approximately 59 wh/kg. A commercial example of this approach was described by T. Ozawa and T. Aita (6) of Sony Corp., where 3, 18650 size lithium-ion cells are paralleled to provide 3ah and 3 cell groups are placed in series to provide 10 volts for a laptop computer. Each cell group would be equipped with electronic cutoffs for both charge and discharge.

Summary

Metallic Lithium-Nickel Oxide cylindrical "D" cells, while having the energy density necessary for the TWS, are not considered ready for procurement at an affordable cost or with the required reliability and safety.

Lithium-Ion, while not providing the full capacity required, currently offers the best combination of capacity, weight, safety and affordability. It is likely, however, that near term demands for the BB2847 may have to be met by the paralleling of several commercial type cells rather than using tailored military "D" size cells.

For the longer term, Lithium-solid polymer electrolyte batteries made by flexible manufacturing techniques, offer the potential of providing a lightweight, low cost, higher capacity rechargeable power source that can replace almost all throwaway battery requirements for the TWS.

References

1. J.M. Cocciantelli, J.P. Dowrmere, M. Pouchard, M. Broussely, and J. Labat, J. Power Sources, 34, 103 (1991)

2. R.J. Staniewicz, M. Broussely, A. Romero, and J. Labat, "Rechargeable Li/V_2O_5 D Cell Development" Proceedings of the 35th International Power Sources Symposium, June 22-25, 1992, Cherry Hill, NJ

3. R.J. Staniewicz, A. Romero, A. Gambrell, "Rechargeable Cells and Batteries Using $LiNiO_2$ Positives" 3rd Lithium Battery Exploratory Development Workshop, June 23-24, 1993, Lake Placid, NY

4. D. Fouchard, W. Ebner, S. Meghead "Development of a Lithium-Ion BB-2847 Battery" Proceedings of the 36th International Power Sources Symposium, June 6-9, 1994, Cherry Hill, NJ

5. R.J. Staniewicz, A. Gambrell, G. Castro "Lithium like Rechargeable Battery" ibid

6. K. Ozawa, T. Aita, "Multicell Pack Using Li-Ion Rechargeable Batteries", Eleventh International Primary and Secondary Battery Technology and Applications, Feb 28-Mar 3, 1994, Deerfield Beach, FL

Effects of Repeated Resistance Testing on the Firing Ability of Igniter EP360-3

Gary Q. O'Day
Eagle-Picher Industries, Inc.
Joplin, Missouri 64801
and
David M. Ryan
Aero Propulsion and Power Directorate
Wright Patterson AFB
Ohio 45433-7251

INTRODUCTION

An igniter is an electroexplosive device (EED) which is typically used to activate thermal batteries, propellants, or other fuels. Being an hermetically sealed unit, the only electrical check is a test of the igniters resistance. This repeated resistance testing causes some concern for certain users. The igniters are rated by All-Fire and No-Fire current pulses. The igniter used for this test is rated at 3.5 Amps, 20 millisecond All-Fire pulse and 1.0 Amp, 5 minute No-Fire pulse which implies that within certain statistical parameters the given pulses will either activate or not activate the igniter.

This report summarizes the work completed under U.S. Air Force contract F33601-93-P-7648, Data Item #0002, issued 11 March 1993 and completed 8 September 1993.

The objective of this test was to determine if desensitization of an igniter occurs due to repeated resistance checks. An EP360-3 igniter (Eagle-Picher Industries, Inc., part number 31-32-026-0) was chosen for this test. This is a dual bridge igniter with only one bridge circuit used for testing.

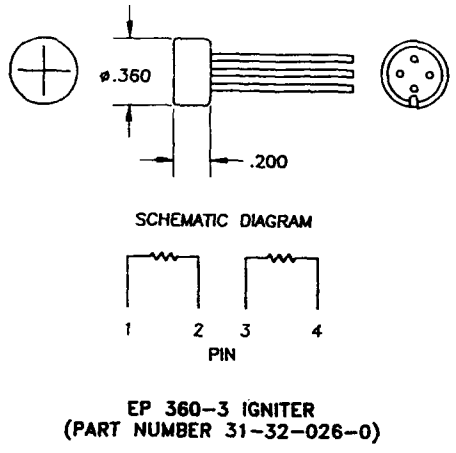

Figure 1 EP360-3 Igniter With Schematic

The testing can be divided into three parts. First, 35 (thirty-five) units were tested to determine the estimated test stimulus required to fire the igniter with a reliability of 99.99% and a confidence level of 95%. This first group was used as a control group.

Second, 40 (forty) igniters taken from the same production lot, had resistance readings taken every 2 (two) minutes (1 milliampere of current for 20 milliseconds) for a total of 10,001 resistance checks.

Third, the group of igniters that had been resistance checked were then tested in the exact same manner as the first group to determine the estimated test stimulus required to fire the igniters with a reliability of 99.99% and a confidence level of 95%. The two estimated test stimuli were then compared to determine if the igniters ability to fire had been impaired.

BRUCETON TEST OF CONTROL GROUP

A Bruceton reliability test was performed on the control group to determine the level at which the units will activate.

The Bruceton Test

The Bruceton Method of Sensitivity Testing provides results from which a statistical estimate of a high assurance of reliability can be established on the assumption that the percentage functioning is related to the test levels by means of a normal error function.

In the first part of the test, five (5) units are tested to determine an approximate level at which 50% of the units will fire (denoted by the letter 'k'). In the second part of the test, the first unit is exposed to a pulse at this level and subsequent units are exposed to levels determined by the previous units ability to fire. An arbitrary level (denoted by the letter 'd') is set as the increment between test levels. If the first unit fires, the next unit is exposed to a pulse at a level of k-d. If the unit does not fire, the next unit is exposed to a pulse at a level of k+d. Each succeeding unit will be tested at a level dependent upon the firing behavior of the previous unit. (i.e. if the previous unit fired, the next unit will be tested at a level 'd' less than the previous level, and if the previous unit failed to fire, the next unit will be tested at level 'd' greater then the previous level.) Thus, the test results will be a sequence of fires (denoted by X) and failures (denoted by O) centered about the 50% firing level.

Fire Current (Amps)	X' Denotes Fire / O' Denotes Did Not Fire																																
	1	2	3	4	5	6	7	8	9	10	11	12	13	14	15	16	17	18	19	20	21	22	23	24	25	26	27	28	29	30	31	32	33	34	35
1.75					X		X														X		X		X		X								
1.70				O		O		X				X		X		X		X		O		O		O		O		X					X	
1.65	X		O						X		O		O		O		O		O										X				O		O
1.60		O								O																				X		O			
1.55																															O				

Test Current	Fire	No-Fire
1.75	6	0
1.70	7	6
1.65	3	8
1.60	1	3
1.55	0	1
Total	17	18

Estimated Test Stimulus = 2.13 Amps

Figure 2. Bruceton Test Data for Control Group

Control Group Testing

Using the above method the 50% firing level (k) was determined to be 1.65 Amperes with a 20 millisecond pulse. The distance between levels (d) was set at 0.05 Amperes. All test pulses will be of a 20 millisecond duration.

The 35 units in the control group were then tested to produce the data shown in Figure 2. The table at the bottom of Figure 2 was then completed and entered into a computer program which calculated the estimated test stimulus, estimated error, etc.

Results

The estimated test stimulus required to fire the control group of igniters with a reliability of 99.99% and a confidence level of 95% was found to be 2.1301 Amperes with an estimated error of 0.0870, which gives a range of 2.0431 to 2.2171 Amperes with a 20 millisecond pulse duration.

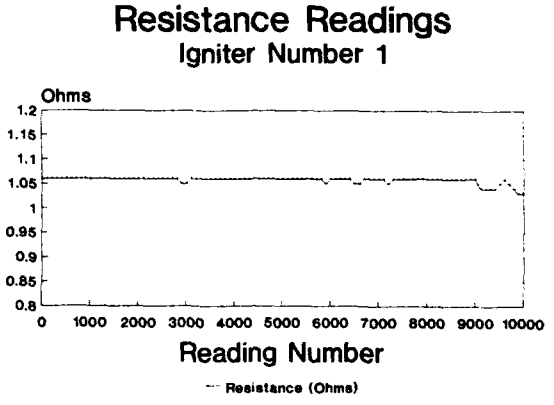

Figure 3. Resistance Readings for Igniter Number 01

RESISTANCE CYCLE TESTING

A second group of 40 igniters were selected from the same production lot. This test group was subjected to a continuous testing of the bridge circuit for a total of 10,001 tests.

The igniters were connected to a Hewlett-Packard 3497A data acquisition system and HP86B computer which sent 1 milliampere of current to each igniter every two minutes. All testing was performed under ambient conditions. A graph of the resistance readings for igniter serial number 01 can be seen in Figure 3.

Results

Comparing the resistance values at the beginning and end of the cycle shows that all of the igniters showed a lowering of resistance but none were significantly lower, with a maximum drop of 0.03 ohms. The specified range of resistance on this igniter is 1.00 +/- 0.10 ohms.

BRUCETON TEST OF CYCLED GROUP

The igniters from the above resistance cycle testing were then tested by the Bruceton Method in the exact same manner as the control group to determine the stimulus level required to activate the igniters.

Results

The data is shown as Figure 4. The estimated test stimulus required to fire the igniter with a reliability of 99.99% and a confidence level of 95% was found to be 1.8625 Amperes with an estimated error of 0.0324 which gives a range of 1.8301 to 1.8949 Amperes.

Fire Current (Amps)	'X' Denotes Fire / 'O' Denotes Did Not Fire																																
	1	2	3	4	5	6	7	8	9	10	11	12	13	14	15	16	17	18	19	20	21	22	23	24	25	26	27	28	29	30	31	32	33	34	35
1.75												X												X											
1.70	X		X		X						O		X				X		X		X		O		X		X		X				X		X
1.65		O		O		X		X		O				X		O		O		O		O				O		O		X		O		O	
1.60							O		O						O																O				
1.55																																			

Test Current	Fire	No-Fire
1.75	2	0
1.70	12	2
1.65	4	11
1.60	0	4
1.55	0	0
Total	18	17

Estimated Test Stimulus = 1.86 Amps

Figure 4. Bruceton Test Data for Test Group

CONCLUSIONS

Effect of testing on resistance

After 10,001 resistance checks at 1 milliampere every 2 minutes, the resistance of the EP360-3 igniter changed a maximum of 3%. This change is well within the normal 10% tolerance specified for the particular igniter. Therefore, it is concluded that repeated resistance testing at 1 milliampere had no immediately significant effect on the igniters resistance.

Effect of testing on sensitivity

The Bruceton test on the control group yielded an estimated test stimulus of 2.1301 Amperes at a 20 millisecond pulse. The Bruceton test on the test group of resistance cycled igniters yielded an estimated test stimulus of 1.8625 Amperes with a 20 millisecond pulse. This is a difference of 13% with the control group requiring a greater current level than the test group. If the resistance cycling had desensitized the igniters, one would expect to see the test group requiring a greater amount of current before activating. In this experiment we have seen just the opposite. This may be due to the inaccuracies of the statistical analysis of the Bruceton test because of the small sample size used.

Group	Estimated Test Stimulus	Estimated Error	Range
Control	2.1301	.0870	2.0431-2.2171
Test	1.8625	.0324	1.8301-1.8949

Table 1. Test Data Comparison

Due to the estimated test stimulus required of the test group not being significantly higher than that of the control group, it can be concluded that continual testing of resistance at 1 milliampere of current for 10,001 checks has no significant effect on the igniters ability to fire.

RECOMMENDED FURTHER TESTING

In an ideal case the estimated test stimulus, plus or minus the estimated error, for each test should overlap if the resistance testing had absolutely no effect on the igniter. The fact that it did not do so for this set of tests may be due to statistical inaccuracies. It would be desirable to perform the Bruceton tests on larger samples or perform more Bruceton tests on control groups to determine if the estimated test stimulus found would fall in the range set by the control group in this test.

All of these tests were performed under ambient conditions. Additional testing may include: resistance cycle testing at high and low temperature extremes, resistance cycle testing in conjunction with temperature cycle testing, and Bruceton testing at high and low temperature extremes or any combination of the above.

Also, it would be desirable to perform testing to determine what will cause a degradation in the igniters ability to fire. Possible tests in this area include: a longer cycle of resistance testing, a higher level of current during resistance cycle testing, and a prolonged period after resistance testing before firing.

REFERENCES

(1) NAVORD Report 2101, "Statistical Methods Appropriate for Evaluation of Fuze Explosive Train Safety and Reliability", 13 October 1953

(2) Eagle-Picher Industries, Incorporated document OP-QC-035, "Bruceton Test Method"

DISPOSAL CHARACTERISTICS OF SELECTED MILITARY BATTERIES

Louis F. Soffer
US Army Communications-Electronics Command
Fort Monmouth, New Jersey 07703

Introduction

Over the past ten years considerable work has been done to assess the disposal characteristics of CECOM-procured military batteries using current US Environmental Protection Agency (EPA) hazardous waste (HW) identification regulations, and state bioassay requirements. This paper presents previous and current test methods, results, disposal requirements and design implications for six classes of military batteries procured by the US Army Communications-Electronics Command (CECOM).

We have assessed the disposal characteristics of Army batteries under Resource Conservation and Recovery Act (RCRA) regulations administered by EPA, and state bioassay requirements. This paper presents findings and regulatory management guidance for CECOM-procured alkaline (ALK), zinc-carbon (LCE), magnesium (MG), lithium-manganese dioxide (Li-MnO_2), lithium-sulfur dioxide (Li-SO_2) and lithium-thionyl chloride (Li-$SOCl_2$) batteries.

Background

RCRA regulations define HW either by listing specific waste streams, or by the identifying specific characteristics under 40 Code of Federal Regulations (CFR) Part 261 Subpart C. Batteries are not listed; and therefore, in order for them to be identified as HW under RCRA, they must be found to be ignitable (D001), corrosive (D002), reactive (D003) or toxic (D004-D043) in accordance with (IAW) established analytical procedures under this regulation. RCRA toxicity regulations became more severe in 1990, when test Method 1311 was changed from the Extraction Procedure Toxicity (EP Tox) test to the Toxicity Characteristic Leaching Procedure (TCLP). This change means, in many cases, that a higher concentration of a TCLP contaminate may be extracted from the sample, than was the case utilizing the EP Tox methodology. A solid waste is determined to be a HW when the extract concentration under TCLP for a particular contaminate is equal to or greater than the "regulatory level (mg/L)" in "Table 1, Maximum Concentration of Contaminants for the Toxicity Characteristic" of 40 CFR 261.24.

All states must utilize RCRA requirements as a minimum for the determination of HW. In addition to RCRA's TCLP the states of Alaska, California, Minnesota, Rhode Island, and Washington utilize bioassay techniques to determine toxicity for HW identification. Bioassay test utilizes an organism's response to a chemical insult to assay toxicity. The measure of toxicity is inversely proportional to the amount of chemical substance to which the organism is exposed. A typical criteria is the lethal concentration (LC) $\leq$500 mg/L, which is fatal to 50% of the test organisms, i.e. LC_{50}, during a 96 hour (96-h) test period.

Previous Findings

CECOM has analyzed MG and Li-SO_2 military batteries[1,2] prior to TCLP requirements. MG batteries were found to be non-hazardous solid waste (NHSW). Li-SO_2 batteries were found to be ignitable (D001), and reactive (D003) under RCRA. The management recommendation for Li-SO_2 batteries suggested that the complete discharge of the battery would eliminate D001 and D003 characteristics, thereby allowing for its disposal as a NHSW. US Army Laboratory Command (LABCOM) analysis of Li-$SOCl_2$ military batteries[3] yielded results and management recommendations similar to those for Li-SO_2 batteries.

Current Efforts

When the TCLP methodology replaced EP Tox we undertook a major study[4] to evaluate ALK, LCE, MG, Li-MnO_2, Li-SO_2 and Li-$SOCl_2$ military batteries for the toxicity characteristic under TCLP. The other RCRA characteristic tests for ignitability, corrosivity and reactivity were not affected by this 1990 regulatory change. In addition, we decided to analyze these batteries utilizing California's (CA) bioassay methodology. The methodology and results are shown below under analysis 1.

A finding of analysis 1 below, indicated that MG batteries discharged to 50% capacity should be characterized as toxic HW for Cr (D007) under RCRA. This finding was challenged by a major battery supplier.[5] The supplier's findings suggested that the TCLP sensitivity for Cr was dependent on the battery's state of charge. This prompted an additional TCLP study[6] to clarify this issue. The methodology and results are shown below under analysis 2.

Analysis 1[4]

Method[7,8]

A random sample, n=42 (7/type), of ALK, LCE, MG, Li-MnO_2, Li-SO_2 and Li-$SOCl_2$ military batteries were selected from depot stock. Prior to analysis ALK, LCE, MG Li-MnO2 batteries were discharged to 50% of capacity to simulate field conditions prior to disposal. IAW solid waste management guidance[2,3] Li-SO_2 and Li-$SOCl_2$ batteries should be totally discharged prior to disposal; therefore, these batteries were totally discharged prior to analysis.

TCLP: The battery samples were then reduced to <9.5mm particle size, and 100g aliquots were extracted IAW TCLP methodology. The extracted leacheates were analyzed for metals, volatile organic compounds and semi-volatile organic compounds, except for pesticides and herbicides, IAW SW-846[9] as required by Method 1311. Metal leacheate samples were analyzed using atomic absorption spectrometry or inductively coupled plasm technique. Volatile organic compounds and semi-volatile organic compounds were analyzed using gas chromatography/mass spectrometry or high performance liquid chromatography as appropriate.

Bioassay: Aquatic bioassays were conducted to further characterize HW. CA's

Table 1

Summary of TCLP Results by Battery Chemical Type
n=42[1], Mean (mg/L)

TCLP Contaminant	Type ALK	LCE	MG	Li-MnO_2	Li-SO_2	Li-$SOCl_2$	TCLP Regulatory Limit
Arsenic	0.53	0.190	0.15	0.062	<0.050	0.10	5.0
Barium	<0.10	0.18	0.88	<0.10	<0.10	0.15	100.0
Cadmium	<0.0030	0.052	0.0033	<0.0030	0.017	<0.0030	1.0
Chromium	<0.010	0.010	9.1[2]	0.012	<0.010	4.2[3]	5.0
Lead	<0.050	0.186	<0.050	<0.050	<0.050	<0.050	5.0
Mercury	0.033	0.040	N/A[4]	N/A	N/A	N/A	0.2
Selenium	<0.050	0.058	0.088	<0.050	<0.050	0.082	1.0
Silver	<0.010	0.036	<0.010	<0.010	<0.010	<0.010	5.0

Notes:
1. Sub-sample, n=7, for each battery chemistry type.
2. Mean value exceeds regulatory limit.
3. Upper 95% confidence limit around mean exceeded regulatory limit.
4. Lithium and Magnesium batteries do not contain mercury.

methodology was selected as a representative test.[8] The TCLP method uses an acetate buffer, which is toxic to some aquatic biota. In order to eliminate this confounding variable, Method 1312 from SW-846 was utilized for extraction, which is not toxic to the Fathead minnow and *Ceriodaphnia*, utilized in CA's methodology. The organisms utilized represent vertebrate and invertebrate species, respectively. Preliminary 48-h LC_{50} acute toxicity tests were conducted to establish dilution ranges. Acute 96-h LC_{50} toxicity tests were conducted. The LC_{50} concentrations (mg of battery/L) reported will kill 50% of the test animals in the specified time period.

Results

TCLP: No volatile organic compounds nor semi-volatile organic compounds were found that exceeded the regulatory limits (RL) established by 40 CFR 261 criteria. The results for "EPA Contaminant" metals are found in Table 1. Fifty percent capacity MG batteries exceeded the 5.0 mg/L RL for Cr. The upper 95% confidence limit around the mean for totally discharged Li-$SOCl_2$ batteries exceeds the 5.0 mg/L RL for Cr. Under EPA's interpretation Li-$SOCl_2$ failed the TCLP RL. Therefore, 50% capacity MG batteries, and totally discharged Li-$SOCl_2$ batteries are considered HW.

Bioassay: Table 2 summarizes the 96-h LC_{50} acute toxicity results for MG, Li-SO_2, Li-MnO_2 and ALK batteries. LC_{50} of $\leq$500

mg/L are identified as HW. Preliminary 48-h acute LC_{50} toxicity tests for LCE (LC_{50}=289 mg/L) and Li-$SOCl_2$ (LC_{50}=2.5 mg/L) batteries identified them as HW under this criteria. 96-h LC_{50} testing for these later two classes of batteries was not required. Li-MnO_2, ALK, LCE and Li-$SOCl_2$ batteries are HW under this bioassay criteria.

Table 2

Acute 96-h LC_{50} Toxicity by Battery Type (mg of battery/L)

Battery Type	Test Organism Fathead Minnow	*Ceriodaphnia*
MG	22,928	18,067
Li-SO_2	691	702
Li-MnO_2	288	73
ALK	246	51

Analysis 2[6]

Method[7]

A random sample, n=20 (5/condition), of military MG batteries were selected from independent government test samples previously obtained. Prior to analysis the samples were assigned and pre-conditioned to four state of capacity conditions: 100% (un-discharged), 50% (50% capacity), 10% (10% capacity), and 0% (totally discharged).

TCLP: The samples were prepared and analyzed IAW procedures described under Analysis 1, above.

Results: MG batteries discharged to ≤50% capacity did not exceed RCRA RL for Cr, see Figure 1. No other metals, volatile organic compounds, nor semi-volatile organic compounds exceeded the RLs established by 40 CFR 261 criteria.

Chromium (mg/L)

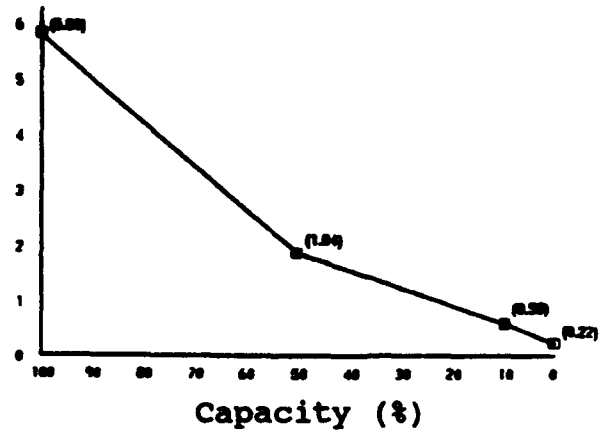

Figure 1. TCLP Analysis of MG Batteries

Discussion

Methods

The EP Tox method uses a structural integrity test (SIT) to determine the particle size prior to extraction. During previous analysis many battery cells survived the SIT intact, and internal battery/cell structures could not be extracted prior to analysis. This model is inadequate as eventually batteries/cells lose integrity in a landfill disposal site. The TCLP does not utilize a SIT. TCLP requires all components to be "crushed, cut, or ground", such that, the sample particles will pass through 9.5mm sieve prior to extraction and analysis. Solids and liquids are amenable to extraction as well as volatiles in a "zero-headspace extractor" utilized by this method.

There is a great difference between EPA's TCLP and bioassay tests to identify HW. Bioassay is independent for the chemical

compound(s) present. TCLP looks for a particular concentration (mg/L) level of a specific element or chemical compound present, which is defined as a HW. Bioassay is only concerned, if the test animal dies at the LC_{50} ≤500 mg/L. These methods provide two different means of assessing toxicity. It is quite possible that more states may adopt bioassay in the future, particularly those with fragile and extensive wetlands.

Findings

Our findings support the manufacturer's data, which indicate that available chromium is affected by the battery's state of charge.[5] It appears that MG batteries with ≤50% charge do not exhibit Cr in excess of the RCRA RLs. Management guidance has been provided to user activities, so that, users may test battery capacity prior to disposal.

Environmental Regulations

The characterization of HW for disposal depends on your location and its applicable regulations. Findings aside, we must deal with "NIMBY", that is the Not in My Back Yard syndrome. I can only suggest that it must be dealt with on a case-by-case basis. It is important to get to know your regulator. Even if findings indicate that the material for disposal is a NHSW, the county officials may not allow the waste at the landfill site without a special permit. And with regard to permits, the disposal site's permit must include your waste stream, or your organization may not use the site.

Waste minimization is another important concept. We have recently commented regarding Docket # F-93-SCSP-FFFFF[10], which affects the recycling and reclamation of batteries. Presently New Jersey's code requires battery recycling. It is important that industry continues to take positive steps to ensure a means to recycle and market spent batteries/cells to reduce the HW stream.

Design

We have already incorporated a complete discharge device in military procured Li-SO_2 and Li-$SOCl_2$ batteries to eliminate their reactivity prior to disposal. Since MG batteries with ≤50% capacity are not HW under RCRA, we may consider the same approach in the future for the MG batteries.

Conclusion

The challenge for the future is to identify, isolate, and properly manage hazardous waste to prevent its entering the waste stream. We should and must minimize waste in order to protect our environment and that of our children. This is called pollution prevention, which is the thrust of the Pollution Prevention Act of 1990. We should strive to reduce the waste at its inception, that is by designing our commodities for reuse, remanufacture or recycling. We should attempt to use less hazardous components. We have reduced the mercury content in LCE and ALK batteries. Maybe we can reduce chromium in MG batteries, or increase the life or cycles of secondary batteries. This will help meet the requirements of Executive Order 12856. Only your innovation can achieve these

aims.

References

(1) Diem, M. and Rosak, D. (1983), Hazardous Waste Special Study No. 37-26-0310-84, Evaluation of Magnesium Batteries Report, US Army Environmental Hygiene Agency (AEHA), Aberdeen Proving Ground (APG), MD 21010

(2) Rosak, D. (1985), Hazardous Waste Study No. 37-26-0427-85, Evaluation of Lithium Sulfur Dioxide Batteries, AEHA, APG, MD 21010.

(3) Kulkarni, R.K., and Rosencrance, A.B. (1986), Technical Report 8507, Safety And Health Hazards Of Disposal Of Lithium Thionyl Chloride Batteries In Sanitary Landfills, US Army Medical Bioengineering Research & Development Laboratory, Ft. Detrick, MD 21701.

(4) Hanson, M., et al. (1992), Toxicity Study of Selected Military Batteries, Martin Marietta Energy Systems Inc., Contract DE-AC05-84OR21400, Oak Ridge, TN 37831.

(5) Letter, Rayovac Corp., 5 September 1991, Subject: TCLP Analysis of BA-4386/U Magnesium Battery.

(6) Painter, P.P. (1993), TCLP Study of Army Procured Magnesium Batteries, Northeastern Analytical Corp. (NAC), NAC Job 924371 Final, Marlton, NJ 08052.

(7) Title 40, Code of Federal Regulations, Part 261, Appendix II (1991), Method 1311 Toxicity Characteristic Leaching Procedure (TCLP).

(8) Polisini, J.M., and Miller, R.G. (1988), Static Acute Bioassay Procedures for Hazardous Waste Samples, California Department of Fish and Game, Water Pollution Control Laboratory.

(9) Test Methods for Evaluating Solid Wastes, SW-846 (Jan. 1990), Rev. 3d Ed., US Environmental Protection Agency, Office of Solid Waste and Emergency Response, Wash., D.C., 20460

(10) Federal Register, 2/11/93, V. 58, No. 27, Subject: Part 260-Hazardous Waste Management System: Subpart C-General Rulemaking Petitions.

TACTICAL POWER FOR MOBILE DIRECTED ENERGY SYSTEMS

Tom R. Childers
Belvoir Research, Development and Engineering Center
Ft. Belvoir, VA 22060

Introduction

This paper discusses some state-of-the-art approaches and options for development of very lightweight prime power source components suitable for a wide range of pulsed load applications. Prime power refers to components which convert available energy (typically kerosene based fuel) into useful electrical power. Typical pulsed loads include High Power Microwaves (HPM), High Power Radars (HPR), Kinetic Energy Weapons (KEW) and High Power Lasers (HPL).

A discussion of two projects undertaken by BRDEC will illustrate some of the approaches available to achieve high power density prime power systems. These projects include:

a. The design of a 1 MW power source for a conceptual airborne application. This effort is discussed in Part 1.

b. The Ground Based Radar (GBR) 1 MW prime power development effort. This is discussed in Part 2.

Concepts and ideas abound using pulse compression techniques to power tactical, mobile pulsed electromagnetic (EM) systems. Tactical mobility is needed for "shoot and scoot" battlefield scenarios. However, successful development of mobile pulsed systems is often hindered by the size/weight of the prime power source. A typical prime power source consists of an engine to convert fuel to mechanical energy, an alternator to create electrical power, and first stage conditioning for power driving the pulsed system. Typically, pulsed systems require d.c. power, either high voltage (HV) or high current. These systems often require large amounts of average power for effective operation.

The pulsed system generally is integrated with a mobile platform (aircraft, land vehicle, or ship). Tactical aircraft usually provide the greatest size/weight constraints, while ships provide the least. Sometimes the existing platform engine can be used; if not, a separate engine must be integrated. Turbine engines provide high power density while reciprocating engines are less power dense. If large rotary (Wankel) engines operating on kerosene based fuels become commercially available in the future, they would provide design and cost flexibility between turbine and reciprocating engines. Research is being conducted on smaller diesel rotaries in the 10 - 100 kW range.

This paper examines current requirements for mobile, tactical prime power systems: small size, low weight, high reliability, and effective system integration.

PART 1: 1 MW Airborne Prime Power Source

The goal of this program was to develop a complete prime power system which could fit inside a 30" diameter, 6' long space inside a missile. The system must convert diesel fuel to 100 kV d.c. to charge a pulsed capacitor. The Belvoir portion included integration of a turbine engine, direct driven alternator and transformer rectifier (TR) unit. Components beyond the TR unit were to be developed by other agencies.

Turbine Engine Design

The airborne power source design effort illustrates a typical special purpose system requiring a turbine. The small space available (30" diameter, 6' long) coupled with high power requirements calls for a lightweight turbine. A diesel fueled ram-air compression turbine engine was chosen to make use of the existing Mach 2 airflow. System considerations required minimizing air scoop drag on the missile. Drag was partially compensated by using the engine exhaust for thrust. The short operating time (4 min) required 5 gallons of fuel for a nominal 1700 hp output. The effort for the 1 MW Airborne Power Source took place in the late 1980s under the auspices of the US Army Harry Diamond Laboratories.

Engine design parameters: 30,000 r/min, 1.25 MW, 200 lbs, 22" long, 18" diameter, 7 lbs/sec mass flow rate, 1,700 degree F turbine inlet temperature. [1]

High Speed, High Frequency (HSHF) Alternator Considerations

Given the various system constraints and requirements, the choice of alternator was fairly clear. High speed operation usually translates to high power density alternators, and matching speed with the engine eliminated gearbox weight. However, development of custom, high speed alternators can be costly and risky. Commercial aircraft alternators are available up to 24,000 r/min, but usually with powers no higher than 200 kW. Some 250-600 kW, 400 Hz air-cooled machines have been designed and built with weights in the 300-600 lb range. HSHF alternators can be used with reciprocating engines at the expense of gearbox weight, which may offset any gains. A 1 MW rated reciprocating diesel engine typically operates at around 1,800 to 2,400 r/min. A turbine engine directly driving a high speed alternator provides a system with the best power density.

A custom HSHF (2 kHz) alternator design was chosen to meet size/weight constraints. The alternator is directly coupled to the engine, thus operating at 30,000 r/min. The alternator is a permanent magnet axial-gap (PMAG) design utilizing a composite wrapped rotor to contain the high mechanical stresses generated when spinning at 30,000 r/min. Permanent magnets simplify rotor design at the expense of direct control of the rotor fields and output voltage. For this application, however, small variations in generator voltage and frequency are acceptable. A small cooling system was designed for the alternator to handle some of the excess heat. Coolant is pumped through hollow stator conductors to absorb conductor losses, maintaining a closed primary cooling loop. Heat is exchanged with a vaporizing coolant which is dumped overboard when pressure relief settings are exceeded. Due to the short operating time, the alternator thermal inertia could absorb a large portion of excess heat.

Alternator design parameters: 30,000 r/min, 8 poles (2,000 Hz), 1 MW average, 4 min duty, 270 lbs, 16" long, 22" diameter, 3-phase, 2 kHz, 1,950 V L-N and WYE output. [2] [3]

First Stage Power Conditioning TR Unit

Typically, the first stage of power conditioning is a rectifier to convert a.c. from the alternator to d.c. This d.c. power usually feeds energy storage/pulse compression circuits. Often a transformer is used before rectification to obtain the desired d.c. voltage. Pulsed systems like KEWs usually require lower voltages

and high currents; the reverse is true for HPL and HPM systems. HPRs can be of two types: tube technology which requires high voltages, or solid state technology which requires low voltages.

High frequency operation means smaller transformers. Thus HSHF alternators are not only lightweight themselves, they allow for smaller, lighter TR units. The transformer core is usually one of the heaviest pieces in a TR unit, and core size decreases with increasing frequency.

The TR design for the 1 MW power source is straightforward using a 3-phase DELTA-WYE transformer and full wave bridge rectification. State-of-the-art HV rectifiers and high frequency operation combine to create high power density. The TR is immersed in dielectric fluid which prevents voltage breakdown and acts as a passive thermal reservoir during operation.

TR unit design parameters: 220 lbs wet, 7 cu.ft., 3-phase DELTA-WYE, 1 MW average, 2,000 Hz, 100 kV d.c. peak output and 150 kV d.c. peak inverse voltage. [4]

Airborne Power System Integration

This section provides an overview of system integration for the power source components and power source integration with the pulsed load. This will illustrate integration issues common to many pulsed systems.

An optimum engine/alternator design speed would minimize weight, prevent operation near critical speeds and reduce technical risk to acceptable levels. Alternator design weight decreased with speed as did the engine design weight; analysis showed 30,000 r/min to be optimum.

The power source was designed to charge an energy storage capacitor, which was the first stage of pulse conditioning. The capacitor is completely discharged within a few microseconds at the end of a 50 ms charge cycle (20 pulses/sec). After discharging, the capacitor initially behaves much like a short circuit. The system's electrical performance was modeled, and alternator and TR reactance was designed to prevent excessive currents during the early portion of the charge cycle. Reactance acts to limit surge currents. Conversely, the reactance was chosen to also assure full charging to the desired 100 kV d.c. peak at the end of the charge cycle. See Fig 1. for a graph of the waveforms during the capacitor charging cycle.

(FIG. 1)

CAPACITOR CHARGE CYCLE

AVERAGE POWER = 1 MW

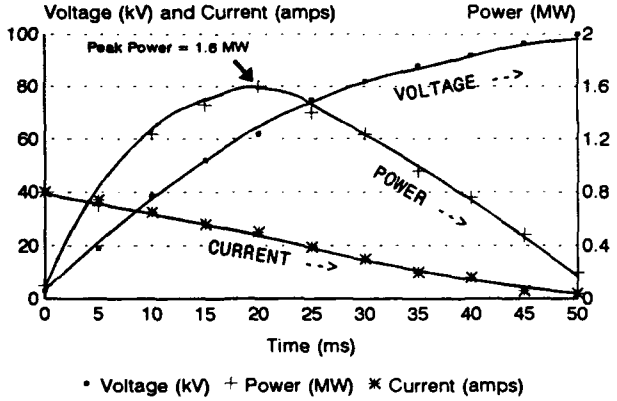

Analysis indicated that peak power flow into the capacitor occurs about midway through the charge cycle. The varying power flow gives rise to cyclic mechanical and electric stresses. The components were designed to withstand these stresses. [5] [6]

Handling excess heat is an ever present issue in compact prime power source design. The best approach is to use efficient components. The alternator and TR unit selected are inherently efficient, operating in the 93% and 97% efficiency range respectively. However, with the high average power required, even these efficiencies give rise to significant waste heat. The relatively short (4 min) operating time allowed the thermal capacitance of the components to absorb much of the waste heat. Longer operating times would necessitate the use of a cooling system designed for steady state operation.

PART 2: GBR Prime Power Development Effort

The system in Part 1 illustrates a case where alternator frequency is a design variable because the load is a pulsed capacitor which requires d.c. However, the GBR system, like most Army and DoD loads, specifies 60 Hz as the input frequency. Design options for the GBR requirement are discussed below.

GBR requirements offer challenges different from the airborne system discussed in Part 1. GBR prime power considerations include C-130 transportability, robust ground mobility, continuous duty operation and noise and IR suppression.

For a traditional 1 MW, 60 Hz power system, the heaviest component is typically the alternator which usually operates at 1,800 r/min. Alternator size and weight can greatly reduced if the speed can be increased. However, increasing speed gives rise to higher frequencies which are not suitable for a 60 Hz specification. To this end, we have explored using a compact HSHF alternator which feeds solid state power conditioning to produce regulated 60 Hz.

The primary issue is whether a system based on a HSHF alternator coupled with power conditioning will reduce overall weight when compared to commercial 60 Hz alternator based system. A 1 MW, 1,800 r/min, 60 Hz commercial alternator weighs about 7,000 lbs. Design efforts with Army Research Lab (ARL), US Navy and industry experts in power conditioning indicate that a 1 MW, high frequency to 60 Hz power conditioner would weigh about 3,000 lbs. The Navy, in particular, has looked extensively at power frequency conversion for multi-megawatt ship electric drive applications.

Table 1. below illustrates the potential weight savings for a 1 MW tactical power system using power conditioning to produce 60 Hz. The Army T-700 turbine was selected as the baseline engine.

Table 1.

Component	Component Weights (lbs)	
	Traditional Design	Advanced Design
Engine	500	500
Gearbox	800	-- (a)
Switchgear	750	-- (b)
Commercial 60 Hz Alternator	7000	--
HSHF Alternator (c)	--	500
Power Conditioning to Produce 60 Hz	--	3000
Cooling for Alternator and Power Conditioning	--	1000
Trailer	6000	6000
Signature Suppressed Housing, Inlet & Exhaust Ducting, Frame and Miscellaneous	6000	6000
Total	21,050	17,000
(a) A gearbox is not needed because the HSHF alternator is directly driven by the engine		
(b) The power conditioning would also act as the switchgear and incorporate fault protection features		
(c) A baseline T-700 speed of 20,000 r/min coupled with an 8 pole alternator produces an output frequency of 1,333 Hz		

In addition to the weight savings illustrated in Table 1., the power conditioning allows the engine to run at its most fuel efficient speed for various loads while still producing 60 Hz (similar to a Variable Speed, Constant Frequency (VSCF) system). Over the long term, fuel costs can become the dominant cost for gen-set operation. The VSCF feature can help to reduce fuel costs.

The alternator can be a wound field design which would offer active output voltage control or a permanent magnet (PM) design which would be simpler and lighter weight. The power conditioning circuit could provide VSCF and constant voltage operation with a PM alternator (perhaps at a smaller speed range when compared to using a wound field alternator).

The power conditioning design selected uses a 3-phase rectifier, d.c. link and Pulse Width Modulation (PWM) to synthesize a 60 Hz output waveform (400 Hz output is also possible). Depending on the voltage, Integrated Gate Bi-polar Transistors (IGBTs) or Gate Turn-off Thyristors (GTOs) can be used for the power switches. IGBTs are suited for lower voltage, high switching frequency designs and vice versa for GTOs. MOS Controlled Thyristor (MCT) switches, once they mature, may combine the advantage of both high voltage and high switching frequency operation with improved efficiency. Higher switching frequencies improve the control characteristics of the PWM circuit while reducing output harmonic distortion.

Commercial 60 Hz alternator technology is relatively static while power switch technology is advancing rapidly with good potential for further weight savings in the future. See Fig. 2. for a conceptual illustration of the power conditioning circuit.

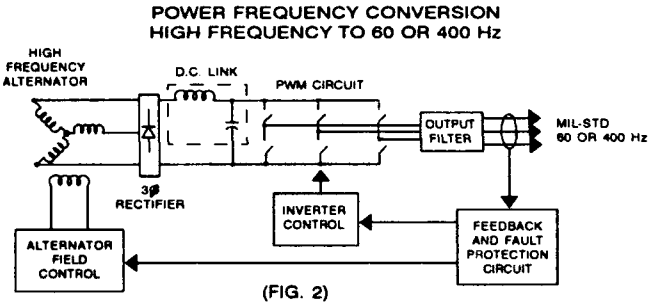

(FIG. 2)

For special purpose loads where a particular frequency is not required, the power conditioning could simply be dispensed with. An appropriate TR unit would then be integrated to provide the desired d.c voltage and current.

CONCLUSIONS

Well developed designs and developmental components exist for fabrication of very lightweight prime power systems suitable for a wide range of mobile, tactical pulsed applications. Standard and non-standard interface frequencies and voltages can be accommodated. Advances in engines, alternators, materials and power switch technologies will allow for continued increases in power density for special purpose and MIL-STD type prime power systems.

REFERENCES

[1] "1,700 HP Ram Air Turbine Engine, Preliminary Design Review and Data Package," 15 March 1989. Prepared by Sundstrand Inc. under contract DAAK70-88-C-0052.

[2] "High Speed Generator Program, Preliminary Design Review," 21 March 1989. Prepared by EML Research Inc. under contract DAAK70-88-C-0053.

[3] "High Speed Generator Program, Preliminary Design Update," 17 April 1989. Prepared by EML Research Inc. under contract DAAK70-88-C-0053.

[4] "High Voltage TR Unit, Detailed Design Review," 18 October 1989. Prepared by Hughes Aircraft Inc. under contract DAAK70-88-C-0054.

[5] "Development of a Compact 1 MW Average Power Source for HPM Applications" in Proceedings of the 5th High Power Microwave Conference, 1990.

[6] "Development of Lightweight Prime Power Source Components for Pulsed Applications" in Proceedings of the 8th National Conference on Pulse Power Technology, 1991.

VEHICULAR POWER GENERATION (IN-LINE)

K. Mike Miller
Power Generation and Environment Control Division
Command and Control Systems Integration, CECOM
Ft. Belvoir, Virginia 22060

INTRODUCTION

Electric Power plays an ever increasing and important role on the modern battlefield. Electric power is essential for operating, maintaining or repairing virtually all of the systems presently fielded. Whether the battlefield scenario calls for Command, Control and Communications operation, weapons systems operation, countermeasure systems operation, or maintenance functions, a power source must be available to the soldier whenever and wherever it may be needed. Where the total energy requirements become significant (more than a few kilowatt-hours), an electric power generator is a necessity.

The requirements placed on electric power generating equipment are changing. With increased CONUS basing of our troops, present and future military operations will require the ability to quickly transport power generation assets to military theaters. This is a real and vital requirement that implies that the size and weight of power generation assets must continue to decrease in order to ease the logistic burdens of transporting these assets.

The Power Generation and Environmental Control Division of CECOM's Command Control Systems Integration Directorate has developed the Vehicle In-Line Power Generation (VILPG) concept as one solution to the Army's requirement for mobile tactical power generation. The concept integrates an electrical generator into the drive train of a tactical vehicle by locating the generator between the vehicle's engine and transmission. This concept has been successfully demonstrated in a 2½ ton tactical truck.

IN-LINE GENERATOR LAYOUT
2-1/2 TON TRUCK

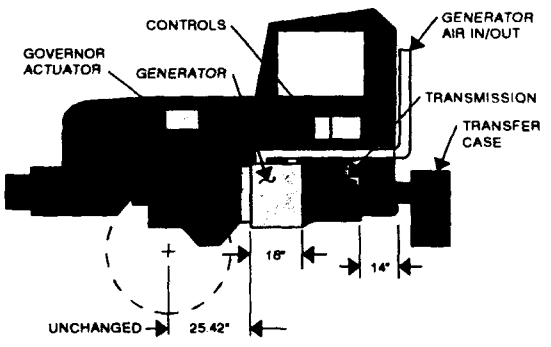

Although adopting the VILPG concept would greatly reduce the requirement for towed power units, it is not proposed as a total replacement for them. In applications for mobile systems which are required to relocate, reposition or otherwise move frequently, the capability to use the vehicle's engine to provide power can reduce the overall size, weight, and cost of the Army's electric power assets and improve operational effectiveness. In applications where the power consumers deploy for periods longer that a few hours, or where the carrier unit needs to be independent from the system being powered, towed power units provide a better solution.

This paper examines the VILPG current and future design and logistic considerations. The paper also outlines potential applications for VILPG technology.

WHY IN-LINE POWER GENERATION?

When considering ways to provide tactical power to Army units, locating a generator in the drive train of a tactical vehicle does not immediately come to mind. The actual power requirement dictates the power generation solution. Depending on the type and amount of power required, different solutions exist.

If the amount of power required by a tactical system is less than 5 kW, a belt driven generator mounted on a vehicle's engine would suffice. For power requirements higher than this, problems appear with this approach. V-belt drives are limited in the amount of shaft power they can transmit, and as the power requirement increases multiple v-belts must be used. This necessitates the use of matched v-belts, which are of the same length. At any particular operating speed higher power demands require physically larger and heavier generators which must be held securely in place by brackets mounted on the engine. The nature of tactical vehicle operations takes them into off-road situations. The accelerations experienced during off-road operation easily lead to bracket failures due to the large mass which must be supported.

Another possibility for producing power would be to use the power take-off (PTO) port provided on large vehicle transmissions. This would offer advantages such as the ability to disengage the generator when it is not required. The problem associated with this solution is the limited volume available between the frame rails of tactical vehicles.

PTOs are typically located at some fixed distance from the center line of the vehicle drive train. The maximum diameter of an electrical machine which can be coupled to the PTO will be limited due to a potential interference problem which exists between the generator and the vehicle frame rail or body. In order to meet the power requirements of the system, the axial length of the generator would have to be increased to account for the small generator diameter. The maximum power capability of a generator is proportional to its volume. This would result in a design which is hard to fabricate and which would be susceptible to failures caused by vibrational resonance.

The maintenance and logistic problems associated with these methods will be eliminated by placing the generator directly between the engine and transmission. Modifications to the drive train must be made to accommodate the increase in axial length that the In-Line generator introduces, but the end result is a piece of electrical equipment which is transparent to the operator when the vehicle is in motion and requires no maintenance to the rotating assembly.

GENERATOR DESIGN

The proposed location of the generator in a VILPG system poses design problems not normally associated with tactical power generators. Commercially available generators are not usually constructed in a way that would allow them to survive in a VILPG application. In designing an In-Line system the most important design consideration is that the introduction of the generator must not compromise the operation, reliability, availability or maintainability of the host vehicle. In the event of a VILPG failure the vehicle should still have the ability to move itself and its occupants out of harms way. This requirement is met by providing a robust mechanical design that considers the total operating envelope for the vehicle performing any of its missions.

A very limited volume is available to insert a generator into the drive train of a tactical vehicle. This constraint limits the generator's physical size. Also, the vehicle engine power and the RPM at which it is produced limits the generator's electrical power capability. This is especially true for missions which require the High Mobility Multipurpose Wheeled Vehicle (HMMWV).

The location of the generator in a VILPG places demands on the generator case which are not seen in conventional applications. The movement and shock loading of the drivetrain while the host vehicle is operating causes large torsional and bending loads to be exerted upon the generator case. The generator case must be capable of handling these loads. Interfacing with the SAE bellhousing on large vehicles and the GM bellhousing on HMMWVs allows the designer to maximize the generator diameter. For instance, an SAE #2 bellhousing allows for a generator diameter of 20 inches. This dimension figures prominently in providing structural stiffness of the generator case, enabling the case to withstand the loads placed upon it.

The shaft of the VILPG must be able to transmit all of the engine power to the transmission when the vehicle is being used in its normal transportation role. In most instances, to produce 20 kW of electric power a standard generator would require no more than 30 HP of input shaft power. The Stewart and Stevenson Medium Tactical Vehicle, an VILPG candidate, can be equipped with an engine rated up to 295 HP. This dictates an obviously larger generator shaft than would be required in a standard configuration.

The In-Line generator must maintain mechanical integrity over the full engine operating speed range. This implies that the generator must be capable of sustained rotor speeds up to 300% above the normal governed speed for electric power generation. Typically 1200 or 1800 r/min is required for 60 Hz utility power applications. The normal design criteria requires generators to survive spinning at up to 125% of their rated operational speed. The higher rotating speed can be compensated for in the construction of the rotor with the addition of reinforcing rings which help hold the rotor assembly together.

The location of the VILPG, the underside of a tactical vehicle, also requires some special design consideration. A 30 inch fording requirement dictates the generator will be partially submerged at times, and thus must be water tight or must survive submersion without harmful effect on operability. The generator also has to be sealed against ingesting mud or dust kicked up by the vehicle's tires when moving.

VILGP SYSTEM INTEGRATION

Integrating a generator into the driveline of a vehicle requires modification of that driveline as well as the addition of other components. As in most integration efforts, the size of the components dictate the difficulty in packaging the end product. For the Vehicle In-Line Power Generator, the components list includes the generator, a governor and governor actuator, and a voltage regulator.

The required drivetrain modifications to the vehicle include altering the front and rear drive shafts to account for the rearward relocation of the vehicle transmission and transfer case. Modifications to the vehicle exhaust system and transmission linkages may also be required.

During the course of demonstrating the VILPG 2 ½ ton truck several questions concerning the concept have arisen. The concerns center on the effect of the generator on the vehicle, on the vehicle engine, and on a broader basis - the mission of the truck.

Engine life can be estimated based on the total amount of fuel the engine will consume before a failure is expected. The higher the hourly fuel consumption rate, the shorter the engine life. The rationale is that if the engine is working hard it will consume more fuel in a given amount of time and wear out faster. The fuel consumption rate of the concept demonstration vehicle is approximately 25% of the amount the engine can consume, so no significant decrease in engine life can be expected.

Providing there is enough room in the underside of a tactical vehicle to accommodate a VILPG no adverse conditions should arise from the installation. As discussed earlier, a design constraint for an In-line generator involves the mechanical strength of the generator case and shaft. Given that this constraint is met, the failure rate of the electrical machine portion of Military Standard family generators and the new Tactical Quiet Generators is approximately 30000 hours mean time between failure. If a failure were to occur in the controls portion of VILPG the host vehicle would still have the ability to operate normally.

BENEFITS

A vehicle equipped with a VILPG offers several benefits to the Army. These include: 1. Increased mobility - limited only by the vehicle's capabilities. 2. Improved deployability - up to 90% net weight reduction and 100% towed volume elimination compared to trailer mounted power sources. 3. Significantly faster time to operation - engine is already warmed and running when the operating locale is reached. 4. Lower logistics costs - truck maintenance equates to generator set maintenance for the most part. The actual amount saved would depend on the application.

Units equipped with VILPGs will have increased mobility because of a decrease in the overall size and weight of the system. For mission-critical operations which require redundant power sources the Vehicle In-Line Generator could function as either the primary or secondary power source. This would not only eliminate the need for a second towed power unit, but also the need for another truck to tow that power source.

The 20 kW VILPG installed in the concept demonstration vehicle added 520 pounds to the weight of that vehicle without increasing the volume of the truck. A MIL-STD towed power unit of similar rating weighs 5000 pounds and occupies 650 cubic feet. The reduction in size and weight is a very substantial benefit when overseas deployments are considered. Displacing/replacing towed power units reduces the amount of equipment which has to be moved by either air, ship, rail or truck.

A unit equipped with the Vehicle In-Line Power Generator will be able to reduce the time required for mission ready operation once it has arrived at its destination. The VILPG equipped vehicle arrives at it destination with its engine running and sufficiently warm to accept load. Preparing for operation only requires engagement of the governor, connecting the cabling to the load, closing the contactor, and operating at will. In contrast, a towed power unit will arrive cold and will require a start cycle and a finite amount of time to sufficiently warm so that it can accept load. A cold ambient condition exacerbates this situation.

Logistics costs can be expected to decrease as the number of tactical generators decrease. There will simply be less equipment that requires maintenance. The additional maintenance to be performed on vehicles equipped with a VILPG will be limited to more frequent oil changes for the vehicle engines. Other than the regular maintenance on the vehicle engine and batteries, the In-Line generator should be extremely low maintenance. This should actually improve the utilization of vehicle maintenance items as most fluids, for example, are changed on an elapsed time basis rather than solely on operating life considerations.

CONCLUSIONS

The introduction of new equipment into the Army is difficult task. The amount of testing required to verify the function and reliability of new equipment is formidable and expensive. In order to defray these costs all of the military services are looking toward duel use technologies, items or systems which can be utilized by both the military and civilian sector. There are numerous civilian applications which require electrical power at remote locations, from construction to oil exploration. The VILPG concept would satisfy these applications quite well.

The mission envisioned for a VILPG equipped vehicle is one in which the vehicle carries a dedicated load. C^4I, military intelligence or contact maintenance functions operating out of vehicle mounted shelters are good examples of operations which require high mobility and readily available electric power. The VILPG provides more tactical capabilities while reducing the costs associated with these capabilities. It is a concept which, when viewed with the entire Army in mind, offers a better overall system solution. Making the most of organizational assets in times of shrinking budgets makes sense.

Nickel-Metal Hydride Cell Development

Bill Hawkins
Advanced Systems Operation
Eagle-Picher Industries, Inc., Joplin, MO

Eagle-Picher Industries has been involved in development of Hydride systems for approximately five years. Both silver and nickel-hydride cells deliver higher energy density, and greater cycle life than their nickel-cadmium or silver-zinc counterparts, while being environmentally benign. Cells, modules and batteries ranging from nominal four to 255 AH capacity have been built and tested. These serve applications as diverse as vehicle propulsion to remote location power back-up to satellite power. This paper will stress hardware built and tested to date.

Metal Hydride Alloys

Eagle-Picher is currently employing an AB5 metal hydride alloy, co-designed with Rhone-Poulenc, the alloy supplier. Electrode fabrication is accomplished by the pressed-powder process. Sintering assist materials are included in the powder blend, as are conductive binders. The alloy of choice is conservatively designed, but tailored to perform well across a wide temperature range, while displaying a long useful life. Typical absorption-desorption curves are shown by Fig. 1.

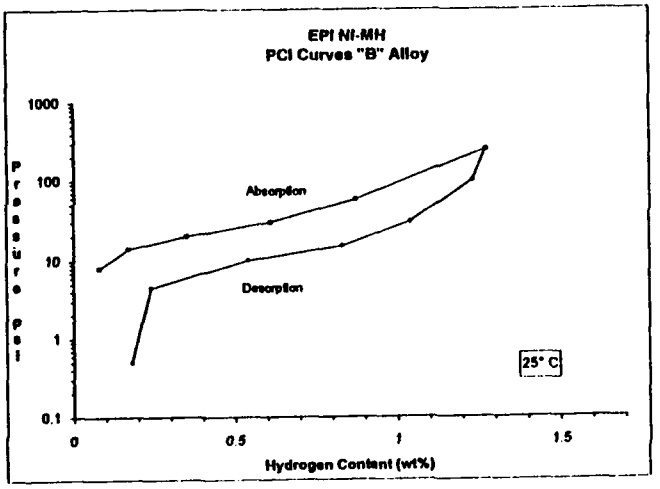

Fig. 1

Nickel-Metal Hydride Cell/Battery Design and Production

Positive electrodes used in the nickel system are the plaque-type, and may be produced by either dry-sinter or slurry type, activated by alcohol or aqueous electrochemical impregnation technique. The separator is typically the conventional non-woven absorbent. Nickel and silver-hydride cells and batteries produced so far have been of the prismatic configuration. (Fig. 2) The largest single number of cells of one type include those supplied to Michigan State

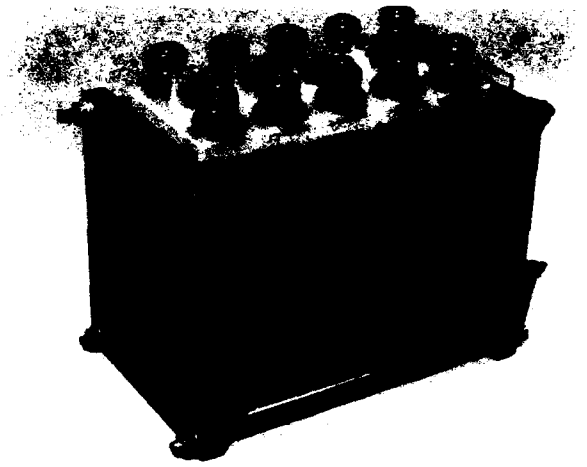

Fig. 2

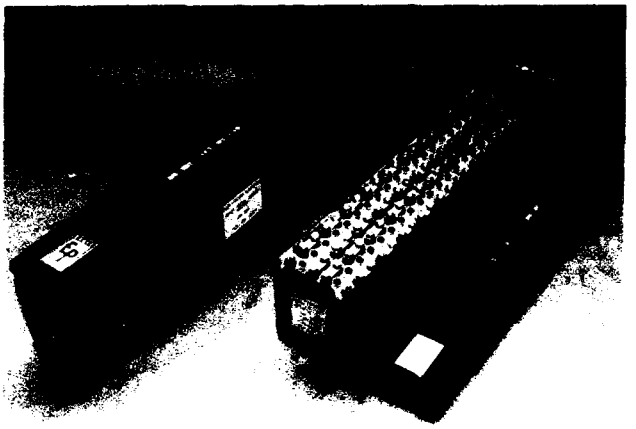

Fig. 3

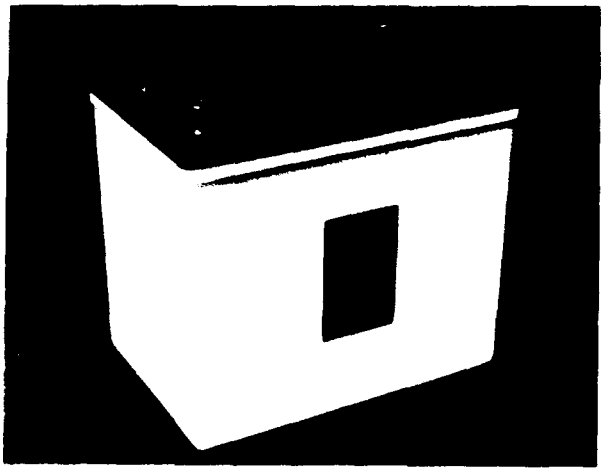

Fig. 4

University. These cells were incorporated into modules for vehicular power (hybrid electric) for the 1993 Ford Hybrid Electric Vehicle Challenge held in Dearborn, MI, on June 1-5. Another configuration which has been constructed for vehicle applications is shown in Fig. 4 These are 6VDC 265 AH modules which were assembled into existing nickel-iron packaging. Eagle-Picher has a long history of supplying batteries for aerospace applications. Nickel-metal hydride cells and batteries are being built currently for this usage. One such battery is shown in Fig.5. Cells of this design have ranged from 4-100 AH These cells are effectively sealed, starved-electrolyte cells in stainless steel cases, using either ceramic or Ziegler compression seals. They feature high-pressure repetitively-operating relief valves as a precaution.

The following table (Table 1) summarizes nickel-metal hydride production to date.

NICKEL HYDRIDE	
43 EA	1.25 AH
52 EA	4 AH
262 EA	10 AH
321 EA	40 AH
12 EA	100 AH
6 EA	180 AH
3 EA (6 MODULES)	255 AH
SILVER HYDRIDE	
120 EA	15 AH

Table 1

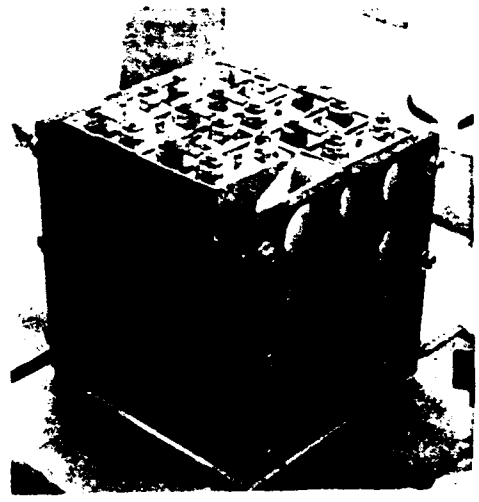

Fig. 5

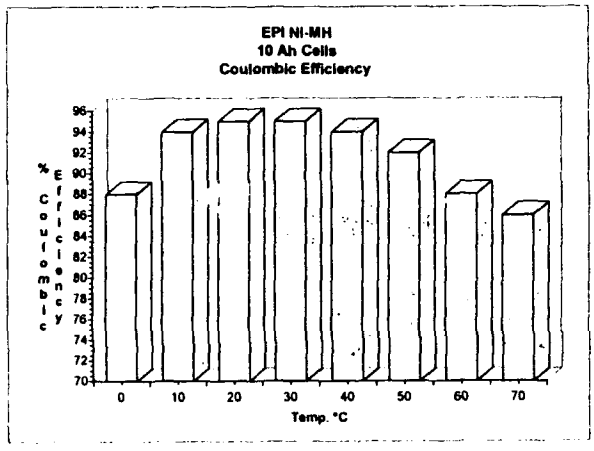

Fig.6

Nickel-Metal Hydride Activation and Testing

The activation of nickel-metal hydride cells employs specific conditioning cycles. Full hydride formation is established as the point at which coulombic efficiency exceeds 95%. Fig. 6 illustrates the capacity spread achieved on 310 RMH-40 cells following conditiong cycles. These 310 cells are from two activation lots. Good cell performance is reproducible.

Nickel-metal hydride cells exhibit excellent performance during rigorous testing. Cell specific-energy (without optimized packaging) with the current hydride alloy is 60 Wh/kg. Using an improved alloy with other advanced cell components will increase cell specific-energy to more than 80 Wh/kg.

Coulombic efficiency testing provides a good measurement of electrochemical system reversibility. Coulombic effiency is defined as the ratio of amp-hours for cell charge (charge in) versus amp-hours of discharge returned (charge out). It also provides a good measure of electrode efficiency by establishing the level of overcharge required for optimal cell operation. As shown in table 2, the nickel-metal hydride system demonstrates equal or superior results to comparable alkaline battery technology such as nickel-cadmium and nickel-hydrogen. A 10 AH cell test group produced an average efficiency of 94% over the temperature tange of 0°C to 20°C. The coulombic efficiency was measured under two different charge conditions for comparison of the rate dependence of the efficiency. All discharges were performed at the C/2 rate (5.0 amp). A coulombic efficiency of 86% was measured at 72°C as an additional data point to determine temperature dependence. This data is presented graphically in fig. 6.

Charge and discharge voltage versus time for RMH-10 and RMH-40 Ah cells for testing from -10°C to 50°C is shown in fig. 7,8,9, and 10. The cell performance is typical for nickel alkaline batteries. Charge voltage is slightly elevated at the colder temperature due to the increased impedance of the electrolyte and separator. Hydride electrode efficiency is also slightly reduced at the lower temperatures. The discharge voltage is slightly depressed for the same reasons. Cell discharge capacity is essentially unaffected over this temperature range.

As described earlier, Eagle-Picher has constructed several nickel-metal hydride 6 VDC batteries, packaged as nickel-iron modules.

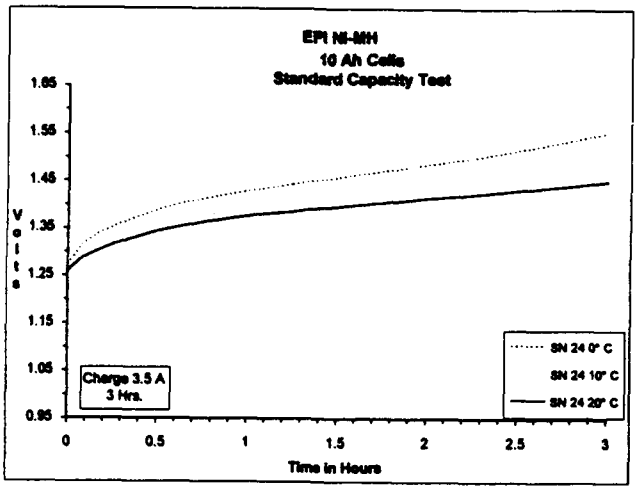

Fig. 7

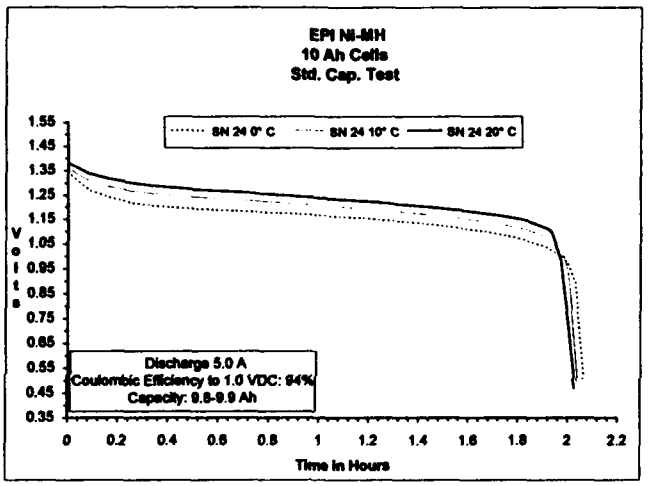

Fig. 8

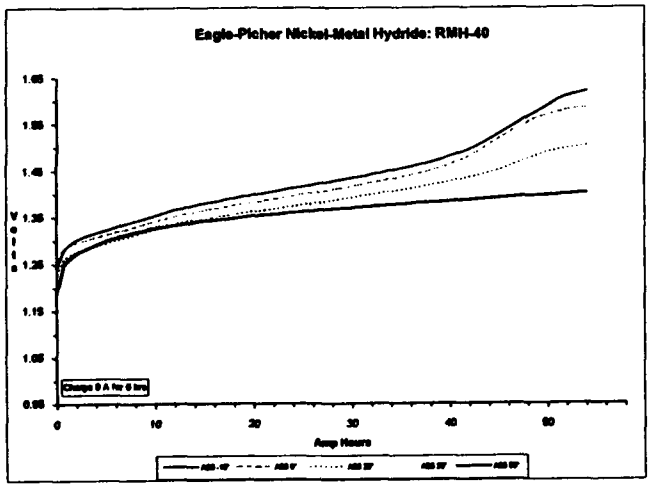

Fig. 9

Charge retention data for Eagle-Picher nickel-metal hydride cells is illustrated in fig. 11. The cell was operated at 10°C with both discharges performed at the C/2 rate. The results show that 92% of the original cell capacity was returned after a 72 hour open circuit stand.

The rate capability of the nickel-metal hydride cells is excellent with good voltage response and high coulombic efficiency. Table 3 summarized typical capacity results for RMH-10 AH cells discharged at various rates ranging from C/2 to 2.5 C. This testing was done at 20°C on a full 20 cell nickel-metal hydride battery. The data shows the average coulombic efficiency as a function of discharge rate under constant current charging conditions. Efficiency varies from 97% at the C/2 rate to 88% at the 2.5 C rate. Cell discharge capacity is nearly independent of discharge rate over this range.

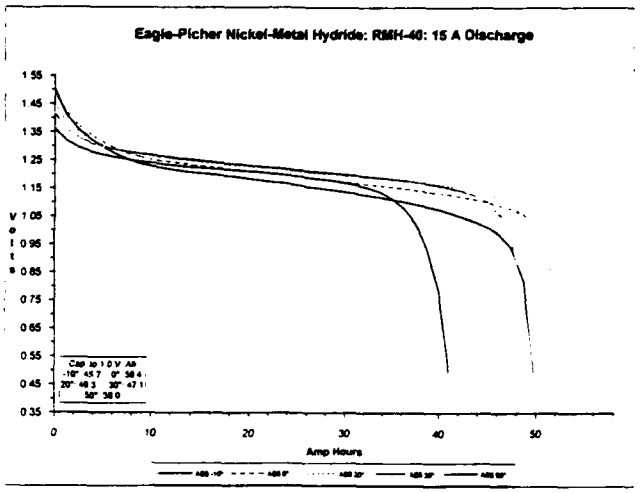

Fig. 10

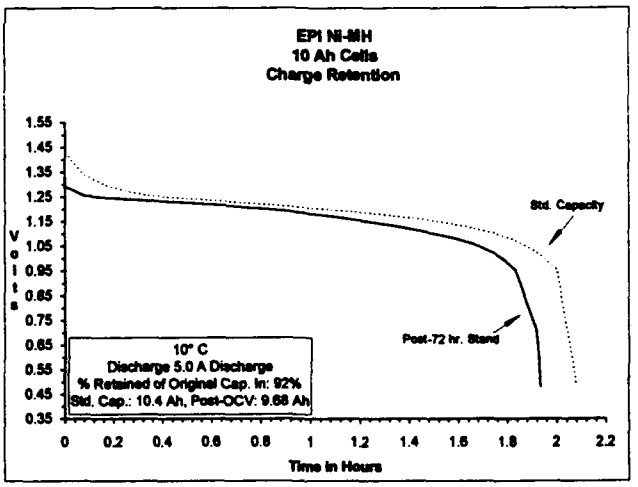

Fig. 11

Test Description (Dischg. 5.0A to 0.5 VDC)	Capacity In (Ah)	Average Coulombic Efficiency
10°C: Chg. 3.5A/3.2 Hrs.	11.2	94%
20°C: Chg. 3.5A/3.2 Hrs.	11.2	95%
0°C: Chg. 5.1A/ 2 Hrs.	10.2	88%
10°C: Chg. 5.1A/ 2 Hrs.	10.2	97%
20°C: Chg. 5.1A/ 2 Hrs.	10.2	96%
SUMMARY OF EFFICIENCY PERFORMANCE RMH-10 CELLS		

Table 2

Test Description	Capacity In (Ah)	Average Coulombic Efficiency
20°C: Chg. 3.5A to 29.14 VDC, Dischg. 5.0A to 20.0 VDC	10.51	96.7%
20°C: Chg. 3.5A to 29.14 VDC, Dischg. 20.0A to 20.0 VDC	10.50	91.9%
20°C: Chg. 3.5A to 29.27 VDC, Dischg. 25.0A to 20.0 VDC	10.2	88%
SUMMARY OF BATTERY PERFORMANCE		

Table 3

Life Testing of Nickel-Metal Hydride Cells

A group of ten selected cells of 10 AH capacity was cycled on LEO orbits at 45% depth. Testing was terminated at 4000 cycles, with cells maintaining 90% of original capacity. Modeling routine have fixed the cycle life probability of this cell design at 16,000 cycles, based upon observed performance data.

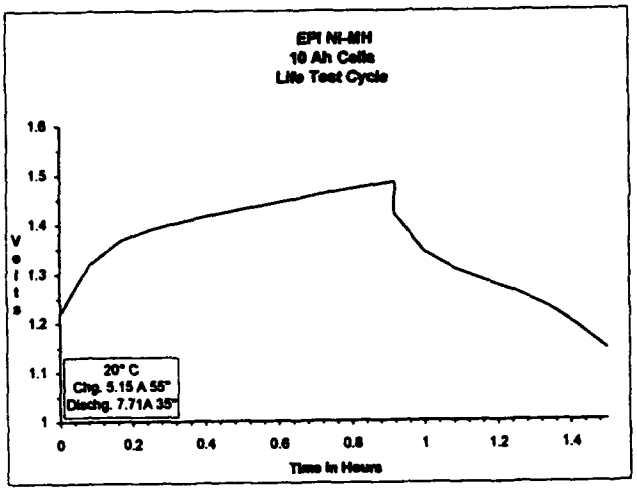

Fig. 12

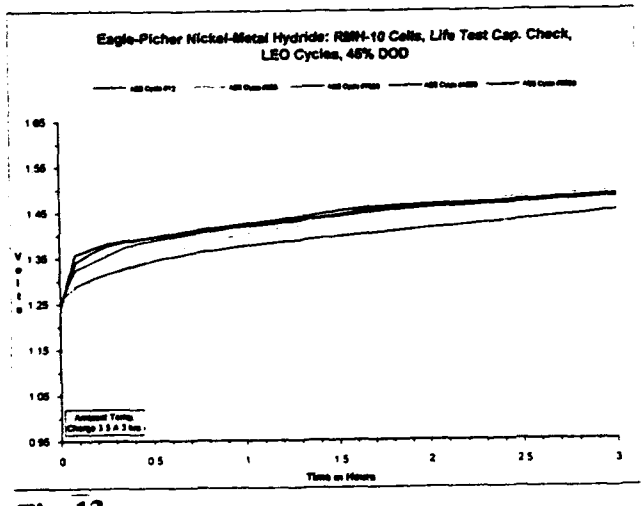

Fig. 13

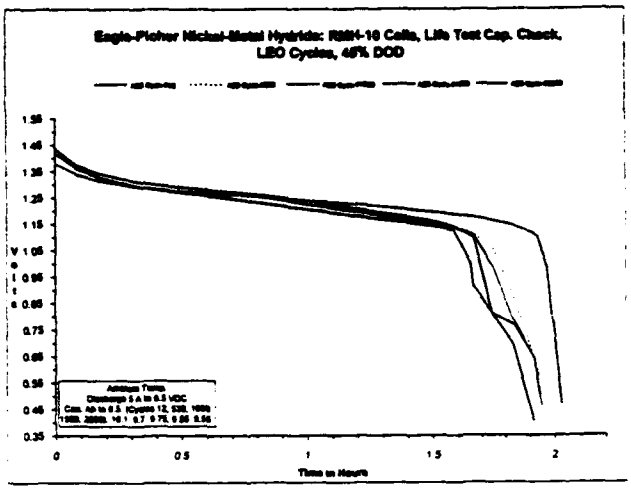

Fig. 14

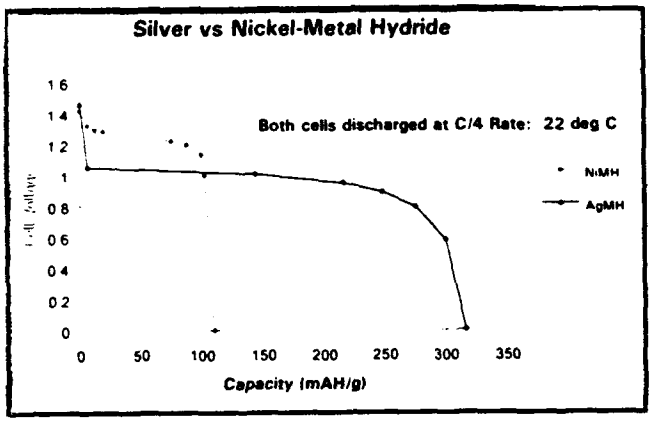

Fig. 15

Silver-Metal Hydride Cell/Battery Design and Testing

The Eagle-Picher silver-metal hydride cells are based upon existing silver-zinc technology. The silver electrode, separator and activation techniques are the same. Replacing the zinc electrode with the metal hydride electrode will increase both the calendar life and cycle life of the silver-metal hydride cells versus silver-zinc cells. Development of the silver-metal hydride system is currently lagging behind the nickel system, but testing of early cells looks promising. Cells were built into the same packaging as nickel-metal hydride cells. This allows for direct comparison of specific-energy. Current 10 AH nickel-metal hydride cells built as silver-metal hydride yield approximately 23 AH. This corresponds to a conservative specific-energy of over 100 Wh/kg. Life testing of these cells is pending.

Fig.15 shows a comparison of capacity versus cell voltage for nickel-metal hydride and silver-metal hydride cells. The inherent higher energy density of the silver system is evident.

References

D. Coates, *Nickel-Metal Hydride and Silver-Metal Hydride Batteries for Aerospace Applications*, 27th IECEC San Diego, CA 1992.

RECHARGEABLE OVONIC NICKEL METAL HYDRIDE BATTERIES FOR CONSUMER , ELECTRIC VEHICLE AND MILITARY APPLICATIONS

S.VENKATESAN, M.A.FETCENKO, D.A.CORRIGAN, P.R.GIFFORD, S.K.DHAR AND S.R.OVSHINSKY

OVONIC BATTERY COMPANY ,
1707 Northwood Drive,
TROY, MICHIGAN 48084

ABSTRACT

Ovonic Nickel Metal Hydride Batteries (Ni-MH) for consumer and EV applications have specific energies of 80 Wh/Kg and energy densities greater than 200 Wh/l. The development of Ovonic EV batteries has been accelerated by the award of USABC contract in May 1992. Presently Ovonic Ni-MH batteries are being produced in various sizes ranging from 1500 mAH AA size cells to 250 AH EV batteries. In this paper some of the latest performance data is discussed and future trends projected. The USABC mid term goals have been met in prototype batteries and in the laboratory. Cycle life test is ongoing.

Ovonic Cells have been subjected to cycling (both charging and discharging) at various temperatures from -20°C to +70°C . Between 80 and 85% of the ambient temperature capacity has been realized at -20°C. The capacity of the cell decreases by about 50% at 70°C. However, capacity returns to rated values at room temperatures. Ovonic cells have achieved low self discharge rates, as low as 10% decrease in one month. This has been achieved by improvement of the metal hydride alloys, positive electrodes and separators.

Due to a high specific power over 200 W/Kg, Ovonic EV cells also have delivered a high energy density under simulated driving profiles like the SFUDS 18-53 KWH packs have been built and tested in electric vehicles where vehicle performance and increased range projections were verified.

OBC Ni-MH modules and individual cells have been subjected to various abuse tests with excellent results. These modules are expected to find uses in military and space based applications. In 1992 OBC was awarded a Phase I SBIR contract to work on the Ni/MH batteries for small satellite applications. Recently contract negotiations on Phase II of this work have begun . Further work is continuing to increase the near-term energy density of the Ovonic Cells from 80 to 120 Wh/Kg and the long term energy density on to 150 Wh/Kg.

Introduction:

Historically, there has been a desire to standardize the power sources in the armed forces so that simplified inventory control and quick replacement is assured. Practically, this has proved difficult to accomplish due to the variety of power requirements different equipment requires. If one battery system could become universal it would be extremely beneficial. The performance characteristics of the Ovonic Ni MH rechargeable battery system promises such a possibility and has provoked renewed interest in standardizing power sources. In this paper Ovonic nickel Metal hydride battery's performance attributes are reviewed and future trends indicated.

The Ovonic nickel metal hydride battery system has been in development since 1979. Although the concept of combining a metal hydride electrode with a conventional nickel electrode to produce a viable rechargeable battery has been studied for over 30 years, identifying an acceptable metal hydride material was not easy. For a metal hydride to be effective as a negative electrode the following criteria have to be met.

*. the metal hydride material should have good hydrogen storage properties: the material should preferably have greater than 1 wt.%. hydrogen storage capacity

*. the thermodynamic properties of the metal hydride material should be suitable for reversible absorption/desorption: the

ΔH value should be about 8 - 10 Kcals/mole

*. the metal hydride material should have high oxidation resistance in alkaline electrolytes so that it will be active even in the oxidizing atmosphere in the cell

*. the metal hydride material should have high corrosion resistance but should not become totally passive

*. the metal hydride material should have sufficient discharge kinetics: i.e, the diffusion coefficient of hydrogen diffusion from the bulk to the surface should be high and the material should possess sufficient catalytic activity.

*. the metal hydride material should also be capable of forming hydrides from molecular hydrogen. This implies that it should have good catalytic activity for the dissociation of hydrogen molecule so that it can form atomic hydrogen which can then be absorbed to form hydrides easily: This property is needed to assure good overdischarge protection.

*. the metal hydride material should be easily manufacturable: it should be easily meltable, size reducible and electrode formable in a relatively simple process.

*. the metal hydride material should not have components that are expensive or the processing should not be complicated such that the production costs go up. Also the scrap and trim recycle capability should exist to increase the material utilization efficiency.

Ovonic Ni-MH technology consists of a family of proprietary alloys developed specifically for electrochemical charging/discharging, which are combined with the conventional nickel /nickel hydroxide positive electrodes with appropriate separators and aqueous potassium hydroxide electrolyte. The heart of the Ovonic technology lies in the proprietary alloys developed for the purpose of reversible electrochemical absorption and desorption of hydrogen. The principal components of Ovonic Metal hydride electrodes and their functions are indicated below.

1. Vanadium:
   - assures good hydrogen storage (VH_2)
   - soluble oxide, porosity to surface (VO_x)
   - high Δ H

2. Zirconium:
   - good hydrogen storage (ZrH_2)
   - high Δ H
   - excellent metallurgy
   - passive oxide (ZrO_2)

3. Titanium:
   - good hydrogen storage (TiH_2)
   - passive oxide (TiO_2)
   - high Δ H

4. Nickel :
   - no hydrogen storage
   - destabilizes ΔH
   - resistant to oxidation
   - catalyst for hydrogen oxydation

5. Chromium:
   - vanadium corrosion inhibitor

In addition, small amounts of other elements are added to alter one or more properties such as high temperature/low temperature performance, self discharge, rate capability etc. The uniqueness of these alloys rests in their disordered microstructures and the presence of multiple phases. These different phases exist very close to each other. Some of these phases act as hydrogen storage media and some act as hydrogen oxidation catalysts, their close proximity assisting each other in the final performance (1- 4). The idea of material modification originally proposed and patented by ECD/OBC (1) is being successfully applied to other metal hydride systems by others in the field.

During charging at the negative electrode atomic hydrogen discharged at the surface is absorbed by the negative electrode, forming the hydride. At the same time the positive nickel electrode gets converted from nickel hydroxide to nickel oxyhydroxide. However beyond a certain charge level oxygen starts evolving at the positive electrode. Since the OBC Ni-MH system has been developed as a maintenance free system, this oxygen evolved should be effectively removed to avoid undue pressure development. This is performed by the recombination of oxygen at the negative hydride electrode. Thus, there is a built-in overcharge protection reaction. Similarly during overdischarge the positive electrode potentials are depressed so far negative that they start evolving hydrogen. This hydrogen is also effectively recombined at the negative electrode.

This is a unique feature that does not exist in nickel cadmium or other nickel based systems. In these systems a small amount of the negative active material (called the anti polar mass) is deliberately added to the positive electrode to take care of a limited amount of overdischarge. The reactions involved in an Ovonic Ni/MH battery is shown in Fig.1.

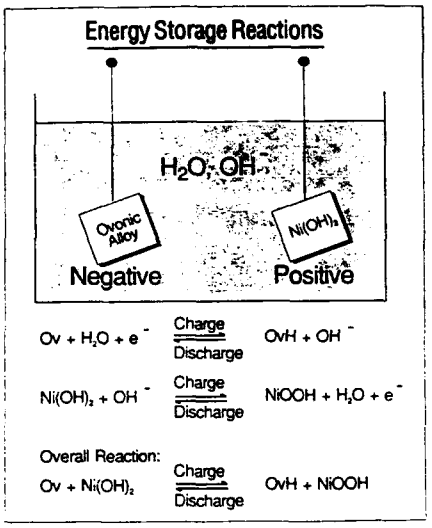

Figure 1

The Ovonic negative electrodes materials are made today in 350 lb lots. In view of their high hardness (greater than Rockwell C 60) these ingots are size reduced by a proprietary hydriding/dehydriding technique followed by a traditional mechanical grinding operation. The powders are pressure compacted in a roll mill onto a nickel screen and sintered in a protected atmosphere. Present generation of Ovonic negative materials have a specific capacity of about 400 mAh/g. In order to realize the full benefit of the negative electrodes it is necessary to combine them with highly efficient and highly loaded positive electrodes. OBC has optimized the conventional chemically impregnated positive electrode. More recently it has also developed a pasted positive electrode technology which has given energy density advantages and cost effectiveness. The pasted positive electrode technology involves pasting a slurry of nickel hydroxide powder with additives and binder(s) onto to a nickel foam /fiber matte, drying and calendering . It is less labor intensive, more reproducible and is light weight.

The performance characteristics of the Ovonic Cells are summarized below.

1. Specific energy : 80 Wh/Kg compared to 30 to 45 Wh/Kg for the best lead acid and nickel cadmium cells.

2. Energy density: >200 Wh/L compared to 90 to 130 Wh/L for the others

3. Power: over 200 W/Kg at 50% Depth of discharge Fig.(2,3,4,5,6)

4. Environmentally friendly: Recyclable, can be disposed of in landfills as non hazardous waste by EPA standards (6,7)

5. Cycle life: over 1000 cycles at 100 % depth of discharge (Fig.3, 4)

6. No maintenance: Totally sealed recombinant technology

7. Operating Temperature: - 20 °C to + 70°C

8. Fast charge: can be fast charged in 15 minutes to 60% charge levels.

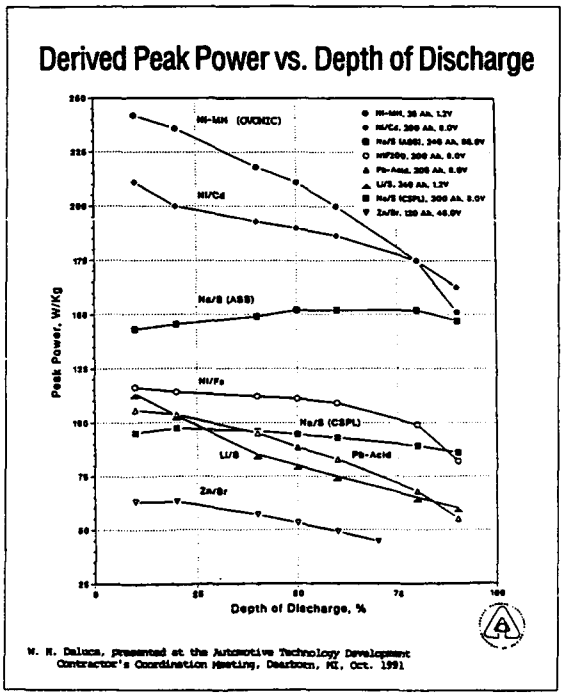

Figure 2

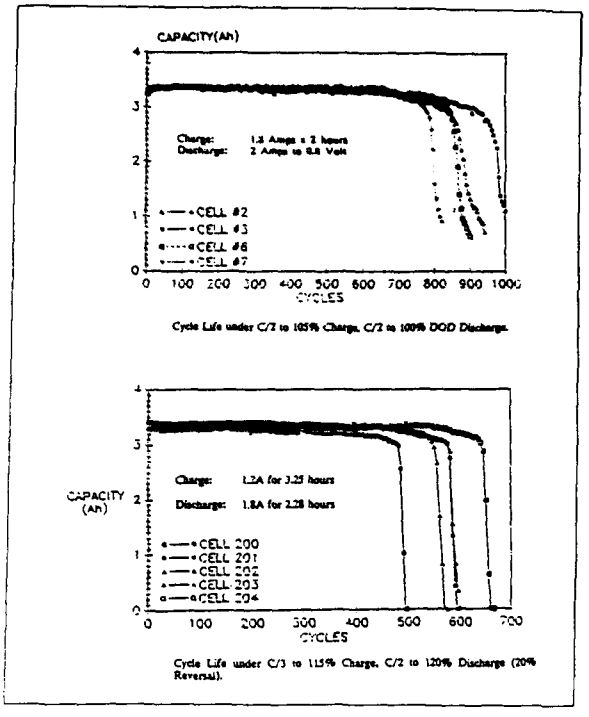

Figure 3

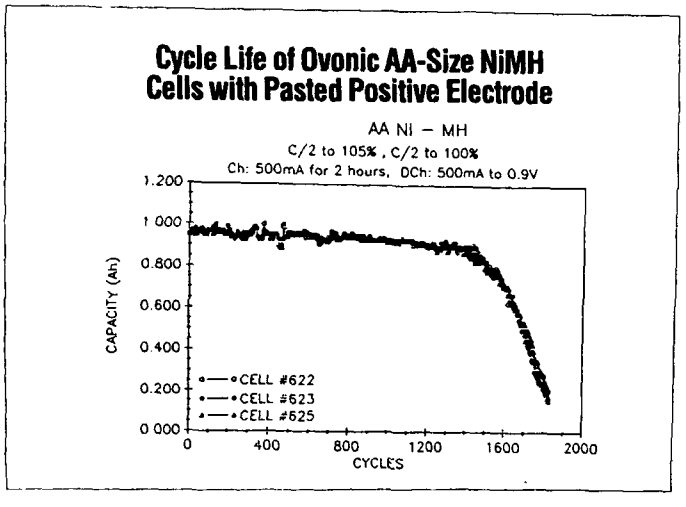

Figure 4

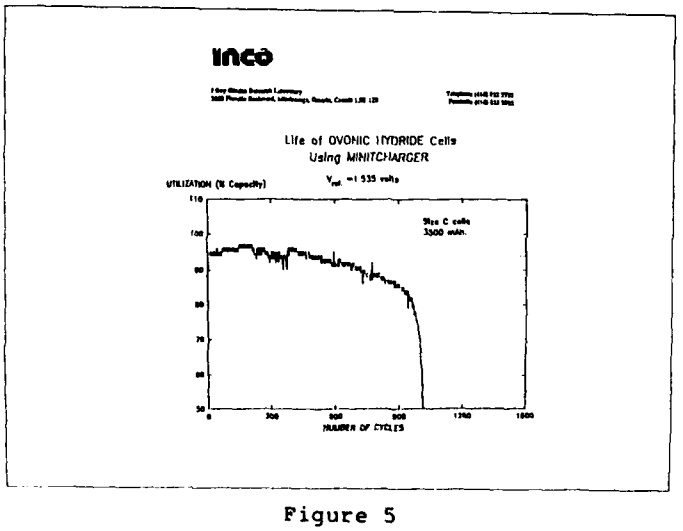

Figure 5

After successfully developing the technology for consumer batteries Ovonic Battery Company has licensed various manufacturers throughout the world. Development of the nickel metal hydride system for electric vehicle applications was started about 4 years ago. Today, prismatic Ovonic cells are produced from 25 Ah to 250 Ah without any tradeoffs in performance. In addition to USABC, this technology has been licensed to Hyundai Motor Company in Korea, Gold Peak Industries in Hong Kong, and Sovlux in Russia.

Temperature performance of the Ni-MH batteries is excellent, capable of being charged and discharged from -20°C to above 70°C. In military applications this is a vital requirement as the military operations could take place in any part of the globe and the equipment should be operational under all conditions. The capacity realized decreases slightly as the temperature is increased and at 70°C about 50 % of the capacity is realized. However once the cells are returned to room temperature full capacity is realized. (Fig. 7). It is well known in the nickel electrode technology that at higher temperatures the nickel positive electrode charging efficiency decreases. If the same fixed amount of charge is being put in , the decrease of charge efficiency will result in lower charge acceptance and hence the capacity output will also be lower. Similarly at -20° C between 80 to 85 % of the ambient temperature capacity is realized. The decrease in the cell capacity at lower temperatures can be explained by the increased polarization at lower temperatures. As the cell reactions indicate, one of the products of reaction is water . If the water is produced inside the pores locally it will reduce the concentration of electrolyte causing the electrolyte to freeze. This will result in polarization. More work is being performed to decrease this polarization.

The excellent power density of Ovonic EV cells has been verified by Argonne National Labs. data. (5). The cycle life of the individual cells ,the modules and the pack have all been excellent.

The self discharge property of Ovonic cells has been considerably improved over the years. This has been achieved by a host of changes introduced in the materials and the technology. Fig. 8 shows that the self discharge improvement has surpassed even the best nickel cadmium cells. As little as 10 % decrease in the capacity of the cell within a month is achievable.

The Ovonic Metal Hydride technology has no limitation in size or capacity. Cells ranging from button cells to large prismatic cells have been built and tested. Similarly electric vehicle prototype modules have been built and tested for cycle life under SFUDS mode. By connecting several of the modules together, a pack is formed. Such packs have been assembled and fitted in vehicles and tested. Figs. 9 and 10 show some of these vehicles. In addition these cells have been developed for NASA for use in small satellites under an SBIR contract award. Phase II of the contract has just been awarded. Fig. 11 shows a typical performance profile for a 6.0 AH prismatic cell. The equivalent Ni/Cd delivered 2.5 Ah.

Ovonic nickel metal hydride cells in lab prototype stage have achieved over 86 Wh/Kg energy density and with improvements in the positive active materials and the negative electrode materials it is expected to increase the energy density will be increased near term to 100 WH/Kg and eventually 150 Wh/Kg in a few years. This increased energy density will result in smaller packs to carry out the same or more functions than

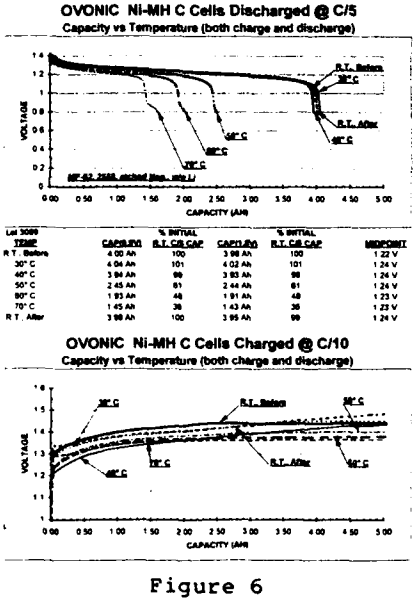

Figure 6

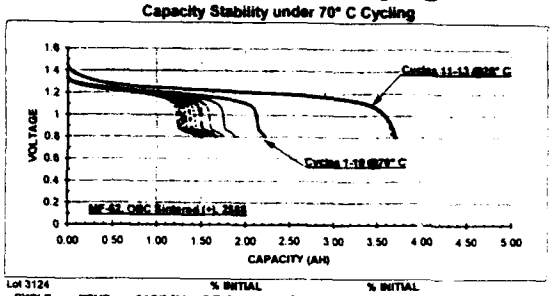

Lot 3124 CYCLE	TEMP	CAP1 (Ah)	% INITIAL R.T. C/5 CAP	CAP1 (Ah)	% INITIAL R.T. C/5 CAP	MIDPOINT
0	20° C	3.90 Ah	100	3.90 Ah	100	1.22 V
1	70° C	2.13 Ah	55	2.12 Ah	54	1.20 V
2	"	1.76 Ah	45	1.74 Ah	45	1.21 V
3	"	1.60 Ah	41	1.59 Ah	41	1.21 V
4	"	1.50 Ah	38	1.49 Ah	38	1.21 V
5	"	1.44 Ah	37	1.42 Ah	36	1.21 V
6	"	1.38 Ah	35	1.37 Ah	35	1.21 V
7	"	1.33 Ah	34	1.31 Ah	34	1.22 V
8	"	1.29 Ah	33	1.28 Ah	33	1.22 V
9	"	1.27 Ah	33	1.25 Ah	32	1.22 V
10	"	1.24 Ah	32	1.23 Ah	32	1.22 V
11	20° C	3.64 Ah	93	3.59 Ah	92	1.22 V
12	"	3.66 Ah	94	3.59 Ah	92	1.22 V
13	"	3.67 Ah	94	3.59 Ah	92	1.22 V

Figure 7

presently possible with a battery pack that is not any bigger than present ones. For example in desert combat conditions with the Ovonic high energy density batteries it is now possible to carry small power packs to power personal air cooling systems or in Arctic conditions personal heating systems.

Summary: Ovonic Nickel Metal Hydride batteries for consumer, electric vehicle and military applications have been produced successfully without sacrificing any of the performance . They have been subjected to extensive in-house testing and by all the licensees of Ovonic Battery Company as well as outside testing by agencies such as the Argonne National Laboratory. Presently electric vehicle power packs are being successfully demonstrated in several EVs.

References:
1. S.R.Ovshinsky: J. Non Crystalline Solids 32, 17 (1979)
2. K.Sapru, B.Reichman, A.Reger, S.R.Ovshinsky, U.S.Patent 4623 597 (1986)
3. S.R.Ovshinsky, S.Venkatesan, M.Fetcenko,S.Dhar : Proceedings of the 24th ISATA International Symposium on Automotive Technology and Automation (Automotive Automation, Croyden, England, 1991)P.29
4.M.A.Fetcenko, S.Venkatesan, and S.R.Ovshinsky: 180th meeting of the Electrochemical Society, Phoenix, Arizona, October 1991
5.W.H.Deluca, Paper presented at the 1991 Annual Automotive Technology Development Contractors Coordination Meeting, Dearborn, MI, Oct.24, 1991
6.C.R.Knoll, S.M.Tuominen, J.Peterson, T.R.McQueary: Proceedings of Battery Waste Management Seminar, S.Wolsky, Editor (Deerfield Beach, Florida, 1990)
7. C.R.Knoll, S.M.Tuominen, R.E.Walsh, J.R.Peterson, Proceedings of the 4th International seminar on Battery Waste Management, S.Wolsky, Editor. (Deerfield Beach, Florida 1991)

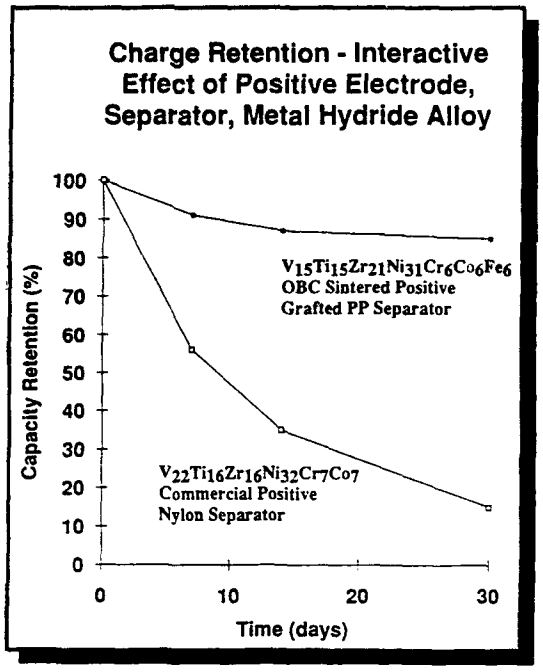

Figure 8

Figure 9

Figure 10

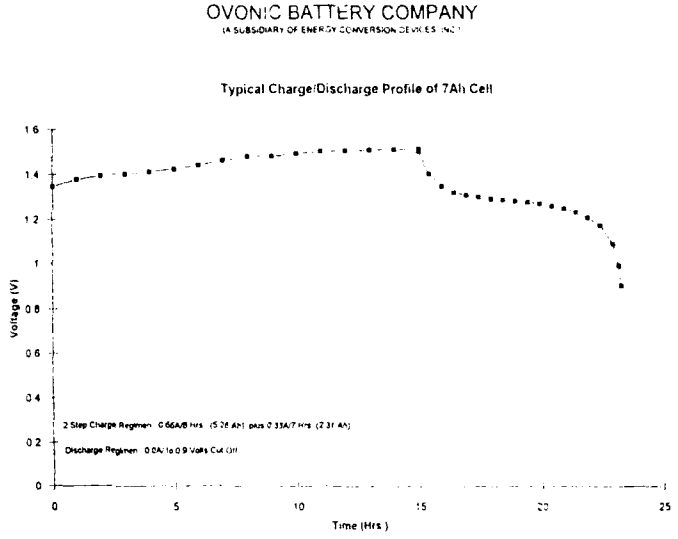

Figure 11

Electrochemical Studies on AB_5 Metal Hydrides

B. V. Ratnakumar, S. Surampudi, S. Di Stefano and G. Halpert
Jet Propulsion Laboratory, California Institute of Technology
4800, Oak Grove Dr., Pasadena, California 91109

Introduction

The ability of certain intermetallic alloys to reversibly absorb significant amounts of hydrogen at low pressures and high potentials is being exploited for several applications. In particular, the replacement of Cd in a Ni-Cd cell with the metal hydride (MH) anodes has resulted in substantial gains in the specific energy, energy density, cycle life and in the environmental compatibility. Also, the Ni-MH cells have the advantages of sustaining high discharge rates, fast charge rates and gas recombination processes during overcharge and overdischarge similar to Ni-Cd. With the voltage and the charge methods also being almost identical, the Ni-MH cells are expected to gain prominence over Ni-Cd in applications ranging from portable electronic appliances to electric vehicles.

Two classes of metal hydrides alloys based on rare earth metals (AB_5)[1,2] and titanium (AB_2)[3] are being currently developed at various laboratories. The AB_5 alloys are essentially based on $LaNi_5$ with various substituents for La as well as Ni to stabilize the alloy during charge- discharge cycling, by reducing the internal stress on hydrogen absorption and/or forming protective surface films. For example, the volume expansion is reduced by a partial substitution of Ni with Co and the interfacial properties improved with small amounts of Al or Si[1]. Sakai et al[4] studied the ternary alloys with different ternary solutes including Mn, Cr, Al, Co and Cu. The cycle life improves upon the substitution of Ni with the ternary solute in the order Mn < Ni < Cu < Cr < Al < Co. A substitution of the rare earth metal site with Ti[5], Zr[6], or other lanthanides such as Nd[1] and Ce[7] render the formation of a protective surface film and enhance the cycle life. This eventually led to the use of relatively inexpensive misch metal, Mm, a naturally occurring mixture of rare earth metals (mainly La, Ce, Pr and Nd) in place of La. The use of misch metal also improved the durability of the alloy, as evident from the long cycle life as well as the quantitative estimates of the surface layers ($La(OH)_3$ and $Mm(OH)_3$) on the cycled electrodes[2]. The alloy formulations currently in use thus contain $(Mm)(Ni\text{-}Co\text{-}Mn\text{-}Al)_5$[8,9], often with other transition metal additives, such as W and Mo.

Despite the fact that the effect of the substitution of La with Ce and Nd were studied independently, the optimum composition of the misch metal has not been reported. Nor are the effects of the La substituents on the electrochemical characteristics of the alloy understood. In this work, a systematic study has been attempted to vary the misch metal composition, especially with respect to the ratio of La and Ce, and to correlate their electrochemical behavior with their performance in alkaline rechargeable cells.

Experimental

These alloys were supplied by Rhone-Poulenc Basic Chemical Co. Out of the several alloys supplied, representative samples were chosen that would vary essentially in the misch metal composition (Table - 1), with the transition metal composition (Ni sites) being approximately similar.

The as supplied alloys were pulverized by ball milling and/or hydrogen absorption - desorption cycles. The MH powder (< 75 μ) was mixed with 20 w% Ni powder (INCO type 255, ~ 1 μ). Electrodes (1" x 1", ~250 mAh) were made from the mixture of MH and Ni powders and 5 w% Teflon, by hot-pressing onto a Ni Exmet. Electrodes for the basic electrochemical studies were prepared by filling the cylindrical cavity in the BAS disk electrodes with the mixture of electrode powders and Teflon, of equal quantities in each case. This would ensure surface area, charge density (mAh/cm^3) and porosity, thus permitting a comparison of different electrochemical parameters of the MH alloys. NiOOH electrodes from an aerospace Ni-Cd cell formed the counter electrode and a Hg/HgO served as the reference electrode. A three-electrode flooded cell with a Luggin capillary for the reference electrode was adopted for the basic electrochemical studies. A prismatic glass cell with nylon (Pellon) separator was employed for the cycle life studies. The electrolyte contained 31 w% KOH solution. Electrochemical experiments were performed with 273 EG&G Potentiostat/Galvanostat interfaced with an IBM-PC. Cycling of the cells was carried out with an in-house automatic battery cycler at constant current (4 mA/cm^2, C/5 rate) to -0.5 V vs. Hg/HgO during discharge and to charge return of 120%.

Results and Discussion

Cyclic Voltammetry : Cyclic voltammetry was carried out in the anodic range from the open circuit potential (~0.6 V vs. Hg/HgO) to 0.4 V vs. Hg/HgO on the virgin alloy, i.e.,

before incorporating any hydrogen therein. This is expected to provide a comparative assessment of the susceptibility of the alloys towards oxidation. The oxidation of the MH alloy forming a passive surface film is one of the prominent modes of failure of the MH electrodes during charge-discharge cycling[3]. Such an oxidation is also responsible for a reduced cycle life in oxygenated environments during overcharge, though the MH alloy is expected to be cathodically protected from oxidation. Also, the voltammetric studies in the above window are relevant to the practical application i.e., during deep discharge, especially when the MH becomes capacity-limiting.

The DC cyclic voltammetric curves of the MH electrodes revealed no peaks corresponding to the oxidation of the major alloying elements, e.g., La, Ce, Ni, Co and Mn. This is not surprising, since the reversible potentials of all the alloying elements (La : -2.9, Ce : -2.87 , Co : -0.73 V, Mn : -1.55 V and Ni : -0.72 V vs. Hg/HgO) are negative to the open circuit potential, such that they would exist only in the oxidized form, as evident from the AES studies on the alloy surfaces[3]. A deoxygenation of the electrolyte hasn't altered the voltammograms, implying that the peaks are related to the hydroxyl ions instead to dissolved oxygen. All the MH alloys exhibited strong peak @ 0.4 V, which may be attributed to the oxygen evolution. Also, its conjugate reduction peak was also observed in the reverse scan. This points to a possibility of using the MH electrode as the current collector for the oxygen reaction in alkaline media, which may be exploited in the fields of rechargeable metal - air cells or fuel cells.

Charge Discharge Behavior

Galvanostatic cathodic (charge) and anodic (discharge) polarization curves were obtained at 17 and 57 mA/cm^2, respectively. The electrodes were overcharged ~400 mAh/g to ensure complete hydriding of the MH alloy. The anodic polarization (discharge) curves (Fig. 1) reveal that the discharge voltages decrease in the order 6025 > 6077 or 6026 > 6039 > IBA 5. The discharge specific capacity obtained under these conditions increases in the order $LaNi_5$ < IBA 5 < 6039 < 6026 < 6025 (Fig. 7). This may be a result of incomplete charging of some of the alloys due to their high (> 1 atm) equilibrium pressure.

Electrochemical Isotherms

Electrochemical isotherms were generated for the MH alloys from the equilibrium electrode potentials at various concentrations of hydrogen in the alloy (state of charge), after effecting absorption / desorption of known quantities of hydrogen by constant current charging and discharging, respectively. The equilibrium electrode potentials are related to the equilibrium hydrogen pressure, P_{H_2} as

E_o (vs. HgO/Hg) = $-0.9324 - 0.0291 \ln(P_{H_2})$

The electrochemical (EC) isotherms during absorption (Fig. 2)are slightly different from the gas phase isotherms, i.e., the inflection in the pressure at the end of absorption is absent, possibly due to the cell internal pressures limited by the present design. The discharge isotherms, on the other hand are much similar to the gas phase isotherms. The absorption equilibrium pressure for the MH alloy decrease in the order 5978 (300 psig) > 6039 (60) > 6077 (40) > 6026, which is the same order for the variation of the specific discharge capacity. Apparently, the equilibrium pressure reflects the chargeability of the alloy under the present conditions. The discharge isotherms reveal the ease of oxidation of the alloys. The desorption equilibrium pressure is to be higher than 10^{-3} to facilitate desorption.

DC Polarization Studies

Often, the kinetics of hydrogen absorption / desorption are slowed down by the addition of (film-forming) substituents added to stabilize the alloy. In order to determine the effects of the substitution of La with Mm (especially Ce) on the discharge / charge kinetics, DC polarization experiments were carried out on the alloys and kinetic parameters were evaluated therefrom. Micropolarization and Tafel experiments were conducted separately on the alloys under potentiodynamic conditions at scan rates of 0.02 mV/s and 0.5 mV/s, respectively. The scan rates were so chosen as to provide near- steady state conditions and yet with minimal changes in the electrode state of charge or surface conditions.

The values of polarization resistance estimated from the slopes of micropolarization curves of different MH alloys (Fig. 3) are fairly identical with a marginal decrease in the order 5978 > 6025 > IBA 5 > 6077 > 6026 > 6039. The Tafel polarization curves (Fig. 4) also seem to be identical for different MH alloys, except for slight differences. The polarization curves were obtained from the anodic segment, to avoid potential fluctuations due to the hydrogen evolved on the electrode during reduction. The curves indicate strong mass transfer effects at high currents. From the Tafel plots, the overpotentials at any c.d. increase in the order 6039 > 6026(6077) > 5978 >IBA5 > 6025. The exchange current densities from the Tafel plots are of the order 10^{-3}-10^{-2} A/cm^2 and the transfer coefficients are 0.12-0.23. The cathodic Tafel segments often show two distinct slopes (e.g., $LaNi_5$), due to the occurrence of hydrogen evolution reaction.

Cycle Life Studies

Finally, the performance of the MH alloys during charge-discharge cycling was evaluated in 250 mAh, negative limited, prismatic, laboratory test cells. Despite the fact that the sealed cells are typically made in the positive - limited mode to permit overcharge mechanism, the present cells were designed to understand the life-limiting mechanisms at the MH electrode. These cells were overcharged by 120% to ensure complete charging. Accordingly, the cycle lives under these conditions are expected to be shorter than in the sealed configuration.

The cycle life of the cells containing different MH alloys are reported in Fig. 5 . As may be expected there is a wide range in the cycle life; the shortest being for $LaNi_5$ that has poor chargeability and increases in the order 6039 < IBA 5 < 6077 < 6026 or 6025. In the course of the cycling the end of charge voltage shows a gradual increase, the voltage decreasing once again in the above order.

Effect of Misch Metal Composition

The above cycling studies may be recast as in Fig. 6, to illustrate the effect of the misch metal composition on the cycle life. As may be seen from the figure, the cycle life improves upon substituting La with Ce, and tends to level off around 30 mol % La and 50 mol % Ce. The initial capacity also seem to improve with an increase in a similar manner ratio. The kinetics of the hydriding are relatively unaffected by the substitution of La with Ce. The optimum composition for the misch metal in the MH alloy would thus contain around 30 mol % of La and 50 mol % of Ce with the remainder being Nd and Pr..

Conclusions

Various electrochemical studies carried out on the MH alloys revealed that the optimum composition for the misch metal in the AB_5 should contain 30 mol % of La and 55 mol % of Ce (Nd and Pr being teh remainder) for the misch metal to decrease the equilibrium pressure, improve the chargeability, and enhance the cycle life with no ill-effects on the kinetics. The MH alloy electrodes facilitate electrochemical reduction or evolution of oxygen which may be exploited in the fields of metal-air cells and fuel cells.

Acknowledgments

The work described here was carried out at the Jet Propulsion Laboratory, California Institute of Technology, under contract with the National Aeronautics and Space Administration. This program is sponsored by the Office of Advanced Concepts and Technology. Gratitude is extended to Dr. Bao-Min Ma of Rhone Poulenc Basic Chemical Co., for providing the MH alloys.

References

1. J. G. G. Willems, *Philips J. Res.*, 39 (Suppl. 1), 1 (1984); J. J. G. Willems and K. H. J. Buschow, *J. Less Common Metals*, 129, 13 (1987).
2. T. Sakai, K. Muta, H. Miyamura, N. Kuriyama and H. Ishikawa, *Proc. Symp. Hydrogen Storage Materials : Batteries and Electrochemistry*, ECS Proc. Vol. 92-5, p. 59 1992); T. Sakai, H. Yoshinaga, H. Miyamura and H. Ishikawa, *J. Alloys and Compounds*, 180, 37 (1992).
3. S. R. Ovshinsky, M. A. Fetcenko and J. Ross, *Science*, 260, 176 (1993); M. A. Fetcenko, S. Venkatesan and S. R. Ovshinsky, *Proc. Symp. Hydrogen Storage Materials : Batteries and Electrochemistry*, ECS Proc. Vol. 92-5, p. 141 (1992).M. A. Fetcenko, S. Venkatesan, K. C. Hong and B. Reichman, *Power Sources*, Vol. 12, p. 411 (1988).
4. T. Sakai, K. Oguru, H. Miyamura, N. Kuriyama, A. Kato and H. Ishikawa, *J. Less-Common Metals*, 161, 193 (1990).
5. T. Sakai, H. Miyamura, N. Kuriyama, A. Kato, K. Oguru and H. Ishikawa, *J. Less- Common Metals*, 159, 127 (1990).
6. T. Sakai, H. Miyamura, N. Kuriyama, A. Kato, K. Oguru and H. Ishikawa, *J. Electrochem. Soc.*, 137, 795 (1990).
7. T. Sakai, T. Hazama, H. Miyamura, N. Kuriyama, A. Kato and H. Ishikawa, *J. Less- Common Metals*, 172-174, 1175 (1991).
8. N. Furukawa et al (Sanyo Electric Co.), *Proc. IBA Meeting*, Seattle, WA, OCT. 12-13 (1990).
9. I. Matsumoto and A. Ohta (Matsushita, Japan), *Proc. IBA Meeting*, Seattle, WA, OCT. 12-13 (1990).

Table -1: Composition of Rhone - Poulenc AB_5 MH Alloys

	COMPOSITION (mol %)							
ALLOY #	**La**	**Ce**	**Nd**	**Pr**	**Ni**	**Co**	**Mn**	**Al**
5978	1	0	0	0	4.96	0	0	0
6025	0.3	0.51	0.07	0.13	3.56	0.76	0.4	0.3
6026	0.25	0.55	0.07	0.13	3.68	0.75	0.4	0.34
6039	0.64	0.25	0.04	0.08	3.51	0.77	0.4	0.31
6077	0.49	0.2	0.09	0.22	3.05	1.5	0	0.53

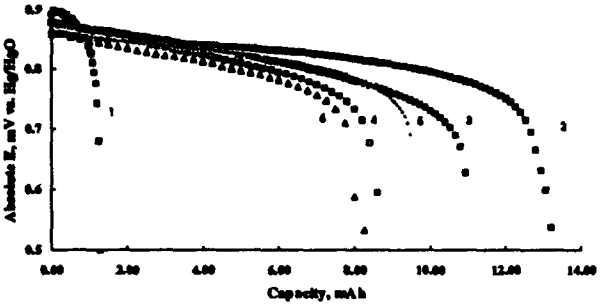

Fig. 1 : Discharge curves of 1) 5978, 2) 6025, 3)6026, 4) 6039, 5) 6077 and 6) IBA 5 MH alloy disc electrodes in flooded glass cell.

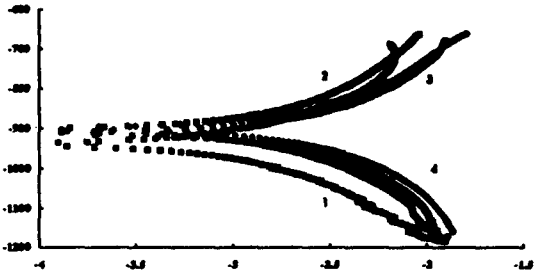

Fig. 4 : Tafel polarization curves of 1) 5978, 2) 6025, 3) 6026 and 4) 6039 MH alloys.

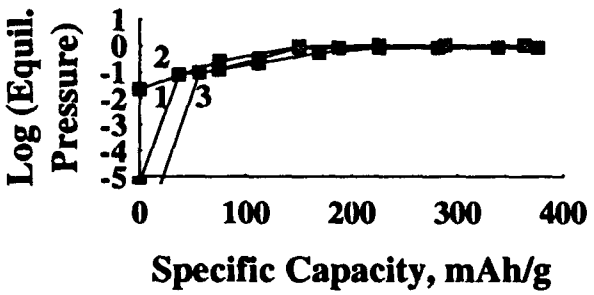

Fig. 2 : Electrochemical isotherms of 1) 6077, 2) 6039 and 3) 6026 MH alloys during hydrogen absorption (reduction).

Fig. 5 : Cycle life curves of 1) 5978, 2) 6039, 3) IBA 5, 4) 6077, 5) 6026 and 6) 6025 MH alloys in ~250 mAh, negative-limited cells @ C/5 charge and discharge.

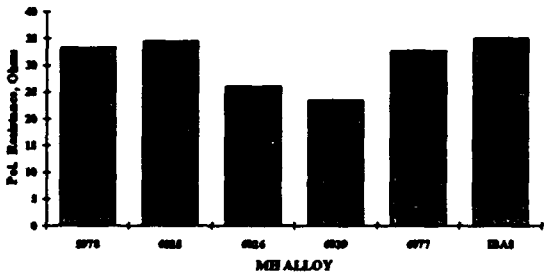

Fig. 3 : Polarization resistances of MH alloys estimated from DC micropolarization experiments.

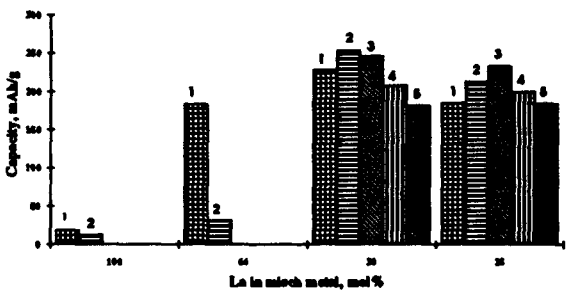

Fig. 6 : Illustration of the dependence of capacity retention during charge-discharge cycling, on the misch metal composition.

Calorimetric Evaluation of Commercial Ni/MH Cells

Eric C. Darcy
NASA-Johnson Space Center, Houston, TX
Brent M. Hughes
Lockheed Engineering & Sciences Company, Houston, TX

Introduction

Development and integration of large capacity nickel/metal hydride (Ni-MH) cells for manned spacecraft applications requires accurately characterizing cell thermal behavior, identifying how it responds to various charge control schemes, and understanding the phenomena which alters it. The on-going effort includes a calorimetric evaluation of various commercial cells with a comparison of several commercial charge control circuits with different charge termination techniques. The end objectives are to determine which cell designs are most suitable for scale-up and to guide the design of future Space Shuttle and Space Station based battery chargers. This paper discusses the plan of the study and its recent findings. These findings come from a comparison of two Ni-MH cell types with a standard Ni-Cd cell while controlled by a constant current charger.

The on-going effort is studying the electrical and thermal performance of cells with the AB_2 (Ovonic, Harding, and Gold Peak) and with the AB_5 (Sanyo, Toshiba, and Furukawa) metal hydride formulations. In this paper, Sanyo's 4/3 A cell (2.3 Ah) is compared to Ovonic's C-cell (3.25 Ah). Therefore, AB_2 refers to an alloy system based on V-Ti-Zr-Ni-Cr [1], while AB_5 refers to a system consisting of rare earth hydrogen absorbing alloys denoted as $MmNi_5$ with inclusion of Ta, Zr, W and Mo [2].

The on-going experimentation is evaluating the effectiveness of various commercial charging control circuits. We have focused on chargers from Benchmarq Electronics, Integrated Circuit Systems, Inc., and Maxim Integrated Products because of their range of operating features and different termination schemes.

The Benchmarq bq2300 charger requires a constant voltage supply to charge at constant current. It uses two main charge termination algorithms. One based on a certain rise in battery temperature ($\Delta T/\Delta t$) and the other on a negative battery voltage slope ($-\partial V/\partial t$). The $\Delta T/\Delta t$ algorithm evaluates a rise in temperature using a thermistor voltage measurement every 34 seconds and is based on a rise calculation made every 68 seconds. The $-\partial V/\partial t$ algorithm operates at the same frequency and ends charge when the battery voltage divided by the number of cells in the battery is lower than the previously measured value by 12 mV. As a back-up, the charger will also terminate when detecting a threshold voltage, temperature, or time.

The Integrated Circuits Systems (ICS) 1702 charger can accept a constant voltage or current supply to control charge using a reverse pulse charge sequence. Figure 1 shows a typical charge waveform with a 1.076 second period consisting of 1.047 second constant current charge pulse, a 4 ms rest, a 5 ms discharge pulse typically set to -2.5 times the level of the charge current, and a 20 ms rest during which the charger makes its voltage measurements. This "burp" charge technique is supposed to prevent the accumulation of gas bubbles on the cell electrode plates. The method has been shown effective with Ni-Cd cells [3]. The ICS charger uses seven charge termination schemes, including a voltage inflection ($\partial V/\partial t$), negative voltage slope ($-\partial V/\partial t$), maximum voltage, temperature slope ($\partial T/\partial t$), maximum temperature, and two charge timers.

The Maxim 712 charger requires a constant voltage supply to charge at a constant current. Its termination methods include zero voltage slope ($\partial V/\partial t = 0$), maximum temperature, and a timer.

Experimental Method

Four cell batteries were cycled by a computer controlled automated system designed in-house. A Macintosh IIcx uses LabVIEW software to send commands to two Fluke Data Acquisition Units and a Kepco Programmer. The Fluke units in turn send a bit pattern to a relay controller which switchs the batteries from states of charge, discharge, and rest. The programmer controls the mode and level of the output of the Kepco bipolar power supplies, BOP 20-10M. For example, during charge a constant voltage of 11 volts is supplied to the Benchmarq charger by the power supply and during discharge this supply is used as a sink to discharge the batteries. Trickle charge is typically controlled by the charger once charge has terminated, but our system allows the user to control trickle by using the power supplies directly.

The calorimetric evaluation is performed with one cell from a battery residing in a measurement chamber of heat conduction calorimeter manufactured by Hart Scientific, Inc.
This calorimeter uses a twin cell approach to measuring heat which cancels out external heat effects.

To date, a cycling comparison at a C rate for charge and discharge with Sanyo and Ovonic Ni-MH cells and the Sanyo Ni-Cd C-cell, model #IN-2000CR, has been completed with the Benchmarq charger. The tests were done at room temperature with cells which had been cycled less than a hundred times.

Results and Findings

Typical single cycle profiles of cell voltage, current, and cell heat rate are shown in Figures 2-4 for each of the three cells. Note that the "Harding C-cell" reference in the figures is interchangeable with Ovonic when referring to the C-cell since Harding is not its manufacturer only its distributor. Harding manufactures only the smaller size cells with the Harding label. The Benchmarq charger appears to terminate charge due to a rise in temperature with both Ni-MH cells prior to $-\partial V/\partial t$ appearing. This limited the charge input at the C rate to no more than one hour. The cell heat profiles show a very pronounced spike just before charge termination. The Ovonic cell heated up earlier in charge than the Sanyo cell. In comparison, the Ni-Cd cell stayed relatively cool until after 100% charge input (vs nameplate capacity). This allowed the Benchmarq charger to detect the negative voltage slope to terminate charge.

Overall, the Ni-MH cells generated significantly more heat on charge then Ni-Cd cells due to the exothermic nature of loading the hydride with hydrogen. Conversely, Ni-MH discharges are much cooler because of the endothermic nature of the hydride releasing hydrogen.

Table 1 compares the electrical and thermal performance of each cell. Electrical criteria include percentage of discharge output base on nameplate capacity, Ah and Wh charge-to-discharge (C/D) ratios, and specific energy. The thermal criteria include Wh_t C/D ratio and charge and discharge efficiencies. Efficiencies are a measure of how much energy is dissipated as heat per electrical input or output and are defined as $(Wh - Wh_t)/Wh$.

The coupling with the Benchmarq charger yielded the most discharge capacity with the Ni-Cd cells and the lowest Ah C/D ratio with the

Sanyo cell. The value of those two criteria are given as averages over 5 to 10 cycles while the others are based on one representative cycle. The Sanyo cell faired better than the Ovonic cell in all categories. The electrical performance of the Sanyo Ni-MH cell is very similar to the Ni-Cd cell except that it yielded a specific energy 46% higher. The charge and discharge efficiencies are nearly identical but reversed between the two.

Table 1. Comparison of electrical and thermal performance of cells cycled with a Benchmarq Electronics bq2003 charger at C rate and at room temperature.

	Ovonic (AB_2)	Sanyo (AB_5)	Ni-Cd
Discharge output (%)	78	87	107
Ah C/D ratio	1.23	1.08	1.15
Wh C/D ratio	1.83	1.38	1.35
Wh_t C/D ratio	2.68	2.10	0.96
Charge eff	0.63	0.77	0.85
Discharge eff	0.75	0.85	0.78
Specific energy (Wh/kg)	33.2	48.0	32.8

Future Work

Calorimetric analysis has shown to be an effective tool to evaluate cell and charger performance. The Benchmarq is not as effective with Ni-MH cells as with Ni-Cd cells. It does not allow for any overcharge input into the Ni-MH cells and thus, subsequent discharge capacities are less than optimum. Continuation of this on-going effort will provide similar comparisons of these and other cells using the other chargers mentioned at varying rates and temperatures.

References

(1) Ovshinsky, S.R., Fetcenko, M.A., and Ross, J. (1993). A Nickel Metal Hydride Battery for Electric Vehicles. Science, 260, pp. 176-181

(2) Tadokoro, M., Moriwaki, K., Nishio, K., Nogami, M., Inoue, N., Chikano, Y., Kimoto, M., Ise, T., Maeda, R., Mizutaki, F., Takee, M., and Furukawa, N. (1992). Development of Hydogen Absorbing Alloys for Nickel Metal Hydride Secondary Batteries. Electrochemical Society Proceedings Volume 92-5, pp. 92-104

(3) Benjamin, F. (1977). System for 20 minute Recharging of Sealed Nickel-Cadnium Batteries. SMPTE Journal, 86, pp. 204-209

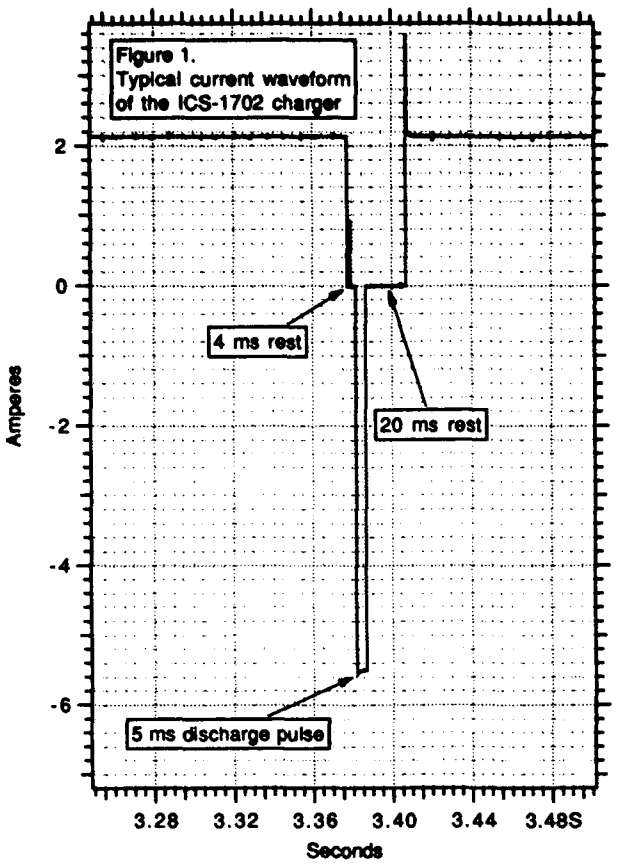
Figure 1.
Typical current waveform
of the ICS-1702 charger
4 ms rest
20 ms rest
5 ms discharge pulse
Amperes
Seconds
2
0
-2
-4
-6
3.28
3.32
3.36
3.40
3.44
3.48S

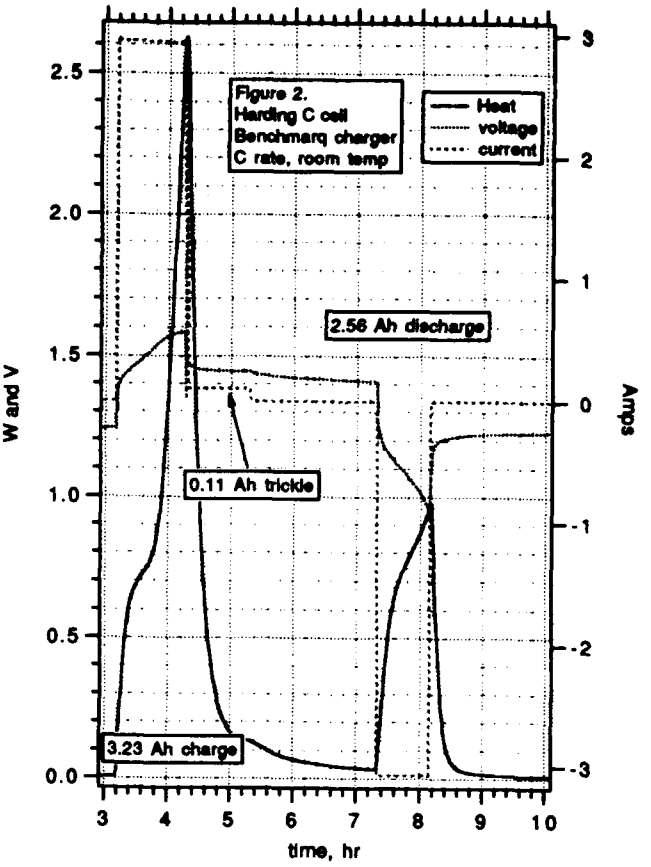
Figure 2.
Harding C cell
Benchmarq charger
C rate, room temp
Heat
voltage
current
2.56 Ah discharge
0.11 Ah trickle
3.23 Ah charge
W and V
Amps
time, hr
2.5
2.0
1.5
1.0
0.5
0.0
3
2
1
0
-1
-2
-3
3
4
5
6
7
8
9
10

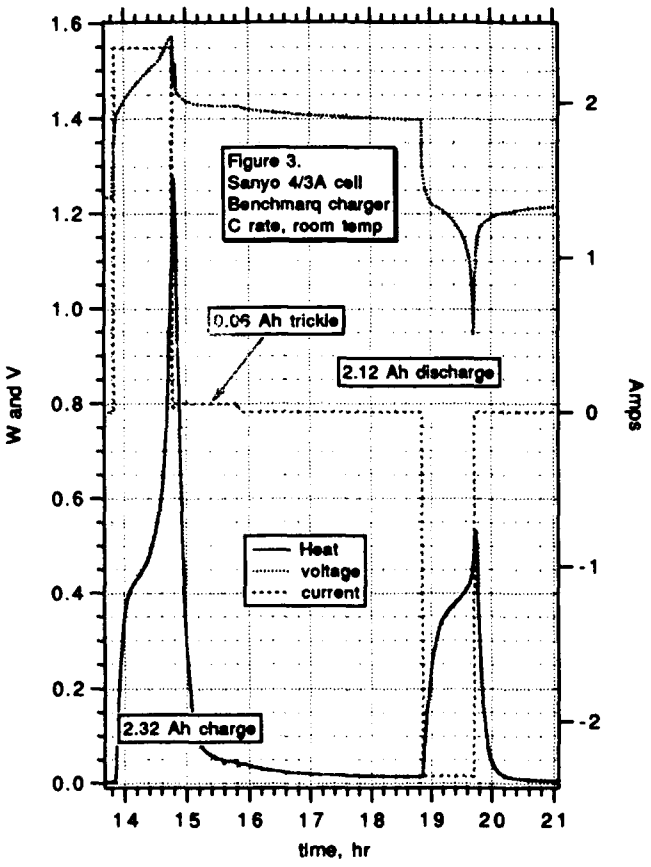
Figure 3.
Sanyo 4/3A cell
Benchmarq charger
C rate, room temp
0.06 Ah trickle
2.12 Ah discharge
Heat
voltage
current
2.32 Ah charge
W and V
Amps
time, hr
1.6
1.4
1.2
1.0
0.8
0.6
0.4
0.2
0.0
2
1
0
-1
-2
14
15
16
17
18
19
20
21

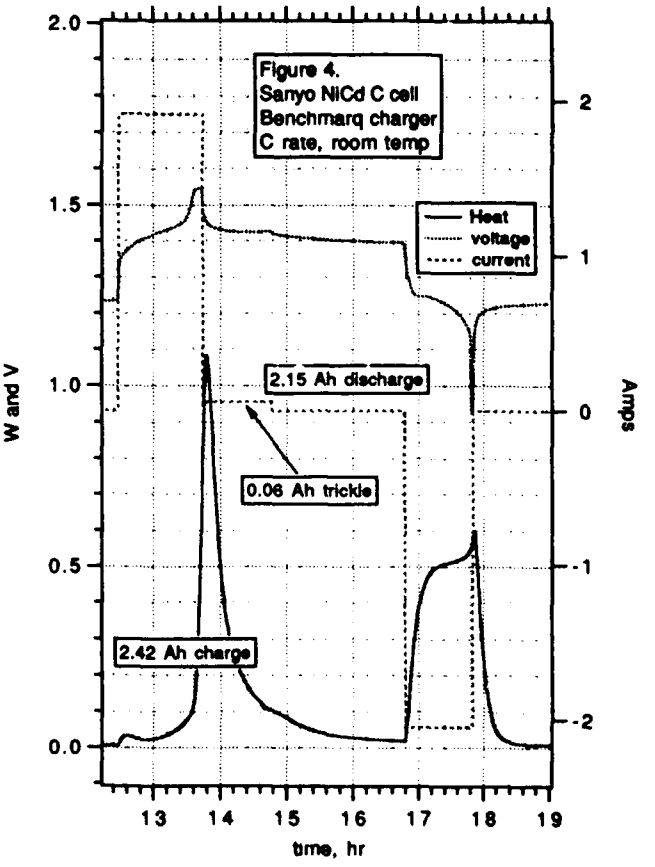
Figure 4.
Sanyo NiCd C cell
Benchmarq charger
C rate, room temp
Heat
voltage
current
2.15 Ah discharge
0.06 Ah trickle
2.42 Ah charge
W and V
Amps
time, hr
2.0
1.5
1.0
0.5
0.0
2
1
0
-1
-2
13
14
15
16
17
18
19

DEVELOPMENT AND TESTING OF SILVER-METAL HYDRIDE BATTERIES

D. K. Coates, C. L. Fox and S. M. Lipka*
Eagle-Picher Industries, Inc.
Joplin, Missouri 64801

* Florida Atlantic University
Boca Raton, Florida 33431

Abstract

Silver-metal hydride is a new battery system under development for aerospace and possible commercial applications. The chemistry is based on extensive experience with the silver-zinc, nickel-hydrogen and nickel-metal hydride battery systems. Silver-metal hydride combines the high energy density of the silver electrode (compared to the nickel electrode) with the longer cycle life of the hydride electrode (compared to the zinc electrode). Silver-metal hydride batteries offer hermetically sealed, maintenance-free operation with improved cycle life over the silver-zinc system. Development work is being done at the materials, electrode and full cell levels. Prototype silver-metal hydride cells have been constructed and are being characterized by electrical testing, cycle life testing and by electrochemical impedance spectroscopy analysis. Improved separator systems are being developed in order to mitigate silver migration and improve performance and cycle life.

Introduction

Some previous work has been done on the silver-metal hydride (AgMH) system by Eagle-Picher[1,2] and in conjunction with Florida Atlantic University[3]. The precursor to AgMH batteries, silver-zinc (AgZn) systems, have been used extensively in military and aerospace applications as both a primary and secondary battery system[4]. Eagle-Picher Industries (EPI) has manufactured thousands of primary and secondary, manually activated and reserve AgZn batteries in many different designs and configurations for a wide variety of military and aerospace applications. These include the Mercury, Gemini and Apollo manned spacecraft, the Lunar Rover, Skylab and many assorted missile and weapons systems such as the Patriot and Tomahawk Cruise missile. EPI AgZn batteries have also powered many solar and electric race vehicles in events such as the GM Sunrayce, the Solar/Electric 300 and the World Solar Challenge in Australia. EPI has extensive experience and manufacturing capability in the production of silver electrodes and silver-based batteries.

Currently, the nickel-metal hydride (NiMH) battery system is in full development and initial commercial production. Significant advances over the past few years in reversible hydrogen absorbing electrode materials have made hydride-based batteries both possible and practical. The major limitation of the NiMH battery is the nickel electrode. One possible solution to significantly increase the energy density of the battery is to replace the nickel electrode with a higher energy density electrode such as silver. The silver electrode has several advantages over other electrodes including the superior conductivity of the silver material. As the silver electrode is discharging, silver-oxide is being reduced to silver metal, which decreases the impedance of the electrode. This continuous decrease of electrode impedance during discharge counteracts polarization effects, resulting in a flat, uniform discharge voltage profile. This effect gives the electrode excellent discharge rate capability as well. AgMH provides an intermediate hybrid system between NiMH and AgZn. The disadvantages of the AgZn system include limited cycle life, limited wet life and an ill-defined end-of-life failure. These limitations are primarily due to zinc migration or "shape change" that occurs in the zinc electrode. Replacing the zinc electrode with the more stable hydride electrode should significantly increase battery life and performance.

Extensive development work is underway to characterize and optimize the AgMH battery system. Work is being done at the materials, electrode and full cell levels. Hydride electrode alloy formulation is a critical aspect of metal hydride battery performance and cycle life. Hydride electrode materials must be formulated and optimized specifically for the silver battery system. Silver electrodes have many advantages over nickel electrodes. While the initial cost of silver metal is higher than nickel metal, this is offset by the ease of manufacture of the silver electrode as compared to the multi-step processing required by nickel electrode manufacturing. Also, the silver electrode doesn't require electrochemically inactive additives, such as nickel powder, to support the active material or increase electrode conductivity. This results in superior energy density and efficiency of the silver electrode.

Flooded electrode testing is being used in preliminary performance and cycle life evaluations. Electrochemical impedance spectroscopy is being used to evaluate and characterize electrodes and cell materials. Improved separator systems are being developed in order to reduce silver migration and improve performance and cycle life. Basic system characteristics such as voltage output, gravimetric energy density, volumetric energy density, rate capability and charge retention are being determined. The AgMH battery has enormous potential as a rechargeable battery system and further development is planned.

Silver-Metal Hydride Battery Chemistry

The silver electrode undergoes two distinct oxidation/reduction reactions during charging and discharging of the battery. These reactions are:

$$2\,AgO + H_2O + 2\,e^- = Ag_2O + 2\,OH^- \qquad [1]$$

$$Ag_2O + H_2O + 2\,e^- = 2\,Ag + 2\,OH^- \qquad [2]$$

Both reactions are reversible and are written as reductions, which corresponds to discharging the electrode. Equation [1] represents the reduction of silver from the +2 oxidation state to the +1 oxidation state. This reaction occurs at a potential of 0.607 volts versus the standard hydrogen electrode. The second reaction [2]

occurs at a voltage of 0.342 volts, corresponding to the reduction of silver +1 to silver metal. Equations [1] and [2] can be combined into an overall reaction for the silver electrode:

$$AgO + H_2O + 2\,e^- = Ag + 2\,OH^- \qquad [3]$$

The chemistry of the hydride electrode has been previously discussed[3]. It can be considered as the alkaline hydrolysis of water followed by the formation of a metallic hydride or as the electrochemical formation of the metallic hydride in the solid phase directly from the aqueous electrolyte. Regardless of mechanistic considerations, the overall reaction at the hydride electrode can be represented by Equation [4]:

$$MH_{(x-1)} + H_2O + e^- = MH_x + OH^- \qquad [4]$$

where M represents a material capable of reversibly forming a metallic hydride and the lower case letter "x" is an integer (x= 1,2,3...) and represents some hydride state of the metal. The reaction is reversible but is conventionally written as a reduction. Combining reactions [3] and [4] yields the overall silver-metal hydride cell reaction that results from combining the silver and hydride electrodes into a secondary alkaline battery. This is represented by Equation [5]:

$$AgO + 2\,MH_X = Ag + 2\,MH_{(X-1)} + H_2O \qquad [5]$$

Reaction [5] represents the overall cell discharge reaction as written. The charge reaction is the reverse. The relative effects of the two major electrode reactions (Equations [2] and [3]) can sometimes be observed in the silver battery as a dual plateau in the charge and discharge voltage profile.

Silver-Metal Hydride Cell Characterization

Figure 1 shows the charge voltage profile for an experimental AgMH cell (silver versus a Hg/HgO reference electrode). The cell uses standard production, sintered silver electrodes and an AB_5 type hydride electrode. Standard AgZn type separator materials were used, including a cellulosic silver migration barrier. The cell was activated with 31% aqueous potassium hydroxide (KOH). The cell was charged at a constant current 0.07 C rate at room temperature. The two-step reaction is clearly visible in the charge voltage versus time curve. The first plateau occurs at a voltage of about 0.25 volts and corresponds to the oxidation of silver metal to the monovalent silver ion. The second plateau occurs at about 0.58 volts and corresponds to the further oxidation of silver to the +2 oxidation state. The voltage increases to about 0.70 volts as the cell is overcharged. The cell was subsequently discharged at the 0.33 C rate.

In Figure 2, the two-step reduction process is visible in the discharge voltage profile. The first plateau occurs at about 0.48 volts and the second at about 0.20 volts. Most of the cell capacity is obtained at the lower voltage. These voltages are the potential of the silver electrode measured relative to the Hg/HgO reference electrode. The observed full cell potential may vary somewhat depending upon the electrode spacing and the separator used.

Impedance measurements were conducted on AgMH cells as a function of state-of-charge (SOC), cycle number and potassium-hydroxide (KOH) concentration (31, 38 and 45 %). Measurements were made on both full and half cells (using a Hg/HgO reference electrode). Impedance measurements were made at 25 cycle intervals at full charge, 50% depth-of-discharge (DOD) and full discharge (500mV total cell voltage). Cycling was performed at the 0.6 C rate to 50% DOD with a 4 to 5% overcharge each cycle.

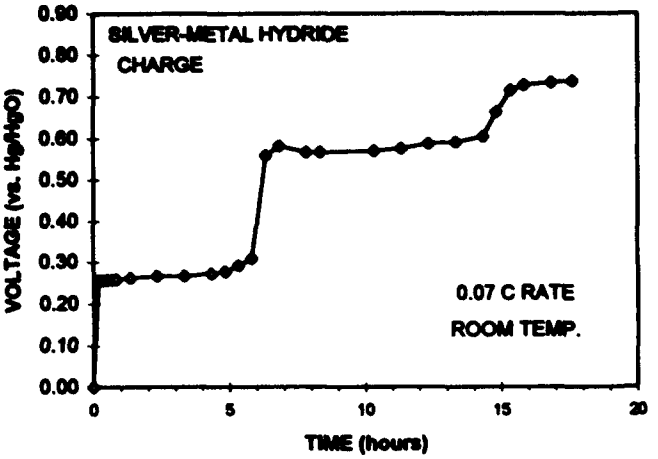

Figure 1. Silver-metal hydride charge voltage versus time

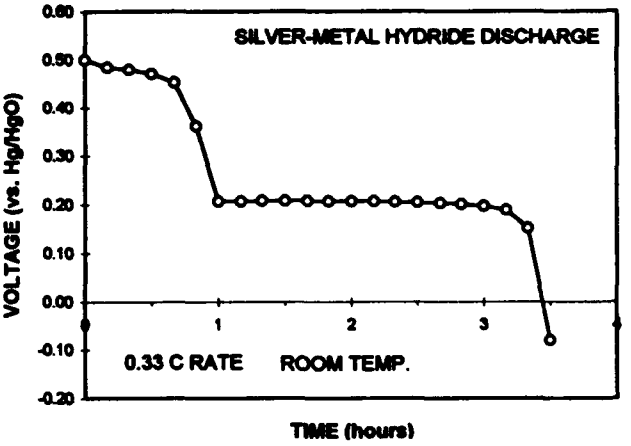

Figure 2. Silver metal-hydride discharge voltage versus time

In general, the ohmic resistance of the AgMH cells increased with cycling. The increase in ohmic resistance may be attributed to the electrolyte concentration changes (decrease in activity), drying out of the separator material and decreased conductivity of the silver migration barrier. At full charge (0% DOD), the impedance data indicates that the total cell impedance was very similar in behavior and magnitude to the impedance obtained for the individual silver electrode. These data demonstrate that the overall impedance of the battery is dominated by the silver electrode.

Impedance data, represented as a complex plane plot, for the full AgMH cell in 31 % KOH at 0% DOD is shown in Figure 3 for various cycles. The data shows that cell impedance was lowest at 3 cycles, increased after 50 cycles and then gradually decreased with additional cycling. This behavior could be explained by the longer period of time required to fully condition or convert the silver into silver-oxides, thus utilizing most of the active material. The data at 3 cycles was dominated primarily by silver metal not fully converted to its oxides thus yielding the observed lower impedance. On further cycling, a greater majority of the silver active material was converted to oxides, which have greater resistivity. Additional cycling to 100, 150 and finally to 200 cycles resulted in a decrease in the active material surface area, trapping of oxygen and pore filling, thus limiting the access of electrolyte to the active material. Again, a fraction of the active material from the fully discharged silver electrode may not have converted entirely to the oxides thus causing a decrease in the total cell impedance.

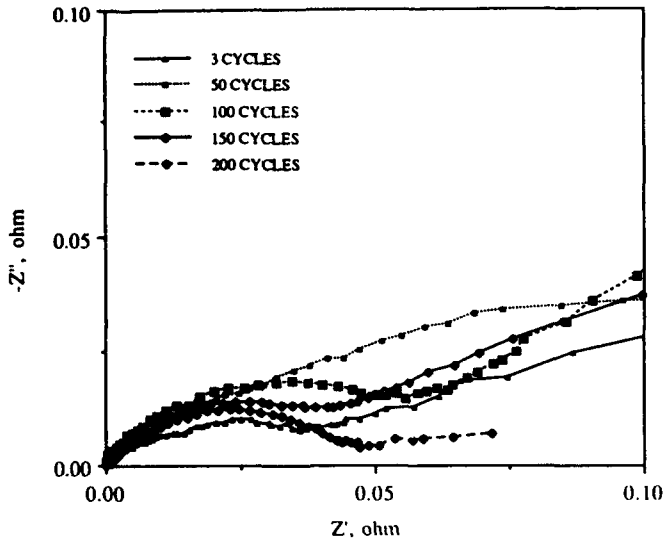

Figure 3. Silver-metal hydride impedance data

At 100% DOD, both the silver and metal hydride electrode impedance magnitudes were similar and contributed almost equally to the total cell impedance. The data for the full cell at 100% DOD in 31% KOH for various cycles are shown in Figure 4 as a complex plane impedance plot. In general, the impedance of the cell increased with increasing cycles. Similar impedance behaviors have been presented by Kaiser[5] due to electrode pore filling and surface smoothing. A similar process may be occurring on the silver electrode surface in which an increasing amount of poorly conductive silver oxides are left unconverted to silver upon cycling. Additional contributions to the increased cell impedance can result from the metal hydride electrode which pulverizes and loses active material; material normally available for hydrogen storage.

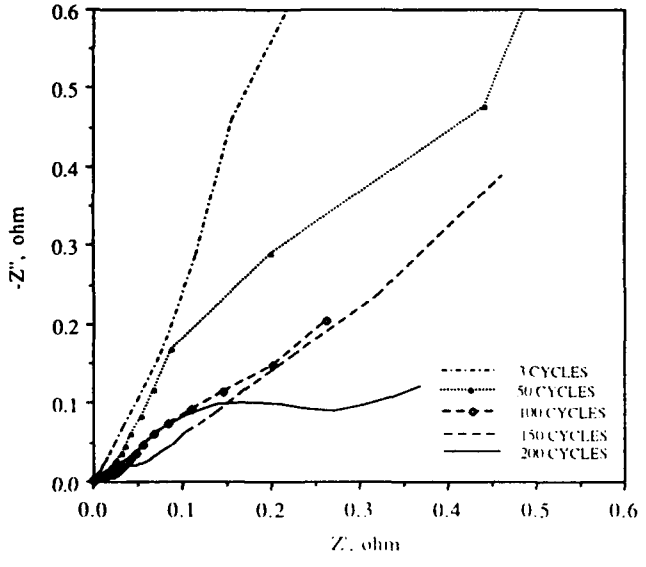

Figure 4. Silver-metal hydride impedance vs. cycling

Silver-Metal Hydride Performance Summary

A sealed aerospace AgMH cell was tested at a variety of charge and discharge rates in order to fully characterize the cell. The cell was built in a standard prismatic configuration in a stainless steel container. The cell was designed to be silver limited with a slight excess of hydride electrode capacity. The cell was operated hermetically sealed with a pressure gauge attached to the fill tube. The cell was vacuum activated with aerospace grade 35% aqueous KOH. A dual-layer separator system was used. Figure 5 shows the cell constant current charge voltage versus the % theoretical capacity for a variety of charge rates, ranging from 0.075 C to 2.0 C. The % theoretical capacity was calculated by multiplying the charge time by the charge current and dividing by the cell theoretical discharge capacity (based on the weight of silver electrode active material in the cell) multiplied by 100%. This is a convenient method of comparing voltage data obtained at different rates on the same x-axis scale. The cell was fully discharged at the C/2 rate after each charge.

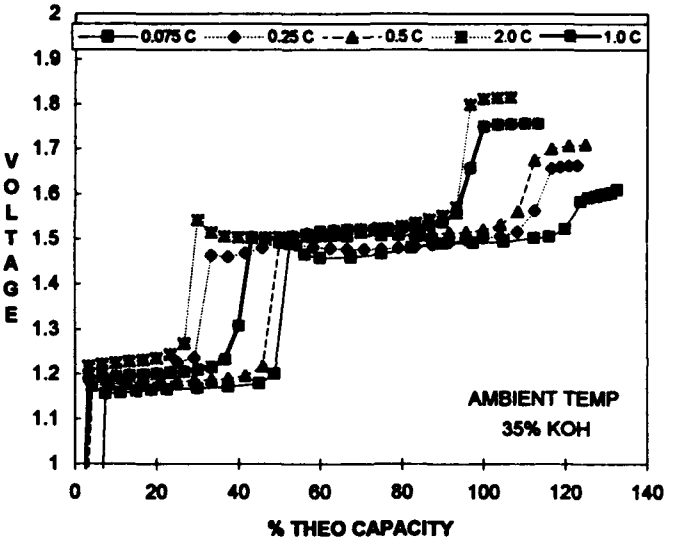

Figure 5. AgMH cell voltage at different charge rates

There is the usual impedance effect of increased charge voltage at higher charge rates. This amounts to a plateau voltage difference of about 75 millivolts over the total range of charging current used. The transition points between voltage plateaus changes considerably at different charge rates. For example, the transition from the initial charge plateau to the second plateau occurs at about 50% SOC at the lowest charge rate (0.075 C). This transition point decreases to about 25% SOC at the highest charge rate (2.0 C). Similarly, the transition from the second charge plateau into overcharge occurs at 120% SOC at a charge rate of 0.075 C and occurs at about 95% SOC at the 2.0 C rate. The cell voltage in overcharge also shows a larger voltage increase than the lower plateaus. Cell overcharge voltage is about 1.55 volts at the 0.075 C rate and increases to about 1.8 volts at the 2.0 C rate.

Figure 6 shows the constant current discharge voltage versus % theoretical capacity for the same cell at a variety of discharge rates. The charge prior to each discharge was done at the 0.10 C rate to eliminate any effects of charging at different rates. The cell was discharged at rates ranging from 0.25 C up to 10.0 C, based on the cell theoretical capacity. The cell was operated hermetically sealed throughout this testing. The cell delivered more than 120% of the calculated theoretical capacity at low rates. Cell discharge capacity was still well above theoretical up to the 5.0 C rate but dropped to 90% of theoretical at the 10.0 C rate. Some residual upper voltage plateau is observed at the lower rates, but this completely disappears above the 3.0 C rate. A single discharge voltage plateau is normally observed in sealed AgMH cells. At normal discharge rates (around C/2) this corresponds to a discharge plateau slightly above 1.0 volt.

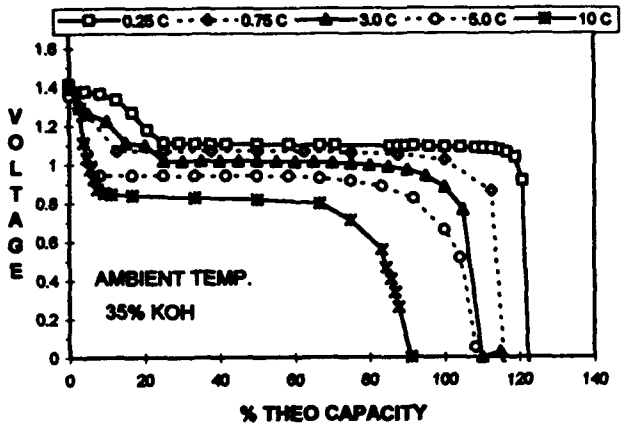

Figure 6. AgMH cell voltage at different discharge rates

A large impedance effect is observed in the discharge voltages in Figure 6. The discharge plateau occurs at a cell voltage of 1.10 volts at the 0.75 C rate and decreases to 0.80 volts at the 10.0 C rate. This is a difference of 300 millivolts. This is at least partially due to the high ohmic impedance imposed by the use of a cellulosic silver migration barrier. In these early prototype AgMH cells, excessive layers of separator and migration barriers were used. Based on subsequent experience and cell performance, the separator layers have been reduced, with a corresponding increase in performance. Separator system optimization remains to be one of the primary areas of continuing R&D.

Figure 7 shows the discharge rate relationship graphically. Cell mid-point discharge voltage (MPDV) is plotted as a function of the constant current discharge rate (expressed as a multiple of the cell capacity "C"). The discharge capacity is also plotted as a function of the discharge rate. Cell capacity is expressed as a fraction of the cell theoretical capacity. The data shows that both the MPDV and the cell capacity are linear as a function of discharge rate, over the range of discharge rates investigated. These discharge rates range from 0.25 C up to 10.0 C, which covers the range likely to be encountered in normal cell operation. The MPDV line has a slope of -0.030 with a correlation coefficient of -0.998, which indicates a good fit of the data to a straight line. The fraction of theoretical capacity data indicates the cell discharge capacity, expressed as a fraction of theoretical, obtained at that discharge rate. These values range from 1.22 theoretical at the 0.25 C rate down to 0.85 theoretical at the 10.0 C rate. The line has a negative slope of -0.369 and a correlation coefficient of -0.993. The cell delivered better than nameplate capacity up to the 5.0 C rate.

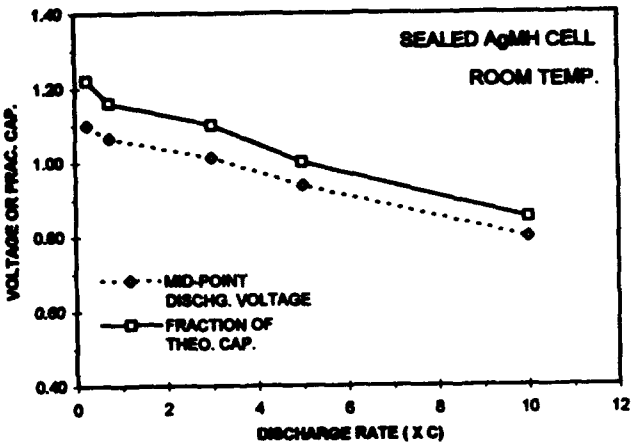

Figure 7. Discharge voltage and cell capacity versus rate

Conclusions

Testing of prismatic aerospace silver metal hydride cells is still underway. The results to date are very promising. It is anticipated that the metal hydride chemistry will function well in aerospace applications, including the more demanding low-earth-orbit missions. The system is ideal for the new generation of small satellites being developed for communications, surveillance and tactical satellite programs. Potential military applications include tactical electric vehicles, swimmer delivery vehicles, underwater power systems, C^4I, communications equipment, GPS receivers, the SOLDIER combat system, battle field computers and any man-portable battery operated equipment. The system may also be useful in premium commercial applications such as cellular telephones, laptop computers and palmtop computers, where the increased energy density, and correspondingly longer run time, offsets the higher initial cost and relatively shorter cycle life of silver-based batteries. The system promises excellent performance and cycle life at a reasonable cost, as compared to other aerospace systems.

References

[1] Coates, D. Proc. 4th Inter. Rechg. Batt. Symp., Deerfield Beach, Florida 1992.

[2] Coates, D. Proc. 27th Intersoc. Ener. Conv. Eng. Conf., San Diego, CA 1992.

[3] Coates, D., Grindstaff, B. and Lipka, S. Proc. 182nd Electrochem. Soc., Toronto 1992.

[4] Jasinski, R. High Energy Batteries, Plenum Press, New York 1967.

[5] Kaiser, H., Beccu, K.D. and Gutjahr, M.A. Electrochemica Acta 21, 539 (1976).

SEALED BIPOLAR NICKEL-METAL HYDRIDE BATTERY

David E. Reisner and Martin Klein

Electro Energy Inc., Danbury, CT

Introduction

The rechargeable nickel-metal hydride (Ni-MH) battery system is quickly gaining acceptance as a practical solution to a vast array of battery exigencies. It's high energy density (E.D.), high power density, long cycle life, and abuse tolerance are attractive performance attributes that complement its safe and environmentally benign character [1,2]. Voltage compatibility (1.2 V) allows for drop-in replacement of the installed base of Ni-Cd.

Electro Energy, Inc., is developing [3-8] a bipolar version of Ni-MH that empowers the Ni-MH system with higher E.D.s and rate capabilities. It is anticipated that the high symmetry and simplicity of the bipolar geometry will ease fabrication and lower production costs significantly. It is expected that this improved performance at lower cost in an ecologically sound battery will have a profound effect in the market place for both small and large batteries.

EEI's innovative technology consists of two electrodes with a separator/insulator sealed in a conductive polymer unit wafer cell. Typically, bipolar cells consist of a bipolar conductive plate centered between anode and cathode. This strict definition follows when individual wafer cells are stacked to form a bilayered bipolar plate.

Conventional Ni-MH cylindrical cells, based primarily on AB_5-type metal hydride alloys, have served commercial applications [9] such as 3Cs devices (cellular phones, notebook computers, and camcorders) since 1991. Use of round cells in prismatic battery cases wastes more than 27% of available packing volume. Sony and Panasonic have responded to this mismatch and both have introduced low-profile prismatic cells for domestic use. Nevertheless, the volume taken up by collector grids, leads, tabs, cell cases, and terminals renders such an approach less than optimal in comparison to a bipolar geometry. The transverse flow of current across the plane of the electrode in the bipolar geometry enhances high rate performance by precluding current flow bottlenecks intrinsic to conventional designs.

The future will undoubtedly witness the use of Ni-MH in industrial applications, hybrid vehicles and EVs. However, prosecution of the large-capacity battery marketplace will be financially driven. At present, conventional Ni-MH spirally wound cylindrical cells cost approximately $1500/kWh. It is estimated [4] that large prismatic Ni-MH batteries of conventional geometry cannot be commercially produced for less than $300/kWh, rendering them uncompetitive with lower performance technologies, even Pb-acid. However, a cost reduction of $100/kWh would significantly enhance the marketability of the attractive Ni-MH chemistry. EEI believes that this reduction can be achieved through the combined use of plastic-bonded nickel electrodes with its proprietary bipolar battery concept [8].

Experimental

The technical challenges to develop a bipolar configuration in the Ni-MH system are formidable. Materials of construction are critical. Specifically, four areas are paramount. The bipolar plate must be electrically conductive, sealable, chemically stable in caustic, and provide adequate interface contact. Hydride alloys must be designed that minimize overpressure on charge. Finally, oxygen must recombine at modest pressures.

Electro Energy, Inc., is developing a sealed bipolar Ni-MH battery that addresses these problems. The unit bipolar cell is shown schematically in Fig. 1. It employs a proprietary 0.004" conductive polymer film (0.26 Ω-cm) that can be heat sealed about anode, separator/insulator, and cathode. Both inorganic and organic separators are being evaluated. The positive and negative electrodes are of dimension 3" x 3" in the experimental cells constructed for the development activities. Measures have been taken to minimize contact resistance and provide an effective conduction path across interfaces. Electrolyte is a conventional 30% KOH solution.

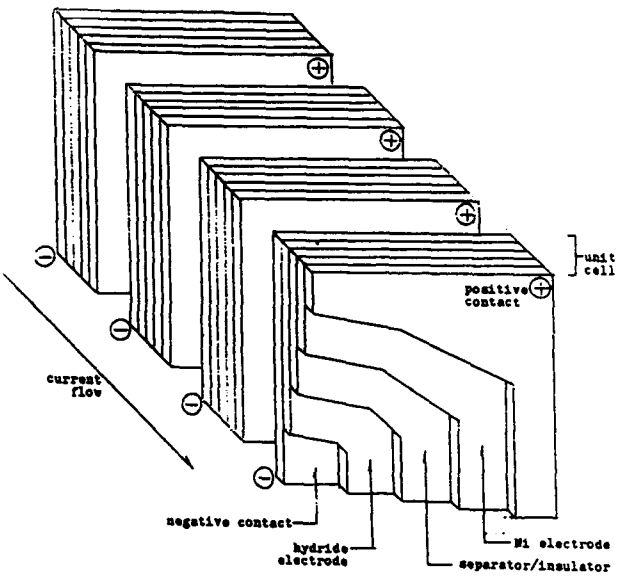

Fig. 1. Bipolar Wafer Cell Concept

Provision has been made for venting, and will be described in a later publication. These unit cells are series connected by stacking them face to face for the desired voltage (see Fig. 2).

The prototype Ni-MH bipolar cell is based on a misch metal (Mm) AB_5-type hydride alloy similar to the International Common Samples [10,11,12]. Misch metal has been used as a low cost substitute for lanthanum in the fundamental $LaNi_5$ metal-hydride alloy formulation which can store up to 6 hydrogens (*i.e.* $LaNi_5H_6$). Substitution of part of the Ni serves to stabilize the hydride materials by forming a protective surface oxide and reduces the equilibrium hydrogen storage pressure.

The alloy $MmNi_{3.55}Co_{0.75}Mn_{0.4}Al_{0.3}$ is representative of the materials used in the EEI cell. Fig. 3 shows first cycle pressure-composition isotherms (PCI) at three temperatures of an EEI-

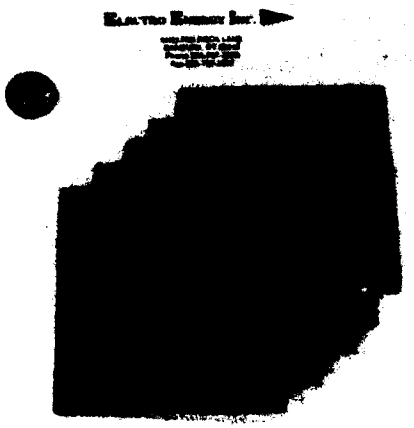

Fig. 2. Unit Cells for Multicell Stack

proprietary formulation of an AB_5-type alloy [13]. A low plateau pressure below one atmosphere is critical for large capacity cells. An equilibrium hydrogen pressure of 1 atm at 25°C corresponds to 3.6 H/f.u. or 288 mAh/g metal-hydride alloy.

Various kinds of nickel positive electrodes have been evaluated in wafer cells, including conventional sintered carbonyl nickel, plastic bonded [14] and foam nickel [15] types. The final choice will be based not only on performance (E.D. and rate) but on future production cost considerations as well. Electrical contact is a significant issue in electrode behavior. Both foam nickel and plastic-bonded type electrodes have demonstrated extended cycle life (see below).

It is anticipated that plastic bonded electrode technology will have a significant effect on Ni-MH battery price reduction. Plate capacities are on the order of 5-6 Ah/in^3 or 200 mAh/in^2 based on the thickness of plates employed. Foam nickel plaques are pressed at 8000 psig resulting in a loading level of approximately 1.6 g/cc voids. Capacities are typically 5.5 Ah/in^3.

Results

Initial studies were done with vented single cells. Cells were cycled eight times daily at a 0.75 C discharge rate at 1.0 A to a 1.0 V cutoff (66% DOD). A period of 63 days is required to achieve 500 cycles. Signs of CO_2 contamination were evidenced through some voltage decay. Replenishment with fresh electrolyte confirmed this. Fig. 4 shows data from a vented cell constructed with a foam nickel plaque (Eltech) pasted with high density active material. Cycle life results are very encouraging. Charge/discharge cycles are shown as high as cycle # 2034. Even at 2000+ cycles, the discharge characteristic still appears stable. The conductive partitions demonstrated excellent durability in the electrolyte without showing signs of increased contact resistance.

More recent studies have focused on the cycling of sealed cells. A metal hydride alloy has been chosen with a low H_2 equilibrium pressure. Fig. 5 shows a family of charge/discharge profiles to cycle # 1012 for a sealed cell employing a plastic-bonded nickel electrode (3" x 3" x 0.035"). Measures have been taken to assure adequate recombination. A 2 hour cycle was chosen at a 50% DOD.

Sealed cells have also been built with foam nickel electrodes. Extended cycle life has been achieved, at a 50% DOD, to more than 2045 cycles (see Fig. 6).

Most recently, EEI has been actively engaged in constructing multicell stacks. Initial studies have been done with vented cells. Fig. 7 shows voltage profiles for a multicell stack of 5 cells (6.0 V) at cycle #125.

Cost

It is difficult enough to achieve acceptable performance results from new battery technologies. It is indeed unusual to provide this improved performance at reduced cost. Klein and

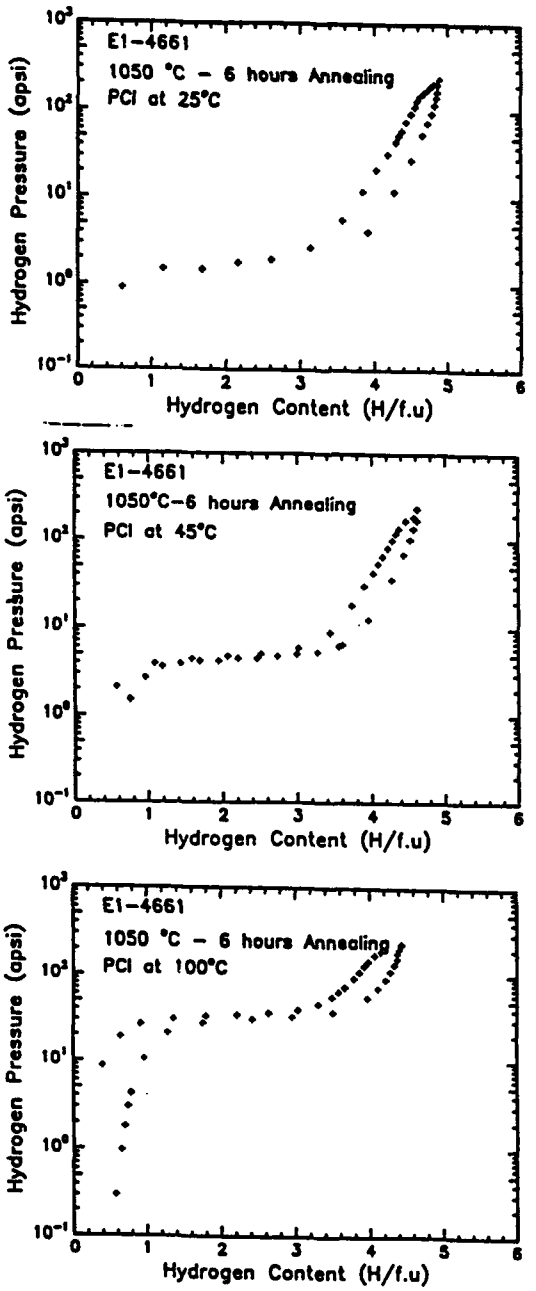

Fig. 3. Pressure Composition Isotherms - EEI Metal-Hydride Alloy

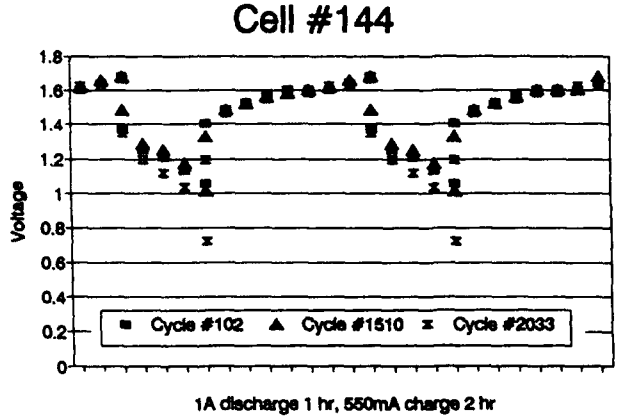

Fig. 4. EEI Bipolar Ni-MH Vented Cell Charge/Discharge Characteristics (Foam Nickel Positive)

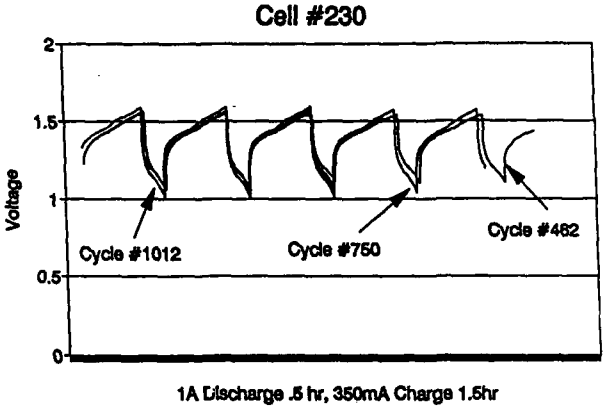

Fig. 5. EEI Bipolar Ni-MH Sealed Cell Charge/Discharge Characteristics (PB Nickel Positive)

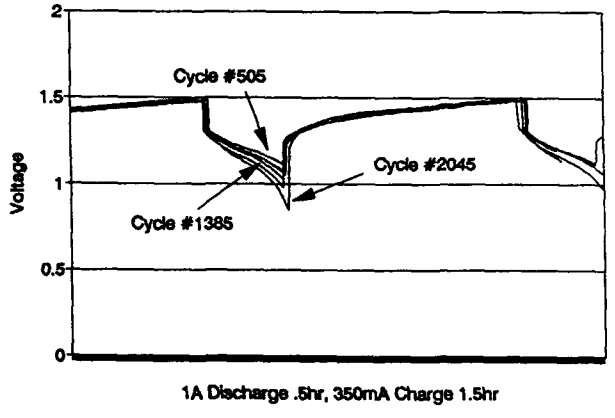

Fig. 6. EEI Bipolar Ni-MH Sealed Cell Charge/Discharge Characteristics (Foam Nickel Positive)

Salkind [4] modeled estimated production costs of materials on a 20 kWh Ni-MH battery comprised of 200 Ah cells based on the hydride alloy $MmNi_{3.55}Co_{0.75}Mn_{0.4}Al_{0.3}$ and a foam nickel positive. Volume production costs of bulk finished materials were calculated at 1.5 times raw metals costs. The total materials cost estimate was $190/kWh, excluding labor, etc.

Revising the cost of misch metal from $10.5/kg to $5/kg [9], reduces the estimate to $178/kWh. Replacing the foam nickel electrode with a plastic bonded electrode comprised of graphite ($1.50/lb) and PTFE ($10/lb), further reduces the production cost to $138/kWh, a 22% cost reduction based on the PB electrode alone. Use of the bipolar configuration would further reduce materials costs in the absence of grids, tabbing, leads, and terminals as well as in the reduction of cell case hardware. Hardware cost reduction of 50% results in a total material cost of 130$/kWh. Anticipated production costs for a conventional foam nickel Ni-MH battery are compared to a plastic bonded bipolar Ni-MH system in Fig. 8. Finally, reduction in labor costs for the system are expected to have a similar effect.

Summary

Initial results for both vented and sealed wafer cells appear very promising. Historically, the successful fabrication of sealed bipolar batteries has been hampered by materials of construction. The results shown above demonstrate that bipolar Ni-MH cells can be sealed and achieve excellent cycle life. Future studies will focus on developing sealed multicell stacks. These prototypes will be tested to evaluate their feasibility for various device applications.

Acknowledgements

The support of the Dept. of Energy (Office of Basic Energy Sciences), the Ballistic Missile Defense Organization and the Air Force (WPAFB), and the National Institutes of Health (NHLBI) are gratefully acknowledged.

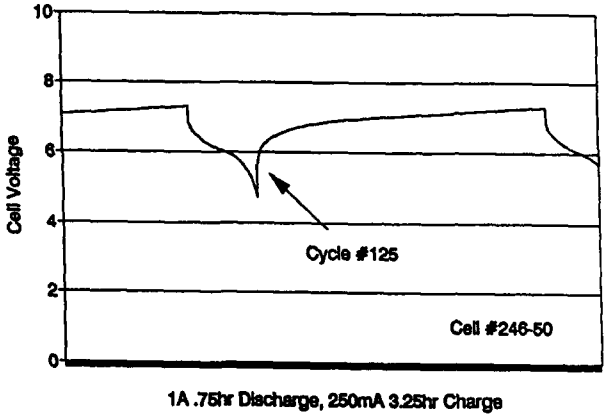

Fig. 7. EEI Bipolar Ni-MH Sealed Cell Stack Charge/Discharge Characteristics (Foam Nickel Positive)

References

[1]. D. Corbus, "Recycling of EV Batts.," Fourth Intnl. Sem. Batt. Waste Mgmt., Deerfield Beach, Nov. 9-11, 1992.

[2]. C.R. Knoll, S.M. Tuominen, R.E. Walsh, and J.R. Peterson, "Recyclability of Ni-MH Rech. Batts.," Fourth Intnl. Rech. Batt. Sem., Deerfield Beach, FL, Mar 2-4, 1992.

[3]. M. Klein, "Potential AF Appls. for Ni-MH Batts.," Proc. 8th Ann. Batt. Conf. Appls. Advs., Long Beach, CA, Jan 12-14, 1993.

[4]. M. Klein and A.J. Salkind, "Design and Cost Anal. of a Ni-MH EV Batt.," Proc. ECS Mtg., Honolulu, HI, May 16-21, 1993.

[5]. D. Reisner and M. Klein, "Design and Preliminary Perf. of Bipolar Ni-MH Batt.," Proc. 28th IECEC, Atlanta, GA, Aug. 9-13, 1993.

[6]. D.E. Reisner, "Bipolar Ni-MH and Other Practicable Approaches to EV Batts.," Proc. S/EV 93, Boston, MA, Oct 21-23, 1993.

[7]. D. Reisner and M. Klein, Bipolar Ni-MH Batt. for HVs," Proc. 9th Ann. Batt. Conf. Appls. Advs., Long Beach, CA, Jan 1-13, 1994.

[8]. U.S. Patent Application filed Oct. 12, 1993.

[9]. A. Kozawa, A. Sato, D. Brodd, and M. Yamashita, "Recent Jap. Prod. and Tech. of Primary and Rech. Li and MH Batts.," Proc. 9th Ann. Batt. Conf. Appls. Advs., Long Beach, CA, Jan 1-13, 1994.

[10]. A.J. Salkind, J.J. Kelley, J.B. Ockerman, M. Klein and J. Weckesser, "Props. of Intnl. Common Sample MH," Ext. Abs. Batt. Div. ECS Fall Mtg., Phoenix, AZ, Oct 13-17, 1991, p. 158.

[11]. T. Sakai, K. Muta, H. Miyamura, N. Kuriyama, and H. Ishikawa, "Ni-MH Batts. Using Rare-Earth Based Hydrogen Storage Alloys," Procs. Symp. Hyd. Stor. Mats., Batts., and Electrochem., ECS Mtg., Phoenix, AZ, Oct 13-17, 1991.

[12]. C. Iwakura and M. Matsuoka, "Appl. Hyd. Storage Alloys to Batt.-Related Fields: Ni-Hydrogen Batts.," Prog. Batts. & Batt. Mats., 10, 81 (1991).

[13]. Rhone-Poulenc, Cranbury, NJ.

[14]. B. Baker and M. Klein, "Hydrophilic Electrode and Method for Making the Same," U.S. Patent 3,898,099.

[15]. D. Reisner and M. Eisenberg, "Conv. and Foam Ni Elodes. in Stabilized High Energy Ni-Zn Batt. System," Proc. 33rd Intnl. Power Sources Symp., Cherry Hill, NJ, Jun 13-16, 1988.

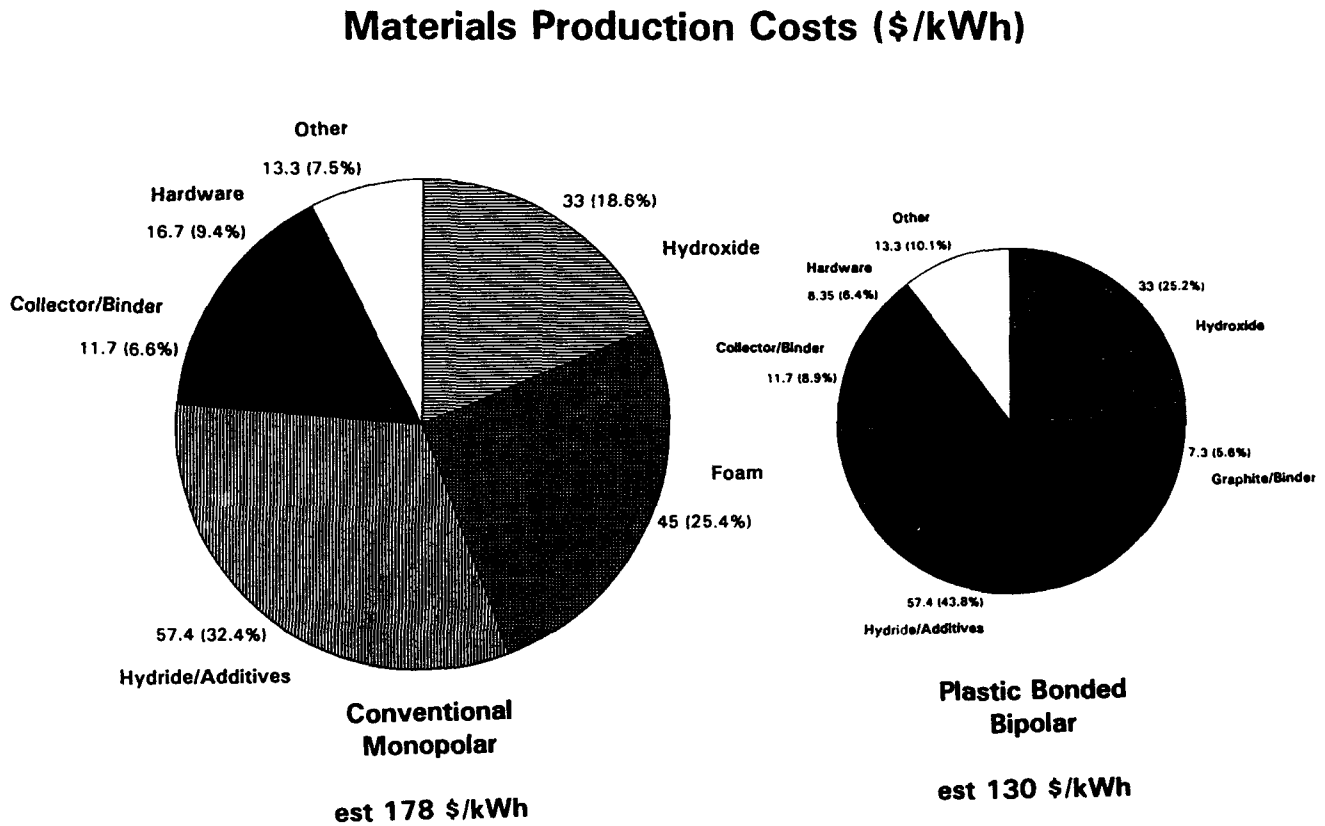

Fig. 8. Estimated Ni-MH Battery Material Production Costs Conventional vs. EEI Bipolar

RECHARGEABLE BIPOLAR LEAD/FLUOROBORIC ACID BATTERY

Gerhard L. Holleck, John P. Hachey and Ernest A. Morin
EIC Laboratories, Inc.
Norwood, Massachusetts 02062

Abstract

Progress in the development of rechargeable bipolar Pb/HBF_4/PbO_2 batteries is reported. High rate operation and excellent low temperature performance delivering ~60% of the room temperature capacity at -50°C have been demonstrated. At the present state of development gas management and capacity fading during extended cycling are the main limitations.

Introduction

For various airborne and/or space borne weapons systems the U.S. Air Force requires power sources which can supply pulsed power at power densities greater than 50 kW/kg. The U.S. Air Force uses batteries also on board of its aircraft to supply power for engine starting and to support a variety of electronic functions. These batteries must be able to operate in very cold weather down to -55°C. They must be capable to deliver high power and in the context of the more electric aircraft also high voltage. Available battery technology is clearly power limited. Here, the newer high energy density battery systems offer no advantage over more well established batteries, for example, the lead acid systems (1).

Lead/lead dioxide fluoroboric acid batteries are used by the military as an inexpensive reserve type primary battery in applications requiring high discharge rates over a wide temperature range (e.g., proximity fuzes (2,3)). Beck (4,5) demonstrated that the system can be electrically recharged using graphite based electrode substrates. Earlier work in our laboratory established the general feasibility of a secondary bipolar Pb/HBF_4/PbO_2 battery for high pulsed power (6). The Pb electrode was particularly well behaved allowing extremely high discharge rates. The reduction of PbO_2 is more complicated and was performance limiting. In the present investigation we identified and quantified aspects of particular importance for the realization of practical bipolar Pb/HBF_4/PbO_2 batteries including oxidation of cathode substrates, capacity fading upon cycling and gas accumulation in the cells.

Battery Concept

To achieve high power densities, and to function effectively at low temperatures, an electrochemical couple, and the battery constructed from it, must satisfy the following requirements:

- Rapid electrode kinetics without passivation
- Thin layer construction
- Highly conducting non-freezing electrolyte
- Bipolar battery configuration

The bipolar rechargeable Pb/HBF_4/PbO_2 battery as schematically illustrated in Figure 1 satisfies all of these conditions and has the potential to achieve a power density of 100 kW/kg and an energy density of 30 Wh/kg in an optimized practical configuration. The battery is unusual in that it uses two electrodes of the first kind. The reaction product for discharge of both electrodes is the same, $Pb(BF_4)_2$, a highly soluble salt in the fluoroboric acid electrolyte. On charge, Pb and PbO_2 are plated back onto the substrates from the common electrolyte according to the following overall equation.

$$2Pb(BF_4)_2 \rightleftharpoons Pb + PbO_2 + 4HBF_4$$

The standard potential of the Pb/HBF_4/PbO_2 couple is 1.59V with the PbO_2 electrode 0.23V less positive than in sulfuric acid electrolytes. The lower potential for PbO_2 should allow the use of graphite as an electrode substrate which would be too readily oxidized in sulfuric acid. Graphite felt and a graphite-filled polymer membrane could then be used as substrates for PbO_2 and Pb. The battery stack illustrated in Figure 1b consists of a repeating sequence of a graphite-filled polymer membrane, a porous polypropylene separator, and a graphite felt layer. The graphite-filled polymer membrane serves as the substrate for the Pb electrode and as the current collector in the bipolar arrangement. The graphite felt provides a three-dimensional, enhanced surface area substrate for the PbO_2, which has the slower kinetics of the two electrode materials. The pores also provide the space needed for the electrolyte.

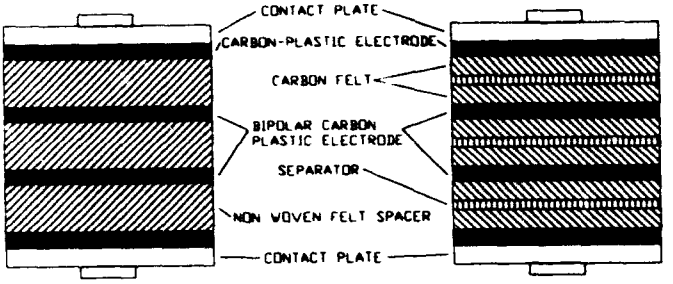

Figure 1. Schematic illustration of bipolar 3-cell Pb/HBF_4/PbO_2 battery configurations.

In principle, the battery can be assembled by simply stacking the individual components. The plastic bipolar substrates can be joined via a heat seal to a plastic gasket bridging the electrolyte space at the periphery. Thus, an integral battery closure is achieved. The battery is then activated through small openings by vacuum filling from a single electrolyte reservoir. In this discharged state, the battery generates no voltage and hence presents no high voltage problems in handling. This is in strong contrast to the difficulties encountered in activating other thin film bipolar arrays which may have voltages up to 200 V/cm. Upon charging, Pb and PbO_2 are plated onto the substrates and HBF_4 is generated in the electrolyte. The result is an active, multicell, bipolar battery generating about 1.6V per cell.

Experimental Procedures

Single cells and bipolar three-cell battery prototypes of the configuration shown in Figure 1 were evaluated in laboratory test fixtures. A typical arrangement is shown in Figure 2. The electrochemical cell was of circular geometry with an active electrode area of 5 cm^2. The electrolyte cavity was defined by a nonconducting rubber gasket and contained various highly porous spacer components, e.g., carbon felt (Technimat 6100-100, Lydall Technical Papers), carbon cloth (Panex PWB-6, Zoltek Corp.), nonwoven polypropylene mat (FS2107, Freudenberg). The separator was a microporous wettable polypropylene (Celgard 3401, Celanese) sandwiched between rubber gaskets. As electrode substrates we used in all cases a highly conductive carbon filled plastic film, based on a PVC copolymer, manufactured by James River Graphics. It was used as 0.005 and 0.010 cm thick film and for the end electrodes also as laminate bonded to aluminum foil. Thin gold coatings were applied to the substrate either by dc magnetron sputtering or by electroplating (Orotemp 24, Technic, Inc.) Intermediate palladium layers were deposited from Pallaspeed DW (Technic, Inc.)

The cells were activated by vacuum impregnation with electrolyte through polyimid microtubing penetrating the rubber gasket. The tubing was subsequently sealed with hot melt adhesive. The electrolytes: 2M $Pb(BF_4)_2$ 1M HBF_4 and 3M $Pb(BF_4)_2$ 1M HBF_4 were prepared from HBF_4 (48-50% solution, Spectrum) and $Pb(BF_4)_2$ (50% solution, Riedel-deHaers). The three molar electrolyte was obtained by water removal under reduced pressure. The cell and battery test procedure consisted primarily of galvanostatic cycling between set voltage limits using an in-house built cycler and a multichannel data acquisition system (BT 8000). A summary of the cell construction and operating variables is shown in Table 1.

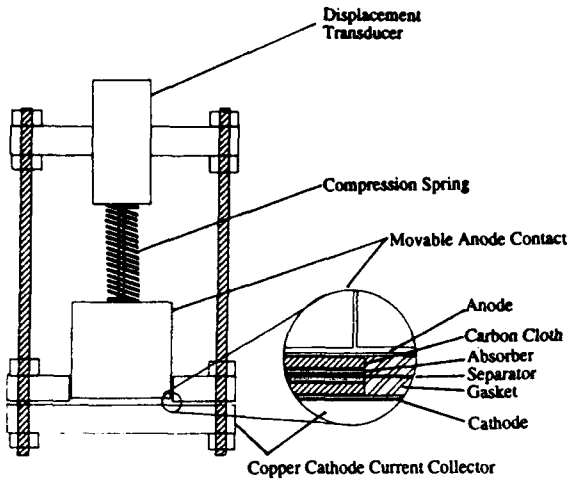

Figure 2. Experimental test arrangement for $Pb/HBF_4/PbO_2$ cells and batteries.

Table 1. Listing of Cell Construction and Operating Variables.

Cell Construction Parameters:	
Carbon Electrode Substrate:	Sheet, felt, cloth
Electrode Spacing.	0.07 to 0.15 cm
Electrode Surface:	C, Au
Cell Configuration:	Divided, undivided
Electrolyte Conc.:	2M $Pb(BF_4)_2$ 1M HBF_4; 3M $Pb(BF_4)_2$ 1M HFB_4
Electrolyte Additives:	None, 0 to 10 mM $Ni(NO_3)_2$
Cell Operating Parameters:	
Charge Mode:	Galvanostatic, pulsed
Charge Current:	2 to 20 mA/cm^2
Charge Voltage Limit:	2.2 to 2.7V
Discharge Current:	2 to 500 mA/cm^2
Discharge Rate:	1 to 200 C rate
Open Circuit Stand:	0 to 90 h
Temperature:	30 to -52°C
Monitored Test Parameters:	
Cell Voltage	
Electrode Potentials	
Cell Capacity	
Cell Resistance	
Gas Generation	

Quantitative measurements of gas generation and consumption in the hermetically sealed cell were achieved via a movable piston coupled to a linear displacement transducer (24 DCDT-050, Hewlett Packard) giving a resolution of ~0.001 cm.

Electrolyte conductivity was measured at 1000 Hz using a YSI conductivity bridge (Model 31) and a commercial dip cell (YSI #344)). A clear (unsilvered) dewar permitted temperature control and solution observation to identify the onset of crystallization. Characteristic results are summarized in Figure 3. With 7.5M HBF_4 and 3M $Pb(BF_4)_2$ 1M HBF_4, no phase separation was observed over the measured temperature range. Ice crystallized from the other solutions starting at the indicated temperatures. In contrast the lead salt precipitated from a four molar solution at about 10°C.

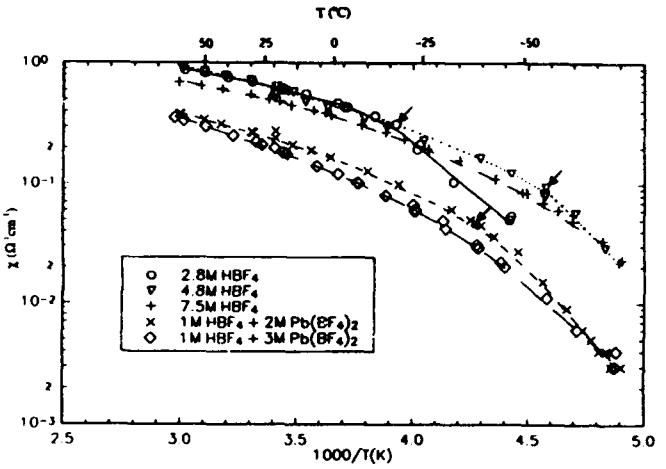

Figure 3. Solution conductivity as a function of temperature for various electrolytes. Start of ice formation marked by arrows.

Results and Discussion

Results

The typical charge-discharge behavior for a $Pb/HBF_4/PbO_2$ battery (configuration b in Fig. 1 with gold coated cathode) is illustrated in Figure 4. The initial PbO_2 formation occurred at a high overvoltage. During discharge some lower oxide remained at the cathode substrate surface conditioning it favorably for the following charge which now occurred at a lower potential (midcharge cell voltage ~1.9V). This also completely eliminated oxygen evolution during charge if overcharge was avoided by charge termination below 2.3V. Some oxygen generation was, however, identified during discharge, especially during early cycles and after battery regeneration as can be seen in Figures 4 and 5. In general, the gas was gradually consumed by diffusion to and reacting at the lead anode. In this specific battery gas consumption was particularly sluggish. Gas chromatographic analysis revealed ~40% O_2, 35% CO and ~25% CO_2 indicating carbon oxidation. Low temperature performance was excellent as shown in Figure 6. The capacity at 100 mA was about 60% and the cumulative capacity 70% of that obtained at room temperature. During cycling we encountered a gradual decrease in capacity. The "lost" capacity could be fully recovered during low rate discharge at about 0.7V. A partial discharge continuation is shown in Figure 7. Following "reconditioning" via complete discharge the original battery performance was restored although the rate of capacity fade was somewhat accelerated probably due to a degradation of the substrate surface quality by remaining reaction products.

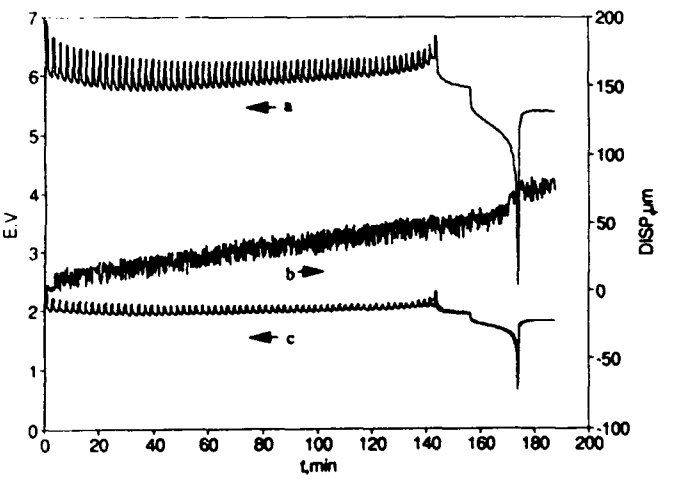

Figure 4. Charge/discharge cycle of battery A. Cycle 1, charge 100 mA for 0.1 s followed by 0.4 s rest, discharge 100 mA. a, battery voltage; b, cell voltage; c, cell stack expansion (piston displacement).

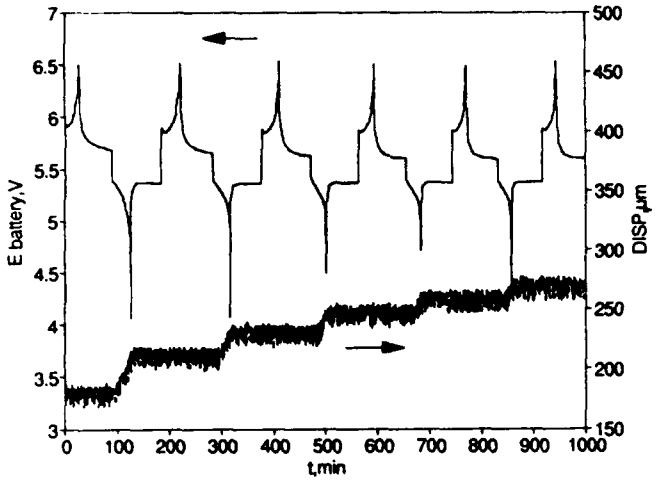

Figure 5. Voltage and displacement of battery A during a test sequence following a complete discharge. Charge and discharge at 25 mA separated by rest periods, cycles 51 to 55.

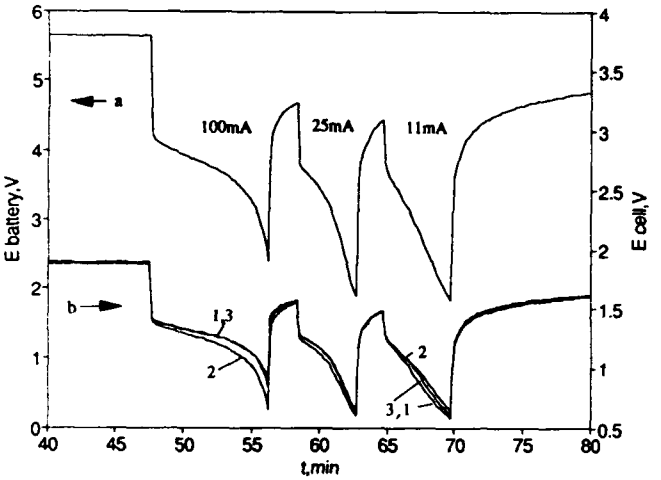

Figure 6. Discharge of battery A at -52°C. a, battery voltage; b, cell voltages.

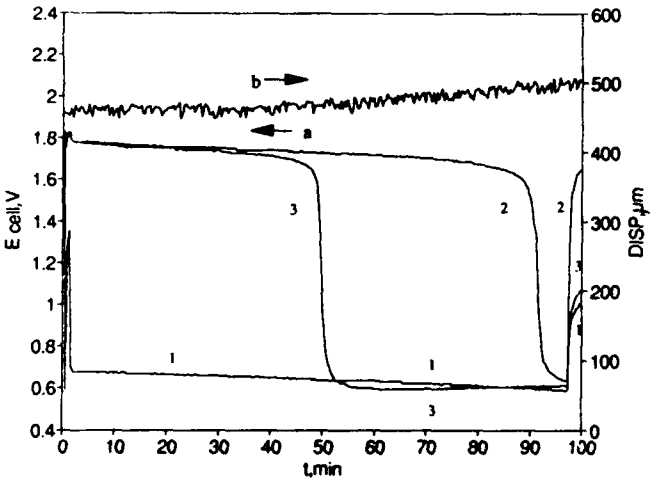

Figure 7. Cell voltage, a, and displacement, b, during continued discharge of battery A, 10 mA, cycle 45.

Discussion

During this investigation we identified the following as critical subject areas:

- Materials stability
- Gas generation and accumulation
- Capacity maintenance during cycling

Materials Stability: The main difficulty arose from the combination of a high acid concentration (7M HBF_4) and a very oxidizing cathode environment in the cell. The carbon-plastic substrate was oxidatively attacked at the cathode resulting in a highly resistive interface layer leading to cell failure via excessive polarization. We identified the formation of graphite oxide at the substrate surface as the cause. In an effort to protect the substrate surface we found gold to be stable in the electrolyte at the cathode potentials. Thin gold coatings deposited onto the carbon plastic substrate greatly enhanced cell performance but eventually failed due to electrolyte penetration between the metal and the carbon substrate. Further development resulted in a well performing stable bipolar carbon plastic electrode substrate of which the cathode side was coated with a thin palladium under layer and a gold overlayer.

Gas Generation and Accumulation: In a hermetically sealed, thin layer bipolar battery no gas accumulation can be tolerated. The corrosion rates of Pb and PbO_2 in HBF_4 are very low but gas would be generated during overcharge of the cell. While O_2 will react with Pb the reaction of H_2 and PbO_2 is very slow. The conventional approach to assure O_2 evolution only by state of charge adjustment cannot be used because both active materials are formed simultaneously from the same electrolyte. However, since overvoltages for H_2 and O_2 generation are high charge termination by cell voltage is practical.

More cumbersome was the generation of oxygen at the cathode during discharge. The amount and rate of gas generation was found to depend on the discharge parameters and especially on cell history. It was greatest at the beginning of cell life and after regeneration via full discharge. It decreased upon cell cycling. This gas generation could be accommodated if sufficient time was allowed for diffusion to and reaction at the anode. The use of dry separators to accelerate gas transport is not applicable in the present system because capacity and discharge performance are directly linked to the amount of electrolyte. Furthermore, we found it necessary to insert a microporous separator (e.g., wettable Celgard) to prevent soft shorting between anode and cathode via Pb dendrites or colloidal lead oxides. Substantial gas generation, e.g., by overcharge or continuous cycling required an overnight rest period for gas consumption.

Carbon substrates at the cathode potential were slowly oxidized. This resulted in the formation of CO and CO_2 as gaseous species. These gases will not be reduced and accumulate in a sealed system gradually degrading its performance and limiting the useful life. Our results suggest that the presence of CO inhibited also the reduction of oxygen at the Pb electrode. While the oxygen liberated during discharge was consumed on charge in the battery without exposed carbon at the cathode it mostly accumulated in the battery with a carbon cloth substrate.

Capacity Maintenance during Cycling: During charge essentially all ionic lead was converted to Pb and PbO_2. Thus, the theoretical and maximum experimental charge capacity was directly proportional to the Pb^{2+} concentration in the electrolyte. The low rate charge efficiency was near 100% in the 2M and only slightly less in the 3M $Pb(BF_4)_2$ electrolyte.

During battery discharge we realized 60 to 80% of the charge capacity. In subsequent cycles the charge capacity was only slightly larger than the discharge capacity and in later cycles the charge in each half cycle became nearly identical. The capacity generally decreased markedly upon continued cycling. Three main mechanisms have been identified as responsible for this effect: 1) Electrode shape change, 2) active material isolation, and 3) accumulation of PbO_x intermediates.

During cell cycling in vertical orientation, we observed the concentration of active material, both Pb and PbO_2 towards the bottom of the cell. This was caused by electrolyte convection due to density gradients during plating and dissolution. In undivided cells this would invariably lead to cell failure via shorting. The phenomenon is similar to that encountered with Zn electrodes in alkaline electrolytes. This problem could be completely eliminated by horizontal orientation of the cell, the use of nonwoven absorber mats and a layer of microporous separator between the anode and cathode compartments.

Active material isolation occurred at the anode and cathode. The former resulted from dendritic or highly porous Pb deposits, which, especially during high rate discharge, dissolved preferentially close to the substrate leaving islands of Pb deposits in the polypropylene absorber mat. Pulse charging and the use of three dimensional conducting substrate matrices (e.g., carbon felt) minimized this effect. Charge termination prior to complete Pb^{2+} ion depletion at the substrate surface would also reduce dendritic deposits but is difficult to implement in a practical battery without compromising energy density.

Active material isolation at the cathode was observed with carbon substrates due to substrate oxidation and formation of highly resistive graphite oxide at the substrate-PbO_2 interface. We solved this problem by protecting the carbon-plastic substrate surface with a thin coating of Pd and Au. Within our test experience this modified substrate was found to be completely stable in the cell environment.

The third mechanism for loss of useable capacity during continued cycling was related to chemical and electrochemical changes at the cathode. The cathode reaction appeared to be quite complex. This was unexpected since in highly acidic solution, cathodic dissolution of PbO_2 must be essentially a heterogeneous process, which means the lattice is dissolved electrochemically layer by layer. In our cell tests we found that a cathode, the normally accessible capacity of which had decreased upon cycling, when discharged below the usual voltage cutoff at reduced rate yielded a large flat capacity plateau at about 0.7V vs. Pb/Pb^{2+} with only moderate rate sensitivity. On open circuit the voltage rose to about 1.1V, a clear indication that we were not merely dealing with a poor ohmic connection of the reaction material. The combined capacity of the regular discharge and the low voltage discharge accounted fully for the total cell capacity. Following such a "regeneration" discharge which apparently removed most of the PbO_x material from the cathode the cell behavior resembled that of a new cell. The rate of capacity decline upon further cycling appeared, however, somewhat accelerated in such a regenerated cell. Apparently, some residual material remaining on the substrate acted as a nucleus or catalyst for this change.

The electrode behavior could be explained via the formation of PbO_x species similar to those discussed for Pb conversion by Dawson (7). These are, however, stable only at higher pH values and thus would require large diffusional gradients or protective surface layers which shielded the material from the high proton activity in the electrolyte. Within the scope of this program we have not been able to investigate these mechanistic aspects. If, as it appears, surface layers play a critical role, changes in electrolyte composition (e.g., impurities or additives) may have a large effect in influencing these side reactions. The only electrolyte additive used in our cell tests was $Ni(NO_3)_2$. It appeared to have a beneficial effect. Whether this was due to the NO_3^- ion (the cathode kinetics is rapid in HNO_3) the NO_3^-/NO_2^- redox reaction or the incorporation of Ni into the PbO_2 deposit (5) has not been established.

Conclusions

Our results demonstrate that the $Pb/HBF_4/PbO_2$ system can be operated as a secondary bipolar battery at relatively high rates (4 to 40 C). Low temperature performance was excellent delivering ~60% of the room temperature capacity at -52°C. At the present state of development gas management and capacity fade during cycling are the main limitations. They need to be addressed before practically attractive bipolar batteries can be constructed.

Acknowledgement

This research was sponsored by the Aero Propulsion and Power Directorate, Wright Laboratory, Aeronautical Systems Division (AFSC), United States Air Force, Wright-Patterson AFB, Ohio.

References

1. R. M. LaFollette and D. N. Bennion, J. Electrochem. Soc., 137 (1990) 3693, 3701.
2. F. G. Turrill and W. C. Kirchberger, Proc. 24th Annual Power Sources Conf., May 19-21, 36 (1970).
3. G. D. McDonald, E. Y. Weissman and T. S. Roemer, J. Electrochem. Soc., 119, 660 (1972).
4. F. Beck, H. Bohn, Ber. Bunsenges. Physik. Chem., 79, 233 (1975).
5. F. Beck in "The Electrochemistry of Lead", edited by A. T. Kuhn, p. 64 (1979).
6. G. L. Holleck and B. H. Jackman, J. Electrochem. Soc., 137c (1989).
7. J. L. Dawson in "The Electrochemistry of Lead", edited by A. T. Kuhn, p. 309 (1979).

RECENT DEVELOPMENTS IN BIPOLAR LEAD/ACID BATTERY TECHNOLOGY AT JOHNSON CONTROLS

Douglas C. Pierce
Advanced Battery Engineering
Johnson Controls Battery Group, Inc.
5757 North Green Bay Avenue
P.O. Box 591
Milwaukee, WI 53201

ABSTRACT

The Bipolar Lead/Acid battery currently under development by Johnson Controls Battery Group, Inc. (JCBGI) is ideally suited for high power, high voltage applications were mass and volume are constrained. The lead/acid battery is an attractive candidate for a bipolar design because of its high power capabilities, well-known chemistry, good thermal characteristics, and widespread manufacturing base. The battery currently being developed is projected to provide a 70-90% reduction in mass and volume over conventional lead/acid batteries and a 30-50% savings over JCBGI's earlier bipolar designs. This development program is currently being funded by Wright Laboratories through the More Electric Aircraft Initiative. Recent progress in the areas of composite bipolar substrate development, battery design, and battery performance will be discussed.

INTRODUCTION

The typical lead/acid cell is usually built in a monopolar configuration with number of electrodes connected in parallel. Within the parallel grouping each individual electrode faces at least one plate of opposite polarity. Three or more of these cells are connected in series to achieve nominal outputs of 6 volts or higher. A bipolar battery differs from the monopolar in that each electrode is made of a positive and negative surface mounted back to back on a conductive interface. Between electrodes are placed a glass mat separator. The advantage to the bipolar design is the shorter, more uniform current path which reduces internal resistance and greatly improves the power capabilities of the battery. (Figure 1)

Figure 1

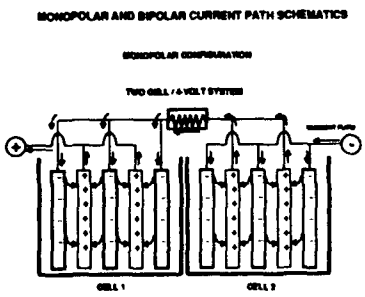

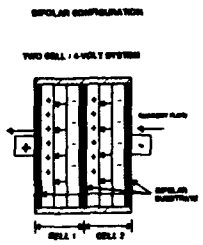

The results of the bipolar advantage can be found in Figure 2. This compares actual discharge discharge data from a quasi bipolar battery and a leading high performance monopolar lead acid battery at the 1 amp/cm^2 discharge rate.

Figure 2

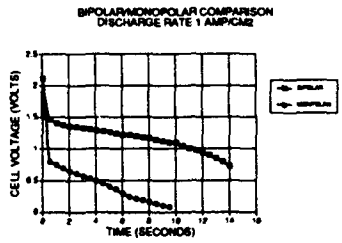

The bipolar design is novel for lead/acid batteries. A lead/acid battery with a laminated lead conductive plastic electrode core was first disclosed by JCBGI as early as 1976. Investigations into this technology continued at a low effort until 1988 when JCBGI was awarded a contract with Jet Propulsion Laboratories through Wright Laboratories to develop a bipolar lead/acid battery. This contract was followed by a DoD contract with JCBGI developing a 430 volt quasi bipolar battery system for the Army that is capable of providing over 100 MegaJoules of energy in the customer specified pulse discharge profile. In September of 1991, JCBGI began second program with Wright Laboratories of 36 months in length, to develop a true bipolar battery for the More Electric Aircraft Technology (BMET) initiative. This program is targeted at introducing the next generation of bipolar lead/acid batteries in September of 1994.

The bipolar lead/acid battery is based on conventional active materials and lead/acid chemistry. The active materials are PbO_2 at the positive electrode and porous Pb at the negative. The two electrode materials are applied on either

side of a conductive substrate and oppose each other across a separator. Both electrodes, and the separator in between them, are nearly saturated with sulfuric acid. The battery incorporates a gas recombinant design where, under normal operating conditions any gas produced in the cell recombines to form water. This eliminates the need for any water addition or battery maintenance. The battery can be designed to include a safety vent that will release excessive gas build up in case of misuse.

Presently, JCBGI has two different bipolar designs under development. The first design is based on electrodes that are made conductive by electrically connecting, through the substrate, the lead grids on either side of the substrate. These electrodes are called "quasi-bipolar" to differentiate them from a substrate that itself is electrically conducting which is called "true bipolar".(Figure 3) The quasi bipolar electrode was designed when a suitable true bipolar substrate could not be developed in the timeframe of the initial contract with JPL. The quasi bipolar design has allowed JCBGI to push forward the technology of bipolar battery development and manufacturing without a true bipolar substrate. While showing obvious power, volume, and weight advantages over monopolar lead acid batteries, manufacturing and cycle life problems limit the future of quasi bipolar batteries for use in many applications.

Figure 3

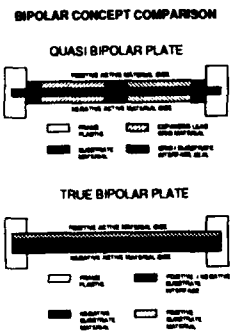

The key to producing a true bipolar battery is the development of a conductive substrate that can withstand the rigors of a lead/acid system. The essential function of the substrate is to provide electronic conduction between the two active materials on each side of the substrate, without permitting ionic conduction, which would short out the cell. The substrate requires not only low resistance, but also chemical stability in sulfuric acid and electrochemical stability at both the positive and negative half-cell potentials. The substrate also must be manufacturable and relatively inexpensive to produce. The substrate requirements are summarized below:

1. Highly Conductive
2. Chemical insolubility in sulfuric acid and in the potential windows of both electrodes.
3. High oxygen and hydrogen overpotentials in sulfuric acid.
4. Inertness to the electrode reactions.
5. Impervious to penetration of the acid electrolyte.
6. Ease of manufacturing and cell to cell sealing.

By developing a true bipolar substrate, the failure mode which caused cycle life problems with the quasi design(ie-grid corrosion) has been removed. The true bipolar design also offers to be much more manufacturable than the quasi design.

JCBGI is currently working with Wright Laboratories on a 36 month contract focussed on developing the true bipolar substrate. Work to date has been very promising. Materials have been identified and proven to be stable in small scale compounding trials. Battery testing results have also been extremely encouraging. Initial work was concentrated on different manufacturing and compounding techniques which will improve the reliability of the substrate material. Optimized compounding parameters will lead to common manufacturing techniques such as extrusion and injection molding. Recent work has been focussed on battery fabrication and testing.

SUBSTRATE FABRICATION TECHNIQUES

The focus of JCBGI's work has been on producing a polymer based bipolar substrate. Resins investigated include LDPE, LLDPE, HDPE, Kynar, and PTFE. Initially these materials were compounded by hand in small batches using a mortar and pestle. This process was very limited in batch size and caused a large degree of variability from trial to trial. The high loading levels needed by some conductive fillers (70-85% by weight) to make the material conductive dictate that special equipment is needed to process the material. JCBGI has been using a twin screw extruder to perform the compounding.

JCBGI began its development using LDPE. The plastic is purchased in powder form which results in a much more uniform dispersion of the filler material and helps eliminate porosity. JCBGI's approach in developing processing parameters was to first prove the stability of the conductive filler, second to optimize part conductivity and eliminate part porosity, and third to reduce part thickness from around 0.070" to 0.015". To prove the stability of the filler, test parts were hand compounded at loading levels of 70-80% by weight, and compression molded to a thickness of 0.070" and stability tested. After a series of successful tests, no change in resistivity after 4 to 30+ days while maintaining a positive potential of 1.5 volts, the emphasis changed towards making the parts thinner, and more conductive.

Because the properties of the filler dictate a loading level of 70-85% by weight is needed to result in part conductivity high enough for use in a battery, JCBGI began investigating additives that would improve the physical properties of the substrate. A number of different additives were thoroughly investigated and only coupling agents were found to provide any real advantage. The others while improving part conductivity, caused additional problems with part porosity.

A series of trials were conducted to optimize the loading level and addition method of the coupling agent. Four different coupling agents were attempted. The coupling agents are used in small quantities, 0.01-1.00% by weight, of the filler. They are designed to bond between the filler and the base resin. The coupling agent improved part conductivity and reduced part porosity at levels between 0.35%-1.00%. At levels higher than

1.00%, the additional material did not offer any improvement over the 1.00% level. It was also found that the order of addition was critical to the performance of the material. It was much more effective to blend the coupling agent with the conductive filler prior to adding the resin.

Most of the development work was done using PE. This material has given JCBGI the best results to date. Recently, JCBGI has also been investigating different resins which would give the substrate more high temperatures capabilities and a more rigid structure. Depending upon the application, the resin with the best properties can be used.

BATTERY ASSEMBLY TECHNIQUES

One of the biggest advantages to using a composite bipolar substrate is the many different options available for cell to cell sealing. Lead sheet substrates have long been investigated for use in bipolar batteries but have obvious drawbacks as far as weight and corrosion. However, the biggest problem with lead sheet may be producing reliable and inexpensive cell to cell seals. A composite substrate, besides eliminating the weight and corrosion concerns, allows one to use any number of inexpensive, existing methods to produce the cell to cell seal.

Both of JCBGI's bipolar designs can utilize the same cell to cell sealing methods. The substrates are designed to be interchangeable in the same tooling. The substrates are first thermally sealed to a non-conductive frame. The electrodes can then be joined together by vibration welding the frames to each other. The plates are stacked on top of each other, with a separator in between.(Figure 4) This allows you to build up the battery voltage in two volt increments without tooling changes. Finally, an acid fill port is then welded into each cell. This method of assembly has been used for all of the quasi battery development with a great deal of success.

Figure 4

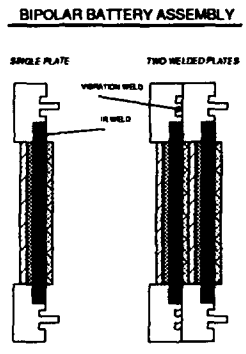

JCBGI has also developed a new, one step sealing technique to replace the initial three step method. This technique performs the initial seal of the substrate to the frame, and the frame to frame seal in one step. In addition the fill port/vent assembly can be designed to be sealed at the same time. The new method eliminates the vibration welding step which has history of dendritic cell failure caused by separator shearing. This improved design also lends itself to be more manufacturable and cost effective than the vibration welding method.

STABILITY TESTING

Stability testing of a bipolar substrate and/or conductive fillers has been developed at JCBGI over many years. The method used for during this development has been the so called "three and four point method" were the bipolar substrate is exposed to a constant potential of 1.5 volts. First, the substrate is sandwiched between the two cells and serves as the working electrode. A constant potential of 1.5 volts is applied to the substrate in the three electrode system were the current is collected at the top of the substrate. After 24 hours the test is switched to a four point test with the current being collected after it passes through the substrate. With the potential remaining at 1.5 volts, the test continues for a minimum of three additional days. Ideally, if the substrate was not porous, the current would remain the same for both the three and four point tests. A rising current during testing would suggest a porous substrate or a non-stable conductive filler.

The second test of the substrate must pass is the conductivity test. The conductivity of the part is measured before and after the stability test. If the conductivity increases more than 10% the part has exhibited either porosity or the conductive filler is not stable. For a conductive filler that is stable, an increase in resistivity would indicate a porosity problem. In parts were the conductive filler is not stable the increase in resistivity is explained by the non-stability of the filler.

BATTERY PERFORMANCE

The quasi design allowed JCBGI to cycle numerous 400 volt bipolar battery strings. This afforded invaluable experience and information regarding packaging, charging, and safe handling of high voltage strings. The 430 OCV strings were packaged in a monoblock container(12"x18"x25") of ten twenty cell batteries in series. The same substrate and packaging design has demonstrated over 100 constant power cycles at two independent locations. Also, the quasi design has demonstrated higher than 1.7 kW/kg in pulse power, laboratory testing at JCBGI.

A bipolar design at JCBGI has demonstrated over 4000+ cycles as well as 3+ amps/in^2 cold crank capability. A composite battery has demonstrated over 150, 100% DOD cycles and 2.5+ amps/in^2 cold crank capability. To date no evidence of substrate failure has been found during post mortem analysis. Conductivity tests of substrates before and after extended cycling have displayed no increase in resistivity. The initial battery testing has clearly shown that the substrate is performing as designed and is able to withstand the rigors of the lead/acid system.

PERFORMANCE PROJECTIONS

Performance projections for the composite and actual test data from quasi battery can be found in the ragone plot in Figure 5. The projections for the substrate were conservative and assumed conventional active materials.

Figure 5

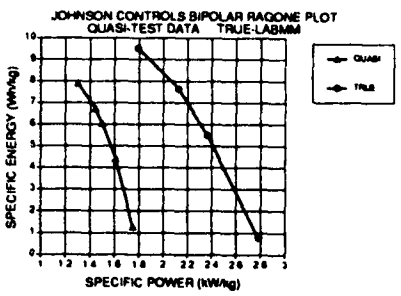

The following table compares the physical characteristics of the composite, quasi and Pb sheet bipolar substrate materials.

Bipolar Technology Comparison

	Pb	Quasi	Composite
Resistivity (Ω-cm)	10^4	10	2
Substrate Thickness (mils)	15	20	15
Substrate Area Density (mg/cm^2)	430	225	130
Failure Modes	Corrosion	Corrosion	None

The composite substrate has a clear advantage over the Pb sheet materials in weight and but not in resistivity. However, computer simulations have shown that battery performance is not extremely sensitive to substrate resistivity for most applications. As the resistivity of the substrate approaches 2 Ω-cm and lower, the change in battery performance at rates as high as 2 amp/cm^2 is negligible.

The composite substrate offers a further advantage over the Pb based materials. The substrate can be specifically tailored in composition for an individual application. Various items can be modified including resin, loading level of conductive filler, and thickness which would obviously change physical characteristics of the substrate. For instance, for a lower rate, energy rich application such as an EV, the loading level of the conductive filler can be lowered to afford a substrate better suited for this application. The loading level could be changed to 70% by weight, which would result in a resistivity of 10 Ω-cm, and an area density of 90 mg/cm^2. The higher resistivity would not dramatically effect battery performance. Also, reducing the weight of the substrate would improve specific energy of the battery system. For higher power applications, the loading level can be increased to decrease the voltage drop across the substrate by making it more conductive.

Using the JCBGI Lead Acid Battery Mathematical Model performance projections can be made for a composite bipolar battery system. Conservative assumptions were made including 0.015" substrate thickness, 2 Ω-cm resistivity, substrate density of 150 mg/cm^2, and conventional active materials performing at 30 ah/#PAM. The following table shows projections for the composite bipolar battery and actual test results for for the quasi design. The energy values are based on the SFUDS profile and power levels are determined at 80% DOD.

JCBGI Bipolar Battery Status

	Quasi	Composite
Power Density (W/L)	946	1350
Specific Power (W/kg)	330	510
Energy Density (WH/L)	122	133
Specific Energy (WH/kg)	38	50

SUMMARY

The Bipolar Lead/Acid battery currently under development at JCBGI shows great promise. While the quasi bipolar design allowed bipolar battery technology to move past many technological hurdles the real future of the battery lies with the composite substrate. A composite bipolar lead/acid battery has been projected to provide specific energy levels of 50 WH/kg and specific power levels of 2.5+ kW/kg. Also, the composite design provides a lightweight, conductive intercell connection which allows for inexpensive and reliable cell to cell sealing methods. Initial market targets have included many government applications such as the More Electric Aircraft for WPAFB, various DoD applications, and Electrical Launch Actuators for NASA. Other applications include automobile batteries, emergency power systems, and electric and hybrid electric vehicles.

ACKNOWLEDGEMENT

The author would like to thank Wright Laboratories, especially Richard Marsh and Richard Flake, for the financial and technological support throughout this battery development. I would also like to thank Dr. Wen Kao, of JCBGI, for answering my endless number of questions and performing all of the computer modeling for this paper.

A New High Rate, Pulse Power, Sealed Lead-Acid Battery

Tristan Juergens, Michael A. Ruderman and Ralph J. Brodd
Bolder Technologies Corporation., 5181 Ward Road, Wheat Ridge, CO 80033

Abstract

A new approach to the design of lead acid batteries has been developed based on the use of very thin lead foil current collectors and very high current carrying capacity. The basic cell construction and the performance characteristics for the new cell are described. Spiral wrap cells based on this electrode concept exhibit extremely high power output with excellent capacity maintenance. Additionally, these cells exhibit flat voltage at all currents, and are capable of very rapid recharge. Applications for this high power technology cover a broad spectrum such as portable power tools, UPS systems, electrically heated catalytic converters, military pulse power applications, engine starting and electric and hybrid vehicles.

Basic Cell Construction

The Thin Metal Film (TMF™) battery technology (1, 2, 3, 4) has been developed at Bolder Technologies. The concept represents a straightforward extrapolation of conventional lead acid technology into a new non-conventional configuration. The original developers of the sealed lead acid gas-recombinant battery technology used thick perforated electrodes and single point current collection (5, 6). This introduced inefficiency in the operation of the cell. The basic element of the present development consists of a thin 0.003" layer of active mass placed on both sides of a solid 0.002" lead foil. The negative and positive active masses have different formulations typical of the industry. The active masses are coated onto the lead foil so as to leave a thin strip of uncoated foil along one edge. The uncoated area forms the contact to the cell terminal. This design produces a 16-19 times increase in the ratio of plate surface area to active material, and a 20-80 times decrease in the path length of the electron flow, when compared to conventional flooded and sealed lead acid batteries. Figure 1 depicts a cross-section of a typical cell. The positive and negative elements are wound together in a spiral wrap configuration with a thin (0.008") glass fiber bibulous separator. The cell is wound in a manner to permit the uncoated strip on the lead foil collector of each element to protrude slightly from the end of the wound cell. Thus, uncoated areas of each plate polarity protrude from opposite sides of the wound cell, similar to capacitor designs. The lead terminals are cast onto the full length of the exposed ends of the spiral wrap cell. The casting serves as a seal, current collector, and manifold for electrolyte distribution. The cell design incorporates a low pressure vent (about 20 psi) into the case. The assembly is then ultrasonically sealed into an ABS housing and vacuum filled with electrolyte.

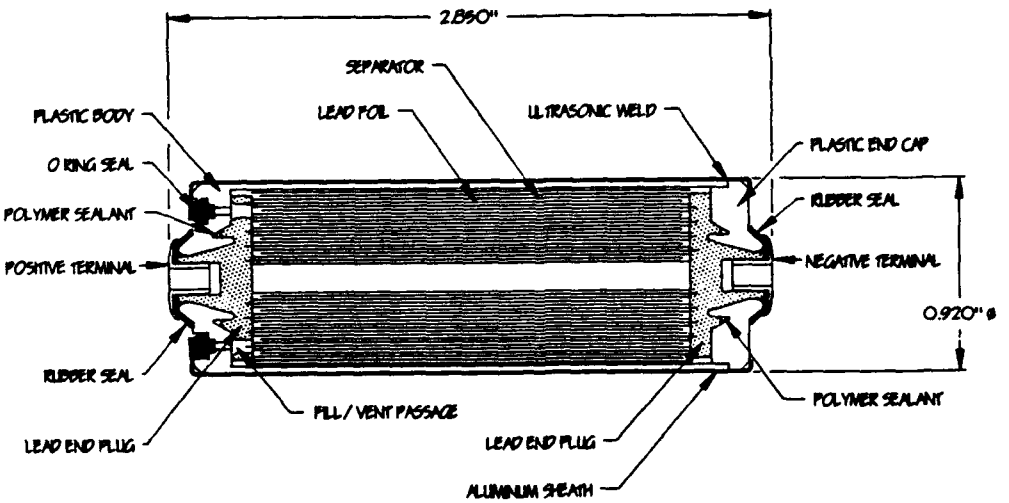

Figure 1. Schematic Cross-Section of the TMF™ Cell.

Performance Characteristics

The TMF™ cell has excellent discharge characteristics. Discharge tests of a 1.5 Ah cell at one, ten and thirty amps yield very flat discharge voltages, even at the 30 amp discharge rate. The voltage is above 2.0 volts for over 50% of the discharge on all three tests. The cells yield over 75% of the low current capacity at the thirty amp rate to a 1.5 volt cut-off.

The use of opposite end current collection produces a uniform current distribution over the electrode surface. The cast-on cell terminal contacts the full length of the current collector. These two key construction features provide a constant low resistance path for current flow across the full electrode surface, combining to minimize cell polarization and increase the operating voltage of the cell. In addition, the low current density and the thin layers of active mass result in high efficiency of utilization of the active materials in the cell, producing excellent cycle life characteristics of over 300 deep discharges and over 15,000 shallow discharges.

The excellent high power capability of the cell follows directly from the cell design and the characteristics of lead acid chemistry. The use of thin metal foil current collectors and thin layers of active mass results in high surface area electrodes. This translates in the cell to a low current density for a given current flow. For instance, at a discharge current of 30 amps, the current density on the electrode surface is about 50 mA/cm^2. The large plate area also reduces the internal impedance of the cell, which is evident in the recharge characteristics as well as the discharge.

The cell can be recharged by any of several regimes, including constant voltage, constant current and constant voltage with a current limit. Figure 2 depicts a typical constant voltage recharge of a 1.2 Ah cell with a voltage setting of 2.65 volts on the charger. A full recharge is accomplished in less than 7 minutes and the cell is 80% recharged in less than 3 minutes. The ability of the TMF™ cell to accept current at very high rates allows flexibility in applications requiring high current discharges followed by rapid recharge.

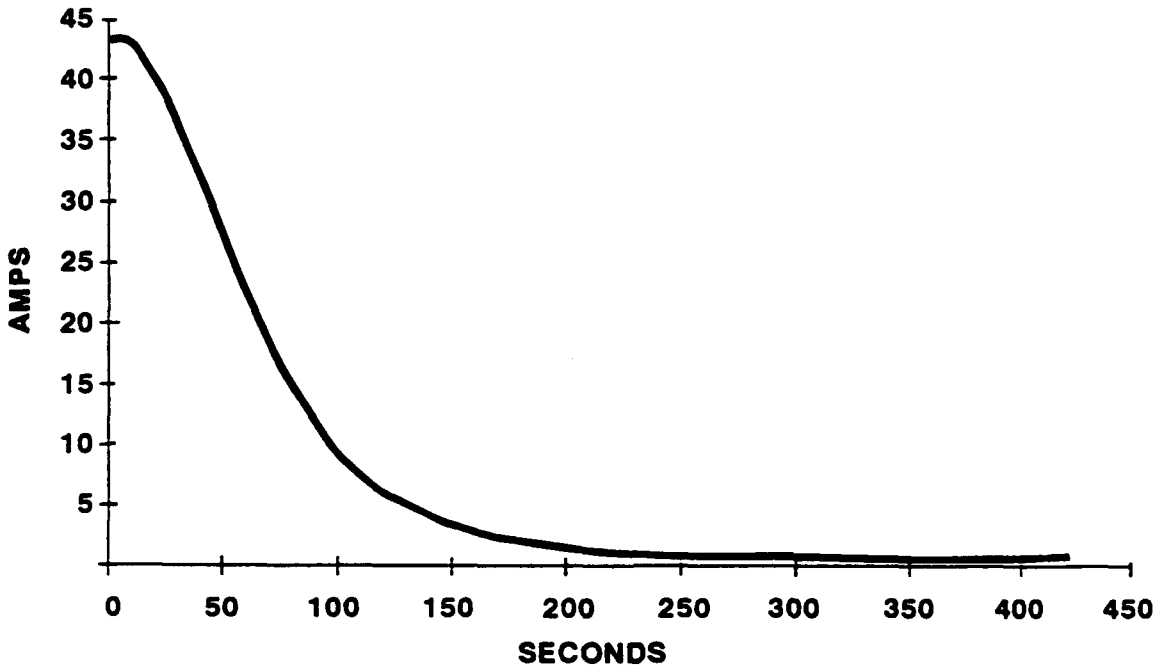

Figure 2. Constant Voltage Recharging of a 1.2 Ah Sub C TMF Cell.

Applications

Figure 3 illustrates the superior discharge profile and voltage maintenance of this new battery. The pulse discharges are modeled after the current profile of an electric drill using a 3/4 in. auger bit in a 2 in. thick redwood board. The constant current load is applied with a 4 sec. "off" and 5 sec. "on" time duty cycle. The "on" time is lengthened as the voltage falls off to maintain a constant energy input. Figure 4 shows the same discharge profile for a standard Ni/Cd pack on the same discharge regime. The TMF™ cell gave 42 pulses while the Ni/Cd battery gave 32 pulses on the same test.

A demonstration of the high power capability of the cell is shown in Figure 5. The peak power performance was determined as a function of depth of discharge according to the USABC procedure (7). The cell delivers peak power of at least 800 W/kg for over 70% of its discharge and gives over 400 W/kg after delivering 90% of its useful life. This is significantly higher performance than any other known battery system now under development. The comparative data in Figure 10 were taken from published reports (8, 9).

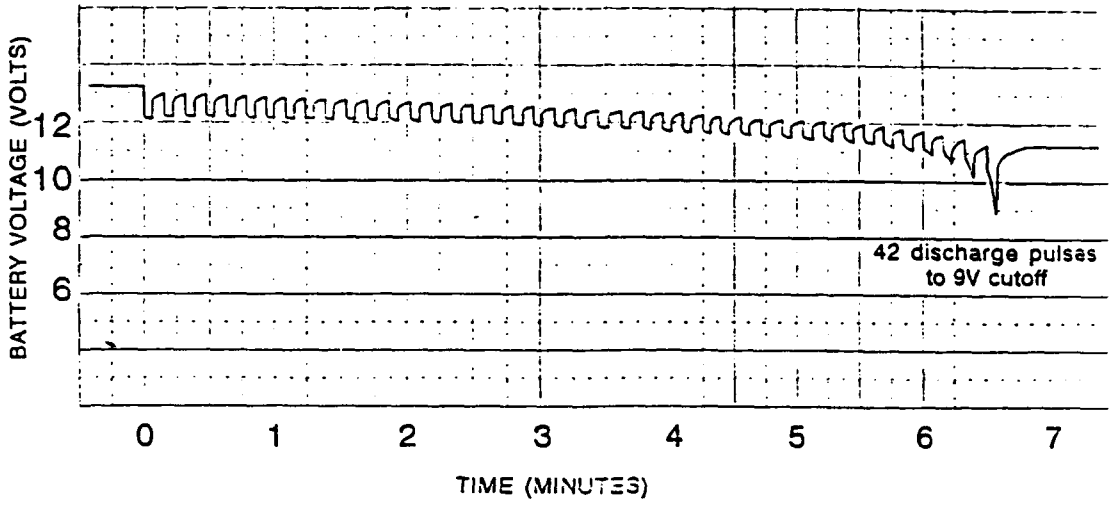

Figure 3. Pulse Discharge of a 12 Volt TMF™ Battery Pack on a Simulated Electric Drill Application.

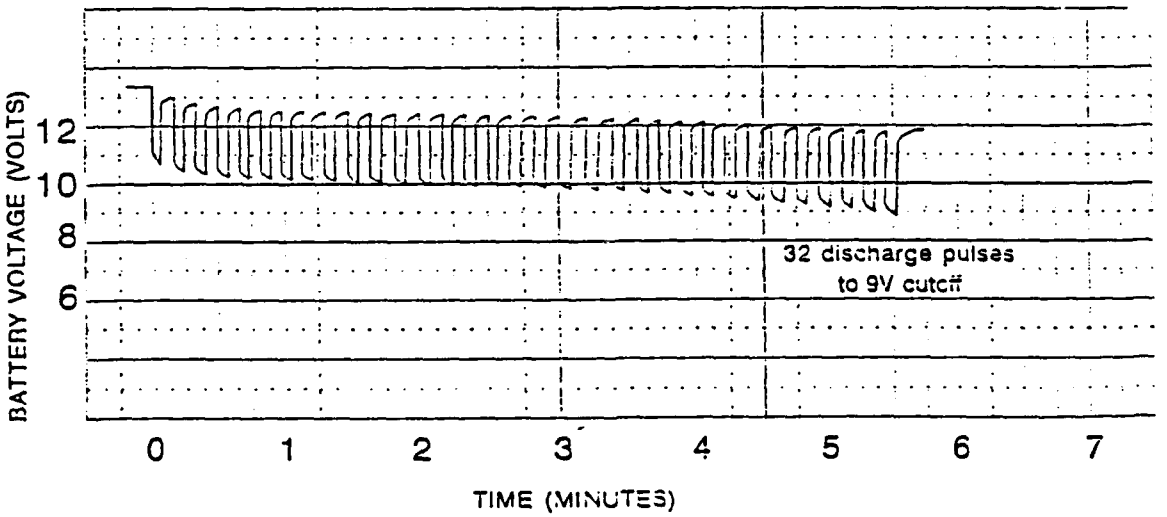

Figure 4. Pulse Discharge of a 12 Volt Standard Ni/Cd C_S Battery Pack on a Simulated Electric Drill Application.

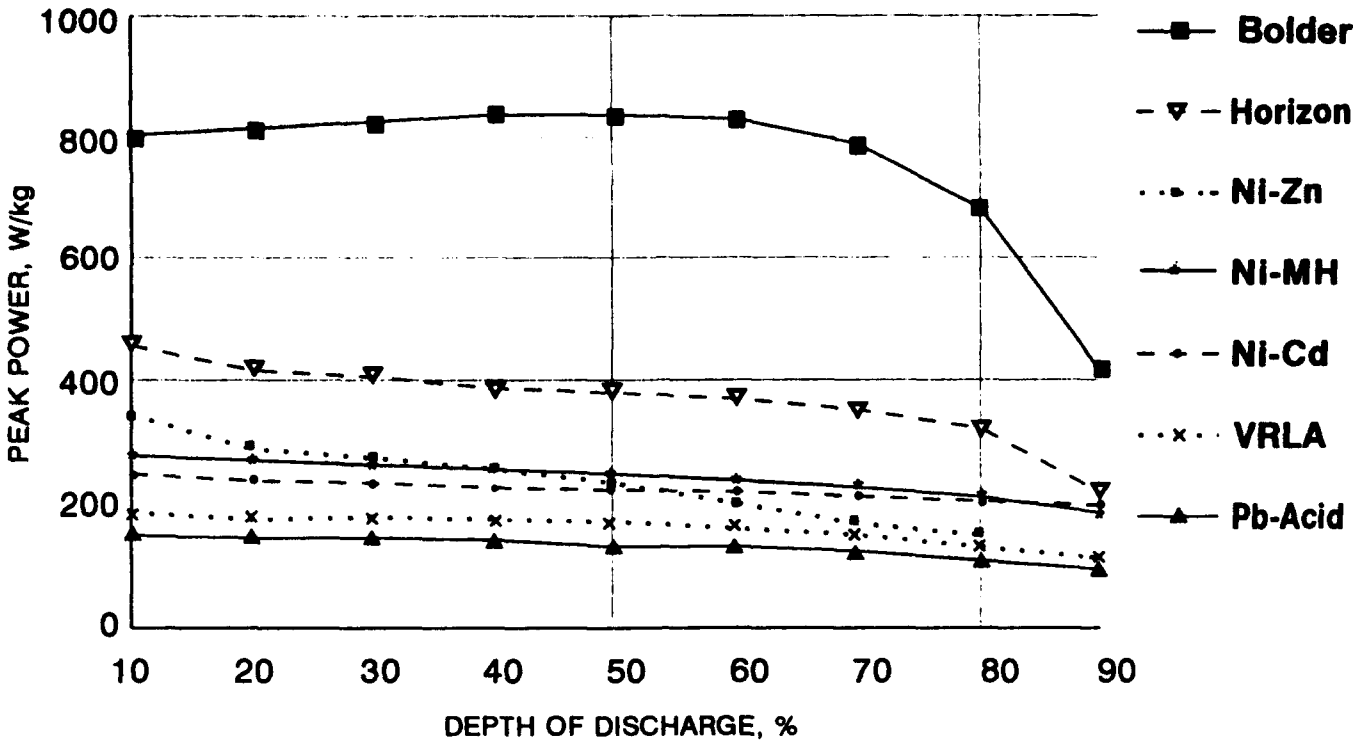

Figure 5. Peak Power Capability of the TMF™ Cell. The Peak Power Capabilities of Other Systems Now Under Development Are Shown For Comparison (8, 9).

Summary

Currently, Bolder Technologies Corporation is producing the Thin Metal Film technology in a 1.2 - 1.5 Ah cell. The basic technology is scalable to both smaller and larger cell sizes with similar performance characteristics. Development work is now underway to produce TMF™ cells in the 10 - 30 Ah range for applications requiring higher capacity unit cells.

References

1. T. Juergens, U.S. Pat. 5,045,086, Sept. 3, 1991.
2. T. Juergens, U.S. Pat. 5,047,300, Sept. 10, 1991
3. T. Juergens, U. S. Pat. 5,198,313, March 30, 1993.
4. T. Juergens, M. Ruderman and R. Brodd, Proc. 9th Annual Battery Conference on Applications and Advances, IEEE, Piscataway, NJ, 1994 , p45.
5. D. McClelland et al, U.S. Patent 3, 3, 862,861, January, 1975
6. D. McClelland et al, U.S. Patent 4,137,377, January, 1979
7. USABC Electric Vehicle Battery Test Procedures Manual, Initial Release, February, 1993
8. W. H. DeLuca, K. R. Gillie, J. E. Kulaga, J. A. Smaga, A. F. Tummillo, and C. E. Webster, Proc. SAE 1992 Future Transportation Conference, August 10 - 13, 1992. (ANL/CF 76681)
9. Technical Summary, Electrosource, Inc.

NEW APPROACH IN THE SYNTHESIS OF POLYMER GEL ELECTROLYTES FOR LITHIUM BATTERIES

Zbigniew Florjańczyk, Ewa Zygadło-Monikowska, Władysław Wieczorek, Wojciech Bzducha, Włodzimierz Krawiec

University of Technology, Faculty of Chemistry, ul. Noakowskiego 3

00-664 Warsaw, Poland

Introduction

The obtaining of systems assuring high ion mobility and at the same time exhibiting good mechanical properties under the working conditions of electrochemical devices is one of the basic problems in the synthesis of solid polymeric electrolytes. Two basic directions can be distinguished in the current studies in this field. The first one is the synthesis of materials capable of stable work at 70 - 120 °C, such as poly(ethylene oxide) blends or crosslinked polymeric matrixes containing polyether segments. The second direction of work leads to the obtaining of materials exhibiting high conductivity at ambient and subambient temperature. Conductivities of the order of magnitude of 10^{-3} - 10^{-5} S/cm has been the goal.

Most of the recent studies in this latter field have dealt with polymer gel electrolytes comprising spatial macromolecular networks, salts and organic solvents.[1-6] They are colloidal systems, in which the organic solvent constitutes 70 - 80 wt. %. In a macroscopic scale the gel behaves like a solid in which the three-dimensional network participates in the deformation process. However, in a microscopic scale in which ion diffusion processes are considered, the gel is a liquid.

The spatial structure may result from specific interactions between the linear polymers chains, e.g. by the formation of hydrogen bonds or micro crystals. However, most often it is formed in a chemical reaction comprising multifunctional monomers or polymer grafting by high energy radiation. These processes are difficult to control and therefore it seems worthwhile to evaluate effective methods permitting the obtaining of gels in two-step processes. First linear polymers would be obtained, which then would be crosslinked as a result of chain polymerization. Such a situation is possible when the monomers used contain functional groups capable of polymerization according to different mechanisms or when the group capable of crosslinking is introduced to the system by the reaction of the previously obtained linear polymer. Two examples of such a strategy are presented in this work. The first one concerns the free radical polymerization of glycidyl methacrylate (GM) in a propylene carbonate and $LiClO_4$ medium and crosslinked by cationic polymerization of the oxirane ring.

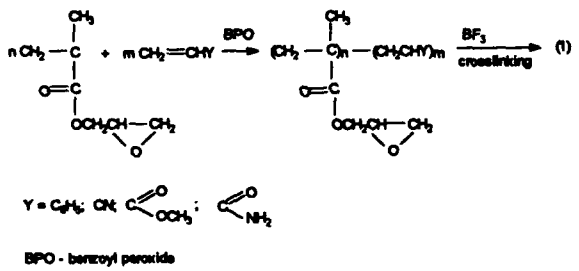

The second method consists in the synthesis of mono conducting gels obtained in the maleic anhydride copolymer with poly(ethylene oxide) glycol derivatives terminated by an allyl group.

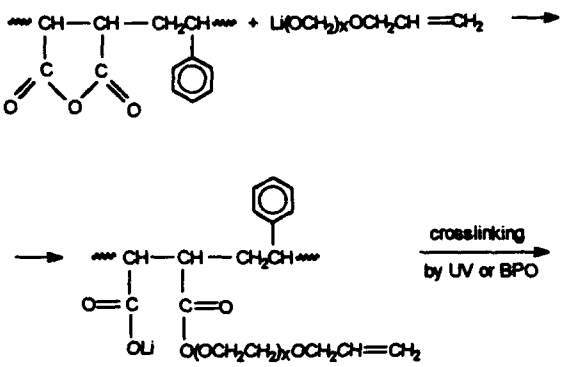

Experimental Procedures

Materials

Monomers, allyl alcohol, DMSO, propylene carbonate and benzoyl peroxide (reagent grade) were purified by distillation. $LiClO_4$ (Aldrich) was dried under vacuum for 24 h at 125 °C. BF_3 etherate (Aldrich) was dissolved in propylene carbonate to form a 20 wt. % solution. *n*-Butyllithium in hexane (15 wt. %, Merck-Schuchard) was used as received. An alternating copolymer of maleic anhydride and styrene was obtained by free radical copolymerization in toluene. The poly(ethylene oxide) glycols terminated by an allyl group were obtained by anionic polymerization of ethylene oxide initiated by NaOH in allyl alcohol according to the general method described elsewhere.[7] The average degree of polymerization was determined by means of ^{1}H-NMR spectroscopy.

Gel Preparation

Method A: Acrylic monomers (~0.3g), $LiClO_4$, propylene carbonate and benzoyl peroxide (0.01g) were placed under nitrogen in glass pressure ampoules and heated at 70 °C for 3 h. The ampoule was then cooled to -78 °C and BF_3 etherate (0.5 wt. % with respect to glycidyl methacrylate) was added. In some experiments additionally 10 cm^3 of acrylonitrile was added and after about 30 seconds the reaction mixture was poured onto Teflon plates, which enabled the obtaining of films. In the other cases the gels obtained were pressed to films between electrodes.

Method B: Maleic anhydride-styrene copolymer (0.5 g) was dissolved in 15 cm^3 of DMSO. The solution obtained was added dropwise to an equimolar amount of poly(ethylene glycol) allyl monoether alcoholate obtained from allyl ether

and *n*-butyllithium. A determined amount of propylene carbonate and 1 wt. % of a free radical initiator or photo initiator were added to the salt obtained. A thin layer of the solution was obtained and the excess of solvents was removed *in vacuo* at 60 - 90 °C. The gels were obtained in the form of a film.

Method C: The solution of the lithium salt obtained as described above was poured onto acidified water. The polymer precipitated was filtered off and purified by dissolution onto water and dried *in vacuo* for 48 h. 0.2 g of the obtained acidic form of the copolymer semiester was dissolved in 3 cm^3 of absolute methanol and converted into a salt by dropping in a *n*-butyl solution. Next, a required amount of organic solvents and initiator were added, a thin layer was poured out and methanol was removed. Gels were obtained by thermal crosslinking at 70 °C for ~1 h or by means of UV radiation.

Conductivity Measurements

AC impedance analysis was used to determine the bulk conductivity of gels. Measurements were performed in the frequency range from 5 Hz to 500 kHz applying stainless steel blocking electrodes. The sample holder was placed in an evacuated glass vessel and vacuum pumped for two hours prior to measurements. The electrode area was equal to 1.5 cm^2 and the sample thickness 0.5 - 1 mm. The samples were kept for 0.5 h at each experiment temperature and was maintained within ± 0.1 °C.

Results and Discussion

Gel electrolytes based on glycidyl methacrylate copolymers

The homopolymerization of glycidyl methacrylate and its copolymerization with styrene or acrylic monomers (presented in Table 1) carried out in propylene carbonate at 70 °C at a 70 - 80 wt. % of the solvent in the presence of 0.5 wt. % of benzoyl peroxide with respect to the monomers is completed after about 2 hours.

Table 1. Conductivity of Gels Based on Glycidyl Methacrylate (GMA) Copolymers with Monomers of Various Polarity[a].

Comonomer	GMA contribution in copolymer mol %	σ_{RT} at 298 K S/cm	E_a kJ/mol
Methyl acrylate	50	2.0×10^{-3}	22.1
Butyl acrylate	50	2.2×10^{-3}	18.4
	50[b]	1.8×10^{-4}	31.8
Methyl methacrylate	30	2.1×10^{-3}	17.1
Acrylamide	50	3.5×10^{-3}	VTF
Acrylonitrile	50	2.2×10^{-3}	VTF
Styrene	60	1.8×10^{-3}	17.6
Poly(ethylene glycol) diglycidyl ether	55	1.9×10^{-3}	

[a] $LiClO_4$: 8 wt. %; propylene carbonate: 80 wt. %; crosslinking agent: BF_3 etherate (0.1 wt. %) (20 % solution in propylene carbonate).
[b] Propylene carbonate: 70 wt. %.

The crosslinking by means of BF_3 etherate was carried out for 15 minutes and IR studies of the gel obtained indicate that all the oxirane rings are practically consumed both in the reactions proceeding at room temperature and at -78°C.

Attempts to obtain stable gels with glycidyl methacrylate homopolymers failed and the polymer formed precipitated in the form of a white solid. The reason for this is the too high crosslinking density and thus too short network segments to successfully bond the solution of the salt and assure elasticity of the system. Stable gels may be obtained when the glycidyl methacrylate monomeric units concentration in the polymer chain ranges between 15 to 60 mol %. Due to the high reactivity of glycidyl methacrylate in free radical polymerization, compounds of high parameter Q values, such as acrylic acid and methacrylic acid derivatives or styrene, should be used as comonomers decreasing the epoxide groups concentration. In Table 1 are presented exemplary ambient temperature conductivity (σ_{RT}) values of gels thus obtained. At a solvent content of 80 wt. % the σ_{RT} values exceed 10^{-3} S/cm. The kind of comonomer used has no essential effect on the conductivity. The highest conductivity values were obtained for systems with acrylamide, which may result from the strongly polar properties of the amide group. The lowest conductivity values were obtained, however, for systems with the least polar comonomer, i.e. styrene. Gels containing 80 wt. % of propylene carbonate exhibit at 0 °C a conductivity of $\sim1\times10^{-3}$ S/cm, at -30° that of above 10^{-4} S/cm, and at -50° that of above 10^{-5} S/cm.

The temperature dependence of conductivity in the 20 - 80 °C range can be analyzed according to the Arrhenius plot (Table 1). It can be noticed that for most of the samples of high propylene carbonate content, the activation energy (E_a) reaches values in the 17 - 22 kJ/mol range. These values are very close to those reported for $LiClO_4$ solutions in propylene carbonate (e.g. ~16 kJ/mol for the optimum salt concentration at 15 °C). Only in some systems with acrylamide and acrylonitrile (Figure 1) the conductivity data are best analyzed using the Vogel - Tamman - Fulcher (VTF) equation: $\sigma = \sigma_0 \times \exp(-B/T-T_0)$, where the pre exponential factor σ_0 is proportional to the activation energy and T_0 denotes the thermodynamic glass transition temperature. As can be seen from Table 2, the T_g values calculated from this equation are very close to the T_g value determined by means of DSC. Thus, the systems studied do not conform to the Addams-Gibbs[8] configurational entropy model developed for solid systems in which T_0 is theoretically predicted to be 50K lower than T_g. This suggests that in gel systems of high solvent content there is no direct relation between the ionic mobility and the motion of polymer network, as predicted by the free volume and configurational entropy theories, but in some systems the chain movements may affect the ion transportation. The values of the pseudo activation energy (B) calculated for these systems are two - three times lower than those reported for solid polymeric electrolytes, e.g. ref. [9,10] DTG studies show that the mass loss up to about 60 °C does not exceed 1.2 %

The conductivity data for several electrolytes based on maleic anhydride copolymers are presented in Table 3. The highest ambient temperature conductivities of above

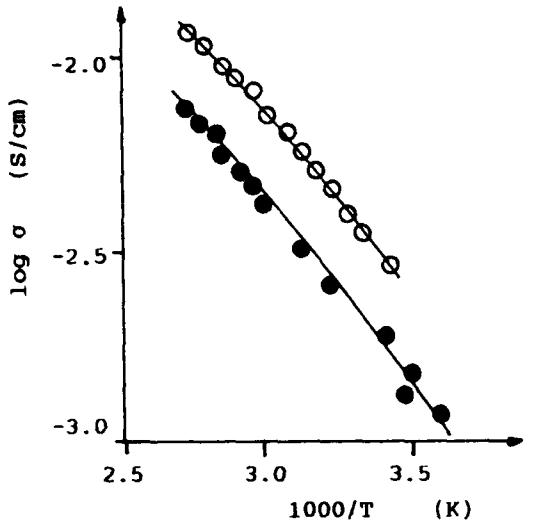

Figure 1. Log conductivity - reciprocal temperatures plots for gel electrolytes based on glycidyl methacrylate copolymers with (•) acrylonitrile and (o) acrylamide. Full lines denote theoretical curves for the VTF equation with parameters given in Table 2.

Table 2. VTF Fit Data and T_g Values for Gel Electrolytes Based on Glycidyl Methacrylate with Acrylonitrile (AN) and Acrylamide (AA).

Comonomer	Temp. range K	A $SK^{0.5}cm^{-1}$	B K^{-1}	T_o K	T_g K
AN	243-369	1.25	435	176	181
AA	291-365	1.92	392	186	188

10^{-4} S/cm are obtained for electrolytes containing three oxyethylene units. The clearly higher conductivity values of these systems than of those where n = 0 indicate that the presence of OCH_2CH_2 units in the side chain has an essential effect on the conducting properties of the gel. Probably even in the presence of the solvents the possibility of internal coordination of lithium ions has a significant effect on the charge carriers mobility and salt dissociation constant. The conductivity decreases with elongation of the oxyethylene chain as a result of a decrease in the charge carrier concentration.

Propylene carbonate and dimethylsulfoxide (DMSO) were used as active solvents of the gels. They constitute 20 - 80 wt. % of the gel. Phase separation of the gel and solvent occurred at higher solvent content. Higher conductivity values are assured when using a solvent mixture than in the case of using systems with one solvent. Systems containing 20 wt. % of DMSO and 20 - 25 wt. % of propylene carbonate seem to be most favorable from the point of view of conductivity and mechanical properties. A further increase in the propylene carbonate content to about 40 wt. % causes only a slight increase in the conductivity of the system. the use of an excess of DMSO causes a worsening of both the mechanical properties and conductivity of the system. We are probably dealing here with a typical for electrolyte chemistry establishing of a certain optimal concentration, determined by a change in the amount and mobility of charge carriers with dilution of the system.

The temperature dependence of conductivity for a majority of systems fulfills the Arrhenius equation and the activation energies determined are of the 22 - 45 kJ/mol range.

Table 3. Conductivity of Maleic Anhydride Copolymers Based Electrolytes.

n[a]	Method of synth.	Plasticizer		Li cont. in	Ionic conductivity	
		DMSO wt. %	PC wt.%	polym. wt. %	25°C S/cm	50°C S/cm
0	C	0	80		$9.0 \cdot 10^{-6}$	$2.2 \cdot 10^{-5}$
	C	30	50		$2.2 \cdot 10^{-5}$	$4.9 \cdot 10^{-5}$
	C	40	40		$1.8 \cdot 10^{-5}$	$7.2 \cdot 10^{-5}$
3	B	10	-	1.76	$1.0 \cdot 10^{-4}$	$2.9 \cdot 10^{-4}$
	B	17	-	1.76	$2.4 \cdot 10^{-4}$	$1.0 \cdot 10^{-3}$
	B	20	20	1.76	$7.7 \cdot 10^{-4}$	$1.9 \cdot 10^{-3}$
	B	21	42	1.76	$8.1 \cdot 10^{-4}$	$2.1 \cdot 10^{-3}$
	C	0	80	1.76	$1.6 \cdot 10^{-5}$	$2.7 \cdot 10^{-5}$
	C	20	25	1.76	$7.8 \cdot 10^{-4}$	$1.9 \cdot 10^{-3}$
	C	20	40	1.76	$8.0 \cdot 10^{-4}$	$2.1 \cdot 10^{-3}$
	C	50	20	1.76	$2.1 \cdot 10^{-4}$	
6	B	20	-	1.32	$2.2 \cdot 10^{-5}$	$8.1 \cdot 10^{-5}$
	B	24	-	1.32	$4.8 \cdot 10^{-5}$	$7.8 \cdot 10^{-5}$
	B	28	-	1.32	$6.1 \cdot 10^{-5}$	$1.3 \cdot 10^{-4}$
7	B	50	-	1.27	$8.6 \cdot 10^{-5}$	$2.7 \cdot 10^{-4}$
	B	22	53	1.27	$1.1 \cdot 10^{-4}$	$2.2 \cdot 10^{-4}$
9	B	20	-	1.06	$7.3 \cdot 10^{-6}$	$3.9 \cdot 10^{-5}$
	B	27		1.06	$2.7 \cdot 10^{-5}$	$1.1 \cdot 10^{-4}$

[a] number of OCH_2CH_2 monomeric units.

For the electrolyte of n = 3 containing 20 wt% of DMSO and 20 wt% of propylene carbonate, investigations were carried out on its stability in the presence of a lithium electrode. We have examined this problem using a.c. impedance spectroscopy of the system comprising a gelled electrolyte sandwiched between two identical lithium metal electrodes.

The ionic conductivity of the sample studied was $8.02 \cdot 10^{-4}$ S/cm at 25°C and $1.78 \cdot 10^{-3}$ S/cm at 50°C giving respective values in relation to the conductivities of the corresponding system of blocking electrodes ($7.7 \cdot 10^{-4}$ S/cm and $1.9 \cdot 10^{-3}$ S/cm, respectively).

In Figure 2 are presented impedance diagrams for a symmetrical Li PGE Li cell at 40 °C. One can easily identify two intercepts on the real axis. The first one at high frequencies may be attributed to the electrolyte resistance (R_E), and the second one at lower frequencies to the resistance of the electrode - electrolyte interface (R_i). From this figure it appears that the resistance of the interface (R_i) increases slightly with time, indicating a relatively slow (but essential) growth of a resistive layer at the interface.

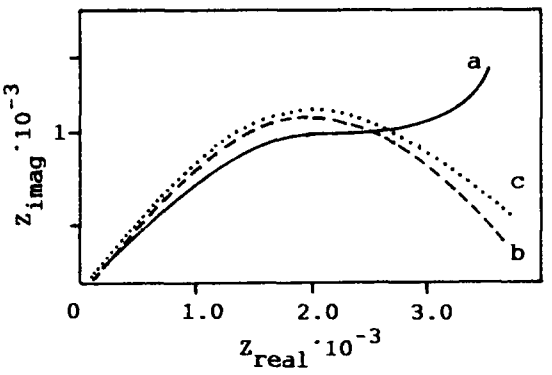

Figure 2. Impedance diagram for a symmetrical Li PGE Li cell at 40°C; a - after 24h, b - 48h, c - 72h.

Since the electrolytes were obtained under carefully controlled water-free conditions, the small passivation layer at the interface cannot be simply related to residual water and formation of an oxide layer. It seems that the effect observed results mainly from a direct reaction between the lithium anode and the electrolyte (especially the plasticizers: propylene carbonate and DMSO). Considering the lithium passivation processes observed in liquid organic electrolyte systems, one cannot exclude that both plasticizers undergo partial conversion to side products in the presence of lithium, which form the passivation layer observed. The results obtained let us suppose that the lithium electrode - PGE interface is affected by passivation phenomena similar to those observed in typical liquid organic electrolytes. Therefore, the selection of an appropriate system of organic solvents considering their stability towards a lithium electrode seems to be an important task in further work. our present studies are devoted to the replacement of DMSO by other organosulfur compounds, and of propylene carbonate by polyethers.

It should be stressed that stable gels based on maleic anhydride copolymers may be obtained also when using other crosslinking groups in side chains of ester groups, or adding multi-functional allyl monomers during crosslinking. A gel of this type checked by us is presented below:

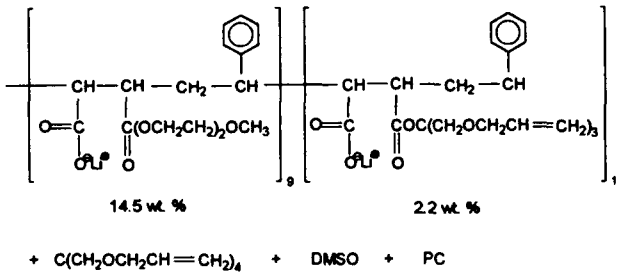

This gel exhibits a conductivity of 7×10^{-4} S/cm at 25°C and activation energy of 17 kJ/mol.

Conclusions

Polymeric gels based on glycidyl methacrylate prepared by the step procedure exhibit one of the highest conductivity values at ambient and subambient temperatures from among the polymeric electrolyte described hitherto. They can be considered as eventual substitutes of liquid electrolytes containing propylene carbonate and lithium salts.

Monoconducting gel electrolytes based on maleic anhydride copolymers are a novel and original system, which seems to be vary attractive due to the low cost of the starting materials. Although the procedure of their synthesis is far from being optimized, the initial ambient temperature conductivity values in the 10^{-4} - 10^{-5} S/cm range and low activation energies seem to be promising.

Acknowledgments

This work was financially supported by the US Department of Defense, Department of the Air Force and Polish State Committee for Scientific Research within the PB/253/3/91 research program.

References

(1) Davous, D., Sebile, B. *Europ. Polym. J.* **1980,** *16,* 347.
(2) Abraham, K. M., Alamgir, M. *J. Electrochem. Soc.* **1990,** *137,* 1657.
(3) Hong, H., Liquan, Ch., Hoejie, H., Rongjian, X. *Electrochim. Acta.* **1992,** *37,* 1671.
(4) Lundsquard, J. S., Yde-Andersen, S. Kokslang, R., Shackle, D. R., Austnin, R. A., Fauteux, D. *Proc. II Int. Symp. on Polymeric Electrolytes,* Siena, **1989,** Scrosati, B., Ed., Elsevier Applied Science, London, New York, **1990,** p. 395.
(5) Huq, R., Kokslang, R., Tonder, P. E., Farrington, G. C. *Electrochim. Acta* **1992,** *37,* 1681; *Solid State Ionics* **1992,** *57,* 277.
(6) Prasad, P. S., Owens, B. B., Smyrl, W. H., Selvaggi A., Scrosati, B. in *Recent Advances in Fast Ion Conducting Materials and Devices* Chowdari, R., Liu, Q. G., Chen, L. Q., Eds., World Scientific, Singapore, **1990,** p. 170.
(7) Gee, G., Higginson, W. C. E., Levesley, p., Taylor, K. J. *J. Chem. Soc.* **1959,** 1938.
(8) Adams, G., Gibs, J. H. *J. Chem. Phys.* **1965,** *43,* 139.
(9) Couvie, J. M., Anderson, A. T., Andrei, M., Martin, A.C.S., Roberts, C. *Electrochim. Acta* **1992,** *37,* 1539.
(10) Mani, T., Stevens, J. R. *Polymer* **1992,** *33,* 833.

Gelioinics for Lithium Battery Applications

G.B.Appetecchi, F.Croce and B.Scrosati
Dipartimento di Chimica, Università 'La Sapienza'
00185 Rome, Italy

In this work we report the results of a systematic investigation on the electrochemical propeties of various highly conducting, gel-type, polymer electrolytes of interest for the development of thin-layer lithium batteries. In particular, the properties and the practical prospects of electrolyte membranes obtained by immoblizing liquid organic solutions of lithium salts in poly(acrylonitrile) and poly(methylmethacrylate) polymer matrices, are illustrated and discussed.

Introduction

Many types of ionically conducting polymers have been developed and characterized in the most recent years[1] . Special interest is today focused on polymer membranes having fast lithium ion transport at ambient and subambient temperatures since they may be exploited as low-resistance separators for the fabrication of high-power, versatile, advanced batteries. Various innovative structures and configurations have been considered for the development of such highly conductive membranes. Generally, the most common concept has been that of trapping liquid solutons into polymer cages. The immobilizaton procedures included UV crosslinking, and gelification and casting. In this paper we describe the properties and the applications of electrolyte membranes obtained by gelification of organic solutions of lithium salts in poly(acrylonitrile) and poly(methylmethacrylate) polymer matrices.

Experimental

Various representative examples of ionically conducting membranes have been considered in this work. Their types and compositions are summarized in Table 1.

Table 1

Type and compostion of gel-type membranes considered in this work.

Sample identification	constituents	molar composition
S-1	PAN-PC/EC-$LiClO_4$	16-23/55.6-4.5
S-2	PAN-PC/EC-$LiAsF_6$	16-23/55.6-4.5
S-3	PAN-PC/EC-$LiN(CF_3SO_2)_2$	16-23/55.6-4.5
S-4	PAN-BL-$LiClO_4$	16-79.5-4.5
S-5	PAN-BL-$LiAsF_6$	16-79.5-4.5
S-6	PAN-BL-$LiN(CF_3SO_2)_2$	16-79.5-4.5
S-7	PMMA-PC/EC-$LiClO_4$	30-19/46.5-4.5
S-8	PMMA-PC/EC-$LiAsF_6$	30-19/46.5-4.5
S-9	PMMA-PC/EC-$LiN(CF_3SO_2)_2$	30-19/46.5-4.5

PAN=poly(acrylonitrile);
PMMA= poly(methylmethacrylate);
PC= propylene carbonate; EC = ethylene carbonate;
BL = γ-butyrolactone.

The preparation of the membranes, as well as the experimental techniques used for their characterization , have been described in previous papers [2,3] to which the reader is referred for further details.

Result and discussion

1.Ionic transport and electrochemical stability.

Figures 1-3 illustrate the Arrhenius plots of the various ionic membranes considered in the present study.

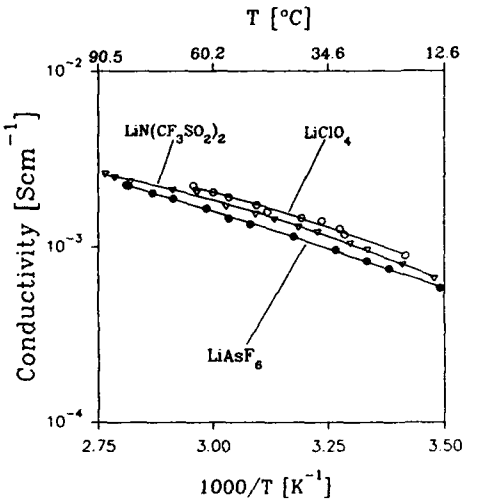

Figure 1-Arrhenius plots of the conductivity of PAN-PC/EC-LiX (samples S-1,S-2 and S-3) ionic membranes.

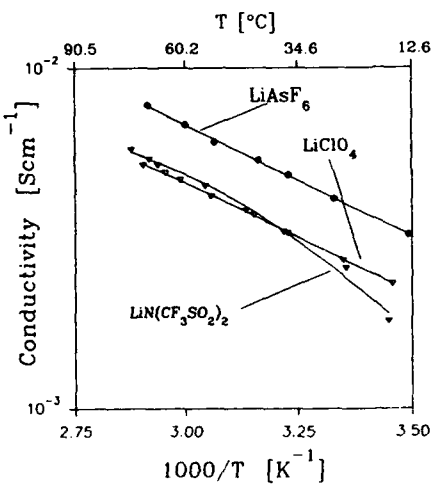

Figure 2 - Arrhenius plots of the conductivity of PAN-BL-LiX (samples S-4,S-5 and S-6) ionic membranes.

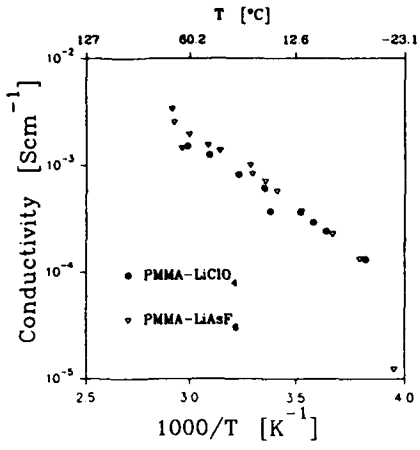

Figure 3-Arrhenius plots of the conductivity of PMMA-PC/EC-LiX (samples S-7 and S-8) ionic membranes.

These plots reveal the most important feature of the membranes which is the exceptonally high ionic conductivity which averages around 10^{-3} S cm^{-1} at room temperature, and 10^{-4} S cm^{-1} at temperatures as low as -20°C. Such fast ionic transport is combined with other key features, such as wide electrochemical stability and high lithum transference number. This is well illustrated in Table 2 which summarizes the electrochemical properties of the various membranes examined in this work.

Table 2

Electrochemical properties at 25 °C of gel-type membranes considered in this work.

Sample electrolyte	conductivity $10^3\,\sigma$ /cm^{-1}	lithium transfer number	anodic stability (V)
S-1)PAN-PC/EC-LiClO$_4$	4.5	0.5-0.6	4.8
S-2)PAN-PC/EC-LiAsF$_6$	4.6	0.6-0.7	4.5
S-3)PAN-PC/EC-LiN(CF$_3$SO$_2$)$_2$	2.0	0.7-0. 8	4.6
S-4)PAN-BL-LiClO$_4$	4.4	0.5-0.6	4.9
S-5)PAN-BL-LiAsF$_6$	6.0	0.6-0.7	4.6
S-6)PAN-BL-LiN(CF$_3$SO$_2$)$_2$	4.0	0.7-0.8	4.7
S-7)PMMA-PC/EC-LiClO$_4$	0.7	0.4	4.6
S-8)PMMA-PC/EC-LiAsF$_6$	0.8	0.6	4.8
S-9)PMMA-PC/EC-LiN(CF$_3$SO$_2$)$_2$	0.7		4.9

From the examination of the data of Table 2 some importatant considerations may be outlined, namely:

i) All the electrolytes considered have comparable transport and electrochemical properties and thus, are interchangeable in terms of these properties. This is a very important aspect since it permits the selection of a system which is the most suitable for a given application. Furthermore, this strongly suggests that the list in Table 2 is far from being exhaustive, and thus by chosing the proper polymer one may immobilize almost any desired liquid electrolyte solution.

ii) The electrochemical stability of the ionic membranes exceeds, on average, 4.5V vs. Li and this demonstrates that they are compatible with high-voltage electrodic couples, such as the Li-V_6O_{13} couple and the Li_xC_6-$LiMO_2$ (M=Co, Ni, Mn...) couple. This makes the membranes suitable for both lithium metal and lithium ion battery fabrication.

iii) The lithium transference number in the ionic membranes is, on average, higher than that usually obtained for the parent pure liquid solutions. This suggests that the role of the polymer component (PAN or PMMA in the case of this work) is much more complex than that of acting as a porous solid support for the liquid solution. Indeed, as discussed elsewhere[4], lithium-7 NMR and dielectric relaxation studies have demonstrated that the polymer component influences the short-range lithium ion mobility and thus, quite likely, also their transference number. Therefore, the term "hybrid electrolytes" often used[5] to classify these gel-type ionic membranes is not fully appropriate. More representative is, in our opinion, the recently proposed[3] term *gelionics.*

Stability of the lithium interface

Detailed investigation based on cyclic voltammetry and impedance spectroscopy [2,3,6] has shown that the lithium electrode is passivated when in contact with gelionic membranes, and that the passivation phenomena affect the electrode cyclability. The extent of passivation varies from case to case which is not surprising since it depends on the level of aggressivity of each given electrolyte component.

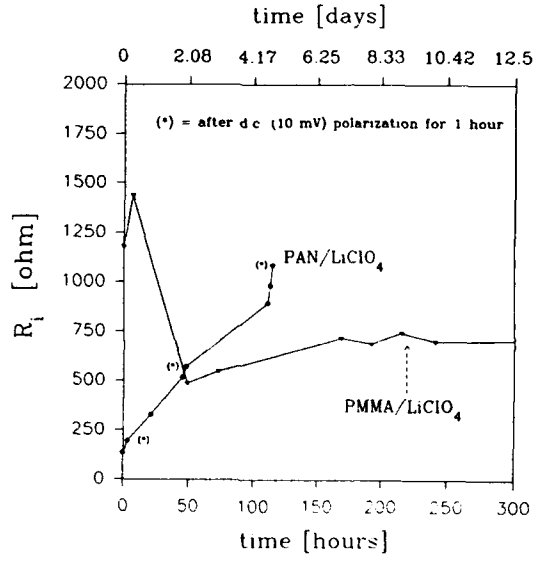

Figure 4- Time evolution at 25 °C of the resistance of the lithium interface in PAN-PC/EC-LiClO$_4$ (sample S-1) and in PMMA-PC/EC-LiClO$_4$ (sample S-7) gelionic membranes. The data in this figure have been obtained by monitoring the impedance response of symmetrical Li/ gelionic membrane / Li cells stored under open circuit conditions.

As an example, Figure 4 compares the time evolution of the resistance of the lithium interface in the two cases of a PAN-based cell and of a PMMA-based cell. The difference in behavior is striking: in the PAN-based medium the resistance continuously increases with a cumulative trend which becomes particularly steep after prolonged time, and which is not even interrupted by occasional current drains; such a dramatic effect is not observed in the PMMA-based medium. The difference in response certainly reflects some major differences in passivation kinetics and thus, in the cyclability of the lithium electrode in the two media. This is confirmed by Table 3 which lists the efficiency of the lithium deposition-stripping process obtained in various PAN-based and PMMA-based cells.

Table 3

Efficiency of the lithium plating-stripping process in gelionics membrane cells at 25 °C. Lithium counter electrode. Stainless-steel substrate.

Sample	type of electrolyte	efficiency (%)
S-1	PAN-PC/EC-$LiClO_4$	72
S-7	PMMA-PC/EC-$LiClO_4$	89
S-8	PMMA-PC/EC-$LiAsF_6$	91
S-9	PMMA-PC/EC-$LiN(CF_3SO_2)_2$	94

Again the data of this table lead to important conclusions regarding practical application prospects of the gelionic membranes considered here, namely:

i)Even for the most favourable cases, the values of the lithium cycling efficiencies are not totally acceptable since they indicate that a consistent fraction of lithium is lost upon cycling. Therefore, the direct use of these membranes as battery separators would require large excess of lithium to assure acceptable (i.e. greater than 500 deep cycles) life to the battery.

ii)Detailed and focussed studies should be carried out with the specific goal of improving the stability of the lithium interface. One approach which has been shown to be quite effective in poly(ethylene oxide) based electrolytes[7] and in PAN-based gelionics[8], may be that of dispersing ceramic powders in the bulk of the membranes. Obviously, other routes should also considered and, particularly, those directed towards the identification of the most stable solvent-lithium salt- polymer combination.

iii) At the present status of (our) knowledge, it appears that if one wishes to successfully exploit the outstanding transport and electrochemical properties of the gelionics membranes, primary lithium metal batteries or lithium metal-free batteries, e.g. rocking chair batteries, should be preferably considered. The validity of this conclusion is presently under consideration in our laboratory by the fabrication and test of thin-layer, plasticlike lithium primary batteries and of new-design, lithium ion batteries.

Acknowledgements

This work has been supported by the US Air Office of Scientific Research, EOARD, under contracts N. SPC-92-4003 and SPC-93-4033. The authors are grateful to Dr. Mark Salomon of the US Army Research Laboratory, Fort Monmouth, N.J., for helpful discussion.

References

1) K.M.Abraham (1993), Applications of Electroactive Polymers, B.Scrosati Ed., Chapman & Hall, London, p. 75
2) F.Croce, F.Gerace, G.Dautzenberg, S.Passerini, G.B.Appetecchi and B.Scrosati, (1994) Electrochim. Acta, in press.
3) G.Dautzenberg, F.Croce, S.Passerini, and B.Scrosati, (1994) Chem.Mater., in press
4) F.Croce, S.D.Brown, S.Greenbaum, S.M.Slane and M.Salomon, (1993) Chem. Mater., 5 p.1268.
5) K.Arbizzani, M.Mastragostino, L.Meneghello, X.Andrieu and T.Vicedo,(1993) Mat.Res.Soc. Symp. Proceedings, vol. 293, p. 169.
6) F.Croce and B.Scrosati, (1993) J.Power Sources, 44, p. 9.
6) K.M.Abraham and M.Alamgir, (1993) J.Power Sources, 44, p.195.
7) B.Scrosati and F.Croce,(1993) Pol. for Adv. Technolgy, 4, p.198.
8) S.Slane and M.Salomon, (1994) in course of publication.

POLYMER-CERAMIC COMPOSITE ELECTROLYTES FOR LITHIUM RECHARGEABLE BATTERIES

Binod Kumar
University of Dayton Research Institute
300 College Park
Dayton OH 45469-0170

and

Lawrence G. Scanlon
Aero Propulsion and Power Directorate
Wright Laboratory
Wright-Patterson Air Force Base OH 45433-7251

Introduction

Solid polymer electrolytes have attracted a great deal of interest. The major motivation for this interest is a technological application - rechargeable and high energy density power sources. The research and development efforts of this decade have contributed significantly toward the identification and definition of issues for further development of solid polymer electrolytes. Ambient temperature conductivity, cationic transport number, electrode-electrolyte interfacial reactions, lithium recyclability, and manufacturability constitute the main issues. These issues need focused attention and satisfactory solutions before solid state polymer batteries become commercially viable.

Polymer-ceramic composite electrolyte is a subset of the general class of solid electrolytes and is continuing to evolve. Only about a dozen papers have been published on this topic. Some of these papers are only exploratory in nature. The purpose of this paper is to briefly review the literature on composite electrolytes, present some preliminary data on polymer-Li_3N composite electrolyte, and then assess the future potential of these electrolytes.

Previous Work

Weston and Steele[1] mixed PEO-$LiClO_4$ polymer complex with α-alumina powder to improve the mechanical stability of these electrolytes. The mechanical stability improved; however, they reported no enhancement in conductivity. Skaarup et al.[2] investigated electrolytes consisting of Li_3N, $LiCF_3SO_3$ and PEO to take advantage of the desirable attributes of inorganic and polymer components of the mixed phase electrolyte. They reported that at small volume fractions of polymers (0.05-0.10) the room temperature ionic conductivity was about a factor of 1,000 larger than that of the single phase polymer and the activation energy for conduction was comparable to that of the inorganic phase. Plocharski and Wieczork[3] investigated PEO-NaI polymer mixed with $Na_{3.2}Zr_2Si_{2.2}P_{0.8}O_{12}$ ceramic powder. They reported at least an order of magnitude increase in the conductivity due to the addition of the ceramic powder which was attributed to an increase in the amorphous phase. Plocharski et al.[4] studied the effect of Al_2O_3 and Nasicon additions in PEO-NaI polymers on conductivity. The conductivity exceeding 10^{-5} S cm^{-1} at room temperature was reported in these composite electrolytes. Skaarup et al.[5] investigated mixed phase electrolyte containing lithium sulphide glasses ($1.2\ Li_2S \cdot 1.6\ LiI \cdot B_2S_3$) and nonconducting polyethylene. Room temperature ionic conductivities of these electrolytes were about 1,000 times higher than that of PEO-based polymer electrolytes. Their results suggested that the polymer phase does not have to be an ionic conducting type polymer and it can be chosen to impart superior mechanical, chemical, and thermal properties. Capuano et al.[6] reported that incorporation of $\gamma \cdot Al_2O_3$ and $LiAlO_2$ in the PEO-based polymer electrolyte increases room temperature conductivity by an order of magnitude. Subsequent work on these composite electrolytes by Croce et al.[7] reported improved lithium-electrolyte interfacial stability. The conductivity enhancement was also reported by Munichandraiah et al.[8] when zeolite was introduced in the PEO:$LiBF_4$ polymer complex. Kumar et al.[9] reported no increase in the room temperature conductivity when a lithium borosulfate glass was incorporated in a PEO:$LiBF_4$ polymer complex; however, the charge transfer resistance decreased by a factor of three due to a small addition of the lithium borosulfate glass. Przyluski et al.[10] investigated (PEO-NaI):SiO_2 composite electrolytes. These electrolytes possessed about an order of magnitude higher conductivity than that of the PEO-NaI electrolytes at ambient temperature. The conductivity enhancement was attributed to a decreased crystallinity which was measured by x-ray diffraction technique. In addition, they also reported improved mechanical and thermal stabilities of these composite electrolytes.

It is interesting to note that most of the reported work has focused on the conductivity, while the main issues in the development of solid polymer electrolytes as pointed out earlier, are conductivity, cationic transport number, lithium-electrolyte interface stability, lithium recyclability, and manufacturability.

Experimental

The composite films were made using reagent grade poly(ethylene) oxide (PEO), lithium tetrafluoroborate ($LiBF_4$), and lithium nitride (Li_3N). The PEO:$LiBF_4$ proportion was used such that the oxygen to lithium ratio was maintained at 8:1. The selection of Li_3N as a ceramic additive to the PEO:$LiBF_4$ polymer complex was based on its reported high lithium ion conductivity[11] and a preliminary experimental report on PEO:Li_3N composite by Skaarup et al.[2] The percentage of lithium nitride varied from 0 to 60%. The ground mixture of the raw materials was compacted in a Carver Press. The compacting parameters, i.e., temperature, pressure, and time, depended upon the composition of the composite electrolyte. Generally, the compacting temperature, pressure, and time were raised as the concentration of Li_3N increased. The compacted composite disc was further thinned on a hot plate between two sheets of teflon, and flattened with a roller. The electrolyte film thus prepared vary in thickness from 0.07-0.15 mm.

Symmetric cells of SS/CE/SS (SS-stainless steel, CE-composite electrolyte) were constructed in a Teflon holder. The cell was contained in an airtight glass vessel with electrical connections. The composite electrolyte film, along with the glass vessel, was annealed between 60-125°C in a helium atmosphere. After annealing the film, electrochemical measurements were conducted in the temperature range 0-100°C using an EG&G Electrochemical System (Model 273A) interfaced with an IBM-compatible computer.

Results and Discussion

The temperature dependence of conductivity of the PEO:$LiBF_4$-40% Li_3N is shown in Figure 1. The figure shows two linear regions intersecting at about 45°C. The room temperature conductivity of this material is approximately $10^{-5.5}$ S cm^{-1}. This conductivity value is approximately an order of magnitude higher than that of PEO:$LiBF_4$ single phase polymer electrolyte. The knee in the conductivity curve signifies a phase transition. For the single phase PEO:$LiBF_4$ electrolyte material, the transition point is approximately 60-70°C and the lowering of the transition point in the PEO:$LiBF_4$-Li_3N composite indicates formation of a chemically distinct, lower melting point phase. The activa-

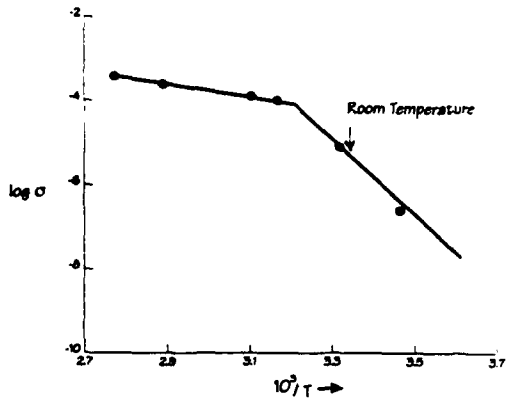

Figure 1. Log σ vs 1/T of PEO:$LiBF_4$-40% Li_3N electrolyte.

tion energy for the lithium transport is significantly decreased above the transition temperature.

Figure 2 depicts the temperature dependence of PEO:$LiBF_4$-50% Li_3N electrolyte. The general features are similar to those in Figure 1. However, the slope of the conductivity curve in the low temperature region was decreased, suggesting lower activation energy for lithium ion conduction. The ambient temperature conductivity is around $10^{-5.7}$ S cm^{-1}. The phase transition temperature of the material remains similar to the PEO:$LiBF_4$-40% Li_3N electrolyte.

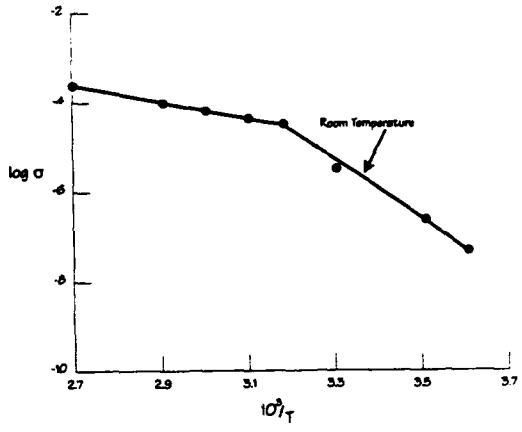

Figure 2. Log σ vs 1/T of PEO:$LiBF_4$-50% Li_3N material annealed at 100°C for 48 hours.

Table 1 presents compositions, ambient temperature conductivity, activation energies (273-323K) and general remarks of the composite materials formulated in this investigation. It is apparent that there is a significant increase in the ambient temperature conductivity as the lithium nitride was introduced in the polymer. The activation energy for lithium ion conduction in the 273-323K varies from 27.2 to 38.81 kcal mol^{-1} with a lack of any consistent trend. In general, the 5% and 25% Li_3N films were easily processed. The films with 40% and 50% Li_3N were slightly brittle and relatively difficult to process.

We intend to analyze the data of this work along with the data reported in the literature on composite electrolytes in view of the first three prevailing issues in the development of commercially viable solid polymer electrolytes; namely (a) conductivity, (b) transport number, and (c) lithium-electrolyte interfacial stability. The analyses would provide a broader view of the attributes and drawbacks of these composite electrolytes. Accordingly, the following discussion is classified into the three aforementioned categories.

Table 1

Compositions and Properties of PEO:$LiBF_4$/Li_3N Composite Electrolytes

Spec. No.	Material Composition	$\frac{\log \sigma \text{ at } 300K}{\Delta E(273\text{-}323K)}$	Remarks
1	95% PEO:$LiBF_4$ 5% Li_3N	$\frac{10^{-6.8}\ S\ cm^{-1}}{27.61\ kcal\ mol^{-1}}$	Easy processing Flexible films
2	75% PEO:$LiBF_4$ 25% Li_3N	$\frac{10^{-6.8}\ S\ cm^{-1}}{27.20\ kcal\ mol^{-1}}$	Easy processing Flexible films
3	60% PEO:$LiBF_4$ 40% Li_3N	$\frac{10^{-5.5}\ S\ cm^{-1}}{38.81\ kcal\ mol^{-1}}$	Slightly brittle films
4	50% PEO:$LiBF_4$ 50% Li_3N	$\frac{10^{-5.7}\ S\ cm^{-1}}{28.04\ kcal\ mol^{-1}}$	Slightly brittle films

Conductivity

Figures 1 and 2 reveal about an order of magnitude enhancement in the ambient temperature conductivity when 40 to 50 percent Li_3N is incorporated in the polymer. Similar results have been reported when $LiAlO_2$, zeolite, SiO_2, Al_2O_3 were introduced in the PEO-based electrolytes. At the same time, there are two reports[1,9] where addition of α-aluminum oxide and lithium borosulfate glass had little effect on the conductivity. It may generally be stated that the ceramic additive in small amounts (< about 50 v%) may have a beneficial but not adverse effect on the conductivity. However, in large amounts (>50 v%) it has an adverse effect.

The mechanism of conductivity enhancement due to these ceramic additives remains uncertain at the present time. The proposed idea that the ceramic additives reduces polymer crystallinity which in turn enhances conductivity appears to have a limited appeal in view of a recent report by Munichandraiah et al.[12] in which they observed no significant increases in conductivity in totally amorphous polymers such as commercial hydrins containing epichlorohydrin repeat units doped with zeolite. The lithium ion conductivity is facilitated in the amorphous phase through the cooperative motion of lithium ion and polymer chains[13]. It is also known that the addition of ceramic particle enhances amorphous phase formation and at the same time raises the glass transition temperature[10] that in turn reduces the segmental chain motion and thereby would have a negative effect on conductivity. Thus, the effects of ceramic additive has two facets: (a) it enhances the volume of the amorphous phase which should help the transport process, and (b) it also increases the glass transition temperature that suppresses polymer chain motion and thus the motion of the lithium ion. These two antagonistic effects of ceramic additive are schematically shown in Figure 3. These effects possibly account for small reported increases in the conductivity. Perhaps the ceramic-polymer grain boundaries structure and chemistry may have an even more important role than the formation of amorphous phase in the electrolyte. The grain boundaries are important because these are the sites of high defect concentration which may allow faster ionic transport. The chemistry and structure of the grain boundaries will be determined by the chemical compatibility between the polymer and the ceramic component. Reactive ceramic such as Li_3N and $LiAlO_2$ may give rise to more defect-rich grain boundaries than the inert ceramic such as SiO_2 and Al_2O_3.

From the preceding experimental data and analyses, it is evident that large increases in conductivity resulting from the addition of ceramic additives is not realizable because of their antagonistic influences on the crystallinity and glass transition temperature.

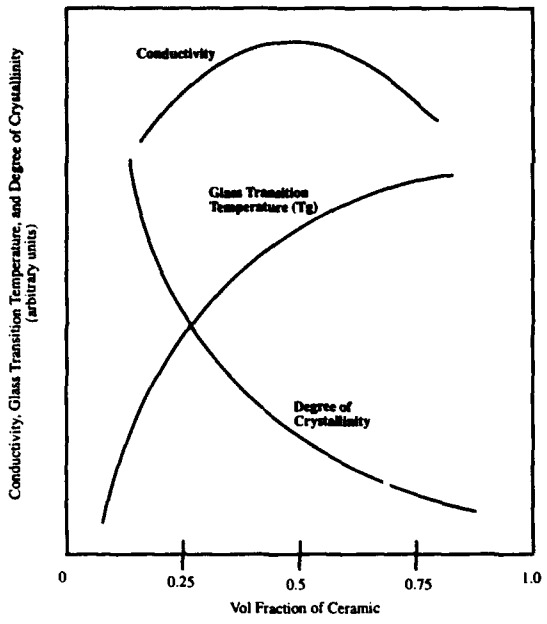

Figure 3. Schematic presentation of conductivity, glass transition temperature, and degree of crystallinity relationship.

Transport Number

The fact that motions of polymer chains contribute to the transport of lithium ion in the polymer electrolytes also has deleterious effects on the transport number. The chain motion also facilitates transport of anionic species and thus the measured conductivity includes contributions from both the species. Some of the polymer electrolytes have cationic transport numbers as small as 0.3[14]. This poses a serious problem for their use in commercial rechargeable batteries. The general observation that solid polymer electrolytes conduct very poorly near or below the glass transition temperature, T_g, remains valid even today and should be an important guideline for future research and development efforts. Above the T_g, polymer chains have significant motion and they remain the primary contributor to the conductivity. Angell[15,16] has analyzed the transport mechanisms in amorphous polymer electrolytes and glassy inorganic solids and generalized the concepts by proposing a parameter known as the decoupling constant, R. The decoupling ratio R is defined as

$$R \approx \tau_s/\tau_\sigma \qquad (1)$$

where τ_s is structural relaxation time and τ_σ is an electrical (conductivity) relaxation time. For glassy inorganic solids, at temperatures below their T_g, R can be of the order of 10^{13}, whereas for polymer electrolytes which are useful above T_g, R can approach or even drop below unity. Typically for solid polymer electrolytes, R is of the order of 10^{-3}, implying three orders of magnitude lower structural relaxation time than the electrical relaxation time.

In general, the decoupling index R is an indicator of the transport number. The larger the value of R, the greater is the cationic transport number. In the polymer-ceramic composite electrolytes, the glass transition temperature increases in proportion to the volume fraction of the ceramic phase. Przyluski et al.[10] reported an increase of 50°C in T_g when 20 wt% hydrophobic SiO_2 was introduced to a $PEO_{10}NaI$ polymer. Angell[15] has shown that at T/T_g=1.2, the R value could be ~10^2 and the transport number could be over 0.9. An increase of 50°C in T_g values in most polymer electrolytes will bring the T/T_g ratio to 1.2 and transport number around 0.9.

The conductivity of polymer electrolytes originates from two distinct processes, i.e., ion hopping and ion transport assisted by polymer chain motion. The measured conductivity is thus comprised of contributions from these two processes. Incorporation of a ceramic additive suppresses the chain motion mediated contribution and thus it must increase the contribution associated with ion hopping such that the conductivity remains the same (the worst case). The ion hopping process is more favorable for cationic species because of its small size and mass than that of the anionic counterpart. This scenario as shown in Figure 4 suggests an enhanced cationic transport number as the volume fraction of ceramic phase is increased.

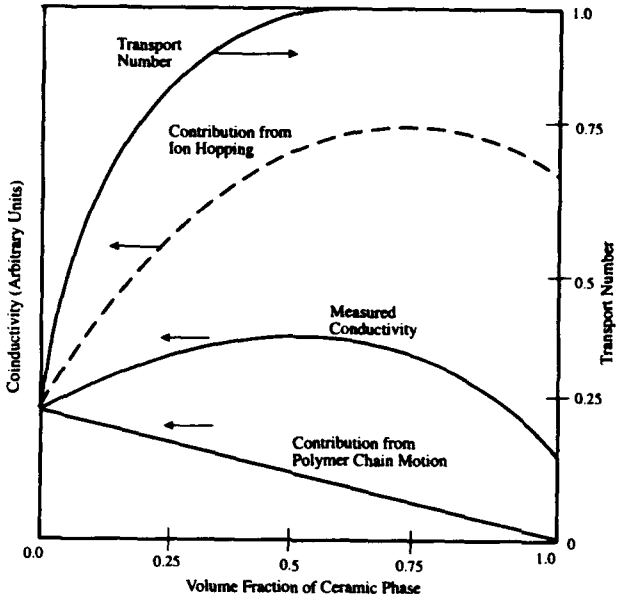

Figure 4. Schematic representation of measured conductivity at ambient temperature, contributions from ion hopping and polymer chain motion, and transport number.

In addition to the aforementioned relationship between the glass transition temperature, decoupling constant, and transport number, there are well-documented experimental data on cationic transport number in solid electrolytes such as β-Al_2O_3, Li_2O-SiO_2, and Li_2O-B_2O_3 glasses. The cationic transport number in these electrolytes is very close to unity. Thus, in polymer-ceramic composite electrolytes although not yet measured, but the theoretical analyses suggest that these materials should have very high cationic transport number.

Interfacial Stability

In a lithium rechargeable battery, the lithium-electrolyte interface is of critical importance. Due to the extreme reactivity of the lithium metal, most of the developed electrolytes passivate lithium. In particular, impurities such as oxygen and water tend to accelerate the passivation mechanism and eventually consume the lithium electrode. The passivation of lithium electrode in non-aqueous-organic electrolyte is a well-recognized and extensively studied phenomenon[17]. Croce et al.[7] have investigated $Li/(PEO)_8:LiClO_4$, $Li/(PEO)_8:LiClO_4$-$\gamma LiAlO_2$, and $Li/PAN\text{-}EC\text{-}PC:LiClO_4$ interfaces using AC impedance spectroscopy. Among the three interfaces, the $Li/(PEO)_8:LiClO_4$-$\gamma LiAlO_2$ interface exhibited the most stable behavior. Croce et al.[7] speculated that the interfacial stability resulted from the scavenging ability of the ceramic powder, γ-$LiAlO_2$ in the electrolyte. Kumar et al.[9] reported suppression of the charge transfer resistance in a $Li/PEO:LiBF_4/Li$ cell by a factor of three when a glass powder of the 0.4 B_2O_3 · 0.4 Li_2O · 0.2 $LiSO_4$ composition was introduced in the polymer electrolyte. The charge transfer resistance is an indirect indicator of the passivation phenomenon and interfacial stability. A few of these symmetric Li/composite electrolyte/Li cells were cycled for over 1,500 cycles at ambient temperature with no obvious problems. Munichandraiah et al.[12] reported that at low

temperatures and low concentrations of zeolite, the exchange current density for Li/Li^+ reaction in a Li/composite electrolyte/Li cell increases. The composite electrolyte consisted of hydrin elastomer doped with $LiBF_4$ and zeolite. The enhanced exchange current density was attributed to the presence of zeolite. The composite electrolytes formulated in this investigation with a composition of PEO:$LiBF_4$-50% Li_3N was also evaluated for Li-electrolyte compatibility. A Li/composite electrolyte/Li cell was cycled at the ambient temperature with a current density of 100 $\mu A\ cm^{-2}$. The flow of current was reversed every hour. The cell functioned for 150 cycles before failure. Although this is a preliminary result, the Li-PEO:$LiBF_4$-Li_3N interface appears to be reasonably stable.

Rechargeable lithium batteries with ceramic electrolytes have been investigated by Bates, et al.[18]. They report virtually no degradation of Li/LiPON glass interface after 5,000 cycles. This result further attests to the ultrastable characteristics of the Li-ceramic interfaces. The electrolyte of the present investigation also contains nitrogen that may form stable oxynitrides and tie up oxygen which is known to passivate lithium.

The experimental evidences are numerous and consistent that the lithium/composite electrolyte interfaces are more stable and efficient than that of Li-polymer electrolyte interfaces. The mechanism for the improved stability and efficiency is not well understood. However, some proposals do exist in the literature and these include scavenging effects of ceramic phase and screening of lithium electrodes with an inert ceramic solid. It will take careful and sustained experimental studies to unfold the underlying mechanisms for improved interfacial stability.

Summary and Conclusions

A brief review of the state of the art of polymer-ceramic composite electrolytes has been presented. Experimental data on PEO:$LiBF_4$-Li_3N composite electrolytes reveals that the addition of Li_3N to the PEO:$LiBF_4$ polymer increases the conductivity by about an order of magnitude at ambient temperature. An analysis of a broader range of composite electrolytes with respect to their conductivity reveals that incorporation of a ceramic solid in a polymer matrix leads to two effects. The first one is the enhancement of amorphous phase which should theoretically enhance conductivity. The second effect is an increase of glass transition temperature with increasing volume fraction of the ceramic phase which should reduce conductivity due to the fact that the polymer chain assisted motion of the conducting ion is suppressed. These two effects are antagonistic in nature and perhaps account for a relatively small increase in conductivity in polymer-ceramic composite electrolytes. Although the benefit from the conductivity point of view is small, all the available information suggest these composite electrolytes should have high cationic transport number due to decoupling of structural and electrical relaxations. Perhaps the possibility of cationic transport number augmentation is the most important feature of these composite electrolytes. Preliminary experimental data on interfacial electrochemistry of lithium-composite electrolyte interfaces reveals promising future. These interfaces are believed to be stable and efficient.

It should be stated here that the electrochemical data on the composite electrolytes is still scarce; nonetheless, they appear to possess many beneficial properties that may lead to their use for commercial purposes.

Acknowledgements

One of the authors (BK) gratefully acknowledges the financial support provided by the Wright Laboratory, Propulsion and Power Directorate under Contract No. F33615-93-C-2350. The authors also express thei. gratitude to Mr. R.A. Marsh for his continued support, encouragement, and constructive criticisms, to Mr. J.D. Schaffer for assistance with experimental measurements involving polymer-Li_3N electrolytes, to Dr. Bruno Scrosati for useful discussions, and to Niki Maxwell for typing and editing the manuscript.

References

1. J.E. Weston and B.C.H. Steele, Solid State Ionics 7, 75 (1982).
2. S. Skaarup, K. West, and B. Zachau-Christiansen, Solid State Ionics, 975-978 (1988).
3. J. Plocharski and W. Wieczorek, Solid State Ionics 28-30, 979-982 (1988).
4. J. Plocharski, W. Wieczorek, J. Przyluski, and K. Such, Appl. Phys. A 49, 55-60 (1989).
5. S. Skaarup, K. West, P.M. Julian, and D.M. Thomas, Solid State Ionics 40-41, 1021-1024 (1990).
6. F. Capuano, F. Croce, and B. Scrosati, J. Electrochem. Soc. 138, 1918-1922 (1991).
7. F. Croce, F. Gerace, and B. Scrosati, Proc., 35th International Power Sources Symposium, Cherry Hill NJ, pp. 267-270 (1992).
8. N. Munichandraiah, L.G. Scanlon, R.A. Marsh, B. Kumar, and A.K. Sircar, Proc., Electrochemical Society, Honolulu HI (1993).
9. B. Kumar, J.D. Schaffer, N. Munichandraiah, and L.G. Scanlon, J. Power Sources 47, 63-78 (1994).
10. J. Przyluski, K. Such, H. Wycislik, W. Wieczorek, and Z. Florianczyk, Synthetic Metals 35, 241-247 (1990).
11. U.V. Alpen, A. Rabenau, and G.H. Talat, Appl. Phys. Lett. 20, 621-623 (1977).
12. N. Munichandraiah, L.G. Scanlon, R.A. Marsh, B. Kumar, and A.K. Sircar, Solid State Ionics, to be published (1994).
13. B. Kumar, P.T. Weissman, and R.A. Marsh, J. Electrochem. Soc. 140, 321-323 (1993).
14. M.B. Armand, in Polymer Electrolyte Reviews 1, ed. J.R. MacCallum and C.C. Vincent, pp. 10-12 (Elsevier Applied Science, 1987).
15. C.A. Angell, Solid State Ionics 9/10, 3-16 (1983).
16. C.A. Angell, Solid State Ionics 18/19, 72 (1986).
17. K.M. Abraham and S.B. Brunner, in Lithium Batteries, ed. J.P. Gabano, p. 371 (Academic Press, London, 1983
18. J.B. Bates, N.J. Dudney, G.R. Gruzalski, R.A. Zuhr, A. Chandhury, C.F. Luck, and J.D. Robertson, J. Power Sources 43, 103-110 (1993).

AN APPLICATION OF RANDOM AND LAYERED POLYMER NANOCOMPOSITES IN LITHIUM POLYMER BATTERIES - A REVIEW

Włodzimierz Kuc, Lawrence G. Scanlon
Aero Propulsion and Power Directorate, Wright Laboratory POOS-2
Wright-Patterson Air Force Base, OH 45433-7251

Emmanuel Giannelis
Department of Material Science and Engineering
Cornell University, Ithaca NY 14853

Introduction

Many routes are presently pursued with the goal of obtaining new materials which could improve the performance characteristics of lithium polymer batteries. Most of the efforts are concentrated on new flexible polymer electrolytes. Unfortunately, polyethylene oxide (PEO) , which has been the widest studied polymeric matrix is highly crystalline at ambient temperature. This limits its conductivity since ionic conductivity is associated with the amorphous PEO phase. Various methods have been applied in order to obtain amorphous and highly conducting PEO-based polymer electrolytes[1]. However, some methods require complicated synthetic procedures or lead to soft liquid-like systems of poor mechanical and electrochemical stability and are environmentally hazardous. Alternatively, the more advanced polymer electrolyte systems may involve interpenetrating polymer networks and composite polymer - ceramic systems. It has been shown that the addition of fine inorganic fillers to PEO based polymeric electrolytes can improve mechanical and electrochemical stability of polymer matrices as well as increase their ambient temperature ionic conductivity[2,3]. Liquan suggested that there is a reciprocal relationship between the ionic conductivity of composite polymer electrolytes (CPE) and the ceramic particle size[4]. This observation was also confirmed by Wieczorek and Scrosati who stressed the importance of grain boundary effects[5,6]. Taking into account these observations and assuming that in polymeric nanomaterials the ceramic grains are so small that the relatively large volume of the solid mixture consists of grain boundaries or interphase regions, we have initiated investigations on CPE containing ceramic species with at least one dimension in the range of 10-30 nanometers. Polymer Nanocomposites represent a new and rapidly developing family of materials with many interesting properties which are not available in conventional micro-sized composites[7,8]. Our investigations cover classic systems obtain by randomly dispersing nanosized (10-40nm) ceramic grains in a polymeric matrix (Fig.1c) as well as layered nanomaterials recently developed by Giannelis and composed of alternating ultra-thin rows of ceramic and polymer[8] (Fig.1a). Initial results of our investigations have shown that both ionic conductivity and interfacial stability of CPE can be further improved by decreasing the ceramic particle size to the range of nanometers[9,10]. Moreover, the Layered Nanocomposite Polymer Electrolytes (LNCPE) create a new and very promising family of composite electrolytes of single ionic conductivity. (Another extremely interesting approach to obtain CPE of single ionic conductivity was recently presented by Peled et. al.[11] who ,within the contract sponsored by NASA, developed a method of covering nanosized Al_2O_3 particles with LiI followed by carefully dispersing the covered particles in a polymer matrix.).

We have also started initial investigations on the use of nano-sized insertion materials, instead of the more commonly used microparticles, as the components of composite cathodes to enhance cathode utilization through increased surface area and ionic conductivity. Initial results of work sponsored by DARPA on vanadium oxide based cathodes, reported recently by Owens and Smyrl, showed enhanced discharge capacity with decreasing particle size (from 70μm to less than 1μm) along with faster discharge rates[12]. This feature was explained by the diffusion of lithium through the ceramic particle which is able to reach equilibrium lithium ion concentrations in a shorter time in the case of smaller particles. Because nanosized MnO_2 and TiO_2 are commercially available and nanosized vanadium oxide is already produced on a laboratory scale, the application of these materials in composite cathodes seems very promising .

Despite a significant number of papers reviewing the properties of different CPE's , a number of important issues involved in both the conduction mechanism and the behavior of CPE's in contact with electrodes, are poorly understood. In most cases, the crucial factors such as the moisture content and ceramic particle size, distribution and electrostatic properties, were not reported. These issues need focused attention and satisfactory solutions before CPE-based rechargeable lithium polymer batteries become commercially available on a wide scale. In this paper we will briefly summarize the part of our investigations on nanocomposite polymer electrolytes (NCPE) and LNCPE as well as indicate the great application potential resulting from the utilization of polymer nanocomposites of different structure and morphology in lithium polymer batteries. Since experimental procedures connected with synthesizing, handling and analyzing of electrolytes have significant influence on their electrochemical properties, a substantial part of this paper will deal with the experimental techniques applied in studies on electrolytes discussed.

General Experimental Methods

Materials

High molecular weight (M.w.≈400,000) PEO, Al_2O_3 of particle size less than 10μm and anhydrous acetonitrile (ACN) of less than 50 ppm of water were received from Aldrich Chemical Co. LTD. High surface area Al_2O_3 of particle size 13 nm and 24 nm were obtained from Degussa Corp. and Nanophase Technology Corp. , respectively. Ultra-dry $LiBF_4$ containing less than 1ppm of water was obtained from Alfa-Ceaser and used as received (the glass ampoules of anhydrous salt were opened in a drybox under a helium atmosphere just before using) The lithium metal (Alfa) was in the form of a ribbon of 0.3 mm thickness. It was rinsed with a mixture of freshly purified hexane and heptane to remove the oil present on its surface (the oil coating applied by the manufacturer inhibited any possible surface reaction of the lithium during storage) and dried prior to use. Since experiments dealing with lithium passivation (e.g. stability and transport number measurements) need a properly prepared electrode, the lithium bulk material was scraped to a metallic luster in a drybox just before using.

Al_2O_3, molecular sieves and PEO were dried over P_2O_5 under vacuum for 48 hours at 150°C, 200°C and 50°C respectively. Anhydrous ACN was additionally dried and stored over dry molecular sieves which decrease the water content of the solvent to about 10 ppm.

LNCPE were synthesized in Prof. Giannelis' Laboratory, Cornell University, Ithaca, NY, according to a previously described procedure[9].

Preparation of Electrolytes

All electrolytes have been prepared and stored in a series of dryboxes (Vacuum Atmospheres Corp.) equipped with a vacuum oven (Vacuum Atmospheres Corp. He-533) and devices for removal and analysis of oxygen and water. The oxygen and water content of the He in the inert atmosphere box was measured continuously with a calibrated O_2 sensor (Vacuum Atmospheres Corp. A/O 316-H) and a solid state moisture sensor (Vacuum Atmospheres Corp. AM-2), both of them sensitive to< 0.1ppm.
The O_2 and H_2O in the dryboxes was kept below 10 ppm and 1ppm, respectively. Transfer of the materials between dryboxes was performed by using hermetically sealed He-filled glass vessels and dessicators, both equipped with O-rings.

The thin films (40-80 μm) of CPE were prepared as follows. The mixture containing 20-22 cc of acetonitrile, 1-1.5g PEO and appropriate weighed quantities of $LiBF_4$ and, whenever required, Al_2O_3 was introduced into a 50 cc sealed mixing chamber of an OMNI Mixer-Homogenizer and stirred ,with periodic interruptions, for 4 hours at 10000 - 16000 rpm. The ratio between the number of monomeric units CH_2CH_2O and the number of lithium in the salt (O/Li) was in all cases fixed at 8/1. The homogeneous solution was then transferred into a 30 cc sealed chamber of the OMNI Ultrasonic Processor where the solution underwent ultrasonic agitation for 1-2 minutes at 20000 KHz, to avoid secondary agglomeration of ceramic particles and remove gas bubbles present in the solution which could significantly affect the casting process. The degassed and warm homogenous solutions were immediately cast onto fine polished teflon molds and introduced into a vacuum dessicator. Then the acetonitrile was slowly (24 hours) evaporated under vacuum and quantitatively collected in liquid nitrogen traps. All the electrolytes obtained in this manner were conditioned for 48 hours over P_2O_5 under vacuum at 50 °C and stored in a drybox, in a vacuum dessicator over dry $CaSO_4$. Homogeneity as well as size of ceramic particles and their distribution in the electrolytes were continuously monitored by Scanning

Electron Microscopy (SEM). By this very fast, fully controlled and environmentally friendly procedure, homogenous polymer electrolyte thin films with no evidence of powder agglomeration, were routinely obtained.

Electrochemical Measurements

All electrochemical experiments were carried out utilizing an EG&G PAR Model 5210 lock-in amplifier and Model 273A Potentiostat/Galvanostat controlled by EG&G PAR Model 270 Research Electrochemistry Software (d.c. polarization) or Model 398 Electrochemical Impedance Software (conductivity and stability measurements) operated by a 486 GATEWAY 2000 computer. Ac impedance was measured with 5 mV ac signal over a frequency range of 100 KHz to 0.1 Hz, and in some cases down to 0.01 Hz, at 6 points per frequency decade. In order to obtain the impedance parameters, all the experimental spectra were analyzed by means of Boukamp's Equivalent Circuit Software, Version 4.5 The fitting procedure was terminated only when the relative errors of impedance parameters remained generally confined below 5% (χ^2 fitting parameter < $5x10^{-5}$).

Disc samples of electrolytes were sandwiched between two equivalent metallic lithium (Li) or stainless steel (SS) electrodes (Electrode surface area 3.14 cm^2 or 1 cm^2). The CPE or Li/CPE/Li systems were introduced between two metallographic grade polished , parallel stainless steel (SS) current collectors. The collectors were kept under a constant mechanical pressure of approximately 10-12 lb./in.^{2} by using calibrated spring loaded terminals. The universal "three electrode" design of the cells allows for the introduction of a reference electrode by inserting , during cell assembly, a 10μm Ni or Al wire between the two layers of electrolyte and plating the wire with lithium from the negative electrode. All samples for the electrochemical measurements were prepared and loaded into sealed electrochemical vessels (each equipped with internal and external wire connections and thermocouple placed near the cell) in the drybox The electrochemical vessels were then removed from the drybox, immersed in the thermostat and the wire leads were connected to the measuring equipment. The temperature of samples inside the electrochemical vessel were constantly monitored with an accuracy of 0.5°C.

The ionic transport number of lithium in CPE's studied, was evaluated by the combination of complex impedance and potentiostatic polarization using lithium electrodes. Li/CPE/Li cells were conditioned at 80°C for 3 hours and then polarized at the same temperature using a voltage of 20 mV for 6-48 hours. Currents were recorded as a function of time until the current was changing by less than 0.5% in 30 min. reaching so called "steady-state" value. The cell impedance was measured just before and after polarization to enable correction for the effect of interfacial resistance.

Ionic conductivity was determined from the a.c. impedance measurements with SS/CPE/SS cell configuration. over the temperature range -20 to 100 °C. The measurements were made every few degrees during heating. After reaching the desired temperature, the cell was kept at that temperature for 30-45 min ,to assure the temperature equilibrium of the sample before the measurement was made. Most of the measurements were done at the open circuit potential (OCP). The a.c. ionic conductivity was calculated from the complex impedance plot with nonlinear computer curve fitting.

The interphase resistance and/or Li-CPE interface were studied by means of a.c. impedance spectroscopy applied to Li/CPE/Li cells at a temperature of 70°C. The change of the impedance was continuously monitored for the first 100 hours after cell assembly when most of the investigated phenomena occurred.

Moisture Determination

Determination of the water content of the electrolyte materials by Karl-Fisher technique was carried out on an automatic Mitsubishi Moisture Meter Model CA-06 equipped with Mitsubishi Water Vaporizer Model VA-06. The moisture content in electrolytes were usually kept below 200 ppm.

Results and Discussion

Figure 2 illustrates the temperature dependence of the ionic conductivity for $(PEO)_8LiBF_4$ - Al_2O_3 nanocomposite electrolytes of various compositions. For comparision, the temperature dependence of conductivity measured for $(PEO)_8LiBF_4$ and $(PEO)_8LiBF_4$ - 10 wt% micro-sized Al_2O_3 electrolytes are also included. One can observe that ionic conductivity of NCPE's varies as a function of nanoceramic content. At first the conductivity increases with the addition of Al_2O_3 reaching a maximum value for electrolytes containing 10 wt% nano-sized Al_2O_3. After that, the conductivity decreases gradually and for samples containing over 30 wt% of alunina falls down below the values received for the undoped $(PEO)_8LiBF_4$ system. The ambient temperature ionic conductivity values obtained for NCPE's of 10 wt% of alumina are one order of magnitude higher than values measured for analogous systems containing microsized alumina. Moreover, the ionic conductivity of optimized CPE exceeds the values recorded for undoped $(PEO)_8LiBF_4$ systems over the whole studied temperature range even at temperatures higher than thePEO melting point (Figure 3). The present observation is similar to that found by Scrosati for $(PEO)_8LiClO_4$ - γ $LiAlO_2$ system[13] and contrary to data reported for systems doped with sodium salts.[14] .Recent studies on NMR imaging of amorphous phase of $(PEO)_8LiClO_4$ - γ $LiAlO_2$ system indicated that the local dynamics of the Li ions, in particular the Li mobility, is not changed by adding the γ $LiAlO_2$ filler what supports the idea that the enhancement of conductivity by adding a filler is caused by stabilizing and increasing the fraction of amorphous phase[15]. However, the fact that characterized by similar Tg values and similar degrees of crystallinity (Table 1) samples containing the same amounts of nanosized or microsized Al_2O_3 show different ionic conductivities over a broad range of the temperature once again proves the importance of grain boundary effects which are clearly visible at ambient temperature and remain noticeable up to 100°C. Similar morphological behaviour of electrolytes containing Al_2O_3 of various particle size was confirmed by polarizing microscope studies at different temperatures (Figure 4).

Figure 5 presents the changes of interfacial resistance versus time recorded at 70°C for $(PEO)_8LiBF_4$ - Al_2O_3 electrolytes of different composition sandwiched between two lithium electrodes. Previous works suggested than the evolution of interfacial resistance with time can be associated with continuous growth of a resistive layer on the Li electrode surface where the passivation layer is a product of the corrosion reaction of Li with electrolyte components[16]. To monitor the morphological changes occuring on Li/NCPE interphase we developed the SEM technique allowing for *post-mortem* examination of the interphase. An exemplary photograph of Li/$(PEO)_8LiBF_4$ - 20wt% nano-sized Al_2O_3 interphase after 2 hours of storage is presented on Figure 6. The changes of interfacial resistance in terms of moisture content, ceramic particle size, equivalent circuit analysis and passivation layer models that are available in the literature were discussed previously[10]. It can be seen (Figure 5) that both the NCPE and conventional micro-sized CPE are much more electrochemically stable in contact with the Li electrode than undoped $(PEO)_8LiBF_4$ electrolyte. Stability of NCPE's in contact with lithium varies with the electrolyte composition reaching the optimum for a system containing 20 wt% nano-sized alumina.

One can also observe that the interfacial resistance of the electrolyte containing nanosized Al_2O_3 is much lower than the interfacial resistance of the analogous microsized electrolyte indicating the importance of greatly increased ceramic surface area for stabilizing the interphase. Figures 7a and 7b show the evolution of Li/$(PEO)_8LiBF_4$ - 10wt% nano-sized Al_2O_3 interphase resistance as a function of time at 70°C for electrolytes containing 200 ppm and 1.5% of moisture , respectively. The influence of the moisture content on the stability of electrolytes is clearly visible. The interfacial resistance of the sample stored in the drybox, in a vacuum dessicator over dry $CaSO_4$ (moisture content below 200ppm) is much lower than for the sample exposed for a long time to drybox atmosphere (moisture content 1.5%). Other experiments have shown that the moisture content in the electrolytes exposed for a short time to the air can rapidly increase reaching the equilibrium value (3-8%) which depends on electrolyte composition. Thus, to allow comparision of the stability of different electrolytes versus lithium electrode the experimental methods, material characteristics and especially moisture content should be described in detail.

The electrostatic charge and surface structure of the ceramic probably affect not only conductivity and stability of NCPE but also the interactions between the filler grains and ions present in the system since the Li_+ transport number measured at 80°C for NCPE (t_+=0.24) is slightly higher than analogous value for undoped electrolyte (t_+=0.20). Aluminum Oxide tends to develop an electrostatically positive charge in contact with polymers - in contrast for example, to silica particles which become charged negatively[17]. One cannot also exclude the influence of hydrogen bonding between anions and OH groups present on alumina surface.

Table 2 presents the ionic conductivity values of LNCPE (Fig.1a) obtained by infusing the galleries existing between the montmoriilonite nano-layers with PEO chains[9]. For this type of LNCPE , the isomorphous substitution of silicon by aluminium in the ceramic layers creates a delocalized negative charge balanced by lithium cations residing in the galleries what leads to systems of single ion conductivity. As can be seen from the Table 2, the ionic conductivity of LNCPE changes slightly in the temperature range from 0°C to 70°C reaching the room temperature value of $1.6x10^{-6}$ S/cm for a system containing 40 wt% of PEO. The ^7Li NMR studies (Figure 8) on LNCPE show a single, motionally narrowed resonance at room temperature. The ^2H NMR spectra recorded for LNCPE containing deuterated PEO were very similar to amorphous bulk PEO and their temperature dependence was strongly correlated with motional narrowing seen in ^7Li NMR [9] indicating strong mutual interactions between lithium cation and infused PEO chains.

Conclusions

The short review of our initial, exploratory works on nanocomposite polymer electrolytes has demonstrated that the application of nanomaterials as components of solid electrolytes can greatly enhance the electrochemical properties of electrolytes in comparison to other composite polymer electrolytes developed up to date. The following conclusions can be drawn:

The ionic conductivity of the optimized NCPE (>10^{-5} S/cm) is about one order of magnitude higher than that for conventional CPE of analogous composition which confirms previously suggested inverse relationships between ionic conductivity and ceramic particle size, proving the importance of grain boundary effects in conduction processes. The influence of ceramic particles on ionic conductivity can be also interpreted in terms of electrostatic interactions and surface structure of the ceramic grains.

The use of nano-sized ceramic particles leads to substantial improvement of the stability of composite electrolytes in contact with lithium electrodes, which reflects the influence of the greatly extended surface area of the nanoceramic powder. The passivation processes observed can be explained in the light of various models proposed in the literature and, in case of NCPE's; the most adequate seems to be Solid Polymer Layer Model. Our investigations have also demonstrated a strong relationship between the electrochemical properties of electrolytes and experimental methods used for their synthesis. The dispersion degree of the ceramic primary particle size in the polymer matrix and moisture content of the electrolytes strongly affects the stability of composite electrolytes in contact with lithium electrodes. Thus, to allow comparisons of data obtained in different laboratories, the experimental methods applied for studies should be described in detail. Moreover, most of the works on passivation phenomena occurring on polymer electrolyte/lithium interface is based on equivalent circuit models adopted from studies on nonaquous electrolytes and subjectively adjusted to polymeric systems. Since the quantitative analysis of the interface in terms of equivalent circuit models should be connected with analysis of the interphase composition, there is a need to develop the new techniques allowing to study morphology and composition of passivation layers. Of great importance seems to be also the application of statistical analysis (based on F-test) which can determine the adequacy of different models to describe a.c. impedance data, establish accuracy of parameters estimation and allow to choose the model of statistically optimal fit. Only the combination of all the techniques mentioned above can lead to correct explanation and simulation of passivation phenomena studied.

The layered nanocomposite solid polymer electrolytes of RT single ionic conductivity of 10^{-6} S/cm create the new family of solid electrolytes of extraordinary properties. It seems, that the conduction processes taking place in the polymer nanolayers do not obey any of proposed ionic transport theories and models developed up to date for polymer electrolytes. An idea of directional conducting polymer nanolayers or nanotubes forms an innovative and very promising approach to synthesize polymer electrolytes of enhanced properties. This idea can be extended in the future on electrolytes consisting of polymeric macrochannels created by crosslinking certain macromonomers in their tubular mesophase status. In our laboratory we started the initial works on computer modeling of such systems, which confirmed the high lithium mobility.

The application of nanomaterials as components of both polymer electrolytes and composite cathodes can lead to build so called "nanobattery" of increased burst power and enhanced performance characteristics.

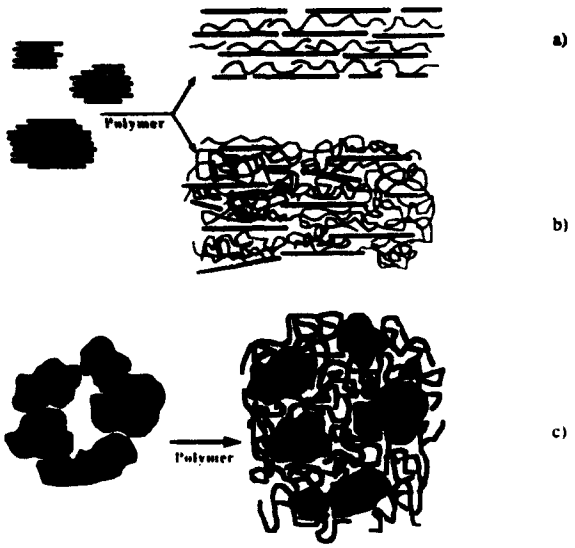

Figure 1. Schematic representation of the structure of composites studied in this work: a) single polymer layers intercalated into ceramic galleries, b) ceramic layers dispersed in continuous polymer matrix, and c) conventional composites composed of ceramic grains finely dispersed in a polymer matrix.

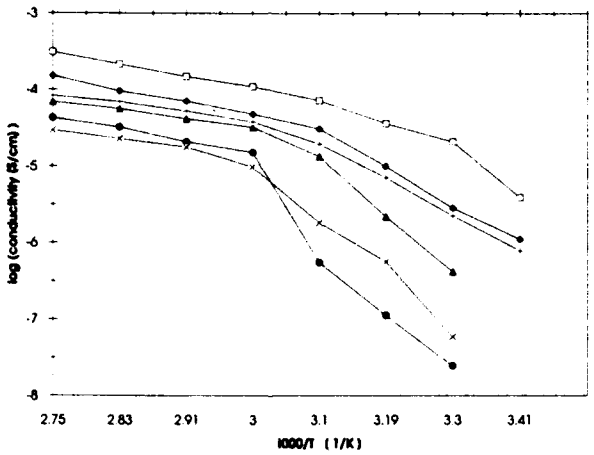

Figure 2. Ionic conductivity versus the inverse temperature of composite $(PEO)_8$ $LiBF_4$ - Al_2O_3 polymer electrolytes at various compositions. (●) 0 wt% Al_2O_3, (▲) 5 wt% nanosized Al_2O_3, (◘) 10 wt% nanosized Al_2O_3, (◆) 20 wt% nanosized Al_2O_3, (x) 30 wt% nanosized Al_2O_3, (+) 10 wt% microsized Al_2O_3

Al_2O_3 [wt.%]	Tg [°C]	T_m [°C]	PEO Crystallinity [%]
pristine PEO	-	64	97
0	-38	58	-
1	-37	55	53
3	-38	53	51
5	-37	54	51
5*	-37	53	51
10	-37	48	28
10*	-33	44	21
20	-38	52	30
20*	-35	56	41
30	-38	52	53
50	-	57	59

Table 1. DSC data for Nanocomposite Polymer Electrolytes containing Al_2O_3 grains of 13nm. (* -sytems containing conventional microsized (<10 μm) alumina).

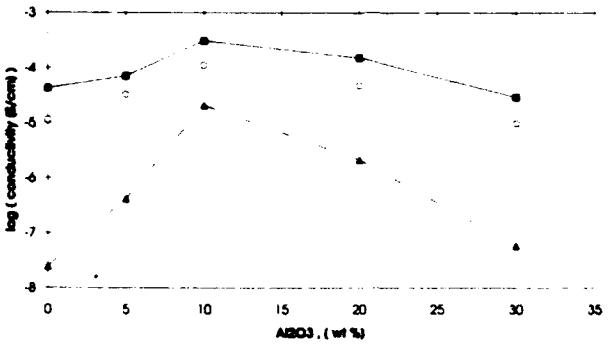

Figure 3. Ionic conductivity versus composition of the $(PEO)_8$ $LiBF_4$ - Al_2O_3 nanocomposite polymer electrolytes at 30°C (▲), 60°C (o) and 90°C (■)

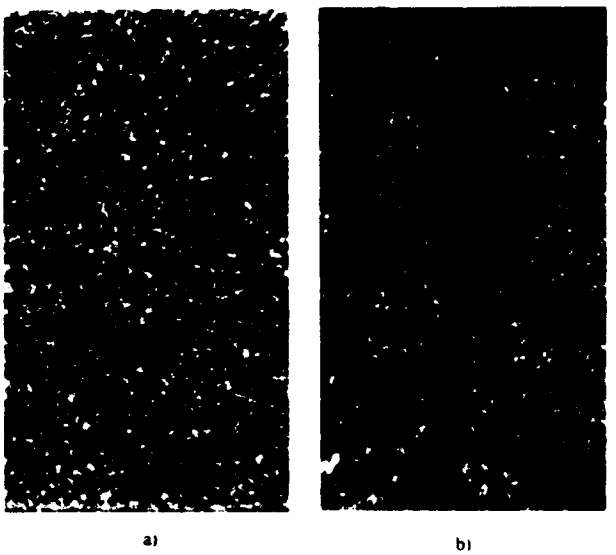

Figure 4. Optical micrographs viewed between crossed polars at 60°C: a) $(PEO)_8$ $LiBF_4$ electrolyte and b) $(PEO)_8$ $LiBF_4$ -10wt% nanosized Al_2O_3 composite electrolyte. Scale bar =0.1 mm

Figure 6. SEM photograph of Li / $(PEO)_8$ $LiBF_4$ -20wt% nanosized Al_2O_3 freezed-fractured interphase. Scale bar = 1 μm

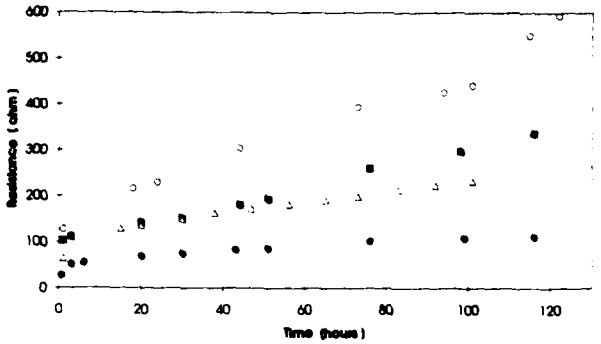

Figure 5. Resistance versus time at 70°C for $(PEO)_8$ $LiBF_4$ - Al_2O_3 composite polymer electrolytes at various compositions. (o) 0 wt% Al_2O_3, , (■) 10wt% nanosized Al_2O_3, (●) 20 wt% nanosized Al_2O_3, (Δ) 20 wt% microsized Al_2O_3.

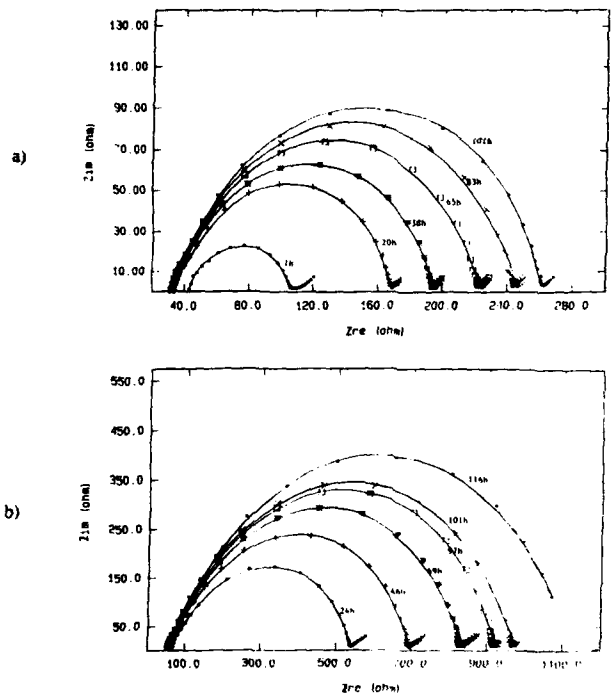

Figure 7. Impedance diagrams of Li / $(PEO)_8$ $LiBF_4$ -10wt% nanosized Al_2O_3 interphase showing the increase in the interphase resistance as a function of time at 70°C for samples containing a) below 200 ppm and b) 1.5% of moisture.

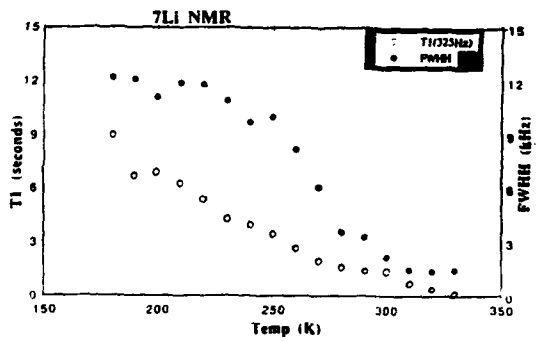

Figure 8. Spin lattice relaxation time (T1) and full widths at half maximum (FWHM) versus temperature, determined from 7Li NMR spectra of *LNCPE of type 1a containing lithiated montmorillonite* and 40 wt% of PEO (O/Li = 6)

Temperature [°C]	0	30	40	60	70
Conductivity [S/cm]	1.0×10^{-7}	1.6×10^{-6}	1.9×10^{-6}	3.9×10^{-6}	4.9×10^{-6}

Table 2. Ionic Conductivity of Layered Nanocomposite Electrolyte versus temperature.

Acknowledgments

The authors express their gratitude to Al Turner, Jeff Schaffer, Cam Rippenhoff, Jim Malone and Marlene Houtz for assistance in developing new experimental techniques and help in preparing electrolytes and carrying out measurements.

References

1. Polymer Electrolyte Review 1 and 2 ed. J.R. MacCallum and C.C.Vincent , Elsevier Applied Science, London 1987 and 1989.
2. J.E Weston , B.C.Steele, Solid State Ionics, 7., 7 (1982)
3. H.Yuankang, C.Zhusheng, Z.Zhiyi, W.Chaoying, C.Liquan, Chem.J.Chinese Univ. (English Edition) Vol.2, No.1, p.97 (1986)
4. C.Liquan, in Materials for Solid State Batteries, ed. B.Chowdari and S.Radhakrishna, World Scientific Pub.Co., Singapore, p.69 (1988)
5. W.Wieczorek, Solid State Ionics, 53-56 , 1064 (1992)
6. F.Capuano, F.Croce, S.Panero, B.Scrosati , The Electrochemical Society Extended Abstracts, Vol.91-2 , p.1017, Phoenix, Arizona, October 13-17 (1991)
7. R.Dagani, Chem.Eng.News, November 23, p.18 (1992)
8. E.P.Giannelis, JOM, March , p.28 (1992)
9. W.Krawiec, L.G.Scanlon,R.A.Vaia, S.Vasudaven. E.P.Giannelis , "Polymer Nanocomposites - a New Strategy for Synthesizing Solid Electrolytes for Rechargeable Lithium Batteries" - to be presented at the 7th International Meeting on Lithium Batteries, Boston MA, May 15-20 (1994)
10. W.Krawiec, L.G.Scanlon , E.P.Giannelis, " Passivation Phenomena at the Lithium - Nanocomposite Polymer Electrolyte Interface" - to be presented at the 4th International Symposium on Systems with Fast Ionic Transport, Warsaw, Poland , May 10-14 (1994)
11. G.Nagasubramanian, A.I.Attia, G.Halpert, E.Peled, Solid State Ionics, Vol.67, 51 (1993)
12. A.L.Xidis, R.T.Atanasoski, B.B.Owens, W.H.Smyrl, , The Electrochemical Society Extended Abstracts, Vol.93-2 , p.43, New Orleans, Louisiana, October 10-15 (1993)
13. B.Scrosati, F.Croce, Polymers for Advanced Technologies, Vol.4, p.198-204 (1993)
14. W.Wieczorek, K.Such, S.H.Chung, J.R.Stevens ," Comparison of properties of composite polymeric electrolytes based on the oxymethylene linked PEO $NaClO_4$ electrolyte with polyacrylamide or Al2O3 additives " - to be published.
15. J.Roos, The Electrochemical Society Extended Abstracts, Vol.93-2 , p.1003, New Orleans, Louisiana, October 10-15 (1993)
16. F.Croce, B.Scrosati, J.Power Sources, Vol.43-44, pp.9-19 (1993)
17. "Highly Dispersed Metallic Oxides", Degussa Corp., Tech. Bull. no.56

THIN LAYER Li/CF_x CELLS WITH POLYMER ELECTROLYTE

Donald Foster and Paul Bramhall
Army Research Laboratory(EPSD), Ft. Monmouth, NJ

Abstract

High energy Li/CF_x primary button cells with plasticized polymer electrolyte have been evaluated for the effect of elevated temperature and thin layer electrodes on cell performance. The electrolyte could be crosslinked by a thermal curing process allowing a greatly simplified method of making the polymer batteries. The usual methods for making liquid electrolyte button cells were performed. After assembling and sealing the the cells, the electrolyte was cured thermally immobilizing it to a gel. The conductivity of the electrolyte after curing was found to be 4 X 10^{-3} S/cm at 25°C. The Li/CF_x were tested over the temperature range of 25°C to 100°C and rates varying from 0.1 mA/cm^2 to 2 mA/cm2. Full CF capacity was realized at 1 mA/cm^2. Full CF capacity was realized at 1 mA/cm^2 continuous discharge at 85°

Introduction

We have developed laboratory scale, thin layer polymer electrolyte Li/CF_x cells and tested them for high energy and high power applications. Future anticipated technological advances such as the cooling unit for the soldier system demand power sources with extremely high energy and power densities, high durability and safety for both the user and the environment. The characteristics of lithium batteries in regard to the above requirements are primarily determined by the materials used for the cathode and the electrolyte.

Carbon monofluoride, CF_x (x=1), has been studied and employed as a cathode active material for lithium batteries for many years [1]. Table 1 compares the energy density of Li/CF_x to several other high energy lithium cells. Li/CF_x has one of the highest energy densities of any electrochemical couple, has a good safety record and is considered to have very good storage characteristics. Further a CF_x cathode contains no heavy metals as most cathode materials do. This makes CF_x one of the most environmentally safe battery systems. Low to moderate rate capability, however, has precluded it from consideration for many applications of interest to the U.S. Army.

Likewise it has been recognized [2] that polymer electrolyte batteries could provide improved safety and handling features over conventional liquid electrolyte systems. Advantages that could be attributed to polymer electrolyte cells are: thin film or thin layer cell construction, bipolar multicell battery construction and greater safety under conditions such as shock, puncture or flame.

Batteries with polymer electrolyte are very low rate compared to liquid electrolyte batteries, however, due to the low conductivity of the polymer electrolyte [3]. To solve the problem, liquid plasticizers have been added to improve the conductivity of the polymer. These plasticized polymer electrolytes can be thought of as a liquid contained by the chains of a high molecular weight polymer forming a gel. Gel electrolytes have been found to have conductivities approaching liquid electrolytes while in principle maintaining the advantages of an immobilized electrolyte [4].

Table 1

Comparison to Theoretical Energy Density of CF_x with Other High Energy Positive Materials for Lithium Batteries

Positive Material	Capacity Ah/gm	Energy Density Wh/kg
CF_x	.894	2190
NiF_2	.554	1370
CuF_2	.525	1650
$SOCl_2$	.451	1578
SO_2Cl_2	.397	1468

This work explores the capability of Li/CF_x batteries with polymer gel electrolyte. Small button cells were used as a test vehicle. To overcome the anticipated problems of low rate capability for Li/CF_x with polymer electrolyte, thin layer electrodes were used to increase the overall surface area, a gel electrolyte was used with high conductivity, and cell operation at elevated temperatures was explored.

Cell Assembly

Because gel and polymer electrolytes will not flow, a different cell fabrication procedure is required. Conventional cell construction for lithium batteries with liquid electrolytes consists of a porous nonwoven separator made of a polymeric material such as polypropylene or Tefzel sandwiched between the lithium foil anode and the porous cathode layer. The liquid electrolyte flows into the pores of the separator and cathode providing a path for ionic conduction throughout the cell and cathode layer.

Solid polymer and gel electrolyte cells are constructed by mixing the solid cathode and polymer electrolyte materials and casting or extruding a solid composite thin layer cathode. Likewise, the electrolyte is usually a free standing solid film or a solid coating on the anode. The completed cell consists of a solid polymer electrolyte layer between a solid lithium foil and solid composite cathode.

This method requires the thin polymer electrolyte to act as electrolyte and separator. Ultra thin layers of heavily plasticized polymer electrolyte may not have the strength to resist penetration of small irregularities in the electrode surfaces. This can result in cell short circuit. Cell performance could further be affected if the lack of a binder in the cathode allows degradation due to volume changes that occur during cell operation.

The procedure for making the cells used in this work is very similar to the techniques used for liquid electrolyte systems. It is based on the electrolyte which contains a crosslinkable polymer. The electrolyte changes from liquid to gel when it is cured thermally. The cathode was rolled using

a Teflon binder onto a foil substrate forming a porous layer . The electrodes were separated by a thin microporous inert material which is completely insoluble in the electrolyte plasticizer. The cells were made by soaking the separator and cathode with the liquid uncured electrolyte. After cell assembly and sealing, the cells were heated to cure the electrolyte thermally. The result is a cell with an immobilized electrolyte but with an solid separator and cathode binder as used in most liquid electrolyte batteries. Figure 1 is a diagram of the finished cell.

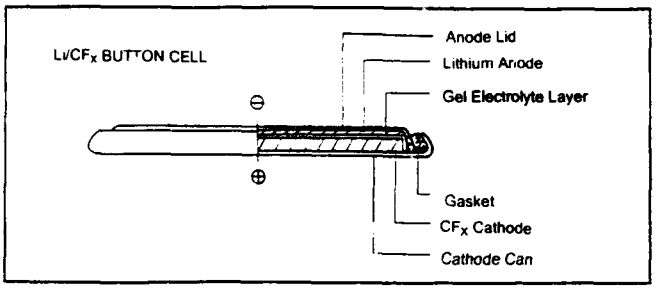

Figure 1. Li/CFx button cell with gel electrolyte.

Experimental Procedure

The electrolyte was a mixture of the following composition: 1M $LiAsF_6$ in propylene carbonate 85%, polyethylene glycol diacrylate PEG-DA 10%, polyethylene oxide PEO (MW=5,000,000) 5%. A small amount of 2,2'-azobisobutyronitrile (AIBN) was added as a crosslinking initiator. The components formed a clear viscous liquid solution.

Conductivity measurements were done in glass conductivity cells with platinum electrodes. The cells were filled with the viscous liquid electrolyte. The cells were heated at 70°C for at least an hour to cure the polymer electrolyte. A.C. conductivity measurements were made at 1 kHz. Temperature control was maintained with a Tenney temperature control chamber. After curing the polymer became a clear gel.

Cathodes were produced by rolling CF_x, carbon and Teflon dispersion in a water and isopropyl alcohol mix. For cathodes produced in house, fluorinated graphite CF_x ($0.95 < x > 1.05$) was used. The cathodes were rolled thin to a thickness of 20 to 100 microns on 25 micron thick aluminum foil. CF_x cathodes were also provided by Ray-O--Vac Corporation for this study. These were also on aluminium foil.

The cells are assembled with the viscous liquid electrolyte before covering. The cell electrodes were 2 cm^2 in area. Porous Tefzel separator and the rolled CF_x and carbon cathode were both soaked with the viscous liquid electrolyte. Because there was considerable free volume on the button cell package containing the very thin polymer electrolyte cell, a small spring assembly was used to keep pressure on the cell and insure good electrical contact throughout discharge. After assembly, the cells are crimp sealed and then stored at 70°C for 90 minutes to cure the electrolyte.

Cells were discharged at constant current load with an AMSEL model 545 galvanostat electrometer. Cells were tested over a temperature range of 25°C to 100°C. Temperature control was maintained with a Tenney temperature control chamber.

Results

Figure 2 shows a plot of the conductivity of the gel electrolyte in this work. At 25°C the conductivity is 4 X 10^{-3} S/cm and at 85°C it is over 10^{-2} S/cm. Although this is still less than the very best liquid electrolytes, it is well above results for the unplasticized polymer systems.

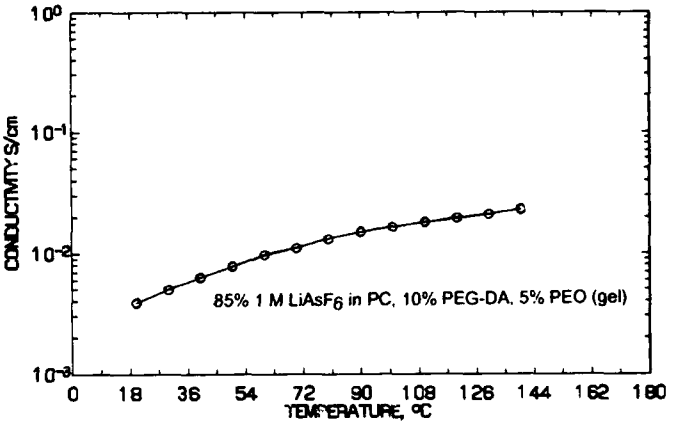

Figure 2. Conductivity of gel electrolyte.

Figure 3 shows the effect of current density on the performance of Li/CF_x cells at 25°C. The capacity decreases rapidly with increasing rate. Increasing the temperature greatly improves the performance of the cells as shown in Figure 4. The rate capability of the cells steadily improved with temperature up to 85°C. Figure 5 shows how the performance varies with rate at 85°C. Further increases in temperature did not improve the performance. It has been shown [5] that at temperatures over 85°C sealing materials such as the polyethylene gaskets used in this study undergo significant degradation at temperatures over 85°C.

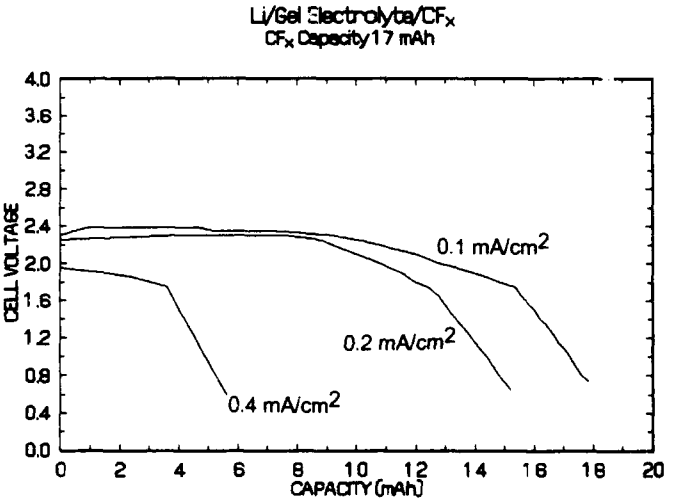

Figure 3. Dischage of three Li/CF_x cells with gel electrolyte at 25°C.

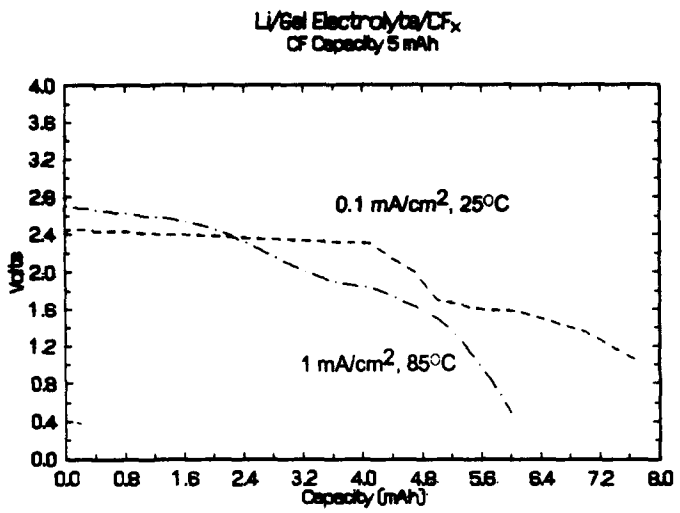

Figure 4. Discharge of Li/CF_X cells with gel electrolyte at 85°C and 25°C.

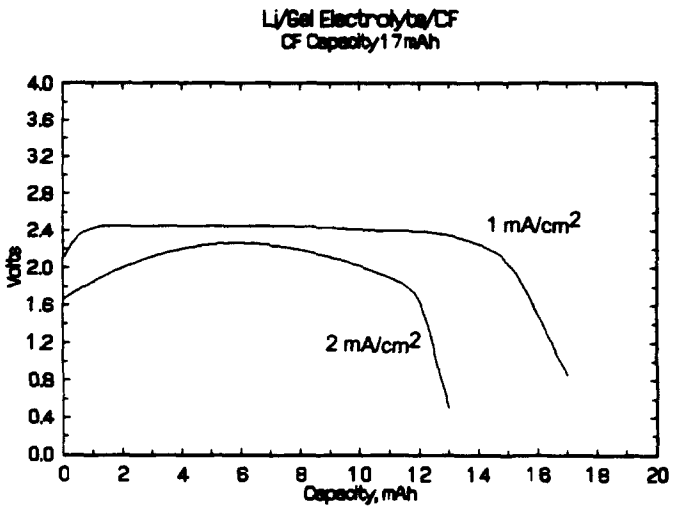

Figure 5. Discharge of two Li/CF_X cells with gel electrolyte at 85°C.

Figure 5 shows that even at 85°C, the cells operate at a reduced voltage at rates over 1 mA/cm^2 at the beginning of discharge. These two cells had cathodes containing only 5% carbon as a conductive additive to the CF_X cathode. Cells with cathodes containing 15% carbon as shown in Figure 4 showed a much flatter discharge curve.

Varying the cathode thickness from 50 micron to 100 micron was not found to effect the performance.

Conclusion

Our results have shown that by raising the temperature to 85°C ano using thin layer cells, the full capacity of the CF_X cells can be obtained at a rate of 1 mA/cm^2. Based on this experimental result, the overall energy density of the cell including current collectors can be calculated. If the current collectors are kept in 12 micron to 25 micron range and the electrodes in the 25 micron to 50 micron range, then energy densities of over 300 Wh/kg and power densities of over 60 W/kg can be achieved. These results neglect the weight of the cell case. However, one of the advantages of a polymer electrolyte system is that the cell casing could be very light weight as compared to other batteries such as SO_2 or $SOCl_2$.

The Li/CF_X battery with polymer electrolyte is a very promising system for Army applications where the batteries can be operated at elevated temperatures. Remaining tasks are to upscale to larger size batteries, produce multicell bipolar cell stacks and investigate the storage and shelf life characteristics.

Acknowledgment

The authors thank Dr. Sid Megahead of Ray-O-Vac Corporation for providing some of the CF_X cathodes used for this study.

References

(1) M. Fukuda an T. Iijima (1985) Lithium and Carbon Monofluoride Cells. Lithium Batteries, J.R. Gabano, Ed., (Academic Press, London), pp. 211-239

(2) B. B. Owens (1992) Rechargeable Lithium Polymer Electrolyte Batteries, Proceedings 35th International Power Sources Symposium, pp 271-2.

(3) M. Gauthier, M. Armand and D. A. Muller (1988), Aprotic Polymer Electrolytes and their Applications, Electroresponsive Molecular and Polymer Systems, T. A. Skotheim, Ed., (Marcel Dekker Inc. New York 1988), pp. 41-95.

(4) K. M. Abraham and M. Muller (1990), Li^+ Conductive Solid Polymer Electrolytes with Liquid-Like Conductivity, J. Electrochemical Soc., 137, pp 1657.

(5) D. Pagoria, et al (1992) Lithium Carbon Monofluoride Batteries Batteries for Extended Ultra High Temperature Storage and Surface Mount Applications, Proceedings of 35th International Power Sources Symposium, pp 7-9.

COMPOSITE ELECTRODE PERFORMANCE IN SOLID POLYMER ELECTROLYTE BASED SYSTEMS

D. Fauteux, A.A. Massucco, M. McLin, M. van Buren, and J. Shi
Arthur D. Little, Inc.
Acorn Park
Cambridge, USA, 02140-2390

ABSTRACT

Performance of electrochemical test cells using composite cathodes based on commercially available V_2O_5 and $LiMn_2O_4$, and a $LiMn_2O_4$ produced by a continuous process developed at Arthur D. Little are compared. Three electrode systems were evaluated in 1) a liquid electrolyte (PC-$LiClO_4$), 2) a PC-based gel electrolyte, and 3) a polymer electrolyte conductive at ambient temperature. The $LiMn_2O_4$ produced using Arthur D. Little process has large and controlled specific surface area and porosity. Consequently this material shows higher exchange current density and higher lithium intercalation capacity than some commercially available type of $LiMn_2O_4$.

INTRODUCTION

The successful development of a solid polymer electrolyte based lithium rechargeable battery technology will require in addition to the development of polymer electrolytes, the development of highly reversible high energy density composite cathodes. Although V_6O_{13} has been extensively used in the past in the formulation of polymer electrolyte based composite cathodes its use in a "commercial" battery system is compromised because of its low average discharge voltage[1] (2.4 Volts versus Li^+/Li^o). It is most likely, for the near term development and demonstration activities, that the polymer electrolyte based composite cathodes will be based on high voltage lithium intercalation materials such as $LiCoO_2$, $LiNiO_2$, $LiMnO_2$, and $Li_xMn_2O_4$. These materials generally require charge voltages in the range of 4 to 4.5 volts versus Li^+/Li^o, consequently necessitating electrolytes which are stable in oxidation to a voltage above 4.5 to 5 V. Few polymer electrolyte systems have clearly demonstrated this range of electrochemical stability.

In addition, polymer electrolyte based composite cathodes must contain a large volume and weight fraction of the lithium intercalation material in order to achieve a high energy density. Most if not all of the polymer electrolyte based composite cathode formulations reported to date also contain an additive, such as carbon or graphite, to improve electronic conductivity. Because of the lower ionic conductivity of polymer electrolyte systems, compared to liquid electrolyte systems, the composite cathode structure must also provide sufficient equivalent porosity to enable ion diffusion in and out of the composite cathode structure without imposing additional polarizations. Generally composite cathode structures are also maintained fairly thin, in the order of 25 to 75 μm, in order to optimize the utilization of the active cathode material capacity.

The role of the uniformity of the particle and of the particle size distribution on the electrochemical performance of lithium intercalation materials has been discussed by Deroo et al. [2]. In his study, Deroo demonstrated the critical importance of achieving a small particle size with a narrow particle size distribution in order to obtain high and uniform reversible utilization of the cathode capacity.

The previous characteristics of polymer electrolyte based composite cathodes; high active solids content, uniform porosity, and reduced thickness, impose severe processing constraints.

In the following report we summarize the results obtained during the characterization of lithium intercalation materials in three different electrolyte systems: a liquid electrolyte system (PC-$LiClO_4$), a PC-based gel electrolyte system, and a solvent free polymer electrolyte system. $LiMn_2O_4$ produced from two different processes, the first one commercial, the second proprietary to Arthur D. Little, and commercial V_2O_5 have been evaluated and their performance are compared. The Arthur D. Little $LiMn_2O_4$ has been produced using a continuous process which yield small $LiMn_2O_4$ particle of high surface area and high porosity. The "as produced" small particle $LiMn_2O_4$ has a bimodal particle size distribution centered around average particle sizes of 1 μm and 4 μm, and a surface area of approximately 18 m^2/g. Subsequent processing of the Arthur D. Little $LiMn_2O_4$ yielded small particles in which the dimensions and surface area yielded a single mode distribution centered around an average particle size of 0.6 μm.

EXPERIMENTAL

Liquid electrolyte system: A 1 molal solution of $LiClO_4$ (Aldrich) in propylene carbonate, PC, (Aldrich) was used as the base line formulation for the liquid electrolyte systems. These liquid electrolytes contained less than 40 ppm of water, as determined by Karl-Fisher coulometric titration.

PC-based gel electrolyte system: A PC-based gel electrolyte was obtained by the admixing of UV-curabled polymer precursors, PC, and a lithium salt. These gel electrolytes were UV-cured (≈200 W) for 1-2 minutes after being over-coated onto the cathode.

Polymer electrolyte system: A polymer electrolyte was obtained by the admixing of curabled polymer precursors, a low vapor pressure plasticizing compound, and a lithium salt. These polymer electrolytes were cured either thermally or with UV light after being over-coated onto the cathode.

Cathode materials characterization: All cathode materials were characterized using a Phillips model 120-1010 x-ray diffractometer (Cu Kα1, 1.5405 Å) . Topography and surface morphology were qualitatively evaluated using SEM, Cambridge Stereoscan 200. Surface area, pore volume distribution, and pore size distribution were measured using N_2 adsorption (Micromeretics ASAP2000) and Hg intrusion (Micromeretics PoreSizer 9320). Densities, (envelope and skeletal) were measured using Hg intrusion and helium pycnometry (Micromeretics 1305). Particle size and particle size distribution were evaluated using a Microtrac Full Range Particle Analyzer.

Electrochemical characterization: 3 electrodes electrochemical cells were used, lithium metal was used as both the anode and the reference electrode. The cell apparent surface area was approximately 5 cm^2. Resistive and capacity contributions were

evaluated using AC-impedance spectroscopy (Solartron FRA-1250 and ECI-1286) in a frequency range from 65 kHz down to 0.1 Hz before and after cycling of the composite cathode materials. Exchange current densities were evaluated using the resistive contribution associated with the charge transfer process.

RESULTS

Liquid electrolyte (base line)

$LiMn_2O_4$: Commercial source

The commercial $LiMn_2O_4$ has a specific surface area of approximately 6 m^2/g. Figure 1.a presents the AC-impedance spectrum of a $LiMn_2O_4$ cathode material obtained from a commercial source. Three features are clearly identified on this spectrum: 1) the resistive contribution associated to the electrolyte (≈ 0.6 Ω), the resistive-capacitive contributions associated to the charge transfer process within the cathode (≈5.2 Ω, ≈30 μF), and a diffusion controlled process at low frequency.

The exchange current density for this commercial $LiMn_2O_4$ cathode material was evaluated to be approximately 458 mA/g After cycling, the AC-impedance spectrum (Figure 1.b) shows a significant increase in the value of the charge transfer resistance.

Charge/discharge voltage profiles, between 2.5 and 4.2 V, show the two voltages plateau, at 2.8 and 4.0 V, corresponding to the reversible intercalation of 1.1 é per Mn_2O_4 (Fig. 2.a).

$LiMn_2O_4$: Arthur D. Little

The $LiMn_2O_4$ used in this study is the "as produced" material and has an bimodal particle size distribution centered around an average particle size of 1 μm and 4 μm, and a large specific surface area of approximately 18 m^2/g. Total pore surface area of pores having diameters larger than 0.01 μm mainly account for this high specific surface area. Figure 3.a presents the AC-impedance spectrum of a $LiMn_2O_4$ cathode material produced using Arthur D. Little's process. As for the commercial sample of $LiMn_2O_4$ cathode material previously described in Figure 1, the AC spectrum (Fig. 3.a) shows three features: 1) the resistive contribution associated with the electrolyte (≈1.3 Ω), 2) the resistive-capacitive contribution associated with the charge transfer process occurring within the cathode (≈1.3 Ω, ≈41 μF), and a diffusion controlled process at low frequency. The exchange current density was estimated to be approximately 1465 mA/g.

The cycling behavior of the $LiMn_2O_4$ is presented in Figure 2.b. Two plateaus are observed. The first one at a high voltage of approximately 4 V and the second one at an average voltage of 2.8 V. The initial discharge capacity correspond to the intercalation of 1.4 é per Mn_2O_4 (Fig. 2.b). After cycling the two plateaus are maintained and their relative proportion is preserved.

Figure 3.b presents the AC-spectrum of the cathode material after cycling. Contrary to what was observed for the cathode using the commercial $LiMn_2O_4$, this cathode showed a decrease of it resistive contribution.

V_2O_5: Commercial source

Figure 4 presents the AC-impedance spectra of a completed cell showing mainly the lithium-electrolyte interfacial resistive-capacitive contribution. The observed (Fig. 5 and 6) behavior of the V_2O_5-based cathode under low current density cycling regimes. initially between 2.8 and 3.8 V and subsequently between 2.0 and 3.8 V, are consistent with the reported behavior of V_2O_5[3].

PC-Based Gel Electrolyte

V_2O_5: Commercial

Figure 7 presents the AC-impedance spectra of a cell made of a V_2O_5-based composite cathode / PC-based gel electrolyte / Lithium anode as measured before and after cycling. The major resistive contribution is associated with the lithium electrolyte interface resistance. The PC-gel electrolyte conductivity was estimated to be near $1x10^{-3}$ S/cm at ambient temperature. Cycling performance of the cell are reported in Figure 8 for a discharge regime of ≈C/10 between 2.0 and 3.8 V.

Polymer Electrolyte

V_2O_5: Commercial source

Figure 9 summarizes the evolution of a V_2O_5-based composite cathode / polymer electrolyte / lithium anode cell impedance as a function of time after fabrication. The cell impedance as measured immediately after assembly (•) and after 64 hours (○) are reported. The cell impedance remains mainly constant during this period of time. Charge/discharge cycles, between 2.8 and 3.8 V, results in the reversible intercalation of 0.3 Li /V_2O_5.

$LiMn_2O_4$: Arthur D. Little

The electrochemical performance characteristics, at a cell level, of composite cathodes containing a mixture made of small particle size-$LiMn_2O_4$ and carbon in a thermally cured polymer electrolyte matrix are presented. These cells have been tested using polymer electrolyte formulations which provide sufficient ionic conductivity at ambient temperature. Evolution of the cell resistance, before and after cycling, as measured by AC-impedance will be discussed. Cycle life performance will also be reported. This experimental work is currently in progress. Detail results will be reported.

CONCLUSIONS

Arthur D. Little has developed a fast continuous process (reaction time of less than 1 minute) for the production of lithium intercalation compounds in the form of small particle of controlled particle size, particle size distribution, and porosity. This process has been used for the production of the cubic spinel $LiMn_2O_4$. Characterization of the electrochemical performance at the cell level demonstrated, that the $LiMn_2O_4$ produced using Arthur D. Little's process, has a high exchange current density which is attributed to the increase in surface area of the cathode material. This attribute is beneficial when the $LiMn_2O_4$ is integrated in gel-polymer electrolyte and polymer electrolyte systems having limited ionic conductivity.

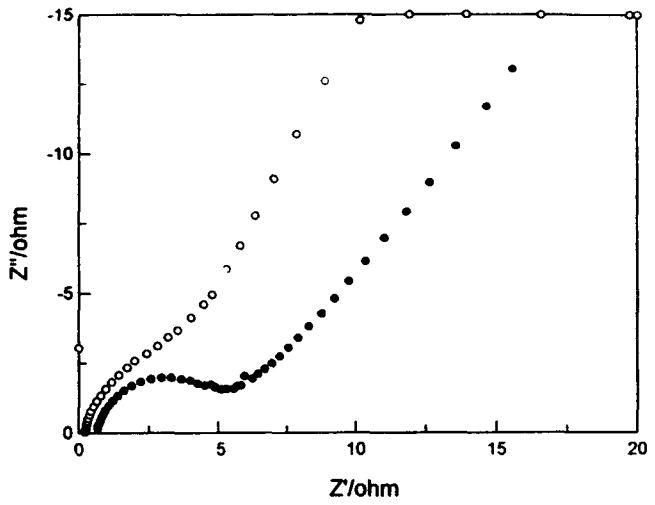

Figure 1: AC-impedance spectra of a cathode made using commercially available $LiMn_2O_4$, in a PC-$LiClO_4$ liquid electrolyte, before (•) and after cycling (○) at a charge discharge rate of ≈C/5

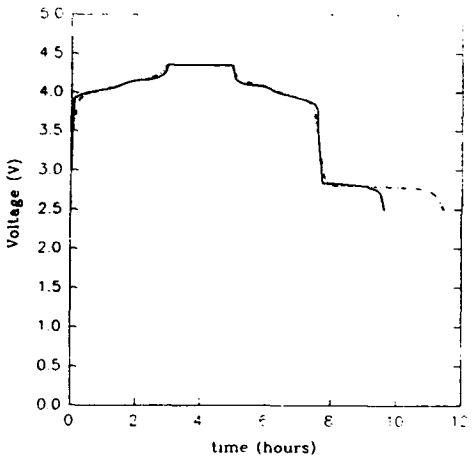

Figure 2: Voltage profile of $LiMn_2O_4$-based cathodes in liquid electrolyte during charge/discharge at ≈C/10 rate, commercial $LiMn_2O_4$ (—) and Arthur D. Little produced $LiMn_2O_4$ (·····) .

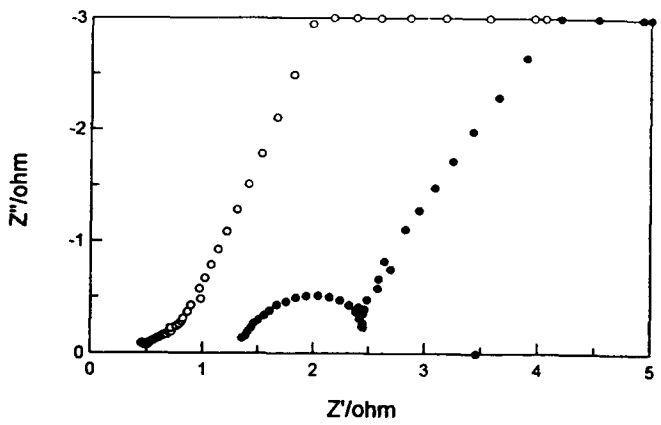

Figure 3: AC-impedance spectra of a cathode made using $LiMn_2O_4$ produced using a continuous process developed at Arthur D. Little, in a PC-$LiClO_4$ liquid electrolyte, before (•) and after cycling (○) at a charge discharge rate of ≈C/5

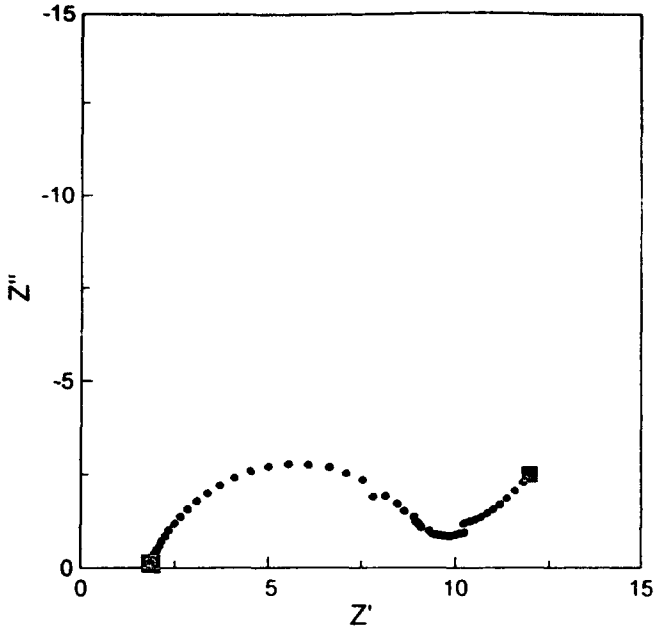

Figure 4: AC-impedance spectrum of a Li/PC-$LiClO_4$ electrolyte/V_2O_5 cell before cycling at ambient temperature

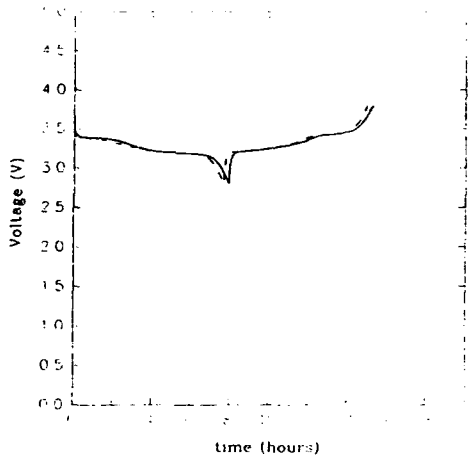

Figure 5: Voltage profile of V_2O_5-based cell in PC-$LiClO_4$ electrolyte, cycled between 2.8 and 3.8 V

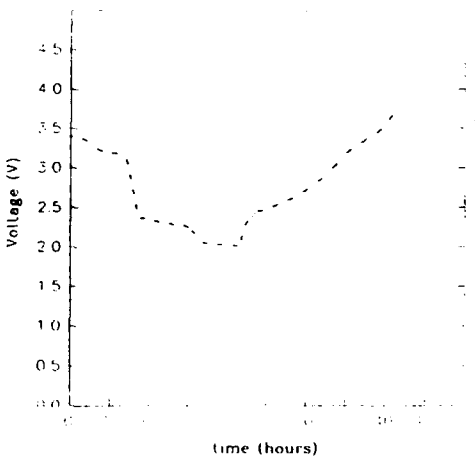

Figure 6: Voltage profile of V_2O_5-based cell in PC-$LiClO_4$ electrolyte, cycled between 2.0 and 3.8 V

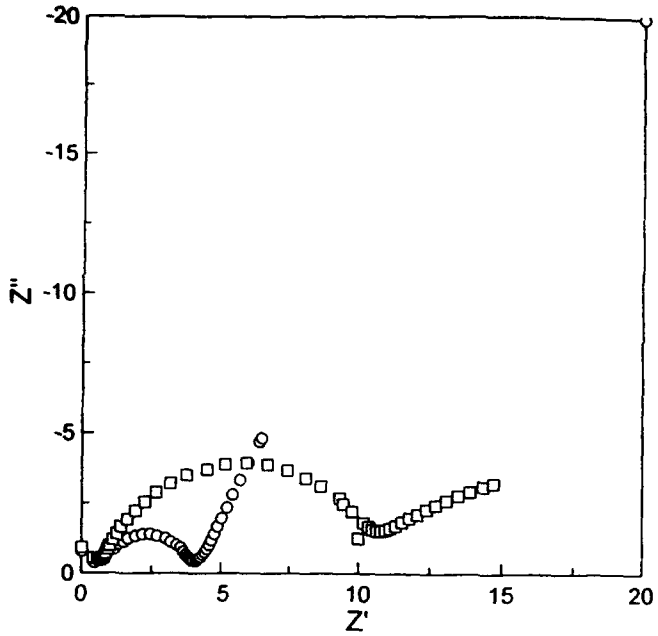

Figure 7: AC-impedance spectrum of a Li/ PC-gel electrolyte/V_2O_5 cell before (O) and after (□) cycling at ambient temperature

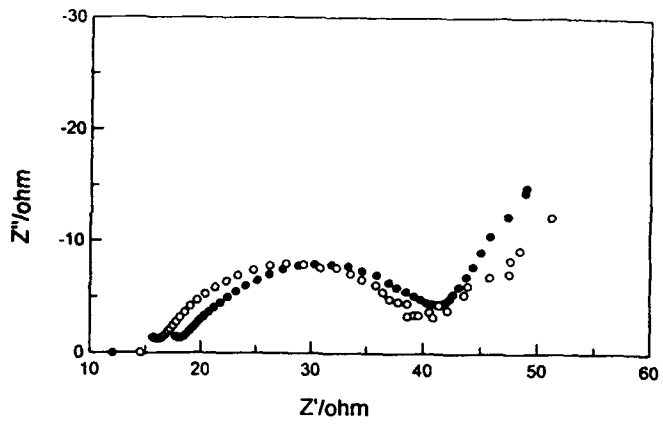

Figure 9: AC-impedance spectrum of a Li/ polymer electrolyte/V_2O_5 cell before (O) and after (●) aging at ambient temperature

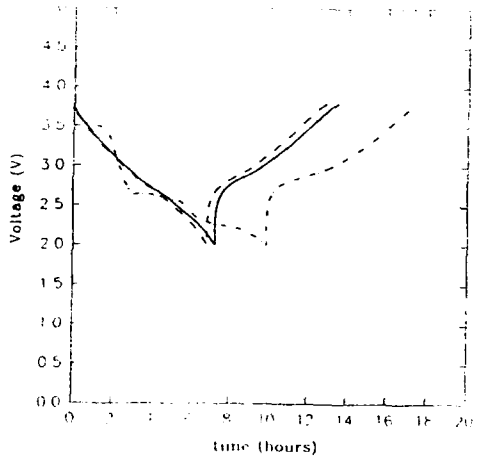

Figure 8: Voltage profile of V_2O_5-based cell in PC-gel electrolyte, cycled between 2.0 and 3.8 V

REFERENCES

1. R.J Brodd, J.T. Lundquist, J.L. Morris and D.R. Shackle, Battery Seminar, Deerfield Beach, Florida, March 194

2. F. Dallard, D.Deroo, D. Foscallo, and J.L. Merienne, J. Power Sourc (1985) 209-213

3. C. Delmas, Chap. 12 in Lithium Batteries, ed. G. Pistoia, Industrial Chemistry Library, Vol.5, Elsevier, 1994

LITHIUM ION INSERTION ELECTRODES: CATHODE MORPHOLOGY AND PERFORMANCE

W.H. Smyrl, R.T. Atanasoski, E.L. Cussler,
B.B. Owens, and M.D. Ward
Corrosion Research Center
Department of Chemical Engineering and Materials Science
University of Minnesota
Minneapolis, MN 55455

The feasibility of Li solid polymer rechargeable batteries has been established as a result of the recent development of ambient temperature solid polymer electrolytes with conductivities on the order of 10^{-3} S/cm. One limitation in the performance of present polymer electrolyte batteries, including those presently under development, is caused by the existing designs of the electrode structures. The program at the University of Minnesota is focused on a comprehensive and coordinated study of novel microporous cathode structures that will lead to a new generation of improved polymer batteries. The conventional approach to electrode design is to fabricate composite structures of small electroactive particles mixed with conductive carbon particles, and perhaps with the polymer electrolyte. The particle size of the electroactive materials is usually above 1 micrometer, and often above 100 micrometers. In the present study, the conventional composite electrode is compared to the behavior of electrode structures produced by two new approaches. The first approach is to synthesize novel electrode structures based on interpenetrating bicontinuous networks that will provide very high surface areas and small pores. The second approach is to prepare microporous electrodes by drying and processing hydrogels derived from sol-gel techniques. The two approaches have yielded electroactive V_2O_5 intercalation electrodes with surface areas above 300 m^2/g. The synthesis and processing activities are complemented by a study of intercalation electrode materials that are silanized derivatives of V_2O_5. We are engaged in a program to assess the relationship between the morphology of the active materials, the structure of the electrodes, the type of electrodes and the mechanisms of the faradaic processes at the positive electrode. We are specifically interested in increasing the rate capability of lithium polymer batteries.

Solid oxide cathode materials which may host the insertion of lithium ions have been of great interest for use in high energy batteries. Such materials offer the possibility for high performance batteries because of their high theoretical specific energy, which is linked to the large departure of the chemical potential of inserted Li below that of the pure metal. As illustrated by Figure 1, the various host compounds offer a wide range of [illegible]rating voltages. The materials also show a considerable [illegible] in the degree of lithium ion insertion.

Development efforts in this field have resulted in commercial Li-ion batteries, as well as various prototype batteries with limited performance and reliability in most cases. The lithium polymer battery is an active area for research at present, both for small cells for computer and microelectronics applications, and large cells for electric vehicles. The polymer electrolyte batteries utilize various oxides of vanadium as the cathode intercalation host. Vanadium oxide hosts are attractive because the theoretical specific energies for such cathodes with lithium anodes can be greater than 1000 Wh/kg, and they are less reactive toward polymer electrolytes than the lithiated oxides of cobalt, nickel, and manganese. However, the experimental cells fabricated with vanadium oxide cathodes suffer from a number of problems including a declining capacity with each cycle as well as generally poor performance at high rates of charge or discharge.

The focus in the present program has been on V_6O_{13} and V_2O_5 materials which have shown promise in various development programs. The former oxide material is probably the most widely used cathode host in polymer batteries, and it has been used in previous work at this laboratory as well. It is prepared by pyrolysis of ammonium metavanadate. Careful control of the pyrolysis conditions are essential in order to obtain high capacity V_6O_{13}. V_2O_5 is prepared by a sol-gel technique wherein a solution of sodium metavanadate is passed through an ion exchange column in order to replace the sodium ion with hydrogen ion. The acidic solution is collected and allowed to set without disturbance for weeks or months, during which time fibrils and ribbons self-assemble in solution and pass through the sol to a gel stage that continues to mature with time. The hydrogel V_2O_5 has attracted widespread interest because of its versatility and properties as an oxidant and host for metal cations.

The V_6O_{13} material is being studied in composite electrodes with carbon additives. The relationship of the performance to the active material particle size and surface area are being assessed as a function of rate at both ambient and elevated temperatures, with liquid electrolytes. The maximum insertion of eight lithium ions can be obtained at elevated temperatures on the first cycle, but for continuous cycling at ambient temperature at a modest rate (i.e., C/10), about 50 percent of the maximum amount of lithium ion insertion is obtained between the working voltages of 3.4 V charge and 1.9 V discharge, under galvanostatic conditions. Very reproducible discharge behavior is observed for particle diameters between 5 microns and 100 microns. Our results for these materials in relatively thin electrode structures does demonstrate that rate limitations arising from diffusion phenomena within the individual particles is partially overcome with small particles.

Examination of a composite mixture of small particle size V_6O_{13} and carbon particles shows the V_6O_{13} particles to be 5 microns or less in diameter, and the carbon particles are 0.1 microns or less. The composite was well mixed and there was no obvious agglomeration of particles. Agglomeration of particles was seen for another mixture made of 100 micron diameter particles. Agglomeration phenomena such as this will not support high rate insertion processes.

V_2O_5 xerogel electrodes may be prepared with different morphologies and surface areas by controlled processing and drying. Spin coated thin films are dense and have smooth surfaces. Dip coated films may be dense when dried slowly or porous when dried rapidly. In both cases the material has been dried under vacuum to a final composition of $V_2O_5 \cdot 0.5H_2O$. The remaining water is held tenaciously and is released only when the material is heated above 300°C.

A discharge curve obtained for a spin coated xerogel V_2O_5 (XRG) film under linear sweep voltammetry conditions shows that about three lithium ions are inserted between 3.8V and 1.9 V. This corresponds to an experimental energy density of 1137 watt-hours per kilogram of electroactive cathode material. A comparison of these results with the theoretical energy density of several other insertion materials is shown in Table 1, and shows that XRG films are superior on this basis.

Multiple continuous discharge/charge cycles have been performed on a V_2O_5 (XRG) film. The film retained over 60 percent of the original capacity after 1000 cycles, and the 'lost' capacity could be recovered by holding the electrode at 3.8 V for several hours at the end of the 1000 cycle test. The coulombic efficiency of the first and second cycles was 94 and 98 percent respectively. The coulombic efficiency of individual cycles was 99.9 percent after 150 cycles. Concurrent mass (quartz crystal microbalance) and charge measurements show that only lithium ions are inserted and released in this system, and that mass reversibility is also observed over an individual cycle. No water was released from the cathode XRG material during the cycling.

Both of the vanadium oxide materials used in the present study show that the rate of insertion of lithium ions is limited by diffusion within the solid oxide and not by the surface injection rate. For thin composite electrodes, utilization of the electrode will be inversely proportional to the discharge (charge) current and directly proportional to the electrode thickness or mass loading. Limitations of transport in the electrolyte phase will eventually become the dominant phenomena for thick electrodes and will cause the utilization to decrease with thickness or mass loading. The transport limitations may be caused by resistance limitations (ohmic drop) in the electrolyte in the pores, or by diffusion in the

pores when all the lithium ions are inserted into the host material. The maximum current for a given utilization may be obtained from such an analysis, and will be used for design purposes.

From the results of the present study, it has been possible to develop the experimental relation between the specific power and specific energy as expressed per unit mass of the oxide electrode materials. Inclusion of the equivalent amount of lithium in the mass would reduce the values by about 10 percent, and therefore it is seen that very thin cathodes are capable of a relatively high level of performance. Of course, the incorporation of such thin cathodes into full size battery designs will further reduce the values by a considerable amount.

Further studies are in progress to analyze performance of thicker films as well as electrode matrix designs that may retain some of the high levels of performance in larger scale electrode and battery designs.

Acknowledgment

This research was supported by ARPA, Contract N/N0014-92-J-1875.

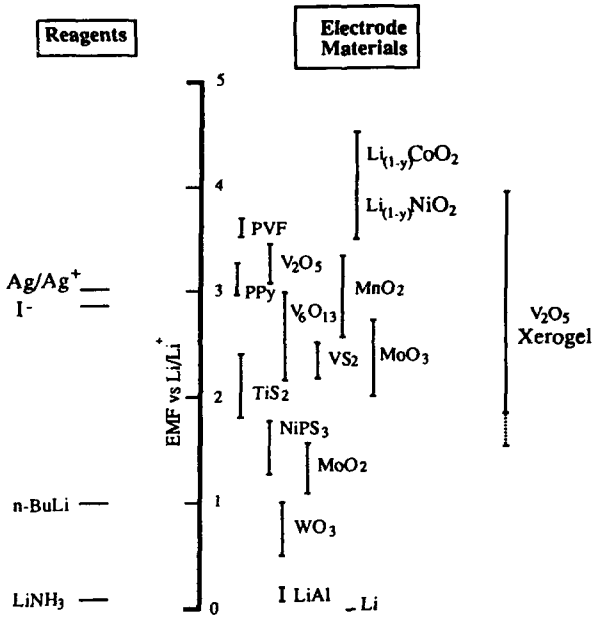

Figure 1. Redox Scale for Li Intercalation Materials and Reagents

Table 1. Theoretical Energy Density of Lithium Insertion Electrode Materials

Cathode	V_2O_5* (XRG)	V_6O_{13}	V_2O_5	TiS_2	$TiSe_2$	VS_2	VSe_2	$NbSe_2$
Energy Density (Wh/kg)	1137	890	460	481	243	505	246	216

* Experimental Energy Density

PERFORMANCE CHARACTERIZATION OF LITHIUM COBALT DIOXIDE CATHODES IN POLYMER-BASED LITHIUM AND LITHIUM-ION RECHARGEABLE CELLS

Weihong Li, Hsiu-Ping Lin and David L. Chua
Alliant Techsystems Inc.
104 Rock Road
Horsham, Pennsylvania 19044

Abstract

This paper reports on the electrochemical performance of the polyacrylonitrile (PAN)-based Li/Li_xCoO_2 and C/Li_xCoO_2 cells. PAN-based polymer electrolyte exhibited ionic conductivity exceeding 10^{-3} S/cm in the temperature range of -20°C to 100°C, and an electrochemical stability window of 2.3 to 4.3 volts. The performance characterization of the $Li/SPE/Li_xCoO_2$ cells employing the PAN-based polymer electrolyte indicated discharge rate capability up to 0.5 mA/cm² (C) during the continuous cycling and 3 mA/cm² (6C) in the pulse discharge mode. Extended cycle life was obtained at 80 to 90 percent depth of discharge. In the PAN-based C/Li_xCoO_2 cells using Calcined Petroleum Coke as the carbon anode, lithium ion intercalation to $Li_{0.4}C_6$ was achievable during the charge and discharge cycling.

Introduction

Continued effort is being devoted to the development of polymer-based rechargeable lithium batteries, since such power systems have the key advantages of high energy density and packaging flexibility.

The development of the third generation polymer gel electrolyte expands system performance capabilities to allow for the potential applications of the rechargeable lithium-polymer batteries at ambient and subambient temperatures. Such gel-type systems, obtained by immobilizing metal salt solvates in a mixture of ethylene carbonate (EC) and γ-butyrolactone (γ-BL) or propylene carbonate (PC) in a polyacrylonitrile (PAN) matrix, exhibited an ionic conductivity exceeding 10^{-3} S/cm at ambient and subambient temperatures. Good dimensional stability was also demonstrated in such polymer electrolyte films as thin as 25 μm using the known film-processing techniques, such as drawdown rod and doctor-blade.

Recently, the exploration of using such gel-type systems in a "lithium-ion" cell has attracted a consistent renewed attention due to its potential of long cycle life and safe operation. In this effort we have evaluated the performance characteristics of the polymer-based "rocking chair" cell, a PAN-based C/Li_xCoO_2 cell using petroleum coke (Conoco) as the anode material.

In this paper, the electrochemical performance of the PAN-based Li/Li_xCoO_2 cell was evaluated by charge/discharge cycling at various current densities and temperatures. The preliminary results on the performance characteristics of PAN-based C/Li_xCoO_2 cell are also discussed.

Experimental

The polymer electrolyte and the $LiCoO_2$ cathode films were prepared by the standard film drawing technique. The components of the desired ratio were first dissolved in the solvent blend of ethylene carbonate (EC) and γ-butyrolactone (γ-BL) at elevated temperature with continuous stirring. The homogeneous viscous solution thus obtained was casted onto the substrate using either the "doctor blade" or the drawdown rod technique.

A two-electrode laboratory cell for cycling test consisted of a lithium foil or a thin film carbon anode, a PAN-based polymer electrolyte film and a $LiCoO_2$ cathode film on a current collector. The laminate was placed between two dielectric plates, encapsulated in the aluminized trilaminated pouch and heat sealed. The charge/discharge cycling tests were conducted on the battery test station (MACCOR).

All material handling and cell fabrication were conducted in a dry room with a controlled humidity (<2% RH).

Results and Discussion

Electrochemical Performance of the PAN-based Li/Li_xCoO_2 Cell

The PAN-based polymer electrolyte developed in this study had an ionic conductivity exceeding 10^{-3} S/cm in the temperature range of -20°C to 100°C[1]. The PAN-based Li/Li_xCoO_2 cell was assembled in the discharged state and showed an open circuit voltage (OCV) of 3.2 volts. The cells had an electrode area of 10 cm² and a theoretical capacity of approximately 10 mAh. The freshly built cells were subject to charge/discharge cycling and pulsing test at various rates and temperatures to demonstrate the electrochemical performance.

Figure 1 shows the typical discharge voltage profiles at various temperatures. At room temperature and above, the system exhibited an average 3.8 volts in discharge cycles, while a slightly lower discharge voltage was observed at 0°C. The discharge rate capability is defined in Figures 2 and 3. In the pulsing experiments, a fully charged cell was subjected to 5-sec discharge pulses at various rates. The results indicated that the cell was capable of maintaining 3.3 volts at 3.0 mA/cm² (6C). Figure 3 compares the voltage profiles of the cells at various discharge rates under the continuous cycling mode. The average 3.8 volts discharge characteristics were clearly demonstrated for discharge rates up to 0.3 mA/cm². Cycling at C rate (0.5 mA/cm²) was also possible although slightly lower discharge voltage was observed. The cyclability of the cell is illustrated in Figure 4. The cycle life of 150 to 200 cycles was achieved at various charge and discharge rates.

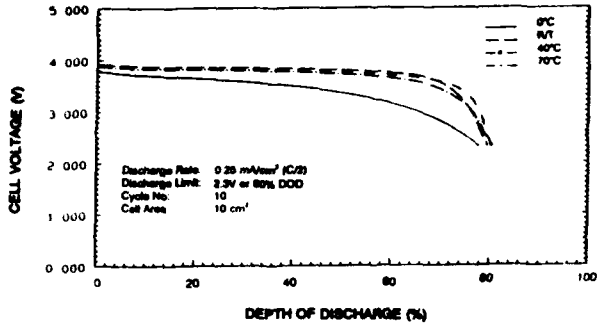

Figure 1. Typical discharge voltage profiles as a function of temperature of Li/SPE/Li_xCoO_2 cell.

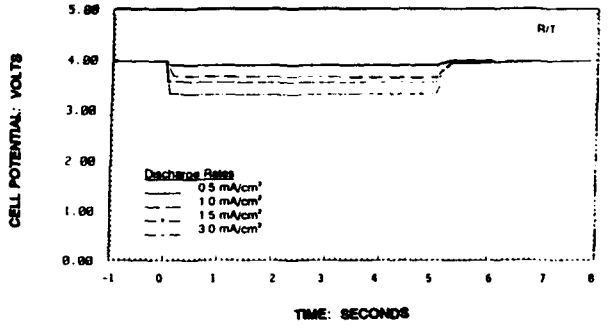

Figure 2. Rate capability during pulse discharge of Li/SPE/Li_xCoO_2 cell.

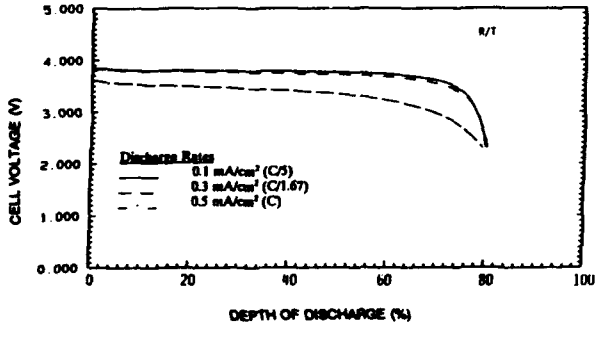

Figure 3. Rate capability under continuous cycling mode of Li/SPE/Li_xCoO_2 cells.

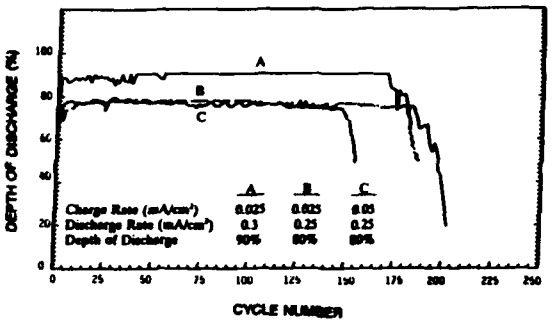

Figure 4. Cycle life performance of Li/SPE/Li_xCoO_2 cells at room temperature.

Performance Characteristics of the PAN-based C/Li_xCoO_2 Cell

The feasibility of using Petroleum coke as the negative electrode in the PAN-based polymer rechargeable cell was evaluated. The carbon anode for the polymer-based C/Li_xCoO_2 cell was processed using the same technique as for processing the cathode film. Petroleum coke can intercalate Li to a composition limit of $Li_{0.5}C_6$, equivalent to a gravimetric specific capacity of 0.186 Ah/g. Figure 5 shows the charge and discharge voltage profiles of a PAN-based C/Li_xCoO_2 cell equipped with a Li reference electrode. The achievable capacity with C/20 charge and C/5 discharge rates yielded a stoichiometry of $Li_{0.4}C_6$. The rate capability of the cell was examined by pulsing a fully-charged cell at various current densities. The results summarized in Figure 6 indicated that the cell maintained 2.7 volts in discharge at 1 mA/cm².

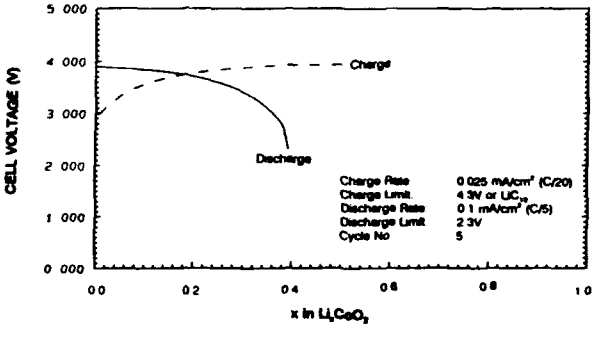

Figure 5. Charge and discharge voltage profiles of a PAN-based C/Li_xCoO_2 cell at room temperature.

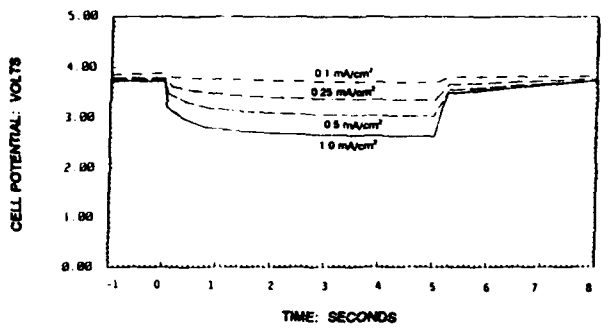

Figure 6. Pulse discharge profile of a PAN-based C/Li_xCoO_2 cell at room temperature.

References

1. W. Li, H-P. Lin and D. L. Chua, to be published in the proceedings of the 184th Meeting of the Electrochemical Society, New Orleans, Louisiana, October, 1993.

2. R. Koksbang, I. I. Olsen, P. E. Tonder, N. Kundsen, and D. Fauteux, J. Applied Electrochemistry, 21, 301 (1991).

Acknowledgement

This work is supported by USAF/Phillips Laboratory and by Alliant Techsystems Inc.'s internal development funds. The authors wish to acknowledge the experimental contributions of Miss Rebecca Morris and Mr. David Hughes. The authors would also like to thank Dr. H. V. Venkatasetty for the valuable discussions.

SOLID-STATE CARBON/$LiNiO_2$ PULSE POWER BATTERIES

M. Alamgir, N. Marchese and K. M. Abraham
EIC Laboratories, Inc.
Norwood, Massachusetts 02062

Solid-state carbon/$LiNiO_2$ cells and two-cell bipolar batteries containing PAN-EC/PC-$LiN(CF_3SO_2)_2$ solid polymer electrolytes have demonstrated high rate capabilities at room temperature with an ability to sustain pulsed discharge currents as high as 50 mA/cm^2. The carbon/$LiNiO_2$ cells retained >80% of the initial cell capacity after 150 full depth of discharge and charge cycles.

Introduction

Bipolar batteries consist of current collector plates whose opposite sides are coated with the cathode and the anode materials. The electronically conducting but ionically insulating bipolar plates shorten the electronic pathway between individual cells and, consequently, bipolar batteries have lower resistance than those configured from a stack of series-connected cells [1]. The internal resistance of bipolar batteries is independent of the cell size. As a result, these batteries are especially suitable as high current pulse power sources, since the power (P) of a battery is inversely proportional to the resistance (R).

$$P = V \cdot I = V^2/R \qquad (1)$$

Bipolar batteries based on liquid electrolytes generally suffer from high rates of self-discharge, due to intercell leakage currents caused by the wicking of the electrolytes over the edge of the bipolar plate. Consequently, fabrication of such batteries using liquid electrolytes is a major engineering challenge. Bipolar batteries containing solid electrolytes are expected to be free of these drawbacks.

There is considerable current interest in developing solid-state batteries based on highly conductive polymer electrolytes- both solvent-free and plasticized [2,3]. However, only the latter electrolytes have sufficiently high conductivities (i.e., $\geq 10^{-3}$ohm^{-1}cm^{-1}) to enable the development of batteries for room temperature operation. The polyacrylonitrile (PAN)-based solid electrolytes developed at EIC belong to this class of electrolytes [3]. Using these electrolytes, we have fabricated solid-state carbon/$LiNiO_2$ cells and bipolar batteries and studied their continuous and pulsed discharge performance at room temperature.

Experimental

PAN-based solid electrolytes were prepared as before [4]. First the polymer was dissolved in a solution of $LiN(CF_3SO_2)_2$ in ethylene carbonate (EC) and propylene carbonate (PC) at 135°C. Electrolytes of 75- 100 μm thickness were then prepared by casting the resulting, highly viscous solution between PTFE shims and cooling to room temperature. Carbon composite anodes were made by pressing a blend of Conoco XP petroleum coke and PAN-EC/PC-$LiN(CF_3SO_2)_2$ electrolyte onto a Ni substrate. $LiNiO_2$ used as the cathode was synthesized by reacting $NiCO_3$ and $LiNO_3$ in O_2 atmosphere. $LiNiO_2$ composite cathodes were prepared from a mixture of $LiNiO_2$, Chevron carbon and PAN-EC/PC-$LiN(CF_3SO_2)_2$ electrolyte by pasting the mixture on a stainless-steel current collector. Bipolar electrodes were fabricated by pressing the $LiNiO_2$ and the carbon electrode mixtures on the opposite sides of a 25 μm stainless-steel substrate. Carbon/$LiNiO_2$ single cells and two-cell bipolar batteries were fabricated by sandwiching the polymer electrolyte between the composite electrodes, monopolar or bipolar, and sealing the package in metallized plastic bags.

Results and Discussion

Equation (1) reveals that besides by lowering the resistance, the power of a battery is increased by increasing its voltage. The $LiNiO_2$ cathode is desirable in this respect, since the Li/$LiNiO_2$ cell exhibits a load potential of about 4V (Fig. 1). The $LiNiO_2$ cathode is also characterized by the high capacity of ~150 mAh/g and good reversibility. While the high voltage of $LiNiO_2$ imposes constraints on the choice of oxidatively stable solid polymer electrolytes, the PAN-based electrolytes have been found to be both chemically and electrochemically stable for use in conjunction with 4V metal oxide cathodes. At room temperature, these electrolytes have a high conductivity of about $1.5 \times 10^{-3} \Omega^{-1}.cm^{-1}$. The conductivities of two PAN-based electrolytes having the compositions of 12 w/o PAN-40 w/o EC/40 w/o PC- 8 w/o $LiN(CF_3SO_2)_2$ and 10 w/o PAN-40.5 w/o EC/40.5 w/o PC-9 w/o $LiN(CF_3SO_2)_2$ in the temperature range of -10 to 50°C are shown in Figure 2.

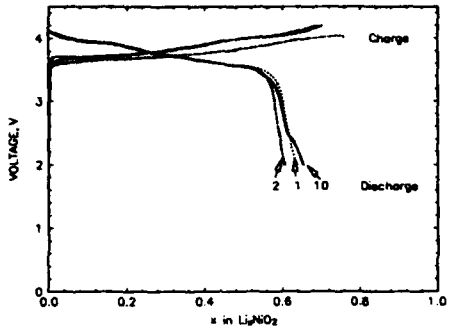

Figure 1. The room temperature cycling performance of a Li/$LiNiO_2$ cell containing a PAN-EC/PC-$LiN(CF_3SO_2)_2$ electrolyte.

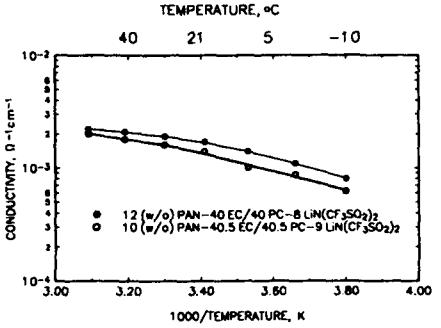

Figure 2. The conductivities of two PAN-EC/PC-$LiN(CF_3SO_2)_2$ electrolytes as a function of temperature.

The PAN-based solid electrolytes are also chemically and electrochemically stable in contact with Conoco petroleum coke, a graphitic carbon intercalation anode, which exhibits a net reversible capacity of ~0.5 Li per C_6 [3]. There is a deintercalation inefficiency of about 0.25 Li per C_6 in the first cycle due to the reduction of the electrolyte.

The performance of carbon/$LiNiO_2$ cells containing the PAN-EC/PC-$LiN(CF_3SO_2)_2$ electrolytes was evaluated first in 10 cm^2 cells using a continuous discharge current of 0.1 mA/cm^2. The cells were cycled usually between 2.0 and 4.0V at room temperature. Figure 3 shows the first two charge and discharge plots of a carbon/$LiNiO_2$ cell. The cell capacity was limited by the anode. Upon activation in the first charge, a capacity of 20.7 mAh was obtained. This corresponds to an intercalation of 0.78 mole of Li per mole of C_6, forming $Li_{0.78}C_6$, and a deintercalation of 0.59 mole of Li from $LiNiO_2$, forming $Li_{0.41}NiO_2$ in the first charge. In the following discharge, a capacity of 13.8 mAh at a discharge voltage of 3.6V was obtained. This implies a 33% loss in capacity in the first cycle, stemming mostly from the carbon anode.

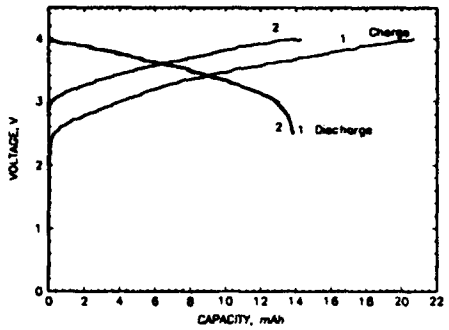

Figure 3. The first two charge and discharge plots of a carbon/$LiNiO_2$ cell at 0.1 mA/cm^2 at room temperature. The capacities of the $LiNiO_2$ and the carbon electrodes were 35.0 and 26.4 mAh, respectively, based on intercalation capacities of 1 Li per $LiNiO_2$ and 1 Li per C_6.

Figure 4 compares data for three cells in which the ratio of the active materials in the cathode to that in the anode was varied. For high cathode to anode ratios, there is an excess of charge input due to plating of Li on the carbon electrode during the first charge. As more and more Li is plated onto the carbon anode in the course of cycling, the cell voltage increasingly resembles that of a *Li/LiNiO$_2$ cell*, as evidenced by the increasingly higher and flatter discharge plateau of the cell in Figure 4a. On the other hand, when the anode is in excess compared to the cathode material, charging the cell to 4.0V does not permit its full intercalation (Fig. 4b). The charge voltage is reached more at the expense of the cathode voltage than of the anode. On discharge, the cell delivers low load voltage. In both of these cases the rechargeability for the cell was poor.

When the cathode to anode mole ratio is about 1.30, the $LiNiO_2$ and the carbon electrode appear to be fully deintercalated and fully intercalated, respectively, in the first charge. The cell then shows excellent rechargeability on subsequent cycling. This is evident by the data in Figure 4c for a cell cycled more than 150 cycles. At the end of this cycling, the cell retained ~80% of its initial discharge capacity at 0.2 mA/cm^2.

To exhibit good cyclability, a carbon/$LiNiO_2$ bipolar battery must not only have an optimum ratio between the cathode and the anode active materials in the cells comprising the battery, but also a careful balance among the capacities of the individual cells. This can be illustrated by the data in Figure 5. When there is a significant imbalance in the capacity of the cells as it is the case in Figure 5a, the cyclability of the battery is poor. The capacity ratio for Cell A to cell B in this battery was 0.71. When the two cell capacities are matched as in Figure 5b, the bipolar battery demonstrates attractive charge and discharge behavior. The ratio of the capacity of Cell A to that of Cell B for the battery in Figure 5b was 0.98.

Both carbon/$LiNiO_2$ single cells and two cell bipolar batteries were galvanostatically pulsed at a series of discharge currents between 1 and 50 mA/cm^2. The pulsewidth was varied between 10 and 50 ms and the interpulse relaxation time was kept at 5x pulsewidth.

Figure 6 shows the initial pulses of a carbon/$LiNiO_2$ single cell discharged at a current density of 10 mA/cm^2. The pulselength was 10 ms. The initial load voltage at this current was about 3V. The voltage traces in Figure 6 show rapid response of the cell voltage to the applied current as well as its fast recovery when the current was turned off. This suggests fast kinetics for the intercalation/deintercalation processes in both the $LiNiO_2$ cathode and the carbon anode. At total of 32,500 pulses to a cutoff of 2.0V were obtained. This translates into a total discharge capacity of 8.9 mAh, which compares well with the capacity of 12 mAh obtained when the cell was continuously cycled at a current density of 0.2 mA/cm^2. The ON and OFF voltages for the cell when pulsed at 10 mA/cm^2 are displayed in Figure 6b.

Figure 7 shows the initial voltage profiles of a two-cell carbon/$LiNiO_2$ bipolar battery pulse discharged at 2 mA/cm^2 for 10 ms. Table 1 gives the specifications for this battery. The battery delivered a total of 150,000 pulses or 6.3 mAh of capacity at a load voltage of 7.5V.

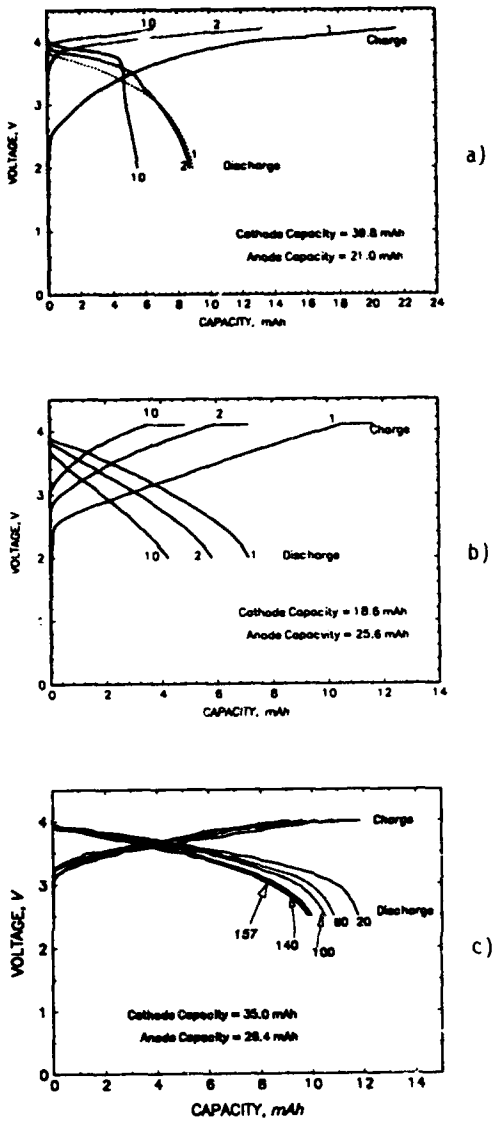

Figure 4. Effect of different cathode:anode mole ratios on the room temperature cyclability of carbon/$LiNiO_2$ cells. Cathode to anode mole ratios, a) 1.79; b) 0.73; c) 1.33.

When the current was increased to 10 mA/cm^2, the average discharge voltage decreased to about 6.5V. A total of 22,500 pulses (or 4.7 mAh of capacity) were obtained (Fig. 8). The battery could also be discharged at a high current density of 50 mA/cm^2 (Fig. 9). The load voltage at this current density was about 5V.

The preceding data demonstrate the usefulness of the PAN-based solid electrolytes in solid-state carbon/$LiNiO_2$ cells and bipolar batteries for room temperature application. Both single cells and bipolar batteries showed good rechargeability, and pulsed discharge capability at currents as high as 50 mA/cm^2.

Acknowledgement

Financial support for this work was provided by the Strategic Defense Initiative Organization, Contract No. F29601-92-C-0099.

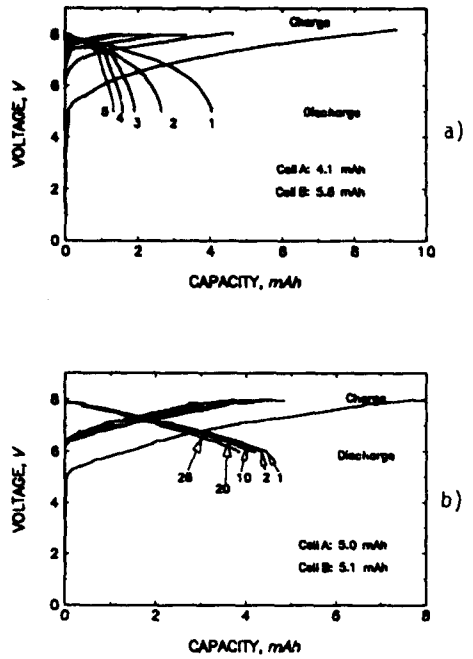

Figure 5. Effect of ratio of cell capacities on the room temperature cyclability of two-cell carbon/$LiNiO_2$ bipolar batteries. Cell A to Cell B capacity ratio, a) 0.71 and b) 0.98.

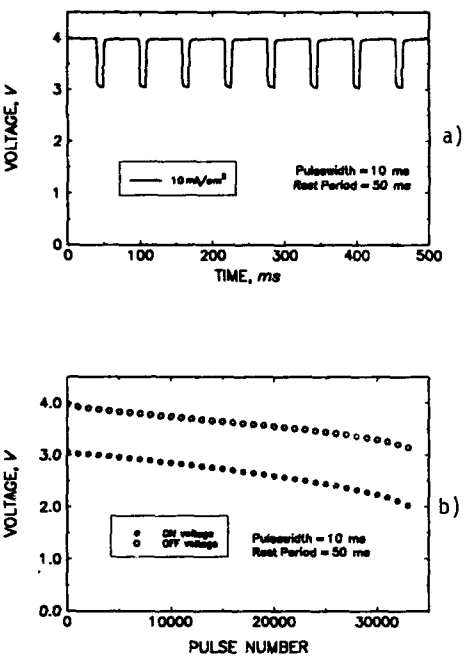

Figure 6. Pulsed discharge of a carbon/$LiNiO_2$ cell at 10 mA/cm^2. A) Initial voltage traces; b) the ON and OFF voltages during pulsing.

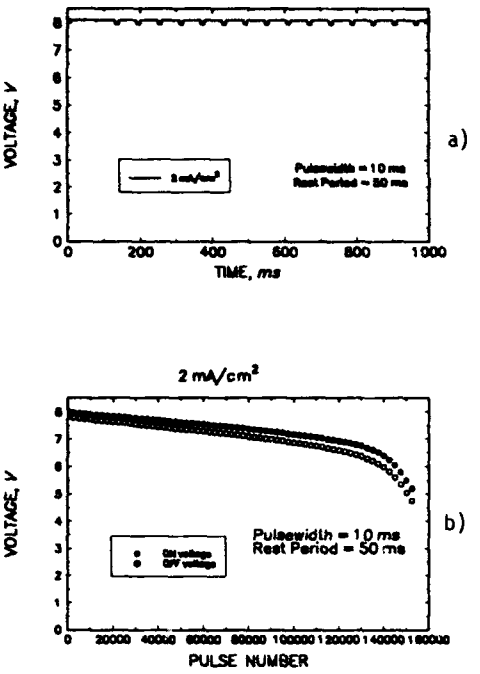

Figure 7. Pulsed discharge of a two-cell carbon/$LiNiO_2$ bipolar battery at 2 mA/cm^2. a) initial voltage traces; b) ON and OFF voltages.

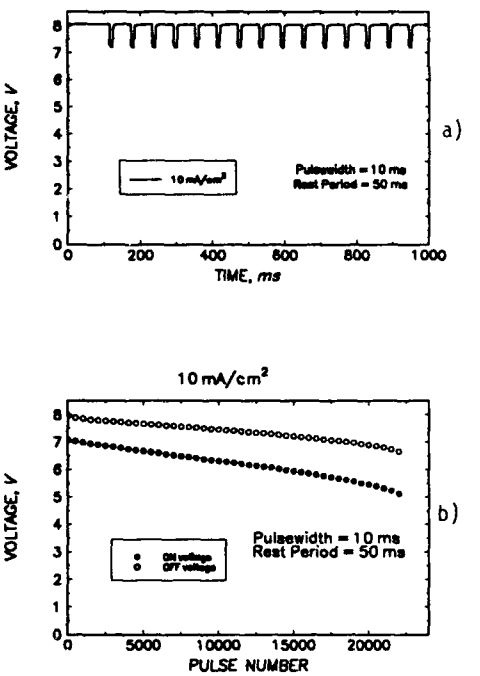

Figure 8. Pulsed discharge of a two-cell carbon/$LiNiO_2$ bipolar battery at 10 mA/cm^2. a) initial voltage traces; b) ON and OFF voltages.

Table 1. Specifications for the 2-cell carbon/$LiNiO_2$ bipolar battery pulse discharged at different currents at room temperature.

		Capacity (mAh)	Capacity Ratio ($LiNiO_2$:Carbon)	Capacity of Cell A to Cell B
Cell A	$LiNiO_2$	9.3	1.37	
	Carbon	7.1		1.05
Cell B	$LiNiO_2$	9.7	1.31	
	Carbon	7.1		

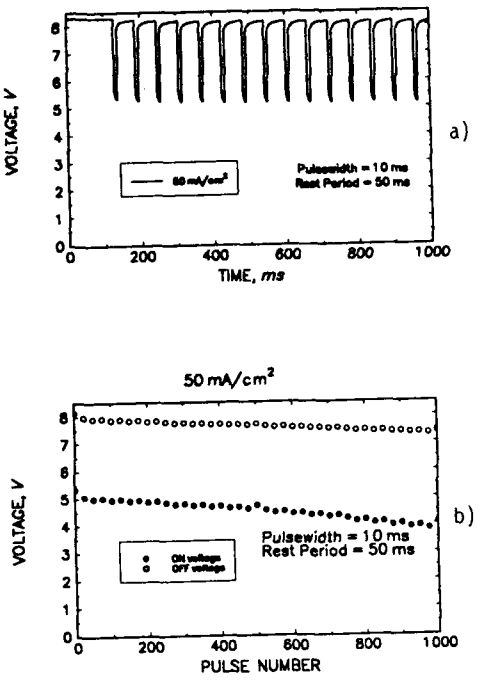

Figure 9. Pulsed discharge of a two-cell carbon/$LiNiO_2$ bipolar battery at 50 mA/cm^2. a) initial voltage traces; b) ON and OFF voltages.

References

1. LaFollette, R. M. and Bennion, D. N., "Design Fundamentals of High Power Density, Pulsed Discharge, Lead Acid Batteries", J. Electrochem. Soc., Vol. 137, pp. 3693-3701, December 1990.

2. Armand, M., Chapter 1 in **Polymer Electrolyte Reviews-1**, J. R. MacCallum and C. A. Vincent, Eds., Elsevier Applied Science, New York (1987).

3. Alamgir, M. and Abraham, K. M., Chapter 3 in **Lithium Batteries** *New Materials, Developments and Perspectives*, Vol. 5 in Industrial Chemistry Library, G. Pistoia, Ed., Elsevier, New York (1993).

4. Abraham, K. M. and Alamgir, M., "Ambient Temperature Rechargeable Polymer Electrolyte Batteries", *J. Power Sources*, **43-44**, 195-208 (1993).

PERFORMANCE CHARACTERISTICS OF LITHIUM ION POLYMERIC ELECTROLYTE CELLS

D. H. Shen, G. Nagasubramanian, C.-K. Huang, S. Surampudi and G. Halpert

Jet Propulsion Laboratory, California Institute of Technology

4800 Oak Grove Dr., Pasadena, California 91106

Abstract

A series of polyacrylonitrile-based (PAN) electrolytes containing $LiAsF_6$ and a number of solvent mixtures including Ethylene Carbonate (EC) + Propylene Carbonate (PC) were prepared, electrochemically evaluated and used as electrolyte in the polymer cells. The typical composition of the electrolyte mixture was PAN ~15 M%, $LiAsF_6$ ~15 M% and solvent mixture ~ 70 M%. The PAN-based electrolyte containing EC, PC and $LiAsF_6$ gave a conductivity of 10^{-3} (S/cm) at room temperature. Both carbon and lithium cobalt oxide composite electrodes were studied versus lithium in small capacity cells. The same electrolyte composition was used in fabricating the composite electrodes. Cells were fabricated and evaluated for cycle life and cathode utilization efficiency. The capacity of the cells is between 5 to 10 mAh. Lithium polymer cells containing either carbon or lithium cobalt oxide showed so far around 40 cycles with minimum loss of capacity. Lithium ion polymer cells (Li_xC /gel/Li_xCoO_2) delivered ~5 mAh capacity in the initial cycles and cycling of the cell is in progress.

Introduction

Lithium polymeric electrolyte rechargeable cells are being actively developed for several applications including consumer electronics and electric vehicles. Polymer rechargeable cells have several advantages over the liquid electrolyte cells: these include 1) reduced propensity for lithium dendrites, 2) enhanced interfacial stability, 3) flexible shape etc. However, the problems related to dendrites and reactivity are not completely eliminated at the lithium electrodes. The development in liquid-based cells is focused on the use of lithium-carbon anodes (termed as lithium ion or "rocking-chair" configuration) in place of metallic lithium to reduce the dendrites and thus improve the cycle life. Additionally, the replacement of lithium with lithium-carbon may improve the safety of the cells. An extension of this concept, i.e., use of Li-C for Li, to the polymeric electrolyte cells is thus expected to further reduce the problems of dendrites and interfacial instability. At the Jet Propulsion Laboratory as part of an on going secondary lithium battery research effort we have initiated preliminary electrochemical studies on the lithium ion polymer cells. Initially, we evaluated the materials properties in small capacity cells. We report below our results on the electrochemical properties of PAN-based gelled electrolytes containing EC + PC + $LiAsF_6$ as well as on the cycling behavior, at room temperature, of Li-Carbon, Li-$LiCoO_2$, and Li_xCoO_2 cells containing the above electrolyte.

Experimental

Electrolyte Preparation:

Gelled electrolytes with different compositions were prepared as given below[1]. Appropriate amounts of the components were weighed before hand. Lithium hexafluoroarsenate was dissolved in the solvent mixture and the temperature of the liquid electrolyte was raised to 100°C followed by the slow addition of PAN. The temperature was maintained at around 100°C till a clear homogeneous viscous liquid was obtained. Thin films were prepared by casting the hot gel between two preheated quartz plates and pressing them together. This procedure yielded thin films with thicknesses ~100 micron. Typical composition of the electrolyte was PAN ~15 M%, $LiAsF_6$ ~15 M% and solvent mixture ~ 70 M%.

Composite Electrodes Preparation:

Composite electrodes with good ionic and electronic conductivities are required in polymer cells to achieve reasonable rates. Li_xCoO_2 -based composite cathodes were used for cell studies. Composite cathodes comprises of Li_xCoO_2 50 w%, acetylene black (for electronic conductivity) 10 w%, and the polymer electrolyte (for ionic conductivity) 40 w%. The Li_xCoO_2 and acetylene black were well mixed by a high speed blender. Gelled polymeric electrolyte (PAN 15 M%; $LiAsF_6$ 15 M% and EC + PC 70 M%) was prepared beforehand followed by the addition of the mixture of Li_xCoO_2 and acetylene black. The hot black slurry was then poured on to a preheated aluminum foil. The slurry was uniformly distributed and coated on the aluminum foil. The composite electrode was cut to size, 1 3/8" x 1 3/8", for later use.

The carbon electrode consists of a commercial graphite subjected to a pretreatment process identified in our earlier studies in organic liquid electrolytes. The carbon electrode gave 240 mAh/gm capacity at C/10 rate. The selected carbon anode and electrolyte materials are being used in conjunction with lithium cobalt oxide composite cathode to fabricate Li ion-polymer cells. The electrodes are sealed in a polyethylene laminated aluminum foil using a sealing technique developed at JPL. Li_xC -based composite electrode was prepared and its electrochemical performance tested. Composite cathodes comprises of Carbon 50 w% and the polymer electrolyte 50 w%. Gelled polymeric electrolyte (PAN 15 M%; $LiAsF_6$ 15 M% and EC + PC 70 M%) was prepared beforehand followed by the addition of preweighted carbon. The hot black slurry was then poured into a stainless steel (SS) mold with a 1 mil thick SS. foil on the bottom. The slurry was then evaporated by convection. The composite electrode was trimmed to size, 1 3/8" x 1 3/8", for cell studies.

Cell Fabrication:

Three types of cells were fabricated. The three types of cells are 1) Li/gel/Li_xCoO_2, 2) Li/gel/Li_xC, and 3) Li_xC/gel/Li_xCoO_2. Two polyethylene laminated aluminum foils were hot sealed on three sides to form an envelop. An electrode stack consisting of lithium anode, polymeric electrolyte, and composite electrodes was assembled and housed in the polyethylene laminated aluminum envelop. The envelop was sealed in vacuum. Four of each experimental Li-Li_xCoO2 and Li-Carbon polymer cells (~10 mAh) were prepared for electrochemical investigations. The cells were assembled in a dry-room with less than 1% humidity. Both types of the cells showed an open circuit voltage (OCV) in the range of 3.0 and 3.2 volts.

Standard electrochemical equipment were used for the electrochemical evaluation of the gelled electrolyte films. AC impedance measurements were made on both uncycled and cycled cells to obtain informations on the bulk and interfacial properties.

Cell Testing:

The laboratory lithium-composite polymer cells were tested at ambient temperature for cycle life performance between the voltage limits described above. A computer controlled battery cycler was used for cycling studies. The cells were charged at a constant current, 1 mA, and followed by taper charge at 4.25V. The cell was discharged at a constant current, 2 mA. The Li-Li_xCoO_2 cells were cycled between 4.3V and 2.6V, and the Li-Carbon cells were cycled between 0.15V and 1V. The full cell was cycled between 2.60 V and 4.25 V.

Results and Discussion

We have investigated the electrochemical properties of the gelled polymer electrolytes, three different types of polymer cells and their cycle life performance. These are described below.

Electrolyte Studies:

Electrolytes films were cut to size (~1 cm^2) and sandwiched between two well polished stainless steel (SS) electrodes (blocking contacts) for both a-c and d c measurements. The a-c measurement was made in the frequency regime 100 kHz to 5 Hz. In Fig. 1 is shown the Nyquist plot for the electrolyte of composition PAN ~15 M%, $LiAsF_6$ ~15 M% and EC +PC ~ 70 M%. The x-axis intercept gives the bulk resistance (R_b) of the electrolyte. The

resistivity (σ) is 10^{-3} S/cm at room temperature. The near perpendicular plot indicates that there is no measurable charge transfer at the interface. In Fig. 2 is shown the d-c voltammetric behavior for the same electrolyte. The electrolyte seems stable in the voltage range 1 to 5 V vs. Li.

Electrochemical Studies of Cells:

Although our aim is to evaluate the a-c behavior of the full cells (LiC composite anode /gelled electrolyte/LixCoO2 composite cathode) as initial studies we investigated the interfacial on bulk properties of the components electrodes using a-c measurements. Experimental cells with Li anode, $LiCoO_2$ composite cathode (~ 10 mAh) and gelled electrolyte were fabricated and cycled at room temperature. In Fig. 3 is shown a-c behavior of lithium cobalt oxide before and after 39 cycles. The value indicate the total resistance is around 2.1 ohms and did not change with cycling. However, Fig. 3b (a-c behavior of the cycled cell) shows the evolution of a semicircle which indicates that interface (between lithium and electrolyte, electrolyte and cathode, or both) changes continuously. In Fig. 4 is shown the a-c behavior of lithium -lithium carbon cell before and after 33 cycles. Although the bulk resistance of the cell is the same (around 2.1 ohms) the interfacial charge transfer resistance is considerably reduced after cycling. This suggests that probably the interface has improved with cycling .

Cell Performance

In Fig. 5 is shown charge-discharge curves as a function of time up to 42 cycles. for a lithium - lithium cobalt oxide cell. The capacity of the cell declined slowly to 3.7 mAh till ~40 cycles. The cycling data for lithium-lithium carbon cell is shown in Fig. 6. The first half cycle is the lithiation of the carbon electrode. A total of 46 mAh was passed. The following cycles exhibited approximately 3 mAh capacity. The capacity difference between the first and the following cycles is attributed to the formation of the surface layer on the carbon material[2]. The discharge capacity for the subsequent cycles remains the same around 3 mAh.

The first three charge-discharge cycles on a full cell (lithiated carbon composite anode/gelled electrolyte/lithium cobalt oxide composite cathode) is shown in Fig. 7. The cell was cycled between 4.25 V and 2.6 V. The initial capacity of the cell was around 5 mAh. The second and third cycles showed a lower capacity. The cycling of the cells is in progress. The data described above are preliminary and further cell studies are in progress.

Conclusions

PAN-based gelled electrolytes were prepared and electrochemically evaluated. The bulk conductivity at room temperature of the electrolyte PAN 21 M%; $LiAsF_6$ 8 M% and EC + PC 71 M% was 10^{-3} S/cm. Small capacity experimental half cells with LiC and $LiCoO_2$ composite electrodes were fabricated and tested for cycle life. These cells could be cycled over 30 cycles without perceptible capacity decline. Performance of the lithium ion polymer cells (LiC/gelled electrolyte/LiCoO2 cathode) is currently being evaluated and the results will be presented in the meeting.

Acknowledgment

The work described here was carried out at the Jet Propulsion Laboratory, California Institute of Technology under a contract with the National Aeronautics and Space Administration

References

1) G. Nagasubramanian, A. I. Attia, and G. Halpert, "A Polyacylonitrile-based gelled electrolyte: electrochemical kinetic studies", J. of Appl. Electrochem., **24** (1994) 298-302.

2) C.-K. Huang, S. Surampudi, A. I. Attia and G. Halpert, Proceedings of the 182nd Electrochemical Soc., Toronta, Canada, October 1992.

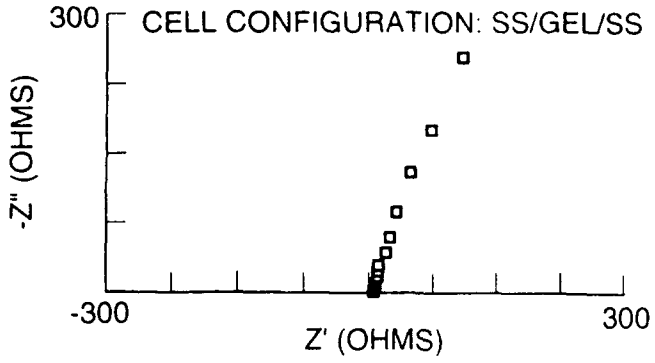

Figure1. NyQuist plot for the electrolyte containing PAN ~20 w%, $LiAsF_6$ ~15 w% and solvent mixture ~65 w%.

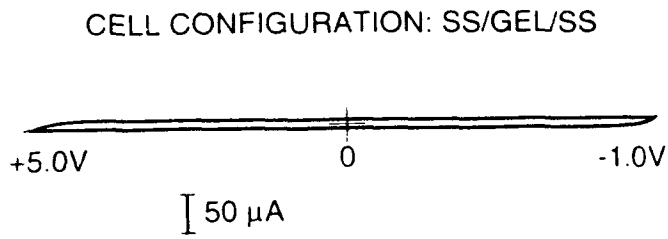

Figure2. D-C cyclicvoltammetric behavior of the electrolyte (same as in Fig.1) sandwiched between two well polished stainless steel electrodes.

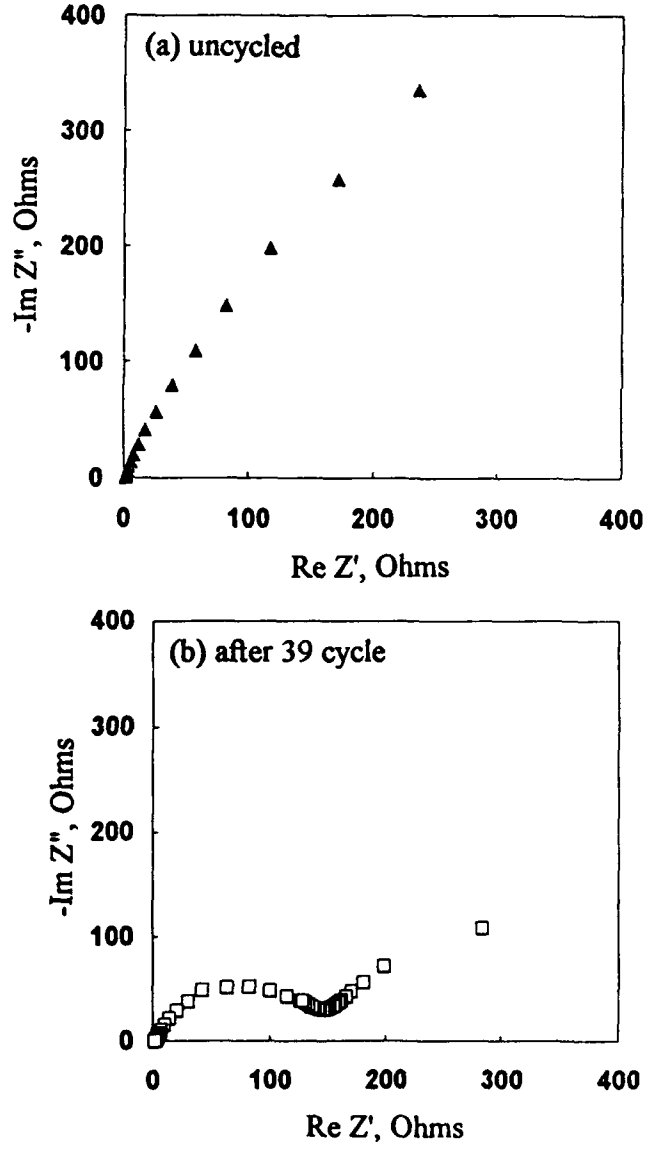

Figure 3. The a-c behavior of lithium-lithium cobalt oxide cell (a) uncycled and (b) after 39 cycles.

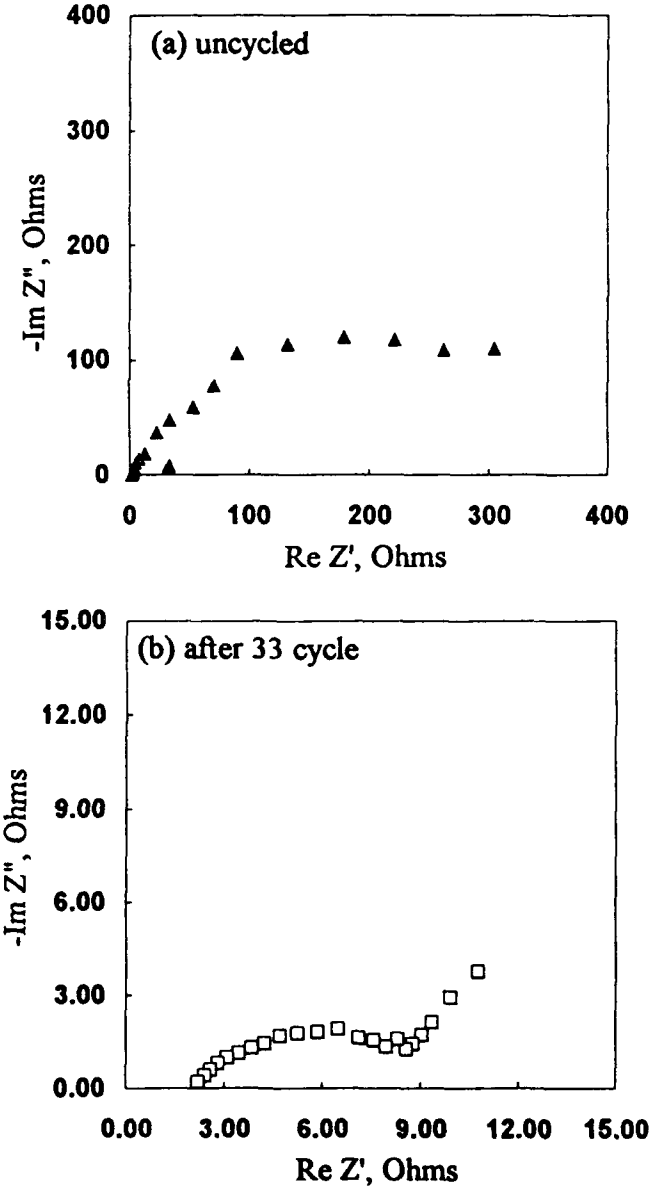

Figure 4. The a-c behavior of lithium -lithium carbon cell (a) uncycled and (b) after 33 cycles.

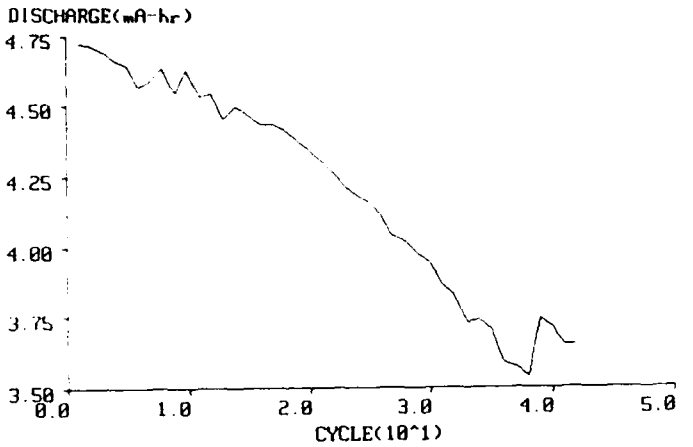

Figure 5. The discharge capacity vs. cycle life of a lithium - lithium cobalt oxide cell.

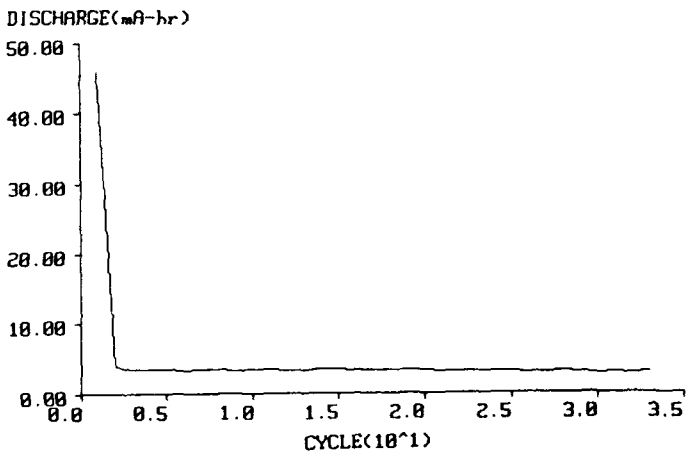

Figure 6. The discharge capacity vs. cycle life of a lithium - lithium carbon cell.

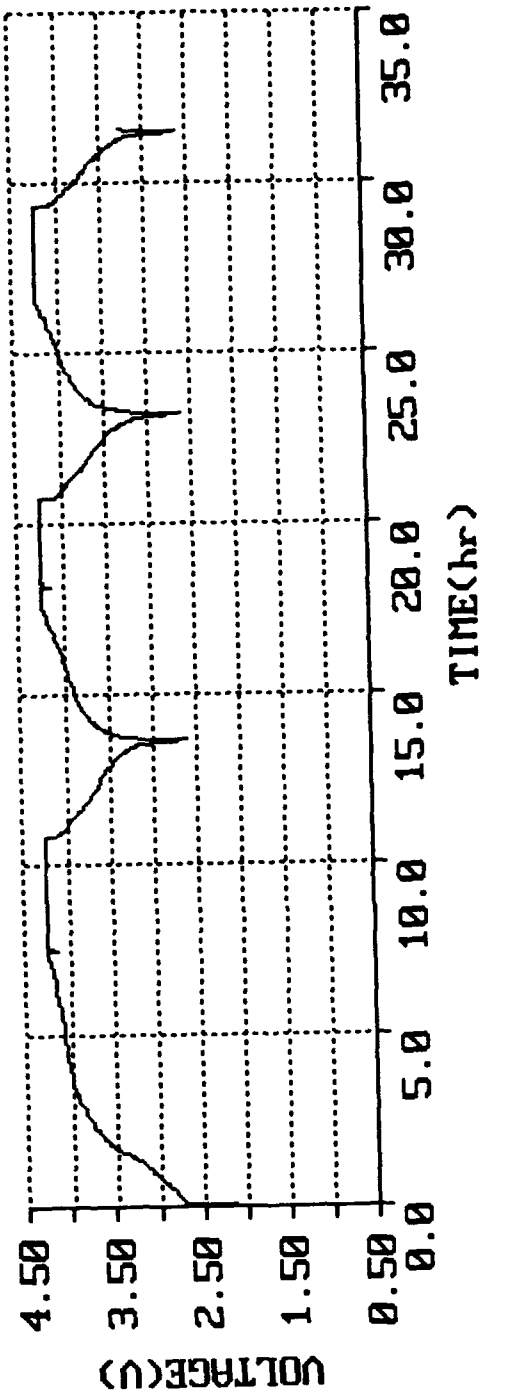

Figure 7. The first three charge-discharge cycles on a full cell (lithiated carbon composite anode/gelled electrolyte/lithium cobalt oxide composite cathode)

RECHARGEABLE ALKALINE ZINC-MANGANESE DIOXIDE BATTERIES

K.Kordesch, L. Binder, J.Gsellmann, W.Taucher, Ch. Faistauer
Technical University Graz, A-8010 Graz, Austria

Introduction

The development of the technology of the Rechargeable Alkaline Manganese dioxide (RAM) - Zinc battery has rapidly progressed over the last few years. Intensive research activities at the Technical University Graz and development efforts at Battery Technologies Inc. (1) have resulted in considerable improvements (2). Between 1989 and 1992 the cycle capacity has beeen more than doubled, the mercury addition to the anode has been gradually reduced and finally eliminated. (Fig.1). Today, the excellent elevated temperature shelf life, which we expect from alkaline MnO_2-Zn primary cells is also a feature of RAM batteries. (3). The technology has been licensed to RAYOVAC, USA and after extensive testing and market surveys in 1992/93, the mass production of RAM batteries started in Fall 1993. Under the trade name "RENEWAL" all four types of cylindrical cells were made available to the consumer market as "Reusable" batteries, together with special charging stations.

The first cycle capacity was chosen to be close to the capacity of the corresponding primary cells to allow a direct replacement in all comparable applications. Recharging is done at a constant voltage of 1.65 V and as a safety precaution, the RAYOVAC stations are mechanically constructed in such a manner, that the charging of primary cells is not possible.

The physical design of cylindrical batteries (Fig.2) has not been changed. Except for the separator material and perhaps the length of the contact nail, there is no noticable difference when compared to a primary battery.

The manufacturing can be done on essentially the same machinery as is used for the productionof primary cells at nearly the same cost. A consumer has therefore a very considerable cost advantage when he directly replaces primary cells in all of his devices. Also the purchase of some other very expensive rechargeable batteries can be avoided in many cases.

On continuous use and 100 percent deep discharge one RAM cell can replace about 80 Zinc carbon or 20 to 30 alkaline primary cells, as is shown in Fig.3. On an intermittent discharge regime, with frequent recharging, the total service time can reach more than hundred times that of alkaline primary batteries, as shown in Fig.4.

However, the most noticeable and consumer-relevant advantage over other types of rechargeable batteries is the good shelf life at elevated temperatures. Fig. 5 presents a comparison of test results achieved at 65 °C with RAM cells, Ni-Cd and MeHy cells.These (Arrhenius' Law) data, expressed in weeks of storage time can also be used to predict the room temperature shelf life for the same numbers of years. This is a well established rule in the battery industry. Historic publications and more recent detailed technical data can be found in the Literature references (4, 5 and 6,)

The RAM System

The MnO_2-Electrode,Discharge Limitations:

The first electron discharge follows the homogeneous proton insertion path and four-valent Mn-dioxide is formally reduced to $MnO_{1.5}$ This reduction process can be followed by neutron powder diffraction spectra. An example is shown in Fig. 6.

The appearence of a new peak below $MnO_{1.6}$ indicates the point where we now stop the discharge to preserve rechargeability. It was found that soluble Mn-species start to appear at continued discharge, especially when the lower voltage 2nd electron range is approached. The Mn-ions find their way to the zinc anode and with no mercury added, the corrosion problem increases, destroying the excellent shelf life characteristics at elevated temperatures. (Fig.5).

A cathode discharge model described by Faistauer (7) , based on work by Wruck (8), points to the different electronic and ionic pathways in thick cathodes which consist of a MnO_2-graphite mix. The manganese dioxide is a poor conductor and relies on the graphite to transport the electrons to the interface, while the KOH in the free pore system (helped by a filler substance) provides the ionic supply. Ideally, the two pathways should be as close as possible in their conductance values. Usually they are considerably diffrent, depending on the layer thickness. The result is a high efficiency of MnO_2-reduction near the separator and a low utilization at the steel can collector side. As a result, the MnO_2 at the separator side is sometimes reduced below the 1 electron level, causing irreversible oxides to be formed. The 2 mm thin cathodes of the AA cells are in this respect far more uniformely and efficiently discharged than the C and D-cathodes (4 and 6 mm thick).

Another strong effect on the discharge and cycle characteristics of MnO_2 cathodes is the depth of discharge. Fig. 7 pictures the change of cycle capacity with reduced depth of discharge. 1 Ah discharge from a AA cell , containing about 8 to 9 MnO_2 corresponds to a usage of 30 to 40 percent of the 1 electron capacity. It actually results in a very useful AA-rechargeable cell. A very large number of 100 % DOD discharge cycles at capacities in the Ah-range of Ni-Cd cells are obtained. Such a performance profile may be desirable for users of devices which are normally completely discharged before recharging. Such cells are not marketed today, but may appear on the OEM-market after optimizing the balance of the capacity limiting zinc anode (which must be made more dense).

The addition of a porosity modifier to the cathode increases the ion availability. As an example , Fig. 8 shows the effect of 10 % $BaSO_4$ addition to the cathode mix. Interesting is that also the initial capacity rises, in spite of the 10 % reduced amount of active material in the same cathodic volume (9).

The cathode also has the capability to react with hydrogen gas produced by corrosion processes at the zinc anode. This is the result of adding 0,1 to 0,5 % of a fuel cell electrode type catalyst, like Ag on acetylene black or carbon. The reduction of the MnO_2 capacity is negligable, but any pressure build-up is avoided, even in the event that a cell is reversed in a series circuit connection. (10).

MnO_2 Overcharge and the O_2-Zn Cycle.

Charging manganese dioxide to higher voltages produces 6-valent manganate, which is soluble and disproportionates into MnO_2 (of the rechargeable type) and into a not rechargeable lower oxide. It was therefore important to prevent the formation of manganate by limiting the charge voltage to about 1.65 to 1.68 V for the present RAM cells. However, it was also found that certain catalysts prevent manganate formation and cause a nearly stoichiometric evolution of

oxygen instead. (11) Fig 9 indicates the initial delay of oxygen evolution on overcharge and the effect of catalysts on O_2 evolution. Fig 10 shows a way to facilitate the uptake of the oxygen gas by inserting a porous cylinder in the center of the cell. The pressurized O_2 gas reaches the large internal zinc interface and forms ZnO. (12)

The Zinc Limitation, Hg-free formulations, Cell Reversal

The zinc powder anode mixture contains KOH and a gelling agent. The amount of Zn determines the depth of discharge of the cathode and thereby the capacity of the cell. Zinc oxide is dissolved into the KOH (or is additionally added as a powder) to make sure that on charge (or overcharge) only oxygen, but no hydrogen can be formed by electrolysis. This is the basis of the previously described oxygen cycle. The cells up to 1993 contained 0.02 % mercury in the zinc. Starting with the 1994 production, no mercury will be added to the anode formulation. Therefore special zinc alloy formulations and/or organic inhibitors are used to reduce the zinc corrosion. However, for rechargeable cells this is not sufficient because the zinc deposited after the first charge is much finer than the original granulated Zn-powder. The mentioned catalysts in the cathode (10) are taking care of the increased H_2-corrosion gassing possibility.

It should also be mentioned that a safeguard for cell reversal is important when cells are connected in series and one cell fails prematurely. In this case also H_2-gas is produced on the MnO_2 side where the catalyst recombines it. O_2 gas is evolved on the nail side. The latter can react with unused Zinc, because even after a 100 % deep discharge some Zn is left (as unconnected particles) in the gel.

The type of gelling agent and other additives are important for the coherence of not amalgamated Zn-particles and for the release of gas bubbles (13). Drop test are used for evaluating such effects.

Present Charging Methods

The presently recommended RAM-charging methods use a constant voltage end point setting. This is equivalent to a taper current charge method. Depending on the size and cost of the charger the cells may be charged in a few hours or simpler, just over night. For a quicker charging process "Pulse Charging" is recommended (Fig.11).The cells are charged in parallel and the voltage sensing is done between the pulses (14)

It was long recognized that the first few cycles of recharging are not efficient if the charge stops at about 1.7 V. Gsellmann (15) suggested a cathodic pre-charging method but it turned out to be too complicated for mass-product manufacturing. With the new **safe** overcharging possibilities (outlined above), a new charging method was devised which increases the capacity of the first recharge cycle by about 25 percent. The cumulative capacity of later cycles increases correspondingly. Overcharging also opens the way for all the devices where series charging and cell equalization is required (like in many OEM-applications).

Discussion of High Power Applications

The advantages of connecting AA cells in parallel to replace the larger D-cells are shown in Fig.12. The reason is that at a high current, the thin cathodes in the AA cells are used 70 % efficiently, while the thick D-size cathodes are only 30 % utilized (16)

A project with the Ontario Ministry of Energy tries to take advantage of these features for the development of small vehicle batteries and solar power chargers (17). High performance series charging of RAM cells bundles has been successfully demonstrated with 6 V series/parallel units. The new improved overcharge and cell equalization possibilities will now extend our capabilities to 12 V and even 24 V series charging with higher uniformity and without single cell control by electronic means.

Solar Charging and New Electronic Circuits (Practical Uses)

Solar charger may now find wide-spread application and acceptance in the consumer market. The previous use of Ni-Cd batteries was unsatisfactory. They discharge rapidly in the sun and the reliability on shelf is poor. The same is true for Ni-Mehydride cells. RAM cells can stand temperatures of 65 °C for weeks, as shown in Fig.5.

In a study aimed at the simplification of chargers, especially for circuits containing only 2 cells in series, which is the case in many devices, radios, and lamps, an overflow current circuit was used. Fig.13 shows such a solar charging circuit with a Zener diode.

In many constant current-charging devices the Ni-Cd cells can be replaced by RAM cells by using the Zener diode circuit (Fig.14).

Studies concerning the rechargeability of the 2nd electron of MnO_2.

In our laboratories we have checked the applicability of the chemically and physically modified manganese dioxide as first described by H.S. Wroblowa (1987) and repeated by many authors in the recent literature. It was found that the high volume of carbon used, makes it impossible to build cylindrical cells with a capacity close to the existing consumer cells. The cell voltage is low and the appearence of soluble Mn-species causes severe corrosion problems with zinc electrodes. Separators with low resistance values are not developed at the time. Replacing the Zn-anode by metalhydrides improves the cycle numbers, but the voltage is even lower. Cells built with electrolytic MnO_2 cathodes and fuel cell H_2-electrodes (18) or metalhydride anodes (19) show a far higher load capability, a better voltage level and good cycle life, using only the 1st electron.

Acknowledgement:

The authors thank the Funds for the Support of Scientific Research in Austria and Battery Technologies, Inc. for their financial support.

References

1. Battery Technologies Inc., (BTI). The BTI Group of Companies, 30 Pollard Str., Richmond Hill, ONT., L4B 1C3, Canada.
2. K. Kordesch, et al., Rechargeable Alkaline Zinc Manganese Dioxide Batteries, 33rd International Power Sources Symp., Cherry Hill, NJ, June 13-16, Proc. pp.817-821, ECS, 1988
3. J.Daniel-Ivad, K.Tomantschger, Electrochem.Soc.Meeting, 1993 in New Orleans, Charge Retention without Hg, Abstract No. 66.
4. "Batteries", Vol.1, Manganese Dioxide, Karl Kordesch, editor, Marcel Dekker, New York, 1974. A new edition is forthcoming.
5. Power Sources 14, Proc. of the 18th Internatl P.S.Symposium. K.Kordesch, L.Binder, W.Taucher, J.Daniel-Ivad, Ch.Faistauer, The Rechargeable Alkaline Zinc-Manganese Dioxide System. P.S.S.Committee, A. Attewell & T.Keily, ed., 1993, pp.193-216.
6. Progress in Batteries & Battery Materials, Vol.12 (1993), IBA-Toronto Meeting. K.Kordesch, J.Daniel-Ivad, K. Tomantschger, The RAM Battery Technology, A Progress Report, pp.52-66
7. Dissertation of Ch. Faistauer, Technische Universität Graz, 1993
8. W.J. Wruck, Dissertation Univ. of Wisconsin, 1984, U.M.I. 1992
9. K. Kordesch, L.Binder, W.Taucher, MnO_2 Additive, Patent 1994
10. K. Kordesch, K.Tomantschger, Catalyst Patents 1990,1991,1992
11. K.Kordesch, L. Binder, Patent, Overcharge Protection of MnO2, Journal of Power Sources, Vol.36, pp.45-56 (1991)
12. K.Kordesch, L. Binder, P. Urdl, ECS-Proc., San Francisco, 1994
13. K.Kordesch, J.Daniel-Ivad, R.Flack, Hg-free Anode Patent 1994
14. K.V. Kordesch, A. Marko, J. ECS., 119, pp.1053-1055 (1972)
15. J.Gsellmann, Habilitation at the Technical Univ. Graz, 1988
16. K.Kordesch, J.Daniel-Ivad, Ch.Faistauer, Hi-Power RAM Cells 82nd Meeting of the ECS., Toronto, 1992, Abstract No.10
17. "Enersearch" project of the Ontario Ministry of Energy, 1992-94
18. K.Kordesch et al., MnO_2-H_2 Battery, Power Sources 13, Proc. 17th Internatl. Power Sources Symp., Bournemouth, 1991
19. J.C.T.Oliveira, Ext. Abstracts, Proceedings of the Electrochem. Soc. Meetings in New Orleans, 1993 and San Francisco, 1994

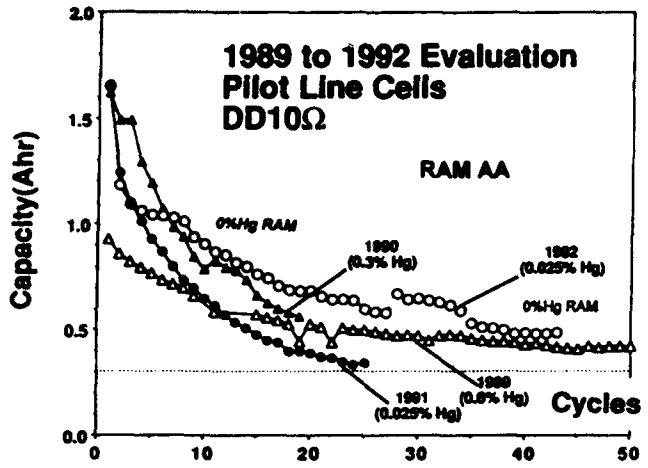

Fig.1: The Progress of RAM Batteries during the years 1989 to 1992

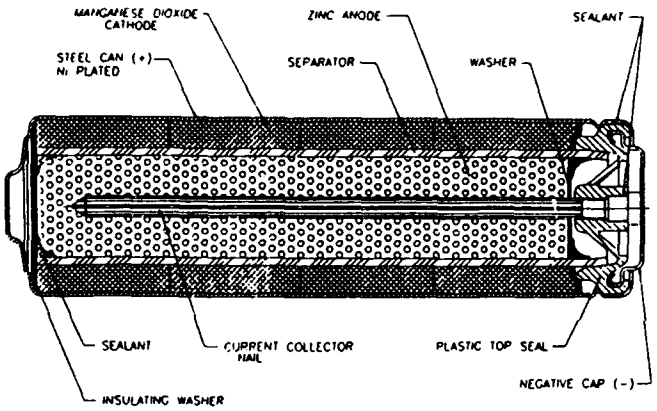

Fig.2: Cut through a AA-size Rechargeable Alkaline MnO_2-Zn Cell

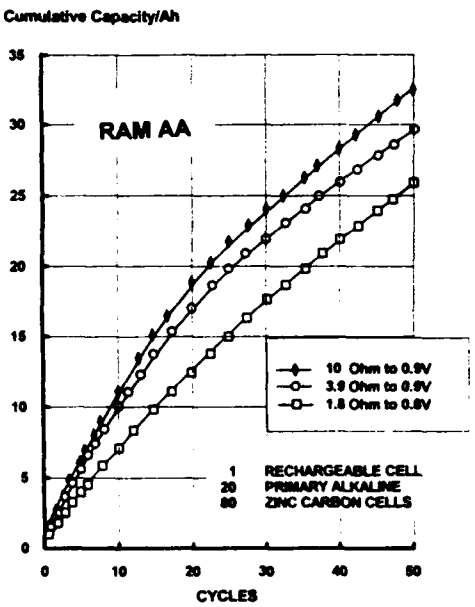

Fig.3: The cumulativ Capacity obtained from AA-size RAM Cells.

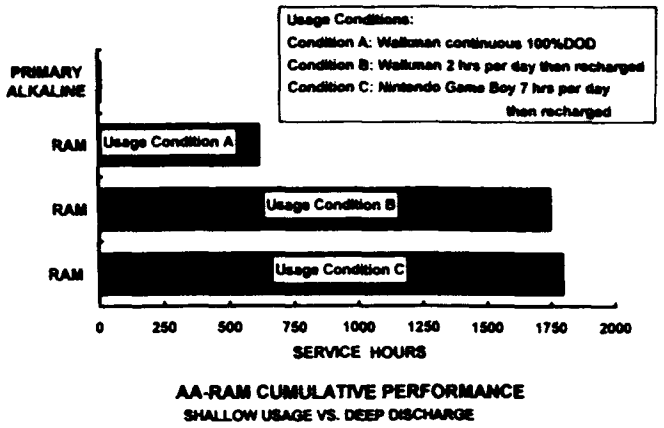

Fig.4: The different service obtained from AA cells when used under daily partial discharge regimes and recharged between uses.

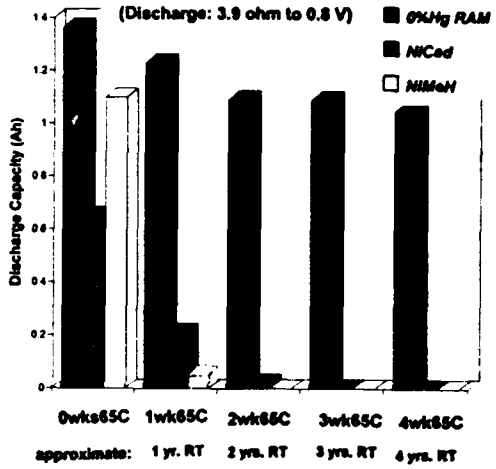

Fig.5: Comparison of the initial capacity and of the performance losses of different rechargeable battery types. at 65 °C.

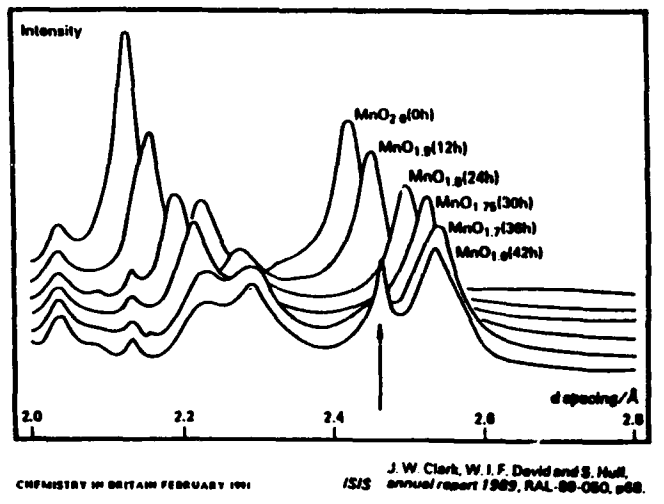

Neutron powder diffraction data of MnO_2 samples from batteries at various stages of discharge. The arrow indicates the position of an additional Bragg peak attributed to the formation of an ordered Mn-O-H phase. The appearance of this phase coincides closely with the point of battery failure.

Fig.6: Diffraction data which show the changes in the MnO_2-structure on discharge near the 1 e^- capacity level. (0.3 Ah/g)

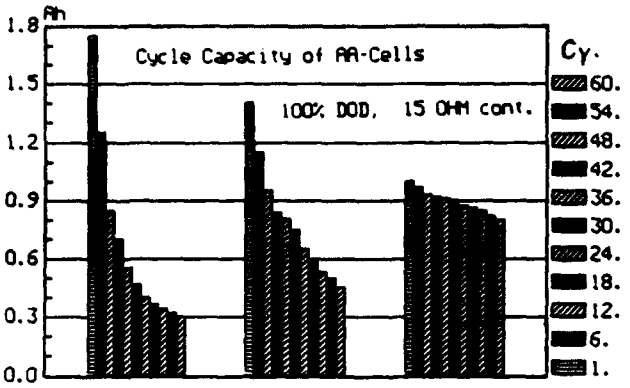

Fig.7: Increasing cycle capacity with less discharge of the MnO_2

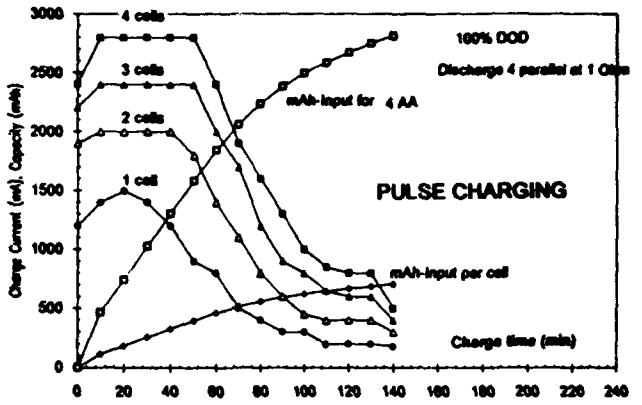

Fig.11: Pulse Charging of RAM cells in a parallel cell arrangement.

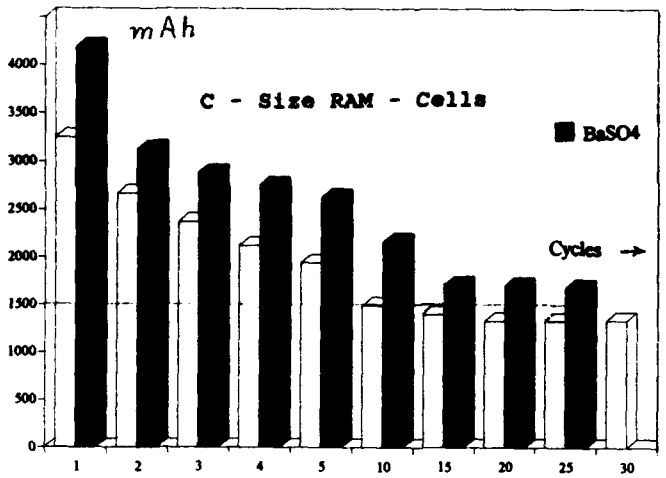

Fig.8: The effect of adding a porous filler to the cathode mass

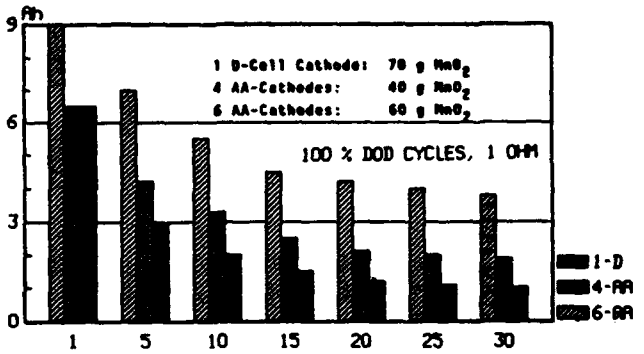

Fig.12: The advantagees of parallel connected AA cells over D-cells "Power Cell": 4 AA cells fit exactly into one D-cell container.

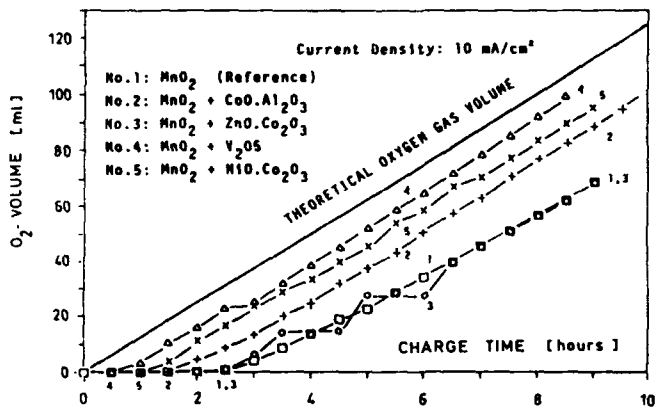

Fig.9: Changing Oxygen evolution efficiency by adding catalysts.

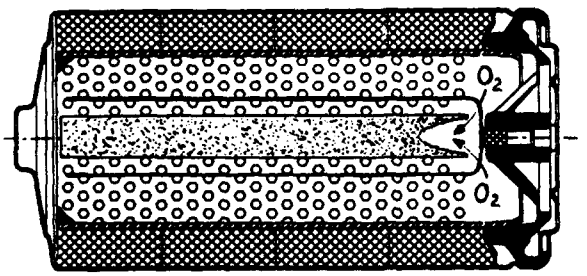

Fig.10: Design of a C-size RAM cell with a porous cylinder in the center of the anode to facilitate O2- gas reaction with the Zn.

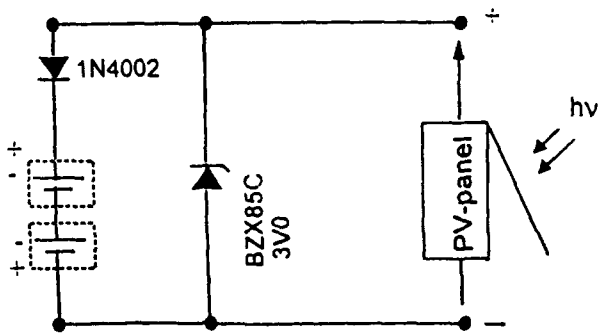

Fig.13: Charging of 2 RAM cells in series by a solar panel. The Zener Diode bypasses any current overflow above 3.4 V.

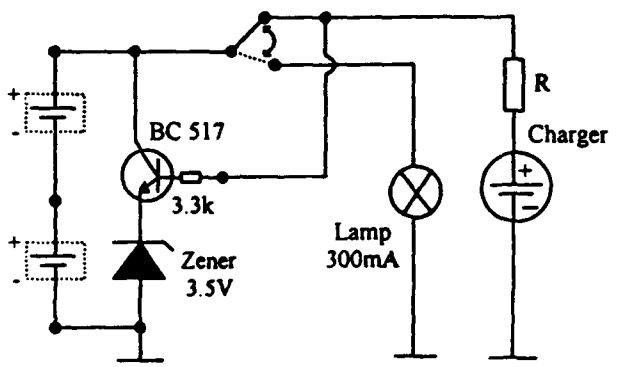

Fig. 14: A stand-by lamp charging circuit with 2 AA RAM cells replacing 2 Ni-Cd cells in a Radio Shack hand-torch.

IMPROVED COMPONENTS FOR RECHARGEABLE ALKALINE MANGANESE-ZINC BATTERIES

Terry Messing, Robert Jacus, and Sid Megahed
Rayovac Corporation, Madison WI

Introduction

Rayovac began manufacturing and marketing a rechargeable alkaline (Zinc/Manganese Dioxide) cell in four sizes (D, C, AA, AAA) in the fall of 1993. These cells and the dedicated chargers (in two sizes) are being marketed under the Renewal® trade name and are experiencing a good reception in the market.

Figure 1: Nominal Capacities of Renewal Cells in AH

	D	C	AA	AAA
First Cycle	5.5	2.8	1.5	0.6
Cumulative (25 Cycles)	90	48	18	8.5

The Rayovac Renewal cell design has several advantages:

Low Cost:

The bobbin type cell design is inherently lower in cost than the spiral wound design used in many rechargeable cell designs. Because the Renewal design used has much commonality with the primary alkaline cell production base the cost picture is further improved.

Charge Stand Times:

The Renewal cell will retain a charge for years similar to its primary analog. This is in sharp contrast to other rechargeable cells which may have lost much of their energy in a few weeks. This characteristic means that effectively the Renewal cell can be recharged and then stored for later use.

Environmental Issues:

The Renewal design presently contains a small amount (0.025% of battery weight) of mercury, however, the design will be mercury and cadmium free. Again the systems based on lead or cadmium have no opportunity to become environmentally friendly.

The rate capability of the Renewal system is adequate for many applications, however there is opportunity to improve that significantly. This paper will discuss the rate capability studies undertaken.

General Experimental Methods

The testing used within this report was performed on a Maccor tester received from the vendor earlier this year. Both AA and AAA Renewal and other cells as indicated were used in this evaluation. The test for the AAA was discharge on a 24 ohm resistor until the voltage fell to 0.9 volts. The cell was then recharged at constant current (150 mA) until the charge voltage rose to 1.65 volts at which time a constant voltage (1.65 V) charge was continued for eight hours. Typically 25 cycles were run on the test samples.

Once every hour of the 24 ohm discharge a 10 second 390 ohm discharge followed by a 10 second 12 ohm discharge was imposed. This discharge is shown in Figure 2.

Figure 2: Typical First Pulse
(One Pulse Per Hour)

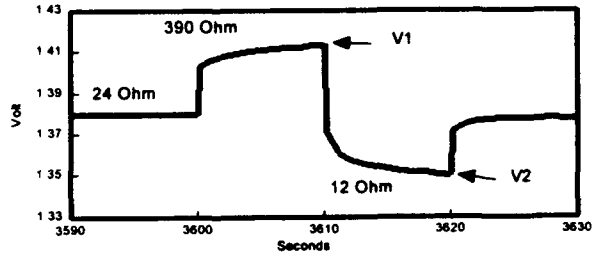

The data reported includes the resistance as calculated via delta voltage divided by delta current between the two points indicated as V1 and V2. When AA-cells were tested the same regime was used except a 12 ohm continuous load with a 195 ohm then 6 ohm 10 second pulses were used.

This method allows the monitoring of the cell resistance as a function of the extent of discharge and as a function of the number of cycles that have been placed on the cell.

In order to obtain a scan of the resistance as a function of discharge rate, constant current discharge for one second followed by a 10 millisecond open circuit was run. Delta voltage divided by delta current resistances were measured between these pulses and the preceding open circuit voltage.

Experiment 1

Renewal AA-cells were evaluated by the resistance scan method. Figure 3 indicates the results.

Figure 3: Typical DC Resistance AA Renewal
10 mS Interrupt

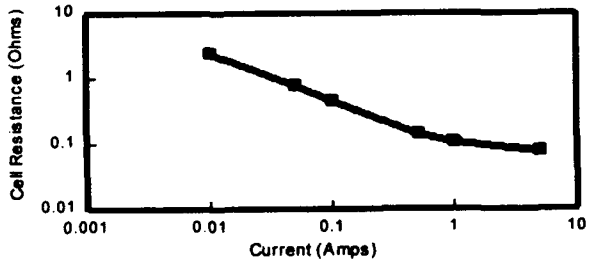

The apparent resistance of this undischarged, (i.e., as manufactured) Renewal cell typically will vary between several ohms at low discharge rates to less than 0.1 ohm at high discharge rates.

Therefore, it is necessary when interpreting this type of DC measurement that the same current densities are used.

Experiment 2

Renewal AAA-cells were evaluated by the hourly interrupt method. Figure 4 indicates the typical results for the first cycle.

Figure 4: Resistance Change, 24 Ohm Discharge
AAA RAM Cell

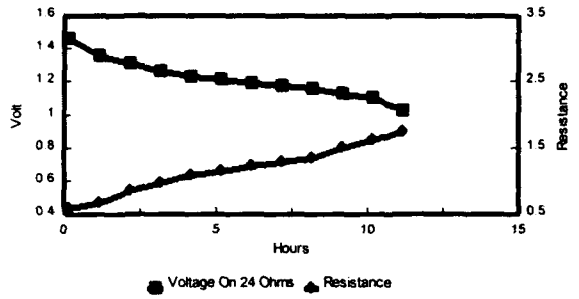

The resistance starts at 0.55 ohms and increases as much as three times in the course of the discharge.

As the cycling of the cell continues the resistance initially in each cycle's discharge is a higher value.

In Figure 5 the initial resistance for the second cycle was 0.55 ohms which increased to 0.9 ohms by the 25 cycle.

Figure 5: Resistance vs Cycle

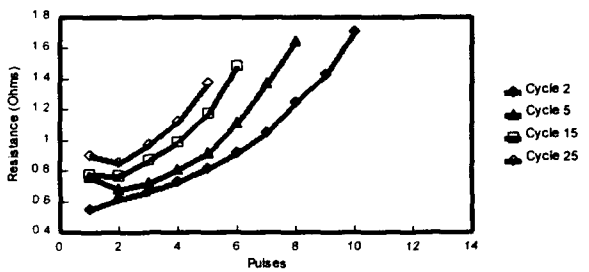

However the maximum resistance developed when the voltage fell to 0.9 volts did not increase. These end of discharge resistances varied between 1.4 and 1.8 ohms.

Finally in Figure 6 the unique shape of the first discharge can be seen as compared to the second cycle. The identical second cycle data was shown in Figure 5 and can be seen as typical in shape for all subsequent cycles.

Figure 6: Resistance vs Cycle
With First Cycle

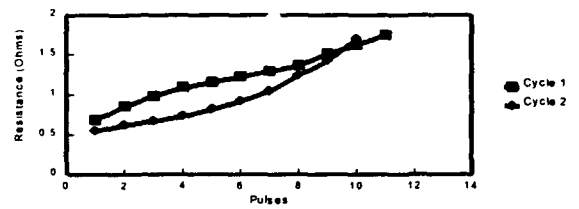

Therefore several observations can be seen as typical of this system in the AAA-cell size. 1) The resistance during each discharge will increase and in the control cell design maybe three times the starting value at the end of discharge. 2) The resistance as each cycle's discharge begins is higher than the preceding cycle's value. The largest increases occur in the first five cycles. 3) The resistance at the end of each cycle's discharge does not increase to the 0.9 volt end point, This is true even as the capacity per cycle decreases, 4) It is speculated that the change in shape of the first cycle curve is related to the zinc form in the anode.

Experiment 3

A Renewal AA-cell was assembled with two platinum wire probes placed immediately on either side of the separator in the anode and in the cathode mass. The probes were in electronic contact with the electrode in which they were placed. The cell was then cycled on the AAA hourly interrupt loads and schedules. A resistance was calculated for both the cell and probe curves and resulted in the following data.

Cycle	Pulse	Cell Resistance	Probe Resistance	Probe as % of Cell
1	1	0.41	0.28	68%
1	15	0.63	0.46	73%
1	28	1.57	1.24	79%
2	1	0.47	0.26	55%

Figures 7 and Figure 8 are graphic displays of the data generated.

Figure 7: AA Renewal, Probe Voltages
Cycle 1 Pulse 1

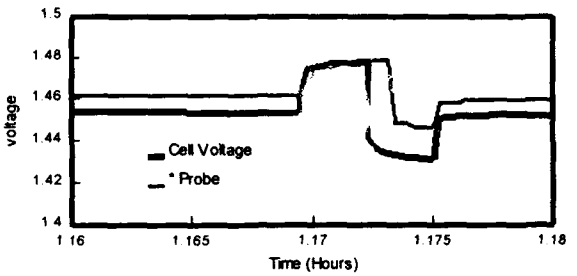

* The voltage between two platinum probes placed immediately on either side of the separator.

Therefore when the cell resistance is at the highest (28th pulse) the resistive loss that might be related to anode or cathode contact resistance is no more than 20 percent of the total.

Experiment 4

Experiment 3 lead us to evaluate the separator resistance contribution to the total cell values. The Renewal design includes a multilayer separator design including barriers. The primary alkaline systems that are commonly available do not have the same degree of separation and do not typically have barriers in them. Therefore three

Figure 8: AA Renewal, Probe Voltages
Cycle 1 Pulse 28

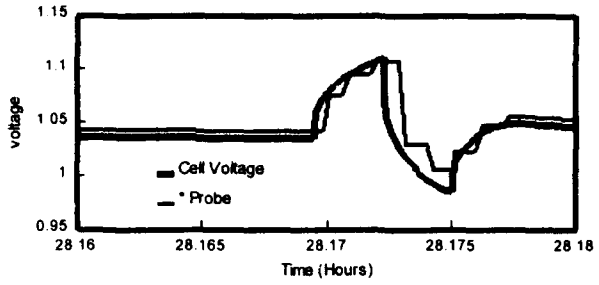

* The voltage between two platinum probes placed immediately on either side of the separator.

typical primary AAA-cells were discharged by the one hour interrupt test. Figure 9 shows the results.

Figure 9: AAA Primary Cell Resistance

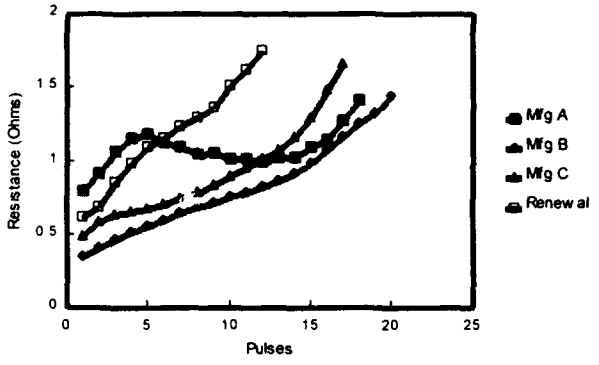

Manufacturer B and C produce primary cells that have a slightly lower resistant initially but which rise in resistance as the cell discharges and reaches the values very similar to the Renewal cell when the cell reaches 0.9 volts. Manufacturer A, which has a relatively high initial resistance, does not experience the same steady rise in resistance.

Therefore, the much lower separator resistances that are used in primary cell designs do not cause a significant decrease in the maximum resistance achieved.

Experiment 5

Separator systems that may decrease the amount of zincate diffusion to the cathode and therefore diminish the increase in cathode resistance, were evaluated. These samples were first evaluated for resistance in a conventional flooded electrolyte set up. The values obtained were:

	Resistivity ohm cm^2
Sample 1	0.65
Sample 2	0.23
Sample 3	0.36
Renewal	0.58

These samples were then assembled into cells and evaluated.

All three samples (Figure 10) on the first cycle show a resistive plateau that is quite different from the control (Renewal) separator . For samples 2 and 3 the ultimate resistance that the cell reaches to 0.9 volts appears to be less than sample 1. However, the initial capacity can also be seen to be somewhat diminished. No shorting was seen in 25 cycles.

Figure 10: AA, Separator Variations
Cycle 1

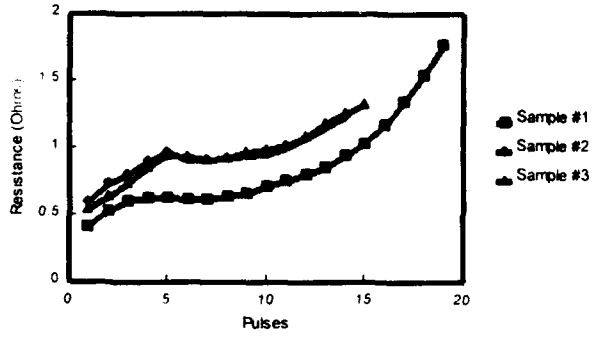

Figure 11 shows the results of cycling sample #1. It can be seen that the plot of the increase in resistance after the first cycle looks very much like the control and no longer has the plateau shape.

Figure 11: AA, Sample #1

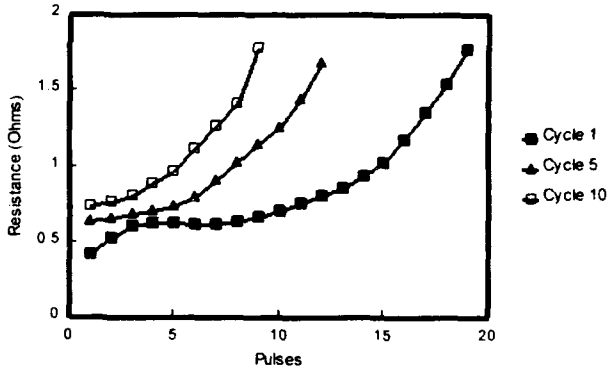

Conclusions

The Renewal AAA and AA-cells are moderate rate cells which have a resistance of 0.4 to 0.6 ohms as measured by the test used in this work. That resistance will increase as the discharge continues and limits the cells pulse capabilities toward the end of discharge. It has been shown that the electronic resistance associated with electrode contact is no more than 20% of the total cell resistance when the resistance is the highest, i.e., towards the end of discharge. This observation indicates that rate improvement projects will be most productive when positioned in the electrode interface/separator systems. Data has been presented to indicate that the separator system

used may influence the resistance increase as the discharge is completed.

We will continue to explore other areas that may effect this resistance.

Acknowledgment

We wish to thank the United States Army Research Laboratory for their support of this work under contract DAAL01-93-C-3362

ADVANCED SILVER ZINC BATTERY DEVELOPMENT

Z. ADAMEDES AND T. TERJESEN
BST SYSTEMS, INC.
PLAINFIELD, CT 06374

ABSTRACT

Historically, silver-zinc batteries have not been capable of reliably providing more than 100 discharge cycles at 100% depth of discharge. This paper describes the development of silver-zinc cells that are capable of extended cycling. These cells incorporate new separator materials, improved negative electrodes and optimized design features which all help to enhance cell performance. Cells fabricated using these new materials and features reliably delivered over 240 cycles without failure and with excellent capacity retention. Thus, the test program has demonstrated a significant advancement in the cycle life of silver-zinc cells.

INTRODUCTION

A systematic development program has been undertaken by BST Systems over the last several years the goal of which was to significantly improve the performance characteristics of the silver zinc cell. The silver-zinc battery holds several distinct advantages over other couples, including high power capability, good gravimetric and volumetric energy density and rechargeability. However, the couple has suffered from limitations in cycle life and attending capacity degradation. These limitations can be directly linked to shortcomings in the separator system and capacity loss due to zinc electrode shape change. This development program has integrated several approaches, including material innovations, to obtain the goal of an improved silver zinc cell.

Among those approaches was to use improved negative electrodes which incorporate the use of a binder material which has been shown to significantly reduce shape change.

Additionally, an improved cellophane-based separator material has been developed by BST Systems (patent pending).

This paper will discuss in Part 1 some of the material improvements made in cell components by BST Systems. In Part 2 the data from a development program incorporating multiple component improvements is presented, the result of which was the demonstration of a 240 cycle cell.

All work presented herein was conducted as part of BST Systems's on-going internal development and improvement program whose goal is to demonstrate and produce enhanced high performance silver zinc cells.

PART 1A: RESTRUCTURED CELLOPHANE

BACKGROUND

In silver zinc secondary battery cells, regenerated cellulose (cellophane) is positioned under pressure between anodes and cathodes. Cellophane when in close contact with a powerful oxidant such as silver divalent oxide (AgO) and in the presence of an electrolyte such as potassium hydroxide (KOH) oxidizes into aldehydes and ketones. This oxidation reaction weakens the structural integrity of the film making it more permeable to migrant metal ions and silver impregnation by colloidal silver which eventually short circuit the cell. The resulting structural weakness of the separator also make the separator more susceptible to zinc dendrite penetration. In practice, multiple layers of cellophane are used to prolong the life of the separator system. This not only adds weight and volume to the cell but also increases the electrolytic resistance of the separator system.

A multi-year separator improvement program has been conducted to improve the separator systems for silver zinc cells. This effort has included the identification of new suitable separator materials as well as the improvement of currently used state-of-the-art materials.

As part of this program, BST Systems, Inc. developed an environmentally benign process that alters the cellophane such that the resultant material exhibits improved resistance to silver penetration. Additionally, the restructured material has similar physical characteristics to untreated cellophane (thickness, color, resistance, etc.). An experimental program was conducted to verify this performance in silver-zinc cells.

EXPERIMENTAL

A film of uncoated unplasticized cellophane was treated according to the method developed by BST Systems. Ten 5 AH cells were fabricated utilizing six layers of this "restructured" cellophane around each positive electrode. Control cells were made with the standard film.

The cells were placed on a cycling program where the cells were charged at a C/10 rate and 100% discharged at a C/5 rate for 50 cycles. At the end of the cycling, the cellophane materials were removed and each layer of the cellophane wrap was analyzed for silver content.

RESULTS

The results of this silver content analysis are presented in Figure 1. The data shows that the cellophane material treated using the BST process has significantly larger quantities of silver in the first layer (layer nearest the cathode). The treated material selectively resists the passage of the dissolved and colloidal cathodic material more effectively than untreated cellophane and has superior resistance to silver penetration.

FIGURE 1

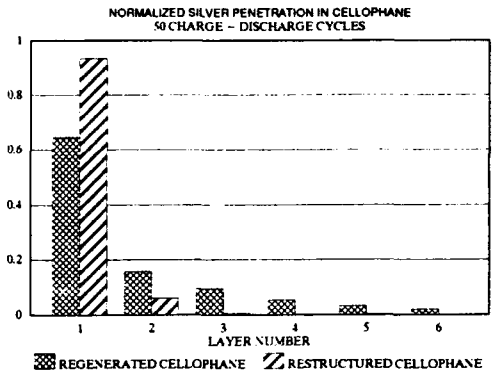

No voltage differences were discernible between those cells built with the restructured cellophane and those built with the untreated cellophane.

PART 1B: DEVELOPMENT OF A SILVER SCAVENGING MATERIAL

BACKGROUND

As discussed above, cellophane is oxidized and weakened by silver divalent oxide (AgO) in the presence of an electrolyte (KOH). The use of a permeable material such as a cellulosic spacer (Aldex paper) or woven polymeric material or non-woven polymeric fabric (nylon or "pellon") has been shown to be effective in reducing the direct contact of the semi-permeable membrane to the silver oxide and inhibiting the transport of the dissolved oxide. However, the attack of the dissolved silver oxide on the cellophane film cannot be prevented by the above type spacer materials. Several materials which showed promise as spacer materials were identified for use and a development program was conducted to quantify their performance. Based on promising preliminary results one material, designated as B239, was selected for further study.

EXPERIMENTAL

Six 12 AH silver zinc cells were fabricated using one layer of B239 placed adjacent to the silver electrode followed by three layers of cellophane. A layer of this material was also placed adjacent to the negative electrodes. Control cells were fabricated using nonwoven polyamide fabric of identical thickness in place of the new material. The cells were then charged at the C/10 rate and 100% discharged at the C/5 rate for a total of ten cycles. Each charge cycle included 5 hours of overcharge to stimulate silver migration. The cells were then dissected and the first, second and third layer of cellophane of each cell was chemically analyzed to determine the silver penetration in the separator.

RESULTS

The results of the silver penetration analysis are presented in Figure 2. The data indicates that this new material has four times more resistance to silver penetration than the non-woven polyamide fabric.

FIGURE 2

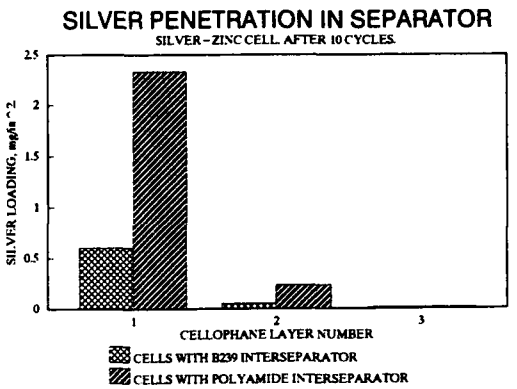

BST Systems has since incorporated this material into a large rechargeable silver zinc cell with excellent results. Cells fabricated using this material met all required voltage and capacity requirement and successfully completed extended testing where the cells were maintained on charge stand or on "float" for over 18 months.

PART 2: THE DEVELOPMENT OF AN EXTENDED CYCLE LIFE CELL

A silver zinc design "concept" was developed and produced in a 5 AH cell configuration. The design concept was a holistic approach to cell improvement and involved the utilization of shape resistant negative electrodes, the use of restructured cellophane and other polymeric materials as well as an optimized system design.

EXPERIMENTAL

Six 5 AH cells were fabricated utilizing the new negative electrodes and the new separator. Cell design details are tabulated in Table 1. Standard 45% potassium hydroxide was utilized. The cells were then cycled according to a regimen consisting of a charge at the C/10 rate followed by a discharge at the C/5 rate. In order to truly tax the cells, all discharges were deep (100% depth of discharge). The cycling was conducted at room temperature until failure occurred.

TABLE 1

L5 CELL DESIGN

# OF POSITIVES:	6
SIZE:	1.75"Wx1.406"h
THICKNESS:	.015"
# OF NEGATIVES:	5 FULL/2 HALF
SIZE:	1.75"Wx1.406"H
THICKNESS:	0.034"
SEPARATOR:	+/PELLON/2T POLYMER/5T C_1/-

RESULTS

Figure 3 illustrates the cycle life performance of the cells. The first failure occurred on cycle 241. Three of the six test cells completed 300 cycles without failure. Cycling was halted shortly thereafter on these cells after the output capacity fell below 50% of the initial capacity.

FIGURE 3

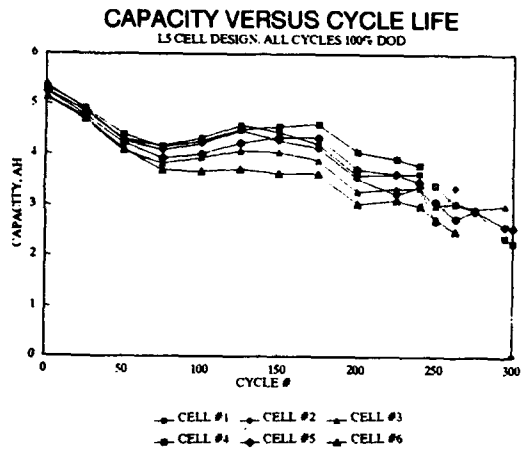

Capacity retention is illustrated in Figure 4. The cells demonstrated exceptional capacity retention over the life of the program. After 100 deep discharge cycles all cells retained approximately 80% of the initial capacity. After 200 deep discharge cycles the cells provided an average of 68% of their initial capacity. The three cells which provided 300 cycles still retained 50% of their original initial capacity. Capacity retention is also tabulated in Table 2.

FIGURE 4

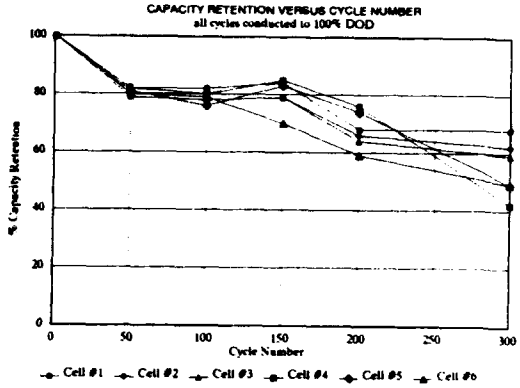

TABLE 2

CAPACITY RETENTION VS. CYCLE NUMBER

	CYCLE #				
CELL	50	100	150	200	END OF "LIFE" (CYCLE #)
1	82%	82%	84%	68%	68% (CYCLE 241)
2	79%	78%	79%	66%	62% (CYCLE 263)
3	79%	78%	79%	64%	59% (CYCLE 295)
4	82%	80%	85%	76%	42% (CYCLE 300+)
5	81%	76%	83%	74%	49% (CYCLE 300+)
6	80%	79%	70%	59%	49% (CYCLE 300+)

Silver utilization continued to be excellent throughout the life of the cells. Silver utilizations were in the order of 2.8 g/AH (357 mAH/g). After 200 cycles, utilizations were in the order of 4.6 g/AH (217 mAH/g). Quantitative data is shown in Table 3. Figure 5 illustrates the silver utilization over 300 deep discharges in graphical format.

TABLE 3

SILVER UTILIZATION AS A FUNCTION OF CYCLE LIFE

(NOTE: ALL DISCHARGES WERE TO 100% DOD)

CYCLE #	OUTPUT CAPACITY (AH)	SILVER UTILIZATION (mAH/g)
1	5.25 AH	351
50	4.23 AH	303
100	4.06 AH	245
150	4.21 AH	255
200	3.53 AH	214
250	3.71 AH	225
300	2.6 AH	158

FIGURE 5

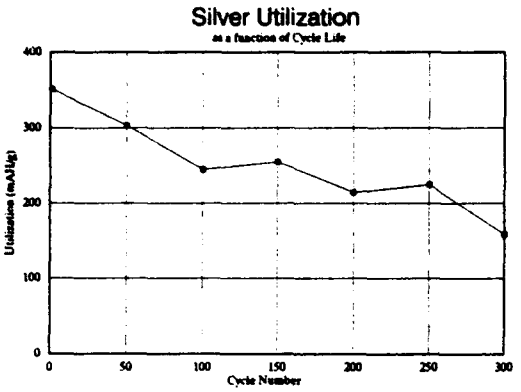

CONCLUSIONS

Significant improvements in silver zinc chemistry have been demonstrated, with 240-300 cycles having been achieved at 100% depth of discharge.

A method of treating the cellophane has been developed resulting in a material that exhibits superior resistance to dissolved cathodic material, colloidal metals and their oxides. The derivative material is semi permeable and similar in electrolytic resistance to that of regenerated cellophane.

Replacement of conventional materials such as woven and non-woven polyamide and cellulosic paper with the new silver scavenging material in cells containing silver cathodes would significantly reduce the rate of failure due to silver migration and would be very effective in long life batteries.

Significant improvements in the cycle life and cyclic capacity retentive capability of silver-zinc secondary cells is clearly possible. For applications where safety, reliability, high energy density and rechargeability is required, extending the cycle capability will enhance the attractiveness of this chemistry.

ACKNOWLEDGEMENT

The authors wish to acknowledge the technical assistance and support of Mr. S. Pirapakaran, Mr. Robert Peterson and Mrs. Susan Belliveau.

DEVELOPMENT OF SILVER-ZINC CELLS OF IMPROVED CYCLE LIFE AND ENERGY DENSITY

Roberto Serenyi
Yardney Technical Products, Inc.
Pawcatuck, CT

Abstract[1]

Substantial improvements to the cycle life and energy density of rechargeable silver-zinc cells were achieved during a Phase I SBIR program, sponsored by the Naval Surface Warfare Center, White Oak Detachment (Dr. S. James), by advancing the state-of-the-art of the negative electrodes and the separators.

The results show a 68% longer cycle life (160 vs 95), and 38% better utilization of active materials, along with 70% higher capacity after 90 cycles, compared with standard cells.

To achieve those improvements we relied on a new class of materials, known as Electro-Permeable Membranes (EPM's), covered by U.S. Patent No. 4,797,190, issued to Mr. Robert L. Peck, with whom Yardney has a licensing agreement. These materials are used as additives and/or coatings for the zinc oxide electrodes and also as coatings for conventional separator materials.

Phase II work, presently under way, has the following main objectives: (1) Optimization of EPM formulations for performance, reliability and ease of manufacture and (2) Development of mass production techniques, for cells of all sizes.

The successful completion of the program will result in improved Ag-Zn cells, capable of 150 cycles as a minimum, at higher energy densities than presently available and with extended wet life, which would be very attractive for a multitude of military, space and commerical applications, such as propulsion for small submersibles, undersea rescue vehicles, torpedoes and targets, communications, short bursts of very high power, missiles (for telemetry, control, rocket stage separation, self-destruct capability), lunar exploration, astronaut's extravehicular activities, television cameras and recorders, surgical instruments, pipeline inspection crawlers, and many more.

Background Information

Present state-of-the-art silver-zinc cells offer the highest energy density among the commercially viable rechargeable batteries (up to 250 Wh/kg), the highest power density (up to 800 W/kg for continuous discharges and 3000 W/kg for short-duration pulses), a relatively low self-discharge rate (3 to 8 percent per month at 25°C, depending on cell design) and a flat voltage during most of the discharge. However, they suffer from two serious drawbacks:

- A relatively short wet life (maximum of two to three years)
- Relatively rapid capacity degradation, which limits the number of useful cycles to 50-150 (or the equivalent number of shallow cycles)

These shortcomings are mostly due to the deficiencies of two of the cell components: the zinc electrode and the separators.

The Zinc Electrode

This component of the silver-zinc system is responsible for the above cycling limitations. The major reasons are shape change and the formation of zinc dendrites.

Shape Change: This is a phenomenon whereby zinc oxide, formed during the discharge, is partially dissolved in the electrolyte and redeposited during the charge in a location different from where it originated. The result is a gradual depletion of the active material at the top and edges of the electrode, which eventually lose all electrochemical activity. As a consequence of shape change, silver-zinc cells lose 50 percent of their initial capacity in about 50 to 150 cycles, depending on design and mode of operation. Within that range, capacity losses occur faster when cells are operated at high charge and/or discharge current densities.

Zinc Dendrites: Zinc dendrites are a sharp, crystalline form of the metal that is produced near the end of charge and during overcharge of the zinc electrodes. These dendrites may puncture the separators, causing irreversible cell failure.

The Separators

Regenerated cellulose in various forms (plain or treated cellophane, fibrous sausage casing) has been used as the main separator for silver-zinc cells since the early days of the development of the system. Indeed it is nearly ideal in many respects, but it suffers from one serious weakness-limited resistance to oxidation by silver oxides, by oxygen, and by the electrolyte. As a result, the life of silver-zinc cells built with regenerated cellulose is practically limited to about two to three years, although some tested under laboratory conditions have lasted over four years.

Technical Objectives

The main technical objective of the program is the advancement of the state-of-the-art of the silver oxide-zinc system through improvements to the negative electrode and the separators.

Improvements to the Negative Electrode

This is not an easy task, as all earlier attempts to achieve anything more than modest improvements were unsuccessful, or in the case of recently published work, remain unproven.

However, YTP believes that substantial improvements can be achieved that would extend the life of the silver-zinc system by a factor of two or better. For that purpose, YTP relied for most of the work on a new class of materials known as Electro-Permeable Membranes (EPM's),

which were invented by Mr. Robert L. Peck of T&G Corporation, a small business concern located in Lebanon, Connecticut.

EPM's are the analog of biological membranes which can keep two different solutions or electrolytes separated indefinitely yet can freely transfer selected ions. They have been described as ionic semiconductors and are the ionic analog of electronic semiconductors.

EPM material consists of a two-polymer blend. One of the polymers is a long chain hydrogel such as used to thicken solutions or to form gels, while the other polymer is a supporting material and can be one of the common plastics such as polypropylene, polyvinyl chloride (PVC), or polyvinyledene fluoride (PVDF). There is a broad range of hydrogels and plastics that can be used.

For use in silver-zinc negative electrodes, various EPM formulations were coated on zinc-oxide particles to provide encapsulated domains expected to remain stable during charge and discharge, thereby maintaining a stable electrode morphology.

Improvements to the Separators

The useful life of silver-zinc cells is normally limited by the zinc negative electrode. However, as soon as substantial advances in zinc electrode technology are accomplished, the need for improved separators will be felt immediately. Again, YTP relied heavily on the EPMs for this purpose by coating them onto existing separator materials. The films that were applied were the following:

- Cellophane, still predominant in rechargeable silver-zinc cells; only one side of the film was coated.
- Celgard 2500, a 1-mil microporous polypropylene (with 45 percent porosity), which in its natural form is hydrophobic and therefore unsuitable as a separator for aqueous electrolyte batteries. The high-water-chain-content EPMs impart good ionic conductivity to these separators while their negligible diffusion rate restricts electrolyte mobility to a minimum, which should minimize the shape change of the zinc electrode. Both sides of the film were coated.

Experimental

The work on Phase I of this program was divided into several tasks, including:

- Development and preparation of EPM formulations for the negative electrode and the separators.
- Development of manufacturing procedures for small quantities of negative electrodes with EPM's and extension to pilot plant quantities.
- Coating of Celgard and cellophane with EPM's.
- Cell design and manufacture.
- Cell testing.

Details of the last two tasks are described below.

Cell Design and Manufacture

A total of 36 cells (4 each of 9 different variations) were built and tested. This number includes 4 standard cells (one variation) and 24 (six variations) with EPM's. All cell packs occupied the entire depth of Yardney's 12Ah cell cavity without spacers. As a result, the cells had variable amounts of active materials and were judged both in terms of overall capacity and capacity per gram of active silver.

Details of the design of the best performing variation of cells with EPM's, designated as V2, compared with that of the standard cells are shown in Table 1 below.

Table 1 - Cell Design Details

Denomination	V1(1)	V2
Positives, number	4	4
Collector	(2)	(2)
Powder (g)	27.7	34.0
Dimensions (in)	1.50 x 2.25	1.50 x 2.25
Thickness (in)	.027	.033
Total active area (in^2)	26.8	26.8
Negatives, number	5 (3f+2h) (3)	5(3f+2h)
Collector	perf. Ag foil	perf. Ag foil
Zinc (g) (4)	23.5	30.4
Additives	1% HgO	3.8% EPM(5)
Thickness (in) (6)	.053/.0285	.064/.034
Construction	Pasted	Mold pressed
Coating	none	none
K ratio (7)	.85	.855
Separators		
Positive	5T C-19 (8)	3T C2500 (9)
Negative	1 P5-bag (10)	1 P5-bag
Coating	none	EPM (11)
Electrolyte	42% KOH	42% KOH

(1) Standard cell
(2) Expanded silver mesh
(3) Three full electrodes (center) and 2 halves at each end
(4) Including additives
(5) Solvent based, code number 17K
(6) Full/half-end
(7) K = mass of active zinc to active silver
(8) 5 turns YTP silver treated cellophane
(9) 3 turns Celgard 2500
(10) 5 mil non woven nylon (Pellon) bag
(11) Code number 2525

Cell Testing

All cells were given three formation cycles and two tests cycles, as shown in Table 2 below.

Table 2 - Formation and Test Cycles

Cycle No.	Charge		Discharge		Drain[1]	
	Current (A)	EOCV	Current (A)	EODV	Current (A)	EODV
F-1	0.3	2.10	4.0	1.10	1.0	1.10
F-2,F-3	0.4	2.05	4.0	1.10	-	-
1-2	0.5	2.05	4.0	1.10	-	-

Note:

[1] When the 4-A discharge has reduced cell voltage to 1.10, the current is lowered to 1 A and the discharge ("drain") is continued, again to a 1.10-V cutoff.

At the end of cycle 2, the cells were divided into two groups (two cells of each variation per group) and tested as follows:

Group A: The cells in this group were cycled continuously on a computer controlled test station , at 40% depth of discharge, with full capacity discharges every 15 cycles, until unable to deliver their shallow cycle capacity (approx. 143 mAh per gram of active silver).

Group B: These cells were used for characterization tests, including gas evolution measurement, and high rate and low temperature discharges.

Test Results

For the sake of brevity, only the results of variations V1 (standard) and V2 (best performing EPM's) are shown.

Cycles 1 and 2

These cycles, performed as stated in Table 2, were used to establish the baseline capacity of the cells. The results were as follows:

Table 3 - Cycles 1 and 2

Variation No.	Cell No.	Output (Ah)		Average, cys 1-2	
		Cycle 1	Cycle 2	Ah	mAh/g(1)
V1	1	9.22	9.58		
	2	9.84	9.95		
	19	9.64	9.84		
	20	9.82	9.73		
	Avg	9.63	9.78	9.70	350.2
V2	5	12.25	12.37		
	6	12.39	12.57		
	23	12.65	12.73		
	24	12.58	12.64		
	Avg	12.47	12.58	12.52	368.2

Note:

(1) milliampere-hours per gram of active silver

Group A: The deep discharge capacity of the cells on this regime is shown in Figure 1; Figure 2 depicts the same data, expressed in mAh/g of active silver. The actual number of cycles to failure (as defined in the preceding paragraph) and the reasons thereof are listed in Table 4.

Table 4 - Cycles to Failure

Cell No.	Variation No.	No. of Cycles	Failure Mode
1	V1	94	LC(1)
2	V1	96	LC
5	V2	159	SS(2)
6	V2	162	SS

Notes: (1) LC = low capacity (negative electrode "shape change")
(2) SS = slow short (silver penetration)

Group B: The most important results of the cells in this group are shown in Tables 5, 6 and 7 below.

Table 5 - Gas Evolution

Variation Number	V1	V2
Gas Evolution (1) $cm^3/hr \times g$ Zn, average	18.3×10^{-3}	5.5×10^{-3}
Gas Evolution (2) cm^3/g Zn, average	0.094	0.028

Notes:

(1) Last 8 hrs of a 24 hr charged stand at 100°F
(2) For a complete discharge at 4.0A at 25°C

Table 6 - Low Temperature Discharges

Variation Number	V1	V2
Discharge (4.0A at 0°C)		
Avg minimum voltage	1.424	1.417
Avg output (Ah)	8.64	10.85
Avg mAh/g silver	312	319
Discharge (4.0A at -20°C)		
Avg minimum voltage	1.209	1.128
Avg output (Ah)	7.36	8.55
Avg mAh/g silver	266	251

Table 7 - High Rate Discharges at 25°C

Variation Number	V1	V2
Average minimum voltage		
at 4.0A	1.475	1.472
at 8.0A	1.436	1.435
at 12.0A	1.407	1.411

Conclusions (Phase I)

Electrical tests performed on the best variation of cells with EPM's (V2) were quite encouraging and justify the expectations originated by preliminary tests. In Group A testing, V2 cells run well ahead of the standard cells in the following areas:

- They had a 68 percent longer cycle life (160 vs. 95).
- They had a 32 percent better silver utilization after 60 cycles and a 38 percent better utilization after 90 cycles.
- The overall capacity was 62 percent better after 60 cycles and 70 percent better after 90 cycles. This margin is very important because it reflects the actual capacity improvement realized in cells of the same external configuration. The improvement results from the combination of a better silver utilization and the additional amount of active materials made possible by using thinner separators.

- The 160 cycles obtained were far more than ever achieved from silver-zinc cells with main separators of the same thickness (less than 0.1 mm).

The performance in Group B testing of cells with EPMs also compares favorably to that of the standard (V1) cells.

- Gas evolution on charged stand and on discharge was only about 30 percent that of the standard cells. This is a very welcome result that is taken as evidence of the lower solubility of negative active material in the electrolyte, which translates into a reduced rate of shape change and, therefore, longer cycle life.
- Voltages at 4.0, 8.0, and 12.0 A were essentially the same as for the standard cells, indicative of good high-rate discharge performance.
- Low temperature performance was good at 0°C but only fair at -20°C, where the minimum voltage was 80 millivolts below the standard cell voltage.

Phase II Work[2]

The Phase II program is a continuation of the Phase I effort with the following main objectives: [1] to demonstrate that improvements beyond those achieved in Phase I are possible, [2] to extend those improvements to all sizes of silver-zinc cells, including those used for torpedo, target and unmanned underwater vehicle propulsion, and to "dry charged" cells, [3] to develop manufacturing procedures adaptable for the production of pilot plant or larger quantities of cells containing the additives and/or coatings, and [4] to develop adequate quality control procedures to insure the reliability of the cells and the reproducibility of the test results.

The most important tasks of Phase II are:

- Further development and preparation of EPM formulations
- Further development of manufacturing procedures for negative electrodes with EPM's, with emphasis on those adaptable to pilot plant or mass production quantities
- Development of quality control procedures
- Cell design and manufacture, which includes 96-8.5 ampere-hour cells, divided into 3 groups and 32-190 ampere-hour cells
- Cell testing, along lines similar to those of Phase I, to determine cycle life, gas evolution and capacity and voltage at high rate and at low temperature

Conclusions (Phase II)

It is too early in the program to draw any clear conclusions. The major accomplishments achieved so far are:

- The fabrication of composite zinc-oxide/EPM electrodes by a mass production method, i.e.: wet pasting
- The fabrication of composite zinc/EPM electrodes by electroforming the above, another mass production technique
- The verification of the viability of the pasted zinc-oxide/EPM electrodes by single electrode cell tests
- The coating of separators (cellophane, Celgard and PVA) with EPMs

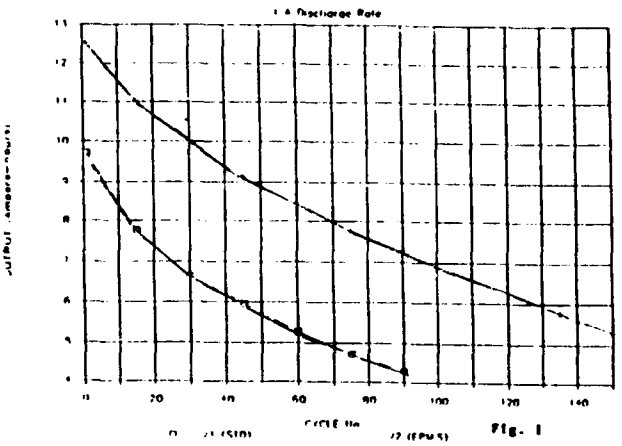

Fig. 1

CAPACITY IN DEEP CYCLES

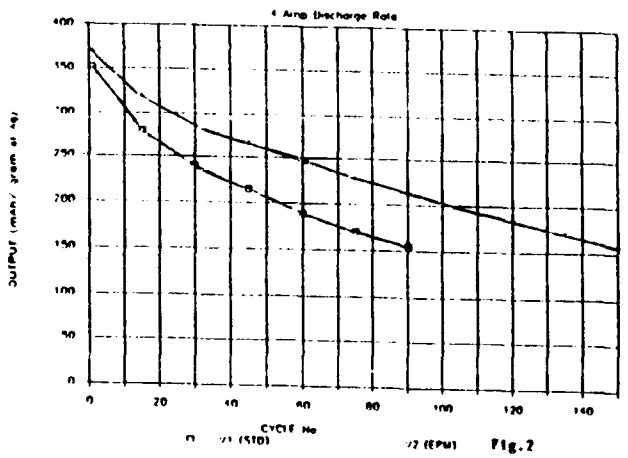

Fig. 2

SILVER UTILIZATION IN DEEP CYCLES

Acknowledgment

This work was supported by the Small Business Innovative Research Office and by the Office of Naval Research, under the High Energy Battery Project.

References

[1] NSWCDD/TR-92/296 : Development of silver-zinc cells of improved cycle life and energy density, 3/3/94

[2] Yardney Technical Products, Inc. SBIR proposal for Phase II of the above program, 6/12/92

AUTOMATIC GENERATION OF SPICE* MACROMODELS OF BATTERIES

Xavier ANDRIEU, David KIERBEL
Alcatel Alsthom Recherche, route de Nozay, 91460 Marcoussis, FRANCE

ABSTRACT

This paper presents the means to automatically obtain behavioral models of primary and secondary batteries based on SPICE modeling. The behavior of the battery is recorded by a frequency signal analyzer in the frequency domain. The response depends on the nature of the electrochemical couple, the physicochemistry, the state-of-health, the state-of-charge and the technology of the cell. A computer software program analyzes the impedance spectra, generates electrical equivalent circuits of the generator and finally produces SPICE input files. The battery macromodel can be used by the large family of analog circuit simulators. The macromodel can be a simple description of the battery in a precise state or a complex representation of the battery working involving the variation of the state-of-charge. That is realized by a succession of discrete models or by incorporating variable components in the macromodel. Examples of modeling are given for nickel cadmium and lithium carbon batteries.

INTRODUCTION

A lot of work has been devoted to the modeling of batteries. Most of the classical models are based on a description of the electrochemistry and the physicochemistry of the batteries. Sophisticated ones can also include a description of the technology and the hardware. If these models are interesting for the understanding of the electrochemical phenomena, they present some limitations. The simulation of a real working from basic data and a theoretical analysis does not still fit well the experimentations and a readjustment of the input parameters can be necessary. As a matter of fact, these models are more interesting for the electrochemists and battery manufacturers for the improvement and the design of cells than for the battery users.

SPICE is a powerful, general purpose circuit analysis program that simulates analog circuits and by far the most popular simulation program being used today by electronicians. The SPICE models of batteries that have already been described [1] allow to simulate dicharge curves at different rates, but do not take into account the complex impedance of the cells and its possible variation with the battery working.

The knowledge of the source impedance is a very important parameter to connect batteries to switching regulators, choppers, motors, actuators, relays, etc... The behavior of a battery-powered system can be disturbed if the system does not match well the battery. That is why it is interesting to modelize an appliance and a battery in the same time. The presented modeling will allow to consider a battery as a common component in a complex electrical circuit.

EXPERIMENTAL

The impedance measurements were carried out in the frequency range 0.1Hz-65KHz, using a frequency response analyzer model 3562A connected to an electrochemical interface model SI 1286, both from Solartron Schlumberger. The batteries used for the experiments were AA VR nickel cadmium from Saft, and lithium carbon US18650 types from Sony. The nickel cadmium batteries were charged at the C rate with an overcharge coefficient of 1.4 and discharged at the C rate. The lithium carbon batteries were charged at constant current (C rate) and at constant voltage (4.2 V) for two hours. The discharges were interrupted at different levels to make impedance measurements. The real state-of-charge of each level was calculated after the complete discharge of the battery. PSpice 6.0 from MicroSim Corporation was used as Spice simulator. The data analysis and PSpice netlist generation programs were written in Visual C++ 1.0 from Microsoft. All the programs run on the IBM PC family.

NETWORK SYNTHESIS

The basis of this modeling is the synthesis of the equivalent electrical circuit of the battery. Until now several methods have been investigated in order to fit experimental data obtained by impedance spectroscopy [2][3][4]. Most of these techniques needs to define the network to fit (structure and number of components) and to provide to the computer entry data (approximative values of the components). The frequency response of a system does not uniquely determine the circuit used to model that response [5]. The proposed synthesis is arbitrary and does not take into account electrochemistry. The impedance spectra recorded at different states-of-charge are analyzed with the following process. The basic hypothesis is that most of the impedance spectra (in the positive real / negative imaginary quadrant) of batteries can be modelized by n RC parallel cells in series (figure 1), that means by a distribution of time constants through an electrical network.

The two main difficulties are the determination of the time constant distribution law and the number of RC cells. The calculation of the capacitor and resistor values, and the determination of the number of RC cells are realized in three steps. Firstly the number of RC cells is fixed and all the resistors have the same value. The computer generates a network consisting of one RC cell and adjusts the capacitance to reduce the gap with the experimental spectrum. A second RC cell is added to the network and the capacitance is still adjusted as previousely. This process is repeated for all the RC cells. At the end, the calculated impedance

spectrum fits well with the experimentation, but the number of RC cells is too high.

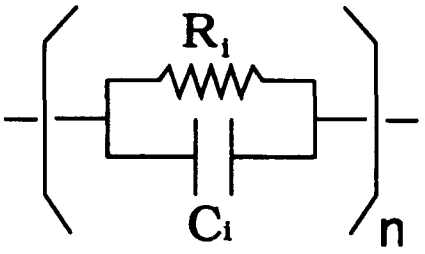

Figure 1. Basic circuit of the battery electric equivalent network

Figure 2 shows the value of the capacitance versus the number of RC cells for an impedance spectrum of a lithium carbon battery. As a matter of fact, this curve presents the distribution of the time constants through the network.

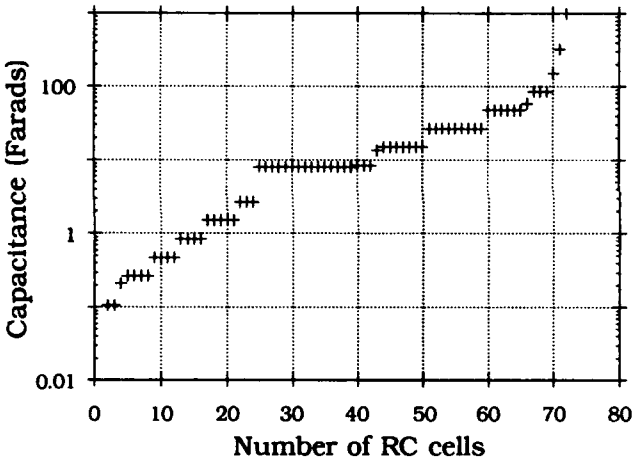

Figure 2. Capacitance versus the number of RC cells for a lithium carbon battery

The second step consists in reducing the number of cells by combining the cells presenting nearly the same capacitance. After this operation, the new computed impedance spectrum differs slightly from the previous one. The third and last step consists in a final adjustement of the synthesized network components by an iterative procedure. Figure 3 shows the experimental and fitted impedance spectra of a lithium carbon battery. The several impedance spectra are recorded during the complete discharge of a battery. The two first steps are only realized once and the final adjustment at each time. That allows to have a continuous variation of the network components with the state-of-charge.

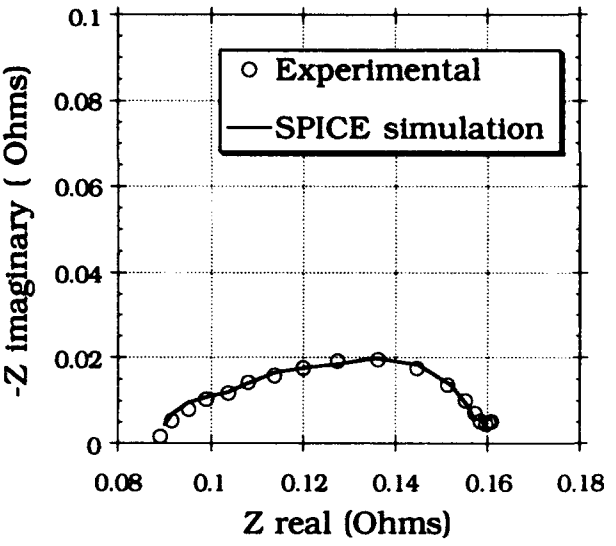

Figure 3. Experimental and fitted impedance spectra of a lithium carbon battery

SPICE MODELING

The first work consists in modeling an electrical network with components varying with the state-of-charge. Each resistor and capacitor of the previous network must be separatly controlled according to a table describing its variation versus the state-of-charge. That is realized by using voltage-controlled resistors and capacitors. The components are obtained with impedance and admittance mutiplier subcircuits (ZX and YX subcircuits in the PSpice library). These subcircuits employ an external component (capacitor or resistor) that is sensed. The output impedance or admittance equals the value of the control voltage times the reference. As a result, the output impedance or admittance is seen by the circuit as a floating resistor or capacitor. Figure 4 shows the simple RC network consisting of two ZX and YX subcircuits in parallel with their reference components.

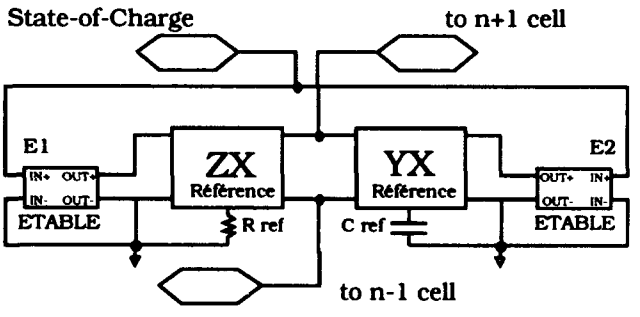

Figure 4. Voltage-controlled RC cell

The values of the components are imposed by a look-up-table voltage-controlled voltage source (ETABLE) that contains their discrete variations. This look-up-table source modelizes the resistance or the capacitance variation versus the state-of-charge. The intermediate values are interpolated. The complete battery equivalent circuit comprises several circuits as described above in series. Each circuit is characterized by its own look-up table. By applying a voltage between 0V to 1V to the SOC input, the impedance spectrum varies continuously from 0 to 100% of state-of-charge. This network is included as a subcircuit in an other circuit that modelizes the discharge of the battery taking into account the voltage variation with the state-of-charge and the energy efficiency with the discharge rates. A possible electric circuit is illustrated in figure 5.

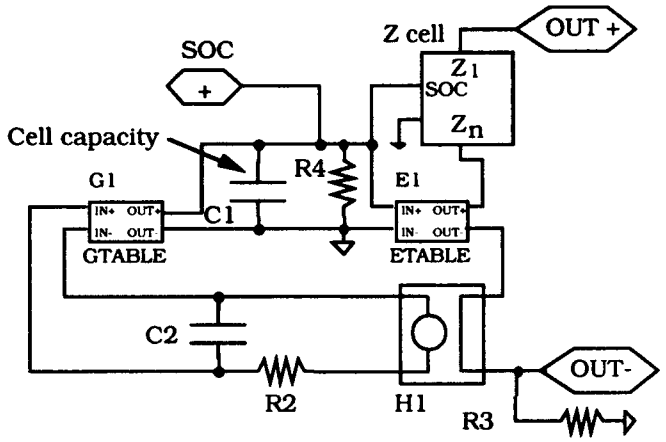

Figure 5. Generic electric circuit of a battery

A look-up-table voltage-controlled voltage source generates the battery voltage according to a memorized voltage profile. This voltage source receives as input the state-of-charge that is calculated by discharging a capacitor (C1) at constant current. The dicharge current is measured in the battery circuit and converted in voltage by a controlled-current voltage source (H1). This voltage is applied through a low pass filter (R2 and C2) to a look-up-table voltage-controlled current source (GTABLE) that discharge the capacitor C1. This table contains conversion and compensation factors to fix the capacity of the battery and to modify the value of the output current as a function of the discharge rate. The purpose of the low pass filter is to not take into account the pulse consumption. The two battery terminals on the electrical diagram are the OUT+ and OUT- labels. The complete battery circuit can be used as a subcircuit in the electrical diagram of a battery-powered application.

GENERATION OF BATTERY MACROMODELS AND RESULTS

The program written for the automatic battery model generation analyzes the data from the frequency response analyzer, computes the equivalent electrical network and generates the PSpice netlist. The frequency response analyzer is programmed through the computer to record successive impedance spectra during a discharge. Data concerning the battery efficiency are introduced separatly and come from discharges at different rates. Figure 6 shows the flow-chart of the complete process.

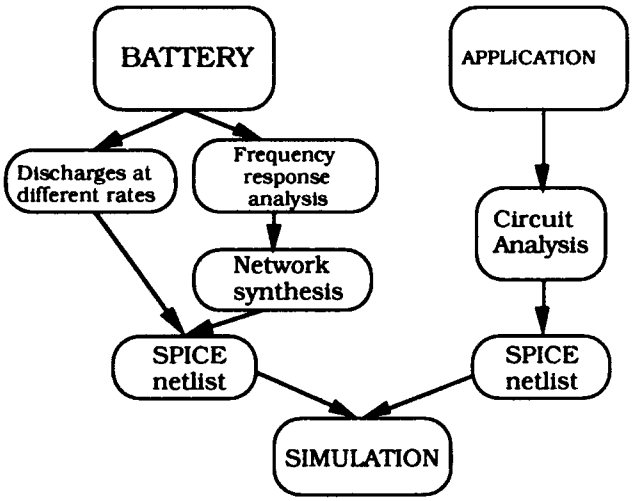

Figure 6, Flow-chart of the battery model generation

Nine impedance spectra were recorded during the discharge for lithium carbon and five for nickel cadmium. After data analysis, the number of RC parallel cells was respectively four and five. Impedance analysis was performed with the SPICE simulator by connecting a frequency swept AC courant generator to the OUT+ and OUT- terminals in the electrical diagram. Figures 3 and 7 show the initial experimental and fitted impedance spectra. A more complete comparison was achieved with varying the state-of-charge. The variation of the modulus and the phase of the impedance of lithium carbon and nickel cadmium batteries with the state-of-charge are illustrated in figures 8 and 9. The fitted results agree very well with the original data through the frequency range and the state-of-charge.

CONCLUSION

One of the main interest of SPICE macromodels of battery is to take into account the environment and to allow to simulate the bidirectional interactions between the battery and the application. In the case of classical electrochemical models, that is very difficult to realize without writting a program for a specific application. SPICE-like programs run on numerous mainframe computers and personal computers, and on various operating systems. So the portability of these models is very good and they allow the users to evaluate batteries in their own application with a simple SPICE simulator. Future improvements will concern the implementation of the impedance variation with the discharge rate, a more precise analysis of the battery efficiency and the influence of the temperature.

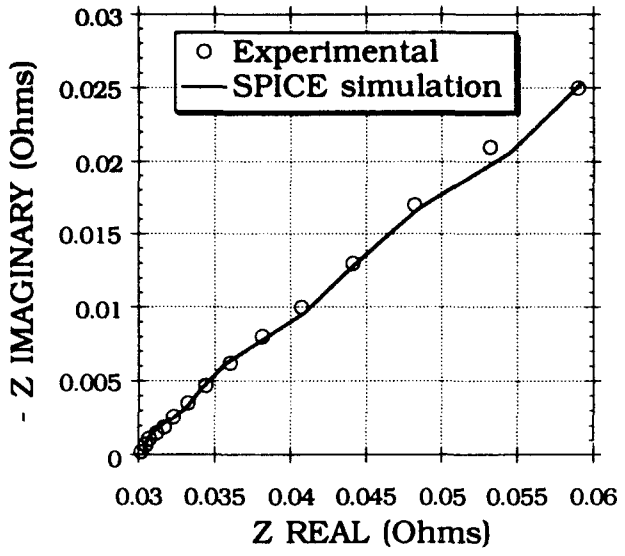

Figure 7. Experimental and fitted impedance spectra of a nickel cadmium battery

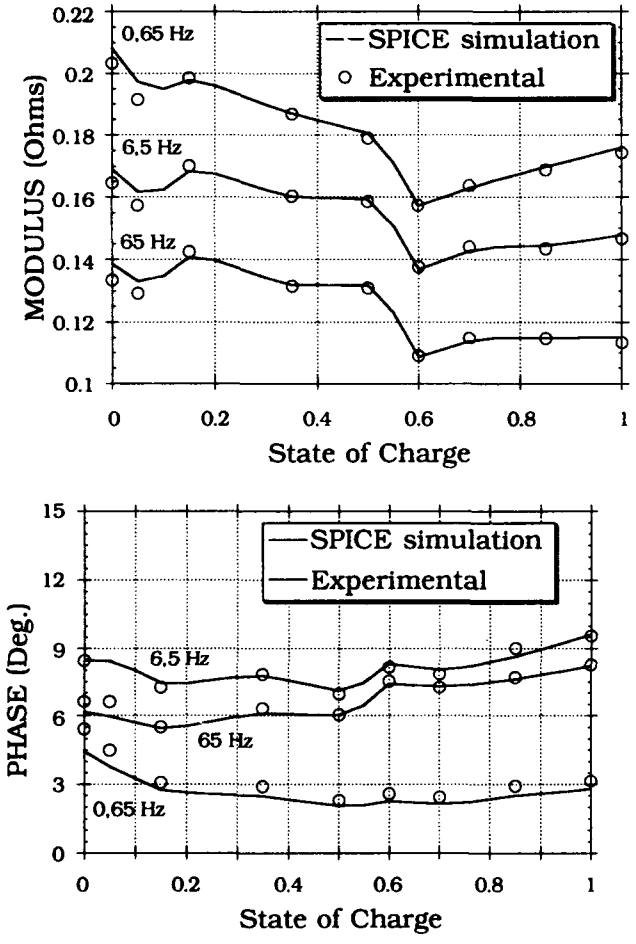

Figure 8. Variation of the modulus and the phase of the impedance of a lithium carbon battery with the state-of-charge

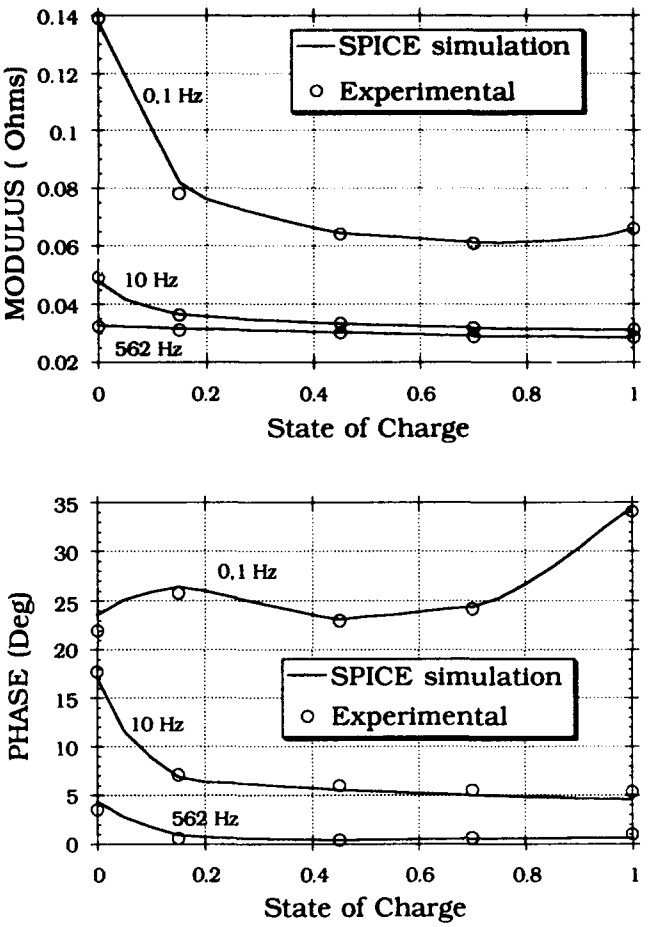

Figure 9. Variation of the modulus and the phase of the impedance of a nickel cadmium battery with the state-of-charge

REFERENCES

* Simulation Program with Integrated Circuit Emphasis

[1] S. C. Hageman. EDN, october 28, (1993), pp 117-128

[2] B.A. Boukamp, Solid State Ionics Vol.20 (1986), pp 31-44

[3] P. Zolotski, J. Electroanal. Chem. Vol.178 (1984), pp 11

[4] J. R. Macdonald, G. B. Cook, J. Electroanal. Chem. Vol.168 (1984), pp 335-354

[5] J. Jacquelin, J.of Non-Crystalline Solids Vol.131-133 (1991), pp 1081-1083

COMMERCIAL NICKEL-HYDROGEN BATTERY DEVELOPMENT

D. K. Coates, C. L. Fox, J. C. Dermott and A. D. Boyt*
Eagle-Picher Industries, Inc.
Joplin, Missouri 64801

*Crowder College
Neosho, Missouri 64850

Abstract

The nickel-hydrogen battery system, extensively used in the aerospace industry, is being developed for terrestrial, commercial applications. Low-cost components, electrodes, cell designs and battery designs are currently being tested. Catalytic hydrogen electrodes have been developed which are compatible with commercial battery cost. Prismatic and spiral-wound cell designs have been built and tested. Common pressure vessel battery designs are also being evaluated. The nickel-hydrogen battery offers potential cycle life unequaled by any other battery system. This makes the battery ideal for remote stand-alone power systems and other applications which require long life and a truly maintenance-free and abuse tolerant battery system.

Introduction

The nickel-hydrogen (NiH_2) battery system has been in production for aerospace applications for more than twenty years[1]. Eagle-Picher currently has NiH_2 batteries operating aboard more than 50 earth-orbital communications and surveillance satellites. Over 100 million cell-hours have been accumulated in actual spacecraft operation, including both low-earth-orbit (LEO) and geostationary-earth-orbit (GEO) satellites. Additional ground-based testing at Eagle-Picher has established cycle life performance of more than 95,000 charge/discharge cycles. This advanced aerospace technology is now being developed for use in commercial, terrestrial applications[2].

The NiH_2 battery system has a number of unique advantages which make it ideal for many commercial applications such as telecommunications, uninterruptible power supplies (UPS), utility load leveling, standby power, electric vehicles[3] and remote location power systems[4]. The NiH_2 battery provides both high energy density and excellent power density. Hydrogen provides a very lightweight, efficient energy storage material. Due to the unique electrochemistry, the NiH_2 system is an inherently fault-tolerant design with excellent overcharge, overdischarge and deep cycle capabilities. The battery is hermetically sealed and truly maintenance-free. The internal hydrogen pressure is a direct linear function of battery state-of-charge (SOC) and thereby provides a simple and reliable method of determining the SOC of the battery. Also, the NiH_2 battery does not contain any toxic materials such as lead, cadmium or mercury and can be readily recycled. Projected battery costs are directly comparable with other nickel battery systems and competitive with lead-based batteries on a life cycle cost basis.

Nickel-Hydrogen Battery Design

A nickel-hydrogen cell develops a potential of about 1.25 volts at the mid-point of discharge, at a C/2 rate. Multiple cells must be combined into batteries for applications requiring higher voltages. Battery design is dependent on the cell design, battery operating parameters and application requirements. Different cell designs require different packaging considerations. A description of several advanced battery designs has been previously published[5].

Common Pressure Vessel Battery Design

The most efficient, low-cost commercial battery designs are common pressure vessel (CPV) applications, containing individual cells such as the prismatic or spiral-wound geometry (Figure 1). The primary requirement at the battery level is hydrogen gas containment and electrical and thermal interface at the system level. The battery container must be hermetically sealed in order to contain the hydrogen gas, without which the battery will not function. The individual cells, connected in series/parallel strings, are contained within the battery container. Multiple containers can be used for a modular approach to larger battery systems. Thermal considerations are minimal except in applications with an ambient temperature above 40 °C. Battery cooling options can be employed for this type of service. Passive cooling methods have been investigated such as the "Cool Cell" technology patented by Zomeworks Corporation. A strain gauge or pressure transducer can be attached to the battery container in order to monitor the battery state-of-charge.

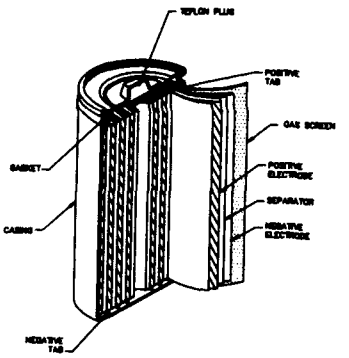

Figure 1. Spiral-Wound Nickel-Hydrogen Cell

A 12 VDC, 120 Ah CPV battery was built in conjunction with Zomeworks Corporation (Figure 2). The cells are a light-weight prismatic design (Figure 3). The CPV battery container was fabricated by Zomeworks. Initial testing on the battery has shown excellent results. A typical charge/discharge profile is shown in Figure 4. The battery charges at a maximum voltage of 15.5 VDC and has a mid-point discharge voltage of 12.2 VDC. The charge and discharge voltage profile is flat and uniform, making the system ideal for interface with photovoltaic charging systems. The performance and abuse tolerance of the battery simplifies the charging system electronics required for reliable operation. The battery delivers 120 Ah at 25 °C. The internal battery pressure is linear as a function of the current during both charge and discharge. The battery has a maximum operating pressure of 180 psi. This operating pressure is simply a function of the free volume available in the battery to contain the hydrogen gas. The battery can be designed to operate at higher or lower pressures. The cell design exhibits low internal impedance which increases the efficiency and rate capability of the battery. This is a prototype battery design for

a stationary commercial application such as telecommunications, utility load leveling or remote power systems.

Figure 2. Terrestrial CPV Nickel-Hydrogen Battery

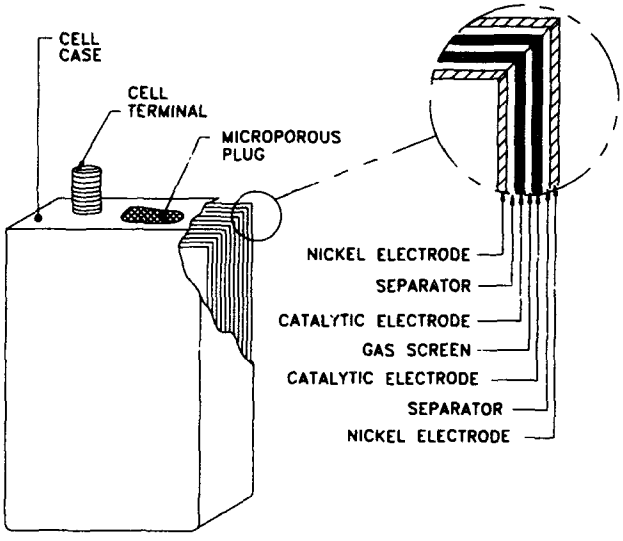

Figure 3. Prismatic Nickel-Hydrogen Cell Design

Dependent Pressure Vessel Battery Design

Dependent pressure vessel (DPV) technology is a modular approach to NiH_2 battery design. The DPV cell design incorporates the best features of the prismatic geometry, while achieving maximum efficiency in hydrogen gas containment. As shown in Figure 5, the geometry of a DPV cell requires some support of the flat surfaces and the cell is partially dependent upon the battery package for gas pressure containment. The cell design has the advantage of a prismatic flat-plate electrode stack (Figure 6). The cells can be readily packaged into a battery or battery module using a simple endplate/connecting rod configuration. A major design advantage is that the battery support structure is efficiently required to restrain the force applied to a portion of the end cell only. As the DPV cells are stacked in series to achieve the desired system voltage, this increment of the total battery weight becomes small. The geometry of the DPV cell also promotes compact, minimum volume packaging and places all cell terminals in close proximity along the length of the battery. The resulting ability to reduce intercell wiring offers additional efficiency and savings.

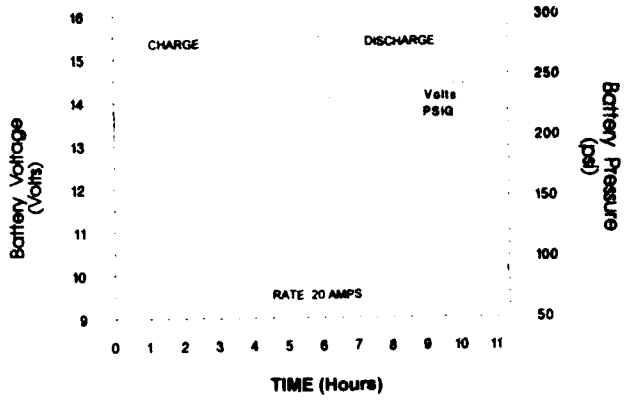

Figure 4. CPV Battery Voltage and Pressure Performance

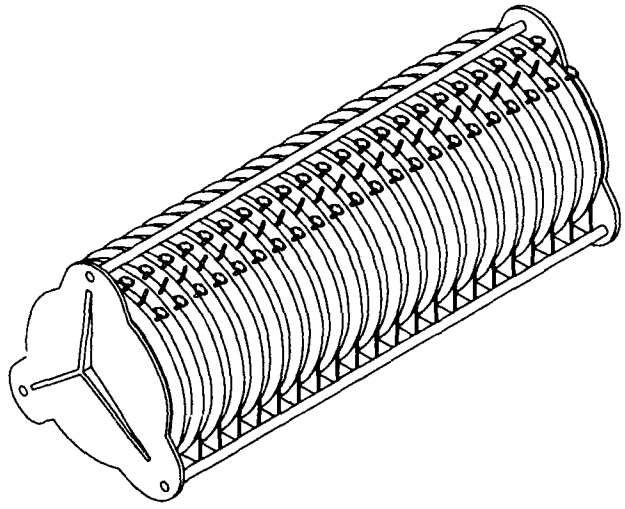

Figure 5. Dependent Pressure Vessel (DPV) Battery Design

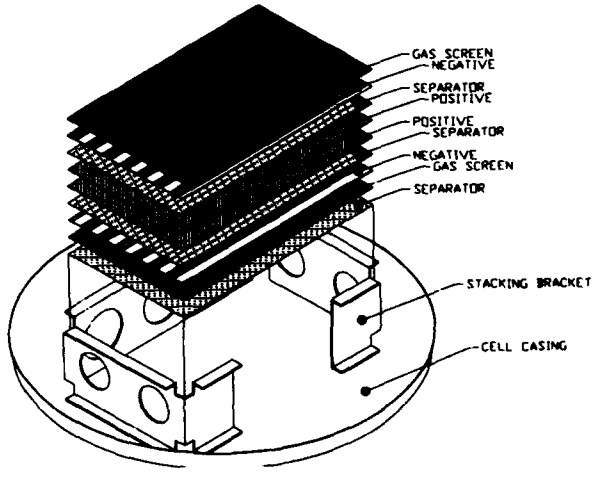

Figure 6. DPV Internal Cell Construction

Tubular Nickel-Hydrogen Battery Design

The tubular NiH_2 battery design is appropriate to the spiral-wound or cylindrical, flat plate cell design. The individual cells can be stacked end-to-end along the length of a tubular pressure vessel. The advantage of this design is that higher operating pressures can be accommodated in a cylindrical container, with less weight of pressure vessel material. This design also offers higher volumetric energy density by minimizing cell pressure vessel volume and by maximizing the battery packaging efficiency. The length and diameter of each modular battery tube would be designed for the specific application. This could be standardized for design simplicity and cost effectiveness. Multiple tubes can be nested together to form a complete battery. This battery design is also applicable to a bipolar NiH_2 cell arrangement. Bipolar cells could be stacked along the inside diameter of the tube. This would provide maximum high current capability for electric vehicle or other high rate or pulse applications.

Low Pressure Nickel-Hydrogen Battery Design

Metallic alloys which reversibly store hydrogen can be used in the NiH_2 system to lower the cell operating pressure. This work was pioneered in the early 1970's by Comsat Laboratories and provided the technology basis for the later development of the nickel-metal hydride battery system. The hydrogen anodic active material is stored as a solid metallic hydride rather than as molecular hydrogen gas. This is a distinctly different application than the nickel-metal hydride battery, in which the hydride material is used directly as an electrochemical cathode or anode. In the NiH_2 system, the hydride forming alloy chemically adsorbs and desorbs the hydrogen produced at a conventional hydrogen electrode. The advantage of this design is that the inherent cycle life limitation of the hydride electrode is avoided. Hydride alloys have the inherent tendency to decrepitate and undergo pulverization, due to volume expansion and contraction which occurs as the electrode is hydrided and dehydrided (charged and discharged).

In the NiH_2 system, the hydride alloy is not used as an electrode and doesn't have to maintain any structural integrity or particle-to-particle bonding. In fact, the reduced particle size and corresponding increase in surface area that occurs during normal cycling increases the efficiency of the material in this application. Another advantage is that the hydride alloy doesn't have to undergo direct exposure to the corrosive alkaline environment, produced in the cell by the concentrated hydroxide electrolyte, oxygen evolution at the nickel electrode and anodic polarization of the hydride material during discharge. Corrosion of the hydride material is a significant problem in the nickel-metal hydride battery. The advantage to the NiH_2 system is that the volumetric energy density of the system is increased, for applications where this aspect is important.

Terrestrial Nickel-Hydrogen Battery Applications

One of the important new areas of terrestrial battery application is independent power systems. These systems generate electricity from a renewable source such as solar or wind energy. Larger systems typically use these renewable energy sources to displace operation of diesel generators, with a resulting savings in fuel and maintenance costs. More commonly, small independent systems of less than 10 kilowatts peak (kWp) utilize no fossil fuels, but rather store a portion of the converted energy for later use. These small systems are typically supplied by solar cells because of their simplicity and reliability.

Application of independent power systems is practical in situations where central electric grids are nonexistent, such as in third world countries and even some remote areas of the U.S. Solar-electric systems are economically competitive with more traditional remote power conversion technologies such as diesel or gasoline generators. The independent systems, such as solar and wind power, are well-suited to remote applications because they eliminate fuel source dependence and the maintenance requirements associated with internal combustion engine-driven generators. While expensive compared to grid-generated power, electricity from solar-driven independent power systems is the solution of choice in remote areas where grid power is not available. These systems vary in size from less than 0.1 kWp for a single home to supply lights and radios, to village-sized systems of 2-10 kWp for residential and commercial uses. While these consumption rates are less than 5% of western standards, even these small inputs of electricity can profoundly impact on the lives of those who receive them.

Third world application of independent power systems provides special challenges, especially in the area of energy storage. System design places a premium on reliability since the availability of parts and qualified service personnel are usually minimal. The storage component of these systems tends to be the limiting factor for reliability. While the solar components have a failure rate of only 1 in 10,000 per year, flooded lead-acid batteries typically last less than one year in these applications. These batteries are short-lived because of frequent and extended periods of low state-of-charge, extended deep cycling and lack of regular maintenance. Storage battery management is usually rudimentary, typically consisting only of high and low voltage cut-offs; more complex controls are seldom used because of reliability issues. The NiH_2 battery has a very flat charge and discharge profile which makes interfacing with a solar array even more efficient. Both the batteries and the expensive solar panels in standard lead-acid based systems are typically oversized by a factor of two to prevent over-discharge and to extend battery life. The use of a long cycle life, abuse tolerant system such as NiH_2 would eliminate the need for excessive overdesign, significantly reducing overall system size, weight and cost. The NiH_2 battery is uniquely suited to interfacing with photovoltaic systems, particularly as this is the normal operational mode in spacecraft applications.

The limitations of existing storage devices in independent power systems suggest that new battery technology could substantially broaden third-world electrification. The following battery traits would be important improvements over currently used technologies; including tolerance to low state-of-charge, long cycle and calendar life, simple monitoring of state-of-charge and sealed, zero-maintenance packaging. The ultimate goal for the energy storage sub-system would be to bring its reliability up to the same standards as the power conversion components, such as the solar arrays. The nickel-hydrogen battery has the necessary performance, reliability and cycle life to make these types of independent power systems both possible and practical.

Conclusions

The nickel-hydrogen system has been successful in replacing aerospace nickel-cadmium batteries for use in earth orbital satellites. Eagle-Picher NiH_2 technology has been fully proven on numerous U.S. and European spaceflight programs. New nickel-hydrogen technology is being developed for both low cost aerospace and commercial applications. Aerospace applications have provided the basis for NiH_2 battery system development. This advanced aerospace technology is being adapted for terrestrial use. The basic technology required for adaptation of the NiH_2 system to low-cost, commercial applications is in place. Low-cost cell components, new cell designs and innovative battery designs have made this transition possible. The advantages of the NiH_2 battery system are unique. The system is ready for many terrestrial applications, such as remote power systems, and with some additional development work the system can be made even more cost effective.

References

[1] Coates, D.K. and Hoofnagle, P.S. (1993). EPI on Charge: Nickel-Hydrogen and Nickel-Metal Hydride Batteries for Spacecraft Power Systems. Space Magazine Vol.9, No.8, Shepard Press, United Kingdom

[2] Coates, D., Roumpf, G. and Baer, S. (1991). Nickel-Hydrogen Batteries for Terrestrial Applications. 26th Intersociety Energy Conversion Engineering Conference Boston, Mass.

[3] Coates, D. and Fox, C. (1994). Multiple Advanced Battery Systems for Electric Vehicles. 9th Annual Battery Conference on Applications and Advances, California State University, Long Beach, California

[4] Stockebrand, T., Baer, S. and Randall, J. (1991). Ideal Use of Nickel-Hydrogen Batteries in Remote Power Systems. 26th Intersociety Energy Conversion Engineering Conference Boston, Mass.

[5] Coates, D.K. (1993). Advanced Nickel-Hydrogen Spacecraft Battery Designs. NASA Aerospace Battery Workshop, Marshall Space Flight Center, Huntsville, Alabama

STRENGHTENING THE WEAKEST LINK

IMPORTANCE OF BATTERY ANALYSIS AND MAINTENANCE

Isidor Buchmann
Cadex Electronics Inc.
Burnaby, British Columbia, Canada

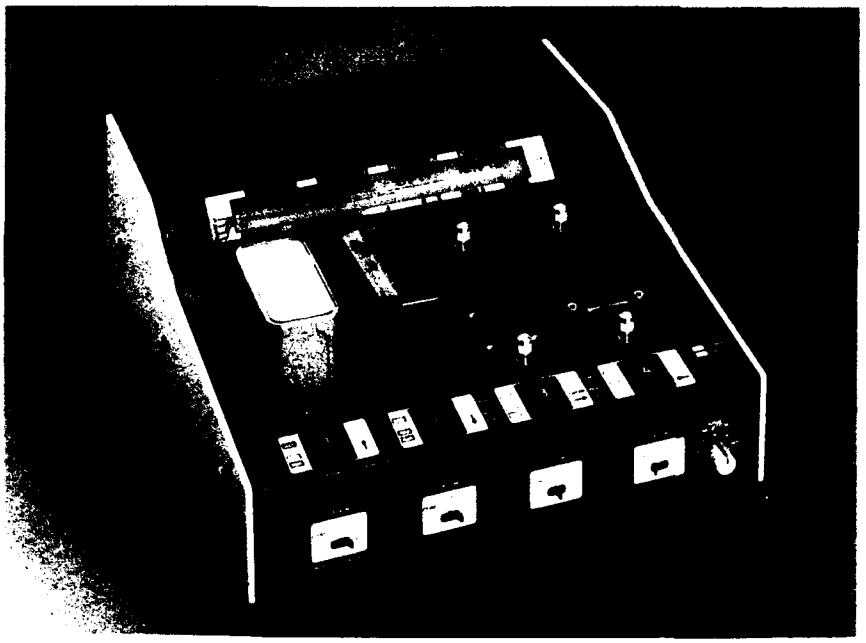

Figure 1 The CADEX C4000 is a programmable battery analyzer capable of servicing NiCd, NiMH and SLA batteries. Four batteries can be processed simultaneously and are tested at their actual voltage and current ratings.

One of the common difficulties with battery powered equipment is the gradual deterioration in performance after the first year of service. Although fully charged, the battery may only deliver half of its original capacity, resulting in unexpected down-time.

Unexpected down-time occurs almost always at the most critical moment. Under normal conditions, the battery holds enough power until recharged. In an emergency situation, more energy is needed and a marginal battery cannot provide the extra power required.

In fact, the Falkland War could have been lost due to marginal batteries. The British Army had assumed that a battery would be fully reliable when recharged in accordance to military procedures. Not so. When command was given to launch the portable missiles, nothing happened. The batteries did not perform and the missiles did not fly that day.

The battery is a mystical "black box" with a mind of its own. It does not change weight, color or shape to indicate state of charge. It simply quits when exhausted.

In many ways the battery exhibits human-like characteristics: it needs good nutrition; it prefers a moderate room temperature, and, in case of the Nickel Cadmium (NiCd) battery, requires regular exercise. The batteries used in the Falkland War were believed to have been affected by a phenomenon referred to as "memory".

Memory: Myth or Fact?

There is some misconception about the word "memory". Memory is commonly blamed for any battery failure known to man. The word **"memory"** is derived from **"cyclic memory"**, meaning that a NiCd battery can remember the depth of discharge applied previously.

Improvements in battery technology have virtually eliminated this phenomenon. Tests performed at a Black & Decker lab, for example, showed that the effects of "cyclic memory" were so minute that they could only be detected with sensitive instruments. After the same battery was discharged for a different length of time, the cyclic memory phenomenon could no longer be detected.

The problem with the modern NiCd battery is not the cyclic memory but the effects of **crystalline formation**. The active materials (nickel & cadmium) of a NiCd battery are present in crystalline form. When the memory phenomenon occurs, these crystals grow, forming spike or tree-like dendrites that cause the NiCd to gradually lose performance. In advanced stages, these crystals may puncture the separator, causing high self-discharge or an electrical short.

The crystalline effect on the NiCd cell plates is similar to the crystal formation during the use of calcium chloride to clear the roads of snow and ice. As the salt absorbs water, crystal formation can be observed.

Preventative Maintenance

Crystalline formation only presents a problem if the battery is left in the charger for days or repeatedly recharged without a periodic full discharge. Such a condition is common with portable communications equipment. It is not necessary to discharge a NiCd before each charge. A discharge to one volt per cell once a month is sufficient to keep the crystal formation under control. Such a discharge/charge cycle is commonly referred to as **"exercise"**.

If exercise is neglected for four months or more, the crystals engrain themselves, making them difficult to dissolve. In such a case, exercise is no longer effective in restoring a battery and **"recondition"** is required.

Recondition is a secondary discharge that slowly drains the battery of its remaining energy. Lab tests have indicated that the NiCd cell needs to be discharged to at least 0.6 volts per cell to effectively dissolve the more stubborn crystalline build-up. When applying recondition, the current must be set low enough to not cause damage through cell reversal.

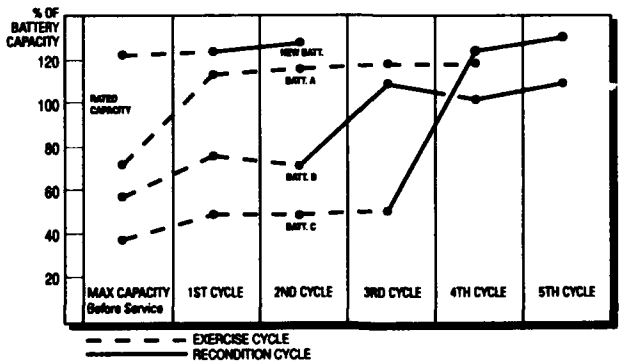

Figure 2 Effects of exercise vs. recondition

Not all batteries respond equally well to recondition. In the study in Figure 2, four batteries afflicted with various degrees of memory are analyzed. All batteries are first fully charged, followed by a discharge to one volt per cell. The resulting capacities are plotted on a scale of 0 to 120%. An additional charge/discharge cycle is applied (dotted line) and the battery capacities are evaluated again.

Battery "A" responded well to exercise. This result is typical of a battery that had been in service for only a few months or had been exercised periodically. Batteries "B" & "C" required recondition (solid line) to recover to full performance. Note that the capacity of the new battery was further enhanced after recondition was applied. When examined after six months of field use, the batteries still showed excellent capacity readings.

Not all batteries will recover with recondition. An older battery may even get worse. If this occurs, the battery is a candidate for retirement. This type of battery may be compared to an old man to whom a vigorous exercise is harmful. On the other hand, an old-timer that has recovered to near full capacity should be re-hired with caution, as it may be subject to high **self-discharge**.

Self Discharge

The NiCd battery has a relatively high self-discharge. If left on the shelf, a new NiCd loses about 10% of its capacity in the first 24 hours. At higher ambient temperature, the self-discharge increases. Likewise, an older battery has higher self-discharge than a new one. A problem arises if a seemingly good battery self-discharges within a day, a phenomenon not too uncommon.

A high self-discharge is caused by a damaged separator. The separator is a thin insulator that isolates the positive and negative cell plates. Once injured, the separator can no longer be improved by exercising the battery. External forces that harm the sensitive separator are uncontrolled crystalline formation due to lack of exercise, poorly designed chargers that boil the battery, and plain old age.

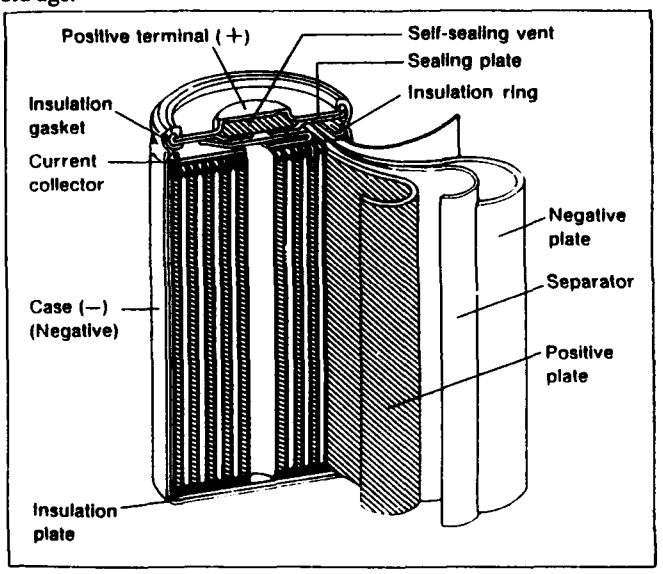

Figure 3 Construction of a NiCd cell

Let us examine the construction of the NiCd cell (Figure 3). The negative and positive plates are rolled up together and placed into a metal cylinder. The positive plate is sintered and filled with nickel hydroxide. The negative plate is coated with cadmium-active material. The two plates are isolated by the separator that is moistened with the electrolyte.

The self-discharge of a battery can be measured with a battery analyzer. To check the self-discharge, first obtain the full capacity of the battery by applying a discharge to one volt per cell. Recharge and store the battery for 24 hours at room temperature (20°C) and measure the capacity again. If the capacity loss during the rest period is more than 30%, discard the battery.

The battery analyzer is not only useful for measuring self-discharge, but more importantly, for exercising and reconditioning batteries to prolong service life. In addition, the analyzer "weeds out" non-performers from the battery fleet.

Battery Analyzers

In the last few years, the technology of battery analyzers has advanced significantly. No longer are we limited to analog units with fixed charge currents and programs that only apply one or two discharge-charge cycles.

The modern battery analyzer (Figure 1) evaluates the battery's condition and implements the appropriate cycles to restore the performance. A recondition cycle is applied automatically if a certain capacity level cannot be reached. Battery chemistry, voltage and current rates are user-programmable. These parameters are stored in the cups or cables and configure the analyzer to the correct function when connected. Over 500 battery-specific cups are available.

The modern analyzer identifies battery packs that contain shorted, mismatched or "soft" cells. The derived battery capacities are organized into residual and final capacities. Problems, such as insufficient capacity reserve at the end of field use, can easily be identified and corrected.

The modern analyzer is capable of charging and discharging the battery at user-defined currents, a feature that allows for testing under true field conditions. A charge and discharge rate of 1C* is up to three times faster than that of a fixed current analyzer. In addition, the capacity readings are more accurate.

The modern analyzer uses *multiple redundant charge-termination algorithms* to ensure the batteries are charged quickly and safely without overheating. Damaging overcharge on a pack with mismatched cells, for example, is eliminated.

The modern analyzer provides user-selectable programs to address different battery needs. For example, **PRIME** prepares a new battery for field use; **AUTO** reconditions batteries unable to reach a user-set target capacity; **CUSTOM** allows the operator to set a sequence of cycle modes composed of charge, discharge, recondition, trickle charge or any combination thereof. Rest periods and repeats can be added as required.

The modern analyzer is easy to operate. Capacity readout in percentage rather than milliampere hours (mAh) is more convenient as the operator does not need to remember the mAh ratings of each battery tested. In addition, simple "pass/fail" lights help to distinguish good batteries from unserviceable ones at a glance.

The modern analyzer offers a printer and computer interface. With printer, service reports and stick-on battery labels can be generated. By attaching the label to batteries, the user is always informed of the battery's history and pending maintenance.

The modern analyzer applies the factory-recommended charge algorithm when servicing NiCd, NiMH and Lead Acid batteries. As new battery chemistries are introduced, EPROM upgrades are made available to enable servicing these batteries also.

**C-Rate is a unit by which charge and discharge times are scaled. NiCd batteries with a rating of up to 1800mAh are commonly charged and discharged at 1800mAh or 1C.*

About the Author
Isidor Buchmann is the founder and Chief Executive Officer of Cadex Electronics Inc. in Burnaby, British Columbia. Mr. Buchmann was active in the radio communications sector and has studied the behavior of NiCd batteries in practical everyday applications.

ELECTRICAL CHARACTERIZATION OF THE NEGATIVE ELECTRODE OF THE USAF 20-YEAR-LIFE MAINTENANCE-FREE SEALED NICKEL-CADMIUM AIRCRAFT BATTERY OVER THE TEMPERATURE RANGE -40 °C TO +70 °C

Za Johnson, Jay Roberts, Darren Scoles
Eagle-Picher Industries Inc.
Power Systems Division
Colorado Springs, Colorado

Abstract

Long life Sealed Maintenance Free Aircraft Batteries are in production and service on several different aircraft. This study presents data on the electrical performance of the negative electrode used in these batteries. The purpose of the study is to demonstrate the charge and discharge performance over temperature, of the negative electrode in order to provide a thorough understanding of the limitations and the potential of the sintered plate, electrochemical impregnated cadmium electrode. This information will be important in comparing the performance to other nickel batteries. The electrode has been found to be very stable as shown by accelerated testing and use in space batteries, and provides a standard for development of the metal-hydride electrode that may be used as a substitute for future aircraft batteries.

Introduction

The Power Systems Department of Eagle-Picher Industries under a research and development contract sponsored by the Battery section of Wright Laboratories, Wright-Patterson Air Force Base, Dayton Ohio, has developed and is testing a sealed nickel-cadmium aircraft battery with a designed life of up to 20 years. The batteries are available in various capacities ranging from 5 ampere-hours to over 100 ampere-hours and with nominal voltages of 12, 24, and 28 volts. Configuration can be designed to fit many different footprints. The batteries are constructed of prismatic, starved-electrolyte, recombinant, nickel cadmium cells enclosed in nylon cell jars. Test data attesting to the reliability and capability of the batteries has been presented at several battery conferences during the last few years. The batteries nave an operating temperature range of -40 oC to +70 oC and deliver rated capacity with repeated cycling over the temperature range -20 oC to +50 oC. Most of the batteries are designed for high-rate performance with a typical internal resistance of 7.0 milliohms for a 40 ampere-hour battery fully charged at room temperature. The cells are constructed using electrodes which are specially designed and manufactured to withstand complete depths of discharge and still be dependable and reliable for thousands of cycles. The sintered substrate is manufactured using nickel powder with very uniform particles this produces pores within the sinter that are small, deep and uniform. This uniformity provides the possibility of electrodes that can be loaded with active material that is deposited uniformly in thin layers. The resulting electrode will have considerably less stresses during a deep discharge.

The capacity of these maintenance-free cells is limited by the positive electrode so that at complete depths of discharge all of the positive active material is fully converted to nickel hydroxide. The positive electrodes are manufactured using a combination of two impregnation processes. The initial active material is impregnated using an electrochemical impregnation process, and the final active material is added using a chemical impregnation process. The combining of these to processes results in very strong and stable positive electrodes with loading levels and energy densities equivalent to those of high capacity nickel electrodes used in flooded nickel-cadmium cells. Because of the efficient and optimized impregnation methods, the electrode is not damaged by the deep discharges that typically occur. Life has been demonstrated to be over twenty thousand cycles in controlled cycling to 40 % depth of discharge. Charge efficiencies of the positive electrode have been found to range from a high of 98% at cooler temperatures and at rates of 1-C or greater; down to a low of 70% at higher temperatures and lower charge rates of C/10. The negative electrode, however is designed and built in a very different manner and exhibits significantly different performance at various operating conditions.

Negative Electrode Design

The negative electrode is designed so as to have considerably more capacity than the positive electrode for several reasons. First, it is always desirable for the cell to be positive capacity limited; the negative electrode must still have charged material remaining after the positive electrode is completely discharged. Second, since the cell has considerable recombination capability for the oxygen generated by the positive electrode during charge and overcharge, and only limited recombination capability for the hydrogen that the negative electrode generates when overcharged. Because of this, it is desirable that the negative electrode never reach a fully charged state. Third, since the oxygen generated by the positive electrode during charge and overcharge is recombined by converting cadmium to cadmium hydroxide on the negative electrode, it is necessary for the negative electrode to always have sufficient excess charged active material (cadmium) to participate in this reaction.

One of the failure mechanisms for all nickel-cadmium cells is migration of cadmium from the pores of the negative electrode out into the separator which electrically insulates the positive electrodes from the negative electrodes. When this occurs it is possible for this negative active material to form an electrical path between the positive and negative electrodes, resulting in a short circuit which can either cause catastrophic failure or reduced capacity because of a high self-discharge rate. The long-life, negative electrode design for these batteries utilizes the special slurry-sintered substrate described previously impregnated with cadmium hydroxide using a sophisticated electrochemical process. In the case of the negative active material it is electro-deposited in very even layers deep within the pores of the substrate and consequently remains trapped within the pores during cycling. Even when most of the active material is discharged and converted to cadmium hydroxide the active material tends to remain deep within the pores. This is a significant step forward in the ability to build a battery capable of thousands of cycles over a long period of time.

The goal of the research supporting this paper is to thoroughly study and characterize this negative electrode in an effort to better understand the effect that its performance has on the overall charge and discharge performance of the long-life sealed aircraft cell. And through the use of accelerated life testing and stress testing of the negative electrode in specially designed negative capacity limited cells, to determine the failure mechanisms as well as the capabilities of the negative electrode.

Production Cell Design

The long life production cells are designed using an negative capacity to positive capacity ratio of approximately 1.8:1. There is one more negative electrode than positive electrode in each cell and the electrodes are physically configured so that a negative electrode is at the outside of each end of the plate stack, and electrodes are alternated negative, positive, negative; throughout the plate stack. The negative electrodes are thicker than the positive electrodes to provide for the increased capacity. The separator used to electrically insulate the negative electrodes from the positive electrodes is a permanently wettable non-woven polypropylene material. The separator was developed by Eagle-Picher Power Systems Division for use in aerospace cells. The separator is made permanently wettable by permanently impregnating the polypropylene fibers with special materials, and the manufacturing procedure for impregnation has been automated to reduce the cost to a level acceptable for aircraft and terrestrial applications.

Test Cell Design

Special test cells were constructed so that the cell would be negatively limited in order to test the effects that temperature and depth of discharge have on the negative electrode. Specifically the cells were designed to have a negative capacity to positive capacity ratio of 1:1.3. This was accomplished by using two specially constructed positive electrodes for every one production negative electrode. The electrodes were physically arranged so that each negative electrode had a positive electrode on either side and except for the two outside positive electrodes all other positive electrodes were back to back with another positive electrode. The separator and inter-electrode spacing used to construct these special test cells were the same as that used in the production cells. And as already mentioned standard production negative electrodes were used so that the study would not have to compensate for changes made to the negative electrode. This configuration was used to manufacture several cells to be tested both in flooded and starved electrolyte conditions. These cells then were divided into various groups and used to complete the testing described in the test plan section.

Desired Information

Information of three different types and in three different general areas was sought and collected from this research. First, was to find out what effect repeated cycling at 100% depth of discharge would have on the life of the negative electrode. And, if repeated cycling to 100% depth of discharge has a deleterious effect on negative electrode life, what specific conditions cause the problems and what mechanisms are responsible. Second, was characterize the negative electrode capacity over the temperature range of -40 °C to +70 °C. Sealed nickel-cadmium cells have reduced charge capabilities at temperatures less than -10 °C, and at temperatures greater than +40 °C. It has been assumed thus far in the development and evolution of the long-life maintenance-free cell that the capacity performance over the temperature range has been dictated by the positive electrode. It has also been assumed that the charge efficiency of the negative electrode is virtually 100% at these temperatures and at the state of charges to which it is exposed. Third, then is to test the negative electrode at various temperatures and charge rates to determine the charge efficiency at these different parameters.

Test Plan

The test plan was divided into three sections with each corresponding to one of the areas of desired information; Life and Capacity Fade, Capacity versus Temperature, and Charge Efficiency vs. Temperature & State of Charge

Life and capacity fade due to fully discharging the negative electrode was carried out in three phases. First, a group of cells were cycled for 200 cycles in the following manner. The cells were charged at a C/2 rate until 110% of the theoretical negative capacity was returned to the cells. The cells were discharged at a C/2 rate until each cell reached 1 volt. The cells were maintained in an environmental chamber at 25 °C and provided enough rest after discharge to allow the cells initial charge temperature to be within 3 °C of 25 °C. After completion of cycling the cells were evaluated for capacity loss and cadmium migration. The second phase of this section was to repeat the above test regime only in this test the cells were discharged to an end of discharge voltage of 0 volts. The third phase of testing was to repeat the cycling with the environmental chamber operating at 50 °C.

Capacity characterization over the temperature range was conducted by cycling a group of cells in an environmental chamber at ten degree intervals from -40 °C to +70 °C. The cells were charged at a C/2 rate until 110% of theoretical negative capacity was returned to the cells. The cells were discharged at a C/2 rate until each cell reached 0

volts. Cells were rested after each discharge until the cell temperature returned to the desired temperature.

Efficiency characterization over the temperature range was conducted by charging and discharging a group of cells in an environmental chamber at twenty degree intervals from -40 °C to +70 °C. The cells were charged at a C/2 rate until 90% of the maximum negative capacity at that temperature was returned to the cells and discharged at a C/2 rate until each cell reached 0 volts. In between test cycles it was necessary to return the cells to 20 °C and fully charge them. The cells were then discharged to 0 volts. This was done in order to be sure that the cells are not positively limited. Efficiency was calculated by dividing the ampere-hours from discharge by the ampere-hours of charge.

Results

The capacity fade and life test cells showed only minimal loss of capacity as a result of 100% depth of discharge cycling.

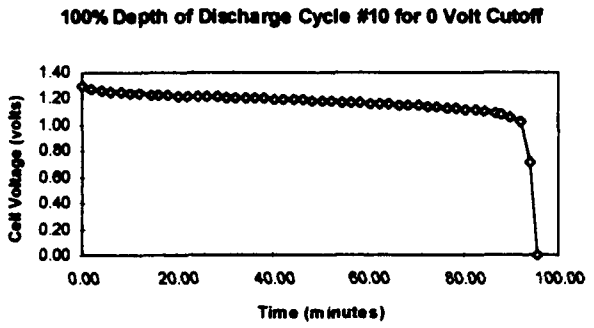

Figure 1

Figure 1 shows a typical voltage discharge curve for the 10th cycle in the 200 cycle regime when the discharge voltage cutoff was set at 0 volts.

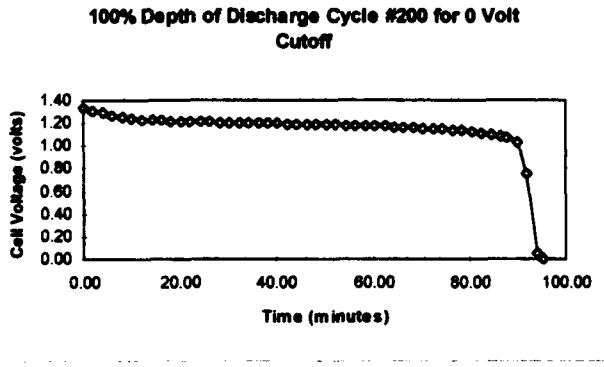

Figure 2

Figure 2 shows the shows a typical voltage discharge curve for the 200th cycle in the 200 cycle regime when the discharge voltage cutoff was set at 0 volts. One can see that the capacity fade was insignificant over the 200 cycle regime.

The cells that were physically disassembled and examined for cadmium migration into the separator showed virtually no movement of the cadmium into the separator. There was small amounts of the negative active material on the surface of the separator, however, an examination of the fibers below the surface with a microscope revealed that the cadmium accumulation was confined to the surface.

The capacity characterization versus temperature data is presented in Figure 3, and shows the capacities to be stable over the temperature range The data presented shows the percentage of maximum capacity achieved at each temperature. The percentage was calculated by dividing the discharge capacity obtained at each temperature by the capacity achieved at 20 °C. The capacity obtained at 20 °C was the maximum obtained and was about 90% of the total theoretical capacity based on weight of active material.

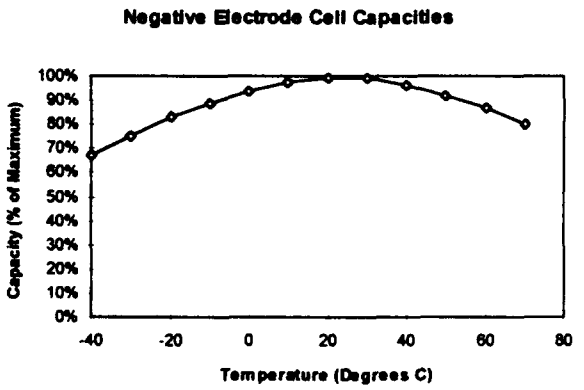

Figure 3

Figure 4 presents the production cell capacity characterization over the temperature range. This information was gathered in another series of testing and is presented here for comparison. Note much higher capacities are possible with an optimized charge algorithm.

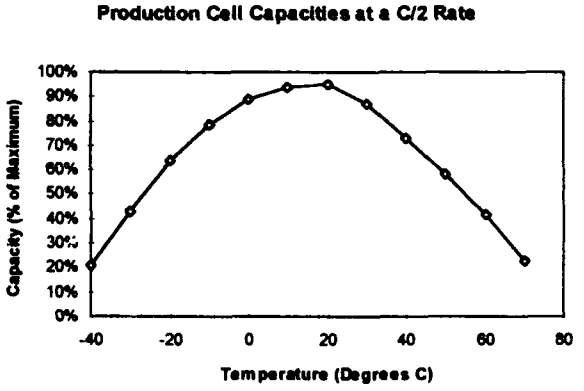

Figure 4

By comparing the two graphs it becomes apparent that the capacity of the production cells is not hindered by the performance of the negative electrode even at the extreme temperatures.

The charge efficiency characterization for the negative electrode testing is summarized in the following graph Figure 5.

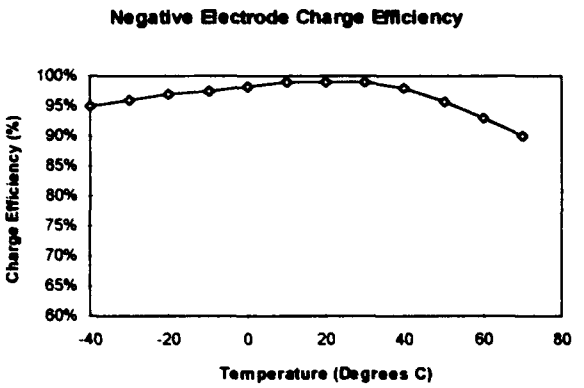

Figure 5

The data shows that the negative electrode is very efficient even when it is close to fully charged . Of course in the production cells the design is such that the negative rarely is charged above 75%.

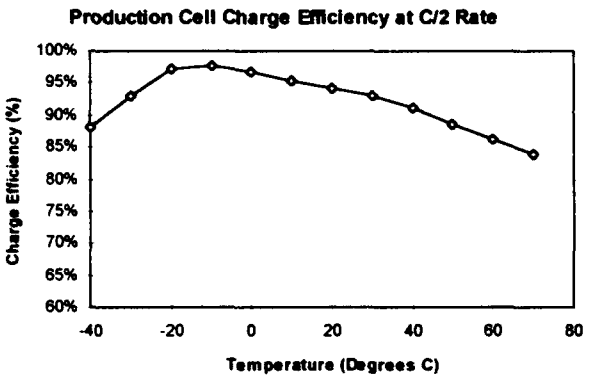

Figure 6

Figure 6 presents similar data from the production cells for comparison. One can see that the negative electrode is much more efficient than the positive electrode and should not negatively affect the performance of the cells.

Conclusions

The specially designed negative electrode used the Eagle-Picher long-life maintenance-free nickel-cadmium battery appears to be capable of meeting all the necessary requirements of: extended life, limited capacity fade, and high charge efficiency. In addition a baseline for negative electrode performance has been developed to provide data for the possible introduction of new negative electrode materials.

Acknowledgments

Part of this work has been supported by the Batteries and Fuel Cells Section, Power Technology Branch, Aerospace Power Division, Wright Laboratory, Wright-Patterson AFB, Ohio 45433.

References

(1) Za Johnson and Tim A. Edgar, "Maintenance-Free Nickel-Cadmium Batteries", Sixth Annual Battery Conference on Applications and Advances, California State University-Long Beach, Jan., 1991.

(2) K. Sense, "Time-to-Failure Analysis for NiCd Batteries in a GPS Orbit", The 1981 Goddard Space Flight Center Battery Workshop, NASA Conference Publication 2217.

(3) The USAF R&M 2000 Variability Reduction Process, Assistant for Reliability, Maintainability, Manufacturing, and Quality, USAF, April, 1991.

(4) Za Johnson and Richard Flake, "Sealed Nickel-Cadmium Batteries", 35th International Power Sources Symposium, Cherry Hill, New Jersey, June, 1992.

(5) Z. W. Johnson, "Separator Qualification and Testing for Sealed Nickel-Cadmium Batteries", Eighth Annual Battery Conference on Applications and Advances, California State University-Long Beach, Jan. 1993.

(6) Z.W. Johnson, J.E. Roberts, and T.M. Kulin, "Charge Efficiency of Sealed Nickel-Cadmium Aircraft Batteries over the Temperature Range of -40 °C to 70 °C", Ninth Annual Battery Conference on Applications and Advances, California State University-Long Beach, Jan., 1994.

VERIFICATION OF LONG TERM WET STAND LIFE OF COMPOSITE FIBER NICKEL ELECTRODES

by

W. A. Ferrando, Code R31
Naval Surface Warfare Center, Dahlgren Division
White Oak, Silver Spring, MD 20903-5000

ABSTRACT

When composite components are used in electrochemical systems, questions often arise concerning the long term stability or corrosion resistance of electrolyte wetted materials. This is particularly true of secondary battery cells. In general, it is quite difficult to carry out a true long term stand life experiment on such materials. Usually, shorter term Arrhenius type elevated temperature simulation experiments are performed, often with some question as to their validity.

A rather unique opportunity has made possible a true long term stability test of the lightweight composite sintered nickel plated graphite fiber electrode. A group of laboratory cells fabricated and first tested during the period 1980-81 and left electrolyte filled and intact at ambient temperature recently have been subjected to further cycling. If significant degradation of the graphite fiber based substrate had occurred in the long exposure to the electrolyte, the cells probably would have become shorted or at least have shown significantly degraded electrical characteristics. In fact, however, the cells showed excellent stability after the long wet storage. After several cycles, the active material utilizations generally returned to levels of the initial tests of a dozen years earlier.

After a lapse of some years, renewed interest has been expressed in the composite nickel electrode technology. This short report describes the sintered nickel plated graphite fiber substrate, electrode fabrication and comparison of the recent data with that of the original tests.

INTRODUCTION

The powder nickel based sintered electrode was developed during the first half of this century and has served well as the electrode of choice for numerous applications. The sintered nickel substrate possesses excellent durability and electrical characteristics. Despite its somewhat high weight and cost, therefore, it has largely withstood most modern attempts to replace it.

New applications, however, require lighter weight cells, which maintain reasonable performance at moderate cost. Ni-Cd, Ni-H_2, Ni-MH and possibly Ni-Zn, represent the next generation of cells beyond lead-acid for many of these applications. A relatively large benefit, therefore, can be realized from development and manufacture of a lightweight, durable and low cost Ni electrode structure as their common element.

BACKGROUND

The composite nickel electrode construction is based upon a patent issued in 1980[1]. It has been reported previously in the proceedings of this Symposium[2] and elsewhere[3,4]. The plaque material consists of nickel plated graphite fiber which is sintered under compression in H_2 atmosphere. Graphite fiber fulfills most closely the requirements for an ideal lightweight substrate indicated in Figure 1. Numerous test electrode plaques have been fabricated using electroless Ni coating on Type VMA pitch mat graphite fiber (Amoco Performance Products, Greenville, SC 29602). The resulting bonded highly porous three dimensional structure utilizes the fiber base both for support of the active material and as current carrier to the collector screen and tab. Figure 2 shows a typical sinter bond within such a plaque.

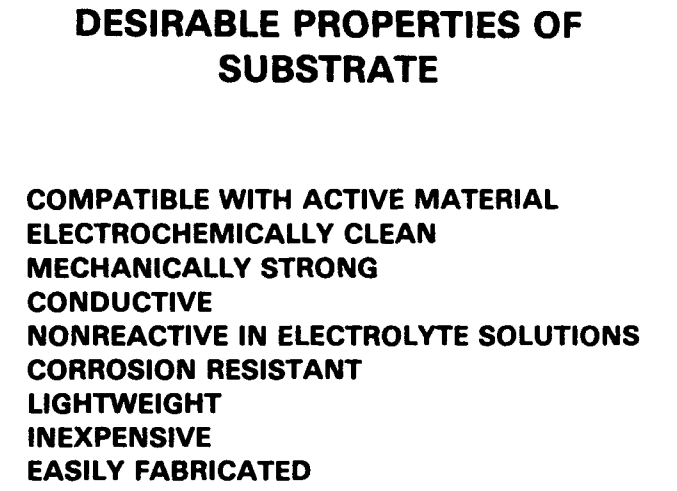

Figure 1. Some Requirements for Lightweight Composite Nickel Electrode Substrate Material.

Other methods recently have been used to produce the composite plaque. These consisted of variations such as sintering randomized chopped electroplated graphite fiber tows, plating of the graphite fiber mat by the nickel carbonyl process and nickel plating of a pyrolized graphite fiber board. To the present, however, the most successful fabrication has been electroless plating followed by compression sintering of the VMA mat.

Figure 2. Typical Sinter Bond Within Composite plaque.

EXPERIMENTAL

While the relatively large average plaque pore sizes (~50 micron) allows ready application of virtually any active material impregnation method, the electrochemical impregnation method of Pickett[5] was employed in the retested cells reported here. This process was carried out in a tank with methanolic based $Ni(NO_3)_2$ solution. The electronegative current typically was applied for 30-60 minutes. Very high specific loadings of the plaques were readily achievable. Computed loadings of 1.6-1.9 g/cc yielding theoretical gravimetric energy densities of 160-210 Ah/kg were typical.

Some substrates later were impregnated by standard chemical impregnation and still later by "suspension" impregnation using fine particle active $Ni(OH)_2$ powder.[6] Conditions must be optimal for these latter methods to achieve loadings approaching those of electrochemical impregnation. In several later test cells, however, comparable results in loading and utilization were obtained by the suspension (pasting) method. The latter method is particularly noteworthy for its' potential cost reduction in fabrication.

Cobalt additive was introduced into the (positive) electrodes by mixing 5-10 wt% $Co(NO_3)_2$ into the impregnation bath. Composite negatives were prepared by an exactly analogous procedure using a $Cd(NO_3)_2$ impregnation bath with no additives.

An early objection to the graphite fiber based composite plaque concerned the possible corrosion (oxidation) of the graphite with cycling and time, leading to substrate deterioration and build up of nonconducting K_2CO_3 in the electrolyte. TABLE 1[7], however, shows the results of electrolyte titration analysis on heavily cycled test cells fabricated under the same conditions during the 1980-81 period as those subsequently retested. The data indicate no K_2CO_3 accretion due to graphitic oxidation over the test periods spanning several months to about one year at that time. These results were an early indication of potential long term stability of the electrode. The last table entry is electrolyte from a commercial cell of unknown pedigree.

TABLE 1
Electrolyte carbonate analysis

Cell	Cycle	Discharge rate (A)	KOH (wt.%)	mg CO_3^{2-} /ml KOH
0	0	0	27	Trace
50	82	0.2 *C*	22	Trace
54	296	2 *C*	34	Trace
57	211	3 *C*	32	Trace
Comm.	~400	Variable	—	170

Description of the Cells/Tests

The electrode substrates were prepared in dimensions of approximately 2.75" X 6" in thicknesses of 20, 30 and 40 mils. In earlier plates, small strips of nickel foil were spot welded to form a current collector grid. Subsequently, expanded nickel mesh was used. The collector was placed between the plated graphite mats and pressure sintered as described.

The sintered composite substrates were electrochemically impregnated with $Ni(OH)_2$ (or $Cd(OH)_2$) as described. The electrodes were installed in specially designed plastic cases with removable panel and O-ring seal (Figure 3). The cells were filled with 30% KOH with no Li+ additive. The separator consisted of a layer each of PERMION membrane (RAI Research Corp., Hauppauge, L.I., NY) and nylon woven material. In general, commercial counterelectrodes were used.

The retests were carried out under substantially the same conditions as the original tests. This was generally continuous charge and discharge cycling at the C/2 rate with discharge taken to approximately 100% depth. The retests were restricted only to those cells observed to have remained wet with electrolyte for the intervening years. For these cells, corrosion processes within the plates would have continued, providing the real time ambient temperature shelf life test of a dozen or so years.

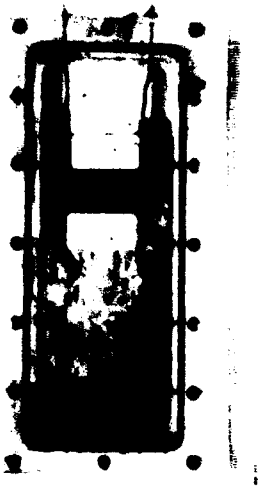

Figure 3. Laboratory Test Cell Accommodating 2.75" X 6" Electrodes.

RESULTS

TABLE 2 displays the data gathered on the retested cells. The fabrication dates, final discharge cycle of original test and several cycles of the retest are reported. There were no shorted cells among those retested. In general, their utilizations returned within a few cycles to approximately those of the earlier tests. Figure 4. shows representative charge/discharge profiles of several retested cells. These are characteristically good cycles typical of Ni-Cd cells in serviceable condition.

Several cells fabricated during the same period as those retested were opened and visually inspected. The composite plates still showed good integrity. Fibers of the plaque substrate could be seen with their nickel plating still intact. A reasonable conclusion to be drawn from these results is the good long term wet stand durability of the sintered nickel plated graphite fiber composite electrode technology.

ACKNOWLEDGEMENT

The author wishes to thank Mr. W. R. Johnson of the NSWC, Crane Division and the Standard Hardware Acquisition and Reliability Program (SHARP) for Sponsorship of this effort.

REFERENCES

(1) W. A. Ferrando and R. A. Sutula, Patent #4,215,190, July 29, 1980.

(2) W. Ferrando, "Fabrication of Prototype Large Scale Composite Fiber Nickel Electrodes", Proceedings - 35th International Power Sources Symposium, p. 141 (1992)

(3) W. Ferrando, W. W. Lee, R. A. Sutula, "A Lightweight Nickel Composite Electrode I: Concept and Feasibility", Journal of Power Sources, Vol. 12, p. 249, 1984.

(4) W. W. Lee, W. A. Ferrando and R. A. Sutula, "Loading and Utilization of Active Material in Nickel Composite Electrodes: Optimization", NSWC Technical Report 84-122, (1984)

(5) D. F. Pickett, "Fabrication and Investigation of Nickel-Alkaline Cells Part I: Fabrication of Nickel Hydroxide Electrodes Using Electrchemical Impregnation Techniques," Technical Report AFAPL-TR-75-34, October 1975

(6) W. A. Ferrando, Patent #4,574,096 March 4, 1986

(7) From W. A Ferrando and R. A. Sutula, "Cycle Life Characteristics of Composite Nickel Electrodes", Proc. Symp. on the Nickel Electrode, The Electrochemical Society, Inc., Pennington, NJ, Vol. 82-4, 1982, p. 276. (by Permission)

TABLE 2

CYCLING OF TEST CELLS

Cell Description	Fabrication Date	Original Cycles/ Utilization *	Test 9/93-1/94 Cycle #/Utiliz.*	Comment
Nickel #41	5/80	499, 36%	500, 15.9% 501, 21.9%	C= 1.9 Ah Elect. very cloudy
Nickel #84	9/80	31, 39.4%	32, 46.9% 35, 67.2%	C= 3.18 Ah Electrolyte clear
Cadmium #62	7/80	81, 74.6% (@ C rate)	82, 62.5% @ C/2 87, 53.8% @ C/2 88, 46.9% @ 2C	C= 1.0 Ah Electrolyte slightly amber
Cadmium #66	4/80	57, 76.3%	58, 68.7% 63, 71.9%	C= 1.66 Ah Electrolyte clear
Nickel: Electroplated Fiber	4/82	None	1, 87.5% 4, 100%+	C= 2.27 Ah Electrolyte clear
Full Composite Cell: 1 Ni, 2 Cd (Cd elect. cycled previously)	3/81	98, 61.3%	99, 73.4% 104, 67.2%	C= 2.83 Ah Electrolyte clear
Multiplate Cell 10 Composite Ni Commercial Cds	2/82	335, 79.1%	336, 50% 341, 78.1%	C=13.8 Ah Electrolyte slightly amber
Multiplate Cell 10 Composite Ni Commercial Cds	2/82	417, 95% (@ C/5)	418, 70% 422, 81.7% (@ C/5)	C=34.5 Ah Electrolyte clear, No addition

* Charge and Discharge at C/2 Rate Unless Otherwise Noted.

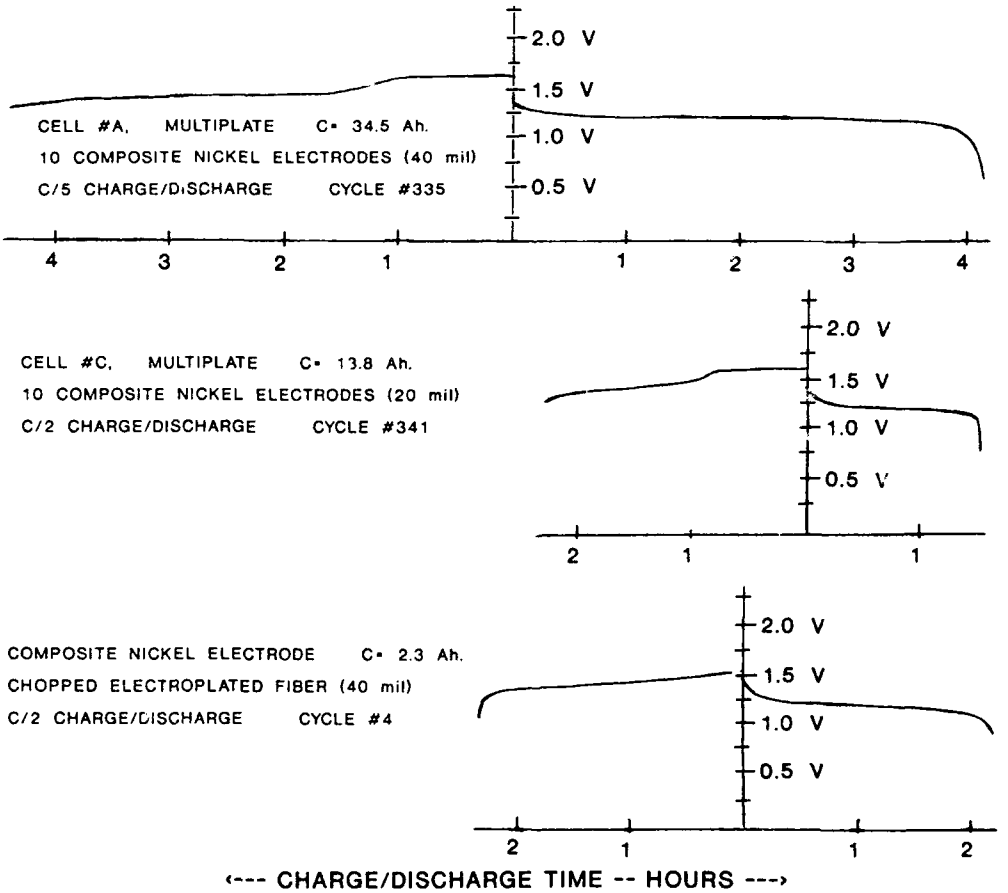

Figure 4. Charge-Discharge Cycles of Several Cells from Continued Test Data

A BRIEF HISTORY OF THERMAL BATTERIES

Walter E. Kuper
Reserve Battery Technology Branch
Electronics and Power Sources Directorate
Army Research Laboratory
2800 Powder Mill
Adelphi, MD 20783-1145

A thermal battery is a primary reserve battery that is activated when the inert solid salt electrolyte is melted by the ignition of an integral heat source. Thermal batteries are recognized as rugged, high-energy-density power sources having wide operating temperature ranges and long shelf lives.

The Beginning

When the proximity fuze was developed during WWII, the batteries available to power it were found to be particularly unsatisfactory in terms of shelf life and operating temperature range.[1] The Navy found it necessary to develop special reserve batteries for the artillery proximity fuzes it had developed. These batteries were activated by setback forces bursting the glass ampule in which the electrolyte was encapsulated. Then spin forces experienced by the shell drove the released electrolyte into the cell cavities of the battery.[2] The National Bureau of Standards Ordnance Development Division (NBS-ODD) developed proximity fuzes for Army ordnance use in nonspin ammunition, such as bombs, mortars, and rockets. The only power sources available were dry cells and, later, wind-driven generators. However, both of these were, in general, unsatisfactory.

After the war, many intelligence reports were collected by the teams of Allied scientists and engineers who investigated the innovative wartime weapons developments of the Germans. Some of these reports were sent by Army Ordnance to the staff of NBS-ODD for review. Among these was a report entitled, *The Theory and Practice of Thermal Cells* by Georg Otto Erb.[3] This report discussed the making, operation, and characteristics of fused salts in primitive reserve cells. This information was reported to the Ordnance Division management with the recommendation that it be investigated.[4] The recommendation was approved and P. J. Franklin was assigned to study this system. Franklin confronted the problems of activating the thermal cell quickly and keeping it compact. He was able to successfully demonstrate thermal cell operation when he used a thermite-type heat powder made by the Catalyst Research Co. (CRC) of Baltimore, MD. When CRC learned how this powder was used, they solicited a contract to develop a thermal battery for NBS-ODD.[5]

The Catalyst Research Corporation Contract

A small contract ($12,600) was awarded to CRC in April 1947 by NBS-ODD to develop a thermal battery for a rocket proximity fuze. After checking the validity of Erb's claims, CRC's workers concentrated on designing an effective cell by seeking the best electrolyte and, most importantly, learning how to heat the cell efficiently. The first cells were made in two ways: (1) by pouring the electrolyte as a carbon tetrachloride slurry and drying it or (2) by pouring molten salt into the cavities of the ceramic washers used to separate the copper or iron and the magnesium electrodes. At this time, binary and ternary combinations of LiOH with $BaCrO_4$, KOH, NaOH, and $LiNO_3$ were used as electrolytes. Early attempts at cell heating included adding the heating material to the electrolyte, or immersing the cells in a body of heat powder. Within a few months, CRC learned how to make large cells that delivered ampere levels of current. In October 1947, NBS-ODD, in a letter[6] to CRC, expressed satisfaction with the progress of the work, told them that the contract was being extended with increased funding, and reminded CRC that a low-current, high-voltage section was also needed.[7]

Early in 1948, in its continuing search for useful salt combinations for electrolytes, CRC found the lithium potassium chloride eutectic, which eventually became the most frequently used electrolyte. Work was started in mid-1948 on the low-current, high-voltage (B cell) section of the battery. To find the best electrolyte and depolarizer for this application, every chemical within reach was tested in tiny test cells or in small crucible cells. During this period, tungstic oxide was found to be a good depolarizer, and calcium metal a good anode.

The original test cells were described as one-half-inch by three-eighths-inch rectangles. In the beginning, these were made of iron and magnesium. The latter, wrapped with asbestos paper which had been impregnated with various electrolytes, served as the anode. Test cells were heated by being held in a Bunsen flame and/or by immersion in heat powder (nickel powder mixed with potassium perchlorate powder and diatomaceous earth). Later, the use of an induction heater was found to give good control of heat for cell testing. Series-connected cells mounted in slots in ceramic disks, and immersed in the heat powder, sometimes worked well. The early B-cell development work is described in a notebook into which Roger Sweet made regular entries between May and November 1948.

By late 1949 it was decided that cells laid flat on tamped heat material worked more efficiently. This arrangement led to the development of the sector cell[8] and the compaction of the heat powder onto asbestos disk. Stack test data using sector cells heated by such heat compacts were reported in April 1950. The cell chemistry, introduced in 1949, was based on nickel and calcium electrodes; the electrolyte was a eutectic mixture of lithium and potassium bromides with 15 percent of potassium chromate added. The electrolyte was carried on impregnated glass cloth.[9]

The Wurlitzer Company and the Mortar Fuze Battery

In 1948, the Rudolph Wurlitzer Company, which had been having difficulty in developing a new wind-driven generator for a mortar proximity fuze for NBS, accepted an option to work on a thermal battery. NBS passed on information gleaned from CRC, and Wurlitzer quickly developed a small button-like B cell (Figure 1) using a silver cup, a magnesium button anode, and a modified, lower melting electrolyte carried on a small asbestos disk. These cells were 0.260 in. O.D. and 0.054 in. high. A number were stacked in mica-lined brass tubes (eventually 15 cells), after which a method of heating the cells was developed (Figure 2). Six such tubes, connected in series, were inserted

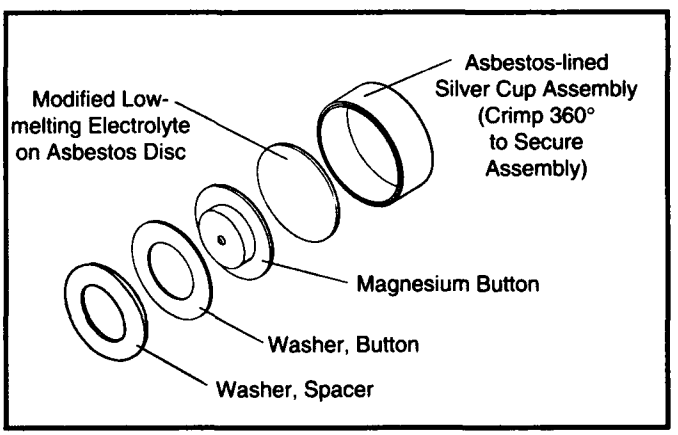

Figure 1. Wurlitzer's small button-like B-cell.

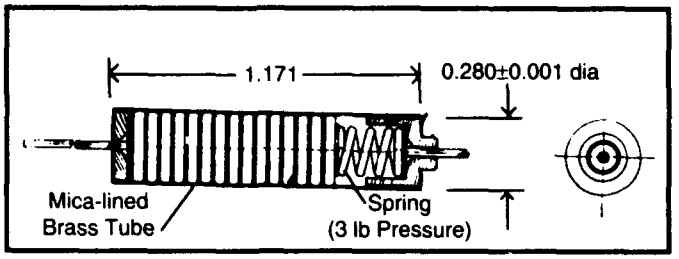

Figure 2. Details of mortar battery B-cell stack.

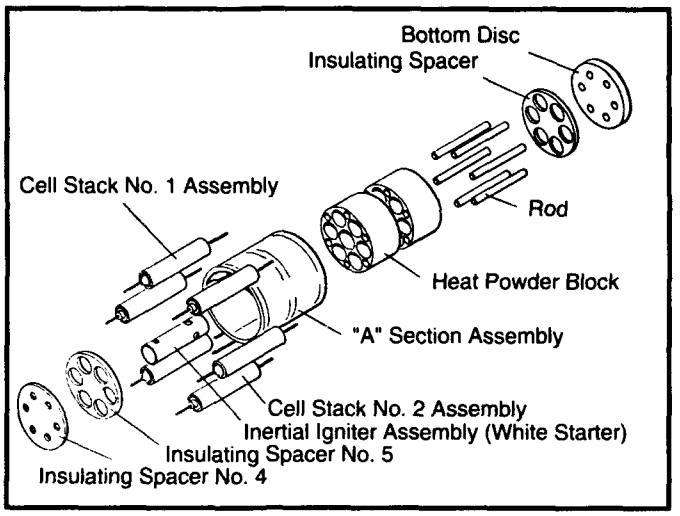

Figure 3. An exploded view of the Wurlitzer mortar fuze thermal battery.

into cavities formed in a three-layer block of compacted heat powder (Figure 3). The battery required an equal number of assembled stacks with opposite polarity at the top (three each) to achieve 90 cells in series that would obtain the required 140-V output. Color-coded end-stack insulators indicated the stack end polarity. Heat was conducted through the tubes to the sides of the cells and then to the electrolyte. The resulting delay in the activation of the B section was within the mechanical delay time that allowed the shell to be well away from the weapon before the fuze activated. The cylindrical A cell that enclosed the stacked-heat powder block was developed later. An inertial starter (actually a two-part match), which was operated by setback forces, was located in the center cavity of the heat block and acted as the initiator of the battery.

The self-contained igniter component designed for the mortar fuze battery was the inertial starter (Figure 4). This device was also used in later battery designs. The inertial starter development resulted from a series of design improvements by several contributors associated with the mortar proximity fuze program. It was originally manufactured by the White Corporation of Milwaukee, WI. This association led to the device being referred to as the White Starter. The inertial igniter assembly is a mechanical device that activates when it experiences a sustained acceleration. The igniter assembly is designed to be relatively drop safe. It is sensitive only to the proper sustained acceleration in a direction parallel to its axis. Such acceleration is obtained when the assembly is properly mounted and fired from a weapon.

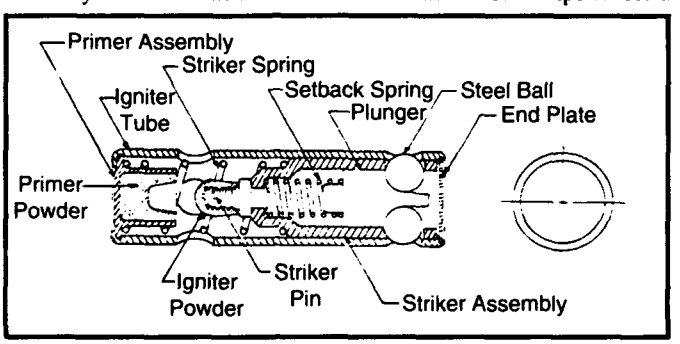

Figure 4. White Starter mechanism.

This battery, packaged in a 1.625-in.-diam by 1.625-in.-high can, supplied nominal voltages of 1.4 V to a 3-ohm load and 140 V to a 10,000-ohm load for 60 s. It activated to minimum voltage in no more than 5 s. The negative bias required by the mortar fuze was electronically generated by means of a resistive network within the fuze.

By 1950, both companies, CRC and Wurlitzer, had developed prototype batteries that would meet the design requirements. However, both batteries still required further refinement of manufacturing processes before regular production could begin.

The Rocket Fuze Battery

The prototype CRC rocket fuze battery[10,11] was based on the ternary electrolyte LiBr-KBr-K_2CrO_4 in all three sections. The A section electrolyte was later changed to the eutectic chloride system because of the better current-per-unit-area capability of this system. Thus, the A section consisted of

$$Mg/LiCl\text{-}KCl\ (eutectic)/WO_3,Ni\ .$$

The system

$$Ca/LiBr\text{-}KBr\text{-}K_2CrO_4/Ni$$

was used in the B section.

The A section was made with two cup-and-cover cells in parallel. The inside surfaces of the cup and cover of each A cell had been coated with a paste of WO_3 depolarizer which had to be baked dry. Two disks of electrolyte-impregnated tape were placed on each side of the centrally located magnesium anode. A nickel lead spotwelded to the anode exited the cell at a small notched opening in the periphery of the cup and cover to avoid shorting the anode to the cathode. The B section was built as a series arrangement of sector cells (Figure 5). Each of the 56 trapezoidal or sector cells had a small piece of electrolyte-impregnated glass tape on each side of a centrally located calcium anode. The calcium was spotwelded to a nickel tab extending from the adjacent cell to make the series connection.

Heat was supplied to the cells by placing them in close contact with the heat powder, Z-2, a blend of fine zirconium (21 percent by weight) and barium chromate powders. This composition supplied 410 calories per gram. In this application, measured quantities of the Z-2 powder had been spread evenly over and then compacted onto thin asbestos paper disks. The flat sides of each cell were pressed against a compacted

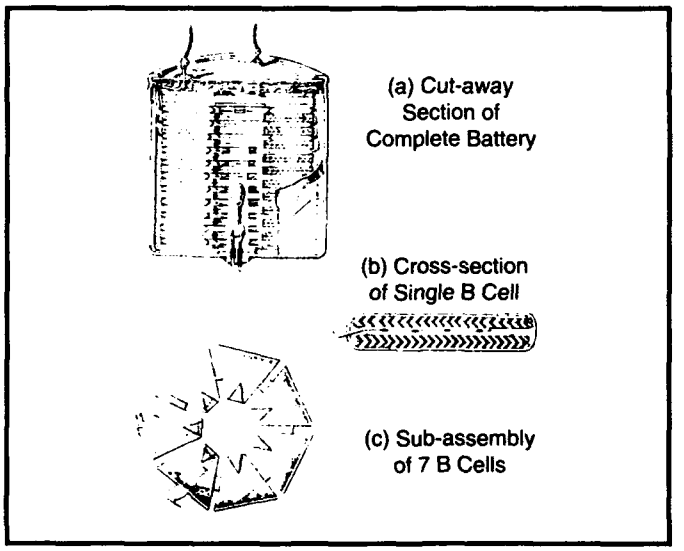

Figure 5. The CRC Rocket Fuze Battery.

powder disk. These heat powder layers on the compacts were fragile and the assembly required careful handling.

The rocket fuze battery, packaged in a 1.625-in.-diam by 1.625-in.-high can, supplied the following voltages and performance characteristics:

"A" voltage:	1.5 V across 3 ohms
"B" voltage:	135 V across 10,000 ohms
"C" voltage:	5.5 V across 100,000 ohms
Activation time:	0.5 s
Life:	30 s

After 1950

In 1950 the Korean War started and the mortar battery was rushed into production. Numerous problems developed which led the ordnance people to worry that the battery was not adaptable to mass manufacture. However, these initial fabrication problems were worked out, and the first major production of a thermal battery for use in a mortar fuze application was initiated in 1951. In this period (1950-51), Minneapolis-Honeywell, Eureka Williams, Pass and Seymour, and Olin-Mathieson were enlisted as additional contractors. The Universities of Florida, Virginia, and Illinois, and North Carolina State College received research and development (R&D) contracts for work on component materials and electrochemical studies during 1951-53. The Electrochemistry Section of NBS also investigated the properties of electrochemical systems.

The Pass and Seymour Company of Syracuse, New York, had the task of preparing the rocket fuze battery for production, and Eureka Williams (EW) was tasked to adapt the rocket fuze battery for mortar use. Eureka felt that the CRC battery leaked too much electrolyte and proposed to replace it with a battery of a new design. The early models of this design had heat-transfer as well as leakage problems. The attempts to overcome these problems eventually led EW to the development of a pellet battery.

At the end of 1950, the Defense community was informed of the existence of thermal batteries by the release of a classified report.[12] This report gave a good summary of the then existing thermal battery technology. It was distributed to approved military agencies to acquaint them with this new battery system in the belief "that basic information should be made available so that this new type of battery can be considered for other requirements."

Shortly after this, the Signal Corps Engineering Laboratories (SCEL) of Fort Monmouth, New Jersey, awarded an R&D contract to CRC for electrochemical system studies and other contracts that led into the development of a series of thermal batteries for other than fuze applications, such as actuators for airplane ejection seats. In 1953 SCEL also awarded contracts to the Eagle Picher Company (EPI) of Joplin, MO, for thermal battery work.

Because of common interests in proximity fuze technology, NBS-ODD had kept the Naval Ordnance Laboratory (NOL) (later renamed the Naval Surface Warfare Center-White Oak, or NSWC-WO) informed of thermal battery developments since the beginning of the CRC contract. In 1949, NOL in coordination with NBS-ODD, began work at CRC and then initiated an independent effort about 1952.

For the same reason, NBS-ODD had informed the British of thermal battery developments about 1950. In 1955, the British began contract thermal battery work at MSA-Glasgow, a corporate affiliate of CRC. Key members of the Glasgow staff trained at CRC.

Calcium-nickel Bimetal Developed at CRC

Improvements in component fabrication for the rocket fuze battery helped upgrade its performance and simplify its manufacture. Thus, a major advance was the development by CRC in 1952 of a high-vacuum distillation process for the deposition of 0.003 to 0.005 in. of calcium metal[13] upon strips of 0.005-in.-thick nickel from which the sector cell parts could be punched. The adoption of this material in battery manufacture by eliminating the spotwelding operation expedited cell ring fabrication and resulted in improved battery performance (Figure 6).

Heat Paper Developed

In 1952, Pass and Seymour vastly improved the usability of the Z-2 heat source material by blending the heat powder with a pulped slurry of inorganic fibers (glass and asbestos) in a Waring blender. The combined slurry was then poured into a sheetmold to form a sheet of paper-like material. This material came to be called "heat paper" and its use greatly simplified both piece-part and battery fabrication.

Heat-paper parts are punched from the damp (excess water having been pressed out) sheet for safety reasons; the parts are dried, sampled for calorimetric content, and sorted by weight. In a properly managed process, the heat content of a part can be controlled on a weight or area basis (i.e., calories per gram or calories per square inch), and the scrap can be reused. The dried material is easily ignited and burns with extreme rapidity. Therefore, it must be handled with great care, and accumulations in battery assembly work areas must be properly controlled and/or kept to a minimum. After the usefulness of this new material had been demonstrated, the University of Florida in 1954 developed and delivered to CRC a paper-making machine designed for heat paper manufacture.

It was also recognized in 1952 that the depolarizer could be made as a paper on the same equipment. This development eliminated the cumbersome process of applying the depolarizer (tungstic oxide) to the cell cup and cover as a slurry or paste and drying or baking it in place. In the bromide electrolyte, which was used in low-current applications, the depolarizer (potassium chromate) was included in the electrolyte mixture, greatly simplifying cell assembly.

Expanding Use of Thermal Batteries

Department of Defense (DoD) contractors had heard of thermal batteries early and, after checking their feasibility for other than fuze power use, were soon obtaining thermal batteries for these new applications. In 1954, the Sandia Laboratories, then a component of the Atomic Energy Commission (AEC), determined that thermal batteries would meet their needs for battery-supplied power very well. Sandia originally contracted with CRC for the development of some thermal battery designs and later placed contracts at all the other thermal battery contractors to build batteries based on these designs. This continued for several years, and then Sandia gradually reduced the number of its contractors, first to EPI, Wurlitzer, and CRC, and finally to only EPI.

Sandia found that the development of a battery for a specific application required closer control than could be managed at a contractor's plant, so it gradually formed its own development laboratory. Sandia made good use of this well-staffed laboratory in the development of its own batteries, and the associated R&D led to advances in technology which, in turn, led to improved battery designs.

In the decade between 1950 and 1960, thermal batteries progressed from marginally operable devices to vital, dependable components of

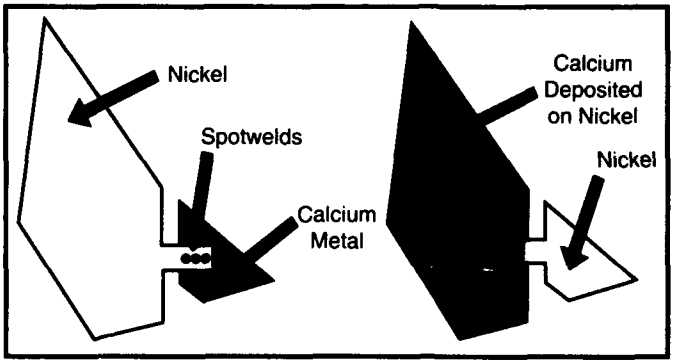

Figure 6. The original CRC sector cell (left) and bimetal sector cell (right).

many missile weapons. Four types of cells were in general use during this period:

(1) The closed cup-and-cover cells, sometimes called "A" cells (Figure 7), were the most popular type, and were made in a range of sizes. These cells could be connected in series and/or parallel and were used for high-current requirements and lifetimes of up to 3 to 5 minutes.

(2) The open-sided sector or trapezoidal cells were used in high-voltage, low-current batteries with many cells in series. Up to 1100 V were obtained with batteries using these cells.

(3) In the open-sided dumbbell cell, the heat source was sandwiched by the folded-over dumbbell faces. The anode was attached to one face, and the combined electrolyte-depolarizer carrier of the cell formed the connection with the neighboring dumbbell cell. This design was frequently used in rapidly activating batteries for short-life pulse applications. Later, the dumbbell cell structure was found ideally suited for use with pellet batteries.

(4) The large rectangular power cell (4.2 x 2.25 x 0.25 in.) with three closed sides was used to deliver currents on the order of 5 A at 6 and 28 V for five or more minutes. These power cells were developed in a program initiated in early 1951 to design a thermal battery to drive the power packs of guided missile fuzes. In the course of this work much was learned about thermal battery design in terms of heat utilization, stack stability and overcoming alloy and electrolyte problems. In the later stages of the project, the superiority of the newly found (1953) depolarizer, calcium chromate ($CaCrO_4$), over tungstic oxide was demonstrated. The two-sided anodes for these cells were made by pressing clean calcium sheet into punched grater-like projections extending out of both sides of the nickel base sheet. This technique of calcium attachment was also widely used to attach calcium to one of the faces of dumbbells. Later, CRC extended their vaporized calcium deposition process to form heavier anode stock for use in these cells as well as in their A cells.

All the above batteries used impregnated glass tape as electrolyte carriers (Figure 8).

The mortar fuze battery, the first thermal power supply to go into production, was manufactured by Wurlitzer, Minneapolis-Honeywell, and EPI. It is estimated that between 1951 and 1967 these companies produced over five million of these batteries. The only application for this battery, however, was as the mortar fuze power supply.

A detailed description of the state of thermal battery development[14] in the mid 1950's (Figures 9 and 10) was incorporated as a section of the report for the Proximity Fuze Symposium held at the Diamond Ordnance Fuze Laboratories (DOFL) in April 1956. DOFL was an Army organization set up in 1953 to absorb NBS-ODD. In 1962 DOFL was renamed the Harry Diamond Laboratories (HDL) and in 1992 HDL was absorbed into the new Army Research Laboratory (ARL).

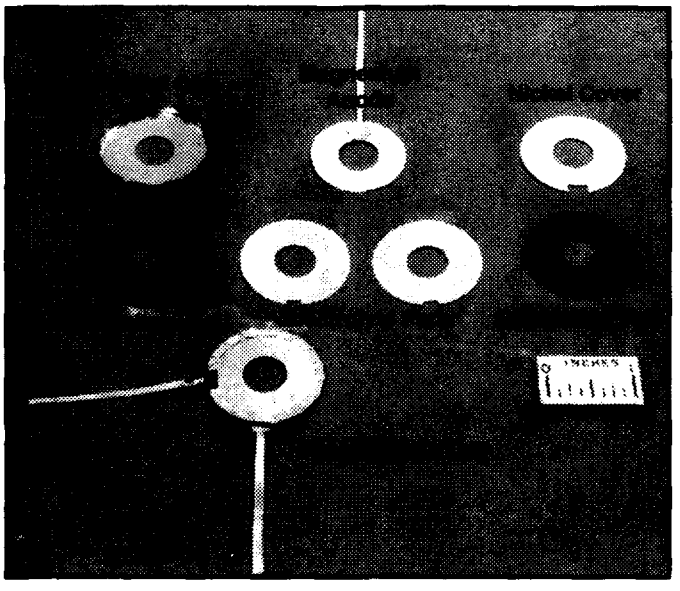

Figure 7. Small cup-and-cover or "A" cell parts layout and assembled cell.

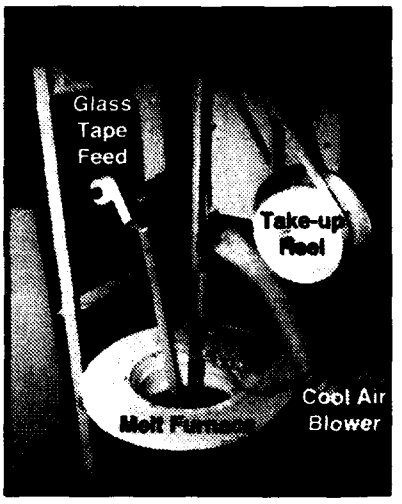

Figure 8. Electrolyte Tape Processing.

Cell Prefusion—A Processing Operation

Battery manufacturers learned that a preconditioning operation for cells or stacks was desirable for proper activation and efficient performance of cells in batteries. The operation was termed prefusion and the various manufacturers had custom-built prefusion equipment for cup-and-cover cells and for sector cell stacks. For A cells, the leads were attached to a resistive load and to a voltmeter. The cell was positioned between two hot platens which were closed upon the cell for a definite length of time and at a predetermined pressure and temperature. The ensuing activation of the cell served to drive out moisture and excess air, allowed the molten electrolyte to soak into the depolarizer, and wetted both anode and collector surfaces, thus

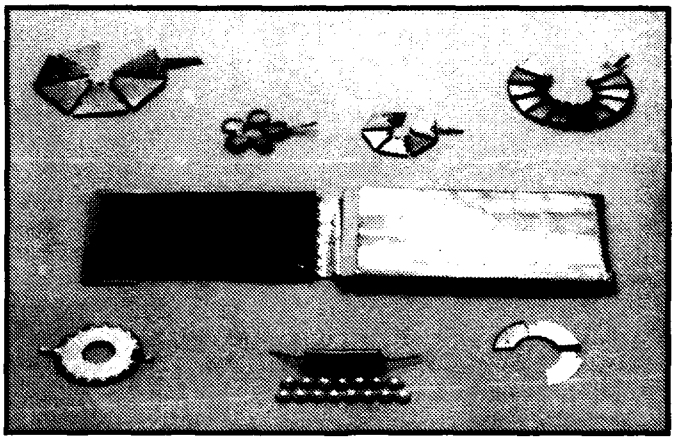

Figure 9. Some representative cells of the mid-1950's.

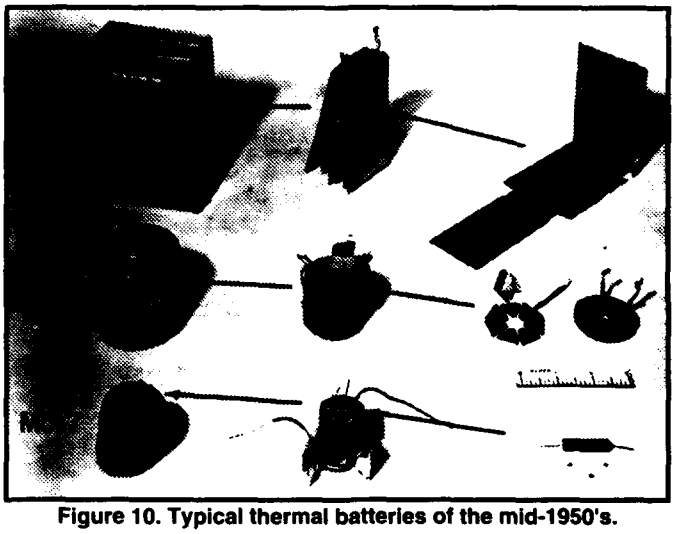

Figure 10. Typical thermal batteries of the mid-1950's.

allowing the cell to activate more rapidly when heated in a battery. Immediately upon completion of the prefusion operation, the cell was rapidly cooled in order to limit consumption of cell component materials.

The prefusion operation also served as a quality control step. The operator of the equipment would reject cells that did not conform to the behavior pattern of correctly made cells. Such rejects were often found deficient in some cell component, such as missing electrolyte or depolarizer pads, or were otherwise misassembled. The prefusion process was also extended to entire stacks of sector cells. In this case, special induction heater coils were developed where the entire stack was prefused in one operation.

Problems Inherent to Thermal Batteries

Manufacturers have always had to contend with some problems that have an adverse effect on the operation of thermal batteries. For example, the electrolyte tended to leak out of the cells of all designs, causing noise due to intercell shorting.

When calcium was used as the anode, a more serious problem was caused by the chemical reaction between the calcium of the anode and the molten lithium chloride of the electrolyte. The reaction of lithium chloride with calcium produces $CaLi_2$, the calcium-lithium alloy. This alloy is believed by some to be necessary for the cell reaction. At the operating temperature of the battery (above 353°C), the alloy is a very mobile liquid metal which can cause intercell shorts. If the alloy makes contact under the right conditions with the depolarizer, particularly $CaCrO_4$, a violent exothermic chemical reaction occurs which affects the voltage and, in the worst case, destroys not only the cell but also the battery. The cell reactions also result in formation of a high-melting-point double salt, $CaKCl_3$, which forms on the surface of the calcium anode and thus blocks access to it by the electrolyte, thereby inhibiting the cell reaction.

Battery designers used various methods to contend with both the electrolyte leakage and the alloy problem. The favorite method was to install barriers of inert materials, such as asbestos or Fiberfrax, within the cells (usually cup-and-cover cells) to restrict alloy flow, and mica disks or asbestos rings between cells to block intercell electrolyte and alloy contacts. To avoid the alloy problem, some early battery designers preferred magnesium to calcium as the anode in their batteries, in spite of the loss of a volt per cell resulting from this selection.

Pellet Batteries Appear

As mentioned earlier, Eureka Williams (EW) was assigned the task of adapting the CRC rocket fuze battery for use in the mortar fuze. EW thought this battery leaked too much electrolyte and proposed another battery design, but found that their new design also had a serious electrolyte leakage problem. After many experiments, they found that leakage would be reduced if the electrolyte were mixed and fused with kaolin. They converted this mixture to an electrolyte carrying pellet. To avoid problems with the calcium lithium alloy, they used a new electrochemical system that they had also been investigating, namely,

$$Mg/LiCl\text{-}KCl\ (kaolin)/V_2O_5, Ni\ .$$

This system had an open circuit voltage of 2.85 and a working voltage of 2.2 to 2.17. EW processed this entire system into a three-layer pellet as follows (Figure 11): measured quantities of magnesium powder, fused electrolyte-kaolin powder, and V_2O_5 powder containing some electrolyte were successively poured into a die cavity and compressed to form a pellet.

The pelletized cell consisted of a nickel dumbbell folded over a heat paper pad. One open face of the dumbbell was coated with a glaze of V_2O_5-B_2O_3, and the other open face was uncoated. The depolarizer end of the pellet was placed in contact with the glazed face of the dumbbell, and the magnesium of the pellet contacted the nickel face of the next dumbbell.[15]

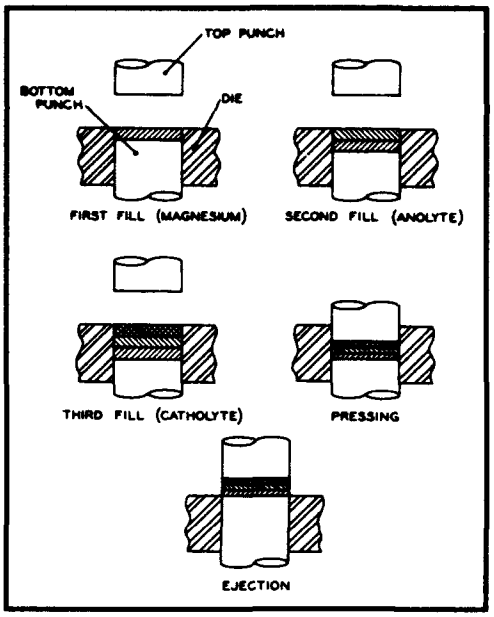

Figure 11. Fabrication of EW three-layer pellet.

This pellet battery work was supported by the Naval Ordnance Laboratory (NOL), as part of a development program for a spin battery that was terminated in about 1955 because of limited funds. Shortly afterwards, however, NOL worked on a battery-powered device that was subject to water impact while the battery was activated. The battery had to operate normally both during and after the impact. NOL had already found that cup-and-cover cell designs tended to squirt electrolyte upon impact, and the operation of the battery was then impaired by electrolyte shorted cells. Recalling its earlier work with the pellet battery, NOL had tests made with pellet batteries, and all tests gave satisfactory results. NOL then decided to use a pelletized design for this application. Later, they extended the use of this pellet battery system to many of their other applications.

Two other thermal battery contractors, CRC[16] and EPI,[17] eventually concluded that the multiple part cup-and-cover cell assembly process was too complex; both sought simpler cell designs. Both companies began to study pellet-type batteries about 1959-60. At this time, CRC made a thorough study of pelletized battery systems in single cell and battery tests. CRC studied the EW pellet design and and did not like it. CRC attempted to develop a single-layer pellet to avoid the "bleeding," "smearing," and "flipping" problems encountered in multi-layer pellet use. Nevertheless, during August 1962, CRC demonstrated its mastery of the EW three-layer pellet design by making a production run of the Navy's Mk 80 battery. But, when CRC went into regular pellet battery production, they as well as Eagle Picher used the two-layer pellet based on the system

$$Ca/LiCl\text{-}KCl\ (kaolin)/CaCrO_4,Fe\ .$$

By the summer of 1962 both CRC and EPI were well-established in pellet battery production using the two-layer system. The depolarizer contained some electrolyte to furnish electrical conductivity to the depolarizer layer during the activation period. Pellets were produced in a die cavity of known volume formed by dropping a lower ram. The cavity was filled with depolarizer powder, the ram was lowered again and the new cavity was filled with the electrolyte mixture. Then, the pressure ram was applied with a predetermined force on the layered materials in the cavity and a two-layered pellet was formed. Iron dumbbells were used to form cells. Calcium attached to one face was placed against the electrolyte side of the pellet; heat paper was sandwiched between dumbbell faces; the other outer, uncoated iron face contacted the depolarizer side of the next cell's pellet.

Cup-and-cover cell batteries were also made and developed by both companies until about 1965, when pellet designs began to take over.[18] Certain special cup-and-cover designs, however, were still being made into the 1980's. Such productions were usually repeat buys of earlier proven designs.

In the mid-1960's there were large procurements (several hundred thousand each) by HDL of three of the earlier developed A,B,C batteries for use in rocket, bomb, and mortar fuzes. These buys marked the phase-out of this technology, because the transistorized fuzes then in development used simpler batteries.

The All-Pellet Battery

In the early 1960's Sandia began development of an all-pellet battery.[19] The heat source was a pelletized blend of fine iron powder and potassium perchlorate. The electrolyte and depolarizer were combined into a single-layer compact (Figure 12) which was made from a homogeneous blend of the eutectic chloride, the calcium chromate, and special silica binder by a prescribed procedure of mixing, ball milling, fusion, and granulation. Calcium bimetal disks or equivalent formed the anodes. The excess iron in the heat pellet acted as the cathode collector and also as the intercell connector in the activated battery. The acronymic name DEB (Depolarizer, Electrolyte, and Binder) was applied to this pellet and to the battery design based on it.

Sandia used the DEB system in its own new designs. CRC, who had done some early investigatory work for Sandia on the system, began using it in production batteries about 1970. EPI used this design in some batteries, but also continued making the two-layer pellet batteries with calcium metal anodes mechanically attached to one face of the dumbbell.

A published article by Jennings discusses the thermal battery technology up to 1970 and includes electrochemistry, cell materials and structures, heating methods, and various battery types.[20]

In 1973, Sandia decided to concentrate on battery development work, and another AEC agency, General Electric Neutron Devices (GEND), became the procurement agency for Sandia-developed batteries. GEND quickly developed the necessary thermal battery fabrication and monitoring facilities and formed an able staff to carry out this new mission.

A 1974 paper[21] by Van Domelan and Wehrle reviews the cup-and-cover technology, touches on the multi-layer pellet system, and details the advantages of the single-layer pellet (DEB) system developed by Sandia.

A New Thermal Battery Manufacturer

In 1966 a small cadre of thermal battery engineers and other specialists left CRC to set up a new company, SCORE, in Cockeysville, MD, to manufacture thermal batteries. The company started by manufacturing cup-and-cover-type batteries based on both the $Ca/CaCrO_4$ and Ca/WO_3 systems and expanded into fabrication of two-layer pellets when they acquired a pellet press. In general, SCORE kept up with developments in the industry, introduced a few innovations of its own and established an energetic R&D group. In 1971 SCORE became affiliated with KDI Corporation and was renamed KDI-SCORE. In 1981, the company was acquired by SAFT, who continued the thermal battery work. In 1989, SAFT also acquired the thermal battery portion of CRC from Mine Safety Appliances. In 1993, however, SAFT discontinued the manufacture of thermal batteries, and planned to use their Cockeysville facilities for R&D work.

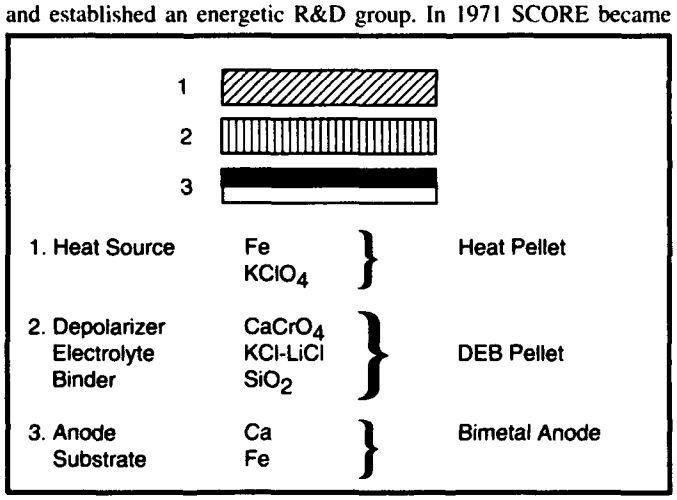

Figure 12. Pellet arrangement in DEB cell.

Wurlitzer's Two-Dollar Thermal Battery

In spite of the emphasis on pellet technology in the 1960's, Wurlitzer, who did not make pellet batteries, developed a small battery in 1967 for an HDL rocket fuze. The battery[22] was intended for high-volume production with a target price of $2.00 per unit.

This nine-cell battery used the electrochemical system

$$Ca/LiCl:KCl = 35:65/V_2O_5\text{-}B_2O_3, Ni$$

and was contained in a can 15/32 in. O.D. and 29/32 in. high. The stack was grounded to the can. The battery activated to 29 ± 3 V in less than 0.3 s and delivered 100 mA for at least 10 s at 20 rps over the temperature range from -40°F to 140°F.

This battery used Wurlitzer's preferred off-eutectic electrolyte which, by reducing the amount of the lower-melting lithium chloride, would melt at a higher temperature and tend to give a slushy electrolyte. These features presumably reduced both the cells' tendency to form alloy and to leak electrolyte. The electrolyte was carried by impregnated crocidolite asbestos paper. The 0.003-in.-thick nickel dumbbell cells were roughly 13/32-in. squares which, when folded over the heat-paper heat source, had one open face coated with vaporized calcium and the other coated with a glaze of $V_2O_5\text{-}B_2O_3$.

This battery was produced at a rate of several thousand per day, 70,000 per month. Wurlitzer made over a million of these batteries, and EPI, the second source, probably made another million. The target price of $2.00 per unit was approached early on, but as the economy changed, the price went up.

Sandia's Long-Life Thermal Battery

In the early 1970's, Sandia considered the possibility of extending the working life of thermal batteries beyond 5 minutes, first working to achieve 15 minutes and eventually reaching a battery life of 60 minutes.[23,24] This success was achieved by following a number of steps, such as lining the battery can with superior thermal insulation, using heat reservoirs (pellets containing a eutectic salt mixture melting at 493°C) at the ends of the stack, utilizing the heat generated by intra-cell reactions, using chemical and mechanical steps to control the calcium-lithium alloy formation, and finally, reducing the load current density on the cell.

Continued work on this design led to the installation of a heat buffer pellet in the middle of the stack and the addition of some $Ca(OH)_2$ to the electrolyte to inhibit alloy formation. The edges of the anodes were also treated to form a thin adherent coating of CaO. The electrolyte modification and the edge treatment apparently did control the alloy problem.

The Lithium, Lithium Alloy, Iron Disulfide System

In the 1960's, Argonne National Laboratory (ANL) began investigating the feasibility of developing a molten-salt secondary battery for vehicular propulsion and load leveling in power systems. It examined the heavier chalcogens as cathodic materials with lithium as the anode. Finding the liquid electrode systems difficult to handle, ANL settled for a lithium aluminum (solid) alloy as anode and iron disulfide and later iron sulfide as the cathodic material. Several contractors worked for ANL on such secondary batteries, studying cell design, materials, heating arrangements, etc. All efforts were directed at building a reliable battery capable of accepting a high number of charge-discharge cycles.

CRC was aware of the work at Argonne and performed work aimed at adapting a lithium anode to primary thermal battery use. CRC filed

for a patent[25] in 1973 on a lithium anode in which the lithium metal was carried on a porous metal, e.g., a fine iron screen that would inhibit the movement of liquid lithium (Figure 13). The screen was mounted in the bottom of a cup. The sides of the cup were folded over a cover formed by a double-layer crocidolite asbestos paper. The outer layer of asbestos was impregnated with the electrolyte, which was absorbed by the inner layer after the battery was activated. Batteries based on this structure went into production in 1975.

CRC later developed a superior version of the lithium metal anode by mixing a fine iron powder into molten lithium. This blended material, when solidified, was rolled into a thin strip from which disks of the mixture were punched. These disks were put into the screen bottomed cell cups, and the sides of the cups were pressed over the periphery of the anode material. The patent[26] states that, at the operating temperature of the battery, this anode softens, does not liquefy, and maintains its dimensional stability during battery operation. A paper by Winchester[27] discusses the performance characteristics of this anode system in batteries. Most, if not all, of CRC's subsequent production used this anode, which CRC referred to as their LAN anode.

The British also had started working with lithium-sulfur cells in the early 1970's. The work also seems to have been influenced by that at ANL and moved on to the use of the iron disulfide cathode and to the design of a primary battery using a lithium-aluminum anode.[28]

During the 1970's and '80's the Air Force's Aero Propulsion Laboratory (APL, Wright Patterson Air Force Base) supported programs to improve thermal battery performance to meet the power and life demands of new sophisticated devices. In 1976, in one of these programs, APL awarded contracts to EPI and SAFT to develop an advanced thermal battery, by optimizing the calcium-calcium chromate system and investigating new electrochemical systems and evaluating their potential worth. Both contractors worked on the $Ca/CaCrO_4$ system and examined a number of other systems; both studied the LiAl/LiCl-KCl (eut)/FeS_2 system early and explored its characteristics, concluding that it was superior to all the other systems with regard to current density, life, and energy output. Furthermore, as a great benefit, there was no lithium-calcium alloy problem. Both companies summarized their findings in their final reports issued in 1979.[29 30]

Sandia also investigated the Li/FeS_2 system at this time, starting with a study of the system Mg/FeS_2 to evaluate the behavior of the cathodic material and following it by studying the system characteristics with lithium alloy anodes.[31] This study showed that the lithium silicon alloy gave better life performance than the lithium aluminum alloy on an anode weight basis. This work was followed by a series of staff reports on investigations of the performance characteristics and chemical aspects of the system.

These developments stimulated a rapid movement away from the use of the calcium-calcium chromate system and has established the lithium or lithium alloy anode/iron disulfide cathode system as the dominant system in use in present-day thermal batteries.

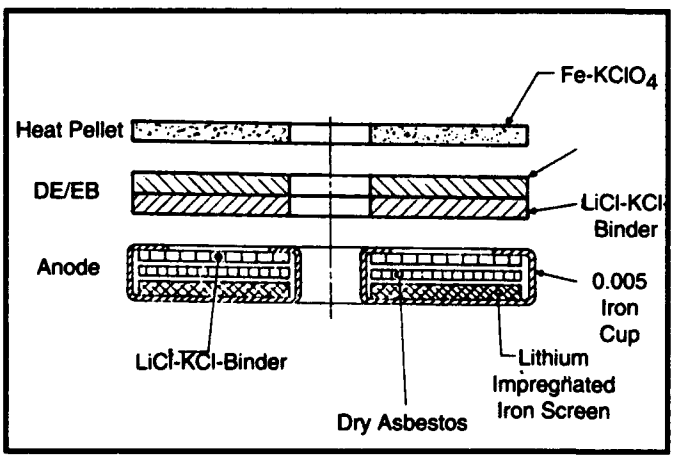

Figure 13. CRC screen-stabilized, molten metal anode cell.

Attewell and Clark review the thermal battery field in a 1980 paper.[32] They briefly discuss the $Ca/CaCrO_4$ system and then proceed with a discussion of the lithium anodes of various types. They point out these these batteries show a marked increase in energy and power density compared with the previous types. They feel that larger batteries than any previously possible with the older system will probably appear and extend the uses of thermal power supplies.

A short historical and technical review of the entire thermal battery field (1984) is presented by Tepper and Yalom[33] in Linden's *Handbook of Batteries and Fuel Cells*.

In use at this time (1993) are three varieties of lithium-based anodes: (1) the physical mixture of lithium metal with iron powder developed by CRC, (2) the lithium aluminum alloy, which was favored by SAFT, and (3) the lithium silicon alloy, which is used by Sandia and EPI. The LiSi offers twice as much available lithium as does the LiAl anode at the working temperature of the battery.

In the 1980's, the search for a better electrolyte than the eutectic chloride revealed two that warranted further investigation, a LiCl-KBr-LiBr eutectic (25-38-37 mole percent) with a melting point at 310°C and an all-lithium halide eutectic LiF-LiCl-LiBr (22-31-47 mol percent) which melted at 430°C. The latter electrolyte was described as superior to the eutectic chloride for high current applications and as ideal for pulse battery applications.

Several papers in the proceedings of the 33rd International Power Sources Symposium (1988) discuss the properties and performance characteristics of additional electrolyte formulations.

The possibility of replacing silver zinc batteries with thermal batteries had been discussed informally for a number of years. A 1984 paper[34] by Gross made the case for such replacement. He discussed the applicable characteristics of both battery types and emphasized the definite advantages offered by thermal batteries. Similarly, in 1988, Briscoe[35] et al. considered many of the same factors and cited the development and qualification of such a battery by SAFT. At this time, additional silver zinc batteries have been replaced by thermals.

Heat Sources

Heat paper was the heat source used in most (the mortar fuze battery used compacted heat blocks) of the thermal batteries made in the 1950's, 60's, and well into the 70's. CRC started to use Z-2 heat powder exclusively about 1950, first as compacts on asbestos disks and Z-2 powder packaged in asbestos envelopes for use in large batteries. Then after mid-1952 CRC started using heat paper based on Z-2. After some experience with this heat paper CRC raised the zirconium content of the heat powder from 21 to 28 percent, when they found that burning Z-2 heat paper could be quenched. This new material was named Z-28.

As batteries became larger, increased amounts of heat powder were used per battery, and the gases generated from the impurities in the constituent materials of the heat powder began to cause pressure problems, i.e., blown out terminal seals and distorted containers. A 1954 DOFL program involving work at DOFL, the University of Florida, and Foote Mineral Company resulted in specifications for both barium chromate and zirconium powders. The specification for the latter was based on the properties of Foote's 120A zirconium powder. Included in this program was the development by DOFL of a special calorimeter,[36] the argon calorimeter, to determine the heat content of thermite-type heat powders. The Parr Company later manufactured this device as the Parr 1411 calorimeter.

In 1958, SCEL sponsored a similar program at CRC[37] to investigate the properties of the constituent materials and heat-paper manufacturing process that affect the performance of the end product. The purity and particle size of the zirconium powder were found to be of great importance with respect to the calorific value and burning rate. The optimum combination, depending on the end purpose, of inorganic

fibers was determined. The quantitative effects of various combinations of components were presented in the report in graphic form so that calorific value, burning rate, tensile strength, flexibility, ash quality, and gas evolution could be predicted and controlled.

These efforts did contribute to improved heat-paper performance, but zirconium heat paper was never completely gasless and battery containers, particularly the larger designs, had to be designed to withstand considerable pressure.

Sandia's Heat Pellet

About 1964, Sandia started the development of the all-pellet battery by converting the heat source to a conductive pellet. After finding a source to produce a fine iron powder of the right particle size and configuration, Sandia blended the iron powder with finely ground potassium perchlorate powder and compressed the mixture. The iron powder was designated NX - 1000 and, at that time, was made by Pfizer. The heat pellet was sufficiently strong for use in a cell stack and could be reliably ignited by a burning heat-paper fuze train. The heat output was controlled by varying the composition of the heat powder mixture. After burning, the remaining metallic iron in the pellet made it electrically conductive so that it acted as an intercell connector. Use of this new heat source in production batteries began in the late 1960's.

New Source of Zirconium Powder

In June 1972, a fire destroyed the Foote Mineral zirconium manufacturing facility. Foote conducted a survey on the future requirements for zirconium, became aware of the growing use of the iron heat pellets, and decided not to replace the facility in view of the limited market and the hazards involved in manufacturing the material.

Foote's departure left Ventron Co. of Beverly, MA, the sole producer of battery-grade zirconium. Using ores from different sources, Ventron produced two types of zirconium, called Type I and Type II, by a magnesium reduction process. Type I zirconium had a larger than usual particle size. Type II zirconium contained particles in the submicron range, which made the dry powder dangerous and potentially ignitable on exposure to air.

Some of the battery manufacturers were concerned about the effects of these two new materials in their established processes. Heat paper made with the Type II material worried manufacturers because of the danger of spontaneous ignition of heat paper during handling, weighing, and battery assembly operations. One company, Eureka, had been using Type I all along and reported no trouble with it. SCORE, when faced with the problem, blended the two types in equal amounts and said they had no problems. Ventron cooperated in overcoming the problem and instituted production controls to reduce the hazards.

With the Foote 120A-grade zirconium no longer available the specification based on it was no longer valid. A new specification, MIL-Z-46189 (dated 02 October 1986), was prepared by the Army Materials Laboratory, working in collaboration with Ventron and with members of the thermal battery community also contributing.

The Calcium Chromate Problem

While not related to heat sources, another material supply problem also arose at this time. The long-time source of an excellent grade of $CaCrO_4$, the most frequently used depolarizer of the period, closed down the plant making the material. Calcium chromate had been targeted by OSHA as a carcinogen, and the company was not interested in replacing the old plant. The supplies of CaCrO4 from other sources were not always satisfactory for a given battery manufacturer's practice, and the replacement sources never did entirely satisfy some users.

This pair of supply problems threatened to close down one important production line and prompted a number of battery- procuring Government agencies (Army, Navy, Air Force, and Department of Energy-DOE) to form a DoD-authorized committee to assess the extent of the users' supply problems with these and any other materials and, if possible, generate replacement sources. The committee's efforts with suppliers and users helped ease the problems and resulted in the erection of an environmentally safe manufacturing facility at GEND (DOE) for calcium chromate. EPI successfully demonstrated a standby plant[38] for zirconium production on an Air Force contract.

Interestingly enough, shortly after these developments, the trend of thermal battery manufacture turned to the wider use of iron-based heat pellets, and calcium chromate was superseded by iron disulfide as a cathodic material.

Contributors

Conversations with the following elicited much historical information on the development of thermal batteries:

Wurlitzer
- Ralph Mead

Catalyst Research Corporation (CRC)
- Joe Gessler, now at SAFT
- Andy Olert, " " "
- Dick Blucher
- Bill Jones
- Bernie Rogers
- Vis Klasons
- Frank DeMarco
- Clint Winchester, now at NSWC
- George Bowser
- D T Breckenridge
- Fred Tepper, now at MSA

Mine Safety Appliances, Pittsburg
- Ron Shakely

Sandia Corporation.
- Norman Rosenberg
- Bob Wehrle (indirectly)
- Ron Guidotti
- R P Clark

Naval Surface Warfare Center-White Oak, (NSWC-WO), formerly Naval Ordnance Lab (NOL)
- David Yalom
- Ben Larrick

Eureka, formerly Eureka Williams, (EW)
- Ralph Zebart
- Lyle Raper
- David Ryan, now with WPAFB

Eagle Picher Industries, (EPI)
- Earl Carr
- Walter McCarter
- Robert Cottingham
- Erwin Walker

Harry Diamond Laboratories
- Charles Ravitsky
- Robert B Goodrich
- Julius Hoke
- Perry Waugh
- Andrew Sabonis
- Harlan Oelke
- Saul Elbaum

References

1. Hamer, Walter J., 25 Years Of Primary Batteries, Proceedings of the Twenty-fifth Power Sources Symposium.
2. The Deadly Fuze, Ralph B. Baldwin, Presidio Press 1980; p 121.
3. Theory and Practice of Thermal Cell by Georg Otto Erb, Publication BIOS/ Cp 2 / HEC 182, Part II, A publication of the Halstead Exploiting Centre, Great Britain.
4. Ravitsky, C., National Bureau of Standards - Ordnance Development Division. Memorandum: "Thermally Activated Reserve Cells," dated 27 June 1946.
5. Letter from O. G. Bennett, Catalyst Research Corporation to P. J. Franklin, National Bureau of Standards, dated 7 February 1947.
6. National Bureau of Standards letter to Catalyst Research Corporation, dated 22 October 1947. Signed by R. S. Walleigh for Harry Diamond, Chief, Ordnance Development Division.
7. The early proximity fuze batteries were A, B, C section batteries; i.e., they supplied voltage and current to the three parts of a vacuum tube circuit. Basically, such a battery is an adaptation of three separate batteries enclosed in a single container. The A section of the battery supplied a heating current at low voltage to the filament of the tube. The B section charged the plate of the tube with a high voltage, usually greater than 100 V. The C section, usually a part of the B Stack of the battery, placed a low bias (negative) voltage on the grid of the tube where the varying potential controlled the flow

of electrons from filament to plate. When transistors replaced vacuum tubes in electronic circuitry, the ABC batteries were made obsolete and they are no longer made.
8. United States Patent. 4,034,143, 5 July 1977, Inventor: Roger G. Sweet, Assignee: Catalyst Research Corporation.
9. The early work with the very hygroscopic lithium salts led to the use of dry boxes using calcium chloride and other drying agents. These were replaced by dry rooms in the effort to keep the work area's relative humidity below 10%. Over time, as experience showed the need for maximum dryness within the battery for optimum battery performance, the relative humidity requirement was reduced to a maximum of 3%.
10. Kaplan, Nathan, and Scillian, Glen L., TR-99, Fuze, VT, T2031E1, Battery, Diamond Ordnance Fuze Laboratories, 1 July 1954. The introduction to this report gives a cursory account of the development of the Rocket Fuze Battery.
11. Hoke, J. U., and Scillian, G. L., TR-186, Fuze, VT T-2061, Battery, Diamond Ordnance Fuze Laboratories, 1 July 1955. This report describes an improved form of the T-2031 Rocket Fuze Battery.
12. Curtis, R. W., and Goodrich, R. B., "Thermal Batteries," National Bureau of Standards, Ordnance Development Division Report 13/7-95R, 6 December 1950.
13. Rogers, M. B., Catalyst Research Corporation Report: Calcium Coating, Vacuum Distillation, NBS Contract Cst-10127, Task Assignment 115.
14. Goodrich, R. B., Thermal Batteries. This paper was excerpted from the Proximity Fuze Symposium held at DOFL 16, 17 April 1956.
15. Nielsen, N. C., Three-Layer Pelletized Cells for Thermal Batteries. Proc. Ann. Power Sources Conf (1969).
16. Blucher, R. L., Shevchenko, D. E., and Sears, L. O., Jr, Thermal Battery Adaption Kit Power Source, Phase I, Catalyst Research Corporation report on Contract DA-36-034-ORD-3692 RD.
17. Doan, D. J., and McCarter, W. K., The Eagle-Picher Company, Couples Department. Comparison of the Pellet Cell Characteristics with the Closed Cell Characteristics In Thermal Batteries, Interagency Advanced Power Group. Proceedings of the Thermal Battery Panel (PIC-BAT 209/8) 4 October 1963, p.7-1. Discusses advantages of the pellet battery over the cup-and-cover design.
18. Goldsmith, H., and Smith, J. T., Thermal Cells in Present Use, Electrochemical Technology, Vol 6, No 1-2, Jan-Feb. 1968, p 16-18. After comparing the performance of cup-and-cover cells against pellet cell designs, the authors concluded that the pellet cell designs were superior.
19. Bush, D. M., "A Pellet Type Thermal Battery," Sandia Laboratories, SC-TM-64-518, April 1964.
20. Jennings, C. W., "Thermal Batteries," The Primary Battery, Vol 2, Edited by Heise, G. W. and Cahoon, N. C., John Wiley & Sons, New York, 1976.
21. Van Domelen, B. H., and Wehrle, R. D., "A Review of Thermal Battery Technology," Intersoc. Energy Convers. Conf, 1974.
22. Mead, R. T., A Low Cost Thermal Battery. Proceedings,Twenty-third Annual Power Sources Conference, 1969, p.137.
23. Bush, D. M., and Baldwin, A. R., A Preliminary Study Into the Feasibility of a Sixty-Minute Thermal Battery, SLA-73-0412. Sandia Laboratories, Albuquerque, NM, April 1973.
24. Baldwin, A. R., "A Sixty-Minute Thermal Battery," 27th Annual Proceedings Power Sources Conference (Atlantic City, NJ 1976), p 152
25. Bowser, G. C., and Moser, J. R.; US Patent 3,891,460, 24 June 1975. Thermal Battery and Molten Metal Anode Therefore.
26. Harney, D. E.; US Patent 4,221,849, Iron-Lithium Anode for Thermal Batteries and Thermal Batteries Made Therefrom.
27. Winchester, C. S., The LAN/FeS2 Thermal Battery System, 30th Power Sources Symposium, 7-12 June 1982.
28. Askew, B. A., and Holland, R., A Novel Design of Lithium-Iron Disulfide Battery for Primary and Secondary Application. Electrochemical Society Extended Abstracts, Fall Meeting, 1975.
29. Dand, P. V., and Press, K. K., "Improved Thermal Battery," Final Report, Wright-Patterson Air Force Base, Ohio, AFAPL-TR-79-027, April 1979.
30. DeGruson, J. A., "Improved Thermal Battery Performance," Final Report, Wright-Patterson Air Force Base, Ohio AFAPL-TR-79-2042, July 1979.
31. Bush, D. M., The Li/FeS2 System for Thermal Batteries, SANDIA 78-0470, Sandia Laboratories, Albuquerque, NM, June 1979.
32. Attewell, A., and Clark, A. J., "A Review of Recent Developments in Thermal Batteries," Proceedings of the 12th International Power Sources Symposium held at Brighton, September 1980, Academic Press 1981.
33. Tepper, Frederick, and Yalom, David, "Thermal Batteries" Section 40, "Handbook of Batteries and Fuel Cells," Edited by David Linden, Copyright 1984, by McGraw Hill, Inc.
34. Gross, Sidney, "Comparison of Lithium Thermal Batteries and Automatically Activated Silver Oxide-Zinc Batteries," Proceedings of the 31st Power Sources Symposium, June 1984.
35. Briscoe, J. Douglas, Chagnon, Guy, Gessler, Joseph L., and Mattson, Donald, "Advances in Thermal Battery Applications" Proceedings of the 33rd International Power Sources Symposium, June 1988.
36. Marcus, I. R., "Measurement of Heat Evolved by Thermite Mixtures, Part III — Standard Calorimetry for Quality Control," DOFL Report TR-576, 15 January 1958.
37. Goodkin, Jerome, "Research on Heat-Producing Compositions, 1 June 1958 through 31 July 1960, Final Report," Signal Corps Contract DA-36-039 SC-75071, DA Proj. No. 3-99-15-102.
38. Smith, D. L., "Production of Zirconium Metal Powder for Rapid Rise Time Thermal Battery Application," Proceedings of the 29th Power Sources Conference, June 1980.

Thermal Battery Chronology

June 1946	C. Ravitsky reviews Erb Report at the National Bureau of Standards Ordnance Development Division (NBS-ODD) and writes memorandum to management recommending further investigation. Management concurs and P. J. Franklin is instructed to investigate.
Dec 1946	P. J. Franklin demonstrates thermal cell feasibility at the National Bureau of Standards Ordnance Development Division.
Feb 1947	Catalyst Research Corporation (CRC) maker of the heat source material used by Franklin: O. G. Bennett, the General Manager, proposes to develop a thermal battery under contract to NBS-ODD.
May 1947	CRC starts work on thermal battery development contract.
Oct 1947	NBS-ODD extends and enlarges scope of contract.
Mar 1948	Wurlitzer starts work on thermal battery for mortar fuze.
1949	Early Wurlitzer thermal battery-fuze field tests.
1950	NBS-ODD decides to use thermal batteries to power all its fuzes.
	Wurlitzer starts limited production of mortar fuze battery.
1950	Early rocket fuze battery ready for field tests.
	NBS issues report "Thermal Batteries."

1951 Signal Corps Electronic Laboratories (SCEL) contract at CRC for R&D work on thermal batteries.

Army Ordnance and NBS-ODD bring in Pass and Seymour, Eureka Williams, Minneapolis Honeywell, and Olin as industrial contractors.

The Universities of Florida, Virginia, and Illinois and North Carolina State College are brought in as R&D contractors.

Bimetal process development started at CRC.

Heat paper developed at Pass and Seymour.

Power battery (guided missile fuze power supply) started at CRC.

1952 CRC begins pilot plant production of calcium-nickel bimetal.

CRC uses heat paper, develops depolarizer paper.

1953 NBS-ODD transferred to Army, renamed Diamond Ordnance Fuze Laboratories (DOFL).

Sandia Corporation looks into thermal batteries.

1954 Heat paper machine developed at University of Florida acquired by CRC.

DOFL begins program for heat powder/heat paper improvement.

British begin thermal battery work at MSA Glasgow.

1955 Sandia Corp. awards contracts to CRC, Wurlitzer, EW, PNS, and Eagle Picher.

EW develops pelletized battery; work sponsored by NOL.

Extensive development and manufacture of batteries using cup-and-cover cells in various sizes.

1960 Pellet work started at CRC and EPI.

1961 DOFL renamed Harry Diamond Laboratories (HDL).

1962 Sandia initiates internal R&D work.

1964 Sandia initiates work on the all-pellet battery.

1966 SCORE, a new thermal battery company, established.

1971 Wurlitzer drops out of the thermal battery business.

KDI Corporation takes over SCORE.

1973 Usual sources of Zr and $CaCrO_4$ powders dry up. Joint Deputies for Laboratories Committee (JDLC) Sub Panel on Thermal Batteries formed to locate new sources and establish standards.

General Electric Neutron Devices (GEND) becomes thermal battery procurement agency for Sandia.

1974 CRC patents cell with lithium metal anode.

1976 Aero Propulsion Laboratory (AFWAL/POOC-1), Wright Patterson Air Force Base, contracts with EPI and KDL SCORE to develop an "Advanced Thermal Battery." Both contractors demonstrate the superiority of the LiAl/FeS_2 system.

1980 Eureka drops out of thermal battery business.

1981 SAFT buys SCORE from KDI.

1989 SAFT buys thermal battery business of CRC.

1992 SAFT ends thermal battery production operations at Cockeysville, MD and converts the facility there into an R&D operation.

1992 Harry Diamond Laboratories (HDL) is absorbed into the new Army Research Laboratory.

EXPERIENCES FROM DEVELOPING ELECTRICAL NON DESTRUCTIVE TESTING FOR THERMAL BATTERIES

Per A. Selånger, Catella Generics AB,
Electrum 232, 164 40 Kista, Sweden
Owe J. Lyrsell, FMV:FL8,
115 88 Stockholm, Sweden
Richard A. Marsh and David M. Ryan,
Wright Lab. Wright-Patterson AFB, Ohio, USA

Abstract

A reliable, practical Electrical Non-Destructive Test (ENDT) method for determining the state-of-health of thermal batteries does not exist for today's users. The Swedish Defence Material Administration, Air Materials Department (FMV) and Catella Generics have undertaken the task to develop an ENDT method for thermal batteries. The approach to accomplish this task is to use statistical analysis of various electrical measurements taken on the thermal batteries and use these results to determine if a failure mode exists in the subject battery. The data to be analyzed will pertain to the batteries' cold open circuit voltage (OCV), cold closed circuit voltage (CCV), cold resistance and cold capacitance. In order to assess or validate the ENDT method developed by FMV and Catella Generics, the Wright Laboratory of WPAFB, OH provided FMV with fifty (50), EAP 12166 thermal batteries produced by Eagle-Picher Industries for evaluation. Unknown to the evaluators, several of these batteries had intentional defects built into the batteries during manufacture. This paper will present the ENDT method developed, the validity test results/conclusions, a discussion concerning the practicality of the ENDT method and future work that is recommended.

Introduction/Background

During the 1980's significant technological advances were achieved in thermal batteries; i.e. increased energy and power density, extended discharge times and the development of large capacity batteries. As a result of these advances, thermal batteries have entered into a wide range of new application areas, i.e. aircraft emergency power. The FMV was the first to introduce thermal batteries as a source of emergency power on board aircraft - JAS 39 multi role fighter. Because of these critical application areas, the FMV has undertaken a project to develop an ENDT method for thermal batteries to determine their state-of-health (or ability to perform the mission) - throughout the thermal batteries' life cycle. The objective of the ENDT method for thermal batteries is to detect manufacturing faults and/or faults which occur during the batteries life cycle while implemented into various weapon systems.

Determining the batteries state-of-health before and after installation into a weapon system would significantly improve system reliability/availability and drastically reduce its life cycle cost. This FMV project to develop a reliable, inexpensive and practical ENDT method for thermal batteries is the first of its type and could have significant cost and reliability impact on the production and use of thermal batteries.

Project objective

The primary task is to identify defect batteries from a specifically prepared population of thermal batteries by the ENDT-TB method. The secondary task is, if possible to point out the different kinds of claimed defects, such as shorted cells, cells with reversed polarity or other defects.

Description of the ENDT-TB concept

Testing samples and their preparation

The test population consisted of a batch of 50 thermal batteries of which some were specially prepared with various types of defects and the others made according to standard manufacturing practice. The batteries were of the EPI, EAP 12166 type. Each battery has a configuration comprising 24 cells divided into two equal stacks with a common ground. The chemistry is the LiAl/FeS_2 system.

The special preparation of defects into the batteries were made in co-operation between Eagle-Picher Industries and Wright Laboratory at WPAFB. The type of defects were cells with reversed polarity, short circuited cells, reduced stack pressure contamination and moisture. The various defects are shown as categories in Figures 1 - 4.

Intentionally, no information other than the type of defects, was initially given to the analyst during the course of the measuring and evaluation part of the project. The analyzing and testing partner was Catella Generics AB.

Experimental

The ENDT-TB measuring procedures were as follow:

* OCV measurements were carried out at +21°C and again +40°C for each stack
* Stack resistance measurements were carried out at +21°C
* Capacitance measurements were carried out for each stack at +21°C.
* Cold discharge experiments were carried out as voltage measurements over a high resistivity load (about 1 Gohm) connected to the battery at +21°C.

The instrumentation used was a Keigthley 617 electrometer for voltage measurements; OCV, cold discharge voltages and resistance. A standard capacitance instrument, Boonton Capacitance Meter Model 72B, was used in the capacitance measurements.

The batteries, after thermal activation were discharged into an 11Ω load. Voltage and current data were collected at a sampling rate of 2 seconds.

The experiences from these measurements are the following:

OCV measurements takes about 30 minutes to reach a reproducible stability at +21°C and 15-20 min. at +40°C. It was necessary in some cases to put the battery on an anti static ground when conducting the OCV measurements.

The cell OCV value was found to be 2.469 VPC. This value is much higher than the value expected from thermochemical calculations. A sulphate contamination associated with the FeS_2 electrode material is identified as the most probable explanation to this observation (1).

Cold capacitance measurements took only a few seconds to stabilize and cold voltage discharge measurements were made after 1 minute.

Resistance measurements were found to be impractical to use due to a very long stabilising time.

Measurements

The battery has four terminals marked +, C, - and M. C for common and M for electrical match. The OCV measurements were carried out over + to C and C to - terminals and presented as +/C respectively C/- in Figures 1 - 2. Corresponding capacitance and cold discharge measurements at the +/C and C/- terminal are also presented in Figures 3 - 4.

Analysis of measurements

Analysis of OCV-measurements: A battery is built of discrete components such as cells. Each cell is assumed to be represented by its thermochemical couple value and a battery by the sum of these cells. A normal battery should be represented by its sum of cell voltages. Abnormal batteries with defects such as short circuited cells or reverse cells assembled upside down (reversed polarity) should all give deviating voltages from the expected value. The precision in such an analysis is dependent on the reproducibility of OCV measurements and the possibility to perform such measurements. The thermal batteries have a very high internal impedance in the cold state, much higher than many conventional voltage measuring instruments. The latter circumstance has been overcome by using a high impedance voltmeter.

The analyzing technique is to divide the measurement value with the OCV cell value characteristic for couple and observe the multiple of "active cells" in the battery. This value should be within some precision to the expected value for a correct battery. The OCV cell value is assumed to be determined in advance for each type of battery.

A battery with one short-circuited cell will show one cell voltage multiple less than a normal battery. A battery with a reversed polarity will show two multiples lower than expected due to its counter current action.

Batteries with other defects such as reduced stack pressure or moisture contamination will not be detected by OCV measurements.

Figures 1 and 2 show actual measurements with correlation to battery type.

Analysis of capacitance measurements: A simple modelling of a battery with a high electrolyte resistance such as an inactivated thermal battery give the formulation for a series configuration capacitance. From such a simple formulation it can be deduced that a short circuit will show a higher value than for the standard battery. The measurement precision and its dependency of the number of cells in a general battery gives a varying precision from case to case.

The potential value of capacitance measurements is its capability to follow aging processes. Air leakage is a potential example of such measurement and changes emanating from mechanical disorders due to long time exposures to vibrations causing changes in the stack geometries.

Analysis of cold discharge experiments: Each stack has its own signature in cold discharge experiments. The voltage observations for such experiments are very much dependent on the resistivity of the cell. A high resistivity gives a low voltage in such experiments. Cell stacks with reduced stack pressure are also not easily detected using x-ray techniques.

Analysis of stack resistance measurements: At the present time, more investigations are necessary in order to avoid the drawbacks of slow stabilization.

An analysing algorithm and a detailed procedure for the ENDT-TB is under preparation.

Outcome of the ENDT-TB testing

Figure 1 and 2 show the correlation of the OCV measurements at +40°C and +21°C with respect to the defects built into the batteries. The statistical control lines correspond to $<OCV> \pm 2\,\sigma$ for good cells.

Figure 1 shows that the "reversed cells" are clearly indicating deviations. Stacks with built-in shorts are not correlating well. It was observed later on the activated discharge curves that the built-in short circuited cells did not show shorts until at a late stage during the discharge. In the early stage of discharge these cells showed normal discharge voltages. The conclusion was that the preparations made were not ideal for simulating a shorted cell.

Figure 3 shows stack capacitance and its correlation to defect types. Capacitance is valuable in the detection of reduced stack pressure defects. The defect type "reversed cells", does not show deviations from the control lines. This was as expected from the simple capacitance model.

Figure 4 shows the cold discharge polarization correlated to defect type. "Low-pressure" type and "reversed cell" types deviate clearly from the main population.

"Moisture" and "Argon back-filling" have not in any case been found to correlate to any measurements.

Table 1 below shows a summary of the correlations to each defect type and diagnostic measurement technique.

Table 1: Outcome of diagnostic testing of thermal batteries with the ENDT-TB method. Y is an applicable and N is not an applicable technique.

Defect type	Diagnostic technique				
	OCV	Capacit-ance	Resist-ance	Cold discharge	Comments
Reversed ly assembl-ed cell(s)	Y	N	N	Y	
Short-circuited cell(s)	Y	Y	N	Y	Not shown in this testing
Reduced stack pressure	N	Y	N	Y	Seems to be of value for checking long term mechanical integrity in vibrational environments
Moisture contam-ination	N	N	N	N	Long term dependence not investigated here
Argon back-filling	N	N	N	N	No indications have been found.

Conclusions

The diagnostic measurements with the ENDT-TB method have enabled the detection of serious failures such as reverse assembled cells and reduced stack pressure. For environmental defects such as moisture contamination and Argon back-filling the ENDT-TB has not shown to be detectable. The short-circuit defects were not detectable and are most probably due to the preparation technique simulating shorted cells.

The ENDT-TB method has shown the potential to complement or replace the more expensive x-ray method for detection of manufacturing defects.

The cold capacitance and cold discharge techniques have the potential for use in determining the state-of-health batteries installed in long term weapon environments.

Recommendations

The use of thermal batteries have created a variety of battery designs. In order to make ENDT-TB a practical method it is recommended to study and evaluate various configurations such as varying internal electrical connections for stacks, stacks in series and in parallell or of various stack voltages.

For the implementation of the ENDT-TB concept into qaulity control (QC), acceptance test procedure or maintenance routines it is recommended to design a test station to initiate an off laboratory experience activity. The task for this activity should be to develop a practical analyzer.

Acknowledgements

We wish to thank Charles Lamb and Joe Wells at Eagle-Picher Industries, Joplin, MO for valuable discussions in the initial stages of this project and also for the preparation of the various defect samples. We also wish to thank Charles L. Hussey, University of Mississippi, for valuable discussions in the thermodynamic identification of the cell OCV value.

References

(1) T. L. Aselage and E. E. Hellstrom, Multicomponent Phase Diagrams for Battery Applications. II Oxygen impurities in the Li(Si)/FeS_2 battery cathode. J. Electrochem. Soc., vol. 134, No. 8, 1977, 1932-1938.

Figure 1 Stack OCV measurements +40°C

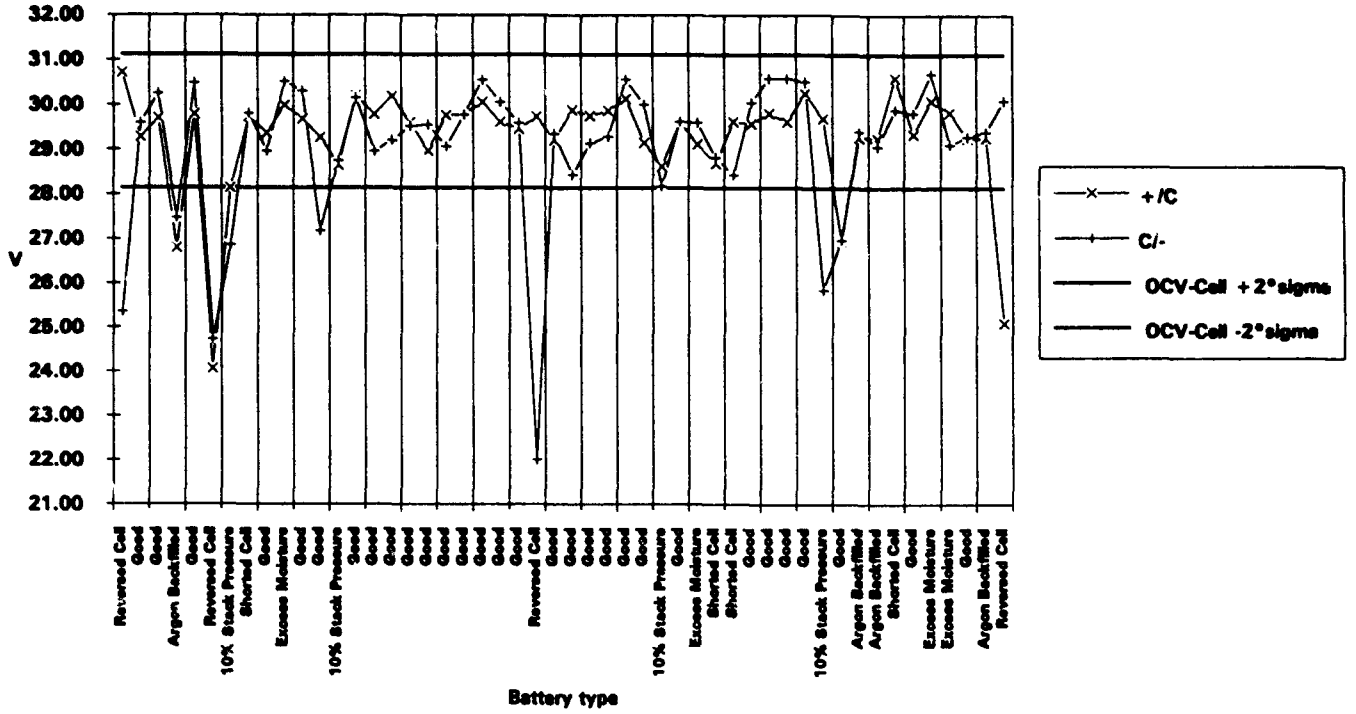

Figure 2 Stack OCV measurements at +21°C

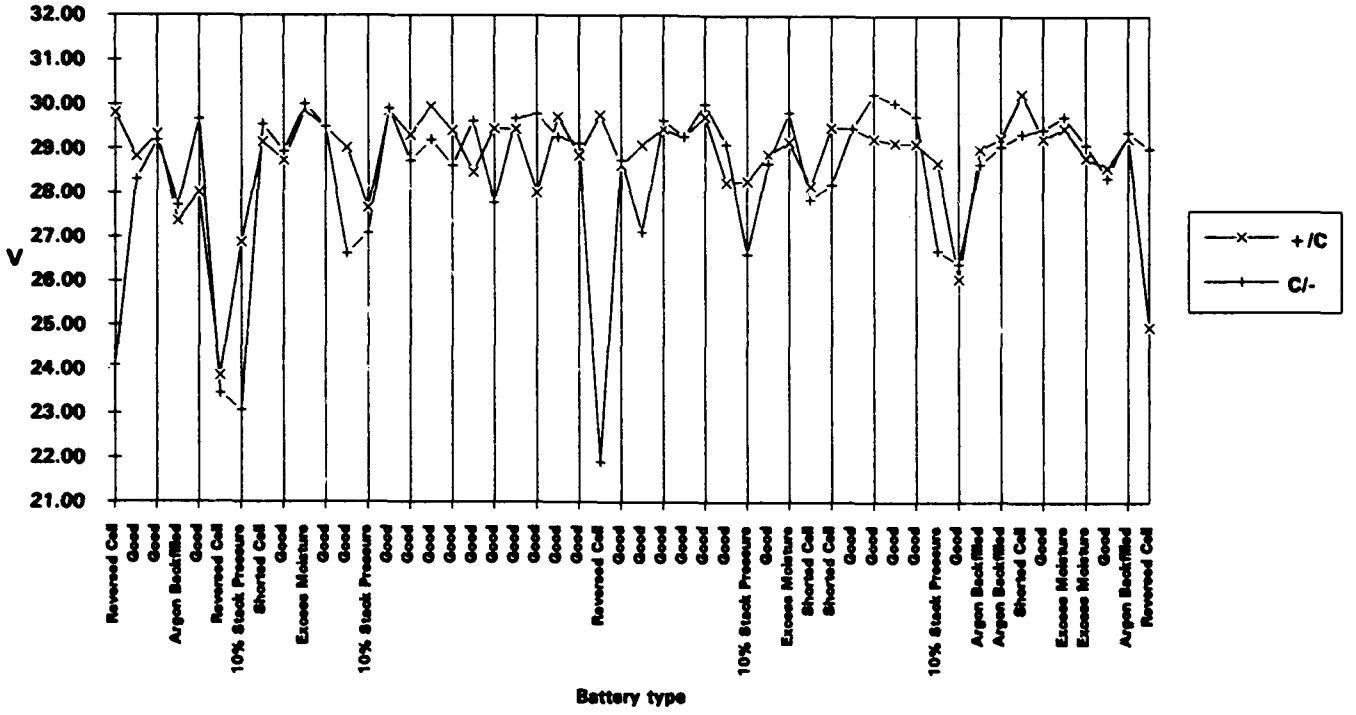

Figure 3 Cold Capacitance versus type of Battery

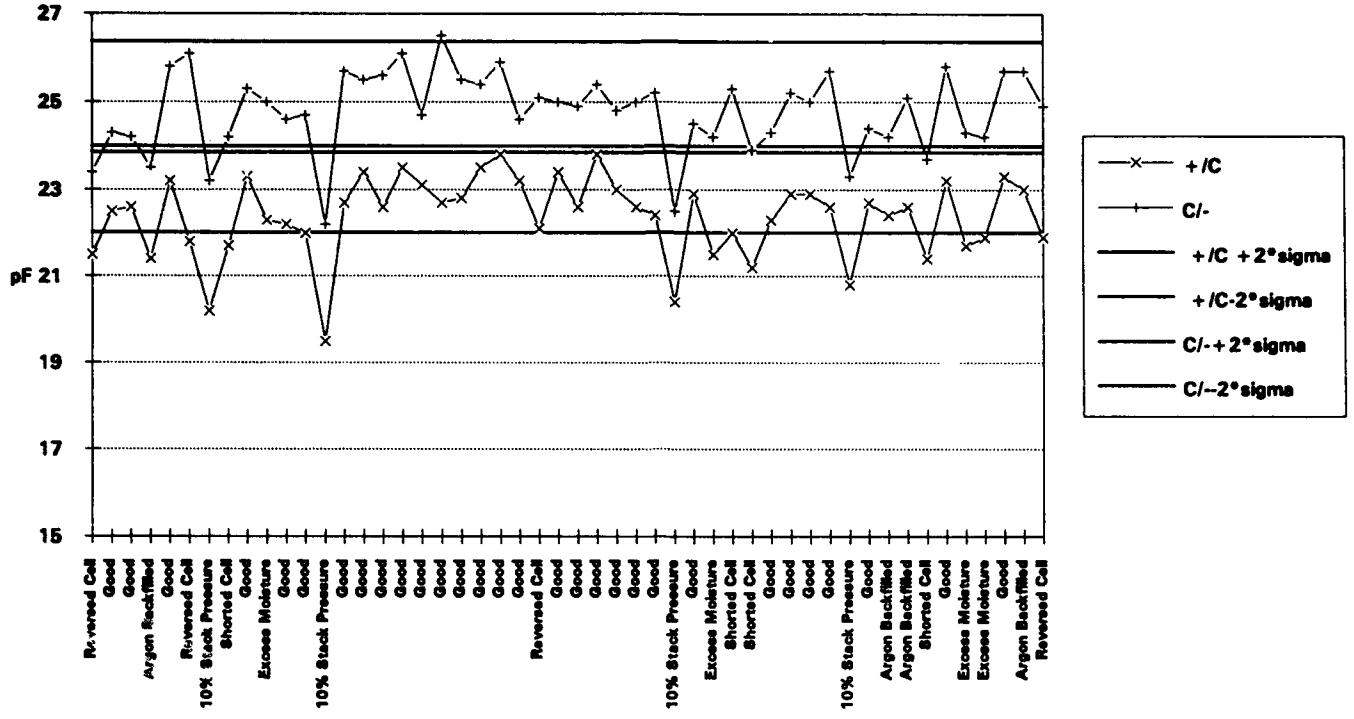

Figure 4 Cold discharge - Voltage measurements over a 1.06 Gohm resistance, +21°C.

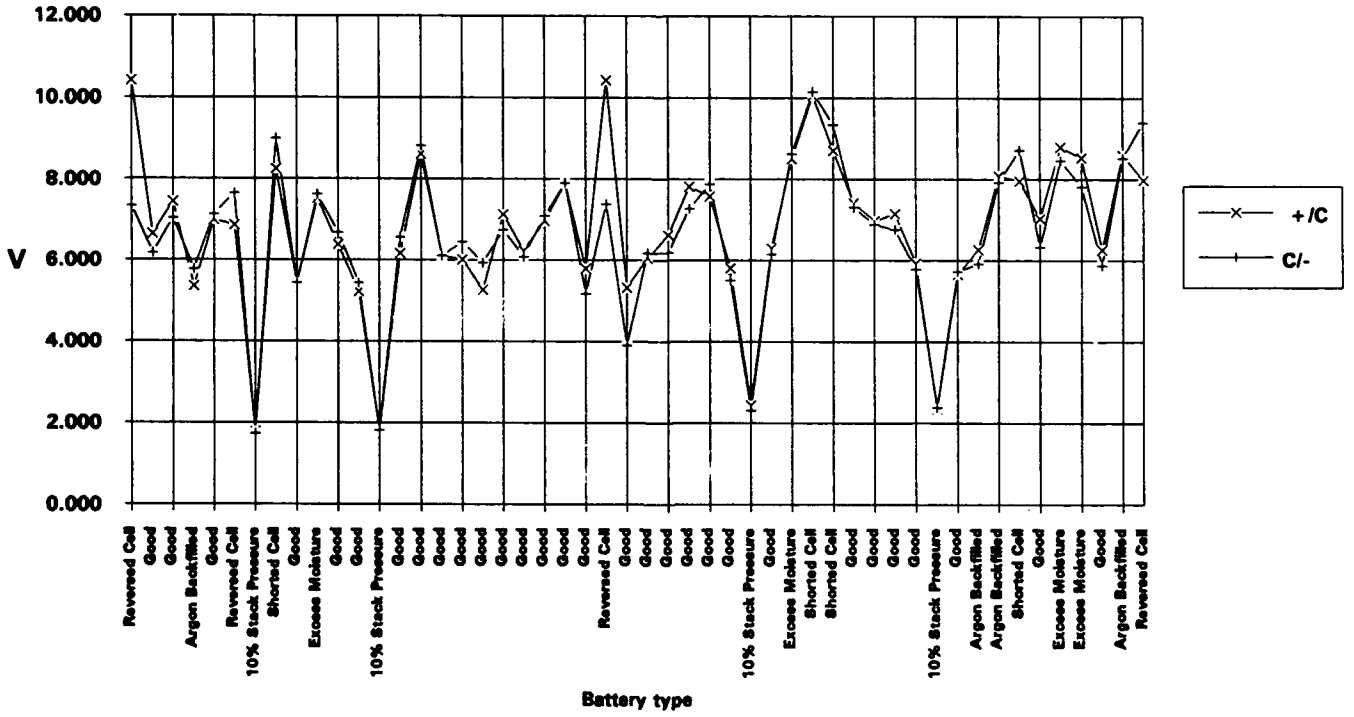

CHARACTERIZATION OF ENERGETIC DEVICES FOR THERMAL BATTERY APPLICATIONS BY HIGH-SPEED PHOTOGRAPHY

Larry R. Dosser
EG&G Mound Applied Technologies*
P. O. Box 3000
Miamisburg, OH 45343
(513)865-4046

and

Ronald Guidotti
Sandia National Laboratory
Battery Development Department
Albuquerque, NM 87185-0614
(505)844-1660

Introduction

Measurement of burn rate, function time, and output properties of components utilizing energetic materials are of primary importance in characterizing not only the reactions of these materials, but also in evaluating the effect of component design changes. High-speed photography at rates of up to 20,000 images per second was used to measure these properties in thermal battery igniters and also the ignition of thermal battery itself. By synchronizing a copper vapor laser to the high-speed camera, laser-illuminated images recorded details of the performance of a component in a unique fashion.[1,2,3] The output characteristics of several types of hermetically-sealed igniters using a $TiH_x/KClO_4$ pyrotechnic blend were measured as a function of the particle size of the pyrotechnic fuel and the closure disc thickness. The igniters were filmed under both ambient (i.e., unconfined) and confined conditions. Recently, the function of the igniter in a cut-away section of a "mock" thermal battery has been filmed. Partial details of these films are discussed in this paper, and selected examples of the films will be displayed via video tape during the presentation of the paper.

Experimental

Two compositions of the pyrotechnic blend, either 33% TiH_x/67% $KClO_4$ or 41% TiH_x/ 59% $KClO_4$ by weight, were used in the igniters. Two particle sizes of the TiH_x, designated as coarse and fine, were also used in the pyrotechnic blend. The coarse material had a mean diameter of 8 microns and the fine material had a mean diameter of 3 microns. The igniters were hot-wire ignited using a 1-ohm bridge and a firing current of 3.5 amps.

The experimental configuration used to record the high-speed photographs of the energetic materials and components is shown in Figure 1. The beam from the copper vapor laser is compressed by a spherical-cylindrical lens combination to form a "laser sheet" that passes across the top of the component. The copper vapor laser operates at a pulse repetition rate of 6 kHz, with an average power of approximately 30 watts. The short pulse width of the laser, about 30 nanoseconds, provides illumination for unique stop-action photographs. The height of the laser sheet is approximately 10 inches, and the camera is positioned to view the component normal to the plane of the laser sheet.

*EG&G Mound Applied Technologies is operated for the U. S. Department of Energy under Contract No. DE-AC04-88DP43495.

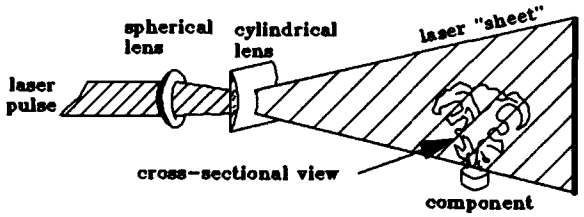

FIGURE 1
HIGH SPEED FILMING WITH COPPER VAPOR LASER ILLUMINATION

The sheet lighting is a particularly useful technique for filming functioning thermal battery igniters. As the igniter functions, the smoke, particulates, and sometimes the closure disc pass through vertically through the laser sheet. Light scattering from the laser sheet is recorded by the camera, and effectively views the internal structure of the flame. The high speed camera was equipped with a rotating prism designed to record two images per frame of film. Since there is only one trigger pulse to the laser for each frame of film, each frame records both a laser-illuminated image and a nonlaser-illuminated image. This permits a ready comparison of each individual igniter, and illustrates the extra information recorded by using the laser. This additional information would be lost if only the visible light generated by the igniter were used to record the details of the igniter function.

Additional high speed filming without copper vapor illumination was done to record the functioning of the igniter in a "mock" thermal battery. A drawing of the "mock" thermal battery is shown in Figure 2. The $Fe/KClO_4$ heat pellets in the stack are separated by stainless steel spacers. The heat pellets contained 88% Fe and 12% $KClO_4$, and were pressed to 55% of theoretical density. The half-battery stack is compressed between graphite blocks machined to accept the heat pellets. The graphite blocks are placed in a steel frame and held tightly in place with a 0.25-inch *thick* lexan^R top and front. The thermal battery igniter fires down through the "battery center" hole defined by the half hole in the heat pellet and the half hole in the lexan^R front. This configuration approximates the environment that the

functioning igniter would experience in an actual thermal battery. The high speed camera was placed as close as possible to the "mock" battery, and with the aid of closeup lenses, high speed films at 6,000 images per second were taken of the ignition process.

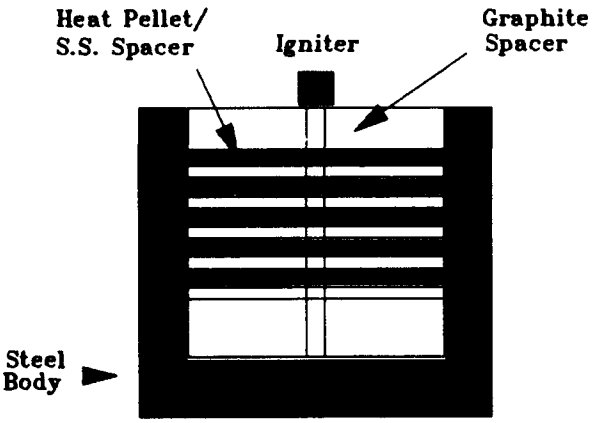

FIGURE 2
"MOCK" THERMAL BATTERY

Results

Many thermal battery igniters were filmed using copper vapor laser illumination. Perhaps the most striking of these results compares identical igniters with the only change being the particle size of the fuel in the $TiH_x/KClO_4$ pyrotechnic blend. Mound currently is the only source for these pyrotechnic blends. Figures 3 and 4 are representative frames from the high speed film of two igniters. Frame no. 7 was selected from the each high speed films, and represents an elapsed time of 1.2 msec after closure disc rupture. Figure 3 shows the output of the igniter loaded with the coarse TiH_x fuel and Figure 4 shows the same type of igniter loaded the fine TiH_x fuel. The difference is striking. The coarse material exhibits a large number of hot particles that continue to burn for a relatively long period of time (more than 3 msec after closure disc rupture). The igniter shown in Figure 4, however, shows mostly burned material and essentially no hot particles. This indicates that most of the fuel was consumed prior to closure disc rupture. The burn time for this igniter is only about 1 msec.

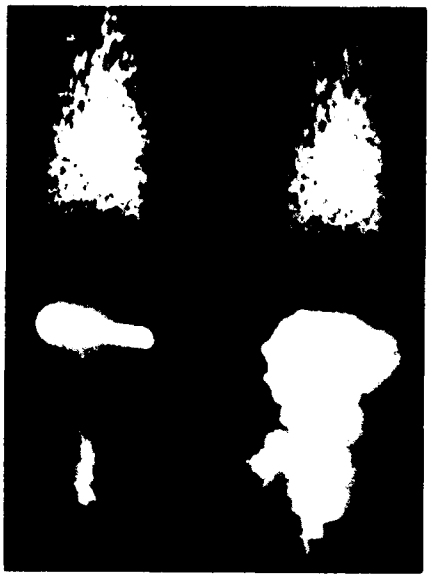

FIGURE 3
COARSE PARTICLE, FRAME 7

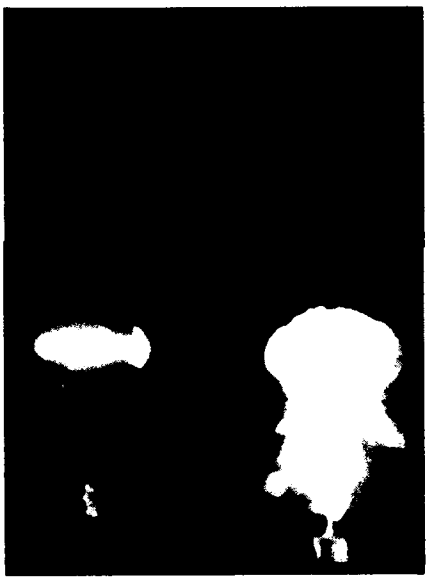

FIGURE 4
FINE PARTICLE, FRAME 7

The function of these igniters in a thermal battery, and the mechanism by which they ignite the battery heat pellets, are of fundamental importance. Results from the ignition of the "mock" battery are shown in Figure 5. There is considerable illumination from the igniter, and hot, luminous gas can be seen propagating between the heat pellets. A detailed frame-by-frame analysis of these films indicates that the pellets may be igniting by the hot gas. In order to more accurately evaluate this hypothesis, the photography must be done at greater magnification. The relative impact of hot gases versus hot particles on heat pellet ignition would further be elucidated by recording experiments using appropriate igniters to provide the desired output characteristics.

FIGURE 5
SINGLE FRAME FROM HIGH SPEED
FILM OF "MOCK" BATTERY

Conclusion

Considerable characterization can be obtained by the high speed filming of the functioning of thermal battery igniters. Details of the igniter function including particle velocity, amount of hot particles produced, function time, extent of combustion prior to closure disc rupture, and the effect of closure disc thickness can be recorded. Examples of this type of information cannot be shown adequately in the few figures in this paper, but are more readily illustrated by the video tape that accompanied this paper.

The effectiveness of the high speed filming technique for detailing the functioning of thermal battery igniters and the subsequent ignition of the thermal battery heat pellets is evident. Clearly, more filming under a higher magnification, and with different igniters, is required to determine whether the heat pellet is ignited by hot particles or by the hot luminous gas produced by the igniter.

References

1. "Ignition and High Speed Photography of Energetic Materials with a Copper Vapor Laser," L. R. Dosser, J. W. Reed, T. C. Girmann, and M. A. Stark, Proc. International Conference on Lasers '87, 770, (1987).

2. "High Speed Photography Energetic Materials and Components with a Copper Vapor Laser," L. R. Dosser, J. W. Reed, and M. A. Stark, Mat. Res. Soc. Symp. 117, 239(1988).

3. "Laser Illuminated High Speed Photography of Energetic Materials and Components with a Copper Vapor Laser," L. R. Dosser, J. W. Reed, and M. A. Stark, Proc. International Conference on Lasers '88, 655,(1988).

Aging Effects and Failure Modes in Thermal Batteries

Harlan L. Lewis, Michael D. Chatelain, Vernon L. Hammersley
Naval Surface Warfare Center, Crane Division
300 Highway 361, Code 609
Crane IN 47522

Introduction

Thermal batteries are energy storage devices which are often presumed not to age under normal ambient storage conditions because they are (1) considered to be hermetically sealed and (2) contain solid electrolytes which are of very low conductivity at ambient temperatures. Thus, Tipper and Yalom[1] state that among their advantages over other primary batteries are shelf lives of 10 to 20yr. However, cell level studies at Sandia National Labs[2] have shown that exposure to moist air contamination equal to an anodic weight gain of only 4% is sufficient to lead to cell failure on test, characterized by (1) higher than normal peak voltage at activation and (2) shorter than normal life during discharge. Recent work at NAVSURFWARCENDIV Crane has indicated that a combination of thermal and mass transport conditions simulate real storage aging effects. Natural internal chemical degradation processes such as auto-oxidation of heat pellets and anodic reactions with entrapped oxygen and nitrogen in the presence of catalytic moisture liberated by mica insulators and separator materials occur more rapidly at elevated temperatures (up to 180F), leading to loss of specification capacity at younger than expected shelf ages.

Of greater significance, though, is reaction with ambient air which may leak into the battery. Two questions arise with respect to loss of capacity in this case. First, how much reactive moist air must be taken up to produce a significant decrease in capacity. Second, on which components in the battery is the leaked moist air having its greatest impact.

At NAVSURFWARCENDIV Crane, studies were initiated to determine at what level of weight gain due to absorbed moist air a class of thermal batteries with lithium-silicon alloy anodes and iron disulfide cathodes would begin to fail the specification requirement for capacity. Then, dissected cells at the same weight gains were submitted to material analysis to determine which components (anode, cathode, electrolyte, heat pellets) suffered the most degradation due to absorbed moist air.

The final evaluation utilizes a mathematical model based on leak rates to predict how many years are required to get the weight gain necessary for a thermal battery to be regarded as no longer reliable, *i.e.*, likely to fail capacity specifications. This then becomes the accepted shelf life.

Experimental

In order to investigate the aging effects of a leak of moist air on thermal batteries on a reasonable time scale, the process is artificially speeded by drilling the case at the top edge with a 3/32in hole, and enclosing the battery in a temperature/humidity chamber with moist air at 80C until a specific weight gain has occurred. The gains studied were 2, 4, 6, and 8% of the total anode weight (since the most active getter in the battery was expected to be the anode, based on the Sandia[2] studies). When a desired weight gain was achieved, the battery was resealed with a high vacuum epoxy resin and function tested for requirement failure.

To then evaluate the effects of the reactant gases on the principal battery components, a new battery which had been subjected to the largest weight gain, 8%, was dissected in a dryroom at the conclusion of the weight gain and the components were transferred immediately to the selected instruments for analysis. The analytical methods chosen included x-ray diffraction (XRD), emission spectroscopy (ES), and x-ray photoelectron spectroscopy (XPS). In addition, individual components were vacuum baked to determine moisture content, and bomb calorimetry (BC) was performed on heat pellets to determine potential loss of calorific output.

Results and Discussion

A sample of insulating disks, wrap, and tape were weighed individually on an analytical balance to 0.1mg precision, vacuum baked at 220F and 10^{-3}torr for 48hr, and then reweighed. In comparison to their initial weight before baking, there was no significant weight change. A similar experiment, conducted on electrolyte samples, yielded similar results. The heat pellets were burned in a bomb calorimeter and the data compared to fresh heat powder data; no significant change in calorific output was observed. Since the cathode material is even less likely to getter any of the reactive gases than those components already mentioned, it was not evaluated by vacuum baking.

Samples of electrolyte wafers from the top and bottom of the cell stack were analyzed by ES; the major elements found were Li, Mg, and Ca. Examination by XRD showed MgO, LiF, and LiBr. No significant difference in diffraction patterns for wafers from the top and bottom of the cell stack was observed. No evidence for significant amounts of hydrated salts was found.

Thus, it seemed likely that the principal absorption of reactive gases would be through chemical reaction with the lithium anodes. Examination of the anodes by XPS with depth profiles (DP) was performed because two questions were important: (1) to what extent were the contaminants spread over the anode surface, and (2) to what depth did the contaminants penetrate the anode.

In the XPS experiments, the surface edge of the bottom disk was examined first. A sector 1.5mm in from the edge was chosen which had a slight purple-red cast; a survey spectrum (Fig. 1)

showed strong oxygen and carbon peaks, and a weak nitrogen peak, typical of surface contamination from exposing the sample to ambient air. When this region was sputtered with argon ions for 10min at 2min intervals, the carbon quickly disappeared while oxygen and lithium contents rose (Fig. 2). As sputtering was continued, the percentage of Li, O, and Si changed as shown in Figs. 3-5. The continued detection of oxygen during sputtering, to an eventual depth of 1.5-2.5x10⁴Å (0.06-0.10mil) in Fig. 3 is most likely an edge effect in the sampling technique, so the depth probe was probably seeing essentially pure alloy beyond a depth of ~5x10³Å (0.02mil). Also it is noted in Figs. 4 and 5 that the alloy composition is heterogeneous, as shown by the erratic data values for Li and Si. Finally, during sputtering it was observed that each time the sample was allowed to rest between sputter intervals for more than 10-15min, the O-peak recovered to two well-defined peaks. The lower binding energy peak (attributed to oxide-O) gradually became more intense with depth than the higher (attributed to hydroxide-O), and in Fig. 6 is presented a montage of O-peaks to exhibit the gradual shift from hydroxide to oxide oxygen with increasing depth. In this figure, plot 244-2 shows one predominant peak for an early depth profile prior to sputtering while 244-8 is after 30min sputter. Then 246-2 shows the oxygen peak recovery prior to the next sputter interval, after the sample had rested, exhibits two peaks with the higher energy peak the larger. After substantially more sputtering, 256-2 shows the oxygen recovery with a shift in percentage to the lower energy peak (oxide-O), and 256-8 shows the O-peak at the end of this sputter period.

The next position on the sample examined was 5.5mm in from the outer edge. In Fig. 7 is a plot of oxygen content, where it is observed that the %O starts at a substantially lower value, decreases more rapidly with depth, and levels out at a somewhat lower value than for the 1.5mm position in Fig. 3. The DP for this sample was taken to about 4.5x10⁴Å (0.2mil), and the same erratic composition values for Li and Si were still observed, indicating continuing inhomogeneity.

Conclusions

The minimum weight gain from moist air which causes a lithium silicon/iron disulfide thermal battery to fail its capacity requirement appears to be about 4%. This percentage of weight gain is dependent on the load profile and extra capacity built into the battery, and is consistent with a worst case percentage (minimum amount of weight gain allowable). Batteries which had a 2% weight increase still met this specification.

No effects of exposure to moist air of any significance were found for any of the components of the thermal batteries except the anodes, in the comparisons as described in the Results section above. The anode degradation by moist air was most pronounced at the outer edges and decreased rapidly toward the center of the plate surface. The depth of penetration appeared to fall off rapidly with distance from the edge. It was also noted that the anodes closest to the drilled hole exhibited an irridescent coloration across the anode surface. This phenomenon decreased in intensity as one proceeded from the plate nearest the hole to the plate furthest away.

The anode alloy samples were found to be heterogeneous in composition for Li and Si. Also, substantial mobility of contaminating reactants was noted for freshly exposed alloy surface, indicating that the reactive agents can be passed across the surface of the anode readily as soon as fresh surface is available. From these observations it is concluded that the entire anode surface is quickly covered with an oxide/nitride film while penetration into the anode occurs more slowly and primarily at the outer edge of the disks. Evidently the loss of 4% of the anode by weight is sufficient to cause the battery to fail its capacity requirement.

References

1. F. Teppler and D. Yalom, "Thermal Batteries," Handbook on Batteries and Fuel Cells, D. Linden, Ed., McGraw-Hill 1984, 40-1.
2. Sandia National Labs, "Capability and Accelerated Aging Study for Li(Si)/FeS_2 Thermally Activated Batteries", document SAND83-1081 of DEC83.

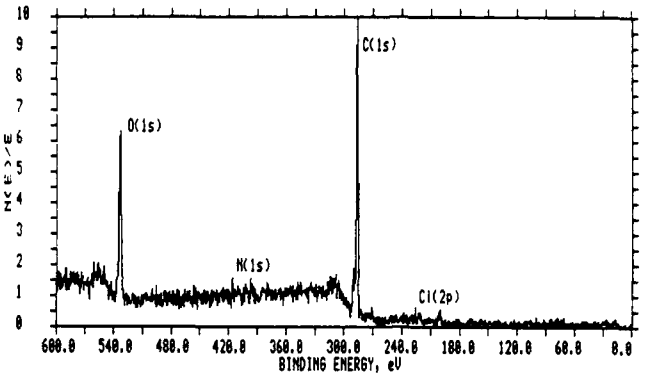

Figure 1. Sample 1, position 1 (1.5mm); initial survey spectrum.

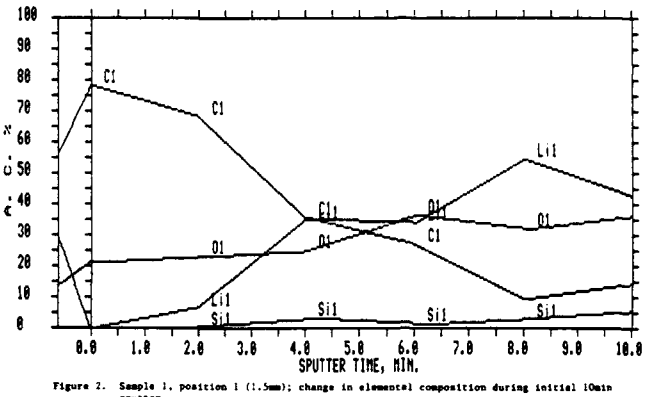

Figure 2. Sample 1, position 1 (1.5mm); change in elemental composition during initial 10min sputter.

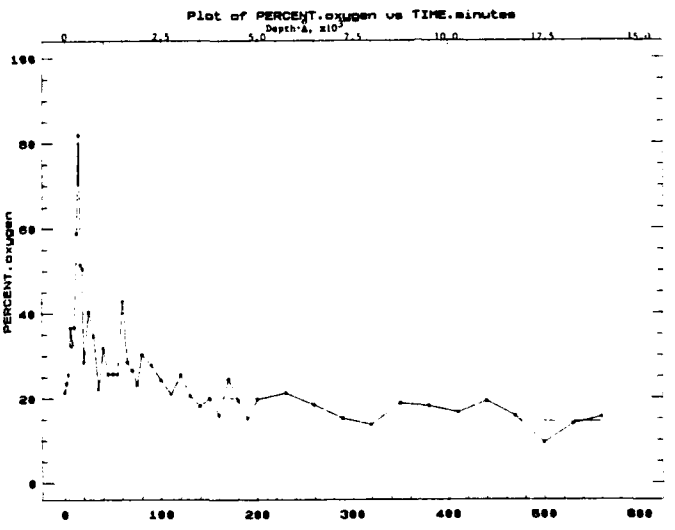

Figure 3. Sample 1, position 1; change in oxygen content with sputtering time and depth.

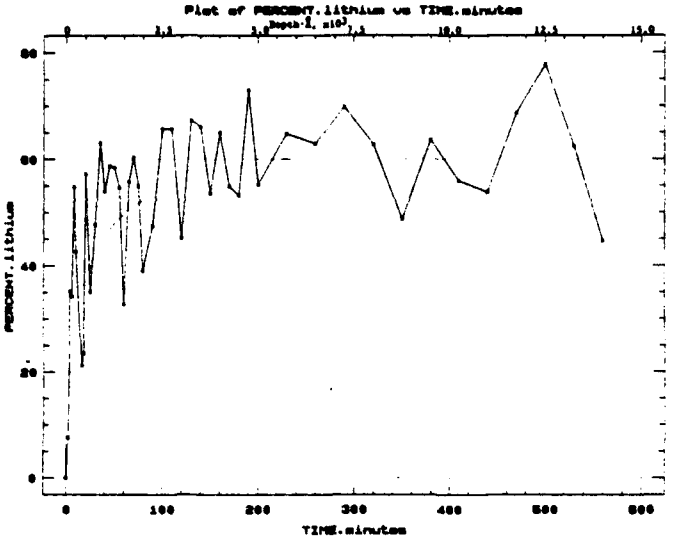

Figure 4. Sample 1, position 1; change in lithium content with sputtering time and depth.

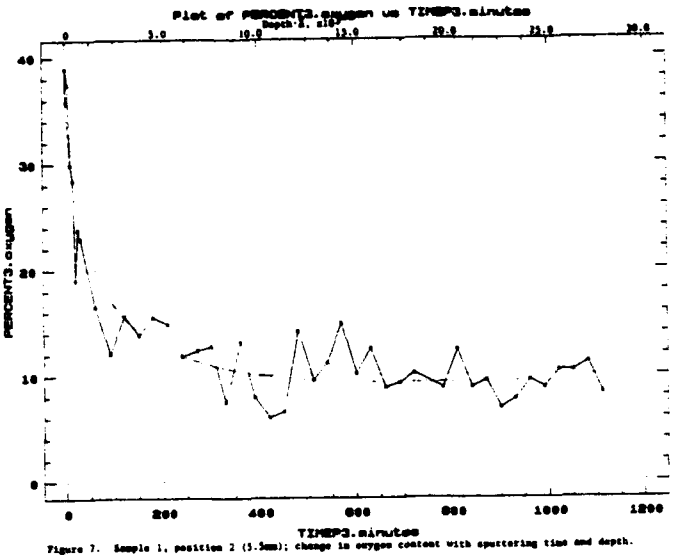

Figure 7. Sample 1, position 2 (5.5mm); change in oxygen content with sputtering time and depth.

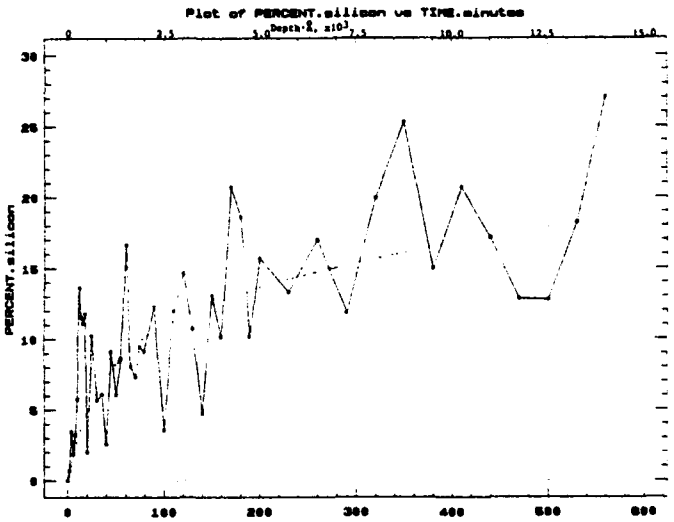

Figure 5. Sample 1, position 1; change in silicon content with sputtering time and depth.

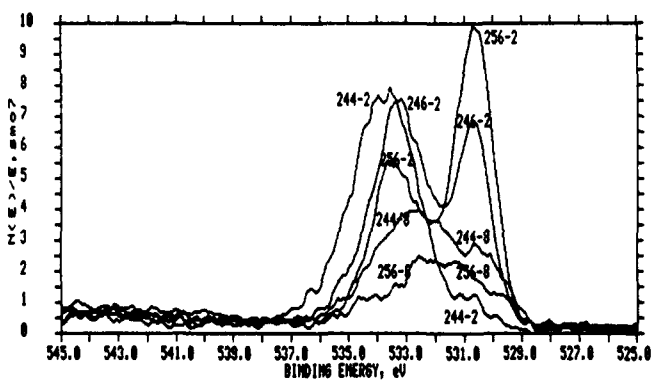

Figure 6. Sample 1, position 1; montage of oxygen spectra at successive sputter depths.

Heat Source for Thermal Batteries: Study on the Coagulation Process

Elisha Rabinovitz, RAFAEL, Haifa, Israel
Chaim Yarnitzky, Department of Chemistry, TECHNION, Haifa, Israel

Introduction

In almost all thermal batteries either the heat source itself or the ignition transfer system is made of zirconium metal powder as fuel, brium cromate as oxidizer and asbstos as a support.

During the production process, these powdered components are dispersed in water. The particles in the dispersion collide, and tend to aggregate. The suspension is filtered, and sheets of a mixed, paper-like material, which can be used as a heat source, result from this process. The aim of this study was to characterize the mechanism of the coagulation process taking place in this heterogeneous system. The research program has been divided into two parts. The first part deals with some electrochemical interface characteristics for each of the components involved. In the second part, the interaction between heterogeneous particles is studied. Defining the main parameters of this process may lead eventually to the replacement of the existing system.

Inter-particle forces

In a dispersion of fine particles in a liquid, frequent collisions between particles occur. Whether such interactions result in a permament contact or whether the particles rebound and stay free is determined by the forces between them. According to the DLVO theory two types of forces are usually considered: Van der Waals attraction forces and the double-layer electrostatic repulsion force. The zeta potential which is the electrical potential at the slip plan between particles and medium can be considered as the potential determining the magnitude of the electrostatic force. Zeta potential becomes zero at the Iso Electric Point (i.e.p.) which is the concentration of the Potential Determining Ions (p.d.i.) at which the number of the positive charges on the surface equals the number of the negative ones.

In addition, steric effects and surface reactions may play an important role in such a process and affect the stability of the dispersion.

The total energy approximation for the interaction energy of two different spheres of radii a_1 and a_2, surface potentials ϕ_1 and ϕ_2, with a distance H between their surface, can be written as:

$$V = \alpha \left(\frac{-A}{12H} + \frac{\epsilon D}{4} f \right)$$

$$\alpha = \frac{a_1 \times a_2}{a_1 + a_2}$$

where A, the net Hamaker constant for materials 1 and 2 in medium 3; ϵ is the dielectric constant of the medium. The repulsion function for the case of constant potential is given by:

$$f = 2\phi_{s1}\phi_{s2} \ln \frac{1+\exp(-\kappa H)}{1-\exp(-\kappa H)}$$

$$+\left(\phi_{s1}^2 + \phi_{s2}^2\right) \ln\left[1-\exp(-\kappa H)\right]$$

Experimental Methods

Data on the powdered materials used in this work are shown in Table I.

Table I

Data of the powders used in this experiment

Powder	Grade	Surface area (sq.m./gr)
Barium Chromate	ALFA	3.05
Zirconium	ALFA	0.23
Asbestos	Chrysotile	11.3

Dispersions of these powders (2 wt% in 0.002M KNO_3 solution (unless otherwise specified) were prepared using freshly distilled water in air-tight containers. An ultrasonic processor was then used to deflocculate the dispersions. The pH of the dispersion was adjusted by adding HNO_3 or KOH.

The zeta potential was determined by microscopic, electrophoretic mobility measurement method, using a ZETAMETER apparatus with a flat cell 10X2 mm and a voltage of 10 V/cm. The i.e.p. was determinated by running two sets of experiments. In the first set, a number of measurements at different p.d.i, concentrations (in a 0.002N KNO_3 solution) has been done, and a curve of the zeta potential vs concentration has been plotted. In the second set, the same dispersion was prepared using 0.01M KNO_3 solution. I.e.p. is the point were the two curves intersect at the point of zero mobility.

Results and discussion

The case of Barium Chromate

The interfacial electrostatic chemistry of the system $BaCrO_4$/solution involves various types of surface species. Each of them can react according to the following set of reactions:

$$CrO_4^{-2} + H^+ \rightleftharpoons HCrO_4^-$$

$$HCrO_4^- + H^+ \rightleftharpoons H_2CrO_4$$

$$Cr_2O_7^{=} + H_2O \rightleftharpoons 2HCrO_4^-$$

and in basic solution:

$$Cr_2O_7^{=} + OH^- \rightleftharpoons HCrO_4^- + CrO_4^{=}$$

$$HCrO_4^- + OH^- \rightleftharpoons CrO_4^{=} + H_2O$$

Most of the reactions taking place at the surface involve adsorption of proton, and that is why protons have also to be considered as p.d.i.'s (in addition to barium and the chromate ions).

The dependence of the zeta potential of $BaCrO_4$ on the pH of the solution is described in figure 1:

As shown, the zeta potential is negative over a wide range of pH. The i.e.p. is found to be at pH value of 4. Based on the equilibrium constants of all the above given reactions, the concentration of barium and chromate species in the solution can be determined for each pH value. At the i.e.p. the concentration of the barium ion is about $4 \cdot 10^{-4}$M which corresponds to a chromate concentration of about $6 \cdot 10^{-7}$M.

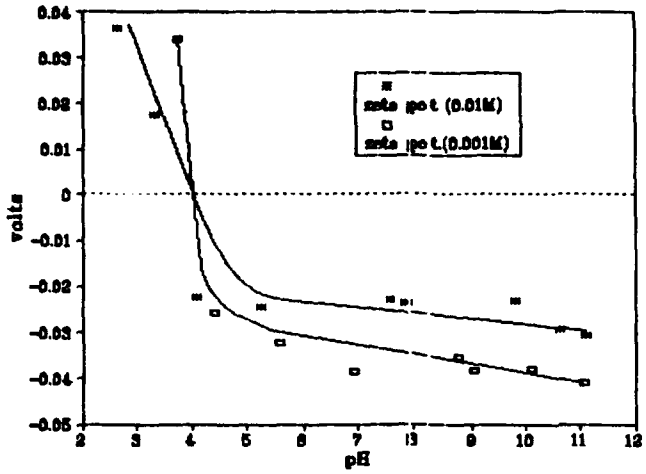

Figure 1. Zeta Potential of $BaCrO_4$ vs. pH

At pH values above 5, the zeta potential remains approximately constant. It is assumed that there is no specific adsorption of hydrogen, hydroxyl or $HCrO_4^-$ ions.

As all solutions are saturated with $BaCrO_4$, the concentration of the barium ion can be calculated for every pH value. Accordingly, figure 1 can be redrawn again as zeta potential vs $p[Ba^{+2}]$. This can be compared with a second experimental set in which the zeta potential of $BaCrO_4$ is measured at a constant pH value of 4.5 (the concentration of p.d.i. in the second set of experiments is changed by adding K_2CrO_4 or $Ba(NO_3)_2$ to the solution).

As can be seen in figure No 2, the zeta potential at constant pH is found to be negative over a wider range of barium concentrations. The i.e.p. is found at the $p[Ba^{+2}]$ value of 2.2 which corresponds to a barium concentration of about $6 \cdot 10^{-3}$M or chromate concentration of $4 \cdot 10^{-8}$M.

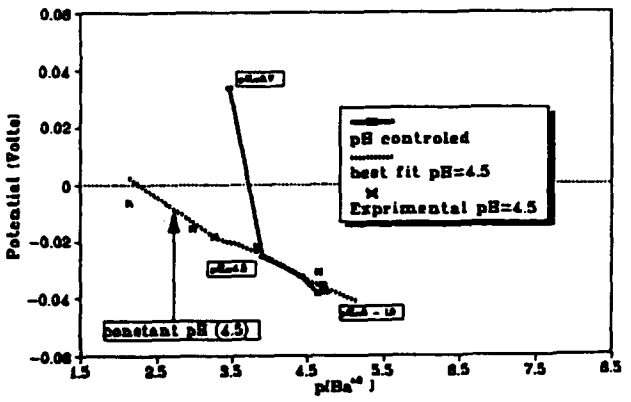

Figure 2. Zeta potential of $BaCrO_4$ vs barium concentration.

The above described results are quite different from those of the previous experiment, wherein the pH of the solution has been varied. The difference between the behaviour of the zeta potential at constant pH and at variable pH can not be related to the specific adsorptin of hydrogen/hydroxyl ion nor to the specific adsorption of bichromate ion. Let us examine the role of the dichromate ion ($Cr_2O_7^{-2}$) in this system.

Figure 3 describes the chromate/dichromate concentration ratio. As shown in Figure 3, the concentration of dichromate at pH values above 4.5 is negligible. At pH values under 4.5 a significant amount of chromate ion are converted into dichromate.

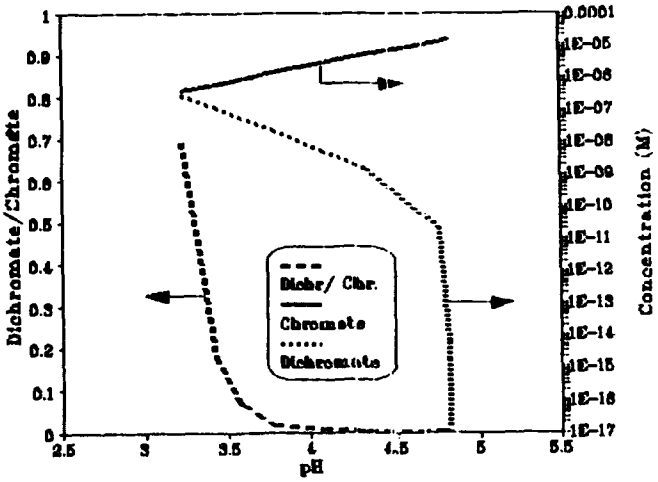

Figure 3. Chromate/dichromate concentration ratio vs. pH

In contrast to all others species in the solution, dichromate can penetrate into the surface of the $BaCrO_4$ crystal lattice. At the same time, the dicromate species in the solution has to be in equilibrium with the dichromate available in the crystal lattice. As the pH of the solution decreases below 4.5, and the solution is enriched in dichromate ions, the concentration of these ions at the crystalline surface must also increase. The change in surface structure seems to be the reason behind the change in the i.e.p.

The zeta potential of zirconium

Zeta potential of the zirconium dispersion has been measured over a wide range of pH. As shown in figure 4, zero electromobility (i.e.p.) is found at pH 4.5.

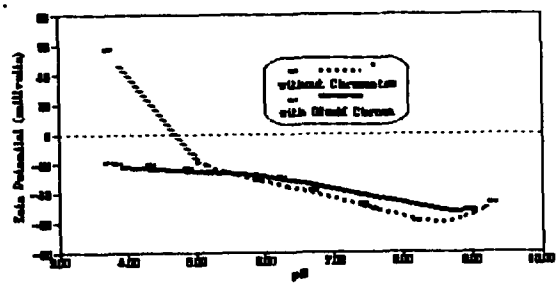

Figure 4. Zeta ptential of colloidal zirconium in 0.002M KNO_3

The zeta potential is found to be negative over all the pH range in the presence of the $CrO4^{-2}$ ion. We assumed that there is a specific adsorption of chromate ion on the surface of the zirconium particles.

The Water/Asbestos Dispersions

When asbestos is dispersed in water, some complex physical and chemical reactions take place. For example, when chrysotile asbestos is dispersed in distilled water, the increase in pH and the concentration of dissociated ions released continues to grow over a period of days. Magnesium is the main ion released. This process can explain why the zeta potential of freshly prepared asbestos dispersion is over +50mV while the zeta potential of washed asbestos is negative. During the production of heat sources based on asbestos, there is always a stage of disintegration involving intensive mixing. During this stage, the dissociation rate increases and positive zeta potential is assumed.

Interparticle interaction energy

Zr-Zr interparticle interaction energy

When a dispersion of zirconium, barium chromate and asbestos is prepared, three types of interparticle interactions may occur: interaction between two identical particles (i.e. two zirconium particles), interaction between two different particles (i.e. a zirconium particle with a barium chromate one) and an agreggate containing a mixture of two which interacts with the third one. A microscopic inspection proves that all possible interparticle interactions occur, leading to coagulation. The only exception is that no aggregate of zirconium particles has been found. In this section we shall discuss the condition for hetero-coagulation of dissimilar dispersions, based on the zeta potential measurements.

Figure 5 describes the interparticle interaction energy of two identical zirconium particles having 1.1μ in diameter, dispersed in a 0.002M neutral KNO_3 solution. The heavy solid line in the figure is the total interaction energy which is the sum of the Van der Waals attraction force (the dashed line) and the electrostatic repulsion force (upper solid line).

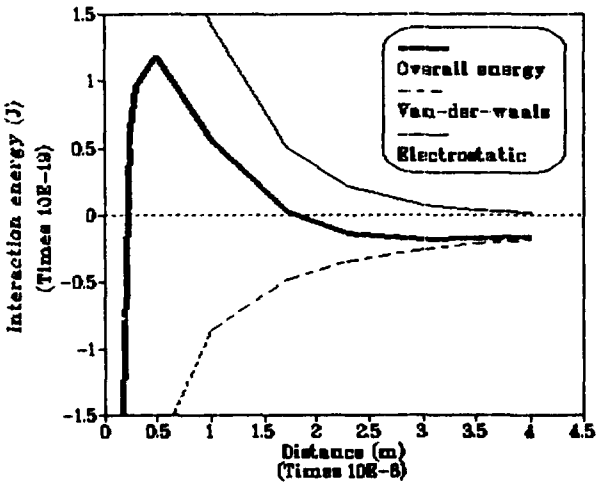

Figure 5. Zr - Zr interaction vs distance

As shown in Figure 5, a high energy barrier exists at a distance of about 10nm, which prevents rapid coagulation (the dispersion is stable). In the same way the interaction energy of particles has been calculated for zirconium dispersions in solutions having different pH values in the range 3.5-8.5.

We found that in the basic pH range and in the pH range below 4, there is a high energy barrier that prevents the coagulation procces. Fast coagulation is expected in the pH range 4-7.

To prove the above prediction, experiments have been conducted in which dispersion of zirconium were prepared with pH ranging from 3 to 9. For each dispersion, sedimentation time has been measured. It has been found that in the pH range of 4-6.5 sedimentaton was fast while outside this range sedimentaton was 2 to 5 times slower.

The interaction energy between zirconium particles in a solution saturated with barium chromate species is of special interest. In the basic pH range, the energy barrier remains. In the lower pH range, due to specific adsorption of chromate ion to the zirconium surface, the barrier is lowered and rapid coagulation occurs.

Chromate - Zirconium interaction

Figure 6 describes the interparticle interaction energy between a $BaCrO_4$ particle and a zirconium one in pH 7. It can be seen that a high energy barrier exists preventing a permanent contact. Yet, before the barrier, a secondary local minimum exists so that unstable flocs can be formed.

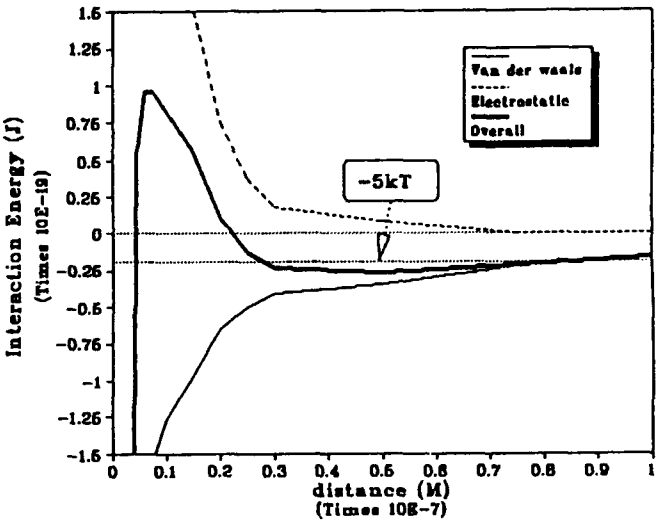

Figure 6. Zr - $BaCrO_4$ interaction (pH=7)

Calculating the interaction energy over the entire pH range shows that there are no barriers in the lower pH range, and flocculation is expected in the basic range. It is also found that there are no barriers when two identical $BaCrO_4$ particles interact.

Conclusions

The mechanism of the heterocoagulation process taking place during the production of zirconium/$BaCrO_4$/asbestos can be understood on the basis of DLVO theory.

It has been found in the case of a dispersion containing Zirconium and $BaCrO_4$ particles that in the pH range of 5.5 and below there is no energetic barrier which can prevent the coagulation of various combination of particles present in the mixture. In such a case the composition of the aggregates is determined statistically, by the number of collisions between the particles which in turn is determined by the composition of the dispersion. In the basic pH

range of such a dispersion, an energy barrier that prevents a permanent contact between two identical zirconium particles exists. Another barrier is also found in the collision between zirconium and $BaCrO_4$ particles. A local minimum in the energetic barrier enables the heterocoagulation.

In the case of zirconium-$BaCrO_4$-asbestos dispersion, under intensive mixing the pH is high and the zeta potential of the fibers is positive. When negatively charged zirconium or $BaCrO_4$ particles penetrate the asbestos gel, they are immediately bound to the fibers. But, unlike the $BaCrO_4$ particles, the zirconium particles prevent other identical particle from binding to each other because of the high energy barrier. Indeed, microscopic inspection has provided evidence of the presence of aggregates made of asbestos fibers and chromate particles, asbestos fibers with zirconium-chromate mixture and even fibres with a single zirconium particle with no zirconium aggregate.

References

(1) R.J. HUNTER (1981). ZETA POTENTIAL IN COLLOID SCIENCE ACADEMIC PRESS.

(2) W.H. VAN RIEMSDIJK, L.C. DE WIT, L.K. KOOPAL, G.H. BOLT (1987) METAL ION ADSORPTION ON HETROGENEOUS SURFACES J. OF COLLOID AND INTERFACE SCIENCE, 116 (2) pp 511.

(3) R.P. TISON (1975) J. OF COLLOID AND INTERFACE SCIENCE, 52 (6) pp. 611.

(4) J.T.G. OVERBEEK (1977) RECENT DEVELOPMENT IN THE UNDERSTANDING OF COLLOID STABILITY J. OF COLLOID AND INTERFACE SCIENCE, 58 (2) 408.

(5) G. FRENS, J.T.G. OVERBEEK (1972) J. OF COLLOID AND INTERFACE SCIENCE, 38 (2) 376.

(6) G.M. BELL, G.C. PETERSON (1972) CALCULATION OF THE ELECTRIC DAUBELE-LAYER FORCE BETWEEN UNLIKE SPHERES J. OF COLLOID AND INTERFACE SCIENCE, 41 (3) pp. 542.

(7) J.T.G. OVERBEEK (1990) THE ROLE OF ENERGY AND ENTROPY IN THE ELECTRICAL DOUBLE LAYER COLLOIDS AND SURFACES, 51.

(8) P. CURRERI, G.Y. ONODA, B. FINLAYSON (1979) AN ELECTROPHORETIC STUDY OF CALCIUM MONOHYDRATE J. OF COLLOID AND INTERFACE SCIENCE, 46 (1) pp 170.

(9) R.J. PUGE, J.A. KITCHENER (1971) THEORY OF SELECTIVE COAGULATION IN MIXED COLLOIDAL SUSPENSIONS J. OF COLLOID AND INTERFACE SCIENCE, 35 (4) pp 656.

IMIDE-BASED ELECTROLYTES FOR MEDIUM-TEMPERATURE RESERVE CELLS

C O GIWA

Materials & Structures Department
Defence Research Agency
Farnborough
Hampshire GU14 6TD UK

Abstract

This paper describes a feasibility study on materials for a medium-temperature (200–350°C) reserve primary cell concept, whose activation is similar to that of thermal batteries in that an electrolyte which was solid under storage conditions would be melted to activate a battery. The aim is a reserve battery of high energy density running at medium-temperature and capable of sustaining a current load of about 50mA/cm^2. Electrolytes studied were LiN $(CF_3SO_2)_2$ and LiN $(CF_3SO_2)_2$–$LiNO_3$–$LiCF_3SO_3$. Thermal analysis and resistance measurements have shown that imide – based electrolytes were stable and capable of sustaining reasonable current densities. The anode was lithium–aluminium alloy and potential cathodes included lithiated vanadium oxide (LVO) and manganese dioxide.

Single-cell test results on the combination LiAl / imide – nitrate – triflate – MgO \ MnO_2 show a capacity of 626 coulombs/g MnO_2 at a current density of 25mA/cm^2 at 275°C. This is equivalent to a specific energy of 540 Wh/Kg MnO_2 of active cell component to 0 volts versus 20% lithium–aluminium alloy.

1. INTRODUCTION

In the last 15 years we have seen a growing effort from several research groups [1-5] aimed at investigating thermally activated cells which utilize electrolytes that melt at medium temperatures. Nitrate - based cells appear to have been widely studied because of their high conductivity (2.1 x 10^{-1} ohm^{-1} cm^{-1}). However, electrolytes containing lithium trifluoromethane sulphonimide have been exclusively examined for use in ambient temperature lithium rechargeable cells as a dissolved salt in the electrolyte for liquid electrolyte batteries and for all-solid-state polymer batteries [6-8]. From the latter investigations, it was concluded that imide - based electrolytes offer improvement in the electrochemical and chemical stability for rechargeable and primary lithium batteries. Because of their high conductivity in the molten state and their thermal stability, imide - based electrolytes have been examined in this work for use in medium temperature reserve batteries. Possible applications for such batteries were not rigidly defined at the start of this investigation but, if successful, this battery was seen as a possible competitor to some designs of lithium ambient temperature reserve batteries. The perceived advantage of the proposed battery over the present reserve batteries would be that the electrolyte would be in-situ between the electrodes ready to be activated and would not require physical displacement from a storage container by action of gas pressure or bellows. The proposed battery could therefore have a higher specific energy and / or power density than the present types.

Information on the transport properties of electrolytes, such as stability, viscosity, resistivity and dielectric constant are of paramount importance during the development of both primary and rechargeable systems. Thus, the aim of this study is to investigate the effective resistance of all - lithium salt electrolytes such as lithium trifluoromethanesulphonimide (LiN$(CF_3SO_2)_2$) - lithium nitrate ($LiNO_3$) - lithium trifluoromethanesulphonate ($LiCF_3SO_3$) and to compare results obtained with neat lithium trifluoromethanesulphonimide. The thermal stability and discharge characteristics of these are also discussed.

2. EXPERIMENTAL

2.1 Chemicals

The lithium trifluoromethansulphonimide ("imide") was a gift from 3M (United Kingdom plc); the lithium trifluoromethanesulphonate ("triflate") and LVO [9] were synthesised at DRA, Farnborough. All other materials were bought from Aldrich Chemical Co.

2.2 Thermal Analysis

Thermal analyses were carried out using combined thermogravimetric analysis (TGA) and differential thermal analysis (DTA). The heating rate was 10°C per minute and samples were heated in a helium atmosphere. The thermogravimetric balance used was a Stanton Redcroft STA1OOO. The results are shown in figures 1 to 3.

2.3 Measurements of the resistance of electrolytes

The effective resistances of electrolyte pellets were measured in the single cell tester, in an argon atmosphere. The single cell tester has been described previously [10]. All electrolyte mixtures were pre-fused in the same atmosphere. Two 3OO mg pellets of 19.9% lithium-aluminium alloy were used to form a sandwich, with the electrolyte pellet (3OO mg) between them. These three pellets were put between flat iron current collectors, which were held between mica insulators and were heated to the required temperature. Currents were passed, and the voltages required to drive the currents through the pellets were recorded. From the currents and voltages the effective resistances were calculated. These resistances included not only the resistance of electrolyte, but also those of the two lithium-alloy pellets, the current collectors, and the two anode -electrolyte interfacial resistances. These effective resistances are shown in table 1 and discussed in section 3.

2.4 Preparation of pellets for electrical discharge

The preparation of pellets for electrical discharges has already been described [5]. The electrolytes used in each test consisted of neat imide LiN$(CF_3SO_2)_2$ or a 90:5:5 mixture of the lithium salts lithium trifluoromethanesulphonimide - trifluoromethane - sulphonate - nitrate. Electrolytes were immobilised on 30% magnesium oxide. A lithium - aluminium alloy containing 19.9% lithium obtained from Lithco was sieved to a particle size <212 microns and used as anode. The temperature and currents at which discharges were carried out are shown in the individual discharge diagrams (figures 4 to 6) and discharge results are summarised in table 2.

3. RESULTS AND DISCUSSION

3.1 Effective Resistance and Stability of Electrolytes

Table 1 summarises the result of the resistivity measurements, whilst figures 1 to 3 show the thermal analyses of neat imide and imide - nitrate - triflate mixture. Lithium imide displayed a complex profile on thermal analysis. Two endotherms were found on heating (see figure 1), the first peak at 155°C being due to a phase change and the second peak at 230°C being due to the melting of the imide. When the sample was allowed to cool and reheated only the upper melting point was found (figure 2). The lower endotherm is probably due to a metastable phase; this thermal analysis indicates that lithium imide is stable in the molten state from 230°C to over 350°C and that it is suitable for use in a medium temperature reserve battery.

The thermal analysis of the all - lithium salt imide - nitrate - triflate mixture ("imide-mix") is shown in figure 3; a sharp melting point of 199°C was found and this mixture was stable to over 350°C. Thus imide - mix electrolyte has a wider operating temperature range (over 150°C) than neat imide.

The effective resistances of imide immobilised on magnesium oxide have been compared with that of imide - mix (see table 1). It can be seen that the resistances of imide - mix were lower than those of neat imide. Thus the imide mix should be a better conductor of lithium ions.

3.2 $LiN(CF_3SO_2)_2$ ("imide") electrolyte

Discharge curves for cells based on neat imide electrolyte are as shown in figures 4 to 6, while table 2 summarises the test conditions. The results in table 2 indicate that the energy density achieved with manganese dioxide alone is low. However, it can be seen clearly that the addition of graphite to cathode did improve the conductivity of the manganese dioxide cathode at 275°C. The energy density attained by LiAl \ imide-MgO \ MnO_2-graphite at 50mA/cm^2 is lower than that of imide - mix - based cell; it can therefore be concluded that the former electrolyte can only give reasonable performance at the lower discharge rate. The sloping discharge profile is an indication that the cell was struggling and also the reaction involved was a one electron reduction as shown below:

$$MnO_2 + xLi \longrightarrow MnO_2Li_x \qquad (2.8V)$$

3.3 $LiN(CF_3SO_2)_2$-$LiNO_3$-$LiCF_3SO_3$ ("imide-mix") electrolyte

Typical discharge curves obtained for imide - mix electrolyte with manganese dioxide are also shown in figures 4 to 6. The cell has an OCV of 2.9V, and gave a better performance than the neat imide cell at 275°C and 300°C at 25 mA/cm^2 and also at the 50mA/cm^2 discharge rate at 275°C; it delivered 61.7%, 68.5% and 84.1% more energy respectively. It can be inferred that these results are due to the lower resistances associated with the imide-mix (see table 1). Figure 6 shows the discharge of a LiAl \ imide-mix-MgO \ LVO-graphite cell. An OCV of about 3.15V was observed and it displayed a sloping voltage curve. It can be seen in table 2 that the energy delivered by this cell increased with temperature at the 50mA/cm^2 discharge rate. The cell discharged at 320°C delivered 243 Wh/kg while the one at 340°C gave 287 Wh/kg, i.e. 18.5% more energy.

4. CONCLUSION

A medium temperature reserve cell has been investigated to provide moderate currents (up to 50 mA/cm^2) at temperatures between 200 and 350°C. Electrolyte mixtures containing lithium trifluoromethanesulphonimide ($LiN(CF_3SO_2)_2$) have adequate conductivity for this application. A mixture containing $LiN(CF_3SO_2)_2$, $LiCF_3SO_3$ and $LiNO_3$ was suitable. The most promising cell appeared to be:

LiAl \ $LiN(CF_3SO_2)_2$-$LiNO_3$-$LiCF_3SO_3$-MgO \ MnO_2-graphite

When discharged at 275°C and at 25mA/cm^2, it yielded over 540 Wh/kg MnO_2.

5. REFERENCES

1. Miles, M. H. and Fletcher, A.N. (1980). Thermal battery utilizing molten nitrate as electrolyte and oxidizer. US Patent Appl. No. 11076

2. Bolster, M. E., Embery, J. and Staniewicz, R. J. (1989). Development of low melting electrolyte system for a LiAl/ Ag_2CrO_4 battery, Extended Abstract Proc. Electrochem. Soc. 98-2, p147.

3. Pereira-Ramos, J. P., Messina, R. and Perichon, J. (1986). Electrochemical behaviour of some transition metal oxides in molten dimethylsulphone at 150°C. J. Appl. Electrochem. 16, pp 379-386.

4. McManis, G. E., Miles, M. H. and Fletcher, A. N. (1985). High performance nitrate cell. US Patent Appl. No 6653115.

5. Giwa, C.O., (1993). Feasibility study of sulphone - based electrolytes for a medium - temperature reserve cell concept. J. Power Sources 42, pp 389-397.

6. Dominey, L.A., Goldman, J. L., Koch, V. R. and Nanjundiah, C. (1990). Stabilization of electrolytes for lithium rechargeable batteries. Proc. Electrochem. Soc. 90-5, pp 56-66.

7. Alamgir, M., Moulton, R. D. and Abraham, K. M. (1991). Solid superionic conductors. Proc.Electrochem. Soc. 91-3, pp 131-141.

8. Waddell, J. E., De Witte J. and Alison, M. (3M Company). Private Communication.

9. Faul, I. (1986). Proc. 32nd Int. Power Sources Symp., Cherry Hill, USA, p636

10. Ritchie, A. G. (1993). Power Sources 14, Proc. 18th Int. Power Sources Symp., Stratford - on - Avon, England, p299.

TABLE 1.

RESISTANCES OF ELECTROLYTE PELLETS
(Ohms)

Electrolyte	Binder Ratio %MgO	Temperature(°C)			
		220	260	275	300
Imide - mix	25	3.67	0.40	0.25	0.22
"	30	7.42	1.23	0.38	0.25
"	35	9.90	1.26	1.01	0.95
Imide (neat)	25	21.00	15.22	0.78	0.43
"	30	33.63	23.02	2.38	0.80
"	35	69.76	48.60	4.43	1.18

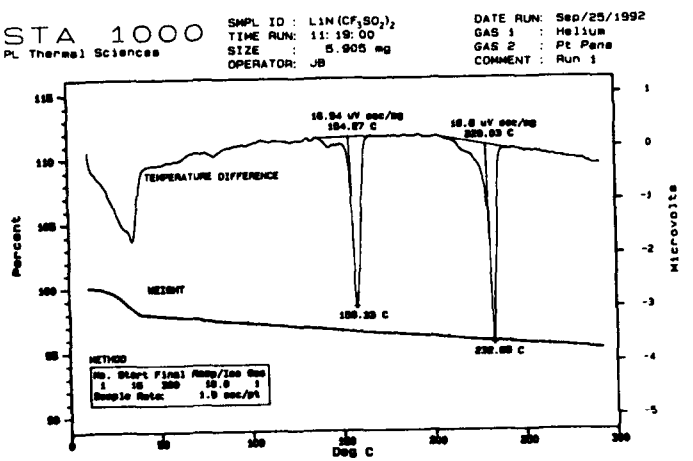

Figure 1 Thermal analysis of $LiN(CF_3SO_2)_2$

TABLE 2

COMPUTATION OF ENERGY FOR SOME IMIDE-BASED CELLS

Cathode / Electrolyte	Temperature °C	Current Density (mA/cm^2)	OCV (V)	Time (min)	Energy Density (Wh/kg)*
MnO_2 - graphite Imide-mix	275	25	2.90	50.5	542.4
MnO_2 - graphite Imide-mix	275	50	2.90	19.0	408.9
MnO_2 - graphite Imide	275	25	2.95	19.5	207.6
MnO_2 - graphite Imide	275	50	2.95	3.0	65.6
MnO_2 - graphite Imide	300	25	2.95	25.5	278.6
MnO_2 - graphite Imide-mix	300	25	2.90	44.5	478.9
MnO_2 Imide	300	25	2.90	14.0	150.4
LVO - graphite Imide-mix	300	25	3.10	35.5	407.5
LVO - graphite Imide-mix	320	50	3.05	10.5	234.0
LVO - graphite Imide-mix	340	50	3.15	12.3	287.0

* Calculated to 0 volts versus 20% lithium - aluminium alloy.

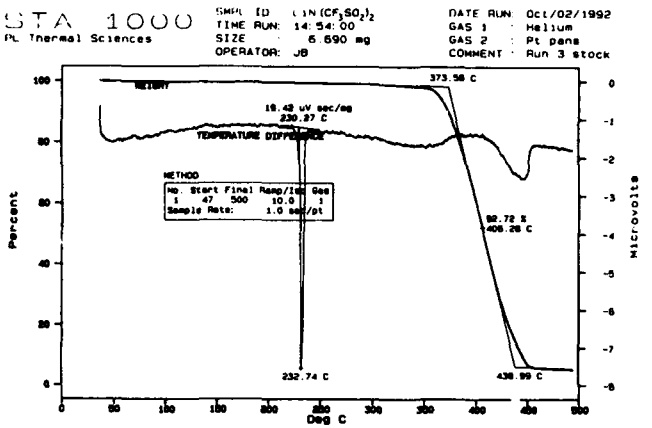

Figure 2 Thermal analysis of $LiN(CF_3SO_2)_2$

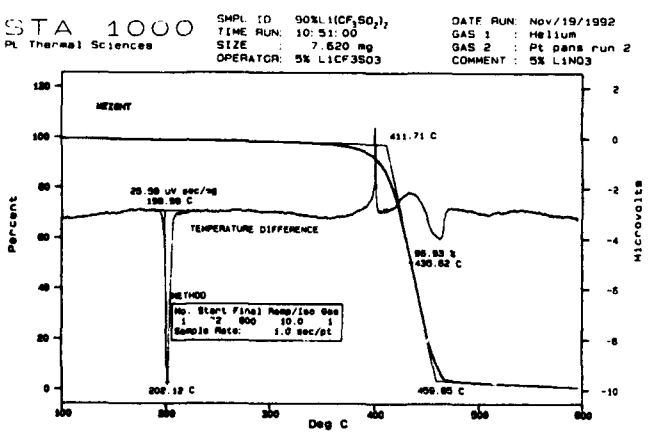

Figure 3 Thermal analysis of imide-mix

Figure 4

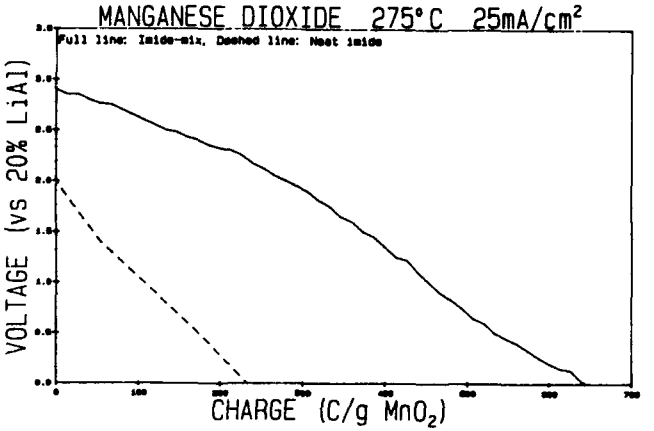

Figure 5

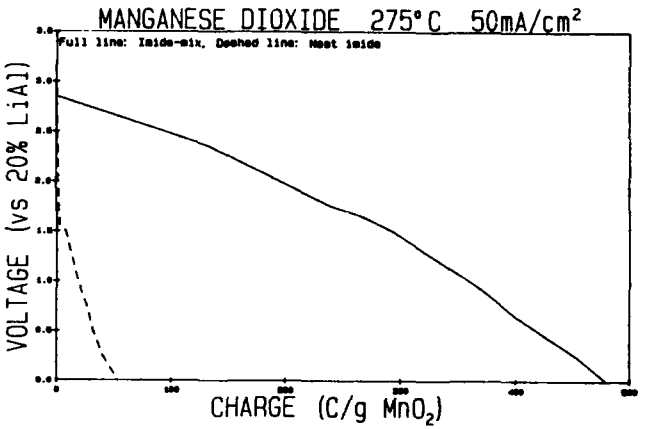

Figure 6

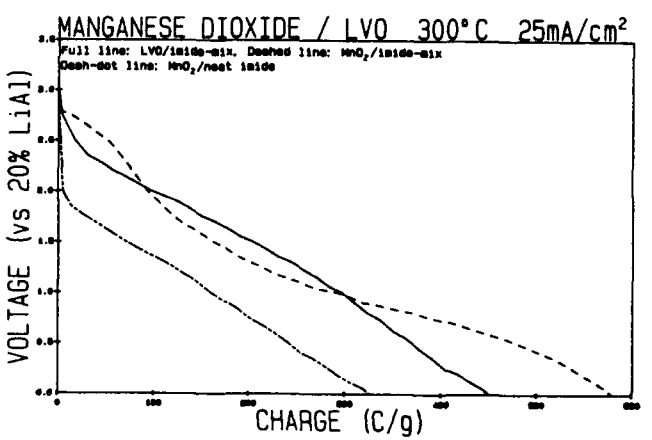

EVALUATION OF TRANSITION METAL SULFIDE CATHODE MATERIALS FOR THERMAL BATTERIES

Steven Dallek and Timothy C. Murphy
Naval Surface Warfare Center, Silver Spring, MD
and
Trung Nguyen
EIC Laboratories, Inc., Norwood, MA

Introduction

Thermal batteries are high temperature, primary, reserve electrochemical power sources employing molten salt electrolytes that are solid and, therefore, non-conductive at normal ambient temperatures. When power is required, an integral pyrotechnic heat source is ignited which raises the internal temperature above the melting point of the electrolyte, thus making it conductive and permitting battery operation. Most thermal batteries are based on the lithium alloy/metal disulfide electrochemical system. The battery consists of a lithium alloy anode, an iron disulfide (FeS_2) cathode, and a lithium chloride-potassium chloride or a lithium fluoride-lithium chloride-lithium bromide eutectic electrolyte. Such batteries have specialized uses for high-power, short-term discharges in a wide range of military applications.

Several projected military applications will require significant advances in the power and energy density capabilities of thermal batteries. It is not likely that a new thermal battery anode material with superior electrochemical properties to lithium and its alloys will be found. The development of new, synthetic transition metal cathode materials, however, with higher thermal stability and higher electrical conductivity than FeS_2 would allow for significant improvements in thermal battery power and energy densities.

The conventional synthetic approach used in the preparation of metal disulfides is the direct reaction of the elements in sealed evacuated silica tubes at elevated temperatures. For example, one of us (S.D.) reported earlier on a process for the preparation of synthetic FeS_2 cathode material for thermal batteries[1]. Mixed transition metal disulfide cathode material can also be prepared directly from the elements, as reported recently by Awano et al[2]. Pure, single phase mixed-metal products, however, are difficult to obtain, even with repeated grindings and firings. In the preparation of Co-rich (Fe, Co)S_2 material, for example, a small amount of CoS_2 was always found as a separate phase[3]. A different approach to the synthesis of transition metal disulfides was proposed by Delafosse et al[4], who prepared CoS_2 and NiS_2 by heating the corresponding sulfates in H_2S. This procedure was used successfully by Bouchard[3] to prepare a series of mixed transition metal disulfides.

In this study, we have synthesized single-phase, mixed transition metal sulfide cathode materials with the compositions $Fe_xCo_{(1-x)}S_2$, $Co_xNi_{(1-x)}S_2$, and $Cu_xNi_{(1-x)}S_2$. The thermal stability, electrical conductivity and electrochemical discharge behavior of the new materials were evaluated and compared to the standard FeS_2 cathode material.

Experimental Methods

Synthesis

The synthesis of the single phase mixed-metal sulfides was carried out using co-precipitated mixed-crystal sulfates. The advantage of using mixed sulfates as a precursor is that hydrated sulfates of Fe, Co, Ni and Cu are isomorphous and readily form mixed crystals. As a result of the homogeneous formation of precipitated mixed sulfates, the formation of finely divided, single-phase, well crystallized materials is facilitated at higher temperatures. The mixed metal sulfates were prepared by mixing solutions of the single metal sulfates in the desired stoichiometry. The mixed sulfate solution was poured into a large batch of acetone to precipitate the mixed metal sulfate crystals which are highly insoluble in acetone. The precipitated sulfate was filtered and dried at 100°C under vacuum. The dry product was heated to 350°C in dry flowing N_2 for 15 minutes. The gas was then changed to a 50:50 H_2S/N_2 mixture and maintained for 6 hours. The resulting sulfide was quenched to room temperature, and residual water was removed by heating the product under vacuum at 300-400°C. To ensure proper stoichiometry, the dry product was heated at 650-700°C in an evacuated quartz tube with excess sulfur for a period of 2-3 days. At the end of the reaction period, the excess sulfur was condensed in a cool region of the tube. The pure mixed metal sulfide was collected under nitrogen and stored in an inert atmosphere. The following series of compounds was synthesized and evaluated in this study: $Fe_{0.8}Co_{0.2}S_2$, $Fe_{0.5}Co_{0.5}S_2$, $Fe_{0.2}Co_{0.8}S_2$, $Co_{0.8}Ni_{0.2}S_2$, $Co_{0.5}Ni_{0.5}S_2$, $Co_{0.2}Ni_{0.8}S_2$, and $Cu_{0.2}Ni_{0.8}S_2$.

Characterization

X-ray Diffraction (XRD): XRD patterns of the new transition metal disulfides were determined using a Rigaku diffractometer fitted with a filtered Cu tube. Si powder was added to the sample to serve as an internal reference.

Thermogravimetric Analysis (TGA): The thermal stability of the new cathode materials and the standard FeS_2 and CoS_2 materials was determined by TGA. A TA Instruments Model 951 or Perkin-Elmer Model 7 thermogravimetric analyzer was used. Samples (10-12 mg) were run in platinum boats at a heating rate of 10°C/min from 20° to 700°C in a flowing atmosphere of argon.

Conductivity Measurements: Conductivity measurements were performed by an AC impedance technique. In this approach, a 5 mV AC signal was applied to the cell in the frequency range from 5 Hz to 100 kHz and the resulting currents and voltages were recorded with the aid of a lock-in amplifier. The resistances of the powder samples were determined from the plot of the imaginary component of the complex impedance (-Z") versus the real component (Z'). The AC impedance measurements were made with an EG&G PARC Model 378 Electrochemical Impedance System, comprised of a EG&G PARC Model 273 Potentiostat/ Galvanostat, a Model 5208 Lock-In Amplifier, and an IBM PC controlled by EG&G PARC software. The sample powder was packed inside a cylindrical cavity with dimensions of 0.5 cm in diameter and 45 cm in length drilled out of a cylindrical block of plastic with a diameter of 34 cm. Two stainless steel rods, which acted as blocking electrodes, were inserted on each side of the cavity and clamped down with a C-clamp. Preliminary experiments indicated that the prepared samples were so conductive that it was necessary to insert a known 1 ohm resistor into the circuit to make the AC impedance measurements possible. A blank measurement was first made to determine the resistance contribution of the 1 ohm resistor, leads and blocking electrodes. The electronic conductivity of the powder was then obtained by subtracting the blank value from the measured value.

Single Cell Discharge Studies: Preliminary evaluations of the electrochemical performance of the new cathode materials were conducted using single cell tests. The individual test cells were constructed with pelletized electrode components. The electrolyte was composed of a mixture of LiCl:LiF:LiBr (25:37:38). It was mixed with MgO in a ratio of 1:1 to form the electrolyte/separator mixture. The anode material was prepared by mixing LiAl powder with the electrolyte in a ratio of 2:1. The cathode material was made by combining the mixed-metal disulfide with the electrolyte in a ratio of 4:1. The electrolyte, anode and cathode mixtures were thoroughly mixed inside a rolling mill for about 2 hours. The homogeneous powder was then pressed with a stainless steel die to form round pellets with an effective surface area of 1.26 cm^2. The cells were constructed by stacking the cathode between two anodes with the electrolyte/separator pellets in between them. The cells were then sandwiched between two stainless steel disc current collectors which were insulated from the compression plates by a layer of insulating mica. The pressure applied to the cell stacks through the compression plate was about 15 psi. The test cells were placed inside a furnace at 520°C under an atmosphere of nitrogen and discharged at a current density of 0.1 A/cm^2. All experimental procedures were conducted in a Dry Room maintained at less than 2% relative humidity.

Results and Discussion

Iron disulfide and cobalt disulfide were prepared separately from the corresponding sulfate precursors to ensure the validity of the H_2S reduction method. XRD patterns obtained for these baseline materials were identical to published data. XRD patterns of the $(Fe,Co)S_2$ series of compounds showed that the initial H_2S reduction step produced an amorphous, non-stoichiometric product. After heat treatment of this material with excess sulfur at 650°C for four days, the XRD pattern clearly indicated the conversion to a highly crystalline and well ordered final product. The $(Co,Ni)S_2$ and $Cu_{0.2}Ni_{0.8}S_2$ materials, on the other hand, were crystalline even before the heat treatment procedure with sulfur.

TGA curves comparing the thermal stabilities of the mixed-metal transition metal disulfides and the standard FeS_2 and CoS_2 materials are shown in Figures 1 and 2. It is seen that the thermal stability of the $(Fe, Co)S_2$ compounds increases with increasing Co concentration. The thermal stability of the $(Co,Ni)S_2$ compounds is highest for the $Co_{0.8}Ni_{0.2}S_2$ phase. The thermal stability of the $Cu_{0.2}Ni_{0.8}S_2$ phase is higher than that of FeS_2 or CoS_2.

The conductivity results are summarized in Table 1. It is seen that the introduction of Co atoms into the FeS_2 structure to form a single phase mixed-metal disulfide significantly increases the conductivity (i.e., decreases the specific resistivity) of the material. The resistivity decreases as a function of increasing concentration of Co atoms. Thus, the conductivity of $Fe_{0.2}Co_{0.8}S_2$ is over 3 orders of magnitude greater than that of FeS_2. Since CoS_2 is a metallic conductor, the incorporation of Co into the semiconducting FeS_2 structure to form the $(Fe,Co)S_2$ phase would be expected to provide increased conductivity. The incorporation of Ni, on the other hand, to form $(Co,Ni)S_2$ is seen to have little effect since NiS_2 is a semiconductor. The high electronic conductivity of the $Cu_{0.2}Ni_{0.8}S_2$ material derives from the metallic conductivity of CuS_2.

Single-cell discharge curves obtained at a current density of 0.1 mA/cm^{-2} are shown in Figures 3 and 4. From these preliminary results, with unoptimized cells, it is seen that $Fe_{0.2}Co_{0.8}S_2$ has a much higher discharge voltage than the standard FeS_2 material.

Summary

New thermal battery transition metal cathode materials with the compositions $Fe_xCo_{(1-x)}S_2$, $Co_xNi_{(1-x)}S_2$, and $Cu_xNi_{(1-x)}S_2$ were synthesized by H_2S reduction of the corresponding mixed-metal sulfate precursors. The materials were characterized by XRD, TGA, conductivity measurements, and single-cell discharge studies.

The $Fe_{0.2}Co_{0.8}S_2$ phase, in particular, has potential as an attractive new cathode material. It has higher thermal stability and substantially lower resistivity than the standard FeS_2 cathode material. Furthermore, the single-cell discharge voltage of $Fe_{0.2}Co_{0.8}S_2$ was significantly higher than that of FeS_2. Thus, the new cathode material may provide for increases in the energy and power densities of thermal batteries.

Acknowledgement

This work was supported by the Naval Surface Warfare Center under the Department of Defense Small Business Innovative Research (SBIR) Program and by the Office of Naval Research under the High Energy Battery Project.

References

(1) S. Dallek et al., "Synthetic FeS_2 Cathode Material for Thermal Batteries," Proceedings of the 33rd International Power Sources Symposium, Cherry Hill, NJ, 13-16 June 1988, pp. 340-345.

(2) A. Awano et al. "Li/$Fe_{1-x}Co_xS_2$ System Thermal Battery Performance," Proceedings of the 35th International Power Sources Symposium, Cherry Hill, NJ, 22-25 June 1992, pp. 219-222.

(3) R. J. Bouchard, "The Preparation of Pyrite Solid Solutions of the Type $Fe_xCo_{1-x}S_2$, $Co_xNi_{1-x}S_2$, and $Cu_xNi_{1-x}S_2$," Mat. Res. Bull., 3, 563-570 (1968).

(4) D. Delafosse and P. Barret, Compt. Rend., 251, 2964 (1960).

Table 1

Resistivity of Single Phase Mixed-Metal Disulfides

Sample	Resistivity, ρ (Ω•cm)
FeS_2	17.72
$Fe_{0.8}Co_{0.2}S_2$	0.088
$Fe_{0.5}Co_{0.5}S_2$	0.021
$Fe_{0.2}Co_{0.8}S_2$	0.005
CoS_2	0.002
$Co_{0.8}Ni_{0.2}S_2$	0.015
$Co_{0.5}Ni_{0.5}S_2$	0.005
$Co_{0.2}Ni_{0.8}S_2$	0.026
$Cu_{0.2}Ni_{0.8}S_2$	0.006

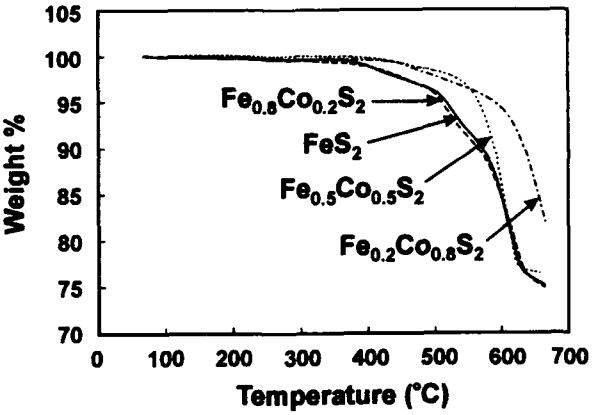

Fig.1: TGA Curves of Transition Metal Disulfides. Heating Rate : 10 °C/min.

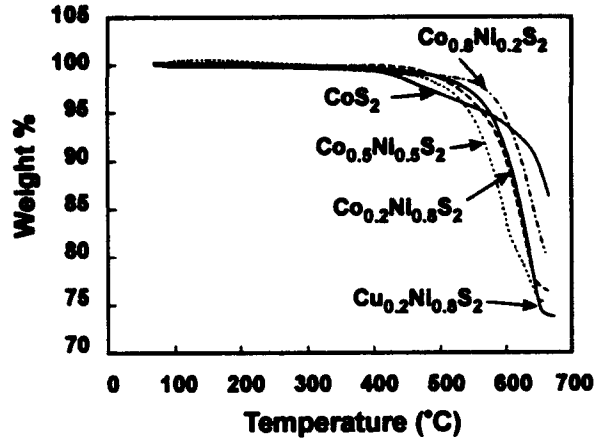

Fig. 2: TGA Curves of Transition Metal Disulfides. Heating Rate : 10 °C/min.

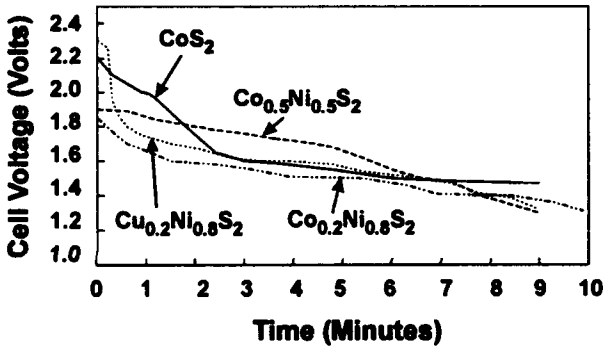

Fig. 3: Single-Cell Discharge Curves of $Co_xNi_{(1-x)}S_2$, $Cu_xNi_{(1-x)}S_2$ and CoS_2 at 0.1 A/cm^2 and 520 °C.

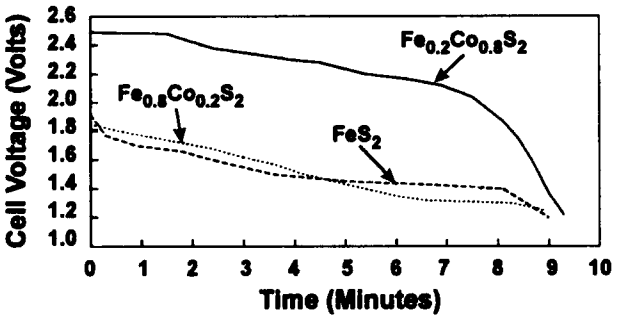

Fig. 4: Single-Cell Discharge Curves of $Fe_xCo_{(1-x)}S_2$ and FeS_2 at 0.1 A/cm^2 and 520 °C.

LITHIUM ALUMINUM / IRON DISULFIDE RECHARGEABLE BATTERIES FOR PULSE POWER APPLICATIONS

J. D. Briscoe
SAFT AMERICA INC
Research and Development Center
107 Beaver Court
Cockeysville, Maryland 21030

Abstract

Advanced lithium aluminum/iron disulfide rechargeable batteries employing molten salt electrolytes are under development at SAFT for pulse power applications. Battery stack arrays consisting of twenty series connected cells operating at 465 degrees Celsius have been cycled at high rates of 3C charge and 75C discharge. The 10 kW cylindrical bipolar battery module employs an integral volume compensating bellows to maintain cell to cell contact while providing for expansion and contraction of the electrodes during cycling. An aluminum iron alloy additive in the negative electrode provides over charge tolerance and cell balancing by a lithium shuttle mechanism. Very high power densities of 3.0 kW/kg and 8.1 kW/l have been demonstrated.

Introduction

Rechargeable LiAl/FeS_2 batteries employing molten halide salt electrolytes are good candidates as power supplies for electric weapon applications. The lithium halide based molten salt electrolytes have high ionic conductivity and are ideally suited for high power densities when compared to aqueous and solid state electrolytes. The lithium aluminum and iron disulfide electrodes have high specific energy and good reaction kinetics. When discharged at a C/3 rate on the upper plateau the system has a theoretical specific energy of 475Wh/kg[1].

$$(2LiAl + FeS_2 \rightarrow FeS + Li_2S + 2Al, 1.66V).$$

The main objective of this R&D effort was to optimize the LiAl/FeS_2 system for high power and to develop and demonstrate 10 kW scaleable battery modules containing 20 series connected, 13 cm diameter sealed bipolar cells. The work plan established a baseline LiAl/FeS_2 cell design and performance. As previously reported[2] negative electrode, positive electrode, separator/electrolyte, cell hardware, and seal studies were conducted using 2.5 cm diameter single cells. Scale-up of the best performing cell design to 13 cm diameter cells and then 10 kW stacks was accomplished. Cell and battery results were compared to target values of 2.9 kW/kg, 33 Wh/kg, 5 MW/m^3, and 56 Wh/l taken from performance guidelines for a future full scale battery as detailed in Table 1. A design concept of the battery is depicted in Figures 1 and 2.

Table 1: Full Scale Battery Performance Guidelines

Energy Storage	100 MJ (27.5 kWh)
Constant Power	2.5 MW
Operating Voltage	500 V
Charge Time	15 - 20 Minutes
Pulse Conditions	12 Shots Over 1 Minute
Pulse Duration	4 Seconds
Pulse Current	5000 Amps
Power Density	5 MW/m^3
Specific Power	2.9 kW/kg
Energy Density	202 kJ/l (56 Wh/l)
Specific Energy	120 kJ/kg (33 Wh/kg)
Battery Volume	<< 3m^3 With a goal of 0.5 m^3
Battery Weight	< 1000 kg

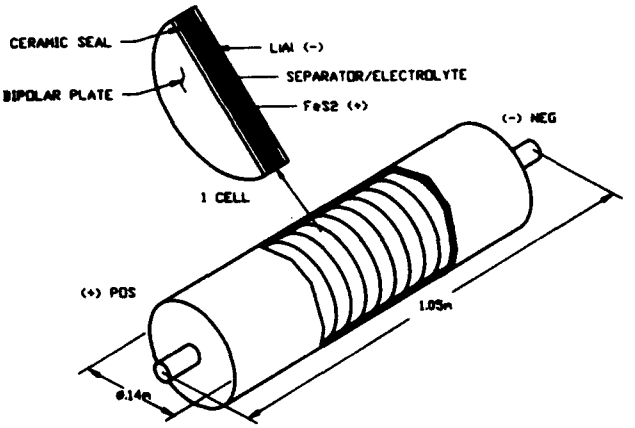

Figure 1: 5 MJ Bipolar LiAl/FeS_2 Module Concept Design

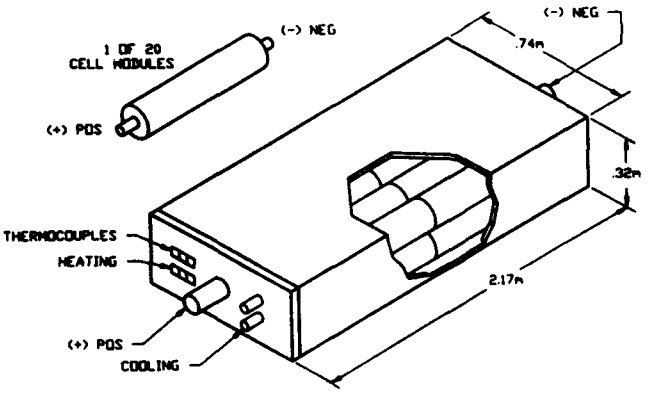

Figure 2: 100 MJ Bipolar LiAl/FeS_2 Battery Concept Design

Experimental

Scale-up to 10 kW battery modules was accomplished beginning with negative electrode, positive electrode, and separator powder mixes that were processed and cold compacted into disks 13 cm diameter using a 400 ton capacity hydraulic press. LiAl electrode disks of 12.9 Ah theoretical capacity were matched with FeS_2 electrodes to obtain a lithium limited cell with negative to positive ratio of 0.86. Overcharge tolerance consisted of additives of Al_5Fe_2 to the negative and NiS and Li_2S to the positive as developed by Argonne National Laboratory (ANL)[3]. The cell chemistry was as follows:

Negative: LiAl, LiBr-LiCl-LiF salt, MgO, and Al_5Fe_2

Positive: FeS_2, LiBr-LiCl-LiF salt, CoS_2, NiS, and Li_2S

Electrolyte/Separator: LiBr-LiCl-LiF salt and MgO

The negative electrode was assembled into a 316 stainless steel cup and a 316 stainless steel screen was placed on top. The cup edge was crimped over the screen and spot welded all around to complete the electrode package. Likewise the positive electrode was assembled using a molybdenum cup and screen. The cell assembly is depicted in Figure 3.

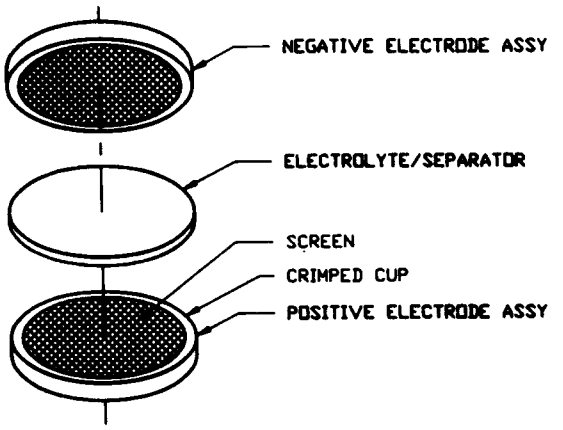

Figure 3: LiAl/FeS_2 Cell Assembly

Twenty cells were stacked in series with two oversized metal foil disks located between each pair of adjacent cells to help decrease electrolyte leakage. The metal disks were bent away from each other at the periphery to form a gap all around. This design provides a more torturous path for electrolyte to travel and reduces leakage currents. The cell stack was placed between horizontal nickel current collector disks inside a stainless steel case as shown in Figure 4.

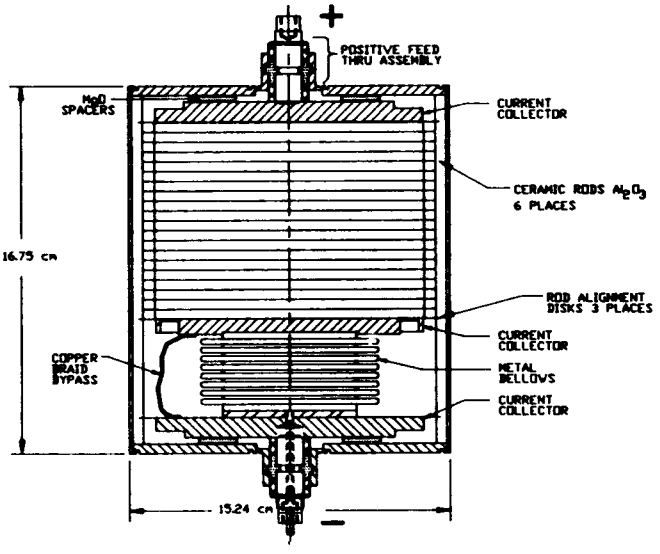

Figure 4: Sectioned View of 20 Cell LiAl/FeS_2 Battery

Alumina ceramic rods were used to electrically insulate the cells from the metal case and to maintain alignment of the stack. The lower disk negative collector was seated on top of a volume compensating Inconel metal bellows resting flat on a second negative collector at the bottom of the case. A copper braid connected the two negative collector plates and served as a current bypass around the highly resistive bellows. The top and bottom current collector plates were isolated from the negative cover assembly by magnesium oxide ceramic spacers. Each plate was tungsten inert gas (TIG) welded to a 1.3 cm diameter nickel terminal. Each terminal was fed through the cover assembly via a boron nitride compressed powder feed through assembly as developed by ANL[4]. The negative and positive cover assemblies were welded into the outer case to complete the battery assembly.

Batteries to be tested were clamped between steel plates with resistance heaters attached and sealed within an insulated test drum container. Because of it's greater length, the 10 kW battery had an additional heater wrapped around the case side. The integral bellows was pressurized with argon gas to provide a force of 55 kg (0.45 kg/cm^2) at operating temperature. The atmosphere inside the drum was purged with argon gas and the battery was heated to 465 ^{o}C. A Bitrode model LCS 500-45 tester with 0-45 volts range and 500 amperes charge and discharge capability was used to test the batteries. Individual batteries were discharged under constant current loads of up to 500 amperes (4 A/cm^2 at 75C rate). Charging consisted of 30 amperes constant current (3C rate) to 2.1 V per cell followed by constant potential taper charging down to low current (<2 A).

Results and Discussions

The optimum chemistry and configuration required for the 10 kW battery was developed by testing many small single cells. Scale-up to full size LiAl/FeS_2 cells was achieved with good success. A comparison of the results of a 2.54 centimeter diameter single cell (EW-43), a three cell battery (EWS5-3) and two twenty cell batteries (EWS5-9 & EWS5-10) is shown in Table 2.

Table 2: Comparison of the Results of Cells and Batteries Tested at 4 A/cm^2

Description	Load (Amps)	Potential (Volts)	Average Capacity (Amp-hrs)	Specific Power (kW/kg)	Specific Energy (Wh/kg)	Power Density (kW/l)
EW-43 1 Cell 2.5 cm	20	0.91	0.222 (47% Util)	3.2	35	8.7
EWS5-3 3 Cells 13 cm	500	2.86	6.8 (53% Util)	3.0	41	8.1
EWS5-9 20 Cells 13 cm	500	18.15	5.6 (43% Util)	3.0	34	8.8
EWS5-10 20 Cells 13 cm	500	14.67	3.3 (26% Util)	2.3	15	6.2

A comparison of the results of EW-43 with EWS5-3 at equivalent current densities of 4A/cm^2 shows that scale-up of the chemistry from a 2.54 cm single cell to a three cell battery with 13 cm diameter cells resulted in similar gravimetric power and energy densities based on the weight of cell components. The power density of battery EWS5-3 was within 6% of cell EW-43. The capacity utilization of the battery was higher by 13%, and the energy density was higher by 6 Wh/kg (17%). This improvement is due to the constant potential charging performed on the battery to equalize the cells. Therefore the battery was charged to a higher state of charge (*SOC*). *This was not done on the small 2.54 cm cells.* EWS5-3 achieved 150 high rate cycles.

The performance of EWS5-10 is representative of a twenty cell battery with cells identical in design to EWS5-3 (with screens). The unusually low power and energy were because of high internal impedance probably

caused by insufficient pressure on the stack resulting in limited wetting of the screens.

In contrast the best performance of a twenty cell battery was EWS5-9 that had cells with no screens. Power densities of 8.8 kW/l and 3.0 kW/kg and energy densities of 353 kJ/l (98 Wh/l) and 122 kJ/kg (34 Wh/kg), were achieved based on the weight and volume of cell components. A complete cycle with rates of 75C discharge and 3C charge (with taper) is shown in Figure 5. Open circuit rest periods of 15 minutes were allowed before and after each discharge. Figure 6 is an expanded discharge plot. The battery produced a peak power at 500 amperes discharge of 11.5 kW.

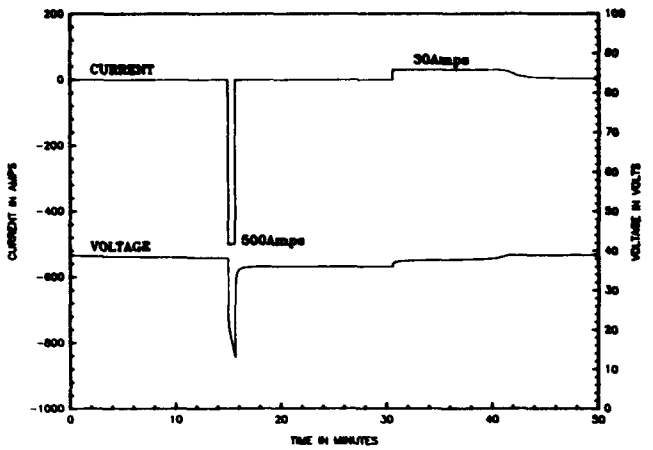

Figure 5: Cycle #6 of 10 kW Battery EWS5-9

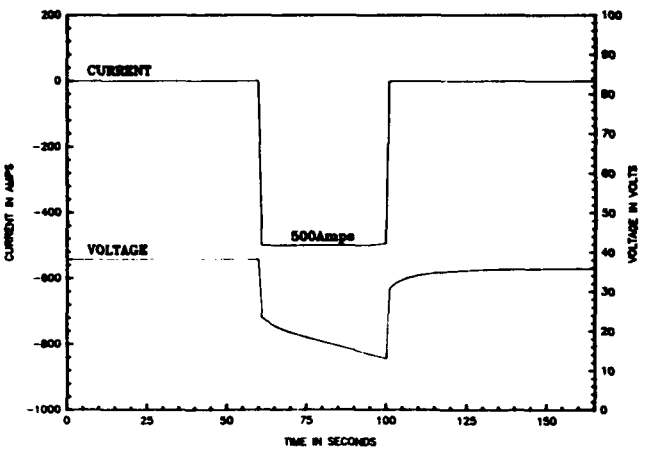

Figure 6: Cycle #6 Discharge of 10 kW Battery EWS5-9 at 4A/cm^2

In order to relate cell stack performance to the battery goals of 2.9 kW/kg and 33 Wh/kg (120kJ/kg) we must apply a burden. The burden represents insulation, heaters, and other hardware required for a full scale battery. If we apply a 25% burden the cell goals are calculated as 3.6 kW/kg and 41 Wh/kg. A plot of specific power versus specific energy of the best three cell and twenty cell batteries is depicted in Figure 7. Both batteries were within 20% of the cell goals. At 500 amperes the three cell battery (EWS5-3) achieved the optimum performance of 3.0 kW/kg and 41 Wh/kg. The 10 kW battery achieved 3.05 kW/kg and 34 Wh/kg.

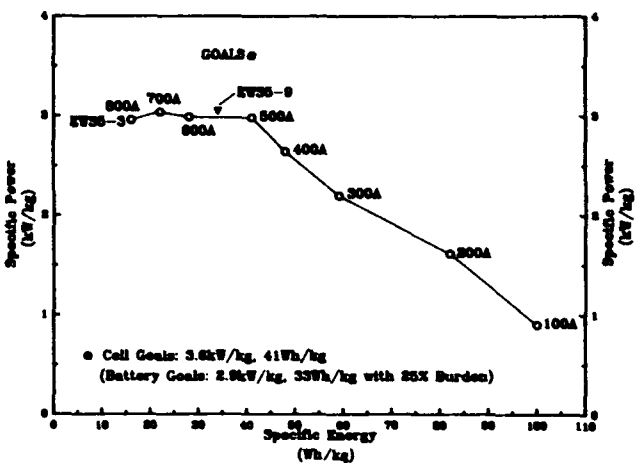

Figure 7: Specific Power vs. Specific Energy of Three Cell (EWS5-3) and Twenty Cell (EWS5-9) LiAl/FeS_2 Batteries

With respect to volume the performance was even better when compared to the goals. In order to achieve a battery size of 500 liters, power and energy densities of 5 kW/l and 56 Wh/l are needed. Using a 25% burden the cell goals are calculated as 6.3 kW/l and 70 Wh/l. Both batteries exceeded these goals as depicted in Figure 8. At 500 amperes battery EWS5-3 achieved 8.1 kW/l and 110 Wh/l. The 10 kW battery EWS5-9 achieved 8.8 kW/l and 98 Wh/l.

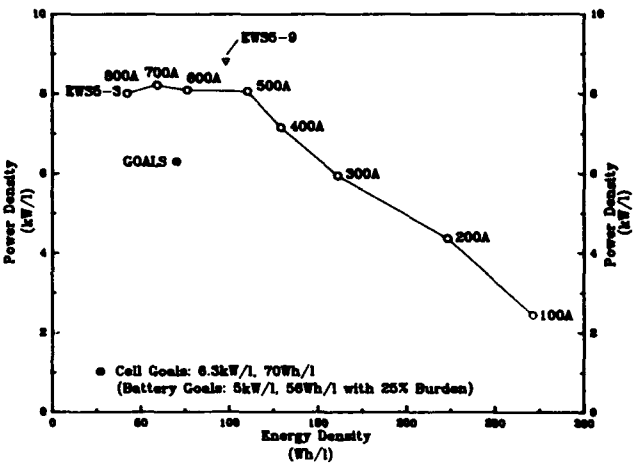

Figure 8: Power Energy vs. Energy Density of Three Cell (EWS5-3) and Twenty Cell (EWS5-9) LiAl/FeS_2 Batteries

Conclusions

Advanced 10 kW battery modules optimized for high power densities of 2.9kW/kg and 5 MW/m^3 are under development at SAFT. Rechargeable LiAl/LiBr-LiCl-LiF/FeS_2 chemistry was developed and optimized for high power in 2.54 cm diameter circular cells. Scale-up of chemistry to 13cm diameter cells and cell stacks was accomplished, and comparable power and energy densities were attained at high rates of 3C (30 A) charge and 75C (500 A) discharge. Power densities of 8.8 kW/l and 3.0 kW/kg and energy densities of 353 kJ/l (98 Wh/l) and 122 kJ/kg (34 Wh/kg) were achieved for a twenty cell 10 kW battery based on the weight and volume of cell components.

Acknowledgment

This work was sponsored by the US Army Electric Armaments Division, ARDEC, and the Army Research Laboratory (ARL).

References

1. P.A. Nelson, and T.D. Kaun, Battery Construction, Testing, and Materials, Molten Salt Techniques, Vol. 4, eds., R.j.Gale and D.G. Lovering, Plenum Publ., London (1991)

2. J. D. Briscoe, R.J. Staniewicz, M. Williams, Rechargeable Pulse Power Lithium Alloy/ Iron Disulfide Batteries, Proceedings of The 35th International Power Sources Symposium, June 22-25, 1992, pp. 294-297

3 T.D. Kaun, et al, Development of Overcharge Tolerance in Li/FeS and Li/FeS_2 Cells, Proc. of the Symp. on Materials and Processes for Lithium Batteries, ed K.M. Abraham, Electrochem. Soc. meeting, Vol. 89-4, p. 383 (1989).

4. E.C. Gay, et al, Li-Alloy/FeS Cell Design and Analysis Report, Argonne National Laboratory Report ANL-84-93 (July 85), p. 8.

DEVELOPMENT OF THE Na/ß"-ALUMINA/S(IV) CHLOROALUMINATE CELL

J. Caja, T. D. J. Dunstan, and G. Mamantov
Molten Salt Technology, Inc.
Knoxville, Tennessee
and
Department of Chemistry
University of Tennessee
Knoxville, TN 37996-1600

Abstract

We present here the results of the development of the rechargeable cell Na/ß"-alumina/S(IV) in molten $AlCl_3$/NaCl as a candidate battery for electric vehicles. Two charge/discharge steps are observed for this cell. In the first step S(IV) is reduced to S(0); in the second, the elemental sulfur is reduced to a complex sulfide. The cell has a theoretical energy density for the two steps of 726 Wh/kg; an open circuit voltage(OCV) > 4.2 V; it operates in the temperature range of 180°C to 250°C. Only the first step was studied in this program. Engineering cells Na/ß"-alumina/S(IV) in molten $AlCl_3$/NaCl were designed and constructed. The cells consisted of the positive mix inside a ß"-alumina tube which was equipped with an α-alumina header. The negative compartment was a stainless steel tube containing sodium. Two types of seal assemblies were used to seal the two compartments: 1) compression seals, 2) a brazed seal. Static and dynamic compatibilities of construction materials with $AlCl_3$/NaCl melts in the presence and absence of sulfur compounds were determined. The electrochemical performance of the cells was tested at 230°C. Open circuit voltage of the charged cells was > 4.2 V; capacity efficiency of the cells was >97 %. It was observed for most of these cells that with cycling the average cell resistance reached a minimum, and then began to increase. This increase in resistance appears to be caused by impurities introduced in the melt during cycling. Cells made of compatible materials(laboratory cells) showed a low resistance which remained constant with cycling. The lowest resistance obtained for these cells was 4.5 Ωcm²; the longest cycle life was 9128 cycles in 14 months; maximum power density was 0.9 W/cm². Deep discharge and overcharge, and freeze-thaw had no effect on cell performance. It was demonstrated that the cell Na/ß"-alumina/S(IV) in molten $AlCl_3$/NaCl made of compatible materials will meet the requirements for applications in electric vehicles.

Introduction

Of the many electrochemical systems which have been considered for battery applications in electric vehicles, those based on molten salt electrolytes appear to be especially promising. The cell Na/ß"-alumina/ S(IV) in molten $AlCl_3$/NaCl is one of these systems; however, its potential for practical applications has not been explored. This cell has been studied at the University of Tennessee since 1976 (1-4); it shows the following characteristics:

Two separate discharge(and charge) steps are observed in this cell. In the first, S(IV) is reduced to S(0) according to the reaction

$$4Na + SCl_3AlCl_4 + 1.5Al_2Cl_6 \underset{\text{charge}}{\overset{\text{discharge}}{\rightleftharpoons}} S + 4NaAlCl_4 \quad (1)$$

Open Circuit Voltage(OCV)= 4.35 V

and in the second, elemental sulfur is reduced to a complexed sulfide according to the reaction

$$2Na + S + NaAlCl_4 \underset{\text{charge}}{\overset{\text{discharge}}{\rightleftharpoons}} NaAlSCl_2 + 2NaCl \quad (2)$$

Open Circuit Voltage(OCV)= 2.75 V

The overall reaction for the reduction of S(IV) to sulfide is described by the equation

$$SCl_3AlCl_4 + 1.5Al_2Cl_6 + 6Na \underset{\text{charge}}{\overset{\text{discharge}}{\rightleftharpoons}} NaAlSCl_2 + 3NaAlCl_4 + 2NaCl$$

Working temperature is in the range of 180°C to 250°C. Energy densities calculated for steps *I* and *II* are 552 Wh/kg and 174 Wh/kg, respectively; for the overall reaction the value is 726 Wh/kg(3).

The acid-base properties of molten chloroaluminates and electrochemistry of sulfur in these melts are crucial for the understanding of the charge/discharge properties of cells that use positive oxidation states of sulfur. Acidic melts are defined as those melts that have an $AlCl_3$/NaCl mole ratio>1. Elemental sulfur can be either oxidized or reduced in both basic and acidic melts. The reduction of sulfur results in a complexed sulfide. The oxidation of sulfur in basic melts($AlCl_3$/NaCl mole ratio<1) leads to S_2Cl_2(+1 oxidation state). In acidic melts the electrochemical oxidation goes through several intermediate oxidation products including S_2Cl_2 to the final reaction product SCl_3AlCl_4 (+4 oxidation state).

Initial studies of this system were carried out at the University of Tennessee using glass laboratory cells. Since 1987 further development of this system was carried out at Molten Salt Technology(MST) with an objective to develop a practical cell.

The results obtained with laboratory cells showed:

- an open circuit voltage >4.2 V.
- high power density(>500mW/cm²) as well as a maximum power density of 1579W/kg (based on the weight of the active components) was achieved for a number of cells.
- more than 1000 deep charge/discharge cycles were obtained for number of cells; for one cell more than 9000 cycles were achieved.
- cells could be charged to 100% of the theoretical capacity.
- charge/discharge efficiency 100%.
- energy efficiency up to 97% of the first plateau.
- loss in cell capacity was not observed after more than 3000 cycles.

Results of an investigation to develop a practical Na/ß"-alumina/S(IV) cell are presented in this paper. Following areas were studied:

1) compatibility of materials
2) seal design
3) cell performance
4) high energy cells.

Experimental

All chemicals used in the cells were of the highest purity. Aluminum chloride(Fluka) and sodium chloride(Malinckrodt) were purified according to standard procedures(5). Sodium(Fisher) was filtered through glass wool before use, and sulfur(Alfa) was used as received. Kovar, 304 Stainless Steel, and the brazing alloys were commercially available. Nickel 200 and tungsten wire were obtained from AESAR. Reticulated Vitreous Carbon(RVC) was obtained from Chemotronics International, Inc., Ann Arbor, Mich. The ß"-alumina tubes with α-alumina headers were manufactured by Ceramatec, Salt Lake City, Utah.

All electrochemical measurements were performed using a 16-channel MACCOR automatic battery test system including an IBM-compatible computer as the Central Processing Unit.

The ß"-alumina tubes were vacuum-dried at 450°C for at least 5 days prior to use. Cells were assembled in the dry box under an inert atmosphere.

Results and Discussion

1) Materials compatibility

The cells were constructed from 304 Stainless Steel which is known to be compatible with molten sodium(6). The melt and its vapors are very aggressive chemically and hence the studies of their effects on stainless steel and on materials used to construct the cell (in particular the seal assembly) were performed. Both static and dynamic compatibility studies were conducted. Dynamic compatibility was determined after

materials had been used in cells during charge/discharge cycling. Static compatibility of materials (304 Stainless Steel, Nickel 200) was determined by measuring the weight loss of coupons (size 1x2cm, thickness 0.15cm, 0.0787cm for stainless steel, respectively) after their immersion in the melts for different periods of time (up to one year) at 230°C.

Results showed that in a slightly acidic melt containing S_2Cl_2, nickel and stainless steel show a very small weight loss. In a highly acidic melt (65/35 mole% $AlCl_3$/NaCl) containing SCl_2AlCl_4 a significant loss in weight was observed for stainless steel; the loss was much less for nickel. The results show that the weight loss for nickel is 31.3mg/cm² after 1 year which corresponds to a depth of penetration of 35.2×10^{-4}cm. Dynamic experiments have shown that tungsten as well as RVC are quite inert with respect to SCl_2AlCl_4. Coiled tungsten wire has been used as the positive current collector in laboratory Na/ß"-alumina/S(IV) cells for long periods of time (17 months) without any apparent attack by the sulfur compounds.

Therefore, the compatibility of tungsten-coated nickel coupons (size 1cmx2cmx 0.0787cm thickness; W coating thicknesses of 19.8µm, 26.6µm, and 32.0µm, respectively) in highly acidic melts containing sulfur(IV) was carried out for 5 months at 230°C. It was observed that W coating remained intact and no tungsten was detected in the melt after 5 months.

2) Seal design

Several engineering cells were designed and constructed. In order to minimize the corrosion of the metal components by the chemicals in the cathode compartment an inside/out cell design was adopted, with the sodium outside the ß"-alumina tube. The main disadvantage of the cells with this configuration is that their capacity is limited by the size of the ß"-alumina tube. An engineering cell consisted of the positive mix inside a ß"-alumina tube which was equipped with an α-alumina header to seal and electrically insulate the sodium and the melt compartments. The negative compartment (anode) was a stainless steel tube containing sodium. Both compartments were sealed employing either compression type of seals (with a bolted flange or with disc springs) or a brazed seal. A coiled tungsten wire was used as the positive current collector. Figure 1 shows the cell design with disc springs.

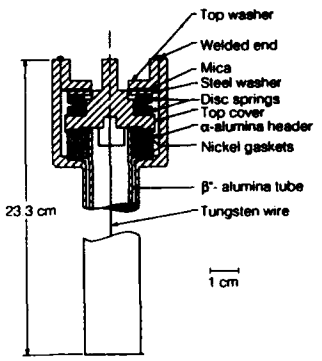

Figure 1 Cell Design with Disc Springs

Brazed seal (metal/ceramic) consisted of an alumina header in which a Kovar ring was bonded to the outer diameter of the header and a nickel (Kovar) ring was bonded to the inner diameter of the header.

3) Charge/discharge performance

Cell capacity ranged from 1.0 to 1.7 Ah. Melt composition (for discharged cells) for majority of cells was slightly acidic (50.4/49.6 mole% $AlCl_3$/NaCl). Working temperature was 230°C. Only the first discharge step (reduction of S(IV) to S(0)) was studied. These cells were charged in the range of 40-90% of the theoretical capacity, and discharged deeply to a cutoff voltage of 3.0 V or lower, depending on the discharge rate.

Typical charge/discharge curves and OCV's for three cycles are shown in Figure 2.

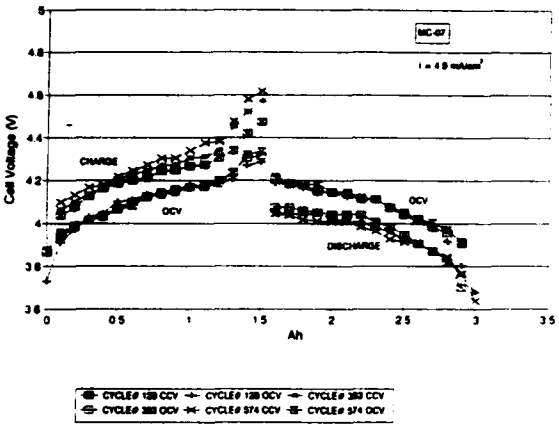

Figure 2 Full Charge/Discharge Curves for the Cell MC-07

Open circuit voltage for the Na/ß"-alumina/S(IV) chloroaluminate cell is a function of the state of charge. It was observed (Table 1) that the OCV of a fully charged cell is >4.2 V.

Table 1

Open Circuit Voltage vs. State of Charge for the Cell MC-02

Cycle #	OCV (V)					
	State of charge (%)					
	0	20	40	60	80	100
57	3.819	4.040	4.134	4.178	4.207	
405	3.810	4.050	4.136	4.179	4.212	4.308

However, it was also observed that the resistance of these cells increased with cycling. Figure 3 shows dependence of the charge and the discharge resistances of three cells (MC-06, MC-07, and GC-09) on cycle number. Difference between the open circuit voltage and the closed circuit voltage divided by the current gave the cell resistance at the particular state of charge. The values for cell resistance obtained at different state of charge (and discharge) were used to determine the average cell resistance during charge (and discharge).

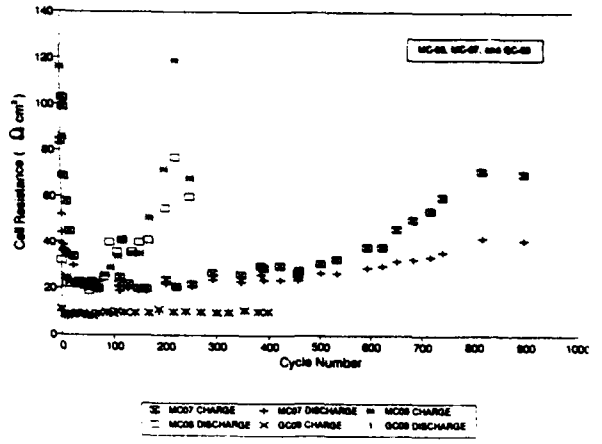

Figure 3 Dependence of the Charge and the Discharge Resistances of the Cells MC-06, MC-07 and GC-09 on Cycle Number.

From Figure 3 it is clear that Cell GC-09 has a lower resistance which increased only slightly with cycling. This cell was a laboratory cell used for comparison with the engineering cells; it employed a ß"-alumina tube from the same batch as cells MC-06 and MC-07. Generally, the cell resistance could be affected by a number of factors. For example, Table 2 presents average laboratory cell resistance during the first 100 cycles as a function of current collectors, initial melt composition, and ß"-alumina treatment prior to cell assembly.

Table 2

Average Laboratory Cell Resistance for Several Current Collectors, Initial Melt Composition, and ß"-Alumina Treatment During the first 100 Cycles

Cell	Current collector	Initial melt	Cell resistance (Ωcm^2)
GC-04[1]	W-coil	acidic	59
GC-15	W-coil	basic	32.5
GC-19	RVC	basic	10.5
GC-06*	W-coil	acidic	31
GC-10*	W-coil	acidic	30.5
GC-28	RVC	basic	7.4
GC-09[2]	W-coil	acidic	8.8
GC-29[2]**	W-coil	basic	4.9

* ß"-alumina tube lead acetate treated.
[1] Without oxygen-getter in the sodium electrode.
[2] New ß"-alumina tube.
** First 1000 cycles.

From Table 2 it is clear that the cell with the RVC current collector has three times lower resistance than the one with the tungsten coil. Also, of the two identical cells the one containing initially a basic melt shows ≈ 50% lower resistance than the one containing an acidic melt.

The laboratory cells contain mainly moisture as an impurity. However, for engineering cells, in addition to moisture, other impurities (e.g. Fe, Cr, Ni from stainless steel) can be generated by the reaction between the vapors of the melt containing sulfur(I) and the top flange or the nickel gasket during charge/discharge and introduced into the melt. For example, the cell resistance for the cell MC-06 increased rapidly with cycling mainly due to the above mentioned reaction in which components of the steel flange (Fe) were introduced into the melt causing an increase in resistance. However, for the cell MC-07, in which the top flange was nickel coated, the cell resistance increased much slower with cycling than for Cell MC-06. The charge/discharge studies showed a relatively low decrease in capacity with cycling. For example, for one cell 8% decrease in capacity after 128 cycles and 20% decrease after 571 cycles, were observed. The observed decrease in the cell capacity is expected from the reaction of sulfur compounds with the top flange. *Post mortem* analysis of the cells showed the presence of metals (Fe,Ni) in the melt as well as of sulfur and chlorine on the lower surface of the top cover. Most of the charge/discharge results were obtained with the engineering cells which employed compression type of seals. However, cells with a brazed seal were also constructed and their performance was evaluated. Cell resistance for these cells began to increase much earlier than for other cells. It was observed that the cells developed a leak on the melt side. The cells with brazed seal employed standard materials with no additional surface protection (e.g. tungsten coating); the seal appeared to be affected by the cathode materials. Results of the studies with cells utilizing stainless steel and nickel show that these materials are less compatible than what was indicated by the static compatibility studies.

All cells with fractured ß"-alumina will show zero resistance. We studied several low capacity cells where the fracture of ß"-alumina caused only a small temperature increase (50°C). Normally, short-circuiting of a cell will not result in cell failure. Deep-discharge and overcharge, and freeze-thaw also had no effect on cell performance. This applies to both engineering cells and laboratory cells.

For the cells that employed compatible materials (laboratory cells) it was observed (for example, for Cell GC-29 in Figure 4) that with continued cycling the cell resistance remained essentially constant, between 4.5 and 5Ωcm^2, until the cell underwent more than 2900 cycles.

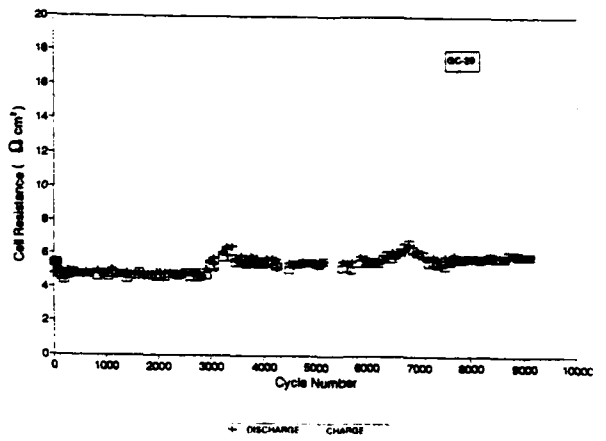

Figure 4 Dependence of the Charge and the Discharge Resistances of the Cell GC-29 on Cycle Number.

Figure 5 shows the effect of overcharge and high current density on the cell resistance. The results show that the cell overcharge had no effect on the cell resistance. This cell was frozen four times (during cycles #64,1025,2770,and 2841). The freeze-thaw had only a negligible effect on the cell resistance. The maximum current density passed through this cell was 0.55A/cm^2.

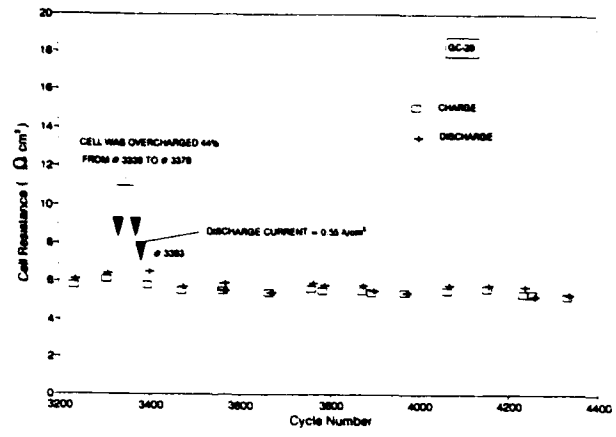

Figure 5 Effect of Overcharge and High Current Densities on the Resistance of the Cell GC-29.

A plot of power delivered vs. current density is shown in Figure 6.

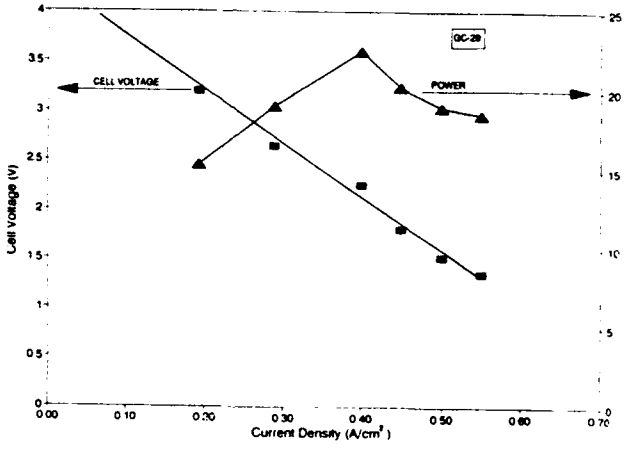

Figure 6 Dependence of the Cell Voltage and Power on Current Density for the Cell GC-29

The results show that the maximum power delivered was 22.5W at 0.40A/cm².

4) High energy cells

All the cells mentioned so far had relatively low concentrations of sulfur(S/Al=0.14); thus their theoretical capacity was low. In the Na/S(IV) chloroaluminate cell the solvent ($AlCl_3$/NaCl melt) participates in the charging/discharging reactions. Its composition changes from basic composition in the discharged state to acidic composition in the fully charged state. Final Lewis acidity depends on the sulfur concentration and the starting melt composition. High sulfur concentration results in a high melt acidity in the fully charged cell. The coulombic capacity of these cells can be increased by adding more sulfur to the melt. It appears that the highest $AlCl_3$/NaCl composition that can be reached in practice lies between 75/25 mole% and 80/20 mole% $AlCl_3$/NaCl.

Two types of high energy cells Na/S(IV) in $AlCl_3$/NaCl can be built depending on the melt composition in the totally discharged state

I) cells that operate almost exclusively in acidic melts

II) cells that operate partly in basic and partly in acidic melts.

Type II cells can achieve significantly higher capacity than Type I cells. Type II cells contain an excess of sulfur, therefore the sulfur in the cathode compartment is only partly oxidized. The capacity density of these cells can be as high as 0.253Ah/cm³ while for Type I cells capacity density is limited to ≈0.164Ah/cm³. Hence overcharge of such a cell causes oxidation of excess sulfur. The useful energy density of the cathode compartment for Type II cell is 80% greater compared to the standard cell(S/Al=0.14). Both Type I and Type II laboratory cells were built and operated. Their charge/discharge efficiency has been 99%. The average OCV of a Type I cell was slightly higher than the average OCV of a Type II cell. On the other hand the cell resistance for Type II cell is higher than for Type I cell. Type I cell achieved a resistance (5.8Ωcm²) which was comparable to other previously studied cells.

Conclusions

Engineering cells Na/ß"-alumina/S(IV) in $AlCl_3$/NaCl melts have been designed and their performance tested. Two types of seal design were utilized: 1) with compression seal, 2) with brazed seal. Materials compatibility studies were also performed. High capacity cells were constructed and their electrochemical characteristics determined as well.

It was determined that both stainless steel and nickel are attacked by the cathode mix with time. The stainless steel is attacked more readily than nickel. However, tungsten and RVC are compatible with the cathode mix. Tungsten coating can be utilized for the protection of nickel and stainless steel. Charge/discharge studies have shown that the cell resistance increases with cycling due to the introduction of impurities (Fe, Ni). However, the cell resistance in laboratory cells is not affected for thousands of cycles. The lowest resistance obtained for one cell was 4.5Ωcm² while the maximum discharge current passed through this cell was 0.55A/cm². The maximum power delivered was 22.5W at 0.40A/cm². Capacity density of high energy cells can be as high as 0.253Ah/cm³.

Finally, based on above results it appears that the cell Na/ß"-alumina/S(IV) in $AlCl_3$/NaCl melt can meet requirements for applications in electric vehicles.

Acknowledgement

This work was supported by the Air Force Systems Command, Wright Laboratory, Wright-Patterson AFB, Ohio 45433-6563, through a Phase II SBIR Contract (Contract No. F33615-88-C-2912).

References

1. G. Mamantov, R. Marassi, J. P. Wiaux, S. E. Springer and E.J.Frazer, in "Proceedings of the Symposium on Load Levelling", N. P. Yao and J. R. Selman, eds., The Electrochemical Society, Princeton, New Jersey, 1977, pp.379-383.
2. G. Mamantov and R. Marassi, U.S. Patent 4,063,005 (1977).
3. G. Mamantov and J. Hvistendahl, J. Electroanal. Chem., 168, 451 (1984).
4. G. Mamantov, U.S. Patent 4,508,795 (1985).
5. R. Marassi, J. Q. Chambers, and G. Mamantov, J. Electroanal. Chem., 69, 345 (1976).
6. Liquid-Metals Handbook, NAVEXOS P-733, Atomic Energy Commission, Department of the Navy, June 1952, Washington, D.C.

SODIUM-SULFUR CELL TESTING

James A. DeGruson
Advanced Systems Operation

Eagle-Picher Industries, Inc.
C & Porter Streets
Joplin, Missouri 64802

Introduction

Eagle-Picher Industries, Inc. (EPI) has been actively involved in the development of Sodium-Sulfur technology since 1986. During this time the cell technology has improved and evolved significantly to the point that complete battery systems are being tested. Most of the effort has been directed toward aerospace applications, however, the technology learned is directly applicable to terrestrial uses. The specific energy achieved for single cells is in excess of 150 W-h/kg. Detailed herein is a brief description of cell and battery construction followed by cell and battery test results showing the advancement of Sodium-Sulfur technology.

Cell Construction

All cells are of the central sodium design meaning that the cathode container has to resist the corrosiveness of the sodium polysulfides. Container designs utilized have employed either molybdenum or stainless steel with chrome plating. The stainless steel containers have demonstrated over 12,000 cycles and the molybdenum containers will cycle indefinitely.

Cell sizes have ranged from 10 Ah through 55 Ah with emphasis on 40 and 55 Ah sizes. Cell designs have incorporated various build parameters which insure proper cathode mixing and sodium availability at the zero g environment of a spacecraft.

Of particular importance to the design of a Sodium-Sulfur battery is consistent cell performance. This is accomplished by controlling the construction of the cell and its components. The β " - Al_2O_3 electrolyte tubes have been investigated extensively[1]. The development efforts have contributed significantly to EPI's understanding of the electrolyte attributes necessary to ensure that performance goals are achieved by the completed cell. The electrolyte inspection techniques incorporated in the EPI Sodium-Sulfur cell manufacturing process include destructive and nondestructive tests. The end result of the manufacturing control is very consistent cell performance.

Cell Performance

Test Equipment Setup

The cycling regime and data acquisition are computer controlled for all testing. The temperature is monitored by the tester but is controlled by temperature controllers with back-up temperature protect circuitry. The cells are connected to the Data Acquisition System (DAS) via a voltage lead and a minimum of one thermocouple. During cycling the computer/DAS will scan the cells at 10 second intervals to determine if any cells are falling out of the current, voltage or temperature limits. Figure 1 shows a typical print-out of the information summarizing a test cycle for four (40 A h)cells. Below the graph in Figure 1, two lines of information per cell are printed. The upper line reflects the charge data and the bottom line is the discharge data. The resistance is shown in milliohms. The graph depicts the cells in the discharge mode at the left, followed by an open-circuit mode for thirty minutes and then the charge regime.

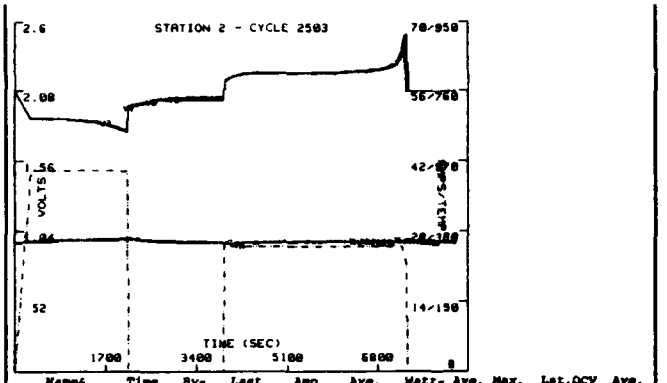

	Name& Cycle	Time (Min.)	By-Pass	Last Volts	Amp Hours	Ave. Amps	Watt-Hours	Ave. Temp	Max. Temp	Let.OCV Pow.Eff	Ave. Resis
3	40-11	56.83	VOLT	2.502	23.65	24.97	52.6	351	363	2.073	
	Cyc# 252	35.00	MA	1.788	23.25	39.85	43.1	357	370	81.9	5.73
4	40-12	57.50	VOLT	2.508	23.90	24.94	53.1	349	361	2.073	
	Cyc# 252	35.00	MA	1.772	23.25	39.85	43.0	355	364	81.0	5.74
5	40-13	57.67	VOLT	2.501	23.96	24.93	53.2	353	366	2.072	
	Cyc# 252	35.00	MA	1.777	23.25	39.85	43.1	359	369	81.0	5.65
6	40-14	57.33	VOLT	2.502	23.84	24.95	52.9	350	362	2.073	
	Cyc# 252	35.00	MA	1.775	23.25	39.85	43.0	357	370	81.3	5.71

Figure 1. Typical print-out of cell summary test data.

Cell Test Data

Figure 1 shows the test data for 4 cells on cycle 252 being charged at a *constant current* of 25 amps to a cut-off voltage of 2.5 volts. The test equipment is set to bypass each cell whenever it reaches this cut-off voltage or a specified time. All four cells of figure 1 reached the cut-off voltage at approximately the same time resulting in an average of 23.8 Ah per cell. Figure 2 shows the test results for the same four cells on the next cycle (253) with a *constant potential* charge averaging 21.5 amps to a cut-off voltage of 2.5 volts. With the constant potential charge none of the four cells reached the cut-off voltage and the charge was terminated by time (70 minutes). This resulted in approximately 5% more capacity being returned to the cells (25.1 Ah versus 23.8 Ah).

With both types of charge reflected in figures 1 and 2, the cell to cell variation was very small. This has been demonstrated in larger groupings of cells tested at EPI and is very important for battery construction[2].

The 40 Ah size cell has been evaluated at EPI over a wide range of discharge/charge rates with the performance continuously being improved. Figure 3 shows cell voltage versus state-of-charge over discharge rates from 10 amps through 40 amps in 5 amp increments. Since the cell performance has proven to be very stable, reproducible, and consistent; EPI initiated work on various battery designs in 1990. This work has been accomplished on internal funding

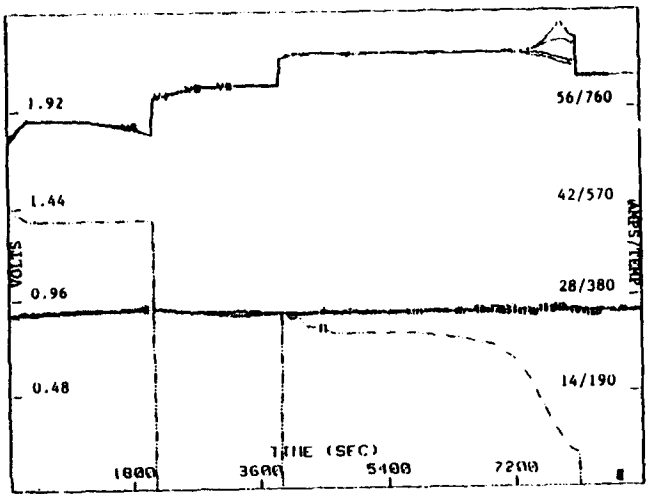

Figure 2. Discharge, open-circuit, and charge profile of four 40 Ah cells (constant voltage charge).

and to facilitate time and cost, the battery constructed has been limited to designs utilizing four-cells.

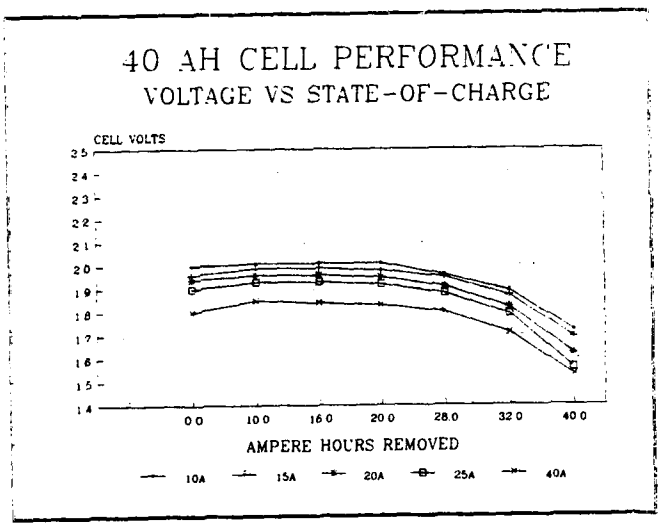

Figure 3. Cell performance at different discharge rates.

Battery Construction

The battery construction consists of two main parts. The first is the cell mounting with electrical and temperature monitoring connections. The second part is the overall enclosure with heaters and thermal insulation. As shown in Figure 4, the cells were built with a flange on the opposite end of the header This flange was bolted to a ceramic plate that was immediately on top of the heater.. The header end of the cell was constructed with a threaded fill tube which also served as the negative terminal. Each cell was fitted with three thermocouples to assess the thermal transfer within the battery enclosure. Each of these thermocouples was secured with a hose clamp.

In addition to the twelve cell thermocouples, three battery thermocouples were attached within the insulated enclosure. The temperatures throughout the battery were consistent with no heat concentrations in any one area. Initially tubes (shown in Figure 4) were used to run the electrical, thermocouple, and heater power wires. Due to heat loss through this arrangement, the tubes were replaced with connectors.

Figure 4. Four cell battery without the insulated enclosure.

The thermal enclosure consisted of a perforated right cylindrical frame surrounded by 100 continuous wraps of multifoil insulation. These wraps are flush with the top of the inner shell with 100 layers of multifoil then placed on top to form the "roof". A stainless steel cover was placed on top of the inner frame and multifoil. The center of the cover had a vacuum connector welded to the top. This allowed monitoring of the vacuum and also allowed varying the vacuum to change the thermal transfer qualities of the enclosure. Table 4 shows the heat loss changing with respect to the amount of vacuum.

Table 1. Battery heat loss data (multifoil insulation).

Temp (°C)	Vacuum (millitorr)	Heat Loss (watts)
300	none	43.77
300	100	16.27
300	190	15.83
400	none	69.83
400	140	24.80

The bottom assembly consisted of 75 layers of multifoil insulation with a top layering of heavier multifoil (15 sheets). The interface of the bottom and top cylinder were gasketed and bolted together. This allowed easy access to make modifications to any internal battery components. A number of different insulation materials and heaters were evaluated in the bottom of the battery. Figure 5 shows the thermal enclosure with the battery and the test panel. The thermal enclosure was made large enough to evaluate cells up to 100 Ah capacity.

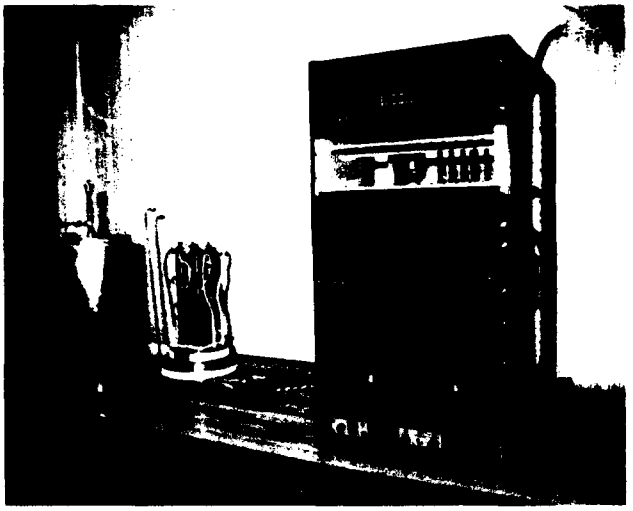

Figure 5. Four cell battery connected to test equipment and thermal enclosure removed.

Battery Performance

Several four-cell batteries have been built. The first battery built did not have a variable vacuum system incorporated into the container and the highest discharge rate achieved was 40 amps (C rate). Higher discharge rates resulted in the internal temperature exceeding the upper limit of 400°C.

The battery shown in Figure 4 was discharged to 60% depth of discharge (DOD) for 1000 cycles with no loss in capacity. Each cycle consisted of a discharge of 48 amps for .5 hours and a charge of 24 amps for 70 minutes. A constant current charge was used and rather than stopping the charge at a battery voltage of 10 volts, the charge was stopped when any one cell reached 2.5 volts. This meant that 3 of the 4 cells were not necessarily charged to their fullest capacity and after iterative cycles could be losing capacity. However the cells performed very consistently and after 1000 cycles, full capacity of the battery was still available. It should be mentioned that during the 1000 cycles, no conditioning cycles were used to revive any cells.

During the 100 minute cycles, the heater input was monitored. The test was initiated at 325°C internally and the heating from discharge was such that no additional heat input from the heater was necessary. The internal temperature approached 400°C during discharge and during charge the temperature dropped back to approximately the 325°C initial temperature. Thus, no heat input was required during the charge part of the cycling regime either. With a variable thermal container, a wide flexibility in rates of discharge are possible. With a fixed amount of thermal insulation and no mechanism for cooling, the Sodium-Sulfur battery's rate of discharge is restrictively dependent upon the thermal conductivity of the battery container.

Conclusion

Thermal management is very important for Sodium-Sulfur batteries but the cells have proven to be very resistant to conditions imposed upon them within a battery. All electrical and thermal test results show that Sodium-Sulfur batteries can provide major improvements in spacecraft power system weight and volume requirements. Additional testing related to the spacecraft's' environmental effects are needed but the low cost of the Sodium-Sulfur battery is an extra incentive for replacing currently used Nickel-Cadmium and Nickel-Hydrogen batteries.

References

1 L. A. Addington, et al., "Fabrication and Testing of Beta"-Alumina Electrolyte Assemblies," *Proceedings of the 35th International Power Sources Symposium*, pp. 391-394, 1992.

2 J. L. Sudworth and A. R. Tilley, The Sodium Sulfur Battery, London: Chapman and Hall, Ltd., 1985, ch 11, pp 349-355.

LITHIUM/BORON ALLOY AS AN ANODE MATERIAL IN PRIMARY OXYHALIDE CELLS

Michael F. Pyszczek and Esther Sans Takeuchi
Wilson Greatbatch Ltd., Clarence, NY

Introduction

Much work has been done in the evaluation and development of lithium alloys for electrochemical applications. While the focus of earlier efforts had been largely in the area of molten salt thermal cells, other studies have explored the use of alloys in both primary and rechargeable lithium systems.

The investigation of lithium-boron alloys in electrochemical cells is believed to have begun in 1972 at the Naval Surface Weapons Center where the alloy evolved from research in high-strength structural materials.[1] Subsequent to this initial report which described the properties of the alloy as an anode in molten LiCl/KCl eutectic electrolyte, a more complete analysis of lithium-boron systems was offered by Dallek et al.[2] and James and DeVries.[3,4] Mixtures ranging from 50-90 atomic percent lithium were studied by differential scanning calorimetry[2], and results suggested that at high lithium concentrations, a two-phase material comprising Li_7B_6 and pure lithium existed.[4] The high lithium alloys were found to be malleable and thermally stable to temperatures approaching 600°C. Szwarc et al.[5] further studied the use of lithium-boron alloys in thermal cells and described the properties of the alloy at thermal battery operating temperatures as being that of liquid lithium immobilized by a porous Li_7B_6 matrix.

The high thermal stability of lithium-boron alloys suggests that it may be possible to develop primary cells with enhanced safety characteristics and reasonable discharge performance. Holmes [6] explored the use of a 68 weight percent alloy in MnO_2 cells utilizing a PC/DME electrolyte. Although the alloy displayed reasonable discharge performance, it was found to generate a highly pyrophoric discharge product. The anode remains reportedly auto-ignited in air, thus severely limiting the potential of this system.

Wilson Greatbatch Limited, in conjunction with NASA, has studied the use of lithium-boron alloys in Li/BCX primary cells. The use of an inorganic electrolyte system was thought to offer the potential of increased cell safety while avoiding the production of pyrophoric discharge products associated with the use of an organic electrolyte. Efforts included an examination of the reactivity of the Li-B anode, and safety and performance evaluation of spirally wound D cells utilizing the alloy as a negative electrode.

Experimental

The lithium-boron alloy used during this investigation was obtained from Cyprus Foote Mineral Company. Compositions ranged from 43 to 44 weight percent lithium ($\approx Li_7B_6$). The material was quite malleable, and demonstrated handling characteristics similar to pure lithium metal. Spirally wound D size test cells were constructed using the Li-B alloy, along with control cells employing pure lithium. BCX depolarizer, consisting of $SOCl_2$ with dissolved BrCl and 1.13M $LiAlCl_4$, was used throughout the experiment. The cell design yielded an electrochemical surface area of 223 cm^2. Cell testing was performed under both constant resistive load and pulse discharge conditions. Temperature effects on cell performance were evaluated for each series of tests. For the pulse testing, the SARSAT regime, consisting of a 50mA background load with 2A, 0.5 sec. pulses applied at 50 sec. intervals was used.

Results

Constant Resistance Discharge

Cells were discharged through resistive loads of 1, 5, 20, 75, and 301Ω under room temperature conditions. Figure 1 presents a performance comparison of the Li-B cells vs. the lithium anode samples.

Figure 1.
Capacity vs. Rate Comparison of LI and LI/B Alloy BCX D Cells.

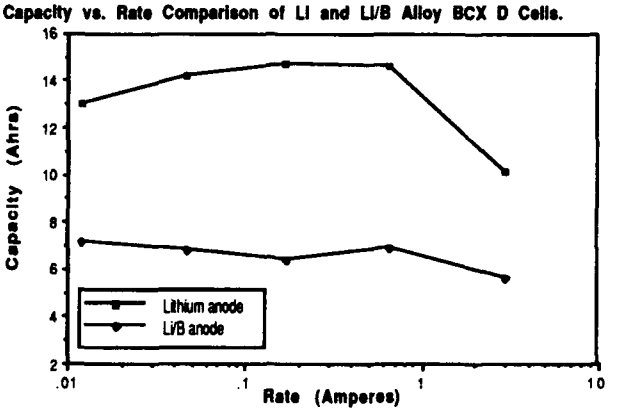

This plot reveals that the Li-B alloy cells deliver only ≈50% of the capacity provided by the control group cells. Based on the average anode mass present in each cell, the results here indicate a 57% utilization of the lithium incorporated in the Li_7B_6 alloy.

Further evaluation was performed by discharging cells through a range of temperatures from 50 to -55°C under a constant 1Ω load. Results expressed as a plot of temperature vs. delivered capacity appear in Figure 2.

Figure 2.
Capacity vs. Temperature Comparison of Li and Li/B Alloy BCX D Cells.

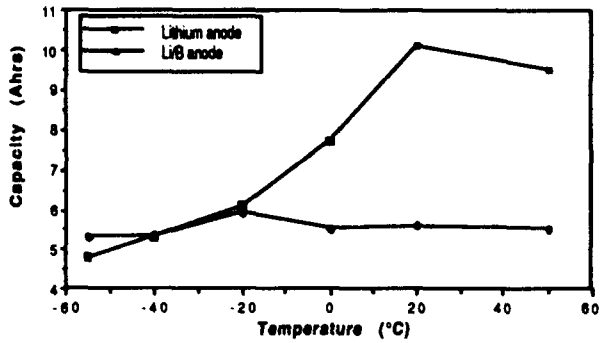

The expected relationship between capacity and temperature is displayed by the curve depicting lithium anode performance. The alloy, however, provides relatively consistent capacity values throughout the range of temperatures. Noteworthy is the observation that as the performance of standard Li/BCX diminishes at -40°C and below, the alloy-containing cells actually provide better capacity.

Additional information regarding the variable temperature performance of these systems is offered as voltage vs. temperature comparisons in Figure 3.

Figure 3.
Voltage vs. Temperature Comparison of Li and Li/B Alloy BCX C Cells.

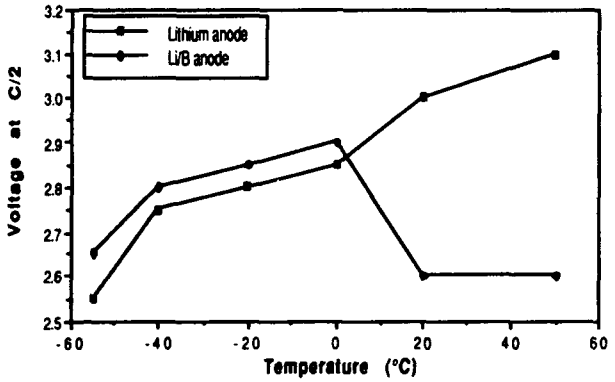

The discharge temperature sensitivity of the Li-B anode cells is again demonstrated in this plot. At 0°C and below the Li-B cells provide a small voltage improvement over the control group, with voltage decreasing quickly as temperature increases. Examination of voltage at half capacity may be misleading due to the shape of the Li-B alloy discharge curve. Figure 4 represents the discharge profile for the 0°C discharge at 1Ω, and clearly illustrates the sloping curve characteristic of these cells.

Figure 4.
Li-B/BCX Discharge at 1Ω, 0°C

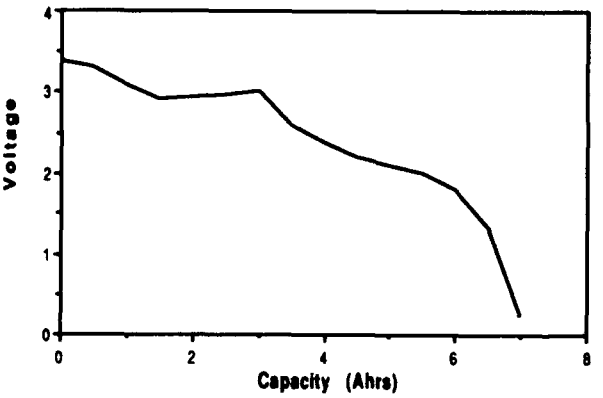

When compared with the Li/BCX curve (Figure 5) gathered under the same discharge conditions, it is apparent that a running voltage comparison may paint only a partial picture of actual cell performance.

Figure 5.
Li/BCX Discharge at 1Ω, 0°C.

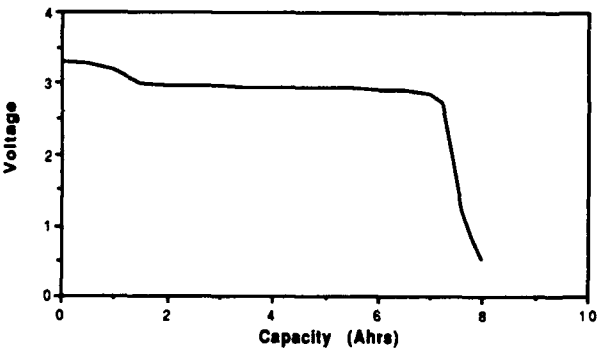

It should be noted that the shape of the Li-B anode curve (Figure 4), showing a step-wise discharge, is consistent with the findings of Larrick [1] when the alloy was employed in a molten electrolyte cell.

Pulse Discharge Testing

Pulse testing was performed on both Li-B alloy-containing test cells and BCX D control cells according to the SARSAT regime described previously. A range of temperatures from 50 to -55°C were also employed during this phase of the evaluation. The plot of temperature vs. time to the 1.5V cutoff shown in Figure 6 summarizes the results of the pulse evaluations.

Figure 6.
Performance Comparison of Li vs. Li/B Alloy BCX D Cells Under SARSAT Pulse Regime.

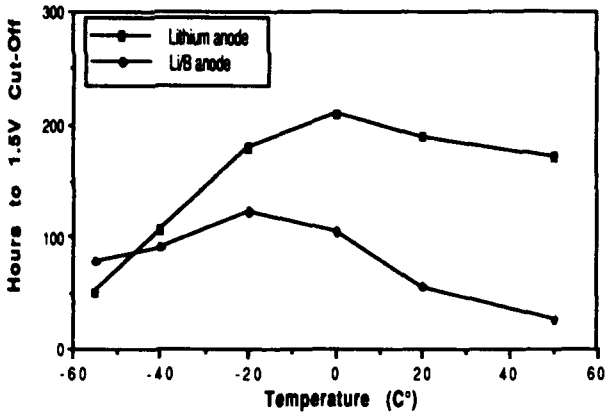

Performance trends that were seen during the constant resistance discharge testing also seem to persist under these pulse conditions. The Li-B alloy cells continue to display poorer behavior as test temperature increases. At the low end of the temperature spectrum, reversal of this performance is seen and substantiates the observations made upon examination of Figure 2.

Safety Testing

Crush and puncture tests were performed on both groups of cells. In all cases the cells vented and burned as a result of the action. No clear difference in the severity of these events based on the anode material contained in the cell could be made.

In response to the observations made by Holmes [6] regarding the pyrophoric nature of Li/B anode residue, cells were disassembled after discharge and examined. Anodes extracted from these cells failed to react in air at humidity levels of 0.5% RH or 75% RH. Contact with water induced activity similar but slightly less vigorous than that of pure lithium. Upon exposure of the depleted Li-B alloy anode to a direct flame, the remaining lithium was consumed, but the residue, presumably boron, failed to burn further.

Conclusions

Although the Li-B alloy demonstrated performance equal or better than Li/BCX cells at temperatures below -20°C, capacity degraded rapidly with increasing temperature. This, along with the sloping discharge profile, suggests that the Li_7B_6 alloy is not suitable as a direct replacement for lithium in primary oxyhalide cells. Safety aspects of cells containing the alloy do not appear to differ appreciably from standard lithium-containing samples. In contrast to previous work in organic electrolyte systems, the residue present at the anode after discharge in an oxyhalide system does not appear to be pyrophoric.

Acknowledgement

The authors gratefully acknowledge the support of NASA for this work and, in particular, Mr. Mort Friedman for his valuable technical assistance.

References

(1) B. F. Larrick, S. D. James, R. Szwarc, Lithium-Boron Alloy- A New Battery Anode Material, Proc. 28th Power Sources Symposium, p. 95 (1978).

(2) S. Dallek, D. W. Ernst, B. F. Larrick, Thermal Analysis of Lithium-Boron Alloys, J. Electrochem. Soc., 126, No. 5, p. 866 (1979).

(3) S. D. James, L. E. DeVries, Structure and Anodic Behavior of Lithium-Boron Alloys in the LiCl-KCl Eutectic Melt, J. Electrochem. Soc., 123, No 3, p. 321 (1976).

(4) L. E. DeVries, L. D. Jackson, S. D. James, Structure and Anodic Behavior of Lithium-Boron Alloys in the LiCl-KCl Eutectic Melt (II), J. Electrochem. Soc., 126, No 6, p. 993 (1979).

(5) R. Szwarc, R. D. Walton, S. Dallek, B. F. Larrick, Discharge Characteristics of Lithium-Boron Alloy Anode in Molten Salt Thermal Cells, J. Electrochem. Soc., 129, No 6, p. 1168 (1982).

(6) R. W. Holmes, Lithium Alloy Anodes in Organic Electrolyte Cells, Abstract 66, p. 107, The Electrochemical Society Extended Abstracts, Vol. 83-2, Washington D. C., October 9-14, 1983.

SELF-DISCHARGE RATE OF LITHIUM THIONYL-CHLORIDE CELLS

Wendy R. Cieslak
Sandia National Laboratories
Exploratory Batteries Department 2223
Albuquerque, New Mexico 87185-0614

Abstract

Our low-rate lithium/thionyl-chloride "D" cell is required to provide power continuously for up to 10 years. The cell was designed at Sandia National Laboratories and manufactured at Eagle-Picher Industries, Joplin, Missouri. We have conducted accelerated aging studies at elevated temperatures to predict long-term performance of cells fabricated in 1992. Cells using 1.0M $LiAlCl_4$ electrolyte follow Arrhenius kinetics with an activation energy of 14.6 Kcal/mol. This results in an annual capacity loss to self-discharge of 0.13 Ah at 25°C. Cells using a 1.0M $LiAlCl_4 \cdot SO_2$ electrolyte do not follow Arrhenius behavior. The performance of aged cells from an earlier fabrication lot is variable.

Introduction

Sandia National Laboratories designs cells and batteries for high reliability weapons applications. Our low-rate lithium/thionyl-chloride "D" cell is required to provide power continuously for up to 10 years. The cell was designed at Sandia and manufactured at Eagle-Picher Industries, Joplin, Missouri. We have previously presented data demonstrating the excellent safety performance of this design.[1] In this work, we present the results of accelerated aging studies that predict long-term cell performance.

Cell Design

The active surface area is 145 cm^2. The cathode is made up of two 0.9 mm thick parts lying together and acting as a single electrode. This allows the parts to slide upon one another while rolling the short, squat spiral stack. In addition, the outer wrap is only single thickness, thereby fully utilizing all components. The cathode uses a 50/50 Shawinigan Acetylene Black/Cabot Black Pearls blend that we have described previously.[2] The separator is a Whatman binder-free borosilicate glass fiber mat.[3] We use 1M $LiAlCl_4$ electrolyte, and, in this study, we evaluate SO_2 as an electrolyte additive to mitigate voltage delay. The theoretical capacity of electrolyte in the cell is 19.3 Ah, and the theoretical Li capacity is 17.6 Ah. At discharge rates of ≥10 mA, the cell capacity is limited by the capability of the carbon cathode to accommodate discharge products. The presence of excess electrolyte is maintained for safety purposes, i.e. to insure that the cell can never run dry. The presence of excess Li may contribute to safety, particularly during over discharge, because it maintains a stable electrode potential. It may also contribute to retention of capacity during long life usage because the cell can afford to lose some Li as a result of corrosion.

To achieve long life, care is taken to purify and dry all parts as well as is practical. The electrolyte is refluxed in the presence of Li for at least four hours. The cathodes are dried in an oil-free vacuum system at 175°C and 30 microns pressure for a minimum of 14 hours. The remaining cell components are dried in a convection oven at 140°C for ≥14 hours. Cells are assembled in a dry room of dew point less than -45°C and filled in an argon atmosphere glove box.

The 304L stainless steel case is of welded construction and uses a glass-to-metal seal of CABAL-12 glass, which is highly resistant to corrosion by Li.[4] The vent mechanism is a 300 psi rupture pressure burst disc manufactured by BS&B Safety Systems. Inc.. The disc operates on a frustum reverse buckling principle, and, as the metal buckles, it tears a score line to open a 3/8" diameter hole.

Accelerated Aging

We accelerated the self-discharge reactions by aging cells in ovens at temperatures from 30°C to 60°C for 63 weeks. At the end of the aging period, each cell was discharged at 25°C under a 50Ω load. The capacity loss was calculated as the difference between the fresh cell capacity, from the average of 12 tests, and the capacity of the aged cell.

Baseline Cells: 1.0M $LiAlCl_4$ Electrolyte

A plot of the logarithm of the capacity loss versus the inverse of the aging temperature yields a linear relationship, Figure 1. This indicates a thermally activated process (Arrhenius kinetics) as expressed by the formula:[5]

$$C(t, T) = C_0 - k_0 t e^{-E/RT}$$

C(t, T) is the capacity loss at time "t" and temperature "T", and the capacity loss at t=0 is defined as $C_0 = 0$. The other parameters are obtained from the least squares fit to the data as shown in Figure 1. Substituting these parameters in the general equation results in the following relationship:

$$C(63 \text{ weeks}, T) = (7.719 \times 10^9) e^{(-7339.2/T)}$$

The value for E/R = 7339.2 and, using R = 1.987 cal/°K-mol, the activation energy E = 14.6 kcal/mol. Activation energies for batteries generally fall in the range of 5 to 15 kcal/mol.[5] Therefore, the capacity loss in these cells shows a relatively strong dependence on temperature. The calculated rate of capacity loss and the [illegible]eration factor as a function of temperature (as [illegible] linear dependence on aging time) are tab[illegible]elow:

TABLE 1

Temperature	Loss, Ah/year	Acceleration Factor
25 °C	0.13	1
30 °C	0.19	1.5
40 °C	0.42	3.3
50 °C	0.68	6.7
60 °C	1.71	13.3

Electrolyte Variation: SO_2 Additive

Cells from the same lot were activated using 1 M $LiAlCl_4 \cdot SO_2$ electrolyte and tested in the same manner as the cells without the SO_2 additive. The fresh cell capacity, standard deviation, and average discharge voltage were unchanged from the baseline cells. After aging, the cells containing SO_2 showed a great variability in their behavior, especially at the higher aging temperatures. For example, one cell aged at 50°C delivered almost no useful capacity, while another delivered more than 14 Ah. The Arrhenius plot, Figure 2, shows these two populations of data in comparison to the baseline cells. The cells containing SO_2 did not behave according to a simple thermally activated process. Instead, some of the cells aged very well, even better than the baseline cells, while others experienced a much higher rate of self discharge. We believe that SO_2 in the electrolyte inhibits growth of the passive film on the anode, as measured by complex impedance analysis.[6] While this effect helps to minimize voltage delay, it may also allow a higher rate of self-discharge to continue. We do not understand why only some of the cells experience the higher self-discharge.

Earlier Cells: 1990 Lot

We also compared cells built in 1990 with those built in 1992. Data from 1990 lot cells tested in the same manner as described above are superimposed on the 1990 lot data, Figure 3. Note th[illegible]e 1990 lot data points show much greater scatter, b[illegible] their average falls very close to the 1992 lot c[illegible]he newer lot implemented improvements in [illegible]rbon cathode fabrication and drying procedures and electrolyte purification techniques, for example, vacuum-drying and refluxing. These changes have substantially increased the cell-to-cell reproducibility.

Summary

We have demonstrated that our baseline 1992 lot cells undergo a self-discharge loss of 0.13 Ah/year at an average temperature of 25°C. The self-discharge reaction is thermally activated, i.e. it follows Arrhenius kinetics. This behavior implies that the mechanism(s) of self-discharge do not change over the temperature range studied. Therefore, elevated temperature aging provides a rapid means of predicting the self-discharge losses for long-term applications. The cause of high variability in self-discharge rate for the cells containing $LiAlCl_4 \cdot SO_2$ electrolyte was not determined. Cells produced in 1992 have smaller variability than those produced in 1990 due to implementation of improved process controls.

Acknowledgments

Prototype lots were built at Eagle-Picher under the direction of David Miller and Tim Counts. Cells were tested at Sandia by Leo Griego. This work, performed at Sandia National Laboratories, was supported by the United States Department of Energy under contract no. DE-AC04-94AL85000.

References

(1) Cieslak, W. R. and Street, H. K., *Safety and Performance of a Long Life Lithium-Thionyl Chloride Battery,* Proc. Eighth Annual Battery Conference on Applications and Advances, Long Beach, CA, January 12 - 14, 1993, Paper #V-7.

(2) Cieslak, W. R. and Street, H. K., *Development of a Moderate Rate Lithium / Thionyl Chloride "D" Cell,* Proc. 34th International Power Sources Symposium, Cherry Hill, NJ, June 25 - 28, 1990, pp. 255 - 258.

(3) Cieslak, W. R., *Compatibility and Performance of Separators in Li/$SOCl_2$ Cells,* Proc. 33rd International Power Sources Symposium, Cherry Hill, NJ, June 13 - 16, 1988, pp. 233 - 239.

(4) Watkins, R. D., et al., *Technology Transfer of CABAL-12 Glass to Support the Fabrication of the MC4050 Power Supply,* Sandia Report SAND88-0498, Printed October 1988, available from National Technical Information Service.

(5) Bro, P. and Levy, S. C., *Reliability Modeling and Accelerated Kinetics,* Quality and Reliability Methods for Primary Batteries, 1990, John Wiley & Sons, Inc., NY, Chapter 10, pp. 127 - 144.

(6) Delnick, F. M. and Baldwin, A. R., *Voltage Delay in Li/$SOCl_2$ Cells for Artillery Applications at -35°C,* Proc. 34th International Power Sources Symposium, Cherry Hill, NJ, June 25 - 28, 1990, pp. 215 - 218.

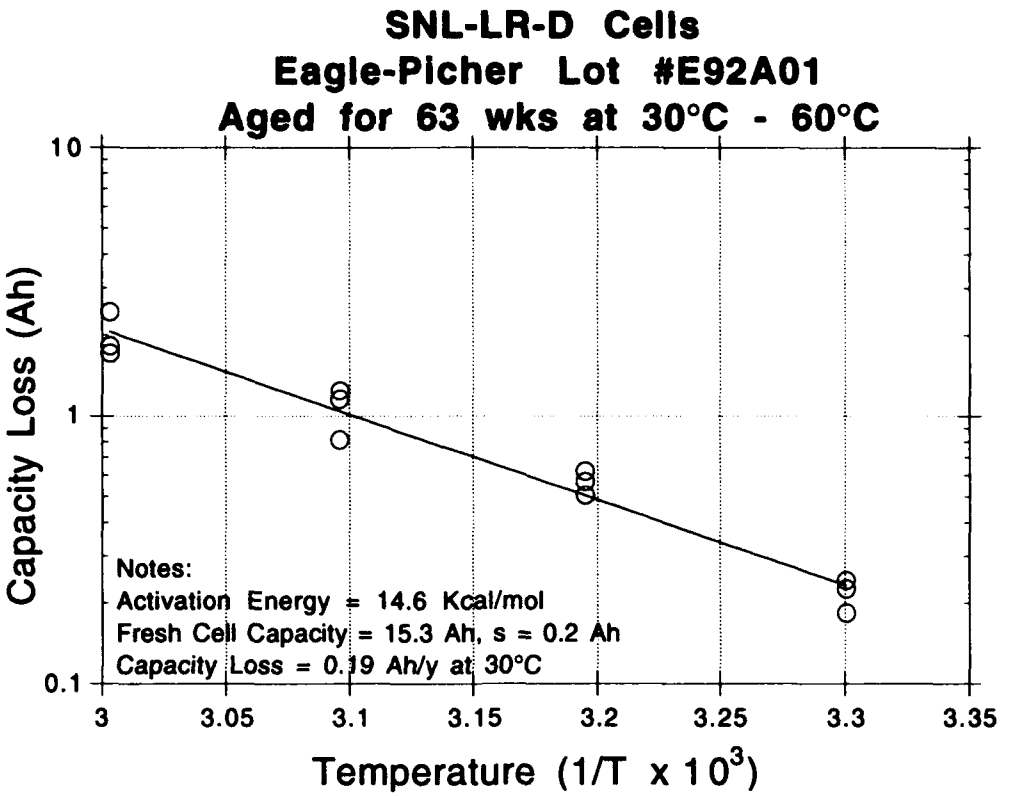

Figure 1. Arrhenius Plot of Cells Activated with 1.0 M $LiAlCl_4/SOCl_2$ Electrolyte (Baseline).

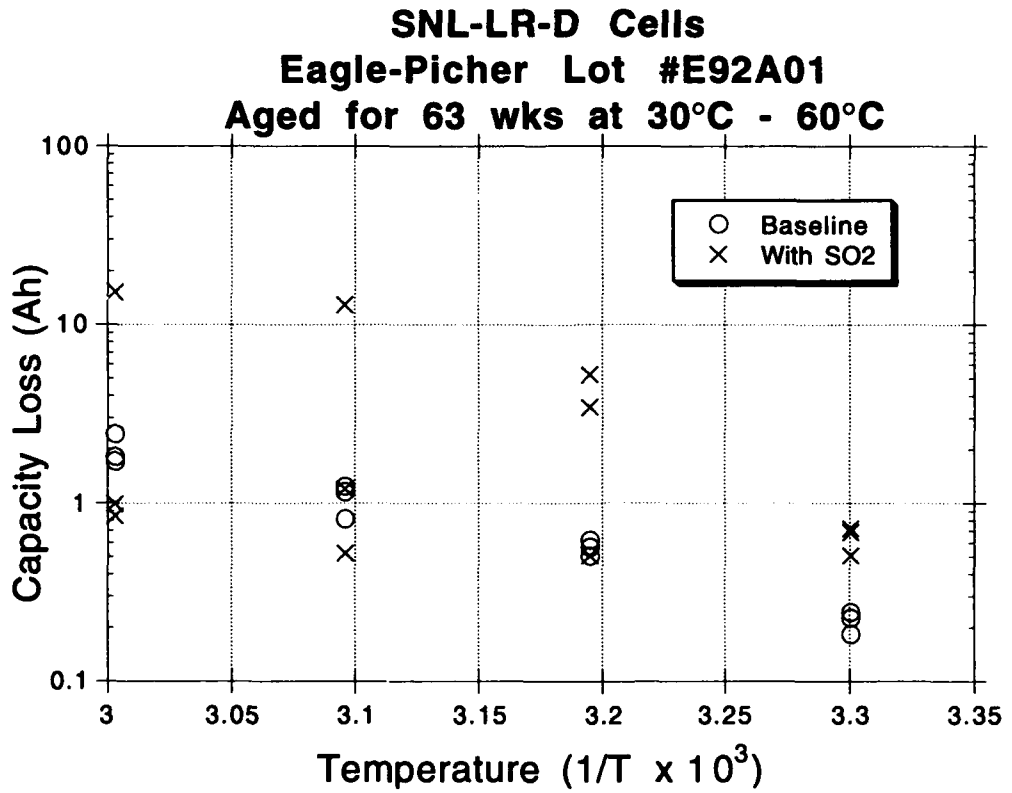

Figure 2. Arrhenius Plot Comparing Cells Activated with 1.0 M $LiAlCl_4 \cdot SO_2/SOCl_2$ Electrolyte to the Baseline Cells.

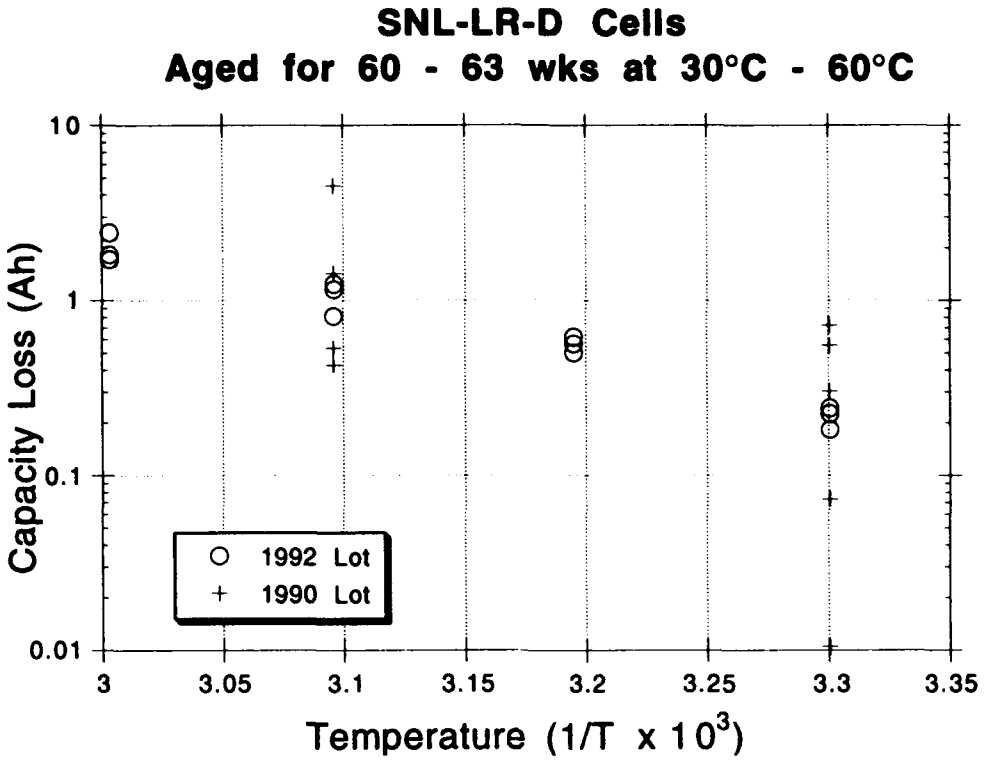

Figure 3. Arrhenius Plot Comparing the 1990 Lot Cells to the 1992 Lot Baseline Cells.

Long Life Reserve Li/$SOCl_2$ Battery For Wide Area Mine

D.L. Miller, R.C. Sheldon, M.A. Manning
Eagle-Picher Industries, Inc.
C & Porter Street
Joplin, MO 64801

Abstract

A battery has been developed which can satisfy the normal reserve application requirements of long storage life and high current discharge while also providing long active life and high specific energy. The 3 pound, 40 $in.^3$ battery was designed to provide a maximum of seven months active life supporting pulses of 3.75 amperes at voltages over 8.0 volts while exposed to temperatures ranging from -35°F to +145°F. In this paper, the battery design, including the novel design characteristic of isolating individual cells while still using a common electrolyte reservoir, will be presented. Also presented is data obtained during environmental testing, both pre and post activation, as well as performance data during various temperature cycles during a seven month discharge and capacity data at select temperatures.

Introduction

The subject battery was developed to supply power for the Wide Area Mine (WAM) family of remote anti tank/vehicle munitions. The battery was designed to withstand system deployment by ground troops using various delivery methods.

The program Statement of Work contained the physical, electrical, environmental and safety requirements. Figure 1 contains a very abbreviated list of these requirements, the ones that were considered to be "Design Drivers". Figure 2 presents the various battery chemistry systems considered for use in battery development and estimates how well each would fulfill the "design driver" requirements. Based upon this information, the reserve lithium thionyl chloride (Li/$SOCl_2$) system was chosen for the development program.

Project Objective

To Deliver a Battery Capable of Meeting the Requirements for WAM Platform Power

Design Drivers

20 Year Unactivated Life
Activation @ -25°F
7 Month Activated Life
2.7 Pounds
38.7 Cubic Inches

Figure 1 Objective/Design Drivers

	WAM Req.	Li/SOCl2	Li-Alloy/FeS2	Zn/AgO
Storage Life	20 yrs	20 yrs	20 yrs	10 yrs
Activation @ -25°F	Yes	Yes	Yes	No
Activated Life	7 Months	7 Months	60 Minutes	24 Hours
Watt Hours/KG	171	171	26	23
Watts/KG	42	42	60	200

Figure 2 Alternative Energy Sources for WAM

Battery Development

The effort to develop a reserve lithium thionyl chloride battery to satisfy the program requirements resulted in the battery design illustrated in Figure 3. The battery is essentially a 40 $in.^3$ cylinder that is 4.2 inches in diameter and 2.9 inches tall. It is mounted to the WAM unit by means of a 5.1 inch diameter .090 inch thick baseplate, which also contains the battery vent mechanism. Electrical connections for battery discharge and igniter firing are made by four recessed terminal pins.

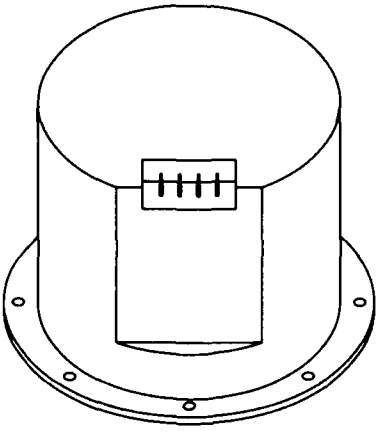

Figure 3 WAM Platform Battery

The basic internal design is illustrated in Figures 4 and 5. The battery contains four series connected horseshoe shaped cells surrounding the cylindrical electrolyte reservoir. Cell electrical connections, venting mechanisms, and electrolyte distribution tubes are located in the ends of the cells (in the open horseshoe area).

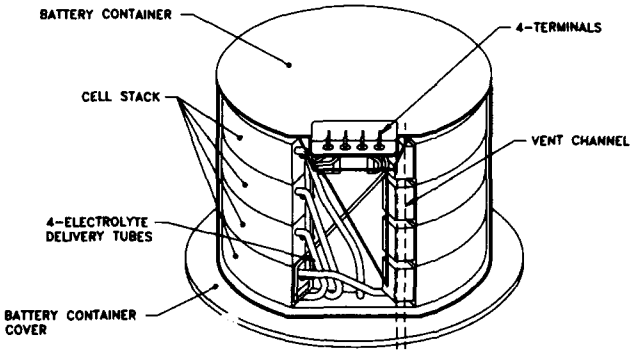

Figure 4 WAM Battery Design

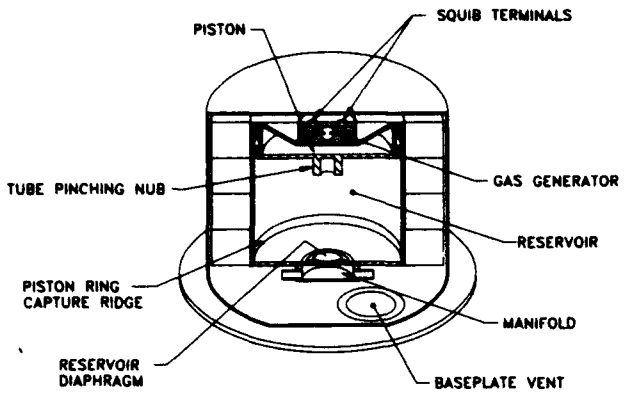

Figure 5 WAM Reservoir Design

Battery activation is initiated by an electrical pulse applied to the igniter which fires the gas generator. The expanding gas moves the piston which pressurizes the electrolyte in the reservoir, breaks the containment burst diaphragm and then forces the electrolyte into the individual cells. The piston continues to move until the leading nub enters the common manifold and seals the cell electrolyte distribution tubes. When the piston reaches full travel, the lock ring expands into a mating groove in the reservoir wall, assuring that the distribution tubes remain closed during the battery's active life and that the piston remains locked in place during all required environmental conditions.

Safety concerns were addressed at all stages of cell and battery development. The efforts were focused on preventing cell and battery internal short circuits and providing mechanisms to control cell and battery responses to abuse conditions. Figure 6 provides a listing of safety features that were incorporated into the cell and battery designs. Measures utilized to greatly reduce the chance of internal cell short circuits included solid electrode substrates (for burr reduction), over-sized separators, optimized component stack compression, internal baffles (to buffer electrolyte entry) and slag barriers (to prevent weld debris from entering the cell stack). As a secondary mesure, a 100% cell capacitance check, performed during vibration, was employed as a measure of design to actual production efficiency. Design measures incorporated to control response to abuse conditions included the placement and sizing of both cell and battery vent mechanisms and the connecting vent channel.

Cell Level

- Solid Electrode Substrates
- Oversized Separator
- Balanced Cells with Optimized Compression
- Electrolyte Baffle
- Slag Barrier
- Venting Mechanism
- 100% Screening (Capacitance)

Battery Level

- Equal Electrolyte Distribution
- Vent Mechanism
- 100% Screening (Capacitance)

Figure 6 Design Incorporated Safety Features

Transportation (49 CFR 173.185)

Safety

- Dead Short Circuit
- 10 Ampere Short Circuit
- Non-Activated Incineration
- Activated Incineration

Environmental

- Thermal Shock (-46°C to 71°C)
- Non-Activated Shock (600g 1.4 ms)
- Activated Shock (1500g .05 ms)
- Loose Cargo Vibration (Activated and Non-Activated)

Performance

- Capacity (-32°C ,24°C ,60°C)
- Mission Profile (Cold Cycle 210 days total)

Figure 7 Successfully Completed Tests

Test Results and Discussion

Batteries were fabricated and subjected to safety, environmental, performance, and transportation tests. Figure 7 provides an abbreviated test summary listing.

Safety testing of the battery design focused on the battery's response to short circuit and fire. Subjecting the activated battery to external dead short circuit conditions resulted in an open cell tab within 10 seconds. Subjecting the battery to an external 10 ampere short circuit also typically results in an open cell tab condition. When the inactivated battery was subjected to an open flame, the battery activated, vented, and burned. Subjecting an activated battery to the same open flame conditions always resulted in the battery exploding. All results obtained were within design expectations and were considered acceptable.

Environmental testing consisted mainly of thermal shock to non-activated batteries, drop shock tests of both activated and non-activated batteries, and loose cargo vibration tests, also on both activated and non-activated batteries. The final battery design was able to withstand all non-activated testing without premature activation or other damage. No activated battery displayed any voltage fluctuations or any other adverse affect to the shock or vibration conditions.

Performance testing consisted of capacity and mission profile tests. Capacity tests included storage, activation, and discharge of batteries at -32°, 24° and 60°C. X-rays of the batteries were also obtained after activation to verify full piston travel and lock. At all three temperatures the batteries were able to meet the required activation time limit (500 ms, maximum) between first voltage and 8.0 volts. Capacities of individual batteries were obtained by discharging each battery at the appropriate temperature at a constant 400 milliamperes. All batteries delivered capacity in excess of the minimum requirement at each required temperature. Specific capacities obtained per test temperature are presented in Figure 8. Long term mission profile tests were performed at the required cold and hot deployment temperature cycles while the batteries were discharged in accordance with the program power profile. This profile included pulses at rates up to 7.5 millliamps per cm^2. One battery was allowed to complete the entire 210 day test profile

at the cold deployment cycle, after which it delivered 3.2 ampere hours during a residual capacity test. The total capacity delivered for this test was 13.0 ampere hours.

The transportation testing was performed in accordance with section 173.185 of CFR 49. Four batteries were subjected to the altitude, thermal stability, vibration, and shock testing per paragraph H.3.ii. None of the batteries displayed any evidence of outgassing, leakage, loss of weight or distortion.

Temperature (°C)	Capacity (Avg.)	Requirement (min.)
-32	11.9 AH	11.0 AH
24	14.6 AH	14.0 AH
60	14.1 AH	13.0 AH

Figure 8 Capacity Test Summary

Conclusion

Eagle-Picher has designed and developed a reserve lithium thionyl chloride battery that exhibits not only the long non-activated shelf life typical of reserve batteries, but also has demonstrated a 210 day activated discharge life fully capable of supporting 7.5 milliamp/cm^2 pulses at any time during this active life. Testing on this 3 pound, 40 in.^{3} battery has been completed to demonstrate its capability to meet and exceed the transportation safety, environmental, and performance requirements of the WAM program. Qualification testing and production have been scheduled for middle and late 1994, respectively.

Acknowledgments

The authors would like to acknowledge that the efforts presented herein were performed for Textron Defense Systems for the US Army, ARDEC, and the Program Manager, Mines, Countermines, and Demolitions, under contract number DAAA21-90-C0018. We would also like to thank Dr. M. Shaw of Eagle-Picher and Ray D'Auteuil of Textron Defense Systems for their advice and support throughout the development program.

UTILIZATION OF THE TAGUCHI APPROACH TO EXPERIMENTAL DESIGN FOR THE ASSESSMENT OF SPIRALLY WOUND LITHIUM OXYHALIDE D CELLS

Pamela J. Size and Esther S. Takeuchi
Wilson Greatbatch Ltd., Clarence, NY

Introduction

The Taguchi Method of Experimental Design was utilized to parametrically assess the effect of four variables in cell design on performance and safety of spirally wound lithium oxyhalide D cells. This approach allows for the examination of many variables at one time through the use of fractional factorial designs. The information collected through such experiments is maximized while the amount of treatment combinations is a fraction of those required of traditional experimental methods. The Taguchi Approach was first introduced into the United States by Dr. Genichi Taguchi in 1980 when AT&T began utilizing his method at their Quality Assurance Center. Xerox and Ford Motor Company began using Taguchi methods in 1982.[1] This approach to experimental design has gained popularity in the United States since then, and has been used at Wilson Greatbatch Ltd. since 1988.

The main structure of the Taguchi approach involves a three step method which includes the System Design, the Parameter Design, and the Tolerance Design. This basic approach can be applied to quality control, engineering, research and development, and problem solving. The System Design, which is the first step in the process, is generated through prior knowledge of the technology involved and is the phase where new ideas are introduced. This is generally thought of as a brainstorming session where the factors in the experiment are determined. The next step in the process is the Parameter Design which identifies the optimum settings of the controlling factors in the experiment and defines the amount of variation in product performance due to each of these variables. Latin Square Designs, or fractional factorials, are introduced at this phase. The third phase in Taguchi methodology is the Tolerance Design which is also a fractional factorial design. This experiment is used to determine the tolerances of the critical factors defined in the Parameter Design. For each of the fractional factorial designs utilized, the data is analyzed by ANOVA analysis which is used to determine the main effects and the percent contribution of each factor in the experiment.

Experimental

Experimental Design

The System Design for this effort identified the four factors to be studied, which were the electrolyte type, the electrolyte concentration, the depolarizer type, and the mechanical cell design. The Parameter Design which best accommodated these four factors was the L18 Latin Square Design. This experimental design requires 18 treatment combinations and can accommodate (7) three-level factors and (1) two-level factor. This basic design is illustrated in Figure 1. Since there were two types of electrolytes, and three levels of each of the other 3 factors, a mixed level experiment was required.

The following formula illustrates how the fractional factorial design reduces the number of treatment combinations required of full factorial designs. For a full factorial design, the number of treatment combinations is:

$$N = L^f \quad [1]$$

where L = # of levels
and f = # of factors

For an experimental design with mixed levels, the equations is modified and becomes:

$$N = L_1^f \times L_2^f \ldots\ldots \quad [2]$$

The number of treatment combinations required of a full factorial experiment which would address this study is equal to $3^3 \times 2^1$ or 54 combinations. This is equal to three times the amount required of the L18 matrix when no replications are made. The Latin Square Experiment reduces the number of treatment combinations while allowing for determination of main effects, % contribution of each factor, and optimum settings of each factor through ANOVA analysis.

Cell Construction

The specific L18 Parameter Design chosen for this experiment is illustrated in Figure 2. The factors studied were the electrolyte type, $LiAlCl_4$ (LAC) and $LiGaCl_4$ (LGC); the electrolyte concentration, 0.6M, 1.2M, and 1.8M; the depolarizer, thionyl chloride (TC), BrCl in thionyl chloride (BCX), and chlorinated sulfuryl chloride (CSC); and the mechanical cell design which differed in working electrode surface area: cell A (123 cm^2), cell B (247 cm^2) and cell C (534 cm^2). D cells of spiral wound construction consisting of lithium anodes and carbon cathodes with a nonwoven glass separator material were used. The cells were vacuum filled with the specific oxyhalide catholyte and hermetically sealed.

Cell Testing

The rate capability and the shelf life determinations for these cells were accomplished through 1A and 3A constant current discharge on fresh cells and cells aged for one year. The cut-off voltage for all discharge tests was 2.0V. A MACCOR Model 3 test measurement system was used to discharge and measure the cells. The temperature of each cell was monitored by individual thermocouples.

The safety issues were addressed under forced-overdischarge (FOD) conditions at 1A and 3A, and high rate short circuit. The FOD test was performed under a constant current at 25±5°C on previously discharged cells that had remained dormant for 3±1 week. Cells tested at 1A were on test for 16 hours and those tested at 3A were on test for 5 hours. ANOVA analysis was conducted on the basis of a rating system designed to assess the level of physical change in cell containment as a result of FOD. The high rate short circuit test was conducted at a constant resistive load of 0.325Ω, with the cells contained in a calorimeter. The heat output for each cell was determined and analyzed by ANOVA methods.

Data Analysis

Lab Partner Software from Sof-Ware Tools was used for the generation of the experimental design and the ANOVA analysis of data. Figure 3 illustrates a sample ANOVA analysis of data from an L18 design similar to the one used in this effort. The ANOVA analysis involves the calculation of the sum of squares in the experiment and the individual factors, including the error in the experimental procedure. The ratio of the variances of each of the factors to the variance of the error, or the F-ratio, is used to determine the confidence level for each factor. A pure sum of squares is calculated based on an assessment of the amount of error in the experiment due to each factor, which is either added or subtracted from that factor's actual sum of squares. From the pure sum of squares, the percent contribution is calculated for each factor based on its fraction of the total sum of squares of the experiment.

Figure 4 illustrates a sample calculation of the main effects of the factors in the experiment. The actual response to the specific performance or safety test is determined for each of the factors and in this way the optimum settings for each of the factors is determined.

Results and Discussion

Rate Capability

The effect of each factor on rate capability of lithium oxyhalide D cells was determined by discharging cells of each configuration at a constant current of either 1A or 3A at 25°C and comparing the operating voltages at 50% DOD. Under a 1A discharge regimen, the operating voltage varied from 3.07 to 3.47V, which was affected the most by the mechanical cell design (42%), with the highest surface area design providing the highest voltages (see Figure 5). The depolarizer had somewhat of an effect on running voltage (22%), and the BCX and CSC depolarizer resulted in higher voltages than the TC depolarizer. Figure 6 illustrates this effect. At the higher rate of 3A, the running voltage is affected only by the depolarizer, and CSC provides better high-rate performance than the BCX and TC depolarizers. CSC results in an average running voltage of 3.26V, compared to 3.07V and 2.97V for BCX and TC respectively.

The effect of each factor on the delivered capacity under both the 1A and the 3A constant current conditions was determined. Under a 1A rate, the capacity was affected the most by the electrolyte and the depolarizer. Cells with LGC electrolyte delivered 20% higher capacities than cells with LAC electrolyte. This factor had a 13% contribution to the overall variation in capacity. The depolarizer contributed 42% to this performance attribute, and the cells with CSC depolarizer delivered the highest capacities. There were three factors affecting the capacity at 3A. The depolarizer, the electrolyte concentration, and the cell design contributed 36%, 23% and 20% to this attribute, respectively. The CSC depolarizer, high molarity electrolyte, and high surface area anode design were favored.

Shelf Life

The effects of the four factors on shelf life were determined by discharging fresh cells under a 1A constant current at 25°C, and repeating the discharge regimen on cells stored for one year. The percent capacity retention was calculated and ANOVA analysis was performed. Figure 7 illustrates the effect of the electrolyte type on capacity retention after one year. The LGC electrolyte resulted in an average capacity retention of 80.7% compared to 32.5% capacity retention for the LAC electrolyte. The three other factors had no significant effect on capacity retention.

Forced Overdischarge

FOD testing at 1A and 3A and 25°C was done both with and without by-pass diodes. Immediately following the test, the cells were assessed regarding any physical change in the cell containment. This assessment was performed using a rating system of 1 - 6, which ranges from no change to case rupture. The data was then analyzed by ANOVA, and the effects of the factors determined. The cell design and the depolarizer type had an effect on cell safety to some degree. Cells with the high surface area design and the BCX depolarizer exhibited the least amount of physical change during FOD.

Short Circuit

The effect of each factor on the short circuit characteristics of D cells was determined by measuring the heat output during short circuit and completing an ANOVA analysis on the data. The factors having the most effect on heat output were the depolarizer type and the electrolyte concentration. Figures 8 and 9 illustrate these effects. The depolarizer resulting in the least amount of heat generated was BCX, contributing 22% to the overall result. The electrolyte concentration contributed to 30% of the result, and the heat output increased with increasing concentration.

Conclusions

The Taguchi approach to experimental design was utilized to assess the effects of four cell design factors on safety and performance of lithium oxyhalide D cells. This method allows for analysis of the four factors with one-third of the treatment combinations of full factorial designs. ANOVA analysis is used to identify the important factors as well as their percent contribution and main effects on the attribute of interest. Additionally, the amount of experimental error can be identified. The rate capability,

shelf life, FOD, and short circuit characteristics were determined for the electrolyte type, the depolarizer type, the mechanical design, and the electrolyte concentration. This study indicated LGC electrolyte had the most significant effect on shelf life. The rate capability was affected the most by the mechanical design and the depolarizer. The high surface area cell and the CSC depolarizer provide the highest running voltages at high rate. The safety attributes studied included short circuit and FOD testing. The high surface area construction and the BCX electrolyte resulted in the least amount of physical change to cell containment during FOD, and the BCX depolarizer and low molarity electrolyte enhance cell safety during short circuit.

Acknowledgements

The National Aeronautics and Space Administration, Lyndon B. Johnson Space Center, is gratefully acknowledged for their financial support of this effort under Contract No. NAS 9-18395.

References

1. T.B. Barker, Engineering Quality by Design, Marcel Dekker, Inc., 1990.

row/column->	1	2	3	4	5	6	7	8
1	1	1	1	1	1	1	1	1
2	1	1	2	2	2	2	2	2
3	1	1	3	3	3	3	3	3
4	1	2	1	1	2	2	3	3
5	1	2	2	2	3	3	1	1
6	1	2	3	3	1	1	2	2
7	1	3	1	2	1	3	2	3
8	1	3	2	3	2	1	3	1
9	1	3	3	1	3	2	1	2
10	2	1	1	3	3	2	2	1
11	2	1	2	1	1	3	3	2
12	2	1	3	2	2	1	1	3
13	2	2	1	2	3	1	3	2
14	2	2	2	3	1	2	1	3
15	2	2	3	1	2	3	2	1
16	2	3	1	3	2	3	1	2
17	2	3	2	1	3	1	2	3
18	2	3	3	2	1	2	3	1

Figure 1. *L18 Experimental Design*

	ELEC	DESIGN	DEPOL	CONC
1	LAC	A	BCX	0.6M
2	LAC	A	TC	1.2M
3	LAC	A	CSC	1.8M
4	LAC	B	BCX	0.6M
5	LAC	B	TC	1.2M
6	LAC	B	CSC	1.8M
7	LAC	C	BCX	1.2M
8	LAC	C	TC	1.8M
9	LAC	C	CSC	0.6M
10	LGC	A	BCX	1.8M
11	LGC	A	TC	0.6M
12	LGC	A	CSC	1.2M
13	LGC	B	BCX	1.2M
14	LGC	B	TC	1.8M
15	LGC	B	CSC	0.6M
16	LGC	C	BCX	1.8M
17	LGC	C	TC	0.6M
18	LGC	C	CSC	1.2M

Figure 2. *Parameter Design*

FACTOR	Df	ΣSQ	VAR	F RATIO	PURE ΣSQ	P(%)
A	1	44.28	44.28	19.67	42.03	13.11
B	2	3.19	1.59	0.71	0.00	0.00
C	2	137.61	68.80	30.56	133.10	41.52
D	2	31.97	15.98	7.10	27.47	8.57
e	46	103.57	2.25		118.02	36.81
TOTAL	53	320.62				

Number of experiments = 54
Sum (experimental values) = 523.36

Correction Factor = 5072.33
Sum of Sq (experimental values) = 320.62

Figure 3. *ANOVA Analysis*

FACTOR:	A	B	C	D
LEVEL 1	237.23	179.05	159.19	159.08
LEVEL 2	286.13	175.74	149.47	171.63
LEVEL 3	-	168.57	214.70	192.65

RESPONSE TABLE (AVERAGES)

FACTOR:	A	B	C	D
LEVEL 1	8.79	9.95	8.84	8.84
LEVEL 2	10.60	9.76	8.30	9.54
LEVEL 3	-	9.37	11.93	10.70

MAIN EFFECTS ANALYSIS

Quality Characteristic:...the bigger the better...

Factors	Optimum Settings	Level	Contribution
Elec. Type	LGC	2	10.60
Cell Design	A	1	9.95
Dep. Type	CSC	3	11.93
Elec. Conc.	1.8M	3	10.70

Total Contribution from significant factors=	43.18
Average Total for all results=	9.69
Estimate of average result (optimum)=	14.10

Figure 4. *Main Effects Analysis*

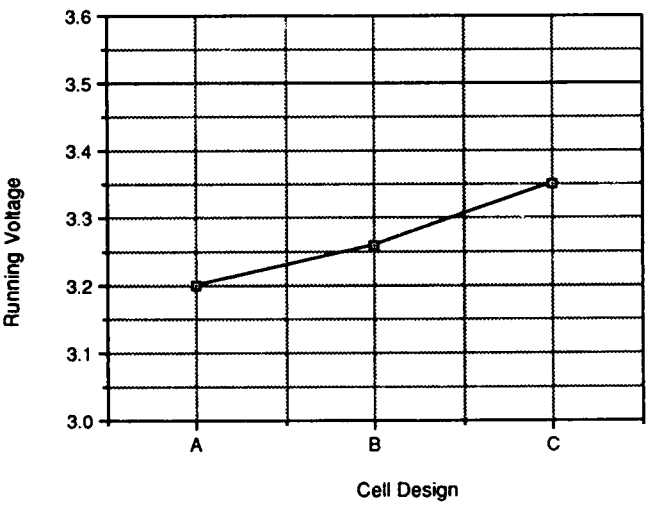

Figure 5 *Effect of cell design on running voltage of cells discharged at 1A and 25°C.*

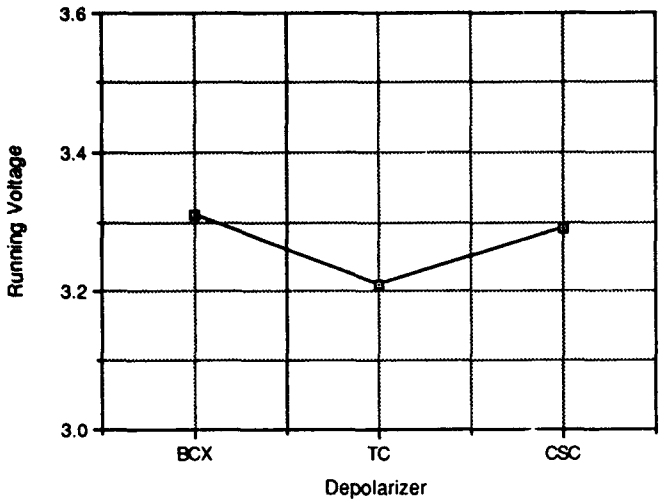

Figure 6 *Effect of depolarizer on running voltage of cells discharged at 1A and 25°C.*

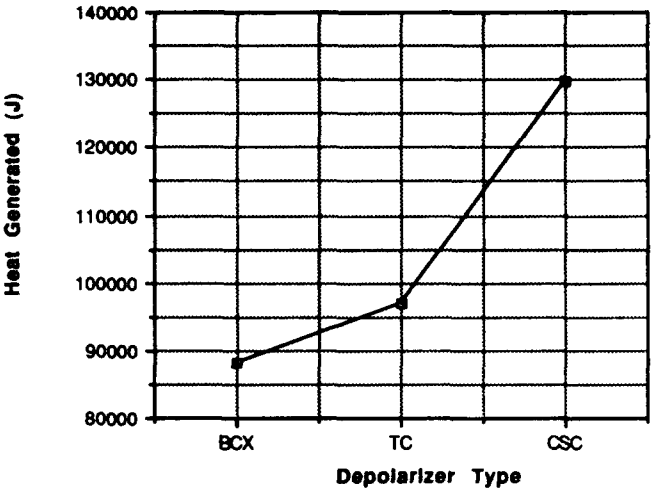

Figure 8 *Effect of depolarizer type on heat generated in D cells under 0.325Ω loads.*

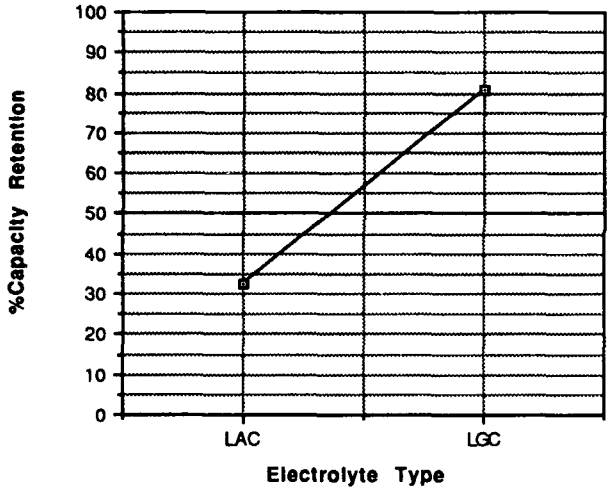

Figure 7 *Effect of electrolyte type on capacity retention after 1 year at 25°C.*

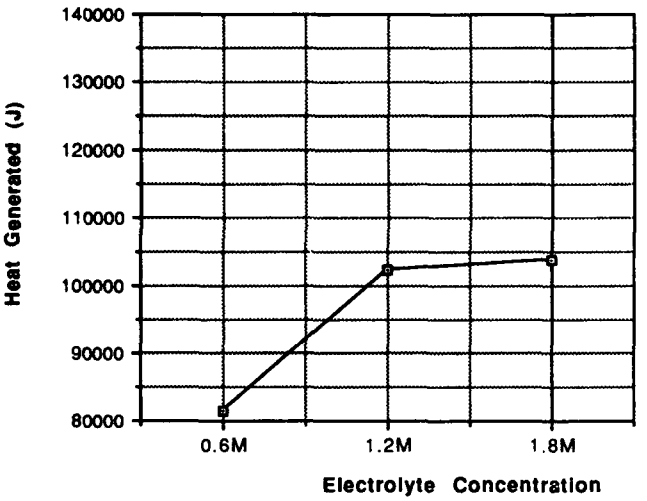

Figure 9 *Effect of electrolyte concentration on heat generated in D cells under 0.325Ω loads.*

DEVELOPMENT OF AA-SIZE CELLS FOR MINE BATTERIES

William P. Kilroy and Julie A. Banner
Naval Surface Warfare Center, Silver Spring, MD

Fraser Walsh
ECO , Somerville, MA

Introduction

The many unique requirements for Navy mines have led to a proliferation of battery designs, with a host of cell sizes and different chemistries. This leads to low procurement quantities, and subsequently to a diminished interest by available suppliers and increased production costs. Commercial lithium AA-size cells were recently evaluated with the objective of identifying a low-cost AA cell production base that would meet mine battery requirements.[1] Our goal was to replace three Hg-based alkaline cell chemistries and still meet the power needs of six Navy mines. The selected cell chemistry had to provide excellent voltage regulation and long storage life, and balance the need for high current pulses against the need for high capacity at low rate discharge. One essential requirement was that the cell had to be non-magnetic. Performance testing of AA-size cells identified the lithium-thionyl chloride (Li-$SOCl_2$) chemistry as the best choice for use in Navy mine applications.[1] A collaborative effort was undertaken to evaluate and improve the AA cell performance to meet specific mine battery requirements. This paper reports the ECO and NSWC development of a nonmagnetic Li-$SOCl_2$ AA-size cell and the effort to optimize cell performance by employing $LiGaCl_4$ electrolyte. The Naval Surface Warfare Center (NSWC) together with EIC Laboratories, Inc. are developing lithium ion-conducting polymer anode films to improve storage life and cell startup. This study will be reported at a later date.

Experimental

The AA cells, manufactured by ECO, are a case negative, hollow core, bobbin design. The cells contain 2.1±0.1 Ah of lithium, 2.8±0.14 Ah of thionyl chloride, and ~0.7g SAB-KB cathode collector. Cells were discharged in sets of four replicate tests at a constant load to a 2.5V cutoff at constant temperature in Tenny environmental chambers. Room temperature (RT) is defined as 20° to 23°C. After selection of the best electrolyte, cells were discharged in sets of three. The cells discharged at -2°C had been equilibrated at -2°C for several days prior to discharge. Short-term high temperature storage was used to simulate long-term ambient storage.

Results and Discussion

Study of Gallium vs Aluminum Salts

Moderate Rate Performance: Test results on commercial AA-size cells revealed that performance problems were most often associated with "old and cold" cells, especially during high rate or pulse discharge. The $SOCl_2$ catholyte proved to have the best overall performance under these conditions.[1] The capacity of spirally-wound Li/$SOCl_2$ cells under high rate discharge has been shown to be improved by employing $LiGaCl_4$ electrolyte.[2,3] However, no appreciable improvement was observed when the cells were discharged at low rates of 1 to 2 mA/cm^2. In contrast, the data in Tables 1 and 2 show the beneficial effects of $LiGaCl_4$ when modified bobbin AA-size cells were discharged at a 175 ohm load (~1 mA/cm^2). After high temperature storage, the average capacity of cells containing the Ga-based electrolyte was superior to cells with the $LiAlCl_4$ electrolyte. After storage, the RT capacity of the 1.8M $LiGaCl_4$ cells was 61% greater than the corresponding Al-based electrolyte.

Table 1

The effect of electrolyte on the capacity of modified bobbin AA-size Li/$SOCl_2$ cells discharged at 20 mA and -2°C

Molar Conc.	Fresh		Stored 7 Days at 70°C	
	$LiAlCl_4$	$LiGaCl_4$	$LiAlCl_4$	$LiGaCl_4$
1.4	1.60	1.59	1.05	1.44
1.8	1.68	1.70	1.28	1.59

Table 2

The effect of electrolyte on the capacity of modified bobbin AA-size Li/$SOCl_2$ cells discharged at 20 mA and 20°C

Molar Conc.	Fresh		Stored 7 Days at 70°C	
	$LiAlCl_4$	$LiGaCl_4$	$LiAlCl_4$	$LiGaCl_4$
1.4	1.73	1.32	0.99	1.15
1.8	1.65	1.59	0.85	1.37

Effects of High Temperature Storage: Since the shelf life of batteries has a significant impact upon the logistics associated with Navy mines, the improved high temperature storage capacity of the $LiGaCl_4$ electrolyte led to further evaluation of the effect of storage on cell capacity. The capacities of $LiGaCl_4$ cells discharged at 20 mA are shown as a function of storage time in Table 3. This unexplained increase in capacity after storage has been observed in #6-size, hollow core bobbin cells.[4] Similar behavior has also been observed with $LiAlCl_4$ cells after 45 days. (See Table 5)

Table 3

The effect of storage time on the average capacity of 1.8M $LiGaCl_4$ AA-size cells stored at 70°C and discharged at 20 mA and RT

Storage (days	0	7	14	28	56
Capacity (Ah)	1.59	1.37	1.22	1.50	1.69

Salt Concentration Study: The effect of $LiGaCl_4$ concentration on the capacity of AA cells as a function of discharge temperature and storage is shown in Table 4.

Table 4

The effect of $LiGaCl_4$ concentration on the average capacity of AA cells discharged to 2.5V at 20 mA after 7 or 14 day storage at 70°C

	Molar Concentration					Temp. (° C)
	0.54	1.40	1.80	2.20	2.60	
Fresh	1.08	1.59	1.70	1.74	1.67	-2
Fresh	1.02	1.32	1.59	1.65	1.53	20
Stored	1.15	1.44	1.59	1.60*	1.45*	-2
Stored	0.88	1.15	1.37	1.51*	1.41*	20

*Cells stored 14 days at 70°C.

The data in Table 4 show that the 2.2M $LiGaCl_4$ electrolyte provided the best overall cell capacity. The $LiGaCl_4$ cells delivered greater capacity at -2°C than at 20°C. This behavior was also observed at 3 mA when discharging cells from another manufacturer.[5]

The "best" cells (1.8M $LiAlCl_4$ and 2.2M $LiGaCl_4$) were also examined at a rate characteristic of mine battery operation, i.e., at 3 mA. Table 5 compares cell capacities as a function of discharge temperature before and after storage.

Table 5

The average cell capacity (Ah) to 2.5V for AA-size cells containing $LiAlCl_4$ and $LiGaCl_4$ discharged at 3 mA

Temp. (°C)	Fresh		Stored at 66°C*	
	1.8M $LiAlCl_4$	2.2M $LiGaCl_4$	1.8M $LiAlCl_4$	2.2M $LiGaCl_4$
-2	1.67	1.83	1.54	1.83
20	1.80	1.75	1.94	1.83

* $LiAlCl_4$ cells stored 45 days; $LiGaCl_4$ cells stored 30 days

In contrast to the high rate data shown in Tables 1 and 2, the Ga-based electrolyte shows little loss in capacity at the 3 mA rate after storage. The RT capacity of cells containing the $LiAlCl_4$ increased after storage, similar to the behavior observed with the $LiGaCl_4$ electrolyte. Cells containing 1.8M $LiAlCl_4$ stored for 45 days at 41° and 54°C also delivered average capacities of 1.90 and 2.01, respectively, when discharged at a 3 mA rate at RT.

Start-Up Characteristics: Even at very low rates, the data confirm the superior low temperature performance of the Ga-based electrolyte. Thus, the 2.2M $LiGaCl_4$ electrolyte was selected for use in further cell development. This choice was validated when the activation times of cells containing $LiAlCl_4$ and $LiGaCl_4$ were examined. The start-up characteristics of fresh 1.8M $LiAlCl_4$ and 2.2M $LiGaCl_4$ cells, discharged with a 200 ohm load for 60 sec., are shown at -2°C and RT in Figures 1 and 2, respectively. When discharged to meet a mine requirement of 0.25mA at -54°C, the Ga-based cells also exhibited a faster voltage recovery. After 48 hours at -54°C, the Ga cells never fell below 3.2V. The Al-based cells required an average 1.5 minutes to reach 3.0V. Fresh Ga-based cells were also capable of activating to 2.8V within 5 sec. at -2°C and to 3.0V at RT under a 27 ohm load.

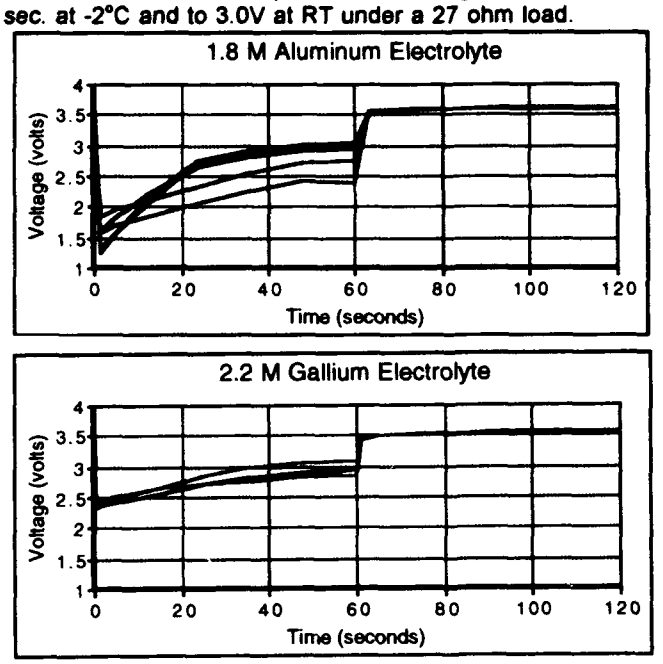

Figure 1. Startup characteristics of fresh 1.8M $LiAlCl_4$ and 2.2M $LiGaCl_4$ cells discharged with a 200 ohm load at -2°C.

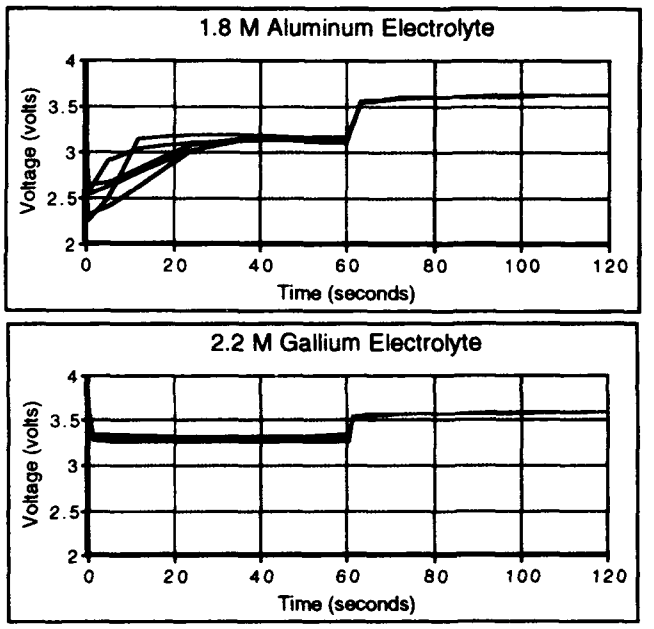

Figure 2. Startup characteristics of fresh 1.8M $LiAlCl_4$ and 2.2M $LiGaCl_4$ cells discharged with a 200 ohm load at RT.

High Rate Performance: Mine batteries may be required to provide high-rate pulses.[5] The cells were discharged at -2°C at 3 mA for about 50 hours prior to application of a pulse with a 9 ohm load.. The Al-based electrolyte cells provided a 275 mA peak current at 2.5V. The Ga-based cells provided 315 mA at 3.0V.

The capacity of commercial $SOCl_2$ AA cells was evaluated to meet a requirement for cells to deliver 0.4 Ah at 50 mA.[5] Power Conversion, Inc. (PCI) and SAFT France bobbin cells met the 50 mA requirement. The capacity of PCI and SAFT cells containing Al-based electrolyte are compared with the capacity of 2.2M $LiGaCl_4$ cells to 2.5V in Table 6.

Table 6

Comparison of Al-based and 2.2M Ga-based electrolyte on the capacity of AA-sized cells discharged at 50 mA and -2°C

Manufacturer	Fresh	Stored 45 days
PCI (Al)	0.89 Ah*	0.72 Ah (41°C)*
SAFT (Al)	0.94 Ah*	0.95 Ah (41°C)*
ECO (Ga)	1.24 Ah	1.42 Ah (55°C)

*Capacity to 2.0V; additional data are reported in reference 5

Performance of Optimized Gallium Cell

Discharge and Pulse Characteristics: Cells containing 2.2M $LiGaCl_4$ electrolyte were subjected to the following peak-load tests: 9 ohms for 100 sec. (P1), 27.5 ohms for 100 sec. (P2), and 100 ohms for 100 sec. (P3). The cells were then discharged at three temperatures at constant load in sets of three cells to compare low, moderate, and high rate capacity. The pulse tests are indicated by P. The capacity to 2.5V is compared to the capacity of an additional set of three cells that were not pulse tested. The results are shown in Table 7.

Table 7

Average Ah capacity of AA-size Li-$SOCl_2$ cells containing 2.2M $LiGaCl_4$ electrolyte with and without initial pulse.

Current	Fresh			Stored 90 days at 55°C		
	-2°C	20°C	50°C	-2°C	20°C	50°C
50 mA	1.24	1.23	1.89	1.37	1.45	1.31
P1	1.24	1.28	1.73	1.40	1.40	1.69
20 mA	1.70[a,a]	1.70[a,a]	1.84	1.68	1.66	1.83
P2	1.63	1.77	1.79	1.64	1.67	1.80
3 mA	1.85[a,b]	1.78[a,b]	1.69	1.79	1.82	1.73
P3	1.85	1.73	1.76	1.93	1.85	1.79

[a]Av. of 7 cells. Includes capacity data from the $LiGaCl_4$ concentration study[a] in Table 4 and NSWC data[b] in Table 5.

Cell Safety Tests: Safety testing was performed in triplicate on 2.2M $LiGaCl_4$ cells after 90 days storage at RT and 55°C. On short circuit, a maximum current of 2.5A and a maximum temperature of 100°C were observed. No ventings occurred. Cells were discharged at a constant current of 50 mA into voltage reversal for 150% of the rated capacity without venting. No venting occurred upon charging. Heating abuse tests resulted in cell ventings between 250° and 290°C. All cells vented from the positive end of their casings.

Prototype Battery Tests: Three mine batteries, composed of AA cells containing the 2.2M $LiGaCl_4$ electrolyte, have been built by ECO and NSWC Crane. Preliminary testing has been completed at MWEA, Yorktown and NSWC, White Oak. All three battery prototypes from ECO performed well under heating abuse tests. After performing low and high frequency vibration and two phase shock tests, all three battery prototypes delivered the rated RT cell capacity.

Summary

A nonmagnetic AA-sized Li-$SOCl_2$ cell has been developed to meet the battery requirements of a variety of Navy mine systems. Test data show the performance of cells has been improved by employing a Ga-based electrolyte. The ECO modified bobbin design, containing 2.2M $LiGaCl_4$ electrolyte, has superior capacity at 50 mA at low temperature when compared to commercial cells containing Al-based electrolyte. Tests performed to date on three different prototype batteries have met environmental, abuse, and RT performance requirements.

Acknowledgement

The authors wish to thank C. Bowers for his assistance in discussing the battery requirements for the mine systems. Funding was supported by NAVSEA via the SBIR program.

References

(1) W. P. Kilroy, J. A. Banner, G.H. Hoff, K.A. Johnson, and W.A. Freeman, Lithium AA-Size Cells For Navy Mine Applications: II Evaluation of Commercial Cells, NSWCDD/TR-92/462, Feb. 24,1994.

(2) W. L. Bowden, J.S. Miller, D. Cubbison, and A. N. Dey, New Electrolyte Salts For Li/$SOCl_2$ Cells, J. Electrochem. Soc., 131,1768, 1984.

(3) W. P. Kilroy, C. Schlaikjer, P. Polsonetti, and M. Jones, Optimized Lithium Oxyhalide Cells, J. Power Sources, 43-44, 715 (1993).

(4) K. Holloway, Captor Mine Phase I - Lithium Battery Testing, ESD 89-123, NSWC, Crane IN 4 Dec. 1989.

(5) J. A. Banner, C. S. Winchester, and W. P. Kilroy, Evaluation of Commercial AA-Size Lithium Cells For Navy Mine Applications, This Journal.

HIGH-RATE LITHIUM THIONYL-CHLORIDE BATTERY DEVELOPMENT

Wendy R. Cieslak and David E. Weigand
Sandia National Laboratories
Exploratory Batteries Department 2223
Albuquerque, New Mexico 87185-0614

Abstract

We have developed a lithium thionyl-chloride cell for use in a high rate battery application to provide power for a missile computer and stage separation detonators. The battery pack contains 20 high surface area "DD" cells wired in a series-parallel configuration to supply a nominal 28 volts with a continuous draw of 20 amperes. The load profile also requires six squib firing pulses of one second duration at a 30 ampere peak. Performance and safety of the cells were optimized in a "D" cell configuration before progressing to the longer "DD" cell. Active surface area in the "D" cell is 735 cm^2, and 1650 cm^2 in the "DD" cell. The design includes 1.5M $LiAlCl_4/SOCl_2$ electrolyte, a cathode blend of Shawinigan Acetylene Black and Cabot Black Pearls 2000 carbons, Scimat ETFE separator, and photoetched current collectors.

Introduction

The customer historically has used a Zn/Ag_2O battery to provide power to the missile electronics. However, the system design team required a lighter weight battery in order to meet new missile performance requirements. While a primary battery system does not often replace a secondary battery, in this case, if the new battery could provide enough capacity to complete three launch attempts and the full mission flight time, then rechargeability would be unnecessary. In addition, going to a primary battery afforded weight savings by eliminating the power cables.

We proposed an active lithium thionyl-chloride battery consisting of high surface area "DD" cells to meet the system requirements, which were as follows:

- Total weight of less than 15 pounds
- Provide 20 amperes (20 A) continuously for 37 minutes (12.3 Ah) to power the computer and stage separation detonators.
- Provide six pulses of one second duration at 30 A to fire the squibs.
- Provide enough excess capacity for three nine-minute launch attempts (additional 9 Ah)
- Nominal 28 to 30 Volts
- Minimum 24 Volts

Our conceptual design of this battery includes 20 "DD" cells wired in two parallel strings with 10 cells in series in each string. Therefore, each cell provides 10 A continuously with 15 A pulses, and total capacity of 10.7 Ah. Most of the development effort in this program concentrated on the cell. Cell performance and safety were optimized in the "D" size cell configuration because of personnel safety concerns and available materials conservation issues. Once a baseline design was established using the "D" cell, the development then shifted to the longer "DD" cell.

Cell Design

The basic cell design is a spiral wound construction. In order to maximize the electrode surface area we incorporate two cathode plates and two anode plates in each cell. The electrolyte is 1.5M $LiAlCl_4$ in $SOCl_2$, and a large excess of electrolyte is present to provide heat sinking, while retaining a minimum free volume in the cell of 4 cc for the "D" cell and 10 cc for the "DD" cell. The cathode uses a 50/50 blend of Shawinigan Acetylene Black and Cabot Black Pearls 2000 carbons with PTFE binder. Each cathode plate is 0.015" thick, to be discharged from both sides. Cell capacity at the design rate of ~6 mA/cm^2 is limited by the practical capacity of the carbon cathode.

Components and Specifications for "D" Cell

- Li theoretical capacity = 9.1 Ah
- Electrolyte theoretical capacity = 17 Ah
- Electrode surface area = 735 cm^2
- Current density = 6.8 mA/cm^2 at 5 A

Components and Specifications for "DD" Cell

- Li theoretical capacity = 17.3 Ah
- Electrolyte theoretical capacity = 32.5 Ah
- Electrode surface area = 1650 cm^2
- Current density = 6.1 mA/cm^2 at 10 A

The separator, Scimat ETFE 200/80/110 microporous membrane, was chosen during our preliminary studies. We designed photoetched Ni current collectors in order to provide a uniform current distribution, low resistance current path, and to avoid edge burrs that might cause shorting. The cell case incorporates a BS&B Frustum Reverse Buckling (FRB) burst disc which operates at 300 ± 25 psi with a 0.375" opening in the "D" cell and a 0.5" opening in the "DD" cell.

Staniewicz, et. al.[1,2] have reported the design of active lithium thionyl chloride batteries for demanding applications. They showed that ETFE separator material and high surface area carbons enhance cold temperature and high rate performance. Our "DD" cell design is similar to theirs, except that we have used longer electrodes; they report 1185 cm^2 of effective interfacial area.

"D" Cell Test Results

Performance Characteristics

Performance testing was conducted in order to demonstrate feasibility and choose the separator material, electrode surface area, and electrochemical

balance. The baseline design was established after twelve experiments. Cells were insulated during the tests to simulate the battery environment.

Two sample tests are shown to illustrate the choice of separator material and the baseline design performance. The tests were run at 5 A constant current. A thermocouple was placed on the cell case.

Cell #8, Figure 1, contained Scimat 200/40/60 separator. Cell #14, Figure 2, contained Scimat 200/80/110 separator. The 200/80/110 separator is thicker than the 200/40/60 separator and it is also more porous. Cells using the 200/40/60 material consistently ran hotter; note the maximum temperature of 130°C for cell #8 versus a maximum of 80°C for cell #14. In addition, cell #8 actually had slightly higher electrode surface area, yielding a current density of 6.2 mA/cm^2 versus 6.8 mA/cm^2 for cell #14. Cell #14 represents the baseline design, which supplied 7.7 Ah at an average of 3.05 V under a 5 A drain rate, and was used for the safety and abuse tests.

Safety and Abuse Characteristics

Safety of the cell and performance of the vent mechanism were characterized by two tests each at the following conditions: 133% overdischarge (reversal), short circuit, charging of fresh cells and charging of previously discharged cells.

Figure 3 shows one of the 133% overdischarge tests (cell #16). Neither cell vented. The cell skin temperature stabilized at approximately 90°C for most of the voltage reversal portion of the test. Therefore, this cell design is extremely resistant to overdischarge at its nominal rate.

The short circuit tests produced venting. The cells ran at least 14 minutes and showed a steady temperature rise during the test, Figure 4 (cell #18). The vent operated at a cell case temperature of <140°C. The vent mechanism functioned properly by providing controlled pressure release, thereby avoiding molten lithium and rapid cell disassembly.

Charging of previously discharged cells caused mild venting. Charging of fresh cells produced energetic venting, Figure 5 (cell #20). The weld holding the cell bottom to the can was torn. Charging of these cells should be prevented, for example, by diode protection.

"DD" Cell Test Results

Performance Characteristics

We used both constant current discharge and the simulated application load profile to characterize "DD" cell performance. The "DD" cells were also encased in thick pipe insulation during the experiments.

The cells vented during constant 10A discharge after 70 to 80 minutes, at a maximum cell skin temperature of 130°C to 135°C, Figure 6 ("DD" cell #3). The capacity of the test shown was 11.9 Ah at an average of 3.15 V.

The cells did not vent in six tests using the application load profile, Figures 7 and 8 ("DD" cell #8). The profile simulated three launch attempts and the mission flight time with the pulses. The launch attempts required 10 A for nine minutes each, and were separated by rest periods of 10 minutes duration (real flight attempts would likely be separated by >1 hour). The mission required 10 A for 37 minutes, plus six 15 A pulses equally spaced throughout the flight time. The maximum cell skin temperature at the completion of the application load profile was only 100°C.

Safety and Abuse Characteristics

Preliminary short circuit tests caused the cell leads to fuse within seconds. No venting occurred. Charging fresh cells produced very energetic venting, similar to charging the "D" cells.

Our program was terminated before the cells were fully characterized and the battery tests were completed because the scope of the missile program was reduced.

Summary

We have developed prototype high surface area "D" and "DD" cells suitable for rates up to 5A and 10A continuous current, respectively. The "D" cells supply ~7.7 Ah at 5A, and may be overdischarged at least 150% without venting. The "DD" cells can only run approximately 70 minutes at 10A (~12 Ah) before venting occurs. However, this is a safe margin for the 37 minutes continuous drain required by the application.

Acknowledgments

Prototype cells were built and tested at Sandia by Leo Griego and Samuel Lucero. This work, performed at Sandia National Laboratories, was supported by the United States Department of Energy under contract no. DE-AC04-94AL85000.

References

(1) Staniewicz, R. J., et. al., *Some Practical Considerations of Lithium Thionyl Chloride Battery Development*, Proc. 34th International Power Sources Symposium, June 25 - 28, 1990, pp. 272 - 274.

(2) Bolster, M. E. and Staniewicz, R. J., *Active Lithium Thionyl Chloride Batteries for High Rate Pulse Applications*, Proc. 35th International Power Sources Symposium, June 22 - 25, 1992, pp. 72 - 77.

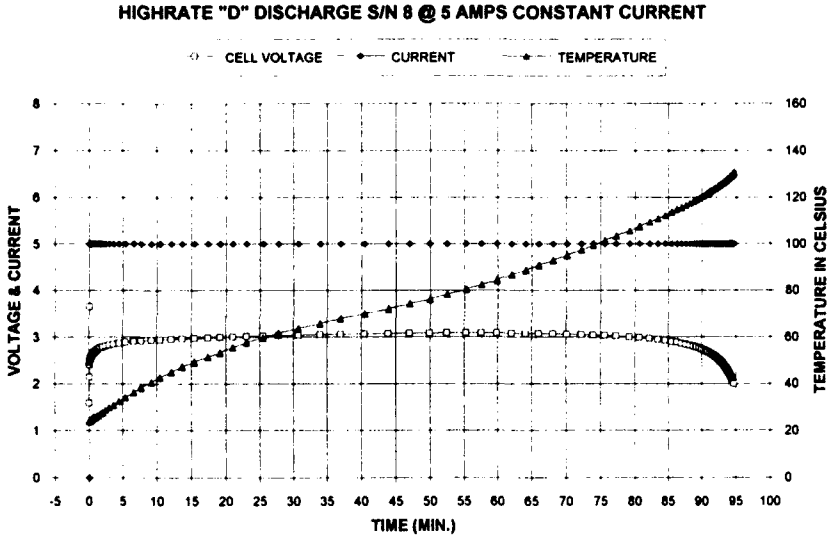

Figure 1. "D" Cell #8 Discharge.

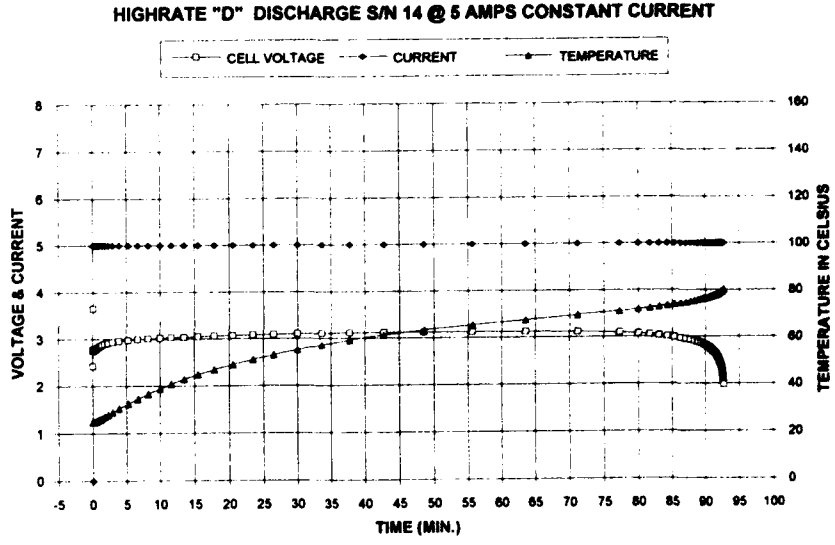

Figure 2. "D" Cell #14 Discharge.

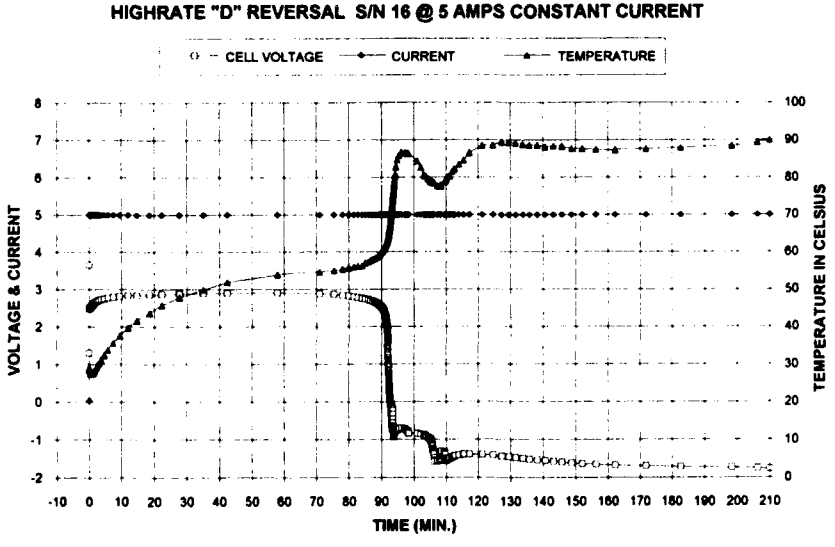

Figure 3. "D" Cell #16 133% Over discharge.

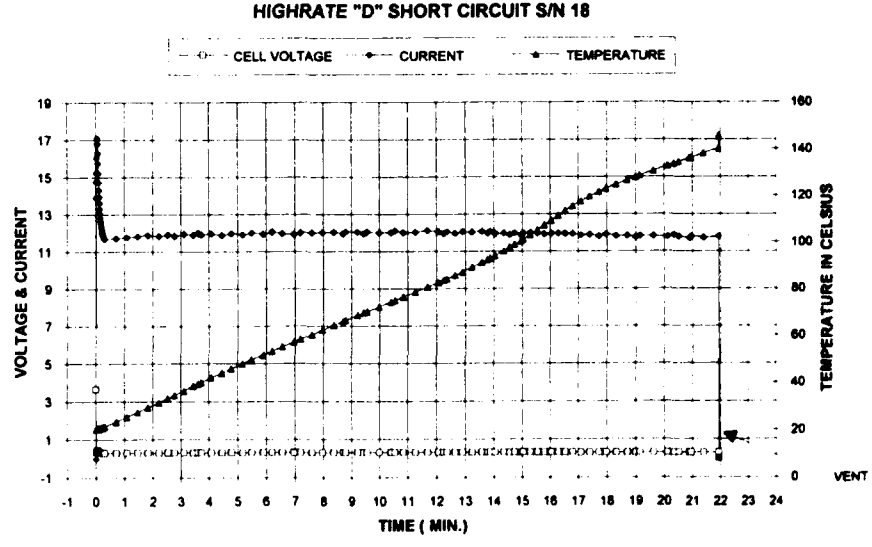

Figure 4. "D" Cell #18 Short Circuit. Actual current may be higher than shown because of uncorrected line losses.

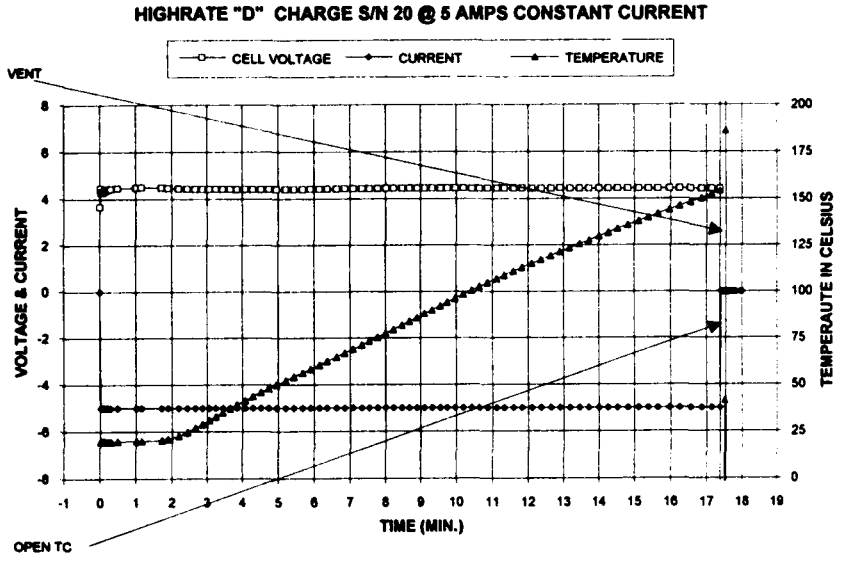

Figure 5. "D" Cell #20 Fresh Cell Charge.

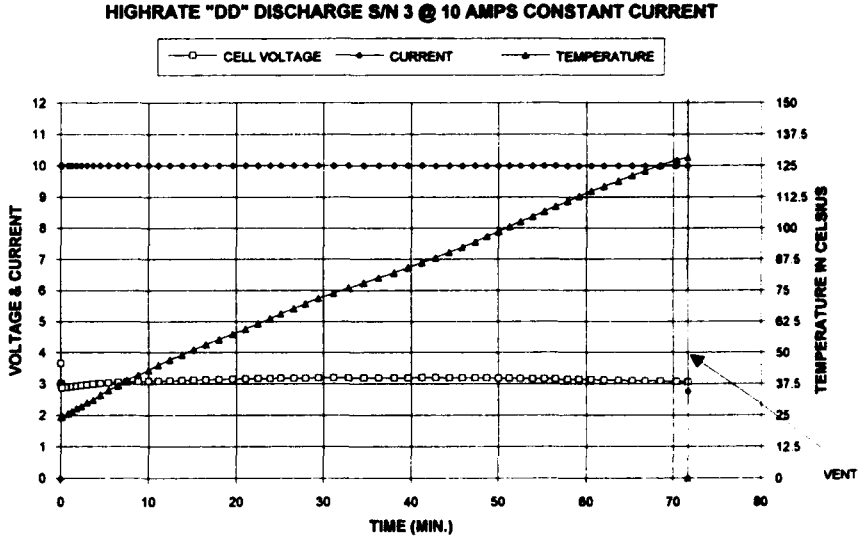

Figure 6. "DD" Cell #3 Discharge.

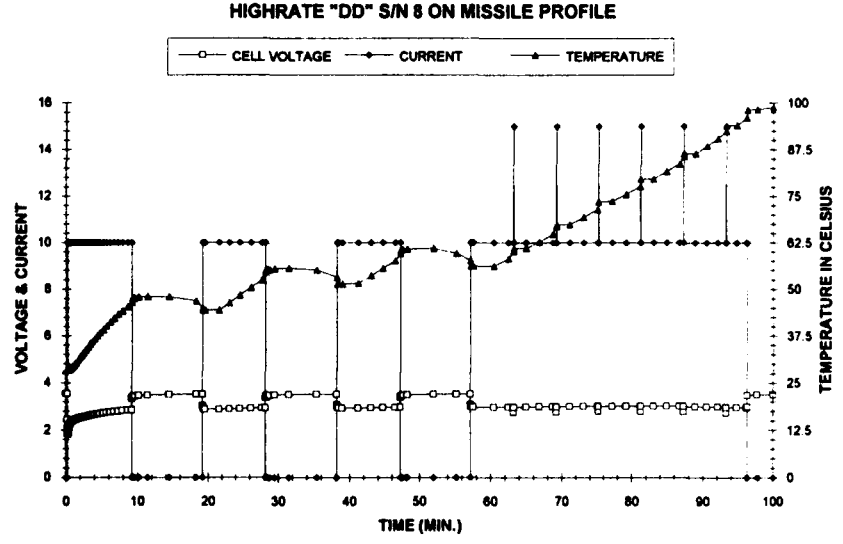

Figure 7. "DD" Cell #8 Discharge on missile profile.

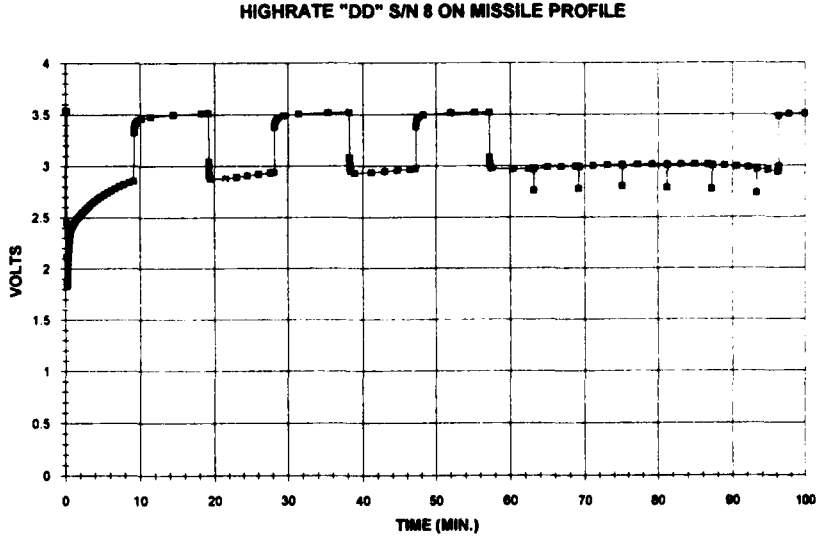

Figure 8. "DD" Cell #8 Discharge on missile profile, expanded voltage scale.

DEVELOPMENT OF A 250 Ah LITHIUM THIONYL CHLORIDE BATTERY

M. J. Milden, H. F. Bittner, J. V. Coggi, The Aerospace Corporation, El Segundo, CA
K. Lejman, General Dynamics Space Systems Division, San Diego, CA
M. Svaleson, Martin Marietta Technologies, Inc., Denver, CO
Maj. T. Conroy, Maj. D. Blehm, USAF Space and Missile Systems Center, Los Angeles, CA
J. L. Firmin, J. P. Semerie, SAFT, Poitiers, France

Introduction

In 1986 several military satellite programs, concerned with a growing launch system performance deficit, sought ways to increase the satellite weight delivered to final orbit. The high rate lithium thionyl chloride primary battery, at that time in the R & D demonstration stage, was identified as a candidate to replace silver zinc batteries. The potential for nearly 50% reduction in battery weight was significant.

The Air Force Space and Missile Systems Center (SMC) awarded two prime contracts for the development and qualification of a battery to replace the 250 Ah primary silver zinc battery utilized on the Titan IV Centaur upper stage vehicle. The requirements/goals for this challenging development effort are shown in Table 1. This paper describes the successful program managed by General Dynamics Space Systems Division (GDSSD), who selected SAFT/France through a competition to develop and qualify a battery for flight.

Table 1. Requirements and Goals for Lithium Development Program

Dimensions	10.8 x 13.3 x 13.4 inches (Direct replacement for silver zinc)
Weight	68 lb (Goal)
Life	6 Year Storage at -18°C 1 Year at 5 to 32°C
Voltage	
MVB	26-32 V
PLB	>29.2 V at up to 60 A (0-85% capacity) >28.0 V at 60-75 A
Voltage delay	<10 msec
Nameplate	250Ah
Safety	ESMCR 127-1
Qualification	MIL STD 1540b

In this paper, details of the cell and battery development program are provided with attention focused on challenges faced during the cell and battery development. When available, references are provided for further information regarding certain aspects of the cell and battery development. Specific results of cellcharacterization and battery qualification tests have been previously published (Refs. 1 and 2).

Program Overview

Based on previous SAFT cell designs, a scaled-up cell capable of meeting the requirements in Table 1 was developed. The Centaur cell is a cylinder with flat plate construction held in place by compression and locating rods through the electrodes. Figure 1 is a representation of the basic cell design. Each cell has a glass-to-metal seal that comprises the positive terminal and two nickel feedthroughs for the negative terminals. A safety burst disk on each cell precludes catastrophic failure.

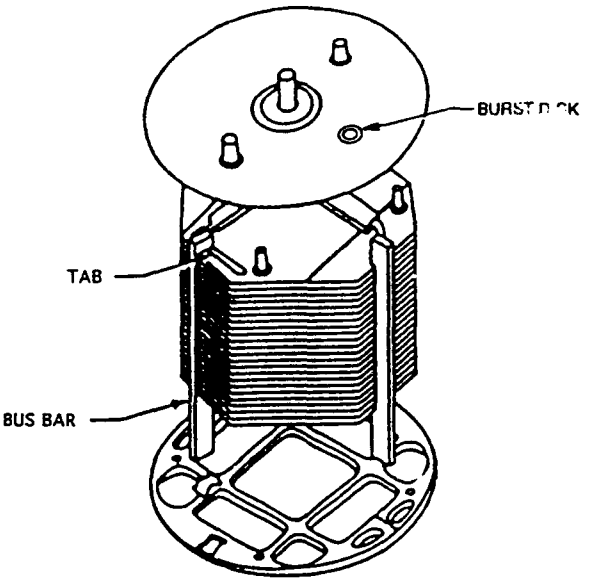

Figure 1. Basic cell design.

The final battery configuration contains two tiers and is shown in Figure 2. The structure consists of a monolithic aluminum machined housing with two layers of machined cavities for the cells; the top layer contains five cells and the bottom layer contains four cells. Mounting legs form an integral part of the structure.

Documentation and configuration control were an important part of this program. Since the ultimate purpose of the effort was to develop a flight qualified

battery, this control system was in place prior to the Critical Design Review and was maintained through the conclusion of qualification testing.

Safety was of paramount importance in the cell and battery designs. The safety program included detailed procedures for handling the cell and battery and extensive safety testing at the cell and battery level. Results indicated that, with proper procedures in place, the lithium thionyl chloride high rate battery can be integrated into an operational environment.

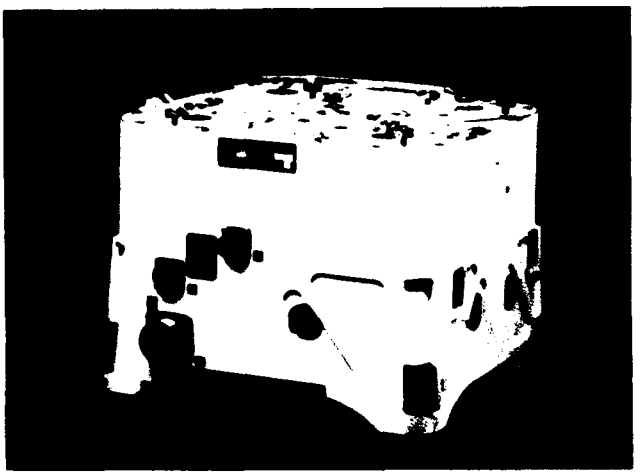

Figure 2. 9VLS250AM battery configuration.

The Centaur lithium thionyl chloride battery has demonstrated compliance to a qualification matrix with only minor deviations and may be considered for use in a flight application (see Ref. 2). Additional efforts in satisfying compliance to deviations, system integration, manufacturing readiness, and flight documentation release await user identification.

Cell Development

Several significant technical challenges were encountered and solved during cell development. These challenges included survival of transmitted vibration levels, electrode tab intergranular cracking, attaining voltage performance, meeting storage requirements, and selection of burst disks.

Engineering development cells were built to verify the ability to withstand the random vibration launch environment, which was 13.7 G_{RMS}, applied to the battery; the cells experienced higher transmitted vibration levels. The initial cell design underwent revisions to meet this environment. Stress relief loops were added to electrode tabs, locating rods were introduced and strengthened, and insulating washers were inserted between electrodes to stiffen the electrode stack. Current collector bus bars were also modified to eliminate sharp corners and doublers were added to high stress areas. Detailed welding schedules were developed to ensure the integrity of the bus-bar-to-electrode tab welds. The resulting cell design survived the required vibration and shock environments.

At the same time intergranular cracks were found in electrode tabs. After extensive work (Ref. 3) it was determined that environmentally assisted stress corrosion was responsible for the cracking. The intergranular cracking had safety implications and was therefore crucial to solve. It was discovered (Ref. 4) that electrically isolated lithium in the cell environment was subject to stripping and plating due to lithium ion concentration gradients formed during discharge. If a lithium anode became electrically isolated from the stack due to intergranular cracking of the tab connection, resulting lithium plating could form an internal short circuit. The only unintentional cell incident that occurred during this development was attributed to this phenomenon. The cell exploded during discharge. The mechanism was confirmed by intentionally clipping the anode tabs of several electrodes in a test cell. The test cell was then discharged identically to the earlier cell. The test cell exploded at approximately the same voltage and discharge capacity.

As a result of analysis and testing, it was determined that the intergranular cracking phenomenon could be precluded by redesigning the electrode substrate with respect to the orientation of the grain structure in the substrate material, which was determined by the rolling direction of the material. Metallographic examination of the cracked tabs indicated that cracking occurred only in substrates whose tabs had grain alignment perpendicular to the length of the tab; no cracking was found in tabs whose grain alignment was longitudinal with respect to the length of the tab. Once this redesign was accomplished, no further intergranular cracking was observed and no other safety incidents occurred.

The stringent mission unique voltage requirement of 29.2 V at up to 60 A was difficult to meet. Electrode surface area was maximized and internal cell resistance was minimized while maintaining the integrity of the cell. Even with these design solutions, it was found that the high voltage requirement could only be met at somewhat elevated temperatures. Figure 3 shows cell voltage as a function of discharge current at ambient temperature and at 40 to 45°C. In order to maintain battery voltage above 29.2 V, the cell voltage must be at or above 3.3 V, and the temperature therefore must be at least 40°C. This temperature also provides for maximum capacity, as indicated in Figure 4. The baseline operating temperature

was therefore 40°C and the majority of cell and battery tests were carried out at this temperature.

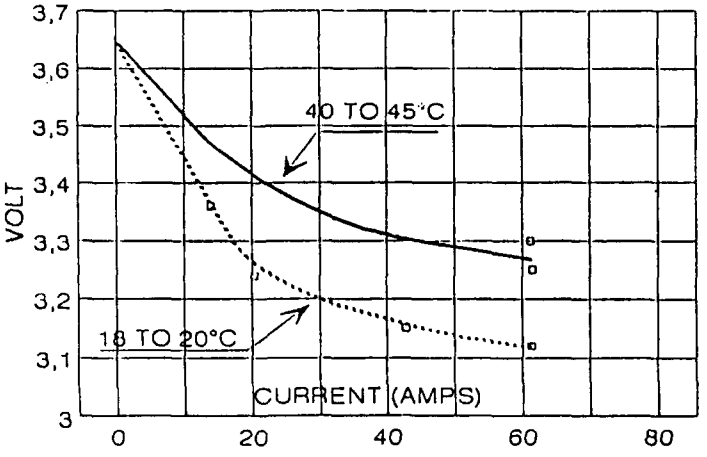

Figure 3. Average cell voltage vs discharge current

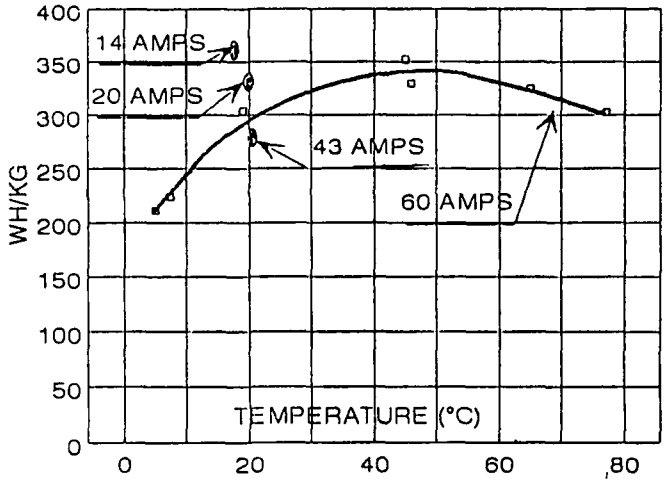

Figure 4. Energy density vs cell temperature

The storage requirements at low temperatures (less than 5°C) have been demonstrated for up to one year. On-going testing will expand that data base and storage times at -18°C with little or no performance degradation for up to 6 years are anticipated. Storage at ambient temperature has been demonstrated for up to 8 months, and it is anticipated that storage at ambient for one year with little or no degradation should be possible. However, the requirement for storage at higher temperatures has not been demonstrated. Although cells can be exposed for short periods to 32°C, longer exposure at this temperature results in increased voltage delay and decreased capacity. This characteristic requires well-controlled storage conditions. Further work will define the storage envelope in terms of temperature and time.

A burst disk vent of 13 bars was initially selected to meet the cell thermal and safety requirements. However, cell-level thermal tests were performed under anticipated worst case hot temperatures which resulted in premature vent operation. It became apparent that the pressure-temperature relationship of the electrolyte solution under these conditions was not well understood. After extensive thermal modeling and testing to characterize the pressure-temperature relationship, a burst disk with a vent value of 22 bars was selected. The higher vent value permitted safe operation under all defined requirements.

Throughout the development, a total of 39 engineering cells were tested to validate design improvements. To characterize the cell design 102 cells were built and organized into a test matrix to measure performance and safety under various mechanical, thermal, storage and time parameters. Results from these tests have been previously published (Ref. 1).

Battery Development

Challenges faced in the battery development included structural integrity to survive vibration and shock, thermal design and modeling, and voltage performance. Much of the battery design work was carried out at the same time that the cell design was undergoing refinement, particularly with respect to the structural and thermal aspects of the cell and battery design, where the designs are interdependent.

Initially, the battery structure consisted of an aluminum housing with nine machined cavities to which mounting legs were attached. The entire assembly was rigidized with a baseplate to which the mounting legs and housing were bolted. This structure failed initial vibration tests. Subsequently the battery was redesigned with the aid of extensive finite element modeling (Ref. 5). The resulting monolithic aluminum battery structure (Figure 2) both survived the mechanical environments and minimized the transmitted environments to the cells. The monolithic structure contributed to increasing the specification battery weight above the initial requirement to 86 pounds. However, the robust structure met all requirements for vibration and shock.

The thermal design of the battery took into account the thermal environment of the launch vehicle and the significant heat generated by lithium thionyl chloride cells during discharge. Complicating the thermal design was the fact that a single battery was developed to meet two different applications, the Centaur Main

Vehicle Battery (MVB) and the Payload Battery (PLB). Each application had a different discharge profile and thermal environment associated with the profile. The thermal design had to maintain minimum temperature to meet the voltage and capacity requirements while limiting the temperature to below the safe operating temperature with respect to the cell burst disk.

Once the thermal environment for the battery was thoroughly defined, the heat generation characteristics of the cells were determined and the thermal characteristics of the battery were modeled. Results from basic research on the heat generation characteristics of lithium thionyl chloride cells (Ref. 6) were combined with results from the Centaur cell characterization tests to determine their heat generation. Detailed thermal models were then developed and validated by thermal vacuum testing carried out as part of the battery qualification program.

For the PLB application, which had the higher voltage requirement, it was determined that an inflight heater was required to maintain minimum temperature in order to provide the minimum voltage. For the MVB application, a ground-only heater was required.

Thermal vacuum testing representing both MVB and PLB applications was carried out under worst case hot and cold conditions (Ref. 7). Test results indicated that the battery met most requirements over the range of anticipated thermal environments. All requirements were met for the MVB application. For the PLB application, however, there were short durations where the voltage fell short of the requirements by 0.5 V or less.

During the battery development three Development Engineering Test (DET) batteries were constructed and tested. Twelve qualification batteries were subsequently built and successfully tested. One DET and five qualification batteries were subjected to vibration and shock; the cells in five of these batteries underwent DPA with no anomalies found. One DET and four qualification batteries were subjected to thermal testing; with the exception of the voltage anomaly for the PLB battery indicated above, all thermal requirements were met. Details of the qualification testing are given in Ref. 2.

Conclusion

The SAFT model 9VLS250AM lithium thionyl chloride battery has completed a program path from development through qualification; the battery was qualified to all of the Centaur MVB battery requirements. The mechanical, electrical, environmental, and safety performance has been demonstrated through testing of over 100 cells and 15 batteries.

References

1. J. P. Semerie and J. L. Firmin, "250Ah Lithium/Thionyl-Chloride Cell Evaluation Test Results", Proc of European Space Power Conference, Sept. 1991, pp 417-422.

2. J. P. Semerie and V. Kandarpa, "250Ah Lithium/Thionyl Chloride Battery Qualification Test Results", Proc of European Space Power Conference, Aug. 1993, pp 799-804.

3. J. A. Wasynczuk, "Environmentally Assisted Cracking of Nickel Strip in $LiAlCl_4/SOCl_2$", Extended Abstracts of the Electrochemcial Society Meeting, New Orleans, LA, Oct. 1993, 93-2, 193.

4. P. Chenebault, "Study of Lithium Plating in $Li/SOCl_2$ Cells Related to Safety Aspects", 36th Power Sources Conference, Cherry Hill, NJ, 1994.

5. R. B. Pan, et al., "Titan Centaur Lithium Battery Mechanical Redesign", Vol 10, Issue 2, pp 33-34 Apr. 1991 Aerospace Quarterly Technical Report.

6. H. F. Bittner, et al., J. Power Sources 26, 441-446 (1989).

7. G. Mckim, et al., "A Method for Thermal Vacuum Test Simulation of Space Environmental Heat Fluxes Closing Heated Plates", Proc. of 14th Aerospace Testing Seminar, Manhattan Beach, CA, Mar. 1993, pp 89-93.

STUDY OF LITHIUM PLATING IN LI/$SOCL_2$ CELLS RELATED TO SAFETY ASPECT

P. CHENEBAULT
SAFT ABD
BP 1039
86060 POITIERS
FRANCE

Introduction

In recent years, lithium/thionyl chloride cells received special interest as energy power source for use in space applications. This results from the high energy density of this system and the resulting weight saving which has a direct impact on mission cost. Moreover, low self discharge rate allows for performance guarantee even after long storage time.

To develop these batteries, difficult requirements have to be fulfil, more specifically regarding shocks, vibrations and thermal environments. In 1988, SAFT began the development of 250 Ah cells according to the specification of battery an US booster.

To satisfy voltage requirements in a large range of current, batteries are made with nine cells connected in series. Large electrode surface is realized in each cell by multiple electrodes assembly in parallel. A detailed description and performance of the SAFT VLS 250 AM cells and 9 VLS 250 AM battery have already been reported [1,2]. For reliability and decrease of internal resistance, each electrode comprises two nickel tabs which are then welded on two different bus bars for parallel assembly. To sustain shocks and vibrations, these tabs have a bent portion acting as stress relief.

During discharge under resistive load (0.33 ohm) after vibration test, one cell (#227) venting violently at the end of discharge when its voltage reached 0.7 volts after voltage fluctuations beginning at 1.7 volts. The discharged capacity was 314 Ah.

This paper presents several experiments performed either on VLS 250 AM cells to identify the origin of this safety hazard or on laboratory cells to determine the failure mechanism of electrodes stacks.

Experiments and results on VLS 250AM cells

Cells failure analysis

Two other cells (#228 and #229) from the same batch than the cell that vented (#227) have been vibrated and then discharged to 0 volt in the same conditions without problems. DPA of these cells revealed rupture of several anode tabs, breaking being located more specifically on the stress relief portion. Safety hazard could not be directly related to these electrical defaults.

A similar cell (#201) was discharged in the same conditions and did not exhibit any problem. This cell had not been submitted to vibrations prior discharge. Compared to the cell #227, the electrolyte volume in cell #201 was exactly the same (743 cm^3) and the delivered capacity was 327 Ah compared to 314 Ah for cell #227. The mean discharge voltage was 3.3 volts, ie 50 mV higher than mean voltage of the vented cell. This demonstrates that discharge conditions as thermal environment were not responsible for cell internal temperature increase and thermal runaway at the end of the discharge. DPA of this cell revealed only one broken tab on an anode. Lower voltage during discharge with cell #227 could result from rupture of several anodic tabs and higher current density.

Different hypothesis have been proposed to explain the anomaly encountered on cell #227:

Hypothesis one:

Decline of electrolyte level and lack of electrolyte with stack drying in the top zone where temperature increases due to higher internal resistance. Lithium deposition can occur and creates dendrites that burn off due to shorting or increasing heat.

Hypothesis two:(similar to hypothesis one)

Decline of electrolyte level and lack of $SOCl_2$ in the top zone which becomes dry and whose impedance increases. This zone becomes progressively inactive and expands. Consequently, current density increases in the bottom part of the stack which remains flooded. This zone has to supply most of the capacity. That implies an increase of lithium consumption in the flooded zone which becomes anode limited (because of a progressive increase of current density, the heat effect in this zone contributes to enhance the lithium selfdischarge). Loss of contact between remaining lithium and nickel foil may occur and leads to voltage fluctuations. The tightness of the contacts between lithium and nickel current collectors increases with possible fusion of lithium (fuse effect).

Hypothesis three:

Short circuits due to separators degradation more particularly by the end of discharged when stresses on separators are increased because of the carbon electrodes swelling by discharge products. In this case, stack compression during cell assembly would be one of the factors influencing cell safety.

Hypothesis four:

Rupture of **both** stress relief on several anodes or cathodes which are insulated from the others (lower discharge voltage). That implies a reduced nominal lithium capacity. The other events are similar to hypothesis 1 or 2 but their extend increases because of the loss of capacity due to stress reliefs ruptures.

Hypothesis five:

Rupture of **both** stress reliefs on anodes or cathodes (lower voltage during discharge). During discharge, lithium deposition due to insulated of electrodes (see explanations given thereafter for lab cells experiments). Because of heat increase at the end of the discharge, chemical reaction of the dendrites with $SOCl_2$ with heat generation may occur. Lithium dendrites may also create shorts between the insulated anode and the carbon electrode facing it.

Experiments on cells

To identify the cause of the safety hazard, three VLS250 AM cells were assembled, each of them having a different defect. These cells have then been discharged but have not been submitted to vibration tests.

Half filled cell (#235): The electrolyte volume of this cell has been reduced deliberately to 435 cm^3 corresponding to a $SOCl_2$ capacity of 278 Ah. This cell has been discharge under a constant current of 42 A with an initial discharge temperature of 10°C (no temperature regulation). The discharged capacity was 207 Ah (cut off voltage of 2.8 volts) and the temperature of the cell alveolous was 50°C in front of the anodic bus bar. This cell has been overdischarged at the same discharge rate during hours without noticeable event.

Cell with increased stack compression (# 269): The stack of this cell has been compressed to 70 kg. This cell has been discharged under a resistive load of 0.35 ohm at 10°C. The delivered capacity was 308 Ah without any anomaly during the discharge.

Cell with insulated anodes (cell #261): In the stack of this cell, three anodes have been electrically insulated by cutting both stress reliefs. These anodes are located in different places of the stack, one at the bottom, the second in the centre and the last one at the bottom. The cell has been discharged using a constant load of 0.35 ohm. The cell exploded when its voltage reached 2.92 volts after a discharged capacity of 314 Ah. No voltage fluctuation was observed.

Conclusion of the cell tests: These tests demonstrate that the most probable hypothesis to explain cell #227 venting is the rupture of both stress relief on an anode. In addition to the cell tests, laboratory cells have been used to study electrochemical mechanism responsible for the creation of a safety hazard.

Experiments on laboratory cells

Lab cells comprising one electrically insulated anode have been assembled. These cells comprises a limited number of electrodes connected in parallel. One of these cell assembly is represented on the figure 1. It is made of disc shape lithium anodes and carbon electrodes. Glass fibber separators are placed between each electrodes (same materials are used for the real cells).

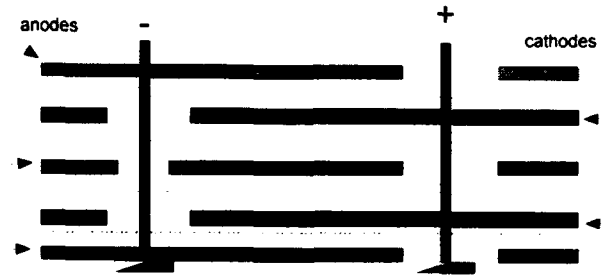

Figure 1: Laboratory cell assembly

In each case, the central anode is electrically insulated from other anodes. The cells is placed in an open PFFE cups in a glove box under inert atmosphere. It is filled with electrolyte (1.35 M $LiAlCl_4$, $SOCl_2$) with a wet stand time of 5 minutes before discharged. Discharge is performed under constant current using a power supply (Keithley 228A).

First experiment: This stack enclosed an insulated anode as illustrated above. It has been discharged under 16 mA/cm^2.

After the discharge, the cell has been disassembled for examination (the cell has not been submitted to overdischarge) and DPA revealed lithium deposits as mentioned on the figure 2.

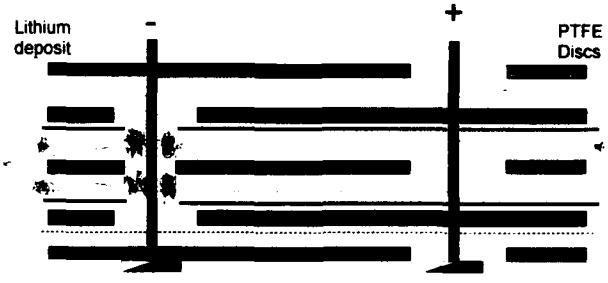

Figure 2: Localization of lithium dendrites in laboratory cell after discharge

Second experiment: To demonstrate the mechanism occurring on an insulated anode during the discharge and to ensure inactivity of the cathode surfaces facing the insulated anode, PTFE discs have been added between the separators and the carbon surface. The central anode has been electrically insulated from the two others as in the previous experiment. During cell DPA, a large amount of lithium dendrites deposit has been observed on the insulated electrodes mainly in the area between this anode and the negative bar. This deposit impregnating the separators burned in air during hydrolysis.

Discussion of experimental results on laboratory cells:
The electrochemical mechanism leading to a lithium deposit certainly results from differences of the lithium ion concentration at the surface of this electrode.
This situation is presented on the figure 3.

During the discharge, reduction of thionyl chloride occurs at the interface of connected electrodes. In this region, depletion of thionyl chloride occurs and promotes an increase of lithium ion concentration in the electrolyte. At the surface of the insulated anode, in the region facing the carbon electrode, the electrolyte concentration remains constant (no lithium oxidation occurs due to electrical insulation and no reduction of thionyl chloride on the carbon electrode). At the periphery or near the anodic bar, the isolated anode can be in contact with highly concentrated electrolyte. That leads to create at the surface of the insulated electrode two region with different lithium ion concentrations. This concentration cell promotes the corrosion of the insulated anode (oxidation reaction on the area facing the carbon electrodes) and lithium deposit at the periphery of this electrode (reduction reaction) where the electrolyte concentration is high.

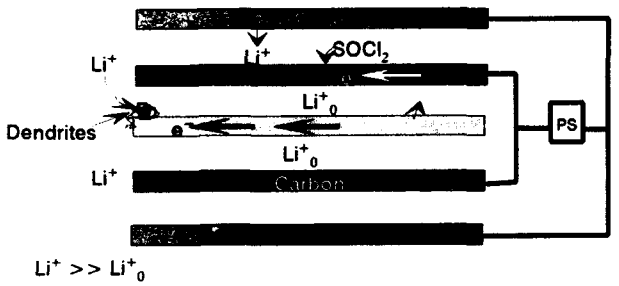

Figure 3: Mechanism of dendrites formation

Conclusions of laboratory experiments: These results clearly demonstrate the possibility of a lithium deposition on a negative electrode when electrically insulated from the others. If the lithium deposit is important, it can penetrate the separator layers and shorts the anode and carbon electrodes. As full capacity is still available for these two electrodes, a thermal runaway can occur either by thermal effect due to short circuit current, dendrites fuzzing or burning.

Recently, explosions of Li/SO_2 cells after vibration have been reported [3]. DPA of these cells clearly revealed a rupture of anodic cold weld between lithium and anodic strip. The authors observed lithium dendrites formation on one end of the insulated anode and lithium corrosion on the other parts. This phenomenon is supposed to create electrical bridges that melt due to current flow, creating the possibility of very localized hot spot able to initiate highly exothermic reaction.

These results are very similar to the observations made on the lithium deposition in the stack that have been discharged in our laboratory. At cell level, similar lithium deposition can occur creating the possibility of thermal runaway.

Discussion of the venting of one VLS 250 AM cell

The previous results show that the simultaneous rupture of the two tabs of an anode is responsible for cell venting. This venting results from a thermal runaway due to lithium dendrites that develop on the insulated anode. Once this phenomenon has been identified, the mechanism of tabs rupture must be studied. It seems to occur because of environmentally assisted cracking of the nickel with metal embrittlement by zero valent lithium. This mechanism has been widely studied and found in $Li/SOCl_2$ cells on the nickel tabs connected to lithium [4]. It can cause cell premature failure. In the case of the VLS 250 AM cell, rupture of brittle nickel tabs by vibrations has certainly be amplified. Modification of the tabs has been made and no venting were obtained either at cell or battery level even after shocks and vibrations.

Conclusions

Venting of one VLS 250 AM cell during discharge after vibration has been studied. It has been found that lithium plating was responsible for a thermal runaway. Lithium plating results from the creation of a concentration cell on an anode which became electrically insulated from the others because of the rupture of its two nickel tabs. This defect is certainly due to nickel embrittlement by environmentally assisted cracking which promotes rupture during vibrations. Modifications of the tabs have been successful and no such defect and safety hazard were obtained.

REFERENCES

(1) J.P. SEMERIE and J.L. FIRMIN, Proceedings of the European Space Power Conference, Florence (Italy), 2-6 Sept. 1991, (ESA SP-320, Aug.1991)

(2) J.P. SEMERIE and V. KANDARPA, Proceedings of the European Space Power Conference, Graz (Austria), 23-27 Aug. 1993 (ESA WWP-054, Aug. 1993)

(3) G.J. Donaldson *et al*, Power Sources 13, The 17th International Power Sources Symposium, Bournemouth, April 1991

(4) J.R SCULLY, W.R CIESLAK, F.S BOVARD, J. Electrochem. Soc., Vol 138, N°8, 2229-2237 (August 1991)

ENTROPY CHANGES IN UNDISCHARGED AND PARTIALLY DISCHARGED OXYHALIDE CELLS

by

M.L. Kronenberg, N.C. Liberto & N. D Isaacs

MSA
38 Loveton Circle
Sparks, MD 21152

Introduction

The accepted discharge reaction for the $Li/SOCl_2$ cell is given in Equation 1.

$$4\,Li + 2SOCl_2 = 4\,LiCl + S + SO_2 \quad (1)$$

With only one exception, most studies carried out during the past 15 years have shown that the entropy change is negative for the $Li/SOCl_2$ discharge reaction which is assumed to proceed as shown in Equation 1 (1-9).

The accepted discharge reaction (10) for the Li/SO_2Cl_2 cell is given in
Equation 2.

$$2\,Li + SO_2Cl_2 = 2\,LiCl + SO_2 \quad (2)$$

Much less work has been done on determining the sign of the entropy change for the sulfuryl chloride system, and part of the work here is directed toward making that determination.

At constant pressure the entropy change is directly proportional to the change in reversible potential with temperature (dE_T/dT). In our investigation the change in OCV with temperature (dOCV/dT) is used to determine the sign of the entropy change for the discharge reactions given above. The way the OCV changes with temperature can change with the depth of discharge if one or more of the reaction products resides in a different phase than it did initially.

In this investigation, d(OCV)/dT was determined on undischarged and partially discharged $Li/SOCl_2$ and Li/SO_2Cl_2 cells by simultaneously monitoring OCV while cooling a cell in a controlled manner. In addition to yielding information about entropy changes in the cell, in certain instances this procedure appears to lead to a direct observation of the thermoneutral potential (T_{TNP}).

Experimental

In our work a simple, rapid non steady state method was used to determine changes in entropy from d(0CV)/dT values. A type K thermocouple is spot welded to the outside surface of a test cell. The thermocouple and cell voltage outputs are fed into a Fluke Model 2286A data logger which is programmed to sample at one minute intervals. The cells were cooled and reheated in a Blue M temperature chamber programmed to ramp from 24 °C at a rate of 0.5 °C per minute to -70 °C. There was a dwell time of up to 2 hours at the lowest temperature followed by a return to 24 °C at the same programmed rate.

The above procedure was followed on both undischarged and partially discharged cells of both chemistries. The $Li/SOCl_2$ cells reported on here used 0.5 M $LiAlCl_4$ as salt and were built in our facility. The Li/SO_2Cl_2 cells were "D" size from Electrochem Industries designated as CSC 3B35 Cells. In addition to sulfuryl chloride these cells are reported to contain small additions of chlorine. The presence of chlorine is not believed to change the nature of the reaction products or otherwise change the main findings of this investigation.

Experimental Results

Using this procedure, the results that we observed for a fresh, undischarged prismatic $Li/SOCl_2$ cell are shown in Figure 1. This is a plot of OCV and outside cell wall temperature as a function of time during a programmed cooling and heating cycle. The temperature of the cooling chamber was changed at a rate of 0.5 degrees/minute from ambient temperature (about 24°C) to -70 °C and return with a soak time of 30 minutes at the lowest temperature.

FIGURE 1 OCV Variation with Temperature
Prismatic Li/SOCl2 Cell

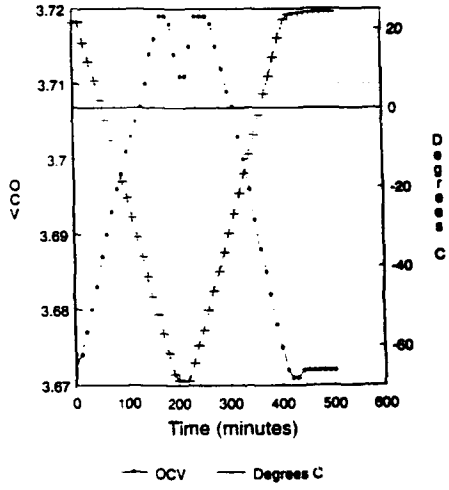

The plot clearly shows the cell OCV and cell wall temperature moving in opposite directions. The OCV peaks at just below 3.72 volts and then moves in the same direction as the temperature, although the temperature is still in the programmed cooling mode. This is the response that would be expected for a cell passing through the thermoneutral potential. The behavior in reverse is repeated on the heating cycle from -70 °C to room ambient temperature. The freezing point of neat thionyl chloride is -105 °C (11). The d(OCV)/dT slope calculated between room ambient temperature and the thermoneutral transition was -0.53 mV/°K.

To estimate the lag effect between the measurement of cell wall temperature and internal cell temperature for this thin prismatic cell, we compared the response of an internal thermocouple in a cell filled with ethylene gylcol to the one that monitored the cooling chamber. The lag effect for the internal thermocouple to reach the same temperature as the chamber air was 5 minutes or less.

The d(OCV)/dT plot for an undischarged CSC cell which is a Li/SO_2Cl_2 based cell containing chlorine is shown in Figure 2. Here again the voltage increases with decreasing temperature. The potential increases upon cooling to just below 3.99 volts. It maximizes at slightly higher voltages upon reversing the cycle. In this experiment the dwell time at -70 °C was two hours. The abrupt decrease in voltage may be due to the initiation of electrolyte freezing since the freezing point for neat sulfuryl chloride solvent is -54.1°C (12) and would be slightly lower than this for the salt containing electrolyte. The slope of d(OCV)/dT is always negative in the region preceding the 1st voltage peak and then changes direction after the voltage peak. The slope in the linear region just preceding the 1st voltage peak is -0.66 mV/°K.

FIGURE 2 OCV VARIATION WITH TEMPERATURE
Undischarged "D" Size CSC Cell

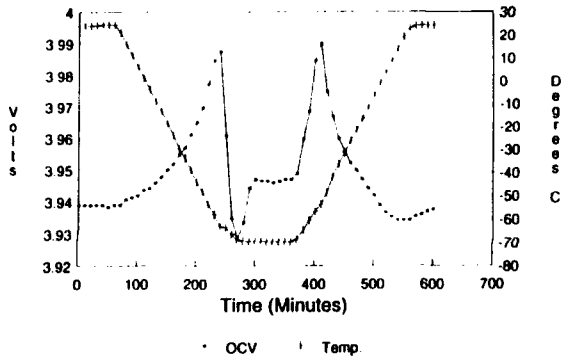

The next group of tests were carried out on partially discharged cells. Figure 3 shows the voltage variation with temperature result for a prismatic $Li/SOCl_2$ cell that was 22.5% discharged. These cell voltage maximums were less on this partially discharged cell than on the fresh, undischarged cell shown in Figure 1. Voltage maximums were slightly less than 3.7 volts. This cell was not a fresh cell, but was stored at ambient temperature for about 1 1/2 years. Here also, the slope of d(OCV/dT) is always negative in the portion preceding the 1st voltage peak. The slope in the linear region just preceding the 1st voltage peak is -1.0 mV/°K.

FIGURE 3 OCV VARIATION WITH TEMPERATURE PLOT FOR 22.5 % DISCHARGED $Li/SOCl_2$ CELL

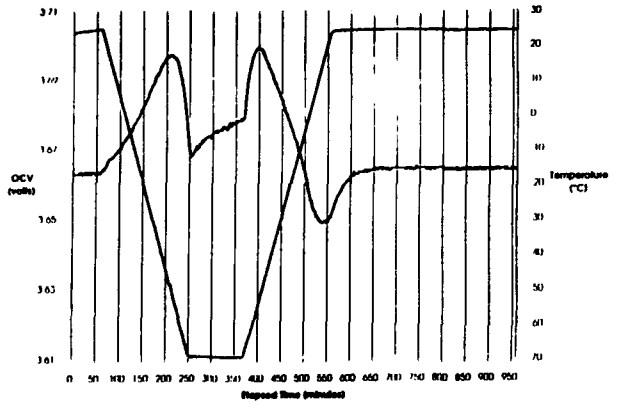

Figure 4 shows the voltage variation with temperature for a $Li/SOCl_2$ cell that was discharged for 45% of its capacity. This cell showed voltage maximums at about 3.71 and 3.73 volts and the voltage peaks were not as pronounced as with the fresh and lower percent discharged cell. Again, the slope of the voltage variation with temperature is negative in the portion preceding the voltage peak and then changes direction. The slope in the linear portion just preceding the 1st voltage peak is -2.0 mV/°K.

FIGURE 4 OCV VARIATION WITH TEMPERATURE PLOT FOR 45 % DISCHARGED $Li/SOCl_2$ CELL

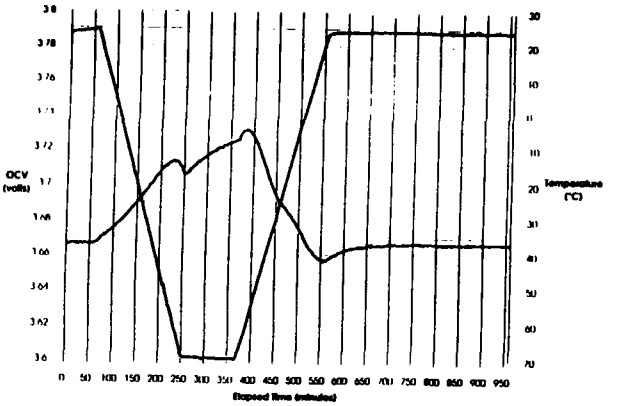

Figure 5 shows the voltage variation with temperature for another $Li/SOCl_2$ cell that was discharged for 68% of its capacity. In this case one voltage peak disappeared and the other peak voltage was more than 3.74 volts. The slope was negative up to the region of the 1st voltage peak and reversed itself. After the 2nd voltage peak it reversed itself again. The slope in the linear region up to where the 1st voltage peak would have been was -2.0 mV/°K.

FIGURE 5 OCV VARIATION WITH TEMPERATURE PLOT FOR 68 % DISCHARGED $Li/SOCl_2$ CELL

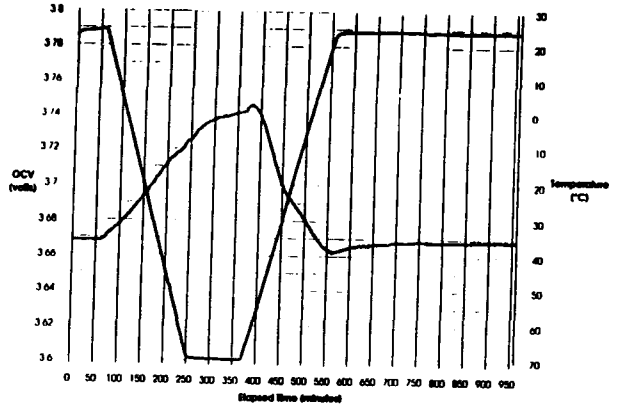

Voltage variation with temperature results for partially discharged CSC cells are shown in Figures 6 & 7. The first cell result shown was from a cell discharged for 2.62 AH and gave voltage peaks that were just under 3.97 volts on the cooling half of the cycle and just above 3.98 volts on the heating half of the cycle. Since this cell has a nominal capacity of 14 AH the percent discharged was about 19%. The slope of the voltage variation with temperature is negative up to the 1st voltage peak and then changes direction. The slope in the linear region just prior to the voltage peak is -0.82 mV/°K.

Figure 6 Voltage Variation With Temp.
Partially Discharged D Size CSC Cell

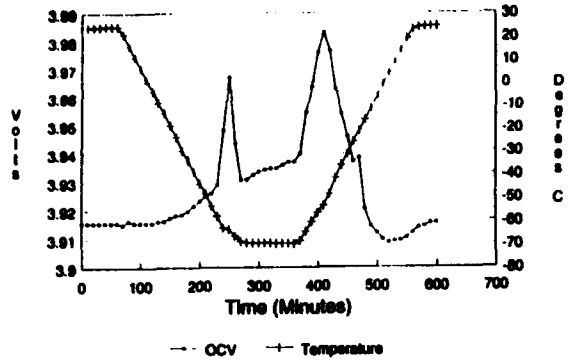

FIGURE 7 Voltage Variation With Temp.
Partially Discharged D Size CSC Cell

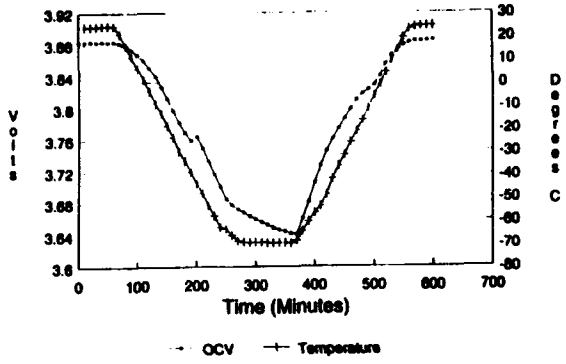

The cell discharged for 8.85 AH (nominal 63% discharged) had no voltage peak and the cell voltage and temperature changed in the same direction, i.e., d(OCV)/dT was positive. This was true over the entire range of heating and cooling cycles. This suggests that significant changes have taken place to products of the cell discharge reaction. The slope of the voltage variation with temperature in the initial linear region is +2.9 mV/°K.

Voltage variation with temperature tests were also conducted under equilibrium or steady state conditions. In these experiments, cells were cooled down in 10 degree steps and allowed to equilibrate at each temperature. Cell voltage readings were taken several hours after standing each temperature. Figure 8 shows the cell voltage variation with temperature for a prismatic $Li/SOCl_2$ cell tested in this way. It is seen that the voltage increased with temperature decrease, as was observed with the transient method. The cell voltage continued to increase to about -40 °C and peaked out above 3.7 volts. Since the voltage measurements were recorded at 10 degree temperature intervals, the true peak voltage may not have been observed. The cell voltage increase between -60 °C and -70 °C can not be explained at this time and will have to be repeated. Several other similar steady state tests on $Li/SOCl_2$ cells gave erratic behavior, even showing positive voltage variation with temperature responses. In a recent work (1) we have shown that cells with internal shorts or other problems that load the cell causing it to deviate from the OCV condition, will not give the normal voltage variation with temperature response that we attribute to tests carried out on fresh cells at OCV. The extent of the deviation needed to give an abnormal response in voltage variation with temperature tests is yet to be determined.

FIGURE 8 OCV VARIATION WITH TEMPERATURE
Thionyl Chloride Cell

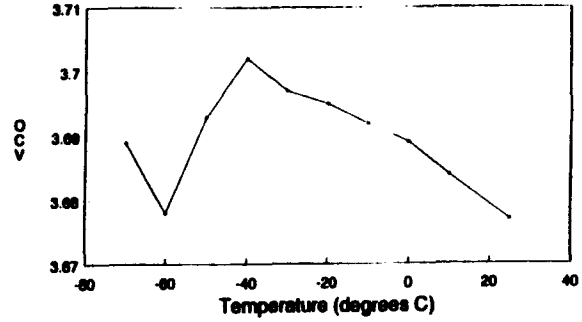

Discussion of Results

The thermoneutral potential value of about 3.72 volts that we obtained for fresh, undischarged $Li/SOCl_2$ cells is in good agreement with most of the results that have been obtained by calorimetric measurements or steady state observations of d(OCV)/dT over the past 15 years (4-11). These results have ranged from 3.66 to 3.88 volts with the exception of Schlaijker et al (ref 7) who reported a value of 3.33 volts which is well below the normally observed OCV of 3.67 volts.

The cell voltage of the undischarged CSC cell increased with decreasing temperature from the OCV to a maximum of about 3.99 volts. The voltage response changed direction at this maximum voltage as would be observed when the thermoneutral potential is attained. The precipitous drop after the maximum may perhaps be attributed to a partial freezing of the electrolyte. The heat of fusion could release heat internally in the cell and cause the voltage to increase since the chamber temperature is no longer decreasing. After that the cell voltage increased with increasing chamber temperature until the thermoneutral potential was again attained and the direction of the voltage/temperature response was again reversed.

With $Li/SOCl_2$ cells that were partially discharged from 22.5 to 68% DOD the double peaks that were observed on cooling and subsequent reheating disappeared with degree of discharge reaching a single maximum at the 68% DOD. Once the first peak disappeared, the voltage variation with temperature did not reverse until the second peak was attained.

The CSC cell partially discharged for 2.62 AH (nominal 19% DOD) gave unsymmetric maxima, one at 3.97 volts and another at 3.98 volts. The cell discharged for 8.8 AH (nominal 63% DOD) gave a voltage variation response with temperature that was in the same direction for the entire cooling and reheating cycle. This observation indicates that there is a positive entropy change in the discharge reaction at this depth of discharge having changed from a negative entropy change at undischarged and low discharge levels. An example of a change that could account for this significant result is a release of a discharge product like SO_2 from a complexed or soluble state in the electrolyte phase to a gaseous product. There has been evidence of free SO_2 at the end of discharge for this cell chemistry. Figure 9 shows the discharge curve for these two cells which was interrupted for the d(OCV)/dT measurements and then completed. The cell capacities were 14.4 AH for the initial lower rate discharge and 14.1 AH for the higher rate discharge. About 0.8 AH of this discharge capacity is obtained from the discharge step just below 3 volts which is most likely due to the cells discharging as Li/SO_2 cells.

FIGURE 9 CSC930 CELL DISCHARGED AT 24 °C

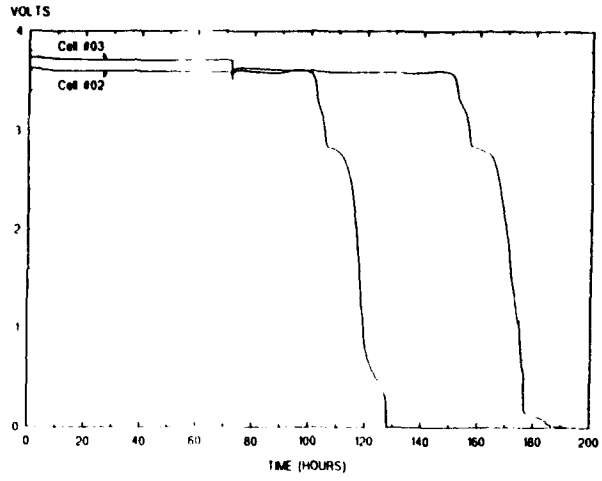

Table 1 summarizes the d(OCV)/dT values obtained from the linear portion of the voltage variation with temperature data just prior to a voltage peak for both undischarged and partially discharged cells for the two chemistries. Entropies calculated from the d(OCV)/dT data are also included in the table.

Table 1. Voltage Variation With Temperature Slopes and Calculated Entropies for Undischarged and Discharged Cells

System	% Discharged	d(OCV)/dT (mV/°K)	Calculated ΔS (Cal/°K-eq)
$SOCl_2$	0	-0.53	-12.2
SO_2Cl_2	0	-0.66	-15.2
$SOCl_2$	22.5	-1.0	-23.0
$SOCl_2$	45	-2.0	-46.1
$SOCl_2$	68	-2.0	-46.1
SO_2Cl_2	19	-0.82	-18.9
SO_2Cl_2	63	+2.9	66.9

Summary of Observations

1. A non-steady state method is being evaluated to examine cell OCV changes with temperature to directly observe the thermoneutral potential and study entropy changes in cells.

2. This method was applied to Li/$SOCl_2$ and Li/SO_2Cl_2 cells.

3. Both Li chemistries showed negative coefficients for OCV changes with temperature on undischarged cells up to a voltage maximum. After reaching the voltage maximum, the coefficient for OCV change with temperature became positive.

4. With fresh Li/$SOCl_2$ cells on both cooling and reheating cycles, the OCV attained a maximum cell voltage close to 3.72 volts, after which the voltage variation with temperature changed direction.

5. The voltage maximum for Li/SO_2Cl_2 cells was close to 3.99 volts, after which the voltage variation with temperature changed direction.

6. Partially discharging Li/$SOCl_2$ cells caused maximum voltage peaks to be significantly changed, and these changes were related to the depth of discharge. The same changes in reversal of voltage variation after passing a modified peak were observed.

7. A partially discharged Li/SO_2Cl_2 cell discharged about 19% of its capacity had shifted peaks, but responded to OCV changes with temperature in the same way as an undischarged cell.

8. A partially discharged Li/SO_2Cl_2 cell discharged to about 63% of its capacity, completely changed its voltage variation with temperature response to give a positive temperature coefficient. This suggests that at this state of discharge, the entropy change for the discharge reaction had changed from negative to positive. This type of change would occur if SO_2 product was no longer confined to the solution phase but was also present in a gaseous phase.

9. Upon completing the discharge of the partially discharged Li/SO_2Cl_2 cells, there was a discharge step just below 3 volts at the normal Li/SO_2 discharge voltage for about 6% of the total discharge capacity.

References

1. M.L. Kronenberg and N.C. Liberto, paper presented at the 1993 Fall ECS Meeting, Extended Abstr. No. 28, p.45, New Orleans, LA, Oct. 10-15, 1993.

2. N.A. Godshall and J.R. Driscoll, J. Electrochem. Soc., 131, 2221 (1984).

3. E.E. Kalu and R.E. White, ibid, 139, 2755 (1992).

4. L.D. Hansen and H. Frank, ibid, 134, 1 (1987).

5. C.R. Schlaijker, F. Goebel and N. Marincic, ibid, 126, 513 (1979).

6. M.H. Miles, ibid, 126, 2168 (1979).

7. P. Bro, Power Sources 7, J. Thompson, Ed., p. 571, Academic Press, N.Y. (1979).

8. H.F. Bittner, B.J. Carter, S.W. Donley and M.V. Quinzio, J. Power Sources, 26, 441 (1989).

9. H.F. Gibbard, Proceedings Electrochem. Soc., 80-4, 510 (1980).

10. S. Gilman and W. Wade, Jr. J. Electrochem. Soc., 127, 1427 (1984).

11. Handbook of Chemistry and Physics, 57th Edition (1974), Robert C. Weast, Editor, CRC Press, Cleveland, Ohio. p. B169.

12. Ibid, p. B166.

HIGH RATE LITHIUM-THIONYL CHLORIDE BIPOLAR BATTERY DEVELOPMENT

P. G. Russell, F. Goebel
Yardney Technical Products, Inc.
82 Mechanic Street
Pawcatuck, CT 06379

Abstract
The lithium/thionyl chloride ($Li/SOCl_2$) electrochemistry is capable of providing high power and high specific power, especially under pulse discharge conditions, when cells containing thin components are arranged in a bipolar configuration. This paper describes recent work concerned with bipolar cell design, cathode evaluation, component manufacturing methods, and the assembly and testing of bipolar modules containing up to 150 cells for Sonobuoy application.

The new generation of active Sonobuoys with increased detection range capability will require improvement in battery performance. The lithium/thionyl chloride bipolar design is capable of meeting the power and energy requirements of these systems (Table 1). The development of a bipolar battery design incorporating ten-inch diameter thin cell components[1] was successful in fabrication and pulse testing of several full size 4-cell stacks, a 20-cell stack and a final 80-cell hermetically sealed 25kW demonstration battery. Performance of this battery was characterized using 2, 4, and 20ms pulses at a ten percent duty cycle. A maximum pulse power of 35kW and specific power of 1.9kW/lb could be demonstrated at a current density of 400mA/cm^2.[2] Although this effort was considered a success, it did point to the need for further cell component utilization if longer pulse times are to be achieved. One goal of the present program is to develop a 10.7kW bipolar module (one-seventh of the torpedo size Sonobuoy power supply) with load voltage in the range 300 to 500 volts.

EXPERIMENTAL

A novel method was developed for manufacturing carbon cathodes. This method starts with a carbon slurry formulation and produces single sheets of cathode material in a sheet mold having uniform thickness and weight. Cathode thickness and carbon content are controlled by changes in the slurry formulation. This method reduced the time required for manufacturing the large numbers of cathodes required for fabrication of bipolar modules containing up to 150 cells. Full size ten-inch diameter cathodes were evaluated in a special fixture with one inch thick steel endplates separated by an O-ring which provides uniform thickness and compression during single cell tests. The final cell gap was adjusted under vacuum to provide proper compression on the cathode/separator components prior to activation with 1.6M $LiGaCl_4/SOCl_2$ electrolyte.

Multicell stacks were fabricated from "bipolar hardware" consisting of bipolar plates and current collecting endplates. Bipolar plates are prepared by bonding thermoplastic Tefzel material to lightly etched nickel substrates. This is an important step since the bipolar plates must maintain the correct cell gap and prevent internal electrolyte leakage between adjacent cells in a bipolar stack. The procedure is illustrated in Figures 1A and 1B. Three Tefzel rings and a substrate are properly aligned between the top and bottom capture mold sections so as to maintain a one-eighth inch Tefzel/substrate overlap, Figure 1A. The two sections are bolted together and maintained under compression during the heating and cooling steps. After melting, the Tefzel material forms a ring of insulation, Figure 1B, with the proper height sealed to the periphery of the nickel substrate. Current collecting endplates are made in a similar manner. In this case, the substrate is a nickel plated copper disk with a nickel tab terminal at the center.

A computer controlled setup provided a constant current of 25A during the pulse and/or continuous discharge performance tests for cathode evaluation in the special fixture. The pulses were 20 seconds in duration with a 10% duty cycle. After 20 cycles of pulse discharge, continuous discharge continued until the cell voltage reached 1 volt. A constant power pulse discharge, 71.4W per cell, was provided by the setup during performance tests conducted on single and multicell submodules. All cell data was stored in a Nicolet System 500 during the constant power pulse tests.

RESULTS AND DISCUSSION

Cathode Evaluation

The variation of cathode utilization(Ah/g) with carbon loading (g/cm^2) is shown in Figure 2. These full size cathodes were evaluated in the special fixture during continuous discharge at 25A, i.e., 50mA/cm^2. The novel cathodes performed better than the standard cathodes made by a calendering procedure, most likely because of the lower apparent density which increases the number of active carbon sites available for $SOCl_2$ reduction. The best result, 1.64Ah/g, was observed for a cathode containing 4.86g carbon, equivalent to a cathode loading of 10mg/cm^2. All further testing was done with cells containing cathodes made by the slurry process described above.

The initial carbon composition contained 80% of a low surface area carbon (60m^2/g) and 20% of a high surface area carbon (>1000m^2/g). The effect of carbon surface area on load voltage during pulse discharge is examined in Figure 3. The end-of-pulse-voltage (EOPV) increased to a maximum of 3V as the high surface area component of the cathode carbon composition was increased from 0 to 60 weight percent. Additional tests confirmed that the 40/60 composition gave the best EOPV values during pulse discharge of full size cathodes at 25A.

Several platinized carbon mixtures were evaluated in an effort to improve the EOPV. The standard 40/60 carbon cathode is compared with the best 40/60 (based on carbon) platinized carbon cathode composition in Figure 4. One characteristic all platinized cathodes had in common was the initial high EOPV followed by a voltage decrease during each additional pulse. A decrease in the number of catalytic platinum sites leaving only active carbon sites due to poisoning by impurities or blockage by locally deposited LiCl, may explain the observed decrease in cell voltage. The EOPV values for one of the standard cathodes increased slightly, most likely because of a small temperature increase, and reached the same value, 3.02V, as the platinized carbon cathode during the twentieth pulse. All 40/60 standard carbon cathodes had EOPV values above 2.9V during evaluation in the special fixture. This standard carbon composition was selected for all further single cell and multicell stack tests.

The effects of current density and duty cycle on the EOPV for full size 40/60 standard carbon cathodes are shown in Figure 5. Increasing the discharge rate while maintaining a 10% duty cycle lowers the EOPV and

causes a rapid fall off in EOPV values, especially at 100mA/cm^2. Increasing duty cycle to 50% has only a slight effect on the 50mA/cm^2 rate while drastically reducing the number of pulses available at 100mA/cm^2.

Cell Design and Stack Assembly

Cell components are sandwiched between adjacent bipolar plates during stack assembly as shown in Figure 6. The lithium anode is rolled onto each bipolar plate and anode endplate prior to stack assembly. Preparation of all cell components and stack assembly procedures were performed in a dry room environment with relative humidity less than two percent. To begin assembly, a carbon cathode is centered on the cathode endplate positioned in the assembly fixture. A glass paper separator is then centered over the cathode and the first bipolar plate is positioned over the assembled components, lithium side down. Each additional cell is assembled in like manner starting with the centering of the second cathode on the first bipolar plate. The anode endplate is the last stack component in the assembly procedure. A fill tube is added to each cell for electrolyte activation after stack sealing. The assembled stack components are compressed to the final height in preparation for stack sealing. The Tefzel insulation rings are sealed along the stack periphery except near the fill tubes (initial three-quarters seal). A 330 watt iron was used to seal the single cell, 4--cell, and 10-cell stacks initially. Each cell is filled individually with the proper volume of electrolyte from a syringe delivery system. A cathode channel design was developed to help distribute electrolyte throughout each cathode. Stack sealing is completed after activation. Each stack is maintained under external compression after activation and during final sealing in preparation for testing. For fabrication of a single cell using bipolar hardware, cell components are assembled between anode and cathode endplates.

Single Cell Tests Using Stack Hardware

Several constant power pulse tests were performed with single cells assembled from stack hardware. The full size 10-inch diameter cathode was down-sized to a 9.25-inch diameter cathode for the torpedo size sonobuoy power source application. Comparison with the full size cathode showed that cell voltage decreased only slightly, i.e; by 50 to 80 mV in going to the smaller diameter cathode. As an example, thirty-one 20 second pulses were obtained during the first constant power continuous pulse discharge test with a 9.25 inch cathode, Figure 7. The average EOPV value in this test was 2.96V from the second through the twentieth pulse.

Multicell Stack Tests

The load voltage in multicell stacks is sensitive to changes in compression on stack components. The external compression was adjusted on several multicell stacks during the initial few pulses in order to maximize stack performance throughout the rest of the test. One result is shown in Figure 8 for a 4-cell stack containing 10 inch diameter cathodes. Thirty-six 20 second pulses were obtained during this constant power continuous pulse discharge test. One characteristic of multicell stacks observed during testing was the increase in voltage, usually during the first 10 to 12 pulses, due to an increase in stack temperature. In this example, the voltage peaked during pulse 13 at 13.56V, for an average of 3.14V per cell. Twenty-seven pulses were obtained during testing of a 10-cell stack, Figure 7. The peak voltage, 31.81V, occurred during pulse 11 for an average of 3.18V per cell.

A 50-cell engineering stack was built with 10-inch electrode components in order to establish a procedure for the assembly, sealing, and activation of large stacks. The stack was assembled as described above. Stack components were compressed between one-inch thick lucite support plates using C-clamps prior to initial stack sealing. It is important that the bipolar plate/Tefzel ring cell assemblies are seated properly, i.e., are compressed into a flat configuration of cells that will maintain proper component contact/compression during activation and testing. The bipolar rings form an uneven vertical surface which must be smoothed in order to insure Tefzel/Tefzel bonding among adjacent rings around the periphery of the stack. The initial three-quarters sealing was done with a 550 watt iron. One layer of a fiberglass/Tefzel composite was applied to the initial seal in order to thicken and strengthen the Tefzel/Tefzel bonded rings.

Compression was relaxed during electrolyte activation which allowed the stack to expand somewhat in the center, part of the normal activation procedure. The cathode could not be uniformally compressed to a flat configuration after activation because of cathode expansion, and as a result, a change was made in the activation procedure to correct this problem. Fourteen pulses were obtained during pulse discharge, Figure 10. Twelve pulses occurred at load voltages above 150V, better than 3V per cell on average. The maximum voltage, 160.75V, occurred during the sixth pulse, for an average of 3.21V per cell.

The first 150-cell bipolar configuration was assembled from three 50-cell stacks connected in series with silver plated copper connectors during pulse discharge. Each 50-cell stack was maintained under compression in a "flat" configuration between one-inch thick lucite disks during the initial three-quarters sealing, electrolyte activation, and final sealing steps. Final compression was supplied with six C-clamps arranged symmetrically around each stack during discharge; three at half the radial distance and three at the periphery. The EOPV values for the 150-cell configuration are plotted in Figure 11. Several of the initial pulses were less than 20 seconds in duration because of problems associated with the high voltage instrumentation/software test setup. Current instability developed during pulse 7 (terminated after 15 seconds) when the power increased to 25.9kW after seven seconds of controlled discharge at 10.7kW. The 19 partial/complete pulses are equivalent to fourteen 20-second pulses.

The high power discharge during pulse 7 may have contributed to the less than expected number of 10.7kW pulses. A second reason would be electrolyte leakage. Minimal leakage occurred during activation of individual cells in each stack, but additional electrolyte was loss prior to and during the test from several small leaks that developed between adjacent Tefzel rings in each of the three stacks.

Assembly and Testing of a 150-cell Bipolar Module

Fabrication and testing of the multicell stacks and problems associated with two 150-cell modules indicated several problem areas which needed to be addressed: Tefzel stack sealing, cell activation, and the handling of large modules, during assembly being the most important. Changes and improvements made in these and other areas are discussed below:

1) The assembly fixture was redesigned so that a uniform compression could be applied to the stack during assembly. Handling is improved since a large module can be rotated under compression in this fixture for ease of sealing and electrolyte activation.

2) The cathode channel design was modified so that the fill tube is no longer compressed between the separator and cathode. This change improved module flatness under compression.

3) The quality of the sealed Tefzel surface was improved by replacing the soldering iron "contact method" with a hot gas welder. This type of welder was observed to melt the Tefzel stack surface without causing extensive degradation of the thermoplastic material.

4) A polarization test was developed to monitor the electrochemical condition of a large module prior to the start of testing.

5) The wicking capability of the cathode was improved by reducing the TFE content of the carbon composition. Several wetting experiments were conducted to compare high and low TFE cathodes. Electrolyte distribution between the cathode and separator components and electrolyte retention by the cathode improved with reduction in the TFE component.

A third 150-cell bipolar module was assembled during a two day period in the production dry room using low TFE cathodes and incorporating the other changes and improvements discussed above. Every effort was made to minimize exposure of the components and module to moisture during the assembly, initial stack sealing, electrolyte activation, and final sealing steps. Several tabs were TIG welded between the anode and cathode honeycomb support structures to provide compression to the module during testing.

Twelve 20 second pulses were obtained during the 10.7kW constant power pulse test. The lowest voltage and EOPV values are plotted for each pulse in Figure 12. Module voltage increased during the first five pulses, then peaked at 498.2v during the sixth 20 second 10.7kW pulse. Module voltage started to drop after the seventh pulse. The pulse test was terminated after the twelfth pulse because of the rapid drop off in voltage between the eleventh and twelfth pulses. Recovery of the OCV to 544V after each pulse was an indication that no internal shorts had occurred. The rapid drop off in module voltage after pulse 7 is evidence that a few cells were weak from lack of an adequate electrolyte content.

ACKNOWLEDGEMENTS

The initial high rate lithium/thionyl chloride bipolar design was developed during a four year program sponsored by Aero Propulsion & Power Lab (Contract F33615-86-C-2677), WPAFB under the technical direction of Richard A. Marsh.

The authors would like to thank Sheila Danahey for her role in bipolar plate development, Hushmuk Patel for his role in slurry cathode development, cell design, and stack assembly, and Fred Thompson and Ed Jackson for providing the high voltage test equipment and programming skills.

Yardney would like to thank the NSWC group and ONR (High Energy Battery Project) for their support of this work, which was performed under Contract NH60921-91-C-0124. The authors would like to thank the Project Manager, Dr. Patricia H. Smith, for all her guidance throughout this effort and the several other contributors for their valuable help during the course of this program: Glen D. Zoski; Charles W. Fleischmann; Stanley D. James; Timothy C. Murphy; and Patrick J. Kelley.

REFERENCES

1. P. Harris, M. Guentert and F. Goebel, Proceedings 34th Power Sources Symposium, June 1990. The Electrochem. Soc., Inc., Pennington NJ, pp 343-345.

2. P. Harris, M. Guentert, High Rate Lithium Development:Final Report for the Period September 1986 to July 1990, WRDC-TR90-2100.

TABLE 1:

Sonobuoy Power Supply Requirements

	Torpedo Size Sonobuoy	A-Size (1) Sonobuoy
Power (Watts)	75,000	4200
Volume limit (inches)	10.5 (D) x 35 (L)	4.5 (D) x 10 (L)
Operating voltage (volts)	300–500	125–250
Pulse width (seconds)	1–20	1–20
Duty cycle (%)	≤ 10	≤ 10
Minimum ping time (seconds)	400	100
Sonobuoy lifetime (days)	8	8

(1) Requirements for 10 module short life thermal battery

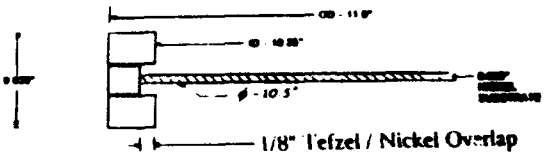

Fig. 1A Tefzel / Nickel Sandwich Prior to Compression Molding

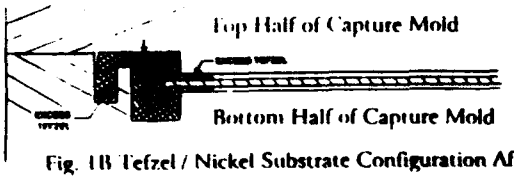

Fig. 1B Tefzel / Nickel Substrate Configuration After Compression Molding

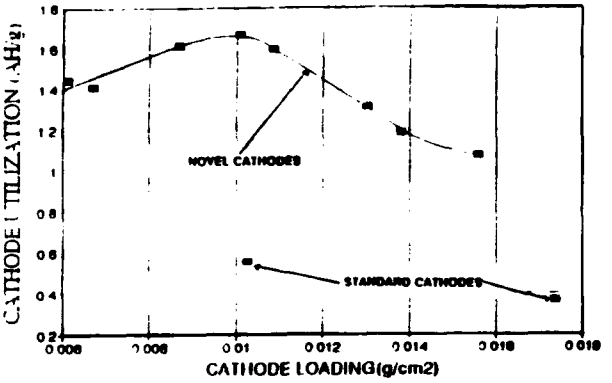

Fig. 2 Cathode Utilization (Ah/g) Versus Cathode Loading (g/cm²)

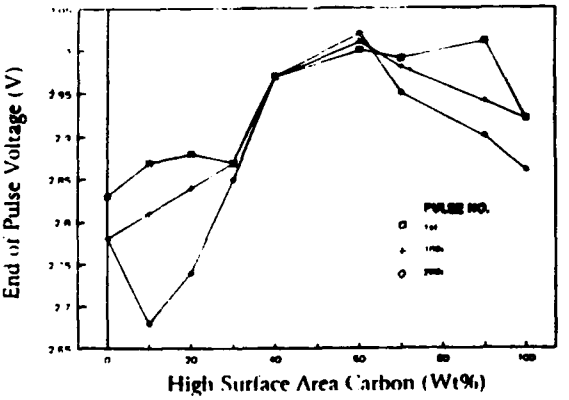

Fig. 3 EOPV Versus Carbon Composition - Twenty 20-Second Pulses

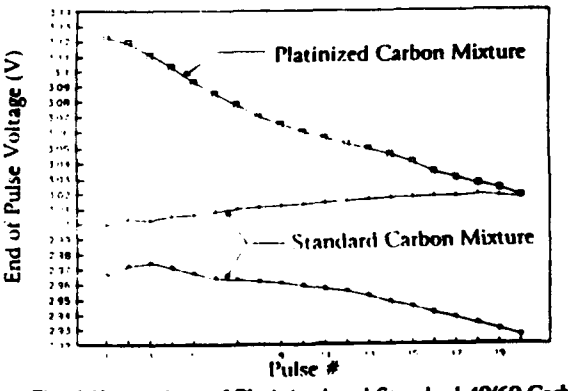

Fig. 4 Comparison of Platinized and Standard 40/60 Carbon Cathodes 20-Second Pulse Discharge at 25A

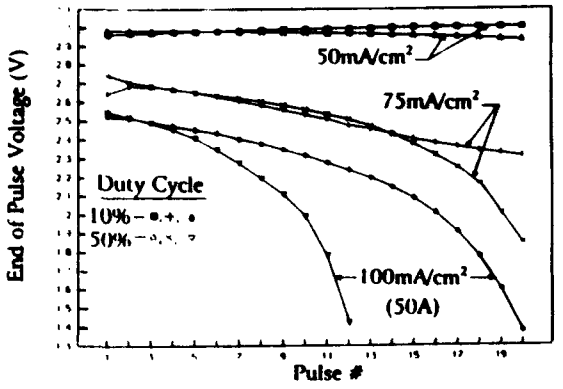

Fig. 5 Effects of Current and Duty Cycle on End of Pulse Voltage

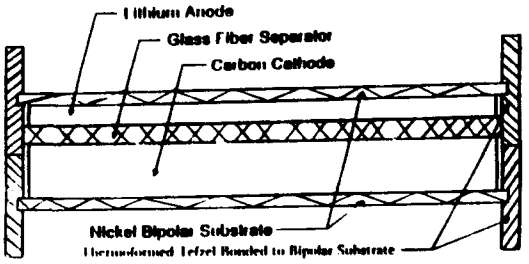

Fig. 6 Single Cell Components in Stack Subassembly

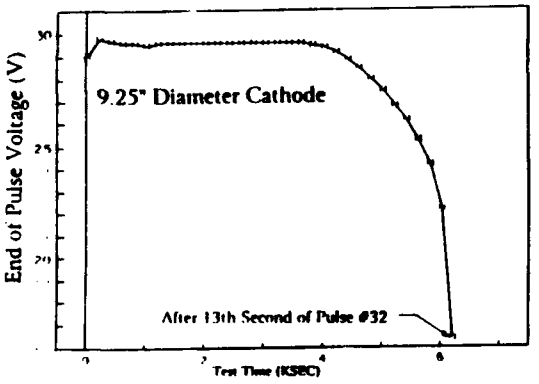

Fig. 7 First Single Cell Constant Power (71.4W) Continuous Power Discharge Evaluation of Cathode for Large Size Sonobuoy Battery

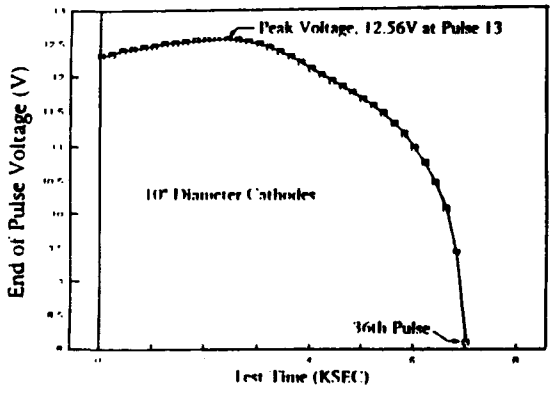

Fig. 8 EOPV for 4-Cell Stack During Constant Power (286W) Continuous Pulse Discharge

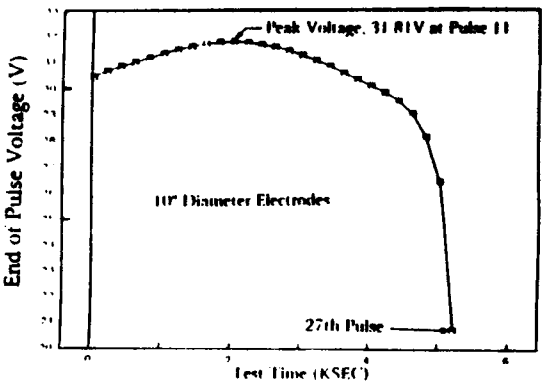

Fig. 9 EOPV for First 10-Cell Stack During Constant Power (714W) Continuous Pulse Discharge

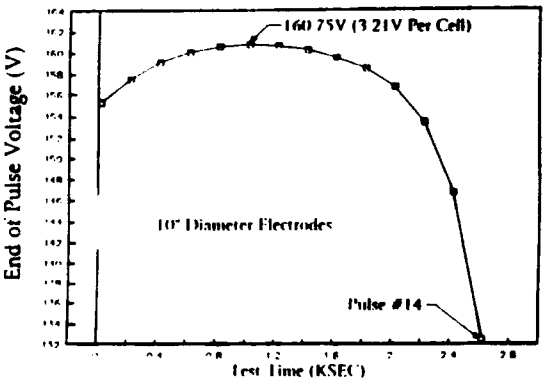

Fig. 10 EOPV for First 50-Cell Stack During Constant Power (3570W) Continuous Pulse Discharge

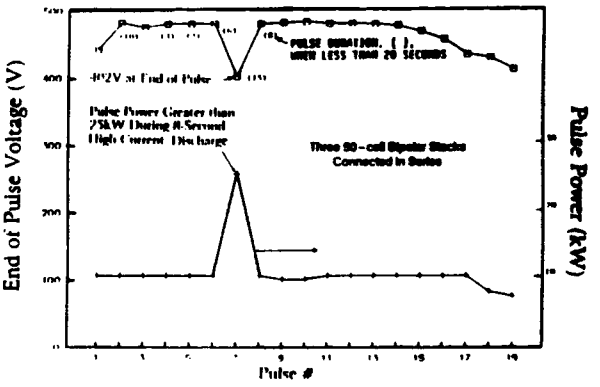

Fig. 11 EOPV for First 150-Cell Bipolar Configuration of Three 50-Cell Stacks Connected in Series During Constant Power (10.7kW) Pulse Discharge Test

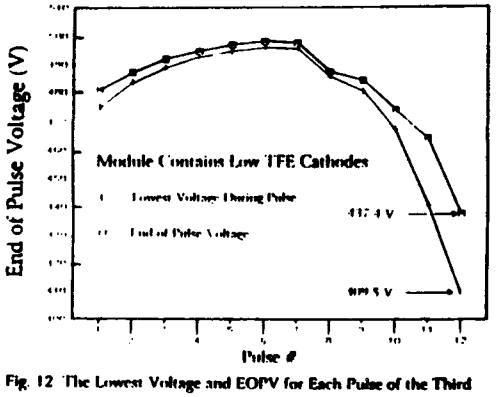

Fig. 12 The Lowest Voltage and EOPV for Each Pulse of the Third 150-Cell Module During the 10.7kW Constant Power Pulse Test

Experimental Simulation of Thermal Behavior of Li/SO_2 primary battery

Young I. Cho[1], Eunsoo Choi[1], and Robert J. Staniewicz[2]
Dept. of Mech. Eng. & Mechanics, Drexel University, Philadelphia, PA 19104
SAFT America, Inc., R&D Center, 107 Beaver Court, Cockeysville, MD 21030

Introduction

The objective of the present study was to conduct heat transfer experiments using a phantom Li/SO_2 battery under controlled conditions in order to examine the effect of various parameters on the thermal behavior of a real Li/SO_2 battery. The lithium sulfur dioxide (Li/SO_2) cells have many desirable characteristics for an electrochemical power source such as high energy density, high operating cell voltage, excellent voltage stability over 95 percent of the discharge, capability of operating over a wide temperature range (-40 to 80°C), exceptionally long storage life and low cost of materials.

In spite of these attractive features Li/SO_2 cells may show hazardous behavior at high rates of discharge [1]. The reports ranged from mild venting to violent explosions and fires. When the Li/SO_2 cell is discharged at a high rate, the internal electrical resistance of the cell produces a high heat generation, which increases the average temperature of the cell. We reasoned that conducting the experiment with actual Li/SO2 cells could result in venting, thus we sought a novel design that eliminated the "real" cells yet could easily be runwithin an ordinary laboratory without unusual dafety measures.

Experimental Method

In order to examine the effect of various parameters on the thermal behavior of the Li/SO_2 battery, the present study developed an alternative method using dummy cells which simulate the heat generations of real Li/SO_2 cells. A phantom Li/SO_2 battery that contained ten dummy cells was constructed as shown in Fig. 1.

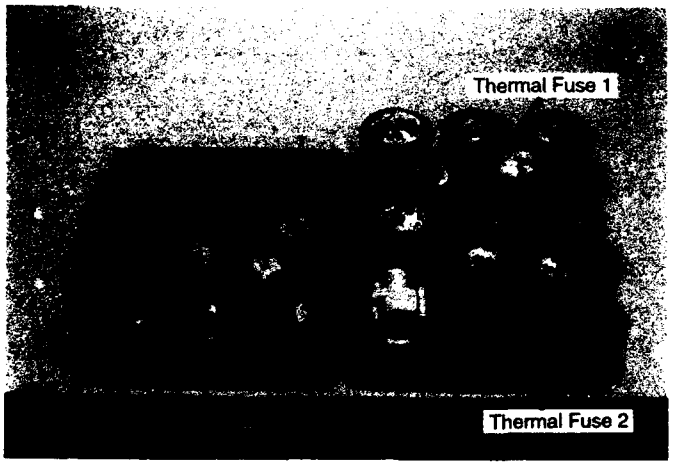

Fig. 1 Photograph of actual Li/SO_2 battery with 10 cells.

Figure 2 shows the top and side views of the battery, which shows ten dummy cells and a flexible board containing two diodes, two electrical fuses and two thermal fuses. The board is placed at the corner of the battery pack and the two thermal fuses are located around the center of the pack, surrounded by five cells, (cells #4 - #7, and #9). Note that thermal fuses disconnect the circuit to avoid danger when the temperature of the pack reaches a critical value. Two diodes are used to prevent reverse or charging currents for safety.

Based on the total thermal mass of the actual Li/SO_2 cell (i.e., 20.07 cal/°C), ten dummy cells were fabricated by filling case cans with molten lead. The identical case cans used in real cells were used. After the lead solidified, a cylindrical cavity of 0.357" diameter and 1.25" depth was drilled at the center of the solid lead where a cartridge heater was inserted to simulate the heat generation in the actual Li/SO_2 battery as shown in Fig. 2, which also shows the locations of fourteen thermocouples. Ten thermocouples (from #1 to #10) were

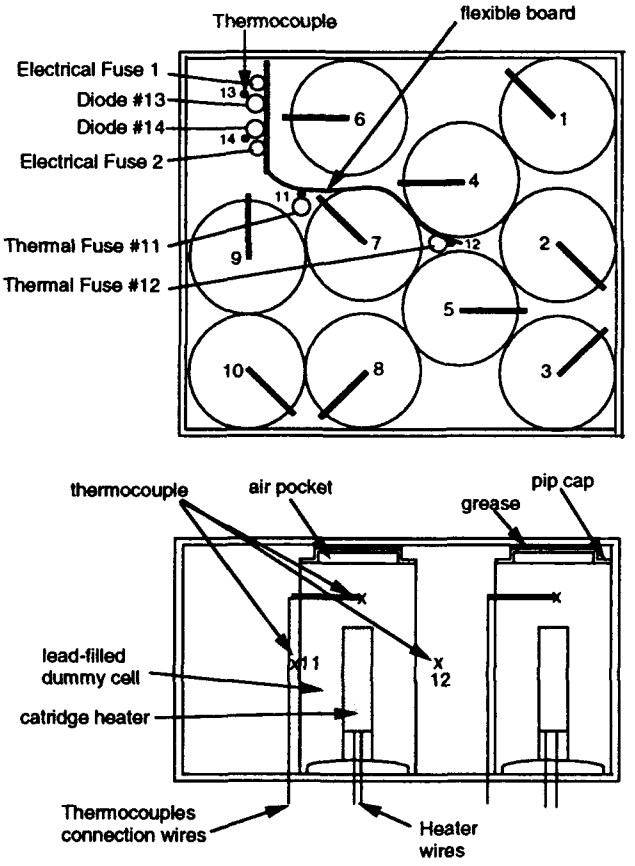

Fig. 2 The layout (top and side views) of ten cells and fourteen thermocouples.

inserted through small cavities drilled at the upper half of dummy cells as indicated by a thick solid line and x mark. In order to monitor the temperatures of diodes and thermal fuses, two thermocouples, #11 and #12, were cemented on the surface of thermal fuses. Two additional thermocouples, #13 and #14, were cemented on the surface of diodes as shown in Fig. 2.

In order to simulate the heat generation due to the discharge of Li/SO_2 cells, high density resistance cartridge heaters from Omega were used. The cartridge heaters were heated using a DC power supply, and the temperature readings were recorded using an IBM computer via a data acquisition system. Since the heat generation rate of each heater critically depends on its resistance, the exact resistance of each heater was measured. The resistance of each cartridge heater is slightly different from each other. Hence, if the same voltage is applied to each heater, there would be a maximum 14% error in the heat generation rate. In order to compensate the difference in resistance, a resistance compensation was made using a nichrome wire so that one could produce exactly the same heat generation rate in each cell. Descriptions of detailed procedures and schematic diagrams of the resistance compensation circuit were given elsewhere [2].

Results and Discussion

There are two sources of heat generations in a battery pack when it is discharged; one is the heat generation from cells and the other is from the control circuit board. The former is the sum of polization heat, entropic heat and chemical heat of the cells, whereas the latter is caused by resistances of the mainly diodes and printed circuits. The effect of the latter on the overall thermal behavior of the battery has not been clearly recognized.

Figure 3 shows the circuit diagram of the control circuit board (i.e., the top figure) and the results of measured voltages with respect to the reference point (i.e., the bottom figure). Since the voltage drop in the connecting track could be significant due to the long distance and narrow width of some tracks, the voltage drop of each connecting track was also measured. The voltage drops in two diodes were almost identical, approximately 0.32V. The voltage drops in electrical fuses were in the range of 0.18-0.22V. Of note is that there was a significant voltage drop in one track between the diode #1 and the thermal fuse #1 as pointed out in the bottom figure (see Fig. 3), indicating room for improvement in future circuit board designs. With the circuit board used in these experiments, there was a significant heat generation occurring in the tracks. One simple way to reduce the voltage drop in the track may be to shorten the distance by rerouting the tracks, use wider ones, or increase the copper thickness.

The heat generation from the cells and control circuit was simulated by supplying DC current to the control circuit from a constant-current DC-power supply outside of the battery pack. The diodes and thermal fuses are electrically connected in series. Figure 4 shows the time history of cell temperature at a 2 amp discharge rate with the flexible board in a temperature-controlled Tenny chamber. Note that the ordinate is the temperature rise from the initial surrounding

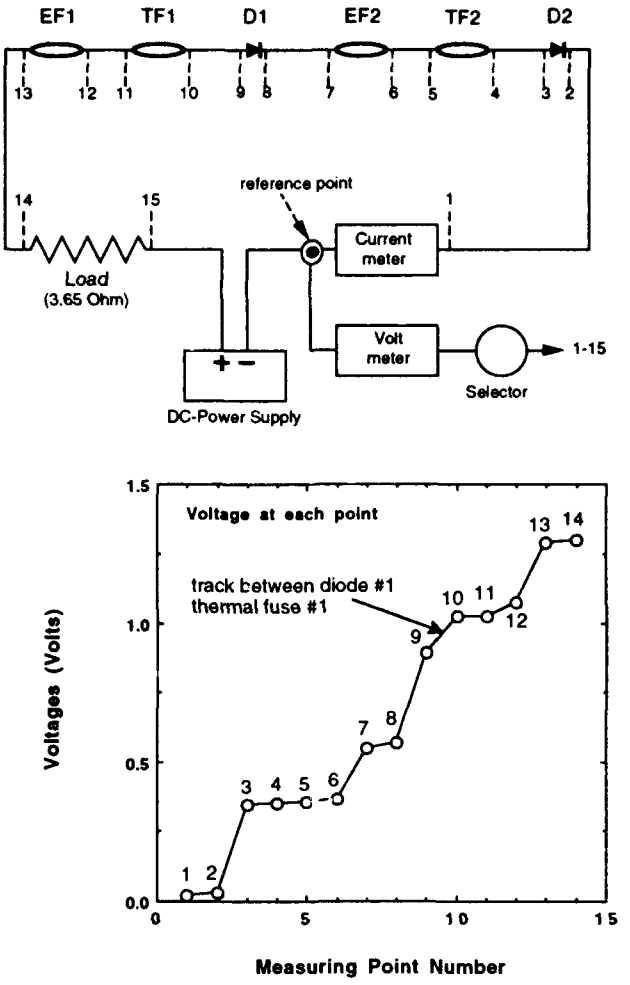

Fig. 3 Top: Schematic diagram for voltage drop measurements of electrical components, Bottom: Results of voltages measured at 14 locations relative to the reference point.

temperature of 25°C. The minimum cell temperature was consistently obtained at cell #3 whereas the maximum cell temperature was obtained at cell #7.

In order to see the effect of the heat generation from the

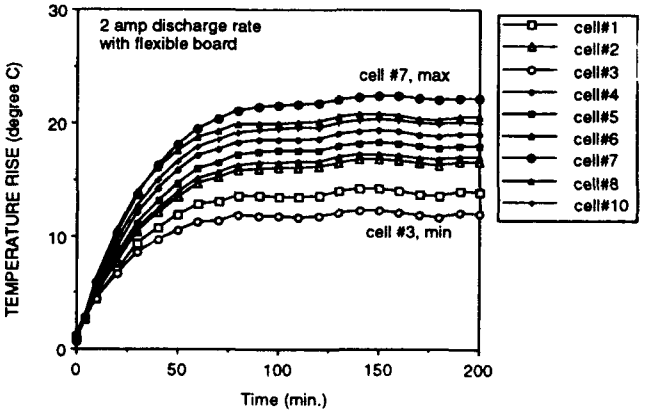

Fig. 4 Temperature rises of cells vs. time.

flexible board, we repeated the test without the board (i.e., no current to the board). Figure 5 shows the comparison of the temperature history (in the form of temperature rise vs. time) for two cases (with and without the flexible board) in the Tenny chamber. Results in Fig. 5 clearly depict that the heat generation from the board significantly increased the maximum cell temperature. The difference between the maximum and minimum cell temperatures decreased from 10°C for the case with the board to 5.3°C for the case without the board, demonstrating the effect of heat generation from the board on cell temperatures.

Figure 6 compares the temperature rise of diodes, thermal fuses, and the maximum/minimum cell temperature rise at the 2 amp discharge rate case. It is of note that the temperature of thermal fuse #11 was substantially larger than the maximum cell temperature #7, whereas that of the thermal fuse #12 was almost identical to the maximum cell temperature.

Diode temperatures were significantly greater than the temperature of #11 thermal fuse. The temperatures of the two diodes rose approximately 64°C from the initial surrounding temperature. Since one diode produces almost the same amount of heat as one Li-SO_2 cell, and the size of a diode is substantially smaller than a cell, the diode temperature increases greatly, to a surprising level. Results presented so far were obtained using 100% duty cycles.

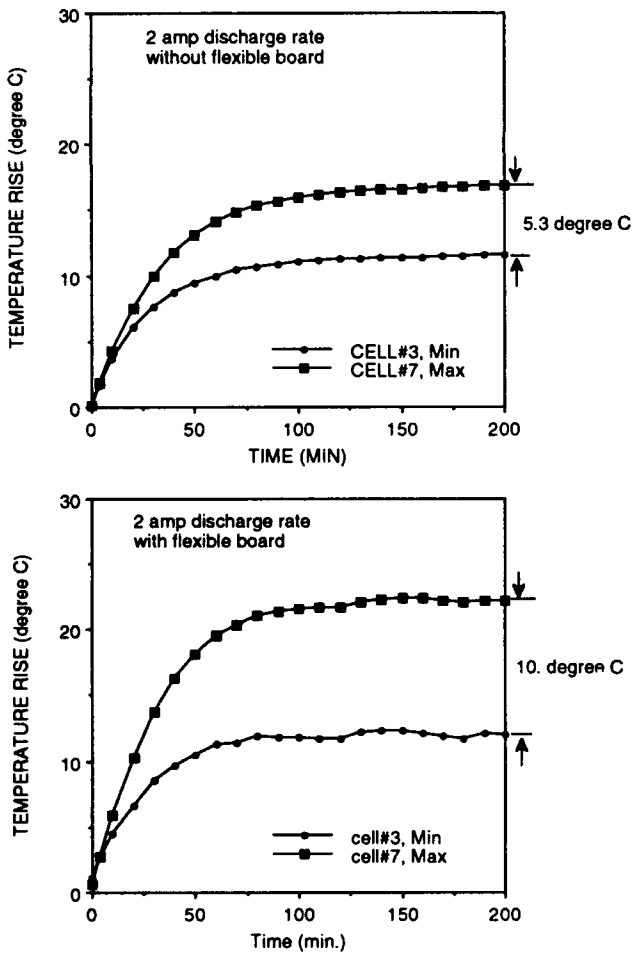

Fig. 5 Comparison of temperature rises of cells #3 and #7 without (top) and with (bottom) control circuit board in Tenny chamber. Both were discharged at 2 amp rate.

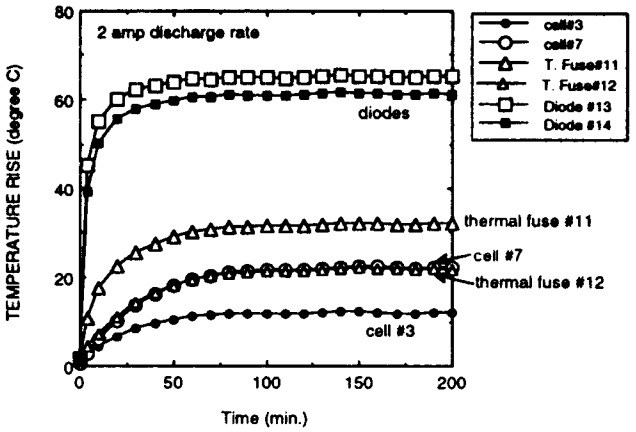

Fig. 6 Temperature rise from key components and max/min cell temperatures

Figure 7 shows the results obtained from 50% duty cycles. The objective of this test was to investigate the thermal behavior of Li/SO_2 batteries when they were discharged at 100% and 50% duty cycles. Figure 7 compares the maximum cell temperature and thermal fuse temperature (#11). Clearly, the temperature reading from thermal fuse #11 was significantly greater than the maximum cell temperature. Since the purpose of having a thermal fuse is to monitor the maximum cell temperature, the current position of thermal fuse #11 does overestimate the maximum cell temperature. Detail results of the 50% duty cycle tests were given elsewhere [2].

Summary

The maximum cell temperature at the 2 amp discharge rate case occurred consistently at cell #7, yielding a temperature rise of approximately 22°C. The thermal fuse #11 (i.e., the one closer to diodes) gives consistently larger temperature readings by almost 10°C

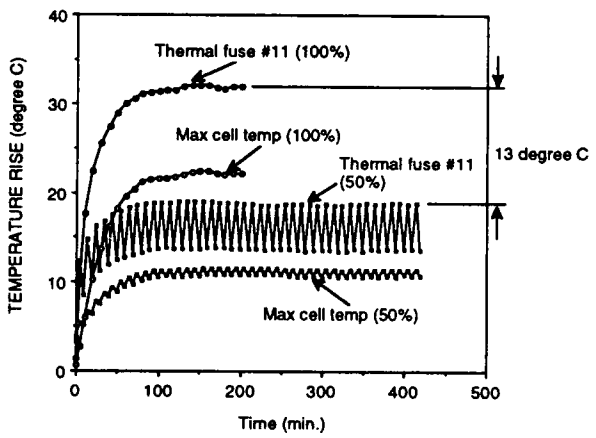

Fig. 7 Comparison of time history of maximum cell temperature and thermal fuse temperatures for 100% and 50% duty cycle cases.

than the maximum cell temperature while the thermal fuse #12 (i.e., the one away from diodes) gives almost identical temperature to the maximum cell temperature. This is an important discovery from a design point of view. Because of the proximal location of the thermal fuse #11 to hot diodes, thermal fuse #11 in the present design recorded a temperature approximately 10°C higher than the maximum cell temperature, rendering a premature opening. The results given in this present study suggests a number of ideas of design improvement from the view point of thermal management of the battery. One example is that manufacturers should carefully select the location of thermal fuses such that thermal fuse monitor the maximum cell temperature correctly.

References

1. Y.I. Cho and D.W. Chee, Thermal Analysis of Primary Cylindrical Lithium Cells, Journal of the Electrochemical Society, Vol. 138, pp. 927-930, (1991).
2. Y.I. Cho, "Thermal Analysis of Li/SO_2 BA-5590 Battery, Phase I and Phase II Final Reports to SAFT America, January 1992 and October 1992.

EFFECTS OF CHEMICAL TRANSPORT AND ENTROPIC COOLING ON LONG-LIFE THERMAL BATTERY DESIGNS, INCLUDING SONOBUOY APPLICATIONS

Charley Lamb
Eagle-Picher Industries, Inc.
Electronics Division, Couples Department
"C" and Porter Streets
Joplin, Missouri 64801

Introduction

Direct chemical transport and entropic cooling are both known to affect the performance of primary thermal batteries. Direct chemical transport, a self-discharge reaction, results in measurable coulombic losses, and is a greater factor in long-life applications, particularly those with long periods of open-circuit or very low current densities. Entropic cooling is less of a factor at low current densities, but becomes important to heat balancing at higher current densities. These phenomena, however, have usually been lumped into utilization-related "adjustment factors" during the battery design/performance analysis phases. Consideration of these effects during example battery developmental builds is illustrated in performance models that quantify the roles these factors have in determining battery performance.

Cell Model

Although crude in some respects, a PC spreadsheet-based cell model has been employed as an aid in the interpretation of selected battery performances. The model allows for the input of material and operating parameters, including:

Anode/cathode types and compositions
Electrolyte type, thickness, and melting point
Cell diameter
Number of cells
Number of parallel stacks
Initial battery polarization
Initial operating temperature
Assumed cooling curve
Load type (constant current or power) and amount

No provision has been made for a thermal model as done by previous researchers using finite element analysis.[1,2] Therefore, the spreadsheet model is most useful for successive iterations of a battery type. Utility for prediction of the performance of a proposed battery is somewhat more limited.

The spreadsheet model defines cell temperature as a function of time, and calculates capacity delivered over the time intervals. Electrolyte resistance is defined as a function of temperature. Capacity losses due to chemical transport at each increment of time and temperature are calculated. The electrolyte resistance functions were obtained by curve-fitting both internal test data and published resistivity data.[3] General equations defining the associated chemical transport losses were derived from published self-discharge data.[4] These transport losses are summed with the current/time capacities, and allow the definition of the possible half-cell voltages from the anode and cathode (which also depend upon temperature). The equilibrium potentials corresponding to each half-cell reaction are those used by Bernardi and Newman.[5] The load potential is, as expected, the sum of the individual half-cell potentials less polarization.

Chemical Transport

For the purposes of the model, the chemical transport factor was most conveniently expressed in terms of capacity (lost) per unit time per unit area of cell interface, or coul-min^{-1}-cm^{-2}. This term, like similar kinetic expressions, is a function of absolute temperature, and varies greatly with electrolyte composition.

Entropic Cooling

Entropic cooling during thermal battery discharge has been variously discussed by several researchers.[2,6,7] The $T\Delta S$ term is usually generated as part of the entropic cooling and resistive heating equation:[7]

$$q = I[-T(\frac{dE}{dT}) + E - V] \quad (1)$$

where q = heat (W)
I = current (A)
T = temperature (Kelvin)
$\frac{dE}{dT}$ = temperature coefficient of discharge reaction (volts/K)
E = open circuit voltage (volts)
V = voltage at current I

Battery Configurations

EAP-12160

The EAP-12160 thermal battery was designed to meet the requirements of the "PRIME" battery in the Advanced Mine Neutralization System. Physical and electrical requirements are:

Discharge Life	1200 seconds
Voltage Range	40 V max., 25 V min.
Load	246 watts constant
Environmental Range	-31°F to +120°F
Case Temperature	350°F max.
Battery Weight	Functional minimum;
Assembly Weight	Not to exceed 7 lb

The physical characteristics of the battery stack assembly are:

Number of Stacks	Two in parallel
Cells per Stack	20
Cell Diameter	3.0 in

The electrochemical system presently used in this battery is Li(Si)/LiBr-LiF-KBr,MgO/ FeS_2.

Performance *vs.* Design: This battery was initially constructed to contain three parallel stacks of 17 cells each. Discharge lives under the constant power load were in excess of 2000 seconds for both "hot"-equilibrated and "cold"-equilibrated units. Figure 1 shows the model prediction and actual performance of the "cold" three-stack design.

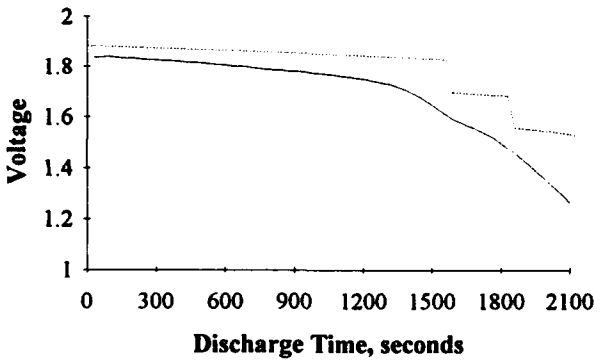

Figure 1. EAP-12160 Discharge Performance Three-stack "cold" battery (——) compared to model (·····).

Because of the large margin in discharge life with a three-stack design, and the modest current densities involved, a two-stack build was proposed. Pellet weights would remain constant, as would cell heat balance and thermal insulation. Internal battery heat content, however, would change because of the effect that changing the current density has on the entropic cooling and resistive heating terms. Figure 2 depicts the battery performance and model prediction for this two-stack "cold" unit. Table 1 summarizes the expected heat effects on both "hot" (initial internal stack temperature of 500°C) and "cold"-stabilized model batteries comparing the differences between a three-stack design and a two-stack design.

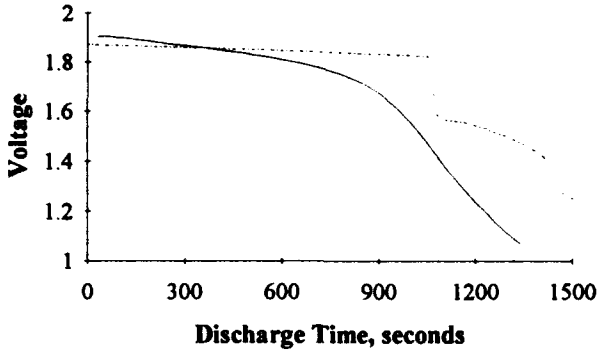

Figure 2. EAP-12160 Discharge Performance Two-stack "cold" battery (——) compared to model (·····).

Table 1. Components of Cell Heat Changes

Battery Configuration	Cumulative Heat Change after 1200 Seconds of Discharge (calories per cell) A			
	Chemical Transfer	$T\Delta S$	I^2R	Total
Three-Stack, "Cold"	+86.2	-185.0	+18.4	-80.4
Three-Stack, "Hot"	+119.0	-196.3	+17.9	-59.5
Two-Stack, "Cold"	+84.2	-287.6	+51.6	-151.8
Two-Stack, "Hot"	+116.1	-309.6	+50.8	-142.6

A) "+" values denote heat released by the cell; "-" values denote heat taken up by the cell.

As noted in Table 1, the two-stack "cold" battery absorbed over 70 calories more per cell during the 1200 seconds of discharge than did the three-stack "cold" battery. Most of this was due to the entropic cooling term, which more than offset the modest resistive heating difference that resulted from the increase in current density. The heat content changes attributable to chemical transfer arise from the loss of 3.22 A-min of capacity for the "cold" units over the 1200 seconds. The "hot" units lost 4.40 A-min of capacity in the self-discharge reactions.

Development Sonobuoy Battery

This thermal battery feasibility/development effort is directed toward a sonobuoy program, a long-life application more typically filled by Li/SO_2 chemistry. The sonobuoy battery (SB) is currently employing a lithium(alloy)/iron disulfide system, and is characterized by the following physical and electrical performance goals:

Battery Weight:	3.0 pounds, max.
Battery Dimensions:	3.25 in dia. by 4.80 in long
Discharge Life:	3600 seconds
Voltage Range:	37 V max., 20 V min.
Environmental Range:	0°C (with -20°C battery) to +35°C (+55°C battery)
Case Temperature:	100°C max. during active life
Electrical Load:	50 - one second pulses of 30 A at 10% duty cycle during 3600 second active life in addition to a 0.200 A constant current background load

Battery Performance: Performance testing has been conducted by applying the 30-A pulses at intervals of 75 seconds during the one hour discharge. Figure 3 graphs a recent "hot" SB test and compares it to the model prediction.

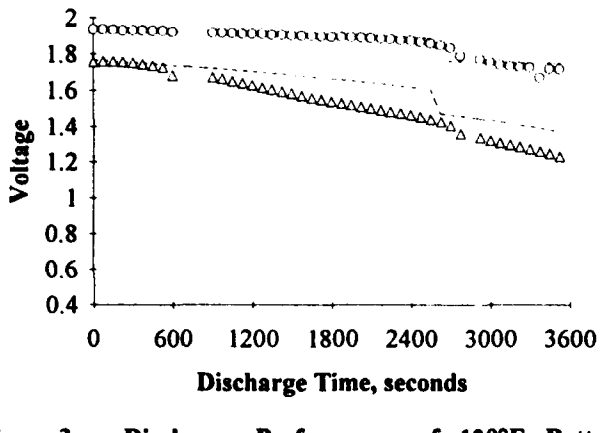

Figure 3. Discharge Performance of 120°F Battery Compared to Model. Data include voltages for battery base load (ooo), model base load ( ), battery pulses (ΔΔΔ), and model pulses (- - -).

Total heat content change over the 3600-second discharge was predicted to be +87.1 cal/cell. The overall generation of heat during battery discharge contrasts sharply to the cumulative cooling associated with the EAP-12160 battery. Much of this heat generation is due to

1) limitation of the I^2R term by the very low average current density, and

2) increase in the amount of chemical transport (self-discharge) by the very long discharge time.

Recent battery discharge lives attained during this ongoing development effort were 2776 and 2850 seconds for "cold"-stabilized units and 3749 and 3762 seconds for "hot" units.

Conclusions

The entropic cooling term, although not a large factor in low-rate cells, is important in total heat management of moderate-rate and high-rate cells. An increase in cell area or number of parallel stacks (usually made during the design phase of a battery to achieve voltage regulation) will directly reduce this term. Chemical transport, on the other hand, becomes more important as battery discharge lives become longer. An increase in cell area will directly increase the degree of self-discharge. As thermal battery performance requirements increase, proper design technique requires careful consideration and management of nderlying contributions to heat content over the entire lives.

References

1. D. M. Bush and R. L. Hughes, *A Thermal Model of a Thermal Battery*, SAND79-0834 (Albuquerque: Sandia Laboratories, July 1979).

2. J. Knight, "A Voltage-Time Model of Lithium-Iron Disulphide Thermal Batteries," *Power Sources 14*, edited by A. Attewell and T Keily (International Power Sources Symposium Committee 1993), pp. 313-326.

3. L. Redey, M. McParland, and R. Guidotti, "Resistivity Measurements of Halide-Salt/MgO Separators for Thermal Cells," *Proc. 34th International Power Sources Symposium*, 1990, pp. 128-131.

4. R. A. Guidotti, F. W. Reinhardt, and J. A. Smaga, "Self-Discharge Study of Li-Alloy/FeS_2 Thermal Cells,"*Proc. 34th International Power Sources Symposium*, 1990, pp. 132-135.

5. D. Bernardi and J. Newman, "Mathematical Modeling of Lithium(alloy), Iron Disulfide Cells," *J. Electrochemical Society*, **134**, 1309 (1981).

6. T. D. Kaun in *Proc. International Workshop on High-Temperature Molten Salt Batteries*, Argonne National Laboratory Report ANL-86-40, pp. B-138-144.

7. H. F. Gibbard and D. M. Chen in *Proc. International Workshop on High-Temperature Molten Salt Batteries*, Argonne National Laboratory Report ANL-86-40, pp. B145-152.

Development of a Two-hour Thermal Battery

Ronald Guidotti and Arlen Baldwin
Sandia National Laboratory
Battery Development Department
Albuquerque, NM 87185-0614

Introduction

The need for a long-life thermal battery with an activated life in excess of 90 minutes presented development challenges with the existing Li(Si)/FeS_2 technology currently being used at Sandia. The technology had been used successfully previously in the development of a one-hour thermal battery.[1] The longer life requirement for the new application, however, necessitated increasing the heat input to the battery to increase the time for maintaining the electrolyte molten. The thermal stability of the FeS_2 cathode material limited the success of this approach, since FeS_2 decomposes to FeS and elemental sulfur vapor when exposed to temperatures in excess of 550°C for any appreciable length of time (e.g., over 10 min).

In comparison, CoS_2 eliminates a large part of this problem because it is thermally stable to about 650°C. Westinghouse researchers have previously shown CoS_2 to be a viable cathode material for high-power, secondary-battery applications when used with the all-lithium LiCl-LiBr-LiF eutectic.[2,3] Because of their success, we explored the use of CoS_2 as a cathode in a long-life primary battery with the LiBr-KBr-LiF eutectic electrolyte developed at Sandia.[4] The low melting point of 313°C and large liquidus range of the LiBr-KBr-LiF eutectic, coupled with its good ionic conductivity, make it ideally suited for such an application. In this paper, we present performance and characterization data for long-life Li(Si)/CoS_2 batteries discharged under a range of conditions with LiCl-KCl and LiBr-KBr-LiF eutectic electrolytes, along with comparative data for Li(Si)/FeS_2 batteries. In addition, we will discuss areas of research that need to be addressed in order to extend the activated lives even more than the nominal two hours achieved in this study.

Experimental Procedures

Materials

The catholytes used in the study contained 73.5% FeS_2 or CoS_2, 25% electrolyte-binder (EB), and 1.5% Li_2O. (All compositions are in weight percent.) The catholytes were fused at 400°C for 16 hours under an argon atmosphere prior to granulating and pelletizing. The EB used in the catholyte was also used for the separator. The LiCl-KCl EB contained 35% Maglite S MgO (Calgon, Pittsburgh, PA) and the low-melting EB contained 25% MgO. The anode was 44% Li-Si and the heat source was 88% Fe/12% $KClO_4$.

The battery stack was insulated with a single wrap of 1-mm Fiberfrax(R) blanket (Carborundum Co., Niagara Falls, NY) and a 10.2-mm sleeve of Min-K TE1400(R) (Schuller Specialty Insulations, Denver, CO) and 12.7-mm Min-K discs on the ends.

Testing

A stack diameter of 50.8 cm (2 in.) was chosen for the design application. The steady-state or background current was 100 mA which corresponds to a current density of 5 mA/cm^2; the pulse current was 10 A for 50 ms and corresponds to a current density of 493 mA/cm^2. The pulse was applied every 10 min throughout the lifetime of the battery. The steady-state voltage was not to exceed 32 V and the minimum voltage during pulsing was not to drop below 22.5 V during discharge. The heat-balance range studied was 82 to 100 cal/g of total cell mass (including the heat pellet). The activation-temperature range for the long-life application was -54°to 82°C.

The initial development work was performed using 10-cell batteries. A total of 18 cells was necessary in the final battery design to meet the voltage requirements.

Results and Discussion

FeS_2 10-Cell Tests

Preliminary evaluation tests were conducted with 10-cell batteries based on FeS_2 and the LiCl-KCl eutectic electrolyte, because data were available for this design for the earlier long-life battery.[1] The optimum heat balance for this design was 92.5 cal/g using Min-K TE1400 insulation, for an activation temperature range of 18° to 37°C, which is not as wide as that for the present application. Preliminary tests performed at -30° and +71°C showed that the one-hour battery design would not meet the new long-life requirements.

Subsequent tests were then conducted using the LiBr-KBr-LiF eutectic in place of the LiCl-KCl eutectic. The test results are summarized in Table 1, along with the preliminary data for the batteries built with LiCl-KCl eutectic. All the batteries used the same heat balance of 92.5 cal/g but those with the low-melting electrolyte were sealed under vacuum, in an attempt to reduce heat losses. Batteries were tested 5 min beyond the original requirement of 3,600 s, to obtain additional performance information.

The batteries with the low-melting electrolyte showed significant improvement in activated lives over the LiCl-KCl-based ones--especially for cold conditions. However, the battery activated at 82°C exhibited significant overheating with strong evidence of thermal decomposition of FeS_2. This manifested itself by a premature drop in voltage due to the FeS_2 --> FeS transition which was the cause of the low voltage at 3,900 s. These data also show that batteries built with the low-melting electrolyte require less heat input relative to those based on LiCl-KCl.

Table 1.

Performance Characteristics of 10-Cell Li(Si)/FeS_2 Thermal Batteries Built with LiCl-KCl and LiBr-KBr-LiF Electrolytes and a Heat Balance of 92.5 cal/g

Electrolyte	Activation Temp., °C	Activ. Life to 13 V, s	St. State Voltage at 3900 s, V	Rise Time to 17.5 V, ms
LiCl-KCl	-30	3,600	Failed	840
LiCl-KCl	+71	5,400	16.3	500
LiBr-KBr-LiF*	-54	4,800	17.1	1,196
LiBr-KBr-LiF*	-40	5,400	17.5	807
LiBr-KBr-LiF*	+82	5,938	14.1	678

* Batteries sealed under vacuum; 100 mA background load; 10 A/50 ms pulse applied every 10 min.

Since the use of evacuated batteries did not statistically increase the activated lives over the standard one, all subsequent tests were conducted with non-evacuated units. Apparently, the gases generated upon activation tend to increase the heat-transfer losses that otherwise would not occur under a high vacuum.

10-Cell Battery Tests

Minimum Pulse Voltage: Subsequent batteries that were tested utilized catholytes based on CoS_2, because of its greater thermal stability relative to FeS_2. The effect of heat balance upon the minimum voltage during pulsing is shown in Figure 1 for 10-cell Li(Si)/CoS_2 batteries activated under cold conditions (-54°C); comparable data for a Li(Si)/FeS_2 battery with a heat balance of 92.5 cal/g are included for comparison. The best results for the CoS_2 batteries were obtained at the highest heat balance of 99 cal/g. The greatest voltage loss occurred for the FeS_2 battery.

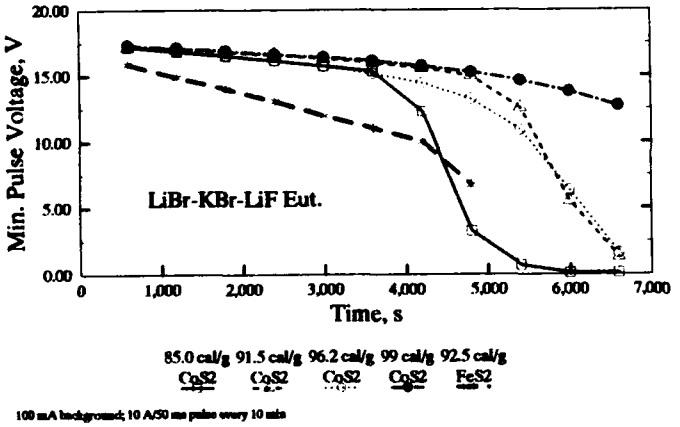

Figure 1. Minimum Pulse Voltage as a Function of Heat Balance for 10-Cell Li(Si)/Metal Sulfide Batteries Using LiBr-KBr-LiF Eutectic Electrolyte and Activated at -54°C.

The effect of heat balance upon the minimum voltage during pulsing is shown in Figure 2 for the batteries activated under hot conditions (82°C); comparable data for the FeS_2 battery with a heat balance of 92.5 cal/g are included for comparison. The best results for the CoS_2 batteries were observed at a heat balance of 85 cal/g. The performance of the FeS_2 battery was intermediate between that of the CoS_2 battery at the lowest heat balance and those at the higher heat balances.

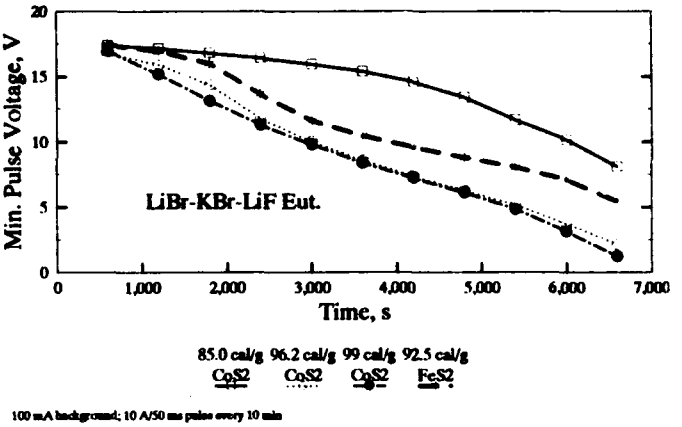

Figure 2. Minimum Pulse Voltage as a Function of Heat Balance for 10-Cell Li(Si)/Metal Sulfide Batteries Using LiBr-KBr-LiF Eutectic Electrolyte and Activated at 82°C.

Internal Impedance: The trends in polarization of the CoS_2 batteries during pulsing followed those observed for the minimum pulse voltage. The relative voltage losses were initially comparable for all of the cold batteries but increased rapidly with the onset of electrolyte freezing. This occurred sooner as the heat balance was reduced. The smallest voltage loss for the hot CoS_2 batteries occurred at the lowest heat balance of 85 cal/g.

The pseudo-impedance of the CoS_2 and FeS_2 batteries (as determined from the voltage drop and change in current during pulsing) is shown in Figures 3 and 4 for activation temperatures of -54° and 82°C, respectively. The performance trends reflected those observed for polarization during pulsing. The initial impedance did not change much as a function of heat balance for the cold CoS_2 batteries. However, the effect of heat balance was more pronounced for the hot CoS_2 batteries. The lowest impedance for the hot batteries occurred at the lowest heat balance.

The impedance of the FeS_2 battery under hot conditions was higher than that for the CoS_2 battery at a heat balance of 85 cal/g and less than those for the higher heat balances. The impedance of the FeS_2 battery under cold conditions, however, was almost three times greater than that of the CoS_2 batteries.

Based on the results of the 10-cell tests, a heat balance of 85 cal/g was selected as optimum for the subsequent 18-cell battery design.

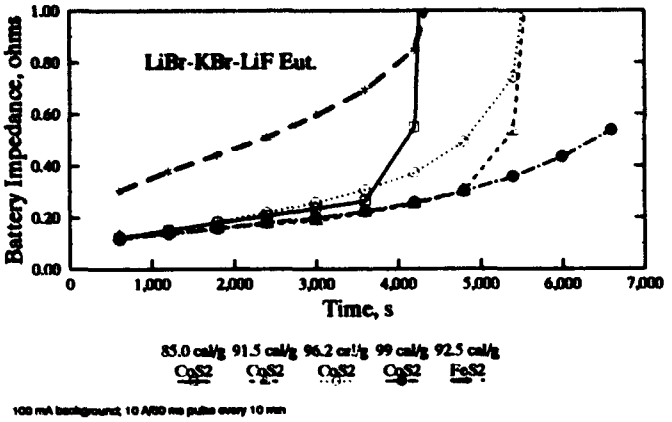

Figure 3. Battery Impedance as a Function of Heat Balance for 10-Cell Li(Si)/Metal Sulfide Batteries Using LiBr-KBr-LiF Eutectic Electrolyte and Activated at -54°C.

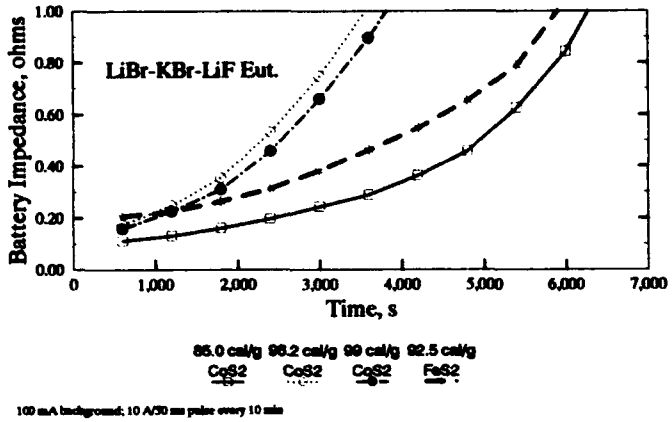

Figure 4. Battery Impedance as a Function of Heat Balance for 10-Cell Li(Si)/Metal Sulfide Batteries Using LiBr-KBr-LiF Eutectic Electrolyte and Activated at 82°C.

18-Cell Battery Tests

The performance of thermal batteries can sometimes be impacted as a result of scale up due to changes in the rate of heat loss associated with size effects. It is sometimes necessary to reduce the heat balance for the scaled-up batteries as a result. For this reason, a limited number of tests were conducted with 18-cell Li(Si)/CoS_2 batteries at a heat balance of 82 cal/g as well as the optimum heat balance of 85 cal/g found for the 10-cell batteries.

Steady-State Voltage: The steady-state voltage under the 100 mA background load is shown in Figure 5 for the 18-cell Li(Si)/CoS_2 batteries activated under both hot and cold conditions. Better results were obtained for the hot batteries at the lower heat balance. However, the decrease in activated life for the cold battery at a heat balance of 82 cal/g was unacceptable. The best overall results were still observed with a heat balance of 85 cal/g.

The performance characteristics for the 18-cell batteries are summarized in Table 2. (The activated life was defined as the time the battery voltage dropped below 18 V, either during steady state or while pulsing.)

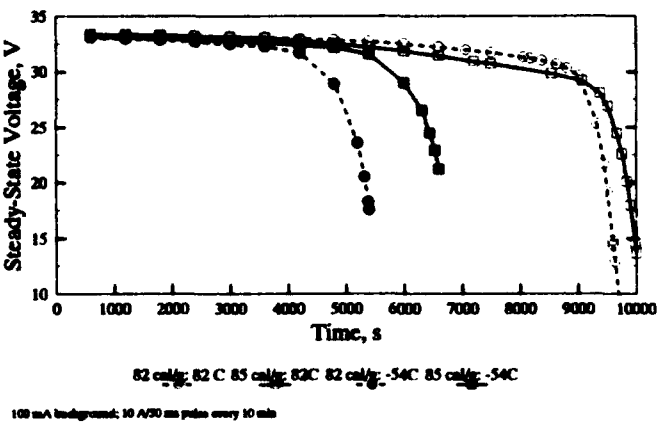

Figure 5. Steady-State Voltage as a Function of Heat Balance for 18-Cell Li(Si)/CoS_2 Batteries Using LiBr-KBr-LiF Eutectic Electrolyte and Activated at -54°C and 82°C

Table 2.

Performance Characteristics of 18-Cell Li(Si)/CoS_2 Thermal Batteries Built with LiBr-KBr-LiF Electrolyte

Activation Temperature, °C	Heat Bal., cal/g	Act. Life to 18 V, s	Rise Time to 17.5 V, ms
-54	85	6,000	790
+82	85	9,550	416
-54	82	5,400	688
+82	82	9,530	420

* 100 mA background load; 10 A/50 ms pulse applied every 10 min.

Activated lives to 70% of peak voltage of 2.65 hours were achieved for the hot batteries and as high as 1.67 h for the cold ones. These are the longest activated lives reported for thermal batteries.

Minimum Pulse Voltage: The corresponding minimum pulse voltages for these 18-cell batteries are shown in Figure 6. The trends displayed are similar to those observed for the steady-state voltage (Figure 5).

Internal Impedance: The internal impedances of the 18-cell batteries are shown in Figure 7. The internal impedances on a per-cell basis were comparable for the 10- and 18-cell batteries.

The sudden increase in impedance reflects the onset of electrolyte freezing. The large temperature range required for activation for the present application--a spread of 128°C--makes it difficult to maximize the activated life under both hot and cold conditions. Increasing the heat balance to extend the lifetime of the cold batteries invariably lead to overheating of the hot ones at the cold optimum heat balance.

Areas of Future Work

We are currently pursuing two main areas of research to increase the lifetime of thermal batteries even further. These involve thermal management and thermal stability of the cathode.

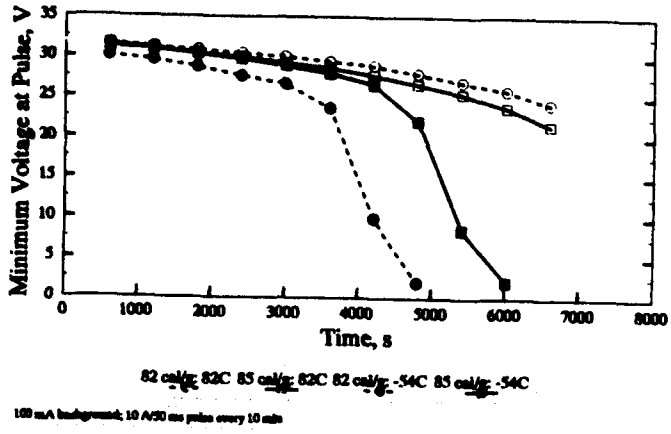

Figure 6. Minimum Pulse Voltage as a Function of Heat Balance for 18-Cell Li(Si)/CoS_2 Batteries Using LiBr-KBr-LiF Eutectic Electrolyte and Activated at -54°C and 82°C

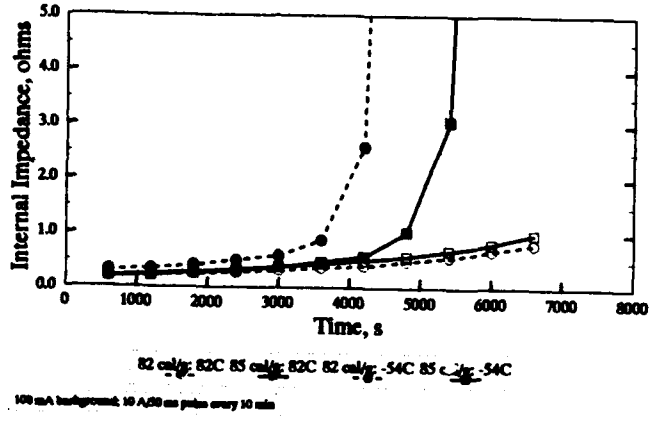

Figure 7. Battery Impedance as a Function of Heat Balance for 18-Cell Li(Si)/CoS_2 Batteries Using LiBr-KBr-LiF Eutectic Electrolyte and Activated at -54° and 82°C

Improved Thermal Insulation: The Min-K type of insulation has the lowest thermal conductivity of any commercial insulation, other than a vacuum-foil type. The latter works well only with larger systems, such as the high-temperature secondary batteries developed at Argonne National Laboratory for electric-vehicle applications.[5] These are impractical for the much smaller thermal batteries because of thermal shunting by conduction at the ends of the battery. This technology would also be prohibitively expensive and would pose production nightmares in terms of assembly and quality control.

Aerogel insulations, on the other hand, offer the potential for even better insulating properties than Min-K under proper conditions. The thermal conductivity of aerogels can be up to a third of that of Min-K insulation.[6] There are problems, however, in high-temperature applications because aerogels are transparent to infrared in the region of 3 to 8 micrometers. It will thus be necessary to add thermal opacifiers to mitigate this problem. We are actively pursuing the use of aerogel insulation for thermal-battery applications as an alternative to Min-K.

Secondary Heating: A second thermal-management approach we are examining is secondary (sequential) heating. This involves the use of two heat sources in the battery. The first would be used as normal and the second one would be ignited much later in discharge to provide a thermal boost to extend the lifetime of the battery. We are depending heavily upon our thermal model for assistance in this work.

Improved Cathodes: The issue of the thermal stability of the cathode will ultimately determine how long a thermal battery can be maintained at a high initial temperature after activation. A cathode with a thermal stability of 700°C or greater is desirable for such an application. We are currently examining a number of cathode materials with high thermal stability and with an emf of at least 2 V vs. Li.

Conclusions

The requirement for a long-life thermal battery with an activated life in excess of 90 min and an activation range of -54° to 82°C cannot be met with the conventional Li(Si)/FeS_2 system using the LiCl-KCl eutectic. By substitution of the lower-melting LiBr-KBr-LiF eutectic for the LiCl-KCl eutectic, it is possible to attain lifetimes of 80-90 min. However, excessive thermal decomposition of FeS_2 results with the hot battery.

Experiments with 10-cell Li(Si)/CoS_2 batteries show that a heat balance of 85 cal/g is optimum for the new long-life application when using the LiBr-KBr-LiF eutectic. Thermal decomposition of CoS_2 becomes noticeable at the highest heat balance of 99 cal/g. In scale-up tests with 18-cell batteries, activated lives in excess of 2-1/2 h for hot condition and more than 1-1/2 h for cold conditions can be attained. Further work is underway to develop alternate insulation and cathode materials to increase the lifetime of thermal batteries even more.

Acknowledgements

The authors wish to acknowledge the assistance of L. M. Moya in the construction and testing of the batteries.

This work was supported by the U. S. Department of Energy under contract DE-AC04-94AL85000 and the U.S. Department of Defense through a contract with Wright-Patterson AFB.

References

1. P. G. Neiswander and A. R. Baldwin, SAND87-0143 (October, 1988).
2. H. N. Sieger, *Proc. 34th Power S ources Symp.*, pp. 334-338 (1990).
3. N. Papadakis, *Ibid.*, pp. 339-342 (1990).
4. L. Redey, M. McParland, and R. Guidotti, *Ibid.*, pp. 128-131 (1990).
5. H. Shimotak, A. A. Chilenskas, R. F. Malecha, and N. P. Yao, *Proc. of 19th Intersoc. Energy Conv. Eng. Conf.*, pp. 793-797 (1984).
6. D. Buttner, E. Hummer, and J. Fricke, in *Aerogels*, J. Fricke, ed., pp. 116-126, Springer-Verlag, New York (1986).

EMERGENCY POWER SYSTEM FOR THE SWEDISH JAS39 LIGHTWEIGHT COMBAT AIRCRAFT

by
Kurt Karlsson
SAAB MILITARY AIRCRAFT
SAAB-SCANIA
LINKÖPING
SWEDEN

1 INTRODUCTION

The Swedish JAS39 Aircraft is a single engine, multirole aircraft - fighter, attack and reconnaissance. It is a small aircraft, to get low price, low operational costs and a low visibility signature. Furthermore it has superb manoeuvrability, reduced stability and uses a digital - Fly by wire - flight control system.

The single engine application makes heavy demands upon the emergency power system. In this system, high capacity, long life Thermal Batteries are used as the power source.

This paper will give a short description of the secondary and emergency power systems and explain the choice of thermal batteries as the emergency power source.

2 SECONDARY POWER SYSTEM

The Secondary Power System (SPS) schematic is given in Fig 1.

SPS can be divided into three subsystems:

1. Auxiliary Power Unit, APU
2. Aircraft Gearbox with accessories, AGB
3. Auxiliary and Emergency Power System, AEPS

Swedish Air Force has required a very flexible base system. Ordinary roads are used for take off and landing. This method of operation requires a self contained aircraft without use of Ground Power Units (GPU). That is the reason why the layout of the SPS was planned as shown in Fig 1.

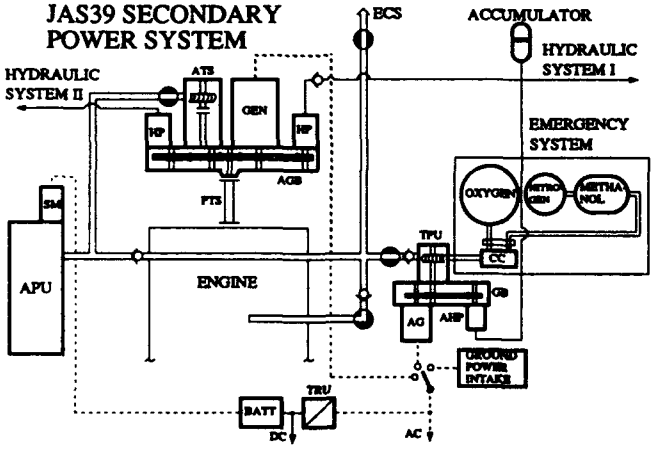

Figure 1 JAS39 SPS schematic.

On ground the APU supplies pneumatic power to the auxiliary system which supplies electric and hydraulic power to the aircraft when the main engine is not running. All checks of the various systems in the aircraft can be performed under this operational mode. If a failure occurs in the AGB or its accessories the main engine supplies pneumatic power to the auxiliary system. If main engine flame out occurs during flight, the EPS supplies electric and hydraulic power to the aircraft.

3 EMERGENCY POWER SYSTEM (EPS)

The EPS is the last link in the power supply chain. When needed it has to start and then produce required power. As the aircraft has reduced stability, no power interrupt is accepted. Most critical is the hydraulic supply. With the small hydraulic accumulator installed in the aircraft a starting time for the EPS of max 1.5 sec is required.

3.1 Original EPS

When the JAS39 aircraft program started, more then 10 years ago, a thorough survey of different methods and principles of EPS were performed. At that time a chemical stored energy system was proven to be the best and was consequently chosen. A bi-propellant system with methanol and gaseous oxygen was chosen, because the monopropellant Hydrazin was not allowed in Sweden.

The hot gas produced in the system could be introduced into the auxiliary turbine therefore driving the auxiliary generator and hydraulic pump. No extra accessories are needed for the emergency mode.

During the development phase of the bi-propellent system it became evident that the system could not be produced as a reliable and safe system within required project schedule. In order to guarantee the aircraft development schedule, Saab installed extra NiCd- batteries and motordriven hydraulic pumps for the emergency power system. Those systems are heavy but are a proven concept in the Saab 37 Viggen aircraft. In the prototype JAS39 aircraft the extra weight and high maintenance cost was acceptable.

The EPS analysis was then repeated and it became evident that thermal batteries with required capacity and performance had been developed.

3.2 New EPS

During the 1980's higher capacity and long life thermal batteries had been developed. Also, small efficient hydraulic packages were available. The attention was drawn to those advances to form the new EPS.

The most promising battery type was the Lithium Aluminium-Iron Disulfide battery and SAFT AMERICA INC was given the task to develop, test and supply that type of battery.

ABEX, Germany was chosen to supply the Hydraulic Package with a French motor from Auxilec.

A joint team with participants from LUCAS - supplier of the AEPS -, SAFT, ABEX and SAAB was formed to perform a feasibility study of the new system.

As time was critical only two months were allocated to reach a decision to change EPS philosophy for JAS39 from hot gas to ther-

mal batteries. A schematic of the new EPS is shown in Fig 2.

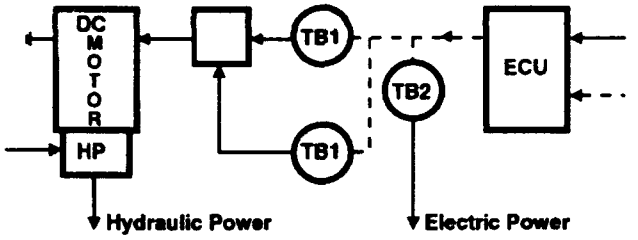

Figure 2 JAS39 new EPS schematic

Originally two battery designs were needed; One to provide power to the hydraulic system and the other to provide power to the aircraft emergency DC bus. From installation point of view two identical battery modules were required for the hydraulic system.

By going to that type of EPS one more hydraulic pump was introduced into the SPS.

Furthermore, no AC-power is available during emergency conditions. It was determined to be acceptable to delete the AC-power if the operating time of the new EPS was increased when changing from hot gas to thermal battery EPS.

4 METHODS AND TOOLS USED TO DEFINE THE NEW EPS

The team initiated the definition of an interim system to be used along with real hardware testing to prove out the concept. Specifications along with performance requirements for the final EPS were defined.

A simulation model of the -"core"- of the hydraulic parts of EPS (thermal battery, DC-motor, hydraulic pump and hydraulic accumulator) - was generated in order to define and specify the requirements of the system and also to provide the interim system for feasibility testing.

The model was built for dynamic simulations. All kinds of operation of the EPS could be studied i.e. start, stop, load changes, steady state, etc.

The characteristics of the above mentioned core items were transformed to equations and actual volumes, masses, torques etc. were introduced into the model.

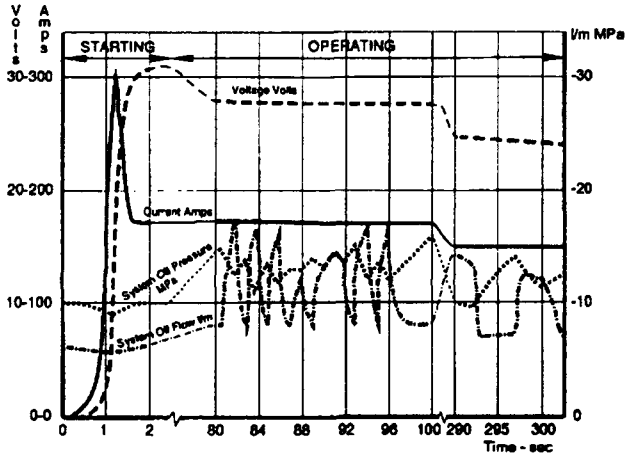

Figure 3 Typical feasibility test results.

SAFT undertook to build a number of batteries for the feasibility testing and ABEX made a hydraulic package available. Testing was performed at different temperatures and the results were very encouraging. The tests showed that it was possible to use thermal batteries for the EPS. Within the required temperature range; the batteries delivered the required capacity, power and duration; also, they were quick to activate and reacted quickly to load changes.

Typical test results are shown in Fig 3.

The battery for supplying the DC-bus was not tested during the feasibility study. However, the study had shown that the proposed system was appropriate and could do the job.

5 DEVELOPMENT AND QUALIFICATION TESTING

The required output from the hydraulic system is specified as a hydraulic oil mass flow versus time and the outlet oil pressure is not allowed to fall below a certain value. Starting and operating times are also important requirements.

Typical figures of required oil mass flow and operating time is shown in Fig 4.

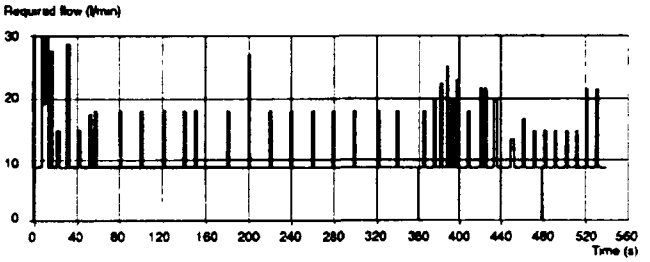

Figure 4 Required emergency oil mass flow.

These requirements were generated from the Flight Control System requirements. Pulse power response from the thermal battery is required.

The EPS is designed to operate after an engine flame out at high altitude down to altitudes which permit APU and engine assisted restarts. After a successful main engine restart the EPS power is not required any longer. If it has not been possible to successfully restart the engine, the pilot will be leaving the aircraft if he can not reach a more immediate airfield or if the APU is not operating. It is not possible to land the JAS39 with only the EPS operating. As a minimum operation of the Auxiliary Hydraulic system is required for a successful aircraft landing.

The battery proposed by SAFT was a lithium primary battery which had low weight/energy-ratio (kg/Ws) and low maintenance cost. It is a Lithium-Iron Disulfide thermal battery with Lithium Aluminium as anode material. The electrolyte is LiCl-KCl-Mg0 melting at approx. 350 °C.

Each module of the batteries has two Electro Explosive Igniters (EEI) for firing of the Heat Source ($Zr/Ba\ CrO_4\ Fe/KClO_4$) which melts the electrolyte. Monitoring systems to check if the batteries have been activated are built into the batteries by fusible links - resistance measuring-.

Battery characteristics are shown in Fig 5 and the final assembly is shown in Fig 6. See also Ref. 1.

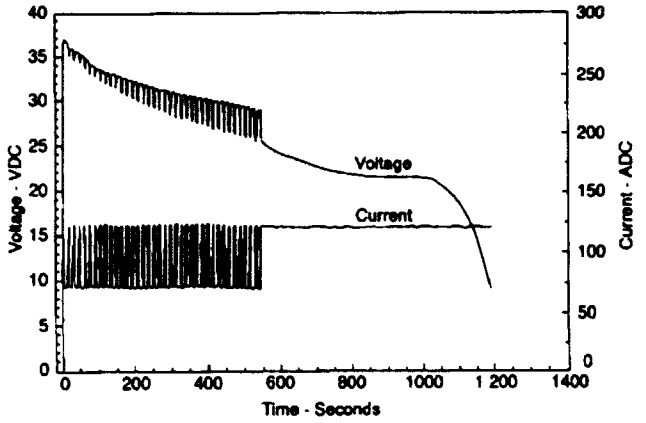

Figure 5 Thermal battery characteristics.

Fig. 5 shows that when the current drawn from the battery is pulsed between two limits a corresponding variation in outlet voltage is obtained, (high current - low voltage). It is also clearly seen that the voltage is decreasing with operational time.

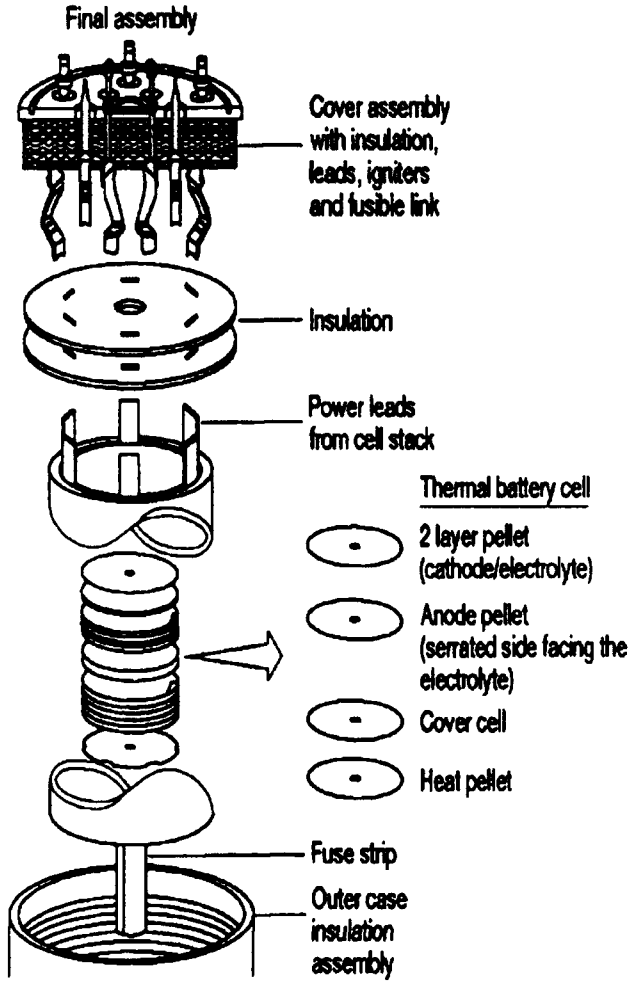

Figure 6 Thermal battery assembly.

The hydraulic pump is a 9 cylinder axial piston pump with a soft cut-off control in order to limit the input/outlet power. Its characteristics are shown in Fig 7.

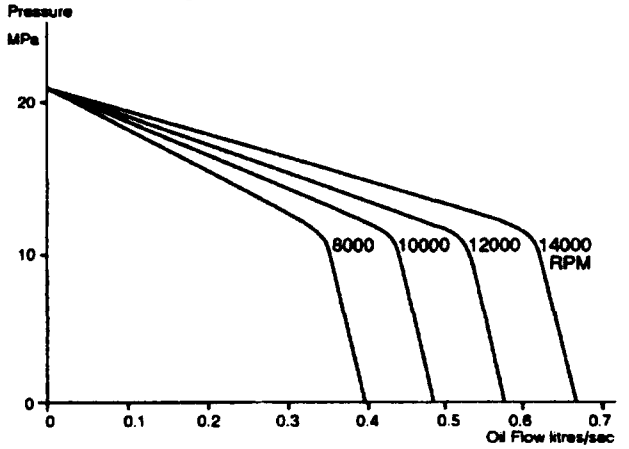

Figure 7 Emergency Hydraulic Pump characteristics.

The DC-motor is a 4 brush, air cooled motor, explosion proof. Its characteristics are shown in Fig 8.

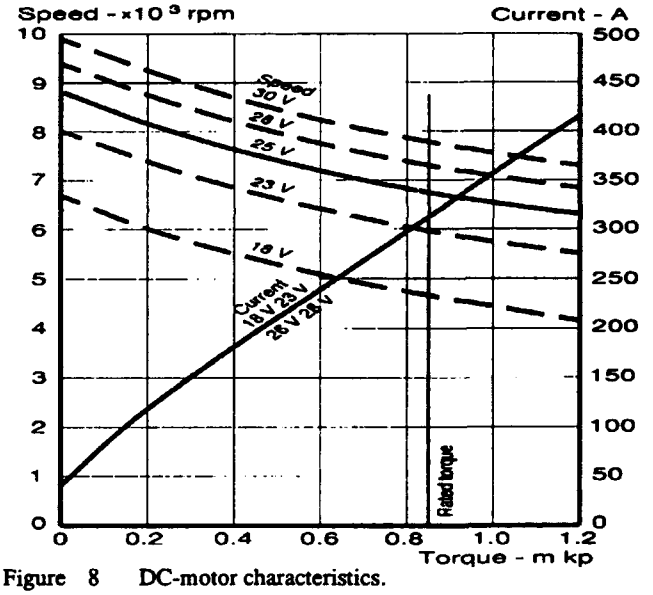

Figure 8 DC-motor characteristics.

Outline drawing of the EHP is shown in Fig 9.

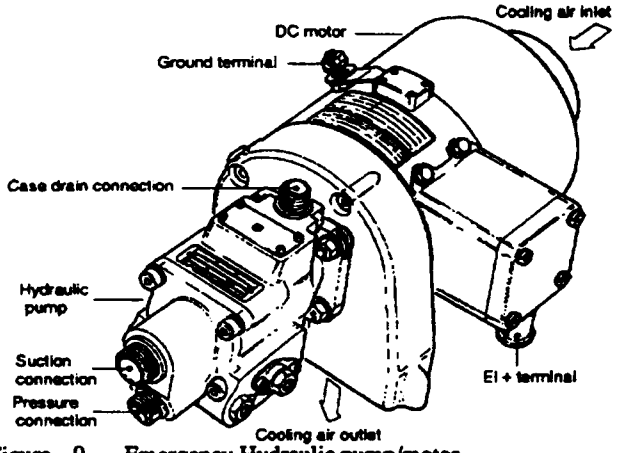

Figure 9 Emergency Hydraulic pump/motor.

Typical results from the simulation model are shown in Fig 10.

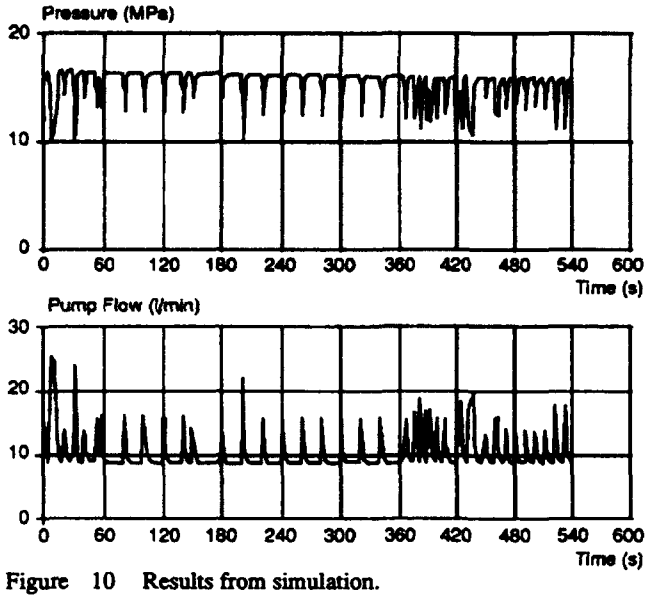

Figure 10 Results from simulation.

An extensive qualification and rig testing has been performed with the EPS.

The system has been successfully tested in the - Iron bird - Hydraulic Rig - Flight Simulator at Saab. The battery system has "flown" the specified emergency profile by a pilot in the Simulator and it has demonstrated over capacity. Since the battery system has demonstrated excess run time (over capacity), redesign to more closely match the system requirements would permit reduction in system weight and volume. An activation of the system in an aircraft on the ground has also been performed to check the installation effects. All performed well.

During qualification testing of the system we have experienced difficulty in meeting the vibration requirements. The failure mode has been shorted cells.

The fusible link design has been modified because in the beginning consistent and repeatable results were not achieved when conducting the system checks.

Currently the EPS uses three identical thermal batteries to provide power to the hydraulic system and the emergency DC-bus.

6 INSTALLATION IN JAS39

The installation of the SPS in the JAS39 is shown in Figure 11. The battery modules are mounted in thermally insulated brackets to protect the aircraft aluminium structure from heat transfer from the high temperature surfaces of the batteries after activation.

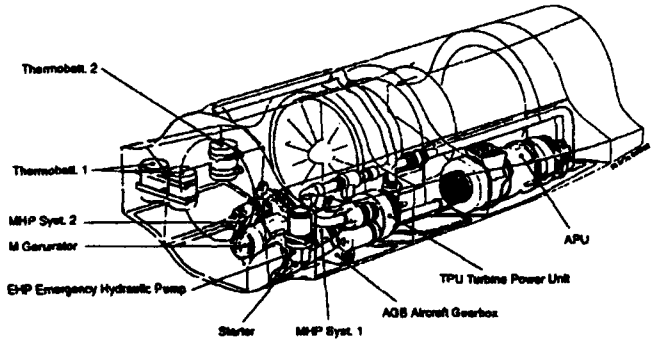

Figure 11 Installation of SPS in the JAS39.

7 WEIGHT LIST

TB hydraulic	24,4	kg
EHP	10,5	kg
TB electric	10,2	kg
TPU	30,2	kg
AECU	7,4	kg
Miscellaneous (Inst)	13,3	kg
Total	96,0	kg

The comparable weight for the original AEPS was 108 kg.

8 ACCESSABILITY AND RELIABILITY

The probability for loss of power from the EPS shall be no more than $4 \cdot 10^{-4}$ during one hour's flight.

The number of Line Replacable Units (LRU) were decreased from 26 to 11 when going from a hot gas system to a thermal battery system.

9 NON DESTRUCTIVE TESTING

The Swedish Defense Materiel Administation (FMV) has initiated a program with the objective to be able to detect different types of failures of the batteries during manufacturing and acceptance processes and also periodically during the service life of the batteries. That method is presented during this conference. See Ref. 2.

In the aircraft the EHP is tested every 200 flight hour. The fusible links are monitored continuously during the flight. The battery igniters are tested with a 10 mA current before every mission. No degradation of the igniters, because of these tests, have been demonstrated according to Ref. 3.

10 LIFE CYCLE COST (LCC)

A comparison of the LCC for the two systems was in favour of the thermal battery system. At this time a service life of the batteries was estimated to 10 years.

11 SUMMARY

The EPS in the JAS39 aircraft of the present layout and as described in this paper is now fully qualified and is operative in the production aircraft. The EPS has been given a simple and straight forward layout with a low weight and few LRU's. With the possibility of monitoring the batteries state of health during the service life an oncondition maintenance will be achieved which will lower the LCC.

Thermal batteries have helped us to solve a difficult design problem in the single engine JAS39 aircraft. A safe and trustworthy system has been installed.

12 REFERENCES

1. **Thermal Battery for Aircraft Emergency Power,** Stephen Kauffman, Guy Chagnon. Proceedings of the 35th Power Sources Conf. 1992.

2. **Experiences from Developing Electrical Non-Destructive Testing for Thermal Batteries.** Per A. Selånger. Proceedings of the 36th Power Sources Conf. 1994.

3. **Effects of Repeated Resistance Testing on Firing Ability of Igniter EP360-1,** G. O'Day. Proceedings of the 36th Power Sources Conf. 1994.

LARGE THERMAL BATTERIES FOR EMERGENCY AIRCRAFT POWER

Joe Wells and Romy Saltat
Eagle-Picher Industries, Inc.
Electronics Division, Couples Department
"C" and Porter Streets
Joplin, Missouri 64802-0047

Introduction

The JAS-39 Grypen fighter aircraft will use three large thermal batteries for emergency electronics and/or hydraulic power in the event of a subsystem or main engine failure. A thermal battery has several advantages including operation at widely divergent temperatures without heater power, fast risetimes to full power, a high energy density, long shelf life, maintenance-free design, as well as environmental and safety considerations. These advantages led to the selection of a thermal battery design over other types of battery electrochemistries, and over alternate systems such as hydrazine and methanol/oxygen.

The original JAS-39 fighter design used one thermal battery for emergency electrical power requirements and two batteries for emergency hydraulic power. These batteries were similar in length and number of cells, but were not identical. Due to enhanced cell performance, Eagle-Picher has been able to offer a single battery design that meets both the emergency electrical and hydraulic needs. This allows total interchangeability of a single design in any of three required battery positions in the JAS-39 aircraft. This interchangeability allows greater economy of scale in battery manufacture as well as reduced depot inventory.

Requirements

The thermal battery for the JAS-39 Aircraft is a relatively large thermal battery at 6.00 inches outside diameter by 8.21 inches long, weighing 9.5 kilograms. The associated wiring harness, connector, and bracket assembly bring the total weight to 10.2 kilograms. A drawing of the battery is shown in Figure 1.

The battery has a nominal 28 Vdc output with the requirements summarized in Table 1 and further discussed below. The battery design must meet an electronics mission at a constant power load of 1.8 kW (approximately 75 to 90 amperes average current) for 540 seconds. Alternately, it must also satisfy the hydraulic mission which requires a 75 ampere base load with pulses up to 200 amperes. The constant power electronics load and the pulsed hydraulic load along with their voltage requirements are shown in Figures 2 and 3 respectively. In addition, the battery must also meet peak voltage and safety concerns during a low discharge rate of 2 amperes.

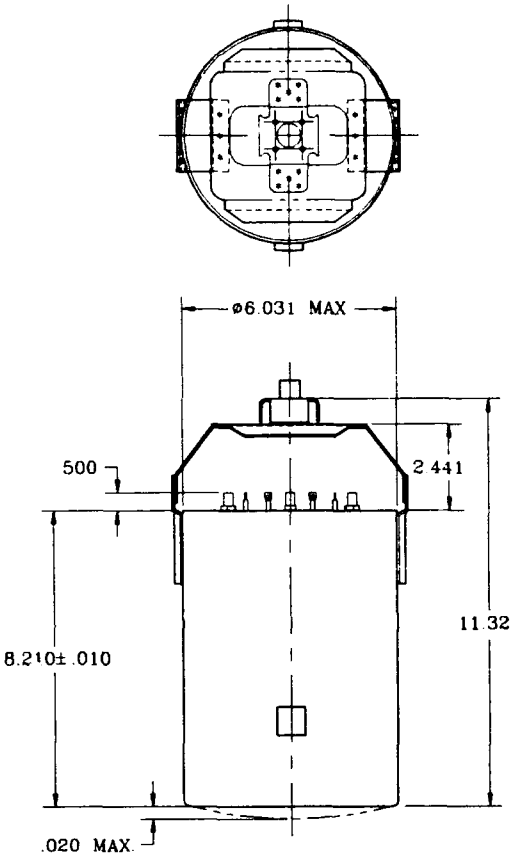

Figure 1. Battery Outline

Table 1. Requirements Summary

Size:	6.00 inches diameter x 8.21 inches long plus connector, cables and brackets
Weight:	9.5 kg (10.2 kg with added hardware)
Mission Life:	540 seconds
Temperature Extremes:	-40°C to +77°C (-40°F to +170°F) plus 30 minute soak at +80°C (+176°F)
Vibration:	10.3 G_{rms} for 1.5 hours/axis
Voltage Range:	31.5 to 23.0 Vdc (Electronics load) 31.5 to 16.0 Vdc (Hydraulic load)
Electronics Load:	1,800 watts constant loading (75 - 90 amps)
Hydraulics Load:	75 amp baseload with pulses to 200 amps
Safety:	2 amps parasitic load

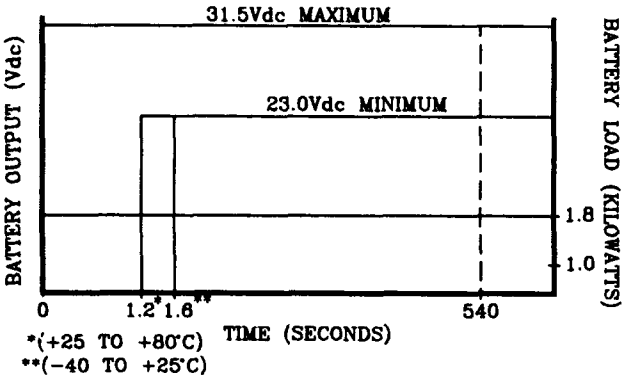

Figure 2. Electronics Load Profile

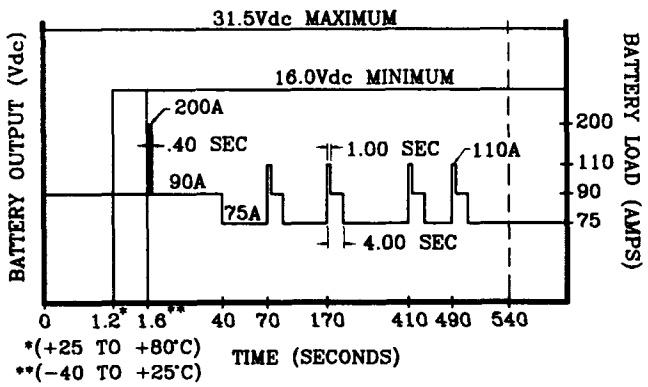

Figure 3. Hydraulics Load Profile

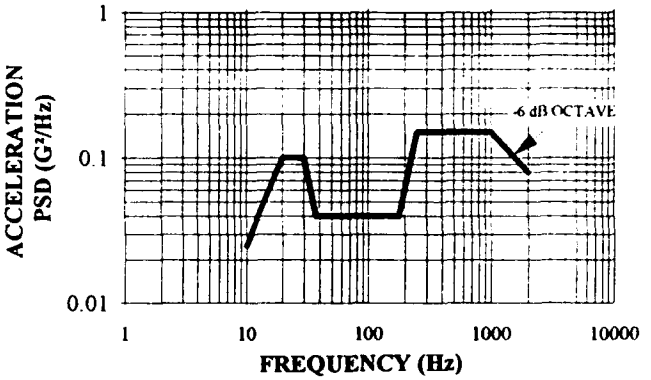

Figure 4. Endurance Vibration Profile

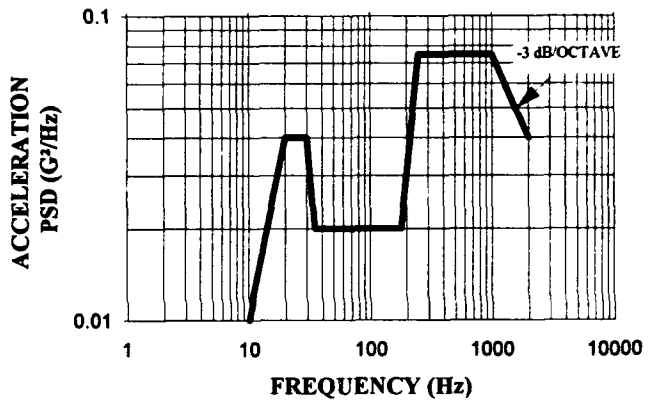

Figure 5. Operating Vibration Profile

The battery activation time shall be less than 1.2 seconds at temperatures above 25°C and less than 1.6 seconds at temperatures between -40°C and 25°C. Activation time is the time interval between the initiation signal and the time at which the battery output reaches 26.0 volts at a 90 ampere load. The battery must meet the electrical performance requirements after extreme temperature stabilization from -40°C to 77°C followed by exposure to 80°C for 30 minutes. The battery must withstand a rigorous endurance random vibration (see Figure 4) of 10.3 G_{rms} for 1.5 hours applied along three mutually perpendicular axes. The operating random vibration profile is shown in Figure 5.

Design Approach

The JAS-39 Battery (Eagle-Picher Part Number EAP-12188) was designed with three stacks of 16 cells connected in parallel as shown in Figure 6 in order to meet the peak voltage requirement of 31.5 Vdc and to reduce the current density. The cells outside diameter is 5.00 inches and the inside diameter is 0.312 inch, yielding an effective area of 19.56 square inches or a total cell area of 58.68 square inches (378.6 cm^2) for three stacks connected in parallel. The battery was developed with standard compositions for all the active materials. The anode contains 44% Lithium(Silicon) alloy and the cathode is Iron Disulfide. The electrolyte is a mix of LiF, LiCl, LiBr, and KBr with 35% magnesium oxide as the binder. The heat source is a standard 84/16 Iron/Potassium Perchlorate. Dual electrode cell construction was used to reduce degradation of the anode and cathode and moderate the thermal energy generated by the heat source in order to achieve performance over the long mission of the battery.

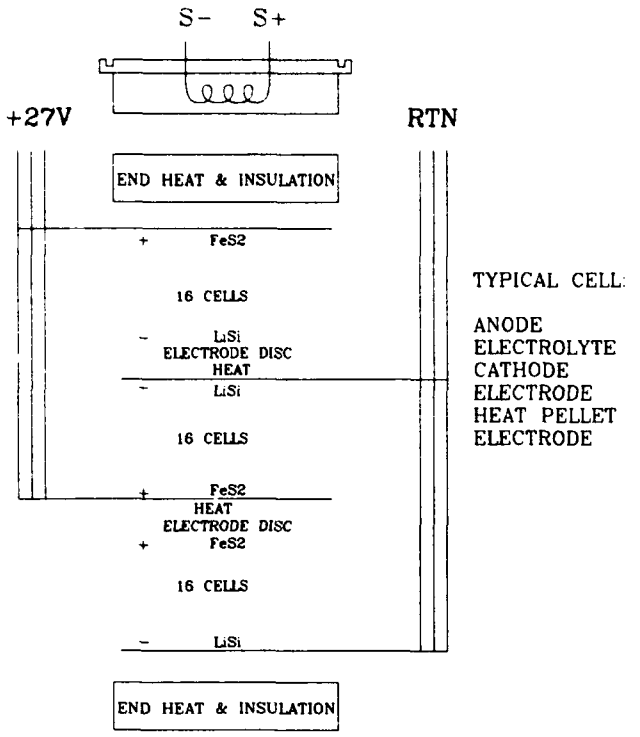

Figure 6. Cell Stack

Actual Performance

Typical performance under the hydraulic load profile at the low temperature extreme is shown in Figure 7. The battery performed for 1322 seconds when subjected to the hydraulic load shown in Figure 3 after stabilization at -40°C. The battery potential dropped from 28.70 volts to 24.70 volts when the 200 ampere pulse is applied after operating under a 90 ampere base load. The voltage drop indicates the battery impedance is 0.036 ohms with the Area Specific Impedance (ASI) 0.065 ohm-cm^2/cell (0.010 ohm-in^2/cell). The impedance stayed relatively low under the final pulse at 490 seconds. The ASI is 0.58 ohm-cm^2/cell (0.09 ohm-in^2/cell), with an excellent voltage margin above the 16.0 Vdc requirement.

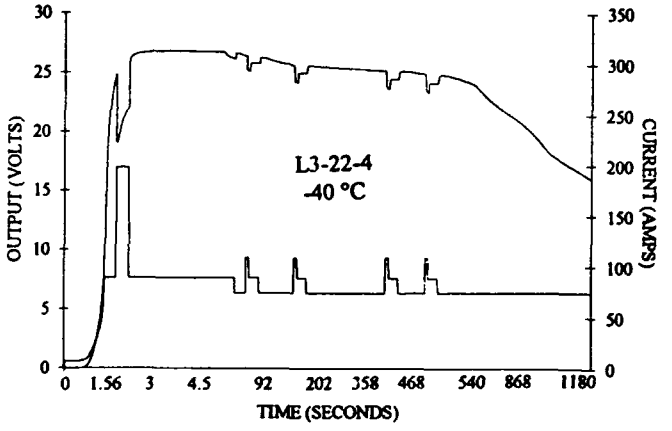

Figure 7. Performance Under Hydraulics Load

Typical performance under the electronics load of 1.8 kilowatts at high and low temperature extremes are depicted in Figures 8 and 9 respectively. The low temperature stabilized battery has a shorter operating life of 600 seconds compared to 1,000 seconds for the high temperature stabilized battery. The operating lives of the low and high temperature batteries are unbalanced by design. To optimize the safety of the battery when installed in the aircraft and during operation under a parasitic load of no more than 2.0 amperes, the amount of heat input to the battery was kept to a minimum. This was accomplished by reducing the weight of the pyrotechnic pellet of each cell with the minimum calorific input to support the mission life of 540 seconds with an approximately 60 second margin when operating at the low temperature extreme.

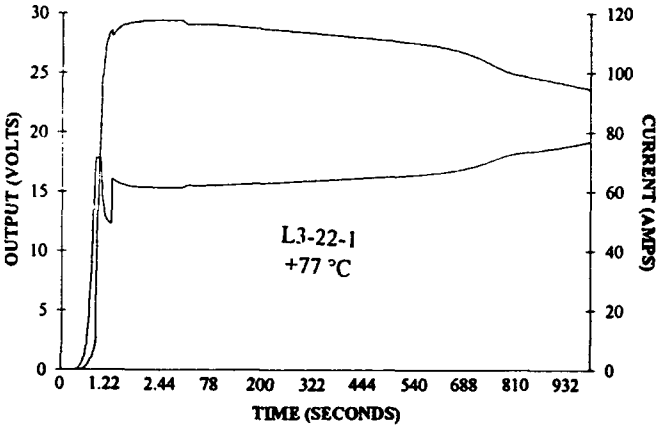

Figure 8. Performance Under Electronics Load

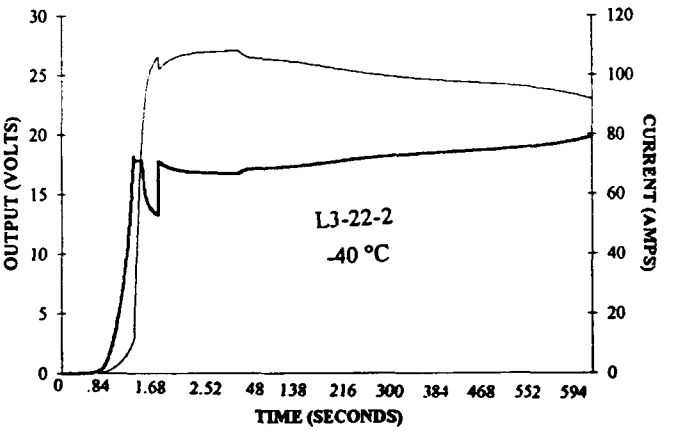

Figure 9. Performance Under Electronics Load

When subjected to a parasitic load of 2 amperes, the high temperature stabilized battery performed for more than 10,000 seconds (2.8 hours) to 23.0 volts, and approximately 13,500 seconds (3.8 hours) to 0 volts as shown in Figure 10. There was no detrimental effect on the structural integrity of the battery container as a result of exposure to the parasitic load. Under this worst case operating condition, the battery case temperature did not exceed 300 °F as depicted in Figure 11. The low case temperature was achieved by the use of Fiberfrax® and high efficiency, flexible Microtherm® insulation.

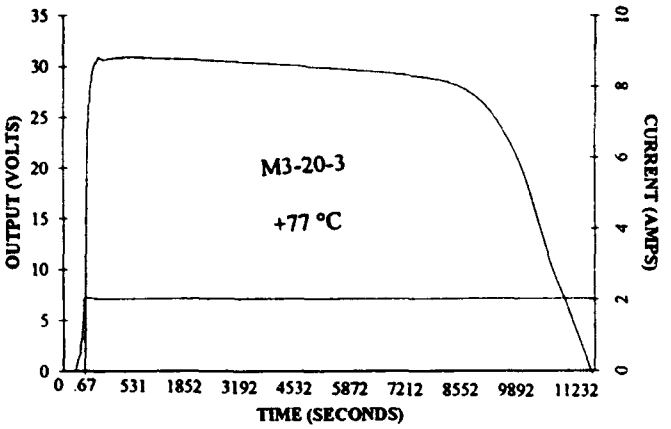

Figure 10. Electrical Performance Under 2 Amperes

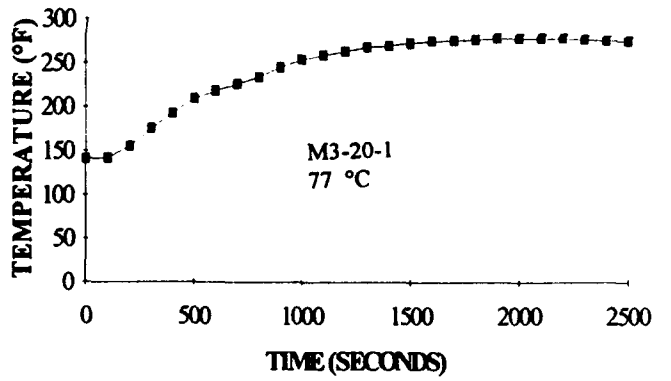

Figure 11. Case Temperature

Based on actual electrical performance, allowable maximum and minimum voltage levels and physical properties, the energy density and specific energy of the battery are shown in Table 2.

Table 2. Battery Energy Density and Specific Energy

Operating Temperature	W-HR/KG	W-HR/L
-40°C	31.70	78.97
+77°C	52.83	131.61

Operating Temperature	W-HR/LB	W-HR/IN^3
-40°F	14.41	1.29
+170°F	24.01	2.16

Conclusions

The EAP-12188 Thermal Battery has been subjected to electrical performance and rigorous environmental testing during development, design verification phase, and qualification testing. The battery as designed by Eagle-Picher Industries Inc., meets all the rigid specification requirements of the JAS-39 Aircraft.

Due to the relatively large size and performance requirements of this battery design, future high power batteries can be enhanced from this baseline design. Foreseen applications include other types of fighter aircraft, commercial aircraft, torpedo, and sonobuoy applications.

Acknowledgments

This work was supported by both Lucas Aerospace Ltd., Hemel-Hempstead, Hertfordshire, England, and SAAB-SCANIA AB, Linköping, Sweden.

THERMAL OPTIMIZATION OF Li(Al)/FeS_2 THERMAL BATTERIES

Frank C. Krieger
Reserve Battery Technology Branch
Electronics and Power Sources Directorate
Army Research Laboratory
2800 Powder Mill Road
Adelphi, MD 20783-1145

Introduction

Ordnance-type Li(Al)/FeS_2 thermal batteries have operating temperatures ranging from 400 to 600°C and are often limited in their lifetimes by heat transfer rather than by electrochemical depletion. The electrochemical capabilities of these systems have been extensively researched, and significant improvements in power and energy densities of the electrochemical cells themselves are not expected.[1] It does appear, however, that many such production-type batteries could be made significantly smaller by improved heat-transfer engineering.

In practice, the heat balance and geometry of most production Li(Al)/FeS_2 batteries are determined empirically. A previously successful ratio of pyrotechnic to cell weight is often used at the beginning of a development program. Batteries are constructed and tested. The ratio of pyrotechnic to cell weights and the amount of pyrotechnic material used at other points in the battery, most notably in the thermal insulation at the cell stack ends, are then adjusted as necessary to produce the required electrical output for the required lifetime.

Computer analyses of the heat-transfer engineering are often done based on thermocouple measurements made during operation. These analyses do not usually include detailed consideration of the internal battery gas environment or of any heat sinking methods that vary significantly from those originally chosen. In the past, such considerations have not been necessary. Very small batteries can be made with simple heat-transfer engineering because of the inherently high power and energy densities of the electrochemical cells (Table 1).

Control of the battery gas environment, especially reduction of the amount of high-thermal-conductivity hydrogen gas, combined with the proper choice of geometry, heat sinking, and chemical heat generation from within the cells, can contribute to significantly smaller, more lightweight batteries. Heat-transfer engineering becomes particularly important as the batteries become smaller and as the required lifetimes increase.[2-4] Combining previous experimental results with finite-element analysis methods now available should provide a more comprehensive picture of thermal-battery heat transfer and permit more rapid analyses of proposed future thermal-battery applications.

This paper describes some of the work that was done on two present (and very different) thermal-battery applications, the MANLOS (Man-Portable Non-Line-of-Sight) airplane and GPS (Global Positioning System) artillery shell. The MANLOS battery is a large thermal battery (38 to 50 V, 40 to 100 A, 98.4-mm diameter, 82.6 mm tall, 1.45 kg, 120-s lifetime) designed to deliver 90 A-min coulombic capacity to a small aircraft motor. The GPS battery is a small battery (11 to 16 V, 1.2 A, 33.3-mm diameter, 35.8 mm tall, 80 g, 145-s lifetime) designed to deliver 2.9 A-min coulombic capacity to an artillery fuze. Both batteries use the electrochemical system Li(Al)/LiCl-LiBr-LiF eutectic-MgO/FeS_2. The MANLOS battery, with its large size and simple geometry, is an excellent vehicle for heat-transfer studies, while the GPS is a small high-spin battery (ultimately 275 rps) with more typical thermal-battery heat-transfer engineering characteristics. Both thermal batteries have typical internal construction in that they are both right circular cylinders with heat pellets in the end thermal insulation for heating the thermal insulation external to the cell stack (Fig. 1); they do not include specialized heat sinks.

Heat Losses and Heat Generation: MANLOS and GPS

Identical cell chemistries and powder batches, processed at ARL, Adelphi, were used in both MANLOS and GPS programs. Batteries were run in vented as well as in sealed condition so that the effect of the gas environment could be verified. Temperature measurements were made with type-K (chromel-alumel) thermocouples. The thermocouple wires were spotwelded to the cell covers, and the wire diameters were varied from 0.254 to 0.0762 mm, as a test of the effect of transients and heat losses along the wires in regions of high-temperature gradients. During the initial temperature transients, readings were taken at a rate of 1000/s. The chemical compositions and masses of the MANLOS and GPS thermal cells and thermal insulators are shown in Table 1.

Table 1. MANLOS and GPS Thermal Cell Characteristics (averaged values for individual cell stack pellets)

A. MANLOS: 28 thermal cells with 29 heat pellets

Component	Mass (g)	Diameter (mm)	Thickness (mm)
Heat pellet	11.3255	76.2	0.6030
E/C pellet	12.0000	76.2	0.8626
A pellet	3.8124	74.9	0.6172
SS collector	2.8100	76.2	0.0831

Total battery thermal insulation mass: 207.54 g

B. GPS: 9 thermal cells with 10 heat pellets

Component	Mass (g)	Diameter (mm)	Thickness (mm)
Heat pellet	0.3990	19.05 × 3.175	0.3518
E/C pellet	0.4173	19.05 × 3.175	0.4770
A pellet	0.1274	19.05 × 3.175	0.3119
SS collector	0.1716	19.05 × 3.175	0.0831

Total battery thermal insulation mass: 17.53 g

C. Thermal cell chemical compositions: Both MANLOS and GPS (weight percents)

Heat pellet is Fe/$KClO_4$(84/16)
E/C pellet is E/C (35/65)
E is MgO/LiCl-LiBr-LiF eutectic (45/55)
C is FeS_2/Fe/E (78/2/20)
A is Li(Al) alloy (20/80)/LiCl-LiBr-LiF eutectic (90/10)
SS is 304 stainless steel

D. Realized power and energy densities for MANLOS electrochemical cells

1. 80 W-Hr/kg
2. 242 W-Hr/l
3. 5.32 kW/kg
4. 16.13 kW/l

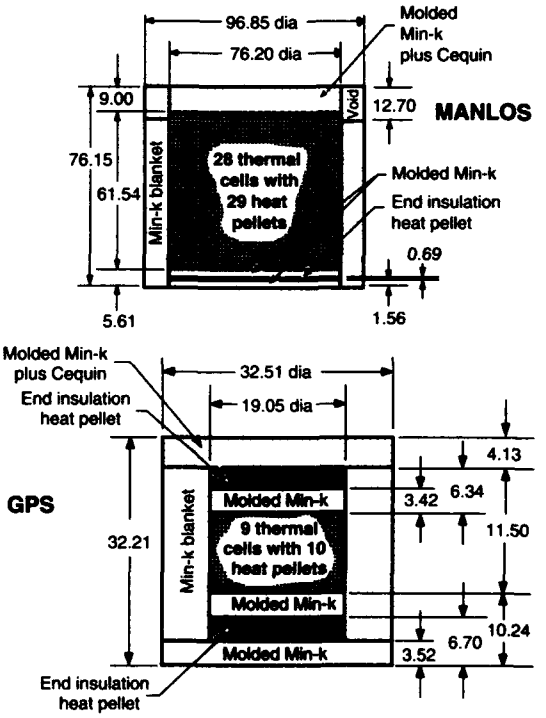

Figure 1. Internal battery constructions. All dimensions are in millimeters. Bottom end insulation heat pellet thickness includes one 0.0813-mm-thick stainless steel cell cover. There is no heat pellet in stack top insulation of MANLOS.

The production MANLOS batteries are to be vented on initiation to reduce the battery case mass, while production GPS batteries are to operate with sealed cases. For the sealed GPS experiment, this paper presents temperature-time curves for a battery with two thermal cells partially short circuited to demonstrate the amount of heat that can be generated from chemical exotherms in these thermal cells.

The temperature-time curves for MANLOS batteries in the vented condition (Fig. 2) and GPS batteries in the sealed condition (Fig. 3) are shown below. For both the MANLOS and the GPS batteries, the top and bottom cell thermocouples were spotwelded to cell covers placed at the extreme ends of the cell stack. MANLOS batteries used a double cell cover at the stack ends to help carry the heavy current. The center cell thermocouple for MANLOS was spotwelded to the cover of the 14th cell from the top of the 28-cell stack, and the cell cover was placed between the heat pellet and the anode. A fourth MANLOS stack cell cover thermocouple was similarly placed in the 25th cell from the top of the 28-cell stack. The individual MANLOS cell covers were all 0.0813-mm-thick 304 stainless steel, 76.2 mm in diameter.

The MANLOS thermocouple that monitored the bottom end insulation heat-pellet temperature was spotwelded to a regular MANLOS cell cover that was placed directly above the bottom end insulation heat pellet. Above this cell cover was a 3.353-mm-thick Min-k disk followed by the cell stack bottom (positive stack end). Below the bottom end insulation heat pellet was a 1.435-mm-thick Min-k disk, followed by a 0.127-mm-thick mica bottom liner above the steel case bottom.

The total internal length of the vented MANLOS battery was 76.15 mm. The top thermal insulation including the lid liner consisted of Min-k (6.79 mm), mica (0.254 mm), and Cequin (1.245 mm) disks, along with glass tape (0.711 mm). The side thermal insulation was a Min-k blanket[4] with a Fiberfrax and glass tape sidewrap. The MANLOS reusable steel case test fixture was uniformly 25.4 mm thick on the top, sides, and bottom.

The sealed GPS battery had 304 stainless steel thermocouple cell covers 0.0813 mm thick, with outer diameters of 19.05 mm and inner diameters of 3.175 mm at the top, bottom, and center of the cell stack. The bottom end insulation heat-pellet thermocouple also used one of these cell covers, which was placed directly on top of the bottom end insulation heat pellet on the cell stack bottom side. This cell cover was separated from the cell stack bottom by a 3.543-mm-thick Min-k disk. The GPS reusable steel case test fixture was 18 mm thick on the sides, with a header thickness of 7 mm and a bottom thickness of 5 mm.

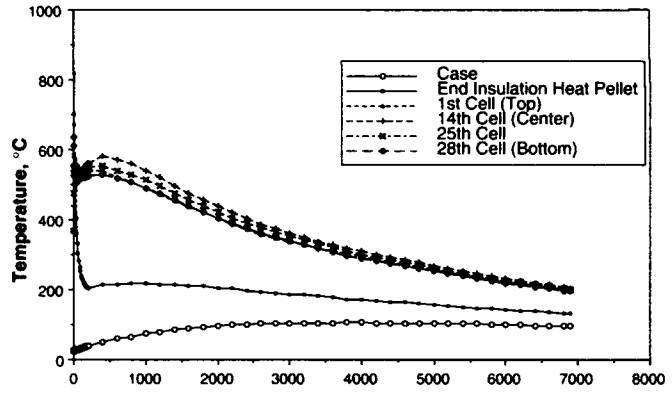

Figure 2. MANLOS battery temperatures (fired in the vented condition at 25°C).

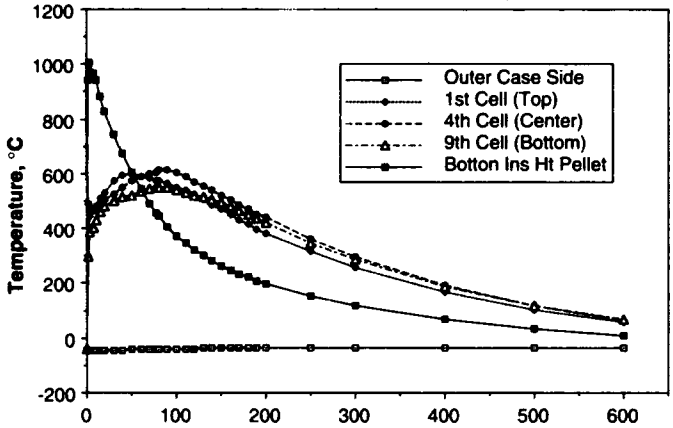

Figure 3. GPS battery temperatures (fired in the sealed condition at −46°C).

Temperature-time data for MANLOS and GPS batteries are shown in tabular form in Tables 2 and 3. These data can be used with the data of Table 1 and the geometry shown in Figure 1 for independent heat-transfer studies. Calculated thermal conductivities for MANLOS and GPS batteries, assuming that all the insulation has the same thermal conductivity, are shown in Figures 4 and 5.

The straight-line comparison of the insulation thermal conductivity versus temperature in Figures 4 and 5 is an experimental value for a previous sealed heat-transfer experiment[3] in which only copper and 84/16 Fe/$KClO_4$ pyrotechnic heat pellets were used with only Min-k blanket thermal insulation. This arrangement was used to eliminate the highly thermally conductive hydrogen gas known to be evolved from other thermal cell components. The thermal conductivities of the thermal insulation in the vented MANLOS battery (Fig. 4) are about 40 percent greater than the values estimated by the manufacturer. This is probably because of the previously mentioned hydrogen.

The manufacturer's value for the thermal conductivity of the Min-k blanket in air is $0.6980 \times 10^{-4} + 1.005 \times 10^{-7} \times T_M$ or 0.899×10^{-4} cal/s-cm-°C at 200°C (where T_M is the median temperature of the thermal insulation in °C). This is compared with the vented MANLOS measured thermal conductivity of about 1.3×10^{-4} cal/s-cm-°C (Fig. 4). The molded Min-k used on the MANLOS and GPS stack ends may have thermal conductivities 20 to 40 percent less than those of the Min-k blanket in the vented MANLOS gas atmosphere.

The method used for the heat-transfer analysis of the time-temperature curves has been reported elsewhere.[3] Although the battery is not operating in a thermodynamically reversible manner, the actual exotherms or endotherms that occur can be measured directly from the cooling curves. These results can then be compared to the basic thermodynamics of the system.[5] Space does not

Table 2. Experimental MANLOS Temperature-Time History

Time (s)	Case	Temperature (°C) 1st cell (top)	14th cell (center)	25th cell	28th cell (bottom)	End ins heat pellet
0	24	25	25	25	25	25
1	24	702	367	367	636	817
2	24	611	438	475	609	673
5	25	590	499	532	555	579
10	25	574	504	543	545	525
15	26	566	504	532	552	490
20	27	561	504	527	555	455
30	28	557	504	522	555	403
40	29	553	506	520	550	362
50	29	550	508	520	546	331
60	29	549	512	520	543	304
70	30	542	513	520	534	283
80	30	539	514	520	531	265
90	32	535	515	520	526	253
100	32	533	518	520	522	241
110	33	531	520	520	520	234
120	33	529	522	521	520	227
130	34	528	528	527	520	221
140	35	531	539	534	520	218
150	36	532	543	54[illegible]	520	214
160	37	532	548	544	520	210
170	37	532	555	545	523	209
180	38	538	557	550	525	207
190	39	540	562	549	525	204
200	40	541	561	549	525	202
400	50	538	582	553	527	214
600	59	522	573	541	519	216
800	66	508	560	530	506	219
1000	74	491	541	513	491	219
1200	80	472	520	497	475	216
1400	85	455	497	476	457	215
1600	90	437	476	456	438	212
1800	93	420	456	438	422	209
2000	96	403	438	422	405	205
2200	99	386	420	404	391	202
2400	100	371	403	391	375	197
2600	103	358	386	378	361	194
2800	104	346	375	365	351	190
3000	105	334	361	354	338	187
3200	105	327	349	343	328	184
3400	105	319	337	331	317	182
3600	105	311	327	322	306	179
3800	106	303	318	310	297	173
4000	106	295	310	301	289	171
4200	105	287	301	293	281	168
4400	105	280	294	285	274	165
4600	105	273	285	278	267	163
4800	104	265	277	270	259	160
5000	104	258	268	262	252	157
5200	103	250	260	254	245	154
5400	102	243	252	247	238	151
5600	102	236	245	240	232	148
5800	101	230	238	233	225	146
6000	100	223	231	226	219	143
6200	99	217	225	220	214	140
6400	98	212	219	215	208	138
6600	97	206	213	209	203	135
6800	96	201	207	204	198	133
6885	95	199	205	201	196	132

permit such a detailed analysis in this paper. Independent analyses can be done with the tabular data and the geometric figures supplied. The two major points that should be emphasized for practical battery technology are the large contribution of hydrogen gas, increasing thermal conductivity and subsequently shortening thermal-battery life, and the large amounts of heat that are generated by the electrochemical cells in the MANLOS and GPS batteries.

Table 3. Experimental GPS Battery Temperature-Time History

Time (s)	Case	Temperature (°C) 1st cell (top)	4th cell (center)	9th cell (bottom)	Bottom end ins. heat pellet
0	-46	-46	-48	-43	-48
1	-46	295	490	295	942
3	-46	445	467	388	1004
7	-46	464	471	403	969
10	-46	479	478	431	941
15	-46	511	494	462	880
20	-46	532	504	480	830
30	-45	573	526	502	745
40	-45	595	549	513	674
50	-43	597	572	522	605
60	-42	590	588	537	546
70	-42	584	598	546	490
78	-41	576	602	550	454
80	-41	574	616	550	446
90	-40	563	614	548	405
100	-40	550	602	542	373
110	-39	538	587	531	347
120	-39	524	569	520	322
130	-38	506	556	515	300
140	-38	487	541	506	280
150	-37	468	522	494	262
160	-37	450	504	478	247
170	-37	432	487	465	234
180	-37	414	471	449	220
190	-37	398	452	433	209
200	-37	382	438	420	197
250	-35	314	360	348	152
300	-35	256	295	285	117
400	-35	167	190	188	67
500	-35	101	116	116	31
600	-35	59	65	68	8

The diluent gas atmosphere in the thermal insulation of the vented MANLOS battery remained at atmospheric pressure and consisted of air (oxygen and nitrogen partially reacted with Li(Al) alloy) contaminated by a small amount of hydrogen gas. Some gases such as methane and ethane would have been present from breakdown of some of the glass adhesive tape, but these gases would not have had a large effect on the thermal conductivity of the thermal insulation. In light of this knowledge and the data for the vented MANLOS battery (Fig. 4), it seems unlikely that the effective thermal conductivity of all the thermal insulation was ever much different from $1.3 \pm 0.2 \times 10^{-4}$ cal/s-cm-°C during the first 1100 s of cooling to an average cell stack temperature of 500°C. On this basis, the entire amount of heat lost from the MANLOS battery during the first 1100 s after ignition was 23,738 cal (1.3×10^{-4} cal/s-cm-°C × 332 cm × 500°C × 1100 s = 23,738 cal; Table 1, Fig. 2).

The effective amount of heat yielded by the cooling masses during this time interval was 7724 cal. After we allow for the amount of heat required to establish a near-steady-state temperature gradient[3] in the thermal insulation (9577 cal), the amount of generated heat was more than three times the amount of heat obtained from natural cooling of the battery components (23,738 – 7724 + 9577 = 25,591 cal). The amount of generated heat was greater than the entire amount of the heat loss from the battery during this time interval (note the nearly constant average cell stack temperature).

The cooling curve also shows that the rates of heat generation vary greatly over short temperature intervals. Some of this behavior might be related to local breakdown of the separator layers and chemical nonuniformities, while some of the behavior can be attributed to natural exotherms and heating due to internal resistances (I^2R, where I is current and R is internal battery resistance) that occur during cell operation.[5] Because the temperature changes used to measure these exotherms are small and the thermocouples are in an active chemical environment, some of these variations may be caused by thermocouple error. Differential scanning calorimetry (DSC) analyses should be used to confirm exotherms and endotherms measured from Table 2 data.

The internal resistance of the MANLOS battery was measured by the current interrupt method to be 0.0967 Ω at 5.4 s, 0.102 Ω at 16.7 s, 0.111 Ω at 60.8 s, 0.113 Ω at 121.2 s, and 0.132 Ω at 151.4 s. The total resistance of the MANLOS internal 304 stainless steel leadwires was calculated at 0.018 Ω. If the internal battery resistance is 0.1 Ω, most of the I^2R heating will be applied to the cell stack. This I^2R heating at 100 A will be 239 cal/s and at 40 A will be 38.2 cal/s. From the computer programs, the effective thermal capacity of the entire MANLOS battery

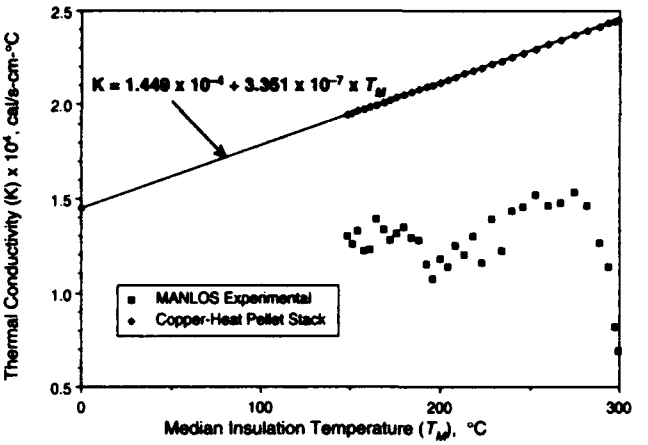

Figure 4. MANLOS thermal insulation thermal conductivities compared with copper-heat pellet stack measurements.

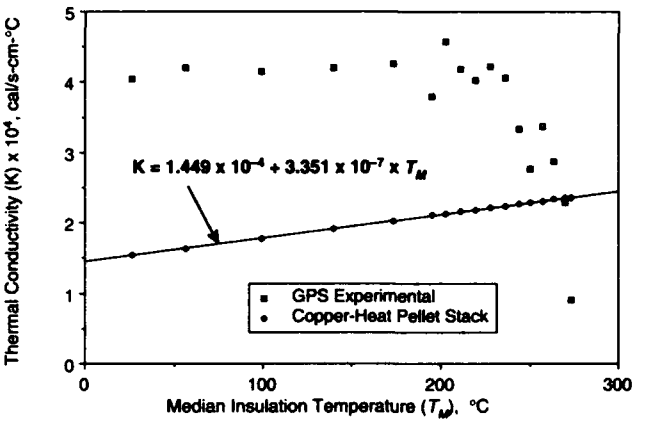

Figure 5. GPS thermal insulation thermal conductivities compared with copper-heat pellet stack measurements.

is 193 cal/°C (458 to 435°C), so that I^2R heating at the 100-A rate should result in an increase in the cell stack temperature of 239/193 = 1.24°C/s while the 100-A current is being drawn, if no heat is lost from the cell stack.

For the GPS battery, Figure 5 combined with previous experience suggests that the effective thermal conductivity of all the thermal insulation during the first 195 s as the cell stack cooled to its minimum operating temperature of 435°C was never much different from 4.1×10^{-4} cal/s-cm-°C. For an average effective cell stack temperature of 500°C (Fig. 3) and a shape factor of 35 cm, the total heat lost from the cell stack during this time was approximately 1511 cal (4.1×10^{-4} cal/s-cm-°C × 35 cm × [500 – (–40)]°C × 195 s = 1511 cal). The effective amount of heat lost from cooling of the GPS components during this time was only 366 cal, so that a total of 1145 cal (3.4 times the heat from natural cooling) was generated from these cells. The amount of heat required to establish the initial near-steady-state temperature gradient in the thermal insulation was 849 cal, so that a total of 1994 cal (1511 – 366 + 849) was generated from the cells. This is 5.4 times the total amount of heat available from the natural cooling.

The internal resistance of the GPS battery measured at 60 and 120 s by the current interrupt method was 0.6 Ω. The I^2R heating under the 1.2-A current was therefore only 0.21 cal/s compared with the measured heat loss rate during operation of 7.8 cal/s.

Transient Experimentation

For the 84/16 weight percent Fe/$KClO_4$ pyrotechnic heat pellet fired under adiabatic conditions at –40°C, the calculated peak temperature is 1413°C. The thermal cells of MANLOS and GPS types of batteries generally should not exceed about 620°C. Defining the initial transient temperature conditions within the first few seconds of pyrotechnic ignition can be a major difficulty. This is particularly true at the

ends of the cell stack, where large amounts of pyrotechnic materials are usually required to prevent excessive cooling of the thermal cells into the thermal insulation heat sink immediately following battery initiation.

When the battery is initiated, heat is lost very rapidly from the pyrotechnic materials and the cell stack until a near-steady-state temperature gradient is established in the thermal insulation. Some studies of this initial transient behavior in MANLOS and GPS are shown below. The results are discussed briefly and are shown in tabular form to facilitate further heat-transfer studies.

For most applications, it has been found experimentally that optimal lifetimes are obtained when sufficient pyrotechnic material is added within the thermal insulation to heat the thermal insulation to the same initial temperature as the thermal cells. Although the excess heat is lost rapidly, this technique prevents rapid initial temperature loss from the thermal cells because of the thermal insulation heat sink effect.

The computer programs used for the thermal optimization of the MANLOS and GPS thermal batteries include the pyrotechnic heat necessary to heat the thermal insulation to the cell temperature. With these computer programs,[1] the calculated peak temperature of the MANLOS battery was 522°C when the battery is fired at +25°C, while the measured value was 542°C at 7.5 s and 547°C at 300 s, if the stack temperature is calculated as 1/4(top + center + 25th cell + bottom) thermocouple readings (Fig. 2, Table 2). The calculated peak temperature for the GPS battery when the battery is fired at -46°C is 518°C, while the measured value is 518°C at 25 s, if the stack temperature is measured as 1/4(top + 2 × center + bottom) thermocouple readings (Fig. 3, Table 3). The GPS stack temperature later increased to 587°C at 85 s because of the heat generated by the two short-circuited thermal cells.

Individual thermal cell heat balances may differ markedly from the total thermal-battery heat balance if large amounts of thermal insulation are used in the battery. For the MANLOS battery, sufficient pyrotechnic was added to each MANLOS thermal cell to raise the individual cell temperature from 25 to 584°C. For the GPS thermal cell, enough pyrotechnic was added to each cell to raise the cell temperature from -46 to 488°C. For most previous designs, the measured peak temperature of the center thermal cell has been within ±20°C of the calculated peak temperature of the individual thermal cells when the 0.254-mm-diameter type-K thermocouple wires are used.

The initial transients for the sealed GPS battery bottom thermal cell and end insulation heat pellet are shown in Table 4 and Figure 6. The calculated adiabatic peak temperature of this end heat-pellet nest was 1377°C, and the thermocouple read the highest value recorded of 1006°C at 3.00 s after the initial recorded temperature rise. The highest measured heat-transfer coefficient for heat transfer from the heat pellet into the cell cover was 49.3 cal/cm²-s.

In a separate GPS experiment, small-diameter (0.0762-mm) thermocouple wires were placed in the GPS bottom end insulation heat-pellet nest to help define the initial heat-pellet transients. The bottom end heat-pellet nest for that experiment consisted of seven heat pellets of total thickness 2.718 mm. Three thermocouple cell covers, each 0.08128 mm thick, were placed in the end insulation heat-pellet nest.

After the very bottom (positive) cell cover of the separate experiment GPS cell stack was a Min-K disk 3.442 mm thick. This was followed by a 0.08128-mm-thick thermocouple cell cover, which was the top thermocouple of the end insulation heat-pellet nest. Then came three heat pellets of total thickness 1.194 mm (1.4839 g), followed by a double (2 × 0.08128 mm thick) thermocouple cell cover. The thermocouple wires (0.0762 mm in diameter) were spotwelded between these two cell covers. Directly below were four more heat pellets of total thickness 1.524 mm (1.9401 g). At the very bottom of the end insulation heat-pellet nest was the third thermocouple cell cover. Beneath this cell cover was a 3.467-mm-thick Min-k disk that rested on the steel case bottom. High-speed transient data for the GPS end insulation heat pellets with the 0.0762-mm-diameter thermocouple wires are shown in Table 5 and Figure 7.

The semilog plot of Figure 7 is of interest because it has been shown previously[6] that heat transfer from heat paper into copper under thermal-battery conditions often shows a linear relationship for the plot of the logarithm of the temperature difference versus time. This rela-

Table 4. Experimental GPS Transient Temperature (0.254-mm-diameter chromel-alumel thermocouple wires) (-46°C ambient)

Time (s)	Temperature (°C) 9th cell (bottom)	Bottom end insulation heat pellet	Time (s)	Temperature (°C) 9th cell (bottom)	Bottom end insulation heat pellet
0.0	-46	-45	1.3	381	970
0.1	131	540	1.4	384	973
0.2	216	734	1.5	381	979
0.3	274	809	1.6	381	982
0.4	309	856	1.7	386	984
0.5	330	887	1.8	382	989
0.6	347	907	1.9	384	992
0.7	359	920	2.0	381	994
0.8	368	930	3.0	384	1006
0.9	374	941	4.0	386	998
1.0	374	950	5.0	426	989
1.1	378	957	5.7	398	980
1.2	380	965			

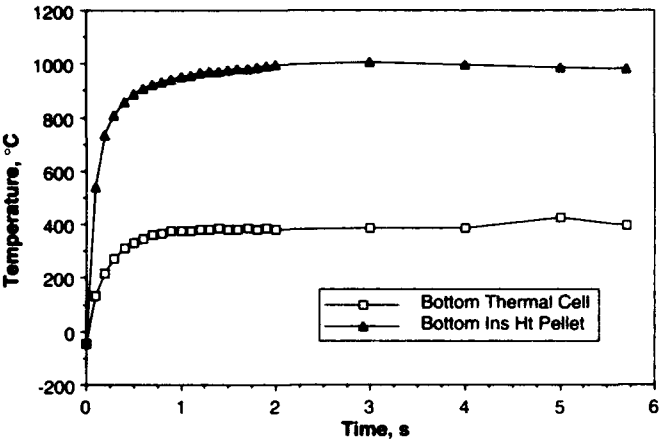

Figure 6. GPS transient temperatures (sealed condition at -46°C).

Table 5. Experimental GPS Transient Temperatures (0.0762-mm-diameter chromel-alumel thermocouple wires) (25°C ambient)

Time (s)	Temperature (°C), bottom end insulation heat-pellet nest Top	Center	Bottom	Time (s)	Temperature (°C), bottom end insulation heat-pellet nest Top	Center	Bottom
0	24	26	24	0.09	219	1079	932
0.01	18	40	21	0.1	569	1248	996
0.02	29	273	31	0.11	793	1270	1043
0.03	22	498	26	0.12	929	1265	1100
0.04	20	534	247	0.13	1007	1237	1121
0.05	21	736	598	0.14	1047	1245	1116
0.06	29	847	742	0.15	1094	1262	1137
0.07	38	935	830	0.2	1171	1223	1161
0.08	173	994	879	0.3	1198	1234	1176

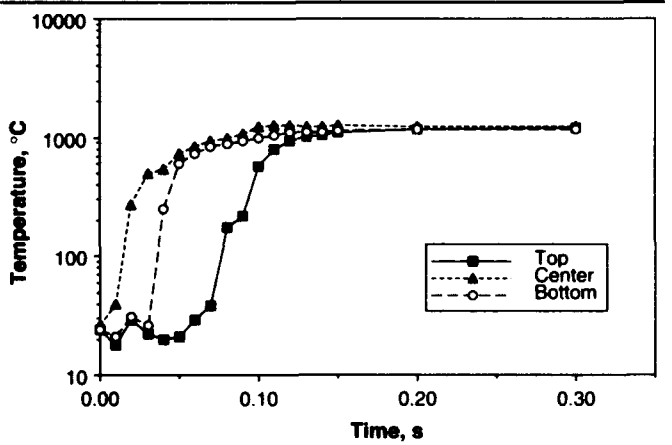

Figure 7. GPS end insulation heat pellet transient temperatures (vented condition at 25°C).

tionship implies that all the heat transfer occurs from conduction (no radiation or convection) if cancelling errors are absent. Since Figure 7 does not show this straight-line relationship, the heat-transfer coefficient is temperature dependent, and radiation heat transfer is probably present.

The calculated adiabatic peak temperature of this end heat-pellet nest was 1365°C, and the middle thermocouple read the highest value recorded of 1270°C at 0.11 s after the initial recorded temperature rise (about 93 percent of the theoretical value). The highest measured heat-transfer coefficient from the heat pellet into the cell cover was 336.6 cal/s-cm^2.

The initial transients for the vented MANLOS battery bottom thermal cell and end insulation heat pellet are shown in Table 6 and Figure 8. The logarithm of the temperature difference versus time is again nonlinear. The calculated adiabatic peak temperature of this end heat-pellet nest was 1317°C, and the thermocouple read the highest recorded value of 822°C at 0.47 s after the initial recorded temperature rise. The low measured peak temperature (about 40 percent lower than the theoretical value) was believed to be caused by the large wires (0.254 mm diameter) drawing heat from the cell cover shortly after pyrotechnic ignition. As the surrounding insulation becomes heated, this error will be reduced. The highest measured heat-transfer coefficient from the end insulation heat pellet into the thermocouple cell cover was 69.9 cal/s-cm^2. When perfect contact between the heat pellet and the thermocouple cell cover was assumed, the finite-element modeler showed a heat-transfer coefficient in the same temperature region of 8699 cal/s-cm^2. Initial temperature increases calculated from the finite-element modeler, assuming perfect thermal contact, were in general agreement with analytically calculated values.[7] The effective thermal conductivity of the cell stack itself was calculated to be $80 \times 10^{-4} \pm 20 \times 10^{-4}$ cal/s-cm-°C from this experiment.

Table 6. Experimental MANLOS Transient Temperatures (0.254-mm-diameter chromel-alumel thermocouple wires) (25°C ambient)

Time (s)	Temperature (°C) Center cell	Bottom cell	End ins. heat pellet	Time (s)	Temperature (°C) Center cell	Bottom cell	End ins. heat pellet
0.0	24	22	23	0.36	115	250	734
0.03	27	21	23	0.37	115	290	759
0.06	29	26	17	0.38	116	318	770
0.1	32	31	21	0.39	120	349	788
0.15	38	32	32	0.4	121	375	796
0.2	43	51	44	0.44	144	464	820
0.25	57	71	109	0.47	158	533	822
0.26	62	76	199	0.5	173	575	817
0.27	68	83	285	0.6	220	639	807
0.28	73	81	353	0.7	257	628	799
0.29	82	88	425	0.8	289	632	785
0.3	87	88	485	0.9	317	634	773
0.31	94	91	546	1.0	342	633	759
0.32	99	105	595	1.1	361	635	747
0.33	104	137	630	1.2	379	638	735
0.34	108	182	678	1.3	392	632	726
0.35	113	218	708	1.37	399	635	722

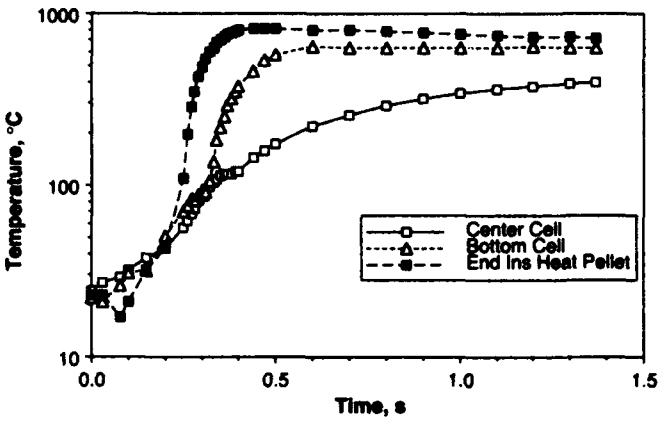

Figure 8. MANLOS transient temperatures (vented condition at 25°C).

Conclusions

Small-diameter (0.0762-mm) type-K thermocouple wires may be used to measure initial transients of heat pellets embedded within the thermal insulation of thermal batteries. For the thermal cells themselves during operation, larger diameter (0.254-mm) type-K thermocouple wires are adequate.

Large amounts of heat were generated by both the MANLOS and the GPS batteries. In both cases, the rates of heat generated were found to be comparable to the rates of heat required for battery operation at constant temperature. Previous battery designs using Li(Al)/FeS_2 with LiCl-KCl eutectic electrolyte have shown cell heat generation rates comparable to the total battery heat loss rates for that system also.[3] Smaller but comparable rates of heat generation have been measured and calculated from thermodynamic considerations for the Li(Al)/FeS system using secondary cells with LiCl-LiBr-LiF eutectic electrolyte.[5] The GPS experiment shows that the amount of generated heat can be increased markedly by intentional short circuits in the thermal cells.

The diluent gas atmosphere increased the heat-loss rate from the sealed GPS battery by a factor of 4 and from the vented MANLOS battery by about 40 percent. These heat losses could be reduced by a reduction in the amount of hydrogen impurities in the battery components and by the use of hydrogen getters such as barium.

Combining control of the cell heat-generation rates with control of the gas atmospheres in present production thermal batteries could dramatically reduce thermal-battery size. Heat generation within the thermal cells themselves should be controllable to specified heat-loss rates by appropriate chemical processing and construction techniques. These techniques should be especially effective in small thermal batteries where large amounts of thermal insulation are required, such as the GPS battery of the present paper or proposed new 30- or 40-mm fuze thermal-battery applications for smart small arms.

ARL is in a unique position to pursue a mission of thermal-battery size reduction through heat-transfer engineering because of its extensive previous experience in thermal-battery chemical processing, construction methods, and heat transfer. Properly applied, the results may be dramatic in terms of size and mass reduction for certain applications. Use of finite-element modeling technology now available will facilitate understanding of the process interactions and greatly accelerate the mathematical optimization of the resulting new thermal-battery systems.

References

1. P. Davis and C. Winchester, "Limiting Factors to Advancing Thermal Battery Technology for Naval Applications," Naval Surface Warfare Center, NAVSWC TR 91-614 (Oct 1991).
2. F. Krieger and R. Comyn, "Fusible Thermostat for Thermal Power Supplies," Harry Diamond Laboratories, HDL-TR-1644 (Nov 1973).
3. F. Krieger, "Heat Transfer Optimization of High-Spin Thermal Batteries," Harry Diamond Laboratories, HDL-TR-2174 (Oct 1990).
4. F. Krieger, "Heat Transfer in High-Current Thermal Batteries," Proceedings of the 35th International Power Sources Symposium, Cherry Hill, NJ, pp 223-226 (June 1992).
5. D. Chen and H. Gibbard, "Thermal Energy Generation of Li(Al)/FeS Cells," J. Electrochem. Soc. **130**, 1975 (1983).
6. D. Carpenter and A. Taylor, "Heat Transfer from Heat Source Material to Copper Disks," VMI Research Laboratories, Report 287-2 (Feb 1970).
7. H. Carslaw and J. Jeager, "Conduction of Heat in Solids," 2nd ed, Oxford University Press, New York (1989).

HIGH ENERGY LITHIUM ANODE THERMAL BATTERIES

Alastair J. Clark, Ian D. McKirdy
MSA (Britain) Limited, Coatbridge, Scotland, UK

Abstract

Data which confirms long stable storage of immobilised lithium anode thermal batteries is presented along with a discussion of recent improvements which have increased specific energy densities up to 120 Wh/kg for large batteries.

Introduction

Thermal batteries have been manufactured in the UK since 1955 by MSA (Britain) Limited, a major thermal battery supplier in Europe. In 1972, MSA (Britain) Limited became involved in lithium thermal battery development on a contract from the UK Admiralty Materials Technology Establishment. The aim was to develop a large lithium anode thermal battery as an underwater propulsion power source. The technology which was developed used immobilised lithium in the anodes with iron disulphide in the cathodes. The pellet construction of the design was closely related to the type of immobilised electrolyte pellet technology that had been used in calcium anode thermal batteries for many years.

At the end of the contract, test results were reported for a large battery, assembled from 10 modules, each 89mm diameter and 575mm long with 80 series cells, (1). The battery powered a motor at an average rate of 33 kW for 13 minutes with a peak power output of 57 kW. The complete 80 cell module in its hermetically sealed container had a specific energy density of 74 $Whkg^{-1}$.

Using different technologies MSA (Britain) Limited later developed and optimised for qualification and production for defence applications many immobilised lithium anode thermal batteries. These were based on proprietary immobilised lithium anodes covered by patents, (2,3). One of these anode technologies generally referred to as "LAN" was fully described by Winchester in 1982, (4). Although immobilised lithium anode thermal batteries have been used to power underwater systems including electronics and propulsion power, their main application has been in guided weapons where they have been used to power guidance electronics, actuator motors, fuses and safety and arming units. They have also been used for power in terminally guided mortars and shells. In military aircraft they have been used to power ejection seat sequencers.

Battery designs which have been manufactured, range from 18mm diameter upwards with voltages from 2 volts to 200 volts. A wide range of current ratings and durations have been covered and designs are available with up to 200 amp current ratings, and with durations of over 30 minutes.

Immobilised lithium anode thermal batteries manufactured by MSA (Britain) Limited have been demonstrated during 15 years of production to be extremely reproducible. As specified for many defence applications, the cells are required to operate over extremely wide temperature ranges of -55°C to 100°C. Qualification testing has demonstrated that they withstand severe vibration, shock, acceleration, temperature cycling and temperature shock environments. Data is available from a number of storage programmes to show that, as required by their applications, they are extremely stable after long periods of storage. The results of one such programme are reported below.

Because many underwater requirements now demand even higher energy densities, MSA (Britain) Limited recently carried out a programme to maximise immobilised lithium anode cell performance. Many of the features which had been introduced to improve the performance of thermal batteries for guided weapons were applied to the optimisation of two battery designs with high capacity cells.

The features which contributed to performance improvements and the results obtained are described and reported below.

Storage of Immobilised Lithium Anode Thermal Batteries

Programme

In January 1984, soon after qualification, MSA set up a long term storage programme on an 89mm diameter, 210mm long, immobilised lithium anode thermal battery. The programme was based on the use of the first two batches manufactured after qualification, and over the next three years during which 20 batches were manufactured, 6 batteries were set aside from each batch so that storage data would also be available to cover materials batches and other production variables. This provided 100 batteries in the first two batches and a further 120 from continuous production.

Batch testing of the 22 batches at +55°C and -30°C gave baseline data before storage, providing 105 results at -30°C and 100 results at +55°C. To date, batteries have now been tested on the aging programme as follows.

Storage Time (Years)	Number Discharged at -30°C	Number Discharged at 55°C
0	105	100
1	5	5
2.5	5	5
5	5	5
6 - 8.5	20 *	20 *
9	5	5

* Batteries from 20 Production Batches

The test load, 23A continuous with pulses to open circuit and to 44A, was designed to allow calculation of internal resistance, in addition to the normal thermal battery parameters of activation time, duration, maximum voltage, etc., derived from the voltage versus time characteristic and frequently used to define thermal battery specification performance.

Results and Discussion

Eight significant performance characteristics were recorded from the voltage versus time discharge curve - Activation Time to 26 volts, Duration to 26 volts, Maximum Voltage, Voltage at 2.4 seconds on 40 amperes, Internal Resistance at 2.4 seconds, Minimum Voltage at 399.9 seconds on 23 amperes, Minimum Voltage at 400 seconds on 44 amperes and Internal Resistance at 400 seconds. These parameters have been used to compare the performance of batteries before and after storage.

In Figures 1 and 2, activation times plotted from the initial batch tests (year zero) at 55°C (100 results) and -30°C (105 results) indicate that the range of initial results is 0.7 to 1.3 seconds at 55°C and 0.8 to 1.4 seconds at -30°C. The results for the stored batteries indicate that they have not changed from the initial range of values even after nine years storage.

Duration plotted in the same manner in Figures 3 and 4 shows no change, with all stored results lying within the original spread.

Voltage at 400 seconds on a load which represents a cell current density of 0.5A cm^{-2} is plotted in Figures 5 and 6. Again there is no indication of any change after storage compared with the initial spread of results.

Internal resistance at 400 seconds, calculated from the voltage change arising from the load change at this time, plotted in Figures 7 and 8 also indicates that this parameter has remained within its original range after storage. This suggests there are no deleterious reactions of the anode surface with traces of moisture unavoidably incorporated into the battery during manufacture. Storage deterioration arising from such reactions, as has been reported during early work on lithium silicon anode systems, (5), is absent from immobilised lithium anode designs.

The other four parameters also indicated that battery discharge performance remains unchanged after storage of up to nine years.

Improvements in Energy Density

Cell Improvements

As noted in the introduction, underwater requirements demand high energy density batteries. Inspection of the makeup of cells used in the original old designs in the light of fifteen years of experience with optimisation of batteries and cells for guided weapons use, indicated two main areas where improvements could be made.

- Increasing the amount of lithium in the anode relative to support materials.
- Reduction in the thickness of the electrolyte/separator layer.

The improvements which were obtained from these changes were evaluated in single cell experiments which have previously been reported, (6). The results obtained from 80mm diameter cells indicated specific energy densities of up to 218 $Whkg^{-1}$. Anodes were evaluated with up to 36% lithium.

Battery Improvements (80mm Diameter Cells)

To confirm that the optimised single cell performance was reproduced in pyrotechnically activated batteries, two battery types were designed using the information generated from single cells. More complete details of the battery designs are given in (6).

Cell Stacks

One battery design - Type A - had 15 series cells (nominal 24V) and was designed to maximise duration performance on a load of 1.12kW. The other battery - Type B - had 25 series cells (nominal 40V) and was designed for a load of 1.32kW.

Battery construction followed principles which have been described elsewhere, (7,8) but compared with the original 80 cell module, the volume of the battery occupied by cells was maximised. Thermal modelling of the two designs was carried out by the DRA Farnborough using a computer model which had been evaluated for immobilised lithium in the designs using MSA (Britain) Limited test data, (9,10). The modelling predictions indicated that with the thermal insulation and end heat design used, battery performance would be limited by electrochemical considerations and not by cooling effects.

Discharge Conditions

Both batteries were discharged into a constant wattage load unit provided by GEC-Marconi Naval Systems, Underwater Weapons Division, set at 1.12kW for Type A and 1.32kW for Type B. Discharges were carried out with the batteries at approximately 20°C in still air.

Discussion and Results

Type A Performance

A graph of the output voltage and load current for battery Type A is shown in Figure 9. From approximately 4 seconds the load regulated at 1.12kW. Over the discharge duration the current increased from 42A (0.83A cm^{-2}) to 75A (1.49A cm^{-2}) The discharge voltage remained above 24V (1.6V per cell) for 348 seconds but 1.12kW was supplied for a further 140 seconds at which time the voltage had dropped to 15V (1.0V per cell). At this point the load ceased to regulate.

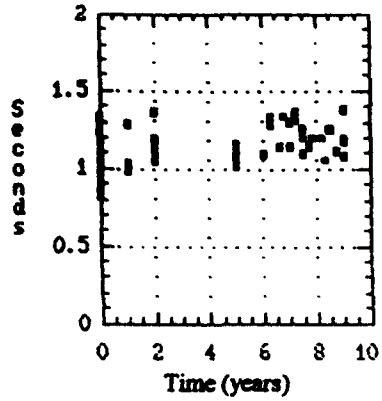

Fig.1 Activation Time v. Storage (Discharged at -30°C)

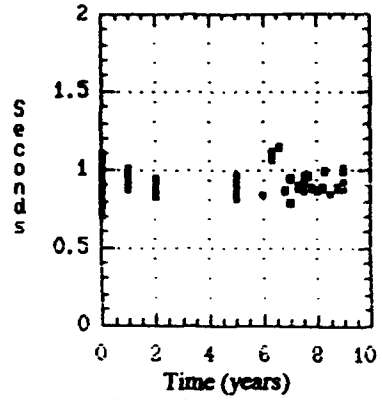

Fig.2 Activation Time v. Storage (Discharged at 55°C)

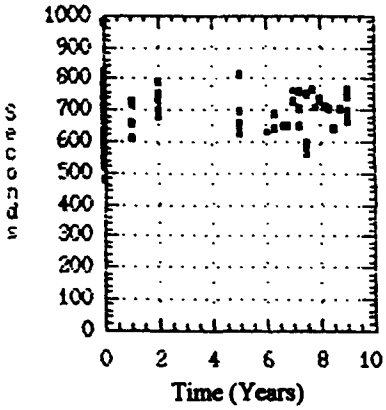

Fig.3 Duration v. Storage (Discharged at -30°C)

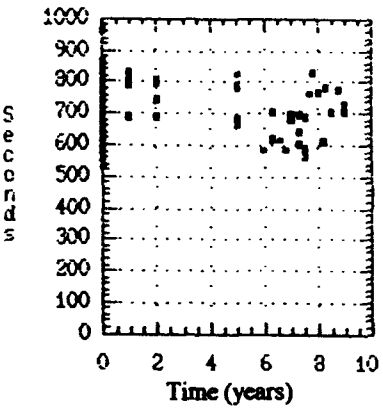

Fig.4 Duration v. Storage (Discharged at 55°C)

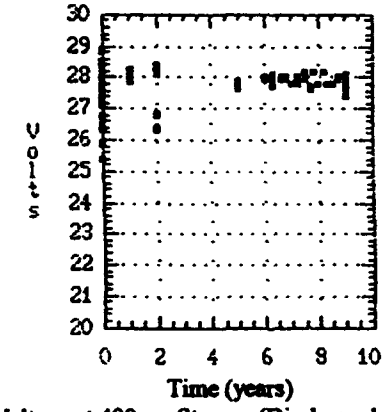

Fig.5 Voltage at 400s v. Storage (Discharged at -30°C)

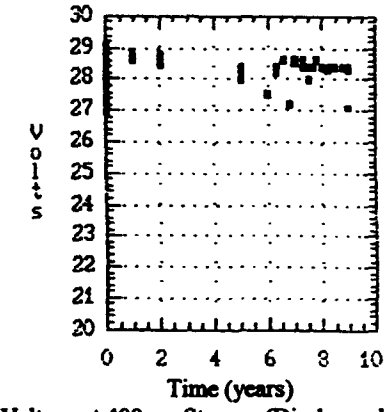

Fig. 6 Voltage at 400s v. Storage (Discharged at 55°C)

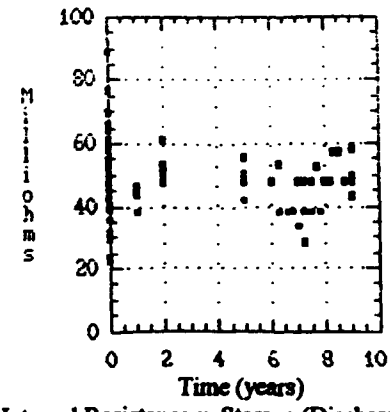

Fig.7 Internal Resistance v. Storage (Discharged at -30°C)

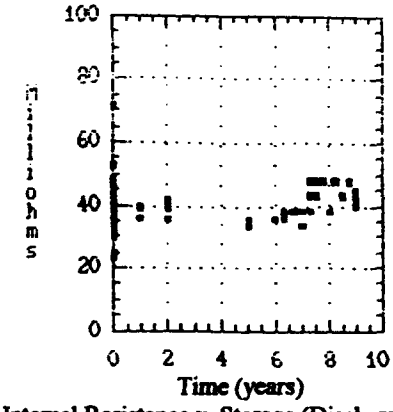

Fig.8 Internal Resistance v. Storage (Discharged at 55°C)

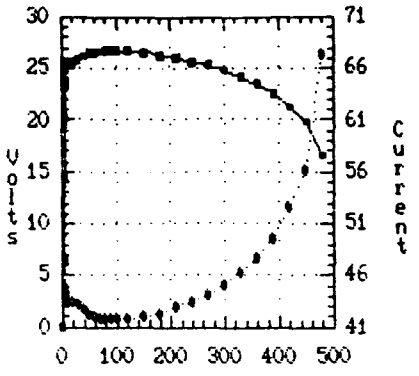

Fig. 9 Voltage & Current on 1.12kW Load Type A

Type B Performance

Similarly for battery Type B, output voltage and load current are shown (see Figure 10). The load regulated at 1.32kW from 4.9 seconds when the voltage had risen to 36V. The battery duration to 36V (1.44V per cell) was 644 seconds but 1.32kW was supplied up to 724 seconds when the battery voltage dropped to 13.2V (0.5V per cell). During the discharge duration, the current rose from 27.5A (0.54A cm^{-2}) to 44A (0.87A cm^{-2}).

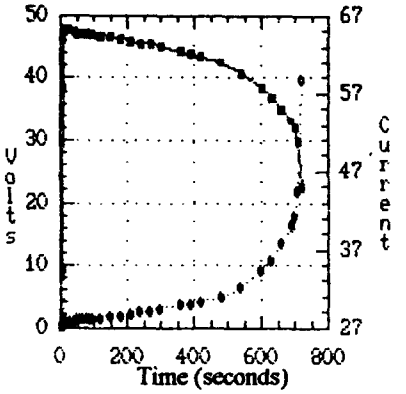

Fig.10 Voltage & Current on 1.32kW Load Type B

Specific Energy Density Improvements

The specific energy densities achieved can be summarised as follows.

Battery Performance	Type A	Type B
Discharge Rate (W)	1120	1320
Total Energy supplied to the Load (Wh)	149	259
Specific Gravimetric Energy Density (Wh kg^{-1})	83	96
Specific Volumetric Energy Density (Wh dm^{-3})	230	260

In both batteries, the performance of the cells including their heat source was 152 $Whkg^{-1}$. The improvement that was achieved is best illustrated by comparison with the performance of the battery manufactured by MSA (Britain) Limited in 1979, (1). In dimensions of 89mm diameter x 575mm long it produced a specific energy density of 74$Whkg^{-1}$. In contrast 106 series cells as used in battery Type A could be fitted in these dimensions resulting in a total energy output of 1100Wh, a power output of 5.6kW for 710 seconds with a voltage regulation of 204 - 127V. The nominal mass for a battery this size would be 10.1kg. Specific energy density is increased to 110 $Whkg^{-1}$ (gravimetric) and 310 Wh dm^{-3} (volumetric), an improvement of 48%.

An analysis of the main components within the battery indicates that this very significant improvement is achieved by the increase of the total cell mass in the battery and an increase in the cell active materials. The utilisation of anode materials in the cell did not change compared with the value determined by the earlier work.

Conclusions

The 9 years storage data presented demonstrates that MSA (Britain) Limited immobilised lithium anode technology batteries are storage stable with no loss of cell capacity as indicated by duration and no change in fuzehead performance or heat source burning rates as indicated by activation time. Improvements in the technology have increased specific energy densities for cells up to 150 Wh/kg and 400 Wh/dm^3, with a corresponding significant increase in battery performance.

Acknowledgements

The authors wish to acknowledge the thermal modelling carried out by Dr. J. Knight, DRA Farnborough and the loan of a constant power load from GEC-Marconi Naval Systems, Underwater Weapons Division. The work on energy density improvements was jointly funded by MSA and GEC-Marconi Naval Systems.

References

(1) Fraser, R.T.M. (1980), "Proceedings of The 29th Power Sources Symposium", Electrochemical Socy., Inc., p43.
(2) Harney, D.E. (1980), "Improvements in or relating to Thermal Batteries", UK Patent Number 2047459.
(3) Baird, M.D. and Clark, A.J. (1982), "Thermal Electric Cells", UK Patent Number 2101395.
(4) Winchester, C.S. (1982), "Proceedings of the 30th Power Sources Symposium", Electrochemical Society Inc.
(5) Searcy, J.Q. and Neiswander P.A., "Proceedings of the 29th Power Sources Conference", Electrochemical Society, Inc., (1980), p38.
(6) Clark, A.J. and McKirdy, I., "Power Sources 14", International Power Sources Symposium Committee, p281.
(7) Attewell, A. (1991), "Modern Battery Technology", Ellis Horwood Limited, p409.
(8) Clark, A.J. (1986), "Chemistry & Industry 6", p205.
(9) Knight, J. and McKirdy, I. (1987), "Power Sources 11", International Power Sources Committee, p491.
(10) Knight, J. and McKirdy, I. (1990), "Proceedings of the 34th International Power Sources Symposium", Institute of Electrical and Electronics Engineers, Inc., p141.

A SHORT LIFE THERMAL BATTERY FOR PULSE POWER APPLICATIONS

J.D. Briscoe, G. Castro, J. Gessler
SAFT AMERICA INC
Research and Development Center
107 Beaver Court
Cockeysville, Maryland 21030

Abstract

High voltage thermal batteries that deliver 4200 W constant power output at power densities of 3.6 W/cm^2 are currently being developed at SAFT. The battery employs the LAN/FeS_2 electrochemical system with an all lithium halide electrolyte operating at temperatures above 445 °C. Utilizing an improved LAN assembly and an optimized two layer electrolyte/cathode pellet, a 36% reduction in cell thickness was achieved in an improved design versus the baseline design. The battery delivers extremely high power densities of 8,750 W/kg and 24,100 W/l while providing energy densities of 37 Wh/kg and 101 Wh/l. The final design measures only 4.1 cm diameter by 13.1 cm length, and delivers over 200 VDC for more than ten seconds.

Introduction

Lithium thermal batteries make excellent primary reserve power sources for military applications requiring high power, fast activation, long shelf life, ruggedness, and high reliability. The lithium and iron disulfide electrodes have high specific energy and fast reaction kinetics. The LiBr-LiCl-LiF molten salt electrolyte (mp = 445 °C) has high ionic conductivity when compared to aqueous and solid state electrolytes. Stacked as a series array of thin circular cells, the battery is activated by an electro-explosive device (EED) that ignites a heat paper fuse train located down the center of the stack and burns the heat pellets located between the cells. The heat produced melts the electrolyte, and the battery delivers high voltage and power.

This paper summarizes the task of improving the State-Of-The-Art of high power thermal batteries for Sonobuoy applications. The battery requirements are detailed in Table 1. Ten batteries are packaged together

Table 1: Short Life Battery Requirements

Power, Watts	4,200
Energy, Watt-Sec	42,000 (10 seconds)
Life, Seconds	10
Minimum Voltage, Pulse	150 VDC (Load)
	50% of OCV
Maximum Voltage, OCV	600V
Minimum Voltage, Regulation (Pulse)	25% of OCV or Peak Volt, Stand-by Load
	(whichever is less)
Stand-by Load	20 to 200 Ohm Approximately
Envelope	4.5" Dia x 10.4" L (10 Units)
Battery Size	4.1 cm (1.60") Dia x 13.2 cm (5.2") L
Weight, Maximum	5.8 kg (12.75 lbs)
	(including mounting)
Weight, Individually	0.48 kg (1.06 lbs)
Activation, Seconds	60% OCV or Stand-by Load Volt Within 0.25
	Seconds
Temperature, Operational	-20 °C to +55 °C

to make an assembly. Individual batteries must produce a continuous 4200 W at 150 V minimum for ten seconds in a maximum envelope of 13.2 cm length and 4.1 cm diameter. The resulting power and energy density goals are 24,138 W/l and 67 Wh/l. In addition the battery must be able to provide the required energy and power after seven years of uncontrolled storage. The battery must also activate in less than 0.25 seconds after temperature storage at extremes of -20 °C and +55 °C. The following discussion summarizes the improvements in design and performance of the short life battery.

Experimental

The LAN/LiBr-LiCl-LiF/FeS_2 electrochemistry was selected as the best choice for this application. LAN is liquid lithium immobilized by a high surface area iron powder[1]. It was chosen over the other commonly used LiAl and LiSi anodes for three reasons. Firstly, it has the voltage potential of pure lithium. Secondly, it has superior rate capability, and thirdly, it can be fabricated into thinner electrodes than the pressed powder alloys. LAN consisting of 17% lithium by weight was cold rolled into thin foil and die cut into disks. Anode assemblies were made by assembling a LAN disk and a expanded metal foil disk into a metal cup and crimping the edge.

The LiBr-LiCl-LiF electrolyte was chosen over LiCl-KCl electrolyte because of its proven performance at high current densities[2]. The lithium salts were processed and fused to make the eutectic salt. Marinco OL magnesia powder was blended with salt and fused to make the electrolyte binder mix. This was ground and sieve sized for pelletizing.

Iron disulfide was selected for the cathode because it has high coulombic capacity, high electronic conductivity, good thermal stability, low reactivity with the molten salt, and very low cost. It was blended with salt and fumed silica (Cabosil) and fused, ground and sieve sized to make the cathode powder. This was pressed along with the electrolyte on a 60 ton mechanical press to make two layer pellet disks.

Heat pellets consisting of a mixture of 84% iron powder and 16% potassium perchlorate powder (299 c/g) were pressed in similar manner. A typical cell is depicted in Figure 1.

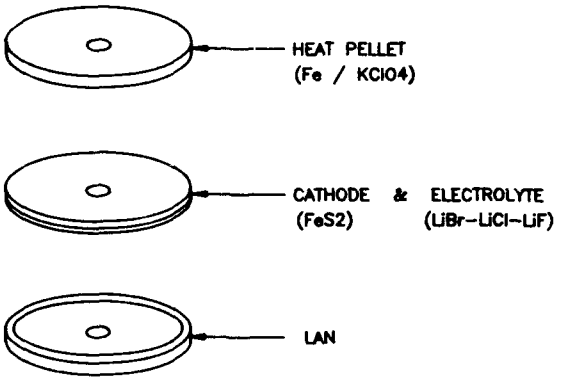

Figure 1: LAN/FeS_2 Cell Construction

A series array of cells with power leads was stacked on a mandrel rod as shown in Figure 2. The stack was wrapped with ceramic fiber paper (Fibrefrax) and glass tape and assembled into a steel case. A heat paper fuse strip consisting of a mixture of zirconium powder, barium chromate and ceramic fibers was placed down the center hole for ignition. A cover assembly with leads, igniter assembly and thermal insulation was welded into the case to complete the battery as depicted in Figure 3.

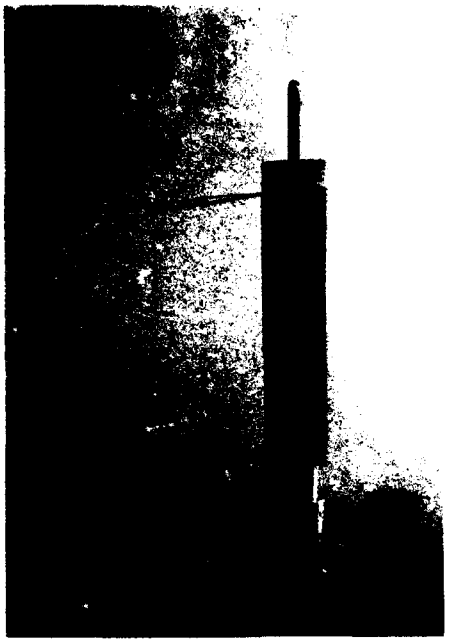

Figure 2: Short Life Battery Cell Stack Assembly

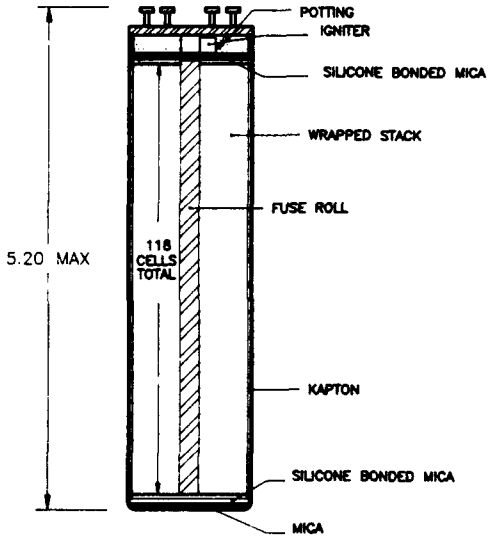

Figure 3: Section View of Improved Short Life Battery

Batteries were assembled and tested to establish a baseline performance. They were conditioned for a minimum of 4 hours at temperature and then removed and activated within 3 minutes in room ambient conditions. A constant load of 4200 W was applied after 0.5 second. The test station consisted of a Compaq 286 microcomputer controlling four Transistor Devices model DLR-400-15-2500A dynamic loads connected in parallel. Electrical performance data were acquired by the computer and stored on the hard disk drive.

Studies to reduce the cell component thickness and to optimize the battery design were conducted concurrent with the testing of baseline design batteries. Thin cells were tested between the heated platens of a conventional cell tester[3] located in a glove box with argon atmosphere. The major emphasis was LAN processing and component thickness reduction since it was calculated that 0.08 mm of LAN is sufficient to meet the capacity requirements, and the LAN assembly was 0.38 mm thick. Improvements in the designs of cell, stack and hardware were combined to make the final battery design. A design verification test (DVT) lot of nine batteries was assembled. Non-operating shock and vibration tests were performed. Four of the batteries were then activated and electrically discharged.

Results and Discussions

Approximately twenty batteries with 100 cells each were assembled using hardware and construction of an existing production design. These were tested to establish a baseline design representing State-Of-The-Art performance. The baseline design weighed 0.68 kg, and was 4.3 cm (1.7") in diameter and 17.5 cm (6.9") high. The best performance of batteries after temperature storage at extremes of -20 °C and +55 °C was 17 seconds life average to 150 volts minimum under a 4200 watt load (3.2 A/cm^2). The power and energy densities were 16.5 kW/l and 6.2 kW/kg and 78 Wh/l and 29 Wh/kg. The average discharge voltage for the first ten seconds was 185 volts for GS-17 (-20 °C) and 190 volts for GS-17 (+55 °C).

An improved short life battery design was developed. As a result of the anode development, we were able to reduce the thickness of the LAN assembly from 0.38 mm (0.015") to 0.20 mm (0.008"). This was accomplished by reducing the thickness of the iron cup, the wire screen, and the LAN. Single cells were tested to verify adequate capacity. The two layer pellet was also reduced in thickness. Consequently the heat pellet thickness could also be reduced because the cell mass to be heated was less. However, the heat pellet became so thin that many were broken during manufacturing and handling. Furthermore, there was concern that non-ignition might be a problem. Therefore we decided to use a thick pellet every two cells of the design. Figure 4 is a sketch showing the improvements in cell component thicknesses. By putting the igniter in the potting below the cover, and removing some insulation from above and below the cell stack, the battery height was reduced to less than 13.2 cm (including terminals). Because of the reduction in cell thickness, 118 cells now fit into the battery.

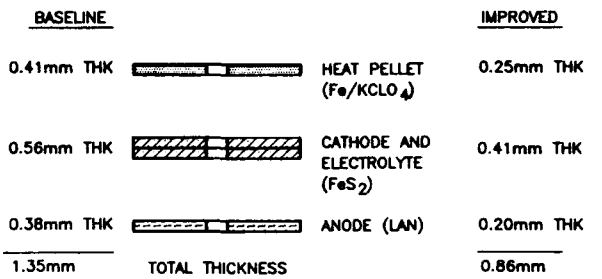

Figure 4: Comparison of Baseline and Improved Cell Component Thicknesses

Table 2 compares the improved battery design with the baseline battery design. The volume and weight of the improved design were reduced by 31% and 33% respectively. A photograph comparing the improved battery with a standard 9 V battery is shown in Figure 5.

Table 2: Comparison of Baseline and Improved Battery Designs

	Baseline	Improved
Diameter	4.3 cm (1.7")	4.1 cm (1.6")
Height	17.5 cm (6.9")	13.1 cm (5.15")
Weight	0.68 kg (1.5 lb)	0.48 kg (1.0 lb)
Total Number of Cells	100	118
Pulse Load	4200 W	4200 W
Nominal Current Density	3.2 A/cm^2	2.1 A/cm^2
	(20.5 A/in^2)	(13.2 A/in^2)

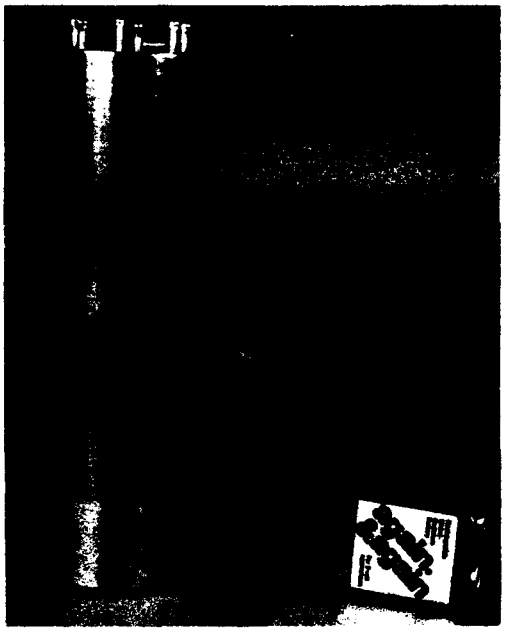

Figure 5: Short Life Thermal Battery

The DVT's were tested, and the results are shown in Table 3. After non-operating shock and vibration tests, the batteries were activated. All four units had a 15 second life to 150 V minimum under a 4200 W load. All electrical requirements were met with the exception of activation. This was undoubtedly due to placing one heat pellet every two cells versus one heat pellet per cell. The power and energy densities were 24.1 kW/l (46% improved) and 8.8 kW/kg (41% improved) and 101 Wh/l (29% improved) and 37 Wh/kg (28% improved). The voltage versus time plot of SL-37 and SL-45 is shown in Figure 6. The average discharge voltage for the first ten seconds was 215 V for SL-37 (-20 °C) and 227 V for SL-45 (+55 °C). This is an 18% higher average voltage than the baseline design.

Table 3: Results of Design Verification Tests

SERIAL NUMBER	SL-37	SL-40	SL-43	SL-45
Conditioning Temperature	-20°C	-20°C	+55°C	+55°C
Peak Voltage	248.2	254.4	254.6	249.1
Rise Time to 150 VDC (Sec)	0.26	0.26	0.31	0.24
Life to 150 VDC (Sec)	15.1	15	15.3	15.1
Life to 200 VDC (Sec	11.9	12.1	13.5	13.1
Voltage at 10.5 (VDC)	206.3	207.6	217.5	215.5
Current at 10.5 Sec (Amps)	20.6	20.5	19.6	19.7

NOTE: 1. Three impact shocks of 100 G applied along longitudinal axis in forward and aft direction for 11 +/- 1 milliseconds.

2. Random vibration applied according to the following ranges for one hour:

Frequency	Power Spectral Density (G^2/Hz)
20 TO 309	0.014
309 TO 1026	Increasing at 3 dB per octave
1026 TO 1126	0.043

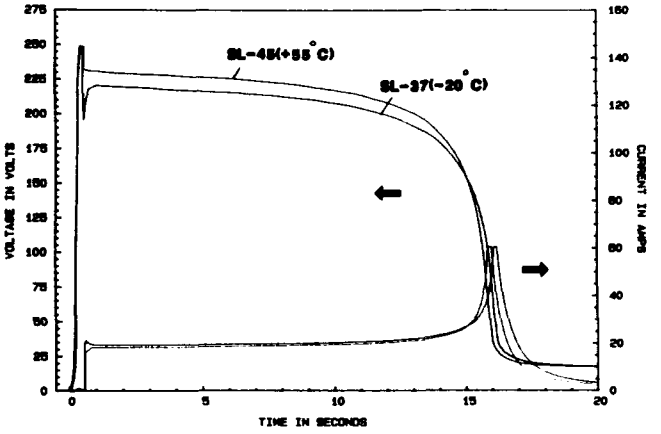

Figure 6: Short Life Battery Discharge Profile

Conclusions

A short life high voltage LAN/FeS_2 thermal battery with ultra high power density was developed for a sonobuoy application. The battery operates at over 200 V and provides a constant 4200 W for 15 seconds at a power density of 3.6 W/cm^2 and an average current density of 2.1 A/cm^2. By developing very thin cell components a 36% net decrease in cell thickness was achieved. Over 40% improvement in power density and over 25% improvement in energy density were achieved over the baseline design. The final battery design achieved power densities of 8,750 W/kg and 24,100 W/l. Energy densities demonstrated were 37 Wh/kg and 101 Wh/l.

Acknowledgement

This work was sponsored by the Naval Surface Warfare Center under the High Energy Battery Project (Contract N60921-92-C-0072).

References

1 Winchester, C.S., The LAN/FeS_2 Thermal Battery System, Proc. of the 30th Power Sources Symposium, pp 23 - 27, 7 - 12 Jun, 1982

THERMAL BATTERY ACTIVATION AND PERFORMANCE UNDER CRYOGENIC CONDITIONS

Joe Wells and Charley Lamb
Eagle-Picher Industries, Inc.
Electronics Division, Couples Department
"C" & Porter Streets
Joplin, Missouri 64801

Introduction

Thermal batteries have a long history of storage and operation at wide temperature extremes in addition to withstanding severe environmental and dynamic conditions without maintenance. These characteristics have made them the battery of choice for most missile and ordnance applications plus evolving new military and commercial applications. Their ability to function at typical military temperatures of -65 °F to +165 °F (-54 °C to +73 °C) is well known. This study evaluated the feasibility of battery mechanical/hermetic integrity, battery activation, and battery function at extremely low temperatures and in combination with low pressure. This includes the viability of both ignitor (or squib) and battery operation at stabilized cryogenic temperatures by immersion in liquid nitrogen at -321 °F (-196 °C). This type of low temperature, in combination with low pressure (10^{-5} torr) would be experienced in a deep space environment. Batteries evaluated were standard Li(Si)/LiCl-LiBr-LiF/FeS_2 designs. The ignitors were production models qualified to MIL-STD-1512.

Background

This paper explores the effects of cryogenic conditions on three major areas which are critical for thermal battery performance. The first was a study of typical materials used in thermal battery construction, and their ability to withstand thermal shock and the low temperature regime. Second, ignitor or squib function and thermal battery pyrotechnic materials were investigated at stabilized Liquid Nitrogen (LN_2) temperatures. The third area was determining the effects of cryogenic conditions and low pressure on battery performance characteristics such as risetime, peak voltage, and battery life.

Experimental

Hermeticity

Glass-to-metal seals using Corning® type 9013 glass beads and 52 iron/nickel alloy terminals per MIL-I-23011 in 304 stainless steel base materials have been the standard in thermal battery designs for many years. Thermal batteries typically require leak rates in the range of 1×10^{-4} to 1×10^{-5} cc of helium /second at one atmosphere differential pressure. This is checked via a timed pressurization and subsequent immersion in hot water. Some new designs require smaller leak rates of 1×10^{-6} to 1×10^{-7}, which dictate the use of helium mass spectrometers. The first experiment was to insure the hermetic seal would not be damaged during exposure to the extremely low temperature or the associated thermal shock of immersion in LN_2 from room temperature equilibrium. A group of 10 thermal battery covers (or headers) were serialized and measured for fine leak rate on a DuPont Model 120 SSA Leak Detector. These 10 room temperature headers were then individually immersed in liquid nitrogen (LN_2) and allowed to stabilize at the LN_2 temperature of -321 °F (-196 °C), which took 4 to 5 minutes. They were then removed from the LN_2 and allowed to return to room temperature. This process was repeated 9 more times for a total of 10 thermal shocks on each header. All 10 headers were then re-checked and the leak rates recorded. The leak rates stayed extremely low and are very near the detection limit of this type of equipment. No specimen showed any significant change in its leak rate as shown in Table 1 below.

Table 1. Header Leak Rate Data

Specimen Number	Pre-Thermal Shock Leak Rate*	Post-Thermal Shock Leak Rate*
1	1.59×10^{-10}	3.19×10^{-10}
2	3.19×10^{-10}	1.59×10^{-10}
3	3.19×10^{-10}	3.19×10^{-10}
4	6.36×10^{-10}	9.6×10^{-10}
5	1.59×10^{-10}	1.59×10^{-10}
6	1.59×10^{-10}	1.59×10^{-10}
7	3.19×10^{-10}	1.59×10^{-10}
8	7.95×10^{-10}	9.6×10^{-10}
9	3.19×10^{-10}	3.19×10^{-10}
10	7.95×10^{-10}	1.92×10^{-9}

* cc of helium/second at 1 atmosphere differential pressure

Pyrotechnics

The second phase of the evaluation was to insure that the ignitors and the pyrotechnic heat powder would function properly at these low temperatures. Ignitors selected for this testing are fully qualified to MIL-STD-1512 and are manufactured by Eagle-Picher (Model EP-360). A comparison of ignitor activation time at +165 °F (+74 °C) and -65 °F (-54 °C) to that at -321 °F (-196 °C) was performed on 30 ignitors. One third of the ignitors were stabilized at +165 °F for 2 hours, and then activated inside the temperature chamber. They were activated via a normal 3.5 Amp/20 millisecond input to the 1.0 ± 0.1 ohm bridgewire. The average activation time was 5.10 milliseconds at +165 °F. Due to the 3.5 Amp limit on the input current and the nominal 1 ohm bridgewire resistance, the voltage applied to the ignitor is approximately 3.5 volts. Once the bridgewire burns open and the ignitor functions, the remainder of the 20 millisecond all-fire pulse is still being applied. This causes the applied voltage to increase dramatically and go off scale. This sharp voltage increase gives the point of ignitor function as shown in Figure 1. This

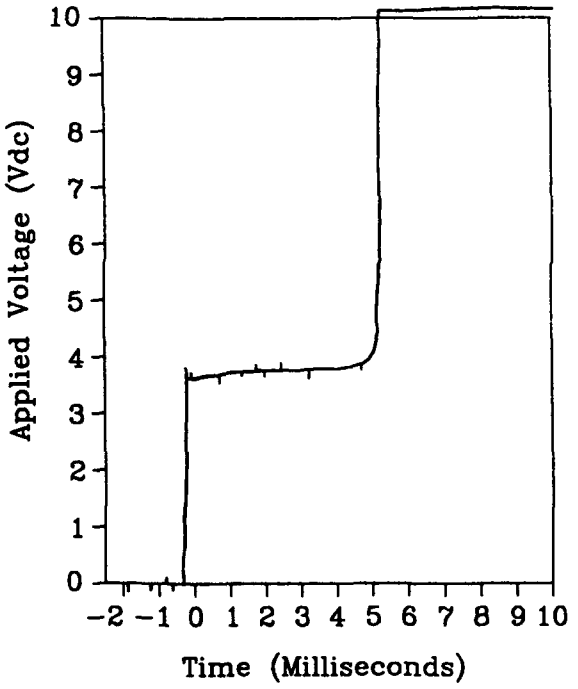

Figure 1. EP-360 Activation Time (+165 °F)

test was repeated on 10 ignitors stabilized at -65 °F for 2 hours, and also activated inside the temperature chamber. They were activated in the same manner via a 3.5 Amp/20 millisecond input to the 1.0 ± 0.1 ohm bridgewire. The average activation time was 5.42 milliseconds at -65 °F. A typical "trace" is shown in Figure 2. The remaining 10 ignitors were submerged in LN_2 for 2 minutes (stabilization occurred after 30-45 seconds), and then activated while immersed. Again, the normal 3.5 Amp/20 millisecond input to the 1.0 ± 0.1 ohm bridgewire was used. A typical "trace" for -321 °F is shown in Figure 3. The average activation time was only 5.69

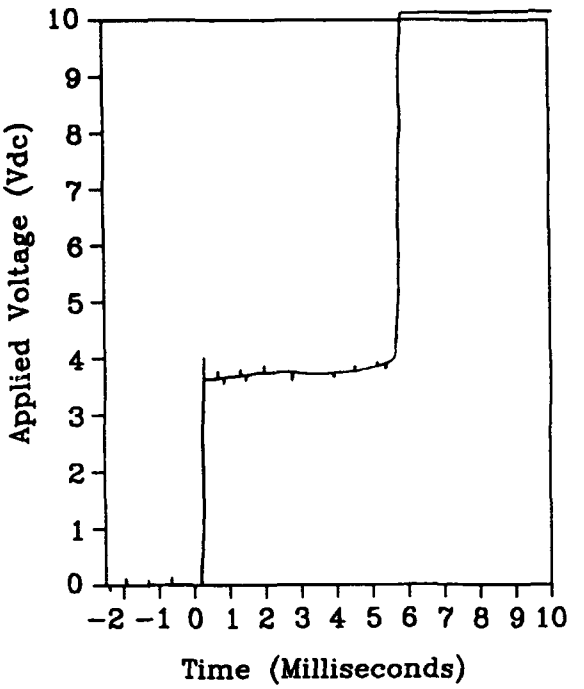

Figure 2. EP-360 Activation Time (-65 °F)

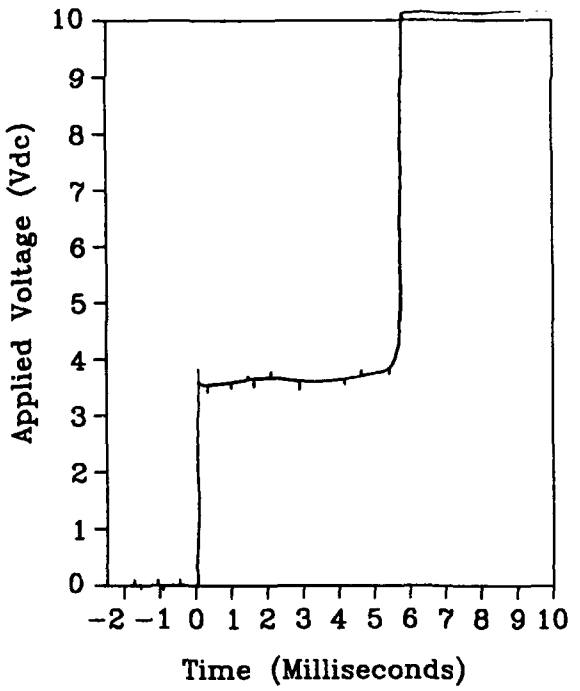

Figure 3. EP-360 Activation Time (-321 °F)

milliseconds at -321 °F and increased by only 0.27 milliseconds from a typical cold military temperature. All 30 squibs tested under these conditions activated. The results and statistical analysis are summarized in Table 2.

Table 2. EP-360 Activation Time vs. Temperature

Sample No.	Activation time at +74°C (+165°F) (in msec)	Sample No.	Activation time at -54°C (-65°F) (in msec)	Sample No.	Activation time at -196°C (-321°F) (in msec)
1	5.44	11	5.48	21	5.68
2	5.00	12	5.48	22	6.08
3	4.80	13	5.52	23	5.84
4	4.88	14	6.00	24	5.60
5	5.24	15	5.32	25	5.28
6	5.00	16	5.52	26	5.36
7	4.96	17	5.00	27	5.48
8	5.00	18	5.40	28	5.24
9	5.28	19	4.92	29	6.76
10	5.44	20	5.52	30	6.00
$\bar{X}$ = 5.10 msec		$\bar{X}$ = 5.42 msec		$\bar{X}$ = 5.69 msec	
σ_{n-1} = .23 msec		σ_{n-1} = .30 msec		σ_{n-1} = .37 msec	

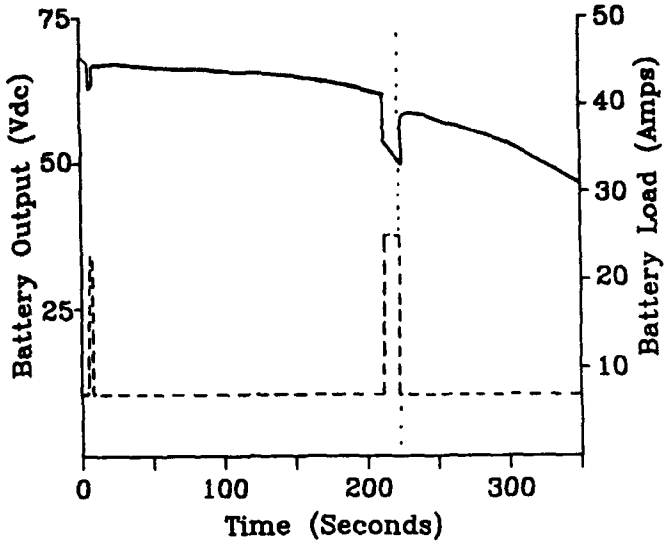

Figure 5. EAP-12053A 6.8 Amp Discharge (-65 °F)

Battery Performance

Having shown that the battery materials could survive the thermal shock and that the ignitors would activate, the next step was to proceed into the effects on battery activation and performance. The test vehicle battery was the EAP-12053A. It is a 2.50 inch diameter by 4.16 inch tall design weighing 2.0 pounds. It is a nominal 60 Vdc output with a voltage range of 72.0 to 45.0 Volts. The EAP-12053A is designed to carry a 6.8 ampere baseload with pulses to 35 amperes for a 222 second mission.

Baseline performance testing was performed on batteries at both +165 °F and -65 °F with the typical discharge curves shown in Figures 4 and 5 respectively. The battery is well heat balanced with both the hot and cold stabilized batteries displaying lives of approximately 360 seconds.

Batteries from the same manufacturing day were then subjected to a series of tests to evaluate performance at LN_2 extremes. Six batteries were immersed in LN_2 for 2 hours with stabilization occurring after approximately 45 minutes. Two batteries were activated and discharged while submerged in the LN_2. Upon activation, the battery cases began to boil the LN_2. Due to the lower starting temperature, the risetimes were slowed by approximately 350 milliseconds and the peak voltages were suppressed by around 4 volts compared to the -65 °F results. A typical discharge curve is shown as Figure 6, with results from all tests summarized in Table 3. The extremely low temperature start and continued heat loss during

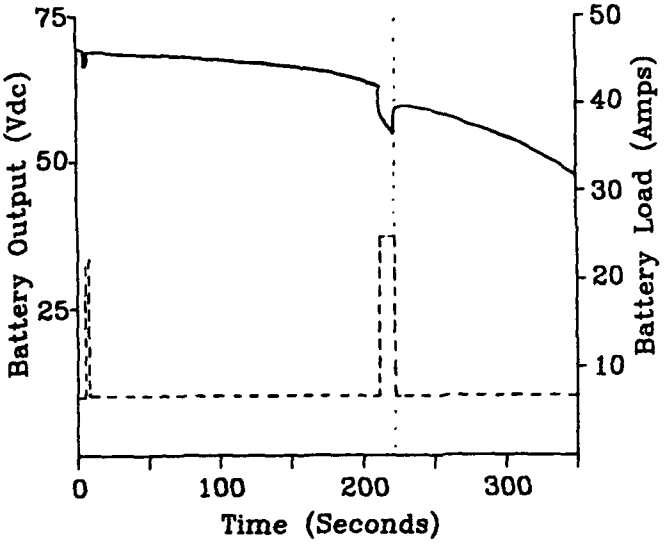

Figure 4. EAP-12053A 6.8 Amp Discharge (+165 °F)

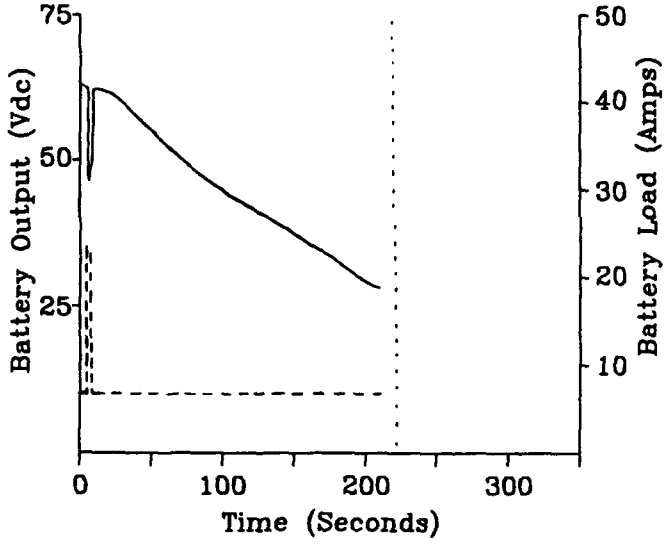

Figure 6. EAP-12053A 6.8 Amp Discharge (-321 °F)

Table 3. EAP-12053A Performance Summary

Temperature	Risetime (msec)	Peak Voltage (Vdc)	Life to 45 Vdc (seconds)	Specific Energy (W-Hr/lb)
+165 °F	.390	69.80	366	21.35
-65 °F	.530	67.45	362	21.12
-321 °F	.880	63.20	98	5.72
-321 °F/ Altitude	.840	63.80	130	7.58
-321 °F/ Altitude/ 750 mA Load	.280	70.40	1673	10.46

battery function (via boiling the LN_2) caused the battery life to 45 volts to be shortened to 98 seconds. An improvement was shown when batteries were removed from the LN_2 and placed into a 10^{-5} torr vacuum. As shown in Figure 7, the battery life was still suppressed compared to -65 °F stabilization, but improved due to the elimination of conductive heat losses.

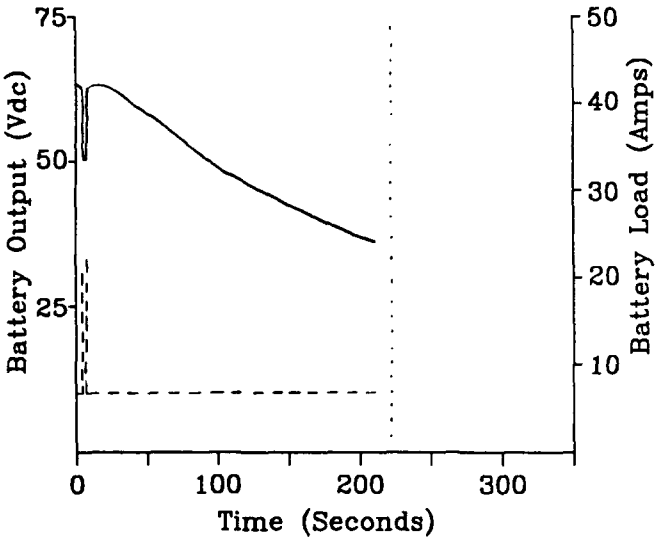

Figure 7. EAP-12053A 6.8 Amp Discharge (-321 °F/10^{-5} torr)

A final battery test was performed on 2 units by removing them from the LN_2, placing them into a 10^{-5} torr vacuum, and testing at a reduced load of 0.750 amperes. The reduced load allowed a higher peak voltage of 70.4 Vdc and an increased life of 1673 seconds to 45 volts. These units were discharged at the 0.750 amp load down to 5 volts and functioned for over 2500 seconds. A typical discharge curve is shown as Figure 8 with the results summarized in Table 3.

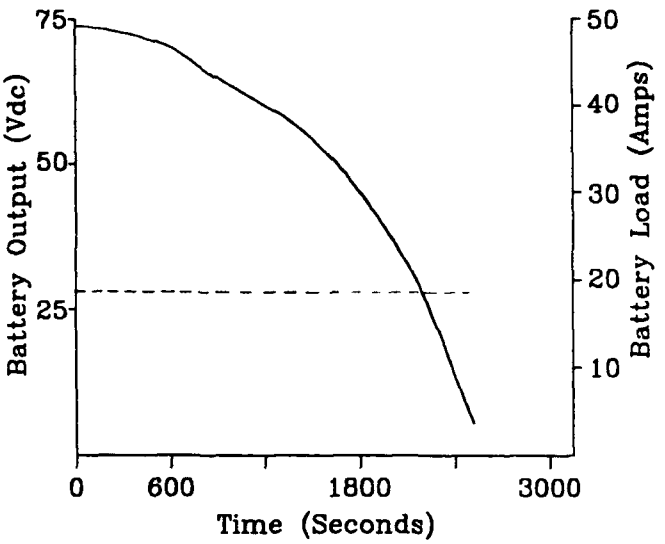

Figure 8. EAP-12053A 0.750 Amp Discharge (-321 °F/10^{-5} torr)

Conclusions

Thermal batteries have added to their proven robustness by the results of this testing. Standard thermal battery hardware has proven its ability to withstand repeated extreme thermal shocks of immersion in LN_2 which are much worse than any foreseen field conditions. Typical thermal battery ignitors have demonstrated their ability to activate during LN_2 immersion and the pyrotechnic material in the battery was also shown to activate with the battery at stabilized LN_2 conditions. The performance of the battery design was shown to be viable under these conditions. The EAP-12053A battery displayed its ability to function at full military temperatures as well as at cryogenic conditions. The lower stabilizing temperature did reduce the battery life but the energy density and power density are still quite good at these lower temperatures.

LITHIUM/MANGANESE DIOXIDE FOIL CELL BATTERY DEVELOPMENT

Thomas B. Reddy and Peter Rodriguez
Power Conversion, Inc., Elmwood Park, NJ

Introduction

Power Conversion, Inc. is carrying out a program to develop a high-rate, high-capacity lithium/manganese dioxide battery in low-cost packaging to increase significantly the cost effectiveness of lithium primary batteries. The initial effort has focused on producing a prismatic cell in a foil-laminate package designed to replace the standard D-size cylindrical cell in the BA-5590/U battery. These cells have been sized to fit ten units inside the BA-5590 battery envelope to form a BA-X590 lithium/manganese dioxide battery. Figure 1 shows a projection of this cell. This design is capable of providing significantly higher capacity than the current LiS02 BA-5590 because of the intrinsically higher capacity per unit volume of Li/MnO2 and because of the more efficient packaging of prismatic cells in a prismatic case. This paper describes the materials evaluation, hardware development, component optimization and cell development phases of this program. Although this paper describes the effort carried out to develop a cell for the BA-X590 battery, this technology may be readily adapted to a variety of other military and commercial applications.

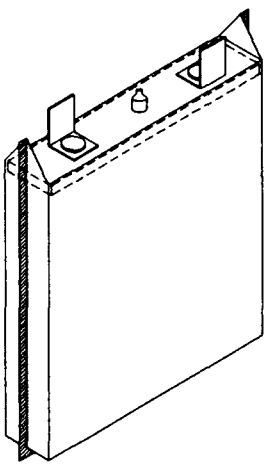

Figure 1: Foil Cell Design Dimensions When Folded: 2.82 high by 2.65 in. wide x0.50 in. thick

Materials Evaluation/Hardware Development

PCI has evaluated eight different types of foil laminates for electrolyte leakage to select a suitable material. Pouches have been formed of approximately the same area as the foil cell, filled with 5 ml. of electrolyte (Lithium Triflate in Propylene Carbonate/Dimethoxyethane), weighed and stored for thirteen weeks at +130°F (54.4°C), the storage conditions specified for the T-test requirement of MIL-B-49458 for Li/MnO2 batteries. Test results are shown in Table 1 in terms of percent weight loss of electrolyte after storage of the seven types of laminate which survived this test. The results show the average loss for three samples of each type tested. Type VI was tested in two different series and the weight loss data show good agreement between the two tests. Five materials show a weight loss of less than 1%, after thirteen weeks, the electrolyte weight loss requirement called out in Paragraph 4.7.12 of MIL-B-49458 for four weeks' storage at +130°F (+54.4°C). Type II and VIII are currently being evaluated in cell hardware. Type II was selected because of its high bond strength to the polypropylene header material as well as its low leakage rate. The Type VIII material is under evaluation because of its very low electrolyte leakage rate.

TABLE 1
Comparison of Electrolyte Loss From Foil Laminate Pouches After Thirteen Weeks' Storage at +130°F

Laminate Type	Series No.	Percent Wt. Loss of Electrolyte
I	1	0.910
II	1	0.655
III	3	1.010
V	3	1.228
VI	3	0.486
VI	4	0.538
VII	4	0.382
VIII	4	0.161

Other hardware components consist of a polypropylene header with an electrolyte fill port and holes for riveted electrical feed-throughs. Polypropylene was selected because of its low cost and higher melting point than polyethylene. Initially, these parts have been machined but will be injection molded in production. See Figure 2 for the header assembly. The foil laminate material is cut to the desired size, a hole punched for the fill port and then heat sealed to the header using a specially designed fixture. Holes are then punched in the foil laminate for the riveted feed-throughs which are adhesive-bonded in place with tabs on top and bottom of the header. Tabs from the electrode array are welded to the internal tabs from the rivet. The foil laminate is then folded around the electrodes and seams formed on three sides using a heat sealer. Ultimately, this sealing operation will be carried out in one step with a specially designed tool. Following assembly of the dry package, it is evacuated and filled with a preset volume of electrolyte on an automated electrolyte fill machine. The fill tube is then welded shut, the cell predischarged and tested.

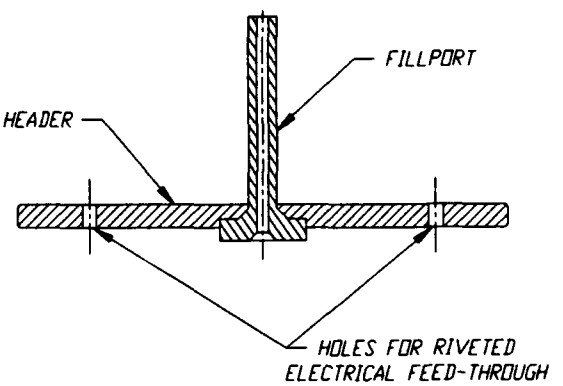

Figure 2: Polypropylene Header Assembly for Foil Cell

Component Optimization Studies

PCI has used both C and D sized cylindrical cells to carry out component optimization studies to select materials for use in the foil cell battery. Table 2 delineates the materials and components which have been evaluated. PCI has evaluated two types of Chemical Manganese Dioxide (CMD) in comparison to an Electrolytic Manganese Dioxide (EMD) and has selected one type of CMD for use since it provides the best overall performance at both +21 and -20°C. Several graphites have been evaluated and one selected based upon the improved voltage response observed when this material is employed. Similarly, several types of expanded metal current collector have been employed (stainless steel vs. aluminum) with two geometries evaluated in the latter material. Table 3 shows typical discharge data at 2 amps and 70°F for Li/MnO2 D cells using two types of MnO2, two types of graphite additive and two types of aluminum current collector. Comparing Row 1 to Row 4, it is evident that the use of the special grade of graphite increases the capacity, operating and start-up voltages with the CMD-Type I. The use of CMD-II gives higher capacity but lower start-up and operating voltages as seen by comparing Rows 1 and 3. The use of a pulled screen gives higher start-up voltage, capacity and operating voltage compared to the standard screen (Row 2 vs. Row 3).

TABLE 2
Materials and Components Evaluated

Cathode Materials
Type of MnO2 (CMD, EMD)
Type of Conductive Additive
Grid Material/Geometry

Anode
Type of Current Collector

Separator
Material (PE, PPE)
Process

Electrolyte
Binary vs. Ternary Solvent Mixture
Type of Salt (LiTriflate, LiImide, LiAsF6, LiClO4)

TABLE 3
Discharge Data for Li/MnO2 D Cells Employing Different Components
All Cells Discharged at 2.00 Amps at +70°F

Type MnO2	Grid Type	Graphite Type	No. Tested	Avg. OCV ± Std Dev. (Volts)	Avg. CCV ±1 Std Dev. at 5 Sec. (Volts)	Capacity to 2.0V Cut-Off ±1 Std. Dev. (amp-hrs.)	Avg. Voltage ±1 Std Dev. (Volts)
CMD-I	Al-Std	Special	3	3.46±0.01	3.14±0.03	7.02± 0.10	2.56±0.03
CMD-II	Al-Pulled	Special	4	3.42±0.01	3.06±0.04	7.78±0.17	2.52±0.03
CMD-II	Al-Std	Special	3	3.37±0.10	3.02±0.04	7.65±0.08	2.47±0.02
CMD-I	Al-Std	Std.	3	3.42±0.03	3.09±0.03	6.60±0.17	2.52±0.03

Based on this discharge data, the use of CMD-Type II in conjunction with the special graphite and pulled aluminum screen provides the highest capacity with good start-up and operating voltages. PCI has also evaluated several types of separator to reduce the cost for this component. Table 4 presents discharge data for Li/MnO2 C cells using two types of separators under two sets of test conditions: 510 milliamp discharge at +70°F (21°C) and 170 milliamp discharge at -20°F (-29° C). At room temperature, the average capacity and start-up voltage are higher for the cells with the Type B material. It is significant to note that these cells operated at -20°F (-29°C) since the Li/MnO2 system is normally rated only to -4°F (-20°C). When discharged at 170 milli-amps, the cells with the Type B separator provided essentially the same start-up voltage and 93% of the capacity observed with the Type A material.

TABLE 4
Discharge Data for Li/MnO2 C Cells Employing
Experimental Separators at Two Test Conditions

Type of Separator (PPE)	Drain Rate (mamps)	Test Temp (F)	No. Tested	Average OCV ±1 Std Dev Volts	Average CCV ±1 Std Dev. at 5 sec. (Volts)	Capacity to 2.0V Cut-Off ±1 Std Dev. (amp-hrs)
Type A	510	+70	3	3.16±0.18	2.58±0.17	2.84±0.14
Type B	510	+70	3	3.34±0.02	2.77±0.06	3.18±0.02
Type A	170	-20	3	3.37±0.01	2.71±0.04	1.98±0.59
Type B	170	-20	2	3.36±0.03	2.72±0.06	1.84±0.64

This data should provide the basis for a cost saving in lithium battery manufacture since the Type B material is significantly less expensive than the separator normally used in Li/MnO2 cells.

Using the materials and components selected for use in the foil cell program, PCI has manufactured and tested D cells. Typical D cell discharge curves are seen in Figures 3 and 4. At 70°F (21°C), a capacity of 9.5 amp-hours at an average voltage of 2.64 volts was achieved at the 2 amp discharge rate (Figure 3). At -4°F (-20°C), a capacity of 6.95 amp-hours with an average of 2.19 volts is obtained on 2 amp discharge. The former value is comparable to that obtained from competitive products while the latter value is twice that obtained by other manufacturers.

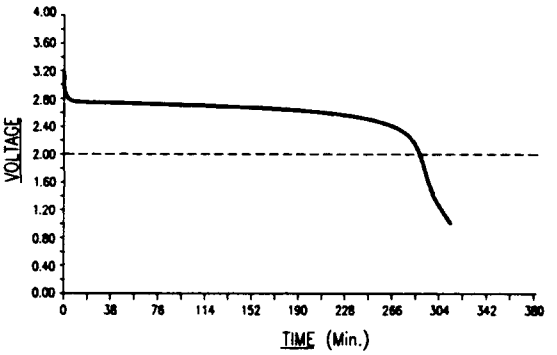

Figure 3: Discharge Curve for Li/MnO_2 D-Cell at 2.00 Amps and +70°F (21°C) Capacity = 9.5 Amp-Hrs.

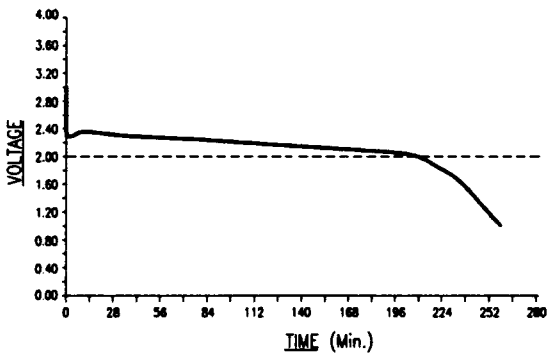

Figure 4: Discharge Curve for Li/MnO_2 D-Cell at 2.00 Amps and -4°F (-20°C) Capacity = 6.95 Amp-Hrs.

Foil Cell Development

PCI's foil cell development has evolved during the course of this program. Initially, cells were fabricated using a parallel plate design but this was found to be labor intensive in assembly. PCI has developed a rapid electrode assembly procedure which it believes to be amenable to automation. Figure 5 shows a discharge curve for a prototype foil cell at the 0.500 amp rate at room temperature. A capacity of 10.2 amp-hours at an average voltage of 2.45 volts was obtained with this cell which used a binary electrolyte. A similar cell was discharged at 1.00 amps and a capacity of 10.1 amp-hours was obtained at an average voltage of 2.25 volts, as seen in Figure 6. The same type of cell was constructed using a ternary electrolyte and discharged at the 1.00 amp rate, giving a capacity of 10.1 amp-hours, as seen in Figure 7. In this case, the average voltage was 2.45 volts, 0.20 volts higher than seen in Figure 6, reflecting the higher conductivity of the ternary electrolyte which is twice that of the binary solvent mixture.

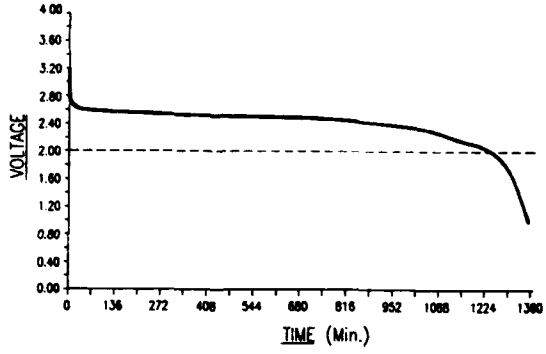

Figure 5: Discharge Curve for Foil Cell at 0.500 Amps and +70°F Average Voltage= 2.45v. Capacity = 10.2 Amp-Hrs. Electrolyte Type 1

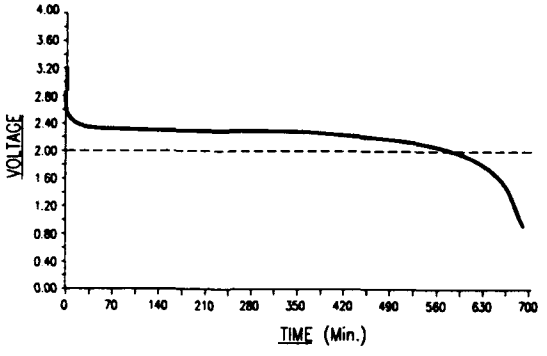

Figure 6: Discharge Curve for Foil Cell at 1.00 Amps and +70°F Average Voltage= 2.25v. Capacity = 10.1 Amp-Hrs. Electrolyte Type 1

In order to simulate actual use inside a battery case where the individual cells will be held in compression, discharge at the 2 amp rate has been carried out with the cell held in compression between parallel plates. Figure 8 shows the discharge curve for this cell which provided a capacity of 11.1 amp-hours at an average voltage of 2.36 volts. The higher capacity obtained at the 2 amp rate undoubtedly reflects the effect of compression on cell performance.

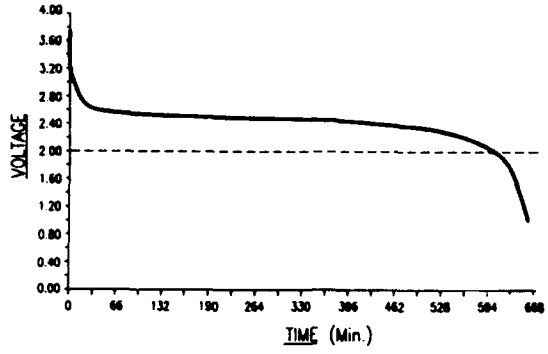

Figure 7: Discharge Curve for Foil Cell at 1.00 Amps and +70°F Average Voltage= 2.45v. Capacity = 10.1 Amp-Hrs. Electrolyte Type 2

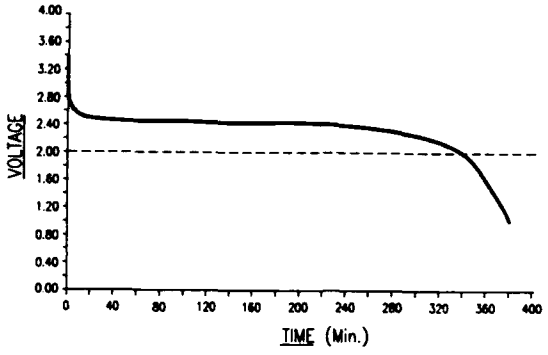

Figure 8: Discharge Curve for Compressed Foil Cell at 2.00 Amps and +70°F Average Voltage = 2.25v. Capacity = 11.1 Amp-Hrs. Electrolyte Type 2

The objective of this program was to develop a cell capable of providing a capacity of 12.5 amp-hours when discharged at 2 amps at 70°F (21°C). This would provide a 78% increase in capacity over the comparable Li/SO2 BA-5590/U. To date, PCI has achieved 89% of program objectives and is confident that with further increases in electrode efficiency that all program requirements will be met.

PCI has emphasized optimizing cell performances in this phase of the program and will carry out environmental and safety testing when the current phase is completed.

Acknowledgments

This work was partially supported by the Electronics and Power Sources Directorate, U.S. Army Research Laboratory, Fort Monmouth, New Jersey. PCI wishes to express its thanks to Mr. Michael A. Brundage and Dr. Harold T. Christopher for their support and encouragement in the course of this program.

High-Rate Lithium Manganese Dioxide Cells Using Shut-Down Separaters

Michael Kohlhase, Klaus Schnelder, John Welsh

Hoppecke Batterien
Brilon, Germany

Shut-down separaters have been available for a number of years but their use has generally been limited to the smaller, spiral wound cells for consumer applications. New shut-down separaters have recently been produced experimentally which show promise to be suitable for the larger, more powerful lithium cells as are used in military applications. The hoped for advantage of the new separaters is that they will make the cells inherently safe against external abuse induced by electrical overload and may even give greater protection against mechanical abuse. If these hoped for benefits are achieved, the protection circuits now employed in lithium batteries could be simplified or even completely eliminated and new markets for the larger lithium cells could be opened up where, up to now, safety concerns have restricted their introduction. In particular, the stringent safety requirements for use (and for transportation) in aircraft may be met with less difficulty.

Lithium manganese dioxide cells were used for the experiments, cells with solid cathodes which contain no toxic or corrosive components and are already recognized by IATA as safe enough to be transported in passenger aircraft. Cells were built with standard and shut-down separaters and were subject to a range of overloads: from marginal overloads at high ambient temperatures to low impedence short circuits. Care was taken to simulate the types of fault that could occur in actual use, for example, incorrectly applied loads or intercell short circuits within a battery.

Mechanical abuse tests such as crushing and nail tests were performed, again comparing the standard and the shut-down separaters. In all cases, videos were made to allow detailed observation of the reactions of the cells if they vented.

The results showed the shut-down separaters function as promised. It proved impossible to make the cells to vent by electrical overload. The cells could be discharged at the 3h rate without the shut-down separater cutting in but, if the discharge rate was significantly increased or if the ambient temperature was too high, the cells shut down well before the venting temperature was reached.

This work shows it is possible to make intrinsically safe lithium manganese dioxide cells using shut-down separaters with the one disadvantage that they are one shot devices: once the shut-down separater has operated the cell cannot recover; this is as opposed to the protection by an external PTC which resets once the load has been disconnected. Many battery packs used for military employ non-replaceable fuse links, also one shot devices, and, in these instances, the shut-down separater does not bring any additional disadvantage.

Finally, it is concluded more work needs to be undertaken, in particular, with the vent design. If the cells cannot be made to vent by electrical overload but only by application of external heat or mechanical abuse, what is the best venting pressure/temperature for a cell? There is a case to be argued that higher venting pressures/temperatures reduce the likelihood of inadvertent venting but will still give protection against an uncontrolled rupture of the cell case. However, many more abusive tests must be carried out before a recommendation can be made.

ULTRA HIGH RATE PULSE PERFORMANCE FROM THE PRIMARY Li/MnO_2 BATTERY

A M Jeffery, M J Sidorowicz
Dowty Batteries, Abingdon,
Oxfordshire, England.

Abstract

The high rate lithium/manganese dioxide primary battery is well established in the market as a safe, reliable and high energy density system. However, still higher rates are always in demand particularly in the area of pulsed discharge regimes. The system is ideal for this type of application due to its inherent instant start-up characteristics and its relatively light weight.

An investigation into the effect of increasing cathode surface area on pulse current capability has demonstrated significant improvement particularly at low temperature. Marked improvement in high rate continuous discharge has also been observed.

It has been shown possible to realise these advances in practical cells without compromising safety in any way.

Introduction

There is a perceived market requirement for a safe lithium/ manganese dioxide primary battery capable of very high power densities in the pulse discharge mode (up to 1 Kw/litre). Such a device would offer a viable, lightweight alternative to thermal batteries for some applications whilst allowing 'push-to-test' health checks to be carried out in service, thereby enhancing user confidence. Military applications such as ejector seat actuation and missile launching and guidance systems could be undertaken in addition to high power consumption transmitting devices.

A major limiting factor to the achievement of very high pulse currents is considered to be the kinetics of the manganese dioxide discharge mechanism. Investigations have been carried out to characterise the effect of electrode area and thickness on pulse capability and also on continuous current discharge.

The characterisation was undertaken utilising the Dowty lithium manganese dioxide coil-pack construction D cell, LiM 336H. The safety implications of an ultra high rate system have also been investigated.

Discussion

The mechanical design of the Dowty LiM 336H has been shown to be fully capable of sustaining higher currents, both continuous and pulsed, than those generated by the standard coil pack. The welded electrode tags, electrode current collectors and cell casing have been designed to offer very low electrical resistance and the construction therefore provided a good vehicle for cell build and testing. The venting system is discussed separately in the section on Safety.

Electrolyte formulation can be optimised for high or low temperatures and rates, but the user almost invariably requires operation over a wide range of temperature and often, a discharge regime which features both high and low current. In Dowty's experience, fine tuning of the electrolyte formulation does not affect rate as much as varying the electrode geometry and constitution.

Similarly, the lithium anode is not as limiting a factor as the cathode in the attainment of high discharge current subject, of course, to the usual constraints of electrode balance, geometry and minimal anodic film formation.

The main rate factor limiting pulse current has been established to be the nature and construction of the cathode. The LiM 336H cell utilises chemically precipitated manganese dioxide of high specific surface area. Much has been written on the heat treatment of various manganese dioxides for use in primary lithium cells and the need to optimise this treatment in terms of temperature, duration and environment.[1-3] It is known that the resulting crystal structure is critical in determining the maximum rate of lithium ion insertion and hence charge transfer. This is true not only for continuous discharge but also for high pulse currents, even initial short duration pulses, where there is clearly insufficient time for Li^+ diffusion within the crystal structure to have any influence on rate. The implication is that optimum crystal structure is essential at the electrolyte/MnO_2 interface as well as within the MnO_2 matrix.

Particle porosity is important in that it can provide a very large surface area for Li^+ insertion. However, this surface area is of little value unless it is accessible to electrolyte. For this reason, the mean pore diameter must be large enough such that a significant proportion of the pore volume can be accessed by electrolyte. The actual mean value of pore diameter required depends on the nature of the electrolyte and, in particular, such properties as surface tension.

It is worth noting here that similar considerations apply to the separator construction. Indeed, it has been found advantageous to employ the maximum mean separator pore diameter consistent with the prevention of inter-electrode shorting.

It has been shown that varying particle size distribution has only a limited effect on high current performance.[5] However, different distributions can markedly influence cathode processing parameters which, in turn, affect the overall cathode porosity. The importance of this porosity in the kinetics of the insertion cathode, and hence the efficiency of the discharge reaction has been discussed previously.[6,7]

However, the characteristics of cathode geometry and their effect on pulse rate capability were the focus of attention of this investigation and cells with varying thicknesses of cathode and balanced anode were constructed resulting in different electrode areas for the D-cell coil pack. Clearly, the thinner electrodes resulted in lower theoretical capacities due to the additional separator and current collector requirements but the system capabilities for short duration, high current pulses over a range of temperatures were studied.

Experimental and Results

Performance

Cathodes of three different thicknesses were manufactured which, when formed into D-cell coil packs, produced geometrical area ratios of 1.00, 1.28 and 1.47 when compared with the standard Dowty cell. These were designated LiM 336H, LiM 336XH and LiM 336VH respectively. In each case the lithium anode thicknesses and areas were adjusted to provide electrochemical balance.

To determine pulse capability the three build standards were tested to establish the current obtainable for a single 1 second pulse at about 1.5V which approximates the maximum power obtainable from the cell. The testing was carried out over a range of temperatures from +65°C to -70°C.

The results are displayed in Fig 1 which shows the pulse current plotted against cathode geometrical area ratio for 336H, XH and VH cells.

It is apparent that the thinner, higher surface area cathodes perform significantly better than the standard 336H configuration at all temperatures. The 336VH delivers a 36A pulse at +65°C and even a 6A pulse at -70°C. It is notable that the lower the temperature, the greater is the advantage of the 336VH compared to the 336H and this is shown by the ratio of pulse currents for the two cells next to the profiles for each temperature in Fig 1. At +65°C, the 336VH shows a 26.3% improvement in pulse current whereas at -70°C the increase is 100% resulting in a significant pulse current at useful voltage.

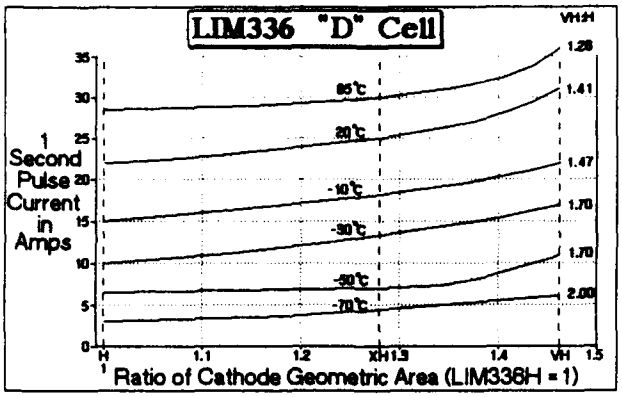

Fig 1: Single Pulse Current

Typical voltage response profiles for the constant current drain from all three cell types are shown in Fig 2 and these illustrate the absence of voltage delay inherent in lithium/liquid cathode systems.

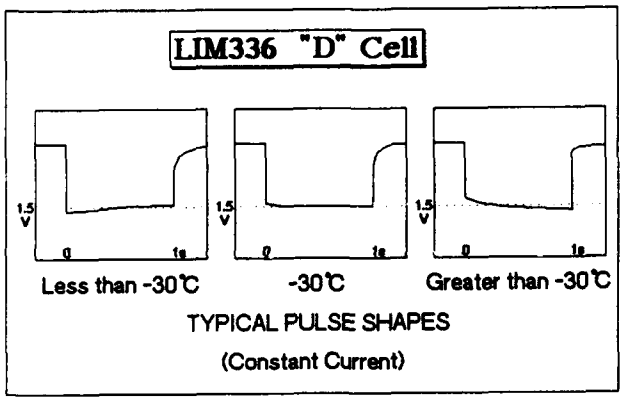

Fig 2: Single Pulse Voltage

It can be seen that for temperatures below -30°C, the cell voltage is rising slightly throughout the 1 second pulse duration, while at -30°C the voltage remains fairly constant and for temperatures above -30°C the voltage exhibits a small decrease. This is thought to be due to the changing balance between cathode polarisation and internal temperature rise resulting from the i^2R heating effect and the exothermicity of the discharge reaction.

At low temperatures, the lower current pulse results in less cathode polarisation and a small temperature rise at the electrode surface produces a slight increase in voltage. At higher temperatures, the magnitude of the current leads to the predominance of cathode polarisation.

These levels of pulse currents are generally sustainable for durations of a few seconds and for frequencies of around one pulse per minute dependent on temperature. For higher pulse durations and frequencies the operating voltage will be lower.

However, as duration and frequency increase for high current pulses, the effects of cell internal heating and temperature rise become more influential in terms of counteracting cathode polarisation. In the limit, this effect is maximised during continuous discharge.

This was investigated by subjecting the three cell types to high rate continuous current at three temperatures. A constant current load of 8.5A to an end point of 1.5V at temperatures of +20°C, 0°C and -15°C was selected. The results are shown in Figs 3,4 and 5 for the three respective temperatures.

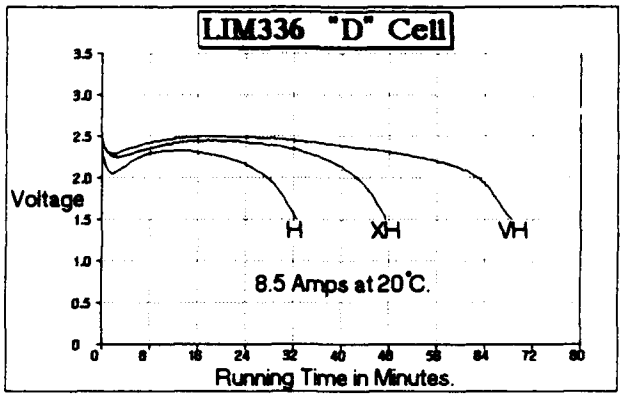

Fig 3: Continuous 8.5A Discharge at 20°C

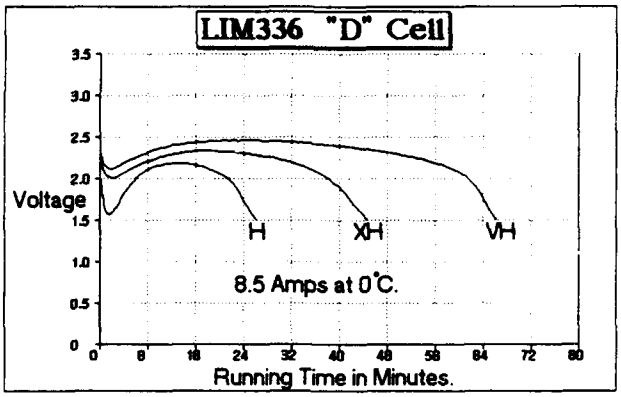

Fig 4: Continuous 8.5A Discharge at 0°C

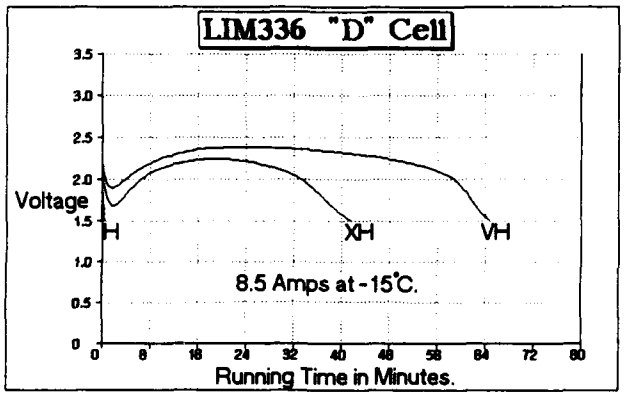

Fig 5: Continuous 8.5A Discharge at -15°C

In all cases the order of discharge duration was VH > XH > H, but the most significant difference was observed at -15°C where the 336H could not sustain the 8.5A load at all whereas the 336VH delivered 9.18 Ah - a duration of 65 minutes.

These results again illustrate the balance between cathode polarisation and internal heating. At -15°C, for example, the 336H suffered cathode polarisation to such an extent and so rapidly that the discharge reaction could not proceed to generate a temperature rise and facilitate further discharge. The 336VH, on the other hand, showed an initial voltage dip to around 1.8V but the reaction proceeded at a sustainable level which induced a rise in temperature to about 60°C by the end of discharge.

The thinner, larger surface area cathode of the 336VH is thus demonstrated to be far superior to the standard cathode at high rate, low

temperature discharge. However, this superiority is offset to some extent by the lower capacity exhibited at moderate rates and temperatures and Fig 6 illustrates this point.

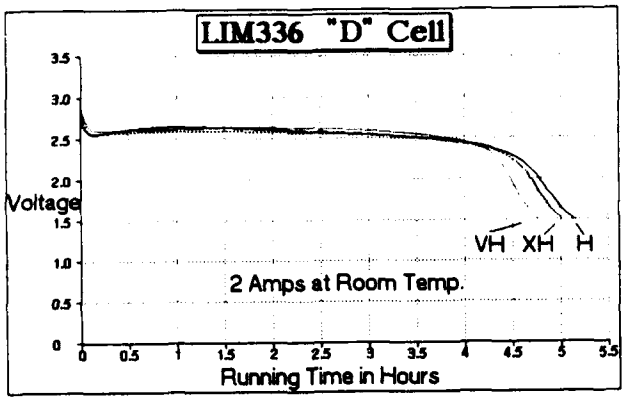

Fig 6: Continuous 2A Discharge at Room Temperature

At 2A constant current and room temperature the order of discharge duration is reversed, H > XH > VH, the actual capacities being 10.2 Ah, 9.9 Ah and 9.6 Ah to an end point of 1.5V.

Safety

In considering the discharge performance of the 336VH in very high pulse or constant current applications, it is recognised that the design must possess fail-safe features to prevent hazardous situations arising from abuse.

A major design feature here is the stainless steel bursting disc which is hermetically welded into the battery case and provides an electrolyte venting path on generation of excess heat. The standard 336H cell contains a disc that vents at a pressure between 200 p.s.i and 250 p.s.i. For the 336VH it was found necessary to lower this pressure to between 150 p.s.i and 200 p.s.i to allow for the faster rate of temperature rise during, for example, short circuit abuse.

The 336VH cell was subjected to a short circuit abuse test through 50 milliohms and Fig 7 shows the current response with time together with the cell case temperature.

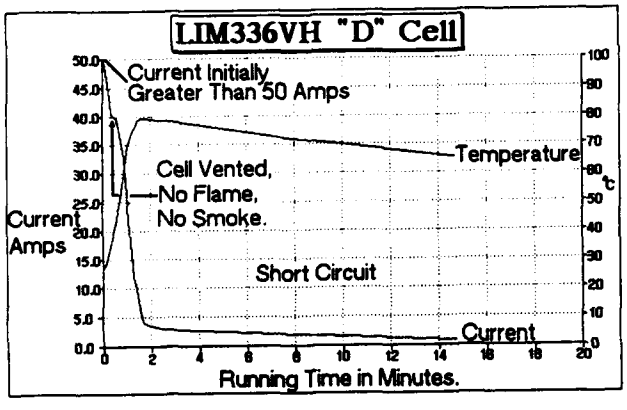

Fig 7: LiM 336VH: Short Circuit

The initial short circuit current was about 70A for a brief period of time but this fell to 40A at about 30 seconds at which point venting occurred with no flame or smoke. The current then continued to fall rapidly for the next 60 seconds reaching 3A, and thereafter a slower decline ultimately reaching zero after about 35 minutes. Meanwhile, a maximum case temperature of 80°C was reached after 90 seconds and declined thereafter to ambient temperature.

A 2A constant forced discharge test was also applied to the 336VH cell and Fig 8 shows the cell voltage and case temperature with time.

All Dowty high rate lithium/manganese dioxide cells are fitted with a copper strip anode current collector. During forced discharge, the anode is completely discharged and no elemental lithium remains at a cell voltage of 0V. At this point, anodic copper dissolution commences and the resulting copper ion deposits on the cathode in the form of dendrites. These dendrites grow into copper "fibres" and ultimately penetrate the separator pores and connect with the original copper strip. This provides an electronically conducting path for the continuing forced current to pass safely without any exothermic electrochemical reactions. The cell is thus left in a permanently safe condition.

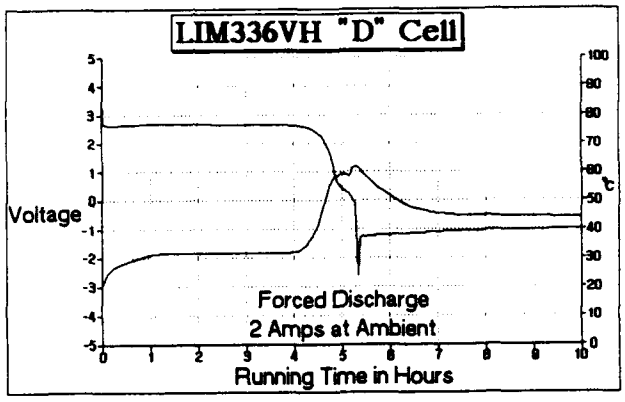

Fig 8: LiM 336VH: 2A Forced Discharge

The effect of this process, which renders the use of a shunt diode unnecessary, is seen in Fig 8. The cell voltage falls to zero at about 5.3 hours and then falls further to about -2.5V. At this point copper deposition is apparent as the voltage rises again to a stable level. The temperature meanwhile reaches a safe maximum of 60°C before declining to ambient.

Thus, short-circuit and forced discharge abuse can both be tolerated safely by the 336VH system design.

Conclusions

There is a need for an ultra-high rate pulse primary lithium/manganese dioxide battery for use in military and transmitter applications over a wide range of temperatures.

Investigations into the effect of geometrical electrode area in the Dowty LiM 336 D-cell have demonstrated much improved pulse current with the absence of voltage delay inherent in liquid cathode systems, and also continuous current discharge capability from higher surface area cathodes.

The improvements in both pulse and continuous current discharge regimes are more significant at lower temperatures. This effect is thought to be primarily due to the balance between the opposing effects of cathodic polarisation and internal heating. Useful pulse currents have been demonstrated at temperatures as low at -70°C, and continuous discharge at close to the C rate has been obtained at -15°C.

The prevention of hazards due to short circuit and forced discharge abuse has been achieved by the use of a low pressure venting system, and an anodic current collector acting as an internal diode.

The characteristic improved performance exhibited by higher surface area cathodes is applicable to other cell sizes in the Dowty product range i.e. ½AA to DD.

Acknowledgements

The authors wish to acknowledge the contribution from A. Stephenson and other workers at Dowty Batteries.

References

1 M. Muller et al, Z Phys Chemie, Leipzing 270 (1989) p321
2 V. Manev, N. Iichev, A. Nassalevska, J Power Sources 25 (1989) p167
3 H. Ikeda, J.P. Gabano (Ed), "Lithium Batteries" London Academic Press 1986
4 H. Ikeda, T. Saito, H. Tamura, Electrochem Soc Cleveland Section Manganese Dioxide Symposium Vol 1 (1975) p384
5 Y.M. Kim, H.Y. Kang, Power Sources 13, 17th Int. Power Sources Symp, Bournemouth 1991, Chap 35 p383.
6 S. Atlung, K. West, J Power Sources 26 (1989) p139 (1989) p177
7 T.J. Lee et al, J Power Sources 43-44 (1993) p709.

LOW TEMPERATURE LITHIUM BATTERY TESTING

Walter A. Traciuski

Applied Power International

1236 N. Columbus Avenue, Suite 41

Glendale, CA 91202-1672

Introduction

There are few batteries that will operate adequately at very low temperatures. This device required two such batteries, one battery (T-1) was required to be discharged for a long duration at a current drain of approximately 2 mA. The second battery (T-2) was required to perform a high current (~2 A) pulse discharge after a 30 mA discharge at temperatures as low as -46°C.

The following is a summary of the test data obtained on recent tests of the T-1 and T-2 batteries. It is broken down into three individual tests:

1. Capacity of three T-1's, one from lot #93 and two from lot # 120.
2. Capacity of one T-2 using a simulated load profile.
3. Performance characteristics of one T-2 over simulated environmental conditions.

Method

Two different lithium battery designs consisting of two different chemistries were tested and evaluated at temperatures ranging from -55°C to +20°C.

A low rate battery (T-1), consisting of two "DD" (Eagle Picher, 29.4 Ah, LCF-112) cells in series using a carbon monofluoride cathode, was tested at a constant temperature of -30°C at varying currents to a nominal two volt cutoff per cell.

The second battery (T-2) was designed for a relatively high current rate pulse application and consisted of 48 "2/3A" (Panasonic, 1300 mAh, CR123A) cells in series-parallel matrix (4 in series X 12 in parallel) resulting in an operating voltage of 12 volts. The cathode for these cells was manganese dioxide.

In the first test the T-1's were discharged by constant resistance using precision Dale resistors. The initial resistance value used was lower than required in actual use to expedite the testing. This was done so that testing could be completed during the term of the contract. As the battery voltage approached the 4 volt cutoff voltage the resistance was increased to reduce the current until the required value was reached. In this way the cells were never discharged below 2 V/cell. The testing was performed at -30°C, again, to expedite the testing. Once the batteries delivered the required capacity for the device, the temperature chamber was lowered to -46°C and the actual discharge rates to complete the testing.

In test number two the T-2 was tested at a constant temperature of -30°C using a constant current discharge which was switched between two different current levels from two different power supplies by use of a Tenor timer. The power supplies were biased by the use of diodes so they could operate in a voltage and current range where they could maintain an accurate constant current. The initial current was 30 mA this was maintained for 300 sec followed by a 2 A pulse which was maintained for 2 seconds. This dual level pulse profile was repeated approximately every hour until the lifetime requirement was met.

In the final test a single T-2 battery was discharged using the same profile as above however the temperature was varied. The initial starting temperature was 20°C and was reduced after each pulse until the cutoff voltage could not be maintained at the 2 A level. Once the battery could not maintain the current without dropping below the cutoff voltage, the chamber temperature was raised to +20°C. The T-2 battery was then discharged approximately 150 mAh and the test sequence was repeated. The voltage data for this test was recorded on a strip chart recorder.

All other data was collected using Schlumberger (now Solartron) Orion 3531 data acquisition system and was accurate to the microvolt level. The chamber temperatures were recorded by the same unit which has the capability of using the thermocouples directly using an internal zero reference. The data was saved to disc and was processed in Excel using Schlumberger (Solartron) 3531 Data to Dif Conversion software for the data conversion.

Discussion

The test plan consisted of:

1.) Capacity testing of one T-1 from lot 93 and two T-1's from lot 120 to confirm the low temperature performance and the meeting of the capacity requirements for the mission and to help determine the lot-to-lot performance variations.
2.) Capacity testing on one T-2 at -30°C to determine if it will meet the mission requirement.
3.) Performance testing on one T-2 to determine the performance parameters over the low temperature range with respect to the depth of discharge.

1.) **Testing of T-1**

a. Place and wire batteries to be tested in an environmental chamber.
b. Reduce the temperature to -30°C±3 °C, soak at that temperature a minimum of 30 minutes.
c. Place a 33 ohm load (~110 mA) across the battery. Observe the results. If the voltage appears to be dropping at a rapid rate and may drop below 3.5 V within 24 hours or is approaching 4 V level, the load resistance may be increased to reduce the current drain. This may be repeated as many times as necessary until one of the following conditions occurs:
   1. The required capacity is reached.
   2. The minimum cut-off voltage is reached (3.5 V) at a current drain of 2 mA.
d. Record the results.

2.) **Testing of T-2**

a. Place and wire the battery to be tested in an environmental chamber.

b. Reduce the temperature to -30°C, soak at that temperature a minimum of 30 minutes.
c. Place a constant current(s) pulse load on the battery consisting of 30±2 mA for 300±5 sec. immediately followed by a 2.0±0.2 A pulse for 2±0.5 sec. This may be repeated as required until one of the following conditions is met:
   1. The required cycle life is met (80 cycles).
   2. The minimum voltage at 2.2 A is reached (8.5 V).

3.) **Performance profile testing of the T-2**

a. Place and wire the battery to be tested in an environmental chamber.
b. Set the temperature at +20°C, soak at that temperature for a minimum of 30 minutes.
c. Perform the same load test as described in 2c above.
d. Reduce the temperature to 0°C, soak for a minimum of 30 minutes and repeat the load test.
e. Reduce the temperature to -20°C, soak for a minimum of 30 minutes and repeat the load test.
f. Reduce the temperature in 10°degree C increments until the minimum voltage of 8.5 V is reached. The temperature increment of 10°C may be reduced to 5°C if it appear that the minimum voltage would be less than 8.5 V if a 10°C was used.
g. After failure to meet the voltage requirement, return the battery to ambient and discharge the T-2, 0.15±0 02 Ah using a constant resistance.
h. Repeat steps 4b-4g.
i. When the required capacity is met the test is complete. Voltage, temperature, and resistance values will be recorded for all tests.

Results

T-1

The first three charts are the constant resistance tests of three T-1's. They were all performed using decreasing current drains as a result of using increasing resistor values for loads. The initial temperature was -30°C which was reduced to -46°C as the actual loads were approached. All of the batteries have met the capacity requirement of 20 Ah however the battery from lot #93 has done so at a lower voltage than the two batteries from lot #120. This lot of cells that had been rejected due to a high temperature exposure during manufacture and was used for prototypes because of their availability. The internal impedance of the cells has been affected but it is not known if this is the reason. It should also be noted that these cells were approximately two years older than the lot #120 cells and this could also be contributory to the increase in internal impedance observed. Possible causes for this internal impedance rise could be due to poor internal wetting or slight amount of corrosion.

T-2 Performance

All the T-2 tests were performed using constant current discharges. The initial current was 29 mA for 300 seconds, immediately followed by a 2 second discharge of 2.16 A. This was accomplished by utilizing an Tenor electronic timer accurate to 0.1 second (for the 300 sec. discharge) and 0.01 seconds (for the 2 sec. discharge). The currents were controlled by the use of constant current power supplies while the battery voltage was being "bucked" by diodes.

The first chart is of the minimum pulse voltage as a result of cycle number. The battery easily met the 80 pulse requirement at a temperature of -30°C. It should be noted that this test was performed in fairly rapid succession and that the response voltage is likely to be significantly higher if a refractory period of several weeks is used as can be seen by the use of two extended refractory periods during the testing. The initial increase in voltage between the first and second cycle is an artifact of this particular battery chemistry and not likely to reappear in later use.

T-2 Characterization

The next five T-2 charts describe the performance profile through the required capacity (0.5 Ah) and over the temperature range of +20°C to -50°C. The fresh T-2 exceeded the voltage requirement of 8.5 V at -50°C. However, later in life this was reduced to -40°C. The 0.535 Ah chart is at approximately 50% of the total potential capacity of the T-2 battery. Over the range of 0-50% DOD the T-2 tested performed almost identically over the observed temperature range. Thus it is likely that the T-2 battery will continue to perform far beyond the requirement.

For the minimum voltage profile testing the -45°C test was actually performed at -46°C which was within the temperature limits required for the testing. This was done to relate the T-2 testing back to the requirement of the T-1 testing.

Summary

The T-1's tested exceeded the requirements for the unit at -46°C and did not drop to the EOL (End-of Life) voltage. The lot 93 T-1 met the requirement at a reduced voltage when compared tom the lot 120 cells. This lot had been rejected by NASA but was used because of the rapid availability for initial testing.

The T-2's have far exceeded the requirements both in lifetime and in low temperature performance. At the required capacity, the T-2 battery tested has exceeded the low temperature performance requirement and does not appear to be degrading. A longer refractory period (i.e. 1-4 weeks) is likely to be beneficial to the performance and will likely extend its useful life.

T-1 TESTING

T-1 (lot #93)

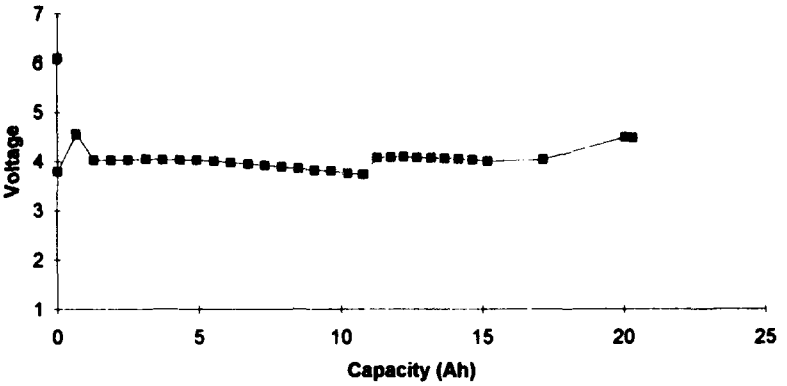

T-1A (lot #120)

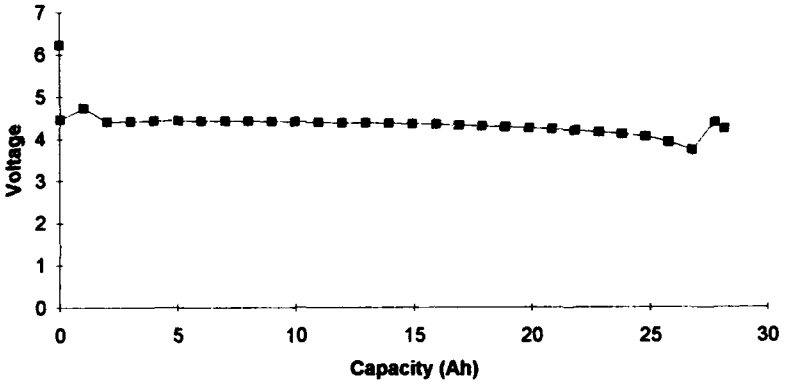

T-1B (lot #120)

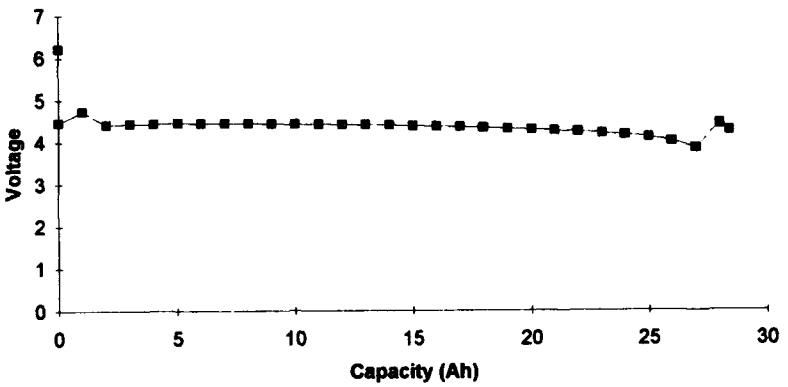

T-2 PERFORMANCE TESTING

T-2 Minimum Pulse Voltage

Temperature -30 C

(Cycle 82 @ -46 C)

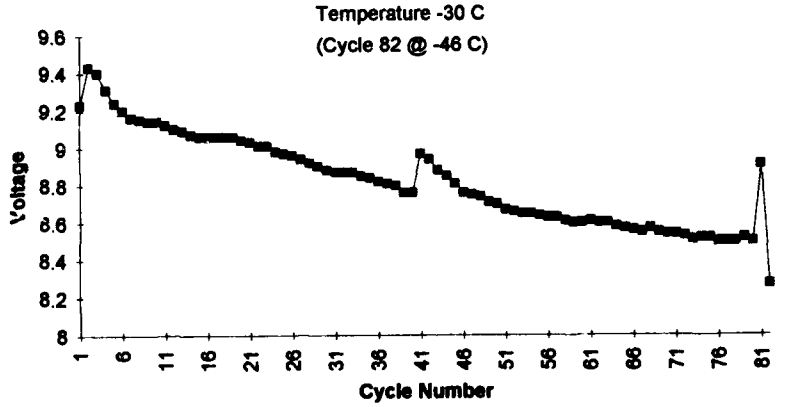

T-2 CHARACTERIZATION TESTING

T-2 Minimum Voltage Profile @ 0.01 Ah

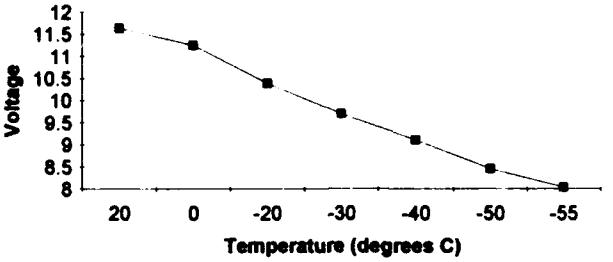

T-2 Minimum Voltage Profile @ 0.145 Ah

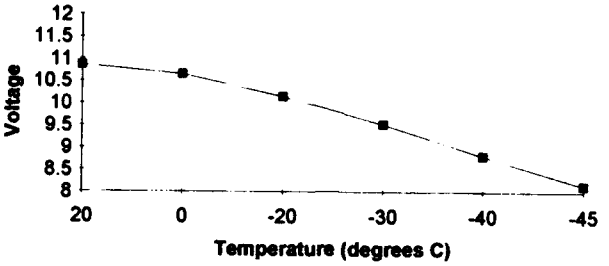

T-2 Minimum Voltage Profile @ 0.275 Ah

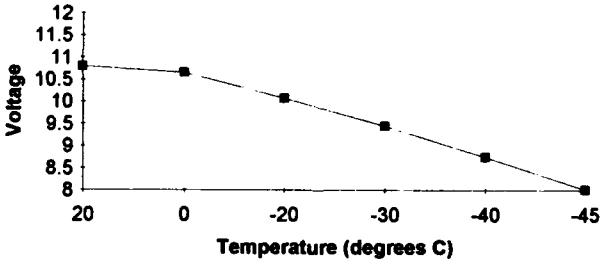

T-2 Minimum Voltage Profile @ 0.405 Ah

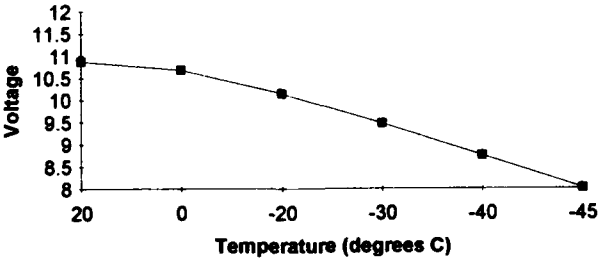

T-2 Minimum Voltage Profile @ 0.535 Ah

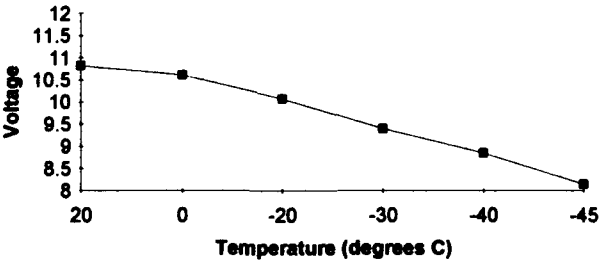

NOTES